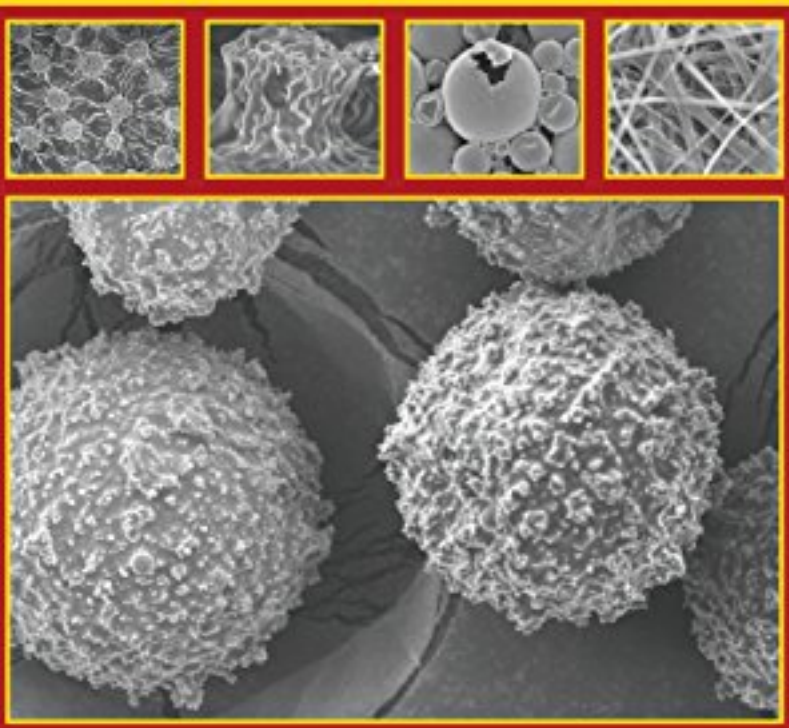
Intelligent Coatings for Corrosion Control



Edited by
Atul Tiwari • James Rawlins • Lloyd H. Hihara

B/H

Intelligent Coatings for Corrosion Control

Intelligent Coatings for Corrosion Control

Edited by

Atul Tiwari, James Rawlins,
Lloyd H. Hihara



ELSEVIER

AMSTERDAM • BOSTON • HEIDELBERG • LONDON
NEW YORK • OXFORD • PARIS • SAN DIEGO
SAN FRANCISCO • SINGAPORE • SYDNEY • TOKYO

Butterworth-Heinemann is an imprint of Elsevier



Butterworth Heinemann is an imprint of Elsevier
The Boulevard, Langford Lane, Kidlington, Oxford OX5 1GB, UK
225 Wyman Street, Waltham, MA 02451, USA

First edition **2015**

Copyright © **2015** Elsevier Inc. All rights reserved.

No part of this publication may be reproduced or transmitted in any form or by any means, electronic or mechanical, including photocopying, recording, or any information storage and retrieval system, without permission in writing from the publisher. Details on how to seek permission, further information about the Publisher's permissions policies and our arrangements with organizations such as the Copyright Clearance Center and the Copyright Licensing Agency, can be found at our website: www.elsevier.com/permissions.

This book and the individual contributions contained in it are protected under copyright by the Publisher (other than as may be noted herein).

Notices

Knowledge and best practice in this field are constantly changing. As new research and experience broaden our understanding, changes in research methods, professional practices, or medical treatment may become necessary.

Practitioners and researchers must always rely on their own experience and knowledge in evaluating and using any information, methods, compounds, or experiments described herein. In using such information or methods they should be mindful of their own safety and the safety of others, including parties for whom they have a professional responsibility.

To the fullest extent of the law, neither the Publisher nor the authors, contributors, or editors, assume any liability for any injury and/or damage to persons or property as a matter of products liability, negligence or otherwise, or from any use or operation of any methods, products, instructions, or ideas contained in the material herein.

Library of Congress Cataloging-in-Publication Data
Intelligent coatings for corrosion control / edited by Atul Tiwari, Lloyd H. Hihara, James Rawlins. – First edition.
pages cm
Includes bibliographical references and index.
ISBN 978-0-12-411467-8
1. Corrosion and anti-corrosives. 2. Protective coatings. I. Tiwari, Atul, editor. II. Hihara, Lloyd H., editor. III. Rawlins, James Wayne, editor.
TA462.I483 2015
671.7'3–dc23
2014034631

British Library Cataloguing in Publication Data
A catalogue record for this book is available from the British Library

For information on all **Butterworth-Heinemann** publications visit our web site at store.elsevier.com

This book has been manufactured using Print On Demand technology. Each copy is produced to order and is limited to black ink. The online version of this book will show color figures where appropriate.

ISBN: 978-0-12-411467-8



Contributors

Annemie Adriaens
Department of Analytical Chemistry, Ghent University, Krijgslaan 281-S12, Ghent, Belgium

Rigoberto C. Advincula
Department of Macromolecular Science and Engineering, Case Western Reserve University, 2100 Adelbert Rd., Cleveland, OH, USA

F.J. Arregui
Sensor Research Laboratory, Electrical and Electronic Engineering Department, Universidad Pública de Navarra, Edif. Los Tejos, Campus Arrosadia, Pamplona, Spain

Imre Bertóti
Department of Plasma Chemistry, Institute of Materials and Environmental Chemistry, Research Centre for Natural Sciences, Hungarian Academy of Sciences, Budapest, Hungary

Kung-Chin Chang
Department of Chemistry, Center for Nanotechnology and Biomedical Technology at Chung-Yuan Christian University (CYCU), Chung Li, Taiwan, ROC

Tami Lasseter Clare
Department of Chemistry, Portland State University, Portland, OR 97207, USA

Attilio M. Compagnoni
Wendel Email Italia, Via Bedeschi 10a, Chignolo (BG), Italy

Alba Covelo
Facultad de Química, Universidad Nacional Autónoma de México, Av. Universidad 3000, Copilco Universidad, Coyoacán, 04510 Ciudad de México, D.F.

Al de Leon
Department of Macromolecular Science and Engineering, Case Western Reserve University, 2100 Adelbert Rd., Cleveland, OH, USA

Flavio Deflorian
Department of Industrial Engineering, University of Trento, via Sommarive 9, Trento, Italy

Eszetr Drotár
Department of Metallurgical and Foundry Engineering, Faculty of Materials Science and Engineering, University of Miskolc, Budapest, Hungary

Miguel Ángel García-Sánchez
Depto. Química, Universidad Autónoma Metropolitana, Av. San Rafael Atlixco No 186, Iztapalapa, Vicentina, 09340 Ciudad de México, D.F.

András Gergely
Department of Metallurgical and Foundry Engineering, Faculty of Materials Science and Engineering, University of Miskolc, Budapest, Hungary

Sunil Kumar Ghosh
Bio Organic Division, Bhabha Atomic Research Centre, Trombay, Mumbai, India, jprakash@barc.gov.in

J. Goicoechea
Sensor Research Laboratory, Electrical and Electronic Engineering Department, Universidad Pública de Navarra, Edif. Los Tejos, Campus Arrosadia, Pamplona, Spain

D. Grigoriev
Max-Plank Institute of Colloids and Interfaces, Am Muehlenberg 1, Potsdam-Golm, Germany

I. Gurrappa
Defence Metallurgical Research Laboratory, Kanchanbagh PO, Hyderabad, India

Abdel Salam Hamdy Makhlouf
Department of Manufacturing Engineering, College of Engineering and Computer Science, University of Texas Pan-American, 1201 West University Dr., Edinburg, Texas, USA

M. Hernaez
Sensor Research Laboratory, Electrical and Electronic Engineering Department, Universidad Pública de Navarra, Edif. Los Tejos, Campus Arrosadia, Pamplona, Spain

Miguel Ángel Hernández-Gallegos
Facultad de Ingeniería, Universidad Nacional Autónoma de México, Av. Universidad 3000, Copilco Universidad, Coyoacán, 04510 Ciudad de México, D.F.

L.H. Hihara
Hawaii Corrosion Laboratory, Department of Mechanical Engineering, University of Hawaii at Manoa, Honolulu, Hawaii, USA

Mingxing Huang
School of Mechanical and Aerospace Engineering, Nanyang Technological University, Singapore

Anthony B. Kaye
Department of Physics, Texas Tech University, Box 41051, Lubbock, Texas, USA

Shengxi Li
Hawaii Corrosion Laboratory, Department of Mechanical Engineering, University of Hawaii at Manoa, Honolulu, Hawaii, USA

Snehal R. Lokhandwala
Shroff S R Rotary Institute of Chemical Technology, Block No. 402, At & Post Vataria, Bharuch, Gujarat, India

I.R. Matías
Sensor Research Laboratory, Electrical and Electronic Engineering Department, Universidad Pública de Navarra, Edif. Los Tejos, Campus Arrosadia, Pamplona, Spain

Carmina Menchaca-Campos
Centro de Investigación en Ingeniería y Ciencias Aplicadas, Universidad Autónoma del Estado de Morelos, Av. Universidad 1001, Col. Chamilpa, 62209 Cuernavaca, Morelos, México

Judith Mihály
Department of Biological Nanochemistry, Institute of Molecular Pharmacology, Research Centre for Natural Sciences, Hungarian Academy of Sciences, Budapest, Hungary

Liana Maria Muresan
"Babes-Bolyai" University, Faculty of Chemistry and Chemical Engineering, Cluj-Napoca, Romania

Zoltán Pászti
Department of Metallurgical and Foundry Engineering, Faculty of Materials Science and Engineering, University of Miskolc, Budapest, Hungary

Jyoti Prakash
Powder Metallurgy Division, Bhabha Atomic Research Centre, Trombay, Mumbai, India

Alberto Quaranta
Department of Industrial Engineering, University of Trento, via Sommarive 9, Trento, Italy

Sandeep Rai
GRP Limited, 510, A Wing, Kohinoor City C-1, Kurla(W), Mumbai, India

P.J. Rivero
Sensor Research Laboratory, Electrical and Electronic Engineering Department, Universidad Pública de Navarra, Edif. Los Tejos, Campus Arrosadia, Pamplona, Spain

Stefano Rossi
Department of Industrial Engineering, University of Trento, via Sommarive 9, Trento, Italy

Mohammed Soltani
RSL-Tech, 9114 Descartes, Montreal, Quebec, Canada

John D. Stenger-Smith
Naval Air Warfare Center Weapons Division (NAWCWD), Polymer Science and Engineering Branch (Code 4L4200D), 1900N. Knox Road (Stop 6303), China Lake, CA, USA

Natasja A. Swartz
Department of Chemistry, Portland State University, Portland, OR 97207, USA

Linda Tavella
Department of Industrial Engineering, University of Trento, via Sommarive 9, Trento, Italy

Atul Tiwari
Department of Mechanical Engineering, University of Hawaii at Manoa, Honolulu, Hawaii, USA

Tamás Török
Department of Metallurgical and Foundry Engineering, Faculty of Materials Science and Engineering, University of Miskolc, Budapest, Hungary

B.M. Tripathi
Powder Metallurgy Division, Bhabha Atomic Research Centre, Trombay, Mumbai, India

Jorge Uruchurtu
Centro de Investigación en Ingeniería y Ciencias Aplicadas, Universidad Autónoma del Estado de Morelos, Av. Universidad 1001, Col. Chamilpa, 62209 Cuernavaca, Morelos, México

Kim Verbeken
Department of Materials Science and Engineering, Ghent University, Technologiepark 903, Zwijnaarde (Ghent), Belgium

Jinglei Yang
School of Mechanical and Aerospace Engineering, Nanyang Technological University, Singapore

I.V.S. Yashwanth
Defence Metallurgical Research Laboratory, Kanchanbagh PO, Hyderabad, India

Jui-Ming Yeh
Department of Chemistry, Center for Nanotechnology and Biomedical Technology at Chung-Yuan Christian University (CYCU), Chung Li, Taiwan, ROC

C.R. Zamarreño
Sensor Research Laboratory, Electrical and Electronic Engineering Department, Universidad Pública de Navarra, Edif. Los Tejos, Campus Arrosadia, Pamplona, Spain

Roohangiz Zandi Zand
Department of Analytical Chemistry, Ghent University, Krijgslaan 281-S12, Ghent, Belgium

Peter Zarras
Naval Air Warfare Center Weapons Division (NAWCWD), Polymer Science and Engineering Branch (Code 4L4200D), 1900N. Knox Road (Stop 6303), China Lake, CA, USA

Preface

Most of the metals in use today have been extracted from thermodynamically stable ores. Hence, when metallic materials are exposed to the environment, they have a strong propensity to revert back to their natural, stable compounds through corrosion. For this reason, the deleterious effects of corrosion have been a concern since ancient times. Today, the wasting away of metals through corrosion is a very costly problem, and numerous studies have estimated that corrosion-related damages account for approximately 3–4% of the gross domestic product of industrialized nations. For the United States alone, the losses due to corrosion are estimated to be on the order of $500 billion per year. One of the most effective ways to prevent these losses is the use of coatings. Coatings were first used in ancient times, when they were made from egg whites, tree sap, and pitch. Today, however, polymer technology and nanotechnology allow engineers to design both functionality and aesthetics into coatings. In this modern world, almost every man-made object is protected or beautified with coatings. As a result, the worldwide coatings industry generates approximately $100 billion per year. As ever higher demands are put on coatings, requiring them to be environmentally friendly, self-cleaning, self-healing, corrosion-indicating, superdurable, and so on, the traditional coatings of yesteryear are gradually becoming obsolete, giving rise to research and development focused on intelligent coatings.

This book comprises a collection of articles written by experts in advanced coating technologies. The introductory chapter describes the fundamental electrochemical principles of metal protection using coatings. Chapter 2 discusses the significance of corrosion and its economic impact, considering a wide variety of current coatings, along with the importance of intelligent coatings. Chapter 3 reviews organic and inorganic pretreatments for metals and alloys, including the use of chromate and phosphate conversion coatings, as well as recent lanthanide-based conversion-coating compositions. In Chapter 4, we introduce economical routes for synthesizing organometallic compounds, the use of organometallic precursors in chemical vapor deposition processes to produce protective coatings, and growth mechanisms for coating applications. Chapter 5 demonstrates the effect of cerium ions on the development of self-healing coatings, and Chapter 6 covers corrosion protection systems that employ zinc-rich hybrid coatings containing polypyrrole and nanoparticles. In Chapter 7, we discuss work on vitreous porcelain enamel coatings containing europium and dysprosium, which have been developed for their luminescent properties. Chapter 8 deals with the self-healing of damaged coatings containing corrosion

inhibitors in nano or micro containers. From a processing standpoint, Chapter 9 provides hard-to-find information on critical parameters involved in transitioning a coating from the laboratory to the pilot plant, and Chapter 10 considers a novel smart quasi-ceramic silicone conversion coating. We also discuss the results of various analytical techniques applied to coatings, and we compare the anticorrosion properties of the quasi-ceramic coating with other commercially available coatings. Chapter 11 explores the use of a conducting polymer as a superhydrophobic coating. Chapter 12 covers various mechanisms of corrosion inhibition using encapsulated corrosion inhibitors, and Chapter 13 discusses the utilization of thermochromic vanadium dioxide in the development of smart coatings. Microencapsulation of corrosion inhibitors in one-part coatings containing organosilane and diisocyanate is the subject of Chapter 14, while, in Chapter 15, we consider the protection of magnesium alloys using a stannate-based self-healing coating. Chapter 16 addresses the use of conducting electroactive polymers for corrosion prevention, and Chapter 17 discusses the control of corrosion in titanium-alloy biomedical implants by means of a series of protective coatings including passive films. Chapter 18 details the use of optical fiber sensors in corrosion monitoring. Chapter 19 points out the importance of waterborne resins formulated with nanoclay as protective, intelligent coatings for cultural heritage objects. Finally, the importance and applicability of Raman and FTIR spectroscopic techniques are the focus of Chapter 20.

We hope that this book provides a useful compilation of information for students from diverse scientific and engineering backgrounds. It can serve as a reference for research students and a technical guide for those from the industrial sector. The editors thank the organizers of the Technical Corrosion Collaboration (TCC), particularly Richard Hays, Deputy Director; as well as the Corrosion Policy and Oversight Office of the United States Under Secretary of Defense for Acquisition, Technology, and Logistics, which gave us an opportunity to collaborate in this area of scientific and industrial importance. We are hopeful that this book will pave new ways for innovative developments in coatings.

Atul Tiwari, Ph.D.
James W. Rawlins, Ph.D.
Lloyd H. Hihara, Ph.D.
USA

Chapter 1

Electrochemical Aspects of Corrosion-Control Coatings

L.H. Hihara
Hawaii Corrosion Laboratory, Department of Mechanical Engineering, University of Hawaii at Manoa, Honolulu, Hawaii, USA

1.1 Introduction

In nature, almost all metals are found in their thermodynamically stable states which are ores that are comprised primarily of oxides, sulfides, and halides.[1] Energy must be expended to extract the elemental metals from the ores. Hence, as soon as the elemental metals are extracted from their ores, they have a propensity to revert back to their thermodynamically stable compounds. In most cases, metals will form oxides when exposed to moisture. If the oxide is porous or does not have good adhesion to the substrate metal, the metal will actively corrode. If the oxide forms a compact impervious layer and has good adhesion, the metal will passivate, resulting in excellent corrosion resistance. In environments that contain aggressive ions, however, the passive film can breakdown, resulting in localized corrosion and very high corrosion rates. Hence, coatings are very frequently needed to suppress corrosion in metals that do not naturally form protective passive films or for aggressive environments that can break down passivity.

Intelligent Coatings for Corrosion Control
Copyright © 2015 Elsevier Inc. All rights reserved.

1.2 Corrosion

For a metal to corrode by aqueous corrosion, water molecules must be present. The metal, however, need not be fully immersed because water can condense on a surface due to temperature fluctuations, even if the relative humidity is lower than 100% (e.g., condensation on cold surface on a warm, humid day), or due to hygroscopic impurities such as airborne salts.[2]

1.2.1 Thermodynamics

Aqueous corrosion is an electrochemical process involving anodic (or oxidation) and cathodic (or reduction) reactions. Dissolution of a metal M, which is an anodic reaction, is represented by the half-cell reaction

$$\mathrm{M} \rightarrow \mathrm{M}^{n+} + n\mathrm{e}^- \tag{1.1}$$

The electrons of the anodic reaction must be consumed by a cathodic reaction for corrosion to proceed. Two predominant cathodic reactions in aqueous corrosion are oxygen reduction (Equations 1.2 and 1.3) and hydrogen evolution (Equations 1.4 and 1.5), respectively. Their half-cell reactions are represented as follows:

$$\mathrm{O_2} + 4\mathrm{e}^- + 4\mathrm{H}^+ \rightarrow 2\mathrm{H_2O}\ (\text{in acidic solutions}) \tag{1.2}$$

$$\mathrm{O_2} + 4\mathrm{e}^- + 2\mathrm{H_2O} \rightarrow 4\mathrm{OH}^-\ (\text{in basic solutions}) \tag{1.3}$$

$$2\mathrm{H}^+ + 2\mathrm{e}^- \rightarrow \mathrm{H_2}\ (\text{in acidic solutions}) \tag{1.4}$$

$$2\mathrm{H_2O} + 2\mathrm{e}^- \rightarrow \mathrm{H_2} + 2\mathrm{OH}^-\ (\text{in basic solutions}) \tag{1.5}$$

Oxygen reduction can only occur in aerated solutions, which contain dissolved oxygen molecules. Hydrogen evolution can occur in both deaerated and aerated solutions.

For example, in an aerated basic solution with oxygen reduction as the cathodic reaction, the overall corrosion reaction can be represented as

$$\begin{array}{c} 2\mathrm{M} \rightarrow 2\mathrm{M}^{2+} + 4\mathrm{e}^- \\ \mathrm{O_2} + 4\mathrm{e}^- + 2\mathrm{H_2O} \rightarrow 4\mathrm{OH}^- \\ \hline 2\mathrm{M} + \mathrm{O_2} + 2\mathrm{H_2O} \rightarrow 2\mathrm{M}^{2+} + 4\mathrm{OH}^- \end{array} \tag{1.6}$$

In a deaerated acidic solution, the overall corrosion reaction of a metal can be represented as

$$\begin{array}{c} \mathrm{M} \rightarrow \mathrm{M}^{2+} + 2\mathrm{e}^- \\ 2\mathrm{H}^+ + 2\mathrm{e}^- \rightarrow \mathrm{H_2} \\ \hline \mathrm{M} + 2\mathrm{H}^+ \rightarrow \mathrm{M}^{2+} + \mathrm{H_2} \end{array} \tag{1.7}$$

where hydrogen evolution is the cathodic reaction.

For corrosion to occur, however, the cell potential, E_{cell}, of the overall corrosion reaction must be positive, which corresponds to a decrease in Gibb's Free energy. E_{cell} is the difference in the *equilibrium* potential of the cathodic half-cell reaction and the anodic half-cell reaction. For example, for the corrosion of a metal in an acidic solution with hydrogen evolution as the cathodic reaction (Equation 1.4), E_{cell} would be calculated as follows:

$$E_{cell} = E_{H^+/H_2} - E_{M^{n+}/M} \tag{1.8}$$

where the equilibrium potential of the half-cell reactions (i.e., E_{H^+/H_2} and $E_{M^{n+}/M}$) can be determined using the Nernst equation:

$$E = E^{\circ} - \frac{RT}{nF} \ln \frac{a_{reactants}}{a_{products}} \tag{1.9}$$

where E° is the standard potential, R is the universal gas constant, T is the absolute temperature, n is the number of electrons transferred in the half-cell reaction, F is Faraday's constant (or charge on one mole of electrons), and $a_{reactants}$ and $a_{products}$ are the activities for the reactants and products, respectively. The value of E_{cell} only indicates if the reaction is thermodynamically possible or impossible, and therefore, the study of kinetics is required to obtain the rates of the corrosion reaction.

1.2.2 Kinetics

In the study of corrosion, polarization diagrams[3] are used to determine the rates of metal dissolution, oxygen reduction, and hydrogen evolution. The thermodynamic driving force for the electrochemical reaction is measured in potential, E, on the vertical axis of the polarization diagram. The kinetics of the electrochemical reaction are measured in current, I, on the horizontal axis of the polarization diagram. Notice that the anodic (Equation 1.1) and cathodic reactions (Equations 1.2–1.5) involve the transfer of electrons, and, therefore, their rates are proportional to the current. Based on Faraday's law, the moles, N, of species reacted is related to the current, I:

$$N = \frac{It}{nF} \tag{1.10}$$

where t is the duration of the current I, F is Faraday's constant (or charge on one mole of electrons), and n is the moles of electrons participating in the reaction:

$$O + ne \rightarrow R \tag{1.11}$$

Anodic reactions generate anodic currents, I_A, and cathodic reactions generate cathodic currents, I_C. The currents are often normalized with respect to the surface area, A, of the electrode:

$$i_A = \frac{I_A}{A} \tag{1.12}$$

$$i_C = \frac{I_C}{A} \tag{1.13}$$

Depending on the metal and environment, metals may have active, passive, or active-passive electrochemical behavior. Active metals and alloys do not form protective passive films and show increasing anodic currents (Figure 1.1) as the potential is increased above the open-circuit or corrosion potential (E_{corr}). Passive metals form protective passive films and have very low dissolution currents (Figure 1.2) at potentials more positive than E_{corr}. Active-passive metals (e.g., Cr, Ni)[4] generally show active, passive, and transpassive regimes on the anodic polarization diagram (Figure 1.3). In the active regime from E_{corr} to the primary passive potential (E_{pp}), the metal dissolution rate increases as the potential increases. In the passive regime, a protective oxide passive film forms on the metal at potentials greater than E_{pp} causing the current to dramatically decrease. In the transpassive regime at more noble potentials, the anodic current again increases either due to passive-film break down leading to metal dissolution or the evolution of oxygen.[2]

Aggressive anions, commonly from the halide group (e.g., Br^-, Cl^-), can prevent passivation, resulting in localized corrosion or pitting of the metal surface. Pitting commences when the electrode potential exceeds the critical value known as the pitting potential (E_{pit}),[2] which also decreases with increasing aggressive-anion concentration (Figure 1.4).[5]

In corrosion, the predominant cathodic reactions are proton reduction and oxygen reduction. In deaerated environments, only the proton reduction occurs; but in aerated

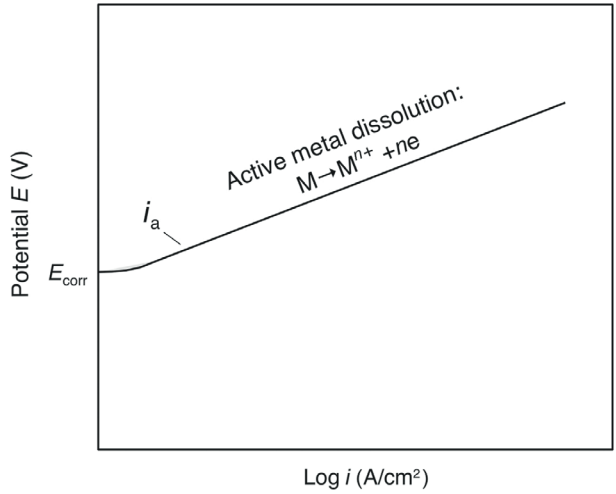


Figure 1.1 Active dissolution of metal due to lack of protective oxide-film formation.

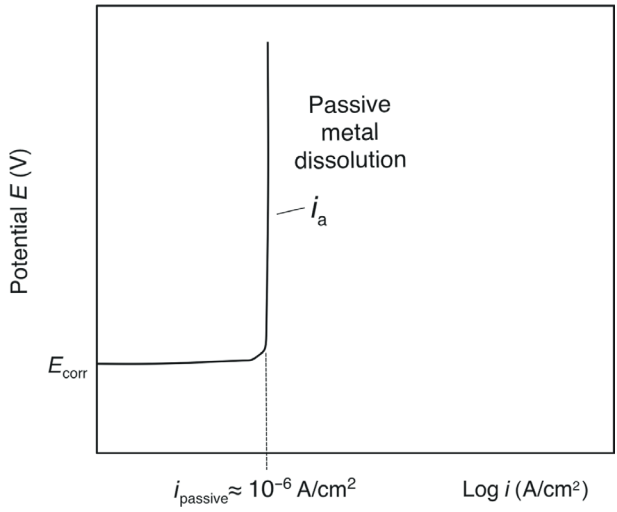


Figure 1.2 Passive dissolution of a metal due to the formation of a protective oxide film.

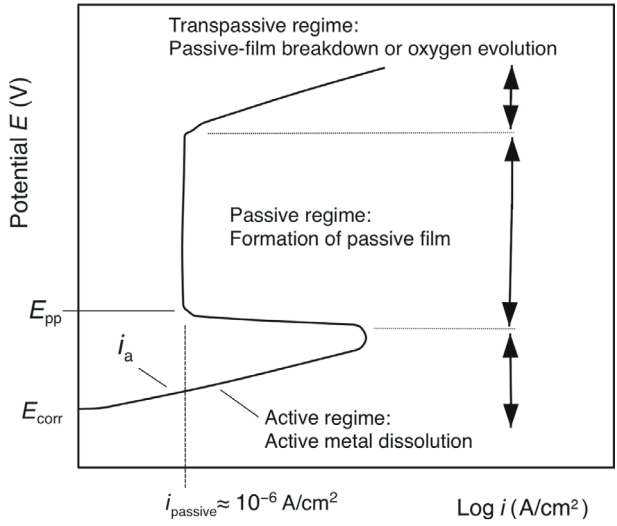


Figure 1.3 Active-passive dissolution with transpassive regime. Protective oxide films forms at potentials above E_{pp}.

environments, both proton and oxygen reduction can occur. Hence, on a polarization diagram, only proton reduction will be seen in deaerated environments, while both proton and oxygen reduction may be seen in aerated environments (Figure 1.5). The current of the oxygen-reduction curve will saturate when the rate at which oxygen molecules reach the cathodic sites is limited by diffusion. The diffusion-limited

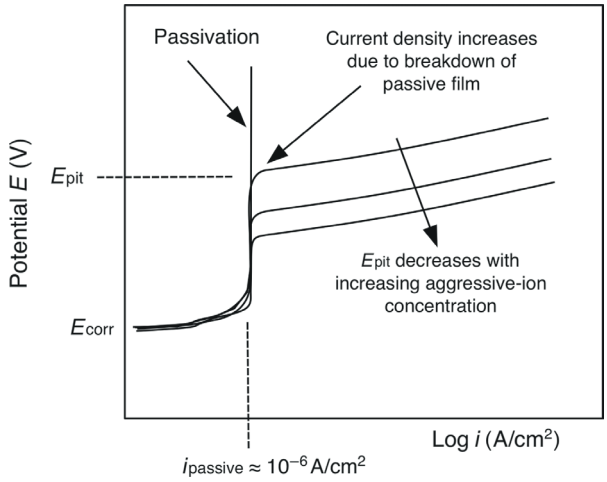


Figure 1.4 Pitting corrosion caused by breakdown of passive film above E_{pit}.

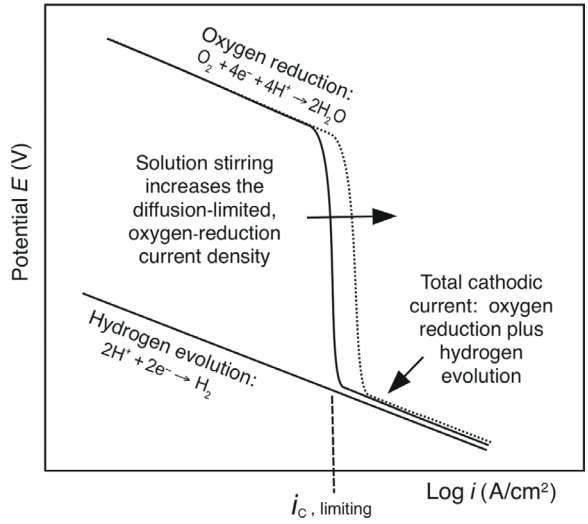


Figure 1.5 Convection by solution stirring reduces the diffusion-layer thickness and increases the diffusion-limited oxygen-reduction current density.

current can increase with higher oxygen concentrations and thinning of the diffusion layer (e.g., by agitation of the electrolyte in bulk solutions or evaporation for thin electrolyte films).

When corrosion occurs, the amount of electrons generated by metal dissolution is equal to that consumed by the cathodic reactions to conserve charge. Hence, the

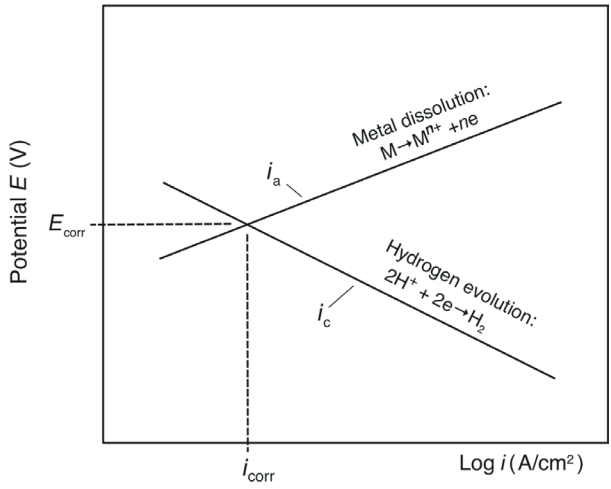


Figure 1.6 Intersection of anodic metal-dissolution curve with the cathodic hydrogen-evolution (or oxygen-reduction if dissolved oxygen is present) curve marks the corrosion potential E_{corr} and corrosion current density i_{corr}.

corroding material assumes the corrosion potential, E_{corr}, where the anodic, i_A, and cathodic, i_C, current densities have the same magnitude, called the corrosion current density, i_{corr} (Figure 1.6).

$$i_A \overset{E=E_{Corr}}{=} i_C = i_{corr} \tag{1.14}$$

1.3 Coatings

Corrosion-resistant coatings and coating systems generally provide one or more of the following characteristics to protect the metal substrate: (i) an impervious barrier to moisture and corrosive species, (ii) corrosion inhibition utilizing corrosion inhibitors, and (iii) cathodic protection. Single-layered, stand-alone coatings or more complex multilayered coating systems can be used. A multilayered coating system may be comprised of a pretreated surface layer and primer layers to enhance adhesion and provide corrosion inhibition to the substrate metal, undercoat layers to enhance durability, and topcoat layers for aesthetics and added environmental resistance (Figure 1.7).

1.3.1 Barrier coatings

Barrier coatings ideally protect the substrate metal by providing an impervious barrier to moisture and corrosive species. Corrosion cannot initiate if moisture is not present; hence, the substrate metal will be free of corrosion if the barrier coating is



Figure 1.7 Coating system comprised of a surface pretreated layer, primer, undercoat, and topcoat.

intact, but will initiate from coating breaches in the presence of moisture and corrosive species. The electrical and electrochemical properties of the barrier coating can also affect the degree of corrosion that initiates at the breaches.

During corrosion, the total anodic current from all sources must equal the total cathodic current from all sources:

$$\sum_j I_{A,j} = \sum_k I_{C,k} \tag{1.15}$$

In the expression above, the currents can be written as a product of the current densities, i, and the corresponding areas, A:

$$i_{A,\text{breach}} A_{\text{breach}} + i_{A,\text{coating}} A_{\text{coating}} = i_{C,\text{breach}} A_{\text{breach}} + i_{C,\text{coating}} A_{\text{coating}} \tag{1.16}$$

The subscripts "A" and "C" are used to denote anodic and cathodic, respectively; the subscript "breach" refers to the exposed substrate region at coating breaches, and "coating" refers to the coating. Solving for $i_{A,\text{breach}}$, which represents the dissolution rate of the substrate at coating breaches, gives

$$i_{A,\text{breach}} = \frac{i_{C,\text{breach}} A_{\text{breach}} + i_{C,\text{coating}} A_{\text{coating}} - i_{A,\text{coating}} A_{\text{coating}}}{A_{\text{breach}}} \tag{1.17}$$

For barrier coatings which are not sacrificial, $i_{A,\text{coating}}$ is taken as zero:

$$i_{A,\text{breach}} = i_{C,\text{breach}} + i_{C,\text{coating}} \frac{A_{\text{coating}}}{A_{\text{breach}}} \tag{1.18}$$

Hence, the anodic dissolution of the substrate at the coating breach, $i_{A,\text{breach}}$, is a function of the cathodic current density of the exposed substrate at the breach and the cathodic current density on the coating multiplied by the coating-to-breach area ratio. Coatings that are electrically conducting and that can support cathodic reactions such as oxygen reduction or hydrogen evolution can have large values of $i_{C,\text{coating}}$. Given that the coating-to-breach area ratio is usually very large (i.e., >100), the dissolution or corrosion at the coating breach, $i_{A,\text{breach}}$, will be concentrated, leading to accelerated localized corrosion (Figure 1.8). Therefore, it is usually not recommended to use noble metals (e.g., copper, silver, gold) as barrier coatings to protect more active metals (e.g., aluminum, steel). It is likely that conductive polymer coatings could also have this effect; hence, barrier coatings that are electrically insulative or that do

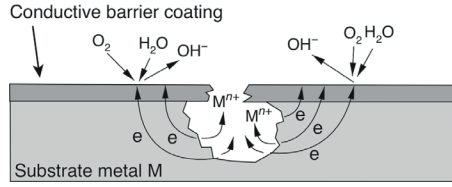


Figure 1.8 Barrier coatings that are electrically conductive and catalytic to oxygen reduction or hydrogen evolution can accelerate corrosion at coating breaches.

not support oxygen reduction or hydrogen evolution are likely to provide much more overall protection. In the limiting case where $i_{C,coating}$ is zero, the corrosion rate at exposed substrate regions at the coating breaches will be equal to the normal corrosion rate of the bare substrate (Figure 1.9):

$$i_{A,breach} \overset{E=E_{Corr}}{=} i_{C,breach} = i_{corr} \tag{1.19}$$

Organic coatings such as epoxies, alkyds, acrylics, etc., are generally applied by spraying or brushing. These coatings are generally permeable to water molecules, absorb moisture, and maintain a concentration of water that is in equilibrium with moisture in the atmosphere. If the coating has good adhesion to the substrate, however, the water molecules remain within the molecular structure of the coating and do not accumulate at the coating-substrate interface.[6] If the coating adhesion is poor due to either the inherent properties of the coating and substrate or the possibility of the substrate surface becoming contaminated—for example, by airborne salts—the water molecules in the coating could accumulate or condense at the coating-substrate interface forming blisters in the coating, which could lead to corrosion.[6] Hence, cracks or breaches in organic coatings are not always necessary for moisture penetration to the substrate interface.

Inorganic coatings such as oxides, nitrides, carbides, and so on, are generally applied by chemical vapor deposition, sputtering, or evaporation, and require vacuum chambers. These coating are often inherently impervious to moisture, but they are

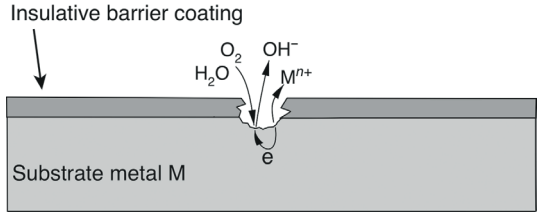


Figure 1.9 Barrier coatings that are electrically insulative or not catalytic to oxygen reduction or hydrogen evolution should not accelerate corrosion at coating breaches.

brittle and can crack and spall. Other inorganic coatings can be grown directly on the substrate metal by chemical or electrochemical processes. Examples are anodized films on aluminum. These films can either be compact and impervious to moisture or porous depending on processing parameters.

To overcome some of the inadequacies of purely barrier coatings, corrosion inhibitors are often added to coating formulations to provide added corrosion protection.

1.3.2 Corrosion inhibitive coatings

Corrosion inhibitors are chemical species that are used to suppress the reaction rates of electrochemical processes to control corrosion. The inhibitors are usually used at low (e.g., parts per million) concentration levels. Anodic inhibitors suppress the anodic reaction rate, which is depicted by shifting the anodic polarization curve to the left (Figure 1.10) to lower current densities, resulting in lower i_{corr} and an increase in E_{corr}. Cathodic inhibitors suppress the cathodic reaction rate, shifting the cathodic polarization curve to the left (Figure 1.11) to lower current densities, resulting in lower i_{corr} but a decrease in E_{corr}. If anodic and cathodic inhibitors are used simultaneously or if an inhibitor suppresses both the anodic and cathodic reactions, both anodic and cathodic curves will be shifted to the left to lower currently densities, resulting in lower i_{corr} and a possible increase or decrease in E_{corr} that will be dependent on the extent of the shift in the anodic and cathodic curves (Figure 1.12).

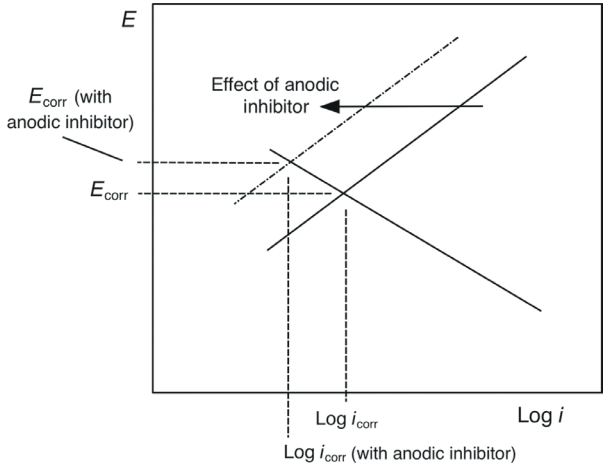


Figure 1.10 Anodic inhibitor suppresses the anodic reaction, resulting in a reduction of i_{corr} and increase in E_{corr}.

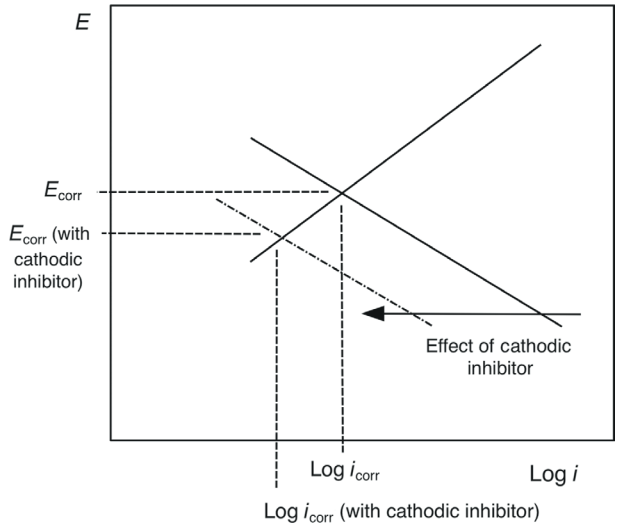


Figure 1.11 Cathodic inhibitor suppresses the cathodic reaction, resulting in a reduction of i_{corr} and decrease in E_{corr}.

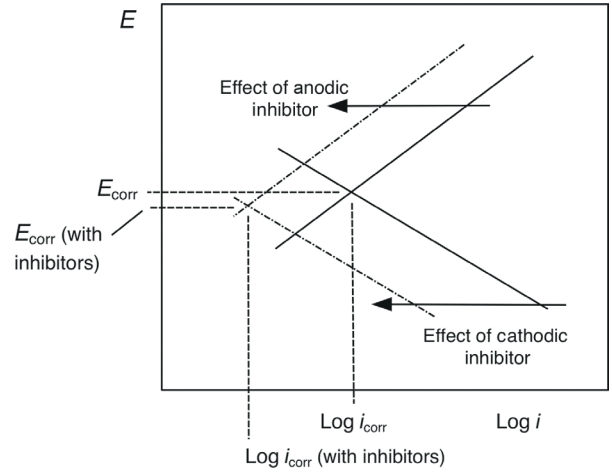


Figure 1.12 Inhibitors suppress both the anodic and cathodic reaction, resulting in a reduction of i_{corr} and possible increase or decrease in E_{corr}.

Inhibitors are often included in surface pretreatments and primers in coating systems. A very effective inhibitor that has been historically used in many applications is hexavalent chromium. However, due to the carcinogenic properties of hexavalent chromium under some conditions, its use is being phased out, which has led to many research and development activities to find or develop less toxic replacements.

1.3.3 Cathodic-protection coatings

In these coatings, the protection mechanism operates on the principle of cathodic protection. The coatings can be either metallic or semiconductive. Metallic coatings have to be electrochemically more active than the substrate metal that is to be protected, and semiconductive coatings have to be n-type semiconductors. The metallic coatings are sacrificial and corrode preferentially to protect the substrate, and the n-type semiconductors operate on the photo-electrochemical effect.

1.3.3.1 Sacrificial metallic coatings

These coatings are consumed or sacrificed to protect the substrate metal. A classic example is galvanized steel where mild steel is protected with a layer of zinc. Typically, with galvanized steels, the zinc coating suppresses the potential of the mild steel at coating breaches and therefore prevents the steel substrate from corroding until a significant fraction of the zinc coating is consumed (Figure 1.13). With the use of polarization diagrams, this process can be described as follows: When a metal M naturally corrodes, it settles at its corrosion potential, $E_{corr,M}$, and corrodes at a rate of $i_{corr,M}$ (Figure 1.14). If the metal M is then electrically connected to a more active metal A (i.e., metal A has a more negative E_{corr} than that of metal M) and both are immersed in the same electrolyte, the potential of metal M and that of the more active metal A will equilibrate to the galvanic potential, E_{galv}. In addition, the corrosion rate of metal M will be suppressed to $i_{diss,M\ (coup\ to\ A)}$ (Figure 1.14) or stop completely if E_{galv} drops below the equilibrium potential for metal M, $E_{M^{n+}/M}$ (Figure 1.14). The corrosion rate of the more active metal A will increase from $i_{corr,A}$ (when it is uncoupled) to i_{galv} when it is coupled to the more noble metal M (Figure 1.14). Hence, metal A will be "sacrificed" to protect metal M.

For cathodic-protection coatings, the sacrificial, active metal used in the coating has to be in electrical contact with the metal substrate that is to be protected. Contact to the substrate can be achieved, for example, by coating the active metal onto the substrate by hot-dipping in a bath of the molten metal, flame spraying the metal, or electrochemically plating the metal from an aqueous bath. Alternatively, particles

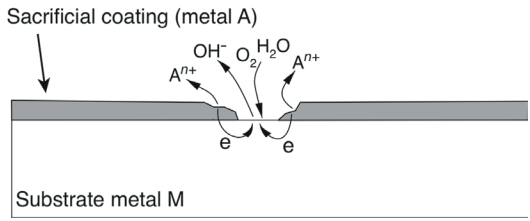


Figure 1.13 Cathodic protection using sacrificial coating.

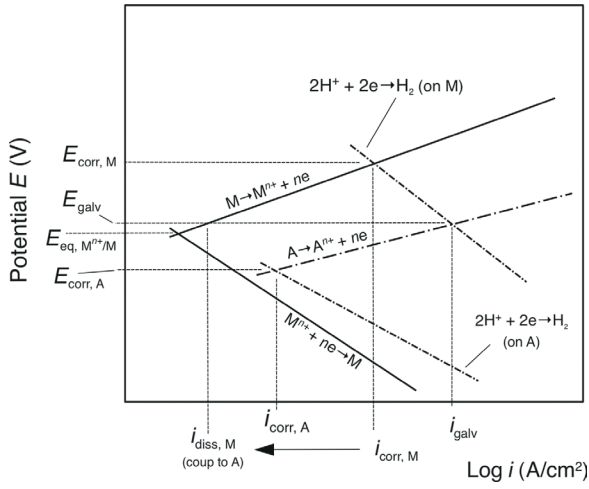


Figure 1.14 Polarization diagrams showing the effect of galvanically coupling an active metal A to a more noble metal M, resulting in the suppression of corrosion of metal M to i_{diss}, M (coup to A).

of the active metal can be incorporated into a binder and then sprayed onto the substrate. The binder can be organic (e.g., chlorinated rubbers, vinyls, epoxies) or inorganic (e.g., silicates).[6] The loading of the active metal has to be sufficiently high (e.g., in the case of Zn coatings, 90-95 wt.% of the dry coating[6]), such that the coating is electrically conductive to allow electrons generated from the corrosion of the sacrificial active metal to migrate to the substrate to induce cathodic protection. The characteristics of the binder can also have secondary effects. For example, when zinc particles are incorporated into inorganic silicate binders, the zinc corrosion products plug defects in the coating as the zinc particles are consumed, making the coating denser.[6] This plugging mechanism is not generally achieved with organic binders. Hence, zinc coatings with inorganic silicate binders may be effective for decades in marine environments compared to months-to-years for zinc in organic binders.

1.3.3.2 N-type semiconductor coatings

Cathodic protection can also be achieved by using coatings that are or contain n-type semiconductors. Cathodic protection is achieved, however, from a photo-electrochemical effect and not by the sacrificial corrosion of the coating. An n-type semiconductor is photo-anodic and under illumination promotes photo-oxidation reactions, such as the oxidation of water. Hence, in the presence of moisture and under illumination, photo-generated electrons from an n-type semiconductor coating could polarize the substrate to more negative potentials to induce

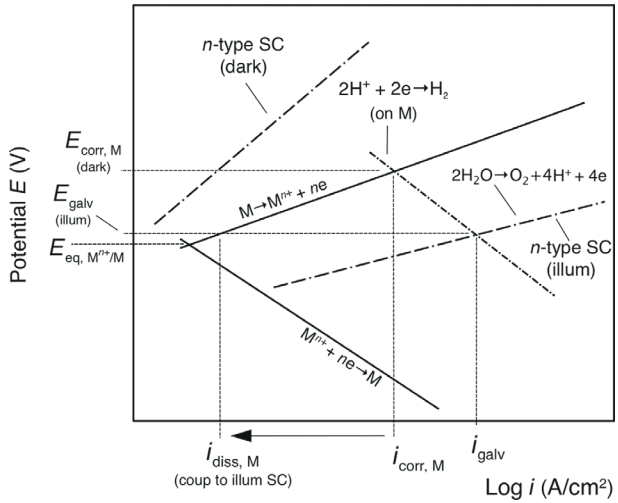


Figure 1.15 Polarization diagrams showing the effect of an illuminated n-type semiconductor (SC) on the corrosion current density of the substrate metal.

cathodic protection.[7] Under illumination, E_{corr} shifts from $E_{corr,\,M\,(dark)}$ to $E_{galv\,(illum)}$, and the dissolution of the substrate decreases from $i_{corr,M}$ to $i_{diss,M\,(coup\,to\,illum\,SC)}$ (Figure 1.15). Due to the requirement of illumination, cathodic protection would only be achieved during daylight periods.

1.3.4 Coating systems

When significant corrosion protection is required, a single layer of coating may not be sufficient, and a more robust coating system may be needed that employs surface pretreatments, primers, undercoats, and topcoats. For example, mild steel can be coated with zinc, pretreated with zinc phosphate, and then top-coated with epoxy (Figure 1.16). With this coating system, the sacrificial zinc layer will cathodically protect the mild steel by galvanic action even if the zinc layer is breached (Figure 1.13). The zinc-phosphate pretreatment increases the adhesion of the epoxy topcoat, which prolongs the life of the zinc coating by suppressing the normal corrosion of zinc. Hence, the zinc will be consumed only when it is needed to protect the mild steel substrate.

When using coating systems, however, it is important that there is compatibility between the different layers, and that they work together or in synergy to enhance overall corrosion protection. Using the wrong combination of coating materials can lead to premature failure. For example, the solvents used in one coating layer could compromise the integrity of an adjacent coating layer, resulting in loss of adhesion or cohesion, etc.[6] Hence, the compatibility and performance of using multiple coating layers should be tested and verified prior to implementation.

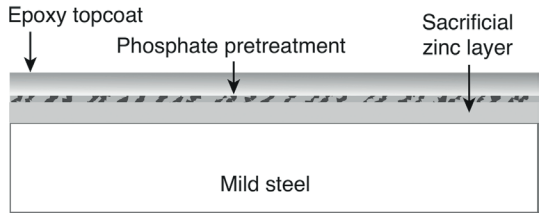


Figure 1.16 Schematic of coating system on mild steel with zinc plating, zinc-phosphate pretreatment, and epoxy topcoat.

1.4 Conclusions

Most metals require the application of a protective coating or coating system to provide an acceptable level of corrosion protection for an intended application. As corrosion of metals is an electrochemical process, it is controlled by moisture content, the chemical environment, and the electrochemical state of the metal. Hence, corrosion can be attenuated by using coatings that effectively control the above parameters. Coating properties such as adhesion, cohesion, imperviousness to moisture, electrical resistivity, catalytic properties for oxygen reduction and hydrogen evolution, corrosion inhibition, and electrochemical potential are all important in the control of corrosion, and how these are controlled or tailored in a coating or coating system will determine the level of corrosion protection achieved.

References

1. Rosenqvist T. Principles of extractive metallurgy. 2nd ed. New York: McGraw-Hill Book Company; 1983.
2. Uhlig HH, Revie RW. Corrosion and corrosion control. 3rd ed. New York: John Wiley & Sons; 1985.
3. Gellings PJ. Introduction to corrosion prevention and control for engineers. Rotterdam: Delft University Press; 1976.
4. Fontana MG, Greene ND. Corrosion engineering. 2nd ed. New York: McGraw-Hill Book Company; 1978.
5. Galvele JR. Present state of understanding of the breakdown of passivity and repassivation. In: Frankenthal RP, Kruger J, editors. Passivity of metals. Princeton, NJ: The Electrochemical Society; 1978.
6. Munger CG. Corrosion prevention by protective coatings. Houston: National Association of Corrosion Engineers; 1984.
7. Ding H, Hihara LH. A "photochemical corrosion diode" model depicting galvanic corrosion in metal-matrix composites containing semiconducting constituents. In: 212th Electrochemical Society Meeting, Washington, DC; 2007.

Chapter 2

The Importance of Corrosion and the Necessity of Applying Intelligent Coatings for Its Control

I. Gurrappa, I.V.S. Yashwanth
Defence Metallurgical Research Laboratory, Kanchanbagh PO, Hyderabad, India

2.1 Introduction

Corrosion is a significant challenge to most of the industries in the world because it causes disasters and massive financial loss.[1] It is essential to remember that corrosion knows no national boundaries and takes place both at ambient and high temperatures. The primary forms of corrosion that have been observed on various materials are given below:

(a) Uniform corrosion
(b) Crevice corrosion
(c) Pitting corrosion
(d) Galvanic corrosion
(e) Intergranular corrosion
(f) Dealloying

Intelligent Coatings for Corrosion Control
Copyright © 2015 Elsevier Inc. All rights reserved.

(g) Erosion-corrosion
(h) Stress corrosion cracking (SCC)
(i) Corrosion fatigue
(j) Microbiologically Influenced Corrosion (MIC)

The susceptibility to degradation by any of these forms of corrosion depends on the nature of materials used, applications, and the surrounding environment. The latest surveys show that the total worldwide, direct annual estimated cost of corrosion (essentially materials, equipment, and services involved with repair, maintenance, and replacement) is approximately US$4 trillion, that is, about 4% of the nation's gross domestic product (GDP) (Figure 2.1). This figure does not include the environmental damage, waste of resources, loss of production, or personal injury resulting from corrosion. Different sectors and related industries are mentioned in Table 2.1. According to corrosion experts, it is possible to save a net of 25% of that annual cost by applying currently available corrosion control technologies. Moreover, it is possible to extend the savings (up to 35%) by innovating and applying intelligent coatings. Therefore, there is a need to innovate an effective, environmentally friendly and economically viable technique for producing and also applying intelligent coatings to minimize corrosion.

Intelligent coatings, also known as smart/self-healing coatings, are multifunctional and contain compositionally optimized inhibiting elements/compounds to respond to the service conditions appropriately. Application of intelligent/smart/self-healing coatings is a cost-effective method of improving the corrosion protection and thereby the durability of metallic structures. A wide range of engineering

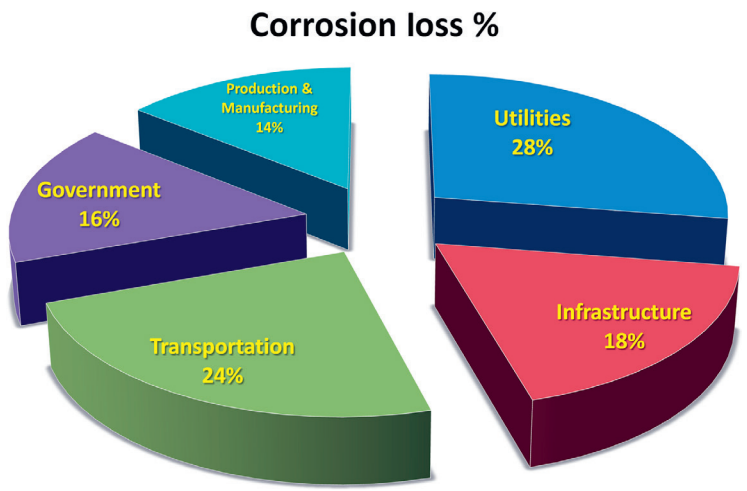


Figure 2.1 Cost of corrosion in different sectors.

TABLE 2.1 Category and Related Industrial Sectors

Category	Industry Sector
Infrastructure	Highway bridges Gas and liquid transmission pipelines Waterways and ports Hazardous materials storage Airports Railway tracks
Utilities	Gas distribution Drinking water and sewer systems Electrical utilities Telecommunications
Transportation	Motor vehicles Ships Aircraft Trains Hazardous materials transport
Production and manufacturing	Oil and gas exploration and production Mining Petroleum refining Chemical, petrochemical, and pharmaceutical Pulp and paper Agricultural Food processing Electronics Home appliances
Government	Defense Nuclear waste storage

structures, from cars to aircraft, from chemical factories to household equipment, can be effectively protected by these coating systems. Intelligent coatings are based on epoxy with polymer and nanoparticulates applied on the structures used at ambient temperatures. However, elevated temperature applications like gas turbine engines used in aero and industrial applications need metallic and ceramic intelligent coatings to enhance their efficiency. Further, the coatings should be multilayered with different compositions applied by varied surface engineering techniques. Here, intelligent coatings have to respond suitably to the surrounding environments and temperatures and enhance the component's life significantly by forming appropriate corrosion resistant films such as chromia or alumina. Hence, the selection of materials and intelligent coatings for a particular application is a challenging task for scientists and engineers. Therefore, intelligent coatings can be divided into low/ambient temperature intelligent coatings and elevated temperature intelligent coatings. The details will be explained in subsequent sections.

2.2 Low Temperature Intelligent Coatings

Traditional coatings like zinc and tin have been utilized for more than one and half centuries as protective coatings providing galvanic protection of defects and as organic or inorganic coatings to protect the substrate (metal/alloy) by acting as a barrier between the substrate surface and the environment. Other types of coatings contain basic pigments that are based on releasing inhibiting compounds such as strontium, calcium, and zinc chromates. The advanced coating contains a small amount of functional additives that enable the coating to provide enhanced functionality. Other coatings have some functionality incorporated into the resin itself. The functionality of the coating depends primarily on the composition or formulation of the coating.

The intelligent coatings provide the best protection by sensing a change in the environment and respond appropriately. Therefore, the intelligent coatings offer multifunctional and multidimensional benefits. With recent developments in nanotechnology, the inherent function of conducting polymers and composite materials can be precisely engineered in such a way that the coating provides intelligent characteristics. The intelligent coatings also overcome the historic usage of hazardous and carcinogenic materials such as hexavalent chromium and cadmium. The drug release concept that has been successfully developed and used for treating various ailments (including heart attacks) provides considerable information for the potential development of intelligent coatings that release corrosion inhibitors.

Development of intelligent coatings that can be produced cost effectively is one of the main issues. Further, the intelligent coatings must possess exceptional performance attributes that justify the additional cost for their manufacture. The developed intelligent coatings must be brought out of the laboratories into reality in the form of proven applications that are commercially viable. The development of newer intelligent coatings will involve multidisciplinary research by materials scientists of varied expertise such as in chemistry, physics, polymers, biology, medicine, and engineering.

Often microbial growths on the surface of materials accelerate corrosion and cause their faster degradation. Under such conditions, intelligent coatings should contain pigments that release toxic compounds so that bacterial growth can be arrested and provide reasonable protection to the substrate material. Another important property of an intelligent coating is its ability to respond to mechanical damage or environmental stresses during service conditions by releasing inhibitors.

Low temperature intelligent coatings can be broadly categorized in many different ways—based on their functional ingredients, applications, synthesis techniques, and so on. The coatings that respond to changes in heat, light, or pressure are sensors; bioactive coatings including antifouling, biodecontamination, and biocatalysis; color shifting coatings; corrosion control coatings; and command destructive coatings. There are intelligent coatings that are difficult to classify including self-lubricating coatings,

superinsulating coatings, self-repair and self-healing coatings, electrically conducting coatings, self-assembling coatings, superhydrophobic coatings, optical coatings, and so on. The intelligent coatings primarily contain functional ingredients within, as mentioned above, and these can be resin itself or a variety of additives such as pigments, nanoparticles, nanotubes, microelectromechanical devices (MEMS), radio frequency identification devices (RFIDs), microencapsulated ingredients, enzymes, antimicrobial agents, and so on, depending upon the application.

Considerable research has been carried out in the area of conducting polymers to develop intelligent coatings because the conducting polymer can form a dense, adherent, and low porosity, passive film on the metal surface and thus prevent corrosion. Some intelligent coatings were developed by employing conducting polymers like polyaniline (PANI) and polypyrrole.[2,3] These materials have a few unique characteristics: first, they are highly stable; second, they are conducting; and third, they hold and release ionic species depending on their state of charge. It is possible to synthesize intelligent conducting polymer coatings by doping ions that release when a corrosion process is sensed.

The other way is to use a combination of inorganic and organic hybrids, which are named as creamers. They are partly organic polymer coupled with an inorganic ceramic. More specifically, they are nanophase-separated metal-oxo clusters connected via a phase coupling agent. The creamer coatings can self-assemble on metallic surfaces to create a passivating preceramic phase, which has been shown to inhibit corrosion even on surfaces in which corrosion has already initiated. These coatings provide mechanical stiffness coupled with the ability to self-heal, deflect high-energy particles protection against deep ultra violet rays, and remain optically transparent.[4]

Tiwari et al. have studied different combinations of coatings, such as a pure epoxy polymer coating, a hybrid coating consisting of epoxy and silicone, a ceramer coating consisting of organo-silicone and a quasiceramic coating consisting of specialty silicone composition. Authors have observed that the hybrid coating exhibits superior nanomechanical properties compared to the pure polymer coating, and the coating containing high silicone levels displayed superior hardness.[5] The hybrid coating had a rough surface that was damaged and partially recovered after the scratch test. The creamer and quasiceramic coatings displayed brittle failure. They have also reported the use of silicone creamer coatings for protection of metals against corrosion.[6]

Two technology enterprises offer energy-efficient, environmentally sound, and attractively priced plant technology (Aquence™) for lean corrosion protection.[7] Aquence is a chemical autodeposition process that draws together decisive commercial and ecological advantages. Aquence is an innovative chemical autodeposition process that provides high-quality corrosion protection without utilizing heavy metals in just a few process stages. The aqueous organic solution builds up a coating film wherever the chemicals come into contact with ferrous metal (Figure 2.2). The

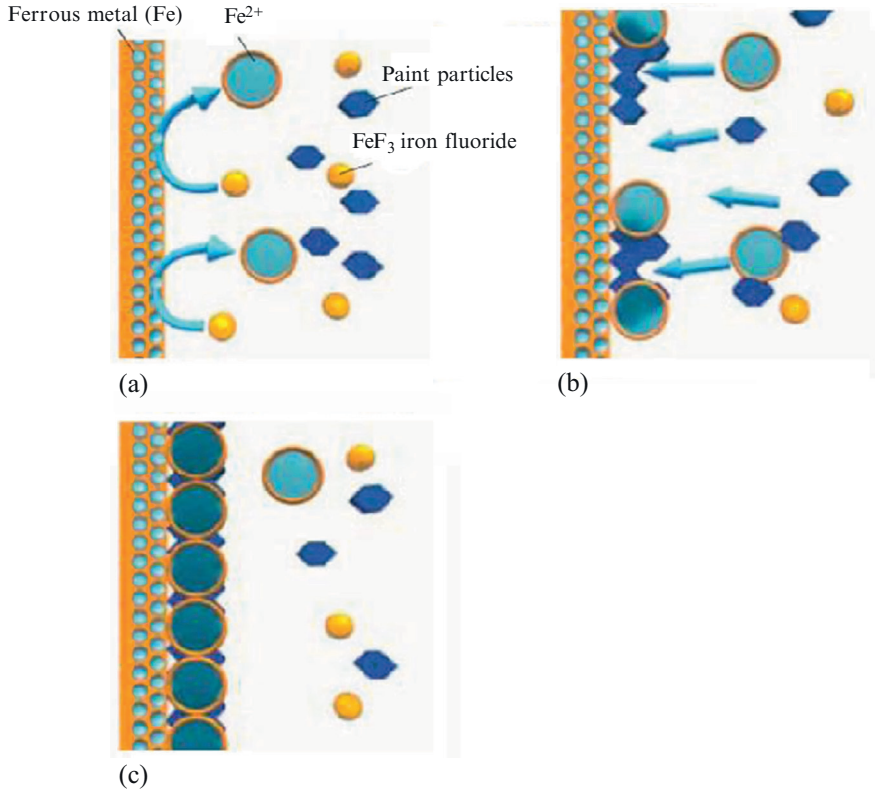


Figure 2.2 Aquence coating formation steps on iron substrate: (a) Fe^{2+} ion releasing; (b) Fe^{2+} ions and paint combining; (c) film formation.[7]

Aquence process produces a coating only where it interacts with ferrous metal; other materials, such as rubber and plastics, remain untreated and are not damaged because low oven temperatures can be selected. Complex parts, like assemblies with prefitted plastic components, can be coated evenly in a single process stage. Uniform contact with the chemicals ensures that even complex assemblies of closely arranged parts as well as cavities can be protected against corrosion. The enhanced hardness and direct bonding of the coating with metal substrate increases durability of the parts.[7]

2.3 Encapsulation for Self-Healing Coatings

Developments in self-healing technology have opened a new area of multifunctional coatings with the potential to increase the lifetime and reduce the enormous costs associated with maintenance of protective coatings. There has been significant research

in this area, particularly for the past decade.[8,9] Synthetic methods are being developed to produce materials with desirable healing properties while maintaining high performance as protective coatings.[10] Accelerated aging testing conducted in this research has shown that corrosion is considerably delayed and reduced (Figures 2.3 and 2.4).

It is essential to note that the use of protective coatings over various substrates is based upon natural systems such as human skin. All protect the underlying substrates.

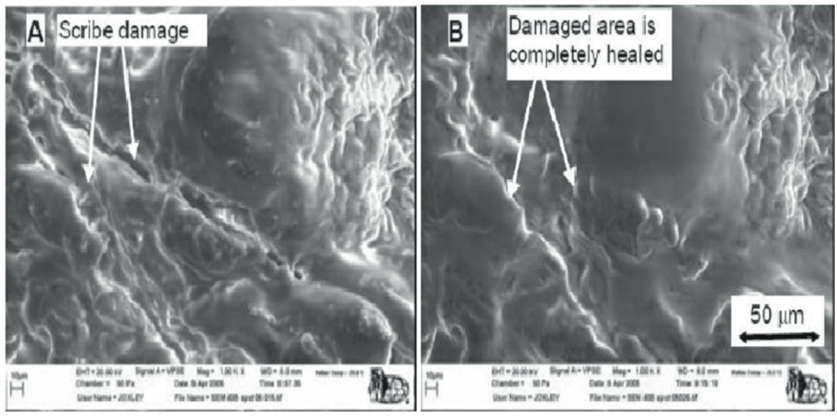


Figure 2.3 Encapsulated coating showing self-healing of a polymer: (a) damaged polymer surface; (b) healed polymer surface.[10]

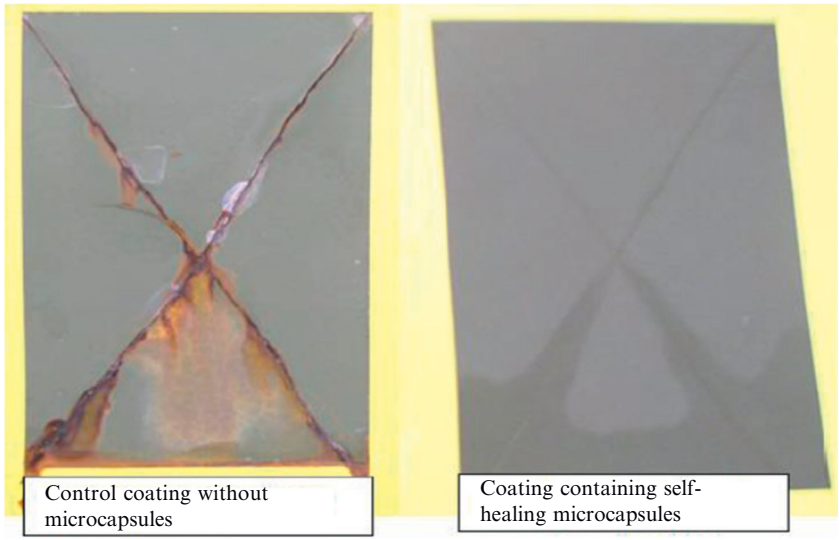


Figure 2.4 The behavior of microcapsules incorporated in polymer primed steels panels.[10]

The main difference with natural protective systems and man-made analogues is their ability to repair themselves after damage. The self-healing of the skin occurs naturally to reproduce an identical surface. Certain plants continually renew the surfaces of their leaves with waxy residue to prevent waterborne contaminant growth such as fungus. Thus, the research in the area of self-healing coatings to add functionality to protective surfaces was inspired by the natural systems.

The main self-healing coatings were prepared by incorporating an encapsulated "healing" agent, which is subsequently released upon damage of the coating. These encapsulation methods have been demonstrated to successfully heal materials after selected events of cuts, scribes, impacts, and deep scuffs on the surface of the coatings (Figure 2.3). These healing materials will re-form the coating over the damaged area, resulting in a protective surface comparable to that of the original undamaged surface. In these coatings, the only initiation source to heal the material is the initial damage event. The use of encapsulated self-healing materials was originally developed by White et al. from University of Illinois. The idea is to embed an encapsulated monomer, dicyclopentadiene (DCPD), into a thermoset composite system. Once cracks were formed in the composite, the capsules rupture, and the DCPD flows into the crack plane via capillary action. The monomer then comes in contact with a catalyst present in the resin, which enables the polymerization into a solid. This innovative concept has been described to be similar to the "self-healing" of cracks in bones (a composite of rigid inorganic hydroxyapatite, collagen, and other flexible organic components).

U.S. Army researchers Kumar and Stephenson demonstrated a self-healing, corrosion-inhibiting coating system for use on outdoor steel structures.[8] Similar research in the area of encapsulated self-healing coatings were performed at Luna Innovations. This concept is similar to the self-healing composites with encapsulated monomers, except that their use will be for protective coating applications. The capsules are broken under stress like a scratch in the coating. Monomers flow out of ruptured capsules into damaged areas to repair coatings via autooxidation processes. For their effective function, the capsules must possess significant structural and chemical integrity in order to withstand normal stress of application and use in a coating.[10] Further, in the case of corrosion prevention, the coencapsulation of corrosion inhibitors have been included to ensure that the resultant healed coating possesses the same inhibition to corrosion as the original coating.[10]

There are several techniques to synthesize the microcapsules like interfacial polymerization,[11] coacervation,[12] *in-situ* polymerization,[13] extrusion, and sol-gel techniques. However, among different techniques, the simple and appropriate technique is *in-situ* polymerization. The comparison among the encapsulation techniques is provided in Figure 2.5. Hence, the majority of researchers have used *in-situ* polymerization as a major technique for fabrication of micro/nanocapsules. The common healant material phase is liquid, because of free flow through the

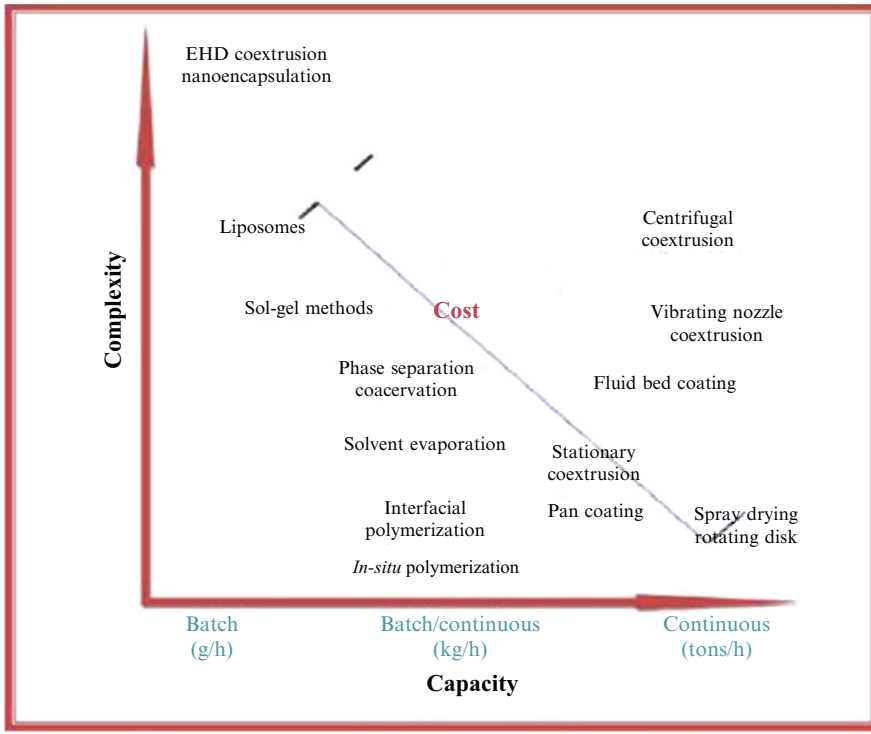


Figure 2.5 Comparison among encapsulation techniques.[14]

crack plane. An excellent review on encapsulation, in particular *in-situ* polymerization, was published by Samazdeh et al.[14]

Nature uses the energy inherent in active base metal surfaces in oxidizing corrosive environment to form passive films. When passive films cannot be formed, for example, for Al in chloride environments, chemical or nanostructures built into the protective coating can be imagined such that the corrosion reaction drives the release of a suitable corrosion inhibitor. This is likely accomplished for suitably doped PANI coatings on Al 2024-T3 exposed to a salt fog environment. Anionic organic ORR inhibitors appear to be suitable dopants. Hamdy et al. have attempted to design a chromate-free anticorrosion intelligent coating for aluminum- and magnesium-based materials for marine, automotive and aerospace applications (Figure 2.6).[15] They reported that a simple vanadia-based chemical conversion coating improves the corrosion resistance of high strength AA2024 alloy.

Nanostructured materials engineering extends the possibility of engineering "intelligent" coatings that can release corrosion inhibitors on demand when, for example, the coating is breached, stressed (mechanically or chemically), or an electrical or mechanical control signal is applied to the coating. Ideally, an "intelligent" corrosion

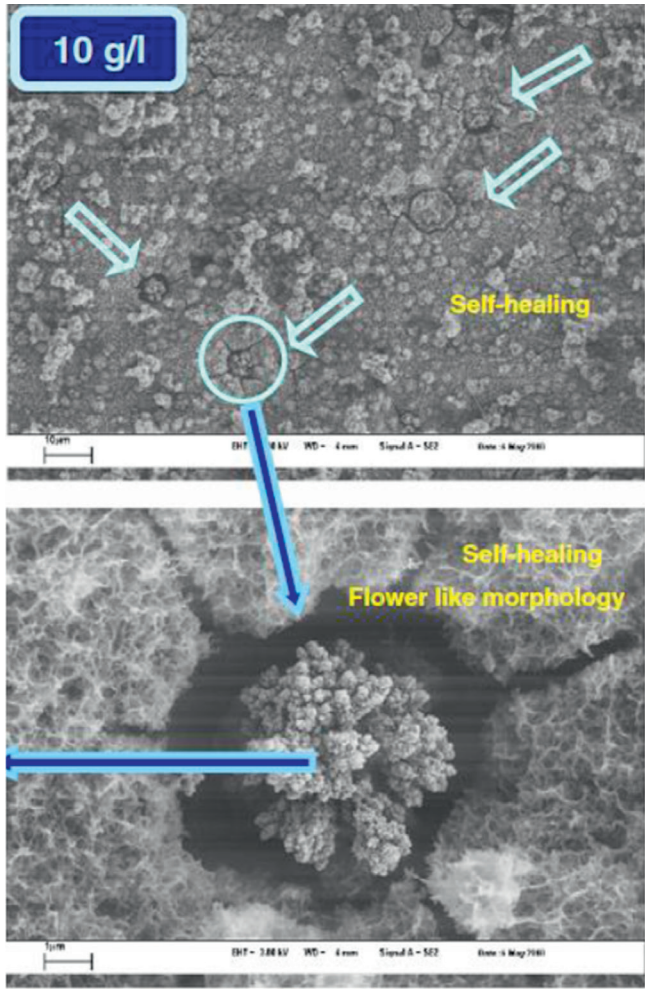


Figure 2.6 The performance of vanadate coating showing the nucleation of vanadium oxide over the corroded zones and the self-healing tendency.[15]

inhibiting coating will generate or release an inhibitor only when demanded by the initiation of corrosion. In an aerated electrolyte, aluminum metal provides about 1.7 V to power a chemical or physical nanomachine to deliver a corrosion inhibitor on demand. Natural passivity, as occurs for steel in nitric acid, makes use of the naturally available driving force to synthesize a "corrosion inhibitor," namely a compact oxide film. In principle, nanoengineered functional coatings can lead to a "smart" active coating that uses the energy inherent in the surface to be protected to produce an inhibiting material when called upon.[16]

Nanocrystalline cobalt (Co) and cobalt/multiwalled carbon nanotube (Co/MWCNT) coatings were prepared by direct current (DC) and pulse reverse current (PRC) electrodeposition from aqueous bath-containing cobalt sulfate, MWCNTs, and so on. Effect of the functionalization of MWCNTs and electrodeposition techniques, that is, DC and PRC, on the microstructure and properties of these coatings revealed that the incorporation of MWCNTs, particularly the functionalized MWCNTs, substantially improve the hardness and resistance to wear and corrosion of the deposited coatings.[17] PRC electrodeposition produces Co and Co/MWCNT coatings that are featured by small grain size, low surface roughness, and more uniform distribution of MWCNTs in the matrix, and consequently display the higher hardness and better resistance to wear and corrosion. The functionalization of MWCNTs favors the codeposition of MWCNTs with Co ions, and then improves the hardness and corrosion and wear resistance of the produced composite coatings. Among all samples, the composite coating incorporated with functionalized MWCNTs produced by PRC electrodeposition exhibited the highest hardness around 1180 $kgf \times mm^{-2}$ and the best resistance to wear and corrosion. The differences in friction and wear behavior of these nanocrystalline Co and Co/MWCNT coatings as a function of treatment of MWCNTs or electrodeposition techniques are attributed to their different hardness, microstructures, and the corresponding wear mechanisms (Figures 2.7 and 2.8).

The successful application of spiro[1H-isoindole-1,9-[9H]xanthen]-3(2H)-one, 3,6-bis(diethylamino)-2-[(1-methylethylidene)amino](FDI) as a "turn-on" early aluminum corrosion detector in epoxy coatings was reported.[18] Electrospray

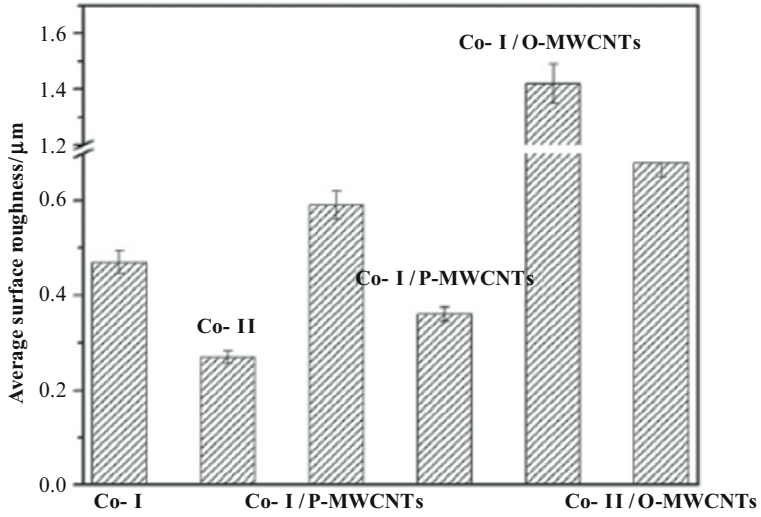


Figure 2.7 Comparison of surface roughness of different nanocrystalline Co and MWCNT coatings.[17]

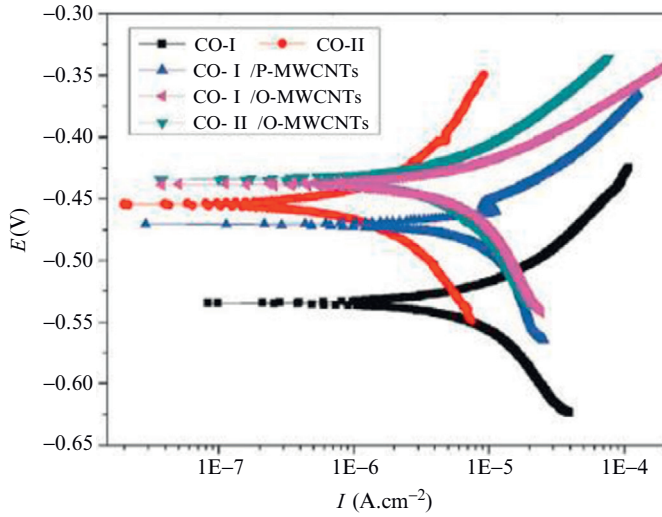


Figure 2.8 Polarization behavior of different nanocrystalline Co and MWCNT coatings in 3.5% mNaCl solution.[17]

ionization mass spectrometry (ESI-MS) and ^{1}H NMR investigations revealed that the nonfluorescent FD1 is sensitive to low pH due to its acid-catalyzed hydrolysis to Rhodamine B hydrazide (RBH) that subsequently becomes protonated to its fluorescent ring-opened form. Both clear and filled FD1-containing smart epoxy coatings were capable of sensing acidic pH produced at the anodic site of localized aluminum corrosion at a low indicator concentration (0.5 wt.%). It was demonstrated by the observation of fluorescent, bright-orange areas corresponding to localized pitting corrosion of the aluminum substrate illuminated by a handheld UV lamp.[18] Therefore, early corrosion of aluminum can be easily and nondestructively detected via "turn-on" fluorescence strategy.

The major structures, such as offshore platforms, ships, submarines, pipes carrying oil, gas, and water, are manufactured from carbon steel and protected from corrosion primarily by paint coatings. During service, the paint coating deteriorates and anodic areas are formed. Particularly the ship hulls have complex structures and paint damage is more likely either due to mechanical damage or during sailing.[19–22] In addition, the underwater hull of the ships have more corrosion sensitive areas like propellers and rudders that are noble to the hull material and are in contact with each other and thus lead to accelerated corrosion. Similarly, the pipelines thousands of kilometers long experience varied environmental conditions that cause disasters. Therefore, it is highly essential to apply an efficient and economic intelligent coating in association with an appropriately designed cathodic protection system in order to protect the structures and pipelines under all operating

conditions. It is important to note that the intelligent coatings alone will not be sufficient for these structures, and the installation of cathodic protection system is a must. However, complementary to a cathodic protection system, the intelligent coatings facilitate and enhance the material life significantly.

2.4 Cathodic Protection

Cathodic protection can be obtained either by using sacrificial anodes or by using an impressed current cathodic protection (ICCP) system. It has been established through experience that the corrosion of structural steel stops when its potential is −800 mV against silver/silver chloride or +250 mV against zinc reference electrode or −850 mV against copper/copper sulfate electrode.

2.4.1 Sacrificial anodes

The principle involved in the development of sacrificial anodes for cathodic protection purposes is that galvanic current flows when two dissimilar metals are electrically connected in the conducting environment. The noble metals are mostly protected by consumption of the less noble metals. Magnesium, zinc, and aluminum alloys are base materials versus mild steel, which is the structural material for the marine structures and, therefore, these alloys produce galvanic current when coupled with mild steel in the seawater, resulting in their sacrificial dissolution for protecting the mild steel.

Sacrificial anodes are often used in preference to ICCP systems when the current requirements are low and when in relatively high conducting environments. Capital investment will generally be lower, and it is often been the most economical method for a short-term protection of marine structures.

2.4.1.1 Advantages of sacrificial anodes

1. Operate independent of electric supply
2. Relatively simple to install; additional anodes can always be fitted if adequate protection is not achieved
3. No electrical hazard to the divers
4. No control to be exercised
5. Eliminate incorrect fitting problems
6. Minimum maintenance costs
7. Low installation costs

However, there are limitations to sacrificial anodes, as well:

2.4.1.2 Disadvantages of sacrificial anodes

(a) Periodic replacement is essential as the life of anodes is limited
(b) Current output cannot be regulated according to the demand (pollution, paint damage, etc.)
(c) They are not economically viable for protecting large and poorly coated pipelines
(d) They require a large number of anodes that results in an increase of frictional drag and weight

2.4.2 ICCP system

This is the most ideal and rugged system that overcomes the above limitations and has been in use in most of the pipelines for protection of ship hulls, offshore structures, and submarines all over the world. In this system, the protection current is drawn through the power supply and is impressed on the pipes/ship hulls/submarines/offshore structures that act as cathodes via inert anodes.

2.4.2.1 Advantages of ICCP system

(i) Large driving potential
(ii) Higher current output
(iii) Flexibility of current output control
(iv) Applicable in almost any resistivity soil environment
(v) Applicable for poorly coated pipelines
(vi) Protects larger and more expensive pipes

Gurrappa has published a significant number of books and research articles on sacrificial anodes and designing smart cathodic protection systems for cooling water pipelines and ship hulls.[23,24]

2.5 High Temperature Intelligent Coatings

As mentioned earlier, the corrosion takes place both at low and high temperatures depending on the service conditions. The desire for ever greater efficiency and increased performance have driven the developments in modern gas turbine engines. These engines require high performance materials to exhibit maximum efficiency by increasing their operating temperatures. Higher operating temperatures lead to high temperature corrosion of the components and thereby reduce their life significantly. Oxidation and hot corrosion are the two overriding factors (under high temperature corrosion) that determine the life of gas turbine engine components. The rate of degradation is slow under oxidation conditions, while it is significantly fast under

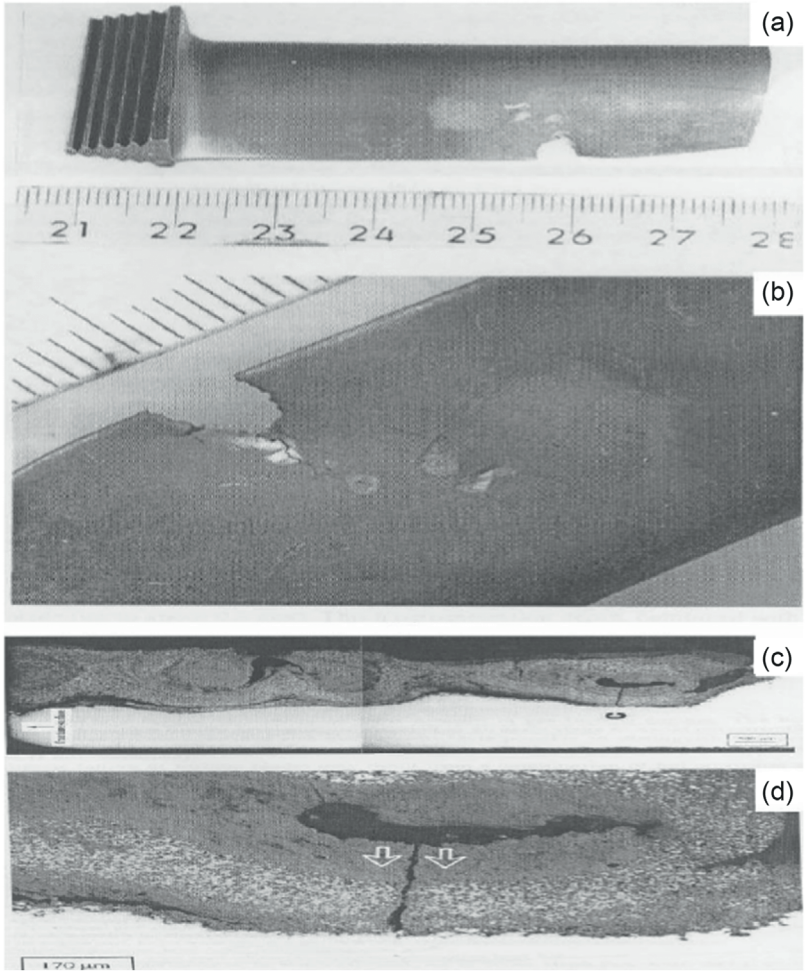


Figure 2.9 Typical failed gas turbine blade due to hot corrosion: (a) macroscopic view of damaged blade; (b) a crack propagating into remainder material; (c) micrograph showing advanced hot corrosion attack; (d) secondary crack propagation.[25]

hot corrosion conditions, and catastrophic failures can result if proper materials in association with appropriate coatings are not used (Figure 2.9).[25,26] Assessment of the current status on hot corrosion problems in gas turbine engines is imperative in order to improve the life of the engines by selecting advanced hot corrosion resistant materials and coatings. This process may help in highlighting the issues that need to be addressed not only to enhance the efficiency of gas turbine engines, but also to avoid failures during service.

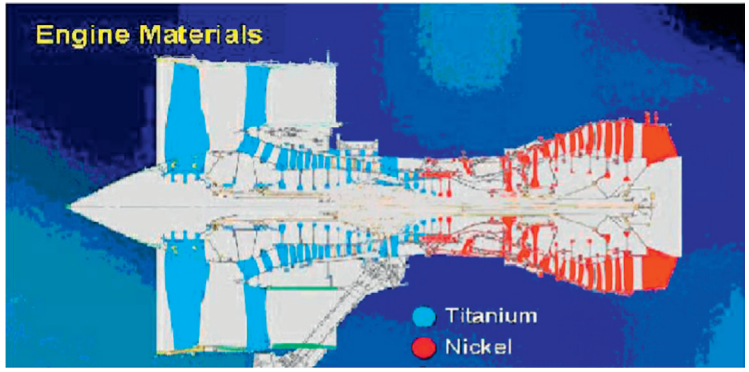


Figure 2.10 Gas turbine engine showing the usage of nickel-based superalloys and titanium-based alloys.[26]

A section of a typical gas turbine engine in which superalloys and titanium-based alloys are used is shown in Figure 2.10. As shown, the hot sections of the engine are dominated by Ni-based superalloys and compressor sections with titanium-based alloys. Advances about three decades ago in processing of Ni-based superalloys allowed evolution of microstructures from equiaxed structures to directionally solidified (DS) multigrain and single crystal (SC) components today. With added capability from compositional flexibility coupled with advances in processing over that time period, high-pressure turbine blade temperatures have increased to about 1250 °C, and metal surface temperature at the hottest locations approach 1150 °C in state-of-the-art gas turbine engines.

One of the most critical components in the engine is the gas turbine blade. The high-pressure turbine blade operates under more arduous conditions of temperature and stress than any component in the engine. Not only does the blade experience high temperature and direct stress, it also experiences rapid temperature transients at various points during the engine cycle. The hot gases surrounding the blade are highly oxidizing and contain high levels of contaminants like sulfur and chlorine if low-grade fuels are used. An ideal superalloy/protective coating should be able to survive this harsh corrosive environment for a designed period.

As mentioned earlier, the efficiency of a gas turbine is proportional to firing temperature. The increase in engine operating temperature meant that the traditional corrosion resistant turbine blade alloys such as IN 738 and IN 939 are no longer strong enough to last the expected 25,000 h of minimum life. It implies that higher strength alloys and single crystal alloys are required for creep strength. Progress in aero and industrial gas turbine blade materials has revealed the fact that in the last decade, dramatic competition in the power equipment industry has boosted the technology to a level that has been achieved recently in aviation turbines. Latest industrial gas

turbines use single crystal, rhenium containing Ni-based superalloys and directionally solidified blades and vanes.

The majority of Ni-based superalloy development efforts have been directed towards improving the alloy high temperature strength with relatively minor concern being shown to its hot corrosion resistance. Further, it is not always possible to achieve both high temperature strength and hot corrosion resistance simultaneously because some alloying elements help to improve hot corrosion resistance while some may help to improve high temperature strength. It is rare that an alloying element leads to enhancement both in high temperature strength and in hot corrosion resistance. This is further complicated for marine applications by the aggressivity of the environment, which includes sulfur and sodium from the fuel and various halides contained in seawater. These features could drastically reduce the superalloy component life and reliability by consuming the material at an unpredictably rapid rate, thereby reducing the load-carrying capacity and potentially leading to catastrophic failure of components.[25,26] Thus, the hot corrosion resistance of superalloys is as crucial as its high temperature strength in gas turbine engine applications. Recent studies have shown that the high temperature strength materials are most susceptible to hot corrosion, and the protective coating plays a key role in effectively combating the hot corrosion problem.[26–31]

2.6 Hot Corrosion

Break down of protective oxide layers by chemical interaction with certain aggressive species contained in the combustion environment can produce accelerated attack on the underlying metal. This process is known as hot corrosion. Hot corrosion takes place mainly because of high concentrations of sulfur, vanadium, and sodium in the fuels, which may be as high as 4%, 0.05%, and 0.01% (all are in wt.%), respectively. Chlorides and sulfates enter the engine with the air; sulfur, vanadium, and sodium oxidize, during combustion, and mostly volatile compounds such as SO_2, SO_3, NaOH, NaO, Na_2O, $VO(OH)_3$, V_2O_5, and V_2O_4 are formed. These compounds condense at 500-900 °C and build up deposits depending on the fuel. Na_2SO_4 is the main component of deposits in engines running on high sulfur and low vanadium fuel. Table 2.2 summarizes the main contaminants that are likely to form in a working environment for three types of gas turbine engines, that is, aero, marine, and industrial gas turbines.

TABLE 2.2 Contaminants in Gas Turbine Fuel and Air

Engine Application	Contaminants
Aero	Na, Cl, S, Ca (all low)
Marine	Na, Cl, S, Mg (all high)
Industrial	Na, V, S, Pb, Cl

2.6.1 Types of hot corrosion

Two different forms of attack have been identified, type-II hot corrosion, and type-I, which occur over, different temperature ranges; 600-750 °C and 800-950 °C respectively. Type-I results from a fluxing process where modification of the sodium sulfate deposit chemistry permits ingress of sulfur into the underlying metal; this produces localized depletion of protective elements, and progressive internal attack occurs. The overall process of type-I hot corrosion produces a characteristic of attack which includes a porous oxide scale, an irregular metal/scale interface, and internal attack with preceding metal sulfides.[26,29]

On the other hand, type-II hot corrosion requires sodium sulfate and sufficient sulfur trioxide to maintain low melting deposit, which readily fluxes the surface oxide. Thermodynamics favor sulfur trioxide formation in the lower temperature range. The associated attack is normally localized, producing pits with a lamellar scale rich in sulfur through progressive fluxing action of the deposits. Here, sulfur generally does not enter the alloy to form internal sulfide with this type of attack.[26]

2.6.2 Mechanism of hot corrosion

Several mechanisms have been proposed for hot corrosion. All the mechanisms involve deterioration of the reaction product barrier that forms on the alloys when the deposits are not present. Basically, the hot corrosion process proceeds in Four stages:

(a) An incubation stage during which the reaction proceeds at a rate essentially similar to that of normal oxidation
(b) An initiation step during which the corrosion is accelerated
(c) A propagation stage during which rapid corrosion takes place and
(d) Ultimate failure of a component

2.6.2.1 Incubation period

During this period, the alloy undergoes normal oxidation similar to that observed in the absence of salt deposit. Initially, the oxides of most of the alloying elements are formed as given below:

$$Ni + 1/2\,O_2 = NiO$$

$$2Cr + 3/2\,O_2 = Cr_2O_3$$

$$2Al + 3/2\,O_2 = Al_2O_3$$

The rapid weight gain of the alloy takes place due to the reaction with oxygen in the initial stages. At the end of incubation stage, thermodynamically stable oxides such as Cr_2O_3 and Al_2O_3 are formed as a dense oxide scale on the surface of alloys.

This oxide scale acts as a diffusion barrier for the ingress of deleterious species such as oxygen and sulfur.

2.6.2.2 Initiation stage

Cracking or spalling of oxide scale occurs in this stage due to the stresses developed during oxide growth. Thus, fresh alloy surface, which is depleted of scale forming alloying elements, is exposed to the action of deposit as shown below:

$$Ni + SO_4^{2-} = NiO + SO_2 + O^{2-}$$

SO_2 will be in the form of dissolved gas.

2.6.2.3 Propagation stage

The propagation stage during hot corrosion is substantially different from the behavior of the alloy in the absence of a deposit. It is accompanied by an exceptionally severe attack of the alloy as a result of fluxing of oxides as shown below:

$$2NiO + 2O^{2-} = 2NiO_2^{2-}\,(\text{nickelate})$$
$$Al_2O_3 + O^{2-} = 2AlO_2^{-}\,(\text{aluminate})$$
$$Cr_2O_3 + 2O^{2-} + 3/2O_2 = 2CrO_4^{2-}\,(\text{chromate})$$

The dissolved sulfur dioxide formed during the initiation period can react with the alloying elements to produce oxides, sulfides, and sulfur.

$$2Ni + SO_2 = 2NiO + 1/2S_2$$
$$4/3Cr + 3/2Ni + SO_2 = 2/3Cr_2O_3 + 1/2Ni_3S_2$$

If the deposits contain chloride ions, it can selectively remove certain elements such as chromium or aluminum from the alloy. This process involves the formation of highly volatile gaseous chlorides inside the pores of the alloy, and thereby metal chlorides diffuse out from the alloy. As a result, mechanical properties of the alloy reduce significantly as the cracks are formed on the alloy surface. The metallic components of these chlorides convert to oxides eventually, but these oxides form as particles and not as continuous layers. Hence, severe attack of the alloy can take place.[26]

The mechanisms have been explained based on acidic and basic fluxing of protective oxide scales depending upon the conditions. The protective oxide scale, for example, Cr_2O_3, is fluxed either as acidic solutes, such as $Cr_2(SO_4)_3$ or CrS, or as basic solutes, such as Na_2CrO_4 and $NaCrO_2$. As a result, the oxide scale can become nonprotective. Such nonprotective scales can be formed by dissolution of the oxide near the alloy surface and reprecipitation as discontinuous particles from the molten

deposit. Rapp and his team[32–34] carried out extensive studies pertaining to hot corrosion fluxing mechanisms, different oxide solubilities, and electrochemical evaluation methods for hot corrosion resistance. Natesan et al.[35] have studied the high temperature corrosion of Ni-based superalloys in coal conversion environments.

As fluxing of the protective scale is crucial in hot corrosion attack, the selection of alloys or intelligent coatings for hot corrosion resistance should be based on the solubility of protective oxides. For a given deposit and environmental conditions, the most favored oxide is the one that has the least solubility and can form a protective scale in the presence of salt film. Figure 2.11 presents the measured solubilities of various oxides in fused Na_2SO_4 at 1200 K.[32] The difference of six orders of magnitude in basicity between minima for the most basic Co_3O_4 to the acidic SiO_2, Cr_2O_3 and Al_2O_3 is striking and is consistent with relevant known alloy systems and coatings under hot corrosion conditions. Cobalt-based alloys and coatings are more vulnerable to acidic fluxing than Ni-based alloys and coatings. Cr_2O_3 is resistant to acidic fluxing because the minimum in its solubility curve corresponds approximately to the acidity of gas turbine environments.

It is extremely essential to assess the intelligent coatings in the laboratory under simulated engine conditions for evaluating their performance since it is not feasible to test each coating directly in the engine. A satisfactory test should yield a prediction of service performance, with an estimation of component life as a desirable objective. Different techniques, which are used for evaluation of various superalloys, and intelligent coatings for hot corrosion resistance, are described later.

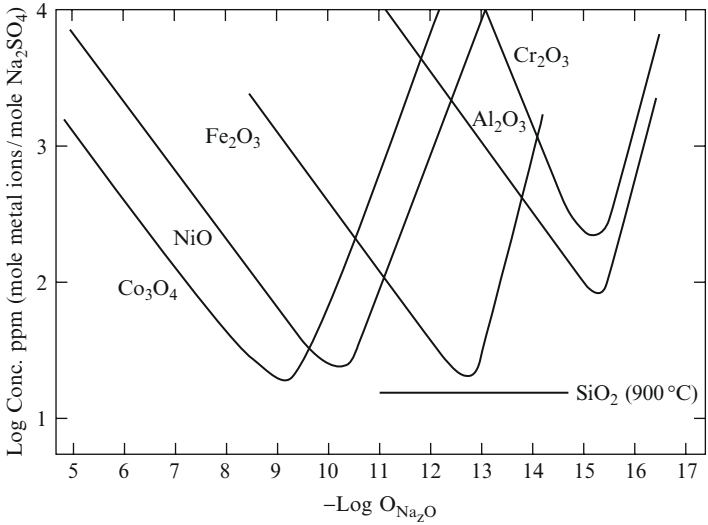


Figure 2.11 Measured solubilities in fused pure sodium sulfate.[32]

2.6.3 Hot corrosion of superalloys

Different superalloys of varied categories, namely, forged alloys such as Nimonic 75, Nimonic 105, and Inconel 718; conventional casting (CC) alloys such as Inconel 713 and Inconel 100; and directionally solidified alloys such as CM 247 LC, MAR-M200, and MAR-M247, were reported for their hot corrosion resistance in different environments. Single crystal superalloys of different generations have been developed. For instance, first generation CMSX-2, TMS-12, TMS-26, PWA1480, and Rene N4; second generation with up to 3 mass percentage rhenium (CMSX-4, Rene N5, TMS 82+ etc.); third generation with up to 6 mass percentage rhenium (CMSX-10, TMS-75, TMS 80+, etc.); fourth generation with rhenium and ruthenium (TMS-138, etc.); and fifth generation superalloys with iridium, ruthenium, and rhenium have been developed.

Single crystal airfoils offer the potential to further improve component high temperature materials strength and by control crystal orientation, can provide an optimum balance of properties. In single crystal material, all grain boundaries are eliminated from the material structure, and a single crystal with controlled orientation is produced in an airfoil shape. By eliminating all grain boundaries and the associated grain boundary strengthening additives, a substantial increase in the melting point of the alloy can be achieved, thus providing a corresponding increase in high temperature strength. The single crystal alloys have been in use in gas turbine engines since 1995. Together with intelligent protective coatings, the new superalloys will provide enhanced growth capability for gas turbine engines in the future.

Figure 2.12 shows the hot corrosion behavior of a few superalloys such as IN 792, CMSX-4, and DMS-4 under type-I conditions. The hot corrosion resistance of CM 247 LC and Rene 80 superalloys under type-II and type-I conditions in chloride and vanadium environments are presented in Figures 2.13 and 2.14. Appreciable corrosion was observed for all the superalloys. It indicates that hot corrosion plays a significant role in causing faster degradation, thereby reducing the superalloy life considerably. Among the superalloys, CM 247 LC was corroded severely, indicating that the superalloy is highly susceptible to hot corrosion. The appreciable corrosion attack of CM 247 LC superalloy was clearly evidenced by observing large cracks (Figure 2.15), broken samples (Figure 2.13), and a large corrosion affected zone (due to appreciable diffusion of corrosive elements present in the environment). Sulfur diffusion and formation of metal sulfides, preferentially chromium and nickel sulfides, are reported to be the influential factor. When sulfide phases are formed in superalloys, Ni-based alloys are inferior to cobalt- and iron-based alloys, which are especially effective in destroying the corrosion resistance of alloys.[26,36–42] In fact, the alloying elements play a significant role and decide the life of superalloys under hot corrosion conditions (Table 2.3).

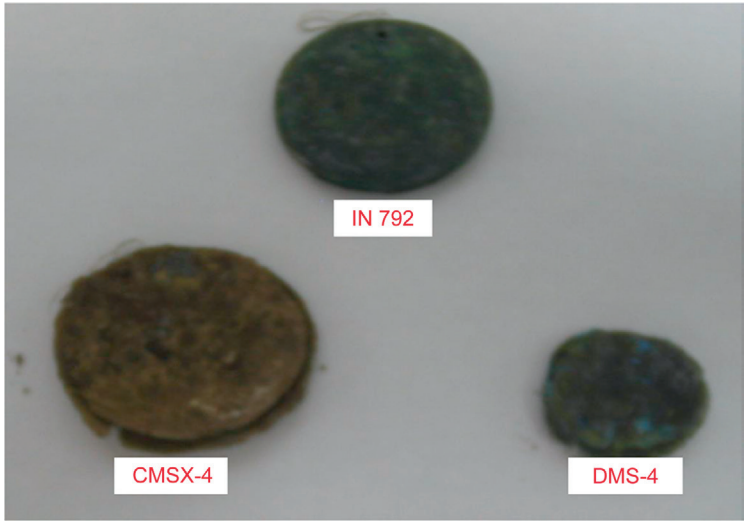


Figure 2.12 Hot corroded superalloys under type-I conditions in marine environment.

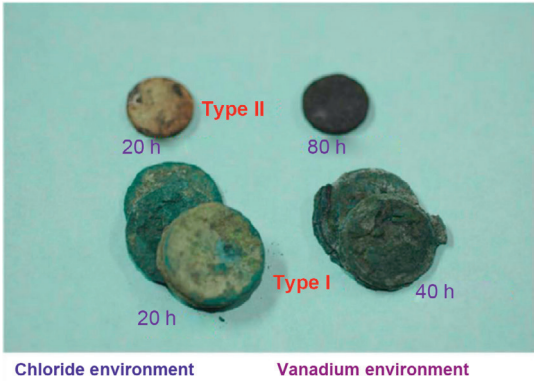


Figure 2.13 Hot corroded superalloy CM 247 LC in chloride and vanadium environments under type-I and type-II conditions.

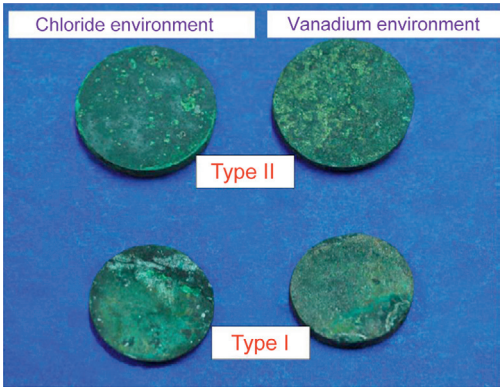


Figure 2.14 Hot corroded superalloy Rene 80 in chloride and vanadium environments under type-I and type-II conditions.

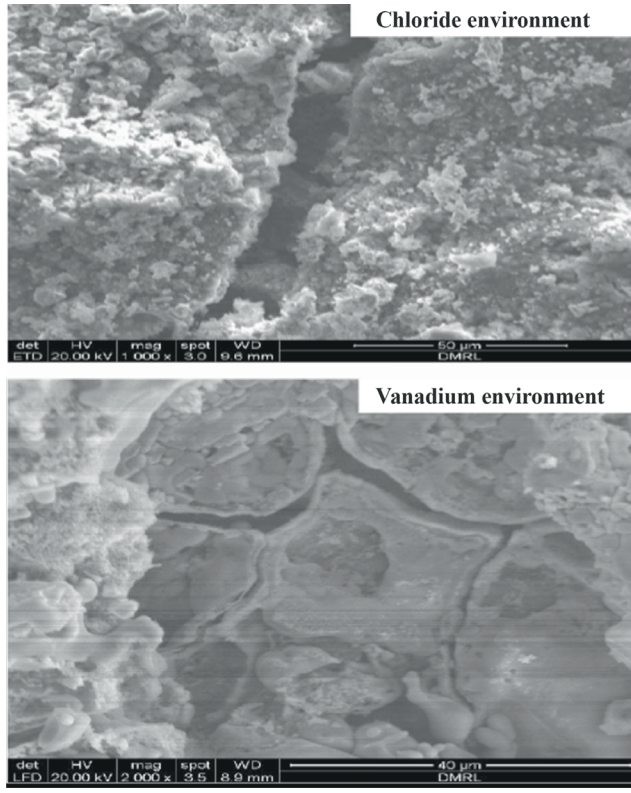


Figure 2.15 Surface morphologies of hot corroded CM 247 LC superalloy in chloride and vanadium environments under type-I conditions.

TABLE 2.3 The Chemical Composition of Selected Superalloys (wt.%)

Superalloy	Ni	Cr	Co	W	Al	Ta	Ti	Mo	Re	Hf	Fe	Mn	Si	Nb
IN 792	Bal	13.5	9.0	1.2	7.6	1.3	5.0	1.2	-	0.2	0.5	-	-	-
CMSX-4	Bal	6.5	9.0	6.0	5.6	6.5	1.0	0.6	3.0	0.1	-	-	-	-
CM 247 LC	Bal	8.1	9.2	8.5	5.6	3.2	0.7	0.5	-	1.4	-	-	-	-
DMS-4	Bal	2.9	7.9	5.8	5.6	8.5	-	-	6.5	0.1	-	-	-	-
Rene 80	Bal	14	9.5	4.0	6.5	-	5.0	1.5	-	-	-	-	-	-

2.6.4 Oxidation characteristics of DMS-4

Figure 2.16 shows an oxidized DMS-4 superalloy, and typical surface morphology of the oxidized superalloy is shown in Figure 2.17.[43] As can be seen, the superalloy was oxidized to the maximum extent by forming thicker oxide scales and was subsequently spalled. It indicates that the rate of formation of oxide scales is considerably high on the newly developed high rhenium-containing and exceptionally low chromium-containing DMS-4 superalloy. This leads to the formation of thick oxide scales over a period of time and subsequently spalled because of adherence problems. The typical results clearly indicate high vulnerability of the newer generation superalloys to high temperature oxidation.

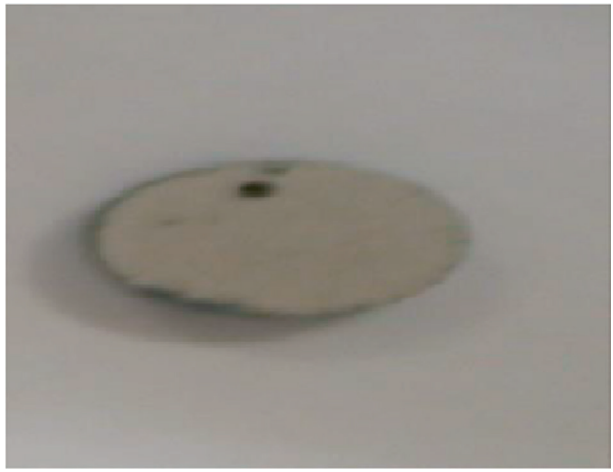


Figure 2.16 Oxidized DMS-4 superalloy at 1100 °C for 100 h.

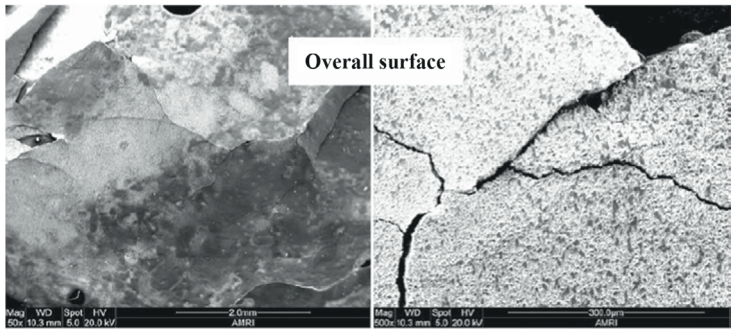


Figure 2.17 Surface morphologies of oxidized DMS-4 superalloys for 3 h at 1100 °C.

It is generally accepted that the temperature capability increases with decreasing Cr content. Therefore, the chemistry of new superalloys was profoundly influenced by reducing Cr content and increasing rhenium (Re) concentration in association with small amounts of iridium, ruthenium with the objective to enhance the temperature capability. As a result, the new generation superalloys contain only 2-3% Cr, but also, instead, contain about 7% Re, 3% Ru, 2% Ir, which is in contrast to the earlier generation superalloys containing about 10% Cr and no Re, Ru, or Ir. It was reported that the rhenium and new alloying elements make the superalloys susceptible to high temperature oxidation and hot corrosion.[44] Its effect is similar to Mo effect on oxidation (i.e., as the high vapor pressure of its oxide). It is because the superalloys cannot form either oxidation or hot corrosion resistant protective scale because of high Re content and other new alloying elements. It clearly stresses the need to apply intelligent protective coatings for their protection under high temperature conditions as the gas turbine blades experience high temperature oxidation and hot corrosion.

2.7 Surface Coating Technologies

The blade coatings are usually of either diffusion coatings (aluminides) or MCrAlY type (where M is Ni or NiCo) (overlay coatings). These coatings can provide protection against oxidation and hot corrosion and act as bond coatings for zirconia-based thermal barrier coating (TBC) systems. In both the cases, slow growth rates and optimum adherence of the alumina and chromia scales formed on the coatings during high temperature exposure are of significance for component life. These requirements can be fulfilled only by using coatings with sufficiently high aluminum and chromium contents. It will ensure protective alumina and chromia scale formation and rehealing, after oxide spallation/reaction with the environment. The life of a coating is mainly limited by aluminum and chromium depletion that occur upon their consumption as a result of alumina and chromia scale growth and also on the repeated spallation and rehealing during the oxidation process. On reaching a stage where the aluminum and chromium level in a bond coating falls below the level at which protective alumina and chromia scale cannot be formed preferentially, faster interaction between the corrosive species present in the environment and the nonprotective oxides of other constituents of the bond coating occurs. This phenomenon significantly affects the coating life under hot corrosion conditions. Further, the constituents of ceramic TBCs react easily with the corrosive species and shorten the coating life significantly. Therefore, the composition of coating is extremely valuable.

2.7.1 Diffusion coatings

In the diffusion coating application process, aluminum is made to react at the surface of substrate, forming a layer of mono-aluminide. For coatings applied over Ni-based superalloys, nickel aluminide is the resulting species. This coating and surface modification process is one of the most widely used for tailoring the surface properties of components.

The most notable improvement in the diffusion coatings has been the incorporation of platinum in aluminide coatings.[45–47] This process involves the deposition of platinum by electrochemical method followed by aluminizing at the suitable temperature for the required period. These coatings became the accepted standard for turbine hot components to combat oxidation as well as hot corrosion. The principal reason for superior performance of these coatings is that the coefficient of thermal expansion of the coating is lower compared to that of underlying superalloy. In addition, platinum enhances the activity of aluminum and allows the formation of continuous alumina scale during high temperature exposure coupled with exceptional adherence, thereby prolonging the life of turbine blades considerably. Failure of coatings under turbine service conditions takes place due to interdiffusion between the coating and the substrate, with the loss of protective capability. Although diffusion coatings are well bonded to the substrate, they have limited compositional flexibility and their usefulness is strongly dependent on the substrate chemistry.

2.7.2 Overlay coatings

To develop coatings with compositions nominally independent of substrates and with capabilities for tailoring to a wide range of requirements for gas turbine applications, overlay coatings emerged. Coatings of this type are generally called MCrAlY (where M stands for Ni or NiCo) and essentially comprise a mono-aluminide component contained in a more ductile matrix of a solid solution. The supply of aluminum for the formation of protective alumina scale comes largely from the dispersed mono-aluminide phase during the useful life of such coatings. Overlay coatings are typically well bonded and have a wide compositional flexibility. Research and development on this type of coatings has led to a variety of compositions, with improved scale adherence. The function of all coatings is to provide a surface reservoir of critical elements that will form highly protective and adherent oxide layers, thus protecting the underlying superalloy from oxidation as well as hot corrosion. Further, MCrAlY based bond coatings play a significant role in providing rough surface for the application of TBCs and to provide protection for the alloy from oxidation and/or hot corrosion. The MCrAlY coatings have been studied extensively for over two decades due to their proven performance over varieties of superalloys in different

applications.[48–51] The effect of aluminum in forming a thermodynamically and chemically hot corrosion resistant layer and thereby improving the life of the components by reducing mass gain in MCrAlY coatings appears crucial. Further, optimum content of aluminum in the coatings is extremely necessary to enhance its lifetime. In fact, it only decides the lifetime of coatings and hence the essentiality of aluminum reservoir in the coatings.

Figure 2.18 illustrates the influence of aluminum on weight loss in the MCrAlY based coating model alloys. It is apparent that aluminum plays a vital role in affecting the hot corrosion resistance of MCrAlY alloys though the concentration of other alloying elements remains constant. The weight loss is maximum for the model alloy containing 6% aluminum, decreases with the increase in aluminum content to 9%, and minimum weight loss is observed for the alloy containing 12% aluminum. The behavior is same for all the model alloys irrespective of cobalt content, that is, whether the cobalt is 10% or 20% (Figure 2.18). Therefore, the minimum amount of aluminum required to be present in the MCrAlY based bond coatings is 9%. It is particularly essential to mention that the optimum content of aluminum required for providing exceptional hot corrosion resistance is 12%, although its effect is marginal when compared with 9% aluminum containing alloys.[36]

It is also necessary to mention that the combination of cobalt and aluminum contents is a must to exhibit appreciable hot corrosion resistance. The recent results clearly showed that cobalt plays a significant role in supporting aluminum to form a chemically and thermodynamically stable oxide scale. The optimum amounts of aluminum and cobalt are to be present in the MCrAlY bond coatings. Hence, the combination of cobalt and aluminum in association with chromium, yttrium, and nickel provides excellent hot corrosion resistance.[38,39]

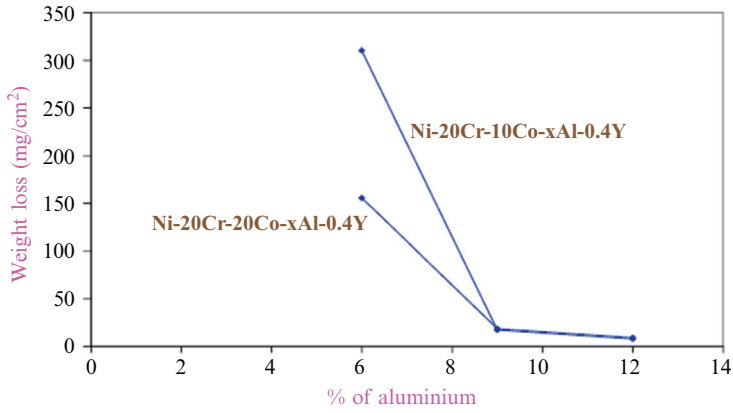


Figure 2.18 Optimum content of aluminum required in MCrAlY coatings for their hot corrosion resistance.[36]

Another crucial aspect is the selection of suitable surface engineering technique by which the coatings are applied. The life of a coating depends not only on coating composition, but also on the surface engineering technique employed for applying the coating. Therefore, selection of appropriate surface engineering technique as well as suitable coating composition (intelligent) becomes a challenging task.

2.7.3 Surface engineering techniques

The following are the most common surface engineering techniques available at present:

(a) Electrodeposition
(b) Diffusion coating processes
(c) Thermal spray techniques
(d) Ion implantation
(e) Hardening and cladding
(f) Selective surface hardening by transformation of phase
(g) Vapor deposition

Electrodeposition, diffusion, and thermal spraying techniques are widely in use to improve the surface of components for hot corrosion resistance. Particularly, thermal spray and vapor deposition techniques are the most efficient techniques for prolonging the life of components significantly.

2.7.3.1 Thermal spraying processes

The coatings applied by these processes have advantage over other techniques. Thermal spraying processes can broadly be divided into the following techniques:

(i) Flame Spraying
(ii) Arc Spraying
(iii) High Velocity Oxy-Fuel Spraying
(iv) Detonation Gun
(v) Air Plasma Spraying
(vi) Vacuum Plasma Spraying

Flame Spraying: In this process, an oxygen-acetylene mixture is passed through a nozzle and ignited to form a combustion flame. In order to form a deposit, the coating powder or wire is fed into the flame, accelerated, and projected onto the substrate. The combustion flame temperature is limited to 3000 °C, and gas particle velocities are relatively low.

Arc Spraying: This process involves the production of molten particles at the tips of two consumable wires via resistance heating. The coating material is subsequently

atomized and projected onto the substrate by a compressed air jet. The process is limited to the spraying of conductive wires relatively cheaply and can achieve high deposition rates.

High Velocity Oxy-Fuel Spraying (HVOF): This process involves combustion of a fuel gas with oxygen at high pressure. This creates high velocity flame propelling powdered coating materials onto a substrate. This technique can produce high-quality coatings for gas turbine applications.

Detonation Gun Spraying: D-Gun and Super D-Gun are developed by Union Carbide. These guns use the energy released by a controlled series of oxygen-acetylene to heat and accelerate the coating powder so as to impart high velocity and propulsion to the powder onto the substrate. The resulting coatings are highly dense and of high quality with a low content of oxide and unprocessed particles.

Air Plasma Spraying (APS): The APS utilizes a DC arc struck between a central inert cathode and an annular copper anode. Moreover, an inert gas is fed into the arc to form high temperature plasma. Powder is fed into the plasma and is ejected at a high velocity towards the substrate.

Vacuum Plasma Spraying (VPS): This process has several advantages over APS. The problems associated with air contamination in the plasma jet are eliminated. Moreover, the plasma jet is longer than air and can achieve ~400-600 ms^{-1} particle velocity that helps in depositing high purity and dense material. A further advantage is coating adhesion.

Kuroda et al. recently developed a novel coating technique called a "warm spray" process that incorporates the advantages of both HVOF and cold spray.[52] Further developments may enable them to develop coatings with enhanced hot corrosion resistance.

2.7.3.2 Electron beam physical vapor deposition (EB-PVD) processes

The electron beam-PVD process has made the most significant impact over the PVD processes in respect of coating rotating blades. The microstructure of the coating is controlled extremely closely in this process, and coating process is slow compared to conventional PVDs. Thermal barrier oxide coatings obtained with this process have a unique columnar structure with high in-plane compliance, which tends to have higher thermal conductivity and has shown to survive a longer thermal cycle life as compared to plasma-sprayed TBC. Table 2.4 provides the comparison of different processes and their limitations.

Figure 2.19 presents a hot corroded diamalloy coated IN 738 with HVOF technique. The surface morphologies of coated superalloy IN 738 (Figure 2.20) revealed poor performance of the coating, indicating that the composition of a coating plays a vital role.

TABLE 2.4 Comparison of Thermal Spray and EB-PVD Processes[53]

Coating Type	Advantages	Disadvantages/Limitations
Diffusion (e.g., aluminides)	Simple to produce, proven ability <900 °C, inexpensive	Thickness limited to 50 µm. Brittle at <750 °C and degrade by interdiffusion. Available compositions are limited
Plasma overlays	High rates of coating and a wide range of compositions are available. Thickness not process limited (100 µm)	Rough surface and single line of sight coating versus EB coatings. Thin multilayers more difficult than EB. About 15% porosity and degrade by interdiffusion
EB-PVD overlays	Good control of microstructure, low contaminant level and control of composition within limits. Layered and graded coatings easily achieved, and multicomponent processing is possible	Low rates of deposition and expensive process. Degrade by interdiffusion
Plasma spray thermal barrier	High rate of coating and a wide range of compositions are available. Layered and graded coatings are possible. Porosity is an advantage and not limited by interdiffusion	Single line of sight coating and difficult to modify microstructure. High stresses generated in coatings
EB-PVD thermal barrier	Good control of microstructure and low contamination level. Layered and graded coatings are possible and not limited by interdiffusion	Low rate of deposition and multiple component processing are possible. Expensive process and generates high stresses, but relieved by structure control

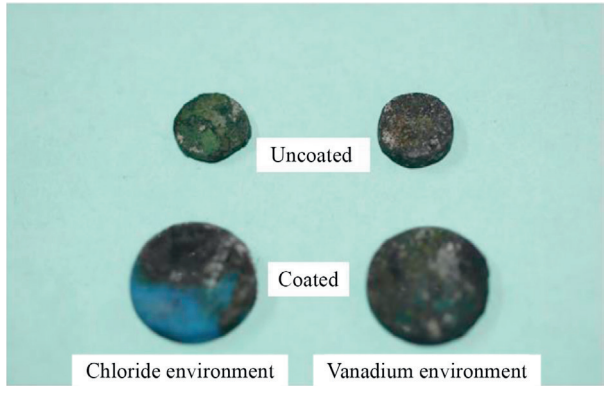


Figure 2.19 Hot corroded diamalloy (HVOF) coated superalloy IN 738 LC in chloride and vanadium environments under type-I conditions.

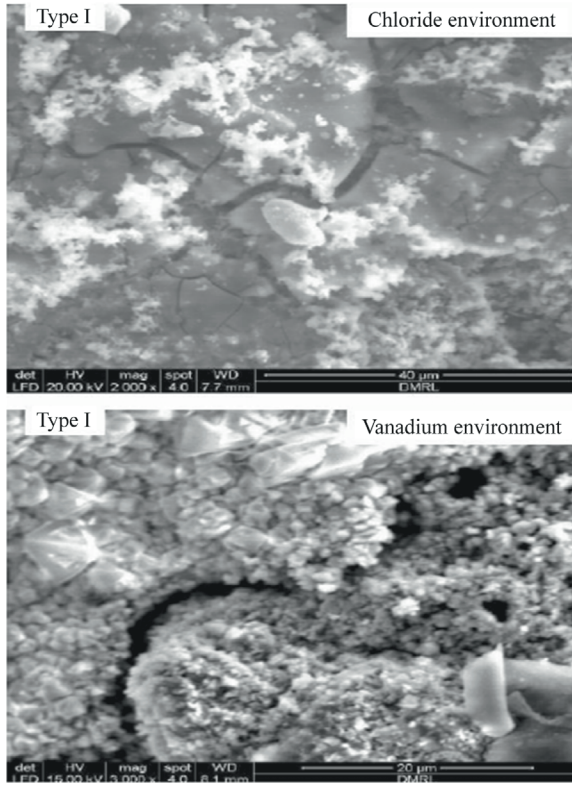


Figure 2.20 Surface morphologies of hot corroded diamalloy (HVOF) coated superalloy IN 738 LC in different environments under type-I conditions.

2.8 Influence of Major and Trace Elements

Traces of silicon and hafnium make the MCrAlY coating highly susceptible to hot corrosion. Traces of silicon or hafnium modify oxide growth rate and the composition of oxide scale, and consequently reduce the coating life significantly. The fluxing of oxide scale also becomes easy when traces of silicon or hafnium is present in the scale. The underlying mechanism is that hafnium and silicon are present in the grain boundaries of alumina scale leach out selectively by readily reacting Si and Hf with chlorine, vanadium, sodium, and sulfur present in the environment to form corresponding compounds. This results in dislodging the grains of alumina scale and creates instability of the oxide scale and thereby reduces the life of coatings significantly. Further, the oxides of silicon and hafnium are soluble in molten basic sulfate, and the basic fluxing dominates in the high temperature hot corrosion region (850-950 °C).

The reaction mechanisms leading to reducing the life of coatings containing silicon or hafnium are given below:

$$HfAl_2O_3 + Na_2SO_4 + NaCl = NaAlO_2 + HfCl_4 + SO_3$$
$$HfAl_2O_3 + Na_2SO_4 + NaCl + V_2O_5 = NaAlVO_2 + HfCl_4 + SO_3$$
$$SiAl_2O_3 + Na_2SO_4 + NaCl = NaAlO_2 + Na_2SiO_3 + SO_3$$
$$SiAl_2O_3 + Na_2SO_4 + NaCl + V_2O_5 = NaAlVO_2 + Na_2SiO_3 + SO_3$$

Kawagishi et al. have proposed an equivalent coating system for high temperature corrosion resistance of Ni-based superalloys.[54] This coating composition is designed to be in thermodynamic equilibrium with the substrate so that no interdiffusion can occur. It is also reported that this coating technique helps in repair of turbine blades. However, hot corrosion resistance of this coating under varied gas turbine engine conditions is yet to be proved because the coating composition is similar to the superalloy.

2.9 Concept of Intelligent Coatings

A primary requirement for a coating to use in high temperature applications is slow growth rates and optimum adherence to the protective scales that form on the metallic coatings during high temperature exposure/service conditions. The gas turbine engines experience both types of hot corrosion as well as oxidation. There is a need to develop intelligent or smart coatings to effectively combat high temperature corrosion problems and to obtain maximum efficiency with reduced failures.

If a single coating can operate successfully over a range of temperatures with different forms of corrosion attack such as type-I and type-II hot corrosion and high temperature oxidation, the coating essentially responds to local temperature in such a way that it will form either an alumina or a chromia protective scale as appropriate. High purity alumina scales offer significant protection against high temperature oxidation and type-I hot corrosion as do chromia scales against type-II hot corrosion. Ideally a single coating should satisfy both the requirements. It Alumina and chromia scale formation is possible for a coating only if it contains chromium- and aluminum-rich graded coatings (Figure 2.21). The base coating should be a standard MCrAlY coating enriched with aluminum at its outer surface and a chromium-rich layer at its inner surface. Under high temperature oxidation and type-I hot corrosion conditions, the outer layer of the coating forms alumina scale, which provides protection and it, offers less protection under low temperature conditions. Under type-II hot corrosion conditions, a chromium-rich layer forms chromia scale at a faster rate and provides protection. Thus, the intelligent coating can provide optimum protection

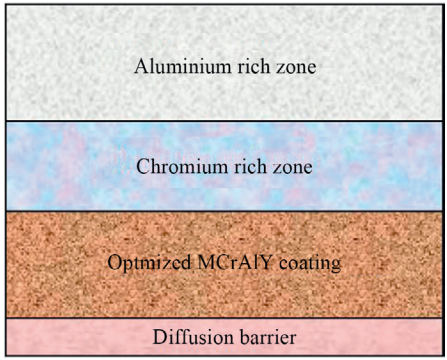


Figure 2.21 Microstructure of an intelligent coating.

by responding suitably to the temperatures that are encountered under actual service conditions of gas turbine engines. This optimum protection is possible because of the formation of the most suitable protective oxide scale in each temperature range of operation envisaged. In this sense, the coating responds to its environment in a pseudo-intelligent manner and hence the name **Intelligent Coating**.

In essence, the development of intelligent coatings design involves the preparation of multilayered coating consisting of an appropriate MCrAlY base, enriched first in chromium and then aluminum to provide a chemically graded structure. The intermediate chromium-rich phase provides protection under low temperature hot corrosion conditions; while the aluminum-rich surface layer provides resistance to high temperature oxidation and type-I hot corrosion. Diffusion barrier coatings prior to chromium- and aluminum-rich layers help in preventing interdiffusion of coating and substrate elements. Thus, the intelligent coating permits operation of gas turbine engines over a wide range of temperatures successfully for more than the designed life and helps in enhancing the efficiency significantly by effectively preventing oxidation, type-I and type-II hot corrosion that are normally experienced in gas turbines.[55–57]

2.9.1 Preparation and Selection of a Suitable Surface Engineering Technique

The development of intelligent coatings is a challenging task. Moreover, selection of suitable surface engineering techniques to produce a quality coating is extremely essential. Probably, selection of a single technique may not help, but a combination of techniques could be useful. Further, order of usage of selected techniques is also vital. Therefore, one has to be extremely careful in selection and utilizing the techniques for production of intelligent coatings in order to achieve maximum efficiency. The intelligent coatings can be task-prepared by using a combination of available surface engineering techniques. Among these, sputtering, thermal spraying, diffusion,

electroplating, and laser treatments are more effective in producing intelligent coatings. Application of a suitable diffusion barrier on the superalloy followed by an optimized MCrAlY coating and chromized treatment to achieve about 70% Cr rich coating and then electroplating of platinum or palladium, followed by pack cementation, enables the desired graded structure. However, detailed research is needed to establish the process parameters of each surface engineering technique, coating thickness, suitable annealing treatments, and so on, to obtain a coating of desired characteristics.

The microstructures of coatings play a significant role in enhancing the life of components. Therefore, obtaining an appropriate microstructure by identifying the suitable surface engineering technique is of paramount importance. The selection of technique for coating preparation should be based on the parameters that are controllable to get the required microstructure. As mentioned earlier, the intelligent coating is a graded coating consisting of different zones (Figure 2.21). Each zone has its specific microstructure with definite composition. The top layer is diffusion-type aluminide, and second is chromium-rich layer followed by suitable MCrAlY coating and a diffusion barrier layer at the bottom. The composition of each zone requires detailed analysis to understand the effect of intelligent coating. The diffusion-type aluminide layer should contain a high amount of aluminum, the second layer should be about 70% rich in chromium, the third layer as that of MCrAlY coating composition, and the bottom diffusion layer should contain heavy elements. The microstructure of each zone varies depending on the coating composition and surface engineering technique used.

2.9.2 Techniques for assessment of intelligent coatings

The following laboratory techniques have been in use for assessing a variety of materials and intelligent coatings for gas turbine engine applications:

(i) Burner rig test
(ii) Furnace test
(iii) Crucible test
(iv) Thermogravimetric test
(v) Electrochemical methods

Burner rig test: This test simulates the operating conditions in gas turbine engines, and the gas composition, pressure, velocity, and temperature. In this test, rigs are composed of a combustion chamber from a small turbine, supplying air from compressors and burning fuel in the usual way. Salt can be sprayed into the combustion chamber. The hot exhaust gases are passed into the sample chamber, where several specimen coupons are placed and rotated in the gas stream. Here, the test variables (such as gas pressure, velocity, sample temperature, salt concentration, and fuel-to-air ratio) can be selected to simulate aero-, marine-, and land-based gas turbine engine's operation.

This test was used extensively for evaluation of a variety of coated and uncoated materials for hot corrosion resistance. It was also established that the tested coatings displayed generally similar behavior during the service. Therefore, this test is more appropriate for evaluating different intelligent coatings to get comparable results with the service conditions of gas turbine engines.

Furnace test: This test employs a furnace with two zones whose temperatures can be controlled independently. The intelligent-coated specimen is placed in one zone, and a crucible containing the test salt is kept in the other zone. With the help of a carrier gas, the vaporized salt is transferred from one zone to other, where it deposits on the intelligent-coated specimen. In this manner, the deposition of salt per unit time can be strictly controlled. In a modified method known as "Dean Test," the corrosion conditions can be controlled from exceptionally mild to extremely severe by simply altering the temperature differential within the two zones. This test was used mainly to study kinetics of various coated and uncoated materials in different environments.

Crucible test: This method involves direct immersion of the intelligent-coated sample to half its length in molten salt in air atmosphere and measurement of weight change to monitor the reaction rate. The gas could be bubbled through the melt or passed over the sample to simulate an oxidizing or reducing environment. This test was used for evaluation of a number of uncoated and coated Ni-based superalloys for hot corrosion resistance. The corrosion test conditions are more severe than that in normal operating conditions of the engines, but it is a simple and helpful test for screening the intelligent coatings.

Thermogravimetric test: It is also called "salt coated test." In this test, an intelligent-coated sample is coated with saturated salt solution, then dried, weighed, and placed in a heated furnace. The sample weight is continuously recorded. In most cases, the weight increases as oxidation proceeds and the vaporization rate is small compared with the oxidation rate. This method can be used for determining the hot corrosion kinetics of different intelligent coatings because the experimental parameters such as gas composition, temperature, and salt loading can be controlled easily and precisely.

Electrochemical methods: This method involves measurement of corrosion current as a result of oxidation-reduction reaction continuously and provides instantaneous corrosion rates. The net reaction is the oxidation of intelligent coating to form oxide scales and the reduction of SO_4^{2-} to a lower oxidation state. Generally, corrosion is accelerated when the salt film is in molten stage such that the intelligent coating and gas are physically separated by the ionically conducting fused salt. Fused sodium sulfate is a dominant ionic (Na^+) conductor like in normal solutions. Thus, the reaction must involve electrochemical steps and hence this method is most ideal for assessing various intelligent coatings as well as other materials for hot corrosion resistance.

The electrochemical polarization of intelligent coatings in molten salts can cause corrosion attack, which is qualitatively similar to that found for a thin salt film in a combustion-product environment. In addition, the results from 600 h of a burner rig test are well comparable with a 4-h electrochemical test method. It proves that electrochemical techniques are extremely helpful in evaluating the intelligent coatings and other materials at a faster rate compared to other tests developed so far. The technique also helps to study reaction mechanisms and online monitoring of intelligent coatings in the actual plants. The merits and demerits of each technique are presented in Table 2.5.

2.9.3 Performance of a developed intelligent coating

Recently, an intelligent metallic coating has been developed, which is optimized compositionally and promotes an appropriate protective scale formation depending on the surrounding environmental conditions that enhance the durability of TBC, and, in turn, the life of CM 247 LC superalloy components. The performances of various compositions of MCrAlY bond coatings applied on CM 247 LC superalloy (without

TABLE 2.5 Comparison of Hot Corrosion Evaluation Techniques

Technique	Advantages	Disadvantages/Limitations
Burner rig test	Simulates gas composition, pressure, velocity, and temperature of gas turbine engines	Complex process and requires long running time. Difficult to control all the parameters accurately
Furnace test	Corrosion conditions can be controlled depending upon the requirements, that is, severe or mild corrosion	Difficult to maintain salt deposition rate for longer times
Crucible test	Most simple and highly useful for preliminary screening of the coatings and materials	Corrosion is severe for alloys or coatings having low or intermediate resistance to hot corrosion
Thermogravimetric test	Precise weight gain measurement Possible under different test conditions, that is, gas composition, temperature, salt composition, etc.	Not useful for predicting the life of coatings and superalloys
Electrochemical test	Fast and useful for ranking the materials based on the oxidation-reduction phenomenon	Yet to be established fully

TBC) were evaluated systematically under type-I conditions in simulating gas turbine engine environments. Among the coatings, NiCoCrAlY coating exhibited a maximum life of more than 300 h (Figure 2.22). The high performance of this coating is due to its ability to form a continuous, adherent, and protective alumina scale on the surface of the bond coating during high temperature corrosion at 900 °C (Figure 2.23).

Table 2.6 presents the life of uncoated CM 247 LC superalloy, intelligent coating as well as different thicknesses of zirconia-based TBCs at 900 °C in simulating gas turbine engine environments. The results indicate that 100 µm thick TBC improved the superalloy life by 450 times to that of bare superalloy. It was also evident that 300 µm thick TBC in association with compositionally optimized 125 µm thick NiCoCrAlY bond coating (intelligent bond coating) enhanced the superalloy life by about 600 times, which was found to be optimum. Thick ceramic coatings could not help in improving the hot corrosion resistance of superalloys further due to adherence problems associated with spallation at higher temperatures. The maximum life of NiCoCrAlY (intelligent coating) + 300 µm thick TBC was attributed to the formation of protective alumina and chromia scales, not only on the surface of bond coating but also on the TBC surface (Figure 2.24). Furthermore, neither

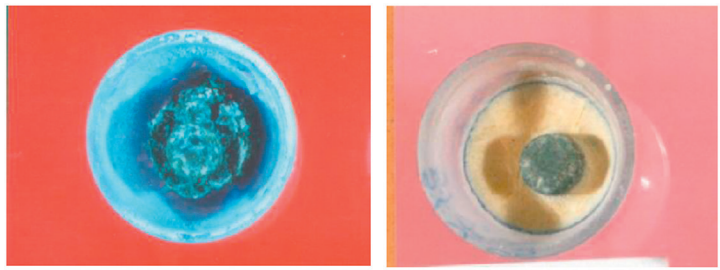


Figure 2.22 The performance of intelligent coating: (a) without intelligent coating (<2 h); (b) with intelligent coating (>300 h).

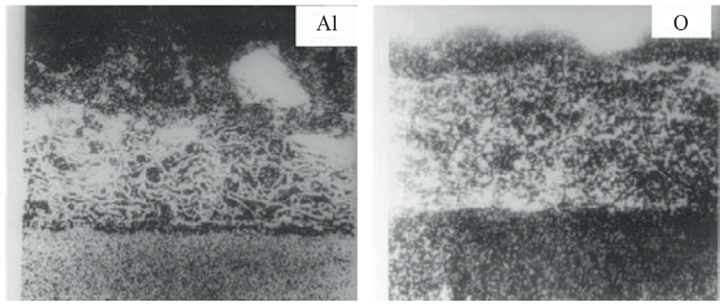


Figure 2.23 Performance of intelligent coating.

TABLE 2.6 Performance of Intelligent Coating on CM 247 LC Alloy + Different Thicknesses of Thermal Barrier Coatings in Vanadium Environments Under Type-I Hot Corrosion Conditions

Type of Coating	Life (Hours)
Uncoated superalloy	<2
Intelligent coating	300
Intelligent coating +100 µm TBC	910
Intelligent coating +200 µm TBC	975
Intelligent coating +300 µm TBC	1175
Intelligent coating +400 µm TBC	1170

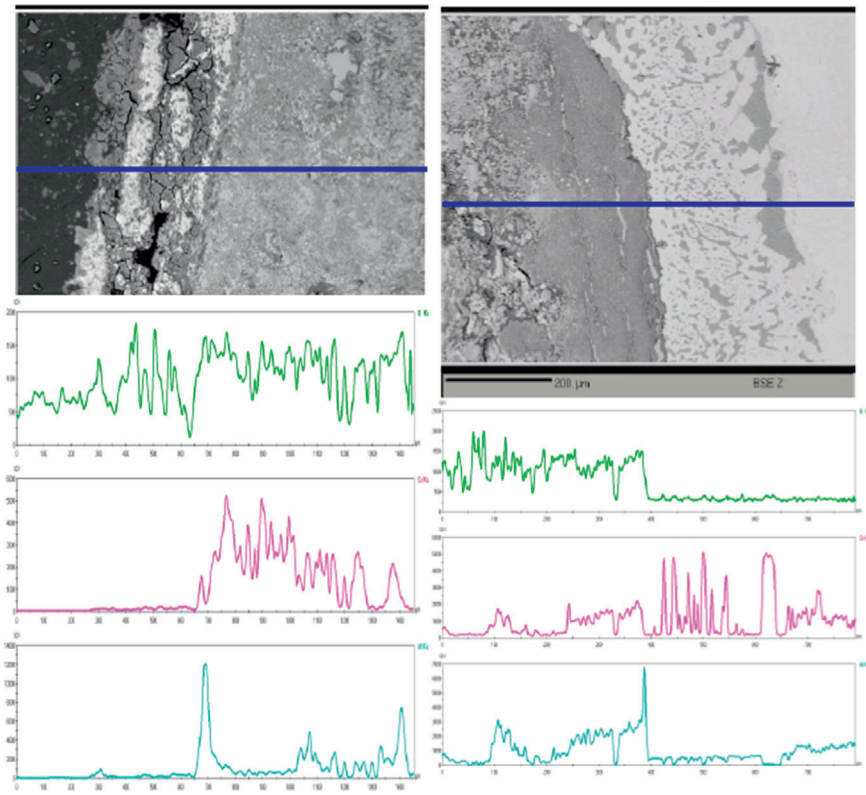


Figure 2.24 EPMA data of hot corroded two-layered intelligent coating showing alumina and chromia scale formation both on top coating surface as well as at the interface.

sulfur nor oxygen was diffused into the coating, indicating an excellent protection provided by 300 µm thick TBC in association with intelligent bond coating to the CM 247 LC superalloy. It is known that TBC reduces the temperature of bond coating/substrate by about 200 °C. It indicates that the substrate or bond coating temperature is about 700 °C only. Under such environmental conditions, that is, at 700 °C, the bond coating promoted chromia and alumina scale formation that is clearly observed in Figure 2.24. It was also observed that the bond coating promoted protective alumina scale formation at 900 °C in the same environments (Figure 2.23). It indicates that the NiCoCrAlY bond coating forms alumina scale at 900 °C, that is, without TBC and chromia and alumina scale in the presence of TBC at the same environmental conditions and provides maximum life to the TBC which in turn i.e. the superalloy components.

Hence, the developed bond coating exhibited intelligence behavior both in the presence and absence of TBC and formed suitable protective scales and hence was named as intelligent bond coating. Other noteworthy observations are the formation of protective alumina and chromia scales on the surface of TBC as well as the prevention of diffusion of corrosive elements like chlorine, vanadium, sulfur, and oxygen. Thus, an intelligent bond coating was successfully developed for TBCs that promote appropriate protective scales preferentially depending on the environmental conditions and enhance the life of superalloy components significantly, which is essential for advanced gas turbines for their increased efficiency. Therefore, it is a potential bond coating for advanced gas turbines of different types, that is, marine and industrial, for their protection against high temperature oxidation, type-I and type-II hot corrosion.

2.10 Conclusion and Outlook

Corrosion prevention over the world, both at ambient and high temperatures, is extremely essential as the financial losses are enormous. It is possible only by designing and developing economically viable and environmentally friendly intelligent coatings over the existing coatings. Research in this direction paved the way for the development of intelligent coatings for ambient corrosion prevention. Further research is needed to understand and develop newer and alternative intelligent coating systems. The design and development of intelligent coatings to combat type-I and type-II hot corrosion and high temperature oxidation in gas turbines are challenging problems for scientists and corrosion engineers. The developmental work in this area has successfully resulted an intelligent coating, which provided an excellent protection to the superalloys against all the concerns that are being experienced by all types of gas turbines. Dedicated research is required both at the laboratory level and field to optimize coating composition, thickness, and microstructure. Additionally,

identification of appropriate surface engineering techniques and their priority of use are needed to prove their performance. Finally, advanced processes and intelligent coatings development efforts are extremely necessary to manufacture modern gas turbine engines that could exhibit ever greater efficiency.

References

1. Gurrappa I, Yashwanth IVS, Gogia AK, et al. The significance of corrosion in titanium based alloys for industrial applications. In: Zhang LC, Yang C, editors. Titanium alloys: formation, characteristics and applications. USA: Nova Publishers; 2013, ISBN: 978-1-62808-329-3.
2. Radhakrishnan S, Sonawane N, Siju CR. Epoxy powder coatings containing polyaniline for enhanced corrosion protection. Prog Org Coat 2009;64:383–6.
3. Yan M, Vetter CA, Gelling VJ. Corrosion inhibition performance of polypyrrole Al flake composite coatings for Al alloys. Corr Sci 2013;70:37–45.
4. Sanchez C, Julián B, Belleville P, et al. Applications of hybrid organic–inorganic nanocomposites. J Mater Chem 2005;15:3559–92.
5. Tiwari A, Hihara LH. Effect of inorganic constituent on nanomechanical and tribological properties of polymer, quasi-ceramic and hybrid coatings. Surf Coat Technol 2012;206:4606–18.
6. Tiwari A, Zhu J, Hihara LH. The development of low-temperature hardening silicone ceramer coatings for the corrosion protection of metals. Surf Coat Technol 2008;202:4620–35.
7. www.durr.com. Surface treatment with Aquence.
8. Kumar A, Stephenson LD, Murray JN. Self-healing coatings for steel. Prog Org Coat 2006;55:244–53.
9. Mehta NK, Bogere MN. Environmental studies of smart/self-healing coating system for steel. Prog Org Coat 2009;64:419–28.
10. Koene BE, Own SH, Selde K. Self healing coatings for corrosion control. In: Proceedings of the first international conference on self healing materials, Noordwijk aan Zee, The Netherlands; 2007. p. 1–6.
11. Shulkin A, Stöver HDH. Polymer microcapsules by interfacial polyaddition between styrene–maleic anhydride copolymers and amines. J Membr Sci 2002;209:421–32.
12. Li CY, Liaw SC, Lai VMF, et al. Xanthan gum–gelatin complexes. Eur Polym J 2002;38:1377–81.
13. Brown EN, Kessler MR, Sottos NR, et al. *In situ* poly(urea-formaldehyde) microencapsulation of dicyclopentadiene. J Microencapsul 2003;20:719–30.
14. Samadzadeh M, Hatami Boura S, Peikari M, et al. A review on self-healing coatings based on micro/nanocapsules. Prog Org Coat 2010;68:159–64.
15. Hamdy A, Doench I, Möhwald H. Intelligent self-healing corrosion resistant vanadia coating for AA2024. Thin Solid Films 2011;520:1668–78.
16. Kendig M, Hon M, Warren L. 'Smart' corrosion inhibiting coatings. Prog Org Coat 2003;47:183–9.
17. Su F, Liu C, Huang P. Characterizations of nanocrystalline Co and Co/MWCNT coatings produced by different electrodeposition techniques. Surf Coat Technol 2013;217:94–104.
18. Augustyniak A, Ming W. Early detection of aluminium corrosion via "turn-on" fluorescence in smart coatings. Prog Org Coat 2011;71:406–12.
19. Gurrappa I, Karnik JA. Physical and computer modelling for ship's impressed current cathodic protection (ICCP) systems. Corr Prev Control 1994;41:40–5.
20. Gurrappa I, Karnik JA. Physical scale modelling for cathodic protection of ships. Corr Prev Control 1995;42:43–7.

21. Gurrappa I, Karnik JA. Development of aluminium alloy anodes for cathodic protection of ships. Corr Prev Control 1996;43:77–85.
22. Kulkarni AG, Gurrappa I. Effect of magnesium addition on the surface free energy and anode efficiency of indium activated aluminium alloys. Brit Corr J 1993;28:67.
23. Gurrappa I, Yashwanth IVS. Significance of aluminium alloys for cathodic protection technology. In: Persson EL, editor. Aluminium alloys: preparation, properties and applications. USA: Nova Publishers; 2011. p. 125–42, ISBN: 978-1-61122-727-7.
24. Gurrappa I. Cathodic protection of cooling water systems and selection of appropriate materials. J Mater Process Technol 2005;166:256–63.
25. Khajavi MR, Shariat MH. Failure of first stage gas turbine blades. Eng Fail Anal 2004;11:589–97.
26. Gurrappa I. Hot Corrosion Studies on CM 247 LC alloy in Na_2SO_4 and NaCl environments. Oxid Met 1999;50:353–83.
27. Wang CJ, Lin JH. The oxidation of MAR M247 superalloy with Na_2SO_4 coating. Mater Chem Phys 2002;76:123.
28. Gurrappa I. Influence of alloying elements on hot corrosion of superalloys and coatings: necessity of smart coatings for gas turbine engines. Mater Sci Technol 2003;19:178–85.
29. Gurrappa I, Yashwanth IVS, Gogia AK. The selection of materials for marine gas turbine engines. In: Konstantin Volkov, editor. Gas turbines. USA: Volkov Konstantin; 2012. p. 51–70, ISBN: 979-953-307-816-7.
30. Gurrappa I, Yashwanth IVS, Gogia AK. The behaviour of superalloys in marine gas turbine engine conditions. J Surf Eng Mater Adv Technol 2011;1:144–149.
31. Gurrappa I, Yashwanth IVS, Burnell-Gray JS. Sulphidation characteristics of an advanced superalloy and comparison with other alloys intended for gas turbine use. Metal Mater Trans A 2013;44:5270–80. http://dx.doi.org/10.1007/s11661-013-1859-8.
32. Zhang X, Rapp RA. Electrochemical Impedance of a platinum electrode in fused Na_2SO_4 melts in SO_2-O_2 environments. J Electrochem Soc 1993;140:2857–62.
33. Rapp RA. Hot corrosion of materials. Pure Appl Chem 1990;62:113–22.
34. Rapp RA. Hot corrosion of materials: a fluxing mechanism? Corr Sci 2002;44:209–21.
35. Natesan K. High-temperature *corrosion* in coal gasification systems. Corrosion 1985;41:646–55.
36. Eliaz N, Shemesh G, Latanision RM. Hot corrosion in gas turbine components. Eng Fail Anal 2002;9:31–43.
37. Gurrappa I. Effect of aluminium on hot corrosion resistance of MCrAlY based bond coatings. J Mater Sci Lett 2001;20:2225–9.
38. Gurrappa I. Development of MCrAlY based bond coatings for hot corrosion resistance. Surf Coat Technol 2001;139:272–80.
39. Gurrappa I. Hot corrosion behaviour of protective coatings on CM 247 LC superalloy. Mater Manuf Process 2000;15:761–9.
40. Gurrappa I. Overlay coatings degradation – an electrochemical approach. J Mater Sci Lett 1999;18:1713–21.
41. Gurrappa I. Thermal barrier coatings for hot corrosion resistance of CM 247 LC super alloy. J Mater Sci Lett 1998;17:1267–72.
42. Gurrappa I. Hot corrosion behaviour of Nimonic-75. J High Temp Mater Sci 1997;38:137–44.
43. Yashwanth IVS, Gurrappa I, Murakami H. Oxidation behaviour of a newly developed superalloy. J Surf Engg Mater Adv Technol 2011;1:130–5.
44. Moniruzzaman M, Murata Y, Morinaga M, et al. Prospect of Ni based super alloys with lo Cr and high Re contents. ISIJ Intern 2002;42:1018–125.
45. Gurrappa I. Platinum aluminide coatings for oxidation resistance of titanium alloys. Platinum Met Rev 2001;45:124–31.

46. Gurrappa I, Gogia AK. Development of oxidation resistant coatings for titanium alloy, IMI 834. Mater Sci Technol 2001;17:581–7.
47. Gurrappa I. High performance coatings for titanium alloys to protect against oxidation. Surf Coat Technol 2001;139:216–21.
48. Leyens C, Fritcher K, Peters M, et al. Transformation and oxidation of a sputtered low-expansion Ni-Cr-Al-Ti-Si bond coating for thermal barrier systems. Surf Coat Technol 1997;94–95:155–61.
49. Brandl W, Grabke HJ, Toma D, et al. The oxidation behaviour of sprayed MCrAlY coatings. Surf Coat Technol 1996;86–87:41–50.
50. Beele W, Czech N, Quadakkers WJ, et al. Long-term oxidation tests on a re-containing MCrAlY, coating. Surf Coat Technol 1997;94–95:41–8.
51. Wang QM, Wu YN, Ke PL, et al. Hot corrosion behavior of AIP NiCoCrAlY(SiB) coatings on nickel base superalloys. Surf Coat Techonol 2004;186:389–97.
52. Kuroda S, Kawakita J, Watanabe M, et al. Warm spraying—a novel coating process based on high-velocity impact of solid particles. Sci Tech Adv Mater 2008;9:33002.
53. Gurrappa I, Yashwanth IVS, Murakami H, Kuroda S. The importance of hot corrosion and its effective prevention for enhanced efficiency of gas turbines, In: Gurrappa I, editor. Gas Turbines. USA: INTECH Publishers (In press).
54. Kawagishi K, Sato A, Harada H. A concept for the EQ coating system for nickel-based superalloys. JOM 2008;60:31–5. www.tms.org/jom.html.
55. Nicholls JR, Simms NJ, Chan WY, et al. Smart overlay coatings – concept and practice. Surf Coat Technol 2001;149:236–44.
56. Gurrappa I. Identification of a smart bond coating for gas turbine engine applications. J Coat Technol Res 2008;5:385–91.
57. Gurrappa I. Design and development of smart coatings for aerospace applications. *Final report*, European Commission; July 2008.

Chapter 3

Smart Inorganic and Organic Pretreatment Coatings for the Inhibition of Corrosion on Metals/Alloys

Peter Zarras, John D. Stenger-Smith
Naval Air Warfare Center Weapons Division (NAWCWD), Polymer Science and Engineering Branch (Code 4L4200D), 1900N. Knox Road (Stop 6303), China Lake, CA, USA

3.1 Introduction

Metals and alloys play a significant role in today's modern world. Metals and alloys have always had a role in past civilizations, but today's complex world requires a variety of coated metals/alloys having multifunctional properties (smart properties). In order for metals and their alloys to effectively survive in many harsh operating conditions, coatings must be used to provide not only surface protection but also a decorative finish. In fact most everyday products are made usable and saleable by having a suitable coating via a surface treatment. Treatments of metals/alloys can impart surface

Intelligent Coatings for Corrosion Control
Copyright © 2015 Elsevier Inc. All rights reserved.

protection of the material, which renders the product/material useful, inhibiting corrosion while retaining economic value. All of these factors have lasting economic impact that contributes to the health and economic well-being of today's modern societies.

3.1.1 Corrosion—definition

Corrosion is normally defined as the "attack on a metallic material by reaction with its environment."[1] Usually one refers to metals when describing corrosion, but nonmetals such as ceramics, plastics, rubber, and so on, can also undergo destruction or deterioration when exposed to various environments. For purposes of this review we will restrict our examination to aqueous/wet environments and methods used to mitigate their corrosive effects.

As a general review we will introduce the several types of corrosion for metals/alloys and their various forms. Corrosion can be divided into three main groups:

- Wet corrosion
- Corrosion in other fluids
- Dry corrosion

"Wet corrosion" refers to metal corrosion occurring in a wet/aqueous environment.[2] The process is almost always electrochemical, and it occurs when two or more electrochemical reactions take place on a metal surface. When a metal is exposed to a corrosive wet/aqueous environment, the metallic nature of the metal is fundamentally changed into a nonmetallic form becoming dissolved species or solid corrosion products. The energy of the system is lowered as the metal converts to a more stable form, in this case nonmetallic corrosion products. This electrochemical process can occur uniformly or nonuniformly across the metal surface, which is called the "electrode" and the ionically conducting liquid is called the "electrolyte." A classic example of this process is the rusting of a steel substrate: the iron metal is converted into a nonmetallic form called "rust."

"Corrosion in other fluids" refers to the corrosion of metals/alloys in nonaqueous environments, such as fused salts sometimes referred to as molten salts.[3] In addition corrosion can also occur in liquid metals.[4] Corrosion in fused salts such as nitrates, halides, carbonates, sulfates, hydroxides, and oxides can cause profound attack on metal alloys via several mechanisms: (1) pitting because of electrochemical attack, (2) mass transport due to thermal gradients, (3) reaction of the constituents of the fused salt with the metal alloy, and/or (4) reactions with impurities present in the fused salt. In addition to fused salts, exposure of metal alloys to liquid-metal environments can cause severe corrosion. Liquid metals are used in industrial applications such as high temperature reducing agents or as coolants due to their excellent heat transfer properties. Corrosion as a result of exposure to liquid-metals can be caused by dissolution, impurity or interstitial reactions, alloying, and compound reduction.

"Dry corrosion" refers to corrosion affecting metals/alloys that are exposed to air or other aggressive gases.[5] For a relatively small number of metals, exposure to gases does not result in corrosion; however, for most metals, exposure to very high temperature gases increases the corrosion rate resulting in corrosion failure. The figure below shows the elements necessary for corrosion under different environments (Figure 3.1).

The three main types of corrosion have been identified and described in detail; we can now turn our attention to the most common forms of corrosion, which are found in wet or aqueous environments. There are eight forms of corrosion, which can be identified based on the appearance of the corroded metal or alloy. These corrosion types are listed below:

- Uniform or general corrosion
- Pitting corrosion
- Crevice corrosion (includes corrosion under tubercles or deposits and filiform and poultice corrosion)
- Galvanic corrosion
- Erosion-corrosion (cavitation and fretting corrosion)
- Intergranular corrosion (sensitization and exfoliation)
- Dealloying corrosion (dezincification and graphite corrosion)
- Environmentally assisted cracking corrosion (stress-corrosion cracking, corrosion fatigue, and hydrogen damage)

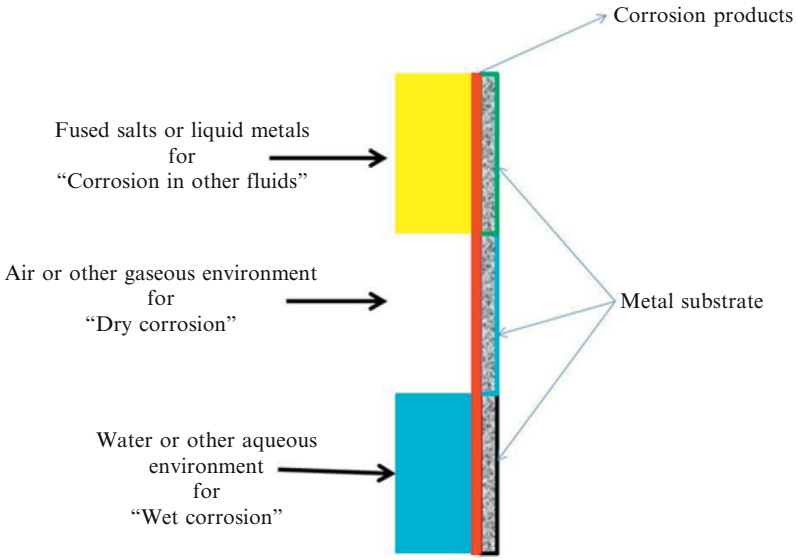


Figure 3.1 Corrosion under different environments.

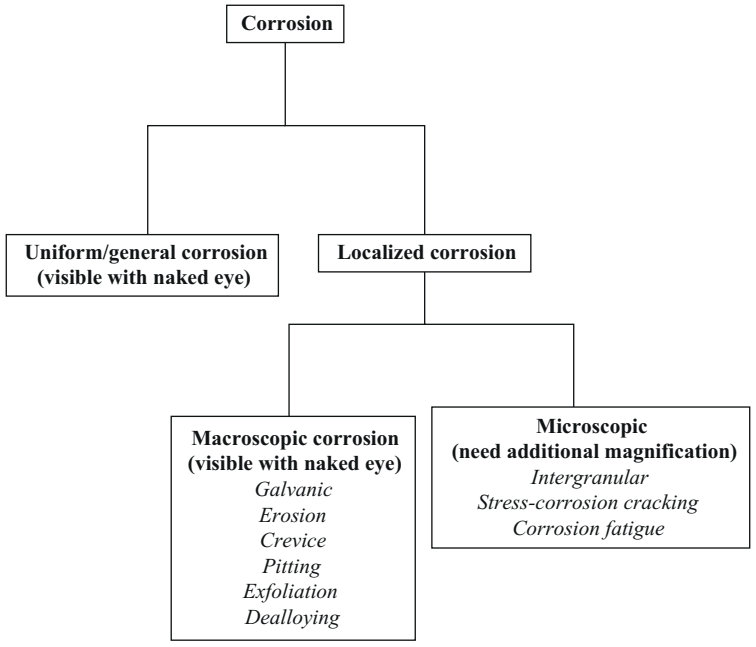


Figure 3.2 Flow diagram representing macroscopic and microscopic forms of corrosion.

The above listed forms of corrosion do not take place independently; there is normally overlap and concurrent forms of corrosion occurring at any time during the corrosion process. Corrosion can also occur at the macroscopic level, which is visible to the naked eye and microscopic level where corrosion occurs in minute amounts and is not visible to the naked eye. In the latter case to examine these effects requires higher magnification before the damage is so severe that it is visible to the naked eye (Figure 3.2). Structural integrity is often compromised after the effects of corrosion become visible to the naked eye.

3.1.2 Costs of metallic corrosion/prevention

Metallic corrosion affects almost every U.S. industrial sector ranging from infrastructure to manufacturing.[6] Aging infrastructure is currently the most important sector affected by corrosion. Recently state and federal agencies have made it a priority to extend their useful lifetimes.[7] Additional sectors (including infrastructure) in today's modern society affected by corrosion are:

- **Infrastructure**—highway bridges, gas/liquid transmission pipelines, waterways/ports, airports, railroads
- **Utilities**—gas distribution, drinking water/sewer systems, electrical utilities, telecommunication

- **Transportation**—motor vehicles, ships, aircraft, railroad cars, hazardous materials transport
- **Production/Manufacturing**—oil/gas exploration/production, mining, petroleum refining, chemical/petrochemical/pharmaceutical production, pulp/paper, agricultural production, food processing, electronics, home appliances
- **Government**—defense, nuclear waste storage

The cost for corrosion repair, maintenance, and replacement affects all facets of the United States and the industrialized world's infrastructure. These costs are not only limited to severe damage compromising public safety, but also environmental damage. Corrosion can disrupt operations requiring extensive repair and replacement of failed assets. Direct corrosion costs in the United States have been estimated at ~$300 billion U.S. dollars annually, accounting for nearly 3.1% of gross domestic product (GDP).[8] Extrapolating to the industrialized world, corrosion costs account for nearly $2.2 trillion U.S. dollars, which represents over 3% of the world's GDP.

3.1.3 Corrosion costs to national economies

As was detailed above in Section 3.1.2, corrosion costs are estimated at ~$300 billion U.S. dollars annually for the United States. This often cited number produced by the National Association of Corrosion Engineers (NACE) Corrosion study of 1998 has been reviewed and updated.[7] G2MT Laboratories have updated this estimate by including both the direct and indirect costs of corrosion and have estimated that all corrosion costs to the U.S. economy are over $1 trillion U.S. dollars for 2013.[9] Additional studies have been conducted throughout the industrialized world. Similar percentage costs to GDP (2-5%) have been found across various economies.[10] Table 3.1 lists several national economies and their associated corrosion costs.

In order to reduce the costs of corrosion affecting various national economies, effective corrosion strategies need to be employed. These existing corrosion-inhibiting technologies include: (1) proper design; (2) proper selection of materials (alloys, metals, plastics, and so on); (3) cathodic protection; and (4) coatings, inhibitors, and

TABLE 3.1 Cost of Corrosion for Several National Economies

Country	Direct Costs of Corrosion ($US Dollars)	Percent (%) of GNP
United Kingdom[11]	$3.2 Billion dollars (1969 US Dollars)	~3.5%
Australia[12]	$0.5 Billion dollars (1973 US Dollars)	~3%
Japan[13]	$9.2 Billion Dollars (1974 US Dollars)	~1.8%

surface treatment. The focus of this review is to provide the reader with an overview of "smart pretreatment coatings," a necessary first step in the prevention and control of corrosion for metals/alloys.

3.2 Designing Smart Coatings for Corrosion Protection

Over the past several decades, coatings have undergone a transformation from simple barrier/decorative coatings to more specialized responsive coatings. These types of coatings that can react or respond to external stimuli are called "smart coatings."[14] Smart coatings have evolved over time from:

- modified coatings with specialized additives, to
- coatings that contain inert ingredients to impart unique properties normally not found in conventional coatings, and finally to
- coatings that can sense and respond to their environment in a consistent and predictable manner.[15]

Nature is the best example of stimuli responsiveness in which living cells have evolved with the ability to respond to continuous and/or intermittent forms of external stimuli. Cells have the ability through reorganization, rebuilding, signaling, and/or reshaping to survive permanent or temporary changes in their environment. This feat is accomplished by the cell membrane as the result of its hierarchically organized multifunctional molecular system.[16] Current research efforts in the coating industry, academia, and government laboratories are trying to develop and adapt the unique features of nature into innovative "smart coatings" for the twenty-first century. These innovative "smart coatings" can have profound effects on everyday living to the most complex of industrial settings.[17]

3.3 Pretreatment Coatings

Pretreatment coatings such as conversion coatings are applied to various metal/alloy surfaces as a first defense against corrosion, but also as an adhesion promoting coating for primers and topcoats.[18] Typically, primers and topcoats do not adhere very well to metal/alloy surfaces without a pretreatment coating. Therefore the following sections will deal exclusively with the pretreatment coating and its ability to act as a "smart coating."

3.3.1 Selecting the proper metal alloy

Prior to depositing the pretreatment coating, the proper metal alloy must be selected. Different metal alloys are known to have various susceptibilities to corrosion

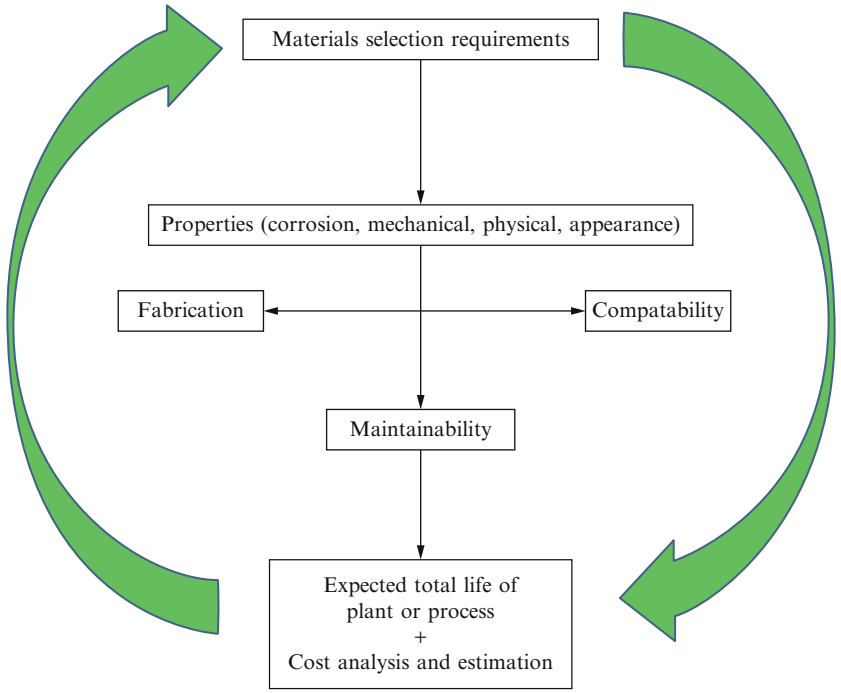


Figure 3.3 Flow diagram for materials selection.

depending on their composition. In order to mitigate these effects, different levels of corrosion protection are needed. The selection criteria are based on the most optimal material required, but this is never a straightforward process. There is the balance of adequate performance versus cost-effectiveness. The selection process is dependent on the type of industry and the corrosive environment that the metal/alloy will be exposed to. Figure 3.3 provides a flow diagram to follow for material selection criteria with the caveat that costs often outweigh the purchase of highly corrosion-resistant metal/alloys in most cases.[19]

3.3.2 Surface Modification

Before we can discuss various "smart pretreatment coatings" on metals/alloys, we must first examine the methods to clean a surface. Before a coating is applied, the surface must be rendered suitable for the pretreatment coating (e.g., conversion coating). This process involves several steps: (1) assessment of surface condition; (2) inspecting for fabrication defects (3) pre-cleaning; and (4) final surface inspection.[20]

The assessment of the surface condition requires inspection of the entire surface to determine the level of contaminants present. These contaminants can be smut,

grease, oil, dirt, rust, corrosion products, salt deposits, and die-release compounds. The presence of these contaminants can dramatically alter the adhesion properties of applied pretreatment coats and subsequent primers and topcoats.

Prior to surface cleaning, any design and/or fabrication defect in the part or substrate to be coated must be removed or repaired. These defects can include excessive pitting, dents, or defects in the metal/alloy component. There are several methods available to remove contaminants from the surface of metals/alloys, which include (1) solvent cleaning, (2) etching cleaners (alkaline and acid etch), (3) desmut or deoxidation, (4) physical cleaning (blasting, abrasion, and/or polishing), (5) acid pickling, and (6) rinsing.[18] Solvent cleaning removes the bulk of smut, grease, oil, dirt, rust, corrosion products, salt deposits, and die-release compounds, but usually requires an additional step such as acid or alkaline etch to remove reactive species. Further cleaning via physical methods is required for the harder steel surfaces where thick or scaly residues are present. This process is not normally used for softer aluminum surfaces. After multiple cleaning processes are complete, a desmut, deoxidation, or pickling step is sometimes used on the metal/alloy to remove any contaminating species rendering an acceptable surface. This provides a surface without weak boundary layers or damage in a reasonable time and cost. A rinsing step is often employed in industrial settings to remove excess reagent(s) and/or solvent(s) from various bath steps and to prevent cross-contamination of the baths. Now that we have reviewed corrosion, metal alloy selection, and cleaning procedures, our next step is to focus on the core of this chapter, which are the various pretreatment coatings commercially available and under development that can act as "smart coatings" as the first line of defense for corrosion inhibition.

3.4 Nonmetallic-Inorganic Pretreatment Coatings

Nonmetallic-inorganic coatings consist of ceramic coating materials, conversion, and anodized coatings. Ceramic coatings such as chemical setting silicate cement lining and porcelain enamels are used for corrosion inhibition. Conversion coats are coatings that convert the natural oxide coating present on a metal surface into a different metal oxide or metal salt. Anodization refers to the oxidation of a metal surface either chemically or electrochemically to generate a thick, dense, passive oxide layer on the metal surface.[21,22] We shall briefly expand on the anodization process for metals because of its importance to conversion coatings. Anodizing has been known since the 1930s, but did not gain widespread and commercial success until the 1970s.[23] There are several metals that can be protected via anodic protection: steels, stainless steels, nickel, nickel alloys, chromium, and aluminum. The "hard anodization" process refers to electrochemically driven surface treatment,[24] and the "standard" process refers to solutions of chromic, sulfuric, or phosphoric acids.[25–27] In response to current environmental and

health warnings about chromium, specifically hexavalent chromium [Cr(VI)][28] non-chromium alternatives have been investigated and commercialized for the anodization of metals. These alternatives comprise lead-tin, cobalt, zirconium, titanium, and silicate processes.[29–32] Anodization converts the existing metal surface to its oxide form or increases the oxide layer thickness, resulting in the formation of a thicker coating. The anodization process provides improved corrosion resistance and paint adhesion, permits subsequent plating, and provides a lustrous decorative appearance to most surfaces. Its facile method, reproducibility, and cost-effectiveness have resulted in its industrywide adaption.

3.4.1 Conversion coatings

Conversion coatings include chromate conversion coatings (CCCs), phosphate conversion coating, and lanthanide-based conversion coating and are deposited onto various metal/alloy substrates such as steel, zinc, aluminum, magnesium, copper, tin, silver, and nickel. Chemical conversion coatings processes are classified by their primary constituent. For example CCCs are mainly composed of chromates, whereas phosphate conversion coatings have as their main component phosphates.[33] The metal/alloy surface is converted into coatings via a chemical or electrochemical process. These types of coatings are used for corrosion protection, increased surface hardness, and added decorative finish and/or as paint primers. Conversion coatings can be very thin 0.00001″ (0.254 μm) or thick coatings 0.002″ (50.8 μm) and can be grown either anodically or by repeated exposure in conversion baths.

Conversion coatings are adherent, insoluble, inorganic crystalline, or amorphous surface coatings that are an integral part of the metal/metal oxide surface. In such films a portion of the base metal is converted into a metal oxide that is less reactive to corrosion than the original metal and improves adhesion for primers. Conversion coatings have gained widespread industrial use due to their strong adhesion properties, high speed of coating formation, and very favorable economics, while providing reproducible and consistent coatings for large-scale industrial use.[34]

3.4.1.1 Chromate conversion coatings

CCCs are normally formed by either chemical or electrochemical treatment of metals/alloys in a solution containing hexavalent chromium [Cr(VI)] with other components.[19,35] This process produces an amorphous protective coating that can be applied to various metals (e.g., steel or aluminum) via immersion or spraying. CCCs are applied to enhance bare or painted corrosion resistance, improve the adhesion of paint or primer coatings, and provide the metallic surface with an appealing decorative finish. The main components of the solutions used for forming CCC films are trivalent chromium [Cr(III)], Cr(VI), the base metal, various oxides, water, and several

additional components such as phosphates, sulfates, and fluorides. CCCs provide excellent bare or painted corrosion protection to the metal. The level of protection afforded by CCCs depends on several factors: (1) type of substrate metal, (2) type of chromate coating used, and (3) chromium coating weight. The mechanism by which Cr(VI) provides corrosion protection has been investigated by numerous researchers over the past several decades. Over the past decade, a general consensus on the mechanism by which CCCs inhibit corrosion has been proposed by several researchers.[36–41] Their research supports the idea that soluble Cr(VI) in CCCs is released to the defect areas in a coating, providing a "self-healing" mechanism that thereby inhibits further corrosion. The soluble Cr(VI) present in CCCs and to a lesser degree in chromated primers acts as a reservoir capable of migrating to defects and inhibiting corrosion. The mechanism of CCCs consists of both a cathodic, inhibiting, insoluble Cr(III) oxide and an anodic, inhibiting, soluble, transportable Cr(VI) species acting in concert with each other. Cr(III) acts as the insoluble, durable, inert coating, and when damage occurs a pH-controlled transport mechanism is enabled releasing soluble Cr(VI) species. The release of the active Cr(VI) inhibitor species in CCC involves the reversible formation of a Cr(VI)-O-Cr(III) mixed oxide. This system is one of the earliest examples of "smart coatings" for corrosion control on various metal alloys.

CCCs have shown over these many decades outstanding corrosion inhibition, and their replacements have not performed as well. However, CCCs and chromate primers are all under increased scrutiny and regulatory oversight by both the U.S and international regulatory agencies. The Cr(VI) compound is a known carcinogenic and toxic material to both humans and the environment.[42–46] Chronic inhalation of Cr(VI) compounds increases the risk for lung cancer, soluble species can cause or exacerbate contact dermatitis, and ingestion can cause irritation and ulcers of the stomach and/or intestine. Cr(VI) is transported into cells via the "sulfate transport" mechanism. As a result of its toxicity, new Cr(VI) OSHA regulations as defined in the February 28, 2006 *Federal Register*, now covers occupational exposure to Cr(VI) for workers during an 8-h TWA period of no more than $5\,\mu g/m^3$.[47] As of January 24, 2013, the National Institute for Occupational Safety and Health (NIOSH) had posted a document entitled "Criteria for a Recommended Standard: Occupational Exposure to Hexavalent Chromium." NIOSH reviewed the critical health effect studies of Cr(VI) and updated its assessment of the potential health effects of occupational exposure to Cr(VI) compounds. The recommendation for the new PEL is $0.20\,\mu g/m^3$ for a workplace environment.[48] This recommendation by NIOSH was advisory only; NIOSH cannot issue a regulatory directive. The European Union (EU) Registration, Evaluation, Authorization and Restriction of Chemicals (REACH) regulations (EC 1907/2006) were adopted in December 2006 and came into force in June 2007. REACH was introduced because many thousands of chemicals are used in the EU, some in very large quantities and with increased risks to human health and to the environment. Cr(VI) is one of the many substances that is highly regulated

by the EU and is currently a substance of very high concern (SVHC). As a result of Cr(VI) toxicity and persistence in the environment, alternative nonmetallic pretreatment coatings have been developed and tested. We shall now review several of these coatings and compare them to CCCs.

3.4.1.2 Phosphate conversion coatings

The phosphating process has been known for over a century, and the bath process consists of dilute phosphoric acid based solutions.[49,19,50] The formation of the phosphate coating requires the precipitation of a divalent metal and phosphate ions onto a metal surface. This treatment provides for a reasonably hard, electronically nonconducting surface coating composed of insoluble phosphate. The insoluble phosphate is contiguous and highly adherent to the underlying metal. The phosphate conversion coating is formed as a result of chemical reactions that transform the surface of the underlying base metal into a corrosion-resistant film. There are three types of phosphate conversion coatings:

- iron phosphates—lightweight, amorphous phosphate coatings that do not contain significant amounts of divalent metal ions
- zinc phosphates—medium-weight, crystalline phosphate coatings that contain divalent metal ions from solution and/or the metal surface
- heavy phosphates—coatings that contain divalent metal ions from solution and from the metal surface

Phosphate conversion coats are applied either via spraying or immersion for bare corrosion protection and/or painted corrosion protection on ferrous and nonferrous metals/alloys. Phosphate conversion coatings can provide effective barrier protection to metal/alloys provided the coating is applied properly. Thicker phosphate conversion coatings can provide better corrosion protection when combined with an overcoat of paint.

3.4.1.3 Lanthanide-based conversion coatings

Nonhexavalent chromium pretreatment coatings have been investigated for the past several decades. The rare earth (lanthanide) elements have received considerable attention due to their unique properties.[18,51,52] The rare earth elements such as cerium (Ce), yttrium (Y), lanthanum (La), neodymium (Nd), samarium (Sm), and praesodymium (Pr) have been investigated for their corrosion-inhibiting properties. The unique properties of the rare earth elements are:

- large atomic radii
- diverse allowable electronic configurations
- formation of multiple oxidation states such as +3 and +4 and occasionally +2

- reactivity with water to form neutral oxides
- formation of stable insoluble mixed oxides
- complex coordination chemistry
- low reduction potential
- instability of lower valence states in alkaline conditions
- precipitates that contribute to the stability and protection of films
- relatively inexpensive
- low toxicity
- low environmental impact[18,53–55]

The pioneering work of Hinton and Wilson used rare earth conversion coatings as alternatives to toxic CCCs.[56–59] Their work focused on cerium salt conversion coats for corrosion inhibition of zinc and aluminum metal/alloys. A cathodic mechanism was proposed by these two researchers to explain the formation of the rare earth oxide coating. The mechanism was based on cathodic reactions generating an alkaline environment, which led to localized precipitation of the rare earth oxides. The precipitated oxides enabled surface protection for the underlying metal alloy, thereby inhibiting corrosion. Further studies by Montemor et al. showed that the mechanism of rare earth oxide formation was a two-stage process, in which Ce-based conversion coatings undergo oxidation from Ce (III) to Ce(IV) state.[60–63]

Cerium-based conversion coatings can be prepared via two routes: (1) deposition of conversion coating onto a metal/alloy substrate is achieved by immersion for several days in simple cerium salt solution at or near neutral pH, or (2) H_2O_2-assisted solution of acidified cerium salt solutions, which results in deposition of cerium-based conversion coating in ≤10 min.[64–67] Ce-based conversion coating have been studied for their corrosion-inhibiting properties on various metals with mixed results for corrosion protection.[18,68–71] Several studies have shown limited to moderate corrosion protection while other studies have shown evidence of poor adhesion limiting its corrosion-inhibiting properties.[72,73]

As was described in Section 3.4.1.1, CCCs inhibit corrosion by dissociation of chromium ions into solution especially in a chloride environment. This dissolution of soluble species can migrate to exposed metal, resulting in the inhibition of corrosion via a "smart release" of chromated species. Similar investigations into the precipitation and dissolution of cerium-based conversion coatings have been investigated by several groups as nonchromium alternatives possessing the same "smart release" mechanism as found for CCCs.[18,74] These initial studies have shown evidence that the lanthanide ions form insoluble hydroxides, which can then provide corrosion protection in the form of cathodic inhibitors. The work based on Scully et al. showed evidence that coatings composed of Al, Co, and Ce did provide self-healing capabilities via a release of Ce ions at pH of 2.[75] Additional work by Heller et al. demonstrated corrosion protection via the formation of an interfacial active layer between

the aluminum substrate and the cerium conversion coating posttreated with 2.5 wt.% NaH_2PO_4 solutions after salt spray exposure.[76–78] However, the as-deposited cerium conversion coatings did not show any interfacial active layers after exposure to salt spray. Further work by Joshi et al. provided additional evidence for the dissolution of Ce species at pH 2, although at pH ≥3 no dissolution of Ce species was detected, and these results showed that the as-deposited coatings were composed of insoluble species that hindered the dissolution and migration of Ce species.[79] The mechanism proposed to account for these results was not determined, but rather dissolution and migration of Ce species were ruled out as possible scenarios. Additional studies using rare earth elements other than Ce such as La, Sm, and Y have been investigated by several research groups.[80–82] Their results showed that like Ce species these compounds are capable of inhibiting corrosion via a conversion film formation.

3.4.1.4 Miscellaneous-based conversion coatings

Additional pretreatment coatings that are non-Cr(VI) have been investigated for several decades now, which include the following systems: pretreatments acting as passivating agents based on molybdates (Mo), permanganates (Mn), vanadates (V), and tungstate (W)[83,84]; fluotitante and fluozirconate conversion coatings[85,86] and trivalent Cr(III) conversion pretreatment (TCP) coatings.[87,88]

Phosphate-permanganate and acidic—(HNO_3 or HF)—potassium-permanganate conversion coatings have been studied by several groups.[89–91] Their results in NaCl solutions showed similar corrosion protection to CCC, however, if Mn is reduced to the divalent oxidation state resulting in the formation of the more soluble Mn(II) oxide species, its corrosion-inhibiting properties are reduced.[92]

The molybdates have been the most studied metal oxyanion compounds to date and their corrosion-inhibiting properties are due to the formation of Mo films that are passivating at anodic sites on a metal surface.[93] Vanadates, molybdates, and tungstates can inhibit corrosion on aluminum when used with other compounds such as chromic species,[94] sulfuric acid,[95,96] and tetraborate solutions.[97] These combinations showed improved corrosion resistance containing the chromate acid species. The chromate anions had exhibited a passivating effect on the aluminum alloy forming stable Al_2O_3 films with further formation of molybdate layers preventing attack of Cl^- ions. The tetraborate solutions showed improved corrosion resistance with thicker anodic films contaminated with higher concentration of molybdate ions.[97]

Conversion coatings based on the group IVB metals, such as titanium (Ti), zirconium (Zr), and hafnium (Hf), have been investigated.[87,98–100] Group IV metal coatings require shorter immersion times (≤10 min) and are a potentially green alternative to CCCs.[101]

In addition, trivalent chromium pretreatment (TCP) coatings have also been investigated and commercialized as a nontoxic, environmentally green alternative to

CCCs.[102–105] TCP coatings are formed by solution immersion in a treatment bath composed of hexafluorozirconates, trivalent chromium oxides, chromium sulfate, and fluorborate salts. The solution is maintained in acidic medium (pH = 3.8-4.0) using either hydrofluoric (HF) or sulfuric acids (H_2SO_4). The color and thickness of the TCP coating can be modified depending on the solution composition, temperature, pH, and immersion time.[106] TCP has been shown to inhibit corrosion on various metals/alloys and has been accepted by the U.S. military as an environmentally friendly, nontoxic alternative to CCCs. Recent work by Swain et al. has investigated the mechanism(s) by which TCP can inhibit corrosion on aerospace aluminum, specifically AA2024-T3.[107] Their work using Raman spectroscopy suggests that mobile CrO_4^{-2} species are present in the TCP film and can diffuse to corroding sites inhibiting corrosion via a passivation mechanism.

3.5 Organic Pretreatment Coatings

We have discussed in detail the various "smart" inorganic pretreatment coatings that are available commercially and that are under investigation. We shall now turn our attention to organic-based "smart coatings." There are various types of organic "smart coatings" that have been commercialized and are under development such as sol-gel and hybrid sol-gel coatings,[108] conductive polymers (CPs),[109] self-assembled films,[110] polyelectrolyte multilayers,[111] controlled release coatings,[112] and biofilms,[113] which all will be presented in the following sections.

3.5.1 Hybrid sol-gel coatings

Over the past two decades sol-gel-based thin films have been investigated by several groups for corrosion inhibition of metal alloys. This research has been spurred by the need for environmentally friendly and nontoxic alternatives to CCCs.[28,46–48,114–116] Significant efforts have been employed to develop sol-gel coatings that can act as adhesion promoters between metal alloys and organic primers/topcoats as well as provide corrosion protection.[117]

There are two methods available to prepare sol-gel coatings via either a hydrolytic method in aqueous media or a nonhydrolytic process in organic media. Either method can produce various sol-gel coatings with different properties. These properties can be controlled via adjusting the composition of the reactive species, organic functionalization, temperature, time, and pH, affecting their potential applications for corrosion protection.[118] Sol-gel based pretreatment coatings have been studied on various metals/alloys, such as copper,[119,120] aluminum,[121] magnesium,[122] and carbon steel.[123] These studies have shown that sol-gel pretreatment coatings exhibit corrosion-inhibiting properties.

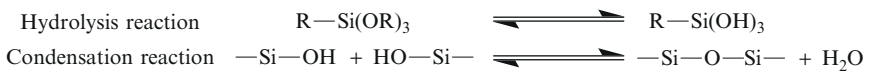


Figure 3.4 Hydrolysis and condensation reactions for producing sol-gel films.

The sol-gel process is based on the hydrolysis and condensation reactions of metal alkoxides [$M(OR)_n$] where M = Si, Ti, Zr, or Al; and R = alkyl group (methyl, ethyl, butyl, and so on) (Figure 3.4).[115,124] The sol-gel process involves two distinct and separate methods for the preparation of the "particles or films," which consists of either an inorganic or organic approach, and the latter is the preferred method. The sol-gel process involves the initial formation of a colloidal suspension or solution referred to as the "sol," which is followed by the formation of the integrated network referred to as the "gel" to give either discrete particles or network polymers.

The sol-gel process typically occurs in four stages:

- hydrolysis
- condensation and polymerization of monomers to form chains or particles
- growth of the particles or chains
- finally, agglomeration of the networks, thickening and formation of the gel[115,118,124]

Inorganic sol-gel pretreatment coatings have been investigated for their corrosion-inhibiting properties, but have suffered from cracking for thick coatings ≥200 nm. Cracking of the sol-gel film is formed during the heating stage when shrinkage of the gel occurs during solvent evaporation.[125] In order for crack-free sol-gel films to be formed, the thickness of the pretreatment film must be ≤100 nm, but their barrier properties are compromised due to presence of micropores in the film. Films produced by the sol-gel method show excellent adhesion between the alloy/metal substrate and primer/paint system.[126]

In order to produce crack-free films, researchers have developed hybrid sol-gel-derived coatings that combine the unique properties of both the inorganics/ceramics with organic polymeric materials.[127] The inorganic/ceramic coatings provide scratch resistance, durability, and improved adhesion between the metal/alloy substrate and organic primer/paint system, whereas the organic components increase flexibility and functional compatibility with the organic primer/paint system.[128,129] There are two classes of organically functionalized sol-gel coatings: (1) nonfunctional organoalkoxysilane and (2) organo-functional alkoxysilanes. Nonfunctional organoalkoxysilane sol-gel coatings are prepared using methyl groups as the organic part for the preparation of the hybrid coatings,[130] whereas, organo-functional alkoxysilanes incorporate such functionalities as epoxy,[131,132] methacrylic,[133,134] acrylics,[135] amino,[136,137] allyl,[138] pyridine,[139,140] or vinyl/phenyl moieties [138,141,142] as the precursor groups for sol-gel formation. These additional functional groups are also available for further polymerization producing sol-gel films with high crosslink densities, improved mechanical

properties, and tailored compatibility of the sol-gel pretreatment coating to the organic primer/paint system. Corrosion resistance using sol-gel films has been dependent on obtaining crack-free films. The hybrid sol-gel films offers several advantages, but still has limitations associated with reduced wear resistance and lower mechanical properties. Incorporation of nanoparticles into a sol-gel network can improve their mechanical properties while providing for corrosion resistance of metals/alloys.[143–146] Further improvements in hybrid sol-gel networks' corrosion-inhibiting properties have focused on introducing corrosion inhibitors with various degrees of success. Incorporation of inorganic inhibitors that are non-Cr(VI) such as phosphates,[147] V,[148] Ce,[147,149–153] and Mo[154,155] compounds as well as organic corrosion inhibitors such as phenylphosphonic acid,[156] mecaptobenzothiazole,[149,157] benzotriazole,[158] and 8-hydroxyquinoline[159] have been investigated for their corrosion-inhibiting properties.

3.5.2 Conductive polymer coatings

Over the past three decades, evidence that CPs such as polyaniline (PANI) and polypyrrole (PPy) could inhibit corrosion has come from the pioneering work of Mengoli,[160] DeBerry,[161] and MacDiarmid.[162,163] Mengoli showed that electrochemically deposited CP coatings on iron (Fe) anodes resulted in an adherent and corrosion-inhibiting film.[160] Further proof was obtained by DeBerry in 1985[161] who showed that PANI electrochemically deposited onto stainless steel showed a change in its corrosion behavior in a sulfuric acid solution, which provided concrete evidence that the PANI films provided anodic protection, thus maintaining a native passive film on the steel metal. There are numerous studies using CPs deposited onto metals/alloys under a variety of conditions such as electropolymerization, solvent-casting, water-dispersive formulations, spray, and dip-coating. These CPs are new "smart coatings" for corrosion protection of ferrous and nonferrous alloys. CPs can function by an anodic protection mechanism for ferrous alloys and therefore can potentially replace such corrosion-inhibiting compounds as Cr(VI) and cadmium (Cd), which are known carcinogenic and environmentally hazardous materials.[42–48,164–166]

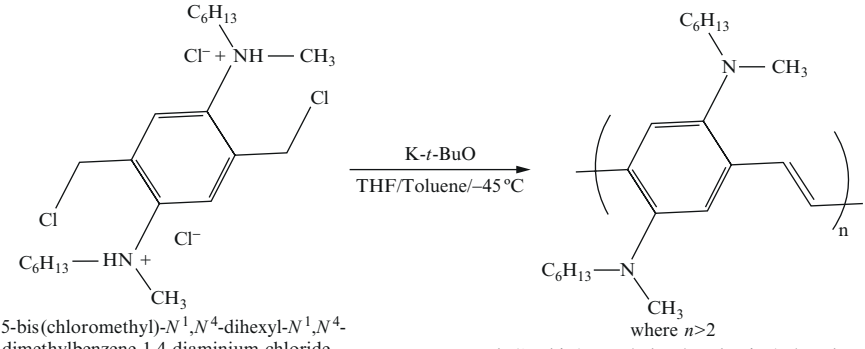
The corrosion mechanism for ferrous alloys as mentioned in the preceding paragraph is via anodic protection for steel alloys, passivation for stainless steels,[167–169] and released dopant ions for mild steels.[170,171] The corrosion protection mechanism for aluminum alloys is still under intense investigation. There are several proposed mechanism(s) by which CPs can potentially inhibit corrosion of aluminum alloys in corrosive aqueous environments.[172] These proposed mechanism(s) are as follows: (1) ennobling of the aluminum alloy,[173] (2) anodic protection/passivation,[174] (3) galvanic and ion-exchange release of oxygen reduction inhibitors,[175] and (4) barrier protection by the reduced form of the CP following an initial galvanic coupling.[176]

Most of the investigations into the corrosion-inhibiting properties of CPs have contained either a nonconductive primer and/or topcoat for enhanced corrosion

protection.[177] Additional work has focused on the corrosion mechanism of CPs via electrochemical and spectroscopic techniques that was also described in the preceding paragraph. There are fewer reports in the literature that focus exclusively on the corrosion-inhibiting properties of CPs as thin films with direct comparisons to the corrosion-inhibiting properties and performance of CCCs. Several recent reports highlight the corrosion-inhibiting properties of PANI, PPy, and PEDOT thin films (<1.0-2.5 μm) deposited on steel alloys with and without topcoats.[178–181]

Researchers at the Naval Air Warfare Center Weapons Division, China Lake, CA synthesized,[182–184] coated, and evaluated a CPs performance both in laboratory[103,185,186] and field testing environments,[187] which was directly compared to CCC. This compound, poly(2,5-bis(*N*-methyl-*N*-hexylamino)phenylene vinylene) (BAM-PPV), (Figure 3.5) was shown to have promise as a viable nontoxic, environmentally friendly alternative to CCCs as reported by Zarras et al.[182–188] The neutral salt fog laboratory results showed that BAM-PPV coated on aluminum alloy could meet the military requirement as a replacement for CCCs. Electrochemical noise method analysis of BAM-PPV coatings showed evidence of a surface passivation mechanism similar to other CPs.[186]

However, when BAM-PPV was coated on aluminum alloy with a non-Cr(VI) primer and topcoat, the neutral salt fog survivability did not match a fully Cr(VI) military coating system [CCC+Cr(VI) epoxy primer+polyurethane topcoat]. A 1-year Air Force field test of BAM-PPV incorporated into a full military coating [BAM-PPV+non-Cr(VI) epoxy primer+polyurethane topcoat] on the C-5 cargo plane's rear hatch door showed equal performance to the fully Cr(VI) military coating.[187] There are several recent reviews available to the reader to get a more comprehensive understanding of CP coatings and their ability to act as "smart coatings" in a variety of corrosive environments.[109,189–191]



2,5-bis(chloromethyl)-N^1,N^4-dihexyl-N^1,N^4-dimethylbenzene-1,4-diaminium chloride

Poly(2,5-bis(*N*-methyl-*N*-hexylamino)phenylene vinylene (BAM-PPV)

Figure 3.5 Polymerization conditions to obtain BAM-PPV.

3.5.3 Self-assembling pretreatment coatings

Self-assembling (SA) molecules are compounds that provide surface protection for the underlying metal or alloy from corrosive environments via the formation of thin films. These SA films can be very thin (~100 Å) and produce flexible, densely packed, stable films capable of blocking electron transfer or inhibiting the transport of corrosive species to the underlying metal or alloy.[192]

SA films are generated when molecules with specific chemical groups are deposited onto a surface have strong affinities for the surface and undergo ordering due to chemical interactions between substrate and SA molecules. In addition to the chemical or physical affinities necessary to form strong interactions on the substrate surface, the type and strength of the intermolecular interactions between the SA molecules that hold the assembly together are equally as important.[193] The SA molecules that are deposited onto substrates (metal or alloy surfaces) are either physically or chemically adsorbed. A significant portion of the research investigating SA films have focused primarily on the self-assembly of *n*-alkanethiolates and related structures on gold substrates. These well-ordered SA films are easily formed under ambient conditions due to the chemical inertness of the gold substrate and the affinity of thiol compounds to chemisorb onto gold.[194]

SA molecules have also been studied for their corrosion-inhibiting properties on various alloys. These SA molecules are specific for certain metals such as alkanethiols for gold,[192–195] silver,[196] and copper[197]; alcohols; amines for platinum[198]; and phosphonate compounds for aluminum.[199] The fabrication of SA films onto either a metal or alloy consists of finding suitable functional groups sandwiched between an aliphatic spacer unit capable of adhering onto the surface of the metal or alloy. The opposite functional group can then react further with the primer layer to form a more robust and durable film (Figure 3.6).

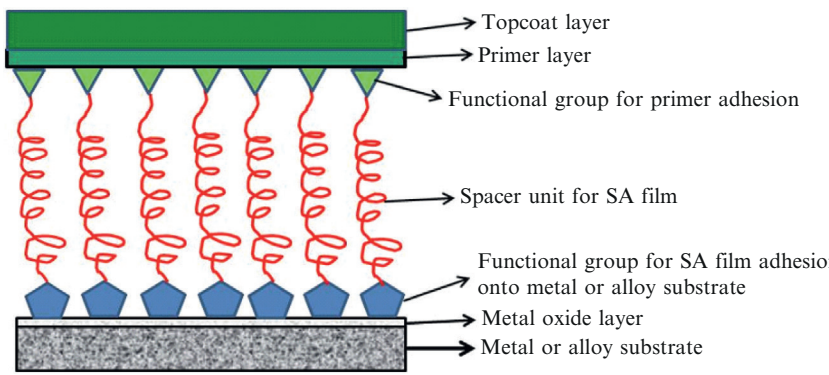


Figure 3.6 Schematic representation of a SA film with primer and topcoat.

SA films can provide effective barriers against the diffusion of oxygen,[200] and/or water.[201] Cross-linking reactions can further enhance the durability and corrosion-inhibiting properties of the SA film.[202] There are several studies of SA films for corrosion inhibition of copper metal using sodium 1-octadecyl-1H-benzimidazole,[203] diethydithiocarbamate,[204] which provided cathodic inhibitor protection, and hexane-1,6-diamine and 2-mercapto-ethanol, which provided evidence for enhanced corrosion inhibition on copper metals.[205] Corrosion inhibition of aluminum metal using octadecylphosphonic acid monolayers was investigated by Grundmeier et al.[206] The 1-tetradecylphosphonic acid SA films deposited on Al 2024 and 1060 showed corrosion inhibition during initial corrosion monitoring,[207] and alkane diphosphonate monolayers on 1050 aluminum showed improved corrosion resistance when the aluminum surface was exposed to oxide formation treatments.[208] Recent work on SA films coated onto iron and steel substrates has been investigated by several groups.[209,210] Adipic acid SA molecules formed compact films onto carbon steel exhibiting reduced electrochemistry on the steel surface[209]; compact and superior seawater stability were found with SA polydopamine/dodecanethiol films on 304 stainless steel[211]; and triazinethiol SA monolayers coated onto zinc treated steel substrates showed improved corrosion resistance but poor water repellency.[212] Brass alloys and magnesium alloys have also been investigated using SA films. In the case of brass alloys several silane SA films inhibited corrosion in 0.2 M NaCl,[213] and SA nanophase particle films provided corrosion protection for AZ31B magnesium alloy in 0.005 M NaCl solution for 354 h.[214]

3.5.4 Polyelectrolyte multilayer films

Polyelectrolyte (PE) films are fabricated by a layer-by-layer (LbL) approach using alternating assemblies of polyelectrolyte pairs consisting of a polyanion and polycation (Figure 3.7).[215] The adsorption of the alternating PE multiple layers is driven by electrostatic interactions, and assemblies of hundreds of alternating polyanions and polycations

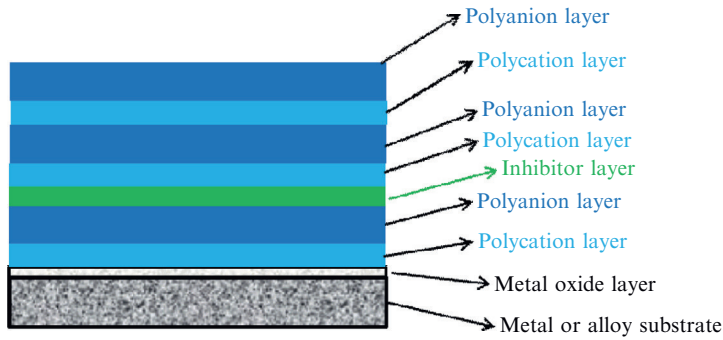


Figure 3.7 Polyelectrolyte (PE) multilayer films.

are possible.[216] The LbL approach for multilayer PE films allows for the precise control over the physical properties of the film (e.g., film thickness and morphology).[217]

The deposition by the LbL approach affords nanometer-scale precision with multifunctional capabilities for the PE multilayer coating, which can exhibit excellent adhesion to the metal or alloy and can "self-heal" to seal surface defects.[218] The PE multilayer films exhibit pH-buffering activity and can stabilize the pH between 5 and 7.5 at the metal surface in a corrosive environment. The PE multiple layer coatings are relatively mobile and also have the ability to seal and eliminate mechanical cracks in the coating via a "self-healing" mechanism.[219] Additionally, active inhibitors can be trapped in the PE multilayer films. The inhibitor is trapped to the layers closest to the substrate for release of inhibitors while maintaining effective substrate barrier properties for maximum corrosion efficiency.[220–223]

3.5.5 Controlled release coatings containing inhibitor-loaded nanocontainers

Controlled release and encapsulation of various materials within an inert host containing the active ingredient, such as drugs, oils, perfumes, and so on, have been studied for several decades.[224–226] Recent efforts have focused on developing encapsulated inhibitors via LbL, polyelectrolytes, copolymer vesicles and interfacial polymerization methods for corrosion inhibition on various metals and alloys.[227] These inhibitor microcapsules can be formulated into coating systems for controlled release of the inhibitor triggered by corrosion to provide a "self-healing" mechanism.[228,229] The size of the microencapsulated inhibitor containers are normally too large ($\geq 1\ \mu m$) to be effective in pretreatment, conversion, or multilayered coatings.

The development of "smart nanocontainers" offers a method by, which nanostructured materials can store the inhibitors, providing a new corrosion-inhibiting system based on a "passive matrix/active container structure" for use in pretreatment, conversion, or multilayered coating systems.[230] Corrosion processes are normally accompanied by local pH changes on the surface of the metal or alloy. Nanocontainers placed near these surfaces can be activated via pH changes or mechanical damage to release the encapsulated inhibitor effectively inhibiting corrosion via a self-healing mechanism. There are numerous literature reports on nanocontainers based on cyclodextrins,[231] mesoporous silica,[232,233] halloysite clays,[234] carbon nanotubes,[235] layered double hydroxides,[236]and titanium dioxide,[237] which have been synthesized and tested for their corrosion-inhibiting properties.[112]

3.5.6 Biofilms as pretreatment coatings

Corrosion control using beneficial biofilms has recently gained interest as a corrosion-inhibiting strategy that is promoted as an environmentally green and

nontoxic alternative to current corrosion control methods.[238] Biofilm formation is a natural process, which consists of a highly organized bacterial community with cells entrapped in a matrix formed by extracellular polymer.[239] The formation of biofilms may impede or accelerate the corrosion process on metals or alloys.[240] The factor that promotes corrosion is the bacteria colonization process on metal substrates. This colonization is nonuniform, producing colonies that are thinner or thicker resulting in anodic and cathodic regions promoting corrosion on the substrate. Additionally corrosion can be impeded if corrosion products formed by the biofilm produce passive layers.[241] The interaction between the metal substrate and biofilm formation depends solely on the type of metal and the degree of microbial activity. The inhibition of corrosion on various metals and alloys using biofilms can be accomplished via several strategies: (1) biofilms secreting antimicrobials,[113,242,243] (2) formation of protective layers,[244,245] (3) biofilms secreting corrosion inhibitors,[246,247] and (4) beneficial biofilms.[248,249]

3.6 Conclusions

A comprehensive review of corrosion inhibition on various metals and alloys using either inorganic or organic pretreatment methods has been presented. Surface pretreatment coatings,whether they are inorganic or organic, serve as the first line of defense in inhibiting corrosion. The selection of the proper pretreatment coating is essential in providing basic corrosion protection for the underlying metal or alloy and promoting adhesion and compatibility between the pretreatment and primer coating. There are a number of pretreatment coatings that are commercially available and are being investigated not only to better understand the complex relationship between metals/alloys and corrosion, but to design and commercialize new pretreatment coatings that are economically viable, environmentally friendly and nontoxic to both humans and ecosystems.

Acknowledgments

The authors would like to acknowledge the financial support of the Office of the Director, Defense Research and Engineering.

References

1. Bardal E. Introduction. In: Corrosion and protection. London: Springer-Verlag; 2004. p. 1–4.
2. Marek MI. Thermodynamics of aqueous corrosion. In: Kori LJ, Olson DL, editors. ASM handbook. Corrosion, vol. 13. Materials Park, OH: ASM International; 1998. p. 18–28.

3. Kroger JW. Fundamentals of high-temperature corrosion in molten salts. In: Korb LJ, Olson DL, editors. ASM handbook. Corrosion, vol. 13. Materials Park, OH: ASM International; 1998. p. 50–5.
4. Tortorelli PF. Fundamentals of high-temperature corrosion in liquid metals. In: Korb LJ, Olson DL, editors. ASM handbook. Corrosion, vol. 13. Materials Park, OH: ASM International; 1998. p. 56–60.
5. Bradford SA. Fundamentals of corrosion in gases. In: Korb LJ, Olson DL, editors. ASM handbook. Corrosion, vol. 13. Materials Park, OH: ASM International; 1998. p. 61–76.
6. Kruger J. Cost of metallic corrosion. In: Revie RW, editor. Uhlig's corrosion handbook. 3rd ed. Hoboken, New Jersey: Electrochemical Society Series; 2011. p. 15–20.
7. Koch GH, Brongers MPH, Thompson NG, et al. Corrosion costs and preventive strategies in the United States. Houston, Texas: NACE International; 1998, Publication No. FHWA-RD-01-156. p. 1–12.
8. Verink Jr ED. Economics of corrosion. In: Revie RW, editor. Uhlig's corrosion handbook. 3rd ed. Hoboken, New Jersey: Electrochemical Society Series; 2011. p. 21–30.
9. Jackson JE. *Cost of corrosion annually in the US over $1 trillion*: *G2MT laboratories report*. http://www.g2mtlabs.com/cost-of-corrosion/; June 2013.
10. Kruger J. Cost of metallic corrosion. In: Revie RW, editor. Uhlig's corrosion handbook. 3rd ed. Hoboken, New Jersey: Electrochemical Society Series; 2011. p. 18–9.
11. Hoar TP. *Report of the committee on corrosion and protection*. Department of Trade and Industry, H.M.S.O. London, UK; 1971.
12. Biezma MV, San Cristobal JR. Methodology to study costs of corrosion. Corrosion Eng Sci Tech 2005;40(4):344–52.
13. Hoar TP. Corrosion of metals: its cost and control. Proc R Soc London, Ser A 1976;348(1652):1–18.
14. Baghdachi J Smart coatings. In: Provder T, Baghdachi J, editors. Smart coatings II. ACS symposium series 1002. Washington, DC: American Chemical Society; 2009. p. 3–24.
15. Brady Jr. RF. Twenty-first century materials: coatings that interact with their environment. In: Provder T, Baghdachi J, editors. Smart coatings. ACS symposium series 957. Washington, DC: American Chemical Society; 2007. p. 3–14.
16. Xia F, Jiang L. Bio-inspired, smart, multiscale interfacial materials. Adv Mater 2008;20(15):2842–58.
17. Baghdachi J. The bespoke design of smart coatings. Eur Coating J 2010;9:17–23.
18. Schuman TP. Protective coatings for aluminum alloys. In: M Katz, editor. Handbook of environmental degradation of materials. Norwich NY: William Andrew Publishing; 2005. p. 345–66.
19. Davis JR. Corrosion: understanding the basics. Materials Park, Ohio: ASM International; 2000 p. 331–358.
20. Khanna AS. Surface preparation for organic paint coatings. In: High performance organic coatings. Cambridge, UK: Woodhead Publishing Ltd; 2008. p. 27–40.
21. Grishina EP, Noskov AV. Electrochemical formation of passivating layers and surface condition during anodic oxidation and corrosion of metals. In: Willard T, editor. Solid state electrochemistry. Hauppauge, NY: Nova Science Publishers Inc; 2010. p. 1–61.
22. Munro JI, Shim WW. Anodic protection-its operation and applications. Mater Perform 2001;40(5):22–5.
23. Riggs OL, Locke CE. Anodic protection. theory and practice in the prevention of corrosion. NY: Plenum Press; 1981, p. 1-260.
24. Montgomery DC. Anodizing. Plat Surf Finish 2007;94(11):12.
25. Vincenzi F, Barba WD, Vincenzi F. A new anodizing process with energy saving. Aluminum Extrusion 2003;8(4):54–8.
26. Konno H, Baba Y, Furuichi R. Formation of porous anodic oxide films containing chromium ions on aluminum. Mater Sci Forum 1995;192–194:379–84.
27. Zhang J-S, Zhao X-H, Zuo Y, et al. The bonding strength and corrosion resistance of aluminum alloy by anodizing treatment in a phosphoric acid modified boric acid/sulfuric acid bath. Surf Coat Technol 2008;202(14):3149–56.

28. Environmental Protection Agency USA. National emission standards for hazardous air pollutant emissions: hard and decorative chromium electroplating and chromium anodizing tanks; and steel pickling-HCl process facilities and hydrochloric acid regeneration plants. Fed Regist 2012;77(182):58220–53.
29. Rabbetts A. Replacements for hexavalent chromium in anodizing and conversion coating. Trans Inst Metal Finish 1998;76(1):B4–5.
30. Critchlow GW. Alternatives to hexavalent chromium process to enhance the durability of bonded aluminum joints. Trans Inst Metal Finish 1998;76(1):B6–10.
31. Matzdorf CA, Nickerson WC, Beck EN, et al. Non-chromium corrosion-resistant coatings for aluminum. Assignee: United States Department of the Navy, USA. *US Patent Number 2007/0095436 A1*; 2007.
32. Sturgill JA, Phelps AW, Swartzbaugh JT. Non-toxic corrosion protection conversion coats based on cobalt. Assignee: University of Dayton, Dayton OH (US). *US Patent Number 7,294,211 B2*; November 13, 2007.
33. Kuehner MA. Phosphate conversion coatings. Met Finish 1985;83(8):15–8.
34. Suzuki I. Corrosion-resistant coatings technology. NY: Marcel Dekker Inc; 1989, p. 10–250.
35. Korinek KA. Chromate conversion coatings. In: Korb LJ, Olson DL, editors. ASM handbook. Corrosion, vol. 13. United States: ASTM International; 1998. p. 389–95.
36. Kendig M, Jeanjaquet S, Addison R, et al. Role of hexavalent chromium in the inhibition of corrosion of aluminum alloys. Surf Coat Technol 2001;140:58–66.
37. Illevbare GO, Scully JR, Yuan J, et al. Inhibition of pitting corrosion on aluminum alloy 2024-T3: effect of soluble chromate additions vs. chromate conversion coating. Corrosion 2000;56(3):227–42.
38. Kendig MW, Davenport AJ, Isaacs HS. The mechanism of corrosion inhibition by chromate conversion coatings from x-ray absorption near edge spectroscopy (XANES). Corros Sci 1993;34(1):41–9.
39. Chidambaram D, Halada GP, Clayton CR. Spectroscopic elucidation of the repassivation of active sites on aluminum by chromate conversion coating. Electrochem Solid-State Lett 2004;7(9):B31–3.
40. Xia L, Akiyama E, Frankel G, et al. Storage and release of soluble hexavalent chromium from chromate conversion coatings equilibrium aspects of Cr^{VI} concentration. J Electrochem Soc 2000;147(7):2256–62.
41. Ramsey JD, Xia L, Kendig MW, et al. Raman spectroscopic analysis of the speciation of dilute chromate solutions. Corros Sci 2001;43:1557–72.
42. Saikia SK, Mishra AK, Tiwari S, et al. Hexavalent chromium induced histological alterations in *Bacopa monnieri* (L.) and assessment of genetic variance. J Cytol Histol 2012;3(2):141.
43. Vignati Davide AL, Beye Dominik J, Pettine Mamadou L, et al. Chromium (VI) is more toxic than chromium (iii) to freshwater algae: a paradigm to revise. Ecotoxicol Environ Saf 2010;73(5):743–9.
44. Sanikow K, Zhitkovich A. Genetic and epigenetic mechanisms in metal cacinogenesis and cocarcinogenesis: nickel, arsenic, and chromium. Chem Res Toxicol 2008;21:28–44.
45. Blisiak J, Kowalik J. A comparison of the in vitro genotoxicity of tri- and hexavalent chromium. Mutat Res 2000;469:135–45.
46. Wetterhahn KE. Hamilton JW, molecular basis of hexavalent chromium carcinogenicity: effect of gene expression. Sci Total Environ 1989;86:113–29.
47. National emissions standards for chromium emissions from hard and decorative chromium electroplating and chromium anodizing tanks, environmental protection agency, *Federal Register*, RIN 2060-AC14; January 25, 1995.
48. *AESF/EPA conference*, *hexavalent chrome PEL AESF presentation*. http://www.nasf.org/nasf-law-regulation.php; January 2004.
49. Naraayanan Sankara TSN. Surface pretreatment by phosphate conversion coatings—a review. Rev Adv Mater Sci 2005;9:130–77.

50. Cape TW. Phosphate conversion coatings. In: Korb LJ, Olson DL, editors. ASM handbook. Corrosion, vol. 13. United States: ASTM International; 1998. p. 383–8.
51. Harvey TG. Cerium-based conversion coatings on aluminum alloys: a process review. Corros Eng Sci Technol 2013;48(4):248–69.
52. Buchheit R, Mahajanam SPV. Ion exchange compounds for corrosion inhibiting pigments in organic coatings. In: Zarras P, wood T, Brough R, Benicewicz BC, editors. New developments in coatings technology. ACS symposium series 962. Washington, DC: American Chemical Society; 2007. p. 108–34.
53. Zhang J-H, Zhang Y-J. Film forming mechanism analysis of cerium conversion coating on zinc coating. Adv Mater Res 2012;557–559:1819–24.
54. Williams G, McMurray HN, Worsley DA. Cerium (III) inhibition of corrosion-driven organic coating delamination studied using scanning kelvin probe technique. J Electrochem Soc 2002;149(4):B154–62.
55. Mansfeld F, Lin S, Kim S, et al. Surface modification of aluminum alloys and aluminum-based metal matrix composites by chemical passivation. Electrochim Acta 1989;34(8):1123–32.
56. Hinton B, Hughes A, Taylor R, et al. The corrosion protection properties of an hydrated cerium oxide coating on aluminum. In: International corrosion congress proceedings 13th Melbourne, November 1996; 1996. p. 337/1–7.
57. Hughes AE, Taylor RJ, Hinton BRW, et al. XPS and SEM characterization of hydrated cerium oxide conversion coatings. Surf Inter Anal 1995;23(7&8):540–50.
58. Hinton BRW, Wilson L. The corrosion inhibition of zinc with cerous chloride. Corros Sci 1989;29(8):967–85.
59. Hinton BRW, Ryan NE, Arnott DR, et al. The inhibition of aluminum alloy corrosion by rare earth metal cations. Corros Australas 1985;10(3):12–7.
60. Montemor MF, Simoes AM, Ferreira MGS, et al. Composition and corrosion resistance of cerium conversion films on the AZ31 magnesium alloy and its relation to the salt anion. Appl Surf Sci 2008;254(6):1806–14.
61. Montemor MF, Simoes AM, Carmezim MJ. Characterization of rare-earth conversion films formed on the AZ31 magnesium alloy and its relation with corrosion protection. Appl Surf Sci 2007;253(16):6922–31.
62. Ferreira MGS, Duarte RG, Montemor MF, et al. Silanes and rare earth salts as chromate replacers for pre-treatments on galvanized steel. Electrochim Acta 2004;49(17–18):2927–35.
63. Montemor MF, Simoes AM, Ferreira MGS. Composition and corrosion behavior of galvanized steel treated with rare-earth salts: the effect of cation. Prog Org Coat 2002;44(2):111–20.
64. Scholes FH, Soste C, Hughes AE, et al. The role of hydrogen peroxide in the deposition of cerium-based conversion coatings. Appl Surf Sci 2006;253:1770–80.
65. Dabala M, Armelao L, Buchberger A, et al. Cerium-based conversion layers on aluminum alloys. Appl Surf Sci 2001;172(3–4):312–22.
66. Aldykiewicz AJ, Davenport AJ, Isaacs HS. Studies of the formation of cerium-rich protective films using x-ray absorption near-edge spectroscopy and rotating disk electrode methods. J Electrochem Soc 1996;143(1):147–54.
67. Campestrini P, Terryn H, Hovestad A, et al. Formation of a cerium-based conversion coating on aa2024: relationship with the microstructure. Surf Coat Technol 2004;176(3):365–81.
68. Lingjie LI, Jinglei LEI, Shenghai YU, et al. Formation and characterization of cerium conversion coatings on magnesium alloy. J Rare Earth 2008;26(3):383–7.
69. Markley TA, Forsyth M, Hughes AE. Corrosion protection of AA2024-T3 using rare earth diphenyl phosphates. Electrochim Acta 2007;52:4024–31.
70. Pardo A, Merino MC, Arrabal R, et al. Carboneras M. Effect of Ce surface treatments on corrosion resistance of A3xx.x/SiC_p composites in salt fog. Surf Coat Technol 2006;200:2938–47.

71. Mora N, Cano E, Polo JL, et al. Bastidas JM, corrosion protection properties of cerium layers formed on tinplate. Corros Sci 2004;46:563–78.
72. Rivera BF, Johnson BY, O'Keefe MJ, et al. Deposition and characterization of cerium oxide conversion coatings on aluminum alloy 7075-T6. Surf Coat Technol 2004;176:349–56.
73. Aballe A, Bethencourt M, Botana FJ, et al. On the mixed nature of cerium conversion coatings. Mater Corros 2002;53:176–84.
74. Bethencourt M, Botana FJ, Calvino JJ, et al. Lanthanide compounds as environmentally-friendly corrosion inhibitors of aluminum alloys: a review. Corros Sci 1998;40(11):1803–19.
75. Scully JR, Presuel-Moreno F, Goldman M, et al. User-selective barrier, sacrificial anode, and active corrosion inhibiting properties of Al-Co-Ce alloys for coating applications. Corrosion 2008;64(3):210–29.
76. Heller DK, Fahrenholtz WG, Geoff E, et al. Directly deposited cerium phosphate coatings for the corrosion protection Al 2024-T3. ECS Trans 2010;28(24):203–15.
77. Heller DK, Fahrenholtz WG, O'Keefe MJ. The effect of post-treatment time and temperature on cerium-based conversion coatings on Al 2024-T3. Corros Sci 2010;52(2):360–8.
78. Heller DK, Fahrenholtz WG, O'Keefe MJ. The effect of phosphate source on the post-treatment of cerium based conversion coatings on Al 2024-T3 and its correlation to corrosion performance. ECS Trans 2009;16(43):47–60.
79. Joshi S, Kulp EA, Fahrenholtz WG, et al. Dissolution of cerium from cerium-based conversion coatings on Al 7075-T6 in 0.1 M NaCl solutions. Corros Sci 2012;60:290–5.
80. Kong G, Liu L, Lu J, et al. Study of lanthanum salt conversion coating modified with citric acid on hot galvanized steel. J Rare Earth 2010;28(3):461–5.
81. Pardo A, Merino MC, Arrabal R, et al. Effect of La surface treatments on corrosion resistance of A3xx.x/SiC_p composites in salt fog. Appl Surf Sci 2006;252:2794–805.
82. Bethencourt M, Botana FJ, Cauqui MA, et al. Protection against corrosion in marine environments of AA5083 Al-Mg alloy by lanthanide chlorides. J Alloys Compd 1997;250(1–2):455–60.
83. Almeida E, Diamantino TC, Figueiredo MO, et al. Oxidizing alternative species to chromium VI in zinc galvanized steel surface treatment. Part 1-A morphological and chemical study. Surf Coat Technol 1998;106:8–17.
84. Almeida E, Fedrizzi L, Diamantinio TC. Oxidizing alternative species to chromium VI in zinc-galvanized steel surface treatment. Part 2-An electrochemical study. Surf Coat Technol 1998;105:97–101.
85. Nordlein JH, Walmsley JC, Osterberg H, et al. Formation of a zirconium-titanium based conversion layer on AA 6060 aluminum. Surf Coat Technol 2002;153:72–8.
86. Deck PD, Moon M, Sujdak RJ. Investigation of fluoacid based conversion coatings on aluminum. Prog Org Coat 1998;34(1–4):39–48.
87. Pearlstein F, Agarwala VS. Trivalent chromium conversion coating for aluminum-a replacement for hexavalent chromium pretreatment. In: Tri-service conference on corrosion, Wrightsville Beach NC. November 17–21, 1997, vol. 2; 1997. p. 12/1–10.
88. Schlosser TM, Musingo EM. Trivalent chromium passivation and pretreatment composition for zinc-containing metals. Assignee: Bulk Chemicals Inc., USA. *US Patent Number 20110100513 A1*; May 5, 2011.
89. Hamdy AS, Hussien HM. Deposition, Characterization and electrochemical properties of permanganate-based coatings and treatments over ZE41 Mg-Zn-rare earth alloy. Int J Electrochem Sci 2013;8:11386–402.
90. Lin CS, Lee CY, Li WC, et al. Formation of phosphate/permanganate conversion coating on ZA31 magnesium alloy. J Electrochem Soc 2006;153(3):B90–6.
91. Chong KZ, Shih TS. Conversion-coating treatment for magnesium alloys by a permanganate-phosphate solution. Mater Chem Phys 2003;80(1):191–200.

92. Srinivasan PB, Sathiyanarayanan S, Marikkannu C, et al. A non-chromate chemical conversion coating for aluminum alloys. Corros Prev Cont 1995;42(2):35–6, 49.
93. Wilcox GD, Gabe DR, Warwick ME. The role of molybdates in corrosion prevention. Corros Rev 1986;6(4):327–65.
94. Zein El Abedin S. Role of chromate, molybdate and tungstate anions on the inhibition of aluminum in chloride solutions. J Appl Electrochem 2001;31(6):711–8.
95. Moutarlier V, Gigandet MP, Normand B, et al. EIS characterization of anodic films formed on 2024 aluminum alloy, in sulfuric acid containing molybdate or permanganate species. Corros Sci 2005;47(4):937–51.
96. Moutarlier V, Gigandet MP, Pagetti J. Characterization of pitting corrosion in sealed anodic films formed in sulphuric, sulphuric/molybdate and chromic media. Appl Surf Sci 2003;206(1–4):237–49.
97. Moutarlier V, Pelletier S, Lallemand F, et al. Characterisation of the anodic layers formed on 2024 aluminum alloy, in tetraborate electrolyte containing molybdate ions. Appl Surf Sci 2005;252:1739–46.
98. Wang SH, Liu CS, Wang L. A comparative study of zirconium-based coating on cold rolled steel. Adv Mater Res 2011;291–294(Pt. 1):47–52.
99. Hamdy AS, Farahat M. Chrome-free zirconia based protective coatings for magnesium alloys. Surf Coat Technol 2010;204(16–17):2834–40.
100. Wang SH, Liu CS, Shan FJ. Corrosion behavior of a zirconium-titanium phosphoric acid conversion coating on AA6061 aluminum alloy. Acta Metall Sin 2008;21(4):269–74.
101. George FO, Skeldon P, Thompson GE. Formation of zirconium-based conversion coatings on aluminum and Al-Cu alloys. Corros Sci 2012;65:231–7.
102. Bhaatia PP, Lomasney GM, Mason US. Trivalent chromium anticorrosive conversion coating for pretreated copper-containing aluminum alloy. *Eur Pat Appl*. *EP255200A1*; February 2, 2013.
103. Zarras P, Prokopuk N, Anderson A, et al. Investigation of electroactive polymers and other pretreatments as replacements for chromate conversion coatings: a neutral salt fog and electrochemical impedance spectroscopy study. In: Zarras P, Wood T, Richey B, Benicewicz BC, editors. New developments in coating technology. ACS symposium series 962. Washington, DC: American Chemical Society; 2007. p. 40–53.
104. Pearlstein F, Agarwala VS. Trivalent chromium solutions for applying chemical conversion coatings to aluminum alloys or for sealing anodized aluminum. Plat Surf Finish 1994;81(7):50–5.
105. Pearlstein F, Agarwala VS. Non-chromate chemical conversion coatings for aluminum alloys. Proc Electrochem Soc 1993;93–28:199–211.
106. Zhang X, van den Bos C, Sloof WG, et al. Comparison of the morphology and corrosion performance of Cr(VI)- and Cr(III)-based conversion coatings on zinc. Surf Coat Technol 2005;199:92–104.
107. Li L, Kim DY, Swain GM. Transient formation of chromate in trivalent chromium process (TCP) coatings on AA2024-T3 as probed by Raman spectroscopy. J Electrochem Soc 2012;159(8):C326–33.
108. Zheludkevich ML, Salvado IM, Ferreira MGS. Sol-gel coatings for corrosion protection of metals. J Mater Chem 2005;15:5099–111.
109. Tallman DE, Bierwagen GP. Corrosion protection using conducting polymers. In: Skotheim TA, Reynolds JR, editors. Handbook of conducting polymers. Conjugated polymers: processing and applications. 3rd ed. Boca Raton, FL: CRC Press; 2007. p. 12-1–42.
110. Rohwerder M, Stratmann M, Grundmeier G. Corrosion prevention by absorbed organic monolayers and ultrathin plasma polymer films. In: Corrosion mechanisms in theory and practice. 3rd ed. Boca Raton, FL: CRC Press; 2012. p. 617–67.
111. Farhat TR, Schlenoff JB. Corrosion control using polyelectrolyte multilayers. Electrochem Solid-State Lett 2002;5(4):B13–5.
112. Zheludkevich ML, Tedim J, Ferreira MGS. "Smart" coatings for active corrosion protection based on multi-functional micro and nanocontainers. Electrochim Acta 2012;82:314–23.

113. Syrett BC, Arps PJ, Earthman JC, et al. Corrosion control using regenerative biofilms (CCURB): an update. Metall Ital 2001;93(7–8):39–44.
114. Balgude D, Sabnis A. Sol-gel derived hybrid coatings as environmentally friendly surface treatment for corrosion protection of metals and their alloys. J Sol-Gel Sci Technol 2012;64(1):124–34.
115. Wang D, Bierwagen GP. Sol-gel coatings on metals for corrosion protection. Prog Org Coat 2009;64(4):327–38.
116. Kasemann R, Schmidt H. Coatings for mechanical and chemical protection based on organic-inorganic sol-gel nanocomposites. New J Chem 1994;18(10):1117–23.
117. Fedel M, Deflorian F, Rossi S. Innovative silanes-based pretreatment to improve the adhesion of organic coatings. In: Sharma SK, editor. Green corrosion chemistry and engineering: opportunities and challenges. 1st ed. Weinheim: Wiley-VCH Verlag GmBH & Co.; 2012. p. 181–209.
118. Kron J, Deichmann KJ, Rose K. Sol-gel derived hybrid materials as functional coatings for metal surfaces. Eur Fed Corros Publ 2011;58(Self-Healing Properties of New Surface Treatments): 105–18.
119. Li Y-S, Lu W, Wang Y, et al. Studies of (3-mercaptopropyl)trimethoxysilane and bis(trimethoxysilyl)ethane sol-gel coating on copper and aluminum. Spectrochim Acta A 2009;73:922–8.
120. Tan ALK, Soutar AM. Hybrid sol-gel coatings for corrosion protection of copper. Thin Solid Films 2008;516:5706–9.
121. Feng Z, Liu Y, Thompson GE, et al. Sol-gel coatings for corrosion protection of 1050 aluminum alloy. Electrochim Acta 2010;55:3518–27.
122. Tan ALK, Soutar AM, Annergren IF, et al. Multilayer sol-gel coatings for corrosion protection of magnesium. Surf Coat Technol 2005;198(1–3):478–82.
123. Norzita N, Haziq M, Zurina M. Development of hybrid nano-sol-gel coatings for corrosion protection of carbon steel. Int J Chem Environ Eng 2012;3(4):267–70.
124. Dimitrev Y, Ivanova Y, Iordanova R. History of sol-gel science and technology (review). J Univ Chem Technol Metall 2008;43(2):181–92.
125. Kurisu T, Kozuka H. Effects of heating rate on stress evolution in alkoxide-derived silica gel-coating films. J Am Ceram Soc 2006;89(8):2453–8.
126. Mayrand M, Quinson JF, Roche A, et al. Heteropolysiloxane coatings on electrogalvanized steel: elaboration and characterization. J Sol-Gel Sci Technol 1998;12(1):49–57.
127. Metroke TL, Parkhill RL, Knobbe ET. Passivation of metal alloys using sol-gel-derived materials—a review. Prog Org Coat 2001;41(4):233–8.
128. Senani S, Campazzi E, Villate M, et al. Potentially of UV-cured hybrid sol-gel coatings for aeronautical metallic substrate protection. Surf Coat Technol 2013;227:32–7.
129. Chen X, Zhou S, Shuxue Y, et al. Mechanical properties and thermal stability of ambient-cured thick polysiloxane coatings prepared by a sol-gel process of organoalkoxysilanes. Prog Org Coat 2012;74(3):540–8.
130. Conde A, Duran A, de Damborenea JJ. Polymeric sol-gel coatings as protective layers of aluminum alloys. Prog Org Coat 2003;46(4):288–96.
131. White SS Jr, Dang HT, Titman S. Abrasion-resistant coating compositions for optical substrates, their manufacture and coated articles therefrom. Assignee: Sailor International Companies General D'Optique, France. *PCT Int. Appl. WO 2000029496 A1*; May 25, 2000.
132. Witucki GL, Vincent HL. Preparation of epoxy-functional silicone resin for powder coating. Assignee: Dow Corning Corporation, USA. *US Patent Number 5,280,098A*; January 18, 1994.
133. Chen Y-H, Liu L-X, Zhan M-S. The preparation and characterization of abrasion-resistant coatings on polycarbonate. J Coat Technol Res 2013;10(1):79–86.
134. Chen J-I, Chareonsak R, Puengpipat V, et al. Organic/inorganic composite materials for coating applications. J Appl Poly Sci 1999;74(6):1341–6.

135. Smarsley B, Garnweitner G, Assink R, Brinker CJ. Preparation and characterization of mesostructured polymer-functionalized sol-gel-derived thin films. Prog Org Coat 2003;47(3–4):393–400.
136. Yu J, Qiu J, Cui Y, et al. Preparation and electro-optic properties of hybrid sol-gel films containing imidizale chromophore. Mater Lett 2009;63(29):2594–6.
137. Menning M, Schmidt M, Kutsch B, et al. SiO2-coatings on glass containing copper colloids using the Sol-gel–technique. Proceedings of SPIE-The International Society for Optical Engineering 1994;2288(Sol-Gel Optics III):120–9.
138. Joshua DuY, Tang Damron M, Zheng G, et al. Inorganic/organic hybrid coatings for aircraft aluminum alloy substrates. Prog Org Coat 2001;41(4):226–32.
139. Kroke E. Novel sol-gel routes to non-oxide ceramics. Adv Sci Technol 1999;15(Ceramics: Getting into the 2000's, Pt. C):123–34.
140. Sugama T, Carciello N, Rast SL. Zirconocene-modified polysiloxane-2-pyridine coatings. Thin Solid Films 1995;258(1–2):174–84.
141. Tamboura M, Mikhailova AM, Jia MQ. Development of heat-resistant anticorrosion urethane siloxane paints. J Coat Technol Res 2013;10(3):381–96.
142. Sheffer M, Groysman A, Mandler D. Electrodeposition of sol-gel films on Al for corrosion protection. Corros Sci 2003;45(12):2893–904.
143. Curkovic L, Curkovic HO, Salopek S, et al. Enhancement of corrosion protection of AlSl304 stainless steel by nanostructured sol-gel TiO_2 films. Corros Sci 2013;77:176–84.
144. Balbyshev VN, Anderson KL, Sinsawat A, et al. Modeling of nano-sized macromolecules in silane-based self-assembled nano-phase particle coatings. Prog Org Coat 2003;47(3–4):337–41.
145. Jang J, Park H. Formation and structure of polyacrylamide-silica nanocomposites by sol-gel process. J Appl Polym Sci 2002;83(8):1817–23.
146. Vreugdenhil AJ, Balbyshev VN, Donley MS. Nanostructured silicon sol-gel surface pretreatments for Al 2024-T3 protection. J Coat Technol 2001;73(915):35–43.
147. Wittmar A, Wittmar M, Ulrich A, et al. Hybrid sol-gel coatings doped with transition metal ions for the protection of AA2024-T3. J Sol-Gel Sci Technol 2012;61(3):600–12.
148. Singh AK, Rout TK, Narayan R, et al. Anticorrosive hybrid sol-gel film on zinc substrates comprising sodium vanadate and colloidal silica. *PCT Int. Appl. WO 2009141830A1*; November 26, 2009.
149. Matter EA, Kozhukharov S, Gyozova A, et al. AA2024 Corrosion protection by hybrid coatings incorporated with Ce(III) and Ce(IV) inhibitors. J Univ Chem Technol Metall 2012;47(5):518–24.
150. Aparicio M, Rosero-Navarro NC, Castro Y, Duran A, Pellice SA. Hybrid Ce-containing silica-methacrylate sol-gel coatings for corrosion protection of aluminum alloys. Eur Fed Corros Publ 2011;58(Self-Healing Properties of New Surface Treatments):202–19.
151. Pirhady TN, Sanjabi S, Shahrabi T. Evolution of corrosion protection performance of hybrid silica based sol-gel nanocoatings by doping with inhibitor. Mater Corros 2011;62(5):411–5.
152. Snihirova D, Lamaka SV, Taryba M, et al. Hydroxyapatite microparticles as feedback-active reservoirs of corrosion inhibitors. ACS Appl Mater Interfaces 2010;2(11):3011–22.
153. Rosero-Navarro NC, Pellice SA, Duran A, et al. Effects of Ce-containing sol-gel coatings reinforced with SiO_2 nanoparticles on the protection of AA2024. Corros Sci 2008;50(5):1283–91.
154. Moutarlier V, Neveu B, Gigandet MP. Evolution of corrosion protection for sol-gel coatings doped with inorganic inhibitors. Surf Coat Technol 2008;202(10):2052–8.
155. Voevodin NN, Grebasch NT, Soto WS, et al. Potentiodynamic evaluation of sol-gel coatings with inorganic inhibitors. Surf Coat Technol 2001;140(1):24–8.
156. Sheffer M, Groysman A, Starosvetsky D, et al. Anion embedded sol-gel films on al for corrosion protection. Corros Sci 2004;46(12):2975–85.
157. Khramov AN, Voevodin NN, Balbyshev VN, et al. Hybrid organo-ceramic corrosion protection coatings with encapsulated organic corrosion inhibitors. Thin Solid Films 2004;447–448:549–57.

158. Chen T, Fu JJ. An intelligent anticorrosion coating based on pH-responsive supramolecular nanocontainers. Nanotechnology 2012;23(50):505705/1–12.
159. Galio AF, Lamaka SV, Zheludkevich ML, et al. Inhibitor-doped sol-gel coatings for corrosion protection of magnesium alloy AZ31. Surf Coat Technol 2010;204(9–10):1479–86.
160. Mengoli G, Munari MT, Bianco P, et al. Anodic synthesis of polyaniline coatings onto iron sheets. J Appl Polym Sci 1981;26(12):4247–57.
161. DeBerry DW. Modification of the electrochemical and corrosion behavior of stainless steels with an electroactive coating. J Electrochem Soc 1985;132:1022–6.
162. MacDiarmid AG, Ahmad N. Polyaniline film on metal surface for preventing corrosion. Assignee: Trustees of the University of Pennsylvania, USA. *US Patent Number 5,645,890*; July 8, 1997.
163. Ahmad N, MacDiarmid AG. Inhibition of corrosion of steels with the exploitation of conducting polymers. Synth Met 1996;78(2):103–10.
164. Jakubowski M. Zinc and cadmium compounds. In: 6th ed. Patty's toxicology, vol. 1. Hoboken, NJ: John Wiley & Sons; 2012. p. 167–211.
165. Tokumoto M, Fujiwara Y, Shimada A, et al. Cadmium toxicity is caused by accumulation of p53 through the down-regulation of Ube3d family genes in vitro and in vivo. J Toxicol Sci 2011;36(2):191–200.
166. Praveen CV, Pradeep Kiran JA, Bhaskar M. Cadmium toxicity-a health hazard and a serious environmental problem-an overview. Int J Pharm Bio Sci 2012;2(4):235–46.
167. Hermas AA, Wu ZX, Nakayama M, et al. Passivation of stainless steel by coating with poly(*o*-phenyenediamine) conductive polymer. J Electrochem Soc 2006;153(6):B199–205.
168. Kraljic M, Zic M, Duic L. *O*-phenylenediamine-containing polyaniline coatings for corrosion protection of stainless steels. Bull Electrochem 2004;20(12):567–70.
169. Wessling B. Passivation of metals by coating with polyaniline: corrosion potential shift and morphological changes. Adv Mater 1994;6(3):226–8.
170. Cook A, Gabriel A, Laycock N. On the mechanism of corrosion protection of mild steel with polyaniline. J Electrochem Soc 2004;151(9):B529–35.
171. Kinlen PJ, Ding Y, Silverman DC. Corrosion protection of mild steel using sulfonic and phosphoric acid-doped polyanilines. Corrosion 2002;58(6):490–7.
172. Yan MC, Tallman DE, Rasmussen SC, et al. Corrosion control coatings for aluminum alloys based on neutral and n-doped conjugated polymers. J Electrochem Soc 2009;156(10):C360–6.
173. Seegmiller JC, Pereira da Silva JE, Buttry DA, et al. Mechanism of action of corrosion protection coating for AA2024-t3 based on poly(aniline)-poly(methylmethacrylate) blend. J Electrochem Soc 2005;152(2):B45–53.
174. Cecchetto L, Delabouglise D, Petit J-P. On the mechanism of the anodic protection of aluminum alloy AA5182 by emeraldine base coatings evidences of a galvanic coupling. Electrochim Acta 2007;52:3485–92.
175. Kendig M, Hon M. Environmentally triggered release of oxygen-reduction inhibitors from inherently conducting polymers. Corrosion 2004;60(11):1024–30.
176. Cogan SF, Gilbert MD, Holleck GL, et al. Galvanic coupling of doped polyaniline and aluminum alloy 2024-T3. J Electrochem Soc 2000;147(6):2143–7.
177. Spinks GM, Dominis AJ, Wallace GG, et al. Electroactive conducting polymers for corrosion control. J Solid State Electrochem 2002;6:85–100.
178. Aradilla D, Azambuja D, Estrany F, et al. Poly(3,4-ethylenedioxythiophene) on self-assembled alkanethiol monolayers for corrosion protection. Polym Chem 2011;2:2548–56.
179. Popovic MM, Grgur BN. Electrochemical synthesis and corrosion behavior of thin polyaniline-benzoate film on mild steel. Synth Met 2004;143:191–5.
180. Tuken T, Arslan G, Yazici B, et al. The corrosion protection of mild steel by polypyrrole/polyphenol multilayer coating. Corros Sci 2004;46:2743–54.

181. Camalet J-L, Lacroix J-C, Aeiyach S, et al. Electrodeposition of polyaniline on mild steel in a two step process. Synth Met 1999;102:1386–7.
182. Irvin DJ, Anderson N, Webber C, et al. New synthetic routes to poly(bis(dialkylamino)phenylenevinylene)s (BAM-PPV). ACS PMSE Prepr 2002;86:61–2.
183. Stenger-Smith JD, Miles MH, Norris WP, et al. Amino functional poly(para-phenylene vinylene)s as protective coatings. Assignee: United States Department of the Navy, USA. *US Patent Number 5,904,990A*; May 18, 1999.
184. Stenger-Smith JD, Merwin LH, Shaheen SE, et al. Synthesis and characterization of poly(2,5-bis(N-methyl-N-hexylamino)phenylene vinylene), a conjugated polymer for light-emitting diodes. Macromolecules 1998;31(21):7566–9.
185. Kus E, Grunlan M, Weber WP, et al. Evaluation of the protective properties of novel chromate-free polymer coatings using electrochemical impedance spectroscopy. In: Zarras P, Wood T, Brough R, et al., editors. New developments in coatings technology. ACS symposium series 962. Washington, DC: American Chemical Society; 2007. p. 297–322.
186. Zarras P, He J, Tallman DE, et al. Electroactive polymer coatings as replacements for chromate conversion coatings. In: Provder T, Baghdachi J, editors. Smart coatings. ACS symposium series 957. Washington, DC: American Chemical Society; 2007. p. P135–51.
187. Zarras P, Anderson N, Webber C, et al. Electroactive materials as smart corrosion-inhibiting coatings for the replacement of hexavalent chromium. Coating Tech 2011;8(1):40–4.
188. Zarras P, Anderson N, Webber C, et al. Novel conjugated polymers based on derivatives of poly(phenylene vinylene)s as corrosion protective coatings in marine environments. In: PACE. September 8–9, 2004, Cologne, Germany; 2004. p. 175–81.
189. Khan MI, Chaudhry AU, Hashim S, et al. Recent developments in intrinsically conductive polymer coatings for corrosion protection. Chem Eng Res Bull (Dhaka) 2010;14(2):73–86.
190. Rohwerder M. Conducting polymers for corrosion protection: a review. Int J Mater Res 2009;100(1):1331–42.
191. Zarras P, Anderson N, Webber C, et al. Progress in using conductive polymers as corrosion-inhibiting coatings. Rad Phys Chem 2003;68(3–4):387–94.
192. Jennings GK, Laibinis PE. Self-assembled organic monolayer films on underpotentially deposited metal layers. Mater Res Soc Symp Proc 1997;451(Electrochemical Synthesis and Modification of Materials):155–60.
193. Smith RK, Lewis PA, Weiss PS. Patterning self-assembled monolayers. Prog Surf Sci 2004;75:1–68.
194. Poirier GE. Characterization of organosulfur molecular monolayers on Au(111) using scanning tunneling microscopy. Chem Rev (Washington, DC) 1997;97(4):1117–27.
195. Rohwerder M, Stratmann M. Surface modification by ordered monolayers: new ways of protecting materials against corrosion. MRS Bull 1999;24(7):43–7.
196. Burleigh TD, Shi C, Killic S, et al. Self-assembled monolayers of perfluoroalkyl amideethanethiols, fluoralkylthiols, and alkylthiols for the prevention of silver tarnish. Corrosion (Houston, TX, United States) 2002;58(1):49–56.
197. Srivastava P, Chapman WG, Laibinis PE. Molecular dynamics simulation of oxygen transport through n-alkanethiolate self-assembled monolayers on gold and copper. J Phys Chem B 2009;113(2):456–64.
198. Sortino S, Petralia S, Conoci S, et al. Novel self-assembled monolayers of dipolar ruthenium (III/II) pentaamine(4,4′-bipyridinium) complexes on ultrathin platinum films as redox molecular switches. J Am Chem Soc 2003;125(5):1122–3.
199. Wapner K, Stratmann M, Grundmeier G. Structure and stability of adhesion promoting aminopropyl phosphonate layers at polymer/aluminum oxide interfaces. Int J Adhes Adhes 2007;28 (1–2):59–70.

200. Ishibashi M, Itoh M, Nishihara H, et al. Permeability of alkanethiol self-assembled monolayers adsorbed on copper electrodes to molecular oxygen dissolved in 0.5 M Na2SO4 solution. Electrochim Acta 1996;41(2):241–8.
201. Jennings GK, Laibinis PE. Self-assembled monolayers of alkanethiols on copper prove corrosion resistance in aqueous environments. Colloids Surf A Physicochem Eng Asp 1996;116(1/2):105–14.
202. Itoh M, Nishihara H, Aramaki K. Preparation and evaluation of two-dimensional polymer films by chemical modification of an alkanethiol self-assembled monolayer for protection of copper against corrosion. J Electrochem Soc 1995;142(11):3696–704.
203. Appa Rao BV, Narsihma Reddy M. Self-assembled 1-octadecyl-1H-benzimidazole film on copper surface for corrosion protection. J Chem Soc (Bangalore, India) 2013;125(6):1325–38.
204. Laio QQ, Yue ZW, Yang D, et al. Inhibition of copper corrosion in sodium chloride solution by the self-assembled monolayer of sodium diethyldithiocarbamate. Corros Sci 2011;53:1999–2005.
205. Tuken T, Kicir N, Elalan N, et al. Self-assembled film based on hexane-1,6-diamine and 2-mercapto-ethanol on copper. Appl Surf Sci 2012;258(18):6793–9.
206. Maxisch M, Thissen P, Giza M, Grundmeier G. Interface chemistry and molecular interactions of phosphonic acid self-assembled monolayers on oxyhydroxide-covered aluminum in humid environments. Langmuir 2011;27:6042–8.
207. Qu J-E, Wang H-R, Zhang Q, et al. Self-assembling behavior and corrosion inhibition of TDPA on differently structured surfaces of 2024 and 1060 aluminum alloys. Int J Mater Res 2012;103(10):1257–64.
208. de Souza S, Yoshikawa DS, Izaltino WAS, et al. Self-assembling molecules as corrosion inhibitors for 1050 aluminum. Surf Coat Technol 2010;204:3238–42.
209. Rajendran S, Sribharathy V, Krishnaveni A, et al. Corrosion inhibitive property of self assembled nano films formed by adipic acid molecules on carbon steel surface. Thin Film Technol 2012;50:10509–13.
210. Liu X, Chen S, Zhai H, et al. The study of self-assembled films of triazole on iron electrodes using electrochemical methods, XPS, SEM and molecular simulation. Electrochem Commun 2007;7:813–9.
211. Chen YY, Chen SG, Chen Y, et al. Surface analysis and electrochemical behavior of the self-assembled polydopamine/dodecanethiol complex films in protecting 304 stainless steel. Sci China Tech Sci 2012;55(6):1527–34.
212. Matsuzaki A, Nagoshi M, Hara N. Corrosion resistance and structure of thiol self-assembly super thin film on zinc coated steel sheet. ISIJ Int 2011;51(1):108–14.
213. Fan H, Li S, Zhao Z, et al. Inhibition of brass corrosion in sodium chloride solutions by self-assembled silane films. Corros Sci 2011;53:4273–81.
214. Guo X, An M. Experimental study of electrochemical corrosion behavior of bilayer on AZ31B Mg alloy. Corros Sci 2010;52(12):4017–27.
215. L'vov YM, Decher G. Assembly of multilayer ordered films by alternating adsorption of oppositely charged macromolecules. Crystallogr Rep 1994;39(4):696–716.
216. Yoo D, Rubner MF. Layer-by-layer modification of surfaces through the use of self-assembled monolayers of polyions. Ann Tech Conf Soc Plast Eng 1995;53(2):2568–70.
217. Quinn A, Such GK, Quinn JF, et al. Polyelectrolyte blend multilayers: a versatile route to engineering interfaces and films. Adv Funct Mater 2008;18:17–26.
218. Andreeva DV, Skorb EV, Shchukin DG. Layer-by-layer polyelectrolyte/inhibitor nanostructures for metal corrosion protection. ACS Appl Mater Interfaces 2010;2(7):1954–62.
219. Andreeva DV, Fix D, Mohwald H, et al. Self-healing anticorrosion coatings based on pH-sensitive polyelectrolyte/inhibitor sandwichlike nanostructures. Adv Mater 2008;20:2789–94.
220. Lari BR, Sabbaghi S. Investigation of corrosion behavior of PAA-PAH polyelectrolyte multilayer nano-film on steel substrates. World Appl Sci J 2011;14(2):199–206.

221. Derakhshandeh R, Lari BR, Sabbaghi S, et al. Control of corrosion in steel substrates by using polyelectrolyte multilayer nano-film. World Appl Sci J 2010;9(10):1129–38.
222. Grigoriev DO, Kohler K, Skorb E, et al. Polyelectrolyte complexes as a "smart" depot for self-healing anticorrosion coatings. Soft Matter 2009;5:1426–32.
223. Faure E, Halusiak E, Farina F, et al. Clay and DOPA containing polyelectrolyte multilayer film for imparting anticorrosion properties to galvanized steel. Langmuir 2012;28:2971–8.
224. Dihora JO, Smets J, Schwantes TA, et al. Microcapsules comprising vinyl polymers for delivery of benefit agents such as perfumes. Assignee: The Proctor & Gamble Company, USA. *WO 2010084480 A2*; July 29, 2010.
225. Zhou M, Leong TSH, Melino S, et al. Sonochemical synthesis of liquid-encapsulated lysozyme microspheres. Ultra Sonochem 2010;17(2):333–7.
226. Wang AJ, Lin YF, Jian CH, et al. Polymeric microspheres for encapsulation of drugs. Assignee: Industrial Technology Research, Taiwan. *US Patent Number 20060141021 A1*; June 29, 2006.
227. Yow HN, Routh AF. Formation of liquid core-polymer shell microcapsules. Soft Matter 2006;2(11):940–9.
228. Calle LM, Li W, Buhrow JW, et al. The benefits of self-corrosion control: multifunctional paints react automatically and rapidly to corrosion. Eur Coat J 2011;11:18–23.
229. Calle LM, Li WN, Buhrow JW, et al. Elongated microcapsules and their formation for use in paints or composites. Assignee: United States Aeronautics and Space Administration, USA. *US Patent Number 20120207921 A1*; August 16, 2012.
230. Puri RG, Meshram RD, Sirsam RS. Recent developments in smart coatings for corrosion protection. Paintindia 2012;62(5):55–61.
231. Chen T, Fu JJ. An intelligent anticorrosion coating based on pH-responsive supramolecular nanocontainers. Nanotechnology 2012;23(50):505705.
232. Chen T, Fu JJ. pH-responsive nanovalves based on hollow mesoporous silica spheres for controlled release of corrosion inhibitor. Nanotechnology 2012;23(23):235605/1–8.
233. Fu JJ, Chen T, Wang MD, et al. Acid and alkaline dual stimuli-responsive mechanized hollow mesoporous silica nanoparticles as smart nanocontainers for intelligent anticorrosion coatings. ACS Nano 2013;7(12):11397–408.
234. Abdullayev E, Lvov Y. Halloysite clay nanotubes for controlled release of protective agents. J Nanosci Nanotechnol 2011;11(11):10007–26.
235. Ling CC, Xue QZ, Jung NN, et al. Collapse and stability of functionalized carbon nanotubes on Fe(100) surface. RSC Adv 2012;2(19):7549–56.
236. Hang TTX, Truc TA, Nguyen TD, et al. Preparation and characterization of nanocontainers of corrosion inhibitor based on layered double hydroxides. Appl Clay Sci 2012;67–68:18–25.
237. Balaskas AC, Kartsonakis IA, Tziveleka LA, et al. Improvement of anti-corrosive properties of epoxy-coated AA 2024-T3 with TiO_2 nanocontainers loaded with 8-hydroxyquinone. Prog Org Coat 2012;74(3):418–26.
238. Videla HA. Biocorrosion and microbial corrosion inhibition: a review. International Corrosion Congress, 18th, Perth, Australia. November 20–24, 2011; Volume 1: plenary 4/1-plenary 4/10.
239. Davey ME, O'Toole GA. Microbial biofilms: from ecology to molecular genetics. Microbiol Mol Biol Rev 2000;64(4):847–67.
240. Zuo R. Biofilms: strategies for metal corrosion inhibition employing microorganisms. Appl Microbiol Biotechnol 2007;76:1245–53.
241. Little B, Ray R. A perspective on corrosion inhibition by biofilms. Corrosion (Houston, TX, United States) 2002;58(2):424–8.
242. Ponmariappan S, Maruthamuthu S, Palaniappan R. Inhibition of corrosion of mild steel using *Staphylococcus* sp. Trans SAEST 2004;39(4):99–108.

243. Mansfeld F, Hsu H, Ornek D, et al. Corrosion control using regenerative biofilms on aluminum 2024 and brass in different media. J Electrochem Soc 2002;149(4):B130–8.
244. Li FS, An MZ, Duan DX. Corrosion inhibition of stainless steel by a sulfate-reducing bacteria biofilm in sea water. Int J Min Met Mater 2012;19(8):717–25.
245. Chongdar S, Gunasekaran G, Kumar P. Corrosion inhibition of mild steel by aerobic biofilm. Electrochim Acta 2005;50(24):4655–65.
246. Ornek D, Wood TK, Hsu CH, et al. Pitting corrosion control of aluminum 2024 using protective biofilms that secrete corrosion inhibitors. Corrosion (Houston, TX, United States) 2002;58(9):761–7.
247. Ornek D, Jayaraman A, Syrett BC, et al. Pitting corrosion inhibition of aluminum 2024 by Bacillus biofilms secreting polyaspartate or γ-polyglutamate. Appl Microbiol Biotechnol 2002;58(5):651–7.
248. Garcia F, Lopez ALR, Guillen JC, et al. Corrosion inhibition in copper by isolated bacteria. Anti-Corros Meth Mater 2012;59(1):10–7.
249. Wood TK, Ornek D, Mansfeld FB. Preventing corrosion on metal or alloy surface with beneficial bacteria biofilms. Assignee: Electric Power Research Institute, Inc. USA. *WO 2002040746*; May 23, 2002.

Chapter 4

Low Temperature Coating Deriving from Metal-Organic Precursors: An Economical and Environmentally Benign Approach

Jyoti Prakash*, B.M. Tripathi*, Sunil Kumar Ghosh†,
**Powder Metallurgy Division, Bhabha Atomic Research Centre, Trombay, Mumbai, India*
†Bio Organic Division, Bhabha Atomic Research Centre, Trombay, Mumbai, India
jprakash@barc.gov.in

Intelligent Coatings for Corrosion Control
Copyright © 2015 Elsevier Inc. All rights reserved.

4.1 Introduction

The performance of composites with metal, intermetallic, or ceramic matrices in many cases depends on the development of suitable coatings to protect against environmental degradation. For example, promising carbon composites undergo damage when thermally fatigued in oxidizing atmospheres.[1,2] Many ceramic matrix composites (CMCs) lose a significant fraction of their room temperature tensile properties after preexposure in air at 1000 °C,[3] and some nonoxide-reinforced oxide matrix composites that are thermochemically compatible in an inert environment form intermediate compounds when exposed to oxygen.[4] Silicon carbide (SiC) and silicon nitride (Si_3N_4) ceramics and composites generally display excellent oxidation resistance but corrode severely in the presence of alkali compounds[5,6] and therefore require protective coatings for use in industrial stack gas environments.[7–9] Protective coatings may provide solutions to these problems if the integrity of the coating can be maintained throughout the projected service life of the component. Among the several key issues that must be considered when selecting coating materials are: (1) the coating must possess the ability to resist reaction with aggressive environments, as well as low oxygen permeability to limit the transport of oxygen, (2) the coefficient of thermal expansion (CTE) of the coating should be close to that of the substrate material in order to prevent delamination or cracking due to the stress caused by CTE mismatch, (3) the coating must maintain a stable phase under thermal exposure. Phase transformation typically accompanies a volumetric change, disrupting integrity of the coating, and (4) the coating must be chemically compatible with the substrate to avoid detrimental chemical interaction.

In the past few years, ceramic coatings have received considerable attention for a variety of reasons, including economics (substitution of expensive alloys by cheaper alternatives, extension of service life of alloys), material protection from wear, corrosion, and erosion, and improvement and development of new material properties.[10–12] Ceramic coatings can be useful in a wide range of applications, such as thermal barriers for gas turbine blades and vanes; hot section parts of diesel engines; materials where wear, corrosion, and oxidation resistance are necessary; electrical insulation in electronic circuit substrates; and nuclear technology and medical applications.[13–17]

There are a number of factors to be considered when developing a coating process for an industrial application. These include capital investment, ease of manufacturing, coating performance, and environmental issues. Although a large number of coating techniques such as electrochemical plating,[18] conversion coatings,[19,20] anodizing,[19] and polymer plating sol-gel coating;[21,22] or plasma polymerization,[23] chemical vapor deposition (CVD),[24] physical vapor deposition (PVD),[25] and so on are available for protecting materials, the widespread use of materials in the industry is still deterred by the lack of appropriate protective coatings that can withstand harsh service conditions. Therefore, a great deal of research is aimed at developing

better, simpler, cheaper coating technologies so we can take advantage of the lower weight and excellent mechanical properties of this material. CVD is the most frequently used technique to deposit thick ceramic coatings (e.g., SiC, TiC, B_4C, TiN, BN, Si_3N_4, TiB_2, MoSi, and Al_2O_3) to protect engineering components against chemical diffusion, wear, friction, oxidation, and corrosion.[26] The cost of CVD for the protective coatings market is generally lower than the functional thin films for the semiconductor industry as it involves coating a large volume of engineering components. Other competing deposition methods for protective coatings are plasma spraying[27] and PVD. However, plasma spraying tends to produce a splatlike structure with a high degree of porosity, microcracks, and surface roughness. A thicker coating is required to provide adequate protection against wear and corrosion, and extensive grinding and polishing postdeposition is required to obtain a smoother surface. Moreover, the splatlike structure is mechanically not as robust as the equiaxed/columnar structure deposited using the CVD and PVD techniques. The PVD method is a line-of-sight process. Therefore, in the PVD process, use of multiple targets and a rotating substrate is often required to improve uniformity of the coating on complex shape components. However, CVD does not have such limitations. In the CVD process of ceramic coating a high deposition temperature is usually required to ensure good adhesion of the thick coating on the substrate as compared to lower deposition temperatures in CVD of thin films. Good coating adhesion is essential for thermal, chemical (corrosion, diffusion resistance), and/or mechanical (e.g., wear, abrasion resistance) properties. Therefore, this requirement limits the use of CVD for applications where the substrate or engineering components are susceptible to high temperatures. For example, the deposition of thick, hard, and wear-resistant coatings onto high-speed cutting tool steels using thermally activated CVD is less suitable because tool steel has a low austenising temperature (450-550 °C). The CVD deposition of protective coatings such as TiC and TiN would require high temperatures (>1000 °C), which is above the tempering temperature of most steels.[28] This leads to softening of the steel substrate, and therefore subsequent heat treatment is required for rehardening, which may cause deformation, change of substrate dimensions, and increase in the cost of production. However, there are other variants of CVD, such as plasma-enhanced CVD (PECVD) and metal-organic CVD (MOCVD), which can lower the deposition temperatures and produce high-quality ceramic protective coatings without degrading the tool steel substrates; but their cost of production is still relatively high compared to the other coating techniques. Many such limitations of CVD coating can be suitably addressed to a great extent by replacing conventional inorganic precursors with metal-organic precursors in CVD coating. In addition, using metal-organic precursors in CVD is economical and environmentally benign. The present chapter covers different variants of coating using metal-organic precursors as well as relatively cheaper synthesis routes for some of the metal-organic precursors that can be used for CVD coating.

4.2 Chemical Vapor Deposition: MOCVD Variant Techniques

CVD of films and coatings involves the chemical reactions of gaseous reactants on or near the vicinity of a heated substrate surface. This atomistic deposition method can provide very pure materials with structural control at an atomic or nanometer scale. Moreover, it can produce single-layer, multilayer, composite, nanostructured, and functionally graded coating materials with well-controlled dimensions and unique structures at low processing temperatures. Furthermore, the unique feature of CVD in contrast to other deposition techniques such as the non-line-of-sight-deposition process has allowed coating of complex shape engineering components and the fabrication of nano-devices, carbon-carbon (C-C) composites, CMCs, and free-standing shape components. The versatility of CVD had led to rapid growth, and it has become one of the main processing methods for the deposition of thin films and coatings for a wide range of applications including semiconductors (e.g., Si, Ge, $Si_{1-x}Ge_x$, III-V, II-VI) for microelectronics, optoelectronics, energy conversion devices; dielectrics (e.g., SiO_2, AlN, Si_3N_4) for microelectronics; refractory ceramic materials (e.g., SiC, TiN, TiB_2, Al_2O_3, BN, $MoSi_2$, ZrO_2) used for hard coatings, protection against corrosion, oxidation, or as diffusion barriers; metallic films (e.g., W, Mo, Al, Au, Cu, Pt) for microelectronics and for protective coatings; fiber production (e.g., B and SiC monofilament fibers) and fiber coating.[24]

The conventional CVD method, so-called thermal-activated CVD (TACVD),[29] uses thermal energy to activate the chemical reactions. However, the CVD reactions can also be initiated using different energy sources. This has given rise to other variants of CVD methods such as PECVD[29] and photo-assisted CVD (PACVD),[30] which use plasma and light, respectively, to activate the chemical reactions. Atomic layer epitaxy (ALE)[31] is a special mode of CVD where a "monatomic layer" can be grown in sequence by sequentially saturating surface reactions. Such CVD variants are useful for the controlled growth of epitaxial films and the fabrication of tailored molecular structures. Flame-assisted vapor deposition (FAVD)[32] uses a flame source to initiate the chemical reaction and/or heating of the substrate. Electrochemical vapor deposition (EVD) is another variant of CVD that is tailored for the deposition of dense films onto porous substrates. Chemical vapor infiltration (CVI)[33] is a form a CVD that has been adapted for the deposition of a dense ceramic matrix during the fabrication of ceramic fiber-reinforced CMCs. Other CVD variants such as pulsed injection CVD[34] and aerosol-assisted CVD[35] use special precursor generation and delivery systems unlike conventional CVD.

MOCVD[36] is a variant of CVD, which has been classified according to the use of metal-organic compounds as precursors. Use of metal-organic precursors in MOCVD has several advantages, such as lower deposition temperature, safe operation, and cost effectiveness. Metal-organic compounds, also known as "metalorganics," contain

metal atoms bonded to some organic radicals. The compounds having one or more direct metal-carbon covalent bonds are called "organometallics." Metalorganics as well as organometallics both can be used as precursors in MOCVD. Use of organometallic precursors has led to the rename of the deposition process as organometallic CVD (OMCVD) to reflect more precisely the choice of precursors used. In conventional OMCVD, the precursor is vaporized at low temperature, under reduced pressure condition and subsequently, metal film is deposited on a substrate surface at higher temperature by adsorption and thermal decomposition of the precursor. The various parameters that control this deposition technique are as following: (1) convection of the gaseous reagents, (2) diffusion of the reagents toward the substrate, (3) adsorption of the reagents onto the substrate, (4) chemical reaction of the adsorbed species producing nuclei and further reaction to give a metal film, (5) desorption of the gas products of the reaction, (6) diffusion of these products through the boundary layer, and (7) gas evacuation of the system (Figure 4.1).

The reader must keep in mind that in all deposition techniques described in this chapter, the important factors which determines the system is surface limited or transport limited are temperature, flow rate, pressure, reactor and substrate geometry. All these parameters are discussed elsewhere.[10] Diffusions at the boundary layer are a complex phenomenon, and results cannot be applied directly from one system to another. The choice of a CVD method among all those described will be made regarding specifications of the deposit in terms of topology, purity, physical properties, process speed, and cost. Different variants of CVD which can use metal-organic precursors are described in detail in the subsequent sections.

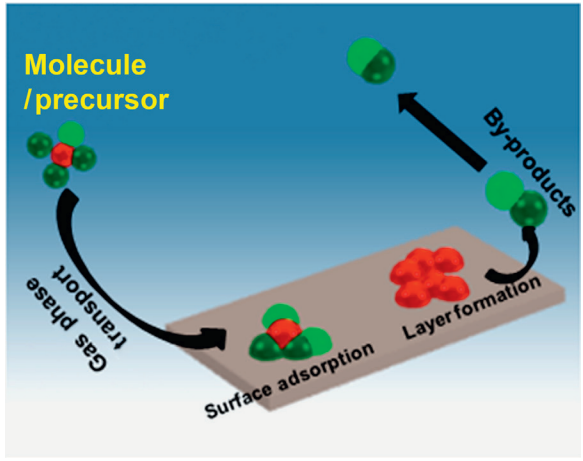


Figure 4.1 Schematic representation of general chemical vapor deposition process.

4.2.1 Laser-induced chemical vapor deposition

In this technique, decomposition of precursor is induced with a laser beam (Figure 4.2).[37,38] Laser-induced chemical vapor deposition (LCVD) has the advantages of better control of the decomposition mechanism compared to the traditional method and being able to function on a substrate-limited surface. This method allows the deposition in confined zones and at low substrate temperature. The process can be carried out with substrates that do not have high thermal conductivity, and the deposit growth kinetics is often faster than those observed with traditional OMCVD. In LCVD, it is also possible to work at higher precursor pressure than in traditional CVD because the growth kinetics here are being limited by gas-phase decomposition. Nevertheless, for most of the applications considered currently—repair of circuits, manufacture of prototypes, and so on—the writing speed remain slow (several ms^{-1} depending on conditions). Deposit resistivity can be optimized toward deposition rate and laser power. Optimum required deposition rate is neither too slow nor too fast and laser power neither too weak nor too strong. Partial pressure of precursor seems to be the critical factor, allowing an increase in deposition rate without loss in the overall deposit quality. To obtain a film with few impurities, the laser must decoordinate all the precursor ligands, avoiding the incorporation of carbon and other elements into the film. The growth rate depends on the wavelength of light used and on the laser power. Photolysis can occur in several stages with

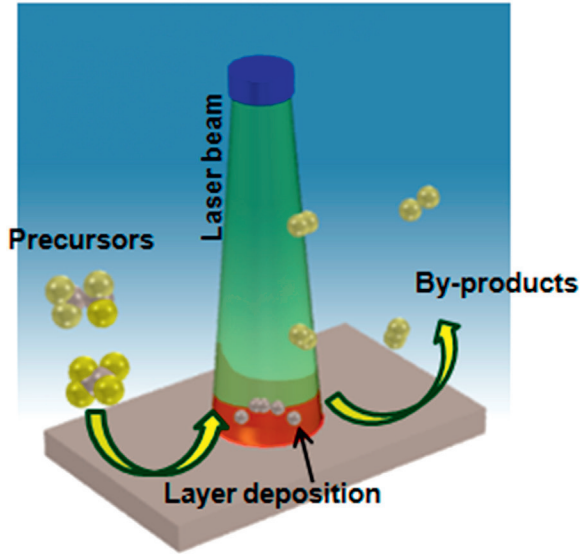


Figure 4.2 Schematic representation of laser induced chemical vapor deposition (LICVD).

quantum yields also dependent on the laser wavelength. Another phenomenon can occur when overheating of the deposit by the laser leads to the precursor desorption.[39] When the laser induces excess heating of the substrate, the deposition cannot be considered pure LCVD, the precursor decomposition becoming primarily thermal and no longer photolytic.

4.2.2 UV-induced chemical vapor deposition

The OMCVD can also be carried out under the irradiation of a UV lamp, which can improve the process of nucleation while lowering the operational deposition temperature (Figure 4.3). In the case of UV-induced chemical vapor deposition (UVCVD) the deposition can be performed in two modes.[40,41] The first, consisting of depositing the precursor on the substrate then irradiation; the second, depositing the metal directly by adsorption, followed by decomposition of the precursor by irradiation of the substrate. In both cases the deposition mechanism has been different and it affects the final coating morphology.

4.2.3 Plasma-enhanced CVD

PECVD is also known as glow discharge CVD (Figure 4.4). It uses electron energy (plasma) as the activation method to enable deposition to occur at a low temperature and at a reasonable rate. Supplying electrical power at a sufficiently high voltage to a gas at reduced pressures (<1.3 kPa) results in the breaking down of the gas and generates a glow discharge plasma consisting of electrons, ions, and

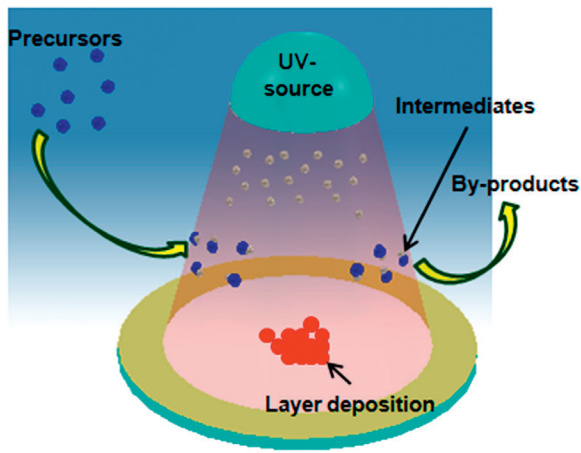


Figure 4.3 Schematic representation of UV induced chemical vapor deposition (UVCVD).

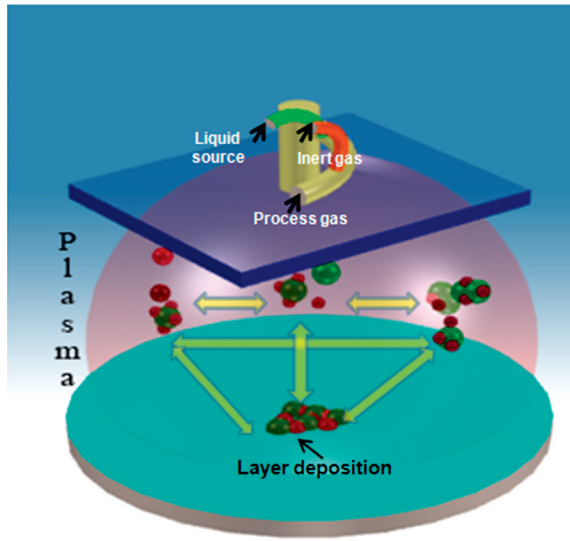


Figure 4.4 Schematic representation of plasma enhanced platinum CVD (PECVD).

electronically excited species. The vapor reactants are ionized and dissociated by electron impact, and hence generated, chemically active ions and radicals that undergo heterogeneous chemical reaction at or near the heated substrate surface and deposit a thin film. The temperature of electron can be in the order of 20,000 °C or higher, while the temperature of the vapor reactants may remain near room temperature, depending on the pressure at which the discharge is operated. The chemical reactions that occur during the glow discharges are complex and can be categorized into homogeneous gas phase collisions and heterogeneous surface interactions. Bell[42] has studied the ways to generate reactive free radicals and ions through the homogeneous gas phase collisions of electrons with vapor reactants and proposed generic examples of electron impact reactions and the rate of reactions. Inelastic collisions between heavy particles during the homogeneous impact reaction have also been considered. Catherine[43] has considered the overall complexity of the plasma process and the growth kinetics during the PECVD of films. This includes the influence of parameters to generate the plasma and the characteristics of such a plasma (e.g., electron ion densities and fluxes, residence time, etc.), which influence the ion energy and substrate temperature. Unlike thermally activated CVD, there is limited available fundamental information about the PECVD process. Hence, it is difficult to establish the relationship between the processing parameters and properties of the films because of the complexity of the PECVD reactions. Therefore, PECVD has the advantage of low temperature depositions where it cannot be met by thermally activated CVD.

4.2.4 Electron beam chemical vapor deposition

Electron beam chemical vapor deposition (EBCVD) is a technology that uses an electron beam to provide localized deposition for nano-scale structures or device fabrication (Figure 4.5). In EBCVD, primary electrons from the beam impact a substrate, causing secondary electrons to be emitted. These secondary electrons play a prominent role in dissociating adsorbed reagent molecules to form a deposit on the substrate and volatiles that are then evacuated from the chamber. The deposition process depends on many factors, including the precursor and the electron beam properties. If the electron beam is not moved relative to the substrate, a dot is grown. A fiber is grown if the growth time is increased. If the beam is moved, lines or other structures can be deposited as in rapid prototyping. High aspect ratio structures can be deposited as supertips on atomic force microscope tips to improve resolution. The resolution of the structures obtained (20 nm for a beam of 30 kV and 7 nm for 200 kV) are better than those obtained with LCVD (10-100 µm) or with ions beams (100 nm). Although deposits resulting from the application of EBCVD contain a lot of carbon,[44] the EBCVD method offers advantages over LACVD: leaving fewer impurities in the deposit and degrading the substrate less.[45] A posttreatment consisting of a heating step in the presence of oxygen decreases the level of impurities. The deposit may then suffer from a volume reduction due to carbon impurity elimination.

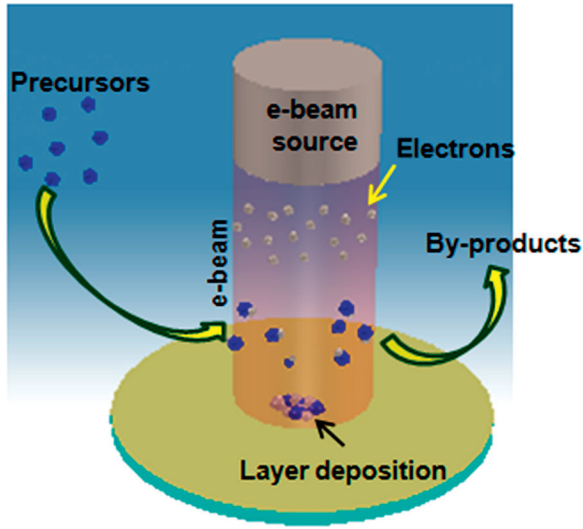


Figure 4.5 Schematic representation of electron beam chemical vapor deposition (EBCVD).

4.2.5 Fluidized bed chemical vapor deposition

Fluidized bed chemical vapor deposition (FBCVD) is one of the most efficient techniques to functionalize, to deposit on, or to coat each individual particle of a powder from gaseous species (Figure 4.6).[46] FBCVD combines two processes. One is the deposition itself, and the other aims in suspending the particles in the deposition zone, most often by flowing a gas upwards through the powder, and in bringing heat to the powder.[47] In contrast to CVD on flat surfaces that often operates in a surface kinetics limited regime, FBCVD is generally transport limited. This is due to the extremely high available growth surface to heated volume ratios (S/V) in the deposition area. Consequently, gaseous precursors are very often totally consumed a few centimeters after their entrance into the fluidized bed reactor, but the high degree of gas solid mixing compensates for this discrepancy and ensures isothermal conditions and uniform deposition.

4.2.6 Atomic layer deposition (ALD)

ALE[31] can be considered a special mode of CVD (Figure 4.7). It is a surface deposition process that can be used for the controlled growth of epitaxial films and the fabrication of tailored molecular structures on the surfaces of solid substrates. "Monatomic layers" can be grown in sequence, which is a characteristic feature of

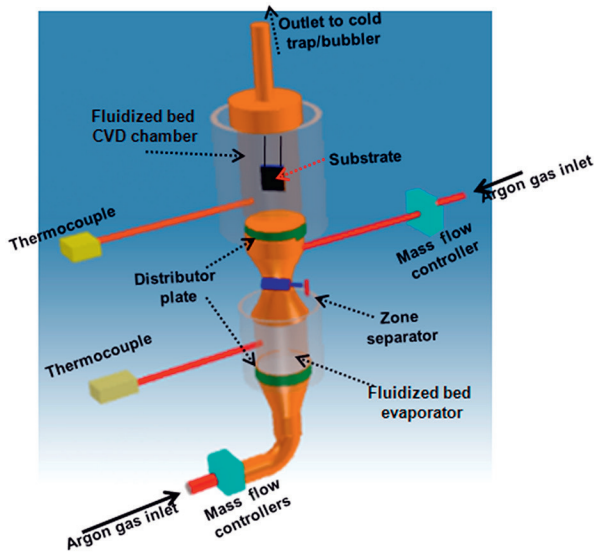


Figure 4.6 Schematic representation of fluidized bed chemical vapor deposition (FBCVD).

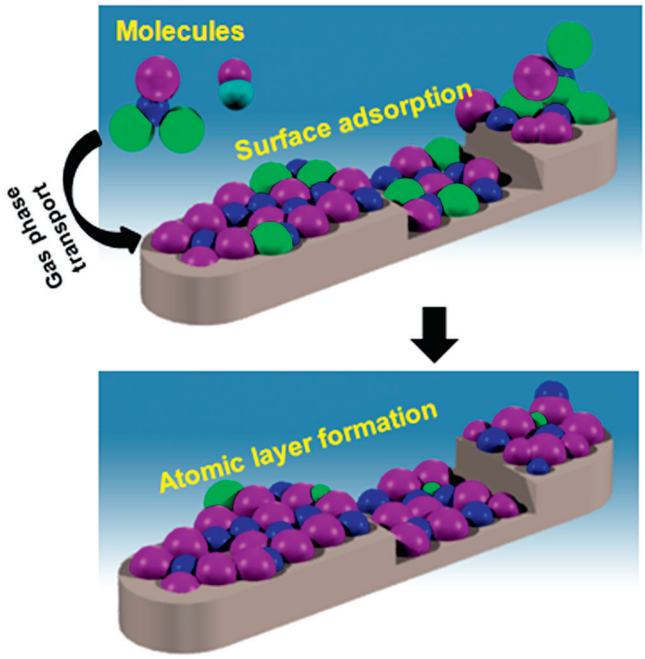


Figure 4.7 Schematic representation of atomic layer deposition (ALD).

ALE. Therefore, the desired coating thickness can be produced simply by counting the number of reaction sequences in the process. The surface reconstruction of the monolayer formed in the reaction sequence will influence the saturation mechanism and the saturation density of the precursor. The ALE reaction sequences are normally performed in an "effective overdosing" condition to ensure a complete saturation of the surface reaction to form the monoatomic layer. Furthermore, such "effective overdosing" condition also provides good conformal coverage that allows uniform coatings onto complex shaped substrates. The sequencing in ALE also eliminates the gas phase reactions and enables a wider choice of reactants (e.g., halides, metalorganics, elemental metal, etc.). The ALE process has the potential to be scaled up for the deposition of high-quality thin films with excellent uniformity and reproducibility onto large area substrate.[48,49] Layer-by-layer deposition processes have been tested with platinum precursors. Precursors, air or oxygen, and inert gases are introduced to the reactor in alternate pulses onto the hot substrate. A single atomic layer is formed through an autolimited growth mechanism. The complex partially decomposes by consuming all the available oxygen adsorbed on the precursor surface and the following oxygen pulse will finish the decomposition. Decomposition products are CO_2, water, and hydrocarbon residues if present in the

starting precursor. Film growth is slow when the deposition starts because of the nucleation step. The films obtained are much uniformed and have a rough surface and highly oriented grains. Adhesion of the films on these substrates is modest, but the amount of all impurities is low and decreases as the air pulse time increases. The decomposition limits its application and makes it also unsuitable for use in ALD conditions.

4.2.7 Focused ion-assisted chemical vapor deposition (IACVD)

Ion beams have been used for the local deposition in the OMCVD process.[50] In ion-assisted deposition, the ion beam decomposes an adsorbed layer of an organometallic precursor. This decomposition generates metal atoms on the surface of the substrate; the organic fragments diffuse away and are exhausted from the system. Film composition will therefore depend on the efficiency of precursor dissociation as well as the efficiency of volatile by-product diffusion away from the sample surface (Figure 4.8). These two parameters both should depend on the relative arrival rates of Ga^+ ions and of precursor molecules on the sample surface in case of Ga source. The effects of Ga^+ ion and precursor fluxes on the platinum film composition and resistivity have been determined for platinum deposition from organoplatinum compounds. Results show that increasing precursor flux at constant ion flux increases Pt and C, but decreases Ga content of the film.[51] Increasing ion-flux, at constant precursor

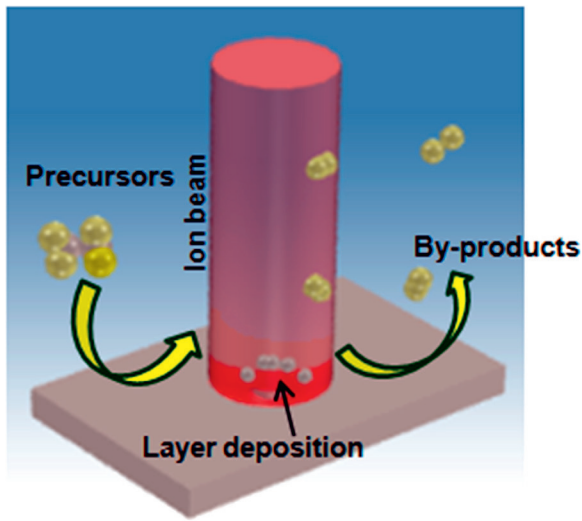


Figure 4.8 Schematic representation of focused ion-assisted chemical vapor deposition (IACVD).

flux, increases Pt content, while decreasing C content of the film. Resistivity neither depends on the film thickness nor on temperature, but was shown to follow C content; films with lower C content have lower resistivity.[51]

4.3 Organometallic Precursors: Economical Bulk Synthesis

In CVD, the solid phase is formed on a surface from a gas phase via one or several chemical reactions.[21] A key issue is the generation of the gas phase, whose composition must be stable during the deposition run. Hence, the choice of the precursors as well as of the delivery scheme is of utmost importance. Since the precursors are usually liquid or solid at room temperature and atmospheric pressure, an evaporation unit is required. Generally, organometallic precursors are preferred rather than halides since they are usually volatile at a much lower temperature (≤300 °C). The organic groups used for synthesis of organometallic precursor compounds broadly belong to β-diketonates, carbonyl and phosphine, cyclopentadienyl, and olefin and allyl family (Figure 4.9). Most commonly used precursors such as tetramethyl-heptanedionate compounds (tmhd: $C_{11}H_{19}O_2$), which are solid at room temperature, belong to the β-diketonates family. These precursors can be dissolved in an appropriate solvent, like monoglyme or octane. However, the β-diketonates exhibit a very poor thermal stability at their volatilization temperature. They tend to decompose before their complete evaporation, forming nonvolatile products. Thus, if they are evaporated in classical units such as a sublimator (for powders) or a bubbler (for liquids), a drift of the vapor pressure occurs upon prolonged heating, which in turn results in a drift of the final cationic composition. This issue became very clear for the deposition

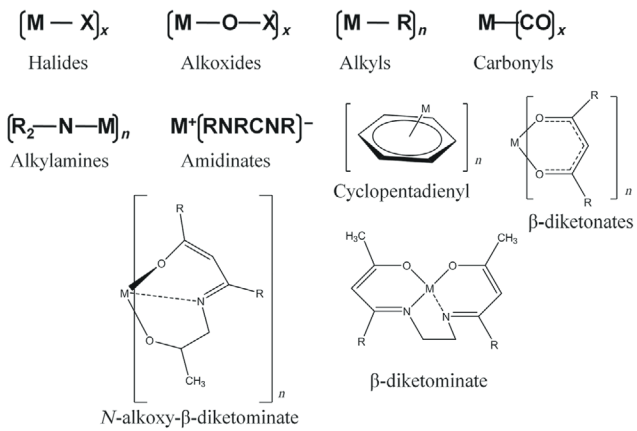


Figure 4.9 The organic groups used for synthesis of organometallic precursor compounds.

of compounds, which requires a stringent control of the stoichiometry. In addition, since the evaporation temperature has to be maintained below the decomposition temperature of the precursor, very low vapor pressures were obtained. These issues can be sorted out by using a suitable delivery system for liquid/solid precursors, a concept that is discussed in a later section. There have been several precursor synthesis routes, but few are selected here for different organometallic compound synthesis on the basis of economy and environment friendly routes. In the next section different organometallic compounds with their mostly used economic and environment friendly routes are discussed.

4.3.1 Organometallic precursors: oxide ceramics

4.3.1.1 Alumina precursors

Alumina (Al_2O_3) films are deposited by CVD to improve the performance of cemented carbide cutting tools, whereby in industry normally only the $AlCl_3$,/CO_2/H_2 reaction gas at temperatures around 1000 °C is used.[52] Instead of halide reaction gases, organometallic precursors enable Al_2O_3 coating at relatively low temperatures. The different reaction systems that were investigated can be classified into two groups: (1) aluminum alkyl compounds such as trimethyl-Al and oxygen or oxygen donors, and (2) aluminum alkoxide compounds. A limiting factor for the MOCVD technique is the high temperature sensitivity of most precursors and the violent reaction with oxygen or water. Most experiments in the literature using Al and O reported deposition using Al organic precursors was carried out at temperatures below 800 °C.[53]

4.3.1.1.1 Synthesis of aluminum isopropoxide

This compound is commercially available. Industrially, it is prepared by the reaction between isopropyl alcohol and aluminum metal, or aluminum trichloride (reaction scheme 4.1 and 4.2):

$$Al + 3iPrOH \longrightarrow Al\left(O\text{-}i\text{-}Pr\right)_3 \tag{4.1}$$

$$AlCl_3 + 3iPrOH \longrightarrow Al\left(O\text{-}i\text{-}Pr\right)_3 + 3HCl \tag{4.2}$$

Using aluminum metal, an older process uses a mercury catalyst (see below), whereas a more recent process does not.[54] In the laboratory, a widely accepted method for preparing aluminum isopropoxide was published in 1936 by Young et al.[55] Their procedure entails heating a mixture of 100 g of aluminum, 1200 mL of isopropyl alcohol, and 5 g of mercuric chloride at reflux. The process occurs via the formation of anamalgam of the aluminum. A catalytic amount of iodine is sometimes added to initiate the reaction, which can be quite vigorous. Young et al. achieved an 85-90% yield, after purification by distillation at 140-150 °C (5 mmHg).

4.3.1.1.2 Synthesis of Al-acetylacetonate

A general method of synthesis is to treat a metal salt with acetylacetone, acacH (reaction scheme 4.3):[56]

$$M^{z+} + z\left(\text{acacH}\right) \rightleftharpoons M\left(\text{acac}\right)_z + zH^+ \tag{4.3}$$

Addition of base assists the removal of a proton from acetylacetone and shifts the equilibrium in favor of the complex. Both oxygen centers bind to the metal to form a six-member chelate ring. In some cases the chelate effect is so strong that no added base is needed to form the complex. Some complexes are prepared by metathesis using Tlacac. In a typical synthesis route for Al-acetylacetonate (reaction scheme 4.4), ammoniacal solution of acetylacetone and aluminum sulfate, $Al_2(SO_4)_3.16H_2O$, solution were prepared. The ammoniacal solution of acetylacetone was added to the aluminum sulfate solution in small portions, with swirling. After complete addition of acetylacetone solution, the pH of solution was measured using blue litmus paper. If the solution was still acidic, ammonia was added by drops until it was just basic. It was left standing for 15 min and then filtered, washed with distilled water, and dried by suction. The product was transferred to a watch glass and air dried. A portion of the sample from cyclohexane was recrystallized. The resulting crystals were isolated by filtration, washed with a small volume of cold cyclohexane and dried in air.

$$Al^{3+} + 3CH_3COCH_2COCH_3 \longrightarrow 3H^+ + Al\left(CH_3COCHCOCH_3\right)_3 \tag{4.4}$$

One of the advantage of present synthesis route was the use of industrial alum $Al_2(SO_4)_3.16H_2O$ as the starting material in order to give alternative uses of this important industrial by-product in the production of alumina. Al-acetylacetonate was used to deposit A_2O_3 coatings on different substrates in the temperature range of 400-600 °C at atmospheric pressure in air.[57]

4.3.1.2 Zirconia, silica, titania precursors

A very versatile technique used for coating zirconia, silica, and titania is by sol-gel method. In this chapter mostly precursors suitable for CVD technique have been discussed, so we will now briefly describe different sol-gel organometallic precursors for zirconia, silica, and titania. This method allows a good reproducibility of coating performances even though some problems have been evidenced due to complex shape substrate and thick film deposition. Moreover, in some cases, coating cracking induced by the thermal treatment performed at the end of deposition has been reported.[58] Usually a thermal treatment at a temperature around 600 °C provides a good chemical homogeneity and good corrosion resistant features to substrates. Nevertheless, some promising results, in terms of corrosion resistance, have been obtained also at lower temperature (400 °C).[59]

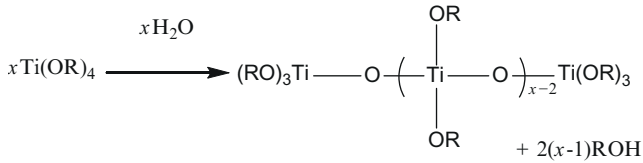
In general terms, the sol-gel process involves three stages: (1) a partial hydrolysis of the metallorganic compound in order to produce reactive monomers, (2) a polycondensation of the reactive monomers, which forms oligomers of colloidal size (sol), (3) and finally an additional hydrolysis, which initiates and further promotes the polymerization and cross-linking of the precursor. The last step, gelation, will produce polymeric compounds of given morphology that upon pyrolysis yield oxide ceramics. The above reactions can be influenced by controlling parameters such as pH, nature, and composition of the solvent, temperature, reaction time, ratio of [RO]/[H_2O] (RO is aloxy group attached to metal), and the type of the R group.[60–62] The nature of the starting metallorganic material undoubtedly constitutes an important parameter which influences all the steps of the sol-gel process. We will not go in further detail of effect of all these parameters and will focus on the deposition chemistry from organosilicon compounds.

4.3.1.2.1 Titania precursors: sol-gel

Titanium alkoxides which after hydrolysis produce amorphous TiO_2 are widely used for titania production in firm of coating/powder. There are two proposed flowsheets (I and II) for the production of low temperature TiO_2.[63,64] The results indicate that anatase is the product in the first case where the washed amorphous TiO_2 after being dispersed in a basic aqueous solution is heated in an autoclave at 200-300 °C. In the second case a mixture of anatase and rutile is obtained following the 16 h calcinations of the thoroughly washed amorphous TiO_2. These differences are believed to be due to different pathways through which hydrolysis and polycondensation take place. The overall reaction (reaction scheme 4.5) despite its simple appearance is more complex because of the possible polymeric form of the alkoxide precursor:

$$\mathrm{Ti(OR)_4 + 2H_2O \longrightarrow TiO_2 + 4ROH} \tag{4.5}$$

Polycondensation can produce Ti-O-Ti bridges (reaction scheme 4.6) which will be preferentially linear if the solutions are diluted.[65] Several other forms can also be produced, O on the conditions and



(4.6)

structure of the alkoxy group, represented by the following general formula $Ti_{3(x+1)}O_{4x}(OR)_{4(x+3).}$[66] Their structures can be more complicated if the possible tetramer $Ti(OC_2H_5)_4$(I) is polycondensed linearly.

Reaction Flow Sheet I:

$$\underset{\text{Precursor}}{Ti(OC_2H_5)_4} \xrightarrow{\text{Hydrolysis}} TiO_2 \text{ amorphous} \xrightarrow[\text{Treatment, pH=10}]{\text{Hydrothermal}} TiO_2 \text{ anatase}$$

Reaction Flow Sheet II:

$$\underset{\text{Precursor}}{Ti(OC_3H_7)_4} \xrightarrow{\text{Hydrolysis}} TiO_2 \text{ amorphous} \xrightarrow[550^{\circ}C, \text{ Oxygen atm, 16h}]{\text{Wash, Calcination}} TiO_2 \text{ anatase}$$

4.3.1.2.2 Silica precursor: sol-gel

The most frequently used and studied precursors for silica are tetraethylorthosilicate (TEOS)[67] and tetramethylorthosilicate (TMOS),[68] and they have been shown to behave differently under similar conditions. This indicates the importance of the molecular structure in the process and the need for more research and studies of the structure/sol-gel relationship in which all the reaction parameters are involved.

Silicon alkoxides are usually used as precursors and their hydrolysis rate can be controlled easily as compared to other faster hydrolyzed derivatives, such as $SiCl_4$ and $Si(OCOCH_3)_4$. Silicic acid and its acetate are also able to produce SiO_2. The solvent will influence the physical characteristics of the final product, and in the case of methanol as the solvent, the porosity of the product will be lower than that produced from TEOS under similar conditions. Similarly, the bulk density increases with temperature and is higher when MeOH is used as solvent.

In the acid-catalyzed system the hydrolysis rate usually decreases with an increase of C atoms in the straight-chain alkoxy group because of an inductive effect, whereas the rate is lowered with increased branching of the alkoxy group of the organosilicon alkoxides due to steric reasons. The polycondensation being a nucleophilic reaction will be influenced by the same factors up to the point at which cross-linking takes place. Other phenomena, such as diffusion and collisions between polymeric chains, are increasingly involved and thus the kinetics are dependent on additional parameters. In general, the hydrolysis reaction is much faster than the condensation. Nevertheless, condensation starts as soon as an alkoxy group has been hydrolyzed and thus the final results of the sol-gel of the silicon alkoxides will be influenced by a combination of the above-mentioned factors. The gelation characteristics of gels produced from methoxy (TMOS), ethoxy (TEOS), and butoxy (TBOS) silicon alkoxides support the above theory. An increase of gelation time is observed when the same alkoxide is used in solvents of increasing molecular weight, for example, MeOH, EtOH, and PrOH. A similar increase is observed with increasing molecular weight of the alkoxide used.[69]

4.3.1.2.3 Zirconia precursor: sol-gel

Alkoxides are the main source of metallorganic precursors for the formation of zirconia. The most frequently used Zr alkoxides (propoxide and butoxide), being liquids,

can be purified by distillation, as is commonly done for the Si and A1 precursors. The Zr gels derived from these precursors can have the weight-loss reaction completed at substantially lower temperatures.

Their hydrolysis pattern is different from those of aluminum and silicon alkoxides, and their tendency toward total hydrolysis is lower than that for the titanium analogues. Zirconium does not give a hydroxide but rather a white gelatinous hydrated oxide ($ZrO_2.xH_2O$) which upon pyrolysis becomes ZrO_2. The hydrolysis of the alkoxides produces several polymeric forms of the zirconyl ion (ZrO^{2+}) which eventually will form ZrO_2 according to the following reactions (reaction scheme 4.7 and 4.8):

$$Zr(OR)_4 + H_2O \longrightarrow ZrO(OR)_2 + 2ROH \tag{4.7}$$

$$2ZrO(OR)_2 \longrightarrow Zr(OR)_4 + ZrO_2 \tag{4.8}$$

Depending on the amount of H_2O added during reaction scheme (4.7), some of the species can be formulated and their thermal decomposition can be represented by reaction (reaction scheme 4.9):

$$Zr(OC_nH_{2n+1})_4 \longrightarrow ZrO_2 + 2C_nH_{2n} + 2C_nH_{2n+1}OH \tag{4.9}$$

but, in reality the process produces a mixture of ZrO_2 and $Zr_2O_3(OR)_2$.[70] Apart from these differences the reactions which take place during hydrolysis and polycondensation are influenced by the same parameters as before, that is, temperature, solvents, the alkoxide/H_2O ratio, and the presence of foreign ions in the solution. A significant phenomenon which is related to the chemical behavior of zirconium and the hydratesoxides rather than hydroxides it forms, is the lack of influence that the alkoxide/H_2O ratio has on the oxide content of the hydrolysis products. Usually, an increase of the hydrolysis H_2O will increase the hydroxyl groups of the hydrolyzable alkoxide, and as a result the oxide content will increase. In the case of the zirconium alkoxides the oxide content is about 80% no matter if the hydrolysis takes place in an excess of H_2O or by atmospheric moisture.

4.3.1.2.4 Zirconia, yttria, silica precursors: CVD precursors

Several yttrium, zirconium, and silicon complexes with acetylacetone, tetramethylheptanedione, hexafluoroacetylacetone, tetramethylethylenediamine, polyether, and amine as ligands were synthesized by adjusting the pH after mixing chlorides/alkoxides of corresponding metals with the corresponding ligand in ethanolic or aqueous solutions. Drake et al.[71] have reported a simple and economical technique to synthesize the adduct complexes of metals using different ligands. Their synthesis for metal complex adducts formation was as follows:

First, this approach aims to coordinatively saturate the metal centers with the combined use of both a chelating chain type ligand, that is, glymes or amines, and a chelating metalated group, for example, a diketonate, functionalized alcohol, diolate, or

acetate (A-R-BH, where A is generally a pendant b-chelating site, R is the hydrocarbon chain linker, and B-H is the predominate site of metalation).[35] The general synthetic strategy is outlined as follows (reaction scheme 4.10):

$$\left[\mathrm{M(OR)}_x\right]_y + 2\mathrm{A\text{-}R\text{-}BH} + \mathrm{L\text{-}L} \longrightarrow \left[\mathrm{M(A\text{-}R\text{-}B)}_x(\mathrm{L\text{-}L})\right] + x\mathrm{ROH} \qquad (4.10)$$

This point is of importance and presumably gives rise to their exceptional stability in the atmosphere, since the chelating ligands are less readily hydrolyzed than would be monodentate alkoxides. Second, the application of multidentate ligands (L-L) has been previously shown to force oligomeric complexes into a more strictly molecular regime, generally reducing the possibility of interactions between monomeric units (although there will always be exceptions to this). Third, this technique of using a preformed metal β-diketonate (either anhydrous or a hydrate) leads to water-free products. Thus hard Lewis bases (either O- or N-based) can utilize the entropic advantages of the chelate effect and facilitate the preparation of anhydrous metal β-diketonates is a low cost route, for example, by the use of simple hydrated complexes prepared via metathesis in aqueous/alcohol media. This latter point has an importance if such materials are going to have real applications as either sol-gel or CVD precursors, where low-cost chemicals that may be manipulated on the open laboratory bench are an important objective.

There were several reports on the synthesis of $Zr(tmhd)_4$, $(thd)_2Zr(OR)_2$, and $Y(tmhd)_3$ and their diglyme, triglyme adducts.[72–75] The kinetic data of evaporation for $Zr(tmhd)_4$ and $Y(tmhd)_3$ are reported in literature. Complete volatility and low temperature range of sublimation/vaporization below 250 °C for $Zr(tmhd)_4$, $Y(tmhd)_3(H_2O)$, and $Y_2(tmhd)_6$(triglyme) make these compounds suitable for use at a lower deposition temperature of substrate in the CVD reactor. The other complex of yttrium, that is, $Y(acac)_3(H_2O)_2$, has shown nonvolatility. The reason for the nonvolatile nature of $Y(acac)_3(H_2O)_2$ is due to its unsaturation of coordination sphere upon heating the complex, leading to oligomerization or poor stability on heating. In addition, the better growth of ZrO_2 and Y_2O_3 has been reported from precursors $Zr(tmhd)_4$ and $Y(tmhd)_3$.

The synthesis, structure, and distinctive reactivity of silicon compounds with coordination numbers greater than five, six, and even higher continue to be an area of lively interest. Ligands of β-diketonates are well-known in the synthesis of hypercoordinate silicon compounds. For example, the first ionic acetylacetonate (acac) silicon complex, $Si(acac)_3Cl.HCl$, was reported in 1903.[76] However, only a few neutral hypercoordinate bis(β-diketonate) silicon(IV) complexes, where (β-diketonate) acetylacetonate, have been reported.[77,78] The first complexes of $(acac)_2SiClMe$, $(acac)_2$-SiClPh, and $(acac)_2SiMe_2$ were reported to be highly unstable, and the isolation yield of $(acac)_2SiMe_2$ was extremely low, only about 10%.[79] The preparation of $(acac)_2SiCl_2$ provided a very poor yield as well.[78] However, $(acac)_2Si(OAc)_2$ is more stable, most likely because of the greater electronegativity of the donor oxygen.[77] There were reports on synthesis of

three new neutral bis(β-diketonate) silicon(IV) complexes (Figure 4.10) in high yield and high purity.[80] The typical synthesis procedure reported in the literature stated that the corresponding compounds can be synthesized by reacting $SiCl_4$ with two equivalent of the corresponding alcohol in the presence of two equivalent of pyridine in a hexane solvent. They are monomeric solids. Thermal analysis revealed they are volatile and thermally stable and, thus, represent promising CVD precursors for depositing high quality transition metal silicate coatings.

4.3.2 Organometallic precursors: nonoxide ceramics

4.3.2.1 Pt, Al, W, Mo precursors

Metallic/alloy coatings have been one of the viable options to coat structural components such as gas turbine to improve their corrosion resistance properties. These components are generally made of metals/alloys or steel. A compatible coating of metal or alloy over these components are generally carried out and organometallic precursors are mostly used for low temperature deposition.

Tungsten, molybdenum, aluminum, and platinum in the form of individual metals or alloys have been extensively used for coating purpose. Carbonyl complexes of metals are widely used as the precursors for metal deposition. The carbonyl complexes of tungsten $W(CO)_6$ and molybdenum $Mo(CO)_6$ metals shows excellent volatility whereas carbonyl complex of platinum is not thermally stable.[81,82] Carbonyls complexes of platinum can, however, be stabilized by the presence of another ligand such as phosphine.[83]

The synthesis of metal carbonyls is the subject of intense organometallic research. Since the work of Mond and then Hieber,[84] many procedures have been developed for the preparation of mononuclear metal carbonyls as well as homo- and hetero-metallic carbonyl clusters.

Some metal carbonyls are prepared by the reduction of metal halides in the presence of high pressures of carbon monoxide under pressure. A variety of reducing agents are employed, including copper, aluminum, hydrogen, as well as metal alkyls

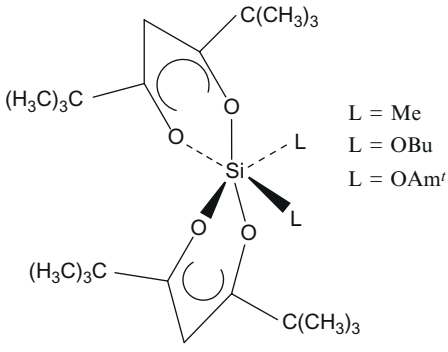


Figure 4.10 Neutral bis(β-diketonate) silicon (IV) complexes. *Reprinted with permission from Ref. [80]. Copyright 2014, with permission from American Chemical Society.*

such as triethylaluminum. Illustrative is the formation of chromium hexacarbonyl from anhydrous chromium(III) chloride in benzene with aluminum as a reducing agent and aluminum chloride as the catalyst (reaction scheme 4.11):

$$CrCl_3 + Al + 6CO \longrightarrow Cr(CO)_6 + AlCl_3 \qquad (4.11)$$

The use of metal alkyls, for example, triethylaluminum and diethylzinc, as the reducing agent leads to the oxidative coupling of the alkyl radical to the dimer (reaction scheme 4.12):

$$WCl_6 + 6CO + 2Al(C_2H_5)_3 \longrightarrow W(CO)_6 + 2AlCl_3 + 3C_4H_{10} \qquad (4.12)$$

$Mo(CO)_6$ is prepared by the reduction of molybdenum chlorides or oxides under a pressure of carbon monoxide, although it would be unusual to prepare this inexpensive compound in the laboratory. The compound is somewhat air-stable and sparingly soluble in nonpolar organic solvents.

Many complexes have been developed for platinum, and among all, a β-diketonate family and a trimethyl-cyclopentadienyl family involve the most-met precursors in the literature.[85–89] The best systems for platinum reported in literature were $MeCpPtMe_3$[87], $EtCpPtMe_3$,[88] and $(cod)Pt(Me)_2$.[89] The compound $EtCpPtMe_3$ is oxygen and water stable at ambient temperature. On the other hand, $(cod)Pt(Me)_2$[89] (Figure 4.11), is less volatile but is easily synthesized in high yield and also gives very interesting results. These precursors benefit from facile decomposition under the CVD conditions. Decomposition is particularly effective and rapid in the presence of oxidizing or reducing gases. The contribution of hydrogen and oxygen as reactive gases also allows notable improvements in the quality of the film deposited and experimental conditions (lowering temperature in particular). Films have therefore been obtained with only traces of impurities, carbon being the most common. A "one-pot" synthesis with a moderate yield (60%) starting from commercially available K_2PtCl_6 has been described, dibromoethane being preferable as a MeLi quencher instead of NH_4Cl for synthesis of $MeCpPtMe_3$.[87] In order to increase the precursor volatility, one hydrogen of the cyclopentadienyl ligand was substituted by a methyl group. The precursor $MeCpPtMe_3$, thus obtained, has a melting point of 30 °C. The main inconvenience with respect to handling of $MeCpPtMe_3$ is its sensitivity toward oxygen and water. With the goal in mind of increasing the precursor volatility, a precursor containing an ethyl-cyclopentadienyl ligand was tested. Deposits were carried out from 350 to 450 °C under 0.7-3 Torr by vaporizing this compound dissolved in *n*-hexane at 130 °C (0.1 M).

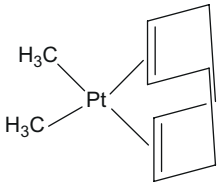
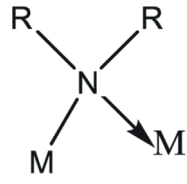


Figure 4.11 Molecular structure of $(cod)Pt(Me)_2$. *Reprinted with permission from Ref. [89]. Copyright 2014, with permission from American Chemical Society.*

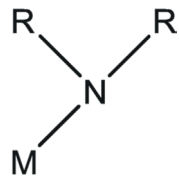
Contrary to the preceding complexes of the same family, $EtCpPtMe_3$ is not oxygen and water sensitive. It is also able to form mixed Pt-C deposits.[88] A synthesis with a 51% yield of this precursor utilizing $Pt(Me)_3I$ and $Na(EtC_5H_4)$ was patented as well as the use of this precursor for platinum OMCVD. The deposit is obtained by bubbling argon in the pure precursor maintained at 35 °C atmospheric pressure and heating the substrate (Si) at 150 °C in the presence of hydrogen. $(cod)Pt(Me)_2$ is a precursor that melts at 100 °C.[89] It was described by Kalck for its use in a FBCVD for the heterogeneous preparation of catalysts and in CVD on graphite.[90]

4.3.2.2 ZrCN and TiCN precursors

Metal carbonnitrides are the important class of compounds that are being used as coating on light metal to improve their performance. The dialkylamino-compounds of the transition metals are of special interest since they bridge the gap between the relatively stable metal alkooxides and the generally unstable metal alkyls. In addition there is the possibility that metal-nitrogen polymers would be formed, either by coordinating-polymerization in (I) (Figure 4.12), during which the lone pair of electrons on the nitrogen forms an intermolecular coordinate bond, or by using the bifunctional primary amine as in (II) (Figure 4.12). In the case of primary amine derivatives there is further possibility that coordination-polymerization will also take place. There are also some factors which might operate against polymerization. Thus in the dialkylamino-derivatives the intermolecular bonds (I) might be prevented by steric effects or by intramolecular coordination involving $d\pi$-$p\pi$ bonds $H{=}NR_2$. In the case of primary amino derivatives there is further possibility that only one of the hydrogens of the NH_2-group would be replaceable by metals and this would prevent polymerization by mechanism (II). Prior to 1959 the only binary dialkylamino-compound of a transition metals or actinide element reported was the tetrakis(diethylamino)-uranium (IV)



(I)



(II)

Figure 4.12 Molecular structure of different metal carbonitrides.

obtained by Gilman and coworkers from the reaction involving uranium tetrachloride and lithium diethylamide.[91] Dermer and Fernelius prepared $Ti[N(C_6H_5)_2]_4$ by treating titanium tetrachloride with sodium diphenyl amide.[92]

It has been shown that the lithium dialkyl amide—metal chloride reaction (I) is suitable for synthesis of numerous dialkylamino-derivatives of titanium, zirconium, vanadium, niobium, tantalum, chromium, molybdenum, and tungsten (reaction scheme 4.13):

$$MCl_x + xLiNR_2 \longrightarrow M\left(NR_2\right)_x + xLiCl \tag{4.13}$$

Most of the dialkylamino-derivatives may be distilled under reduced pressure although in some cases [e.g., Nb(V), Ta(V) compounds] interesting thermal decomposition occurs. The aliphatic dialkylamino-compounds are readily hydrolyzed or alcoholyzed but arylamino-derivatives are relatively more stable. Some interesting steric effects are observed in the dialkylamino-compounds while in the primary amino-compounds a number of polymeric derivatives are obtained. Only in the case of $Zr(NMe_2)_4$ is there any evidence of polymerization at the boiling point of benzene and it is noteworthy that the compound is significantly less volatile than the corresponding titanium derivative. From a consideration of the steris effects demonstrated in the aminolysis of these tetrakis-(dialkylamino)-derivatives it is deduced that the absence of polymerization is a consequence of the powerful shielding of the central atom by the dialkylamino group.

In Table 4.1 some of the metallorganic compounds of type tetrakis(diethyl)-aminometal ($M(N(C_2H_5))_4$) are mostly used for deposition of such compounds; for example, $Zr(N(C_2H_5)_2)_4$ and $Ti(N(C_2H_5)_2)_4$ are used for coating of ZrCN and TiCN, respectively. Using plasma-assisted CVD method the deposition temperature of such compounds is been drastically reduced to 180 °C which is very useful for coating metals/alloys.[93,94]

TABLE 4.1 Metalorganic Compounds of Type Tetrakis(Diethyl)-Aminometal of Titanium and Zirconium

Sr. No.	Compound	Physical State	Boiling Point (°C/mmHg)
1	$Ti(NMe_2)_4$	Yellow liquid	50/0.05
2	$Ti(NEt_2)_4$	Orange liquid	112/0.1
3	$Ti(NPrn_2)_4$	Red liquid	150/0.1
4	$Ti(NBu_{1/2})_4$	Red liquid	170/0.1
5	$Zr(NMe_2)_4$	White solid (mp. 70 °C)	80/0.05
6	$Zr(NEt_2)_4$	Green liquid	120/0.1
7	$Zr(NPrn_2)_4$	Green liquid	165/0.1
8	$Zr(NBu_{1/2})_4$	Green solid	180/0.1

4.3.2.3 SiC precursors

SiC is the most widely used material, especially for corrosion-resistance application. So in this section we provide a detailed description of organosilicon compounds synthesis as SiC precursor is given.[95] In the past many SiC coatings have been produced by the CVD technique; however, most SiC coatings deposited have been grown at relatively high temperatures of 1300-1380 °C and at atmospheric pressure, using separate precursors for Si and C.[96–100] For instance, SiH_2 or Si_2H_6 have been used for Si, and CH_4 or C_3H_8 have been used for C.[101] Combination of methyltrichlorosilane (CH_3SiCl_3 or MTS) and hydrogen is the most popular single molecular precursor, partially because methyltrichlorosilane contains the same number of silicon and carbon atoms. To achieve an optimal oxidation resistance, it is important that stoichiometric SiC is deposited. Although the C/Si molar ratio in methyltrichlorosilane is one, deposition of silicon with SiC is encountered at a temperature below 1000 °C, whereas carbon is deposited with SiC above1600 °C. The mechanism of SiC deposition can be regarded as two independent subsystems, that is, the deposition of carbon and the deposition of Si.[102] Equal rates will result in stoichiometric SiC. Detailed knowledge of the kinetics in the gas phase and on the surface is, however, limited, especially for chlorine-containing SiC precursors like CH_3SiCl_3. The gas phase kinetic for the SiH_4-hydrocarbon system is relatively well understood,[103,104] but more knowledge of the surface chemistry is needed. The use of methyltrichlorosilane requires a source of hydrogen gas to combine with the chlorine atoms liberated during decomposition. The reaction forms hydrogen chloride as a by-product, which must be removed, thus requiring a scrubber as part of the equipment. Since the hydrogen chloride is corrosive all equipment must be corrosion resistant. Table 4.2 shows examples of conventional SiC precursors and their applications.

Recent practice of using halogen-free single source compounds in CVD is, in some cases, enjoying low deposition temperature and accurate stoichiometry. Since the single molecular precursor already has a Si–C bond in the precursor itself, it does not need further activation energy to make a Si–C bond in the film, resulting in epitaxial temperatures below 1000 °C. Many research groups have thus performed growth of SiC either on different substrates using single precursors: Golecki et al.[105] had grown single crystalline epitaxial cubic(100) films on (100) Si substrates at 750 °C by low pressure CVD, using methylsilane, CH_3SiH_3 and H_2. He got the stoichiometric SiC composition at low temperature because methylsilane can generate vapor that is stable at room temperature. The drawbacks of methylsilane are very low boiling point (–57 °C) pyrophoric and irritant gas and commercially available at high cost. Steckl et al.[106] have grown the cubic SiC on Si using the precursor trimethylsilane, and they have investigated the effect of temperature, flow rate of precursor on on-axis Si (100) and off-axis Si(111) substrates.

TABLE 4.2 Conventional SiC Precursors and Their Applications

SiC Precursors	Condition of Synthesis		Application
	Temperature (°C)	Pressure (kPa)	
CH_3SiCl_3	1323-1673	n.r.	Coating
	1200	1.7	Coating
	973-1073	10-35	
	973-1173	10-100	Composite (CVI)
	1052-1070	2-13.3	
CH_3SiCl_3/CH_4	1273-1523	4.6	Coating
$SiCl_4/CH_4$	1200-1400	100	Coating
$(CH_3)_2SiCl_2$	1473-1600	n.r.	Coating
$SiCl_4$/carbon	1300-1500	100	Coating
SiH_4/C_xH_y	1573-1723	100	Electronic

n.r. = not reported.

The use of trimethylsilane to form amorphous or polycrystalline SiC films is also known in the art. For instance, Kaplan et al.[107] have described the formation of SiC coatings on video disks using trimethylsilane in a glow discharge CVD process. Trimethylsilane gas is colorless, noncorrosive, and nonpyrophoric precursor, but excess carbon deposition is formed during SiC deposition. There are other organosilane type precursors available to get SiC film. Yasui et al.[108] have used dimethylsilane to get cubic SiC film while Avigal et al.[109] have grown the SiC on the Si-SiC-C system using different precursors such as tetramethylsilane (b.p. = 26-28 °C), diethylsilane (b.p. = 56 °C), and tripropylsilane (b.p. = 171 °C). The SiC has been grown in the range of 700-1400 °C regardless of the atmosphere, but the films are contaminated with inclusions of silicon and free carbon. They found that pyrolysis of tetramethylsilane in H_2 produces less free carbon than in the presence of helium. It was also noticed that at lower temperature the CH_3 deposits more free carbon while at higher temperatures the C_3H_7 deposits more free carbon. Tetramethylsilane, diethylsilane, and tripropylsilane are stable at room temperature. First two precursors have low vaporization temperature and tripropylsilane has high vaporization temperature. All three precursors are safe to handle but are costly.

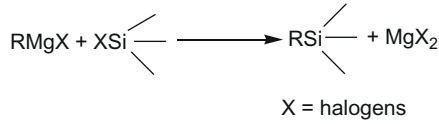
Jeong et al.[110] have prepared thin films of cubic SiC on Si(100) by high vacuum MOCVD using diethylmethylsilane [DEMS, $(C_2H_5)_2(CH_3)SiH$] (b.p. = 78 °C) at various temperatures. DEMS is stable at room temperature, nontoxic, and not explosive. With a deposition temperature of 900 °C, relatively well oriented 3C-SiC layers were obtained. When the deposition temperature was increased from 700 to 900 °C, there was an improvement in crystallinity and grain size. However, above 900 °C

crystallinity decreased with increasing temperature and growth time due to a crystal shape change. These results show that the deposition temperature and time are important factors for influencing film crystallinity and carbon deposition.

Kim et al.[111] have used a new precursor dimethylisopropylsilane [$(CH_3)_2CHSiH(CH_3)_2$] (b.p.=66-67 °C) to deposit cubic SiC films on Si(100) and Si(111) substrates at the temperature range of 750-970 °C using low-pressure organometallic chemical vapor deposition (LP-OMCVD). They found that at low temperature amorphous SiC films and free carbon were deposited. They got cubic-type SiC films on uncarbonized Si(100) surfaces at 850 °C and a polycrystalline cubic SiC film on a carbonized Si(100) substrate at 960 °C. But they were not successful in obtaining epitaxial growth of cubic SiC on carbonized Si (100) using the same precursor.

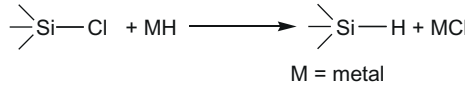
There are many synthesis routes described in literature of above organosilane precursors. We will discuss some of the economical synthesis routes of potential organosilicon precursors for SiC. In general in these methods first chlorine substituted silanes are taken that may be a product or by-product of a technical process (for example, methyldichlorosilane is a technical product which is obtained as a by-product of the direct synthesis).

The organic groups can be introduced into these chlorinated silanes by the Grignard process (scheme 4.1) in which only the Si–Cl bond (but not the SiH bond) is involved. The Grignard reaction is of fundamental importance for the whole field of organosilicon chemistry.[112] It utilizes organomagnesium compounds to transfer organic groups to silicon (reaction scheme 4.14):



(4.14)

Conversely, the chlorine in chlorosilanes already containing organic substituents can be replaced by hydrogen (scheme 4.2). Reactions with metal hydrides, such as lithium tetrahydroaluminate,[113] lithium hydride,[114] sodium hydride,[115] and the reactive aluminum tetrahydroborate $Al(BH_4)_3$[116] are most suitable for the reaction, which proceeds in principle as follows (reaction scheme 4.15):



(4.15)

The action of aluminum tetrahydroborate on trimethylchlorosilane can be represented schematically in reaction scheme (4.16):

$$2Al(BH_4)_3 + 6(CH_3)_3SiCl \longrightarrow Al_2Cl_6 + 3B_2H_6 + 6(CH_3)_3SiH \qquad (4.16)$$

The reaction with sodium hydride dispersed in mineral oil or another inert high-boiling hydrocarbon requires temperatures of 175-350 °C.[115] The addition of

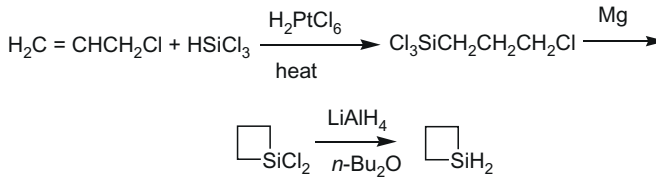
catalysts can lower the reaction temperature or increase the yield. Alkylborons, boricacid esters, and triethylaluminum are suitable catalysts.[117,118] An interesting embodiment of the substitution reaction consists in passing the halogen compound through a eutectic melt of an alkali-metal halide containing lithium hydride. In this way, at 360-400 °C dimethyldichlorosilane yields dimethylsilane $(CH_3)_2SiH_2$ with 95% conversion and 89% yield.[119]

Boo et al.[120] have used a new single molecular precursor 1,3-disilabutane containing two silicons and carbon atoms. They have grown the Cubic SiC films on the Si(100) and Si(111) substrates in the temperature range 650-900 °C by LP-OMCVD using this precursor. Polycrystalline cubic SiC films were formed on Si(100) substrates at such a low temperature as 650 °C. The films obtained on carbonized Si(100) substrates at temperatures higher than 850 °C show improved crystallinity in their X-ray diffraction patterns. On the other hand, highly oriented SiC films in the [111] direction were formed on carbonized Si(111) substrates at 900 °C.

The precursor 1,3-disilabutane which contains silicon and carbon atoms at a ratio of 1:1 was obtained by reduction of 1,1,3,3-tetrachloro-1,3-disilabutane. The synthesis of 1,1,3,3-tetrachloro-1,3-disilabutane was reported by Jung[121] as follows.

The reaction of (chloromethyl) methyldichlorosilane with elemental silicon and hydrogen chloride using copper as a catalyst and cadium as a cocatalyst leads to the attachment of a silicon atom to the organochlorosilane molecule, producing 1,1,3,3-tetrachloro-1,3-disilabutane. Reduction of this compound with metal hydrides (e.g., lithium aluminum hydride) in ether replaces the chlorine atoms with hydrogen atoms. The final compound is 1,3-disilabutane.[122]

Steckl et al.[123] have grown the SiC films on different substrates using silacyclobutanes. In these precursors deposition of carbon occurs in SiC film, because of Si:C ratio is 1:3. Silacyclobutane is synthesized according to reaction scheme (4.17).



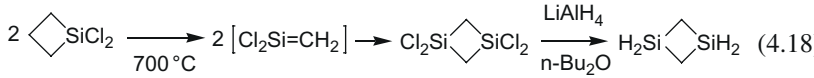
(4.17)

The 3-halopropyltrichlorosilanes are prepared by addition of trichlorosilane to an allylhalide with chloroplatinic acid as catalyst. The 1,1-dichloro-1-silacyclobutane[124,125] can be prepared from $Cl_3SiCH_2CH_2CH_2Cl$ using magnesium powder. This 1,1-dichloro-1-silacyclobutane is reduced using lithiumaluminumhydride in n-butyl ether at 0 °C to get silacyclobutane, $(CH_2)_3SiH_2$.

Another precursor that is used because of the same number of silicon and carbon atoms is 1,3-disilacyclobutane. Larkin et al.[126] and Chadder et al.[127] have used this precursor to get stoichiometric SiC, but this precursor needs relatively high temperature to grow SiC film and it has tedious synthesis route. It can be prepared by the $LiAlH_4$

reduction of 1,1,3,3-tetrachloro-1,3-disilacyclobutane. This 1,1,3,3-tetrachloro-1,3-disilacyclobutane is obtained by pyrolyzing 1,1-dichloro-1-silacyclobutane[128] at 700 °C according to methods described by Nametkin et al.[129] This type of pyrolysis reaction is of considerable interest and it is postulated to go through the $[Cl_2Si{=}CH_2]$ intermediate.

The process is given in reaction scheme (4.18):



(4.18)

The strained cyclic molecule 1,3-disilacyclobutane allows to grow β-SiC film at a temperature >300 °C lower than possible with a similar straight chain reagent. It is proposed that decomposition of the cyclic precursors directly produces intermediates that can lead to deposition of stoichiometric SiC. The synthesis routes of cyclic compounds are completed and tedious. Cyclic precursors are promising for both the deposition of single crystal films at high temperature as well as for polycrystalline and single crystal films at low temperature.

Takahashi et al.[130] have used the hexamethyldisilane (HDMS) (b.p. = 112-114 °C) to get cubic SiC films on Si and other substrates. At temperatures lower than 1100 °C the growth rate is limited by thermal decomposition of HMDS molecules. At higher temperatures, the growth rate is limited by thermal diffusion of $(CH_3)_n$-Si-H_{4-n} species through stagnant gas layers at the substrate surface. Temperature dependence of crystallinity of grown films reveals that the gas system is effective for low temperature epitaxy. With and without buffer layers, single-crystalline 3C-SiC containing twinnings were grown on a Si(111) substrate at 1100 °C. In the case of Si(100) substrates, single crystals were grown only with a buffer layer. Even though growth temperatures were as low as 1100 °C, crack lines were observed in a 5 μm thick layer grown on a Si(111) substrate. HDMS is stable at room temperature and gives codeposition of free carbon with SiC film.

Shen et al.[131] have described a method for making the SiC ceramic precursor compound, 2,4,6-trimethyl-2,4,6-trisilaheptane (TMTSH), which comprises reducing chloromethyl-dimethylchlorosilane with lithium aluminum hydride in a suitable solvent to form chloromethyldimethylsilane; reacting the chloromethyldimethylsilane with magnesium to form the corresponding Grignard reagent; coupling the Grignard reagent with methyldichlorosilane; and recovering 2,4,6-trimethyl-2,4,6-trisilaheptane. It has been demonstrated that the deposition of SiC occur on a substrate at deposition temperature 1400 °C and pressure about 760 Torr. Whereas for deposition of SiC at low temperature such as at 600 °C, low system pressure about 10^{-10} Torr was required. The SiC precursor is a chlorine-free, single molecular compound rather than a polymer, oligomer, or mixture of compounds, oligomers, or reaction products. The main chain of the compound is composed of repeating

Si-C units. The carbon-to-silicon ratio in the precursor compound is 7:3. This chlorine-free carbosilane contains no elements other than silicon, carbon, and hydrogen and is therefore highly suitable for CVD and CVI applications. TMTSH provides higher deposition rate and higher yield than can be achieved with methyltrichlorosilane. Other benefits include ease of preparation, handling, storage, and transportation. The composition is noncorrosive. In addition, the silicon-to-carbon (Si:C) ratio is relatively low and can be controlled by control of parameters which affect the deposition rate. Carbon content of the coating can be varied from a slight excess of carbon to near stoichiometric ratio of silicon to carbon using nitrogen as a carrier gas. No solvents or reactive secondary gases are required. A carrier gas is not essential, but nitrogen, hydrogen, argon, or other suitable carriers can be used to vary flow rates and partial pressure of the TMTSH. Nitrogen, hydrogen, or mixtures are used to control the stoichiometry of the coating.

An alternate of the single molecular precursors are the organometallic polymer precursors, especially polysilanes and polycarbosilanes. These polymer compounds that contain polysilanes and polycarbosilanes must be volatile for CVD use. Generally the polymers of sufficiently high molecular weight, crosslinks before significant volatilization occurs. Such cross-linking before volatilization is highly undesirable for the application under consideration, where excessive silicon and carbon remain in polymer and do not come in vapor form. Presently research is going on to get a polymer precursor that gives stoichiometric SiC film and can be used in the CVD process, but so far no precursor has been obtained in our knowledge which fulfills all criteria of an ideal precursor.

In the commercially available precursors for SiC, presently precursors are available with the name CVD 2000 and CVD 4000.[132] CVD 2000 is a single molecular organometallic liquid precursor while CVD 4000 is a single component liquid precursor having the basic structure of $[SiH_2\text{-}CH_2]_n$. Their synthesis routes have not been disclosed and have high cost. In our lab we have developed an economical synthesis process to synthesize a precursor that is halogen free and stable in atmosphere and low sublimation temperature. Its synthesis involves reaction of dichloromethane with silicon powder having a specific size in a specially designed fluidized bed. A schematic diagram of fluidized bed is given in Figure 4.13. The typical reaction involves the reaction of silicon with dichloromethane at 350 °C, and the product was condensed and collected in a vessel. The collected product was distilled at 150 °C at atmospheric pressure, and later on distilled product was reduced with lithium aluminum hydride. The final compound that was named CVDP has shown up to 95% volatility at 200 °C. This compound was further used for graphite substrate coating and has given promising results. Currently we are not revealing much about the synthesis and coating process since it is in a process of publication/patent. A comparative study of precursors CVD 2000 and CVD 4000 with other commercially available precursors is given in Table 4.3.

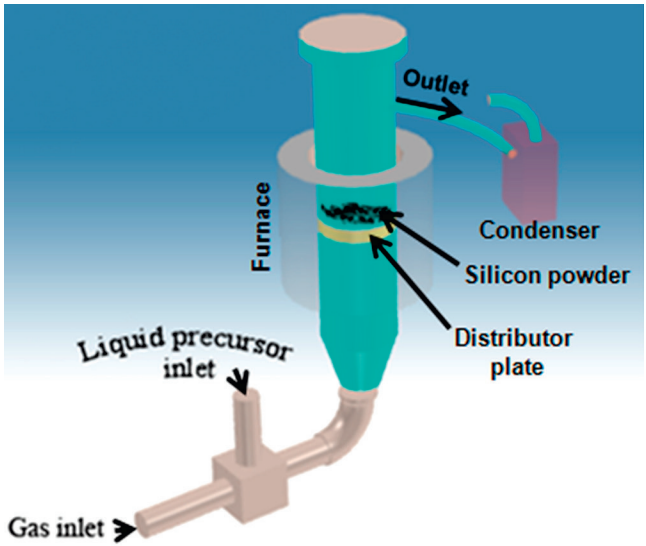


Figure 4.13 Schematic representation of fluidized bed system for precursor synthesis.

4.4 Liquid Delivery Systems: Effect of Solvent

In most of the cases of OMCVD, the solid/liquid precursors were heated under reduced pressure for vaporization. The solids can vary in their shape or crystallinity, which can affect their volatility. Various systems of vaporization have been developed and adapted for use with pure liquid precursors or solutions. The first system described is that of the bubbler, where the precursor is pulled through the liquid by the bubbling of a gas. The liquid can be heated (and the entire line, up to the reaction chamber to avoid recondensation) or cooled according to the volatility of the precursor and the desired precursor flow. This system was adapted with regulators and sensors in order to have a partial pressure of precursor constant in the furnace. It is the simplest and widely used system. The second system used for precursor delivery is direct liquid injection system. A direct liquid injection system has been described where the solution is injected by syringe directly into a vaporization chamber. The syringe can be replaced by volumetric pumps, mixing the solvent and precursor and delivering the solution in a constant fashion or according to a preprogrammed set of instructions. The third kind of system is the improvement of liquid injection system. An improvement to liquid injection systems in terms of precision was the development of pulsated liquid injection where micro-quantities of precursor solution are injected sequentially. A comparative OMCVD Pt coating study under very similar experimental conditions, employing two precursor delivery systems, has been reported: comparing Pt OMCVD films obtained from $MeCpPtMe_3$ with a TriJet™ liquid delivery system and

TABLE 4.3 Comparison of Different SiC Precursors

	CVD 2000	CVD 4000	MTS	Silane	Organometallic Precursors Developed in our Lab
Precursors	Only CVD 2000	Only CVD 4000	MTS plus H_2 (in exact ratios)	Silane plus methane (CH_4)	Mixture of organosilicon compounds (CVDP)
Precursors hazards	Flammable (FP = 51 °C)	Flammable (FP = 9 °C); air, moisture reactive at 140 °C	Corrosive, toxic, flammable (FP = 3 °C); moist air and water reactive at 20 °C	Pyrophoric	Easy to handle; noncorrosive and nontoxic
% SiC in precursor	63% SiC (25% C, 12% H)	91% SiC (9% H)	27% SiC (71% Cl, 2% H)	Silane—87% SiC (13% H), Silane+Methane—83% SiC (17% H_2)	(CVDP) Approx. 83% SiC
By products of the CVD process	H_2 and Methane (CH_4)	H_2	HCl (highly corrosive) as well as H_2 and silanes	H_2	H_2, CO/CO_2
Coating composition Si:C	Varies with substrate temp., 1:1 + 5—15% carbon	1:1 ± 0.5%	1:1 ± 1.2% plus Cl and trace metals	1:01	1:1 ± 5%, no trace metal deposition
Deposition temperature	800-900 °C	600-900 °C	1000-1400 °C	1200-1500 °C	700-1000 °C

a conventional bubbler.[133,134] The properties of the deposits grown using the two different precursor delivery systems were found to be very similar, making a comparison between the two deposition techniques nontrivial. Although the use of a conventional bubbler leads to fast deposition of Pt films, controlling the amount of consumed precursor is difficult. Conversely, the liquid injection system enables perfect control over the quantity of precursor used, but results in a slower rate of film growth. In this study, the use of cyclohexane gave positive results due to its low chemical interference with the oxidative decomposition of platinum precursor. Even for liquid precursors, the use of a solvent is often needed to control precursor delivery. Aerosol flash evaporation using solutions give good results in terms of accuracy. In general, the choice of solvent remains unexplained and its effects upon deposition are not described in detail. They can play a role by interacting with the second even the first sphere of metal coordination and thus stabilize the metal complex. It is also possible to dissolve in the solution a suitable quantity of free ligand in order to stabilize the complex. Another potential effect of solvent is to increase the vapor pressure of the precursor by an azeotropic effect. The more commonly used solvents are: acetylacetone, pentane, cyclohexane, tetrahydrofuran (THF), and *n*-hexane.

4.5 Organometallic Precursor Chemistry

Single source precursors have been preferred over multisource precursors to overcome the problem of vapor phase control and homogeneity of the unstable precursors. The single source precursor is contained in a closed container under an inert gas at room temperature; a small quantity of the precursor is introduced into an evaporator held at a high temperature, where it is being flash volatized. This allows fast evaporation of the precursor and a shorter delivery time of the vapor precursor to the reaction zone, which also leads to a higher growth rate (e.g., mm/s) than the conventional bubbler method. This technique also enables the use of precursors with lower volatilities than the classical multisource precursors and the composition of the vapor is the same as the mixture of precursors, thus allowing the synthesis of multicomponent films (including those containing Ba, and rare earth elements) with a better control of composition and stoichiometry and higher reproducibility. The use of single source precursors also simplifies the control of process parameters of the MOCVD process.

Volatility and decomposition of the precursor is a key stage in the formation of the coating. Fast and complete precursor decomposition usually ensures that a coating of good purity and a good quality is obtained. The chemical nature of the precursor is the dominant factor here, requiring stability under the vaporization conditions and decomposition only under the deposition conditions. Selvakumar et al.[135] have established that volatility of CVD precursors are the important factor for effective coating. The most important quantitative characteristic of volatility is the pressure of

saturated vapor of the compound at defined temperature. Thermogravimetry method has been used for determination of vapor pressure, enthalpies of sublimation and evaporation, and solid-state kinetics of chemical reactions for volatile precursors. Transpiration technique, which is also known as the gas entrainment technique, was used for determination of vapor pressure over a wide range of pressures. In this study the kinetic parameters for sublimation and evaporation of volatile metal complexes by nonisothermal studies were evaluated. Different organometallic compounds of Fe, Cr, Cu, Si, Al, Ni, Ga, Sc, La, Mg, Mn, Y, Zr, and Sr exhibited substantial volatility below 600 K without residue. The added advantage is their excellent air/moisture stability, making it amenable for use under ambient conditions. The complete volatility and low temperature range of sublimation/vaporization below 600 K for all studied compounds make it suitable for use at a lower deposition temperature of the substrate in the CVD reactor.

4.6 Nucleation and Growth Mechanisms

According to the operating conditions used, the precursor flow and temperature can be the main contributor to the nucleation process, that is, by the formation of new crystallites or with the growth of the initially formed crystallites[136,137] (Figure 4.14). Under conditions favoring nucleation, the film obtained appears as a small crystallites, the consequent aggregation of which results in good connectivity between the grains and nearly an absence of holes and hence, a low resistivity. Under conditions supporting growth, the film is made up of large crystallites. Various physical factors influence the prevalence of nucleation or growth at the time of film formation. Due to this parameter being of a kinetic nature, the temperature is very important, the phenomena of growth and nucleation not utilizing same activation energies. The gas composition sometimes has significant effect on the nucleation. Nucleation can be supported by the nature of the substrate at the beginning of deposition and also by the nature of the gas used. For example, the addition of steam that will produce hydroxy groups; the consequences of which are limitation of atom diffusion and then of crystal growth.

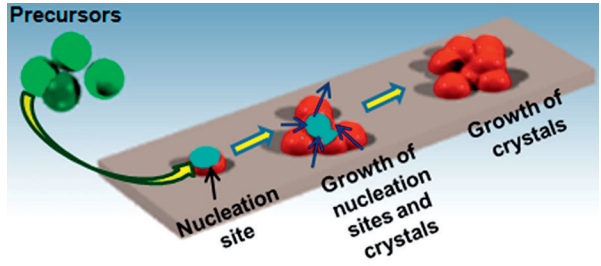


Figure 4.14 Schematic representation of nucleation and growth mechanism.

Nucleation is also supported by precursor "supersaturation," obtained by increasing the precursor concentration in the phase gas. Decomposition in phase gas can also contribute to the nucleation process. Generally during deposition, small grains are formed by nucleation on the substrate surface initially; bigger grains are then formed onto this first layer. A process has been developed in order to produce smooth films with small grains throughout the thickness of the film, and for that purpose, the deposit is performed in two stages (Figure 4.14). First, the growth conditions support nucleation, the agglomeration and the formation of a smooth initial film. Second, film growth with small grains is favored. When the quantity of evaporated precursor for the formation of the initial film is reached, the operating conditions are changed; the temperature, the pressure, and the oxidizing concentration are lowered.

4.7 Coating Damage Mechanisms

A schematic illustration of the principal damage mechanisms and partial processes[138] that take place between a substrate, its coating, and its environment are illustrated in Figure 4.15. The effects of oxygen attack at high operating temperature are highlighted and will be discussed in more detail; however, other aggressive species, for example, Cl_2, Na_2SO_4, and H_2, are also important.

In the case of oxygen permeation, an oxide scale may form at the substrate/coating interface, and this can be either beneficial or detrimental. If a dense compact scale is formed, it may provide additional protection against ingress of oxygen; however, the molar volume expansion of the reactant products can induce stresses which damage the protective coating. In addition, volatile species, for example, CO, N_2, $SiCl_4$, may evolve as reaction by-products and these gases must diffuse outwardly to the surface. If their diffusion is restricted, gas bubbles will form, and, under certain conditions, the internal pressures can rise to the point of disrupting the coating. If oxygen or other reactive species penetrate to the composite surface, selective attack may occur along matrix/fiber interfaces and damage the coatings that have been introduced to enhance interfacial sliding. Localized attack may progress rapidly down these interfaces and cause deterioration in overall mechanical properties. This can be a particular problem in brittle matrix composites where prior matrix cracking has occurred and in composite systems subjected to thermal or thermomechanical fatigue.

A major consideration in the application of any coating is uniform adherence between coating and substrate. Usually, the coating process is selected to provide acceptable adherence, and great care is employed to minimize or eliminate surface contamination. Coating systems must be chosen that will be thermochemically stable at operating temperature, and differences in thermal expansion between coating and substrate must be kept to a minimum. It is not always possible to balance these factors, and compromises in CTE mismatch are often accepted. The result can be an unacceptably high stress level that eventually leads to spallation or cracking. Actually,

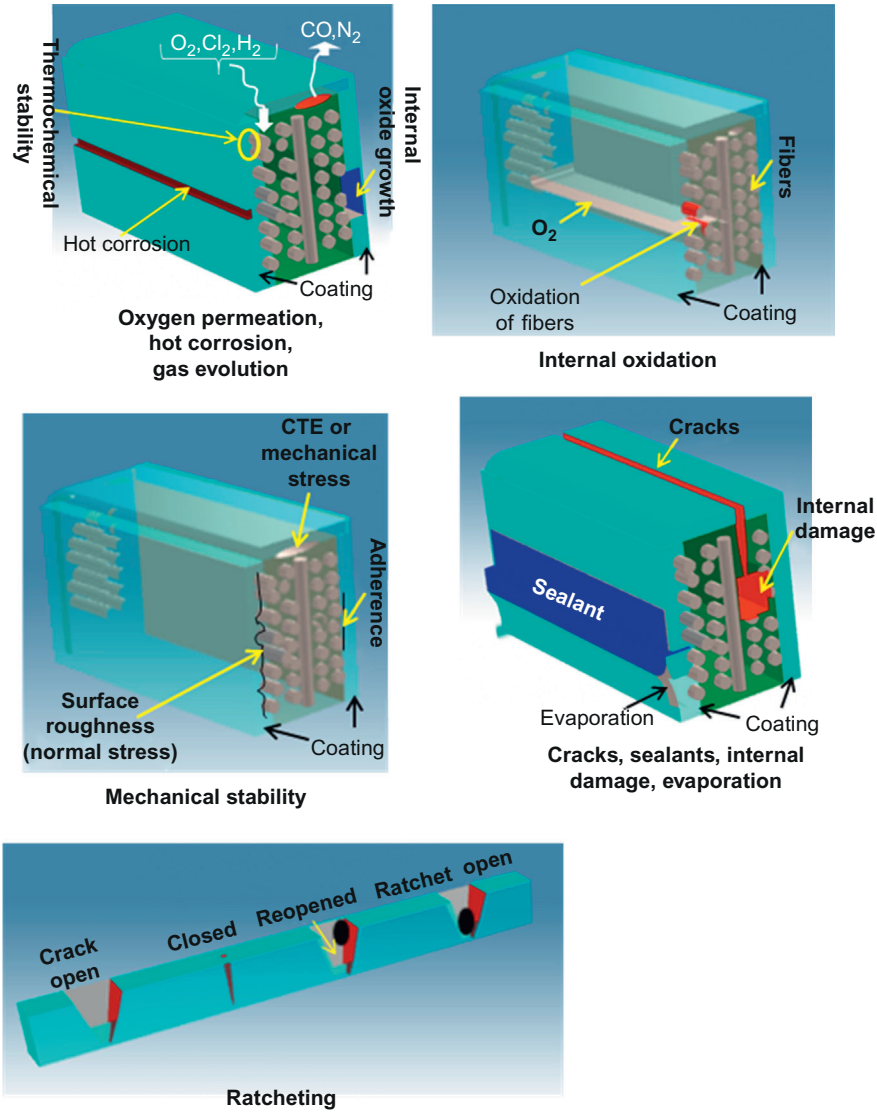


Figure 4.15 A schematic illustration of the principal damage mechanisms in high temperature and corrosive environment. *Reprinted with permission from Ref. [138]. Copyright 2014, with permission from Elsevier.*

the formation of cracks, pinholes, or other coating defects is inevitable, that is, there is no perfect coating system. Thus, crack management becomes a major consideration in the development of engineered coating systems. Cracks may open and close with the application of loads or through exposure to thermal cycling. If the openings are sufficiently large at a reactive temperature, the ingress of molecular oxygen or

other aggressive species will lead to internal damage. One approach is to utilize glass sealants or employ additives that have self-healing properties during high temperature exposure. Coatings which employ sealants can be effective; however, finding a sealant that is functional over a large temperature range is a challenge.

Oxygen permeability was identified as an important criterion in the selection of protective coatings. Composites are particularly susceptible to attack along matrix fiber interfaces or internally within matrix cracks. Thus, if aggressive species penetrate the coating, they can rapidly diffuse into the interior of the composite and cause damage. The result of internal oxidation and interface degradation generally, and sometimes significantly, reduces mechanical performance. A by-product of many interface reactions is a volatile gas. If these internally generated gases are unable to diffuse outwardly to the surface, gas bubbles will form and pressures can build to the point where damage occurs. Ceramic composites/coatings are being considered for expanded use in combustion system hot sections or in gas discharge regions. The presence of Na, S, or V impurities in the combustion products can lead to molten sulfate vanadate condensates which are extremely corrosive. Enhanced oxide solubility in these deposits is capable of rapidly degrading coating effectiveness, which may increase oxygen permeation or enable attack by other aggressive species. While thermochemical compatibility between aggressive environments and the composite is usually the primary factor in the selection of a coating system, mechanical stability is often the determining factor in whether a coating can provide its intended function. Large differences in CTE can usually not be tolerated and will limit thermal cycle resistance. The application of graded interfaces can be beneficial when properly designed to minimize certain types of damage, such an interlaminar shear or across-ply cracking. However, grading is not generally an answer to the amelioration of large CTE mismatches for the prevention of in-plane cracking.

Since perfect coatings are not a practical reality, some sort of crack or flaw management philosophy is an essential part of coating design. Thinner coatings produce smaller cracks that are a factor in controlling the ingress of molecular species. The coating must be designed so that the cracks heal themselves at operating temperatures, or sealants must be employed to fill and close openings.

4.8 Conclusion and Outlook

Protective layer coatings of refractory ceramics on substrate materials are applied usually to protect the substrate materials in harsh conditions such as oxidative and corrosive environments. Based on application, coating materials having desired properties such as high melting point, good thermal and chemical stability, and thermal expansion coefficient close to the substrate material are chosen. The class of materials

extensively used for protective coatings includes carbides and nitrides of transition metals (titanium, zirconium) and of nonmetal (silicon). Furthermore, oxides such as silica, alumina, titania, and zirconia, are also applied for protective coatings. Among the several coating methods which are available to derive coating of such materials, the CVD process based on organometallic precursors is very promising by virtue of cost effectiveness and being environmentally safe. Additionally, this process is advantageous to derive high-quality protective coatings over the substrates without the substrate degradation. There are different modes of CVD such as LCVD, UVCVD, PECVD, EBCVD, FBCVD, ALD, and IACVD that can utilize organometallic precursors for protective coating of the substrates in an economical and safer manner. The selection, synthesis, and liquid delivery system of organometallic precursors are of utmost importance for desired coating. Significantly large numbers of synthesis methods are available for synthesizing organometallic precursors using cheaper chemicals. In addition, efficient liquid delivery systems, such as bubbler, direct liquid injection by syringe, preprogrammed volumetric pumps, and pulsated liquid injection for injecting organometallic precursors into the vaporization chamber, are also available. Therefore, the MOCVD technique has the potential for producing a good-quality protective coating on substrates in an economical and environmental friendly manner.

References

1. Hiroshi H, Takuya A, Yasuo K, et al. High-temperature oxidation behavior of SiC-coated carbon fiber-reinforced carbon matrix composites. Composites: Part A 1999;30:515–20.
2. Tsung-Ming W, Wen-Cheng W, Shu-En H. Temperature dependence of the oxidation resistance of SiC coated carbon/carbon composite. Mater Chem Phys 1993;33:208–13.
3. Anwesha M, Dipul K, Nijhuma K, et al. Oxidation behavior of SiC ceramics synthesized from processed cellulosic bio-precursor. Ceram Intern 2012;38:4701–6.
4. Hermes EE, Kerans RJ. Degradation of non-oxide reinforcement and oxide matrix composites. Mater Res Soc Symp Proc 1988;125:73.
5. Aksay IA. Molecular and colloidal engineering of ceramics. Ceram Intern 1991;17:267–74.
6. Otsuka A, Matsumura Y, Hosono K, et al. Long term oxidation of a SiC fiber-bonded composite in air at 1500 °C. J Eur Ceram Soc 2003;23:3125–34.
7. Tietema R. Large-Scale industrial coating applications and systems. Comprehensive Mater Process 2014;4:519–61.
8. Prakash J, Venugopalan R, Paul B, et al. Study of thermal degradation behavior of dense and nanostructured silicon carbide coated carbon fibers in oxidative environments. Corros Sci 2013;67:142–51.
9. Venugopalan R, Prakash J, Nuwad J, et al. Morphological study of SiC coating developed on 2D carbon composite using MTS precursor in a hot wall vertical reactor. Int J Mat Res 2012;103:1251.
10. Chattopadhyay DK, Raju KVSN. Structural engineering of polyurethane coatings for high performance applications. Prog Polym Sci 2007;32(3):352–418.
11. Voevodin AA, Zabinski JS, Muratore C. Recent advances in hard, tough, and low friction nanocomposite coatings. Tsinghua Sci Tech 2005;10:665–79.

12. Rhys-Jones TN. Metallic and ceramic coatings: production, high temperature properties and applications. Corros Sci 1990;30:959–60.
13. Mordike BL, Ebert T. Magnesium: properties—applications—potential. Mater Sci Eng A 2001;302:37–45.
14. Dulera IV, Sinha RK. High temperature reactors. J Nucl Mater 2008;383:183–8.
15. Gray JE, Luan B. Protective coatings on magnesium and its alloys—a critical review. J Alloys Compd 2002;336:88–113.
16. Treccani L, Yvonne Klein T, Meder F, et al. Functionalized ceramics for biomedical, biotechnological and environmental applications. Acta Biomater 2013;9:7115–50.
17. Prakash J, Ghosh S, Venugopalan R, et al. Study of properties of SiC layer in TRISO coated particles grown using different alkyl-silicon compounds. AIP Conf Proc 2013;1538:26–9.
18. Wang CY, Yao P, Bradhurst DH, et al. Surface modification of Mg_2Ni alloy in an acid solution of copper sulfate and sulfuric acid. J Alloys Compd 1999;285:267.
19. Mittal CK. Chemical conversion and anodized coatings. Trans Metal Finishers Assoc India, Metal Finishing 1993;34:34.
20. Luo JL, Cui N. Effects of microencapsulation on the electrode behavior of Mg_2Ni-based hydrogen storage alloy in alkaline solution. J Alloys Compd 1998;264:299.
21. Mazia J. Paint removal (Striooina organic coatings). Metal Finishing 1990;88:466.
22. Schmidt H, Langenfeld S, Nab R. A new corrosion protection coating system for pressure-cast aluminium automotive parts. Mater Design 1997;18:309.
23. Gray JE, Luan B. Protective coatings on magnesium and its alloys—a critical review. J Alloys Compd 2002;336:88–113.
24. Luan B, Pierson HO. CVD/PVD coatings. Corrosion 1987;13:456, ASM Handbook.
25. Helmersson U, Lattemann M, Bohlmark J, et al. Ionized physical vapor deposition (IPVD): a review of technology and applications. Thin Solid Films 2006;513:1–24.
26. Choy KL. Chemical vapour deposition of coatings. Prog Mat Sci 2003;48:57–170.
27. Varacalle Jr. DJ, Lundberg LB, Herman H, et al. Titanium carbide coatings fabricated by the vacuum plasma spraying process. Surf Coat Technol 1996;86–87:70–4.
28. Zhang J, Xue Q, Li S. Microstructure and corrosion behavior of TiC/Ti(CN)/TiN multilayer CVD coatings on high strength steels. Appl Surf Sci 2013;280:626–31.
29. Mathur S, Kuhn P. CVD of titanium oxide coatings: comparative evaluation of thermal and plasma assisted processes. Surf Coat Technol 2006;201:807–14.
30. Vidal S, Maury F, Gleizes A, et al. Photo-assisted MOCVD of copper using Cu(hfa)(COD) as precursor. Appl Surf Sci 2000;168:57–60.
31. Niinistö L. Atomic layer epitaxy. Curr Opin Solid State Mater Sci 1998;3:147–52.
32. Yates HM, Brook LA, Sheel DW, et al. The growth of copper oxides on glass by flame assisted chemical vapour deposition. Thin Solid Films 2008;517:517–21.
33. Luo R. Friction performance of C/C composites prepared using rapid directional diffused chemical vapor infiltration processes. Carbon 2002;40:1279–85.
34. Teren AR, Thomas R, He J, et al. Comparison of precursors for pulsed metal-organic chemical vapor deposition of HfO_2 high-K dielectric thin films. Thin Solid Films 2005;478:206–17.
35. Wang HB, Xia CR, Meng GY, et al. Deposition and characterization of YSZ thin films by aerosol-assisted CVD. Mater Lett 2000;44:23–8.
36. Desu SB. Metallorganic chemical vapor deposition: a new era in optical coating technology. Mater Chem Phys 1992;31:341–5.
37. Tamir SB, Rabinovitch K, Gilo M, et al. Laser induced chemical vapor deposition of optical thin films on curved surfaces. Thin Solid Films 1998;332:10–5.
38. Jensen CJ, Chiu WKS. Open-air laser-induced chemical vapor deposition of silicon carbide coatings. Surf Coat Technol 2006;201:2822–8.

39. Braichotte D, Garrido C, Bergh HVD. The photolytic laser chemical vapor deposition rate of platinum, its dependence on wavelength, precursor vapor pressure, light intensity, and laser beam diameter. Appl Surf Sci 1990;46:9.
40. Marsh EP. Nucleation and deposition of PT films using ultraviolet irradiation. *US Patent, US 6204178 B1*; 2001.
41. Marsh EP. Nucleation and deposition of platinum group metal films using ultraviolet irradiation. *US Patent Appl. 2006/0014367 A1*; 2006.
42. Bell MS. Plasma composition during plasma-enhanced chemical vapor deposition of carbon nanotubes. Appl Phys Lett 2004;85:1137–9.
43. Labelle CB, Laua KKS, Gleason KK. Pulsed plasma enhanced chemical vapor deposition from CH_2F_2, $C_2H_2F_4$, and $CHCIF_2$. MRS Proc 1998;511:75–7.
44. Botman A, Mulders JJL, Weemaes R, et al. Purification of platinum and gold structures after electron-beam-induced deposition. Nanotechnology 2006;17:3779.
45. Kempshall BW, Giannuzzi LA, Prenitzer BI, et al. Comparative evaluation of protective coatings and focused ion beam chemical vapor deposition processes. J Vac Sci Technol B 2002;20:286.
46. Vahlas C, Juarez F, Feurer R, et al. Fluidization, spouting, and metal-organic CVD of platinum group metals on powders. Chem Vap Depos 2002;8:127.
47. Perez-Mariano J, Lau K-H, Sanjurjo A, et al. Multilayer coatings by chemical vapor deposition in a fluidized bed reactor at atmospheric pressure (AP/FBR-CVD): TiN/TaN and TiN/W. Surf Coat Technol 2006;201:2174–80.
48. Ritala M, Leskelä M. Chapter 2 – atomic layer deposition. In: Handbook of thin films, vol. 1; San Diego, CA: Academic Press; 2002. p. 103–59.
49. Knodle WS, Chow R. Molecular beam epitaxy: equipment and practice. In: Handbook of thin film deposition processes and techniques. 2nd ed. New York, USA: Noyes Publications; 2001. p. 381–461.
50. Telari KA, Rogers BR, Fang H, et al. Characterization of platinum films deposited by focused ion beam-assisted chemical vapor deposition. J Vac Sci Technol B 2002;20:590.
51. Tao T, Ro J, Melngailis J, et al. Focused ion beam induced deposition of platinum. J Vac Sci Technol B 1990;8:1826–9.
52. Catoirea L, Swihart MT. High-temperature kinetics of $AlCl_3$ decomposition in the presence of additives for chemical vapor deposition. J Electrochem Soc 2002;149:C261–7.
53. Jensen K, Kern W. Thermal chemical vapor deposition. Thin Film Processes 1991;1:283–368.
54. Helmboldt O, Hudson LK, Misra C, et al. Aluminum compounds, inorganic. In: Ullmann's encyclopedia of industrial chemistry. Weinheim: Wiley-VCH; 2005.
55. Young W, Hartung W, Crossley F. Reduction of aldehydes with aluminum isopropoxide. J Am Chem Soc 1936;58:100–2.
56. Fernelius WC. Inorganic syntheses. New York: McGraw-Hill Book Company; 1946.
57. Rodriguez P, Caussat B, Iltis X, et al. Alumina coatings on silica powders by fluidized bed chemical vapor deposition from aluminium acetylacetonate. Chem Eng J 2012;211–212:68–76.
58. Lacourse WC, Dahar S, Akhtar MM. Fiberizable $Si(OC_2Hs)_4$-H_2O-C:HsOH sols with stabilized viscosity. J Am Ceram Soc 1984;67:C200.
59. Artaki I, Zerda TW, Jonas J. Solvent effects on the condensation stage of the sol-gel process. J Non-Cryst Solids 1986;81:381.
60. Hench LL. Use of drying control chemical additives (DCCAs) in controlling sol-gel processing. In: Hench LL, Ulrich DR, editors. Science of ceramic chemical processing, vol. 52. New York: Wiley-Interscience; 1986.
61. Orcel G, Hench U. Use of a drying control chemical additive (DCCA) in the sol-gel processing of sodasilicate and soda borosilicate. Ceramic Eng Sci Proc 1984;5(7–8):546–55.

62. Jada SS. Study of tetraethyl orthosilicate hydrolysis by in situ generation of water. J Am Ceram Soc 1987;70:C298.
63. Yan MF, Rhodes WW. Low temperature sintering of TiO_2. Mater Sci Eng 1983;61:59.
64. Heistand RH, Oguri Y, Okamura H, et al. Synthesis and processing of submicrometer ceramic powders. In: Hench LL, Ulrich DR, Hench LL, Ulrich DR, editors. Science of ceramic chemical processing. New York: Wiley-Interscience; 1986. p. 482.
65. Bradley DC, Gaze R, Wardlow W, et al. Structural aspects of the hydrolysis of titanium tetraethoxide. J Chem Soc 1955;3977–82.
66. Boyd T. Preparation and properties of esters of polyorthotitanic acid. J Polym Sci 1951;7:591–3.
67. Yoldas BE. Introduction and effect of structural variations in inorganic polymers and glass networks. J Non-Cryst Solids 1982;51:105.
68. Bradley DC, Mehrotra RC, Gaur DP. Metal alkoxides. London: Academic Press; 1978.
69. Klemperer WG, Mainz MM, Millar DM. A molecular building-block approach to the synthesis of ceramic materials. In: MRS symposia proceedings; Better ceramics through chemistry II, Pittsburgh: MRS; 1986. p. 3–20.
70. Bradley DC, Factor MM. Pyrolysis of some alkoxides. I. Thermal stability of some zirconium alkoxides. J Appl Chem 1959;9:435.
71. Drake SR, Miller SAS, Williams D. Monomeric group IIA metal β-diketonates stablized by multidentate glymes. J Inorg Chem 1993;32:3227–35.
72. Varanasi VG, Besmann TM, Anderson TJ. Equilibrium analysis of CVD of yttria-stabilized zirconia. J Electrochem Soc 2005;152:C7–14.
73. West G, Beeson K. Low-pressure metalorganic chemical vapor deposition of photoluminescent Eu-doped Y_2O_3 films. J Mater Res 1990;5:1573–80.
74. Luten H, Rees JW, Goedken V. Preparation and structural characterization of, and chemical vapor deposition studies with, certain yttrium tris(β-diketonate) compounds. Chem Vap Depos 1996;2:149–61.
75. Weber A, Suhr H, Schumann H, et al. Thin yttrium and rare earth oxide films produced by plasma enhanced CVD of novel organometallic π-complexes. Appl Phys A 1990;51:520–5.
76. Dilthey W. Ueber Siliciumverbindungen. Chem Ber 1903;36:923–4.
77. Pike RM, Luongo RR. Silicon(4) compounds containing 1,3-diketo ligands. J Am Chem Soc 1966;88:2972.
78. Thompson DW. A new fl-diketonate complex of silicon(IV). Inorg Chem 1969;8:2015–8.
79. West R. Silicon and organosilicon derivatives of acetylacetone. J Am Chem Soc 1958;80:3246.
80. Chongying X, Thomas HB. Synthesis and characterization of neutral cis-hexacoordinate bis(β-diketonate) silicon(IV) complexes. Inorg Chem 2004;43:1568–73.
81. Elschenbroich C, Salzer A. Organometallics: a concise introduction. 2nd ed Weinheim: Wiley-VCH; 1992, ISBN: 3-527-28165-7.
82. Rand MJ. Characteristics of PtSi – Si contacts made from CVD platinum. J Electrochem Soc 1975;122:811.
83. Marriott JC, Salthouse JA, Ware MJ, et al. The structure of tetrakis(trifluorophosphine)nickel and tetrakis(trifluorophosphine)platinum determined by gas-phase electron diffraction. J Chem Soc D: Chem Commun 1970;595–6.
84. Herrmann WA. 100 Jahre Metallcarbonyle. Eine Zufallsentdeckung macht Geschichte. Chem Unserer Zeit 1988;22:113–22.
85. Marboe EC. Deposition of metal on glass from metal formates. *US Patent US2430520*; 1947.
86. Martin TP, Tripp CP, DeSisto WJ. Composite platinum/silica films deposited by chemical vapor deposition. Chem Vap Depos 2005;11:170.
87. Choi W-G, Choi E-S, Yoon S-G. Pt thin film collectors prepared by liquid-delivery metal-organic CVD using $Pt(C_2H_5C_5H_4)(CH_3)_3$ for $LiCoO_2$ thin film cathodes. Chem Vap Depos 2003;9:321.

88. Kwon J-H, Yoon S-G. Preparation of Pt thin films deposited by metalorganic chemical vapor deposition for ferroelectric thin films. Thin Solid Films 1997;303:136.
89. Dryden NH, Kumar R, Ou E, et al. Chemical vapor deposition of platinum: new precursors and their properties. Chem Mater 1991;3:677.
90. Hierso J-C, Feurer R, Kalck P. Platinum and palladium films obtained by low-temperature MOCVD for the formation of small particles on divided supports as catalytic materials. Chem Mater 2000;12:390.
91. Jones R, Karmas G, Martin G, et al. Organic compounds of uranium II, uranium(IV) amides, alkoxides and mercaptides. J Am Chem Soc 1956;78:4285–6.
92. Dermer O, Fernelius W. Die einwirkung von titantetrachlorid auf organische stickstoffverbindungen. Z Anorg Chem 1953;221:83–5.
93. Rie K-T, Wöhle J. Plasma-CVD of TiCN and ZrCN films on light metals. Surf Coat Technol 1999;112:226–9.
94. Kudapa S, Narasimhan K, Boppana P, et al. Characterization and properties of MTCVD TiCN and MTCVD ZrCN coatings. Surf Coat Technol 1999;120–121:259–64.
95. Prakash J, Sathiyamoorthy D. Organometallic route to the chemical vapor deposition of silicon carbide film. Int J Mech Eng Mater Sci 2008;1(2):93–108.
96. Steckl AJ, Li JP. Epitaxial growth of β-SiC on Si by RTCVD with C3H8 and SiH4. IEEE Trans Elec Dev 1992;ED-39:64–74.
97. Nishino S, Suhara H, Ono H, et al. Epitaxial growth and electric characteristics of cubic SiC on silicon. J Appl Phys 1987;61:4889–93.
98. Ueda T, Nishino H, Matsunami H. Crystal growth of SiC by step-controlled epitaxy. J Cryst Growth 1990;104:695–700.
99. Powell JA, Larkin DJ, Matus LG, et al. Growth of high quality 6H-SiC epitaxial films on vicinal (0001) 6H-SiC wafers. Appl Phys Lett 1990;56:1442–4.
100. Morosanu CE. Thin films by chemical vapor deposition. Amsterdam: Elsevier; 1990.
101. Liaw P, Davis RF. Epitaxial growth and characterization of β-SiC thin films. J Electrochem Soc 1985;132:642–8.
102. Fischman GS, Petuskey WT. Thermodynamic analysis and kinetic implications of chemical vapor deposition of SiC from Si-C-Cl-H gas systems. J Am Ceram Soc 1985;68:185–90.
103. Stinspring CD, Wourmhoudt JC. Gas phase kinetics analysis and implications for silicon carbide chemical vapor deposition. J Cryst Growth 1988;87:481–3.
104. Koh JH, Woo SI. Computer simulation study on atmospheric pressure CVD process for amorphous silicon carbide. J Electrochem Soc 1990;137:2215–8.
105. Golecki I, Reidinger F, Marti J. Single-crystalline, epitaxial cubic SiC films grown on (100) Si at 750 °C by chemical vapor deposition. Appl Phys Lett 1992;60:1703–5.
106. Madapura S, Steckl AJ, Lobada M. Heteroepitaxial growth of SiC on Si(100) and (111) by chemical vapor deposition using trimethylsilane. J Electrochem Soc 1999;146:1197–1202.
107. Kaplan M, Matthies DL, Princeton NJ. Metallized video disc having an Insulating layer thereon. *U.S. Pat. No. 3,843,399*;1974.
108. Yasui K, Hashiba M, Narita Y, et al. Comparison of the growth characteristics of SiC on Si between low-pressure CVD and triode plasma CVD. Mater Sci Forum 2002;367:389–93.
109. Avigal Y, Schieber M, Levin R. The growth of hetero-epitaxial SiC films by pyrolysis of various alkyl-silicon compounds. J Cryst Growth, 24/25. 1974. p. 188–190.
110. Jeong SH, Lim DC, Jee H-G, et al. Deposition of silicon carbide films using a high vacuum metalorganic chemical vapor deposition method with a single source precursor: study of their structural properties. J Vac Sci Technol 2004;B 22:2216–9.

111. Boo J-H, Yu K-S, Lee M, et al. Deposition of cubic SiC films on silicon using dimethylisopropylsilane. Appl Phys Lett 1995;66:3486–8.
112. Curran C, Witucki RM, McCusker PA. Electric moments of organosilicon compounds. I. Fluorides and chlorides. J Am Chem Soc 1950;72:4471–4.
113. Finholt AE, Bond JAC, Wilzbach KE, et al. Prepared from PhSiCl3 and LiAlD4 by analogy to the procedure for PhSiH3. J Am Chem Soc 1947;69:2692–6.
114. Ponomaranko VA, Mironov VF. Bull Acad Sci USSR, Div Chem Sci (Engl Transl) 1954;1954:423.
115. Beleg. *Pat. 553496* [U.S. Prior. 19.12.1955].
116. Goodspeed NC, Sanderson RT. Organo-silicon compounds. XXVII. Reduction of alkoxychlorsilanes by means of metal hydrides. J Inorg Nucl Chem 1956;2:266–8.
117. German Appl. (West German) 1055511 [15.12.1956], *Brit Pat 823483* (German prior. (West German) 3.11, 12.12, and 15.12; 1956).
118. Zakharkin LI. Bull Acad Sci USSR, Div Chem Sci (Engl Transl) 1960;1960:2079.
119. Sundermeyer W. Eureopean Research Associates S.A., German Appl. (West German) 1080077 (8.8.1957).
120. Boo JH, Yu KS, Kim Y. Growth of cubic SiC films using 1,3-disilabutane. Chem Mater 1995;7:694–8.
121. Jung IN, Yeon SH, Han JS. In: Organometallics: a concise introduction, vol. 12. Weinheim: Wiley-VCH; 1993, p. 2360. ISBN: 3-527-28165-7, 2nd ed.
122. Jung IN, Lee GH, Song CH. *Korean Patent Appl. No. 1992, 92, 4705*; 1992.
123. Steckl AJ, Yuan C, Li JP, et al. Growth of crystalline 3C-SiC on Si at reduced temperatures by chemical vapor deposition from silacyclobutane. Appl Phys Lett 1993;63:3347–49.
124. Cambell PG. Ph.D. thesis. Pennsylvania State University; 1957.
125. Vdovin VM, Nametkin KS, Grinberg PL. Dokl Akad Nauk SSSR 1963;150:799.
126. Larkin DJ, Interrante LV. Chemical vapor deposition of silicon carbide from 1,3-disilacyclobutane. Chem Mater 1992;4:22–4.
127. Chadder AK, Parsons JD, Wu J, et al. Chemical vapor deposition of silicon carbide thin films on titanium carbide, using 1,3 disilacyclobutane. Appl Phys Lett 1993;62:3097.
128. Laane J. Synthesis of silacyclobutane and some related compounds. J Am Chem Soc. 1967;89:1144–47.
129. Nametkin NS, Vdovin VM, Zavgalov VI, et al. Izv Akad Nauk SSSR Ser Khim 1965;1965:929.
130. Takahashi K, Nishino S, Saraie J. Low-temperature growth of 3C-SiC on Si substrate by chemical vapor deposition using hexamethyldisilane as a source material. J Electrochem Soc 1992;139:3565–71.
131. Shen Q, MacDonald LS. Silicon carbide precursor. *U.S. Patent No. 6,730,802*;2004.
132. Silicon carbide precursors-CVD 2000 & CVD 4000, Ceramics PA. New York, USA: Starfire Systems. www.starfiresystems.com.
133. O'Brien P, Pickett NL, Otway DJ. Developments in CVD delivery systems: a chemist's perspective on the chemical and physical interactions between precursors. Chem Vap Depos 2002;8:237–9.
134. Baumann PK, Doppelt P, Fröhlich K, et al. Platinum, ruthenium and ruthenium dioxide electrodes deposited by metal organic chemical vapor deposition for oxide applications. Integr Ferroelectrics 2002;44:135–142.
135. Selvakumar J, Nagaraja KS, Sathiyamoorthy D. Relevance of thermodynamic and kinetic parameters of chemical vapor deposition precursors. J Nanosci Nanotechnol 2011;11:8190–7.
136. Prakash J, Ghosh S, Sathiyamoorthy D, et al. Taguchi method optimization of parameters for growth of nano dimensional SiC wires by chemical vapor deposition technique. Curr Nanosci 2012;8:161–9.
137. Prakash J, Kumar Ghosh S, Sathiyamoorthy D. Catalyst-free chemical vapor deposition for synthesis of SiC nanowires with controlled morphology. In: Wang ZM, editor. Silicon based nanomaterials. Springer: New York, USA. 2013.
138. Courtright EL. A review of fundamental coating issues for high temperature composites. Surf Coat Technol 1994;68–69:116–25.

Chapter 5

Synthesis and Evaluation of Self-Healing Cerium-Doped Silane Hybrid Coatings on Steel Surfaces

Roohangiz Zandi Zand*, **Kim Verbeken**†, **Annemie Adriaens***

**Department of Analytical Chemistry, Ghent University, Krijgslaan 281-S12, Ghent, Belgium*

†*Department of Materials Science and Engineering, Ghent University, Technologiepark 903, Zwijnaarde (Ghent), Belgium*

5.1 Introduction

Industrial equipment commonly faces the problem of corrosive degradation. While corrosion cannot be entirely avoided, it can be controlled and delayed by using well-designed alloys, corrosion inhibitors, protective coatings, and cathodic protection.[1] Chromate coatings provide excellent protection against corrosion; however, their carcinogenicity has caused them to be banned in Europe since 2007, and a global ban is likely.[2]

Intelligent Coatings for Corrosion Control
Copyright © 2015 Elsevier Inc. All rights reserved.

As alternatives to chromate-based surface treatments, several classes of new pretreatment systems have been developed. Pretreatments employing functional silane coatings are particularly promising because they provide different chemical functionalities on a wide range of substrates, both metallic and nonmetallic. Silane coatings are generally uniform, robust, and reliable. They also present lateral resolution in the nanometer regime.[3] Their good barrier properties arise through the formation of a dense—Si–O–Si—network, which hinders the penetration of corrosive species to the substrate. Thus, the effectiveness of silane coating pretreatments strongly depends on the barrier properties of the film.[4–6] These barrier properties can be enhanced through the addition of small amounts of chemicals with specific properties, such as self-healing.[7]

Recent investigations of sol-gel processes have aimed to develop sol-gel coatings doped with environmentally compatible inhibitors, such as cerium compounds.[7–10] These systems can combine the barrier properties of sol-gel coatings with the ability of the cerium ions to inhibit corrosion.[3,10] Cerium ions inhibit corrosion by migrating through the coating to the location of attack (a defect in the coating) and then reacting to passivate the site. Therefore, they act as cathodic inhibitors at active sites through the precipitation of insoluble cerium hydroxide at local regions of high pH.[10,11]

Cerium nitrate can improve the protection of galvanized steel substrates from corrosion when used either as a conversion film[12–14] or as a corrosion inhibitor through its addition to a silane formulation.[3,15–17]

The anticorrosion properties of silane coatings can also be improved by the addition of oxide nanoparticles. The nanoparticles can be synthesized in the films, as demonstrated for sol-gel coatings,[5,18] or they can be added to the pretreatment solutions.[18] Mg alloys pretreated with sol-gel coatings containing ZrO_2 and CeO_2 nanoparticles have been reported to show enhanced corrosion protection (due to the CeO_2) and improved wear resistance (due to the ZrO_2).[18]

Montemor et al.[5,18] reported a new approach that involves the modification of bis- [triethoxysilylpropyl] tetra sulfide silane (BTESPT) with nanoparticles such as CeO_2, SiO_2, or CeO_2–ZrO_2. Improved corrosion resistance could also be achieved by initially activating the nanoparticles with cerium nitrate. Ceria nanoparticles were shown to be very effective fillers, improving both the barrier properties of the silane coatings and the overall corrosion resistance. The protective behavior depends on the concentration of nanoparticles; their activation with cerium ions leads to thicker and more protective silane films.

This chapter reports the creation and evaluation of self-healing properties in cerium-doped silane hybrid coatings (SHCs), which could be used as environmentally compatible protective coatings for steel surfaces that are subject to corrosion in specific environments. We focus on two different types of steels: austenitic 304L stainless steel (SS) and hot-dip galvanized steel (HDG). In NaCl solution, 304L SS has been reported to have greater corrosion resistance than HDG.[19,20] The effects of

various factors on the microstructure, morphology, and protective properties of the coatings were tested using both these substrates. The tested factors were the concentrations of cerium ions and the use of additives, including bisphenol A (BPA), cerium nitrate, and CeO_2 nanoparticles.

The influences of cerium and BPA on the microstructures of the coatings were examined using Fourier transform infrared (FTIR) spectroscopy. The morphological and microscopic features of the coated substrates were evaluated using atomic force microscopy (AFM) and scanning electron microscopy (SEM). After corrosion testing, SEM was used to evaluate the samples. Corrosion of the sol-gel coatings was assessed via neutral salt spray tests, electrochemical impedance spectroscopy (EIS), and potentiodynamic polarization tests.

5.2 Experimental Procedure

5.2.1 Sample preparation

The silane solution was prepared by dissolving 4.084 mL 3-glycidoxypropyltrimethoxy silane (GPTMS) (Merck, New Jersey, USA) in a mixture of 0.5 mL aqueous HCl (pH = 2) (H_2O/Si mole ratio = 0.5[21]) and an aqueous dispersion of activated ceria nanoparticles. The ceria nanoparticles (10 wt.% in water, particle size <25 nm, Sigma Aldrich, St. Louis, USA) were activated by ultrasonic dispersion in an aqueous solution of cerium nitrate (Fluka, Buchs, Switzerland). The solution was placed in a sealed beaker and stirred at room temperature for 30 min at 240 rpm to hydrolyze and condense the silane precursors. BPA (Merck) was then added to the solution as a cross-linking agent. It was dissolved by mixing the solution for 80 min. To accelerate the condensation reaction, 0.0152 mL 1-methylimidazole (MI) (Merck) (MI/Si mole ratio = 0.01) was added to the solution, which was then stirred for 5 min. A clear, colorless, homogenous solution resulted. A set of silane solutions (S1-S11) with different molar ratios of CeO_2/Si, $Ce(NO_3)_3$/Si, and BPA/Si was also prepared (Table 5.1).

The metallic substrates were 304L stainless steel and HDG. The 304L SS was comprised of Fe with the following additives (by mass): 17.65% Cr, 8.59% Ni, 1.75% Mn, 0.41% Si, 0.25% Mo, 0.017% C, 0.45% Cu, 0.032% P, 0.0050% S, and 0.0049% Al. Coupons (4.98 cm^2 area and 0.1 cm thickness) were made for the AFM, SEM, and electrochemical tests. Plates (7 × 15 × 0.1 cm) were used for the salt spray tests. The galvanized steel specimens each had an ~8 µm zinc coating, which had an area density of ~112 g/m^2.

The 304L SS specimens were successively ground with 600 and 1200 grit emery paper and degreased with acetone in an ultrasonic bath for 10 min. Chemical etching was performed by immersing the samples in an alkaline solution (1 M NaOH) for 5 min at 50 °C. After rinsing in tap water and then in deionized water, the cleaned

TABLE 5.1 Composition of the Cerium-Doped Silane Coating Solutions

	Molar Ratio (mol%)		
Set	CeO_2/Si	Ce $(NO_3)_3 \cdot 6H_2O$/Si	BPA/Si
S_1	—	—	0.500
S_2	—	0.200	0.500
S_3	—	0.200	—
S_4	—	0.100	0.500
S_5	0.100	—	0.500
S_6	—	0.001	0.500
S_7	—	0.005	0.500
S_8	—	0.010	0.500
S_9	—	0.050	0.500
S_{10}	0.050	—	0.500
S_{11}	0.025	0.025	0.500

S_1 and S_2 used to study the effects of cerium addition on the corrosion performance of silica hybrid coatings (SHCs).
S_2 and S_3 used to study the effects of BPA on corrosion performance of SHCs.
S_4 and S_5 used to study the effects of CeO_2 and $Ce(NO_3)_3$ on corrosion performance of SHCs.
S_1, S_4, S_6, S_7, S_8, and S_9 used to study the effects of cerium concentration on corrosion performance of SHCs.
S_1, S_9, S_{10}, and S_{11} used to study the effects of activated ceria nanoparticles on corrosion performance of SHCs.

substrates were dried in air. The galvanized steel specimens were degreased using an alkaline cleaner. They were then washed with distilled water and dried in air.

Both types of sample were immersed in silane solution for 60 s. The coated specimens were dried at room temperature for 24 h. They were then cured at 25-130 °C for 90 min to initiate extensive cross-linking in the hybrid films.[22] The thicknesses of the coatings were measured by profilometry (Check line 3000 pro, Germany).

5.2.2 Analytical Methods

FTIR measurements of the coated samples were carried out using a Bio-Rad 575C spectrophotometer in the mid-IR range (4000-400 cm^{-1}). All spectra were taken at an incident angle of 45° normal to the surface of the specimen, with a spectral resolution of 4 cm^{-1}. For each measurement, 64 scans were collected.

AFM images were obtained under ambient conditions using a multimode scanning probe microscope (Digital Instruments, USA) equipped with a Nanoscope IIIa controller. 5×5 μm scans were recorded in tapping mode using a silicon cantilever (OTESPA, Veeco). Nanoscope software (version 4.43r8) was used to analyze the surface roughness, after the recorded images were modified using an automated X-Y-plane fit.

SEM measurements were performed using an XL30 SEM microscope equipped with an energy-dispersive X-ray spectroscope. The silane coatings were observed before and after EIS measurements. Secondary electron images were collected at 15 and 20 kV.

Corrosion of the coated substrates was evaluated via the ASTM B117 standard neutral salt spray test[23] using a 5% NaCl solution. Prior to exposure, the back and edges of the plates were covered with adhesive tape. An artificial scratch that reached the substrate was made in the coating to allow assessment of possible delamination. Visual examination of the macroscopic surfaces was carried out at intervals throughout the exposure.

EIS and potentiodynamic polarization tests assessed the corrosion of the silane-treated substrates in a 3.5% NaCl solution. An Autolab PG-STAT 20 potentiostat equipped with a frequency response analyzer module was used to assess a three-electrode system, which consisted of an Ag/AgCl KCl_{sat} reference electrode, a platinum mesh counter electrode, and the sample as the working electrode. EIS was performed at room temperature at the open circuit potential. Data were obtained as a function of frequency (over the range 10^5-10^{-2} Hz) using a sine wave with peak-to-peak amplitude of 10 mV. The samples were immersed in the electrolyte solution for 30 min before measurement, and measurements were conducted periodically. For each experiment, the measurements were repeated four times. Impedance fitting was performed using the appropriate equivalent circuits, using Z-view software (Scribner Associates Inc.).

Potentiodynamic measurements were performed over the range −1500 to 1000 mV versus Ag/AgCl KCl_{sat}, at a rate of 1 mV/s. These measurements were also performed four times. Tafel extrapolation (conducted according to the ASTM Standard G3-89, 2004)[24] was used to determine I_{corr} and E_{corr}.

5.3 Results and Discussion

5.3.1 Effects of cerium ions and BPA on the microstructure and the corrosion protection of SHCs on 304L stainless steel

Magnified FTIR spectra of the SHC (S_1) and the cerium-doped SHC (Ce-SHC) (S_2) in the regions 500-1300 cm^{-1} (Figure 5.1a) and 2800-4000 cm^{-1} (Figure 5.1b) show main features that include bands corresponding to Si−O−Si sequences, OH groups, and $-CH_2$ groups.

- The strong peaks between 1000 and 1200 cm^{-1} are associated with the Si−O−Si/C−O−C asymmetric bond stretching vibration,[25] which is the structural backbone of the hybrid material.[25] The high-frequency band near 1020 cm^{-1} is assignable to the antisymmetric stretching of oxygen atoms. The bands at intermediate frequencies around 750-800 cm^{-1} are attributable to the symmetric stretching of the oxygen atoms.

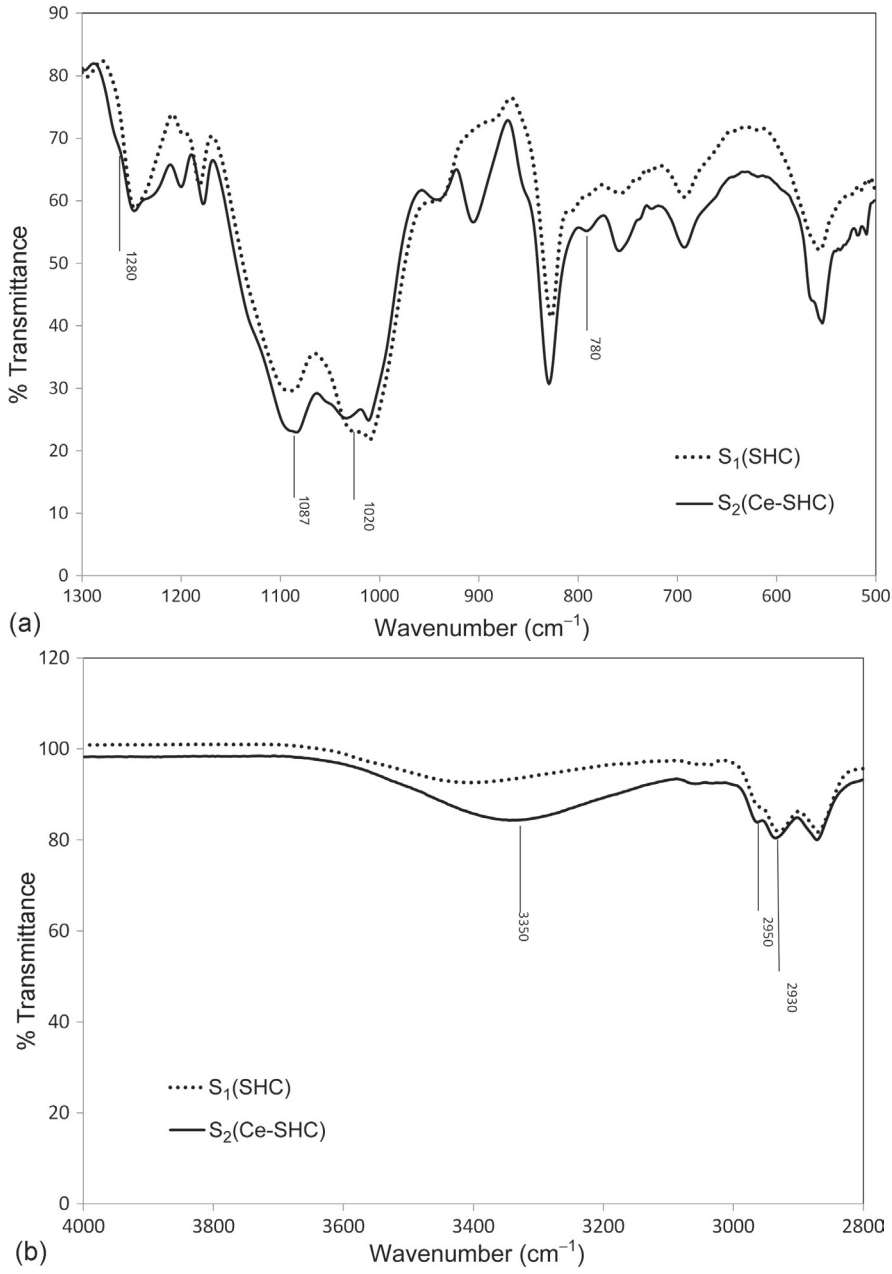


Figure 5.1 FTIR spectra of 304L SS substrates pretreated with silane hybrid (S_1) and cerium nitrate-doped silane hybrid (S_2) coatings: (a) magnified region from 500 to 1300 cm^{-1} and (b) magnified region from 2800 to 4000 cm^{-1}. *With kind permission from Elsevier.*[32]

- The $-CH_2$ group incorporated into the silica group is indicated by the two weak absorption peaks at about 2930 cm^{-1} and 2950 cm^{-1}, which can be assigned to symmetric and asymmetric stretching of the $-CH_2$ bonds present on the silicon moiety.[26] The presence of this hydrocarbon unit reveals a certain degree of planarization of the coating macromolecular chains. The intensities of the 1087 cm^{-1} band and the 780 and 2950 cm^{-1} shoulders increase in the Ce-doped sample (S_2), demonstrating that the incorporation of cerium nitrate leads to improved condensation.
- The broad band centered near 3400 cm^{-1} is assigned to residual Si–OH stretching vibrations and hydrogen-bonded water,[27] which possibly formed during the hydrolysis of the alkoxy groups of GPTMS.

The effects of BPA, an aromatic diol, on the cross-linking of organosilica networks via the chemical coupling of the aromatic diol and epoxy-functionalities were also studied by FTIR spectroscopy. Cerium-doped silica hybrid coatings with and without BPA (Ce-SHC, BPA=0) (S_2 and S_3) were analyzed. The magnified spectral regions of interest are 500-1300 cm^{-1} (Figure 5.2a) and 2800-4000 cm^{-1} (Figure 5.2b). The bands due to asymmetric epoxide ring deformation at 758 and 902 cm^{-1} in sample S_3 are of similar intensity, which allows monitoring of the coupling reaction between the epoxy functionalities of the organosilica networks and the diol cross-linkers. These bands almost disappear in the FTIR spectra of sample S_2, indicating the chemical bonding of organosilica networks in a cross-linked network.[28] The bands due to Si–O–Si in sample S_3 (centered at 1100 cm^{-1}) become more intense and broader relative to those in sample S_2. This is attributable to the direct connection of epoxy silanes and propyl trimethoxy silane in sample S_3, which resulted in the formation of a very brittle film.

A standard corrosion resistance evaluation using salt spray was used to assess the three sol-gel film coatings. Photographs after 2000 h of salt spray exposure (Figure 5.3) illustrate that the SHC (S_1) (average thickness 19.2±6.5 µm) and the cerium-doped SHC (S_2) (average thickness 57.7±12.0 µm) did not show any signs of blistering, delamination, or corrosion. The samples retained their original shiny surfaces. However, the Ce-doped silica hybrid coating without BPA (S_3) (average thickness 57.1±4.0 µm) showed limited resistance to the salt spray; it exhibited blistering and delamination after exposure for 148 h. The first signs of corrosion appeared after exposure for 1600 h.

Potentiodynamic polarization measurements were carried out to estimate the effects of cerium and BPA on the corrosion resistance of the SHCs. Potentiodynamic polarization curves (Figure 5.4) were recorded after the bare and pretreated 304L SS substrates with the three coatings (S_1-S_3) were immersed for 3 h in a neutral 3.5% NaCl solution. Table 5.2 lists the electrochemical parameters derived from these curves.

The limiting current density for oxygen reduction and the anodic current density for all the coated specimens were lower than those for the uncoated 304L SS. This suggests that the corrosion protection was due to both the blockage of

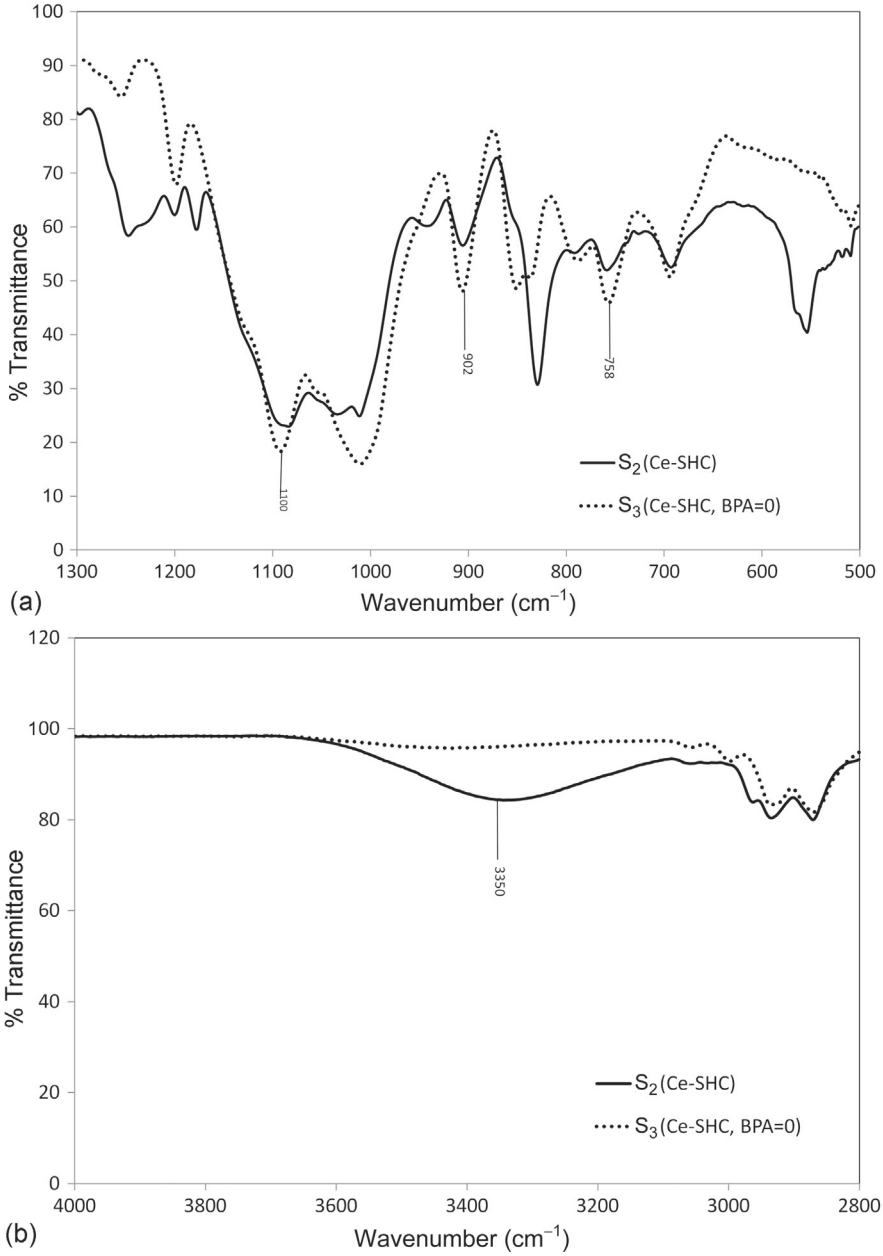


Figure 5.2 TIR spectra of 304L SS substrates pretreated with cerium nitrate-doped silane hybrid (S_2) and non-BPA cerium nitrate-doped silane hybrid (S_3) coatings: (a) magnified region from 500 to 1300 cm^{-1} and (b) magnified region from 2800 to 4000 cm^{-1}. *With kind permission from Elsevier.*[32]

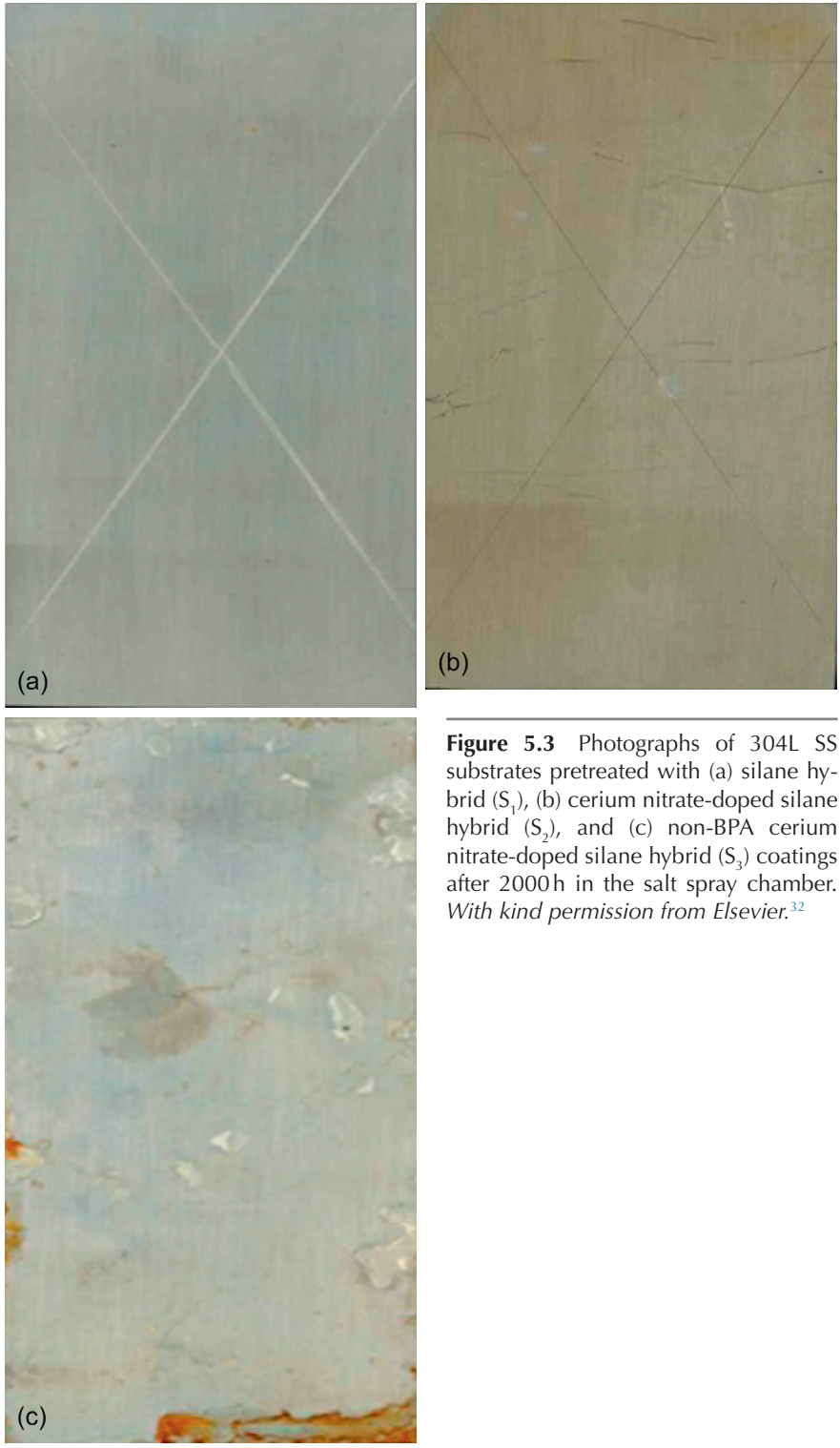


Figure 5.3 Photographs of 304L SS substrates pretreated with (a) silane hybrid (S_1), (b) cerium nitrate-doped silane hybrid (S_2), and (c) non-BPA cerium nitrate-doped silane hybrid (S_3) coatings after 2000 h in the salt spray chamber. *With kind permission from Elsevier.*[32]

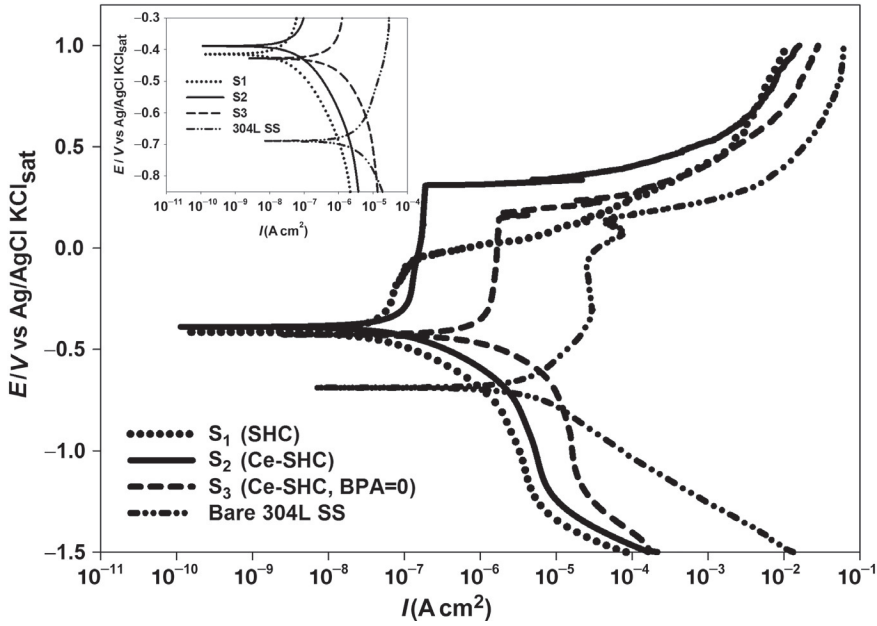


Figure 5.4 Potentiodynamic polarization curves of 304L SS substrates both bare and pretreated with silane hybrid (S_1), cerium nitrate-doped silane hybrid (S_2), non-BPA cerium nitrate-doped silane hybrid (S_3) coatings obtained after immersion for 3 h in a 3.5% NaCl solution. The inset plot has potential depicted as the difference between the imposed and corrosion potentials, which allows better separation of the anodic and cathodic polarization effects. *With kind permission from Elsevier.*[32]

TABLE 5.2 Electrochemical Parameters Obtained from the Polarization Measured in a 3.5% NaCl Solution

Sample	E_{corr} (V)	I_{corr} (A cm^{-2})	b_c (V/dec)	b_a (V/dec)	Passive Area (V)
Bare 304L SS	–0.690	3.97×10^{-6}	0.331	0.243	–0.326 to –0.086
S_1: SHC	–0.414	2.30×10^{-8}	0.264	0.103	–0.269 to –0.030
S_2: Ce-SHC	–0.389	4.48×10^{-8}	0.297	0.100	–0.233 to 0.308
S_3: Ce-SHC(BPA=0)	–0.427	5.10×10^{-7}	0.315	0.101	–0.312 to 0.181

With kind permission from Elsevier.[32]

the surface with the reduction of oxygen and metal dissolution in the pores of the coating layers. Sample (S_1) showed a decreased corrosion current density, I_{corr}, of around 2.30×10^{-8} A cm^{-2}. Its corrosion potential (–0.414 V) is more positive than that of the bare sample. Nevertheless, Figure 5.4 shows a very limited passive region of approximately –0.269 to –0.030 V over its corrosion potential.

The addition of cerium ions in coating S_2 led to further reductions of corrosion current density and corrosion potential. A distinct passive region emerges that extends over a several hundred mV range of 0.233 to +0.308 V over the E_{corr}.

The poor performance of the S_3 coating that lacked BPA may have been due to the permeability of the coating, which occurred due to cracks or porosity. This permeability allowed the aggressive electrolyte to reach the metal surface and initiate corrosion, indicating that the omission of a cross-linker can significantly affect the corrosion resistance of cerium-doped SHCs.

SEM images of the bare and coated 304L SS samples recorded after potentiodynamic polarization testing in a neutral 3.5% NaCl solution (Figure 5.5) each show localized corrosion. Exfoliation of the corrosion products, cracks (Figure 5.5a–c), and pits (Figure 5.5d) of different sizes are visible. The damage around some of the cracks and pits (Figure 5.5a–d) indicates preferential localized attack, which occurred after the applied potential exceeded the breakdown potential. This localized attack promoted the hybrid film to deteriorate and delaminate, possibly due to hydrolysis reactions at the interface. The diffusion of oxidant ions and the corrosion rate both increased, causing an accumulation of corrosion products at the interface, which promoted the formation of the defects and microcracks that are shown in Figure 5.5a–c. Samples S_1 and S_2 showed improved corrosion resistance, as suggested by the E_{corr} and I_{corr} values (Table 5.2).

Impedance spectra were recorded for the bare and coated 304L SS substrates after immersion for 3 h in a 3.5% NaCl solution (Figure 5.6). The uncoated sample showed an EIS spectrum characterized by two time constants. The time constant at higher frequencies was assigned to the presence of an oxide/hydroxide film on the substrate and that at lower frequencies was due to corrosion activity. The total impedance of the substrate was below $5.86 \times 10^5\,\Omega\,cm^2$. Significant amounts of corrosion products were observed.

Samples S_1 and S_2 also showed two time constants: one at higher frequencies, attributed to the presence of the silane layer, and a lower frequency constant due to the charge transfer reaction associated with oxidation of the substrate. The Bode phase angle plot for sample S_3 shows a different time constant at middling frequencies that can be attributed to cracking and corrosion activity at the surface of the substrate. This likely resulted from the absence of the cross-linker (BPA) causing brittleness in the film, which led to microcracks and delamination of the film.

Both the SHC (S_1) and the cerium-doped SHC (S_2) showed low-frequency system impedances that were about one order of magnitude greater than those shown by the bare sample and sample S_3 (Figure 5.6b). This was probably due to the coating blocking the aggressive electrolyte from reaching the reactive metal surface. The lower impedance shown by sample S_3 was due to the creation of defects and cracks in the coating, which allowed the diffusion of the aggressive electrolyte to the substrate.

EIS of samples S_1 and S_2 evaluated their barrier properties and inhibition mechanisms. Phase angle plots and bode modulus for samples S_1 (Figure 5.7)

and S_2 (Figure 5.8) were recorded at intervals while the samples were immersed in a 3.5% NaCl solution for 22 days.

Impedance measurements of the noninhibited system (S_1) display a slight evolution of the barrier properties associated with the hybrid coating. This behavior is related to water uptake, which occurred during the first days of immersion in the electrolyte. After 22 days, the noninhibited system displayed lower barrier effects.

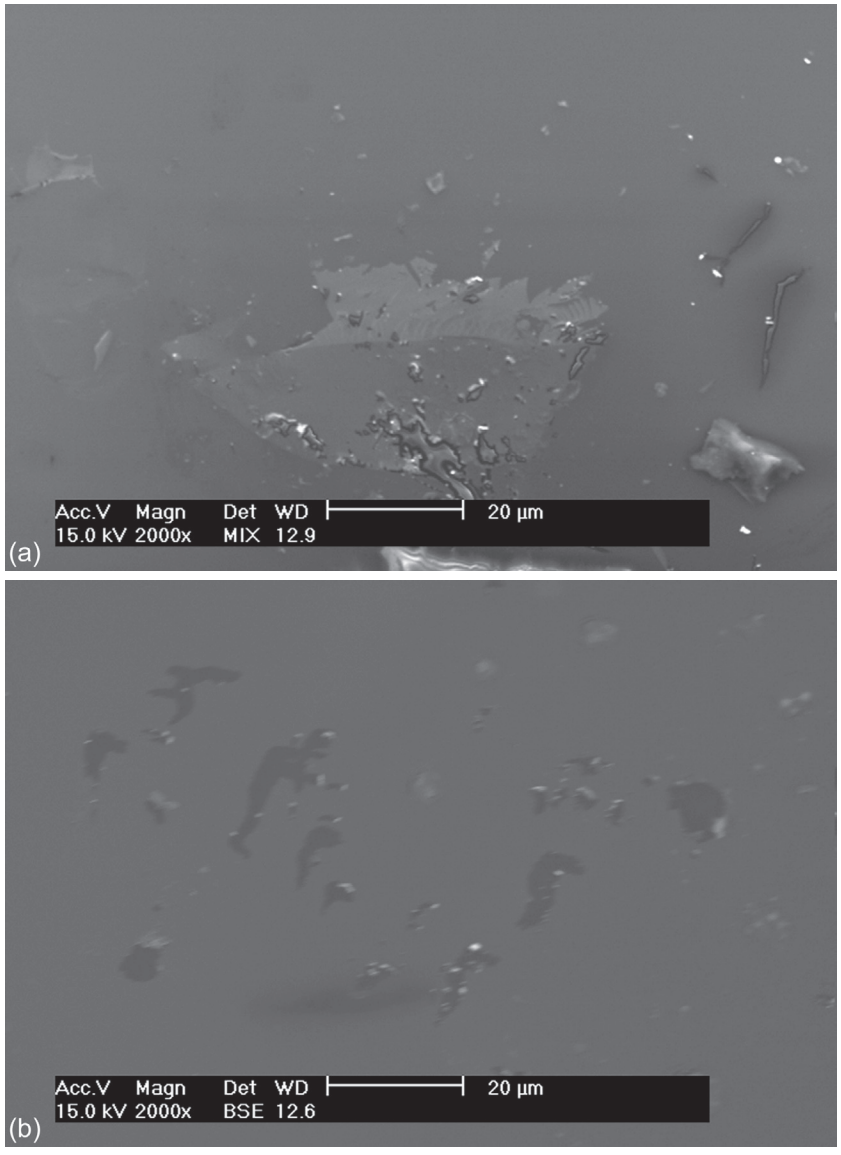


Figure 5.5 SEM micrographs of (a) silane hybrid-coated (S_1), (b) cerium nitrate-doped silane hybrid-coated (S_2)[32]

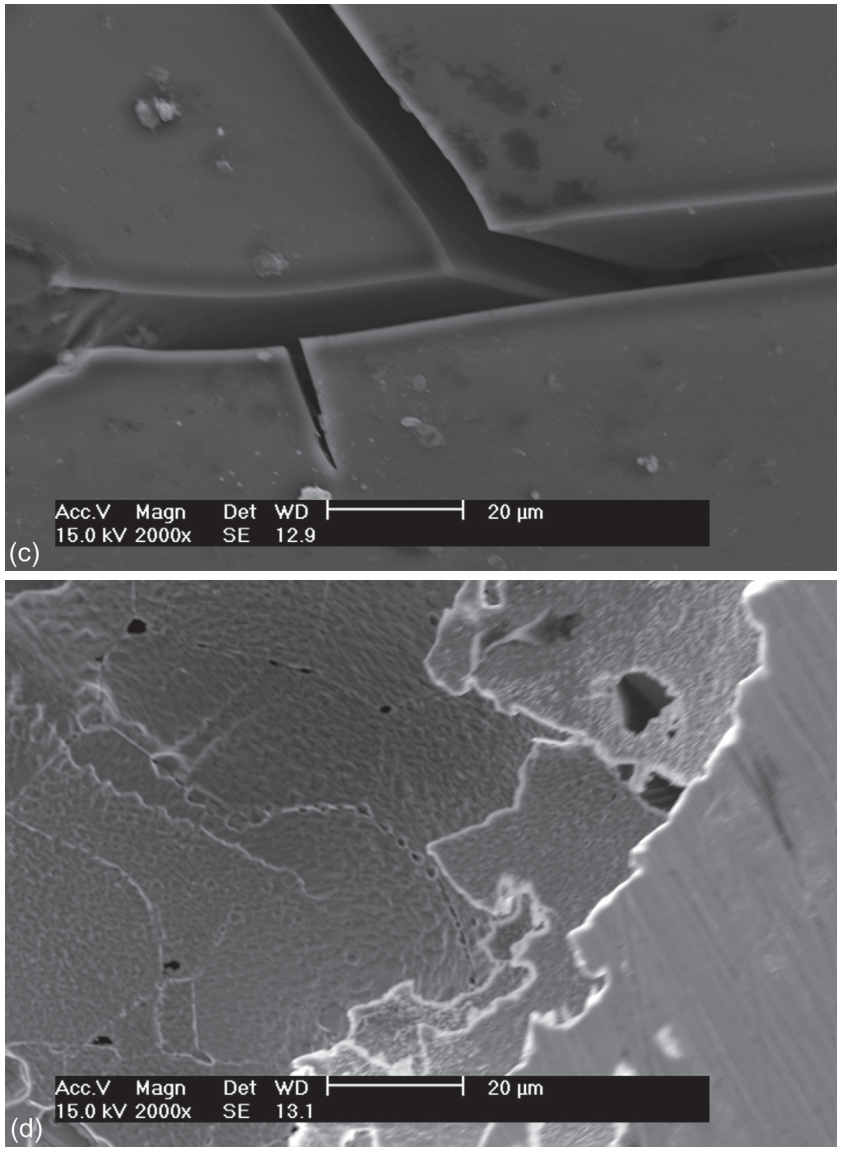


Figure 5.5, cont'd (c) non-BPA cerium nitrate-doped silane hybrid-coated (S_3), and (d) bare 304L SS obtained after potentiodynamic polarization in a neutral 3.5% NaCl solution. *With kind permission from Elsevier.*[32]

The system containing cerium species (S_2) offered better protection than the noninhibited (S_1) system, and its barrier properties remained constant for longer. The inhibited system showed slower electrochemical evolution than the noninhibited one because the inhibiting effect of cerium ions slowed the corrosion kinetics.

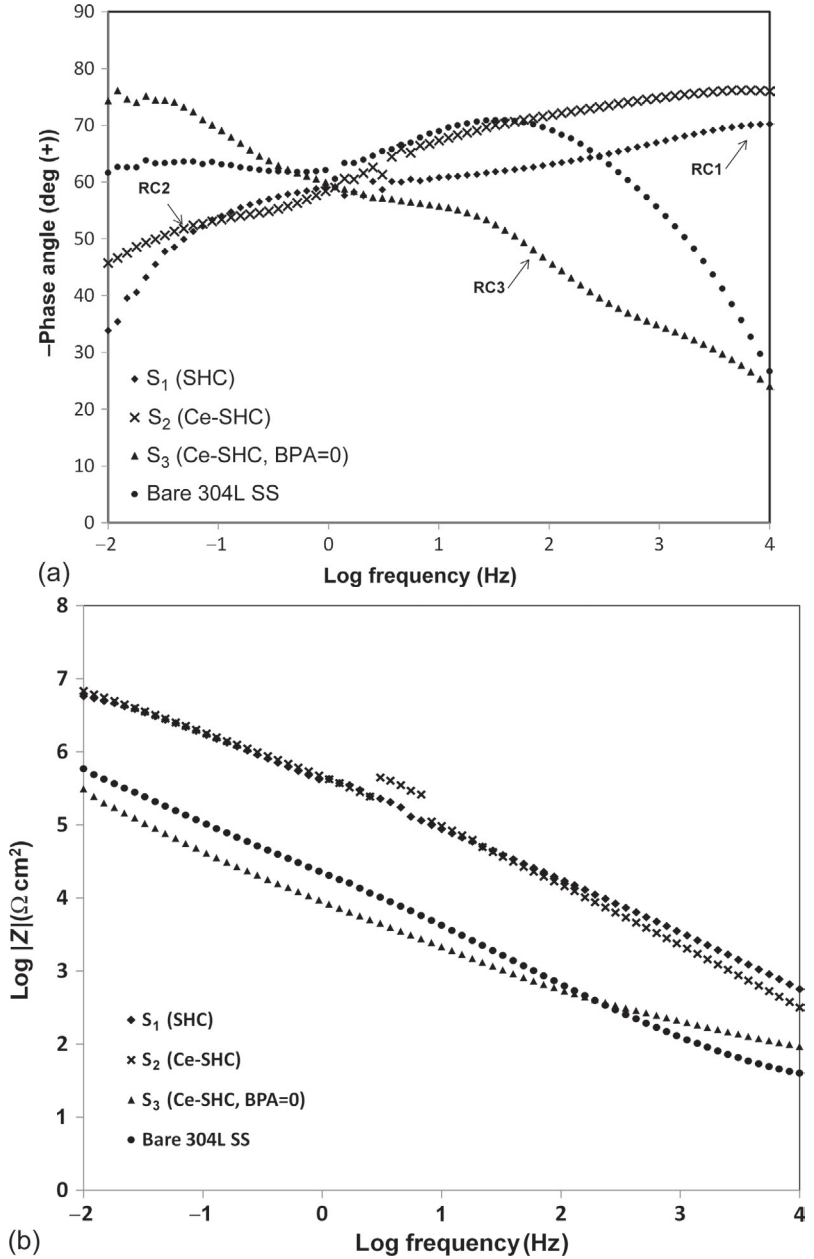


Figure 5.6 EIS phase angle plots (a) and bode modulus (b) for bare and silane hybrid-coated (S_1), cerium nitrate-doped silane hybrid-coated (S_2), and non-BPA cerium nitrate-doped silane hybrid-coated (S_3) 304L SS substrates after immersion for 3 h in a 3.5% NaCl solution. *With kind permission from Elsevier.*[32]

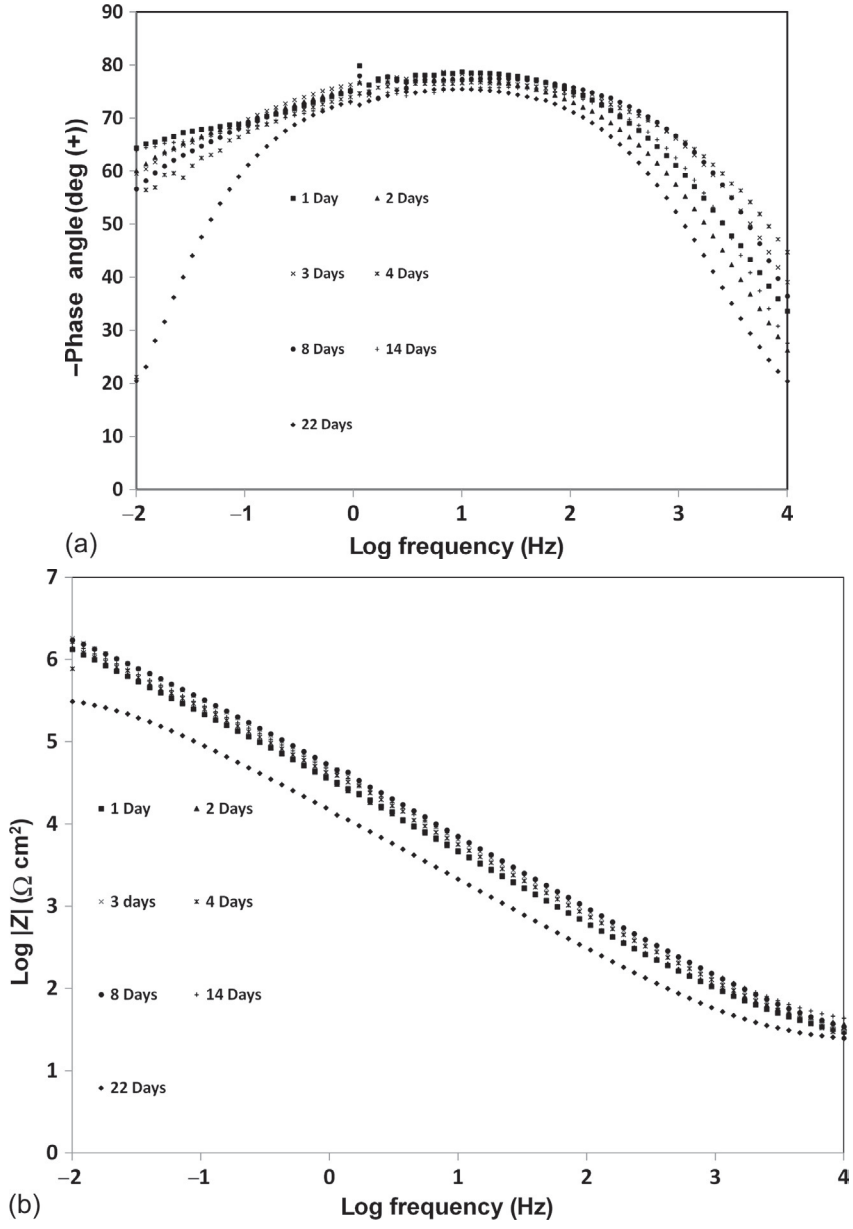


Figure 5.7 EIS phase angle plots (a) and bode modulus (b) for silane hybrid-coated (S_1) 304L SS during immersion in a 3.5% NaCl solution. *With kind permission from Elsevier.*[32]

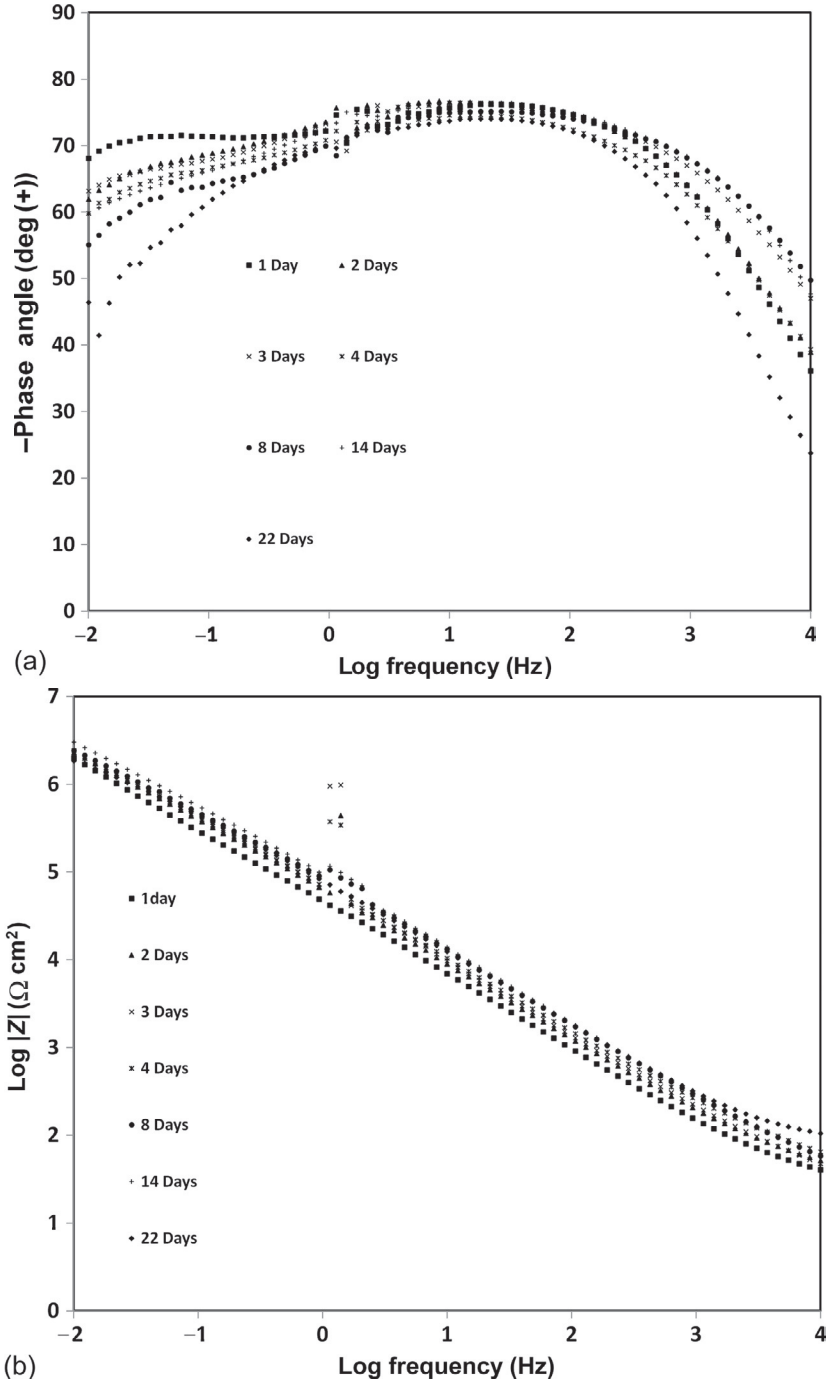


Figure 5.8 EIS phase angle plots (a) and bode modulus (b) for cerium nitrate-doped silane hybrid-coated (S_2) 304L SS during immersion in a 3.5% NaCl solution. *With kind permission from Elsevier.*[32]

The corrosion features of the samples were further explored through analysis of the EIS spectra analysis using equivalent electric circuits. To simulate the impedance plots, the constant phase element (CPE) was used instead of an "ideal" capacitor to explain the deviations from the −1 slope in the Bode modulus plot. CPE can be described by Equation (5.1):

$$Z_{\mathrm{CPE}} = \frac{1}{Y_0 (j\omega)^n} \tag{5.1}$$

with $-1 < n < 1$[8].

In this equation, n is a coefficient associated with system homogeneity (being 1 for an ideal capacitor), ω is the frequency, and Y_0 is the pseudocapacitance of the system (expressed in $\Omega\,\mathrm{cm}^{-2}\,\mathrm{s}^n$) that can be represented by:

$$Y_0 = \frac{e\varepsilon\varepsilon_0 A}{d} \tag{5.2}$$

In the Equation (5.2), ε_0 is the permittivity of free space (expressed in F/m), ε the dielectric constant of the surface film, d the thickness of the coating (in μm), A the exposed area (in cm^2), and r the roughness factor.[8]

The impedance response of sample S_1 after immersion for 22 days suggests nonideal dielectric capacitive behavior, which includes the electrolyte resistance (R_s), polarization resistance (R_{po}) of the corroded areas, and the nonideal capacitance of the coating (CPE_c) (Figure 5.9a). The equivalent circuit shown in Figure 5.9b models sample S_2 after similar immersion. It consists of similar elements: R_s, CPE_c, and R_{po}, related to porosity or defects to the passage of the electrolyte. The extra parameters included in the circuits (CPE_{dll} and R_{ct}) represent the presence of a double layer between the metal surface and the electrolyte, which led corrosion products to the pores. CPE_{dll} is related to the nonideal capacitance of the double layer, and R_{ct} is related to the charge transfer resistance of the metal. Table 5.3 lists the fitting parameters for the models presented in Figure 5.9a and b. The lower polarization resistance shown

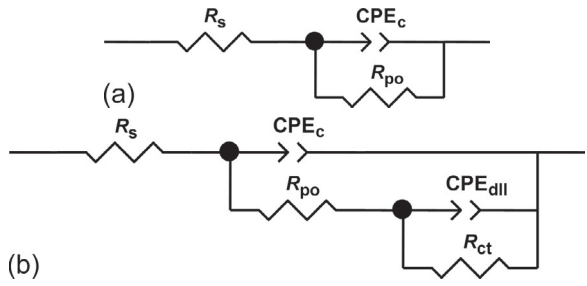


Figure 5.9 Equivalent circuits used for numerical fitting of EIS data for (a) silane hybrid-coated (S_1) and (b) cerium nitrate-doped silane hybrid-coated (S_2) 304L SS substrates after immersion for 22 days in a 3.5% NaCl solution. *With kind permission from Elsevier.*[32]

TABLE 5.3 Parameters Obtained from Fitting Data for 304L SS with Silica Hybrid (S_1) and Ce-Doped Silica Hybrid (S_2) Coatings After Immersion for 22 Days in a 3.5% NaCl Solution

Sample	R_s ($\Omega\,cm^2$)	CPE_c ($\Omega^{-1}\,cm^{-2}s^n$)	n_c	R_{po} ($\Omega\,cm^2$)	CPE_{dll} ($\Omega^{-1}\,cm^{-2}s^n$)	n_{dll}	R_{ct} ($\Omega\,cm^2$)
S_1: SHC	22.59	1.42×10^{-5}	0.839	3.67×10^{5}	—	—	—
S_2: Ce-SHC	22.59	2.61×10^{-6}	0.828	7.44×10^{5}	1.23×10^{-6}	0.506	6.49×10^{6}

With kind permission from Elsevier.[32]

by the system containing sample S_1 is associated with water uptake through the pores and/or defects in the coating. It is likely linked to an increase of exposed area.

The electrochemical parameters derived from the polarization curves, together with the EIS results, reveal the persistent protection offered by the cerium-doped SHCs. Increased immersion would likely lead to the release of cerium from the defects in the coatings. The cerium would then produce insoluble hydroxides when it reacts with hydroxyl groups from cathodic reactions.[8,29] These hydroxides, together with the corrosion products, decrease the cathodic current and, therefore, reduce the overall corrosion rate.[29]

5.3.2 Electrochemical Assessment of the Self-Healing Properties of SHCs Modified with Cerium Nitrate and Cerium Oxide Nanoparticles on 304L Stainless Steel

Cerium-modified SHCs can supply self-healing abilities, which can automatically repair the corroded areas, thereby providing more durable corrosion protection. Self-healing is defined as the partial recovery of the protective properties of the coated system when damaged.[5,30] It is evaluated by applying an artificial defect to a coated surface and monitoring the electrochemical behavior via EIS.[5,30] The self-healing abilities of cerium-modified SHCs on 304L SS substrates were electrochemically investigated before and after defect application. The coated samples were immersed in the electrolyte for one week before a defect was created on their surfaces. Cerium nitrate and cerium oxide nanoparticles were used as cerium sources, and the surface morphology and electrochemical behaviors of the sol-gel coatings doped with cerium nitrate were compared with those of sol-gel coatings containing cerium oxide nanoparticles.

304L SS specimens pretreated with sol-gel coatings modified with $Ce(NO_3)_3{\cdot}6H_2O$ (S_4) and CeO_2 nanoparticles (S_5) were observed by AFM (Figure 5.10). Sample S_4 showed a comparatively smooth nanostructure surface with a root mean square (RMS) surface roughness of 0.227 nm. The low color contrast in the top view image (Figure 5.10a) suggests limited heterogeneity of the coating thickness. No agglomerates were observed on the surface.

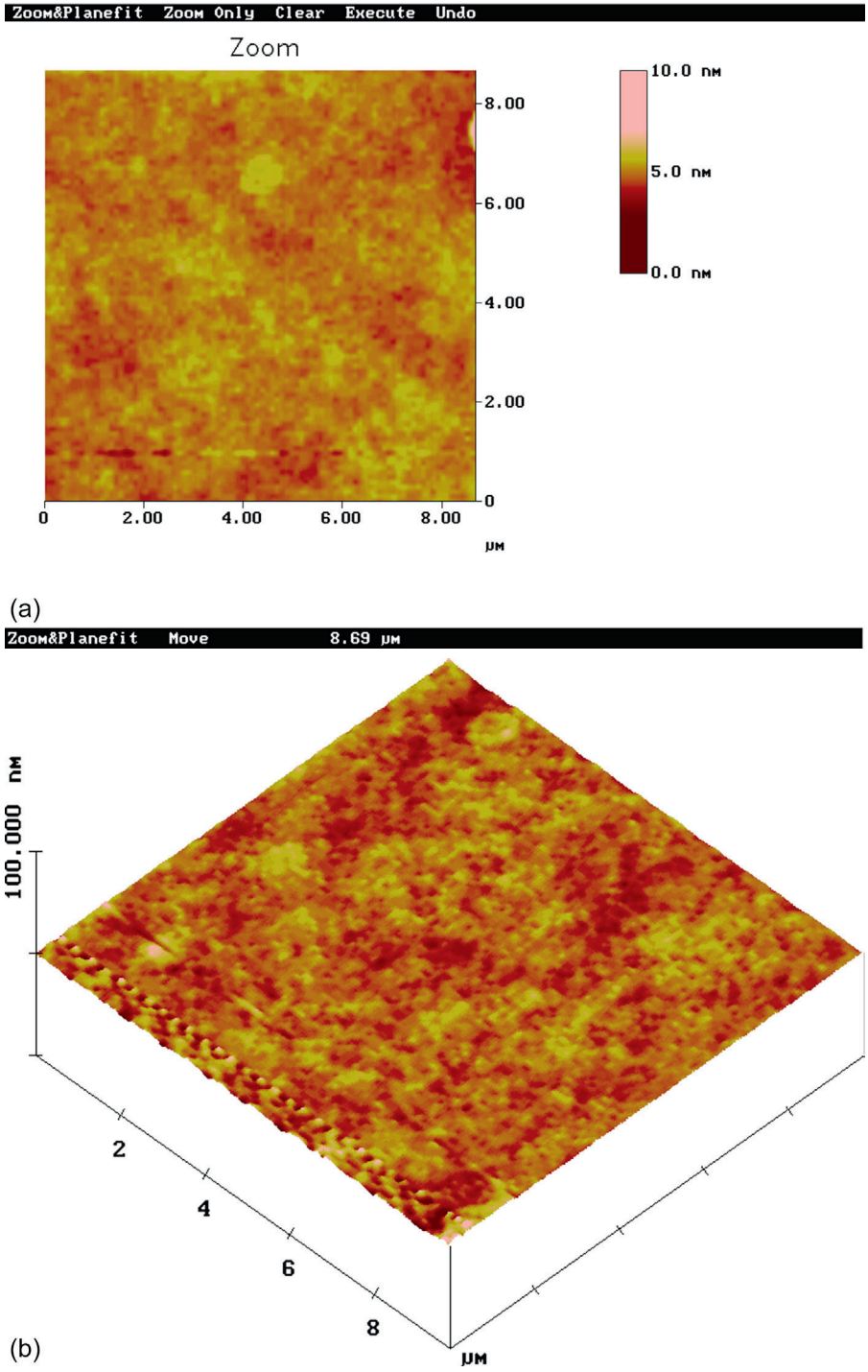
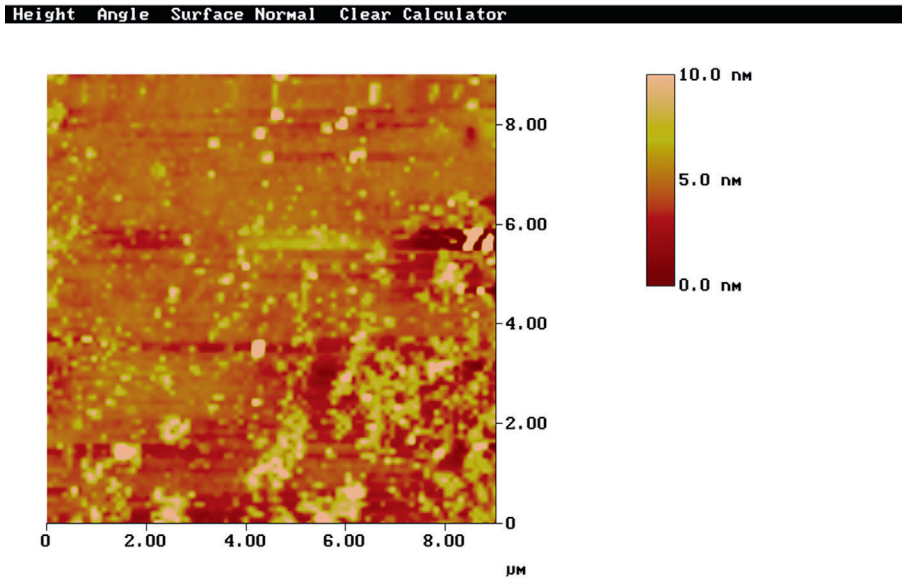
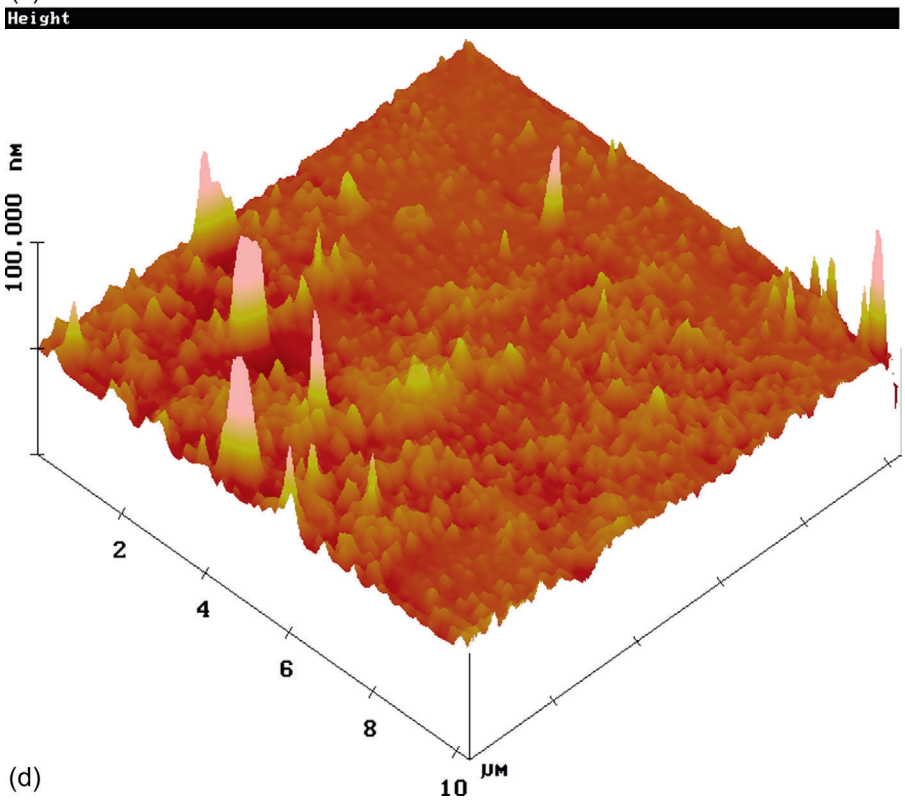


Figure 5.10 AFM (a, c), top-view (b, d), and topographic images of 304L SS pretreated with silane hybrid coatings modified with (a, b) cerium nitrate (S_4) and (c, d) CeO_2 nanoparticles (S_5).

(Continued)



(c)



(d)

Figure 5.10, cont'd

Sample S_5 clearly showed nanosized particles incorporated into the film matrix with a relatively uniform distribution. The RMS roughness was 2.145 nm. The several larger particles observed in the hybrid matrix appear to be agglomerations of smaller particles. The sharper color contrast in the top view image (Figure 5.10c) suggests stronger height differences. The color contrast is uniformly distributed throughout the image, again suggesting some variation of the coating thickness.

Photographs of the 304L SS pretreated with $Ce(NO_3)_3{\cdot}6H_2O$ (S_4) and CeO_2 nanoparticle modified coatings after 2000 h of salt spray exposure (Figure 5.11) show that the coatings gave different levels of protection. Coating S_4 (average thickness $60.6 \pm 11.96\,\mu m$) (Figure 5.11a) did not blister or delaminate and retained its originally shiny surface, while coating S_5 (average thickness $60.66 \pm 13.51\,\mu m$) (Figure 5.11b) exhibited slight blistering around the scratched area (circles in the figure). Overall, good long-term corrosion protection appears to have been achieved by the silane sol-gel coating modified with $Ce(NO_3)_3{\cdot}6H_2O$ (S_4).

Impedance spectra for the coating S_4, both with and without an applied defect, were recorded at intervals during immersion (Figure 5.12a). The impedance at low frequencies (LF) shown by the pristine sample was close to $1.95 \times 10^6\,\Omega\,cm^2$ during the first hours of immersion. After immersion for 3 days, it dropped slightly ($1.6 \times 10^6\,\Omega\,cm^2$). This was associated with water uptake through pores and/or defects in the coating.[8] Longer immersion (3-7 days) led impedance at LF to increase rapidly and remain high.

After immersion for 7 days, a defect was induced on the coating to create a corroding area. The impedance at LF markedly decreased 1 h after application of the defect (close to $1.19 \times 10^5\,\Omega\,cm^2$). This was an expected consequence of the damage. Further immersion for 1 day led the impedance at LF to increase further to $1.6 \times 10^6\,\Omega\,cm^2$. Yet longer immersion led the LF impedance to decrease slightly. This change is attributable to the self-healing effects of $Ce(NO_3)_3{\cdot}6H_2O$ on the areas of corrosion.[31] The self-healing originated from the release of cerium near the defect. The cerium then produced insoluble hydroxides by its reaction with hydroxyl groups from cathodic reactions.[32] These hydroxides, together with the corrosion products, decreased the cathodic current and consequently reduced the overall corrosion rate.

The shape of the phase angle plot (Figure 5.12b) indicates two time constants before and after the application of the defect. The high-frequency process is attributable to the response of the silane film; the low-frequency time constant is due to the response at the interface of the film with the substrate.

The coating modified with CeO_2 nanoparticles (S_5) showed a different trend. The total impedance of the system was lower than that of the S_4-modified sol-gel film. Impedance decreased rapidly with increased immersion, both before and for 5 days after the application of the defect (Figure 5.12c). Impedance increased 7 days after the application of the defect, suggesting that the coating was still providing some protection.

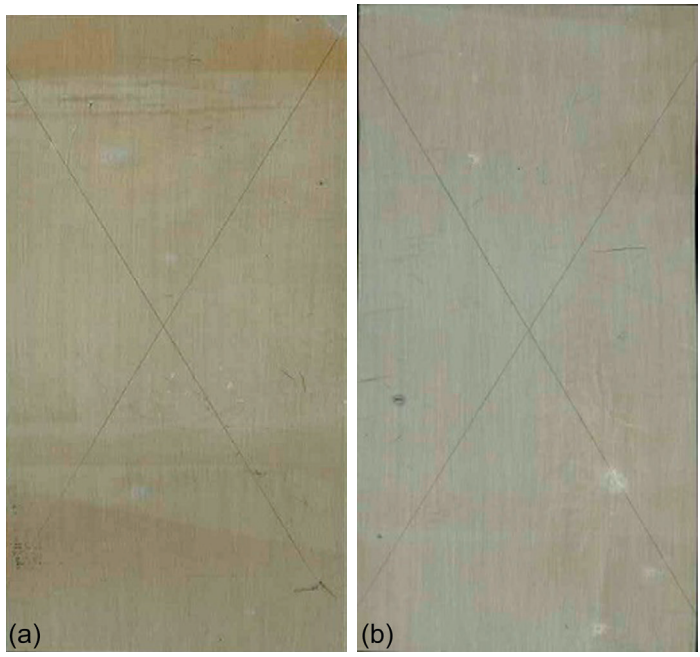


Figure 5.11 Photographs of 304L SS pretreated with silane hybrid coatings modified with (a) cerium nitrate (S_4) and (b) CeO_2 nanoparticles (S_5) after 2000 h of salt spray exposure.

The EIS spectra show two time constants before the application of the defect and during early immersion (Figure 5.12d). Increased immersion led the low-frequency time constant to lose its prominence, while the high-frequency time constant remained well defined. After the application of the defect, the phase angle plot shows one time constant at high frequencies, which is ascribable to corrosion on the substrate, although no coating degradation was observed for the sol-gel coating containing CeO_2 nanoparticles.

The EIS measurements were further analyzed by fitting the experimental plots to equivalent electrical circuits (EECs), while taking into consideration the number of time constants and the quality of the fits.[33] The equivalent circuit for the system with coating S_4 (Figure 5.13a) consists of: the electrolyte resistance, R_s; the nonideal capacitance of the coating, CPE_c; the resistance to the passage of the electrolyte presented by pores or defects, R_{po}; the nonideal capacitance of the double layer between the metal surface and the electrolyte, which soaks the corrosion products near the pores, CPE_{dll}; the charge transfer resistance of the metal, R_{ct}; and the Warburg finite impedance, W. The Warburg impedance and the CPE, with an n value around 0.5 (representing "infinite diffusion"), are used to model the increasing ionic conductivity that occurred owing to corrosion inside the pores.[8]

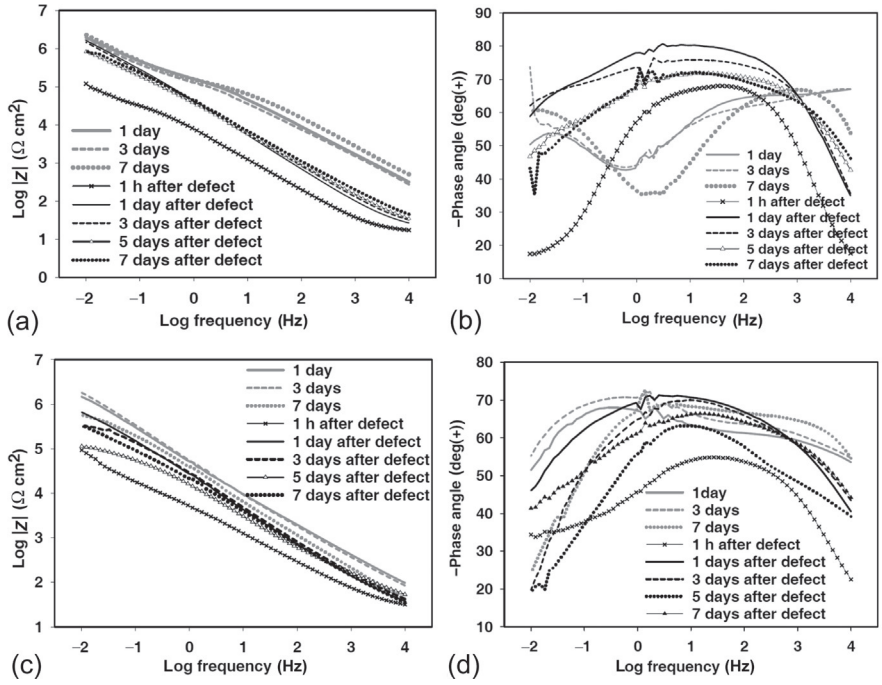


Figure 5.12 EIS Bode modulus (a, c) and phase angle plots (b, d) for 304L stainless steel sample pretreated with silane hybrid films modified with (a, b) cerium nitrate (S_4) and (c, d) CeO_2 nanoparticles (S_5). Spectra were obtained during immersion in a 3.5% NaCl solution before and after the application of a defect.

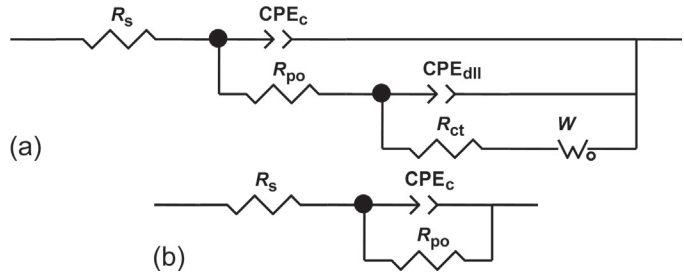


Figure 5.13 Equivalent circuits used for numerical fitting of EIS data during immersion in a 3.5% NaCl solution. (a) Cerium nitrate-modified silane hybrid coating before and after defect application, CeO_2 nanoparticle-modified silane hybrid coating before defect application; (b) CeO_2 nanoparticle-modified silane hybrid coating after defect application.

Impedance results for the S_5 coating were fitted using two different equivalent circuits. Before the application of the defect, two time constants were required to simulate the EIS spectra (Figure 5.13a); only one was required after (Figure 5.13b).

Figures 5.14 and 5.15 depict the evolution of the parameters used in the numerical simulation of the experimental results. The system with the S_4 coating showed a high-frequency resistance that decreased slightly during the first hours of immer-

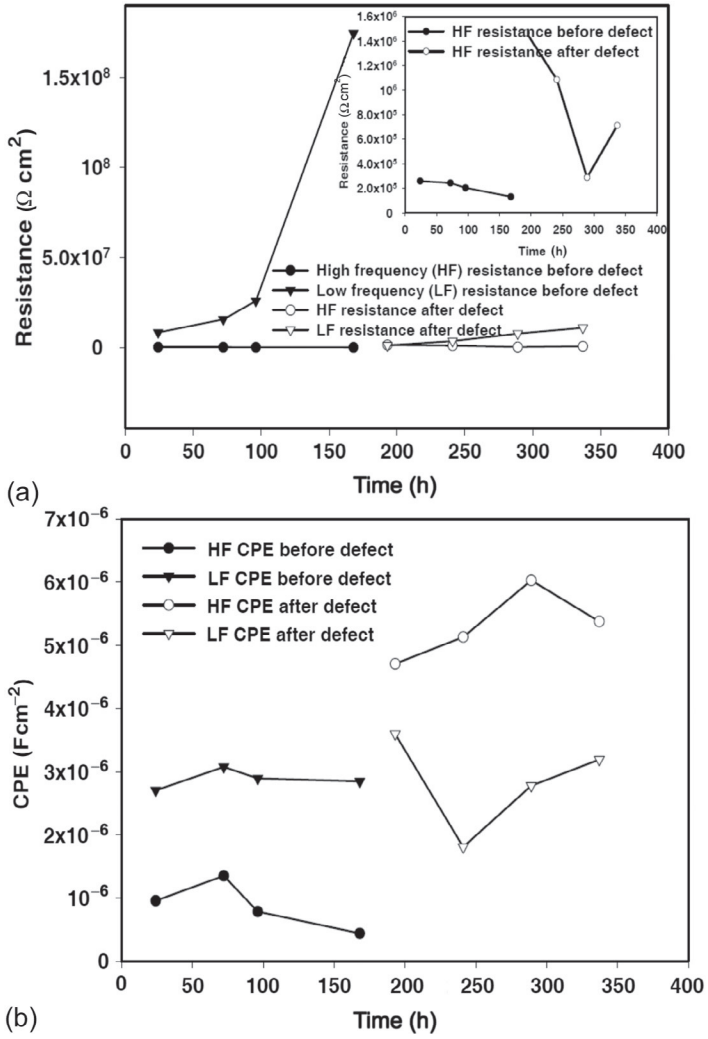


Figure 5.14 Evolution of fitting parameters for the silane hybrid coating modified with cerium nitrate (S_4) during immersion in a 3.5% NaCl solution. Values were obtained by numerical fitting using the equivalent circuit depicted in Figure 5.13a.

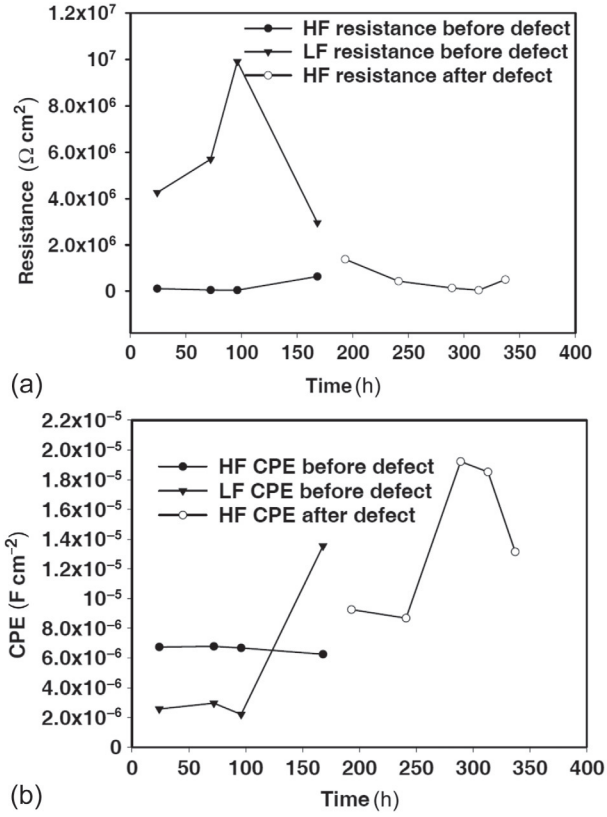


Figure 5.15 Evolution of fitting parameters for the silane hybrid coating modified with CeO_2 nanoparticles (S_5) during immersion in a 3.5% NaCl solution. Values were obtained by numerical fitting using the equivalent circuits depicted in Figure 5.13a and b.

sion before the application of the defect (Figure 5.14), following the development of conductive pathways inside the silane film.[5] The resistance remained nearly constant (around $1.32\times10^5\,\Omega\,cm^2$) during immersion for 7 days. The high-frequency CPE values were around $9.5\times10^{-7}\,F\,cm^{-2}$ and decreased slightly with time. The low-frequency behavior was characterized by a resistance that increased from $8.404\times10^6\,\Omega\,cm^2$ during the first hours of immersion to $174\times10^6\,\Omega\,cm^2$ after immersion for 7 days. Its CPE values were around $2.7\times10^{-6}\,F\,cm^{-2}$ and remained nearly constant during the 7 days of immersion.

The high-frequency resistance increased 1 day after the application of the defect ($1.47\times10^6\,\Omega\,cm^2$); it subsequently decreased slightly until the end of the experiment. The CPE values were around $4.7\times10^{-6}\,F\,cm^{-2}$ and increased with time. Unlike the high-frequency resistance, the low-frequency resistance increased from

$1.2\times10^{6}\,\Omega\,cm^{2}$ 1 day after defect application to $11\times10^{6}\,\Omega\,cm^{2}$ 7 days after defect application. The CPE values decreased from $3.6\times10^{-6}\,F\,cm^{-2}$ to $3.19\times10^{-6}\,F\,cm^{-2}$. The evolution of the fitting parameters shows that the silane coating partially recovered its protective properties. Because the low-frequency behavior can be assigned to corrosion at the interface, it is possible to conclude that the corrosion was retarded.

The system with coating S_5 showed slightly increased resistance after immersion for 7 days before the application of the defect (Figure 5.15). This can be ascribed to cerium oxide or hydroxide blocking the pores or defects.[5,31] The CPE values were around $6.74\times10^{-6}\,F\,cm^{-2}$ and remained nearly constant during the 7 days of immersion. At LF, resistance increased with time, indicating that cerium oxide/hydroxide formed with the release of CeO_2 from the sol-gel matrix.[5,30] After immersion for 7 days, the resistance decreased to $2.95\times10^{6}\,\Omega\,cm^{2}$, indicating pitting corrosion on the substrate. Correspondingly, the CPE values increased rapidly during immersion owing to the breakage of the oxide/hydroxide layer.[5,30]

After the application of the defect, the sample showed slightly decreasing resistance for the duration of the immersion test, indicating degradation of the coating. The CPE values dropped after 3 days of immersion to $8.68\times10^{-6}\,F\,cm^{-2}$, reached a maximum, and then decreased again ($13.15\times10^{-6}\,F\,cm^{-2}$) owing to saturation of electrolyte in the sol-gel film.

The electrochemical tests showed that modification of the silane sol-gel coating with cerium ions (S_4) resulted in a protective coating with barrier properties and/or corrosion inhibiting activity. The improved barrier properties were correlated with increases of reactive silanol groups [$-Si(OH)_3$] and condensed species that could increase the viscosity of the silane solution and the coating thickness.[4]

Further assessment of the mechanisms associated with the electrochemical behavior of these systems was conducted through potentiodynamic polarization measurements. The curves obtained from the scratched samples after 1 h of immersion are depicted in Figure 5.16. Table 5.4 lists the electrochemical parameters obtained from these measurements.

The $Ce(NO_3)_3$-doped sol-gel coating (S_4) showed a lower corrosion current density, I_{corr}, (around $1.36\times10^{-7}\,A\,cm^{-2}$) than the sol-gel coating containing CeO_2 nanoparticles (S_5), and its potential was shifted higher (–0.408 V). This coated sample shows a passivation range of approximately –0.340 to +0.013 V over its corrosion potential. This behavior was improved by the barrier properties of the coating.[32]

Coating S_5 presented a continuous potential range characterized by a control mechanism of equilibrium in the oxidation and reduction reactions. It also showed a wide passive plateau of –0.403 to +0.092 V above the corrosion potential.

The d.c. polarization results show that the presence of the cerium compounds favorably shifted the corrosion potential, decreased the anodic currents, and altered the kinetics of the anodic processes.[32] These effects were much more marked for coating S_4 than for coating S_5.

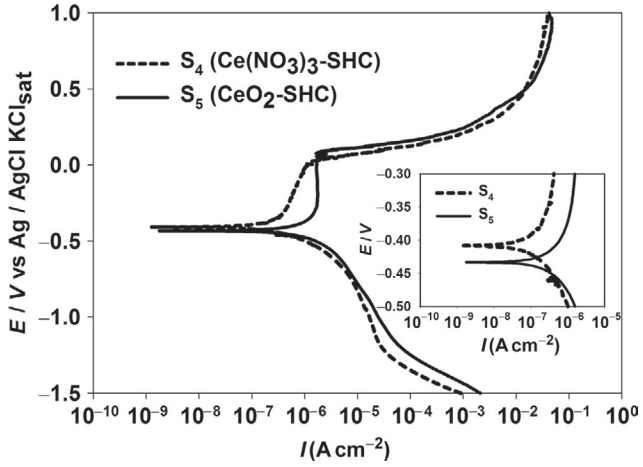


Figure 5.16 Potentiodynamic polarization curves of silane hybrid coatings modified with cerium nitrate (S_4) and CeO_2 nanoparticles (S_5) obtained after immersion for 1 h in a 3.5% NaCl solution. The inset plot has potential depicted as the difference between the imposed and corrosion potentials, which enables better separation of the anodic and cathodic polarization effects.

TABLE 5.4 Summary of Electrochemical Parameters Obtained from the Polarization Measured in a 3.5% NaCl Solution

Sample	E_{corr} (V)	I_{corr} (A cm^{-2})	b_c (V/dec)	b_a (V/dec)	Passive Area (V)
S_4: $Ce(NO_3)_3$-SHC	–0.408	1.36×10^{-7}	0.187	0.950	–0.340 to 0.013
S_5: CeO_2-SHC	–0.434	4.99×10^{-7}	0.230	0.116	–0.403 to 0.092

5.3.3 Influence of Cerium Concentration on the Microstructural Features and Corrosion Protection of the Cerium-Doped SHCs on HDG Substrates

The protective behavior of the cerium-doped SHCs depends also on the dopant concentration.[7] Dopant concentration must be optimized because too high or too low concentrations negatively affect the barrier properties of the coating.[1,7] Therefore, HDG substrates were tested with SHCs containing various molar ratios of cerium nitrate dopant [0.000 (S_1), 0.001 (S_6), 0.005 (S_7), 0.010 (S_8), 0.050 (S_9), and 0.100 (S_4)]. The lower corrosion resistance of the HDG in comparison to the 304L SS allows better assessment of the effects of the cerium concentration upon the anticorrosion performance of the silane coatings.

Microstructural observation of the nondoped (S_1) and the 0.05 M cerium nitrate-modified (S_9) SHCs before immersion in a 3.5% NaCl solution revealed smooth surfaces without any cracks or defects (Figure 5.17). However, the S_1 coating showed several agglomerations (Figure 5.17a), which may be ascribed to the relatively high viscosity of the sol.[11] The heterogeneities in the coating might lead to regions more prone to corrosion.

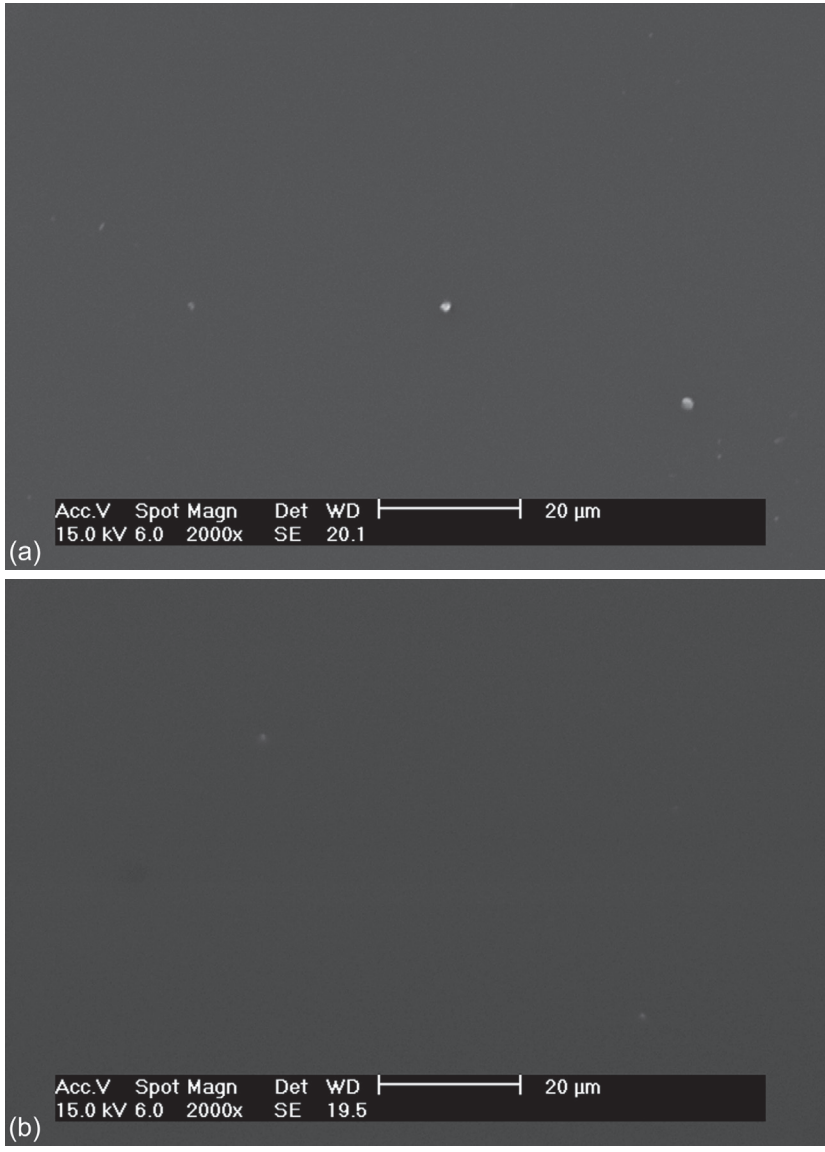


Figure 5.17 SEM micrographs of silane hybrid coatings doped with (a) 0.000 M (S_1) and (b) 0.05 M (S_9) cerium nitrate on HDG prior to immersion in a 3.5% NaCl solution.

After immersion for 72 h in a 3.5% NaCl solution, localized corrosion was observed for all coatings (except S_9). Exfoliation of the corrosion products and cracks of different sizes were observed. These localized attacks could promote the deterioration and delamination of the films and were possibly due to hydrolysis reactions at the interface. Corrosion was enhanced by the diffusion of the oxidant ions, which caused corrosion products to accumulate at the interface and promoted the formation of defects and microcracks.

The S_9 coating remained homogenous and crack-free after immersion for 120 h (not shown). Further immersion for a total 144 h led to the appearance of cracks. Comparison of the specimens after immersion for 144 h (Figure 5.18) suggests that the lowest and highest tested concentrations of cerium reduced corrosion inhibition in the sol-gel matrix and weakened the coatings.

Coating S_1 (average thickness: $2.7 \pm 0.2\,\mu m$), which lacked cerium nitrate dopant, showed limited resistance in the neutral salt spray test. Corrosion was visible to the naked eye after exposure for 120 h. Coatings S_7 and S_8 (average thickness: 5.5 ± 0.2 and $7.6 \pm 0.2\,\mu m$, respectively) showed corrosion after 168 h, while coatings S_6 and S_4 (average thickness: 6.4 ± 0.2 and $11.5 \pm 0.2\,\mu m$, respectively) showed corrosion after 240 h. The best performance in the salt spray test, with respect to general and localized corrosion, was shown by coating S_9 (average coating thickness: $8.4 \pm 0.2\,\mu m$), which contained 0.050 M cerium nitrate. Corrosion was detected after 336 h of exposure.

The coating that lacked cerium nitrate showed delamination, which increased rapidly during exposure to the salt spray. The coatings that incorporated cerium nitrate also showed increasing delamination during exposure, but with markedly reduced rates; for example, the coatings with 0.001 M (S_6) and 0.050 M (S_9) cerium nitrate showed comparatively little delamination after exposure to the neutral salt spray for 336 h. Images of the specimens after salt spray testing for 336 h are shown in Figure 5.19.

The different corrosion behaviors of the five samples containing cerium nitrate can be modeled using hybrid networks with limited capacities for inhibitor uptake. A low concentration of inhibiting cerium nitrate leads to improved barrier properties and, therefore, to improved uniform corrosion protection. Increased cerium nitrate content leads to increased porosity, which reduces the barrier properties of the coating and so lowers the protection against corrosion.[11,25,34,35]

Corrosion near the scratch behaved differently from the uniform corrosion elsewhere. Increasing the cerium concentration significantly reduced delamination. For instance, the coatings with 0.050 M (S_9) and 0.1 M (S_4) cerium nitrate showed less delamination near the scratch than those with lower cerium nitrate contents. The limited delamination in the presence of higher concentrations of cerium nitrate suggests the presence of a corrosion-inhibiting species.

Impedance spectra of the six HDG samples were recorded after 24 h of immersion in a 3.5% NaCl solution (Figure 5.20a). The impedance at LF initially increased with increasing cerium nitrate concentration from 0.000 to 0.050 M. However, above this critical concentration, impedance at LF reduced slightly.

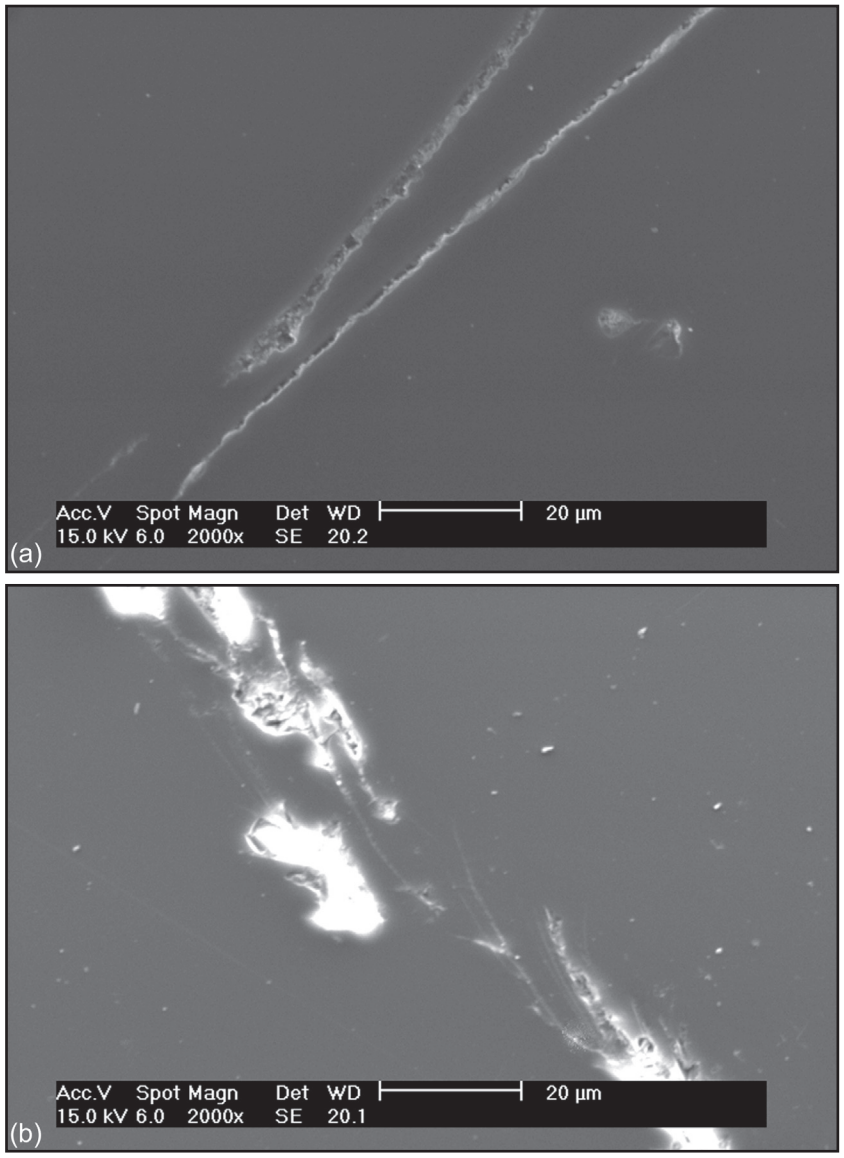


Figure 5.18 SEM micrographs of silane hybrid coatings doped with (a) 0.000 M (S_1), (b) 0.001 M (S_6),

The shape of the phase angle plot in Figure 5.20b indicates the presence of two time constants. The high-frequency time constant is attributable to the response of the silane film, and low-frequency time constant to the response of processes at the film-substrate interface.

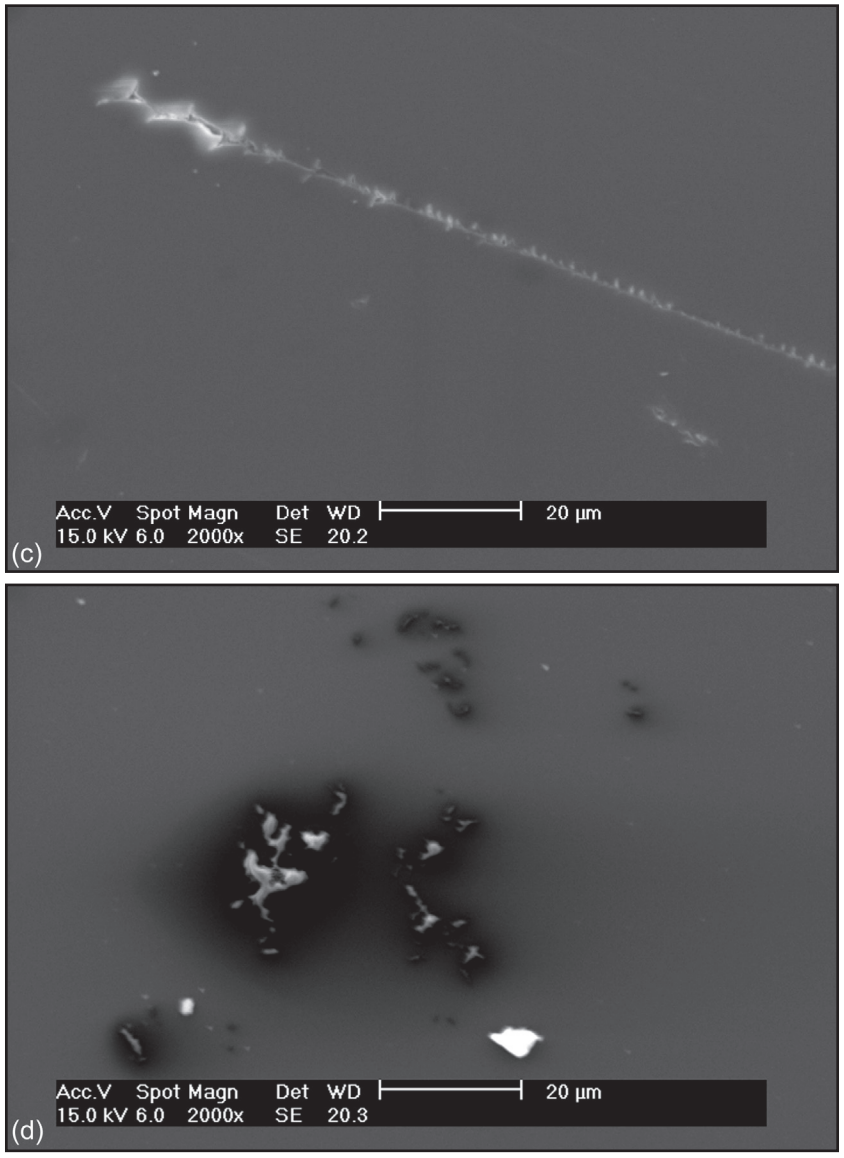


Figure 5.18, cont'd (c) 0.005 M (S_7), (d) 0.01 M (S_8),

(Continued)

EIS Bode modulus (Figure 5.21a) and phase angle (Figure 5.21b) plots of the various coatings after immersion for 144 h in a 3.5% NaCl solution consistently show clear decreases of impedance at LF. This can be attributed to the hydrolytic degradation of the coatings. The impedance at LF of coatings doped with cerium nitrate

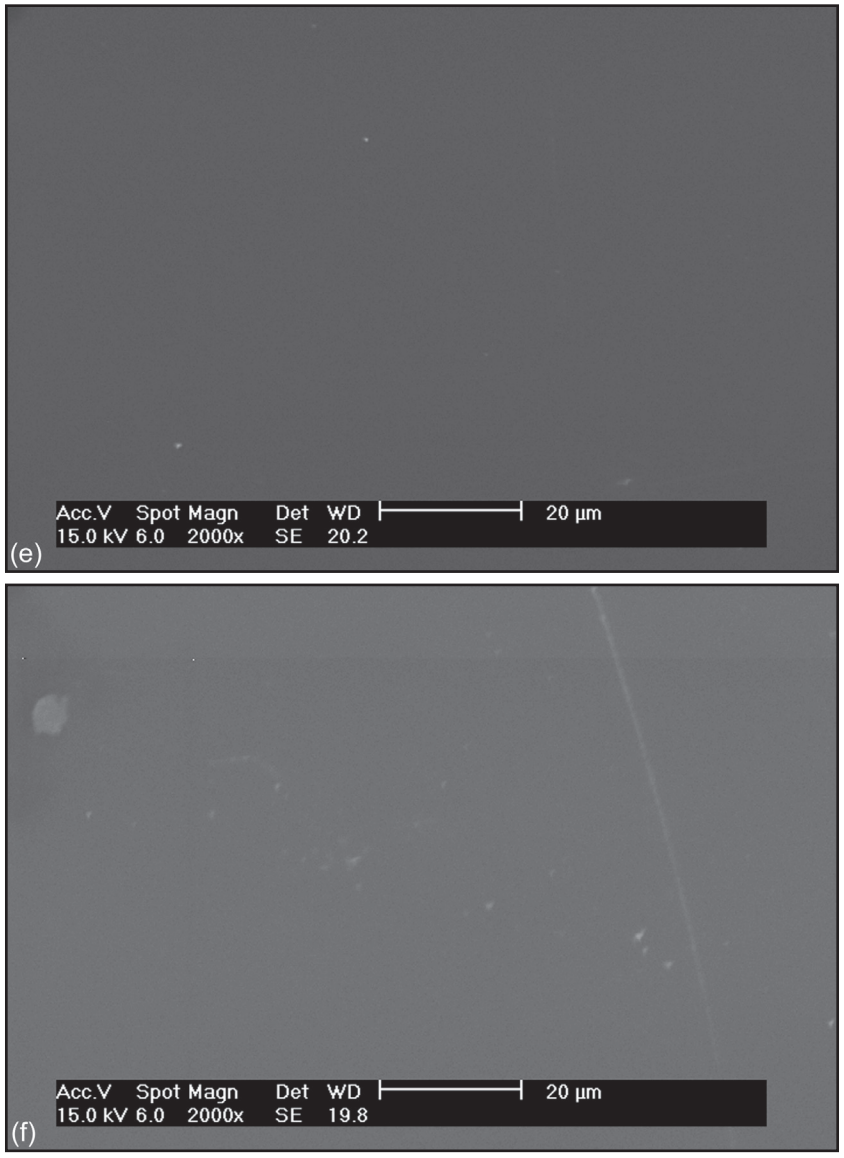


Figure 5.18, cont'd (e) 0.05 M (S_9), and (f) 0.1 M (S_4) cerium nitrate on HDG after immersion for 144 h in a 3.5% NaCl solution.

(except coating S_9) dropped to <300 Ωcm^2. However, the exception, doped with 0.05 M cerium nitrate, retained a higher impedance at LF of 337 Ωcm^2. The dependence of corrosion resistance on the cerium concentration indicates the significance of controlling the cerium concentration for optimal protection.[1,7]

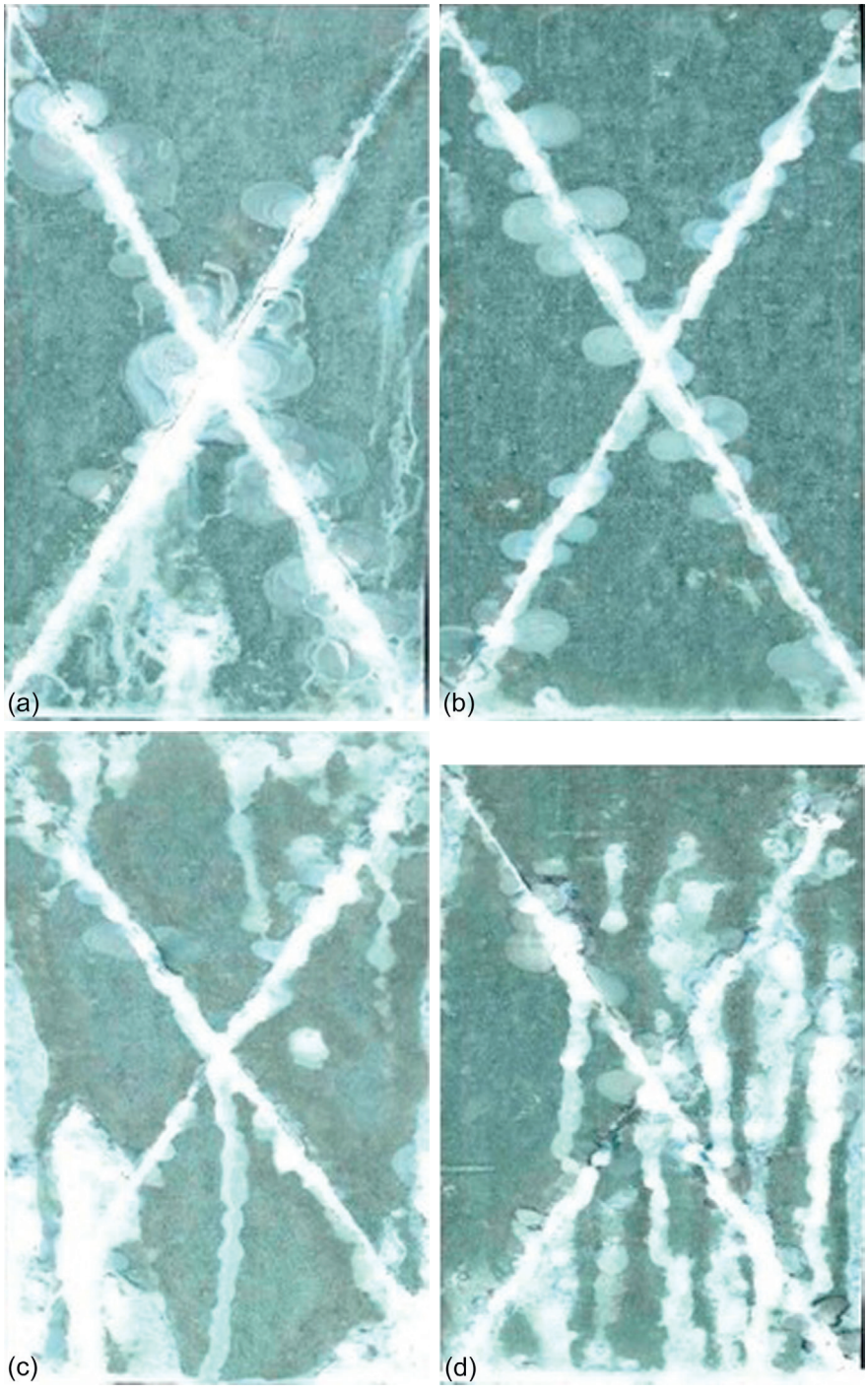


Figure 5.19 Photographs of silane hybrid coatings doped with (a) 0.000 M (S_1), (b) 0.001 M (S_6), (c) 0.005 M (S_7), (d) 0.01 M (S_8),

(Continued)

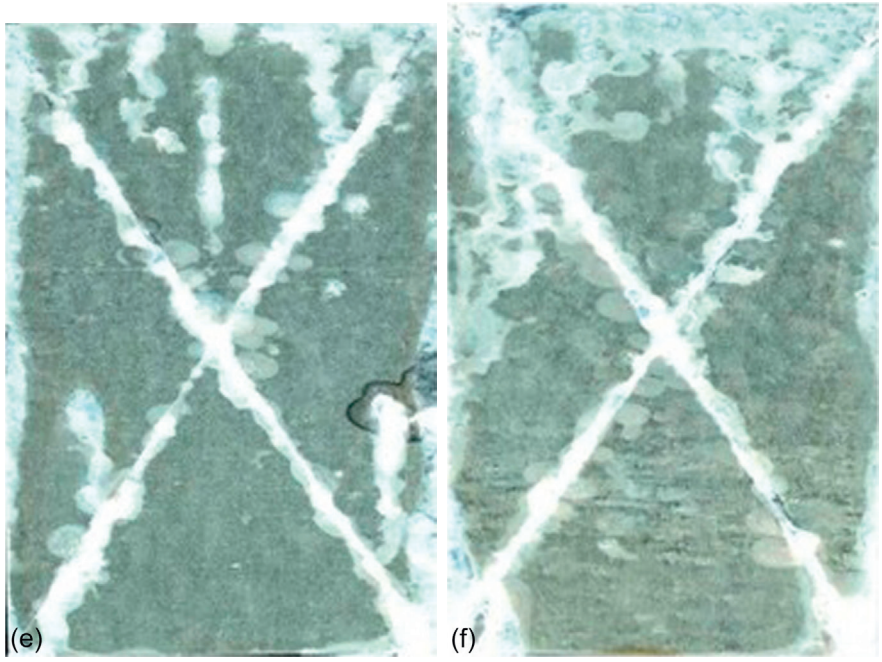


Figure 5.19, cont'd (e) 0.05 M (S_9), and (f) 0.1 M (S_4) cerium nitrate on HDG after salt spray exposure for 336 h.

The EIS results can be interpreted by numerical fitting using the equivalent circuit depicted in Figure 5.22. In this equivalent circuit, R_s is the resistance of the electrolyte; CPE_c and R_c represent the capacitance and resistance of the hybrid coating, respectively; CPE_{dll} is the capacitance of the electrochemical double layer at the metal-electrolyte interface; and R_{ct} is the charge transfer resistance of the metal.

The evolution of the properties of the coatings during immersion was assessed by plotting their capacitance and resistance (Figure 5.23). The coatings doped with 0.005 and 0.050 M cerium nitrate had the lowest capacitance during the 144 h of immersion, demonstrating that they were of the greatest thickness (Figure 5.23a). During immersion, capacitance remained largely consistent, with only a small increase, associated with electrolyte uptake, visible after 24 h. Increased cerium nitrate doping significantly influenced the capacitance of the coatings, which was raised by about an order of magnitude in the coating with 0.100 M cerium nitrate. This increase was due to a decrease of the coating thickness and/or a higher porosity, either of which would increase conductivity.[7] During immersion of the coating containing 0.100 M cerium nitrate, film capacitance significantly increased because of water uptake. This was due to the reduced barrier properties of the highly loaded film, which

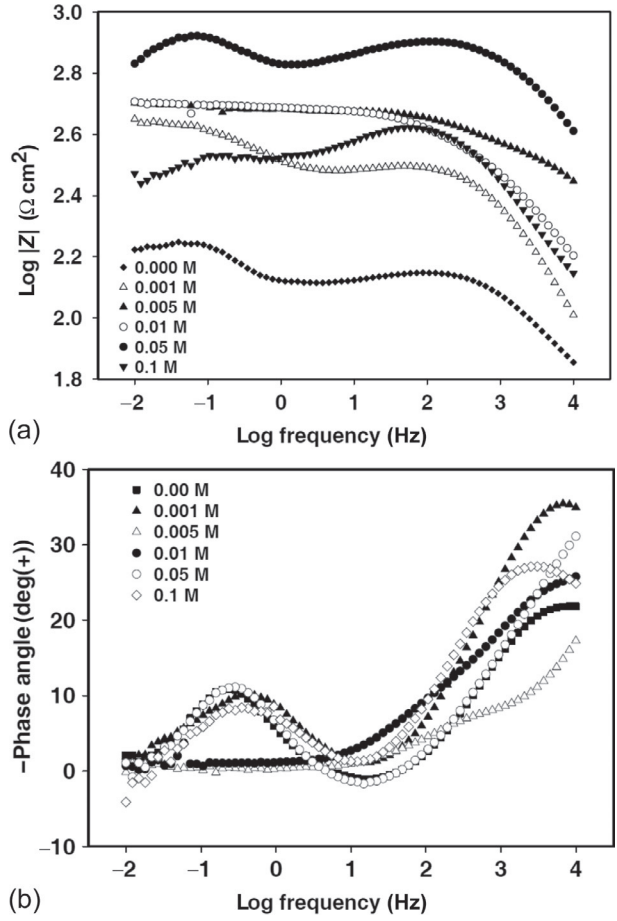


Figure 5.20 EIS Bode modulus (a) and phase angle plots (b) for HDG pretreated with silane hybrid coatings doped with different concentrations of cerium nitrate obtained after immersion for 24 h in a 3.5% NaCl solution.

is in accordance with previous results of cerium-doped silane coatings on aluminum alloys (reported by Schem)[11] and on galvanized steel (reported by Trabelsi).[7]

The evolution of the coating resistance (Figure 5.23b) is an important characteristic of the barrier properties of a protective layer.[7,11] Upon initial immersion, the highest resistance was shown by the coating containing 0.050 M cerium nitrate. A small increase of coating resistance occurred during the first 24 h of immersion, probably due to swelling of the matrix and consequent closing of nano/micropores.[11] Resistance subsequently decreased slowly during the remainder of the 144 h immersion test, reflecting the stability and good barrier properties of the coating. In contrast, the coatings containing the lowest concentrations of cerium nitrate (0.000-0.005 M) rapidly

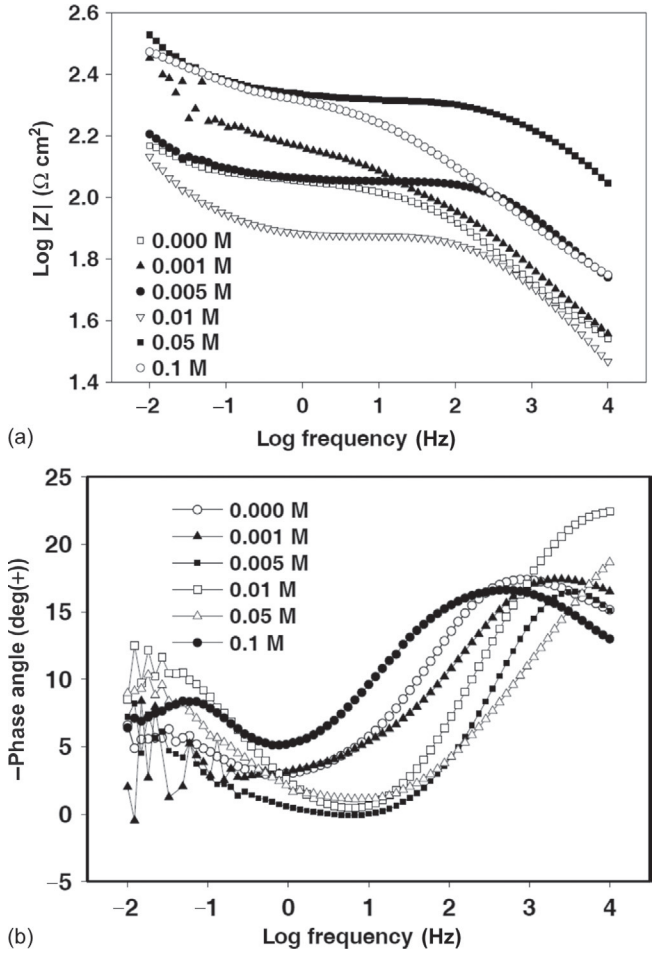


Figure 5.21 EIS Bode modulus (a) and phase angle plots (b) for HDG pretreated with silane hybrid coatings doped with different concentrations of cerium nitrate obtained after immersion for 144 h in a 3.5% NaCl solution.

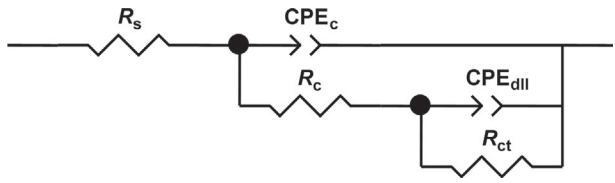


Figure 5.22 Equivalent circuit used for numerical fitting of EIS data for silane hybrid coatings doped with different concentrations of cerium nitrate during immersion in a 3.5% NaCl solution.

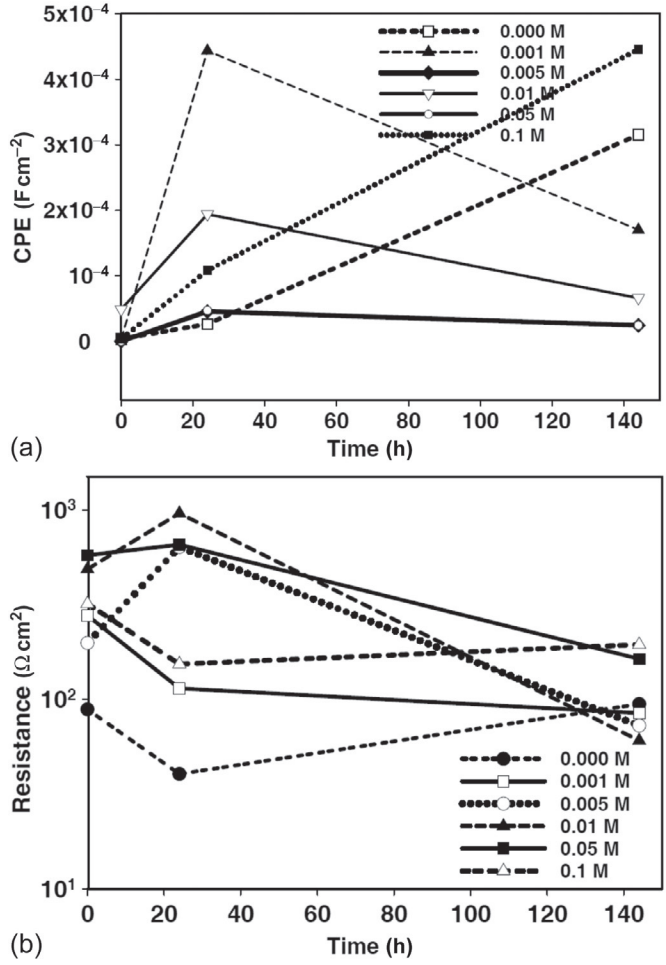


Figure 5.23 Evolution of coating (a) capacitance and (b) resistance during immersion in a 3.5% NaCl solution obtained by numerical fitting using the equivalent circuit depicted in Figure 5.22.

lost their barrier properties; resistance decreased throughout the immersion test. This fast decrease was related to the formation of new defects and pores in the coatings.[11] The behaviors of resistance and capacitance suggest that there is an optimum level of cerium nitrate doping for the silane solutions.[7]

The concentration of cerium nitrate also affected parameters characteristic of the corrosion process; corrosion is associated with the development of a time constant in the low-frequency range of the EIS spectra. Over the first 24 h of immersion, charge transfer resistance, which is inversely proportional to the corrosion rate,[7] increased as cerium content increased from 0.000 to 0.050 M (Figure 5.24a). Greater doping

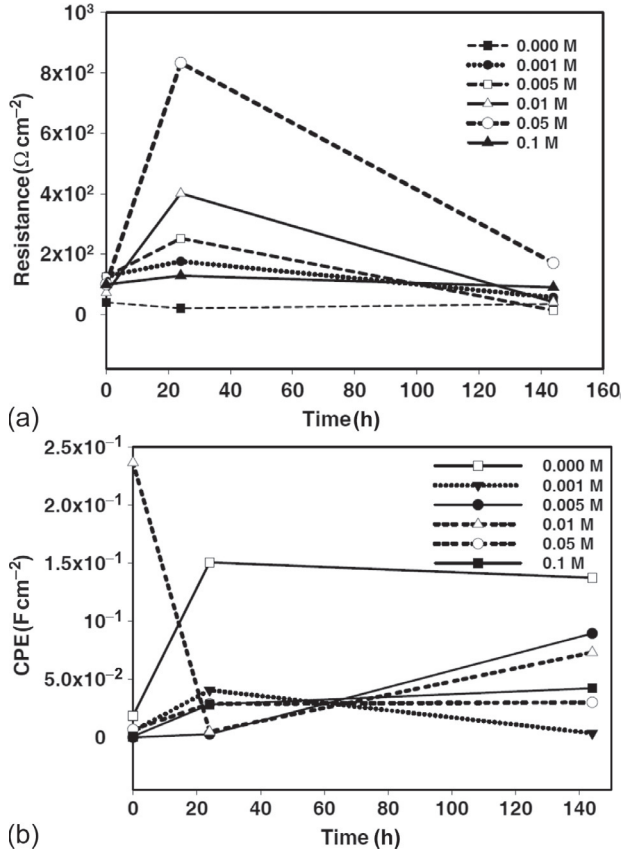


Figure 5.24 Evolution of (a) charge transfer resistance and (b) double layer capacitance during immersion in a 3.5% NaCl solution obtained by numerical fitting using the equivalent circuit depicted in Figure 5.22.

led to a significant reduction of charge transfer resistance. All coatings showed decreasing resistance during immersion for 144 h, although the highest resistances were shown by the coating doped with 0.050 M cerium nitrate. This behavior indicates the good resistance of the doped coating against the onset of corrosion.[7]

The double layer capacitance (Figure 5.24b) of all the coatings increased during the immersion test. The EIS results also show that the coatings doped with 0.000 and 0.001 M cerium nitrate corroded soonest, with the first signs of corrosion detected after 24 h. The others coatings showed corrosion after 96 h (except for that containing 0.05 M cerium nitrate). These results are in good agreement with the observations of coating resistance and indicate that there is an optimal level of cerium doping. The coating with the highest concentration of cerium nitrate showed lower barrier properties, and so allowed corrosion.[7]

Potentiodynamic polarization measurements were carried out to estimate the effects of cerium concentration on the corrosion resistance of the coatings (Figure 5.25). The corrosion current (I_{corr}) and corrosion potential (E_{corr}) were determined by Tafel extrapolation[1,24] and show the effects of the different doping levels (Table 5.5). There are two significant differences between the curves of the nondoped coating and that containing 0.050 M cerium nitrate: E_{corr} shifted to a greatly less negative value and cathodic current density (A/cm^2) markedly reduced. The difference in E_{corr} directly reflects the degree of coverage of the coating over the entire substrate.[36] Good coverage provides a continuous nanoporous coating layer, which causes E_{corr} to shift to a more positive value. The reduction of cathodic current density is attributable to the inhibition of the cathodic reaction at the corrosion site, particularly the oxygen reduction reaction.[36,37] Similar behavior has been reported by Zhong et al.[1] for the magnesium alloy AZ91D in 3.5% NaCl solution after the addition of cerium nitrate. Their results suggest that Ce^{3+} ions react in a first stage with OH^- ions, which are generated in the cathodic zones of the alloy, leading to the formation of localized areas rich in cerium. These are then involved in blocking the cathodic sites, which is reflected in the reduced corrosion rate. Hence, such a reaction, which leads to the corrosion of steel, appears to be retarded by a silica coating containing an inhibitor of 0.05 M cerium nitrate.

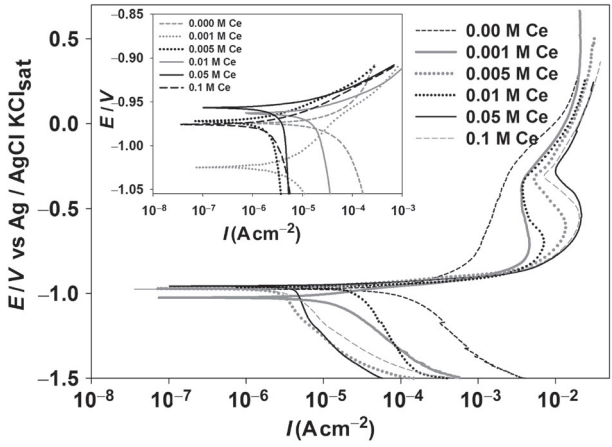


Figure 5.25 Potentiodynamic polarization curves of silane hybrid coatings doped with different concentrations of cerium nitrate obtained after immersion for 1 h in a 3.5% NaCl solution. The inset plot has potential depicted as the difference between the imposed and corrosion potentials, which allows better separation of the anodic and cathodic polarization effects.

TABLE 5.5 Summary of Electrochemical Parameters Obtained from the Polarization Measured in a 3.5% NaCl Solution

Sample	E_{corr} (V)	I_{corr} (A cm^{-2})	b_c (V/dec)	b_a (V/dec)	Passive Area (V)
S_1: 0.000 M	–0.974	3.57×10^{-5}	0.060	0.093	–0.792 to –0.241
S_6: 0.001 M	–1.025	3.48×10^{-6}	0.043	0.057	–0.815 to –0.348
S_7: 0.005 M	–0.972	1.18×10^{-6}	0.017	0.066	–0.829 to –0.320
S_8: 0.01 M	–0.963	6.01×10^{-6}	0.014	0.027	–0.838 to –0.341
S_9: 0.05 M	–0.957	1.74×10^{-6}	0.047	0.009	–0.864 to –0.289
S_4: 0.1 M	–0.976	1.02×10^{-6}	0.016	0.027	–0.840 to –0.304

5.3.4 Evaluation of Corrosion Inhibition by Silane Coatings Filled with Cerium Salt-Activated Nanoparticles on HDG Substrates

The protective behavior of silane films loaded with activated CeO_2 nanoparticles was next assessed. The nanoparticles were activated with cerium ions to improve the corrosion resistance and to reduce agglomeration of the nanoparticles due to stabilization of their surface charge.[5]

AFM images of HDG substrates with both nonmodified (S_1) and cerium-modified silane coatings were recorded (Figure 5.26). The top-view image of coating S_1 (Figure 5.26a) shows a comparatively smooth nanostructured surface with an RMS surface roughness of 0.608 nm. There is little color contrast in the image, suggesting low heterogeneity in the coating thickness and a good distribution of silica particles. However, the topographic image of this film (Figure 5.26b), which shows substrate features, reveals some large particles that likely resulted from the agglomeration of smaller particles on the surface.[25,38] The effects of the cerium dopant and nanoparticles on surface morphology were assessed relative to these images. The silane coating modified with $Ce(NO_3)_3$, (S_9) showed a smooth nanostructured surface with an RMS surface roughness of 0.402 nm (Figure 5.26c and d). The low color contrast in the top-view image suggests limited heterogeneity in the coating thickness; no agglomerates were observed on the surface.

The top-view image of the coating modified with nonactivated CeO_2 nanoparticles (S_{10}) (Figure 5.26e) shows a number of CeO_2 nanoparticles uniformly distributed in the silane coating, which had an RMS roughness of 8.421 nm. Some agglomerates were visible in the topographic image (Figure 5.26f). The sharper color contrast of the topographic image suggests larger height differences. The color contrast was uniformly distributed throughout the image, indicating heterogeneity of the coating thickness. Similar observations were reported by Phanasgaonkar et al.[25]

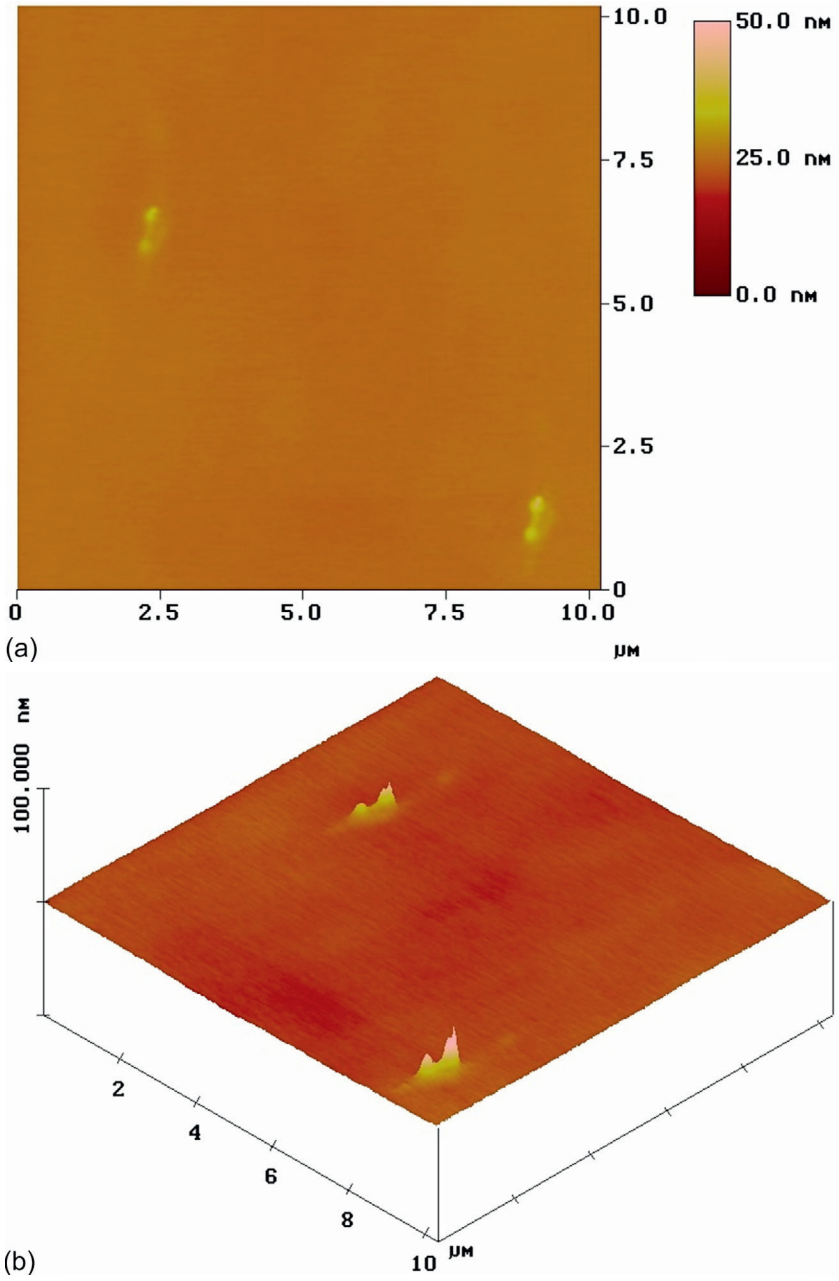
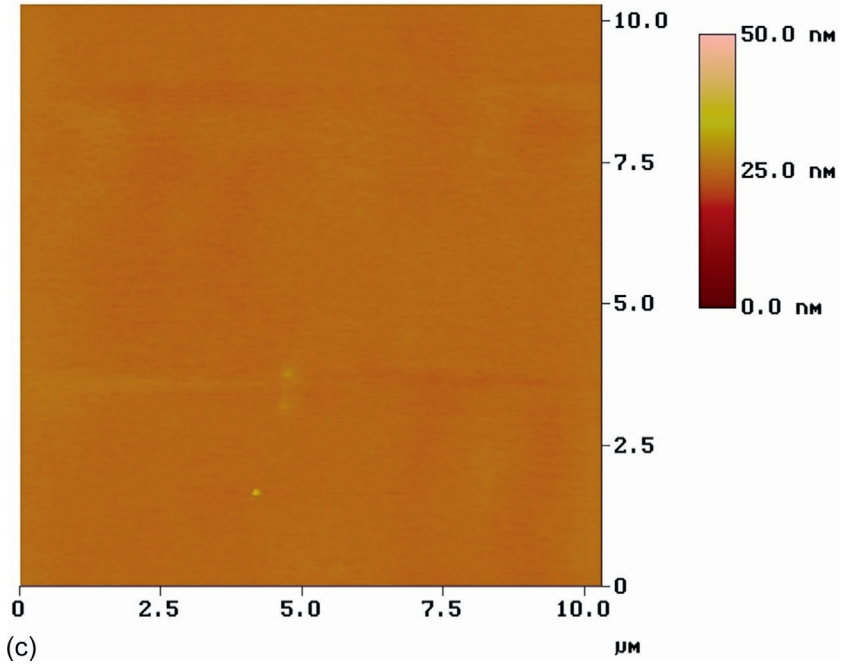


Figure 5.26 AFM (a, c, e, g), top-view, and (b, d, f, h) topographic images of HDG with (a, b) a blank silane hybrid coating (S_1) and silane hybrid coatings modified with (c, d) cerium nitrate (S_9), (e, f) CeO_2 nanoparticles (S_{10}), and cerium nitrate-activated CeO_2 nanoparticles (S_{11}) (g, h).

(Continued)



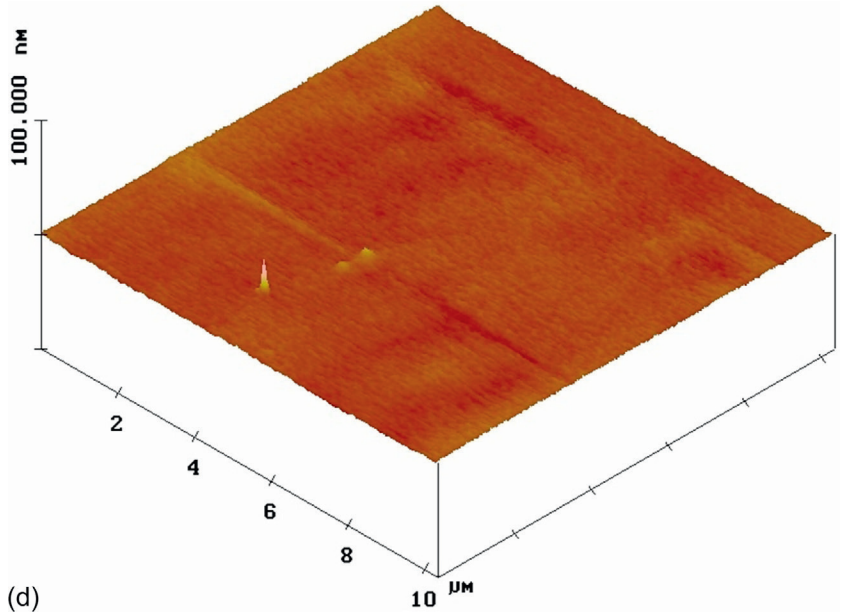


Figure 5.26, cont'd

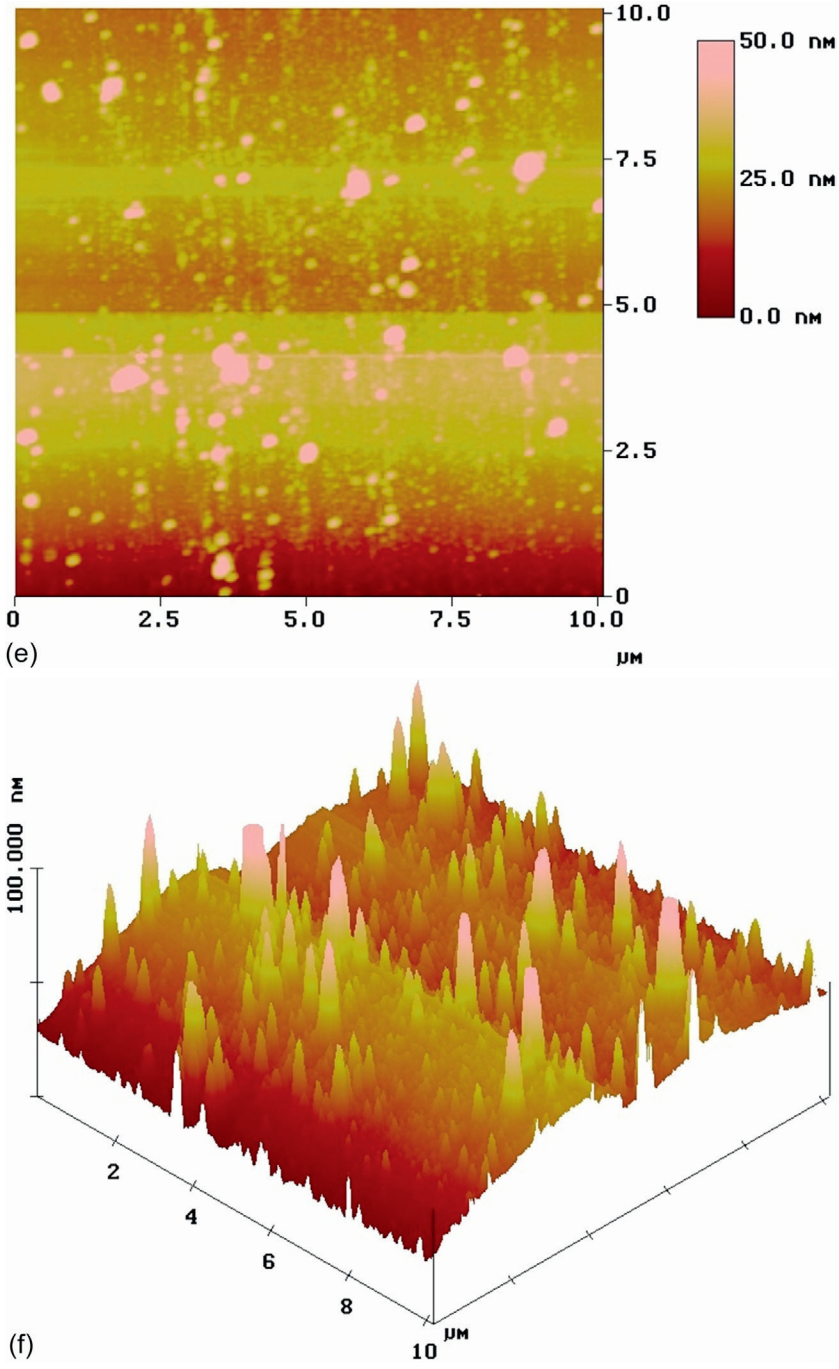
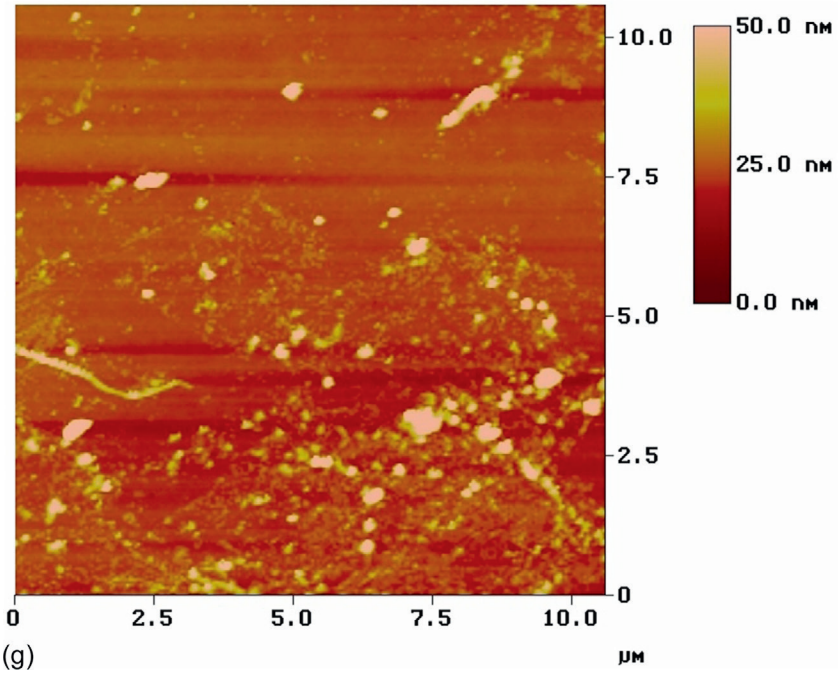


Figure 5.26, cont'd

(Continued)



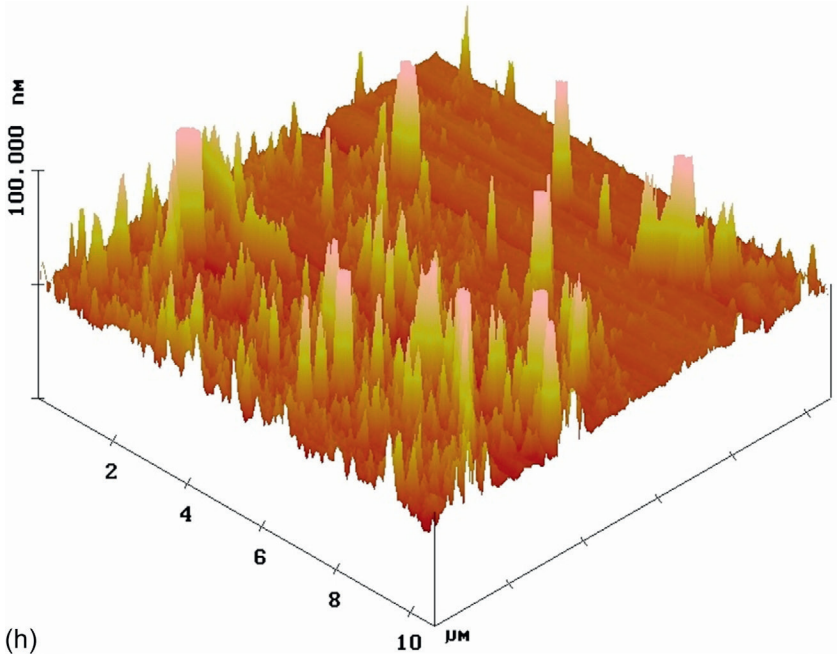


Figure 5.26, cont'd

The top-view image of the silane film filled with activated CeO_2 nanoparticles (S_{11}) (Figure 5.26g) reveals a number of CeO_2 nanoparticles uniformly distributed in the silane coating, which had an RMS roughness of 6.210 nm. Little color contrast is shown, indicating low heterogeneity of the coating thickness. The topographic image (Figure 5.26h) shows that the outer surface layers of this coating contained nanometer-scale particles and agglomerates. These results suggest that the addition of cerium ions altered the surface morphology of the coating modified with nonactivated CeO_2 nanoparticles.

SEM revealed the effects of the CeO_2 nanoparticles on the microstructure and qualitative chemical composition of the various silane coatings. Figure 5.27a shows the surface of the typical blank silane coating (S_1) prior to immersion in a 3.5% NaCl solution. It appears uniform and defect- and crack-free. However, several white agglomerates appeared in the coating matrix, which were identified by EDX (energy dispersive X-ray analysis) as being Si-rich (Figure 5.27b). It is likely that these features were clusters of nanoparticles formed in the outermost layers of the silane film.[1,39] The coatings doped with cerium nitrate (S_9) (Figure 5.27c) and nonactivated cerium oxide nanoparticles (S_{10}) (Figure 5.27d) contained particles of many different sizes. These particles were equally distributed in the coatings, and no microscale pores or cracks were observed. The silane film filled with CeO_2 nanoparticles activated with cerium ions (S_{11}) showed fewer and smaller silica agglomerations than the blank silane film (Figure 5.27e). EDX analysis of this region (Figure 5.27f) clearly showed the presence of cerium and silicon peaks, indicating that the addition of activated CeO_2 nanoparticles led to the decomposition of the silane chains and a reduction in the size of the particles in the sols.[1,25]

The thicknesses of the silane films were also determined using SEM. The silane coatings modified with cerium nitrate (S_9) and nonactivated cerium oxide (S_{10}) nanoparticles showed thicknesses of ~2.16 and 4.97 µm, respectively. Thickness increased to ~6.77 µm for the coating filled with CeO_2 nanoparticles activated with cerium ions (S_{11}). All modified films were thicker than the blank silane film (S_1) (~1.89 µm), suggesting that thicker or better cross-linked coatings formed in the presence of the activated ceria nanoparticles, as also observed by Montemor et al.[18] and Garcia-Heras et al.[34] This modification of the coating matrix could improve the resistance to oxidation of the substrate.[25]

SEM images of the nonmodified and cerium-modified silane coatings obtained after EIS testing (Figure 5.28) indicate the ability of the sol-gel coatings to protect the HDG substrates. All the coatings showed localized corrosion after immersion for 144 h in a 3.5% NaCl solution: exfoliation of the corrosion products and cracks of different sizes were observed. These localized attacks promoted the deterioration and delamination of the hybrid film, possibly due to hydrolysis reactions at the interface. Additionally, the diffusion of the oxidant ions became faster, and the corrosion rate increased, causing an accumulation of corrosion products at the interface and at the same time promoting the formation of defects and micro-cracks.[16] However, the SEM results showed that the barrier properties

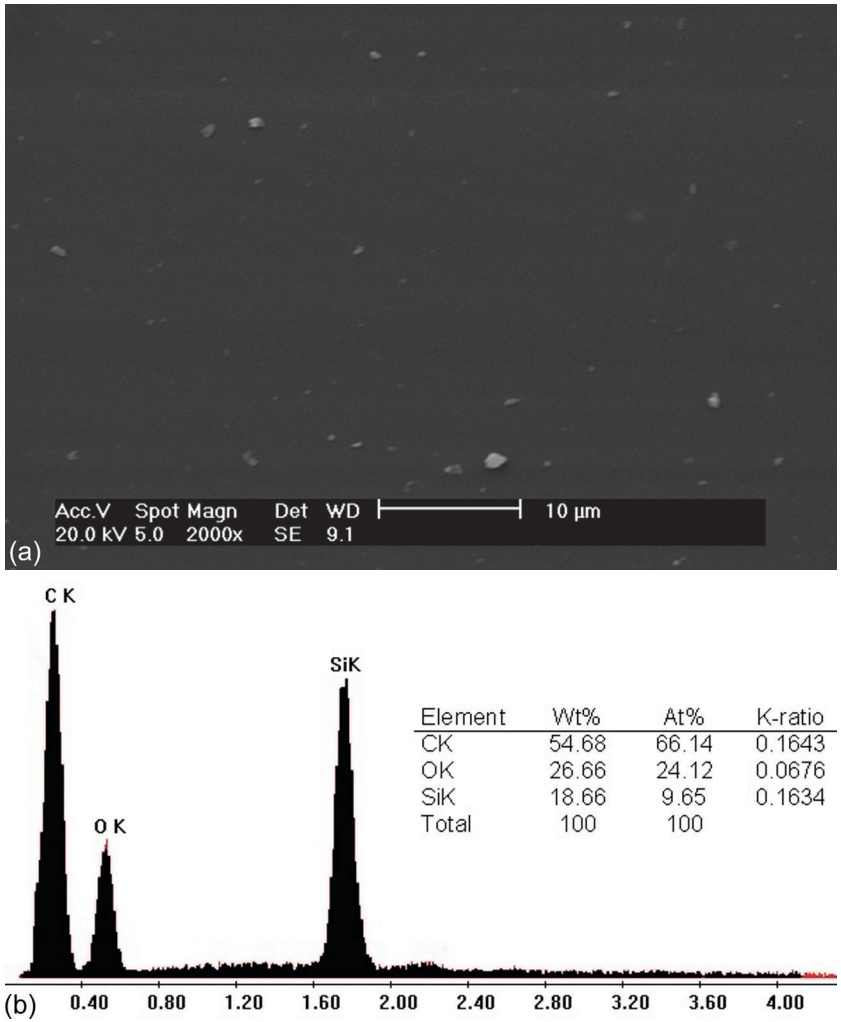


Figure 5.27 SEM micrographs (a, c, d, e) and EDX spectra (b, f) obtained from the indicated regions of HDG pretreated with (a, b) a blank silane hybrid coating (S_1) and silane hybrid coatings modified with (c) cerium nitrate (S_9), (d) CeO_2 nanoparticles (S_{10}), and (e, f) cerium nitrate-activated CeO_2 nanoparticles (S_{11}) prior to immersion in a 3.5% NaCl solution.

of the films containing the activated nanoparticles (S_{11}) (Figure 5.28d) were improved, likely as a consequence of the increased film thickness. The presence of the cerium ions also promoted the formation of reactive silanol groups in the silane molecules, leading to a higher degree of cross-linking, higher silicon content, and, therefore, more homogeneous films with better barrier properties, as has been confirmed by Montemor et al.[18]

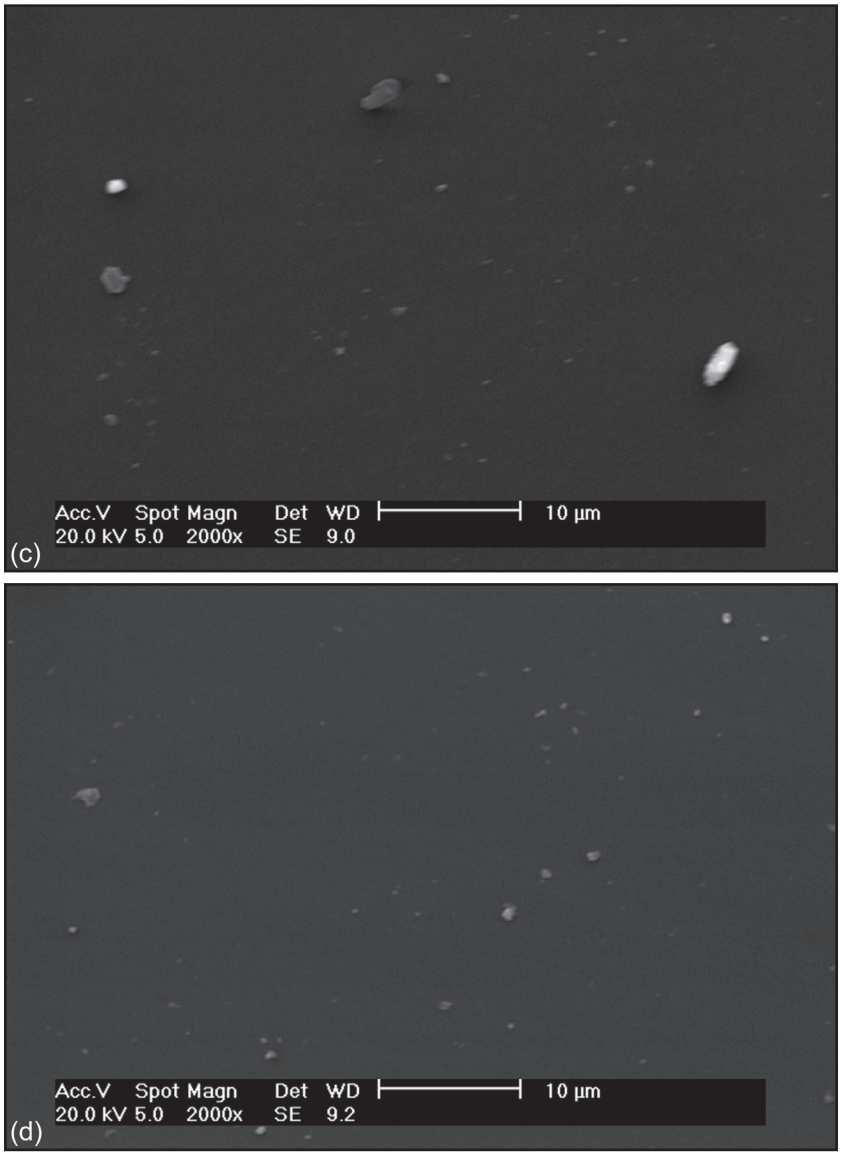


Figure 5.27, cont'd

(Continued)

To detect possible differences among the differently modified silane films, 144 h salt spray tests were performed (Figure 5.29). At the initial stages of exposure, all coatings showed the sacrificial dissolution of zinc in the artificially scratched area. The breakdown of the coating layers progressed with time; eventually the zinc coatings degraded, resulting in the formation of white rust.[40]

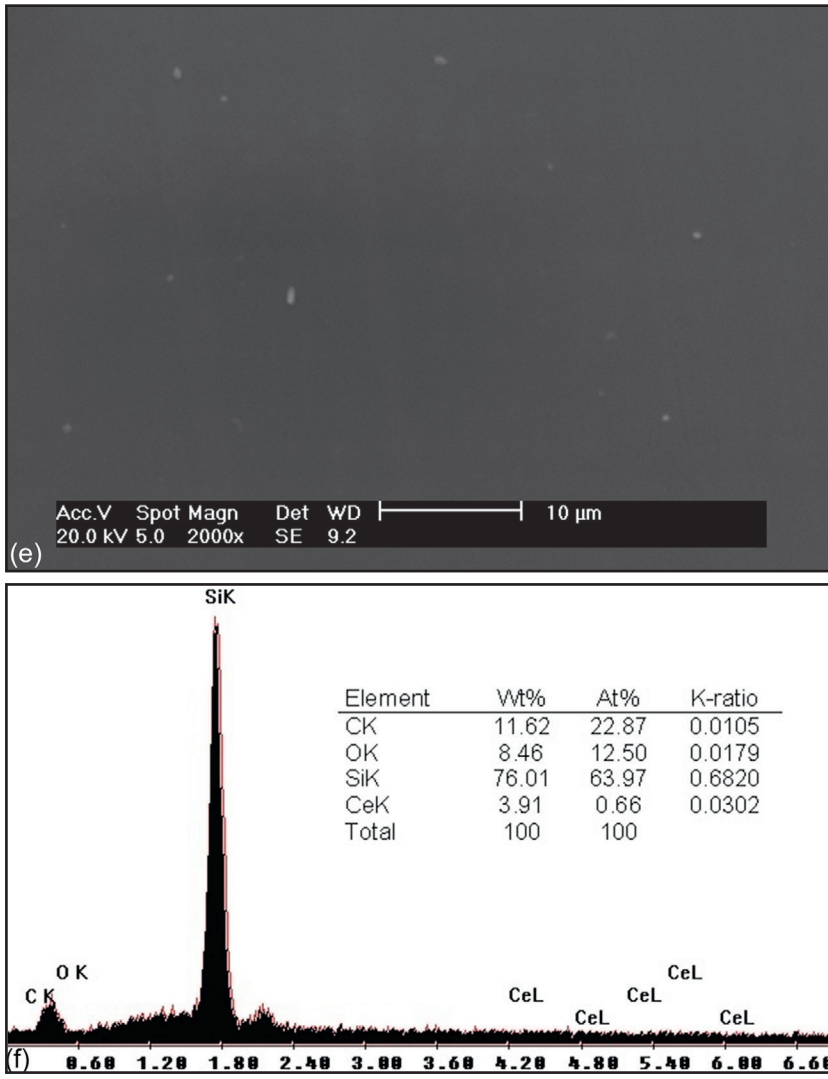


Figure 5.27, cont'd

For the blank silane-coated substrate (S_1), delamination increased rapidly during salt spray exposure. The modified silane coatings still showed increased delamination during exposure, but at markedly reduced rates. For example, the silane coating filled with activated CeO_2 nanoparticles (S_{11}) suffered comparatively little delamination after exposure for 144 h, indicating its stability and barrier properties.

EIS spectra of the coated galvanized steel substrates show that the nonmodified-silane-coated sample (S_1) (Figure 5.30a) exhibited lower impedance than that with the

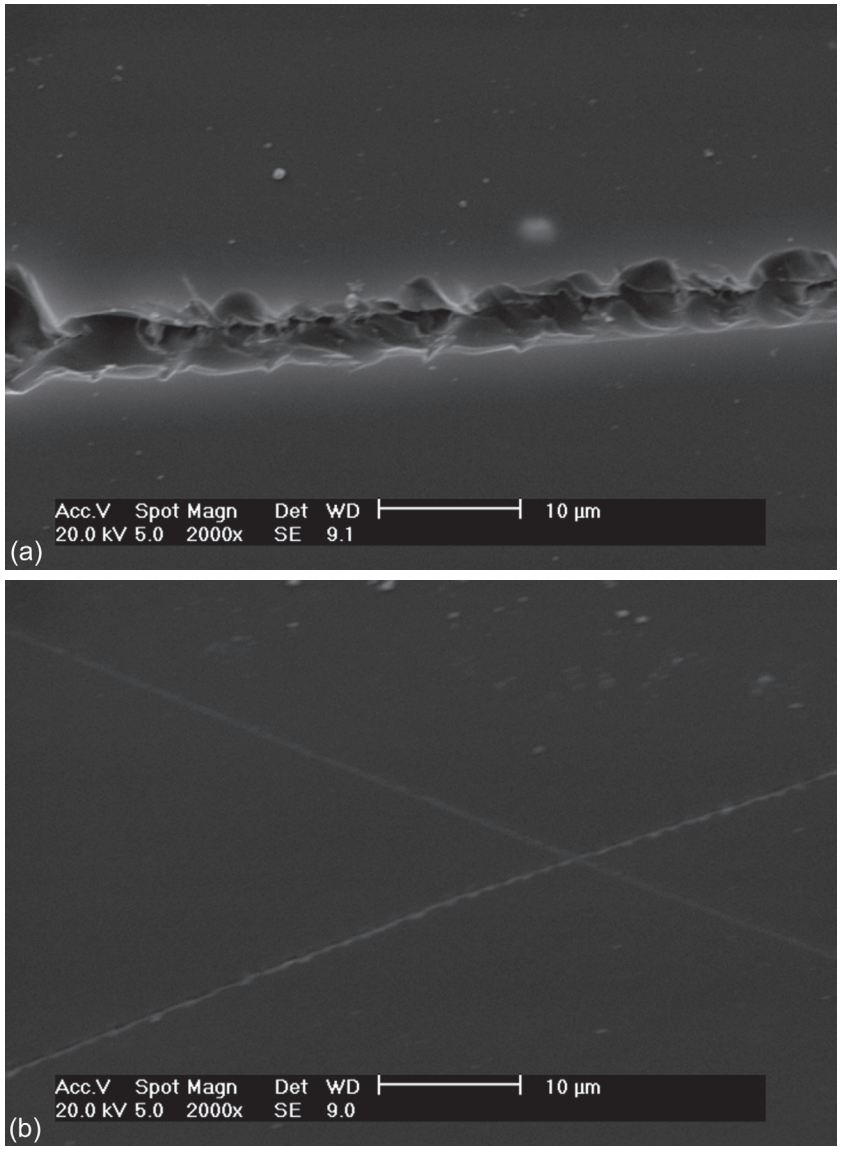


Figure 5.28 SEM micrographs of HDG pretreated with (a) a blank silane hybrid coating (S_1) and silane hybrid coatings modified with (b) cerium nitrate (S_9),

(Continued)

$Ce(NO_3)_3$-modified coating (S_9) (Figure 5.30c). Furthermore, in the presence of cerium nitrate, total impedance remained approximately constant for the duration of the 144 h test in a 3.5% NaCl solution. This was due to both the better barrier properties and the corrosion inhibition abilities.[32]

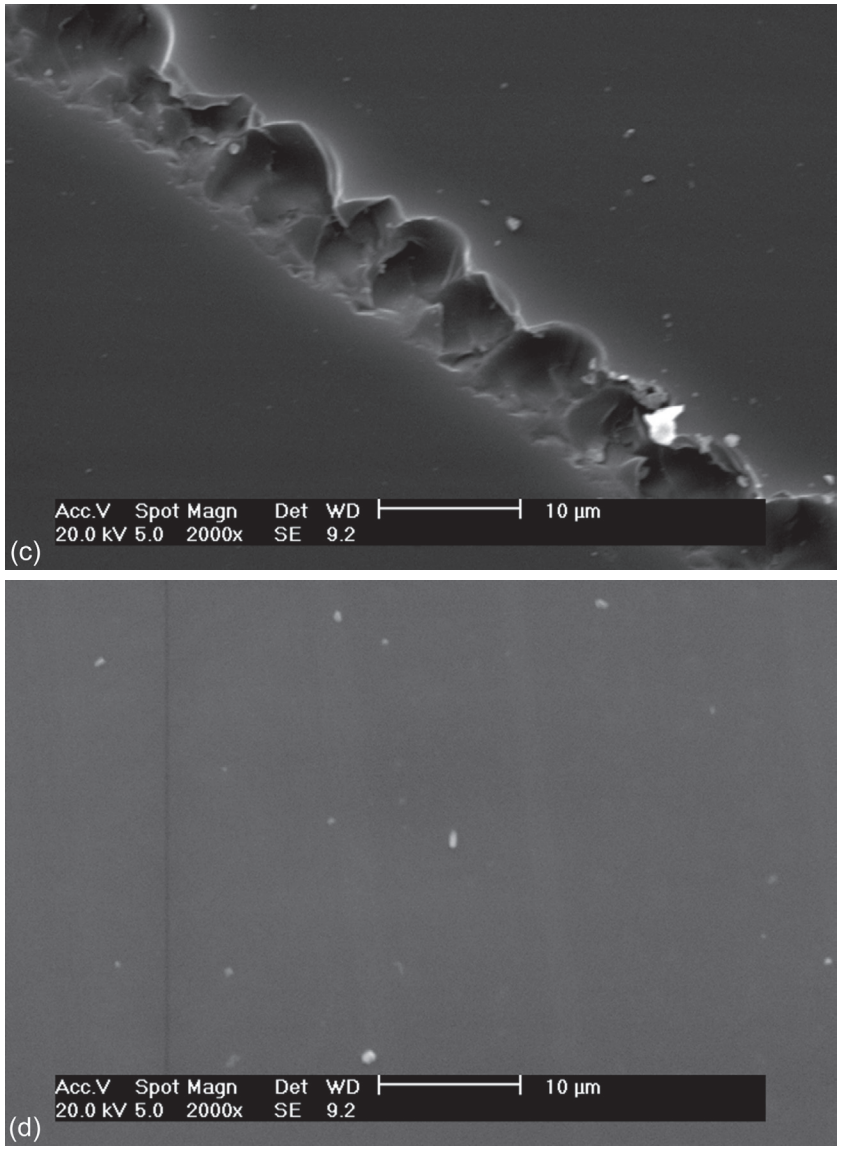


Figure 5.28, cont'd (c) CeO_2 nanoparticles (S_{10}), and (d) cerium nitrate-activated CeO_2 nanoparticles (S_{11}) after immersion for 144 h in a 3.5% NaCl solution.

EIS Bode plots obtained for the silane coatings filled with CeO_2 nanoparticles (S_{10} and S_{11}) (Figure 5.30e and g) show that total impedance was lower for the system containing nanoactivated CeO_2. The addition of cerium ions led to a significant increase in impedance. For example, after immersion for 24 h, the total impedance

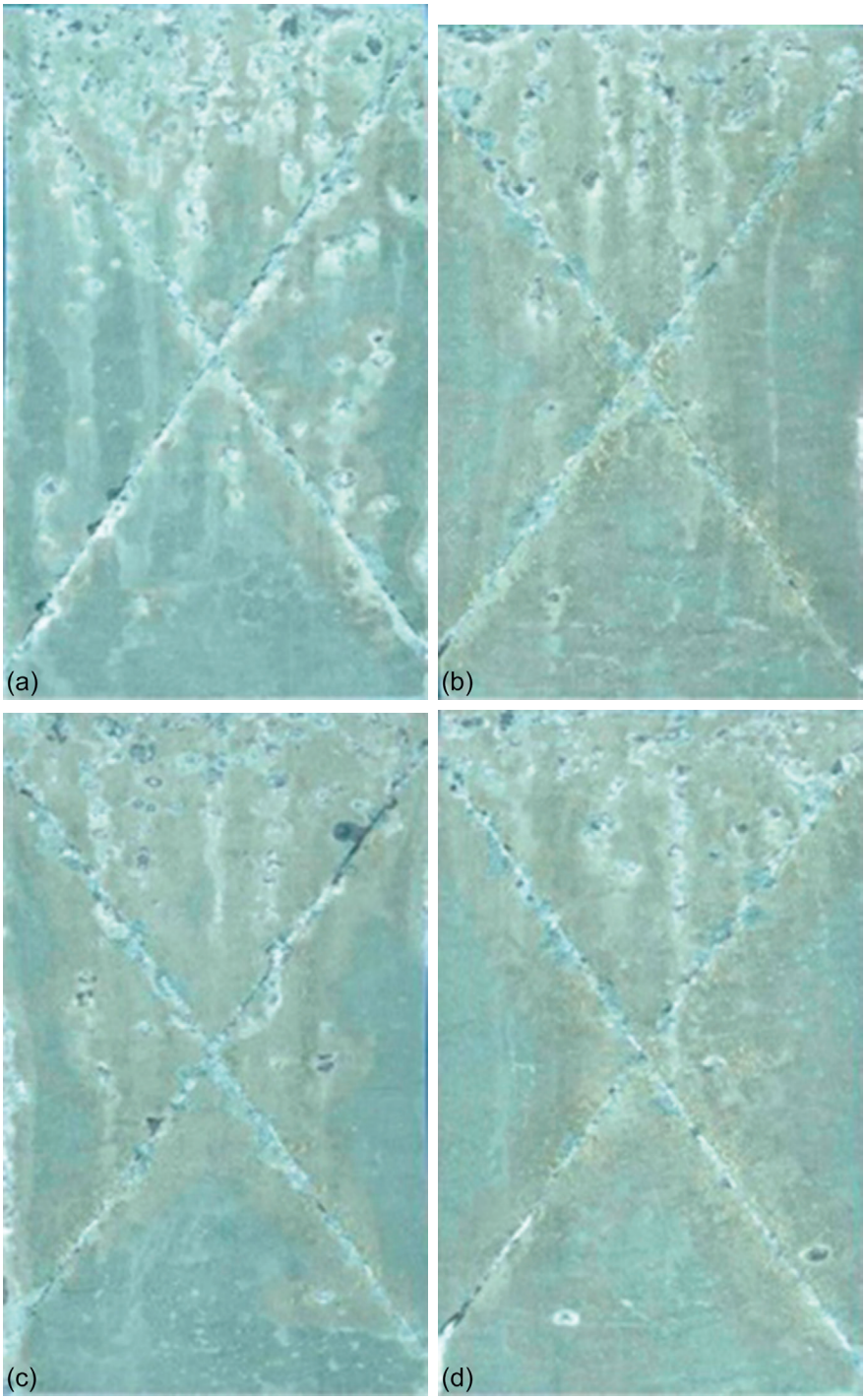


Figure 5.29 Photographs of HDG pretreated with (a) a blank silane hybrid coating (S_1) and silane hybrid coatings modified with (b) cerium nitrate (S_9), (c) CeO_2 nanoparticles (S_{10}), and (d) cerium nitrate-activated CeO_2 nanoparticles (S_{11}) after 144 h of salt spray exposure.

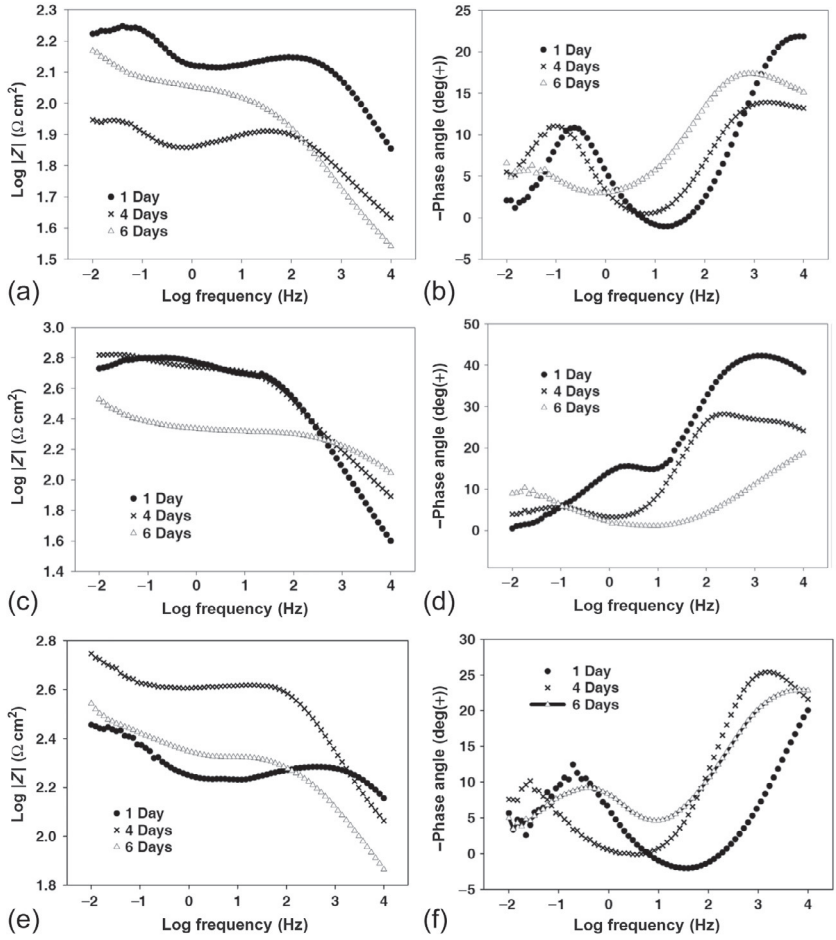


Figure 5.30 EIS Bode modulus (a, c, e, g) and phase angle plots (b, d, f, h) for HDG pretreated with (a, b) blank silane hybrid coating (S_1) and silane hybrid coatings modified with (c, d) cerium nitrate (S_9), (e, f) CeO_2 nanoparticles (S_{10}), and (g, h) cerium nitrate-activated CeO_2 nanoparticles (S_{11}) during immersion for 144 h in a 3.5% NaCl solution.

of the system containing activated CeO_2 was more than two orders of magnitude higher than that of the system filled with nonactivated CeO_2. This finding has also been noted previously[5,15] and was attributed to the likelihood of nanoparticles agglomerating and creating large defects in the coating, which promotes the uptake of the aggressive solution, and therefore promotes corrosion. The activation of the nanoparticles with cerium ions enhanced the protective properties of the modified silane films by increasing the thickness of the film and/or reducing its porosity.[18]

The shape of the phase angle plot indicated the presence of two time constants (Figure 5.30b, d, f, and h): one attributable to a high-frequency response of the silane film and one to a low-frequency response of the processes occurring at the silane film-substrate interface.

A more detailed interpretation of the EIS results can be made by numerical fitting using the equivalent circuit depicted in Figure 5.22.

Figure 5.31 shows the evolution of the resistance and capacitance of the coatings during immersion in a 3.5% NaCl solution. The high-frequency resistance values (Figure 5.31a) generally decreased during the first hours of immersion owing to the development of conductive pathways inside the blank silane film (S_1).[30] During early immersion, the highest resistance was shown by the coating modified with $Ce(NO_3)_3$ (S_9), whose resistance then dropped sharply after a few hours. The high-frequency resistance of the coating with nonactivated CeO_2 nanoparticles (S_{10}) reached a maximum and then started to decrease. The initial increase of the high-frequency resistance in the last two systems (S_9 and S_{10}) was attributed to swelling of the matrix and the consequent closing of nano/micropores.[11]

The high-frequency resistance of the system filled with activated CeO_2 nanoparticles (S_{11}) increased more gradually. The initial EIS response was nearly capacitive over the entire frequency range, and the resistance remained above 233 Ωcm^2. Its continued slow increase over the 144 h test led to a significant overall increase. Compared with the blank silane film, the modified silane films showed significantly improved barrier properties.

The evolution of capacitance during the immersion test is shown in Figure 5.31b. Coating S_{11} showed the lowest capacitance of the four considered systems, and it was the thickest of the coatings. Its capacitance remained relatively consistent during the immersion, with only a small increase after 96 h, which was associated with the uptake of electrolyte.[5,11] In contrast, the blank silane film showed significantly increased film capacitance after 96 h of immersion. This was due to water uptake, which was facilitated by the reduced barrier properties of the film.[5]

The evolution of the high-frequency fitting parameters indicated that the addition of nanoparticles reinforced the barrier properties of the film. The addition of cerium to the nanoparticles markedly influenced the capacitance and resistance of the coatings, and the systems filled with cerium-activated CeO_2 nanoparticles showed the best protection. These results are in accordance with those of Schem et al. regarding aluminum alloys with silane coatings filled with CeO_2 nanoparticles[11] and those of Montemor et al. regarding galvanized steel with silane coatings doped with Ce salt-activated nanoparticles.[5]

The evolution of the fitting parameters associated with the low-frequency behavior of the EIS spectra (Figure 5.32) gives information on the electrochemical activity at the silane-zinc interface. For the system pretreated with the silane coating (S_1), the initial CPE values (Figure 5.32a) were of the order of 0.0187 $F cm^{-2}$. During 96 h of

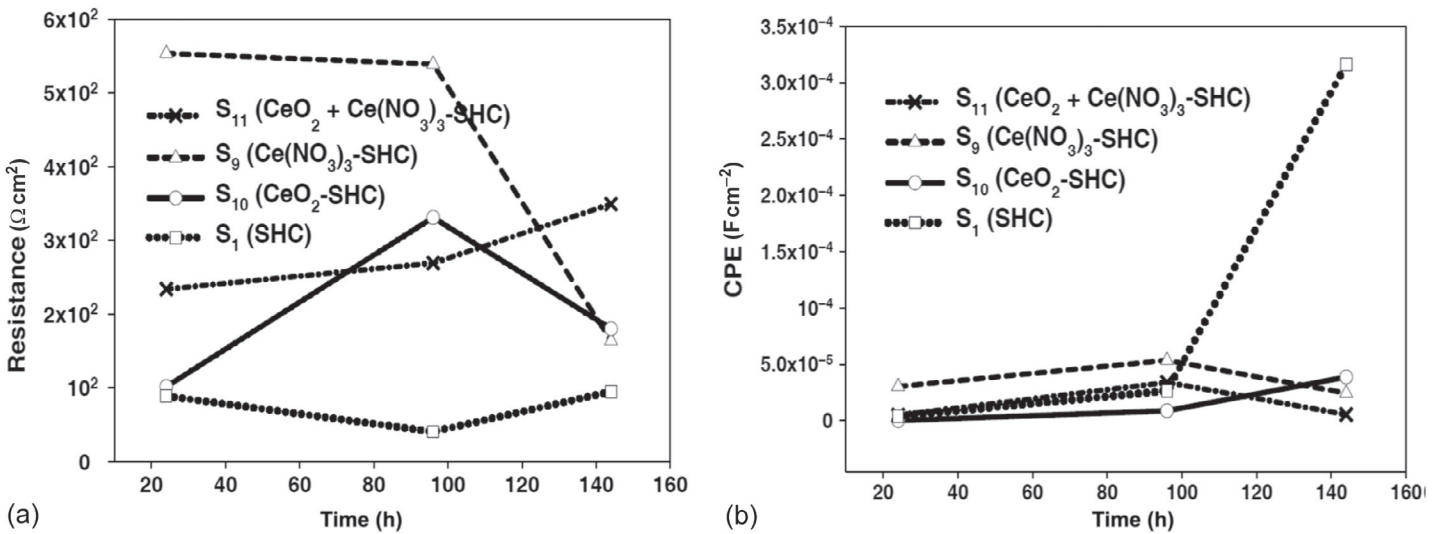


Figure 5.31 Evolution of coating (a) resistance and (b) capacitance during immersion in a 3.5% NaCl solution obtained by numerical fitting using the equivalent circuit depicted in Figure 5.22.

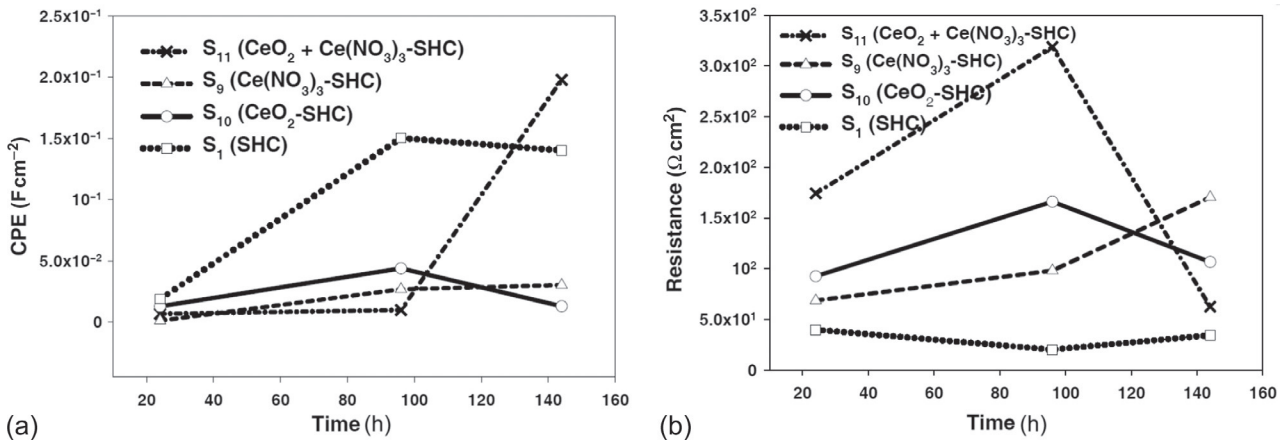


Figure 5.32 Evolution of (a) double layer capacitance and (b) charge transfer resistance during immersion in a 3.5% NaCl solution obtained by numerical fitting using the equivalent circuit depicted in Figure 5.22.

immersion, CPE values increased and then stabilized at ~0.1402 F cm^{-2}. This agreed with the evolution of the low-frequency resistance (Figure 5.32b) of the blank silane film, which gradually decreased during this period, from 39.81 to 20.24 Ω cm^2, before stabilizing at ~34.42 Ω cm^2.

The systems modified with CeO_2 behaved distinctly. In the absence of cerium ions (S_{10}), after 96 h, the CeO_2-filled system showed CPE values of ~0.0438 F cm^{-2}; its resistance increased from 92.54 Ω cm^2 during the first hour of immersion to ~166.20 Ω cm^2. After 144 h, CPE and resistance had increased slightly to 0.0129 F cm^{-2} and 106.60 Ω cm^2, respectively. The activation with cerium ions had significant effects on both the low-frequency CPE and the resistance. During immersion for 96 h, the CPE values of sample S_{11} were below 9.7601×10^{-3} F cm^{-2}, and the resistances increased to over 318.80 Ω cm^2. Resistance gradually decreased during the immersion test. Resistance and CPE eventually approached the values shown by the silane coating modified with $Ce(NO_3)_3$ (S_9). The low-frequency resistance increased during immersion, indicating that cerium oxide/hydroxide was stably formed with the release of $Ce(NO_3)_3$ from the sol-gel matrix.[31] The low-frequency resistance reached close to 170.62 Ω cm^2 after 144 h, indicating the continuous accumulation of cerium oxide/hydroxide during immersion. In addition, the CPE increased gradually to ~0.0301 F cm^{-2} after 144 h, four orders of magnitude lower than the value measured for the blank silane coating, suggesting that the inhibition products had filled the originally electrolyte-saturated pores at the coating-substrate interface.[31]

In some cases, the low-frequency resistance increased after a few hours, accompanied by a decrease in CPE. Because corrosion was localized, the precipitation of the insoluble and passive corrosion products likely occurred at these locations, decreasing the corrosion activity at the interface.[5] In fact, the most pronounced changes were observed for the blank silane film, which presented the poorest barrier properties and was therefore the most prone to early corrosion attack, as was observed by Montemor et al.[5]

Polarization curves were recorded after 1 h of immersion in the electrolyte (Figure 5.33). Parameters (I_{corr} and E_{corr}) derived from the curves (Table 5.6) indicate the different effects of the cerium modification on the silane coatings. The shifting of the cathodic polarization curves to lower current densities indicates the enhanced protection at the cathodic sites offered by coating S_{11}. The corrosion potential of sample S_{11} (–0.934 V) is indicative of its notably greater corrosion resistance when compared with samples S_1 (–0.974 V), S_9 (–0.959 V), and S_{10} (–0.987 V).

The poor performance displayed by coatings S_1 and S_{10} may have been attributable to permeability associated with cracks or porosity, which allowed the aggressive electrolyte to come into contact with the metal surface, thus initiating corrosion.[30] These results are consistent with the SEM micrographs, which show cracks and

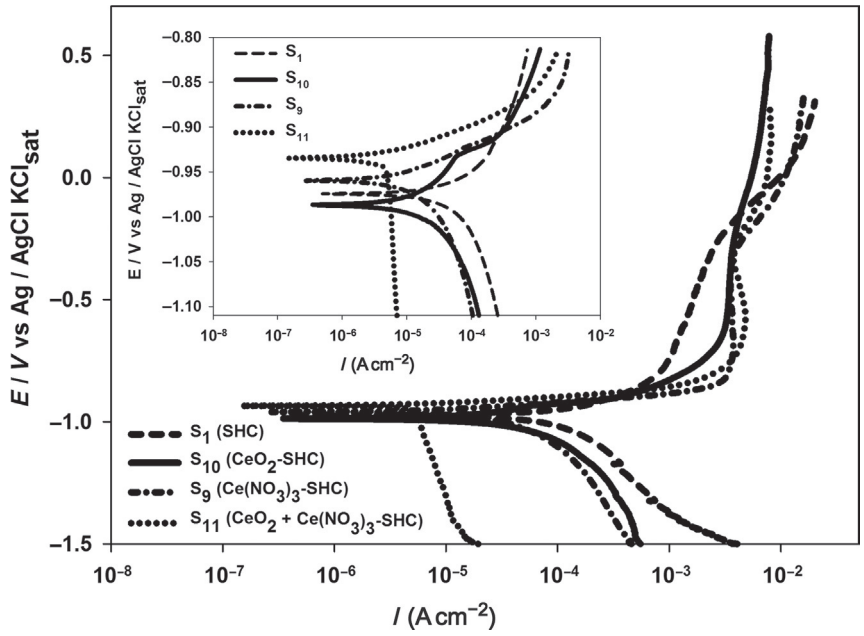


Figure 5.33 Potentiodynamic polarization curves for HDG pretreated with blank silane hybrid coating (S_1) and silane hybrid coatings modified with cerium nitrate (S_9), CeO_2 nanoparticles (S_{10}), and cerium nitrate-activated CeO_2 nanoparticles (S_{11}) obtained after immersion for 1 h in a 3.5% NaCl solution. The inset plot has potential depicted as the difference between the imposed and corrosion potentials, which allows better separation of the anodic and cathodic polarization effects.

TABLE 5.6 Summary of Electrochemical Parameters Obtained from the Polarization Measured in a 3.5% NaCl Solution

Sample	E_{corr} (V)	I_{corr} (A cm^{-2})	b_c (V/dec)	b_a (V/dec)	Passive Area (V)
S_1: SHC	–0.974	3.57×10^{-5}	0.060	0.093	–0.792 to –0.241
S_9: $Ce(NO_3)_3$-SHC	–0.959	3.22×10^{-6}	0.022	0.022	–0.832 to –0.320
S_{10}: CeO_2-SHC	–0.987	4.90×10^{-6}	0.031	0.026	–0.677 to –0.262
S_{11}: CeO_2+$Ce(NO_3)_3$-SHC	–0.934	1.11×10^{-6}	0.015	0.012	–0.809 to –0.327

delamination in these coatings after immersion for 144 h in 3.5% NaCl solution (Figure 5.28). Similar behavior has been reported by Montemor et al.[5] for galvanized steel substrates in 0.005 M NaCl solution.

5.4 Conclusion and Outlook

Cerium-doped SHCs employing GPTMS and BPA, as a cross-linking agent, were synthesized via a sol-gel method and fabricated on treated steel surfaces (either austenitic 304L stainless steel or HDG). The use of these substrates allowed investigation of the effects of various parameters that influence the microstructure, morphology, and protective properties of the coatings. These parameters include the concentrations of cerium ions and additives such as BPA, cerium nitrate, and CeO_2 nanoparticles.

FTIR spectroscopy and SEM confirmed the formation of crack-free cerium-doped SHCs with Si−O−Si structural backbones and $-CH_2$ groups incorporated into silica network. The resulting films were transparent and homogenous. The lack of cross-linking agent (BPA) in the linear cross-linked cerium-doped SHC caused it to show cracks, be very brittle, and withstand corrosion poorly.

Comparatively smooth nanostructured surfaces with low heterogeneity of coating thickness were observed in the silane coatings modified with cerium nitrate rather than CeO_2 nanoparticles. The use of CeO_2 nanoparticles led to high heterogeneity of coating thickness.

Corrosion testing indicated that the CeO_2 nanoparticles gave good corrosion inhibition properties to scratched surfaces because of their ability to complex with other species, therefore contributing to the stabilization of the passive film via an anodic inhibition mechanism. Modification of the silane solution with cerium nitrate led to improvements in the barrier properties, corrosion inhibition, and the self-repair of defects. The cerium ions can change the silane solution chemistry, promoting the formation of reactive silanol groups and more condensed species.

Electrochemical studies indicated general improvements due to the incorporation of cerium nitrate, although the performance of the coated substrate depended on the doping level. Too low or too high cerium concentrations led to reduced corrosion inhibition in the sol-gel matrix. EIS and polarization results confirmed that the optimal corrosion resistance was obtained at a cerium concentration of 0.05 M.

Modifying the silane coatings with cerium salt-activated CeO_2 nanoparticles led to improved barrier properties and corrosion resistance and decreased coating capacitance. The incorporation of activated CeO_2 nanoparticles reduced the cathodic current density by two orders of magnitude and shifted the voltage to more positive values (compared with the blank silane-coated substrate) during polarization in 3.5% NaCl solution.

Acknowledgments

The authors wish to acknowledge Ghent University for financial support and Arcelor Mittal Gent for providing the materials. The authors would also like to thank Peter Mast, Michel Moors, Christa Sonck, Veerle Boterberg, Sandra Van Vlierberghe, Babs Lemmens, and Vitaliy Bliznuk for technical assistance.

References

1. Zhong XK, Li Q, Hu JY, et al. Effect of cerium concentration on microstructure, morphology and corrosion resistance of cerium-silica hybrid coatings on magnesium alloy AZ91D. Prog Org Coat 2010;69(1):52–6.
2. Shchukin DG, Zheludkevich M, Yasakau K, et al. Layer-by-layer assembled nanocontainers for self-healing corrosion protection. Adv Mater 2006;18(13):1672–8.
3. Cabral AM, Trabelsi W, Serra R, et al. The corrosion resistance of hot dip galvanised steel and AA2024-T3 pre-treated with bis-[triethoxysilylpropyl] tetrasulfide solutions doped with Ce(NO3)(3). Corros Sci 2006;48(11):3740–58.
4. Deflorian F, Rossi S, Fedel M, et al. Electrochemical investigation of high-performance silane sot-gel films containing clay nanoparticles. Prog Org Coat 2010;69(2):158–66.
5. Montemor ME, Feffeira MGS. Cerium salt activated nanoparticles as fillers for silane films: evaluation of the corrosion inhibition performance on galvanised steel substrates. Electrochim Acta 2007;52(24):6976–87.
6. Wang HM, Akid R. Encapsulated cerium nitrate inhibitors to provide high-performance anticorrosion sol-gel coatings on mild steel. Corros Sci 2008;50(4):1142–8.
7. Trabelsi W, Cecilio P, Ferreira MGS, et al. Electrochemical assessment of the self-healing properties of Ce-doped silane solutions for the pre-treatment of galvanised steel substrates. Prog Org Coat 2005;54(4):276–84.
8. Pepe A, Aparicio M, Duran A, et al. Cerium hybrid silica coatings on stainless steel AISI 304 substrate. J Sol-Gel Sci Techn 2006;39(2):131–8.
9. Trabelsi W, Triki E, Dhouibi L, et al. The use of pre-treatments based on doped silane solutions for improved corrosion resistance of galvanised steel substrates. Surf Coat Tech 2006;200(14–15):4240–50.
10. Rosero-Navarro NC, Pellice SA, Duran A, et al. Corrosion protection of aluminium alloy AA2024 with cerium doped methacrylate-silica coatings. J Sol-Gel Sci Techn 2009;52(1):31–40.
11. Schem M, Schmidt T, Gerwann J, et al. CeO2-filled sol-gel coatings for corrosion protection of AA2024-T3 aluminium alloy. Corros Sci 2009;51(10):2304–15.
12. Aramaki K. Self-healing mechanism of a protective film prepared on a $Ce(NO_3)(3)$-pretreated zinc electrode by modification with $Zn(NO_3)(2)$ and Na_3PO_4. Corros Sci 2003;45(5):1085–101.
13. Aramaki K. The inhibition effects of cation inhibitors on corrosion of zinc in aerated 0.5 M NaCl. Corros Sci 2001;43(8):1573–88.
14. Aramaki K. Preparation of self-healing protective films on a zinc electrode treated in a cerium(III) nitrate solution and modified with sodium phosphate and cerium(III) nitrate. Corros Sci 2004;46(6):1565–79.
15. Montemor MF, Trabelsi W, Zheludevich M, et al. Modification of bis-silane solutions with rare-earth cations for improved corrosion protection of galvanized steel substrates. Prog Org Coat 2006;57(1):67–77.
16. Zand RZ, Verbeken K, Adriaens A. Influence of the cerium concentration on the corrosion performance of ce-doped silica hybrid coatings on hot dip galvanized steel substrates. Int J Electrochem Sci 2013;8(1):548–63.
17. Zand RZ, Verbeken K, Adriaens A. Evaluation of the corrosion inhibition performance of silane coatings filled with cerium salt-activated nanoparticles on hot-dip galvanized steel substrates. Int J Electrochem Sci 2013;8(4):4924–40.
18. Montemor MF, Ferreira MGS. Analytical characterization of silane films modified with cerium activated nanoparticles and its relation with the corrosion protection of galvanised steel substrates. Prog Org Coat 2008;63(3):330–7.

19. *Report of International Nickel Company (INCO), Corrosion resistance of the austenitic chromium nickel stainless steels in chemical environments*; 1963.
20. Marder AR. The metallurgy of zinc-coated steel. Prog Mater Sci 2000;45(3):191–271.
21. Zand RZ. *Investigation of corrosion, abrasion and weathering resistance in hybrid nanocomposite coatings based on epoxy-silica* [Thesis]. Azad University-Tehran North Branch; 2005.
22. Zand RZ, Verbeken K, Adriaens A. The corrosion resistance of 316L stainless steel coated with a silane hybrid nanocomposite coating. Prog Org Coat 2011;72(4):709–15.
23. ASTM B117-11 standard practice for operating salt spray (fog) apparatus, G01.05, book of standards 2011; Volume: 03.02.
24. ASTM standards for corrosion testing of metals. 3rd ed. W. Conshohocken, PA: ASTM International; 2008.
25. Phanasgaonkar A, Raja VS. Influence of curing temperature, silica nanoparticles- and cerium on surface morphology and corrosion behaviour of hybrid silane coatings on mild steel. Surf Coat Tech 2009;203(16):2260–71.
26. Tiwari A, Hihara LH. High silicone content barrier coatings for corrosion protection of metals. *TRI-service corrosion conference, Denver*; 2007. p. 1–17.
27. Mosher BP, Wu CW, Sun T, et al. Particle-reinforced water-based organic-inorganic nanocomposite coatings for tailored applications. J Non Cryst Solids 2006;352(30–31):3295–301.
28. Zandi-zand R, Ershad-langroudi A, Rahimi A. Organic-inorganic hybrid coatings for corrosion protection of 1050 aluminum alloy. J Non Cryst Solids 2005;351(14–15):1307–11.
29. Pepe A, Aparicio M, Cere S, et al. Preparation and characterization of cerium doped silica sol-gel coatings on glass and aluminum substrates. J Non Cryst Solids 2004;348:162–71.
30. Moutarlier V, Neveu B, Gigandet MP. Evolution of corrosion protection for sol-gel coatings doped with inorganic inhibitors. Surf Coat Tech 2008;202(10):2052–8.
31. Shi HW, Liu FC, Han EH. Corrosion behaviour of sol-gel coatings doped with cerium salts on 2024-T3 aluminum alloy. Mater Chem Phys 2010;124(1):291–7.
32. Zand RZ, Verbeken K, Adriaens A. Corrosion resistance performance of cerium doped silica sol-gel coatings on 304L stainless steel. Prog Org Coat 2012;75(4):463–73.
33. Zheludkevich ML, Serra R, Montemor MF, et al. Nanostructured sol-gel coatings doped with cerium nitrate as pre-treatments for AA2024-T3—corrosion protection performance. Electrochim Acta 2005;51(2):208–17.
34. Garcia-Heras M, Jimenez-Morales A, Casal B, et al. Preparation and electrochemical study of cerium-silica sol-gel thin films. J Alloys Compd 2004;380(1–2):219–24.
35. Ballarre J, Jimenez-Pique E, Anglada M, et al. Mechanical characterization of nano-reinforced silica based sol-gel hybrid coatings on AISI 316L stainless steel using nanoindentation techniques. Surf Coat Tech 2009;203(2):3325–31.
36. Sugama T. Cerium acetate-modified aminopropylsilane triol: A precursor of corrosion-preventing coating for aluminum-finned condensers. JCT Res 2005;2(8):649–59.
37. Hosseini M, Ashassi-Sorkhabi H, Ghiasvand HAY. Corrosion protection of electro-galvanized steel by green conversion coatings. J Rare Earth 2007;25(5):537–43.
38. Montemor MF, Trabelsi W, Lamaka SV, et al. The synergistic combination of bis-silane and CeO_2 center dot ZrO_2 nanoparticles on the electrochemical behaviour of galvanised steel in NaCl solutions. Electrochim Acta 2008;53(20):5913–22.
39. Palomino LM, Suegama PH, Aoki IV, et al. Electrochemical study of modified cerium-silane bi-layer on Al alloy 2024-T3. Corros Sci 2009;51(6):1238–50.
40. Shibli SMA, Chacko F. CeO_2-TiO_2 mixed oxide incorporated high performance hot dip zinc coating. Surf Coat Tech 2011;205(8–9):2931–7.

Chapter 6

Hybrid Zinc-Rich Paint Coatings: The Impact of Incorporation of Nano-Size Inhibitor and Electrical Conducting Particles

András Gergely[*], Zoltán Pászti[*], Imre Bertóti[†], Judith Mihály[‡], Eszetr Drotár[*], Tamás Török[§]

[*]Department of Metallurgical and Foundry Engineering, Faculty of Materials Science and Engineering, University of Miskolc, Budapest, Hungary

[†]Department of Plasma Chemistry, Institute of Materials and Environmental Chemistry, Research Centre for Natural Sciences, Hungarian Academy of Sciences, Budapest, Hungary

[‡]Department of Biological Nanochemistry, Institute of Molecular Pharmacology, Research Centre for Natural Sciences, Hungarian Academy of Sciences, Budapest, Hungary

[§]Department of Metallurgical and Foundry Engineering, Faculty of Materials Science and Engineering, University of Miskolc, Budapest, Hungary

Intelligent Coatings for Corrosion Control
Copyright © 2015 Elsevier Inc. All rights reserved.

6.1 Introduction

Application and investigation of zinc-rich paints (ZRPs) dates back a long time[1] with an enormous amount of scientific and engineering achievements. There were some works aiming to characterize liquid ZRPs,[2] working out their modeling by means of electrochemical impedance spectroscopy (EIS),[2,3] analyzing the duration of active-passive protection terms[4] andpretreatment of the surface of steel substrate rust converter[5] and investigating the influence of salt contamination of the interface,[6] pointing out the difference between the early-stage and later-stage diffusions of zinc and iron corrosion products impacting the overall protection performance. A number of studies have disclosed the effects of pigment volume concentration (PVC),[7–12] the zinc grain size range from microns to the nanometer range[12–17] or the spherical and lamellar[8,10,18] shape[8,18–20] of the pigments. Nonetheless, a combination of the spherical and lamellar pigments gives the best performance.[10,21] To disclose the impact of the binders, several organic vehicles, inorganic binders, and organic-inorganic hybrid compositions were developed by the industry partly to substitute organic paint coatings with volatile organic carbon (VOC) components and seek long, service life-capable high performance solutions. Among the organic ones, epoxy[21–23] and alkyd binders[24,25] are the most frequently used. However, there are many eco-friendly alternatives such as the inorganic silicates[13,26,27] and alkyl-silicates[15,23,28–31] or alkyl-silicone modified silicates,[18] featuring much more efficient and long-term service (meaning low VOC content and isocyanate-free technology). In comparison with organic coatings, these hybrids have many advantages, such as high durability, hardness, good gloss and color retention, along with resistance to atmospheric degradation and heat, and low chemical affinity toward oxidation (almost missing cathodic delamination during prolonged exposure). All these features come from the chemical structure and the increased stability of the inorganic substance used in considerable amounts, making these compositions more attractive compared to many other alternatives. Nevertheless, careful laboratory and field testing is needed every time to assess the actual delivery of these systems so as to appropriately meet application targets. However, strict VOC regulations can be met by another approach so the interest in a solvent-free powder is understandable. Powder coatings[32,33] tested in flowing conditions[34] were formulated with electrically conductive and semiconductive auxiliary particles such as carbon black[35,36] and polyaniline[37] to reach electrical percolation or render inhibition in the matrices. Some studies found di-iron phosphide a proper agent to enhance electrical conductivity and to improve the performance of inorganic ZRPs[38] to a level similar to that of graphite and aluminum powders.[39] Therefore, some degree of galvanic protection is allowed to occur at lower zinc contents than the critical PVC, depending on the relative

amount of the conducting additive and the overall paint composition. The most favorable ratio of substitution of zinc was pointed out at quite high contents of 20, 15, and 15 wt.% for di-iron phosphide, graphite, and aluminum, respectively. However, the large content of such additives proved to be inappropriate or even far deteriorating, leading to greater rates of zinc self- and bimetallic corrosion for the same time scale.

Besides the use of pure zinc,[21] development of the ZRPs included testing numerous zinc compositions with alloying elements of especially aluminum[18,40] and in some cases magnesium.[41] The latter type efficiently protects even aluminum alloys, which generally means a lower, inhibited corrosion rate of the pigments compared to pure magnesium-rich coatings. In addition, in some cases development led to the application of surface modified zinc with either derivatives of phosphoric or phosphonic acid, which helped to inhibit zinc corrosion and lowered galvanic activity of the coating.[42] The application of additives such as zinc oxide[8] and high-quality well-dispersed clay minerals[16,32] at very low zinc content (as little as 10 wt.%)[17] indicated firm barrier behavior and long-term galvanic function. Another evolution branch is to employ hybrid pigment-particle compositions based on the aspect of partial replacement of zinc dust with intrinsically conducting polymers like Polyaniline (Pani),[32,38,43] Polypyrrole (PPy) supported either with carbon black[44] or nano-size alumina,[45] pristine,[46] and modified carbon nanotubes (CNTs).[47] The former semiconductors act as auxiliary corrosion inhibitors, and the latter ones were used to facilitate electrical percolation. Both additives led to improved protection characteristics on various scales. On the one hand, CNT-embedded stand-alone PPy[48] and polyaniline films[49] indicated minor positive results, whereas only poor protection was obtained by the CNT-poly(*o*-phenylenediamine) composite.[50] In addition, thin waterborne polyurethane films containing oxidized CNTs showed moderate protection functionality.[51] However, on the other hand, there were studies reporting lower corrosion resistivity of metals when connected to CNTs,[52–55] which was interpreted on the basis of microgalvanic action between metallic matrixes and the CNTs. Similarly, effective galvanic coupling between epoxy composites of graphite and metallic substrates immersed in either quiescent or flowing seawater are well known, and both the greater composite and fiber area aggravate the phenomenon.[56] Galvanic corrosion can even occur when moisture absorption can take place through the epoxy outer-layer matrix to the graphite fibers. These composites are effective cathodes for oxygen reduction in seawater, featuring a similarity to a bimetallic setup composed of two dissimilar metals. So, successful application of especially the nano-size electrically high conducting carbon forms is expected to face some hardships. Furthermore, particles such as ultra-fine glass fibers deteriorate protection properties[57] although hardness and adhesion of the coatings are positively affected. A very special approach was to encapsulate diisocyanate monomer resin with microsize nickel-zinc

alloy shells to provide self-healing characteristics.[58] Nevertheless, performance of this technology is not yet comparable to liquid ZRPs.

In general, electrical percolation of the ZRPs is necessary to activate their proper protection function. Pigments are usually assumed to be homogeneously distributed in organic coatings, and the voids may form not only when PVC is reached or exceeded by a critical degree but even below it. That was proven by a study that expounded on the basis of a phenomenological theory, pointing out the relevance of the coarseness parameter and the relationship with the smallest densely packed pigment clusters, leading to density fluctuations on the formation of voids below and above the CPVC.[7] So, in relation to forestalling the formation of voids spanning coatings while obtaining electrical percolation, it is highly recommended to apply metallic grains of small size at lower contents than the critical PVC, which depends on the density of the vehicles and metallic pigments as well as their sizes and shapes. This is all in favor of attaining high barrier function with durable and efficient galvanic function in addition to complying with certain economical and environmental requirements.

In case of the nano-size zinc containing coatings, it must be noted that highly efficient galvanic activity (at reduced film permeability) is often due to the better connectivity of the pigments because of the lower average distance between the grains. Interparticle distance decreases with decreasing size of the particles,[59,60] resulting in decreasing electrical percolation thresholds as a consequence of increasing spatial density of electrical coupling connections and infinite volume spanning cluster formation of the pigment-particles. Then osmosis-driven blistering should be absent because of the low coarseness, high packing density in the coating. This is obviously due to the large size of dense pigment clusters allowed by the favorable ratio of micron- and nano-size spherical grains despite the overall compositions close to the critical PVC. This finding agrees with the theoretical considerations discussed earlier.[61] The concept of nano-size in relative amounts of grains has been proven.[14] The ratio of nano-size metallic grains can and should be increased at the expense of the micron-size particles as the overall zinc content decreases[15] for the sake of keeping high profile protection characteristics.

In this chapter, corrosion protection characteristics of two sorts of zinc-rich hybrid coatings containing either inhibitor or conductor types of nano-size particles are compared. All the main features of the hybrid coatings are compared with conventional liquid ZRPs represented by one typical formulation with an electrically percolating structure. The protective nature and performance of the zinc-rich hybrids are interpreted on the basis of electrical properties and spatial distribution of the nano-size particles. This work is part of an effort to find appropriate particles to enhance the protection performance of traditional liquid ZRPs with the electrically nonpercolating structure of the solid fillers.

6.2 Experimental

6.2.1 Materials and synthesis

6.2.1.1 Preparation of the nano-size particles

Multiwalled carbon nanotubes (MWNT-30 type nanotubes with average diameter of 40 nm, supplied by Shenzhen Nanotech Port Co. Ltd., China) were dispersed by ultrasonication in the mixture of aqueous ethanol and acetic acid (by the volume mixtures of 10:1:3) twice for 30 min. To ensure enhanced dispersity as well as stability of the dispersions and to facilitate exfoliation, poly(4-ammonium styrenesulfonic acid, 30%, Aldrich) and sodium dodecyl sulfate (98%, Aldrich) were used and are later referenced as PSS and SDS, respectively.

For preparation of the nano-size particles, pyrrole (98%, Aldrich) was dissolved in water-dispersed sol of fumed alumina (AluC, BET surface: $100\,m^2\,g^{-1}$, Evonik Industries AG, Germany) and the colloid was stirred intensively for 2 h. In case of the alumina-supported PPy type particles, the procedures of polymerization and deposition were carried out in aqueous ethanol (at a content of 13% by volume) dispersed alumina sol. Initial pyrrole concentrations were 1.94×10^{-2} and 1.192×10^{-1} M, whereas alumina contents were 2.44 and 4.76 wt.% solely to the alumina and the nanotube containing dispersions, respectively. PSS content and SDS concentration of the nanotube containing mixture were 2.15 wt.% and 2.43×10^{-3} M. For oxidative polymerization of pyrrole, the solution of iron(III) nitrate (97%, Fluka) was added to the vigorously stirred sol to obtain an iron(III)-pyrrole molar ratio of 8×10^{-1}. When the mixture became homogeneous, 1 M nitric acid solution (~1 ml) was added immediately to set the pH to 3. Then the mixture was stirred slowly for 6 h then let stagnant for 16 h. Suspensions were filtrated and the solid was washed 12 times (to remove SDS), then particles were dried and ground. Composition of the nano-size particles is summarized in Table 6.1.

TABLE 6.1 Composition of the Nano-Size Particles in Weight % Determined by Elemental Analysis Based on the Nitrogen Element (on the Average of Three Measurements)

Samples	Alumina Content (wt.%)	Types of the MWCNTs	MWCNT Content (wt.%)	PPy Content (wt.%)	Charging Efficiency[a] of PPy (%)
p1	96.6	MWCNT-30	-	3.28	$3.7\pm5\times10^{-3}$
p2	77.9	LS NC7000	14.01	4.48	$2.1\pm4\times10^{-1}$

[a]Coulombic efficiency of PPy was derived from the voltammetry charging currents normalized to the surface of platinum working electrode and mass of measured samples (on the average of five measurements).

6.2.1.2 Preparation of paint coatings

Paint coatings were layered on standard low-carbon, cold-rolled steel panels (RS type CRS, roughness; 25-65 micro-inches, complying with ASTM A1008.1010, A-109 and QQS-698 standards) used as received from Q-Lab Ltd. Particles were dispersed by 20 min mortar grinding and milling in dissolved epoxy (at a polymer concentration of 50 wt.%).

The organic solvent was composed of 80:10:10 volume % of xylene (Fluka), 1-methoxy-2-propanol (Fluka) and 2-butanon (Aldrich). Suspensions of the particles were mixed with component A—stabilized zinc-rich masterbatch (HZO Farbenzinkstaub, Norzinco GmbH) in epoxy (Epoxidharz CHS141, bisphenol-A epoxy resin, Prochema). Component B—poly(amido amine) cross-linking agent (Durepoxy H15VP, USNER) was added to the suspensions, stirred to homogenize and diluted to get desired wet concentration. Primer coatings were roll-blade casted on steel panels in 90 μm wet thickness (35±5 μm dry thickness) and let cure for a week at room temperature. Top-coatings were layered on hardened epoxy in an overall wet thickness of 120 μm (80±5 μm dry thickness) with Macrynal SM 2810/75BAC hydroxyacrylic resin (CYTEC Industries Inc.) cured with aliphatic polyisocyanate resin: hexamethylene diisocyanate (Desmodur® N75MPA/X, Bayer Material-Science LLC) which was dissolved in the mixture of *n*-butyl acetate, xylene, and isobutanol (2:2:1). Coatings were let dry and cure for three weeks at room temperature. Scribes were made by a blade as X-cuts. Composition of the paint coatings is detailed in Table 6.2.

TABLE 6.2 Composition of the Hardened Paint Coatings

Coatings	Particles	Weight% and Volume Fraction of PPy in the Primer	Weight% and Volume Fraction of PPy in the Epoxy Vehicle	Weight% and Volume Fraction of MWCNTs in the Primer	Weight% and Volume Fraction of MWCNTs in the Epoxy Vehicle	Zinc
Z	-	-	-	-	-	90 (55.8)
H1[a]	**p1**	0.107 (2.8×10^{-3})	0.364 (3.9×10^{-3})	-	-	70 (25.8)
H2[b]	**p1**	0.060 (1.9×10^{-3})	0.301 (3.2×10^{-3})	-	-	80 (37.0)
H3[a]	**p2**	0.144 (3.8×10^{-3})	0.493 (5.3×10^{-3})	0.450 (5.3×10^{-3})	1.542 (7.3×10^{-3})	70 (25.8)
H4[b]	**p2**	0.079 (2.6×10^{-3})	0.408 (4.3×10^{-3})	0.245 (3.6×10^{-3})	1.275 (6.0×10^{-3})	80 (37.0)

[a]Nano-size particles were at 3.21 and 11.0 wt.% in the primer and the epoxy binder, respectively.
[b]Nano-size particles were at 1.75 and 9.1 wt.% in the primer and the epoxy binder, respectively.

6.2.2 Methods

6.2.2.1 Characterization of the nanotube and the nano-size particles

6.2.2.1.1 Elemental analysis

To obtain composition of the nano-size particles, elemental analysis was performed by a Vario EL *III* micro and macro CHNOS elemental analyzer (Elementar Analysensysteme GmbH, Germany) with about 4 mg sample. Data were used to derive information given in Table 6.1.

6.2.2.1.2 Electrokinetic potential

Zeta-potential characterization of the nanotubes was performed in water by Malvern Zetasizer Nano ZS equipment at a dispersed phase content of 4×10^{-2} M of carbon. Electrophoretic mobility of the particles was measured by Laser Doppler Velocimetry then Henry's equation was used to determine electrokinetic potentials based on the Smoluchowski approximation. The values of density (2300 kg m^{-3}) and refractive index (2.000) were used for MWCNTs, whereas refractive index (1.330), density (998.21 kg m^{-3}), and dynamic viscosity (1.002 Pas, at 20 °C) of water were used for calculations. Measurements indicated electrokinetic potentials of −17.6 mV of the pristine MWCNTs at pH of 6. Electrokinetic potential of the nanotubes with the applied quantity of surfactant and polyelectrolyte proved to be sufficient to stabilize dispersity of the mixture during preparation of the nanoparticles.

6.2.2.1.3 Cyclic voltammetry

Three-electrode cell configuration was applied for the electrochemical measurements. A platinum spiral ($A\approx13$ cm^2) and saturated calomel electrode (SCE) were used as counter and reference electrodes, respectively. A platinum disc working electrode (diameter of 13 mm) was incorporated in a Teflon tube. Pressed pellets of the particles were attached to the working electrode by a Teflon bracket and wetted with 0.1 M acetonitrile solution of sodium perchlorate (Aldrich) used as electrolyte for the measurements. PPy contents of the pellets were reduced at −0.4 V for 30 min, then voltammetry scanning was performed at a rate of 10 mV s^{-1}. Capacitive current transients are normalized to unit mass of the particles and the surface of working electrode. Prior to repeatability of the measurements and to avoid limitations in ionic mass transport, around 0.15 g of the samples was pressed with a maximum pressure of 250 kg cm^{-2}. Half an hour dwell-time preceded voltammetry investigation to ensure proper wetting and swelling of the sample pellets.

6.2.2.1.4 Fourier-transform infrared spectroscopy

PPy structure in the particles was investigated by Fourier-transform infrared (FTIR) spectroscopy using a Varian Scimitar 2000 FT-IR spectrometer (Agilent

Technologies, Inc., USA) equipped with a broadband Mercury Cadmium Telluride (MCT) detector and a "Golden Gate" attenuated total reflection (ATR) unit with diamond ATR element. 128 scans were coadded with a spectral resolution of 4 cm^{-1}. All spectra were ATR corrected using the Varian Resolution Pro 4.0 spectral handling software package.

6.2.2.1.5 Transmission electron microscopy

Powder form of the particle samples was crushed under ethanol and deposited onto copper grids covered by carbon supporting films. Transmission electron microscopy (TEM) data were acquired with a FEI MORGAGNI 268(D) microscope (FEI Co., The Netherlands) operated at 100 kV, with tungsten filament (top-entry; point-resolution = 0.5 nm).

6.2.2.1.6 Rheology

To obtain complementary microstructure information beyond TEM observations based on interaction, the particles dispersed with dissolved alkyd binder were studied by basic rheology study. Owing to the difference between statistical and kinetic percolation thresholds, particle concentration (3.846 wt.%) was set to inferior content ranges for series of samples in epoxy resin of the cured hybrid ZRPs. Three-dimensional (3D) distribution and interaction of the particles in dispersions provides valuable information on the structure of the particles in the dry and cross-linked organic binder that is relevant to interpret protection function of the hybrid coatings.

Measurements were done by a HAAKE RheoSress RS1 rotational rheometer (Thermo Fisher Scientific Inc., USA) equipped with a cone/plate sensor (2° angle, Ø 35 mm) used at a temperature of 25 ± 0.3 °C. After three days of swelling, particles were dispersed by half an hour mortar grinding of *n*-butanol and xylene (7:93) dissolved alkyd resin (distilled tall oil, SYLVATAL™ 25/30LT, Arizona Chemical, Gersthofen, Germany). Frequency and amplitude sweep tests were performed at a frequency of 1 Hz and the stress of 1 Pa, respectively. Between the stages of increasing and decreasing anisotropic mechanical load testing, steady rheology characterization with constant rate and stress dynamic measurements were carried out keeping deformation rate at 300 s^{-1} and applied stress at 200 Pa constant for 33 and 5 s, respectively. Composition of the colloid mixtures are presented in Table 6.3. Particle contents in the rheology-characterized mixtures were set to inferior amounts in epoxy binder of the coatings because kinetic percolation is measured at lower solid phase content than electrical percolation relating to statistical geometric arrangement of solid inclusions at the same dispersity.[62] This is because the volume exclusion effect of the highly anisotropic particles is more sensitively measured, and mobility restriction of dissolved polymer becomes more pronounced than 3D volume spanning electron conduction ability of the nanotube networks.[63,64] At the same aspect ratio (~10^2), nanotube volume fraction above the geometrical

TABLE 6.3 Volume Fraction (φ) of the Rheology Characterized Dispersions Containing the Nano-Size Particles in Dissolved Alkyd Resin at a Solid Phase Content of 3.846 wt.%

Particles	Alumina (φ)	PPy (φ)	MWCNT (φ)	Thixotropy[a] ($Pa\,s^{-1}$)	σ[a] (Pa)
D1	1.61×10^{-2}	1.32×10^{-3}	-	78,522	7.4
D2	1.30×10^{-2}	1.76×10^{-3}	2.45×10^{-3}	28,350	6.5

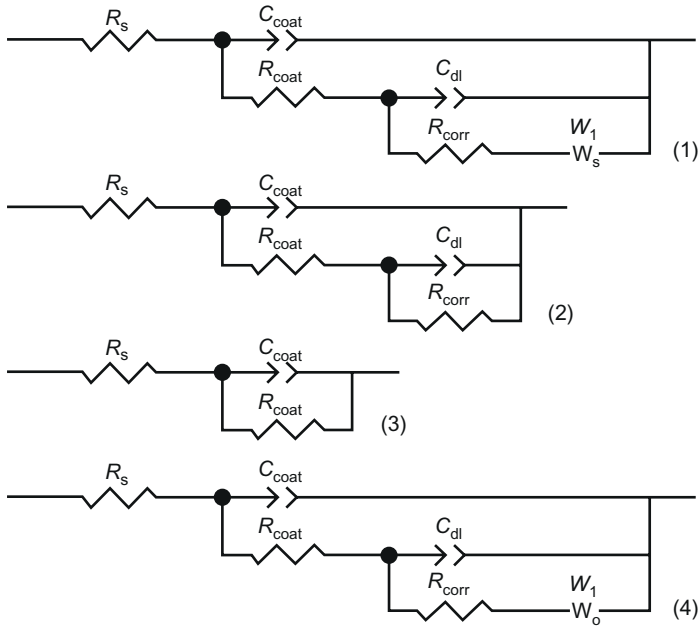
[a]Thixotropy index and yield stress were determined by constant rate and force mode measurements, respectively.

percolation threshold (~5×10^{-3}) is a semidilute dispersion, implying the onset of nanotube interactions.

6.2.2.2 Characterization of paint coatings and low carbon steel substrates

6.2.2.2.1 Electrochemical impedance spectroscopy

A platinum spiral, SCE, and glass-tube-fitted paint coatings covered steel panels ($A=5.3\,cm^2$) were used as counter, reference, and working electrodes, respectively. Immersion tests were performed with an electrochemical cell configuration proposed by Kendig et al.[65] which is known as "Rapid Electrochemical Assessment of Paints" method. The electrochemical cell and the Zahner IM6eX potentiostat-frequency analyzer (Zahner-elektrik GmbH and Co., Germany) were placed into two grounded Faraday cages wired to each other. OCPs were measured in an open cell configuration. Then impedance measurements were carried out in the frequency range of 10 kHz and 20 MHz applying sinusoidal perturbation of 20 mV. The most probable electrical circuits with the lowest number of discrete elements were used for modeling. In all cases, resistance of the electrolyte solution ($R_s=25\,\Omega$) was assumed to be the same for all samples as measured with bare steel electrodes by the same cell geometry. Equivalent electrical circuits (presented below) used for impedance fittings are referenced as follows: $R_s(Q_c(R_p(Q_{dl}(R_{ct}W_s))))$ (1), $R_s(Q_c(R_p(Q_{dl}(R_{ct}))))$ (2), $R_s(R_p(Q_c))$ (3), $R_s(Q_c(R_p(Q_{dl}(R_{ct}W_o))))$ (4). Coating (Q_c, denoted as C_{coat}) and double-layer (Q_{dl}, denoted as C_{dl}) capacitances were substituted and better described by constant phase elements because of some frequency dispersion, whereas pore (R_p, denoted as R_{coat}) and charge-transfer (R_{ct}, denoted as R_{corr}) resistances were coupled parallel according to the capacitive elements as shown in the circuits of (1-4). To describe semiinfinite and finite type mass transport processes (as detected during the time scale of investigation) taking place through some of the coatings and fit diffusion related tail in low-frequency region of the impedance data, open (W_o) and short (W_s) Warburg elements were used for fitting. Impedance fitting was performed with the 3.1c version of the Zview program (Scribner Associates, Inc.). Applied electrical circuits with data summarizing figures are listed in appropriate place of the results section.



6.2.2.2.2 Glow-discharge optical-emission spectroscopy

This technique was employed owing to its capability to detect elements in ppm quantities to have a clear overview on the effect of mass transport of the species found in the electrolyte used for the immersion test. The analysis was started with sample preparation; removal of the top coat by gentle polishing with emery paper (#600), leaving the epoxy primer intact (in a thickness of 40 µm). Elemental depth profiling experiments were performed using a GD-Profiler 2™ radio-frequency glow-discharge optical-emission-spectrometer (GD OES) instrument (HORIBA Jobin Yvon S.A.S., France). Samples were investigated under argon atmosphere at a constant pressure of 500 Pa. Prior to high sensitivity detection of the elements, sputtering was performed at a constant power of ~50 W. Settings were optimized to obtain ideal shape of the craters and acceptable resolution. Flushing time was 20 s, whereas the anode diameter was 4 mm. Depth profile data are presented over 40 µm of the primer coatings with an additional 20 µm sputtered depth in the steel substrates on average. Ion intensities were normalized to the maximum carbon intensity with the help of the intensity data from argon (Fi). Without standards of paint coatings and a well defined zinc-rich composition, depth-profile results with relative element intensities serve as a first-approach comparison before and after the immersion tests, whereas some of the element intensities were multiplied for the sake of comparison.

6.2.2.2.3 X-ray photoelectron spectroscopy

Although there are some limitations in the information provided by this technique due to the statistical manner of sampling and model based fitting evaluation results, this is a sensitive and very surface-specific detection method to provide valuable information on the presence, relative ratio, and chemical nature of the elements in the steel/coating interface. Immersion tested paint coatings on the steel panels were removed by three times of 5 min ultrasonication in the mixture of dichloromethane, methanol, toluene, and tetrahydrofurane (6:1:1:1). XPS spectra were recorded from the steel surface on a Kratos XSAM 800 spectrometer operated at fixed analyzer transmission mode using Mg $K\alpha_{1,2}$ (1253.6 eV) excitation. Pressure of analysis chamber was lower than 1×10^{-7} Pa. Wide scan spectra were recorded in the 100-1300 eV kinetic energy range, applying pass-energy (80 eV) in 0.5 eV steps with 0.5 s dwell time. High-resolution spectra of characteristic photoelectron lines of constituent elements, and the C1s region for carbon-containing layers were recorded at pass-energy (40 eV) by 0.1 eV steps with 1 s dwell time. Chemical states of the constituents were determined by XPS database.[66,67] Kratos Vision 2000 software was used for quantifications with experimentally determined sensitivity factors. Spectra were referenced to the energy of C1s line of polymeric or hydrocarbon type adventitious carbon set at 285.0 eV binding energy and, if it was applicable,to the Fermi edge (0.0 eV binding energy) of the iron substrate.

6.2.2.2.4 Immersion and salt-spray chamber corrosion tests

Immersion tests were carried out for 254 days with 1 M sodium chloride solution at room temperature, changing the electrolyte in a 42-day period. Corrosion tests were performed by a spray/prohesion/humidity cabinet (SF/MP/AB100, C+W Specialist Equipment Ltd., UK) installed with a Jun-Air (OF302, Gast Manufacturing Inc., USA) oil-free compressor. The 45 min cycles were divided into two phases. In the first 25 min, samples were exposed to salt fog combined with prohesion. Dosage rate of the sodium chloride solution (5 wt.%) was at 7 $cm^3 min^{-1}$. Temperature of the chamber was set to 35 °C, and the salt solution was heat up to 45 ± 3 °C. In the second phase, the temperature was held at 35 °C for 20 min without application of salt mist. Test cycles were repeated for 142 days. Evaluation of the corrosion propagated samples was made according to the principles of the EN ISO 4628:2005 standard.

6.3 Results

6.3.1 Investigation of the nano-size particles

6.3.1.1 Cyclic voltammetry

Cyclic voltammetry is able to reveal characteristic differences and minor changes in electrochemical activity of the intrinsically conducting polymers, including their

derivatives and composites. In addition, due to the mechanism of mediated electron transfer reaction, anodic corrosion inhibition function of the particle samples is strongly influenced by redox activity of PPy and conductivity of the nano-size particles regardless of its free-standing or supported form, applied as a stand-alone film or in composites—paint coatings. Therefore, particles were voltammetry tested, and the most representative scanning results are shown in Figure 6.1.

Moderate electroactivity of the PPy was noticed during investigation of the **p1**. The redox activity related capacitive current density well exceeded the double-layer capacitance and adsorption resulted background current measured with bare platinum electrode. The first capacitive current response and consecutive scanning gave similar curves with the location of oxidative peak potentials at –0.1 V, but much lower oxidative-reductive charges, indicating good electrochemical reversibility. The low and progressively decreasing current transients by sequential scanning and the low charging efficiency (Table 6.1) are due to the very low electrical conductivity of **p1**, containing the undoped semiconducting type polymer as a thin superficial layer on the alumina at the contents (~4 wt.%) of just around the percolation threshold in the sample.[68]

In case of the **p2** powder sample, orders of magnitude greater than anodic-cathodic capacitive current transients were measured not just as first scanning but as consecutive curves, which reflect far higher electrical conductivity. Oxidation peak potentials were easily recognized at 0.0 V, but reduction peak potentials could only be scarcely identified at –0.35 V, meaning noticeable electrochemical revers-

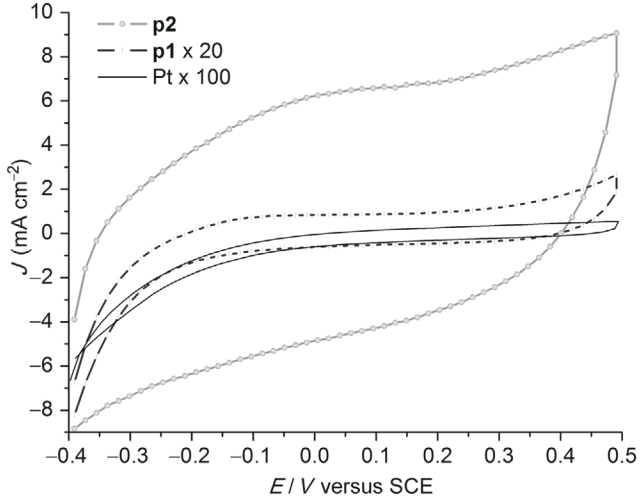


Figure 6.1 Cyclic voltammmograms of the PPy modified alumina (**p1**) and the PPy modified alumina/MWCNT (**p2**), and base current measured with the bare platinum working electrode (Pt).

ibility of the PPy content. The voltammogram is less affected by the lower ohmic potential drop during the measurement as a consequence of high conductivity of the sample. This is due to the geometrical, statistical percolation of the MWCNTs and so the result was electrical percolation in the **p2** at MWCNT content of 14 wt.%, whereas the onset of electrical percolation was found at 9 wt.% nanotube contents. The transient profile and the scale of capacitive currents with coulombic efficiency of $2.1 \pm 3 \times 10^{-1}$ at low relative amount of PPy manifest altogether mediocre electrical conductivity of the partially doped PPy, supported partly by the PSS modified nanotubes. Shift of the peak potentials compared to neat and alumina supported PPy is partly attributed to a greater extent of conjugation and less electron deficient state of the PPy because of the high relative amount of the nanotubes and effective electron transfer from them. However, hindered charge mobility through the network is connected to the sterical structure of PPy deformed by PSS, causing limited conjugation in the polymer segments. This is because the low amount of homogeneously dispersed nanotubes was modified with large amount of immobile PSS complexed PPy film, and the polyelectrolyte limits the extent of conjugation in PPy by distortion and conformational adjustments leading to energy barrier to slow down electron conduction.[69]

6.3.1.2 Fourier-transform infrared spectroscopy

In Figure 6.2 FTIR spectra of the nano-size particles are compared to each other and the free-standing PPy samples prepared in water (PPy1) and aqueous ethanol (PPy2). In the PPy1 spectrum the characteristic bands of PPy are found at 1528 and 1467 cm^{-1} corresponding to the νC–C and νC=N stretching vibrational bands of the pyrrole ring (arrows), respectively, while the bands at 1285 and 1142 cm^{-1} belong to the C–H deformations.[70,71] The weak, but well-defined band at 1093 cm^{-1} corresponds to the in-plane deformation mode of NH_2^+ of protonated PPy backbone.[72] In case of the PPy2, a doublet at 1554 and 1531 cm^{-1} in the C–C stretching region was identified, which was attributed to the combination of intra-ring C=C and inter-ring C–C stretching vibrations.[73] Furthermore, slight blue-shift of the peaks suggests a more compact 3D structure of the PPy2. As for the alumina supported PPy (**p1**), spectral features of the polymer film changed. The new bands at 1634 and 1340 cm^{-1} are assigned to the deformation vibration modes of protonated species, NH_2^+ of doped PPy. The broad, intensive band around 1120 cm^{-1} corresponding to the C–H in-plane deformation vibrations suggest a compact 3D structure of the thin polymer film. The blue-shift of C=C/C–C inter and intra-ring vibration (arrow) can also be explained by enhanced electron delocalization in the PPy segments.[74]

In the spectrum of MWCNT incorporated particles (**p2**), the main C=C/C–C band of PPy inter- and intra-rings around 1550 cm^{-1} (arrow) is slightly blue-shifted compared to the one of the neat polymer (around 1530 cm^{-1}).[46] Supramolecular

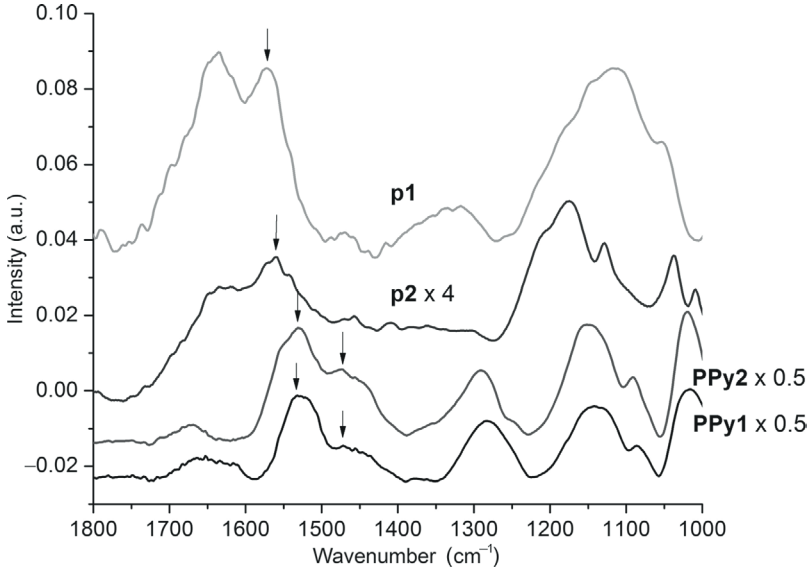


Figure 6.2 FTIR spectra of the PPy modified alumina (**p1**) and the PPy modified alumina/MWCNT (**p2**) samples with the spectra of neat PPy prepared in water and aqueous ethanol mixture (**PPy1** and **PPy2**).

assembly is partly accounted for the effect, leading to more efficient, enhanced electron delocalization along the PPy network. However, suppressed C–H deformations at 1294 and 1047 cm^{-1} suggest a coplanar (characteristic) structure of the PPy segments throughout the backbone. Blue-shifted bands (at 1575 and 1220 cm^{-1}) agree with the deprotonated state of the PPy,[75] resulting in moderate electrical conductivity but good electroactivity based on high redox activity and reversibility of the polymer. Typical thin PPy film structure is indicated by the low intensity bands of –C–H in plane bending and C–N stretching at 1038 and 1173 cm^{-1}, respectively. As to the PPy/PSS complexes, lower PPy bands intensities were detected and partial incorporation of the PSS into PPy modified nanotubes-alumina was evidenced by the PSS bands in the spectrum. Despite the masking phenomenon of S=O bands at ~1220 cm^{-1}, a well-defined νC–N stretching band was detected at 1180 cm^{-1}, which is in connection with the PPy conductivity mechanism undergoing via electron hopping by bipolarons near N–C bonds.[76] No sign of oxidative degradation, that is, the presence of carbonyl bands in the spectrum, was detected.

6.3.1.3 Transmission electron microscopy

In Figure 6.3a–f, TEM images of the nano-size particles are presented. Figure 6.3a depicts the loosely aggregated flocs of the alumina-supported PPy particles at submicron-scale, interacting through moderate spatial density of interlinks at micron-scale. The

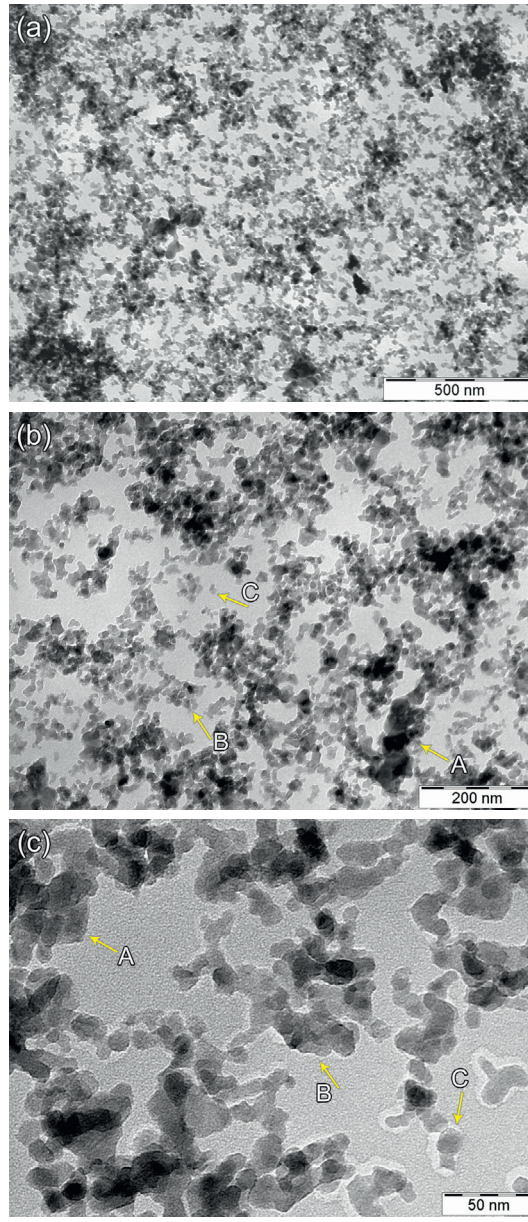


Figure 6.3 TEM images of the (a–c) PPy modified alumina (**p1**) and

(Continued)

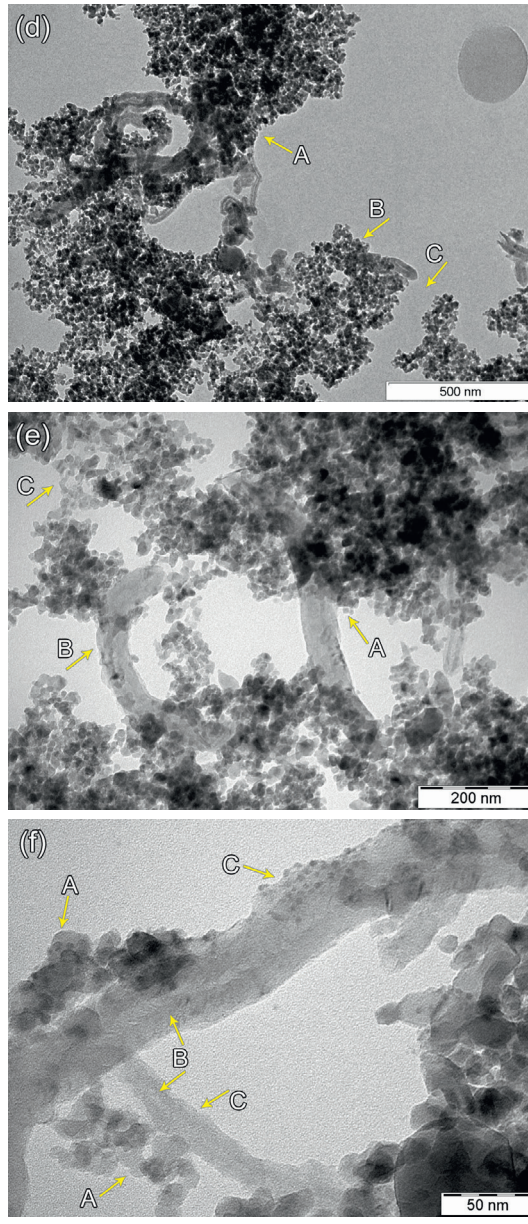


Figure 6.3, cont'd (d–f) the PPy modified alumina/MWCNT (**p2**) particles.

highly and evenly dispersed particles exhibited markedly extended interparticle interactions, infinite association, and 3D cluster formation of the particles (**p1**). By taking observation at higher magnification (Figure 6.3b), the reason for the well-dispersed and associated distribution of the particles became obvious. PPy modification of alumina leads to a minor proportion of coalescencelike aggregation of the particles (arrowed by A), the majority of bridging type—loosely aggregated particles (arrowed by B) and some fraction of almost individually dispersed particulates with thin PPy film coatings. The latter ones were core-shell type particles (B and C) that were merged to give globularly structured multiphaselike structures (A) found in moderate proportion around the size range of 200 nm with weak tendency toward agglomeration. The complete coverage with thin PPy film could be well observed (Figure 6.3c), and size distribution of the aggregates showed smaller contribution around 200 nm (A), predominant fraction at 100 nm (B), and much smaller proportion below 100 nm (C).

As it is shown in Figure 6.3d, the nanotube incorporated sample indicated much lower dispersity, more pronounced aggregation (A) of particles (**p2**), and loosely assembled arrangement on micron-scale (B) with finite size of aggregated particle-floc interactions (C). The PPy modified alumina was partly strongly (Figure 6.3e, A) and less coherently (B and C) aggregated with the nanotubes, but not evenly distributed along the MWCNTs (B and C). However, the nanotubes were almost evenly dispersed and their filaments supported microgel flocs with extended 3D interconnection of the particulates with low spatial density. PPy deposition resulted in reversible aggregation and some degree of coalescence of the alumina (Figure 6.3f, A) around the MWCNTs (B) but all of the alumina and nanotube support was completely covered with thin polymer film (C). Large-scale aggregation of the **p2** compared to the **p1** is due to the codeposition of PPy/PSS complexes causing a double-flocculent effect. The **p2** sample is regarded as a nonuniform, inhomogeneous particle composed of anisotropic filaments and nano-size isotropic particles in the form of randomly distributed submicron voluminous island-like arrangements. Although cluster topologies and dispersibility of the **p2** was far inferior to the **p1**, its electroactivity allows effective improvement of galvanic function of the ZRPs with zinc contents lower than critical PVC, while the **p1** type particulates can only facilitate inhibition of the sacrificial metallic pigments and may enhance the barrier nature of the paint coatings.

6.3.1.4 Rheology characterization of dispersion of the nano-size particles

Dynamic measurement results are presented in Figures 6.4a and b. Strong viscoelastic response of dispersion of the **p1** (**D1**) is revealed by the high storage and the lower loss moduli over a wide-frequency domain (Figure 6.4a). Pseudo-solid flow behavior is associated with the medium spatial density interlinked, coherent microstructure of the sol. The elastic-viscous transition with an intersection at ~3 Hz

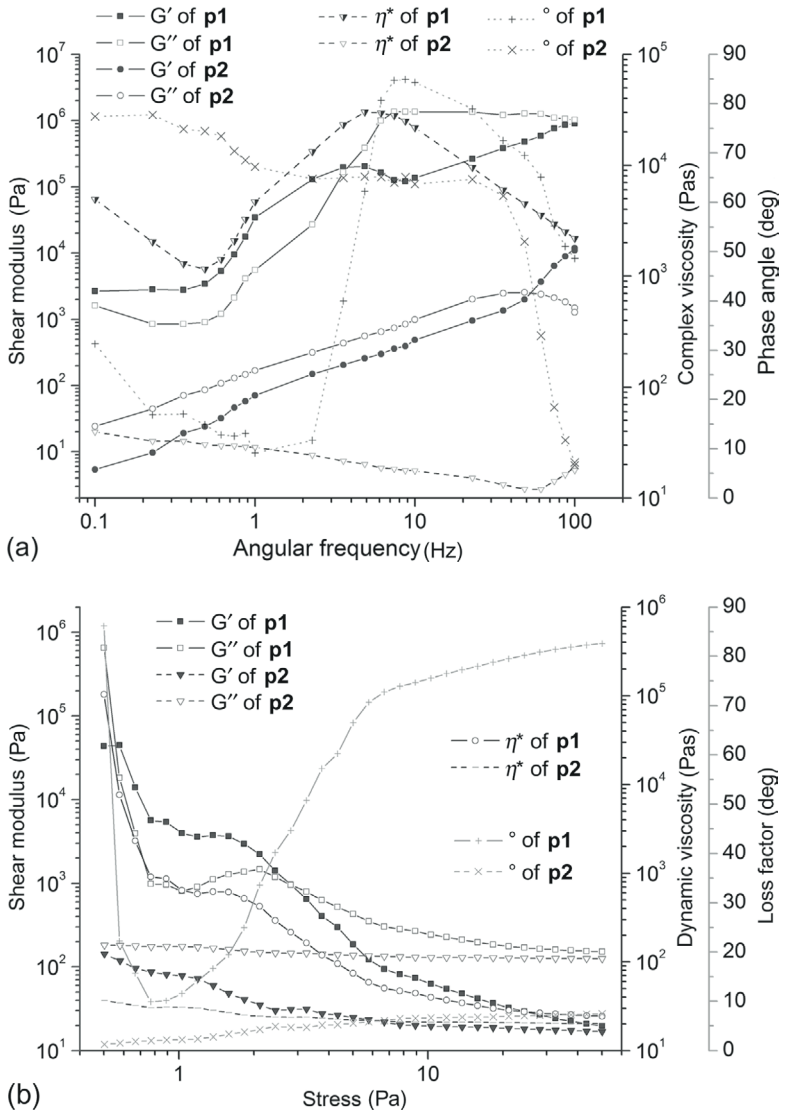


Figure 6.4 Dynamic rheology test of particle dispersions: (a) frequency and (b) stress sweep results measured at a stress of 1 Pa and the frequency of 1 Hz, respectively.

reflects moderate stress-induced deterioration of the 3D associated colloid system. The steeply increasing loss factor also indicates such a quasi-solid and viscous transition. Considerable ramp in the complex viscosity is attributed to the large extent of interparticle interactions of the highly dispersed filler phase. The plateau between 10 and 100 Hz in the loss factor supports moderately high strain rate yielded deterioration in the colloid structure.

The amplitude sweep test revealed two stages of stress-activated attrition in the macro- and microgel structure of the **D1** along with elastic-viscous transition signified by intersecting storage and loss moduli at 10 Pa (Figure 6.4b). The former is connected to the less extensively interlinked floc system and moderately coherent association of the particles within the microgel flocs, whereas the latter is most probably in accordance with the stress amplitude (critical stress level) induced collapse of the coherent pseudo-solid gel system. However, decreasing complex viscosity confirms effective shear-induced reorientation, disruption of 3D particle associations.

As for the **D2**, the wide angular frequency range constant ramp of low storage and somewhat higher loss moduli besides the high phase angle in the loss factor over wide range mean a viscous flow characteristic with the absence of effective 3D particle associations and coherent microstructure of the colloid system. Nonetheless, the intersection of moduli at 50 Hz and the sharply decreasing phase angle unanimously reveal a transition from sol to gel behavior that is associated with the straining caused structure build-up, loose and low spatial density interaction of the microgel flocs in the dispersion. This is confirmed by the stress sweep test that indicated out-of-range intersection of ~0.4 Pa.

The lack of hydrogen bonding between alumina and the dispersant led to inefficient interfacial interactions. So, hydrated alumina repels much of the alkyd matrix, since insignificant rheology control of unmodified alumina is connected to the weak van der Waals forces between the solid and the vehicle. Thus, Newtonian flow of dissolved vehicle and its dispersion with bare alumina gave constant complex viscosity with wide range linear ramp of storage and loss moduli associated with rapid relaxation processes. Greater loss and lower storage moduli evidenced viscous flow characteristic due to the lack of association of unmodified alumina and coherent microstructure of the colloid system. High surface/volume ratio and dispersity of the alumina led to increased hydrodynamic resistance, greater volume exclusion effect of the nano-size filler. Therefore, remarkable interfacial forces in the **D1** are obviously related to the thin film PPy content interacting effectively with the lipophile matrix because of the match of solubility parameters.[77] Enhanced interfacial attractive forces between the liquid phase-dissolved polymer matrix and the highly dispersed particles are responsible for the high mobility restriction of the polymer segments and the effective load transfer related massive flow resistance.

Constant rate and stress load results are shown in Figure 6.5a and b, whereas creep test data are presented Figure 6.5c. In case of the visco-elastic type **D1**, the high strain rate domain located large hysteresis and the different slope of shear-thinning effect are connected to the various strength and scale of particle associations and rearrangements (Figure 6.5a). The high forward (fw.) and backward (bw.) apparent dynamic viscosities at all strain rates leading to considerable thixotropy index mean moderate reorientation rate of the particles and

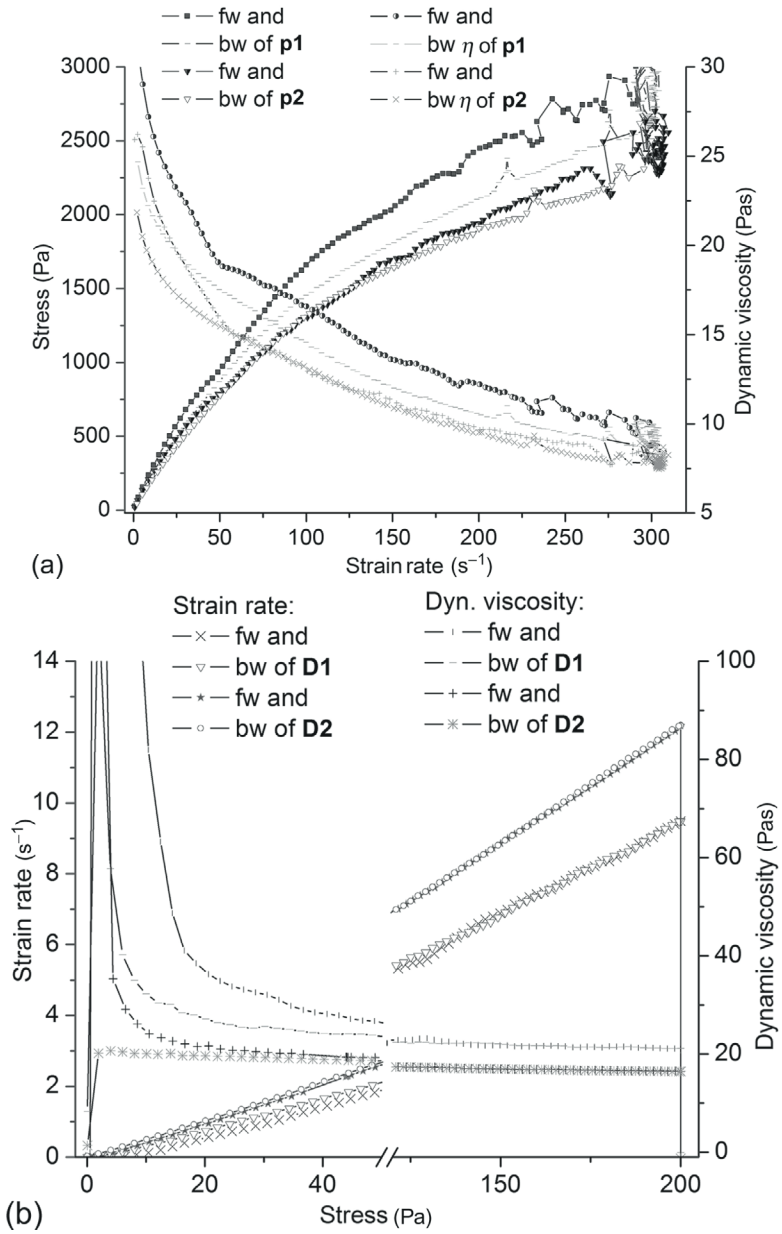


Figure 6.5 Steady rheology test of particle dispersions: forward (fw) and backward (bw) test results; (a) the applied shear stresses, (b) strain rates, and

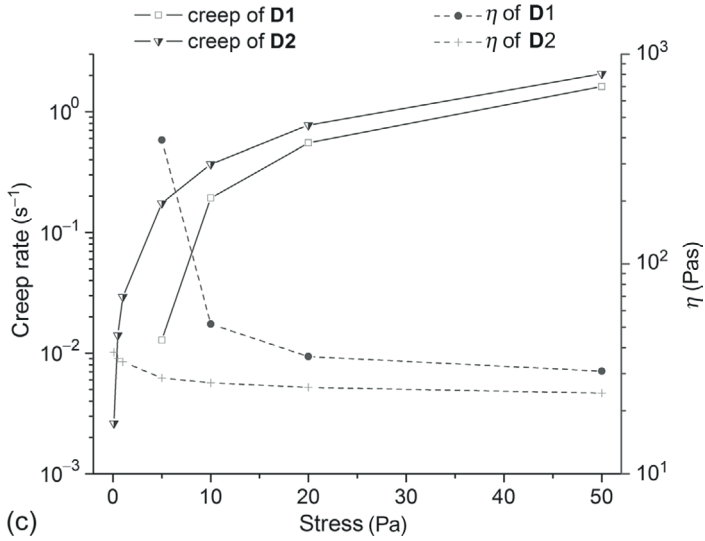


Figure 6.5, cont'd (c) creep rates along with the apparent dynamic viscosities.

slow recovery of the colloid structure. Besides the large thixotropy, continuous shear-thinning is connected to increasing deterioration and disruption of the interlinked flocs with subsequent gradual floc attrition-activation of bridging and coalescence aggregated or flocculated particles. Nevertheless, all interparticle interactions seemed to diminish with durable straining at high rates, leading to complete disruption of the microgel floc system which was indicated by the asymptotic hydrodynamic flow resistances at the heist rate (the same was measure to the alumina dispersion). The high yield stress (Figure 6.5b) and the remarkable creep resistance at low stress loading (Figure 6.5c) suggest a highly interlinked floc system, well-interacted microstructure of the highly dispersed **p1** particles (featuring high, effective volume fraction).

As for the rather visco-plastic type **D2**, the high shear-thinning in a pseudo-plastic viscous way suggests fast rotational orientation of the nanotube filaments with low hindrance to relax and build up (Figure 6.5a). Moderate thixotropic nature (28,350 Pa s^{-1}) and the lower yield stress (6.5 Pa, Table 6.3) also support the idea of rapid relaxation and fast reorientation of the nanotube-loaded **p2** particles. Apparent viscosities were high despite volume fraction of the nanotubes with an average aspect ratio of 100 were under the rheology percolation threshold at volume fraction of 7×10^{-3},[78] in the semidilute regime of the bare MWCNTs. Furthermore, fast rupture of floc interactions (slow recovery) and the gradual minor attrition of anisotropic filaments (faster recovery) are concluded along with a mediocre particle dispersity and the resulted less effective load

transfer, low stress threshold-resistance to yield to flow and creep (Figure 6.5c). In dispersions of the **p2** type particles with lower relative amount of the nanotubes (between 8.5 and 14 wt.%), no effect of infinite cluster formation, geometrical (statistical) or kinetic percolation of the nanotubes and their filamentous particles but high thixotropicity was experienced by all measurement methods. So, electrical percolation of the **p2** by its higher relative MWCNT content is suggested to transfer into statistical and kinetic percolation threshold measured by rheological methods.

6.3.2 Investigation of the paint coatings and steel substrates

6.3.2.1 Immersion test with EIS monitoring

OCP and impedance data acquired during the immersion test are presented in Figure 6.6a and b–f with assessment of the samples summarized in Table 6.4. Based on the evaluation of impedance data, fitting parameters of discrete elements of the most probable electrical circuits are given in Figures 6.7 and 6.8. The traditional type zinc-rich **Z** coated steel panel exhibited mixed potentials below –0.9 V over the first half of the test (~3000 h), which means stable and viable galvanic function of the primer, cathodic polarization of the steel surface, and thermodynamic immunization protection of the steel substrate against corrosion. However, this should partly mean inefficient corrosion inhibition of the substrate by the interfacially precipitating corrosion products. This long-term stage of active protection was allowed by the highly porous primer and the intense anodic action of the zinc. Weak barrier nature of the **Z** is reflected by the small and decreasing impedance moduli besides the high low-frequency phase-angle minimum and breakpoint frequencies shifting toward the high-frequency range (Figure 6.6b), which is a consequence of inefficient pore-blocking effect. After an initial deactivation at 552 h, continuous drops in the impedance moduli correlated with the slowly anodic shifting OCPs. Uniform surface polarization, partially diminishing galvanic function of the **Z** became obvious after

TABLE 6.4 Evaluation of the Immersion Test Results

Coatings	Degree of Blistering Size and Density	Degree of Delamination	De-Adhesion of Coatings
Z	2 (few)	Considerable	Inhomogeneous
H1	0 (none)	None	-
H2	0 (none)	Complete	Homogeneous
H3	0 (none)	None	-
H4	1 (few)	Slight	Inhomogeneous

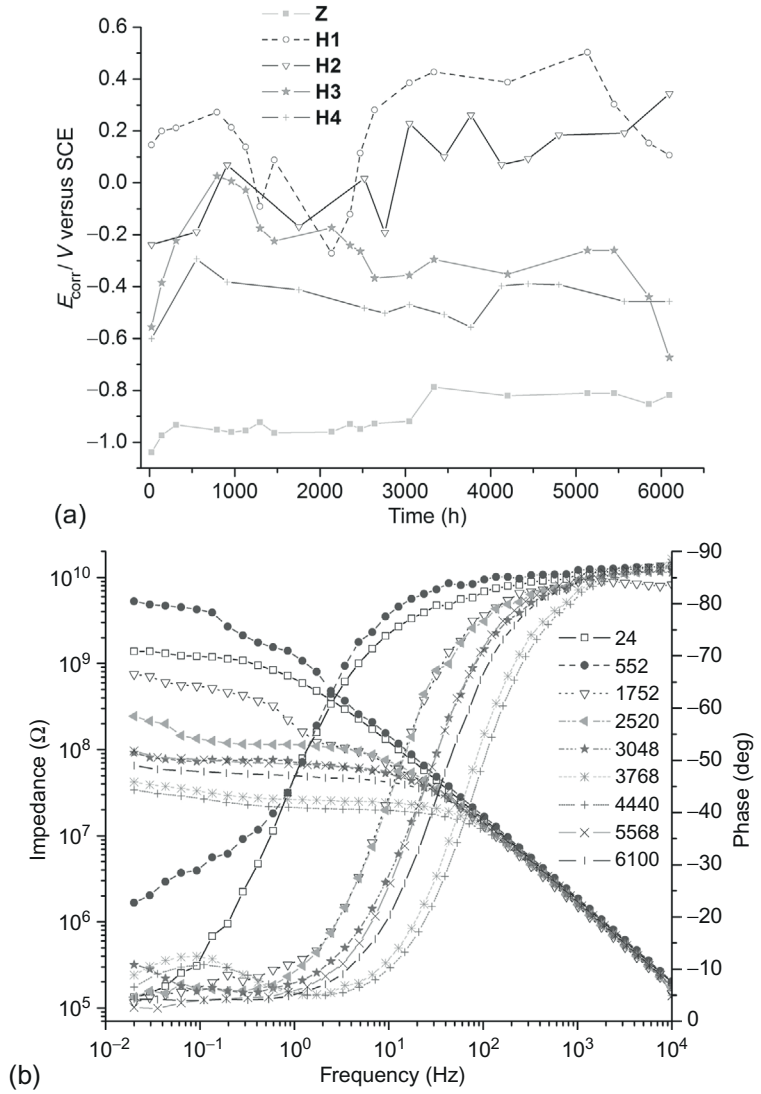


Figure 6.6 Immersion test: (a) corrosion potential and (b–f) electrochemical impedance spectra (in Bode representation) of steel panels coated with the zinc-rich **Z** and the **H1-H4** hybrid coatings.

(Continued)

3000 h, whereas evolving some mechanical blockage and recoveries of the barrier nature could be identified at 552, 4800, and 6100 h of immersion. Intense sacrificial and self-corrosion of part of the zinc pigments (around 30%) was appointed by cross-sectional SEM observations, finding corroded phase at grain boundaries. Thus, intense sacrificial action of zinc led to high rate of oxygen reduction reactions and

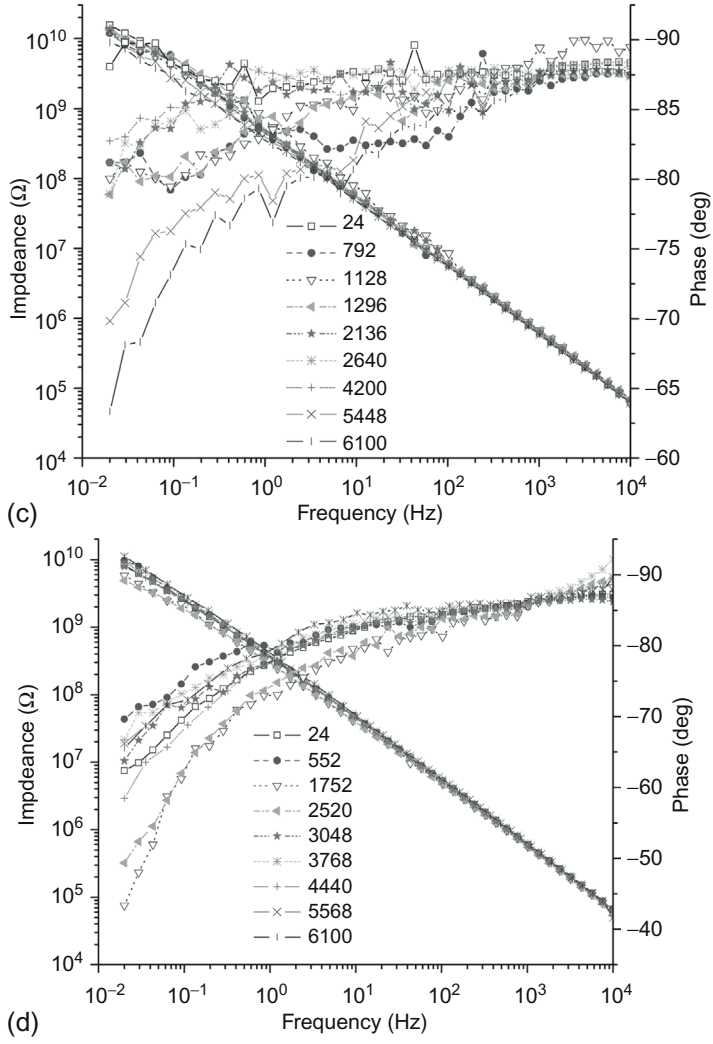


Figure 6.6, cont'd

obviously the evolution of strongly alkaline milieu especially at the interface. So, the primer severely delaminated relating to oxidative degradation,[79,80] and saponification of the binder, no macroscopic corroded spots were detected on the steel surface. Interestingly, some degree of cathodic protection was even available at 6000 h, obviously in inhomogeneous lateral distribution as corrosion potential of the system remained around –0.8 V, which is considered to be a threshold to provide enough anodic current output for cathodic immunization of steel substrates (under fairly protecting barrier coatings) even in performance demanding circumstances.[81]

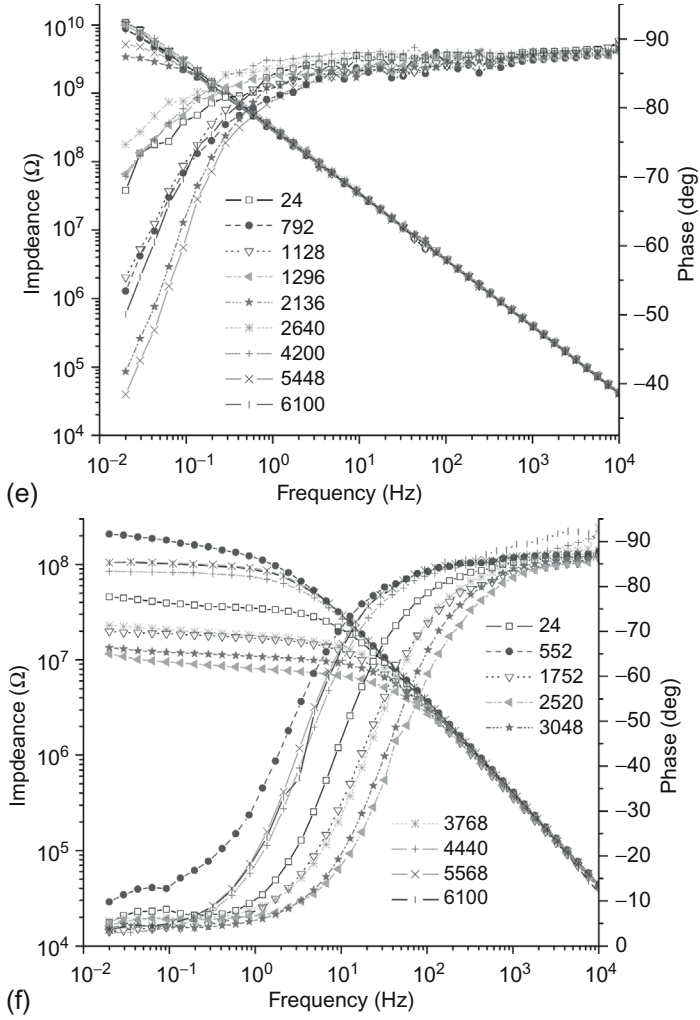


Figure 6.6, cont'd

The OCPs between 0.2 and 0.3 V and the high impedance moduli (Figure 6.6c) signify markedly slow initial activation by the electrolyte, evidencing a very efficient barrier character of the **H1** lasting for around 1500 h. These data suggest significant resistance control of the coating (unfortunately masking the corrosion potential) besides a remarkable shrinkage in the specific anodic area of zinc. Although some activation of the primer and its zinc content with a highly restrained galvanic action are thought to take place based on the OCP having shifted to around –0.3 V

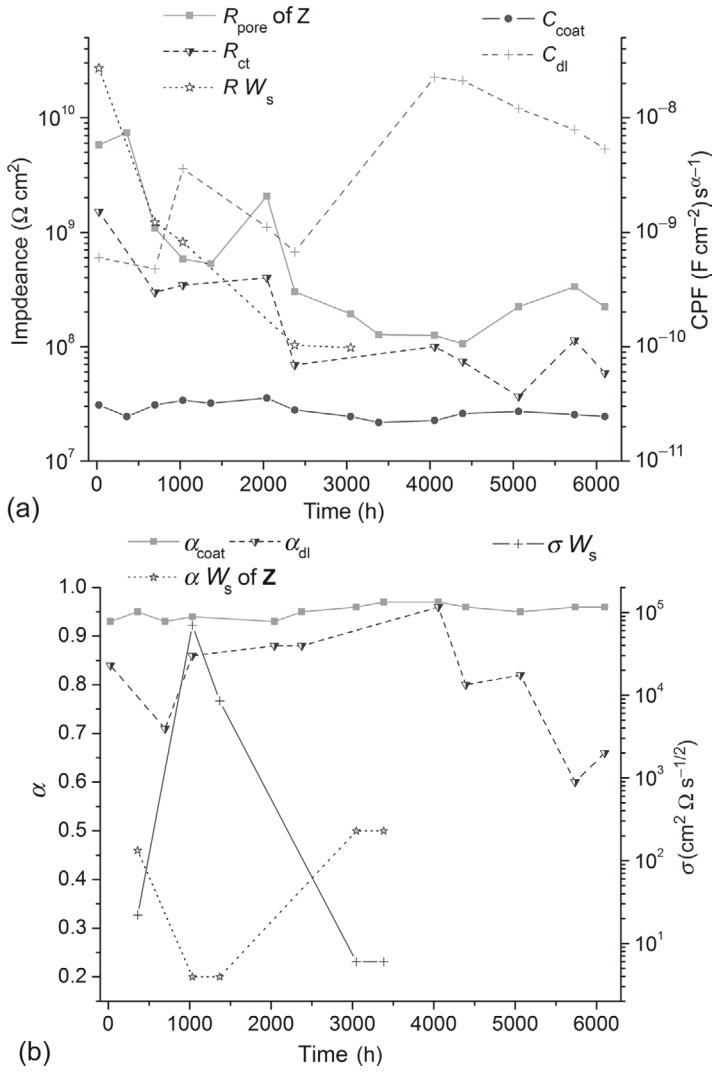


Figure 6.7 Fitting results of the impedance data acquired in immersion test of (a and b) the traditional type zinc-rich **Z**. The following modeling equivalent electrical circuits were used for impedance fittings: $R_s(Q_c(R_p(Q_{dl}(R_{ct}W_s))))$ (1), $R_s(Q_c(R_p(Q_{dl}(R_{ct}))))$ (2).

at the time of 2000 h, it should not be considered as a capacitive feature of the coating. Accordingly, the impedance spectra revealed ignorable changes in the inbound mass transport regime, that is, electrolyte infiltration processes. The wide range of nonideal capacitive phase response is attributed to the nonperfect geometry of the measuring cell with its inhomogeneous current distribution and the uneven coating surface both at the primer/top coat and the top coat/solution interface. After a minor activation at 2000 h, durable passive protection by the **H1** coating seemed to recover

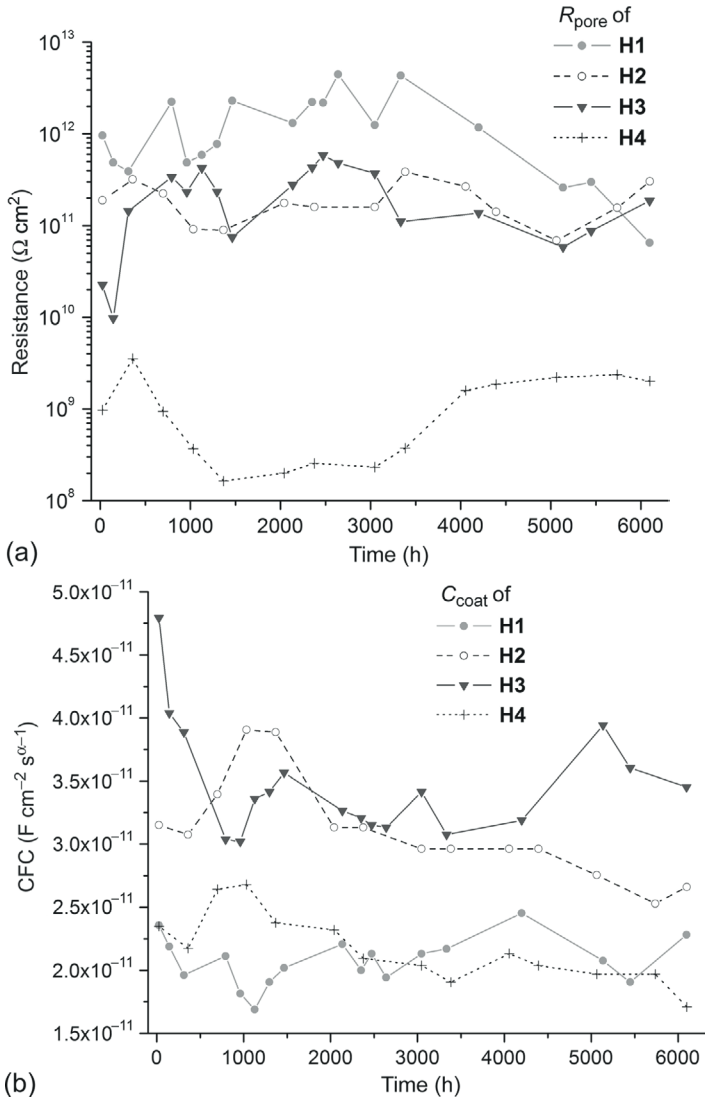


Figure 6.8 Fitting results of the impedance data acquired in immersion test: (a–c) the **H1-H4** samples and (d and e) parameters of the second parallel circuit elements modeling the **H4**. The following equivalent electrical circuits were used for impedance fittings to the **H1-H3**; $R_s(Q_c(R_p))$ (3) and to the **H4**; $R_s(Q_c(R_p(Q_{dl}(R_{ct}W_o))))$ (4).

(Continued)

at ~2400 h of the immersion and lasted for over 3000 h, owing probably partly to the very low amount of accumulation of corrosion products. Remarkable anodic shift of the OCPs to around 0.4 V and the considerable resistance control (above $10^{10}\,\Omega\,cm^2$ by the coating) mean very low rate of oxygen reduction reaction undergoing at the steel substrate acting as an oxygen electrode as it was given by Evans.[82] It was pointed

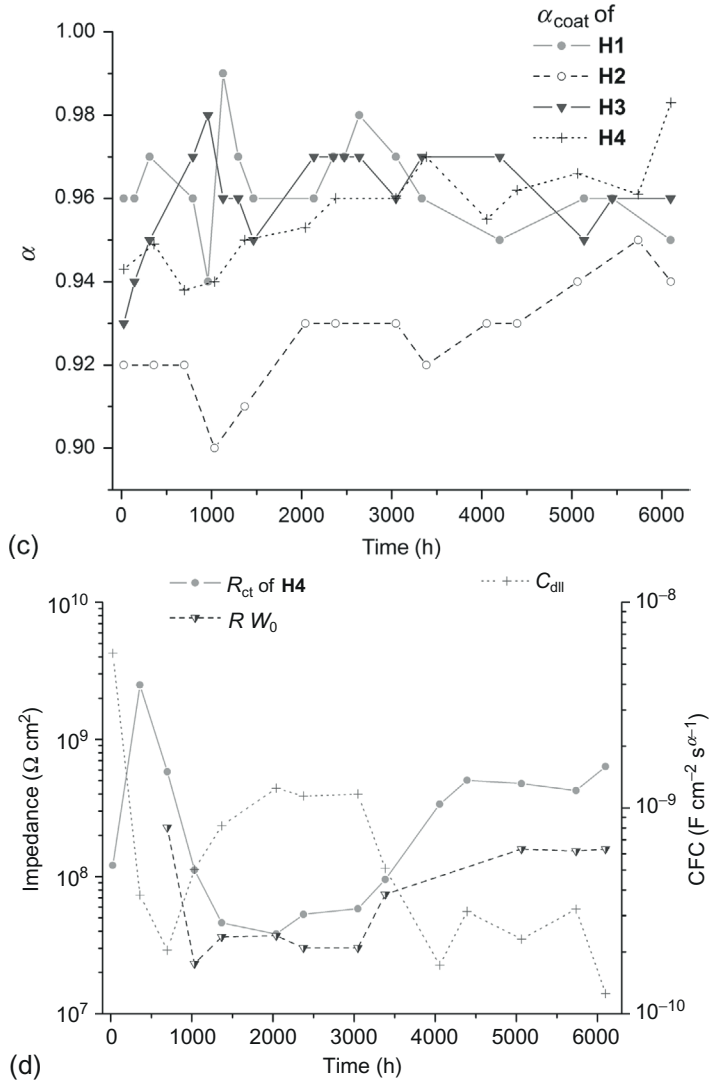


Figure 6.8, cont'd

(Continued)

out that corrosion potentials and oxygen reduction on passive films of metal oxides and thermal oxide electrodes occur at 0.4 V and in galvanic coupled cases at 0.2 V versus SCE.[83] In comparison with the initial state of the primer, it means notably small active anodic areas and low rate of zinc dissolution. However, the firm barrier nature of the **H1** seemed to deteriorate at 5000 h when OCPs turned to change to the cathodic direction and decreasing low-frequency impedance was accompanied with

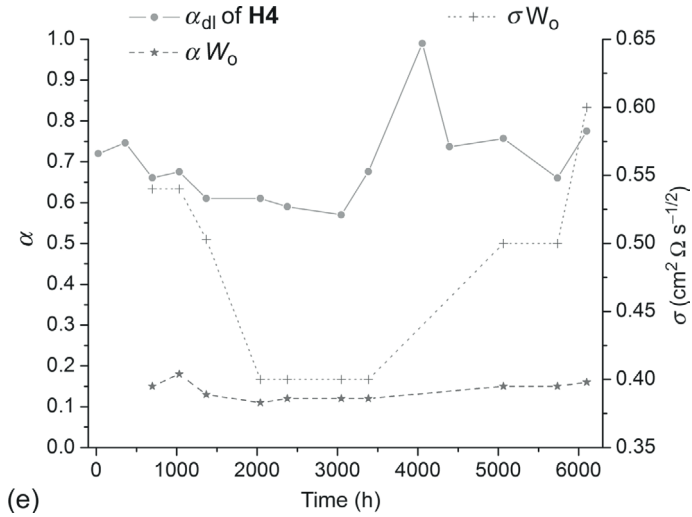


Figure 6.8, cont'd

increasing low-frequency phase-angle minimum. According to the robust passive character, no impact of the corrosion processes such as delamination, blistering, and steel rusting were experienced.

Similar function of the **H2** coating was noticed based on the slightly fluctuating but continuously increasing corrosion potentials and the durable highly resistive behavior (Figure 6.6d). A slightly altered protection characteristic of the **H2** hybrid (with some similarities partly to the **Z** and the **H1**) is recognized both in the corrosion potential pattern and impedance data as a function of time. The measurement of more anodic OCPs at ~1000, 3000, and 4000 h all coincided well with the increasing capacitive nature of the coating, giving bit higher impedance amplitudes and a lower phase minimum in the low-frequency domain. Steady changing tendency of the OCPs toward the more anodic range supports the idea of progressively restrained anodic action of zinc (decreasing active surface) and galvanic function of the coating. Impedance spectra revealed coating activation at 1752 and 2520 h by the increasing low-frequency phase-angle even though impedance moduli remained practically unaffected, suggesting a minor proportion access by the penetrating electrolyte-slightly increasing volume and area of pores in the primer. In comparison with the **H1**, the more frequent activation and recovery of the coating can probably be attributed to the short-term pore-filling action by the smaller amount of accumulating corroded species in a bulk phase of the primer which should be hardly leachable. In addition, as almost the same strongly anodic shifted corrosion potentials were measured with lower resistance control in the case of **H2** compared to **H1** in the end (as a convergence), which obviously suggest more effective corrosion inhibition at the steel surface by the precipitating and insulating corrosion products and which

should also mean the absence of evolution of alkaline milieu in the interface with an altogether low rate of oxygen reduction reaction. As a result, no corrosion spots on the steel surface could be detected (Table 6.4). Nevertheless, some oxidative deterioration might as well happen owing to complete delamination of the coating. This cathodic delamination phenomenon is in agreement with the interfacial electron transfer reactions undergoing even under firm barrier coatings as it was experienced to neat epoxy-top coated system. So, the highly dispersed PPy-coated alumina particles based primers provided efficient passive protection, long-term mechanical blockage besides the lack of evidence of cathodic protecting functionality in immersion tests.

In case of the **H3** loaded with nanotube incorporated particles (Figure 6.6e), the OCP and impedance changes evidenced efficient barrier characteristics and some cathodic function in the early activation up to ~400 h and the latter steady periods from 2500 h. Considerable passive protection is well reflected by the high impedance amplitudes over the entire test along with the low phase minimum (between −75° and 55°) either in the early and the late period of the test or the location of breakpoint frequencies in the low-frequency domain (over ~1 Hz) measured in the medium and late periods. The somewhat decreasing impedance moduli up to ~1300 h are related to very fast activation and blockage of the coating accompanied with anodic shifting corrosion potentials. As electrical percolation of the coating relies on the medium dispersed **p2** particles (with far nonpercolating micron-size isotropic zinc), the nanotube supported filaments provide interconnections between both the zinc grains and the steel substrate. The insulation at spanning clusters seemed to slowly diminish as OCPs turned changing in steps toward the cathodic range at 1500, 2500, and 5500 h, ending in a suppressed cathodic potential of −0.7 V. All these stages were followed with minor recoveries in the barrier function, which were highlighted by the more capacitive coating nature at ~1300, 2600, and 6100 h besides the slight anodic changes in the OCPs. The most efficient pore-blocking action was identified at around 2600 h probably resulting in improved cathodic function of the coating. This means some shrinkage in the active anodic surface of the sacrificial pigments in bulk phase of the primer but remaining electrical connection at the steel/coating region causing relatively high oxidative degradation of the epoxy binder in the interface (see Section 6.3.2.3).

Similarly to the **Z**, the **H4** coating led to the evolution of well stabilized corrosion potentials initially at −0.4 V until ~2000 h, −0.5 V up to 3500 h and −0.6 V till ~4000 h. Based on the corrosion potential changes, moderate variations in the coating state are thought to take place at 500 and 4000 h. From 4000 h to the end of immersion test, OCPs remained −0.4 and −0.5 V. Impedance data indicated recoveries in the barrier function; a short-lived evolution at ~550 h and a prolonged one from 3000 h lasting to the end (Figure 6.6f). The first is attributed to a minor coating deactivation by the pore-filling corrosion products, which was followed by moderate extent of electrolyte infiltration over the next 2500 h. Rest of the term from 3500 h

was recognized as partial inhibition and passive protection by the precipitation of corrosion products both at the coating/steel interface and bulk phase of the primer. The stable OCPs around –0.5 V suggest moderate electrical interaction of the zinc facilitated by the nano-size particles, resulting in restrained galvanic function and some degree of cathodic protection. The small second time-constant at 0.1 Hz until ~550 h manifests redox reactions taking place at continuously decreasing proportion of the steel surface. Both the **H3** and **H4** coatings exhibited very good condition without blistering. No cohesion or adhesion loss of the **H3** was experienced, whereas only minor de-adhesion of the **H4** was noticed, hinting on the low rate (or short-term) and small extent (inhomogeneous) distribution of interfacial electron transfer reactions leading to partial cathodic delamination failure. Interestingly, no sign of precipitated zinc corrosion products at grain boundaries was found in cross-section of the **H3** and **H4** hybrid primers by SEM observations.

By analyzing impedance data based on the applied modeling circuits, pore resistance of the **Z** decreased until 4500 h in a similar way to the charge-transfer resistance with an absolute minimum around 5000 h (Figure 6.7a and b). Coating capacitance was found slightly affected but mostly following coating resistance changes in a reversed manner as a function time in accordance with our expectation. This was parallel with the continuously decreasing resistance of the finite diffusion element, indicating less hindered mass transport through the coating (represented in the low-frequency domain) whose effect on the impedance spectra could be identified up to 3500 h. Halved exponent of the Warburg element and by several orders of magnitudes greater diffusion coefficient between around 1000 and 1300 h are interpreted as more hindered mass transport of the electrolyte, which is typical porous diffusion through coatings. Interestingly, it did not translate into much greater coating capacitance, but found coincided with markedly increasing double-layer capacitance identified with local and absolute maximums around 1000 and 4000 h, respectively. So, lower scale of dispersion in the Warburg impedance describing finite diffusion should obviously result from the inhomogeneous spatial distribution of mass transport in the primer, partial dissolution and transport of corrosion products in the interface at higher pH (alkaline milieu because of the reduction reactions concentrated on the steel interface) and some precipitation taking place in bulk and outer region of the primer in a neutral or slightly acidic milieu.

Intermittent uptick in the pore resistance around 400, 2000, and 5800 h (measured as greater low-frequency impedances) concur with minor enhancement of the coating barrier nature by the corrosion products which lasted for short-term as a consequence of leaching, that is, outbound mass transport leading to faster depletion of the primer. In addition, double-layer capacitance tended to turn to local minimums as coating resistance became greater, which agrees with the previously mentioned hypothesis. Corrosion inhibition of steel by the precipitating corrosion products is supposed to happen and insulate partially the primer from its substrate

between 3000 and 4500 h of exposure as OCPs manifested nonviable or incomplete cathodic polarization of the interface (positive shifted corrosion potentials) besides the enhanced coating activation by the electrolyte. This is in line with the easily detectable swelling spots over the coating and the large amount of corrosion products in cross-section and at the steel surface detected by scanning electron microscope and X-ray photoelectron spectroscopy. Whilst the double-layer capacitance seemed to be well decreasing in the later stage, minor increase of the coating and charge-transfer resistances can be explained by a more stabilized recovery in mechanical blockage and lower rate of electron transfer reactions, especially oxygen reduction reaction in the coating/steel interface. Fading inhibition by the piles of accumulated corrosion products did not entail in ensuing evolving appreciable cathodic immunization. In fact, diminishing galvanic protection of the substrate is connected to partial fading of electrical percolation as a result of accumulation of pore-filling species inside the bulk primer and at steel interface. On the one hand, the several orders of magnitude higher charge-transfer resistance compared to bare steel under similar conditions (R_{ct} ~$3.5\times10^{3}\,\Omega\,cm^{-2}$)[84] points out valuable corrosion inhibition efficiency throughout the entire test. On the other hand, exponent of the double-layer capacitance at 600 at 5800 h suggests clear impact of the mass transport regime in the coating/steel interface and near bulk region of the primer as parameters of the constant phase element can partially be transferred to parameters of the Warburg element.

In case of the hybrid samples, only one parallel circuit was used for fitting (Figure 6.8a–e). The high barrier type **H1** and **H3** exhibited enhanced passive protection between 500 and 3200 h while the **H2** and **H4** showed decreasing efficiency of pore blocking over the same period. In addition, difference between the generally higher pore resistance of the nanotube free **H1** and **H2** coatings (~10^{11}-$10^{12}\,\Omega\,cm^{-2}$) compared to the MWCNT incorporating **H3** and **H4** counterparts (~10^{8}-$10^{10}\,\Omega\,cm^{-2}$) was evidenced. Nevertheless, the **H1**, **H2** and **H3** coatings are regarded as highly cross-linked, homogeneous I type coatings, whereas the **H4** based on its coating resistive behavior is respected as a lower cross-linked, inhomogeneous D type coating. So, greater zinc content with lower spatial density of cross-linking in the primer led to lower pore resistance (despite structure of the filler phase enclosed by the binder), whereas incorporation of increasing amount of surface modified nanotubes leads to the same effect on a much larger scale even though smaller relative amounts of particles and nanotubes were loaded in both the primer and the binder at higher zinc contents (Table 6.2). The profiles of capacitance changes, more exactly the constant changes of the constant phase elements, by time were found similar to the similar formulations, the **H1** and **H3** as well as the **H2** and **H4** (Figure 6.8b). Furthermore, pore resistance increases in most cases coincided with decreasing coating capacitance. Despite the lower particle content, constant phase element of the **H2** remained consistently above that of the **H1**, which was comparable to the difference between particle contents of the primers, and some convergence to the

end as resistance of the coatings showed intersection around 6000 h. This may be explained by the greater zinc content with its increased initial interfacial area and the effective interaction with the highly dispersed particles increasing porosity of the **H2**. Active zinc surface and porosity would surely decrease by time entailing in more positive OCPs as coating resistance was slightly affected in the meantime. Interestingly, coating capacitance of the less porous **H3** was markedly greater than that of the **H4**, indicating an opposite tendency compared to the **H1** and **H2** hybrids. This can be attributed to increased content of the nano-size particles and their geometrically closely arranged aggregates in the form of percolating filaments in the **H3**. No double-layer capacitance type component could be assigned to the hybrid samples, so corrosion inhibition with interfacially deposited corrosion products can be surmised by comparing pore resistance, coating capacitance, and OCPs. So, remarkable inhibition function and slight cathodic surface polarizing ability of the **H4** are suggested, but no such valuable action should be connected to other hybrids as their pore resistances were far higher. Exponent of the constant phase element was close to ideal capacitive behavior except for the **H2** manifesting the highest porosity in the early test stage (Figure 6.8c), which became similar to the other coatings in the second half of the test period.

Compared to the electrically percolating **H1**, **H2**, and **H3** coatings (on different scales), the **H4** was both electrically percolating and electrolytically permeating as a consequence of combination of high zinc and specific particle (**p2**) contents. In comparison with the **H3**, coating capacity constant of the **H4** decreased by the scale expected by the lower PPy and alumina contents in the binder even though its pattern over time was similar to the **H2** featuring the same coating formulation. Permeable initial structure of the **H4** formulation is reflected by the need of additional circuit elements giving with at least a second time constant in the lower frequency domain (Figure 6.8d and e). Although charge-transfer resistance assigned to the **H4** remained at ~$10^7\,\Omega\,cm^{-2}$ between 1400 and 4000 h, its later stage magnitudes of ~$10^8\,\Omega\,cm^{-2}$ became appreciable connecting to more pronounced corrosion inhibition at the steel surface in comparison with the **Z**. Double-layer capacitance related constant phase element was more steady and at least an order of magnitude lower (Figure 6.8d) than that was measured to the **Z** (Figure 6.7a). In partial connection, the greater double-layer capacitance between 1000 and 3200 h correlated well with lower pore resistance of the **H4**. The exponent of the constant phase element describing double-layer capacitance was around 0.7 lower than the **Z** by 0.15 on average, which means highly porous interfacial range between the coating and the steel surface (Figure 6.8d). In case of the **Z**, such an exponent in the last stage of the test is connected to the considerable amount of corrosion products detected on the steel surface obviously affecting surface porosity and the mass transport processes through the porous layer coupled to its outer part in the bulk phase of the primer. This exponent of the **H4** became ideal capacitive (~1) at

4000 h and accompanied with increased pore and charge-transfer resistance along with lower double-layer capacitance and anodic shifted OCPs, suggesting efficient pore sealing in the interface and the primer. The semi-infinite diffusion modeling type Warburg element was used for fitting mass transport related impedance contributions in the **H4**. Although its resistance was comparable to the **Z**, it showed opposite tendency to change from 1000 h. The very low exponent ~0.15 (Figure 6.8e) is partly attributed to the highly heterogeneous deterioration at the steel surface (as it was described with a number of unit cells to thick coatings by Mansfeld et al.[85]) and it probably means long spatial range of porous diffusion processes which are partly reflected by exponents of the constant phase elements associated with the coating and double-layer capacitance. However, in comparison with the **Z**, concentrating in the coating range near the steel surface, much higher dispersion of the Warburg impedance should be accounted as a result of higher pH gradient in the coating/steel interface and much hindered mass transport in the primer; insignificant dissolution and transport of the alkaline dissolved corrosion products and a large proportion of precipitation in the inner phase of the primer under a neutral or slightly acidic milieu.

Impedance data of the **H1**, **H2**, and **H3** coatings showed low phase angle minimums over the low-frequency domain reflecting the absence of coating breakdown in accordance with the evaluation routines, degradation monitoring, and prediction of coating failures.[86] This is corroborated by the impedance/frequency slope of −1 over the 10^2-10^4 Hz range obtained to all coating samples, which is another evaluation routine of coating degradation.[87] As for the ennobled OCPs measured on the hybrid samples in immersion tests (pronounced resistance control similarly to neat, un-pigmented epoxy), the observations can be explained by the effect of interfacial oxygen reduction reactions undergoing under electrolyte deprived, dry condition as a consequence of highly cross-linked, least penetrated coatings. According to literature data,[82] oxygen reduction occurs around 0.4 V and (if galvanic coupled) at 0.2 V versus SCE on passive metal oxide electrodes and thermal oxide electrodes, respectively. This is in agreement with Evans;[81] freshly exposed steel substrates with epoxy coatings feature excellent barrier function, exhibiting OCPs of around 0-0.25 V when polymer coated steel reacts as an oxygen reduction electrode. In this potential range, the ratio of corroding area can be lower than 10^{-3}% of the overall geometrical surface. As the proportion of the anodic area increases, potential of the coated steel must decrease converging to around −0.65 V. So, the systems with very good barrier coatings experience considerable potential drops when surface area of the corroding metal substrate is small, since increasing potential is a useful degradation monitor. Because potential of pure zinc in seawater is approx. −1.050 V[11] iron must have acted as cathode in vicinity of the sacrificial pigments in all cases. According to the prediction of Evans,[81] 99.99% of the coating coverage is located in area of the Evans diagram under the current of ~10^{-11} A cm^{-2} over any

OCP measured for the hybrids. On the other hand, voltage drops were defined in the range of 10^{-3}-10^{-2} V to the **Z** and the **H4**, showing increasing and steady tendencies over measured periods, respectively. In case of the **H1**, **H2**, and **H3**, much greater voltage drops were calculated around 10^{1} and 10^{0}-10^{-1} at current densities of ~50 pA cm^2, exhibiting overall decreasing tendencies. So, hybrid samples can be termed as high barrier coatings in agreement with engineering classification based on DC current measurement.[88]

To estimate dry effective relative permittivity-initial capacity of the ZRPs, the exponential mixture rule known as the Lichteneker-Rother model, which was successfully for epoxy matrix based systems of nano-size alumina[89] and zinc oxide,[90] was utilized[91] to calculate dielectric constants of the primers composed of epoxy, nano-size alumina, PPy, CNTs, and zinc oxide. In accordance with the presumption and method of the Brasher-Kingsbury relationship,[92] thickness of the coatings was assumed to remain constant during immersion tests even though polymers swell by moisture uptake. Estimated water uptake of the epoxy binder and the coatings of the samples using the impedance data defined CPE related capacities is as follows; the **Z** 22-33% and 10-14%, the **H1** 4-12% and 3-9%, the **H2** 9-19% and 6-14%, the **H3** 7-14% and 5-10%, the **H4** 2-10% and 1-6%, respectively. Furthermore, according to the analysis of a nested pair model based breakpoint frequency evaluation method,[93,94] to make a prediction on relative increase in the defective area besides the standard classification evaluation procedure,[95] breakpoint frequencies crossing at −45° in the phase diagram of the Bode represented impedance data and estimated relative increase in the redox active area on the steel surface associated partly with delamination of the coatings were used to appraise coating/steel samples over immersion test periods, which are summarized in the following: the **Z** over 10^{0}-10^{2} Hz with the increase of up to 5×10^{4} (10^{-5}-10^{-3}% overall), the **H1** over 10^{-3}-10^{-2} Hz with the increase remaining below of 2×10^{1} (lower than 10^{-6}% overall), the **H2** over 10^{-2}-10^{-1} Hz with the increase of up to 10^{2} (lower than 10^{-6}% overall), the **H3** over 10^{-3}-10^{-1} Hz with the increase of up to 5×10^{2} (lower than 10^{-5}% overall), the **H4** over 10^{0}-10^{2} Hz with the increase of just below the 10^{5} times (10^{-5}-10^{-2}% overall). The latter is also referred to as surface ratio of the pores, percentage of total cell area with damage or defect area percentage of the coatings, which proved to describe well hybrid ZRPs but underestimate the traditional ZRP type **Z**. This is probably because evaluation requires proportional validity of the breakpoint frequency to the redox active surface area of the metallic substrate by satisfying the following requirements; (1) breakpoint frequency is independent of coating thickness so it is proportional to disbonded area, (2) the area of corroding metal is the same as the pore area, and (3) dielectric constant of the coating is constant over the corrosion propagation period. The second and the third assumption cannot be complied with by the **Z** but may well be met by the hybrid ZRPs after some days of exposure (at least constant or steady state of the pore and coating surface ratios).

6.3.2.2 Glow-discharge optical-emission spectroscopy

Depth profile data of the main elements detected in primers of the **H2** and the **H4** are given in Figures 6.9 and 6.10. In line with the firm barrier nature of the coatings indicated by the impedance spectroscopy results, none of the coating elements especially zinc and oxygen was found depleted or enriched in entire cross-section of the primer after the immersion test. In comparison with carbon and zinc as the main elements

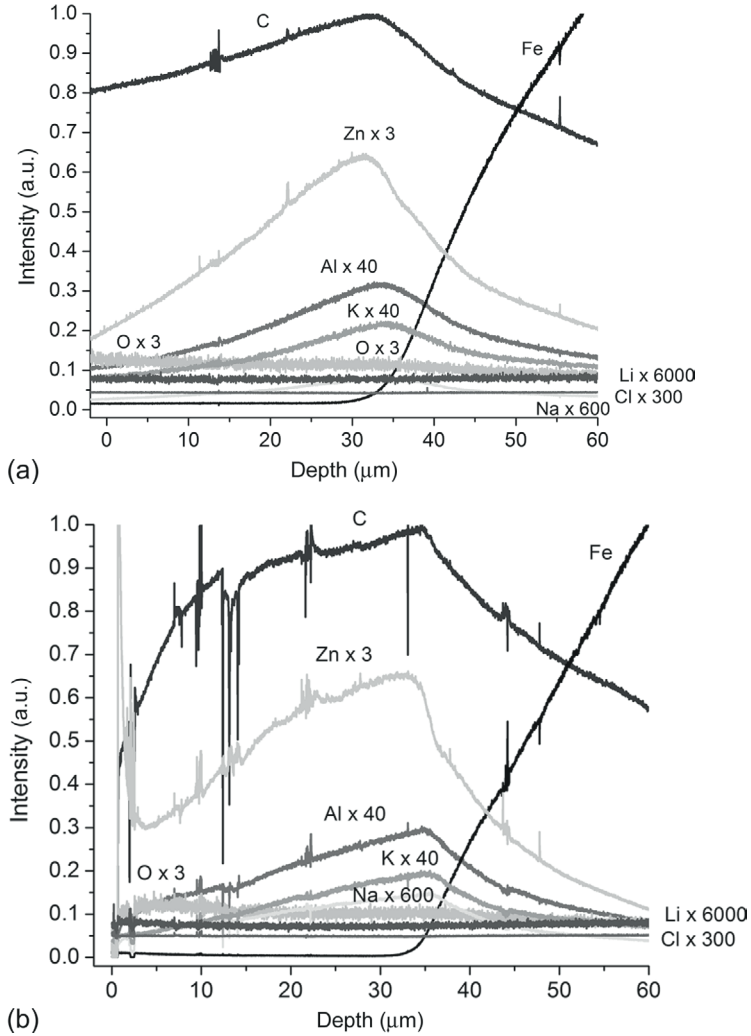


Figure 6.9 Relative intensities of the elements detected by GD OES in cross-section of the **H2**: (a) before and (b) after the immersion test.

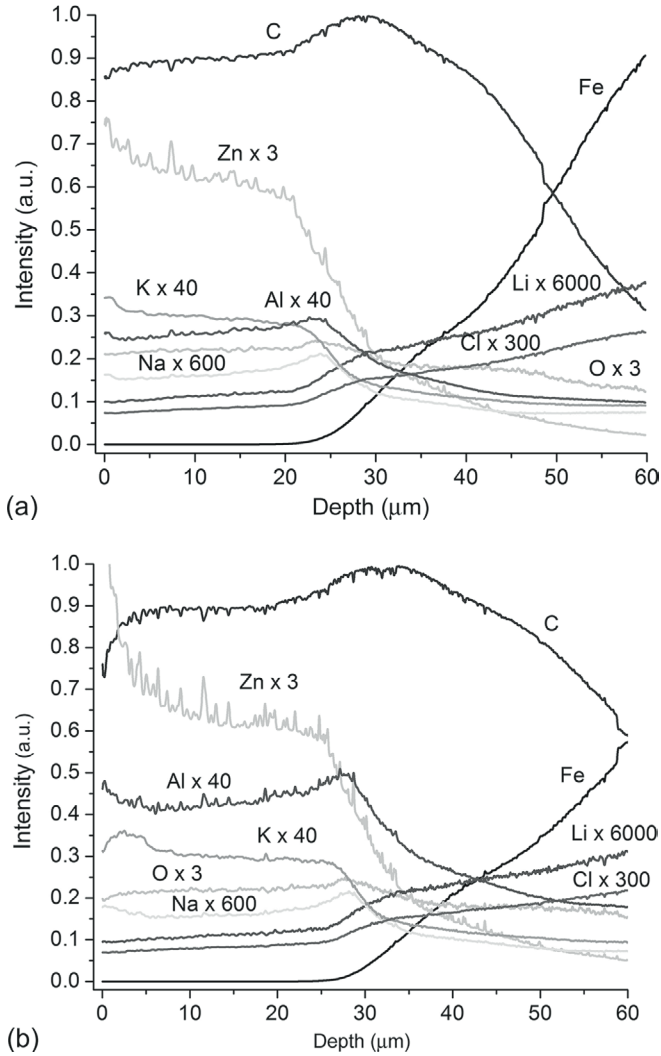


Figure 6.10 Relative intensities of the elements detected by GD OES in cross-section of the **H4**: (a) before and (b) after the immersion test.

in atomic % in bulk phase of the primers, no species of the electrolyte solution were detected in greater relative quantities after propagation but most of the elements such as aluminum, sodium, and potassium was found proportional to the zinc content obviously because they could be its impurities. This should mean very low ionic permeability-conductivity of the zinc-rich hybrid coatings including the **H4** even though impedance data of the latter suggested porous nature of the coating with pore resistance between 10^7 and $10^8\,\Omega\,cm^2$.

6.3.2.3 *X-ray photoelectron spectroscopy*

XPS detected regions acquired from the surface of steel panels of the immersion tested **Z** and **H1-H3** samples are presented in Figure 6.11a–d, where intensities of the peaks correlate with the element contents. Relative quantities of the detected

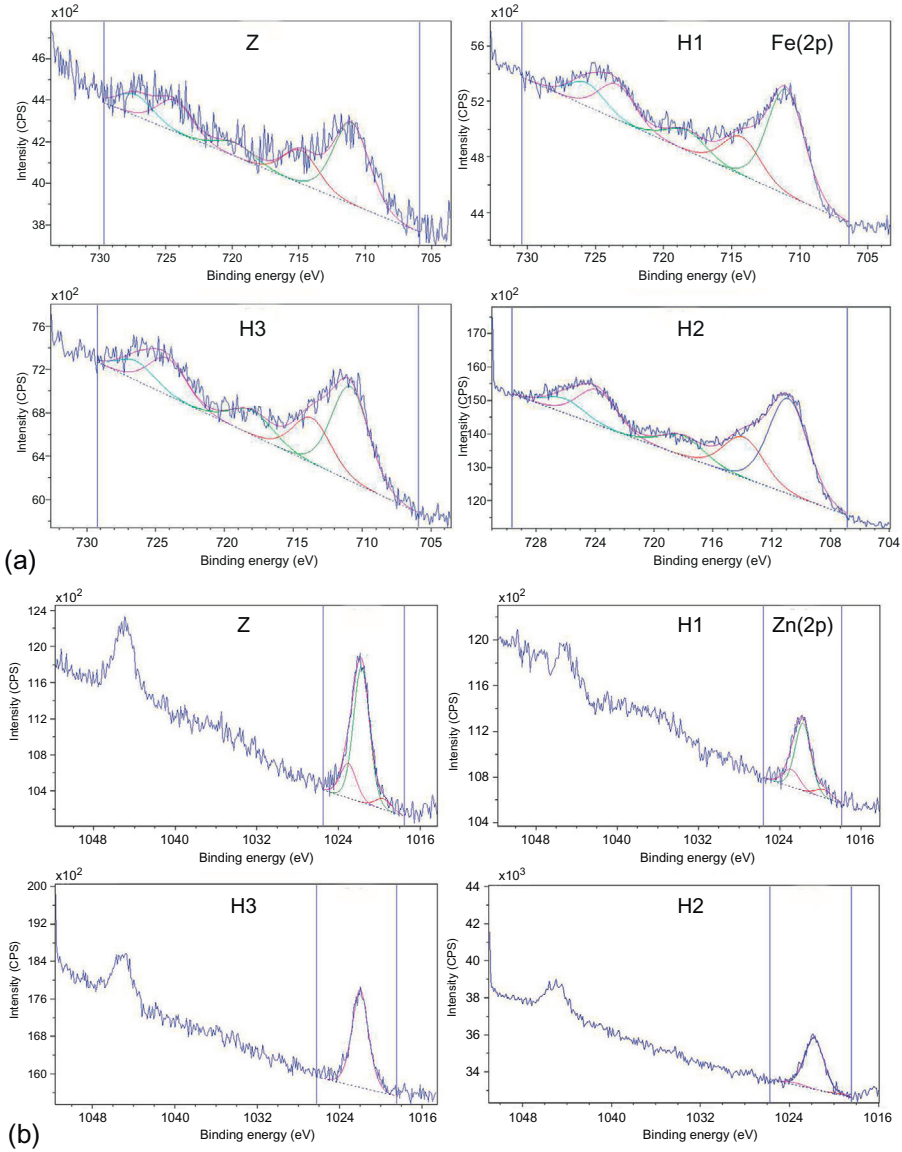


Figure 6.11 XPS spectra regions acquired from steel surface of the immersion tested samples: (a) Fe 2p, (b) Zn 2p,

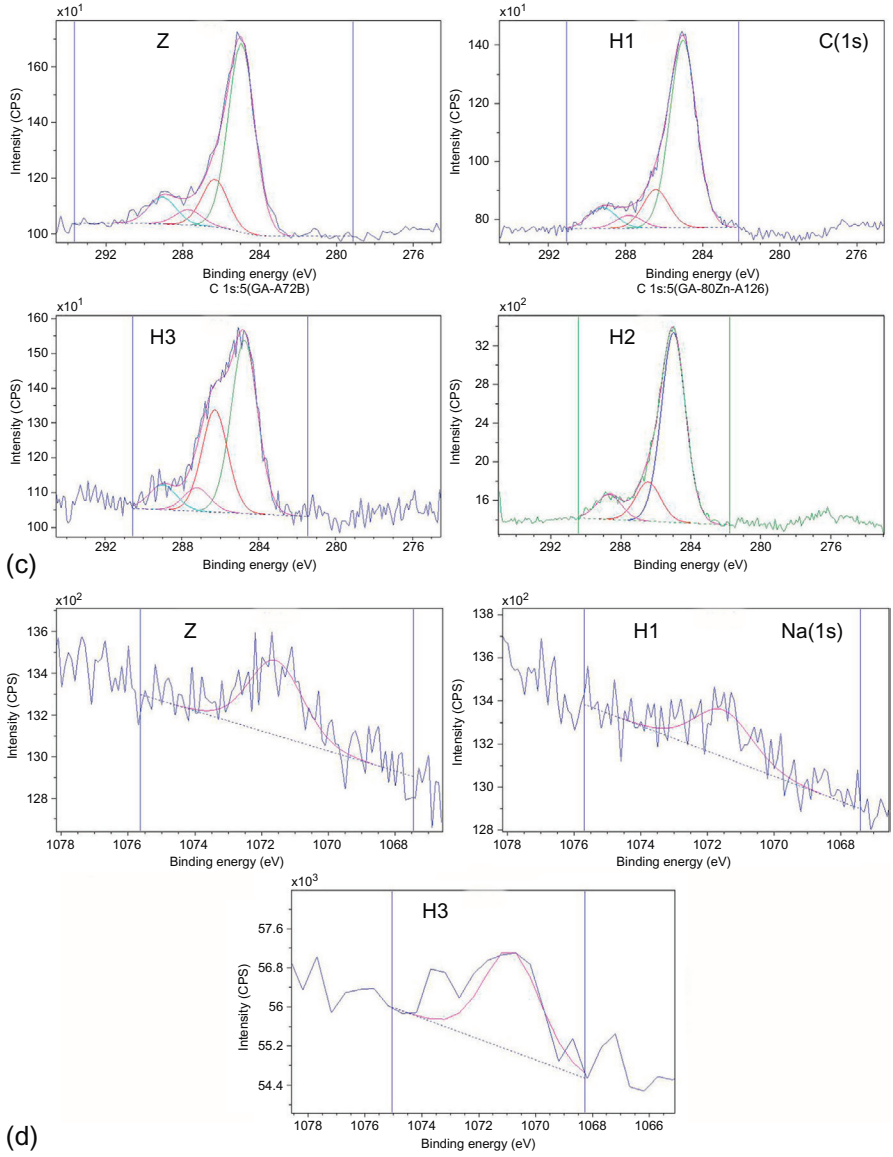


Figure 6.11, cont'd (c) C1s, and (d) Na 1s.

elements and components are considered to be more adequate for qualitative analysis and the data are given in Table 6.5, whereas proportion of the main elements and components related to the result of corrosion processes are summarized in Table 6.6 to have overview on the function and characteristic of the coatings.

TABLE 6.5 Ratio of Elements Detected by XPS on the Surface of Immersion Tested Paint Coated Steel Panels

Coated Samples	Elements (Region)	Binding Energy (eV)	Chemical State (Relative Proportion)	Content (Atomic%)
Z	Fe 2p	710.9	Fe_xO_y (thin Fe(III) rich phase)	7.5
		706.8	Fe(O)	0.08
	Zn 2p3/2	1022.2	ZnO	4.5
		1024.0	$Zn(OH)_2$	0.14
		1019.6	Zn(O)	0.1
	O 1s	530.2	Fe_xO_y	18.1
		531.8	–OH, O=C–	19.7
		533.4	OO–C	4.2
	C 1s	285.0	C–C	25.3
		286.6	–C–O	5.5
		288.6	–C=O	4.0
		289.7	–C=O(O)	1.1
	Na 1s	1072.1	Na_2O, NaCl, Na_2CO_3 or phosphates	1.7
	K 2p3/2	292.8	Halogenide and phosphate	0.3
H1	Fe 2p	711.5	Fe_xO_y (thin Fe(III) rich phase)	14.5
	Zn 2p	1021.7	ZnO	2.8
		1022.9	$Zn(OH)_2$	0.8
		1019.6	Zn(O)	0.3
	C 1s	285.0	C–C	27.4
		286.4	–OH	5.6
		287.9	–C=O	1.3
		289.0	–C=O(O)	3.2
	O 1s	531.5	O=C–, HO–Fe and Zn	14.7
		530.0	O–Zn and Fe	21.5
		533.0	OO–C	3.9
	Na 1s	1071.5	Na_2O, NaCl, Na_2CO_3 or phosphates	0.8

TABLE 6.5 Ratio of Elements Detected by XPS on the Surface of Immersion Tested Paint Coated Steel Panels—cont'd

Coated Samples	Elements (Region)	Binding Energy (eV)	Chemical State (Relative Proportion)	Content (Atomic%)
H2	Fe 2p	711.1	Fe_xO_y (thin Fe(III) rich phase)	16.9
	Zn 2p	1021.7	ZnO	4.4
		1022.9	$Zn(OH)_2$	0.2
	C 1s	285.0	C–C	25.5
		286.4	–OH	5.5
		288.7	–C=O(O)	3.5
	O 1s	531.5	O=C–, HO–Fe and Zn	15.3
		530.0	O–Zn and Fe	25.0
		533.0	OO–C	3.7
	Na 1s	1072.1	Na_2O, NaCl, Na_2CO_3 or phosphates	0.2
H3	Fe 2p	710.7	Fe_xO_y (thin Fe(III) rich phase)	5.3
		713.4	$Fe(OH)_x$ (partial)	1.6
	Zn 2p	1022.0	ZnO and $Zn(OH)_2$	8.1
	C 1s	284.8	C–C	16.6
		286.3	–OH	9.7
		287.2	–C=O	2.3
		289.0	–C=O(O)	2.5
	O 1s	531.2	O=C–, HO–Fe and Zn	16.8
		530.4	O–Zn and Fe	10
		529.8	OO–C	10.4
	Na 1s	1072.1	Na_2O, NaCl, Na_2CO_3 or phosphates	1.6
	K 2p3/2	292.8	Halogenide and phosphate	0.4

Iron was detected as a mixture of the 2^+ and 3^+ valence states in the **Z** and found predominantly in its 3^+ valence state in the **H1-H3** besides occasionally a small contribution of metallic iron which feature obviously came from the metallic phase under the thin oxide film (Figure 6.11a). Oxidized iron phase compared to traces of the binder (carbon) was found in much greater relative proportion in the

TABLE 6.6 Ratio of the Elements Derived from XPS Data Measured at the Surface of Steel Specimens of the Immersion Tested Samples

Elements	Z	H1	H2	H3
Total Zn/Fe content	0.6	0.2	0.3	1.0
Fe content/Total C	0.21	0.39	0.49	0.17
O-bound C/total C content	0.3	0.3	0.3	0.5
Alkaline/Fe content	0.3	0.1	0.01	0.3

H1 and **H2** (Table 6.5) than in the **Z** and **H3** comparable to each other. In case of the **Z** even severe delamination and de-adhesion was observed, since the enhanced amount of carbonaceous remnants can be connected to oxidative degradation of the epoxy, which is in accordance with prolonged intense galvanic function of the primer, interfacial electron transfer reactions, and oxygen reduction reactions. Some metallic zinc could be detected in the **Z** and the **H1** but the majority of the zinc oxide was found as dominant phase with inferior contribution of the hydroxide species (Figure 6.11b). Very similar to what was found in connection with the carbonaceous matter, a relative amount of zinc oxide precipitated in the interface (with respect to iron-oxide) showed high ratios in the **H3** and the **Z** and much lower in the **H1** and **H2** (Table 6.6). This is a sensitive measure of overall rate (over the entire test period) of electrically coupled bimetallic corrosion, that is, galvanic function of the primers, which confirmed intense action of the **Z** and the **H3**, and lower rates in the nanotube-free hybrid ZRPs. Although repeated measurements exhibited much lower zinc corrosion in steel/coating interface of the **H3** formulation, such a ratio of corroded species generally exceeded the level found in the **H1** and **H2** type coatings on average (as a consequence of resistance control), which signifies impact of the electrically well percolating structure of the filler phase and the available corrosion preventing the ability afforded to the steel substrate. It is also closely connected to the anodic current output of the zinc-rich primer system and its utilization efficiency for cathodic protection of the steel substrate. In relation to the corrosion inhibition effect by the interfacially accumulating zinc corrosion products, this feature was obviously more efficient in the hybrids than in the **Z** where the generated alkaline milieu and high porosity of the primer allowed less efficient accumulation of the precipitated corroded species at the interfaces as suggested by the measured corrosion potentials and evaluated resistance and capacities of the coatings. Oxygen containing species indicated varied composition as a result of high relative amounts of oxides/hydroxides of iron and zinc. Regarding the oxygen region of the spectra of the **H3**, chemical state of zinc could not be resolved to components but corroded iron species were managed to assign to oxides and hydroxides. The facts that no iron corrosion spots were visually observed on

the steel surface protected by the hybrids and the Fe 2p spectra showed the same characteristics as the native iron oxides formed under ambient conditions.[96] This supports the presumption that most of the steel surface became oxidized before the immersion test and the hybrid coating must have provided viable corrosion prevention over the test period.

The overall oxidative conversion-degradation of the epoxy binder was almost the same in all investigated samples (Table 6.6). However, the ratio of oxidized carbon components indicated a characteristic deviation in the **H3** in the form of more pronounced hydroxyl type degradation (rather than carbonyl or carboxyl type) when compared to other samples (Figure 6.11c). This obviously means that enhanced electron transfer reactions between the primer and steel substrate should have taken place, whereas catalytic effect of the MWCNTs toward ORR[10] was not suppressed by the semiconducting PPy film.

According to the tendency of galvanic function of the coatings and oxidative degradation of the organic binder (besides the consequence of the various cross-linking degree of the binder depending on the relative amount of solid inclusions), considerable amount of sodium was found both in the **Z** and the **H3** along with potassium (clearly above the detection limit and in greater ratio to sodium than in the electrolyte) (Figure 6.11d) but low amounts were found in the **H1** and **H2** close to the detection limit without any sign of potassium.

6.3.2.4 Salt-spray chamber test

Evaluation of the samples after salt spray testing is summarized in Table 6.7, whereas photographs of the samples are shown in Figure 6.12. Test results of the **H1** type coatings pointed out firm barrier function, considerable resistance against delamination and prevention of iron rust formation around the scribed areas. The scale and later stage deterioration of the coating suggested good protection. The **H2** exhibited an altogether much better protection characteristic with

TABLE 6.7 Evaluation of Salt Spray Chamber Test Results

Coatings	Degree of Blistering Size and Density		Degree (Ri) and Area (%) of Rusting over Intact Surface	Corrosion Grade and Delamination Around Scribes
Z	3	2 (few)	Ri 3, 1	Grade 3—slight
H1	3	3 (medium)	Ri 3, 1	Grade 2—slight
H2	2	3 (medium)	Ri 2, 0.5	Grade 2—very slight
H3	3	2 (few)	Ri 3, 1	Grade 3—slight
H4	3	2 (few)	Ri 2, 0.5	Grade 2—slight

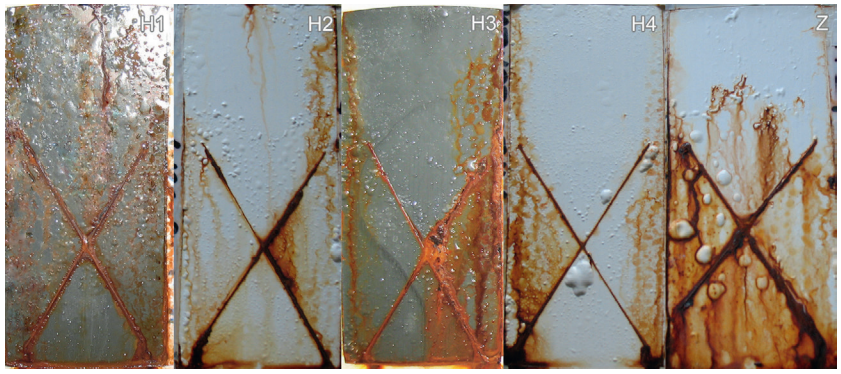


Figure 6.12 Photographs of the cyclic salt spray tested paint coatings.

very good active corrosion prevention around the scribed areas and resistance against delamination. Even buried areas seemed to be in a better preserved state with a lower scale of coating degradation, which supports the notion of quite good semiactive/passive protection nature. Only some proportion of the buried areas were scattered with a small size of blisters but only the larger ones, about half of them in number, were related to iron rust formation. These are the result of optimal hybrid formulation; high zinc and the low specific particle contents, leading to low porosity and electrolytic conductivity besides good utilization of the low anodic current output for steel protection. Robust protection nature is emphasized by the almost uniform way of small scale corrosion around scribes, lower degree of staining and the later stage of coating deterioration along with the very low migration progress of delaminating fronts.

Both the nanotube-loaded **H3** and **H4** samples exhibited very good condition with the lowest scale of blistering over intact areas along with good and excellent resistance against delamination around scribed areas, respectively. Lower susceptibility to blistering over buried areas is in accordance with the directly non-interconnected or moderately interconnected structure of fillers (measured as threshold of rheological and electrical percolation by the nano-size particles), allowing to afford dominating passive protection feature of the coatings. Nevertheless, a notable difference was identified in their corrosion prevention functionality; the rate of staining, amount of iron rust formation was far the best in the **H4**, especially in the intersection and an altogether good condition of the **H3** was noticed.

Due to the high zinc PVC, coating porosity and cross-linking density of the binder, the **Z** afforded only moderate resistance against blistering, but viable corrosion prevention at scratched areas. It also provided an acceptable degree of protection over the intact surface against rusting and blistering, but the latter was clearly inferior to most of the hybrids. This is the consequence of an increased rate of coating deterioration

partly because of the accumulation and subsequent leaching of the massive amount of corrosion products, which was noticed to occur after 40 days of exposure.

6.4 Discussion

To interpret the protection mechanism of the nanotube-free hybrid ZRPs, the following assumptions are taken into account. Statistically even distribution of spheroids of both the zinc pigments and the nano-size particles are considered at average sizes of 3 μm and 30 nm, respectively. So, active interfacial area between the two sorts of particles is estimated of ~6% of the entire zinc surface, allowing electrical interaction within a distance volume range of 10 nm in vicinity of the metallic grains. The latter is the typical maximum interparticle distance where electrical percolation takes place in polymeric composites by an electron tunneling mechanism.[97,98] This should be valid when the impact of solvation related swelling, unbundling, or bridging aggregation of the PPy segments partially restricts mobility and settling of the particles are neglected. By an average density of $\sim 2 \times 10^{20}\,m^{-3}$, PPy covered nano-size alumina particles provide less coherent and low density paths across the binder, restricting highly the electrolyte ingress. Owing to the significant difference (at least $10^4\,cm^2\,s^{-1}$) between mass transport in bulk phase and interphase along grain boundaries,[99] one can have a notion of full activation and partial passivation of the interacting zinc grains in the hybrid ZRPs. The overall zinc corrosion should be very limited and inhibited corresponding to the impact of nano-size particles on composites[100] and the interfacial interaction ability of nano-size composites with metallic surfaces.[101] Furthermore, semiconducting particles should affect the sacrificial anodic current output of zinc. So, the overall mechanism probably involves partial p-n junction regulation as a result of interconnected n- and p-type semiconductors of generated zinc oxide and PPy.[102] This function was evinced leading to improved protection performance based on the mechanism of a semiconductor altered sacrificial function of the metallic pigments.[8]

On the other hand, anodic current output and its density must always exceed current density of the protected substrates. In ZRPs protected substrates, corrosion rate is cathodically controlled. Hence, corrosion potential of the system approaches anodic OCPs when current density is just above the equivalent corrosion current. In an immersion test zinc corrosion is controlled by diffusion processes because charge-transfer resistance in the coating/steel interface should be smaller than the Warburg impedance (even though it is affected by the marked voltage drop). Considering that 2-5 and 5-20 $mA\,m^{-2}$ cathodic current is needed to maintain stable protection of steel substrates under fair and poor coatings by impressed current systems in stagnant and low velocity conditions, respectively,[103] such a range of anodic current output must be provided by the **H2** (and the **H4**) formulation as it is learned from the salt spray test results. Thus, galvanic function of the hybrid ZRPs (with

nonpercolating zinc content) should take benefit from moderate interaction and low spatial density of the nano-size particles. Nevertheless, a major part of the particles was dispersed at a size range of 50 nm, although they were surely not evenly distributed in the binder. The latter leads to facilitated electrical percolation, infinite cluster formation by the particles and the zinc pigments. Calculations suggest contributed electrical conductivity of the hybrid primers when particles are of 10 nm diameter, which is in agreement with the aspects of double and multiple percolation theory[61,104] establishing a relationship between decreasing size of conducting particles and percolation thresholds of the composites.

To interpret galvanic function of the nanotube-loaded hybrid ZRPs and the role of PPy modified nanotubes, the effects of the pristine nanotubes should be first examined. Simplified model interpretation, electrical circuit of the nanotube connected zinc and steel is as follows. The 3D network of zinc particles are connected together and to the steel by the CNTs. Longitudinal current conduction between the metallic electrodes of zinc and steel is called current drainage (I_D) undergoing in a longitudinal direction through the axis of the nanotubes. Current conduction in a transversal direction (perpendicular to the axis of the nanotubes) is hereby named as current leakage (I_L) between the anodic zinc and cathodic functioning steel electrodes. With similar properties, graphite is routinely used in impressed current based cathodic protection systems as it is an efficient anode[105] but graphite incorporation into paint formulations is known to cause devastating consequences.[57] In our approach, PPy film on the nanotubes is to alter perpendicular electrical conductivity, increase resistance on the surface of the MWCNTs by less conducting layers to the surrounding media, while the majority of their tips are thought to remain uncoated (resistance of the pristine CNTs in a longitudinal direction). The amount of nanotubes necessary for a spatially interconnected network is identified by percolation thresholds. Although there is usually a difference between kinetic and statistical percolation thresholds because of the particle movements and dynamic aggregation or a system with static paths of randomly distributed filler,[62] some of the rheology terms are related to either of these percolation thresholds which are relevant to establish relationships between structure of the polymer composites and their electrical properties.[106,107] In addition, further assumptions need to be made as follows: the nanotube-loaded hybrid ZRPs are uniformly accessed by the electrolyte and the reaction with the main depolarisator such as oxygen is limited by the rate of electrolyte infiltration activating sacrificial action of the thin oxide layer covered zinc pigments. MWCNTs with high surface and electrical conductivity behave as indifferent electrodes, leading to greater rate of anodic and cathodic reactions. Cathodic processes are due to the mesoscopic galvanic cell formation with metallic components.

MWCNTs are good electrical conductors ($\sim 1.8 \times 10^3\,\mathrm{S\,cm^{-1}}$)[108] with the conductance of individual tubes up to $G \sim 490 G_0$[109] where longitudinal conductance is quantified as $G = nG_0$ and where n is an integer number and the G_0 equals to $\approx 77.5\,\mu\mathrm{S}$.[110]

Current-carrying capacity of up to 7.27 mA and the conductance of ~460 G_0[11] are more than enough for hybrid coatings to afford comparable anodic current output to metallic substrates (~10^{-1} mA cm^{-1}) as traditional ZRPs.[111] Because CNTs facilitate electrical connection of zinc and the steel substrate, nano- and mesoscopic galvanic cells form from certain particle content. This should lead to decreasing utilization efficiency of anodic current output, causing lower protection by the coatings and ineffective immunization of the substrate. What is more, increased surface ratio by the cathodic nanotubes only aggravates the situation.

Although simple galvanic setup of zinc and steel electrically coupled by the nanotubes was discussed,[96] nanotubes as uncoated conductors supplied by the electrolyte and depolarisator species act as cathodes, which results in a high rate of cathodic reactions offset by anodic reactions on zinc and iron. Potential drop along the nanotubes weakening longitudinal electron transport can be disregarded, since a high rate of cathodic reactions should take place and a large proportion of the anodic current output is wasted over the entire length of the nanotubes (as $R_{perp} < R_{long}$). MWCNTs conduct an electrical current of huge density though efficiency of galvanic coupling is limited by conductivity of the low quantity of diluted electrolyte[112] since the shorter the distance from individual metallic species is, the higher the probability of the reduction reaction should be, especially under the conditions of an electrolyte deprived and diluted milieu. Hence, CNT assisted corrosion of zinc and iron must be limited by mass transport of the depolarisator, resulting in a much shortened lifetime of the coatings and steel substrates. The formation of coupled electrodes can also be discussed by modified or unmodified drain-current systems, and then galvanic efficacy of nanotube-loaded traditional ZRPs should be very low because anodic current output of the zinc would not support steel protection, whereas low current drainage at junctions on both ends of the MWCNTs could occur in the neighborhood of zinc and steel electrodes. Acceleration by drain-current system depends on resistance of the wedging-in component, so the higher the resistance is, the higher the potential drop isand the lower the current between the two ends are. The efficiency of drainage of a sacrificial setup should be very low because of the low volume range perpendicular current leakage by the MWCNTs at the expense of parallel transport of coupling between the two electrodes ($I_L > I_D$). Thus, efficiency of this system to collect and drain anodic current to steel must probably fail. When CNTs are electrically coupled to either the zinc or steel surface then corrosion rate of both must be high. If orientation results in about the same distance from both types of electrodes, then their increased rate of corrosion should undergo parallel.

Exohedral modification of the nanotubes with a p-doped semiconductor such as a PPy aims at overcoming most of these shortcomings. Then the system is composed of two metallic electrodes; zinc and steel wired to each other by the modified MWCNTs as “plastic sheathed” current conductors. This is in agreement with the standard of impressed cathodic systems.[105] So, the aforementioned mechanism is

altered to a favorably decreased rate of perpendicular current leakage on the CNTs as a result of greater resistance of the normalized component passage ($R_{perp} > R_{long}$ so $I_L < I_D$). Thus, the ratio of longitudinal transmission increases or in other aspects the degree of current drainage increases since the rate of accelerated bimetallic corrosion becomes greater. This is a better view to construct galvanic cells with optimal setup properties, electrodes of varied nobility connected by isolated electrical conductors to eliminate cathodic behavior of the nanotubes.

Percolation or tunneling based junction potential drop, the resistance at junctions should be lower than resistance of the PPy film restricting the rate of reduction reaction of the depolarisator in transversal direction as a current leakage. The resistance at nanotube-zinc junctions is also related to tunneling as to the CNTs and zinc-iron electrodes. Thus, electrical connections of zinc and steel must take benefit from the 3D percolating arrangement of the highly anisotropic filaments of the nano-size particles. Moderate number and spatial density of the ionic conducting paths results in enhanced electrolyte penetration through the nanotube-loaded hybrid ZRPs (as it is reflected by EIS data). The higher conductivity electrolyte milieu in bulk phase of the primer leads to activation of greater scale. By that increased amount of anodic current output leads to efficient drainage by modified nanotube based galvanic coupling. Increased density of the nanotubes within an order of magnitude in binders (compared to compositions of the **H3** and **H4**) is required to maintain acceptable efficiency of anodic current drainage, conduction of current provided by increased sacrificial action of zinc to the steel substrate at lower barrier capable coatings (the so called "fair coatings" with specific resistance of $\sim 10^7\,\Omega\,cm^2$). So, higher proportion of the zinc grains is to be wired to each other and to the substrate to maximize drainage ratio of the anodic current output and minimize the leakage loss. However, this must be subject to optimize partly due to the fact that hydrophilic modified nanotubes increase enormously the electrolyte permeation but sacrificial current utilization can only keep up quite moderately. This suggestion is supported by the fact that electrical conductivity of the nanotube-loaded polymer composites generally improves with increasing number of junctions per unit area or volume, facilitating electron transport along networks and occupied paths.[113,114] In addition, aggregated nanotube assemblies always give higher electrical conductivity of their composites when the relative amount of the nanotubes is close to the percolation threshold,[115] whereas convergence to the quality of nano-size filler loaded composites results in the evolution of more advanced functionalities of the hybrid coatings.

Otherwise, there should be an upper limit in mass ratio of the MWCNTs and the zinc grains to obviate large-density mesoscopic galvanic cell formation with enhanced surface area of the cathodic part. In this aspect, the lower diameter type MWCNTs are more favorable to maintain appropriate electrical connection of the sacrificial grains at the lowest amount of solid filler resulting in a medium extent of cathodic surface area. On the other hand, segments of the electrically highly

conducting particles provide a chance to alter surface area ratio of the zinc anodes and steel cathodes by varying the sum of electrically connected grains with substrates to set percolating thickness, volume ranges beside the traditional way to alter volume concentration, size, and shape of the anodic pigments. By the herewith delineated approach, ~20 wt.% decrease in zinc contents can be achieved in primers, depending on type of the nanotubes and composition of the particles, retaining or even enhancing protection performance of the conventional ZRPs. Galvanic function of all hybrid ZRPs with low zinc content can only be interpreted on the basis of multiple percolation theory.[61] In a system composed of multiple phases, orientation of the lower dimension structure like the PPy film is preferential at the interface of at least two immiscible phases such as epoxy, alumina, and/or the MWCNTs. Owing to the fact that nano-size materials[116] can form conducting paths without macroscopic percolation, [117] arrangement of the nano-size particles and composition of the primers result in decreased electrical percolation threshold.

6.5 Conclusion

There are a number of ways to improve traditional metal-rich coatings. When auxiliary conducting particles are applied, then dispersity of the particles should be preferably high, especially in the case of isotropic particles. Some meso-scale assembly and arrangement of the anisotropic particles are always preferred. However, the most relevant aspects of feasibility of the conducting additives are the high electrical conductivity and the slightest ability toward reduction of potential depolarisators.

According to the described interpretation relaying on the PPy modified nanotubes, the nano- and micron-size carbon allotropes with 1D elongated highly anisotropic concentric structure are identified as potential candidates to improve ZRPs in case of carefully designed particle compositions and coating formulations.

In the standpoint of spatial arrangement of meso- and nano-scale particles and finely balanced functionality, the mixture of nano- and micron-size particles should lead to emergence of nano-engineered “wise-coatings,” acting in accordance with actual circumstances set by barrier function of the coatings, diffusion rates of the electrolyte, and depolarisator species.

Thus, in comparison with the PPy modified alumina/CNT loaded hybrids and conventional ZRPs, the better protecting hybrid primers are represented as moderate permittivity, charge storage capacity systems with low dielectric loss by low water uptake.

Acknowledgment

Gábor Lassú is gratefully acknowledged for his GD OES measurements.

References

1. Ross TK, Wolstenholme J. Anti-corrosion properties of zinc dust paints. Corros Sci 1977;17(4):341–51.
2. Abreu CM, Izquierdo M, Keddam M, et al. Electrochemical-behavior of zinc-rich epoxy paints in 3-percent NaCl solution. Electrochim Acta 1996;41(15):2405–15.
3. Hammouda N, Chadli H, Guillemot G, et al. The corrosion protection behaviour of zinc rich epoxy paint in 3% NaCl solution. Adv Chem Eng Sci 2011;1(1):51–60.
4. Abreu CM, Izquierdo M, Merino P, et al. A new approach to the determination of the cathodic protection period in zinc-rich paints. Corrosion 1999;55(12):1173–82.
5. Singh DDN, Yadav S. Role of tannic acid based rust converter on formation of passive film on zinc rich coating exposed in simulated concrete pore solution. Surf Coat Technol 2008;202(8):1526–42.
6. Shi H, Liu F, Han E-H. The corrosion behavior of zinc-rich paints on steel: influence of simulated salts deposition in an offshore atmosphere at the steel/paint interface. Surf Coat Technol 2011;205(19):4532–9.
7. Fishman RS, Kurtze DA, Bierwagen GP. The effects of density fluctuations in organic coatings. J Appl Phys 1992;72(7):3116–24.
8. Jagtap RN, Patil PP, Hassan SZ. Effect of zinc oxide in combating corrosion in zinc-rich primer. Prog Org Coat 2008;63(4):389–94.
9. Rodríguez MT, Gracene JJ, Saura JJ, et al. The influence of the critical pigment volume concentration (CPVC) on the properties of an epoxy coating. Part II. Anticorrosion and economic properties. Prog Org Coat 2004;50(1):68–74.
10. Giudice C, Benitez JC, Linares MM. Zinc-rich epoxy primers based on laminar zinc dust. Surf Coat Int 1997;80(6):279–84.
11. Selvaraj M, Guruviah S. Optimisation of metallic pigments in coatings by an electrochemical technique and an investigation of manganese powder as pigment for metal rich primers. Prog Org Coat 1996;28(4):271–7.
12. Vilche JR, Bucharsky EC, Giudice CA. Application of EIS and SEM to evaluate the influence of pigment shape and content in ZRP formulations on the corrosion prevention of naval steel. Corros Sci 2002;44(6):1287–309.
13. Montes E. Influence of particle size distribution of zinc dust in water-based, inorganic, zinc-rich coatings. J Coat Technol 1993;65(821):79–82.
14. Schaefer K, Miszczyk A. Improvement of electrochemical action of zinc-rich paints by addition of nanoparticulate zinc. Corros Sci 2013;66(1):380–91.
15. Canosa G, Alfieri PV, Giudice CA. Environmentally friendly, nano lithium silicate anticorrosive coatings. Prog Org Coat 2012;73(2–3):178–85.
16. Bagherzadeh MR, Mousavinejad T. Corrosive inhibition behavior of well-dispersible aniline/p-phenylenediamine copolymers. Prog Org Coat 2012;74(4):589–95.
17. Arianpouya N, Shishesaz M, Arianpouya M, et al. Evaluation of synergistic effect of nanozinc/nanoclay additives on the corrosion performance of zinc-rich polyurethane nanocomposite coatings using electrochemical properties and salt spray testing. Surf Coat Technol 2013;216(1):199–206.
18. Zhang L, Ma A, Jiang J, et al. Anti-corrosion performance of waterborne Zn-rich coating with modified silicon-based vehicle and lamellar Zn (Al) pigments. Prog Nat Sci: Mater Int 2012;22(4):326–33.
19. Jagtap RN, Nambiar R, Hassan SZ, et al. Effect of zinc oxide in combating corrosion in zinc-rich primer. Prog Org Coat 2007;58(1):253–8.
20. Li XF, Cui XM, Liu SD, et al. Preparation and characterization of inorganic zinc-rich coatings based on geopolymers. In: Zhang C, Chen N, Hu J, editors. Inorganic thin films and coatings. Key engineering materials, vol. 537. 2013. p. 261–4.

21. Faidi SE, Scantlebury JD, Bullivant P, et al. An electrochemical study of zinc-containing epoxy coatings on mild steel. Corros Sci 1993;35(5–8):1319–28.
22. Pereira D, Scantlebury JD, Ferreira MGS, et al. The application of electrochemical measurements to the study and behaviour of zinc-rich coatings. Corros Sci 1990;30(11):1135–47.
23. Shreepathi S, Bajaj P, Mallik BP. Electrochemical impedance spectroscopy investigations of epoxy zinc rich coatings: role of Zn content on corrosion protection mechanism. Electrochim Acta 2010;55(18):5129–34.
24. Gervasi CA, Di Sarli AR, Cavalcanti E, et al. The corrosion protection of steel in sea water using zinc-rich alkyd paints. An assessment of the pigment-content effect by EIS. Corros Sci 1994;36(12):1963–72.
25. Baczoni A, Molnár F. Advanced examination of zinc rich primers with thermodielectric spectroscopy. Acta Polytech Hung 2011;8(5):43–51.
26. Peart J. Point-counterpoint: organic vs inorganic zinc-rich in the field in defense of inorganic zinc-rich primers. J Protect Coat Linings 1992;9(2):46–53.
27. Øystein Knudsen O, Steinsmo U, Bjordal M. Zinc-rich primers—test performance and electrochemical properties. Prog Org Coat 2005;54(3):224–9.
28. Feliú Jr S, Morcillo M, Feliú S. Deterioration of cathodic protection action of zinc-rich paint coatings in atmospheric exposure. Corrosion 2001;57(7):591–7.
29. Díaz I, Chico B, de la Fuente D, et al. Corrosion resistance of new epoxy–siloxane hybrid coatings. A laboratory study. Prog Org Coat 2010;69(3):278–86.
30. Real SG, Elias AC, Vilche JR, et al. An electrochemical impedance spectroscopy study of zinc rich paints on steels in artificial sea water by a transmission line model. Electrochim Acta 1993;38(14):2029–35.
31. Akbarinezhad E, Ebrahimi M, Sharif F, et al. Synthesis and characterization of new polysiloxane bearing vinylic function and its application for the preparation of poly (silicone-co-acrylate)/montmorillonite nanocomposite emulsion. Prog Org Coat 2011;70(1):39–44.
32. Marchebois H, Keddam M, Savall C, et al. Zinc-rich powder coatings characterisation in artificial sea water: EIS analysis of the galvanic action. Electrochim Acta 2004;49(11):1719–29.
33. Meroufel A, Touzain S. EIS characterisation of new zinc-rich powder coatings. Prog Org Coat 2007;59(3):197–205.
34. Marchebois H, Joiret S, Savall C, et al. Characterization of zinc-rich powder coatings by EIS and Raman spectroscopy. Surf Coat Technol 2002;157(2–3):151–61.
35. Marchebois H, Touzain S, Joiret S, et al. Zinc-rich powder coatings corrosion in sea water: influence of conductive pigments. Prog Org Coat 2002;45(4):415–21.
36. Marchebois H, Savall C, Bernard J, et al. Electrochemical behavior of zinc-rich powder coatings in artificial sea water. Electrochim Acta 2004;49(17–18):2945–54.
37. Meroufel A, Deslouis C, Touzain S. Electrochemical and anticorrosion performances of zinc-rich and polyaniline powder coatings. Electrochim Acta 2008;53(5):2331–8.
38. Feliú Jr S, Bastidas R, José M, et al. Effect of the Di-iron phosphide conductive extender on the protective mechanisms of zinc-rich coatings. J Coat Technol 1991;63:67–72.
39. Ling C, Xue JZ, Hui M, et al. Effects of conductive pigments on the anti-corrosion properties of zinc-rich coatings. Adv Mater Res 2013;652–654:1830–3.
40. Bastosa AC, Zheludkevich ML, Klüppel I, et al. Modification of zinc powder to improve the corrosion resistance of weldable primers. Prog Org Coat 2010;69(2):184–92.
41. Plagemann P, Weise J, Zockoll A. Zinc–magnesium-pigment rich coatings for corrosion protection of aluminum alloys. Prog Org Coat 2013;76(4):616–25.
42. Park JH, Yun TH, Kim KY, et al. The improvement of anticorrosion properties of zinc-rich organic coating by incorporating surface-modified zinc particle. Prog Org Coat 2012;74(1):25–35.

43. Armelin E, Martí M, Liesa F, et al. Partial replacement of metallic zinc dust in heavy duty protective coatings by conducting polymer. Prog Org Coat 2010;69(1):26–30.
44. Armelin E, Pla R, Liesa F, et al. Corrosion protection with polyaniline and polypyrrole as anticorrosive additives for epoxy paint. Corros Sci 2008;50(3):721–8.
45. Gergely A, Pfeifer É, Bertóti I, et al. Corrosion protection of cold-rolled steel by zinc-rich epoxy paint coatings loaded with nano-size alumina supported polypyrrole. Corros Sci 2011;53(11):3486–99.
46. Avakian RW, Horton SD, Hornickel JH. Cathodic protection coatings containing carbonaceous conductive media. *US Patent, 7,422,789*; 2008.
47. Gergely A, Pászti Z, Bertóti I, et al. Novel zinc-rich epoxy paint coatings with hydrated alumina and carbon nanotubes supported polypyrrole for corrosion protection of low carbon steel: part II: corrosion prevention behavior of the hybrid paint coatings. Mater Corros 2013;64(12):1091–1103.
48. Ionita M, Pruna A. Polypyrrole/carbon nanotube composites: molecular modeling and experimental investigation as anti-corrosive coating. Prog Org Coat 2011;72(4):647–52.
49. Martina V, De Riccardis MF, Carbone D, et al. Electrodeposition of polyaniline–carbon nanotubes composite films and investigation on their role in corrosion protection of austenitic stainless steel by SNIFTIR analysis. J Nanopart Res 2011;13(11):6035–47.
50. Salam MA, Al-Juaid SS, Qusti AH, et al. Electrochemical deposition of a carbon nanotube-poly(o-phenylenediamine) composite on a stainless steel surface. Synth Met 2011;161(1–2):153–7.
51. Hu ST, Kong XH, Yang H, et al. Anticorrosive films prepared by incorporating permanganate modified carbon nanotubes into waterborne polyurethane polymer. Adv Mater Res 2011;189–193:1157–62.
52. Fukuda H, Szpunar JA, Kondoh K, et al. The influence of carbon nanotubes on the corrosion behaviour of AZ31B magnesium alloy. Corros Sci 2010;52(12):3917–23.
53. Aung NN, Zhou W, Goh CS, et al. Effect of carbon nanotubes on corrosion of Mg–CNT composites. Corros Sci 2010;52(5):1551–3.
54. Li Q, Turhan MC, Rottmair CA, et al. Influence of MWCNT dispersion on corrosion behaviour of their Mg composites. Mater Corros 2012;63(5):384–7.
55. Turhan MC, Li Q, Jha H, et al. Corrosion behaviour of multiwall carbon nanotube/magnesium composites in 3.5% NaClElectrochim Acta 2012;56(20):7141–8.
56. Aylor DM, Murray JN. The effect of a seawater environment on the galvanic corrosion behavior of graphite/epoxy composites coupled to metals. *Research and development report, CDNSWC-SME-92/32*, Naval Surface Warfare Center, Bethesda, MD; August 1992.
57. Hao Y, Liu F, Shi H, et al. The influence of ultra-fine glass fibers on the mechanical and anticorrosion properties of epoxy coatings. Prog Org Coat 2011;71(2):188–97.
58. Patchan MW, Baird LM, Rhim Y-R, et al. Liquid-filled metal microcapsules. ACS Appl Mater Interfaces 2012;4(5):2406–12.
59. Jing X, Zhao W, Lan L. The effect of particle size on electric conducting percolation threshold in polymer/conducting particle composites. J Mater Sci Lett 2000;19(5):377–9.
60. Levon K, Margolina A, Patashinsky AZ. Multiple percolation in conducting polymer blends. Macromolecules 1993;26(15):4061–3.
61. Gergely A, Bertóti I, Török T, et al. Corrosion protection with zinc-rich epoxy paint coatings embedded with various amounts of highly dispersed polypyrrole-deposited alumina monohydrate particles. Prog Org Coat 2013;76(1):17–32.
62. Bauhofer W, Kovacs JZ. A review and analysis of electrical percolation in carbon nanotube polymer composites. Compos Sci Technol 2009;69(10):1486–98.
63. Zhu J, Wei S, Yadav A, et al. Rheological behaviors and electrical conductivity of epoxy resin nanocomposites suspended with in-situ stabilized carbon nanofibers. Polymer 2010;51(12):2643–51.
64. Kim YJ, Shin TS, Choi HD, et al. Electrical conductivity of chemically modified multiwalled carbon nanotube/epoxy composites. Carbon 2005;43(1):23–30.

65. Kendig M, Jeanjaquet S, Brown R, et al. Rapid electrochemical assessment of paint. J Coat Technol 1996;68(863):39–47.
66. Moulder JF, Stickle WF, Sobol PE, et al. Handbook of X-ray photoelectron spectroscopy. Eden Prairie, Minnesota, USA: Perkin-Elmer Corp; 1992.
67. Wagner CD, Naumkin AV, Kraut-Vass A, et al. NIST X-ray photoelectron spectroscopy database, Version 3.4. Gaithersburg, MD: National Institute of Standards and Technology; 2003. http://srdata.nist.gov/xps/.
68. Cho G, Glatzhofer DT, Fung BM, et al. Formation of ultrathin polypyrrole (PPY) films on alumina particles using adsorbed hexanoic acid as a template. Langmuir 2000;16(10):4424–9.
69. Vernitskaya TV, Efimov ON. Polypyrrole: a conducting polymer; its synthesis, properties and applications. Russ Chem Rev 1997;66(5):443–57.
70. Tian Y, Yang F, Yang W. Redox behavior and stability of polypyrrole film in sulfuric acid. Synth Met 2006;156(16–17):1052–6.
71. Socrates G. Infrared and Raman characteristic group frequencies. Baffins Lane, Chichester, England: John Wiley & Sons; 2001.
72. Omastova M, Trchova M, Kovarova J, et al. Synthesis and structural study of polypyrroles prepared in the presence of surfactants. Synth Met 2002;138(3):447–55.
73. Tian B, Zerbi G. Lattice dynamics and vibrational spectra of pristine and doped polypyrrole: effective conjugation coordinate. J Chem Phys 1990;92(6):3892–8.
74. Liu L, Zhao C, Zhao Y, et al. Characteristics of polypyrrole (PPy) nano-tubules made by templated ac electropolymerization. Eur Polym J 2005;41(9):2117–21.
75. Blinova NV, Stejskal J, Trchová M, et al. Polyaniline and polypyrrole: a comparative study of the preparation. Eur Polym J 2007;43(6):2331–41.
76. Patil AO, Heeger AJ, Wudl F. Optical properties of conducting polymers. Chem Rev 1988;88(1):183–200.
77. Hansen CM. Hansen solubility parameters: a user's handbook. Boca Raton, FL: CRC Press; 2007.
78. Shaffer MSP, Fan X, Windle AH. Dispersion and packing of carbon nanotubes. Carbon 1998;36(11):1603–12.
79. Sorensen PA, Dam-Johansen K, Einell CE, et al. Cathodic delamination of seawater-immersed anticorrosive coatings: mapping of parameters affecting the rate. Prog Org Coat 2010;68(4):283–92.
80. Nguyen T, Hubbard JB, Pommersheim JM. Unified model for the degradation of organic coatings on steel in a neutral electrolyte. J Coat Technol 1996;68(855):45–56.
81. Recommended Practice DNV-RP-B101. *Corrosion protection of floating production and storage units.* Det Norske Veritas; 2007.
82. Evans UR. The corrosion and oxidation of metals. London: Edward Arnold; 1961.
83. Wilhelm SM. Galvanic corrosion caused by corrosion products. In: Hack HP, editor. Galvanic corrosion, ASTM STP 978. Philadelphia: American Society for Testing and Materials; 1988. p. 23–34.
84. Hammer P, dos Santos FC, Cerrutti BM, et al. Carbon nanotube-reinforced siloxane-PMMA hybrid coatings with high corrosion resistance. Prog Org Coat 2013;76(4):601–8.
85. Mansfeld F, Kendig M, Tsai S. Determination of the long term corrosion behavior of coated steel with AC impedance measurements. Corros Sci 1983;33(4):317–29.
86. Mansfeld F, Tsai CH. Determination of coating deterioration with EIS: I. Basic relationships. Corrosion 1991;47(12):958–63.
87. Tsai CH, Mansfeld F. Determination of coating deterioration with EIS: part II. Development of a method for field testing of protective coatings. Corrosion 1993;49(9):726–37.
88. Bacon RC, Smith JJ, Rugg FM. Electrolytic resistance in evaluating protective merit of coatings on metals. Ind Eng Chem 1948;40(1):161–7.
89. Singha S, Thomas MJ. Permittivity and tan delta characteristics of epoxy nanocomposites in the frequency range of 1 MHz–1 GHz. IEEE Trans Dielectr Electr Insul 2008;15(1):2–11.

90. Singha S, Thomas MJ. Dielectric properties of epoxy nanocomposites. IEEE Trans Electr Insul 2008;15(1):12–23.
91. Lichtenecker K, Rother K. Die herleitung des logarithmis- chen mischungsgesetzes als allegemeinen prinzipien der staionaren stromung. Physikalische Zeitschr 1931;32:255–60.
92. Brasher DM, Kingsbury AH. Electrical measurements in the study of immersed paint coatings on metal. I. Comparison between capacitance and gravimetric methods of estimating water-uptake. J Appl Chem 1954;4(2):62–72.
93. Haruyama S, Asari M, Tsuru T. In: Kendig MW, Leidheiser H, editors. Electrochemical society proceedings series. Proceedings of the symposium on corrosion protection by organic coatings [abstract 87-2]; Pennington: Electrochemical Society; 1987. p. 197–207.
94. Hirayama R, Haruyama S. Electrochemical impedance for degraded coated steel having pores. Corrosion 1991;47(12):952–8.
95. Hack HP, Scully JR. Defect area determination of organic coated steels in seawater using the breakpoint frequency method. *Ship materials engineering research and development report*, David Taylor Research Center; 1990.
96. Bhargava G, Gouzman I, Chun CM, et al. Characterization of the "native" surface thin film on pure polycrystalline iron: a high resolution XPS and TEM study. Appl Surf Sci 2007;253(9):4322–9.
97. Fiuschau GR, Yoshikawa S, Newnham RE. Resistivities of conductive composites. J Appl Phys 1992;72(3):953–9.
98. Sherman RD, Middleman LM, Jacobs SM. Electron transport processes in conductor-filled polymers. Polym Eng Sci 1983;23(1):36–46.
99. Reed-Hill RE. Physical metallurgy principles. 2nd ed. New York: Van Nostrand; 1973 p. 418–22.
100. Rothon RN. Mineral fillers in thermoplastics: filler manufacture and characterization. Adv Polym Sci 1999;139:67–107.
101. Gergely A, Pászti Z, Hakkel O, et al. Corrosion protection of cold-rolled steel with alkyd paint coatings composited with submicron-structure types polypyrrole-modified nano-size alumina and carbon nanotubes. Mater Sci Eng B 2012;177(18):1571–82.
102. Patil RC, Radhakrishnan S. Conducting polymer based hybrid nano-composites for enhanced corrosion protective coatings. Prog Org Coat 2006;57(4):332–6.
103. Joseph RD. Metals handbook, ASM international, vol. 1. 9th ed. Ohio: Materials Park; 1978. p. 758.
104. Jing X, Zhao W, Lan L. Threshold in polymer/conducting particle composites. J Mater Sci Lett 2000;19(5):377–9.
105. von Baeckman W, Schwenk W, Prinz W. In: Handbook of cathodic corrosion protection, theory and practice of electrochemical protection processes. 3rd ed Houston: Gulf Professional Publishing; 1997. p. 209.
106. McClory C, McNally T, Baxendale M, et al. Electrical and rheological percolation of PMMA/MWCNT nanocomposites as a function of CNT geometry and functionality. Eur Polym J 2010;46(5):854–68.
107. Zhu J, Wei S, Yadav A, et al. Rheological and electrical analysis in carbon nanofiber reinforced polypropylene composites. Polymer 2010;51(3):2643–51.
108. Ando Y, Zhao X, Shimoyama H, et al. Physical properties of multiwalled carbon nanotubes. Int J Inorg Mater 1999;1(1):77–82.
109. Li HJ, Lu WG, Li JJ, et al. Multichannel ballistic transport in multiwall carbon nanotubes. Phys Rev Lett 2005;95(8):086601 (1–4).
110. Dekker C. Carbon nanotubes as molecular quantum wires. Physics Today 1999;52(5):22–8.
111. Yan M, Gelling VJ, Hinderliter BR, et al. SVET method for characterizing anti-corrosion performance of metal-rich coatings. Corros Sci 2010;52(8):2636–42.
112. Uhlig HH, Revie RW. Corrosion and corrosion control. New York: John Wiley & Sons; 1985.
113. Xiao G, Tao Y, Lu J, et al. Highly conductive and transparent carbon nanotube composite thin films deposited on polyethylene terephthalate solution dipping. Thin Solid Films 2010;518(10):2822–4.

114. Blackburn JL, Barnes TM, Beard MC, et al. Transparent conductive single-walled carbon nanotube networks with precisely tunable ratios of semiconducting and metallic nanotubes. ACS Nano 2008;2(6):1266–74.
115. Aguilar JO, Bautista-Quijano JR, Avilés F. Influence of carbon nanotube clustering on the electrical conductivity of polymer composite films. eXPRESS Polym Lett 2010;4(5):292–9.
116. Suzuki YY, Heeger AJ, Pincus P. Percolation of conducting polymers on a gel. Macromolecules 1990;23(21):4730.
117. Fizazi A, Moulton J, Pakbaz K, et al. Percolation on a self-assembled network: decoration of polyethylene gels with conducting polymer. Phys Rev Lett 1990;64(18):2180–3.

Chapter 7

Innovative Luminescent Vitreous Enameled Coatings

Stefano Rossi[*], **Alberto Quaranta**[*], **Linda Tavella**[*], **Flavio Deflorian**[*], **Attilio M. Compagnoni**[†]

[*]*Department of Industrial Engineering, University of Trento, via Sommarive 9, Trento, Italy*

[†]*Wendel Email Italia, Via Bedeschi 10a, Chignolo (BG), Italy*

7.1 Introduction

Porcelain enamel is an inorganic coating of a vitreous nature that can be applied to both glass and metallic substrates, such as steel and aluminum alloys, using different techniques. *Enamel* is a term of medieval origin derived from the Germanic *smaltjan*, which means *melt*. This coating, in fact, is produced from vitreous flakes which, with the addition of pigments and additives, are fired at relatively high temperatures (between 780 and 850°C, in the case of steel substrate). Then, as a matter of fact, enamel is essentially glass and does not require the application of any kind of toxic substances, such as solvents or other chemical components.[1]

During the heat treatment there is fusion of the frit flakes and solubilization of most of the oxides and compounds added during the mill grinding. The vitreous flakes, called *frit*, are obtained by the melting, rapid cooling, and subsequent grinding with the other materials that constitute the glass. Porcelain enamel is an ancient material. Due to its characteristics of brightness and durability this material has been

Intelligent Coatings for Corrosion Control
Copyright © 2015 Elsevier Inc. All rights reserved.

used for many centuries in artistic fields for manufacturing jewels, art objects, religious items, and other pieces, owing to its attractive appearance with brilliant colors. With the advent of the industrial revolution in the eighteenth century, the use of enamel began to spread, and it was used in several products on an industrial scale, such as household goods, furnishings, and interior decoration items.[2] In recent decades vitreous enamel has been used both for decorative purposes and for protection against corrosion and for its engineering properties. Today there is a tendency to try to combine in a material, and particularly in the coating, more properties of different natures. These coatings are therefore called *intelligent* or *smart* materials or coatings. Even the enamels have followed this trend. In recent years, the research has tried to combine in these layers different functional properties, such as antibacterial properties and optical properties with corrosion and high temperatures.

The research to produce luminescent enamels, the object of this chapter, has the purpose of bringing together the excellent functional and aesthetic properties of this traditional type of coating with the luminescence characteristic, which could lead to new uses of the enamel. Luminescent materials, such as polymers, organic coatings, and inks are already on the market; however, these products are based on pigments that do not show corrosion resistance at high temperatures. In addition these materials do not often present resistance to natural weathering, UV radiation, and chemicals.

The luminescent enamel could have interesting commercial applications (components of outdoor furniture and interior design, architecture, applications in the safety field). Applications in fields in which luminescent paints are not suitable could be very interesting. Luminescent enamel is a not material that is much studied. In the literature, there are very few references to this material. The properties of these innovative materials are not well studied, especially considering their resistance to weathering. The purpose of this work is to study and characterize some types of luminescent porcelain enamel considering both microstructural and the luminescence properties.

To consider several possible applications, it is necessary to investigate the properties of the material using tests that simulate different types of aggressive environments in order to check the maintaining of the luminescent properties during exposure to aggressive environments and whether the addition of luminescent pigments could reduce or modify the excellent properties of traditional porcelain enamel. In addition, it is not known if the heat treatment of enamel curing could modify the behavior of luminescent pigments.

7.2 The Most Important Properties of Vitreous Enamel

Porcelain enamel presents numerous properties that allow many applications in different fields. This type of layer is one of the best methods to guarantee corrosion protection in numerous environments due to its glassy nature, the absence of defects, and its high thickness and excellent adhesion. Figure 7.1 shows the typical cross-section of an enamel layer.

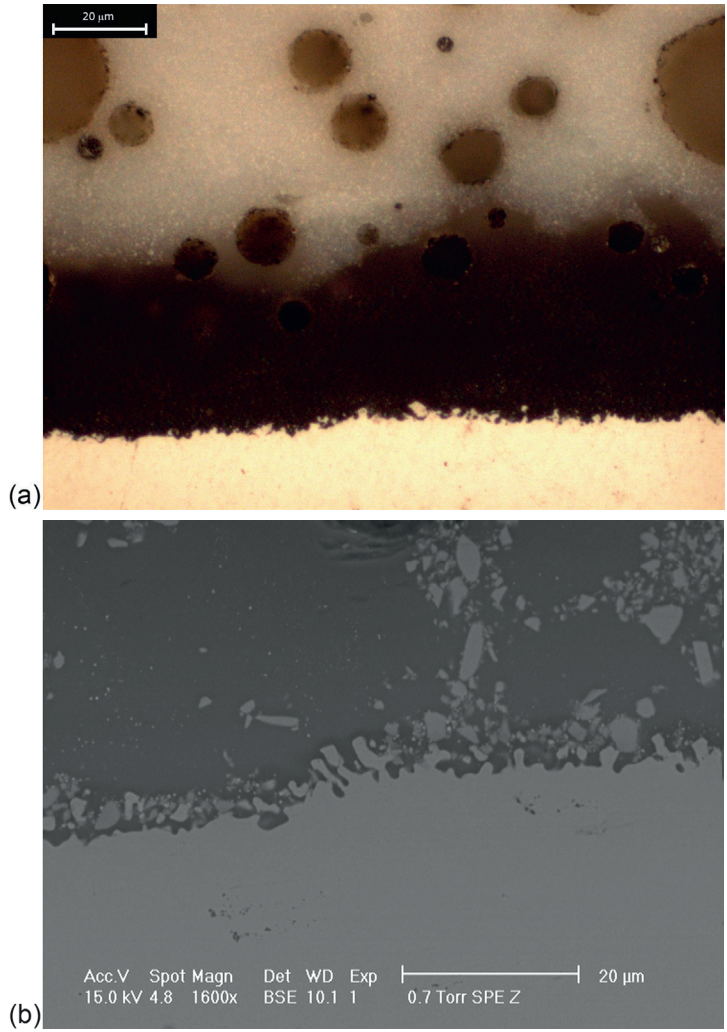


Figure 7.1 Typical cross-section of a vitreous enamel coating deposited on steel substrate (a) and the interface between glassy matrix and steel substrate (b).[1]

The excellent adhesion is obtained during the process of curing. During the thermal treatment the oxidation of the iron of the substrate happens with the formation of oxides with a dendritic growth. These physical-chemical reactions occurring at the interphase enamel/metal guarantee a strong adherence between the two materials, thus providing the enamel/metal system with good mechanical properties and excellent corrosion resistance.

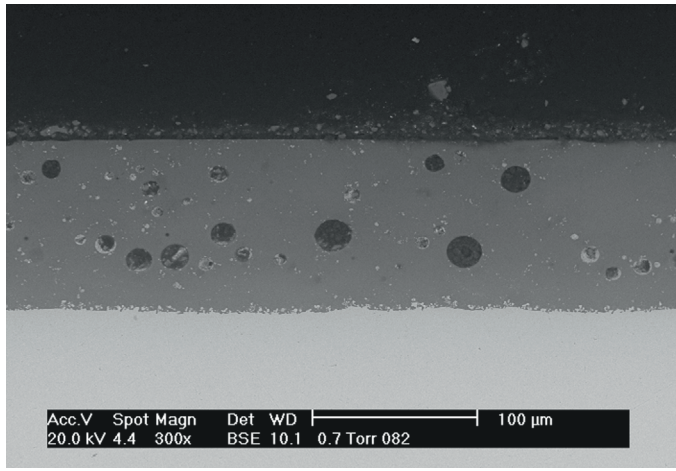


Figure 7.2 Typical porosity present in an enamel layer.

The firing temperature is between 760 and 870 °C. During this process the different components interact in enamel glass, gas bubbles can be produced, and the layer surface is leveled. Then, a diffusion process of the melted frit is present, obtaining excellent adhesion properties thanks to the presence of oxides including cobalt.[3,4]

From Figure 7.2 it possible to observe the typical porosity formed during the curing process due to the development of gas and water vapor. The porosity remains limited to the layers closest to the substrate. In addition, this porosity is not interconnected and then the contact between aggressive environment and metallic substrate is avoided. Due to this aspect and to chemical inertia of the glass matter, this coating shows excellent corrosion protection. Thanks to the glassy nature, the coating is resistant to most of the solutions with the exception of strong basic solutions of fluoridric acid. The enamel shows also resistance to high temperature and it is easily cleanable.[3–5]

The glassy nature of the matrix and of the colored pigments produces an excellent resistance to UV radiation with the maintaining of the color.[4]

The hardness also provides good resistance to mechanical damage, the exclusion of impulsive collisions, due to the brittleness of the glassy matter. This coating, in addition to good protection properties, shows very interesting aesthetic qualities connected with its vitreous nature. Its smooth surface provides high gloss and a great color palette with different color shades and textures with special effects available.[2,4]

By modifying the frits chemical composition it is possible to control the properties of the layers, improving some aspects. For example, potassium feldspar and zirconium silicate are added in the frit composition to promote the pyrolytic properties at high temperatures and to improve flame resistance, avoiding unaesthetic surface changes.

Usually, in order to guarantee a very good adhesion a groundcoat enamel ensures the adhesion between the coating and the substrate; the followed covercoat enamels provide different surface properties.[1]

7.3 Luminescent Properties

Luminescent materials have the characteristic of emitting light when excited by cathode rays, UV radiation, or visible light.

The luminescence is a physical process derived from electronic transitions: only some materials exhibit this phenomenon, such as phosphors.[6]

Usually the luminescent material is formed by a matrix doped with activators, which can be a transition metal or rare earth ions that act as emitting centers. When the material is irradiated with a suitable wavelength, the activators absorb the energy, reaching an electronic excited state. The absorbed energy must equal to the distance between the two energy levels. This condition is unstable, and the system goes back to the ground state by releasing the energy in the form of radiation emission.[7]

To obtain materials that show at the same time luminescent properties and not radioactive or toxic aspects, the addition of rare earths to the oxide matrix is very frequent. The optical excitation of rare earth ions occurs by means of transitions between the 4f orbitals or form 4f to 5d levels. Some tetravalent ions (Ce^{4+}, Pb^{4+}, Tb^{4+}) and some trivalent ions (Dy^{3+}, Eu^{3+}) have transitions between 4f levels; while other trivalent (Ce^{3+}, Pb^{3+}) and bivalent (Sm^{2+}, Yb^{2+}, Eu^{2+}) ions have transitions between 4f and 5d levels.[7]

Luminescent materials, which exhibit the phenomenon of the afterglow, are particularly interesting. In fact, in these materials the luminescence can be observed for a long time after the end of the excitatory pulse. This phenomenon is possible by the storage of excitation energy in the lattice for a certain time period.[7] This category includes the *long-afterglow phosphors,* which have a luminescence decay time ranging from seconds to minutes.

Considering rare earths, a phosphor can be obtained by exploiting the electronic transitions in the energy levels of europium and dysprosium ions, in particular the electronic transfer from Eu^{2+} to Dy^{3} during arousal and from Dy^{3+} a Eu^{2+} during the release.[6] At this type of luminescent pigment often strontium is added, which helps to increase the emission intensity.[8]

7.4 Luminescent Porcelain Enamel Coatings

In this chapter luminescent porcelain enamel is considered, which emits a light radiation after being irradiated with UV or visible light due to the adding of pigments containing europium and dysprosium.

The luminescence properties of these pigments is ensured by the electronic transitions of europium ions, while the presence of dysprosium ions is fundamental to obtain a long afterglow. In particular the latter ions act as hole traps capturing the gaps formed by the excitement of the europium ions.[9]

In europium and dysprosium doped matrices, Dy^{3+} is indispensable to obtaining a long luminescence decay time, and, in the same time, its concentration influences the emission spectra. This has been verified by Song et al.[10] in Al_2O_3-SiO_2 glasses doped with Eu and Dy, where an increasing of Dy concentration leads to an increase in green emission effect, which was attributed to the presence of defects in the lattice.

7.5 Materials and Experimental Procedures

Low-carbon steel panels (10×10 cm) were coated with different luminescent vitreous enamel systems made of three layers. The first was the ground layer, which functioned to guarantee good corrosion protection and adhesion of the coating;[3] the second one guarantees corrosion protection; and the top layer shows the luminescent properties. The coatings are obtained by wet spraying in an industrial laboratory (Wendel Email Italia, Chignolo d'Isola—BG). Drying and firing treatments at a temperature of 850 °C were carried out (three applications and two firing processes).

The first two layers present a typical commercial composition based on SiO_2, B_2O_3, Na_2O, and other oxides; TiO_2 was added in the intermediate layer as an opacifier agent. The total thickness of both layers together is 220 µm.

To produce the luminescent deposit a standard frit was used with an adding of 50% wt. of luminescent pigments, containing europium and dysprosium oxides, and of 1% wt. of visible color pigments. The other components of the frit were typical of enamel with the presence of Al_2O_3, SiO_2, SrO, MgO, CaO, and B_2O_3.

The luminescent pigments are made of a vitreous matrix, 50% wt. Al_2O_3, 25-30% SiO_2, 30% wt. SrO, 10-15% wt. MgO, 2% wt. CaO, 1-2% wt. B_2O_3 wt. with the addition of Eu_2O_3 and Dy_2O_3.

To permit the wet application to the frits are added 5% wt. clay, 0.5% wt. sodium aluminate, and 50% wt. water, producing the necessary slurry.

Three different types of samples are investigated considering the visible color and the luminescent effect produced with different Eu/Dy ratios, as shown in Table 7.1 In addition the dimension of luminescent pigments used for samples M1 and M2 are smaller than those used for sample M3.

The microstructural characterization was carried out on both the cross-section and the surface using an ESEM Philips XL30 microscope. The typical properties of traditional enamel, such as corrosion protection, resistance of color, and gloss and abrasion resistance, were evaluated to observe if the presence of luminescent can affect these properties. The luminescent properties of the different layers and their

TABLE 7.1 Characteristics of Luminescent Layers

Luminescent Enamel Layers	M1	M2	M3
Ratio Eu/Dy	1.2	4	0.6
Visible color	White/light yellow	Light blue	Yellow
Luminescent emission color	Sky blue	sky blue	Blue green
Thickness of luminescent layer [μm]	170	240	95

persistence during accelerated testing were also evaluated. Luminescent characteristics were evaluated measuring the emission spectrum (excitation wavelength of 350 nm) and excitation spectra (emission wavelength 500 nm), using a Jasco spectrofluorimeter FP6300. To evaluate the stability of the properties, different accelerated tests were then carried out, normally performed on coatings and enamels. An exposure to UV-A radiation for 500 h, following ASTM G154 standard, was made. Before and after the exposure the color was measured using a spectrometer CM-2600d Konica Minolta with illuminant D65/10° following the international method CIELab.[11–13] Several parameters were considered. The total color differences ΔE^* before and after the test was calculated as follows in Equation (7.1):

$$\Delta E^* = \left((\Delta L)^2 + (\Delta a)^2 + (\Delta b)^2 \right)^{1/2} \tag{7.1}$$

where L is the lightness (0 is black, and 100 is white), a is the red-green variation (positive values are red, negative values are green, and 0 is neutral), and b is the yellow-blue variation (positive values are yellow, negative values are blue, and 0 is neutral).

To check the endurance of the luminescent properties in case of cyclic stimulus, 24 cycles of alternate radiation exposure, consisting in 1 h of UV-A exposure followed by an hour without irradiation, were carried out. During this test, the performance of the luminescence as a function of time was continuously monitored using an Ocean Optics Spectrometer USB4000. To collect the emission, a 600 μm silica optical fiber was fixed in front of the sample. As reference sample, the light reflected from a white, not luminescent enamel was measured during the cycles. The spectra and the signal as a function of the time was analyzed by means of SpectraSuite. During the cycling test the intensity of the maximum peak of the spectrum (associated with a particular wavelength) in function of time test was monitored with a measurement every minute.

From the emission spectrum, detected by the optical fiber, was subtracted the reflected spectrum of the UV-A lamps from the white enamel in order to obtain as a result only the emission spectrum of the luminescent enamel. To evaluate the chemical resistance, the samples were subjected to both acid and alkaline attack. For the acid resistance test, the enamel specimens were immersed for 24 h in a 10%wt. citric

acid solution at room temperature at around pH 2, following ASTM C282. For the alkaline solution resistance test, the samples were immersed in a 52.64 g/l solution of tetra potassium pyrophosphate at pH 10 for 6 h at 96 °C.

To evaluate the produced damage, color, gloss, and roughness were measured at the beginning time and after 3, 6, 9, and 24 h of immersion. A glossmeter digital Erichsen NL3A was used for the measurement of gloss. The roughness was measured using a MAHR MarSurf PS1 tester at a measurement length of 5.6 mm and a cut-off length of 0.8 mm. R_a was recorded as an average value of five measurements. The device measures at an accuracy of 0.01 µm. Using the spectrofluorimeter, luminescence characteristics were measured before and after the attack.

After immersion the surface and the cross-section were observed using an environment scanning electronic microscope ESEM Philips XL30 to observe the possible damage of the luminescent enameled surface.

To investigate the corrosion protective properties and to check the possible influence of the presence of luminescent layers, samples with an artificial linear defect of 2 mm wide were exposed in a salt spray chamber, according to ASTM B117, for a total of 1000 h. After 500 and 1000 h of exposure, the state of the surface close to the defect was observed using the optical microscope Zeiss Stemi 2000-C to evaluate the adhesion of the luminescent enamel and the possible presence of enamel detachment phenomena.

To evaluate the potential reduction of the luminescence characteristics, the luminescence was measured at the beginning, after 500, and after 1000 h of exposure, using the Jasco spectrofluorimeter FP6300. Finally the resistance to mechanical damage and maintenance of the luminescence properties were evaluated. An abrasion Taber test according to ASTM D-4060 with the use of Taber Abraser 5135 was carried out. H22 grinders with 1 kg applied weight were used.[14,15] The wheels were composed of vitrified clay, silicon carbide, and alumina particles embedded in an organic matrix. After 1000 cycles the change of color, gloss, and surface roughness were measured to highlight the produced damage on the surface. The gloss measured at angle of 60° obtained from the average of more than 12 measures considered.

Roughness measurements R_a, 12 for each sample, were carried out. The decrease in luminescence was evaluated using a FP6300 Jasco spectrofluorimeter. Luminescence spectra were collected on each sample from several points.

To highlight the damage morphology, the samples surfaces were observed using a scanning electron microscope. To study the change of the corrosion protection properties produced by mechanical damage, the abrasion test has been carried out up to the loss of protection. To highlight the protection properties loss, electrochemical impedance spectroscopy (EIS) measurements were the carried out. This technique is widely used to evaluate the protective properties of coatings.[16–18]

The measurements were carried out in a classic three-electrode system: the sample was the working electrode, a platinum counter electrode was used, and Ag/AgCl (0.205 V vs. standard hydrogen electrode SHE) was used as the reference electrode.

The analyzed area was 30.43 cm^2, corresponding to the circularly damaged area during an abrasion test. The electrolyte was a 3 wt.% Na_2SO_4 solution.

The electrochemical impedance measurements were carried out every 1000 abrasion cycles. The EIS measurements were carried out using a potentiostat and a Frequency Response Analyzer instrument (Princeton PARSTAT 2273) connected to a PC. The AC perturbation amplitude was 15 mV, the frequency ranged from 10^5 to 10^{-2} Hz. The EIS data are fitted using a simple equivalent electrical circuit made of a capacity in parallel with a resistance R(RQ),[16,18] using the *Z SIMP WIN* fitting program. The first resistance is the electrolyte resistance, the R_p is the coating resistance, and the C_p represent the coating capacity.

The R_p threshold of $10^6\ \Omega cm^2$ is considered as the limit of the loss of protection properties of the coating.[2,14] Below this threshold, in fact, the coating could be considered not protective. After 8000 cycles of abrasion the samples surface were observed at an optical microscope Zeiss Stemi 2000-C to highlight the damage morphology and to highlight the difference among the luminescent samples.

7.6 Results and Discussion

7.6.1 Characterization of enamel layers

Figures 7.3–7.5 show the cross-section of the different samples. Considering the microstructural analysis of the samples, it is possible to observe the presence of rather large closed porosity (diameter up to 40 µm), in particular at the interface between

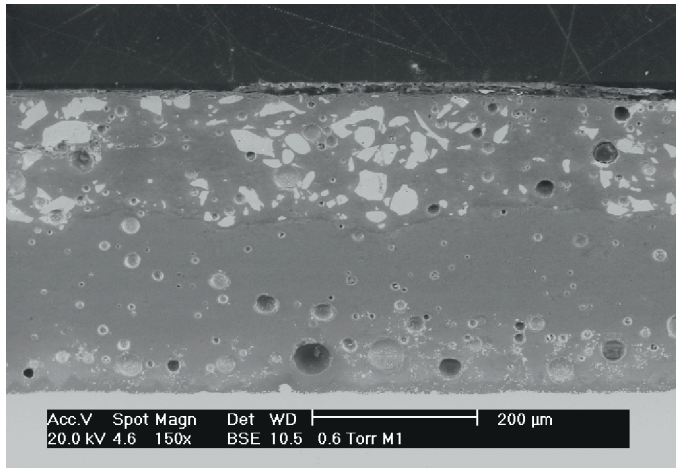


Figure 7.3 Microstructural cross-section of sample M1.

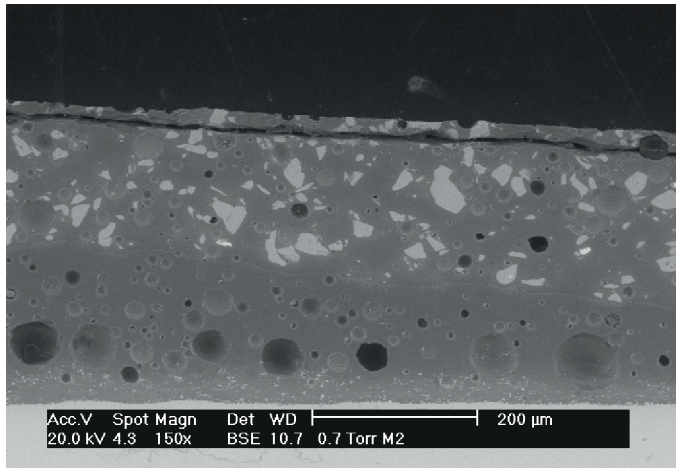


Figure 7.4 Microstructural cross-section of sample M2.

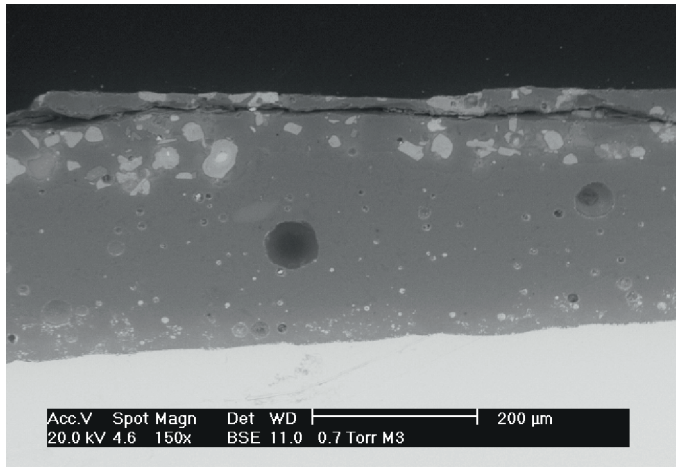


Figure 7.5 Microstructural cross-section of sample M3.

the enamel ground layer and intermediate one; on the contrary in the ground layer and in the finish luminescent layer the pores were smaller and less frequent. These are the typical porosity results of the vitreous enamel formed during the curing process of the coating.[1,3]

In all three samples the presence of dendrites at the interface between the enamel layer and the steel substrate is observed: this interpenetration of the two materials provides good adhesion of the protective deposits, which show good corrosion protection properties.[1,3]

Observing the luminescent deposit, the particles of strontium oxide, light particles, are concentrated more in some areas and show a variable size with a maximum value of 35 µm.

For sample M2 the particles of strontium oxide are mainly concentrated in the inferior half thickness of the luminescent layer; toward the surface, in fact, few particles are present.

Only sample M3 shows the particles of pigments emerging on the surface; these particles are also not homogeneously distributed in the thickness but are concentrated in some areas.

Figure 7.6 shows the surface of the samples. It is possible to observe that in the case of sample M3, the luminescent particles are clearly present on the surface.

The presence or absence of the particles on the surface is likely due to the different nature of the luminescent pigments used in the three types of enamels. The luminescent pigments used in samples M1 and M2 present a small size and therefore are easily embedded in enamel deposition slurry. On the contrary, in the case of sample M3 the luminescent pigments present a significantly larger dimension and during the application some particles remain on the surface; during the firing process these particles are not completely incorporated in the glass matrix.

A mapping by EDXS analysis of the rare earths (europium and dysprosium) showed that these elements are fairly homogeneously dispersed in the luminescent layers. Figure 7.7 shows the emission spectra of the samples. From the emission spectra it can be concluded that these luminescent enamels are characterized only by the electronic transitions of Eu^{2+} ions since transitions related to Eu^{3+} are not observed.[10] On the spectra, two broadbands are present, peaked at 467 nm (blue) and 491 nm (green), respectively. Moreover, as the concentration of dysprosium increases (M2 < M1 < M3) the contribution of the peak in the green, related to the defects in the matrix, increases.[10]

From the excitation spectra (Figure 7.8) it is possible to observe the presence of three peaks. Samples M1 and M2 show spectra with the same shape, with a main peak at 361 nm and two secondary peaks at about 325 and 400 nm. Sample M3 presents a slightly different and wider excitation spectrum, with the main peak with a higher relative intensity and shifted to 365 nm.

7.6.2 Trend of protective properties

The samples were exposed to 500 h of UV-A radiation. Figure 7.9 shows the total change of color: the difference of the color for all samples comprised between 2 and 2.6 points, hardly noticeable by the human eye. Therefore it is possible to affirm that the pigments which produce appearance of the enamel do not present sensible damage due to the resistance of the oxide compounds.

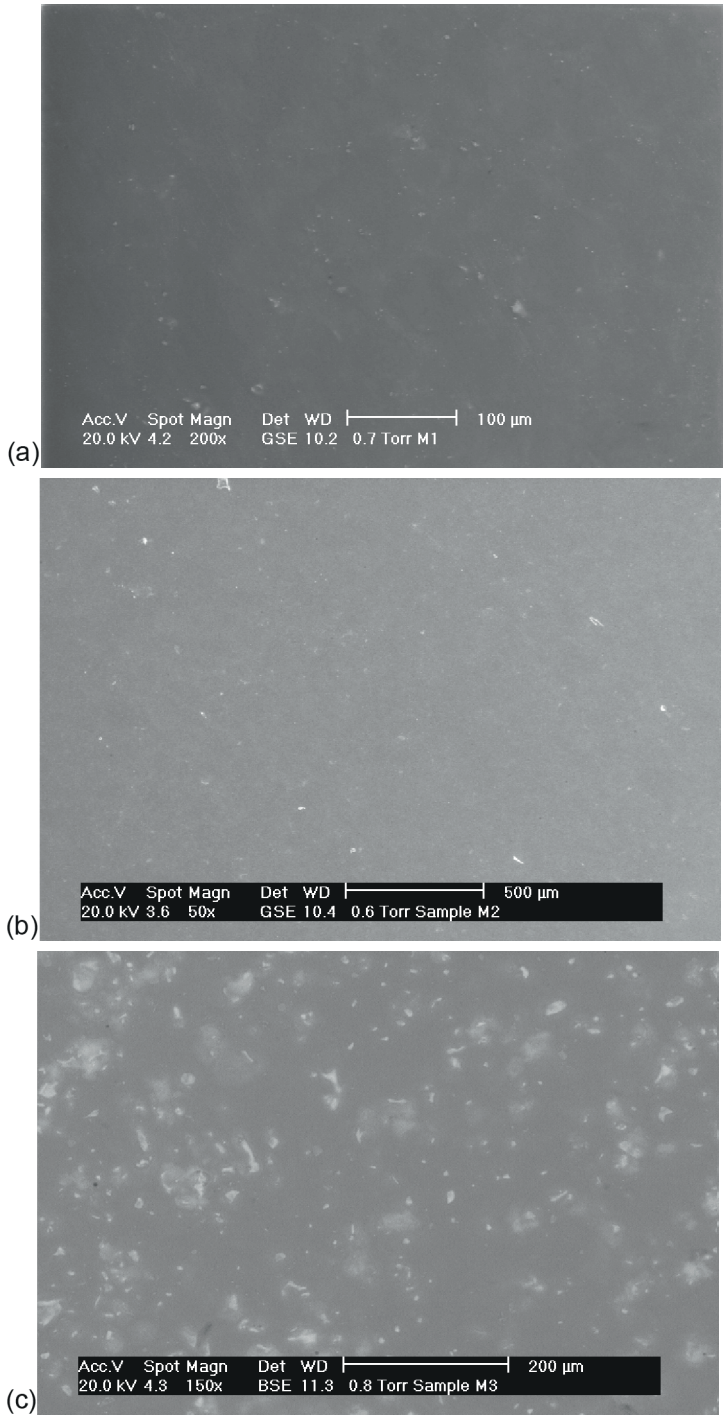


Figure 7.6 Surface of the studied samples: (a) sample M1, (b) sample M2, and (c) sample M3.

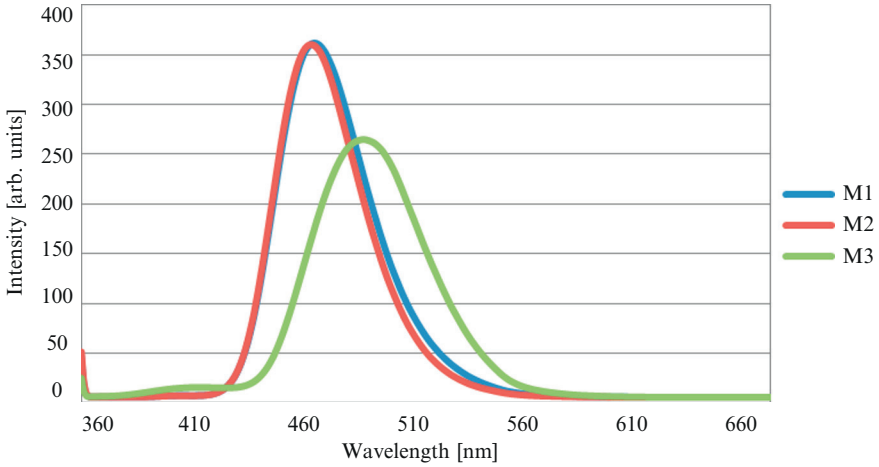


Figure 7.7 Emission spectra of the luminescent enameled layer excited by a radiation with 350 nm wavelength.

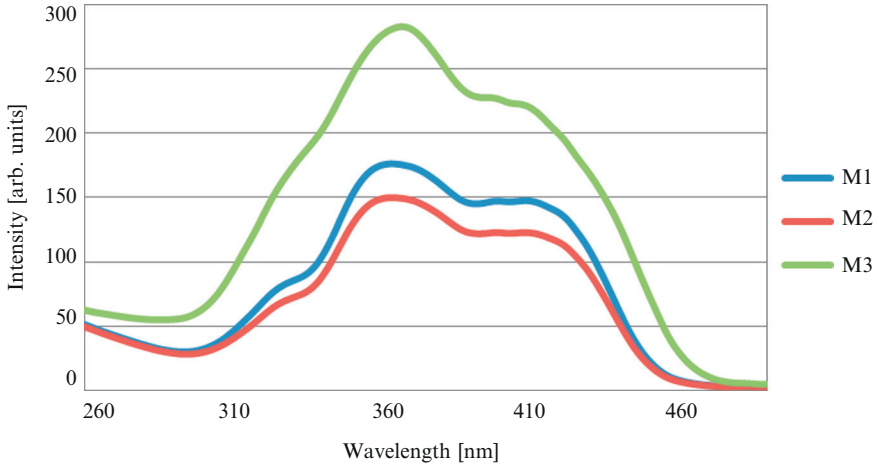


Figure 7.8 Excitation spectra of the luminescent enameled layers.

Considering the different color parameters, sample M1 becomes slightly darker, sample M2 slightly changes to green, and sample M3 changes towards yellow. However, in all cases the variations remain very limited.

Let us now consider the resistance to chemical solutions.

Figure 7.10 shows the variation of gloss before and after 3, 6, 9, and 24 h of immersion in citric acid solution.

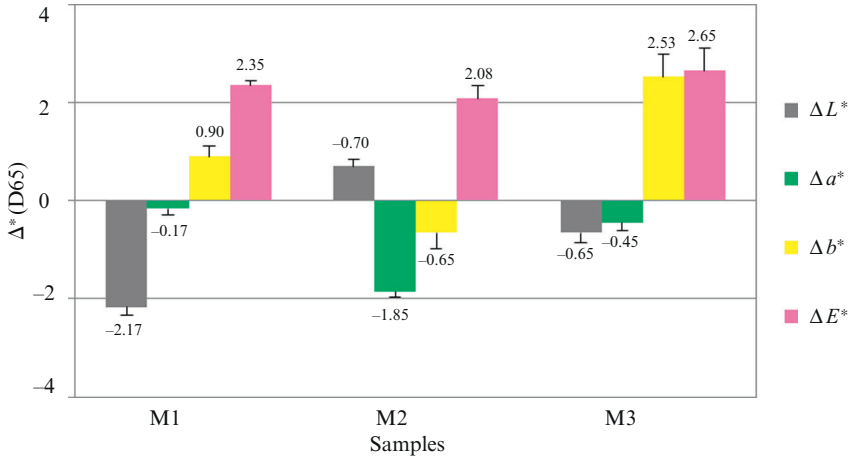


Figure 7.9 Color changes of luminescent enameled samples after 500 h of UV-A continuous exposure.

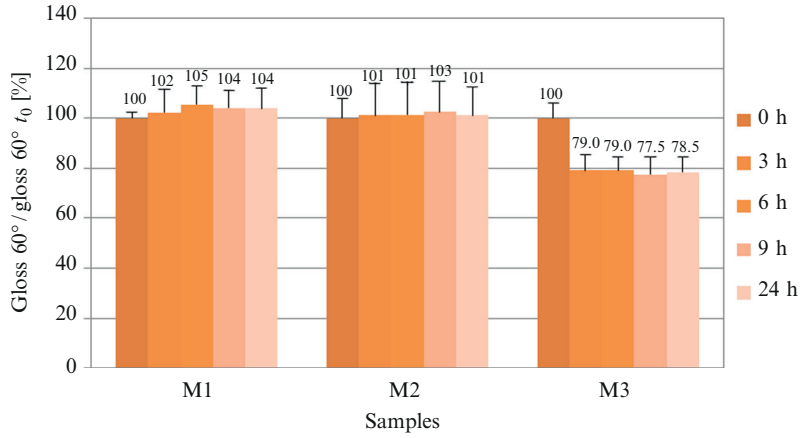


Figure 7.10 Gloss change at 60° of the samples at starting time and after 3, 6, 9, and 24 h of immersion in citric acid solution.

For samples M1 and M2 the values of gloss did not show perceptible changes, indicating an excellent resistance of these samples to the acidic environment. On the contrary, sample M3 showed a sensible decrease of gloss. This decrease is observed already after the first 3 h of immersion; after this time, the value remained practically constant. It is possible to conclude that the damage of the surface starts in a short time. The roughness change values (Figure 7.11) confirm this result. In fact the roughness and the gloss are well connected.

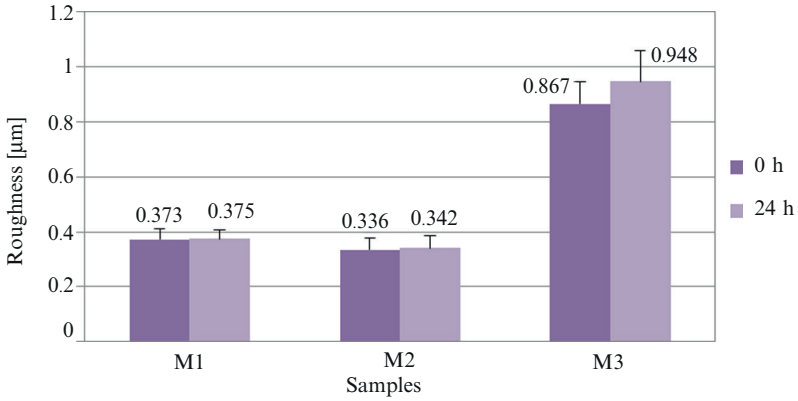


Figure 7.11 R_a [µm] roughness values of the sample before and after 24 h of immersion in citric acid solution.

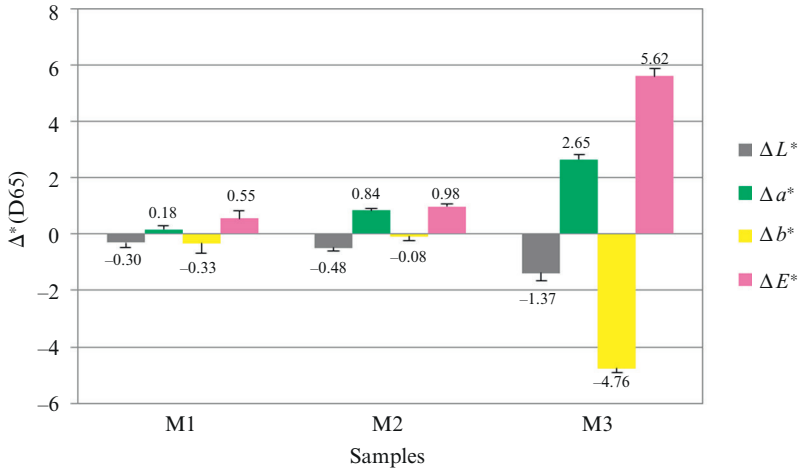


Figure 7.12 Change of color of the samples after 24 h of immersion in citric acid solution.

Considering the color change (Figure 7.12), only sample M3 presents a significant change in the color that turns into the blue and red.

From these experimental data, it is possible to conclude that samples M1 and M2 show a very good resistance to the acid environment presenting an unchanged surface aspect. Sample M3, instead, degrades in the acid solution.

Considering the aspects of surfaces of the samples after 24 h of immersion (Figure 7.13), sample M3 presents localized attacks mainly close to the particle emerged on the surface with consequent roughness increasing and gloss decreasing.

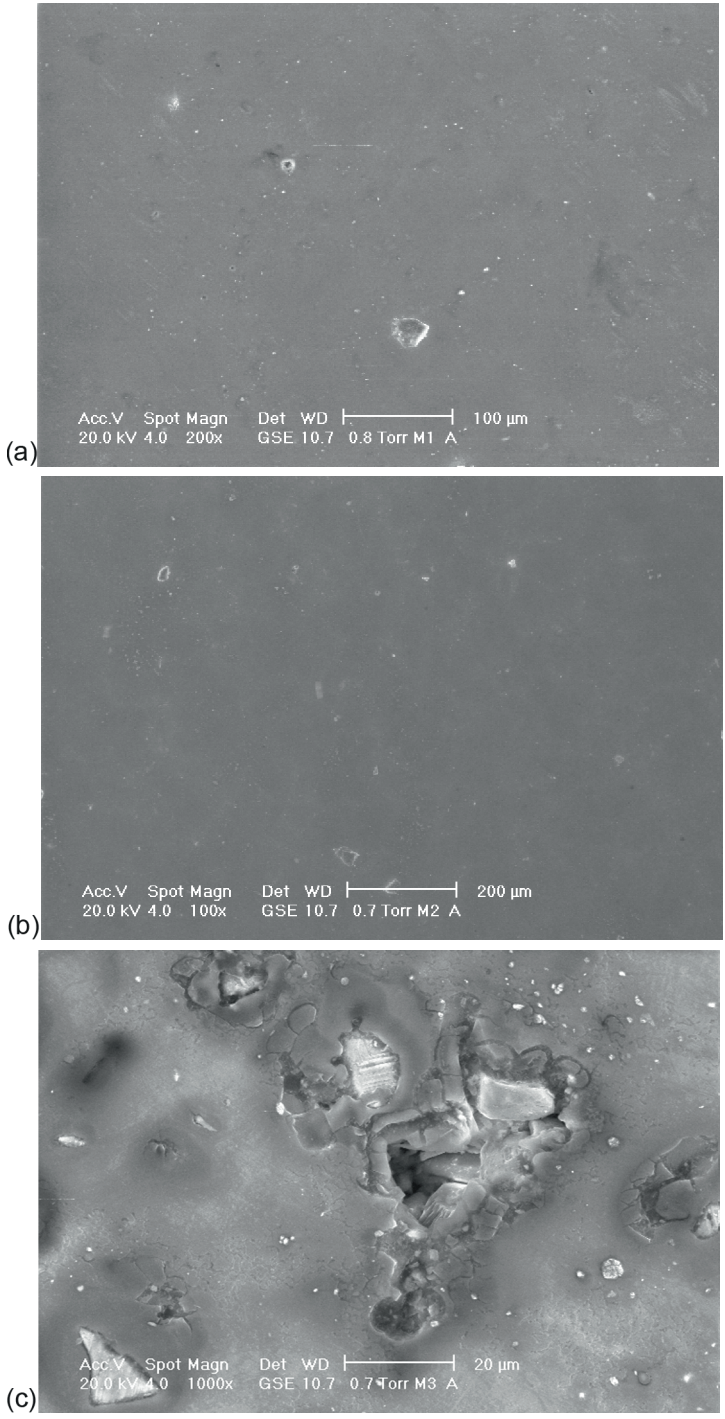


Figure 7.13 (a) Surface of sample M1 after 24 h of immersion in citric acid solution. (b) Surface of sample M2 after 24 h of immersion in citric acid solution. (c) Surface of sample M3 after 24 h of immersion in citric acid solution.

The cause of this different behavior among the samples could be associated with the presence of emerged particles on the surface in the sample M3 and that increasing the roughness could facilitate the start of the chemical attack (Figure 7.14).

A totally different behavior is observed during immersion for 24 h in an alkaline solution of potassium pyrophosphate at 96 °C. In this case, samples M1 and M2 show a considerable variation in both the gloss (Figure 7.15) and the roughness (Figure 7.16). Unlike the previous behavior in acid solution, in this case the decrease of gloss begins after 3 h, but a continuous decrease with immersion time is observed. The degradation process continues during immersion, producing at the test end a significant roughness

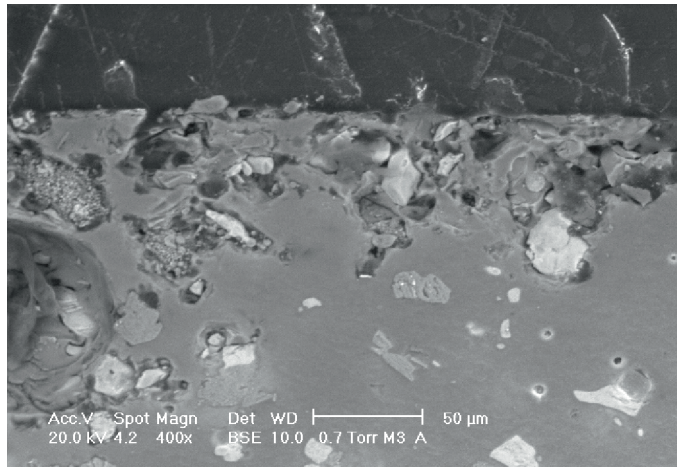


Figure 7.14 Cross-section of sample M3 after 24 h of immersion in citric acid solution.

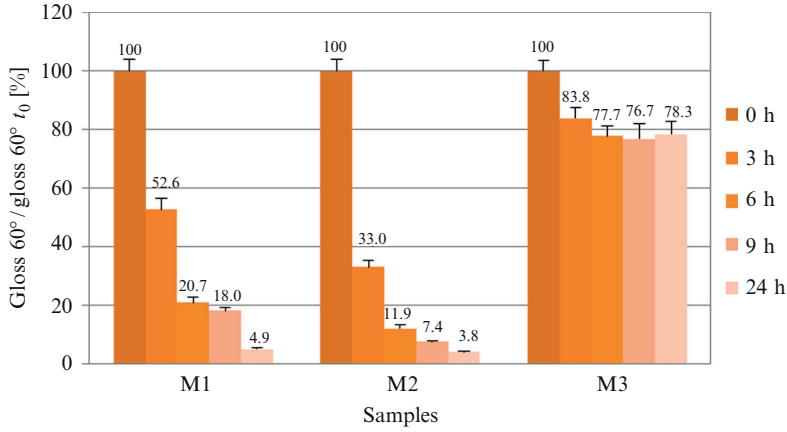


Figure 7.15 Percentage gloss change at 60° compared to the initial value for the samples during immersion in alkaline potassium pyrophosphate solution (before immersion and after 3, 6, 9, and 24 h).

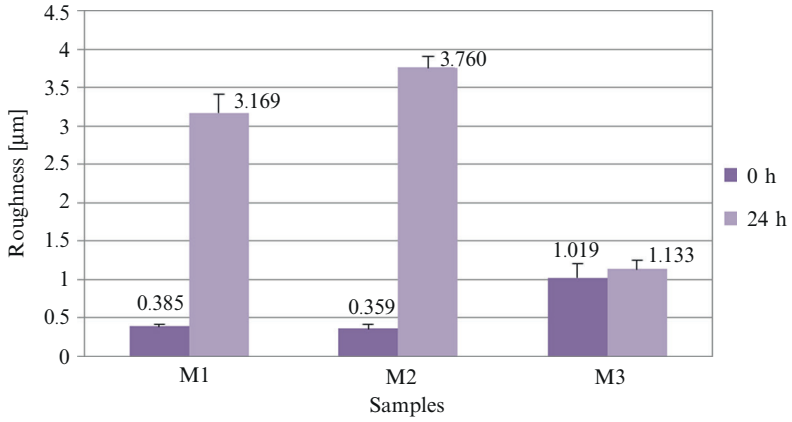


Figure 7.16 R_a [µm] roughness values of the samples at beginning and after 24 h of immersion in alkaline potassium pyrophosphate solution.

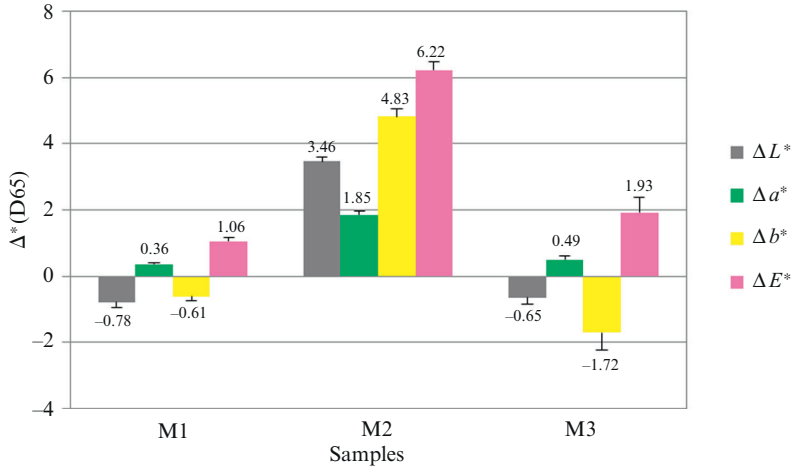


Figure 7.17 Color change of the samples of after 24 h immersion in potassium pyrophosphate solution.

increase. Sample M2 shows the highest variations. On the contrary, sample M3 produces a very limited decrease in gloss, which after 3 h remains unchanged.

The roughness indicates considerable degradation of the surface for samples M1 and M2. Considering color parameters (Figure 7.17), only the sample M2 presents an observable color change appearing lighter and more yellow.

The surface of the samples M1 and M2 after 24 h of immersion in alkaline solution appears highly degraded with the attack of the glassy matrix (Figure 7.18a and b). Sample M3, on the contrary, shows higher resistance to this environment with the presence at the end of the test of only localized attacks of small dimensions (Figure 7.18c).

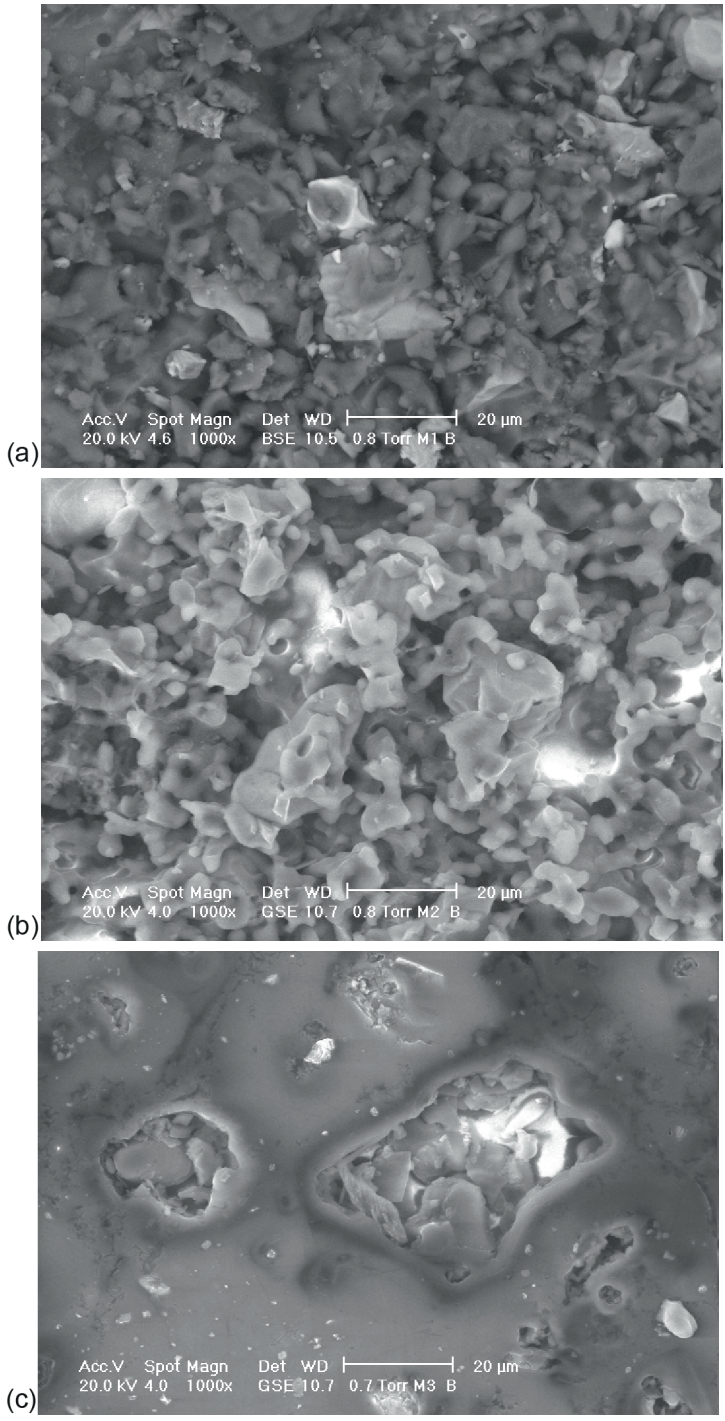


Figure 7.18 (a) Surface of sample M1 after 24 h of immersion in alkaline solution. (b) Surface of sample M2 after 24 h of immersion in alkaline solution. (c) Surface of sample M3 after 24 h of immersion in alkaline solution.

The alkaline solution tends to attack the glass matrix. The cause of this different behavior among the samples could be associated with the presence of particles emerged on the surface. The presence of these particles appears to help the chemical resistance of the enamel, hindering the dissolution of the glass matrix attacked by the alkaline solution and making a barrier between the solution and the glassy matrix (Figure 7.19a and b). M1 sample results less damaged than M2 one, probably due to the higher presence of unsolubilized particles in the upper part of the luminescent enamel layer.

Considering the exposure to salt spray atmosphere, typical accelerated corrosion test, it is possible to observe that after 1000 h of exposure luminescent enamels show

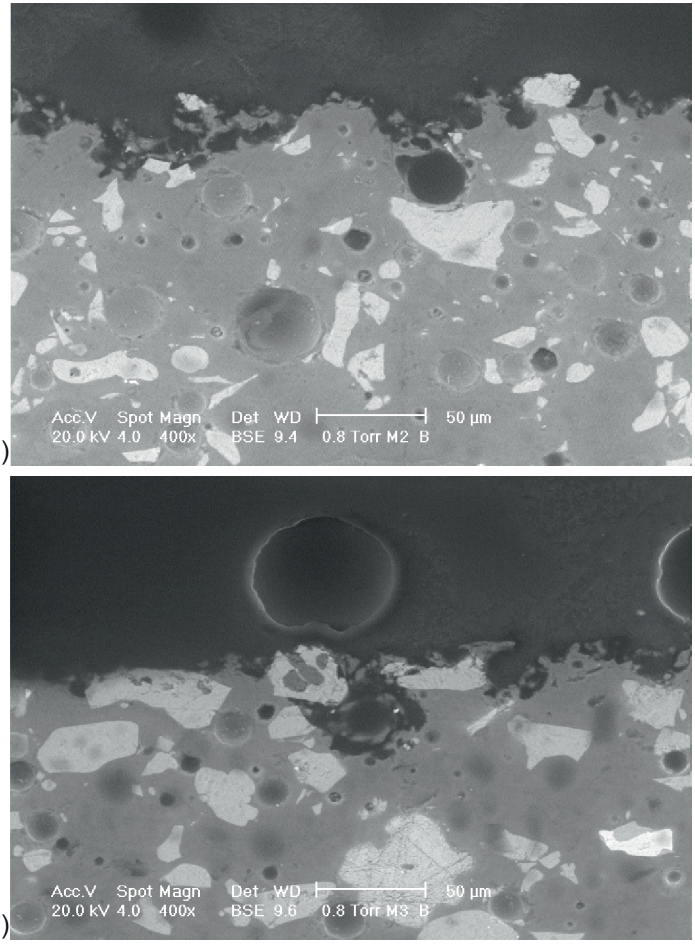


Figure 7.19 (a) Cross-section of sample M2 after 24 h of immersion in alkaline solution. (b) Cross-section of sample M3 after 24 h of immersion in alkaline solution.

an excellent protection against corrosion, typically of enamel coatings. In all cases no detachment of the coating close to the artificial scratch is observed (Figure 7.20). This excellent behavior is due to the inertia of the glass matter together with the excellent adhesion with the steel substrate. Furthermore, the adhesion loss is not present even with corrosive phenomena of the substrate, in correspondence of the defect. This fact confirms that the chemical composition changes of the frit necessary to obtain the luminescent effect do not adversely affect the protective properties of the coatings.

Finally the resistance of abrasion is considered. 1000 cycles of abrasion test produce a great surface modification of the samples with the removal of part of the luminescent enamel layer and with a formation of a widespread defectiveness. In all samples a remarkable increase of roughness was present (Figure 7.21). After the 1000 abrasion cycles, a corresponding high decrease in the gloss values equaled about 20 for all three samples (Figure 7.22).

The abrasion action produced a significant change in the color of the enameled surfaces, highlighting visible noticeable differences (Figure 7.23). Samples M2 and M3 show the greatest variation in the color tone. The sample M2 tended to become lighter and changed to yellow. The sample M3 changed toward blue.

Considering the damaged surfaces in all samples, the abrasive grinders create grooves and scratches in the glass matrix (Figure 7.24). The typical texture of damage with the cross morphology could be recognized, typically produced during the abrasion caused by the grinding wheels.[14]

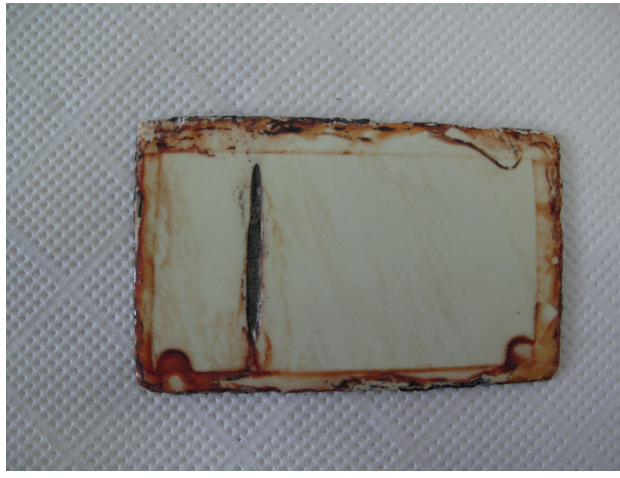


Figure 7.20 Sample M3 with artificial scratch after 1000 h of salt spray exposure.

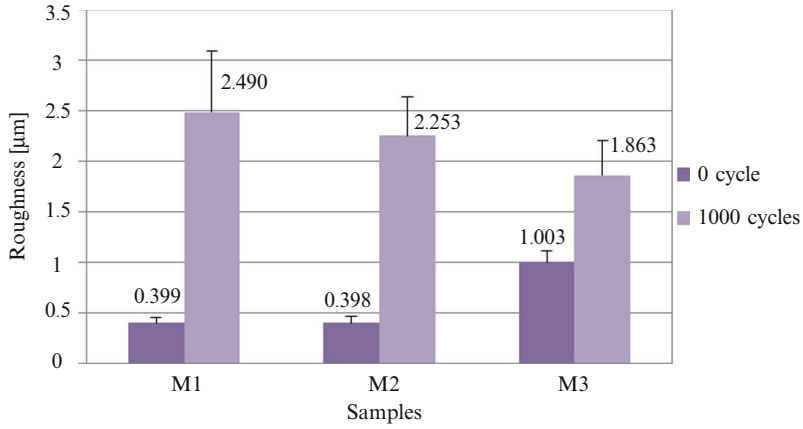


Figure 7.21 R_a roughness values [µm] of the samples before and after 1000 abrasion cycles.

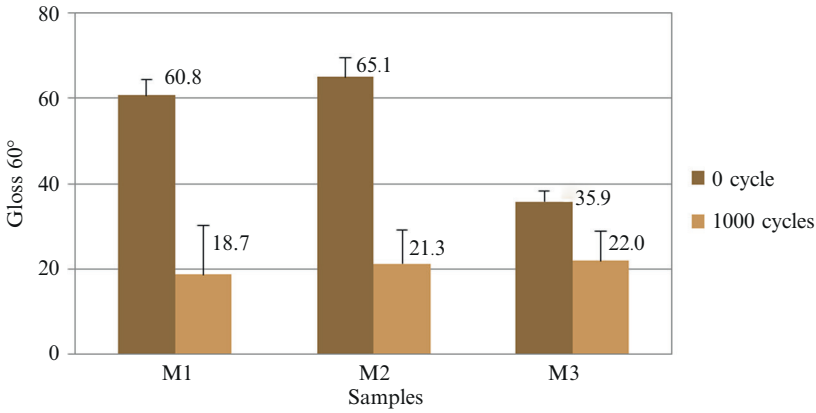


Figure 7.22 Gloss (60°) of the samples after and before 1000 abrasion cycles.

Considering the cross-section of the abraded samples (Figure 7.25a–c), it is possible to note that the mechanical damage is not homogeneous in the area where the grinders insist. In the more internal part the damage is higher with a sensible reduction of the luminescent layer thickness. On sample M3 in several areas the luminescent deposit was practically totally removed.

Thousand cycles of abrasion did not damage the intermediate layer and in all samples also the presence of cracks was not observed. The protective properties were thus preserved for all three samples. To have information about the mechanical damage necessary to have the loss of corrosion protection, other cycles of Taber test were carried out. Every 1000 cycles the protective capacity of the samples was evaluated by electrochemical impedance measurements.

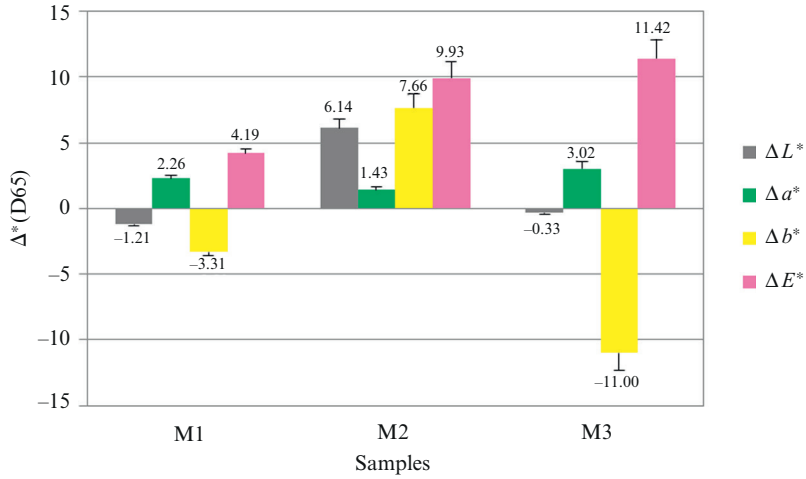


Figure 7.23 Color changes of the samples after 1000 abrasion cycles.

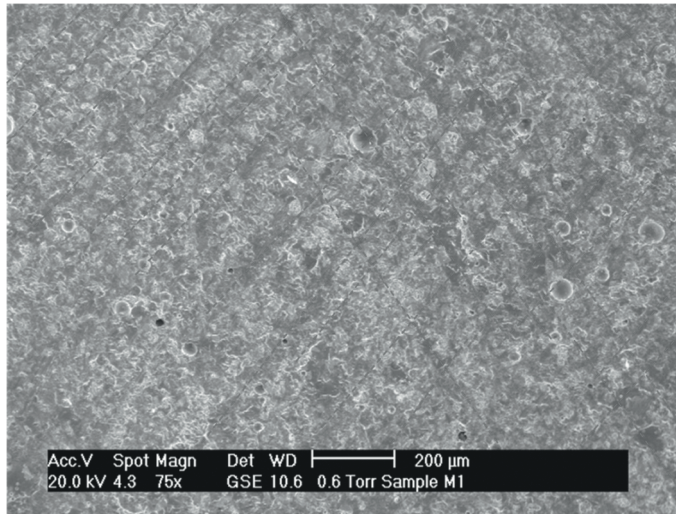


Figure 7.24 Surface of M1 sample after 1000 abrasion cycles. It is possible to recognize the typical cross scratches produced by the grinders.

Figure 7.26 shows the trend of the coating resistance obtained from fitting of impedance data in function of number of abrasion cycles. All three samples initially presented a high corrosion protective characteristic. The loss of these properties was obtained only after 7000 cycles for sample M2, 8000 cycles for M1, and 10000 cycles for sample M3. For protective properties loss it was necessary to completely remove the luminescent enamel layer and almost all of the intermediate enamel layer,

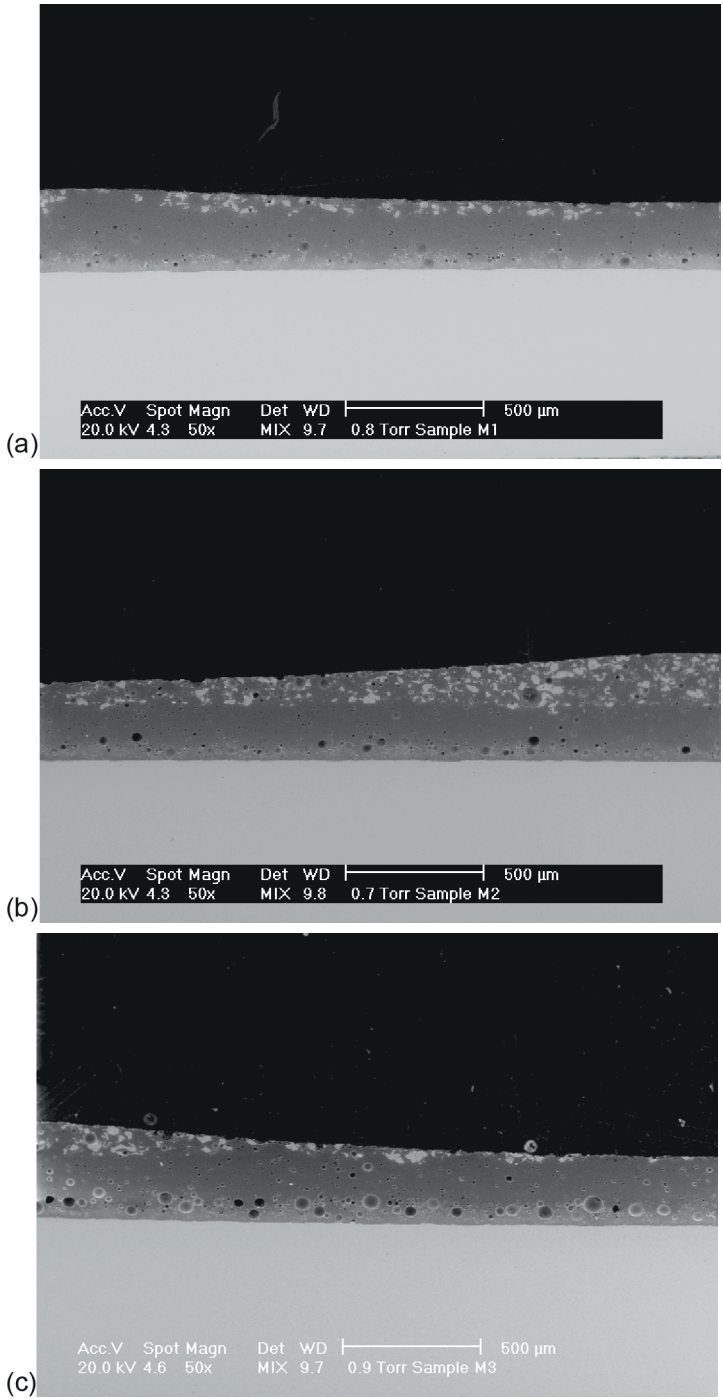


Figure 7.25 (a) Cross-section of sample M1 after 1000 abrasion cycles. (b) Cross-section of sample M2 after 1000 abrasion cycles. (c) Cross-section of sample M3 after 1000 abrasion cycles.

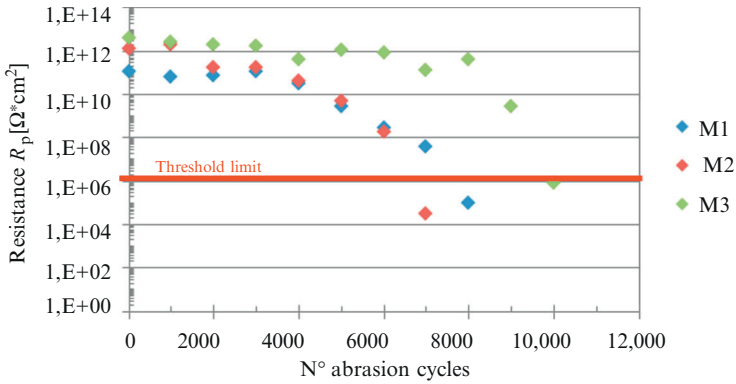


Figure 7.26 R_p coating resistance of the enamel luminescent samples in function of the number of abrasion cycles.

which was the first layer responsible for the corrosion protection. A nucleation of cracks that reach the steel substrate was also necessary.

The different number of abrasion cycles required to compromise the protection properties of the enamel samples is not connected with the thickness values. Probably statistical nucleation of defects is the determinate aspect. Considering the high number of cycles needed for the protection loss, it is possible to affirm that the protective capacities of all three samples was very high and there was no difference between luminescent enamel systems in comparison with the traditional enamels.

7.6.3 Trend of luminescent properties

Figure 7.27 shows the value of the intensity of the main peak of the emission spectrum of samples before and after 500 h of continuous UV-A exposure. No changes in intensity, shape, and position of the emission and the excitation spectra are observed. It is possible to conclude that UV-A exposure does not produce measurable modification on the luminescent pigments and then on the properties of the coatings.

A cyclic UV-A exposure test was carried out to highlight if the loading and unloading action led to a reduction in efficiency of the pigments. The exposure to cyclic UV-A radiation does not produce damage or alteration of the luminescent pigments such as to cause decreases in the emission intensity. Figure 7.28a–c presents the trend of the intensity of the main peak of the emission spectrum for each sample during the cycles of loading and unloading. For all samples neither decrease in intensity with increasing numbers of cycles nor delays of the response was observed. After 24 cycles, the intensity of the peak appeared to be the same as that of the first cycle. The difference in intensity between the samples can be ascribed to little variations of the fiber position during each measurement run.

The effect of immersion tests in acid and alkaline solutions on the luminescence properties was also analyzed. The immersion of the samples for 24 h in citric acid solution did not cause any change in the excitation and emission spectra. Shape, position, and intensity of these spectra (Figure 7.29) remained within the range of

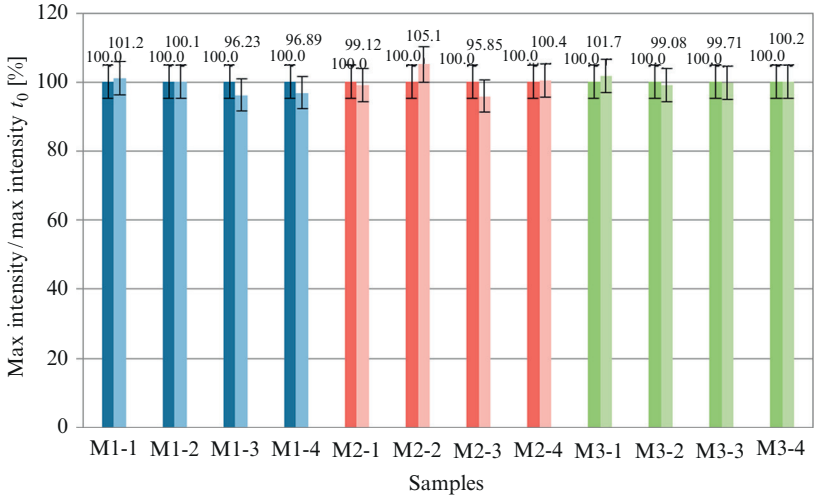


Figure 7.27 Intensity of the main peak of the emission spectrum (excitation wavelength 350 nm) of the luminescent enamel samples before and after 500 h of UV-A exposure. For every measured point, the values were normalized to the intensity of the initial peak of that point. For each sample, four tests in different areas of the surface were made.

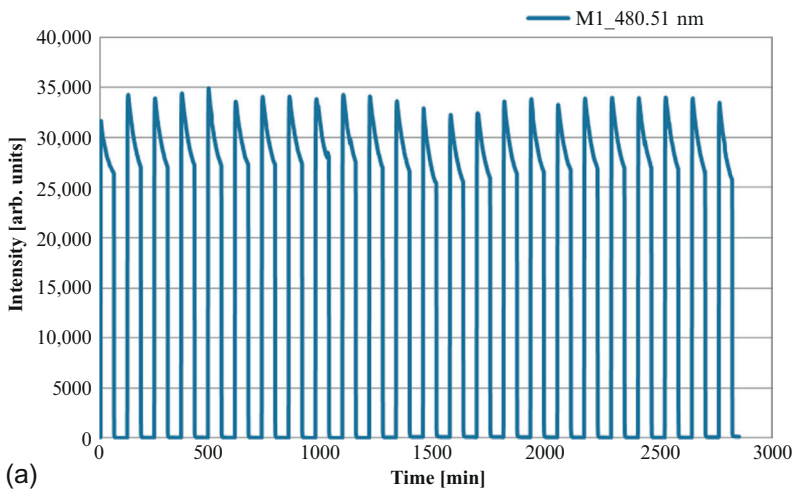


Figure 7.28 (a) Trend of the intensity of the main peak of the emission spectrum of sample M1 during cycles of loading/unloading of UV-A radiation (1 h lamps on + 1 h lamps off).

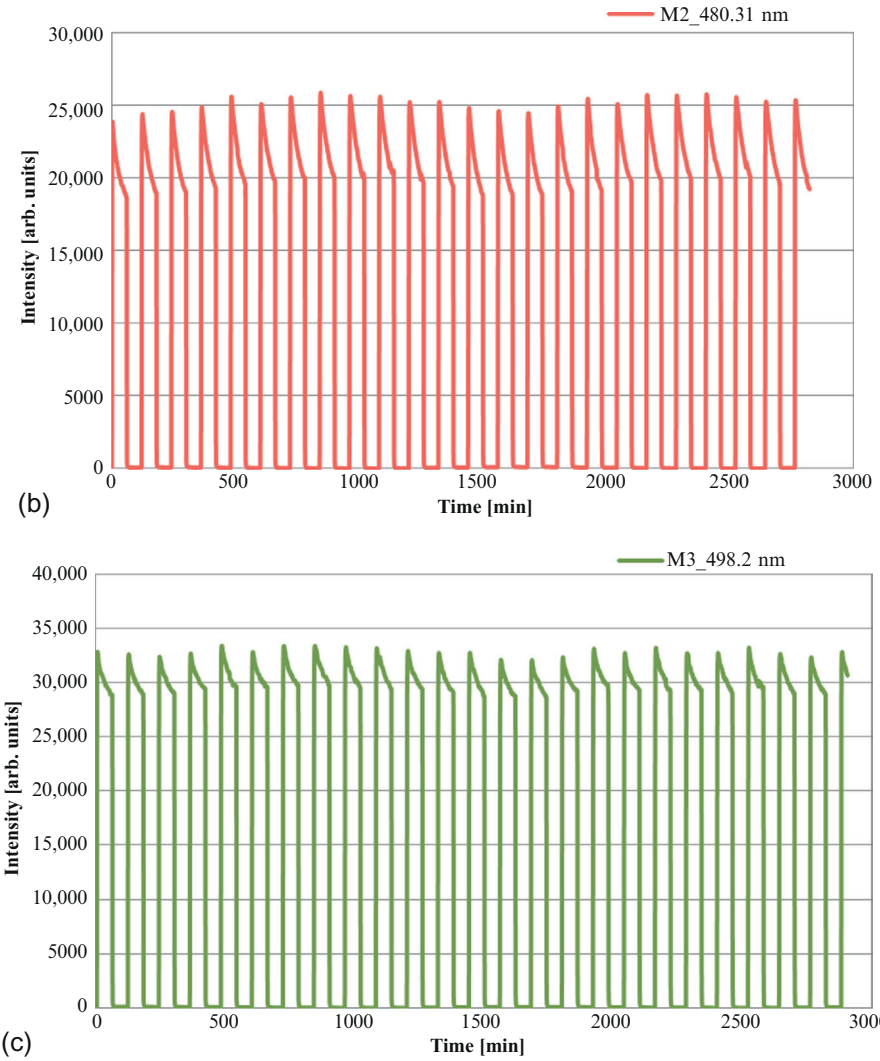


Figure 7.28, Cont'd (b) Trend of the intensity of the main peak of the emission spectrum of sample M2 during cycles of loading/unloading of UV-A radiation (1 h lamps on+1 h lamps off). (c) Trend of the intensity of the main peak of the emission spectrum of sample M3 during cycles of loading/unloading of UV-A radiation (1 h lamps on+1 h lamps off).

the instrument reproducibility error. Considering these results, the removal of few micrometers in these enamel layers does not lead to measurable changes in luminescence characteristic. This conclusion is confirmed by the behavior of sample M3. In fact, this sample, after the acid immersion, shows small localized surface attacks with possible removal of pigments, but no decrease of the emission intensity was observed, indicating the maintenance of the homogeneity of the luminescent pigments.

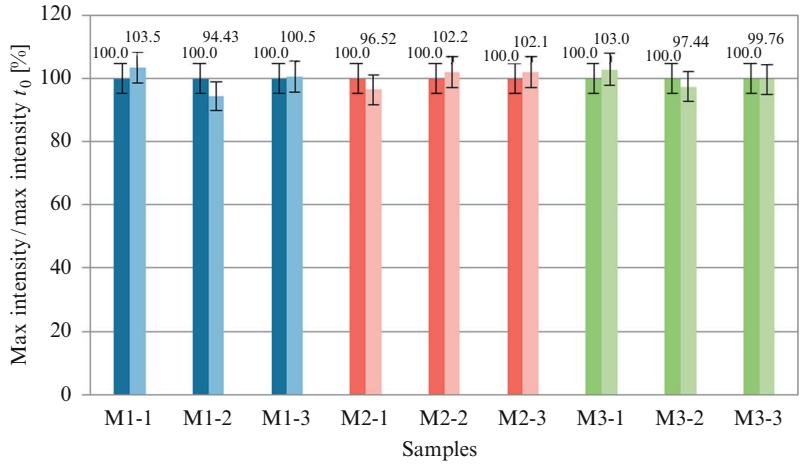


Figure 7.29 Intensity of the main peak of the emission spectrum (excitation wavelength 350 nm) of the enamel samples before and after immersion in acid solution. For every measured point, the values are normalized to the intensity of the initial peak of that point. Initial values (left) and after 24 h of immersion (right).

Even the immersion for 24 h of the luminescent enamel samples in potassium pyrophosphate alkaline solution did not produce changes in the excitation and emission spectra of the sample M3. Considering the decrease of light emission (Figure 7.30), only the sample M2 showed a decrease in some points, probably due to the higher roughness produced during the aggression alkaline, which hinders the absorption and emission process.

Thousand hours in salt fog chamber exposure of luminescent enamel samples did not produce any modification of the luminescent pigments. No changes in intensity (Figure 7.31), shape, and position of emission and excitation spectra were observed in all types of deposits.

Finally, an abrasion test is considered to evaluate if mechanical damage produces reduction of the luminescent characteristics. Figure 7.32 shows the trend of the intensity of the main peak before and after 1000 cycles of the Taber abrasion test. It is possible to observe that the mechanical damage causes a decrease in the luminescent properties. All samples, in fact, presented a decrease in the intensity of both emission and excitation spectra. The decrease of the intensity of the emission peak, in fact, followed the trend of the abrasion damage distribution, which were more marked in the inner part of the contact area where the thickness was more reduced.

For every sample, the removed layer was of several microns, causing an appreciable reduction of the luminescence intensity, but the percentage of reduced intensity was different.

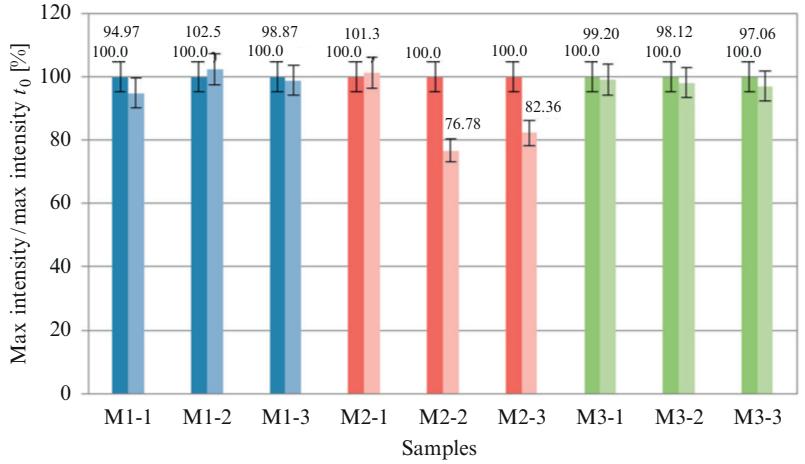


Figure 7.30 Intensity of the main peak of the emission spectrum (excitation wavelength 350 nm) of the enamel samples before and after immersion in alkaline solution. For every measured point, the values are normalized to the intensity of the initial peak of that point. Initial values (left) and after 24 h of immersion (right).

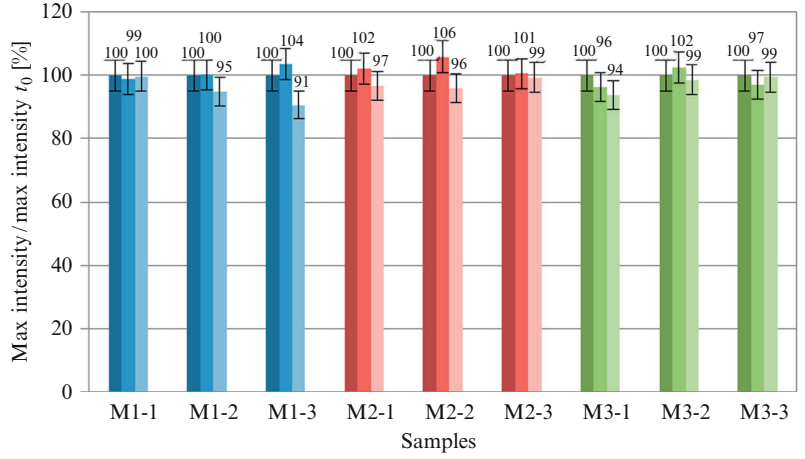


Figure 7.31 Intensity of the main peak of the emission spectrum (excitation wavelength 350 nm) of the enamel samples before state (left), after 500 h, (middle) and after 1000 h (right) of salt spray exposure. For every measured point, the values are normalized to the intensity of the initial peak of that point.

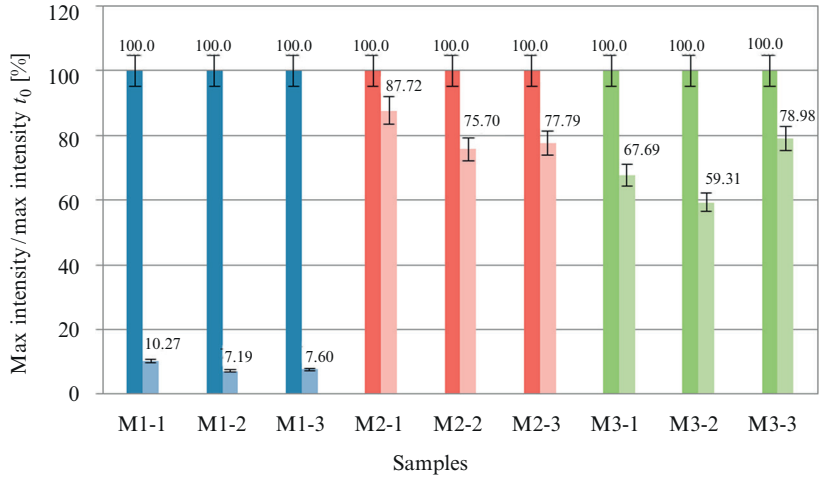


Figure 7.32 Intensity of the main peak of the emission spectrum (excitation wavelength 350 nm) of the luminescent enamel samples before (left) and after (right) abrasion cycles. For each measured point, the values are normalized to the intensity of the initial peak at that point.

Sample M1 shows the higher emission reduction, with the loss of more than 90% of the initial intensity, while sample M3 shows a decrease of 40% and sample M2, 25%. Taking into account the thickness of the layers (M3 < M1 < M2), the difference in behavior is not fully understood, but it can be ascribed to different distributions and homogeneities of the luminescent pigments along the layer thickness.

7.7 Conclusion

The porcelain enamels are glass coatings deposited on steel that guarantee, at the same time, excellent technical properties and aesthetic-perceptive ones. The vitreous matter, which constitutes these coatings, is inert in many environments and aggressive substances. Thanks to the deposition and curing technologies, the adhesion between the enamel layer and the steel substrate is very good, and it remains even in the presence of defects and cracks in the coating and corrosive phenomena on the noncovered substrate.

The luminescent enamel layers obtained with an adding of rare earth compounds such as europium and dysprosium are an interesting example of smart coatings, which show very particular optical properties together with the traditional one, presenting at the same time eco-friendly and nonhazardous aspects.

In literature there are no studies on these innovative coatings. Thus, the aim of this chapter is to present experimental tests to check whether the presence of the

luminescent layer would change the traditional enamel properties and to highlight the degradation resistance of these luminescent layers. Three different types of luminescent enamel systems were studied, which differ in the ratio between the rare earths, (europium and dysprosium), that produce the luminescent emission. Different size of the luminescent pigments was considered. The emission spectra were due to the contribution of two peaks (one in blue and one in green), and the increase of dysprosium increased the contribution of the green peak.

M1 and M2 luminescent enamels showed a different behavior to chemical solutions than did the M3 deposit. Only sample M3 was subject to attack by the citric acid solution with the formation of localized attacks, which produced a gloss decrease, increase in roughness, and color change. On the contrary, the particles, which were emerged in the surface, seemed to hinder the aggression on the glassy matrix in alkaline solutions. In this environment, sample M3 results showed much less damaged than that shown in samples M1 and M2, presenting only small localized attacks. These last two types highlight a heavy damage of the glass matrix with a dramatic gloss drop, roughness increasing, and degradation of color pigments. The dimension of luminescent pigments and their position in the enamel layers played a fundamental role in these behaviors.

The luminescent emission intensity remained constant after UV-A radiation exposures (both continuous and cycled tests) and also after salt spray chamber exposure, indicating that the luminescent pigments would not undergo any alteration in aggressive environments. From the experimental data, it is also possible to assume that the thickness of the enamel layer can affect the luminescent emission intensity, but that only great material removals may cause the appreciable decrease in intensity of luminescent emission; the removal of localized few μm does not involve measurable changes in luminescence.

The presence of the external luminescent enamel layer does not affect the excellent resistance properties of the traditional enamel systems. The corrosion protection properties are lost only with great mechanical damage caused by the total removal of the luminescent layer and almost all of the intermediate layer, and, at the same time, the production of cracks.

References

1. Rossi S, Scrinzi E. Evaluation of the abrasion resistance of enamel coatings. Chem Eng Proc 2013;68:74–80.
2. Scrinzi E, Rossi S. The aesthetic and functional properties of enamel coatings on steel. Mater Design 2010;31:4138–46.
3. Andrews AI, Pagliuca S, Faust WD. Porcelain (vitreous) enamels and industrial enamelling processes—the preparation, application and properties of enamels. Mantova: The International Enamellers Institute; 2011.

4. Rossi S, Scrinzi E, Compagnoni AM, et al. Enamel and design. The potential of enamelled materials. Bologna: Fausto Lupetti Editore; 2011.
5. Ubertazzi A, Wojciechowski N. Vitreous enamel. Milano: Ulrico Hoepli Editore; 2002.
6. Buxbaum G, Pfaff G. Industrial inorganic pigments. 3rd ed. Weinheim: Wiley-VCH; 2005.
7. Blasse G, Grabmaier BC. Luminescent materials. Berlin: Springer-Verlag; 1994.
8. Bartwal KS, Ryu H, Singh BK. Effect of Sr substitution on photoluminescent properties of $BaAl_2O_4:Eu^{2+}$, Dy^{3+}. Physica B 2008;403:126–30.
9. Lin Y, Tang Z, Zhang Z, et al. Preparation and properties of photoluminescent rare earth doped SrO–MgO–B_2O_3–SiO_2 glass. Mater Sci Eng B-Adv 2001;86:79–82.
10. Song CF, Yang P, Lu MK, et al. Enhanced blue emission from Eu, Dy co-doped sol–gel Al_2O_3–SiO_2 glasses. J Phys Chem Solids 2003;64:491–4.
11. Hunt RWG. Measuring colour. New York: Wiley; 1987.
12. Overheim RD, Wagner DL. Light and colour. New York: Wiley, John & Sons; 1982.
13. Hunter RS, Harold RW. The measurement of appearance. New York: Wiley; 1987.
14. Rossi S, Deflorian F, Fontanari L, et al. Electrochemical measurements to evaluate the damage due to abrasion on organic protective system. Prog Org Coat 2005;52:288–97.
15. Rossi S, Deflorian F, Scrinzi E. Comparison of different abrasion mechanisms on aesthetic properties of organic coatings. Wear 2009;267:1574–80.
16. Macdonald JR. Impedance spectroscopy: emphasizing solid materials and systems. New York: Wiley; 1987.
17. Barsoukov E, Macdonald JR. Impedance spectroscopy: theory, experiment and applications. Hoboken: Wiley; 2005.
18. Scully JR, Silverman DC, Kendig MW. Electrochemical impedance: analysis and interpretation. Philadelphia: American society for testing and materials; 1993.

Chapter 8

Anticorrosion Coatings with Self-Recovering Ability Based on Damage-Triggered Micro- and Nanocontainers

D. Grigoriev
Max-Plank Institute of Colloids and Interfaces, Am Muehlenberg 1, Potsdam-Golm, Germany

8.1 Introduction

8.1.1 Corrosion as a global economic problem

The tremendous annual detriment directly resulting from corrosion of metallic materials and structures and the corresponding huge economic impact is a very important issue worldwide. According to a study conducted in 1999-2001 by CC Technologies Laboratories, Inc., supported by the U.S. Federal Highway Administration (FHWA) and the National Association of Corrosion Engineers (NACE), the total annual estimated direct cost of corrosion only in the United States is an overwhelming $276 billion.[1] Similar results were reported for Europe, where every year more than €200 billion need to be invested just to recover losses related to corrosion degradation.

Intelligent Coatings for Corrosion Control
Copyright © 2015 Elsevier Inc. All rights reserved.

Thus, even in the most economically advanced countries the material losses and performance failure costs connected with corrosion are estimated to be 3-4% of GDP.[2,3] The corresponding information for the less economically developed countries is only partially accessible but seems to be more dramatic.[2] Therefore, preventing corrosion and improving corrosion protection are nowadays the most important tasks challenging the community of corrosion scientists, engineers, and technologists.

8.1.2 Methods for combating corrosion: short overview

Because the corrosion process begins usually on sites where a metallic construction adjoins an aggressive surrounding, the typical place of the corrosion occurrence is the surface of the metal of which this construction is made, or, speaking more strictly, the interface between the metal and a medium. Thus, to date, all known approaches for preventing and controlling corrosion are directly or indirectly related to the stopping or slowing of the interfacial/surface reactions of the corresponding metal (alloy) with the aggressive environment. This can be achieved in many different ways. These ways may be generalized into two categories: one is a big group of approaches using chemical or physicochemical modification of the entire bulk material; and the second is an even more numerous group of approaches related to the surface/interfacial modification of the material to be protected.

Typical examples of approaches from the first group are the use of various corrosion-resistant alloys,[4,5] polymers,[6–8] and composite materials,[9] or catodic protection.[10]

On the other hand, such approaches as use of different organic,[11] ceramic,[12] and metallic protective coatings,[13] anodic protection,[14] application of diverse corrosion inhibitors[15–18] can be mentioned as conventional instances of the second group.

Among the wide variety of interfacial protective approaches only briefly named above, the use of organic coatings is probably the most common and economically sound approach to improve corrosion protection and, therefore, durability and performance of metal products and constructions in an extremely broad area of applications ranging from aviation to household appliances.

Depending on the metallic substrate to be protected and on the particular requirements of a coating's anticorrosion efficiency and its other properties, a modern organic protective coating may be a quite complex construction. Excluding all cases of specific applications with special demands on the anticorrosive performance, a conventional contemporary anticorrosion coating can be regarded as a layered structure most commonly composed of three layers beginning from the substrate: a thin pretreatment layer, a primer, and a topcoat.

In some cases, the anticorrosion performance of these layered build-ups can be provided merely by the good isolation of the metal substrate from the corrosive environment, that is, the corrosion protection of these coatings has only a passive character because none of the layers included in the coating contain any additives that can

prevent the onset of corrosion or slow down its propagation. Therefore, any damage to the mechanical integrity of the coating matrix in the case of such a passive coating is connected with the total failure of its protection performance at least in vicinity of the damaged site and, as a consequence, leads to the unrestricted development of corrosion.

Therefore, the addition of different anticorrosive agents, predominantly inorganic anticorrosion pigments,[19,20] to a passive matrix became more and more common to impart at least some active anticorrosion function to a passive coating.

Especially successful was the application of hexavalent chromium compounds (Cr VI). These substances were widely used to create pretreatment conversion films.[21,22] Because of the strong oxidation effect of chromates, the metal substrate to be protected plays the role of reductant, and on its surface the tight solid film of hydrated chromium (III) oxide is formed.[23,24] The relatively thin conversion film obtained in this manner possesses very good barrier properties and can moreover confer on the coating the ability to heal itself upon damage. This ability is provided by the excess of chromate ions that become embedded into the conversion layer during its formation but remain only physically bonded with this layer. As a result, they can be easily released upon destroying the mechanical integrity of the coating exactly at the injured site and react again with the metal substrate, providing both cathodic and anodic passivation of the surface.[25,26]

Additionally, the gradual release of chromates incorporated in the matrix of the conversion film and their subsequent transfer to surface defects via the contiguous aqueous phase impart the long-term protection to it.[27–29]

Chromate conversion films are usually prepared by chemical treatment and have a low thickness. Thus, the amount of excess chromates that can be accumulated inside these films is not sufficient[30] for the sustained corrosion protection of the substrates. To increase the sustainability of the protective effect, chromate anticorrosive pigments such as $CaCrO_4$, $SrCrO_4$, or $BaCrO_4$ should be incorporated into the more extended primer layer.[31–35]

However, the oxidative power of chromates causes several very serious negative effects: importantly, high environmental toxicity coupled with this health concern show correlations between chromate pollutions and different cruel deceases such as cancer or gene damage.[36] These health and environmental incompatibilities as well as the safety problems related to them were the driving forces to ban the use of chromates in corrosion protection solutions and to eliminate them from various applications.[37]

To date, the use of chromates has been stopped in almost all main industries and steadily increasing efforts are being made to find environmentally benign substitutes. Different alternative solutions have been suggested. A number of compounds of several transition metals in a high oxidation state have been used for chemical conversion coatings, such as titanium,[38] vanadium,[39] zirconium and niobium,[40] manganese,[41,42] cobalt,[43] molybdenum,[44] tungsten and silicon,[45] cerium,[40,46–49] and other

rare earth metals.[50,51] Other endeavors embrace such techniques as electrochemical chromate-free oxidation treatment (anodizing),[52–54] diverse organic-inorganic pretreatments,[55,56] and the application of organic inhibitors directly onto the metal substrate surface.[57] Another attempt to find appropriate alternatives to chromates was reported by Dufek and Buttry.[58]

One of the most conventional methods to replace toxic chromates in organic anticorrosion coatings is the use of various inorganic pigments on the basis of zinc compounds (especially, zinc phosphate) for addition to the primer layer.[20] These essentially less harmful additives have, however, an essentially lower protective efficiency. To attain an appropriate level of anticorrosion performance, much higher amounts of zinc phosphate should be included in a coating formulation. As a consequence, the growing ecological impact of their use on the environment, especially in the long-term, has to be taken into account. These concerns have already initiated the development of coating solutions free of zinc phosphate use,[59] with the goal of its gradual elimination in the future.

Unfortunately, an equivalent substitution for chromates has until now not been found. Moreover, most of the studies of chromate-free protective solutions have unambiguously led to the conclusion that chromates provide outstandingly better anticorrosion performance compared with any other coatings developed so far. Therefore, the application of Cr (VI) compounds has been temporarily allowed as an exception in some industries, such as the aerospace industry, where the very high requirements for anticorrosion performance are mandatory because of enhanced safety standards.[60] Simultaneously, the community of anticorrosion specialists continues more and more intensive tries to propose and to develop novel additives, techniques, and approaches for corrosion protection in order to attain solutions with equivalent to or even better performance than that of chromium (VI) compounds.

The direct incorporation of corrosion inhibitors in one of the layers (pretreatment, primer, or even topcoat) in the protective organic coating is a most obvious way to impart to this coating the ability to react actively to the corrosion-inducing factors.[61–63]

However, a lot of different obstacles can occur at this straight-line solution because of the specific physicochemical properties of the inhibitors applied and their interactions with other components of the coating system. These interactions can lead to a significant impairment or even to the failure of the protective performance of the coating.

Optimal effectiveness of an inhibitor can only be attained if its concentration in the closest proximity to the damaged site is in a certain “proper” range. Thus, too low inhibitor solubility will lead to its lack in the damage environment and consequently to the weak feedback activity. Whereas the solubility is too high, the substrate can only be protected for a relatively short time, after which the inhibitor depletion state will be rapidly attained. High osmotic pressure is another drawback related to the

too high inhibitor solubility, which usually results in strong blistering and even delamination of the coating matrix from the substrate under protection. The osmotic pressure can also accelerate the water penetration across the coating, thus acting as a semipermeable membrane and causing the destruction of the passive coating matrix.[64] Moreover, the adverse chemical interactions between inhibitor and other components of the coating matrix lead to significant shortcomings in its stability and to the worsening of the barrier properties of the coating system as a whole.[65] The structural, chemical, and acidic/alkaline properties of the passive matrix determine the intensity of its interaction with the inhibitor and therefore the release rate of the latter. Furthermore, the freely dispersed state of an inhibitor leads quite often to its spontaneous leakage, causing a surface depletion of the inhibitor during aging.[66]

8.2 Micro- and Nanocontainers-Based Approach to the Protective Organic Coatings: Self-Healing Versus Self-Protecting

The idea to incorporate the previously encapsulated active agents in various materials or coatings to make them self-healing or self-restoring has been initially inspired by numerous examples from the living nature. First of all, the skin of humans and various mammalians as well as some other tissues demonstrate unique features to recuperate its integrity after being injured by external impacts (self-restoring) and to disable several types of aggressive species, mainly of environmental origin, adhering to its surface (self-protecting). It is also notable that the named abilities are always activated by external destructive factors, playing the role of on-demand triggers, such as integrity damage, or chemical or microbial attack, working in a very sustainable manner.

Efforts to mimic these natural features in diverse artificial engineering materials in order to impart to them the ability to reestablish their functionalities autarkically was started approximately three decades ago. Proposed in the early 1990s[67,68] and elaborated initially for the self-repair of materials integrity in the bulk,[69] this concept was then transferred to interfaces, mainly to organic anticorrosion coatings for metal substrates.[64,70–72]

The active feedback behavior of micro- or nanostructured material is essentially determined by its specific design. To date, the following approaches can be distinguished to fashion the fine structure of self-repairing materials: (1) based on incorporated micro- or nanocontainers, (2) based on embedded network of microcapillaries ("vascular"), and (3) intrinsic.[73]

Because of universality and high variability in realization, approach connected with the use of micro- or nanocontainers (further—"containers") embedded in the material matrix is the most established now. Incorporation of containers loaded with

diverse active agents enables the active feedback of the system upon the action of factors leading to the material damage because these work simultaneously as opening triggers for the containers and therefore for the release of active agents.

Most frequently, so-called sealants are used for the encapsulation in containers providing to the bulk phase of material the reestablishment of its mechanical integrity and the corresponding mechanical properties. Hence, the amount of sealing agent encapsulated in the containers applied for this purpose has to be sufficient for filling up the cracks in the interior of material bulk. This requires the use of quite large, typically micrometer-scale containers with the considerable volume fraction in the bulk.

Upon transfer of the same concept to the almost two-dimensional case of protective coatings, it is necessary to take into account several intrinsic constraints limiting the highest possible volume of the encapsulated sealant. First, this volume is closely related to the size of containers. Second, the containers volume fraction within the coating matrix also restricts the sealant volume that could be potentially released at the fracture site. These two parameters of the containers plurality are of key importance for their applicability in a certain coating. Only containers with size of several times smaller than the thickness of the coating can be embedded without damaging their integrity. Moreover, too high volume fraction can cause the formation of polydisperse container aggregates with the upper size cut-off exceeding the coating thickness.

The quantitative estimation of the protective capacity of the coating with the sealant-filled containers can be done as follows. Let us take into consideration a protective coating with thickness H and depth D which is damaged by a rectangular scratch with the width L and the depth attaining the surface of the metal substrate (Figure 8.1).

The monodisperse spherical core-shell containers with the size $2R$ and core radius r filled with sealing agent are homogeneously distributed in the coating matrix with the volume fraction φ. Only containers located at position $x \leq r$ related to each scratch face will be damaged at the scratch propagation. Thus, all these containers are distributed in the part of the coating matrix adjacent to the scratch which volume can be given by a simple expression:

$$V = 2HDr \tag{8.1}$$

Volume of all containers distributed within this matrix volume is then:

$$V_c^t = 2HDr\varphi \tag{8.2}$$

Obviously, number of containers N_c in the same volume is given by the ratio of their total volume to the volume of a single container:

$$N_c = V_c^t / V_c^s = \frac{2HDr\varphi}{4/3\pi R^3} \tag{8.3}$$

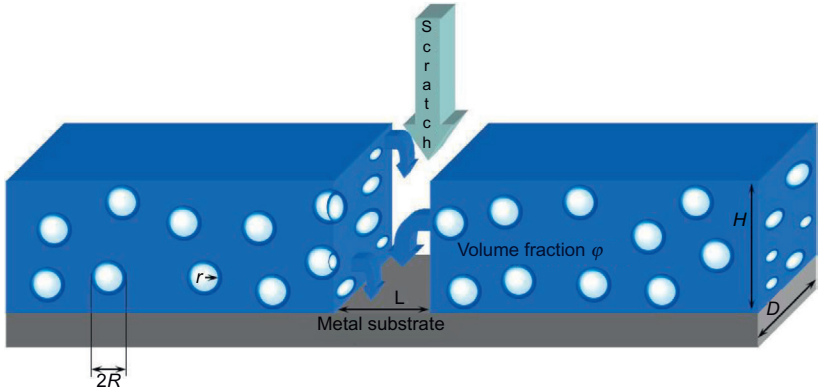


Figure 8.1 Illustration of the scratch propagation along the protective container-based coating on the metal substrate affecting the embedded containers. *These materials are reproduced with permission of NACE International.*

Multiplying the amount of the sealant encapsulated in the single container and by their number (Equation (8.3)) the total amount of sealant encapsulated within the damaged volume is obtained as:

$$V_s^t = \frac{2HDr^4\varphi}{R^3} \tag{8.4}$$

Part of the scratch which can be filled up by the total encapsulated sealant is given by the ratio of volume expressed by Equation (8.4) to the total scratch volume:

$$\alpha = \frac{V_s^t}{V_{Scr}} = \frac{2HDr^4\varphi}{R^3HDL} = \frac{2r^4\varphi}{R^3L} \tag{8.5}$$

If the thickness of the container shell is negligible small comparing to its diameter, that is, if $R \sim r$, the Relation (8.5) can be simplified to the form:

$$\alpha = 2\frac{R}{L}\varphi \tag{8.6}$$

The physical meaning of this relation is straightforward: For any reasonable volume fraction (for instance, for $\varphi = 0.1$) of containers with the size 10 μm and very thin shells, damage caused by the scratch can only be completely sealed when the latter has a width <1 μm, that is, only submicrometric scratches can be recovered.

Considerably larger defects whose onset is also quite probable during the service life of a typical protective coating cannot be sealed even partially when a protective coating based on the containers filled with the sealing agent will be implemented in practice. The demonstrated limitations in the performance of self-repairing anticorrosion coatings based on the containers filled with sealants determine the predominant

loading of the containers rather with protective agents (e.g., corrosion inhibitors) than with sealing ones.

The situation with the maximal amount of the sealing agent released from containers upon damage can be significantly improved, if the elongated containers, that is, containers with the aspect ratio other than unity are incorporated into coating matrix.[74] The strongly elongated containers with the aspect ratio of 10 can release an almost twofold higher amount of sealing agent. Moreover, the orientation of these containers to the crack plane can also influence the sealing efficiency of the containers-based coating: if all containers are situated perpendicular to the plane of crack, up to four times higher improvement is expected. On the other hand, parallel orientation of containers and the crack leads to the decrease of the sealing capacity up to 50%. However, even the use of elongated containers filled with the sealant cannot ensure the complete self-restoring of the scratches with widths essentially exceeding the range of several micrometers.

On the contrary, efficiency of the encapsulated inhibitor for the protection of the bare metal substrate freshly created by the scratch is considerably higher: Let us imagine spherical containers with $R = 1\,\mu m$ and $\varphi = 0.05$ filled with an inhibitor possessing a molecular weight M_w of 500 g/mole and a density ρ of 1 g/cm^3.

Following the similar consideration as previously, the maximal value of inhibitor that may be adsorbed on the scratch surface can be calculated as

$$\Gamma_{max} = \frac{2HR\rho\varphi}{M_w L}, \tag{8.7}$$

where L and H are width of the scratch and the thickness of the coating, respectively.

Assuming a quite realistic coating with the thickness $H = 70\,\mu m$, one obtains $\Gamma_{max} = 0.014/L$ μmole/m^2. In other terms, Γ_{max} values of some tens of micromoles per square meter are derived for typical millimeter-range scratches. These values are at least one order of magnitude higher than common saturation adsorption values Γ_∞ reported for some organic inhibitors.[75,76] As a result, defects of the coating surface with even larger centimeter-wide areas can be fully protected by the inhibitor amounts released from abovementioned containers.

Therefore, the term "self-protecting"[77] in relation to coatings is more appropriate to use than "self-healing" since their physical integrity is usually not reestablished due to the protective effect of inhibitor released from containers, whereas the "main" anticorrosion functionality of such a coating can be completely recovered.

The key element of novel self-protecting anticorrosion organic coatings is a plurality of micro- or nanocontainers embedded in the coating matrix and possessing the triggered on-demand ability to release protective agents. In the following paragraphs of this work, the attention will be concentrated on the different types of containers applied in novel coatings, approaches and techniques used for their preparation, their

morphology and release properties, distribution in coatings after curing, as well as the anticorrosion performance of container-based organic coatings.

8.3 Types of Containers and Methods of Their Preparation

Several types of nano- or microcontainers can be used for incorporation in the matrix of new self-protecting coatings: containers based on layered double hydroxides (LDHs); containers with porous or hollow ceramic core primarily soaked with inhibitor and then encased by polyelectrolyte (PE) shell with stimuli-responsive ability; containers with porous or hollow ceramic core impregnated by inhibitor and sealed then with the stimuli-responsive stoppers at the pores ends; and polymeric and composite containers possessing inhibitor-rich core and stimuli-responsive shell prepared on the basis of direct or inverse emulsions. All these types of containers have their specific peculiarities related to their preparation, loading with active agents (inhibitors), and incorporation in the coating matrix, which are discussed in more detailed in the next sections.

8.3.1 Nano- or microcontainers on the basis of LDHs

LDHs, also called as hydrotalcite-like substances,[78] are naturally occurring clay-based nanostructured microparticles. Their composition can be expressed by the following general formula $(M^{2+}_{1-x}M^{3+}_{x}(OH)_2)A^{n-}_{x/n}\cdot mH_2O$ where the cations M^{2+} can be represented by Mg^{2+}, Zn^{2+}, Fe^{2+}, Co^{2+}, Cu^{2+}, and so on, and M^{3+} can be represented by Al^{3+}, Cr^{3+}, Fe^{3+}, Ga^{3+} and others. Possessing a brucite-like structure with octahedral holes where some divalent cations were exchanged with various trivalent ones, LDHs compensate this excess of positive charge by intercalation of different guest anions between the host hydroxide layers located in the hydrated interlayer galleries.[79] These anions can be exchanged with various species, thus allowing the preparation of a wide range of new material with application-specified properties, for example, as storage and delivery carriers for biologically important compounds and drugs; as selective media in separation science; and as polymer additives.[79] The LDHs have also been applied as catalysts and catalyst supports,[80] polymer stabilizers,[81] and traps of anionic pollutants.[82]

The application of hydrotalcite-like compounds in corrosion protection has covered different areas. In some studies, the LDHs have been produced *in situ*, on the top of metallic substrates as protective films.[83] The targeted synthesis of LDH layers with inhibitor intercalation immediately in the vicinity of substrate under protection is the simplest method for corrosion protection using this type of nanocontainers.[84] Hydrotalcite-based conversion films have demonstrated good corrosion protection,

and some research groups have been trying to improve the interaction between these conversion films and organic coatings.[85]

An alternative method is the use of these anion-exchangeable clays as potential inorganic host particles for different corrosion inhibitors and their incorporation in protective organic coatings. Due to considerable adsorption capacity of LDHs, the twofold aim can be achieved: not only the release of the substances that impart active protection, but also the trapping corrosive anions like chlorides or sulfates. These corrosive species may be replaced by different corrosion-inhibiting anions like nitrates, chromates,[86] vanadates,[87] or divanadates.[88] In the latter case, the coatings doped with Zn/Al LDH-nanocontainers provide a well-defined self-protecting effect and confer anticorrosion properties of organic coating comparable or even superior to the currently used environmentally unfriendly chromate-based systems.

A new class of materials with emerging importance within the LDH family are LDHs loaded with organic anions.[89] Several successful syntheses of these materials were performed recently. Williams and McMurray prepared LDHs with such organic species as benzotriazole (BTA), ethyl xantate, and oxalate[90] by rehydration of commercial hydrotalcite ($Mg_6Al_2(OH)_{16}{\cdot}CO_3{\cdot}4H_2O$). The resulting layered systems were inserted into a poly(vinylbutyral) coating prepared by a bar cast on the top of AA2024-T3 aluminum alloy.

LDHs intercalated with 2,5-dimercapto-1,3,4-thiadiazolate were prepared in a similar way[91] and then the inhibiting properties of this anion with respect to the oxygen reduction reaction on copper were studied.

In another recently developed possibility, Poznyak et al.[78] used Zn-Al and Mg-Al LDHs loaded with quinaldate and 2-mercaptobenzothiazolate. The containers were synthesized via anion-exchange reaction. Spectrophotometric measurements demonstrated that the release of organic anions from these LDHs into the bulk solution was triggered by the presence of chloride anions, proving the anion-exchange nature of this process. A significant reduction of the corrosion rate was observed when the LDH nanopigments were present in the corrosive media.

The mechanism by which the inhibiting anions can be released from the LDHs underlines the versatility of their environmentally friendly structures and their potential application as nanocontainers in self-protecting coatings.

8.3.2 Containers with ceramic core and polyelectrolyte/polymeric shell

Naturally occurring or previously synthesized mesoporous or hollow micro- or nanoparticles are used for the preparation of this containers type. Several examples of micro-and nanoparticles commonly applied for this purpose are presented in the Figure 8.2.

Regardless of whether the ceramic particles are of artificial or natural origin and independent of their chemical nature, the extended porous core of these particles can

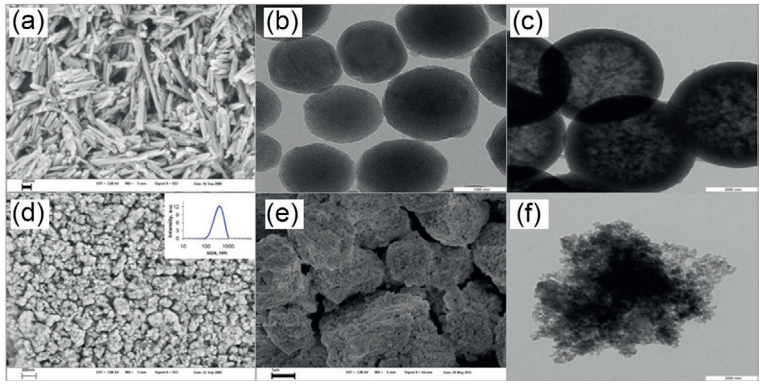


Figure 8.2 Mesoporous or hollow micro- and nanoparticles used for the preparation of containers ceramic core: (a) halloysite nanotubes, scale bar below denotes 200 nm; (b) spherical mesoporous silica (SMS) nanoparticles, scale bar denotes 100 nm; (c) spherical hollow silica (SHS) nanoparticles, scale bar denotes 200 nm; (d) mesoporous TiO_2 nanoparticles, scale bar below denotes 200 nm; (e) commercially available silica microparticles, scale bar denotes 1 µm; (f) commercially available aluminum modified silica submicroparticles; scale bar denotes 200 nm. *These materials are reproduced with permission of NACE International.*

serve as a robust scaffold on the next steps of containers assembly. Simultaneously, this spongelike reservoir can be loaded with various active compounds, in our particular case, anticorrosion coatings, with diverse corrosion inhibitors. The loading capacity is determined by the total volume of cavities, gaps, or pores available and can vary in the range between ~15 vol% for halloysite nanotubes (HS) and nearly 70 vol% for the silica nanoparticles with the highest porosity.

Halloysites nanoparticles represent one particular type of naturally occurring aluminosilicates with the average composition ($Al_2Si_2O_5(OH)_4 \cdot nH_2O$). In contrast to kaolin and many other aluminosilicates, halloysite nanoparticles have the shape of tubes (Figure 8.2a) with the typical average length between 2 and 5 micrometers and 50 and 15 nm for the outer diameter and for the diameter of the hollow cylindrical cavity along the particle major axis, respectively.[92] It is suggested, that this tubular shape of halloysite particles can to be caused by an irregular replacement of Al^{3+} by Fe^{3+} in the octahedral positions (3-10 wt.% of Fe_2O_3) due to geochemical processes in the earth's crust.[93]

Unlike naturally occurring halloysites, spherical silica nanoparticles with much higher porosity can be prepared by the surfactant-templated polycondensation method. Size of these particles, their morphology, as well as the size distribution and structure of pores are determined by the type of the soft template applied in the synthesis (surfactant micelles or emulsion droplets) and by the physicochemical conditions in the system controlling the kinetics of hydrolysis and polycondensation.

When micelles of the cationic surfactant cetyltrimethylammonium bromide (CTAB) were chosen as template particles distributed in a sodium hydroxide solution, the hydrolysis of the subsequently added tetraethoxysilane (TEOS) and following gradual polycondensation of arising silanol molecules on the micellar templates led to the so-called spherical mesoporous silica (SMS) nanoparticles (Figure 8.2b). SMS particles have well-expressed, two-dimensional, hexagonally arranged cylindrical pores with the diameter of 3.5 nm and demonstrate very high values of the specific area and the total pore volume, 1000 m^2/g and 1 cm^3/g, respectively.

In the case of initial premixing of TEOS and CTAB, subsequent dispersion of this mixture in a water-ethanol medium, and raising the pH value in the continuous phase of the resulting emulsion to 11.5 with ammonium hydroxide, the formation of spherical hollow silica (SHS) nanoparticles was observed (Figure 8.2c). This type of silica nanoparticles does not show any structural order of pores, but has a quite dense shell and a highly porous inner cavity. The average pore diameter of these particles, their specific surface area, and the total pore volume demonstrate, however, values quite similar or even equal to those for SMS nanoparticles—3.5 nm, 1000 m^2/g, and 0.9 cm^3/g, respectively.

Another example of artificial porous ceramic nanoparticles, preliminary prepared for containers cores, are the nanoparticles of the mesoporous titania (TiO_2). These particles are synthesized via heterophase oxidation of titanium carbide (TiC) micron-sized powder by the concentrated nitric acid. Subsequent multiple washing with H_2O yielded (Figure 8.2d) the titania nanoparticles with average size of 400 nm and the moderate polydispersity (PDI = 0.35). These spongy ceramic scaffolds have a quite broad pore size distribution, with the mean value of 10 nm and a considerable total pore volume of about 0.35 cm^3/g, which allow the sufficient loading of containers with various corrosion inhibitors.

Several kinds of mesoporous silica micro- or submicroparticles which can be immediately used for the fabrication of microcontainers are nowadays available on the market for reasonable prices. For instance, Figures 8.2e and f show two sorts of such particles, with the average sizes of 3.7 µm, but very high total pore volume of 2.0 cm^3/g as well as of 500 nm and 0.75 cm^3/g, respectively.

In connection with the characterization of ceramic core porosity, the question arises: what degree of porosity is enough to incorporate the inhibitor amount, sufficient for the effective corrosion protection?

Using the same formalism as at the derivation of Equation (8.7) and following discussion, let us imagine a microcontainer on the basis of the spherical porous ceramic core with the radius of 1 µm and volume fraction of pores of 20 vol%. Assuming further that only a half of this volume may be loaded with the inhibitor released upon coating damage, the volume of efficient inhibitor loaded in a single container becomes

$$V_{\text{eff}} = \frac{0.2 \times 4 / 3\pi R^3}{2} \tag{8.8}$$

Following the previously introduced (page 8) typical values for the density ρ, molecular weight M_w of inhibitor and its saturation adsorption $\Gamma_{\max}$ on the surface of metallic substrate of 1 g/cm^3, 500 g/mole, and 5×10^{-6} mole/m^2, respectively, the maximal area of substrate that can be protected by inhibitor released from this microcontainer can be estimated as

$$A_{\max} = \frac{V_{\text{eff}} \rho}{M_w \Gamma_\infty} = \frac{0.2 \times 4 / 3\pi R^3 \rho}{2 M_w \Gamma_\infty} \approx 16 \times 10^{-10}\ \text{m}^2 \tag{8.9}$$

This area corresponds to the area of a square with the side length of 40 μm. One thousand of these containers can already protect an area of 1.6×10^{-6} m^2 which can be imagined as area of the scratch with the length of 16 mm and width of 100 μm, that is, as area of a quite common almost macroscopic defect occurring in the practice. Ratio of the total volume of these containers to the scratch volume can give the necessary volume fraction of containers providing the full protection of this scratch. Assuming again an organic coating with the thickness $H = 70$ μm, this fraction can be estimated as ~0.37×10^{-4}, that is, even at such a very low containers fraction the effective protection of substrate can be achieved. Of course, the presented numerical estimation of the inhibitor load capacity for containers with the porous ceramic core is quite simplified, but even in this case it demonstrates how efficient can be the application of these containers in the new anticorrosion organic coatings.

Next important step in the preparation of containers described in this section consists in the soaking of the chosen active agent or inhibitor into the pores or cavities of the container ceramic core (loading of the core). For this purpose, the corresponding porous or hollow micro/nanoparticles are added to the concentrated solution of the inhibitor in an appropriate solvent or to the pure inhibitor (if an inhibitor is a liquid) and this mixture is then subjected to the multiple cyclic vacuumization in a desiccator.[71] The applied procedure provides the significant acceleration of the solution penetration and uptake in the especially narrow pores normally sealed with the tiny gaseous stoppers (nanobubbles) and enhances finally the amount of the inhibitor loaded in the containers. Moreover, the confined volume of narrow pores lead to the considerable decrease of the mobility of inhibitor molecules, which contribute as a consequence to the essentially extended release time for inhibitor impregnated into porous core and make therefore the release more sustained.

This peculiarity of the inhibitor molecules constrained in the confined volume of pores was used recently[94] for the preparation of the self-protecting anticorrosion coatings for the aluminum substrate where the remarkably slower kinetics of the inhibitor release was observed for the larger core particles possessing the longer pores and providing more interaction sites between inhibitor molecules and pores

walls. This prolonged release enabled the good long-term corrosion inhibition also for the protective organic coatings with the mesoporous nanocontainers without any polyelectrolyte or polymeric shells.

An important precondition required for the successful impregnation step is at least a good or, better yet, a complete wetting of particles material with the corresponding solution or liquid inhibitor. Thus, a thorough selection of a proper solvent with the good wetting ability to a specific ceramic material forming the core of container and simultaneously with the excellent solvency for the chosen inhibitor is necessary for the high efficiency of containers loading. Typically, high loading values of ceramic mesoporous containers with the inorganic inhibitors are attained from their aqueous solutions whereas organic inhibitors are less water-soluble and can be essentially better loaded from organic solvents of intermediate polarity such as short-chain alcohols, ketones and esters. Some examples of inhibitor loaded hollow or mesoporous cores particles discussed previously are presented in Figure 8.3.

The final stage of containers assembly procedure is the layer-by-layer (L-b-L) alternate adsorption of opposite charged polyelectrolytes onto ceramic cores for the formation of PE shells around them. Cationic polyelectrolytes such as poly(diallyldimethylammonium chloride), PDADAMAC; polyallylamine hydrochloride (PAH); polyethylene imine (PEI) and anionic ones like poly(sodium 4-styrene sulfonate), PSS; polyacrylic acid (PAA); poly(methacrylic acid), PMA, can be mentioned as typical individual building blocks for the shell assembly where specific properties desired for a certain shells of future containers can be varied using different combinations of corresponding polyelectrolytes. Schematically, the process of containers build-up and its last step—the L-b-L polyelectrolyte deposition—is demonstrated in Figure 8.4. Amount of deposition and washing steps between the changes from cationic to anionic polyelectrolyte depends on the desired thickness of the shell to be created and on requirements to its final composition.

An envelope formed by polyelectrolyte multilayers around loaded ceramic porous or hollow container core significantly decelerates or almost completely stops the premature leakage of the inhibitor from the container. Moreover, utilizing a certain combination of polyelectrolytes for the shell assembly can provide it special sensitivity to the pH changes in the local surrounding; this factor can also be used as a specific trigger for the controlling of shell permeability or for the containers opening. The creation of such pH-sensitive shells of micro- or nanocontainers can particularly be achieved by deposition of weak cationic or anionic polyelectrolyte in alternation with strong oppositely charged polyelectrolyte. Both types of polyelectrolytes are almost fully dissociated in the neutral pH range and attract each other electrostatically in the container shell. This complete charge compensation within the shell leads to its neutrality and quite high density, especially in the dried state.

In the case when a weak polyelectrolyte is included in the shell composition, it becomes less dissociated in vicinity of either its pK_a or pK_b value depending on the acidic or basic character of this weak polyelectrolyte. As a consequence, the shift

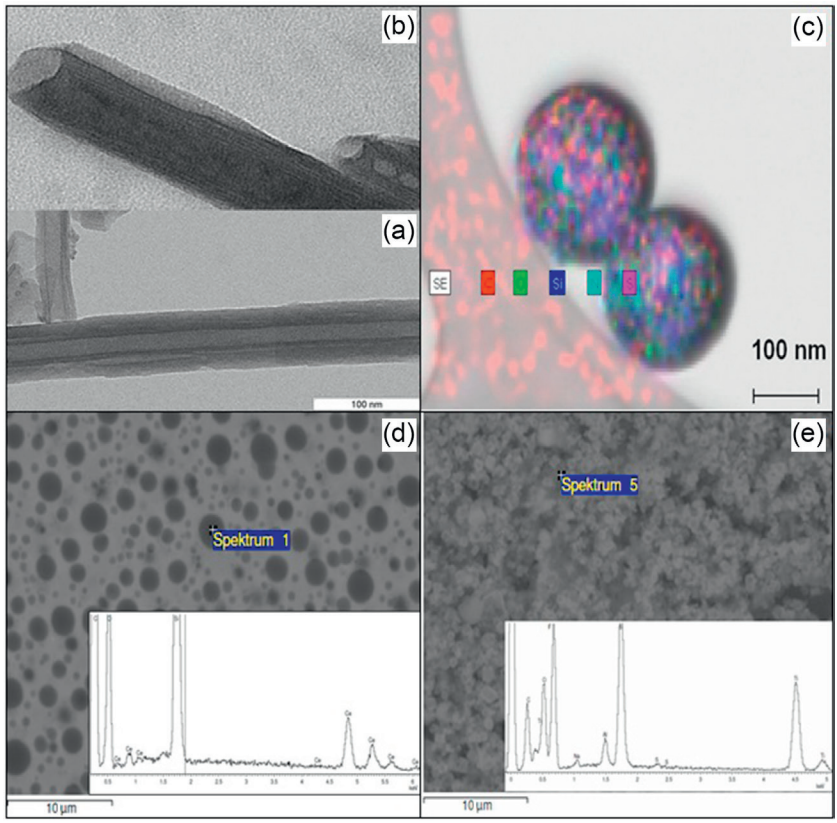


Figure 8.3 Ceramic container cores filled with inhibitors: (a and b) empty halloysites and halloysites filled with ammonium molybdate, respectively; (c) SHS silica particles filled with mercaptobenzothiazole (MBT); (d) commercially available silica microparticles filled with cerium nitrate; (e) commercially available aluminum modified silica microparticles filled with sodium hexafluorotitanate. *These materials are reproduced with permission of NACE International.*

of pH value toward basic (for a weak cationic polyelectrolyte) of acidic (for a weak anionic polyelectrolyte) leads to the distortion of the charge compensation in the container shell and finally to its swelling due to electrostatic repulsion between individual layers. The opened state of containers is then achieved.

Usually, the onset of corrosion and further development of this process leads to the local pH changes that can be remarkable nearby the cathodic or anodic sites on the substrate. The corresponding specific sensitivity of containers shells converts this effect accompanying corrosion into a trigger for the opening of containers and for the release of the encapsulated inhibitor on-demand. Thus, the protective coating with embedded containers of this type demonstrates self-protecting anticorrosion functionality.

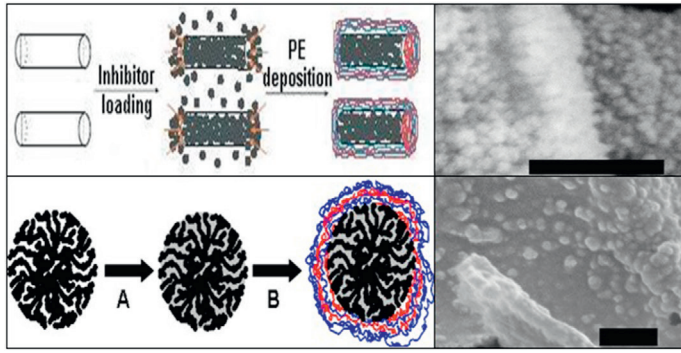


Figure 8.4 Schema of assembly steps in the preparation of ceramic particle-based nano- or microcontainers. The second step on the left top and bottom pictures represents the L-b-L alternate PE adsorption halloysite nanotubes and mesoporous ceramic particles, respectively. Microphotographs on the right show the surface of mesoporous ceramic particle before (top) and after (bottom) deposition of PE multilayer; scale bars denote in both cases 200 nm. *These materials are reproduced with permission of NACE International.*

8.3.3 Containers with ceramic core and stimuli-responsive stoppers at the pores endings

The main component of this type of containers is almost identical to the one described in the previous paragraph: This is a porous or a hollow ceramic core of micro- or nanodimensions which has also to be initially impregnated with the corrosion inhibitor or other active agent. Only one specific feature here is of higher importance than for the abovementioned containers with ceramic core and polyelectrolyte shell—even in the case of a core with the hollow interior, the presence of small, through pores in the shell of this ceramic particle is essential for the build-up of this containers type (Figure 8.5). Firstly, these pores are necessary to load the

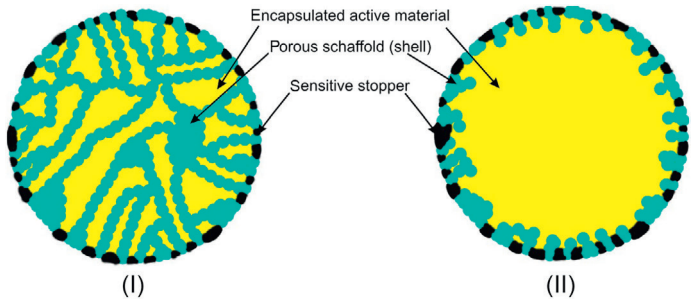


Figure 8.5 Schematic illustration of porous (I) and core-shell (II) nanocontainers with stimuli-responsive stoppers at pores endings.

inner part of the porous or hollow ceramic particle serving as a containers core. Again, being immersed into the liquid to be loaded, the particles have to be subjected to multiple vacuum cycles. After an appropriate uptake of the substance to be loaded is accomplished, the last stage of containers preparation is commenced. In contrast to the ceramic containers with the continuous polyelectrolyte multilayer shell, no enclosure of entire core particle is performed to isolate the container load from the surrounding medium and to prevent its premature release from containers. To attain the closed state of containers, the outer endings of pores in the ceramic porous or hollow particle are sealed with the insoluble stoppers made of substances that are the products of chemical or physical interactions between encapsulated corrosion inhibitor or solvent/dispersing agent and an additional external compound. For example, these stoppers can be made of ionic complexes or aggregates arising as a result of interfacial physical processes, such as interfacial precipitation, coacervation, or gelation. Therefore, the second important feature of pores is their role of "holders" for the stoppers formed at the pores outlets. The size, tortuosity, and the surface chemistry determine the ability of pores to be successfully sealed by a certain type of stoppers. Sometimes, an additional stabilizing of the pores openings or the chemical modification of their surface is necessary.[95]

The release of the encapsulated inhibitor toward the containers exterior can be on-demand switched on by several triggers that are, again, either the factors causing corrosion or the factors arising as a consequence of the corrosion process. As most typical triggering factors a change of pH, concentration of specific ions, ionic strength, or temperature can be mentioned. Local changes of these parameters nearby of containers in the closed state cause the swelling or dissolution of stoppers and therefore the opening of containers leading to the stimuli-responsive release of inhibitor or other active agent.

The simplest realization of this idea was recently reported by Abdullayev et al.[96,97] where the halloysite nanotubes were employed as core particles. Here, the hollow lumen inside halloysites was simultaneously used as a single big pore for loading and then for the sealing of its outer ends with the stoppers. After the halloysite nanotubes were filled with the corrosion inhibitor BTA, the endings of tubules were closed by the insoluble stoppers, preventing the spontaneous release of the enclosed inhibitor. The formation of the insoluble complexes between BTA and bivalent copper cations was utilized for the nanocontainers sealing. The stimuli-responsive opening of containers was carried out by the addition of a concentrated ammonia solution to the aqueous suspension of containers. Due to formation of very stable, but soluble copper-ammonia complexes and because of pH increase leading to the formation of the anionic form of BTA, the stoppers were irreversible removed and the entrapped BTA was released in the containers' exteriors. The subsequent introduction of these containers in the organic coatings for the corrosion protection of copper and aluminum showed their considerably better and sustained anticorrosion performance as

compared with standard ones. Later, the corresponding U.S. patent application[98] was made on the basis of this material.

More recently, the extended concept of these containers was also applied as a patent.[99] In this patent, not only cylindrical hollow halloysites were proposed as containers cores, but also many other types of mesoporous or hollow ceramic micro- and nanoparticles. Moreover, various possible chemical as well as physical mechanisms for the stoppers creation were shown along with the inhibitor complexation reaction.

The possibility to utilize the different chemical mechanisms of stoppers opening was demonstrated very recently for the mesoporous silica-based nanocontainers with pores sealed by the insoluble complex between copper ions and BTA.[95] Two external factors—the decrease of pH value below 5 and increase of sulfide ions concentration in the exterior solution led to the decomposition of copper-BTA complexes and to dissolution of stoppers followed by the release of active agents such as inhibitor BTA or antibacterial agents benzalkonium chloride or triclosan. By the incorporation of containers loaded by the corresponding agents into the coating matrix, the protective organic coatings with the enhanced anticorrosive, antibacterial, or multifunctional performance were prepared.

8.3.4 Containers on the basis of direct or inverse emulsions

As can be seen from previous sections, preparation of containers based on the use of ceramic hollow or mesoporous micro- or nanoparticle as scaffold and impregnable container core is a multistep process. Loading capacity and the number of loading cycles depend on the porosity of the scaffold as well as on the pores size distribution and can be additionally complicated in the case of narrow pores. This procedure may become even more complex when the containers load and containers core are composed of the substances with essentially different polarities. Furthermore, the polarity mismatches between core and dispersion medium where the containers were initially dislocated can make the total procedure overcomplicated.[100] Together with at least two-step deposition of PE shells of containers, the entire fabrication of this containers type is not always simply and economically sound enough.

On the contrary, the paradigm in the preparation of nano- or microcontainers based on the utilization of emulsion as a starting point reveals a number of advantages over the techniques dealing with the particulate porous or hollow cores which were discussed above. Most important, the emulsion-based concept is the straightforward one where the droplets of emulsions play a twofold role: as soft (liquid) template particles and as loaded cores of the containers to be prepared. This simultaneous multipurpose use of emulsion droplets allows the significant reduction of number of stages during the containers fabrication. The second big advantage in using an emulsion as an initial system for the containers preparation is the liquid state of both the dispersion medium

and dispersed phase at the beginning of assembly. First, this reduces significantly the amount of energy, that is, comminution work that has to be applied for the preparation of the colloidal system, especially in the presence of surfactants decreasing additionally the interfacial tension. Second, the liquid state of the dispersed phase facilitates the exact regulation of concentrations of all components and enables not only the fine adjustment of the active agent content and its distribution in the container, but also the precise control of containers size distribution by means of hydrophobes and surfactants.

Another benefits connected with the emulsion route for the containers preparation are the possibility to prepare containers with core/shell morphology and encapsulation of liquid ingredients. This situation may, for instance, frequently occur at the preparation of containers for biomimetic self-protecting anticorrosion coatings where the liquid encapsulated in containers resembles a biological liquid first of all blood in the skin. Thus, in case of destructive external impact, the strong immediate feedback of this coating will be achieved.

Obviously, the fabrication of oil-in-water (O/W, direct) or water-in-oil (W/O, inverse) emulsion serves as a springboard for all specific realizations of the emulsion-based concept. Thus, the liquid/liquid interface between dispersion medium of an emulsion and the plurality of droplets constituting its dispersed phase or this plurality itself functions as locus in quo where the formation of the container proceeds. A broad variety of techniques yielding finally the micro- or nanocontainers may be grouped into two wide classes depending on the nature of processes leading to the containers formation: (1) approaches using the physical phenomena for their creation and (2) techniques utilizing different chemical reactions at the interface of emulsion droplets or *in-situ* reactions in their bulk with eventual subsequent merging and segregation of the growing prepolymers at the interface (Figure 8.6).

This general classification is considered in more details in the next sections of this chapter on the basis of several types of containers prepared by the particular methods from these two groups. Concrete containers taken as corresponding examples will be used to discuss the methods applied for their preparation, mechanisms of their formation, and advantages and drawbacks in order to provide the self-protecting anticorrosion coatings the abilities to mimic the active feedback properties of living matter.

8.3.5 Containers based on the interfacial physical phenomena

8.3.5.1 Containers obtained by means of solvent induced interfacial precipitation

At the application of this method for the preparation of containers, the emulsion droplets serve as soft template particles at whose interface the component forming the shells of the future containers starts to precipitate because of changes in the

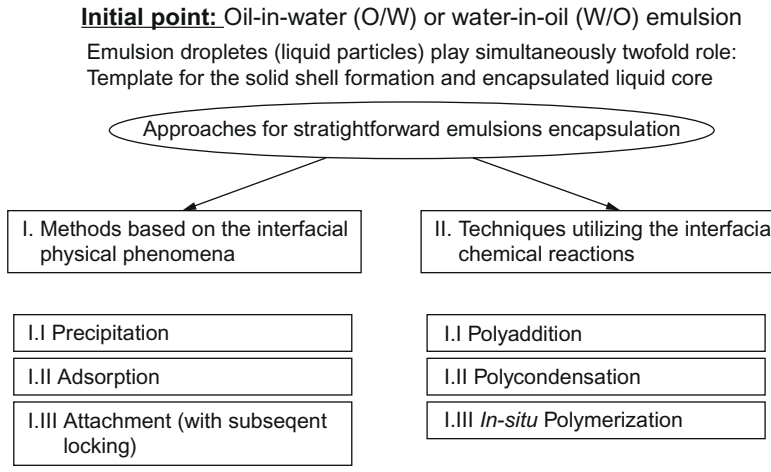


Figure 8.6 Subdivision of emulsion-based methods for the preparation of micro- and nanocontainers.

physical or chemical parameters (composition) in the system. The same droplets contain also the substance to be loaded into containers and function therefore as their future cores. The shell-forming component is at the beginning completely dissolved in the emulsion droplets and both phases of this disperse system (emulsion) remain initially homogeneous. Several changes occurring in the system can disturb the solubility of the shell-building component and lead to start of its precipitation.

In the simplest case, changes in only one physical parameter of the system such as temperature can cause a serious lowering of the miscibility of the shell-forming component with other components in one phase of the two-phase disperse system leading to its precipitation at the droplets interface.

The decrease of the solubility of the shell-forming compound with subsequent precipitation can be also induced by changes in the phase composition—either by removal of the solvent having a good solvency for this compound (further—"solvent") from the system or by addition of the solvent possessing a poor solvency for it (further—"nonsolvent") to the system. Since the dispersed phase is a nonautonomous one, the phases are unequal against the independent changes of their compositions. If the shell-forming component is initially dissolved in the dispersion medium, its solubility there could be distorted almost without any effects on the composition of the dispersed phase. Moreover, a precipitation from dispersion medium is additionally favored by the presence of the emulsion droplets according to the heterogeneous nucleation mechanism that proceeds at their interface. Typical processes leading to the interfacial precipitation from the dispersion medium are evaporation of the solvent from this phase or its dilution by the nonsolvent, that is, solvent evaporation-induced precipitation (Figure 8.6), or dilution-induced precipitation.

In the spatially opposite case, precipitation starts from the interior of emulsion droplets, and triggers analogous to these for the dispersion medium can only be activated by the involving of the surrounding dispersion medium. Therefore, the solvent or nonsolvent, respectively, should at least be sparingly soluble also in the dispersion medium of the emulsion to be transferred through it from/to the emulsion droplets with the initially dissolved shell-forming component. Interfacial precipitation from the dispersed phase can additionally be influenced by curvature and confined character of its particles.

In the end, the formation of either containers with the core/shell morphology and liquid core or compact solid containers is attained.

Micro- and nanocontainers for the self-protecting anticorrosion coating containing the water-repelling agent sodium docusate (AOT) were prepared in our group,[101] exploiting the solvent evaporation-induced interfacial precipitation in an O/W emulsion. The oil phase of the O/W emulsion was prepared by the mixing of water-immiscible dodecane with ethyl acetate (EA) sparingly soluble in water at the components ratio 5:9. In this composite solvent, ~9.5 wt.% of polystyrene (PS, $M_w = 34$ KDa) and 5 wt.% of sodium docusate, related to the total oil phase composition, were dissolved. Phosphate buffer solution with pH 7 saturated by EA at normal conditions was used as an aqueous dispersion medium of the emulsion. To this solution, 135 mg of nonionic surfactant Triton X-100 was added as emulsifying agent. Then, 10 v/v% rough O/W emulsion was prepared by means of Vortex-shaker (stage 7, for 1 min) and processed finally for 3 min with the high speed rotor-stator homogenizer Ultra-Turrax (IKA Werke, Staufen, Germany). After that, this emulsion was either left for the EA evaporation under the fume hood with continuous stirring at 150 rpm for 12 h or, to accelerate the removal of this solvent, firstly diluted ten times with Milli-Q water and then treated by the dry nitrogen bubbling for 5 h. Volatile EA was completely evaporated and an aqueous dispersion of PS micro- and nanocontainers containing a solution of AOT in dodecane was obtained. The zeta-average size of containers measured by DLS intensity (zetasizer Nano ZS Malvern, UK) was 1570 nm with PDI = 0.8 reflecting the strong polydispersity of containers visible also on the qualitative level in the Figure 8.7. Such a broad containers size distribution is a typical consequence of the emulsion preparation by means of a high speed rotor-stator homogenizer like Ultra-Turrax. Interestingly that the containers obtained only by the gradual evaporation of EA without acceleration showed lower polydispersity with PDI = 0.6 probably because of the Ostwald ripening in the initial emulsion droplet that kept in this case their liquid state longer. Several partially deformed containers with the concavities in the shells observable in the Figure 8.7 can be considered as an indirect argument for their core/shell or multicompartment morphology. On the other hand, this containers structure may be also deduced from the very low miscibility of core material (diluted docusate solution in dodecane) with the aqueous dispersion medium.

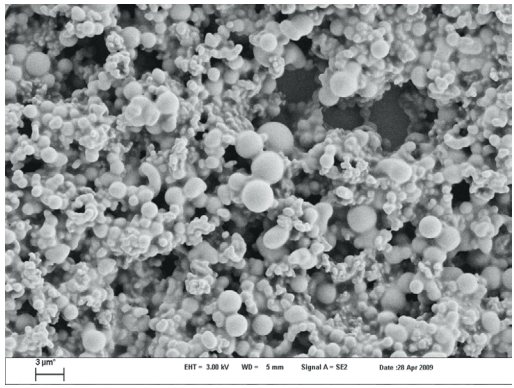


Figure 8.7 Micro- and nano-containers with polystyrene shells containing a solution of water-repelling agent sodium docusate in dodecane obtained by the solvent evaporation-induced interfacial precipitation. *These materials are reproduced with permission of ICE Publishing.*

In spite of the simplicity and relatively low costs of interfacial precipitation method in its various concrete realizations, there are also a lot of challenges and drawbacks connected with some technical peculiarities of this method and with the properties of containers obtained in this manner related to their embedding into coating matrix. Solvents used for the dissolution of shell-forming component(s) have to be either completely or at least sparingly soluble in the dispersion medium, most often aqueous one. These solvents should be also volatile enough to assure a reasonable time of complete evaporation and formation of the container shell. Therefore, the application of this method in both solvent evaporation-induced precipitation and dilution-induced precipitation types will lead to serious amounts of environmentally dangerous wastes such as volatile organic compounds (VOC) or VOC-contaminated water, especially when upscaled to the industrial extent. Because of such environmental concerns, the industrial realization of the interfacial precipitation method may be additionally complicated by the necessity to install quite expensive recycling set-ups.

Another problem is that polymers used for the formation of containers shells are the preformed polymers, which should be well-soluble in several solvents of intermediate polarity ensuring the good miscibility with both aqueous and oily phases. Thus, the relatively low cross-linking degree of polymers employable for this purpose is required. However, the high solubility of shell-forming polymers in the solvents of moderate polarity excludes automatically the incorporation of containers made of these polymers by interfacial precipitation in the coatings on the basis of organic solvents and restricts their use only to water-borne coating formulations. Moreover, even in this case, the coating formulations with relatively high curing temperature can also be a subject of doubt as the low cross-linking degree of polymer will cause its melting already on the curing step with subsequent destruction of containers.

8.3.5.2 Containers prepared by the use of layer-by-layer (L-b-L) polyelectrolyte interfacial adsorption

Notwithstanding that the L-b-L interfacial adsorption method became well-established worldwide in cases of plane solid[102] and colloidal solid[103] templates in the last three decades, its extension to the liquid colloidal templates (emulsion droplets) was elaborated not so long ago. Several details of this technique were partially used already in some works issued in the middle 2000s.[104–106]

These attempts were, however, seriously restricted either by employing specific chemicals or by application of unique preparation conditions. So, Tjipto and coworkers[106] have used the special substance (4′-pentyl-4-cyanobiphenyl) forming nematic liquid crystals as material for the droplets of O/W emulsion to be encapsulated. At the encapsulation of various food-relevant emulsions, both amounts of hydrophobic bioemulsifiers and the preparation conditions used evidences that the initial solid or solidlike layer was formed at the interface before the container shell formation by L-b-L polyelectrolyte deposition was started.[104,105]

Universal approach to the preparation of loaded micro- and nanocontainers based on the direct emulsion encapsulation by polyelectrolyte L-b-L adsorption was developed only recently.[107] Using this approach, the liquid colloidal templates (droplets of O/W emulsion) were composed of water-immiscible substance dodecane. To stabilize the dispersed phase of initial emulsion and to ensure the significant interfacial charge of droplets for the beginning of polyelectrolyte adsorption, the oil phase was doped by small amount of cationic surface-active precursor Dioctadecyldimethylammonium bromide (DODAB). Because of dodecane's very low solubility in nonpolar solvents, 30 v/v% of chloroform was added to dodecane in order to improve the precursor solubility in the oil phase. The droplets of O/W emulsion, however, did not contain any detectable traces of chloroform during the polyelectrolyte deposition steps because of its considerable solubility in the aqueous media. Colloidal stability of initial emulsion was achieved due to a concentrated monolayer of strongly positively charged DODAB (zeta-potential was about +90 mV) at the surface of each droplet. The L-b-L assembly was done by the subsequent adsorption of oppositely charged polyelectrolytes from their concentrated (20 mg/ml) aqueous salt-free solutions. The creamed upper layer of the positively charged initial emulsion was added dropwise to the oppositely charged solution of PSS upon continuous stirring, ensuring its good adsorption with the subsequent overcharging of the droplets interface. The excess of the remaining free polyelectrolyte was washed out by pure Milli-Q water. The second encapsulation step was done in an aqueous solution of cationic PE PDADMAC or PAH in the same manner (Figure 8.8). The further repetition of the alternating adsorption steps leads to the formation of containers with desired shell thickness depending on the particular final demand. Resulting containers had Z-average size of 4.2 μm and were quite monodisperse (PDI = 0.32). The dried droplets of O/W

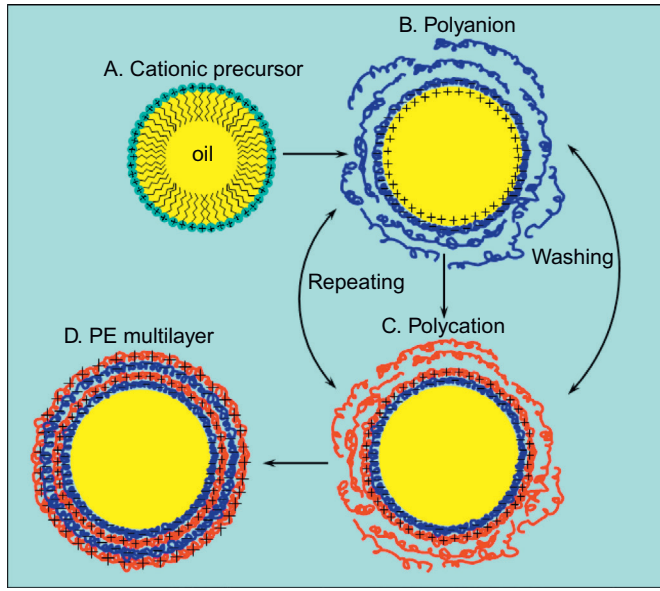


Figure 8.8 Alternate layer-by-layer (L-b-L) polyelectrolyte adsorption on the interface of emulsion droplet—a depiction of deposition steps. *These materials are reproduced with permission of ICE Publishing.*

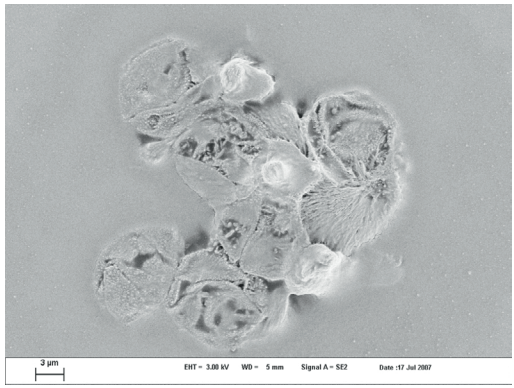


Figure 8.9 Microcontainers on the basis of dodecane-in-water O/W emulsion with PE shells made of four subsequently adsorbed PSS and PDADMAC layers. *These materials are reproduced with permission of ICE Publishing.*

emulsion encapsulated by the L-b-L interfacial adsorption technique are presented in the figure. Since the procedure of drying leads, in the case of PE oil-filled containers, to their collapse, especially on the steps connected with the preparation of SEM samples, the oily containers cores cannot be kept intact, and only wrinkled polyelectrolyte containers shells are observable (Figure 8.9), supporting the polyelectrolyte multilayered shell assembly around O/W emulsion droplets.

Following the proposed paradigm for the straightforward preparation of the emulsion-based polyelectrolyte containers[107] further progress in this field was achieved.[108,109] Wackerbarth et al.[108] reported polyelectrolyte microcontainers on the emulsion basis with six layers of biopolyelectrolytes for the potential application in the food industry. The authors of Ref. 109 have presented the successful polyelectrolyte encapsulation of highly unstable polyunsaturated natural oils for the purpose of storage and degradation protection by introducing the natural antioxidant compound (tannic acid) as a shell constituent in alternation with the biocompatible oppositely charged polyelectrolyte.

Container prepared via polyelectrolyte L-b-L direct emulsion encapsulation technique can be envisaged as quite applicable in several types of protective coatings, especially water based, imparting to them some unique functionalities independent of the nature of components encapsulated in the core. This can be achieved due to the many polyelectrolytes available for L-b-L container shell assembly. Purposeful choice of polyelectrolytes for the containers shells allows their opening by numerous environmental or artificially introduced triggers such as temperature,[110] pressure,[111] changes in pH,[112] ionic strength, electrochemical potential, and therefore enables the specific stimuli-responsive protective ability of coatings carrying these containers.

Nanometric accuracy provided by polyelectrolyte L-b-L deposition on the each step of the container build-up allows very fine adjustment of their size and the shell thickness that also can be of high practical importance in many research and industrial fields.

On the other hand, some drawbacks of polyelectrolyte containers obtained by the L-b-L interfacial adsorption should be also mentioned here making their utilization in many types of self-protecting coatings problematic. Even at deposition of polyelectrolytes with lowest M_w the permeability of shell for low-molecular agents loaded into containers remains high disabling the possibility of sustained release for these substances and use of such type of containers in the media with good solvency for the core material. Low mechanical stability of the polyelectrolyte shells at any reasonable number of polyelectrolyte layers in the shell is the other source of trouble. It can be significantly improved by the increase of L-b-L deposition steps and subsequent annealing at higher temperature,[110] such an overcomplication makes the fabrication costs rise and thus is unacceptable for many potential application fields. At the same time, the use of soft emulsion-based containers with L-b-L polyelectrolyte shells is imaginable in the water-borne coating formulations with the quite mild curing conditions and ductile coating matrices.

8.3.5.3 Containers on the basis of irreversible interfacial attachment—formation of Pickering emulsions

Noticeable phenomenon of emulsions stabilization due to spontaneous attachment of the partially hydrophobic/hydrophilic micro- or nanoparticles at the O/W or

W/O interface underlies this method of preparation of emulsion-based nano- and microcontainers.

This "strange" behavior of such particles is known since the beginning of twentieth century[113,114] and can be strictly described in terms of particle energy change at its transition from the bulk location to the interface[115]:

$$\Delta G_{\text{att}} = -\pi r^2 \gamma_{\alpha\beta} \left(1 \pm \cos\theta\right)^2 \tag{8.10}$$

Thermodynamically, even in the case of small nanoparticles, this transition is practically irreversible because of the huge depth of the potential energy of the particle located at the interface and is therefore commonly called not "adsorption" but "attachment." Due to these reasons, the partially hydrophobic/hydrophilic particles form spontaneously a tight mono- or even multilayer at the emulsion droplets interface and act as building blocks for the containers shells. Again, the emulsion droplets serve as a template for the formation of the particulate shells and work at the same time as reservoirs for the loaded active agent.

The interfacial activity of particles can be an intrinsic property of them connected with their specific affinity to certain types of solvents. In this case even the pristine particles with unmodified surface are able to concentrate at the interface between droplets of this solvent and the external continuous phase.[116] However, this peculiarity is more frequently imparted to the particle by its surface modification using various types of surfactants[117,118] bonded electrostatically or covalently to the particle material.

Electrostatic mechanism of the modification does not presume the formation of the proper chemical bonds between surfactant molecules and particle surface, but is rather a result of the equilibration of the complex physical interactions between these molecules, particles, and surrounding medium (solution). Therefore, the small amounts of free surfactant molecules always persisting in the system can occasionally interfere with the corrosion inhibitor or other protective agents in the core-forming emulsion droplets and impair the mechanism of the interfacial particle attachment. To avoid this undesired situation, the thorough selection of appropriate nonreacting and noninteracting surfactants and protective components should be made before fabrication of containers. The indicated problem will, however, not arise at all when inhibitor molecules possess by themselves the certain surface activity and can therefore simultaneously cause the partial hydrophobic modification of the particle surface. Many corrosion inhibitors are weak organic acids, bases, or amphoteric compounds having functional groups partially or fully ionized in a certain pH range and therefore becoming hydrophilic. In the case when residual organic moieties of inhibitor molecules are hydrophobic enough, the entire molecule will demonstrate the amphiphilic behavior in the same pH range, that is, will act as a surfactant. Haase et al. utilized the corresponding ability of the amphoteric corrosion inhibitor 8-hydroxyquinoline (8-HQ)[119] to become considerably protonated at the

pH <5.5 (pK_a = 5.13) and to be adsorbed electrostatically on the surface of negatively charged silica nanoparticles (Ludox TMA) in order to make them partially hydrophobized and therefore interfacially active. These particles stabilize the O/W emulsion droplets forming the multilayers at their interface that can be considered as particulate containers shells (Figure 8.10). The droplets of dispersed phase are composed of Diethyl phthalate (DEP) with dissolved 8-HQ and function as containers cores with the already loaded inhibitor. The containers size distribution and the amount of nanoparticles in the containers shells are well-expressed functions of pH in the range from ~4.4 to 5.6. At pH 4.4 the monodisperse containers with volumetric average size of 4.5 μm and PDI of about 0.4 were obtained. This pH-dependent behavior can be related to the continuously increased interfacial activity of silica nanoparticles hydrophobized by the gradually growing amount of the adsorbed 8-HQ upon pH drop. Below the pH 4.4, protonation degree of 8-HQ and subsequently its concentration in the dispersion medium attain the values enabling the formation of an 8-HQ bilayer on the surface of silica nanoparticles. The hydrophobe-hydrophobe interaction of the overlapping aromatic rings is suggested to be a driving force for this effect. As a result, the positively charged protonated groups of 8-HQ molecules in the outer part of bilayer are oriented toward dispersion medium and re-hydrophilize the particles in the containers shells. The rapid destruction of the containers is observed in this pH region, leading to the immediate burstlike release of the encapsulated inhibitor. This pH-sensitivity as well as the mechanical rupture of containers could be utilized as triggers for the containers opening and stimulated inhibitor release when the containers become embedded in the matrix of a self-protecting anticorrosion coating.

Emulsion-based containers fabricated by means of interfacial attachment of nano- or microparticulate building blocks forming the container shell reveal several advantages in the preparation routine and in the handling that follows, fashioning them as potential candidates for the use in the various self-protecting coatings. Fabrication of micro- and nanocontainers by means of the interfacial attachment

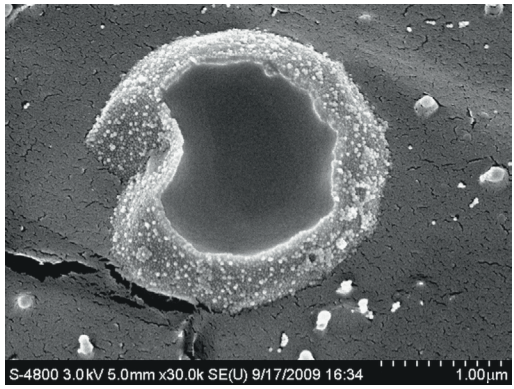


Figure 8.10 Multilayered nanoparticulate (Ludox TMA) shells of micro- and nanocontainers with liquid core containing corrosion inhibitor 8-HQ. Cryo SEM image. *These materials are reproduced with permission of ICE Publishing.*

method is usually quite simple procedure that includes as a rule only two steps—(1) preparation of particles as building blocks for the shells of future containers due to their partial hydrophobization (O/W) or hydrophilization (W/O) and (2) addition of them to the two-phase system containing all components of containers during or immediately before the emulsification with subsequent processing leading to the ready containers. Sometimes this procedure can be even further simplified to the practically one-pot process.[116] Because of its simplicity, this preparation pathway may often be economically sound and has a high practical relevance. Wide variety of particles of different chemical nature and of immiscible solvents with diverse polarities available facilitates an almost unlimited number of achievable containers types thus making the method very versatile. Comparing with the types of the emulsion-based containers described above, containers prepared by the interfacial attachment of particles demonstrate much higher robustness[120] and are therefore more suitable for the incorporation into self-protecting coatings with hard coating matrices. However, the main problem in the application of containers prepared by interfacial attachment remains the heterogeneity of their shells comprised of many fine particles joined at the surface of each emulsion droplet to a mono- or multilayer with the lot of gaps between individual building blocks. This discontinuous structure of the container shell reduces considerably its mechanical properties, especially comparing with these of the individual particle in the shell and increases its permeability drastically. The latter could be very critical when the containers loaded with the oil-soluble protective agent are mixed with a solvent-based coating formulation able to wash out the containers load immediately after their addition into coating mixture.

To enhance the mechanical strength of containers and make them more seamless, single particulate elements of the containers shells should be locked at the interface and joined together. It can be done for instance by the local high energy treatment[121] where the high intensity ultrasound was used for this purpose. The second possibility is the interlinkage of particles in the shell by the deposition of additional polyelectrolyte layers atop it. This, on the one hand, complicates the process of the containers preparation by one more step, but on the other hand can significantly improve the integrity and permeability of their shells. Moreover, the polyelectrolyte deposition could impart to shells certain additional valuable features connected with the properties of polyelectrolyte layer like selective pH sensitivity and so on. Figure 8.11 shows containers on the basis of Pickering emulsion droplets made of 1.5 M solution of 8-HQ in dimethyl phthalate (DMP) coated with three polyelectrolyte bilayers composed of pairs PAH/PSS or PAH/PAA. Alternate deposition of polyelectrolytes not only did not disturb the initial containers size distribution with volume-average size of 2.5 μm and PDI = 0.35, but also did lead to the significantly higher stability of containers that remained almost not deformed during the SEM sample preparation.

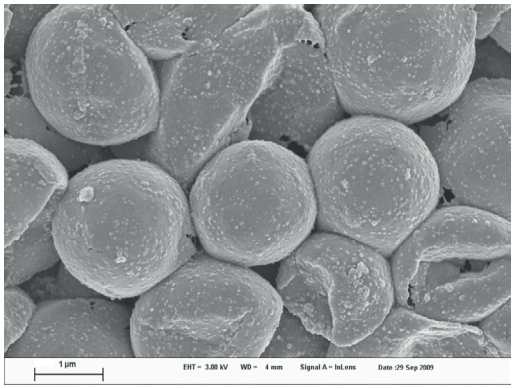


Figure 8.11 Core/shell microcontainers with nanoparticle shells obtained by interfacial deposition locked subsequently with the L-b-L adsorption of six polyelectolyte monolayers [PSS/poly(allylamine hydrochloride, PAH]. *These materials are reproduced with permission of ICE Publishing.*

8.3.6 Containers prepared by the interfacial or bulk chemical reactions in emulsion droplets

In the chemical methods of containers fabrication, containers form in the course of a chemical reaction proceeding either at the interface between emulsion droplets and dispersion medium around them or in the droplets interior.

Following to this natural division related to the reaction location, also the containers obtained by means of the corresponding reactions could be classified in two big groups: containers prepared using the interfacial polyaddition or polycondensation reactions and containers obtained by *in-situ* emulsion polymerization proceeding usually in the bulk of emulsion droplets.

8.3.6.1 Containers via interfacial polyaddition/interfacial polycondensation

At the containers synthesis by interfacial reaction in an emulsion, at least one of the reactants is distributed outside droplets in the continuous phase of emulsion whereas the others are dissolved in the droplets. Initially, the reactants have sufficiently different polarities and are predominantly soluble only in one of the coexisting phases excluding their interpenetration in the adjacent phase and premature reaction between them. Moreover, reactants have to remain phase-separated all the time when reaction goes on and meet each other only at the interface of emulsion droplets. If the product of such an interfacial reaction is soluble neither in the droplets of the emulsion nor in the medium around them, containers with the core/shell morphology will be synthesized. In the more frequently arising case, however, the resulting product is soluble or swellable in the droplets of dispersed phase, and particles with the compact morphology occur.[122,123] Depending on the release of low-molecular side products, the interfacial polyaddition (without side products) or interfacial polycondensation (with) reactions can be discriminated.

The encapsulation of the mixture of protective agents possessing simultaneously the functionalities of corrosion inhibitors and water repellents was carried out recently[124] by the interfacial polyaddition technique for the further application in the self-protecting anticorrosion coatings. The oil phase of the future O/W emulsion was composed of mixture of two protective agents, trimethoxy(octadecyl)silane (TMODS) and trimethoxy(octyl)silane (TMOS), Poly[(phenyl isocyanate)-co-formaldehyde] trifunctional pre-polymer participating in the reaction of shell formation as well as solvent (DEP) enabling the miscibility of all components.[124] This mixture was firstly dispersed in an aqueous medium by means of nonionic polymeric emulsifier polyvinyl alcohol (PVA) under intensive stirring for 3 min with high speed rotor-stator homogenizer Ultra-Turrax (IKA Werke, Staufen, Germany).

Resulting emulsion was added to the phosphate buffer solution containing the second water-soluble reactant glycerol and polyaddition reaction catalyst 1,4-diazabicyclo [2.2.2]octane (DABCO). The formation of polyurethane (PU) containers shells at the interfaces of droplets was occurred according to the following reaction scheme:

$$n\mathrm{OCN-R-NCO}+n\mathrm{HO-R'-OH}\rightarrow\left[-\mathrm{R-NHC(O)OR'-}\right]_n \qquad (8.11)$$

The reaction mixture was then left for 1 h at 65 °C under continuous stirring and subsequently overnight without heating and stirring for the completion of containers formation. Suspension of obtained micro- and nanocontainers was dialyzed in order to remove residual glycerol and PVA and then separated by centrifugation at 13,000 rpm. Finally, quite polydisperse microcontainers with the well-expressed core/shell morphology (Figure 8.12) were isolated.

The size distribution of resulting PU containers demonstrated two peaks representing two main fractions of containers in the mixture—one at 1.0 μm and the second one—at 5.5 μm. At the increasing of rate of the high speed rotor-stator homogenizer from 11,000 rpm through 16,000 rpm to 22,000 rpm, the area of the first peak was continuously increased with the subsequent reduction of the second one remaining,

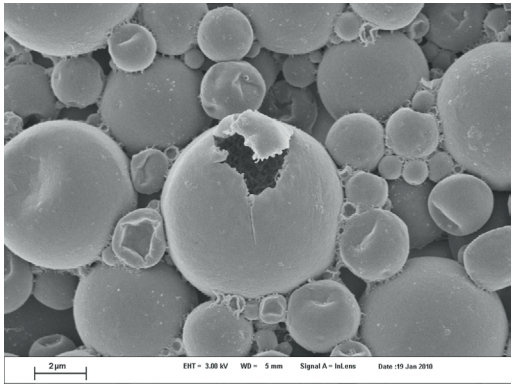


Figure 8.12 SEM images of microcontainers synthesized by interfacial polyaddition technique with encapsulated mixture of bifunctional protective agents and polyurethane shells. *These materials are reproduced with permission of ICE Publishing.*

however, still bimodal. Such a bimodal particle size distribution can be considered as polymerized replica of an initial O/W emulsion predestined by its droplets size distribution[125] almost always showing a high polydispersity if the high speed rotor-stator homogenizer was applied for the emulsification process. Utilization of ultrasound for this purpose leads as a rule to narrower and frequently monomodal droplet size distribution in the original emulsion.[126] Application of this comminution method in the considered case of containers with PU shells was unfortunately impossible because of numerous sonochemical effects accompanying the collapse of cavitation bubbles upon ultrasound propagation. Reactive isocyanate functional groups in the pre-polymer molecules quickly underwent side reaction with water molecules and highly reactive products of the water thermolysis (free radicals, hydroxyl-carrying species, etc.).

The incorporation of a small amount of these containers into the conventional coating (~6 wt.% microcontainers in relation to the total mass of the dry coating) provides to itself protecting features: Being mechanically damaged, the modified coating reveals not only recovered corrosion protection at the site of scratch, but also dewetting ability for the aqueous corrosive media.

Figure 8.13a and b demonstrate example of containers obtained by the interfacial polycondensation technique. The containers presented here have silica shells and are filled with the corrosion inhibitor mercaptobenzothiazole (MBT) dissolved in the organic solvent dibenzyl ester. These two compounds along with the shell-forming component TEOS were mixed together to form the oil phase of the future emulsion. An oil phase was dispersed in an aqueous phase with pH = 11.5 using the cationic surfactant CTAB, and the resulting emulsion was then left overnight at 65 °C.

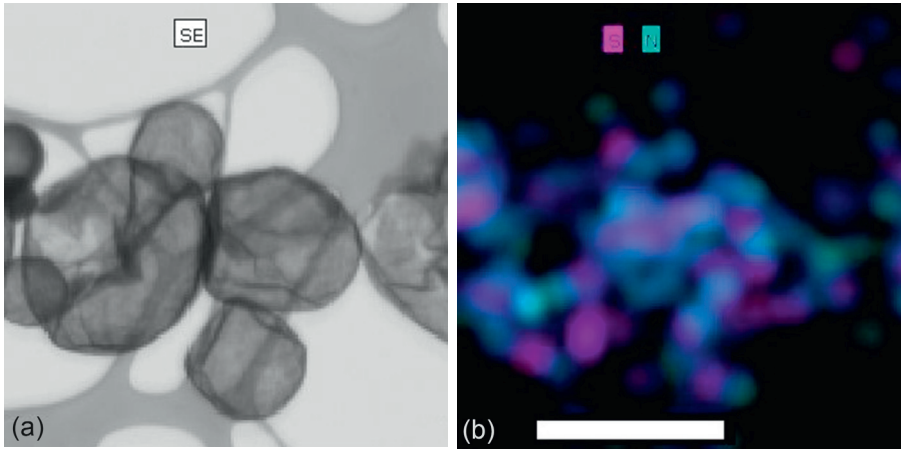


Figure 8.13 (a) Nanocontainers with silica shell loaded with corrosion inhibitor mercaptobenzothiazole; TEM picture, scale bar denotes 1 µm. (b) Nanocontainers with silica shell loaded with corrosion inhibitor mercaptobenzothiazole; EDX mapping, scale bar denotes 1 µm. *These materials are reproduced with permission of NACE International.*

Formation of container shell made of silica was achieved due to gradual hydrolysis of TEOS with the silanols as semi-products and their subsequent condensation on the surface of liquid colloidal template[127]:

$$\mathrm{Si(-OEth)_4' + H_2O \xrightarrow{-EthOH} (OH)Si(-OEth)_3 \xrightarrow{+(OH)Si(-OEth)_3} \xrightarrow{-H_2O} (EthO-)_3\,Si-O-Si(-OEth)_3} \tag{8.12}$$

At the end, the polydisperse submicrocontainers (zeta-average size 700 nm, PDI = 0.43) loaded with MBT (see EDX spectrum in the Figure 8.13b) were collected.

These containers can be successfully applied in the anticorrosive self-protecting coatings in cases when the corrosion is caused or followed by the pH increase. The dissolution of silica shell in this pH range can lead to the corrosion-triggered release of inhibitor.

Similarly, the containers of other composition with compact morphology were obtained for self-protection purposes by the interfacial polyaddition method. This type of containers made of polyurea and the corrosion inhibitor 2-methylbenzothiazole (MeBT) was used in the self-protecting anticorrosion coatings for the aluminum substrate.[123] Formation of the compact morphology can be explained as a result of the high affinity of MeBT to the polymer network. Due to very good solvency of this liquid inhibitor for polyurea, MeBT becomes homogeneously distributed over the whole droplet volume, forming a gel with a high amount of the liquid component. At the same time, crosslinked polymer network can hold the structure of the resulting particles together, ensuring their solid state. These microgel particles combine the attractive properties of both solids and liquids, making them perfect candidates for usage in self-protecting anticorrosion coatings. The solid state of the particles ensures good mechanical stability of the resulting coating system. The liquid component (MeBT), being entrapped in the solid matrix, retains its mobility providing the coating system with self-protecting abilities. The introduction of only a few parts of the particles in an organic coating allowed the significant improvement of its corrosion protection performance, as was shown by scanning vibrating electrode technique and electrochemical impedance spectroscopy.[123]

Figure 8.14 shows another example of containers obtained by the interfacial polycondensation technique. These containers have polyamide shells and are filled with the corrosion inhibitor Ce(III)-tris-(bis-2-ethylhexyl) phosphate dissolved in the organic solvent dibutylphosphate. These two compounds along with the shell-forming component terephthaloylchloride (TPC) were mixed in the weight ratio 2:13:5 for inhibitor, solvent and TPC, respectively, to form the oil phase of the future emulsion. Oil phase was dispersed in the Milli-Q water using the nonionic emulsifier PVA and the resulting emulsion was then added to the second aqueous phase containing combination of bi- and pentafunctional amines—ethylenediamine and tetraethylene-

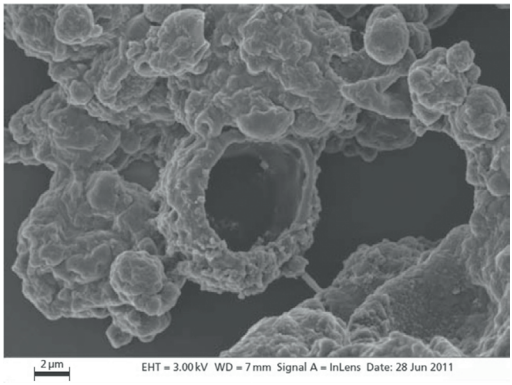


Figure 8.14 Micro-and nanocontainers filled with the corrosion inhibitor Ce(III)-*tris*-(bis-2-ethylhexyl) phosphate dissolved in the organic solvent dibutylphosphate and possessing the polyamide shells prepared by the interfacial polycondensation technique. *These materials are reproduced with permission of ICE Publishing.*

pentamine in the ratio ensuring the trifunctionality of the final mixture. The rapid formation of containers shells according to the reaction:

$$n\,\mathrm{H_2NRNH_2} + n\,\mathrm{ClOCR'COCl} \leftrightarrow \left[-\mathrm{NHRNHCOR'CO}-\right]_n + 2n\,\mathrm{HCl} \quad (8.13)$$

was accomplished by the release of HCl as the low-molecular side product and was therefore conducted in the highly basic medium containing fivefold excess of amines relating to the TPC amount. The obtained containers had a mean size of 6 µm and were highly polydisperse (PDI = 0.7) because of very cautious conditions during their preparation (use of high speed rotor-stator homogenizer at lowest stirring rate, short comminution time, etc.).

These containers may be promising for the applications the anticorrosive self-protecting coatings in cases when the corrosion is caused or followed by the pH decrease. The dissolution or strong swelling of the polyamide shell in this pH range will lead to the corrosion-triggered release of inhibitor.

8.3.6.2 Containers through in situ emulsion polymerization

Realization of this technique of containers preparation presumes that all reactants needed for the synthesis are contained in the emulsion droplets from the beginning. These droplets serve as reservoirs for reactants and protective agents and play simultaneously the role of liquid colloidal reactors and are only kinetically stabilized against the premature onset of polymerization reaction. After the O/W or W/O emulsion with desired properties such as stability, concentration, droplet size distribution and so on is prepared, the chemical (initiator substance, catalyst) or physical (T, UV-light etc.) triggers are activated to switch on the reaction and it runs until the attainment of the real equilibrium state corresponding to the completion of the polymerization.

The polyepoxy containers loaded with the corrosion inhibitor MeBT for the use in self-protecting anticorrosion coatings on the aluminum substrates were prepared by *in-situ* polymerization method[101] by the following steps. The mixture of reactants needed for the formation of polyepoxy shells of containers was initially prepared of the 1:1 combination of aromatic and aliphatic epoxy-monomers trimethylolpropane triglycidyl ether and tris(4-hydroxyphenyl)methane triglycidyl ether, respectively. A 20% of MeBT related to the total mass of the mixture was then added. The final step in the preparation of oil phase of the future emulsion was the addition of the second reactant for the *in-situ* polymerization reaction—diethylenetriamine in the amount ensuring the slight excess of the stoichiometric equivalence with the sum of both epoxy components. The oil phase was dispersed in the 2 wt.% aqueous solution of the nonionic emulsifier PVA using Ultra-Turrax at 16,000 rpm for 5 min. The obtained O/W emulsion was then doped with a small amount of polymerization catalyst tetrabutylphosphonium bromide to increase the reaction rate to a reasonable level. The mixture was left overnight under moderate stirring to complete the polymer formation. The resulting containers are very polydisperse (see Figure 8.15), with the volume-average size of 2.3 µm (PDI = 0.96), and have obviously the core/shell morphology revealing the phase separation in the emulsion droplets in the course of the polymerization reaction leading finally to the segregation of core and shell parts of containers. Again, the significant improvement of the container size distribution by the creation of the more monodisperse initial O/W emulsion via utrasonication was not possible because of the immediate reaction of monomers with water and especially with the products of sonochemical processes. Because of presence of free amino groups in the structure of the epoxy polymer that is obtained, the containers reveal high positive surface charge (zeta-potential of about +45 mV) and are therefore well dispersible in various aqueous media, for instance, in the water-based

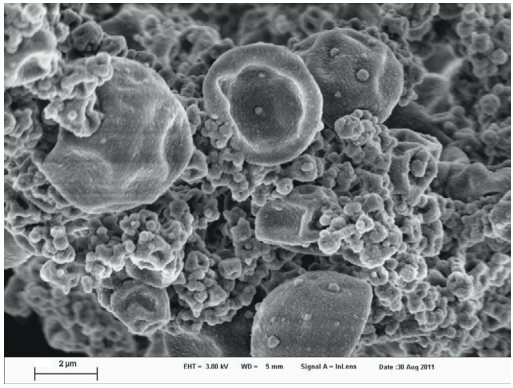


Figure 8.15 The polyepoxy micro- and nanocontainers filled with the corrosion inhibitor methylbenzothiazole (MeBT) obtained by *in-situ* polymerization method of O/W emulsion. *These materials are reproduced with permission of ICE Publishing.*

liquid coating formulations. Moreover, the introducing of epoxy monomers with the functional groups easily hydrolyzable in the acidic or basic medium (like ester groups) allows their opening in these media and finally acid- or base-triggered release of protective agents from the containers.

Sometimes, the combination of several emulsion-based methods of container fabrication leads to better results than the application of each of these methods alone. Solid micro- and nanocontainers for the self-protecting anticorrosion coatings were prepared via interfacial deposition of droplets-stabilizing SiO_2 nanoparticles with subsequent *in-situ* polymerization of their liquid cores.[128] Oil phase of the initial Pickering emulsion was composed either of styrene with dissolved corrosion inhibitor 8-HQ, hydrophobe hexadecane (HD) and polymerization initiator azo-bis-(isobutyronitril) (AIBN) or of styrene, corrosion inhibitor MBT, 4-vinylpyridine (4VP) as a solubilizing agent for MBT, HD, and AIBN. The weight percent ratios of all components were 193:45:10:2 or 255:90:130:20:4, respectively. The silica nanoparticles (Ludox TMA, Sigma) were used for the creation of particulate shells of the future containers. Noteworthy, that no additional steps for making silica partially hyhrophobic and therefore intefacially active were needed: 8-HQ acts as SiO_2 particle hydrophobizing agent and as, simultaneously, the encapsulated inhibitor, 4VP also hydrophobizes silica, acts as a MBT cosolubilizer, and becomes copolymerized with styrene. Variation of the amount of silica introduced in the liquid/liquid system during the comminution step (ultrasonication, VCX 505, Sonics & Materials Inc. Newton, USA) allowed the size controlling of the interim containers with the oily liquid core simply by the almost complete consumption of particles due to their interfacial deposition. The higher was the ratio of nanoparticles mass to the oil volume R, the smaller were the droplets of corresponding Pickering emulsion, independent of the ultrasonication power (W = 40 W) applied to the system. The size distribution of the nanosilica-stabilized emulsion droplets was always satisfactorily narrow: at $R = 0.09$, the number-average size was 2.3 μm with PDI = 0.45; at $R = 0.32$, the number-average size was 600 nm with PDI = 0.35; and at $R = 0.91$, the number-average size was around 260 nm with PDI = 0.2. It is also important to emphasize here that before and during the ultrasonic treatment the system was purged for 7 min by the nitrogen flow and ultrasonication was carried out under continuous cooling in the ice bath. These measures allowed the complete avoiding the undesired premature polymerization on the dispersion step. Finally, the polymerization of the liquid cores was initiated by heating the whole mixture up to 65 °C for 24 h. These solid containers (Figure 8.16) were introduced in the conventional water-based alkyd coating formulation that was then deposited on the aluminum specimens. The coatings with entrapped containers showed considerably better corrosion resistance than unmodified ones, as was confirmed by EIS and SVET measurements (Figure 8.17).

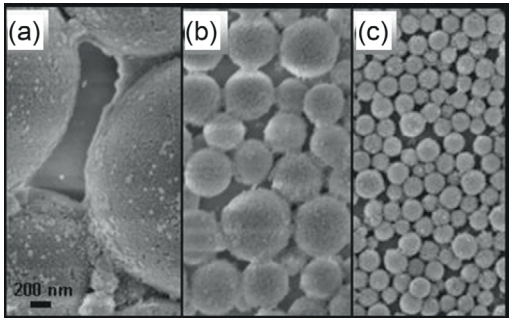


Figure 8.16 SEM micrographs of silica-PS/8-HQ micro- and nanocontainers stabilized initially by the interfacial deposition and finally synthesized by *in-situ* polymerization method at different silica mass to oil volume ratios ($m_{particle}/V_{oil}$): (a) 0.09 (b) 0.32 (c) 0.91 g/ml. *These materials are reproduced with permission of ICE Publishing.*

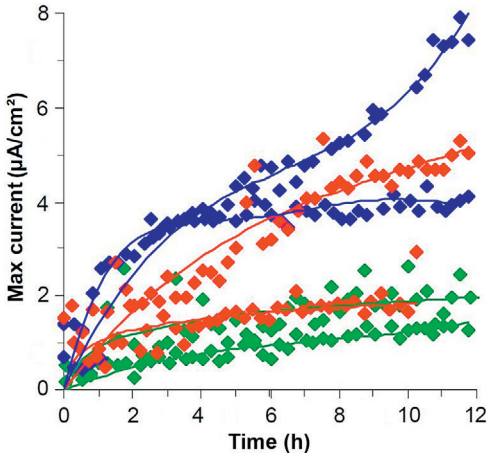


Figure 8.17 Results of measurements by the scanning vibrating electrode technique (SVET) obtained for scratched blank and modified alkyd coatings on aluminum in 0.1 M NaCl solution. Coatings: without containers—1, with 10 wt.% of containers—2, coating with 20 wt.% of containers—3. *These materials are reproduced with permission of ICE Publishing.*

8.4 Release of Active Agents from Containers

Release kinetics of an active agent (corrosion inhibitor) entrapped in containers is very important characteristic of them influencing strongly the rate and intensity of protective feedback of the coating in which these containers are incorporated. Of course, there are some other factors that can also affect the feedback kinetics like distribution of containers in the coating matrix, its permeability for molecules of encapsulated agent as well as for the molecules from ambient medium and so on, but the release properties of containers themselves remain the main parameters that determine their selection for the particular practical application. Basically, shell thickness and indirectly related to it permeability predestine the release kinetics from container. Both these parameters can be widely varied at the containers assembly. The precisely controlled thickness of containers shells can be designed by the exact components ratio during the synthesis of polymeric containers either via interfacial or via *in-situ* polymerization methods. In case of containers with the ceramic core

and polyelectrolyte shell, even the nanometric accuracy is possible through the number of individual steps of alternate polyelectrolytes deposition.

Together with absolute thickness of the container shell, the chemical nature of the shell material is essential for the kinetics of release especially in regard to the chemistry of the encapsulated active agent and to the medium where the container should be then dispersed. If the product of interfacial or bulk polymerization reaction is swellable in the containers cores due to good solvency of liquid inhibitor or auxiliary cosolvent used for the homogenization of oil phase prior emulsification step, the resulting containers do not acquire the core/shell morphology but are rather compact gel particles,[122,123] revealing slow and sustained release of the encapsulated substance. Solubility or swellability of shell-forming material should be also taken into account on all steps of containers incorporation in the final coating. Containers have to remain stable already on the stage of their mixing with the coating formulation (free-standing containers) and then during the subsequent application and curing steps until their exposure to the aggressive surrounding (containers embedded in the coating matrix).

To examine the influence of certain components of the coating formulation where the containers should be distributed before the application step, the release from the containers freely dispersed in the medium mimicking this solvent mixture has to be studied. For instance, the containers with ceramic cores and polyelectrolyte shells are suitable mainly for the use in aqueous coating formulations because of the polar character of their shells. In order to check how these media can influence the shell properties and therefore the release behavior of containers they were incubated in buffer solutions with different pH values and the corresponding release kinetics were investigated. The results of this study are given in Figure 8.18a showing fast and almost complete release of active agent (corrosion inhibitor BTA) in acidic and basic pH ranges. These findings are consistent with the strong swelling of polyelectrolyte complexes made of two weak polylectrolytes—basic PAH and acidic PAA in the same pH windows. Swelling of polyelectrolyte shells of containers is therefore responsible for the opening of containers and release of inhibitor at low and high pH values which can be used as triggers for the protective feedback activity of coatings containing this containers type.

In contrast, Figure 8.18b shows the example when the medium impact on the containers shells leads to the very fast release of the encapsulated active agent. Burstlike release of the antibiofouling and antibiocorrosion agent 4,5-dichloro-2-*n*-octyl-4-isothiazolin-3-one (DCOIT) from PU microcontainers in an ethanol medium demonstrates clearly the complete inapplicability of this containers type for use in the coating formulations with the ethanol-like media.

For containers with porous or hollow ceramic core, the shape of hollow lumen and pore size distribution are additional factors that contribute significantly to the final rate of release. Figure 8.18c demonstrates that in the case of especially high

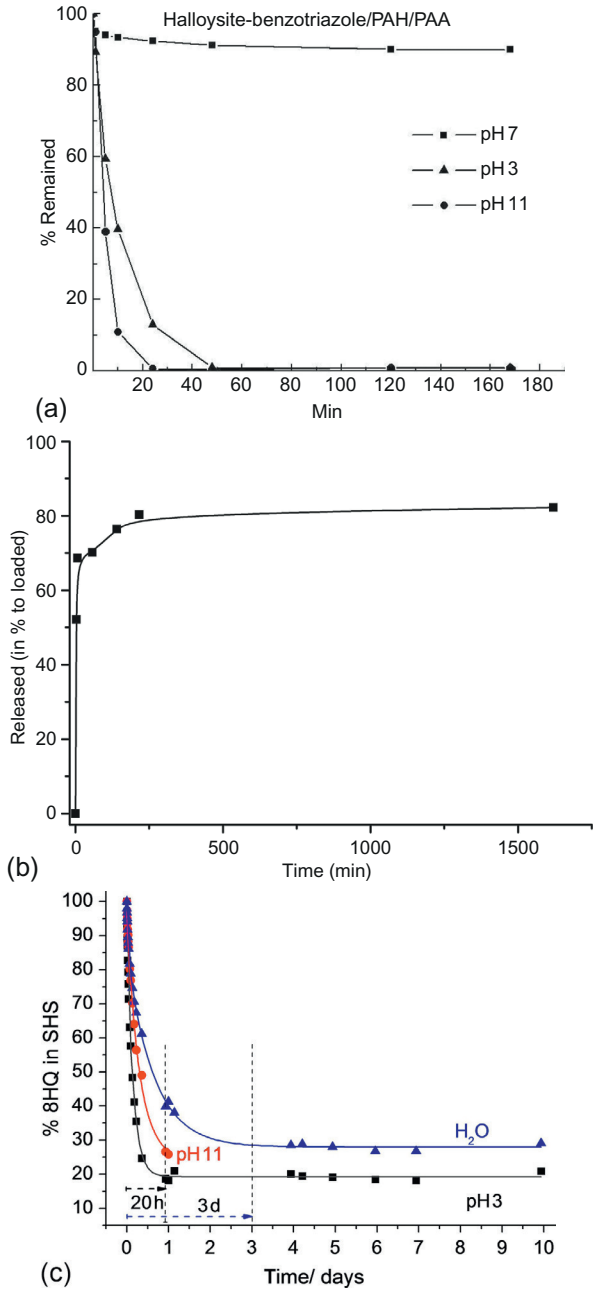


Figure 8.18 (a) Release kinetics from containers freely distributed in media: halloysite-based containers enveloped in polyelectrolyte shell loaded with benzotriazole at different pH in the aqueous medium. (b) Release kinetics from containers freely distributed in media: Containers with polyurethane shells loaded with 4,5-dichloro-2-*n*-octyl-4-isothiazolin-3-one (DCOIT) in ethanol medium. (c) Release kinetics from containers freely distributed in media: SHS silica containers loaded with inhibitor 8-hydroxyquinoline (8-HQ) at different pH in the aqueous medium. *These materials are reproduced with permission of NACE International.*

porosity of the core and very fine pores (containers made on the basis of SHS silica nanoparticles), the release of the loaded substance from the core may last a considerable time. Changes in the pH value of the surrounding medium affect the release kinetics additionally because of the corresponding changes in the surface charge of the ceramic core and amphoteric character of the loaded inhibitor 8HQ.

Combination of containers providing both fast and continuous slow release in the same coating matrix seems to be especially suitable for an optimal protective performance of this coating. Initial strong burstlike release at the site of the damage ensures the high local concentration of inhibitor or other protective agent leading to the immediate creation of its protective layer on the metal surface whereas the following gradual release of small portions of inhibitor over long-term period provides the sustainability of the protection.

8.5 Distribution of Containers in the Matrices of Novel Protective Coatings

Homogeneity of containers distribution in the matrix of the protective coating is another very important parameter that can strongly influence not only the stimuli-responsive ability of novel coatings, but also affect their barrier properties. Traditionally, the proper size of containers for the incorporation in a coating is believed to be optimal if they have the size of about 10% as compared with the thickness of the coating layer in which they are embedded. This ratio between coating and containers dimensions ensures the maintenance of the coating integrity also after incorporation of containers including the most critical situation when some small aggregates of containers will be formed during some steps of the coating application or coating processing. However, even in almost ideal case of small and nonaggregated containers, the formation of local areas with the enhanced concentration of containers within coating matrix may lead to the deterioration of barrier properties of this coating and subsequently to the failure of its anticorrosion performance.[129] Moreover, location of containers predominantly in a certain part of the coating matrix can also influence the response rate of novel coating to the damaging impacts. As it was shown very recently,[130] increasing the distance between containers localization and metal surface to be protected led to better barrier properties, but worsened the active corrosion inhibition. The opposite situation when containers are located close to the substrate caused the decrease of passive protection of the coating.

Distribution of containers in the matrix of the cured coating is closely related to their dispersibility in the initial coating formulation. This characteristic, in turn, depends on the interplay between the interaction of containers with themselves (cohesion) and with solvent components of the coating formulation (adhesion). If the work of adhesion exceeds the work of cohesion the wetting of containers by the

coating formulation medium is energetically disadvantageous and they tend to form aggregates. In the best case of lower adhesion work, the good wetting of containers is achieved and they may be dispersed well in the coating formulation. Other important preconditions for stability of containers dispersion are electrostatic or steric barriers around containers preventing their aggregation. On the other hand, such factors as high density difference between material of containers and the formulation medium as well as presence of other particles (in the worst case—of opposite charge), such as particles of the color pigment, can lead to the destabilization of the entire coating formulation even prior application and then to the very inhomogeneous distribution of containers in the matrix of the cured coating.

Creation of electrostatic or steric barriers protecting containers from the premature aggregation can be performed by means of their surface modification. Most frequently, substances having the surface activity are used for this purpose including ionic, nonionic and polymeric surfactants. Modification of containers surface by surfactants can also essentially improve their wettability by the formulation medium providing their better dispersibility in this formulation. In this manner, the stable dispersions of quite polar containers may be prepared not only in polar (aqueous) media, but also in the media with much higher hydrophobicity.[131]

Containers with polymeric shells of significant polarity such as PU, polyurea (PUa), and polyamides, are well-dispersible in media with high to moderate polarity because of their essential surface charge stabilizing containers from coagulation. These containers can be successfully introduced into water-based coating formulations as for instance shown in Figure 8.19a and b. Core/shell containers with the PU-shells and DCOIT loading for the self-protecting coatings against biofouling and biocorrosion are presented in the Figure 8.19b as already embedded into the polyepoxy coating matrix. These containers were prepared similarly to the pathway described above for the alkoxysilanes filled PU containers. Only the difference was that instead of alkoxysilanes mixture, the dispersed phase of the initial O/W emulsion contained about 55 v/v% of 10 wt.% solution of DCOIT in the mixture of octyl- and nonylbenzene.

At the same time, the polar nature of solvent-free powder coatings (polyester and polyepoxy) allowed the homogeneous distribution of not only containers with PUa shells, but also of much more polar halloysites-based containers (Figure 8.19c and d, respectively).

8.6 Protective Performance of Container-Based Organic Self-Protecting Coatings

Self-protecting functionality of novel coatings is determined by the type(s) of active agent(s) loaded in the containers that are incorporated in the coating matrix. Thus, first

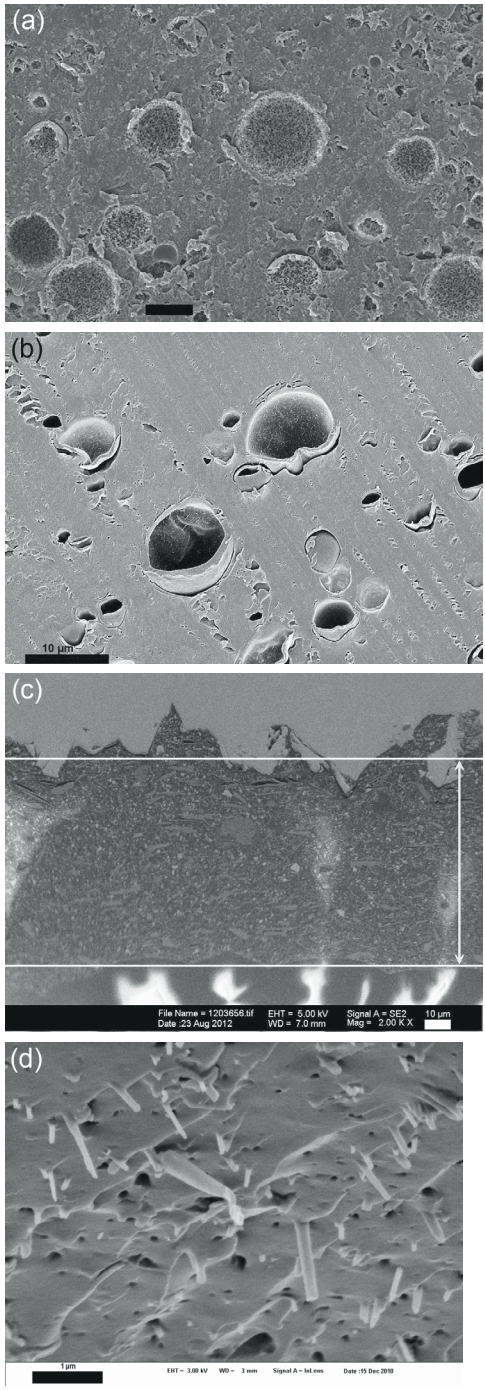


Figure 8.19 (a) Distribution of nano- and microcontainers in the coating matrix: PU microcontainers loaded with the siloxanes mixture in a model epoxy coating; scale bar denotes 3 µm. (b) Distribution of nano- and microcontainers in the coating matrix: PU microcontainers loaded with the biocide DCOIT in a model epoxy coating; scale bar denotes 10 µm. (c) Distribution of nano- and microcontainers in the coating matrix: halloysite-based nanocontainers with PE shells loaded with corrosion inhibitor 8HQ in a model epoxy coating on the steel substrate; scale bar denotes 10 µm, arrow shows the coating thickness. (d) Distribution of nano- and microcontainers in the coating matrix: halloysite-based nanocontainers with PE shells loaded with corrosion inhibitor benzotriazole (BTA) in a polyester powder coating; scale bar denotes 1 µm. *These materials are reproduced with permission of NACE International.*

of all, not only anticorrosion, but also antifouling, dewetting, and many other types of active functional coatings, are realizable. Because of the special construction of containers shells, their opening is triggered by the factors accompanying the onset or development of destructive events, such as corrosion and biofouling. When the coating of a container is damaged as a result of a destructive attack, nearby containers also become mechanically and/or chemically affected. Therefore, the release of the protective agent happens exactly on the damaged or affected site, only on demand and just in the quantity not exceeding the amount really necessary for the termination of destructive processes. This "smart" behavior of new active coatings leads to very slow depletion of the active agent, and a very sustained protective performance is achieved compared with conventional coatings. Moreover, through the fact that some consequences of a certain deterioration process can act as triggers for the release of active agents and finally for the return of the coating to the almost fully recuperated state, the self-recovering of the main protective function of the coating is attained.

Specimens made of AA2024 aluminum alloy were coated with water-based two-part epoxy paint formulation containing 10 wt.% of inhibitor-loaded micro- or nanocontainers. The anticorrosion performance of these coatings was then compared with the performance of standard coating possessing 15 wt.% of inorganic anticorrosion pigment by means of a filiform corrosion test according to DIN EN 3665. Results of this test are presented in Figure 8.20 and reveal that not only formulation with nanocontainers based on the mesoporous silica nanoparticles, but

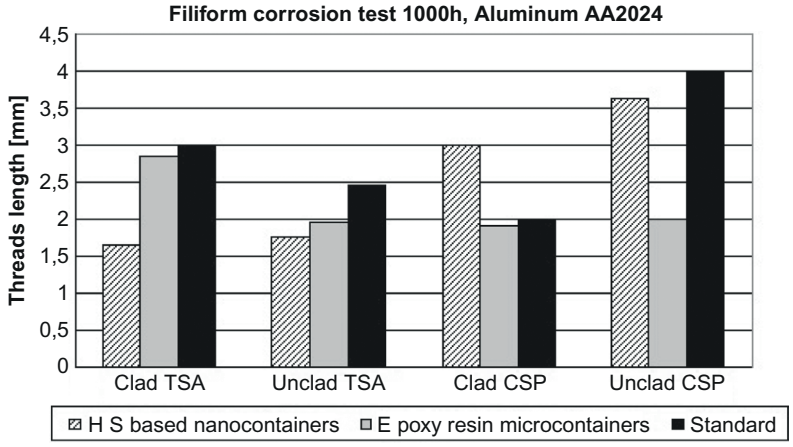


Figure 8.20 Average threads length obtained in a filiform corrosion test for a two-part epoxy paint formulation containing 10 wt.% of inhibitor-loaded micro- or nanocontainers in comparison to standard coating formulation: (patterned) halloysite-based nanocontainers filled with inhibitor 1; (gray filled) epoxy resin-based core/shell microcontaioners filled with inhibitor 2; (black filled) standard coating formulation.

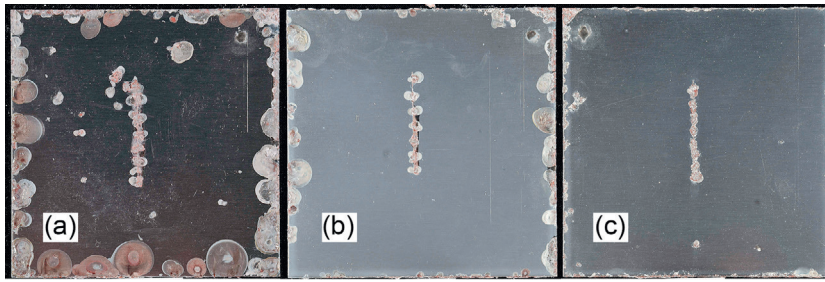


Figure 8.21 Anticorrosion performance of novel containers-based protective coatings: (a) aluminum specimen coated with a standard acrylic coating versus (b) aluminum specimen with the same coating doped with 5 wt.% of empty halloysites-based nanocontainers and (c) aluminum specimen with the same coating doped with 5 wt.% of halloysites-based nanocontainers possessing PE shells and loaded with corrosion inhibitor mercaptobenzothiazole. CASS test duration—240 h. *These materials are reproduced with permission of NACE International.*

also core/shell microcontainers with an epoxy shell and inhibitor-rich core have better performance than the standard formulation.

The halloysite-based nanocontainers embedded in an acrylic coating improved its corrosion protection performance significantly compared with standard coatings used previously for the same purpose. The results of copper accelerated acetic acid salt spray test (CASS-Test) performed in accordance with the specifications of ASTM B368 showed essentially longer maintenance of coating integrity in the area around the artificial scratch and at the cut edges as well as much lower delamination for the coating containing inhibitor loaded halloysites (Figure 8.21). This enhanced anticorrosion efficiency of novel coating was achieved due to lower depletion of inhibitor from tubuli-shaped containers possessing PE shells, making the inhibitor release much more sustained.

Figure 8.22 shows two another successful applications of inhibitor loaded halloysite-based nanocontainers. Powder-coated steel specimens were subjected to a neutral salt spray test (NSS-Test) according to ASTM B117 for 500 h. As can be seen, independent of the chemical composition of the coating matrix, introduction of inhibitor-loaded nanocontainers led to significant improvement of anticorrosion performance of the coating both for corrosion development on the scratched site as well as for the extent of delamination around the scratch.

8.7 Conclusions

A novel approach based on the incorporation of active agent filled nano- or microcontainers in the matrix of protective coatings leads to the essential improvement of



Figure 8.22 Anticorrosion performance of novel containers-based protective coatings. (a) Steel specimen coated with a standard polyepoxy powder coating versus (b) steel specimen coated with the same coating doped with 5 wt.% of halloysites-based nanocontainers possessing polyelectrolyte shells and loaded with corrosion inhibitor 8-HQ and (c) steel specimen coated with the same coating doped with 5 wt.% of halloysites-based nanocontainers possessing polyelectrolyte shells and loaded with corrosion inhibitor BTA; (d) steel specimen coated with a standard polyester powder coating versus (e) steel specimen coated with the same coating doped with 5 wt.% of microcontainers possessing polyepoxy shells and loaded with corrosion inhibitor methylbenzothiazole and (f) steel specimen coated with the same coating doped with 5 wt.% of microcontainers possessing polyepoxy shells and loaded with corrosion inhibitor 8-HQ. *These materials are reproduced with permission of NACE International.*

their resistance to various environmental attacks and to more sustained anticorrosion performance, especially combined with the traditionally proven corrosion protection solutions.

Nano- or microcontainers are a key element of the new protective organic coatings and characteristics of these containers such as composition, morphology, and size determine essentially the protective efficiency of the coating.

Environmentally friendly LDH-based nanocontainers revealed a high versatility of their structures and may have a significant potential for applications in self-protecting coatings.

Efficient and robust nanocontainers can be prepared on the basis of naturally occurring or preformed hollow or mesoporous nanoparticles with subsequent formation either of an L-b-L polyelectrolyte shell or pore stoppers sensitive to the specific corrosion related triggers.

Fabrication of polymeric and composite nano- or microcontainers via the emulsion route is other versatile approach allowing preparation of containers with core/shell, multicompartment or compact (on demand) morphology, and size in the range from some micrometers to some tens of nanometers, wide variety of loaded corrosion inhibitors both in solid and liquid state, as well as shell components for optimal incorporation in different coatings.

Embedding of containers with different active agents (inhibitors, biocides, dewetting agents, etc.) can provide not only the active coatings with single specific feedback-active functionality, but also multifunctional (simultaneous embedding of several containers types) protective coatings.

References

1. Koch GH, Brongers MPH, Thompson NG, et al. Corrosion costs and prevention strategies in the United States. *Report No. FHWA-RD-01-156*. Washington, DC: Federal Highway Administration; 2001.
2. Schmitt G, Schütze M, Hays GF, et al. Global needs for knowledge dissemination, research, and development in materials deterioration and corrosion control. New York: World Corrosion Organization (WCO); 2009.
3. McCafferty E. Introduction in corrosion science. New York: Springer; 2010.
4. Bendall KC. Corrosion resistant alloys—an industry-wide overview of applications. Anti-Corros Method M 1995;42(2):12–5.
5. Ahluwalia H, Uhlenkamp BJ. The importance of quality in corrosion-resistant alloys in biopharmaceutical manufacturing. Pharmaceut Tech 2008;32(2):164–77.
6. Pacitti J. Plastics for corrosion-resistance applications. Anti-Corros Method M 1964;11(1):18–24.
7. Pritchard G. Anti-corrosion polymers: PEEK, PEKK and other polyaryls. Toronto: ChemTec Publishing; 1995.
8. Schweitzer PA. Mechanical and corrosion-resistant properties of plastics and elastomers. New York: Marcel Dekker; 2000.
9. Bogner B. Composites for chemical resistance and infrastructure applications. Reinf Plast 2005;49(10):30–4.

10. von Baeckmann W, Schwenk W, Prinz W, editors. Handbook of cathodic corrosion protection: theory and practice of electrochemical protection processes. Houston: Gulf Publishing; 1997.
11. Khanna AS. High performance organic coatings. Cambridge: Woodhead Publishing; 2008.
12. Gao W, Li Z, He Y. High temperature oxidation protection using nanocrystalline coatings. In: Saji VS, Cook R, editors. Corrosion protection and control using nanomaterials. Cambridge: Woodhead Publishing; 2012.
13. Maaß P, Peißker P, editors. Handbook of hot-dip galvanization. Weinheim: Wiley; 2011.
14. Roberge PR. Handbook of corrosion engineering. New York: McGraw-Hill; 2000.
15. Sastri VS. Corrosion inhibitors. Principles and applications. New York: Wiley; 1998.
16. Raja PB, Sethuraman MG. Natural products as corrosion inhibitor for metals in corrosive media—a review. Mater Lett 2008;62(1):113–6.
17. Saji VS. A review on recent patents in corrosion inhibitors. Recent Patents Corr Sci 2010;2:6–12.
18. Zhao XD, Yang J, Fan XQ. Review on research and progress of corrosion inhibitors. Appl Mech Mater 2010;44–47:4063–6.
19. Etzrodt G. Pigments, inorganic, 5. Anticorrosive pigments. Ullmann's encyclopedia of industrial chemistry, vol 27. Weinheim: Wiley; 2012. p. 343–57.
20. Buxbaum G, Pfaff G, editors. Industrial inorganic pigments. Weinheim: Wiley; 2005.
21. Osborne JH, Blohowiak KY, Taylor SR, et al. Testing and evaluation of non-chromated coating systems for aerospace applications. Prog Org Coat 2001;41(4):217–25.
22. Osborne JH. Observations on chromate conversion coatings from a sol-gel perspective. Prog Org Coat 2001;41(4):280–6.
23. Xia L, McCreery RL. Chemistry of a chromate conversion coating on aluminum alloy AA2024-T3 probed by vibrational spectroscopy. J Electrochem Soc 1998;145(9):3083–9.
24. Sinko J. Challenges of chromate inhibitor pigments replacement in organic coatings. Prog Org Coat 2001;42(3–4):267–82.
25. Chidambara D, Vasquez MJ, Halada GP, et al. Studies on the repassivation behavior of aluminum and aluminum alloy exposed to chromate solutions. Surf Interface Anal 2003;35(2):226–30.
26. Kendig MW, Buchheit RG. Corrosion inhibition of aluminum and aluminum alloys by soluble chromates, chromate coatings and chromate-free coatings. Corrosion 2003;59(5):379–400.
27. Zhao J, Frankel G, McCreery RL. Corrosion protection of untreated AA-2024-T3 in chloride solution by a chromate conversion coating monitored with Raman spectroscopy. J Electrochem Soc 1998;145(7):2258–64.
28. Xia L, Akiyama E, Frankel G, et al. Storage and release of soluble hexavalent chromium from chromate conversion coatings—equilibrium aspects of Cr-VI concentration. J Electrochem Soc 2000;147(7):2556–62.
29. Zhao J, Xia L, Sehgal A, et al. Effects of chromate and chromate conversion coatings on corrosion of aluminum alloy 2024-T3. Surf Coat Tech 2001;140(1):51–7.
30. Berger R, Bexell U, Grehk TM, et al. A comparative study of the corrosion protective properties of chromium and chromium free passivation methods. Surf Coat Tech 2007;202(2):391–7.
31. Le Bozec N, Nazarov A, Persson D, et al. The role of chromate in preventing undermining coatings on hot dip galvanised steel surfaces. In: Sinclair JD, Frankenthal RP, Kalman E, Plieth W, editors. Corrosion and corrosion protection. The electrochemical society proceeding series, Pennington, vol. 2001–22; 2001. p. 81–90.
32. Carlton GN. Hexavalent chromium exposures during full-aircraft corrosion control. AIHA J 2003;64(5):668–72.
33. Prosek T, Thierry D. A model for the release of chromate from organic coatings. Prog Org Coat 2004;49(3):209–17.

34. Gao Y, Ana U, Wilcox GD. Corrosion inhibitor doped protein films for protection of metallic surfaces: appraisal and extension of previous investigations by Brenner, Riddell and Seegmiller. Trans Inst Met Finish 2006;84(3):141–8.
35. Scholes FH, Furrnan SA, Hughes AE, et al. Chromate leaching from inhibited primers. Part I. Characterisation of leaching. Prog Org Coat 2006;56(1):23–32.
36. Twite RL, Bierwagen GP. Review of alternatives to chromate for corrosion protection of aluminum aerospace alloys. Prog Org Coat 1998;33(2):91–100.
37. Directive 2000/53/EC of the European Parliament and of the council of 18 September 2000 on end-of life vehicles. Official J Eur Comm 2000;L269:34–43.
38. Tsai YT, Hou KH, Bai CY, et al. The influence on immersion time of titanium conversion coatings on electrogalvanized steel. Thin Solid Films 2010;518(24):7541–4.
39. Zou ZL, Li N, Li DY, et al. A vanadium-based conversion coating as chromate replacement for electrogalvanized steel substrates. J Alloy Compd 2011;509(2):503–7.
40. Ardelean H, Frateur I, Marcus P. Corrosion protection of magnesium alloys by cerium, zirconium and niobium-based conversion coatings. Corros Sci 2008;50(7):1907–18.
41. Hughes AE, Gorman JD, Harvey TG, et al. Development of permanganate-based coatings on aluminum alloy 2024-T3. Corrosion 2006;62(9):773–80.
42. Zhao M, Wu SS, Luo J-R, et al. A chromium-free conversion coating of magnesium alloy by a phosphate-permanganate solution. Surf Coat Tech 2006;200(18–19):5407–12.
43. Hughes AE, Gorman JD, Harvey TG, et al. SEM and RBS characterization of a cobalt based conversion coating process on AA2024-T3 and ALA7075-T6. Surf Interface Anal 2004;36(13):1585–91.
44. Magalhaes AAO, Margarit LCP, Mattos OR. Molybdate conversion coatings on zinc surfaces. J Electroanal Chem 2004;572(2):433–40.
45. Li Z, Dai C, Liu Y, et al. Study of silicate and tungstate composite conversion coatings on magnesium alloy. EPC 2007;27(1):16–8.
46. Kobayashi Y, Fujiwara Y. Corrosion protection of cerium conversion coating modified with a self-assembled layer of phosphoric acid mono-*n*-alkyl ester. Electrochem Solid-State Lett 2006;9(3):BI5–8.
47. Lin CS, Li WJ. Corrosion resistance of cerium-conversion coated AZ31 magnesium alloys in cerium nitrate solutions. Mater Trans 2006;47(4):1020–5.
48. Hosseini M, Ashassi-Sorkhabi H, Ghiasvand H. Corrosion protection of electro-galvanized steel by green conversion coatings. J Rare Earth 2007;25(5):537–43.
49. O'Keefe MJ, Geng S, Joshi S. Cerium-based conversion coatings as alternatives to hex chrome. Met Finish 2007;105(5):25–8.
50. Yang X, Wang G, Dong G, et al. Rare earth conversion coating on Mg-8.5Li alloys. J Alloy Compd 2009;487(1–2):64–8.
51. Kong G, Liu R, Lu J-T, et al. Study on growth mechanism of lanthanum salt conversion coating on galvanized steel. Acta Metall Sin 2010;46(4):487–93.
52. Knudsen OO, Tanem BS, Bjorgum A, et al. Anodising as pre-treatment before organic coating of extruded and cast aluminium alloys. Corros Sci 2004;46(8):2081–95.
53. Niu LY, Jiang ZH, Li GY, et al. A study and application of zinc phosphate coating on AZ91D magnesium alloy. Surf Coat Tech 2006;200(9):3021–6.
54. Alanazi NM, Leyland A, Yerokhin AL, et al. Substitution of hexavalent chromate conversion treatment with a plasma electrolytic oxidation process to improve the corrosion properties of ion vapour deposited AlMg coatings. Surf Coat Tech 2010;205(6):1750–6.
55. Hansal WEG, Hansal S, Polzier M, et al. Investigation of polysiloxane coatings as corrosion inhibitors of zinc surfaces. Surf Coat Tech 2006;200(9):3056–63.

56. Liu JR, Guo YN, Huang WD. Study on the corrosion resistance of phytic acid conversion coating for magnesium alloys. Surf Coat Tech 2006;201(3–4):1536–41.
57. Hernandez-Alvarado LA, Hernandez LS, Miranda JM, et al. The protection of galvanised steel using a chromate-free organic inhibitor. Anti-Corros Method M 2009;56(2):114–20.
58. Dufek EJ, Buttry DA. Inhibition of O_2 reduction on AA2024-T3 using a Zr(IV)-Octadecyl phosphonate coating system. Electrochem Solid-State Lett 2008;11(2):C9–C12.
59. http://www.duboischemicals.com/pcp/files/ZirconizationWhitePaper.pdf [accessed 22.08.2013].
60. Velterop L. Phosphoric sulphuric acid anodising: an alternative for chromic acid anodising in aerospace applications? ATB Metallurgie 2003;43(1–2):284–9.
61. Brooman EW. Modifying organic coatings to provide corrosion resistance part I: background and general principles. Met Finish 2002;100(1):48–53.
62. Brooman EW. Modifying organic coatings to provide corrosion resistance: part II—inorganic additives and inhibitors. Met Finish 2002;100(5):42–53.
63. Brooman EW. Modifying organic coatings to provide corrosion resistance part III: organic additives and conducting polymers. Met Finish 2002;100(6):104–10.
64. Shchukin DG, Möhwald H. Self-repairing coatings containing active nanoreservoirs. Small 2007;3(6):926–43.
65. Raps D, Hack T, Wehr J, et al. Electrochemical study of inhibitor-containing organic-inorganic hybrid coatings on AA2024. Corros Sci 2009;51(5):1012–21.
66. Vreugdenhil AJ, Woods ME. Triggered release of molecular additives from epoxy-amine sol gel coatings. Prog Org Coat 2005;53(2):119–25.
67. Dry CM, Sottos NR. Passive smart self-repair in polymer matrix composite materials. Proc SPIE 1993;1916(7):438–44.
68. Dry CM. Procedures developed for self-repair of polymeric matrix composite materials. Comp Struct 1996;35(3):263–9.
69. White SR, Sottos NR, Geubelle PH, et al. Autonomic healing of polymer composites. Nature 2001;409(15 February):794–7.
70. Shchukin DG, Zheludkevich ML, Yasakau KA, et al. Layer-by-layer assembled nanocontainers for self-healing corrosion protection. Adv Mater 2006;18(13):1672–8.
71. Shchukin DG, Möhwald H. Nanocontainers for entrapment of corrosion inhibitors. Adv Funct Mater 2007;17(9):1451–8.
72. Hughes AE, Cole IS, Muster TH, et al. Designing green, self-healing coatings for metal protection. NPG Asia Mater 2010;2(4):143–51.
73. Blaiszik BJ, Kramer SLB, Olugebefola SC, et al. Self-healing polymers and composites. Annu Rev Mater Res 2010;40(5 April):179–211.
74. Mookhoek SD, Fischer HR, van der Zwaag S. A numerical study into the effects of elongated capsules on the healing efficiency of liquid-based systems. Comp Mater Sci 2009;47(2):506–11.
75. Wang X, Liu C, Li XF, et al. Photodegradation of 2-mercaptobenzothiazole in the γ-Fe_2O_3/oxalate suspension under UVA light irradiation. J Hazard Mater 2008;153(1–2):426–33.
76. Ferreiro EA, De Bussetti SG, Helmy AK. Sorption of 8-hydroxyquinoline by some clays and oxides. Clays Clay Miner 1988;36(1):61–7.
77. Ghosh SK. Self-healing materials: fundamentals, design strategies, and applications. Weinheim: Wiley; 2009, p. 102.
78. Poznyak SK, Tedim J, Rodrigues LM, et al. Novel inorganic host layered double hydroxides intercalated with guest organic inhibitors for anticorrosion applications. ACS Appl Mater Interfaces 2009;1(10):2353–62.
79. Williams GR, O'Hare D. Towards understanding, control and application of layered double hydroxide chemistry. J Mater Chem 2006;16(30):3065–74.

80. Albertazzi S, Basile F, Vaccari A. Catalytic properties of hydrotalcite-type anionic clays. In: Wypych F, Satyanarayana KG, editors. Clay surfaces: fundamentals and applications. Amsterdam: Elsevier; 2004. p. 496–546.
81. Sorrentino A, Gorrasi G, Tortora M, et al. Incorporation of Mg-AI hydrotalcite into a biodegradable Poly(3-caprolactone) by high energy ball milling. Polymer 2005;46(5):1601–8.
82. Palmer SJ, Frost RL, Nguyen T. Hydrotalcites and their role in coordination of anions in Bayer liquors: anion binding in layered double hydroxides. Coord Chem Rev 2009;253(1–2):250–67.
83. Buchheit RG, Mamidipally SB, Schmutz P, et al. Active corrosion protection in Ce-modified hydrotalcite conversion coatings. Corrosion 2002;58(1):3–14.
84. Tedim J, Zheludkevich ML, Salak AN, et al. Nanostructured LDH-container layer with active protection functionality. J Mater Chem 2011;21(39):15464–70.
85. Leggat RB, Taylor SA, Taylor SR. Adhesion of epoxy to hydrotalcite conversion coatings: II. Surface modification with ionic surfactants. Colloids Surf A 2002;210(1):83–94.
86. Williams G, McMurray HN. Anion-exchange inhibition of filiform corrosion on organic coated AA2024-T3 aluminum alloy by hydrotalcite-like pigments. Electrochem Solid-State Lett 2003;6(3):B9–B11.
87. Mahajanarn PV, Buchheit RG. Characterization of inhibitor release from Zn-Al-$[V_{10}O_{28}]^{6-}$ hydrotalcite pigments and corrosion protection from hydrotalcite-pigmented epoxy coatings. Corrosion 2008;64(3):230–40.
88. Zheludkevich ML, Poznyak SK, Rodrigues LM, et al. Active protection coatings with layered double hydroxide nanocontainers of corrosion inhibitor. Corr Sci 2010;52(2):602–11.
89. Theng BKG. The chemistry of clay-organic reactions. New York: Wiley; 1974.
90. Williams G, McMurray HN. Inhibition of filiform corrosion on polymer coated AA2024-T3 by hydrotalcite-like pigments incorporating organic anions. Electrochem Solid-State Lett 2004;7(5):B13–5.
91. Kendig MH, Hon M. A hydrotalcite-like pigment containing an organic anion corrosion inhibitor. Electrochem Solid-State Lett 2005;8(3):B10–1.
92. Joussein E, Petit S, Churchman J, et al. Halloysite clay minerals—a review. Clay Miner 2005;40(4):383–426.
93. Lvov Y, Price R. Halloysite nanotubules a novel substrate for the controlled delivery of bioactive molecules. In: Ruiz-Hitzky E, Ariga K, Lvov Y, editors. Bio-inorganic hybrid nanomaterials. London: Wiley; 2008. p. 454–80.
94. Borisova D, Akcakayıran D, Schenderlein M, et al. Nanocontainer-based anticorrosive coatings: effect of the container size on the self-healing performance. Adv Funct Mater 2013;23(30):3799–812.
95. Zheng Z, Huang X, Schenderlein M, et al. Self-healing and antifouling multifunctional coatings based on pH and sulfide ion sensitive nanocontainers. Adv Funct Mater 2013;23(26):3307–14.
96. Abdullayev E, Price R, Shchukin D, et al. Halloysite tubes as nanocontainers for anticorrosion coating with benzotriazole. ACS Appl Mater Interfaces 2009;1(7):1437–43.
97. Abdullayev E, Lvov Y. Clay nanotubes for corrosion inhibitor encapsulation: release control with end stoppers. J Mater Chem 2010;20(32):6681–7.
98. Lvov YM, Abdullayev E. Microreservoir with end plugs for controlled release of corrosion inhibitor. US 2011/0297038 A1.
99. Shchukin D, Grigoriev D, Möhwald H. Corrosion inhibiting pigments and method for preparing the same. EP2604661A1, US 2013/0145957 A1.
100. Moya S, Sukhorukov GB, Auch M, et al. Microencapsulation of organic solvents in polyelectrolyte multilayer micrometer-sized shells. J Colloid Interface Sci 1999;216(2):297–302.
101. Grigoriev DO, Haase MF, Fandrich N, et al. Emulsion route in fabrication of micro and nanocontainers for biomimetic self-healing and self-protecting functional coatings. Bioinspir Biomim Nanobiomater 2012;1(2):101–16.

102. Decher G, Schlenoff JB. Multilayer thin films. Sequential assembly of nanocomposite materials. Wiley: Weinheim; 2003.
103. Sukhorukov GB, Fery A, Brumen M, et al. Physical chemistry of encapsulation and release. Phys Chem Chem Phys 2004;6(16):4078–89.
104. Guzey D, McClements DJ. Formation, stability and properties of multilayer emulsions for application in the food industry. Adv Colloid Interface Sci 2006;128–130:227–48.
105. Nilsson L, Bergenståhl BJ. Adsorption of hydrophobically modified anionic starch at oppositely charged oil/water interfaces. J Colloid Interface Sci 2007;308(2):508–13.
106. Tjipto E, Cadwell KD, Quinn JF, et al. Tailoring the interfaces between nematic liquid crystal emulsions and aqueous phases via layer-by-layer assembly. Nano Lett 2006;6(10):2243–8.
107. Grigoriev DO, Bukreeva T, Möhwald H, et al. New method for fabrication of loaded micro- and nanocontainers: emulsion encapsulation by polyelectrolyte layer-by-layer deposition on the liquid core. Langmuir 2008;24(3):999–1004.
108. Wackerbarth H, Schön P, Bindrich U. Preparation and characterization of multilayer coated microdroplets: droplet deformation simultaneously probed by atomic force spectroscopy and optical detection. Langmuir 2009;25(5):2636–40.
109. Lomova MV, Sukhorukov GB, Antipina MN. Antioxidant coating of micronsize droplets for prevention of lipid peroxidation in oil-in-water emulsion. ACS Appl Mater Interfaces 2010;2(12):3669–76.
110. Köhler K, Shchukin DG, Sukhorukov GB, et al. Drastic morphological modification of polyelectrolyte microcapsules induced by high temperature. Macromolecules 2004;37(25):9546–50.
111. Shchukin DG, Gorin DA, Möhwald H. Ultrasonically induced opening of polyelectrolyte microcontainers. Langmuir 2006;22(17):7400–4.
112. Mauser T, Déjugnat C, Möhwald H, et al. Microcapsules made of weak polyelectrolytes: templating and stimuli-responsive properties. Langmuir 2006;22(13):5888–93.
113. Ramsden W. Separation of solids in the surface-layers of solutions and 'Suspensions' (observations on surface-membranes, bubbles, emulsions, and mechanical coagulation). Preliminary account. Proc R Soc Lond 1903;72(477–486):156–64.
114. Pickering SU. Emulsions. J Chem Soc Trans 1907;91(1):2001–21.
115. Binks BP. Particles as surfactants—similarities and differences. Curr Opin Colloid Interface Sci 2002;7(1–2):21–41.
116. Frelichowska J, Bolzinger M-A, Chevalier Y. Pickering emulsions with bare silica. Colloids Surf A 2009;343(1–3):70–4.
117. Gonzenbach UT, Studart AR, Tervoort E, et al. Ultrastable particle-stabilized foams. Angew Chem Int Ed 2006;45(21):3526–30.
118. Schmitt-Roziéres M, Krägel J, Grigoriev DO, et al. From spherical to polymorphous dispersed phase transition in water/oil emulsions. Langmuir 2009;25(8):4266–70.
119. Haase MF, Grigoriev D, Moehwald H, et al. Encapsulation of amphoteric substances in a ph-sensitive Pickering emulsion. J Phys Chem C 2010;114(41):17304–10.
120. Ferri JK, Philippe C, Gorevski N, et al. Separating membrane and surface tension contributions in Pickering droplet deformation. Soft Matter 2008;4(11):2259–66.
121. Grigoriev D, Miller R, Shchukin D, et al. Interfacial assembly of partially hydrophobic silica nanoparticles induced by ultrasonic treatment. Small 2007;3(4):665–71.
122. Latnikova A, Grigoriev DO, Möhwald H, et al. Capsules made of cross-linked polymers and liquid core: possible morphologies and their estimation on the basis of Hansen solubility parameters. J Phys Chem C 2012;116(14):8181–7.
123. Latnikova A, Grigoriev D, Schenderlein M, et al. A new approach towards "active" self-healing coatings: exploitation of microgels. Soft Matter 2012;8(42):10837–44.

124. Latnikova A, Grigoriev DO, Hartmann J, et al. Polyfunctional active coatings with damage-triggered water-repelling effect. Soft Matter 2011;7(2):369–72.
125. Barrére M, Landfester K. High molecular weight polyurethane and polymer hybrid particles in aqueous miniemulsion. Macromolecules 2003;36(14):5119–25.
126. Abismaïl B, Canselier JP, Wilhelm AM, et al. Emulsification by ultrasound: drop size distribution and stability. Ultrason Sonochem 1999;6(1–2):75–83.
127. Grigoriev D, Akcakayiran D, Schenderlein M, et al. Protective organic coatings with anticorrosive and other feedback active features: micro- and nanocontainers based approach. Corrosion 2014;70(5):446–63. http://dx.doi.org/10.5006/0976.
128. Haase MF, Grigoriev DO, Möhwald H, et al. Development of nanoparticle stabilized polymer nanocontainers with high content of the encapsulated active agent and their application in water-borne anticorrosive coatings. Adv Mater 2012;24(18):2429–35.
129. Borisova D, Möhwald H, Shchukin DG. Influence of embedded nanocontainers on the efficiency of active anticorrosive coatings for aluminum alloys part I: influence of nanocontainer concentration. ACS Appl Mater Interfaces 2012;4(6):2931–9.
130. Borisova D, Möhwald H, Shchukin DG. Influence of embedded nanocontainers on the efficiency of active anticorrosive coatings for aluminum alloys part II: influence of nanocontainer position. ACS Appl Mater Interfaces 2013;5(1):80–7.
131. Hollamby MJ, Fix D, Dönch I, et al. Hybrid polyester coating incorporating functionalized mesoporous carriers for the holistic protection of steel surfaces. Adv Mater 2011;23(11):1361–5.

Chapter 9

Important Aspects Involved in Pilot Scale Production of Modern Paints and Coatings

Sandeep Rai*, **Snehal Lokhandwala**†

**GRP Limited, 510, A Wing, Kohinoor City C-1, Kurla(W), Mumbai, India*

†*Shroff S R Rotary Institute of Chemical Technology, Block No. 402, At & Post Vataria, Bharuch, Gujarat, India*

9.1 Introduction

Bringing new products to market as quickly as possible is a proven and successful business strategy for growth as applied by every industry. A systematic and methodical approach to minimize risks pertaining to process and product quality in developing new technologies is vital for the survival of the company. It is a well-known fact that pilot plants play an essential and crucial role in realizing R&D concepts into commercially viable processes for chemicals, catalysts, fuels, and other products. Pilot plants are equally valuable for the quick and fast development of modern paints and coatings at the root level, which falls under the category of fastest moving consumer goods.

Pilot plants processes are of paramount importance to minimize the risk associated with developing new and unproven technologies. The main difference in the characteristic of a pilot plant and a commercial plant is that its main output ("product") usually is data—not a large volume of physical goods/products as in

Intelligent Coatings for Corrosion Control
Copyright © 2015 Elsevier Inc. All rights reserved.

the case of a commercial reactor. These data include engineering design information for the commercial plant, impact of operating parameters on process efficiency and product quality, raw material quality requirements, development of safe standard operating procedures, and estimation of capital and operating costs. It is, therefore, essential that pilot plants be relatively more robust and flexible in functions/operations than their commercial manufacturing counterparts. Normally, pilot plants withstand extremes in process conditions, as optimum manufacturing temperatures, pressures, and other elements of the process are unknown and have yet to be established.

Detailed engineering aspects involved in pilot scale production of modern paints and coatings are of enormous importance for the successful and hassle-free scale-up of formulations as per the market demand.

In this chapter, we briefly review and describe the various engineering aspects involved in pilot scale production of polymeric binders (aqueous and solvent-based), intermediate dispersions, and final paint and coatings formulations.

9.2 Definition

Any pigmented liquid, liquefiable, or mastic composition designed for application to a substrate in a thin layer and that is converted to a solid, protective, decorative, or functional adherent film after the application is called a paint or coating.

Paint or coating is comprised mainly of four ingredients: pigments and extenders, resins/mediums/binders, solvents/thinners, and additives.

Pigments: Pigment may be defined as a solid material, in the form of small discrete particles, insoluble in the medium in which it is employed. Pigment provides density, color, protection, opacity, and fastness to light.

Pigments have the following properties:

- Color: For decorative effect or esthetic appeal
- Opacity: Power to hide or obliterate
- Fastness to light: Ability to retain its color when exposed to light
- Tinting strength: Ability of a colored pigment to tint a white base
- Reducing strength: Ability of a white base to resist tinting

Resins: Resins are solid, semisolid or liquid substances of nonuniform and often high molecular weight, which in the solid state usually possess a softening or melting range and exhibit conchoidal (shell-like) fractures. They have a general tendency to flow at room temperature. Resins are, in general, raw materials, for example, binders, curable molding compositions, adhesives, and coatings. Some types of medium are glue, casein, oils, alkyds, amino, nitrocellulose, urethanes, chlorinated rubber, and epoxy.

Solvents: Solvents/thinners are the liquid materials added to the binder to reduce the overall viscosity/flow of the system. Solvents have characteristics such as solvent power, BP, rate of evaporation, flash point, flammability, chemical stability, color, odor, toxicity, and cost. Solvents (mostly hydrocarbons) may be classified as aliphatic (kerosene, mineral turpentine), aromatic (toluene, xylene), ketones (acetone, MIBK, and MEK), and esters (ethyl acetate, butyl acetate).

Solvents have the following applications:

- Provide flow
- Increase and ease Paint ability
- Dissolve the resin
- Control the drying properties of the paint
- Ensure uniform drying
- Dissolve film formers

Additives: Additives constitute the group of products that is used in relatively small amounts to give paint or coatings one or more desirable properties. It provides wetting, facilitates dispersion, facilitates and controls drying, and prevents bacterial attacks. There are different types of additives: wetting agents, dispersing agents, antisettling agents, antiflotation agents, flow control agents, antiskinning agents, pH stabilizers, thixotropic agents, thickeners, bactericides, fungicides, and freeze thaw stabilizers. Pilot plant trials of these additives are relevant for developing new and alternate sources/suppliers of these critical raw materials/chemicals.

Additives have the following applications:

- Viscosity can be increased or decreased
- Settling can be prevented
- Skinning can be prevented
- Drying can be accelerated
- Foaming can be eliminated
- Thixotropic can be created
- Gloss can be increased or decreased
- Improve stability of formulation during intermediate processing and storage
- Flow and leveling can be improved

9.3 Dispersion Process

Dispersion is breaking down the pigment agglomerate and homogenous mixing of pigment into a resin such that every pigment particle is entirely surrounded by resin. To facilitate the dispersion, some dispersion aids are added to the pigment, which

have a greater ease of adsorption onto a pigment surface and are themselves attracted to the resin.

The solids have a definite structure, nonflowing, rigid, compact, micronized solids entrap air, intermolecular attraction, and surface tension whereas liquids have no clear structure, flow, and innumerable molecular structure and have molecules close to each other, intermolecular attraction, and surface tension.

Dispersion Process—Liquid/Solid: Powdered solid has air entrapped during micronization. Thus, we have three phases involved when we mix solid powder with liquid. The purpose is to mix the liquid with solid powder and remove the air.

The factors affecting dispersion are

- Solid-liquid interface
- Intermolecular attraction
- Surface tension

Stages of Dispersion Process: It is necessary for any coating or paint manufacturer to disperse the dry pigment into part of the medium of the coating. Dry pigments consist of agglomerates of crystals of pigment.

The dispersion process has four stages:

- Grinding
- Wetting
- Separation
- Stabilization

Grinding: Grinding is a process of breaking the agglomerates by using some external force, such as impact, shear, or both.

Wetting: Wetting involves displacement of air from the surface of the pigment particles and aggregates by the medium in which dispersion is to be affected.

Separation: The objective of this process is to separate the pigment agglomerates into individual crystals.

Stabilization: This is key to making a good dispersion. If the dispersion is not stabilized, the pigment particles will be attracted to each other and undergo flocculation.

9.4 General Process for Paints and Coatings

There are three main routes through which the paint is produced (Figure 9.1). This route is used mainly for solvent-based paints and coatings. It is also known as the sand mill route. The sand mill route consists of Twin Shaft Disperser (TSD) and a sand mill. TSD is used for premixing purpose, and the sand mill is used for grinding or size reduction purposes.

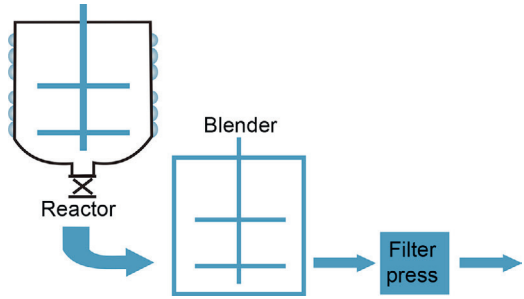
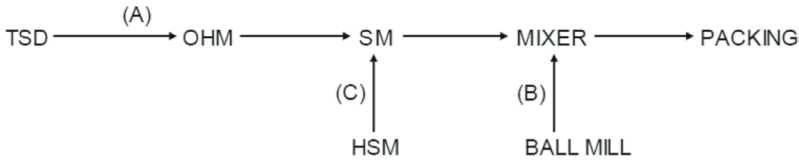


Figure 9.1 General process for paints and coatings.

These routes are



TSD: Twin shaft disperser
OHM: Overhead mixer
SM: Sand mill
HSM: High-speed mixer

This route contains the following tasks:

- Premixing
- Grinding
- Thinning and tinting
- Quality assurance
- Packing

(A) Paints and coatings having extremely hard pigments are made by this route because they cannot be dispersed or grinned in TSD/sand mill.

(B) In this route, the task of TSD and OHM is accomplished by HSM. This route is preferred in pilot plants wherein the finished paint or coating for evaluation is required in extremely less quantity.

Thinning and tinting are the key tasks in pilot plant production of modern paints and coatings. Tinters belong to a group of additives. Tinters are mainly used for

getting the required shades of the paint batches as per the market need. Following are the routes that are used while preparing the tinters:

ATTRITOR → TINTERMIXER
TSD → OHM → SM → TINTERMIXER
BALL MILL → TINTERMIXER
HSM → SM → TINTERMIXER

9.5 Pilot Plants

Pilot plant is defined as a small version of a planned industrial plant, built to gain experience in operating the final plant. It is a small-scale industrial plant in which problems can be identified and solved before the full-scale plant is built. Pilot plant is often referred to as an experimental industrial *plant* in which processes or techniques planned for use in full-scale operation are tested in advance. A pilot plant allows investigation of a product and process on an intermediate scale before a large amount of money is committed to full-scale production.

In general, a pilot plant can be used for the following:

(a) Making product and process corrections based on evaluation results obtained for laboratory studies and their optimization and validation prior to scale-up
(b) Development of prototype new recipes and formulations
(c) Acquiring data to justify whether to go for full-scale production and, if found positive, designing and constructing a full-size plant or modifying an existing plant
(d) Development of alternate and cheaper sources of raw materials
(e) Generation of thermochemical data and reaction trends
(f) Evaluation of performance of critical raw materials/chemicals/additives
(g) Customer complaint investigation

9.5.1 Step by step scaling up

9.5.1.1 Reactors

Bench scale and lab scale systems are vital early-stage tools for assessing and scaling up new technology. Such systems are highly automated and customized for the application and are treated as a precursor to larger pilot and demonstration scale plants. Typical size of bench/lab reactor varies from 1 to 5 L.

For successful production of any product on a mega scale, pilot plant is a necessary tool to study the process involved. It also gives us a complete idea of the parameters that are of vital importance in getting a maximum yield and a product

of high quality. Pilot plants provide the first window of the process development world. Performance/application tests are carried out to determine, or confirm, yield and other relevant data under a variety of operating conditions. Reactor size at the pilot plant scale typically ranges from 10 to 100 L.

Demonstration plants differ from pilot plants as the equipment and process flow sheet resemble much more closely to commercial scale operations. Demonstration plants can have significantly higher capital and operating costs than a pilot plant and are typically only employed when the process technology itself is already quite well developed. Reactor volumes typically fall within the 100-1000 L range.

9.5.1.2 General steps involved in scale-up

(a) The product economics are to be defined based on projected market size and competitive selling.
(b) Laboratory experiments and scale-up planning are conducted simultaneously.
(c) Critical monitoring parameters are defined in the proposed process.
(d) A pilot plant is constructed considering SHE requirements, cleaning and sanitizing systems, packaging, and waste handling systems.
(e) The product and the process results of pilot plants are evaluated, including process economics to make any corrections, and a decision on whether to switch to a full-scale plant are taken. Figure 9.2 exhibits conceptual business modeling of a new product development.

Another frequently used word in scale-up is kilo lab, but it differs from pilot plant as shown in Table 9.1.

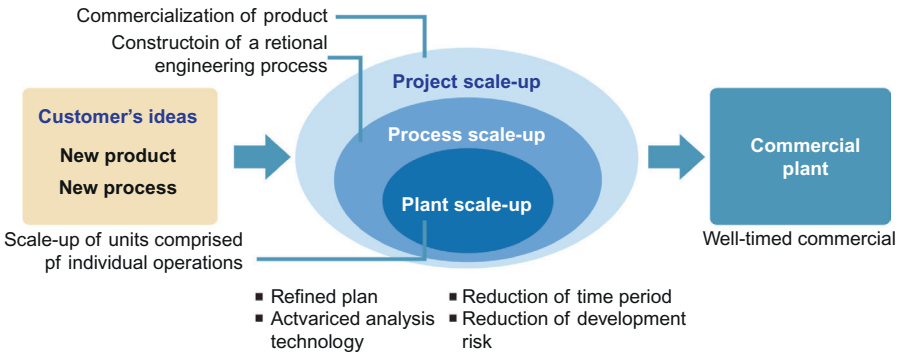


Figure 9.2 General steps involved in scale-up.

TABLE 9.1 Comparison Between Kilo Lab and Pilot Plant

Kilo Lab	Pilot Plants
■ Can be fitted into lab buildings	■ Are separate buildings
■ Restricted by fire code to lower floors and have localized blast protection	■ Use group H for high hazard
■ Building not generally suited for large amounts of solvents	■ Can handle solvents by drum or piped in
■ Likely glass plants used	■ Usually have steel or glassed-steel vessels
■ Volume taken can be 1-5 L	■ Volume selected can be 10-100 L

9.5.2 Pilot plant layouts—major issues

Pilot plants not only are necessary for process parameters and product quality point of view, but should be easy to approach. They should also have ease of operation and maintenance. Safety and disposal of toxic raw materials/by-products should also be given due importance in terms of usage and disposal while designing and commissioning. The critical parameters to be taken into account while designing and installation of pilot plant are depicted in Figure 9.3.

9.5.3 Process equipment and its support units

Table 9.2 shows the list of vital support units required for the process equipment used in a pilot plant for paints and coatings.

The basic requirement for pilot plants of paint and coating is to generate data for proper scale-up. A main criterion for processing is proper dispersion using suitable

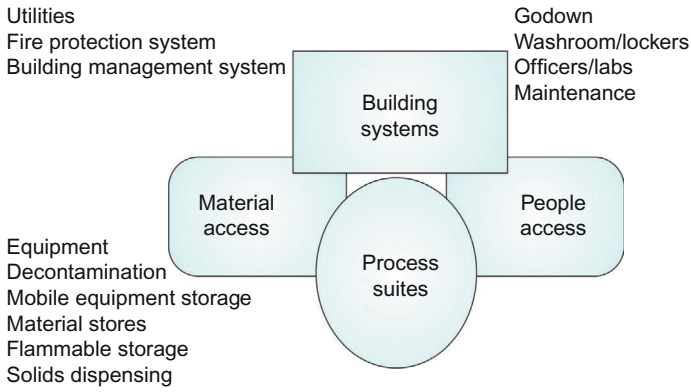


Figure 9.3 Pilot plant layouts—major issues.

TABLE 9.2 Equipment Used in a Pilot Plant for Paints and Coatings

Process Units	Support Units
Reactors—pressure and nonpressure	Suitable PCS/DCS control unit
Mixing vessels	Temperature control module
Pumps	Suitable heating/cooling system
Scales	A suitable and easily accessible control room
Ball mill—mixer	Air compressor
TSD: Sand mill—mixer	Suitable safety health and environment-related devices
HSM: Dyno mill—mixer	
Attritor—mixer	
Direct mixer	
JPT	

binders, which are essentially water-based or solvent-based polymers. Polymeric binders in use for paints and coatings include waterborne acrylic, styrene-acrylic emulsions, SBR, XSBR, NBR, XNBR emulsions, and solvent-based alkyd resins.

9.5.4 Types of pilot plant for water and solvent-based polymeric binders

The pilot plants for modern paints and coatings can be broadly classified as aqueous emulsion based pilot plant and solvent-based resin pilot plants.

9.5.4.1 Aqueous emulsion based pilot plant

These emulsions are the product of radical polymerization of unsaturated monomers in an aqueous medium. Their vital applications include binders for paints and plasters, paper and packing materials adhesives for wood, and binders and laminating materials for paper, textile, and leather processing. Such a polymerization is preferred to solution polymerization because of processing without organic solvents, shorter batch times, and constant product viscosities regardless of the rate of polymerization. The main components involved in this pilot plant are:

(a) Monomers: Major used monomers are vinyl propionate, vinyl acetate, butadiene, styrene, and acrylic and methacrylic derivatives. In order to achieve the desired finished product properties, a blend of monomers is used.

(b) Emulsion stabilizers: Surface active agents are required for stabilization of polymer particles during the formation of micelles during polymerization. It is observed that the emulsion produced with protective colloids could exhibit higher viscosities and large particle diameter compared to the polymers generated using just emulsifiers.

(c) Emulsifiers: In general anion-active and nonionic emulsifiers such as alkyl sulfates and -sulfonates, alkylethersulfates and -phosphates, sulfosuccinates, and ethoxylated fatty alcohols or nonylphenols are frequently used. The stabilizers for such emulsifiers are water soluble, high molecular organic compounds such as polyvinyl alcohol, hydroxyl ethyl cellulose, and polyvinylpyrrolidone.

(d) Initiators: The polymerization process requires water-soluble initiators such as ammonium or potassium peroxidisulfate and, less frequently employed, hydrogen peroxide.

(e) Buffers: During the polymerization process pH-value of the reaction mixture affects the saponification rates of some monomers (vinylic and acrylic esters) and, therefore, requires the presence of small quantities of buffers such as phosphates, carbonates, acetates, or borates.

(f) Water: Fully demineralized water is preferred because the presence of electrolytes in the process water has an adverse effect on the polymerization process. The qualities of water also affect the diffusion of monomer molecules partly through the water phase into the micelles of the emulsifier and formation of initiator radicals.

The batch emulsion polymerization is executed either by the monomer feed or the emulsion feed process.

Monomer Feed Process: In this process, an initial quantity of monomers, initiators, emulsifiers, or protective colloids and part of total water are fed into reactor. After attaining the desired temperature (generally 45-80 °C), the remaining quantity of monomers and other ingredients are charged at controlled rates.

Emulsion Feed Process: In this process a preemulsion is prepared from monomers, water, emulsifier, and initiator. A part of the preemulsion is transferred to the reactor and heated to up to desired temperature. The balance of the preemulsion is then added at a preset flow rate when the reaction has initiated. In Figure 9.4 various feeding modes such as continuous, semicontinuous, and direct dosing are schematically shown.

As another option, a part of the process water along with emulsifier and additives are charged to the reactor and finally adding a part of the preemulsion. After initiating the polymerization reaction, the remainder of the preemulsion is fed to the reactor at a preset rate. After the completion of the reaction, further initiator is added and the batch is maintained at reaction temperature to reduce the residual content of free monomers. Finally the batch is cooled and transferred to a cooling and mixing tank where auxiliary materials, such as plasticizers, defoaming agents, microbicides, and, if required, neutralizing agents, are added, and the batch is adjusted to the final product specification.

The main advantage of this process is that heat generated during the polymerization can be controlled by the cooling water circulation in the limpet coil of the reactor.

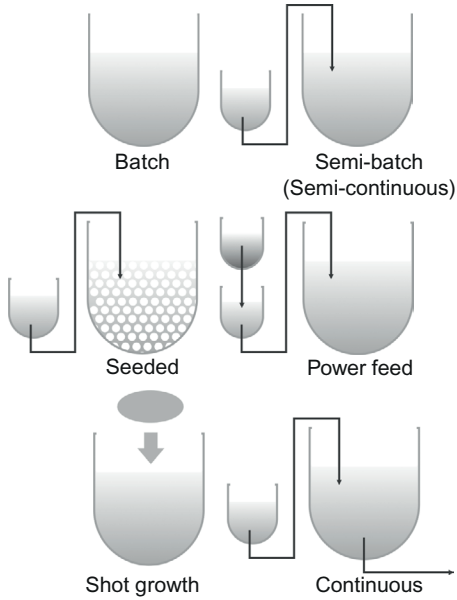


Figure 9.4 Different feed processes.[1]

Even the employment of an agitator with a drive designed for infinitely variable shaft speeds, an efficient blending, and heat removal at low shear forces are achieved.

A polymer emulsion pilot plant consists mainly of the following equipment:

(a) Charge equipment for raw materials with load cells for emulsifier tank, monomer blending tank, initiator and accelerator tanks and reactor, and automatic charge valves
(b) Emulsifier manufacturing equipment with tank, agitator, and transfer pump
(c) Monomer blending and feeding equipment with monomer blending tank, and initiator and accelerator tanks, each equipped with agitator, transfer pump, and flow meter
(d) Reaction equipment with reactor, reactor agitator, and distillation system. Butadiene-based emulsions require pilot plant with mechanical seal and appropriate safety equipment such as rupture disc
(e) Vacuum equipment with vacuum pump
(f) Heating and cooling circuit (primary and secondary) with circulation pump, heat exchanger,and control valves
(g) Cooling and blending equipment having cooling and blending tank and agitator
(h) Filter equipment with product pump and product filter
(i) Process control equipment and instrumentation with personal computer and software controllers, switch and control boards for the installation of the load equipment, and PLC

State of the art pilot plant for polymer emulsion includes high agitation efficiency, low shear rates, and excellent heat transfer using highly polished reactor and reactor agitator surfaces in contact with the product to facilitate cleaning operations. New technologies come with fully automatic process control through a personal computer with specifically developed user friendly software for a comfortable plant manipulation, optimum process operation, and reproducible product characteristics. A pilot plant for taking up development work for a butadiene (gaseous monomer) recipe such as styrene butadiene and acrylonitrile butadiene rubbers is shown in Figure 9.5.

9.5.4.2 Solvent-based resin pilot plants

Resins are the condensation/addition polymers that are formed by reacting monomer functional groups. It is the film-forming material and provides gloss and adhesion to paint and coating. These binders are also used to bind the pigment and extender to the substrate.

Resin plays a vital role in overall paint formulation, such as:

i. It converts liquid coating into solid film after application as a thin film by air-drying or drying mechanism.

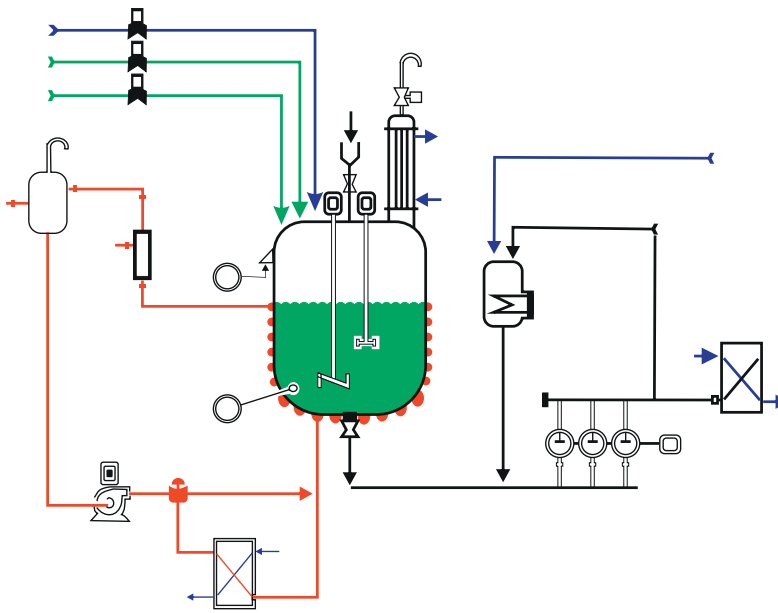


Figure 9.5 Pilot plant for aqueous lattices.

ii. It provides gloss to finished paint and coating films.
iii. It provides flexibility and hardness to the paint film.
iv. It facilitates paint and coating adherence to the surface.
v. It imparts resistance to water, alkali, and abrasion.
vi. It helps in the easier dispersion of pigment and extender in a uniform way on the substrate.

Different types of binders used in the modern paints and coating industries are alkyd resin, nitrocellulose, amino resin, polyesters, phenolics, chlorinated rubber, acrylic resin, epoxy resin, silicone resin, and polyurethane.

Resin pilot plant includes substantial equipment like pilot reactor, blender, and filter machine. The pilot plant contains accessories such as nitrogen gas line with rota meter, temperature and pressure indicators, sampling port, condenser, separator with auto siphon pot, and vacuum pump. Normal utilities required are heating media, cooling tower, compressor, chilling plant, nitrogen and instrument air, and so on. During resin processing, few important physical and chemical properties are monitored in pilot plants, for example, color, clarity, viscosity, acid value, % nonvolatiles (120 °C/1 h), hydroxyl value, finish on Hegmann gauge, weight per liter, dilution viscosity, and drying characteristics. Process control in resin pilot plants includes measurement of water of reaction, stirring speed (RPM) and type of agitator, addition time of ingredients, reaction time, temperature, steam pressure, and so on.

9.6 Major Equipment Used in Paints and Coating Industry

Mixers, mills, and filters are the major equipment used in production of paints and coatings. It is, therefore, necessary that pilot plants for paints and coatings must contain small replicas of the above equipment for effective and accurate data for scale-up. However, the principle remains the same, only the size differs. Figure 9.6 shows a schematic diagram of reactor and accessories required for polymeric binders.

9.6.1 Mixers

Mixers are used to achieve homogeneity between different components of paints and coatings. Mixers are used in the following operations:

- Mixing oils or resins
- Decreasing the viscosity of resins and varnishes
- Mixing pigments and fillers with coating materials
- Mixing additives with paints or varnishes

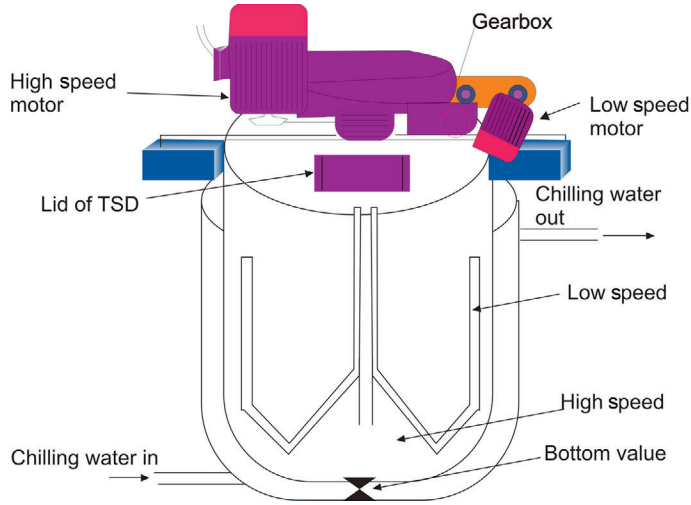


Figure 9.6 Pilot plant for solvent-based polymers.

- Adding solvents or diluting agents (thinner) to paints to adjust the viscosity
- Preparing emulsion (water-based) paints

There are several types of mixers used in the paint and coating industry depending upon their suitability for different end applications. Choice of mixer type depends on viscosity, density difference between components, and solid particle size.

There are different types of mixers:

- Manual mixers
- Automatic mixers
- Kneaders
- Colloid mills
- Rotary churns
- Mixing by air streams

VisiMix—an engineering modeling tool that simulates mixing and heat transfer in stirred tanks was used by Solutia in product and process development. This tool was successfully used to assess the mixing and heat transfer capability of a pilot reactor for a new resin product. It was also exceptionally useful to design pilot plant agitation configuration for a new process and to scale-up a lab reactor to a pilot vessel to match the particle size distribution of the final product.[2]

Figure 9.7a–q[3] shows impellers and mixers useful in both pilot plants of modern paints and the coating industry.

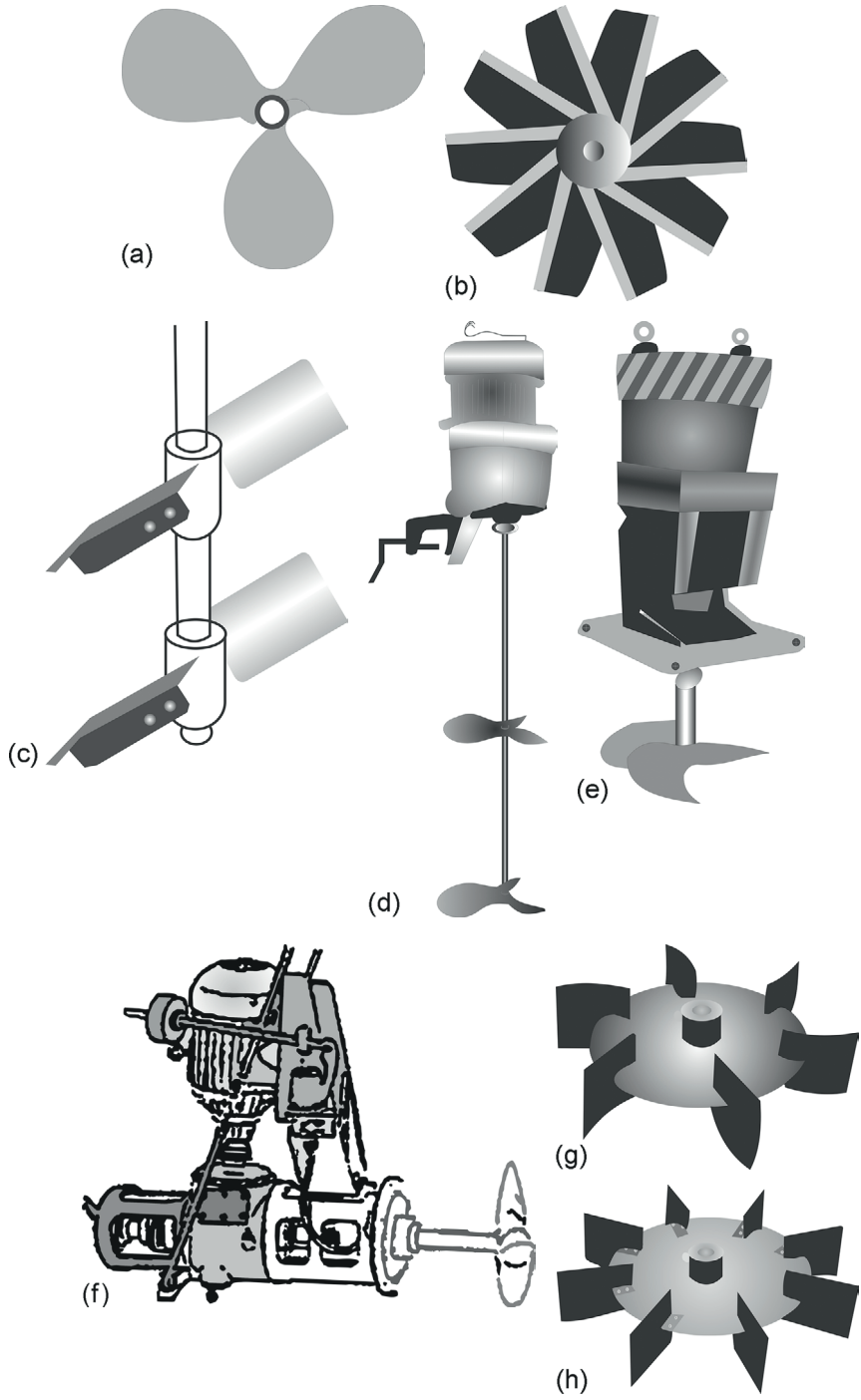


Figure 9.7 High-speed mixer. (a) Axial flow propellers. (b) Axial flow propellers. (c) Axial flow propellers. (d) Axial flow propellers. (e) Axial flow propellers. (f) Axial flow propellers. (g) Turbine propeller. (h) Turbine propeller.

(Continued)

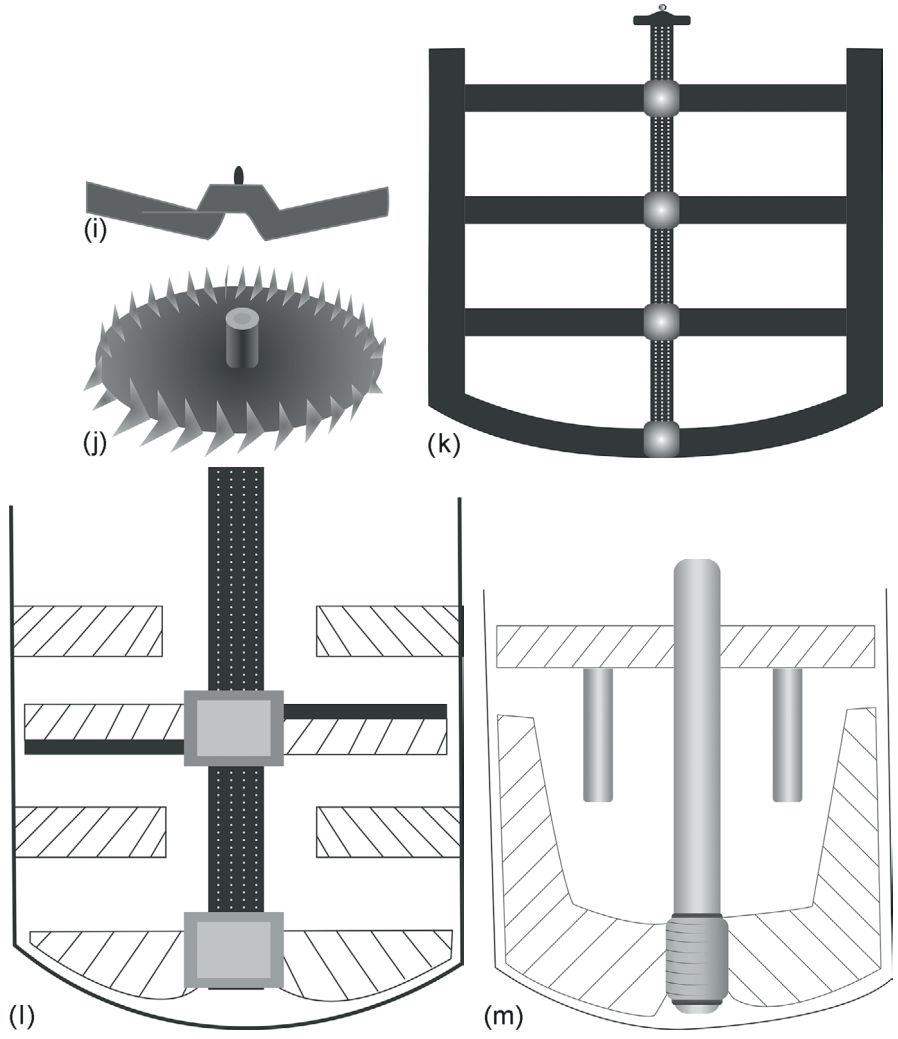


Figure 9.7, Cont'd (i) Paddle propeller. (j) Radial flow propeller. (k) Paddle stirrer. (l) Paddle stirrer. (m) Anchor stirrer.

The mixers usually consist of the mixing tank, usually vertical, and one or more impeller(s) driven by an electrical motor; the mixing tank may also have vertical baffles. The impeller consists of a shaft assembled with one or more mixing blades propellers. Propellers can be divided into two main types, axial and radial flow propellers.

Axial flow propellers as shown in Figure 9.7a–f is considered the most commonly used in paints and coating industry. The impeller in Figure 9.7d is fixed in the wall of the mixing tank with suitable inclination; it can be also fixed vertically at the

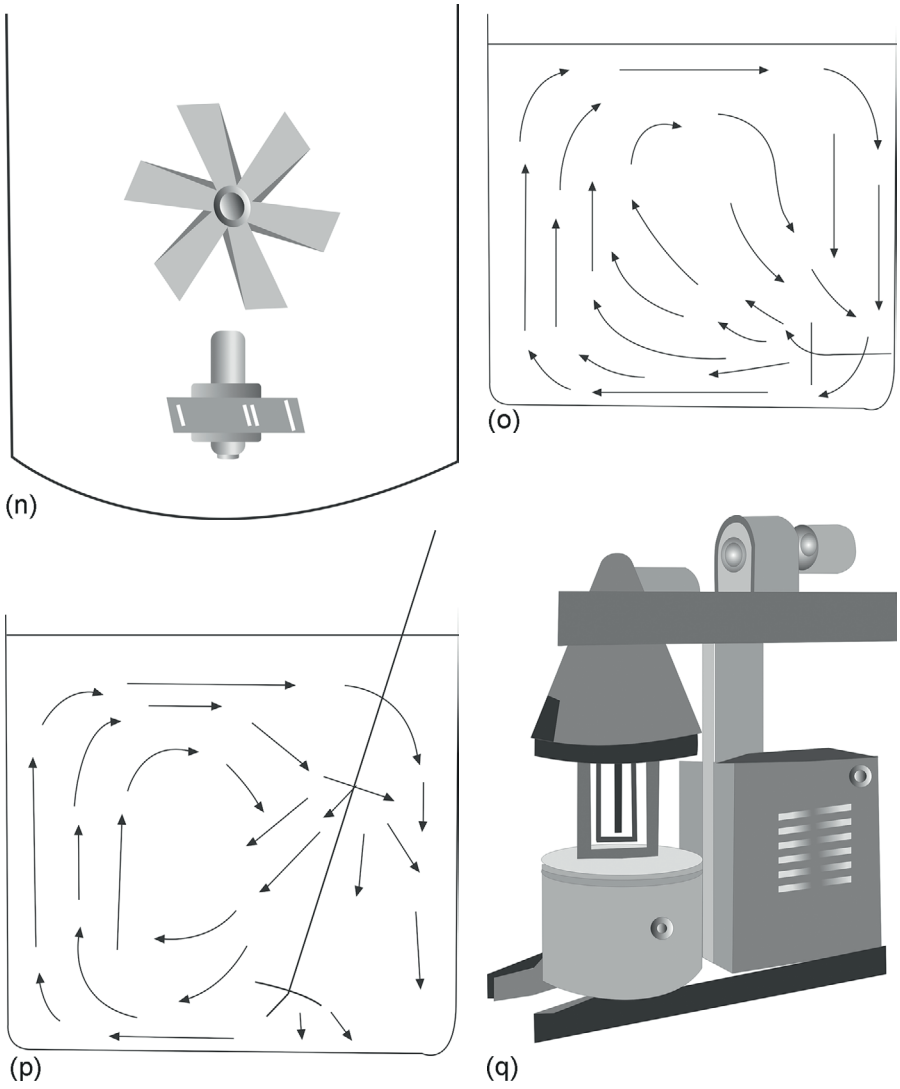


Figure 9.7, Cont'd (n) Multiple vane stirrer. (o) Motion of the inclined propeller. (p) Motion of the inclined propeller. (q) Kneader.

(Continued)

axis of mixing tank using vertical baffles. These impellers rotate at speeds between 1150 and 1750 rpm. The vertical type as shown in Figure 9.7e is used in preparing colloids and rotates at speeds between 350 and 420 rpm via gearbox. The inclined high-speed type is used for the preparation of various kinds of emulsions. The type shown in Figure 9.7f is used to mix liquids that are free from solid particles.

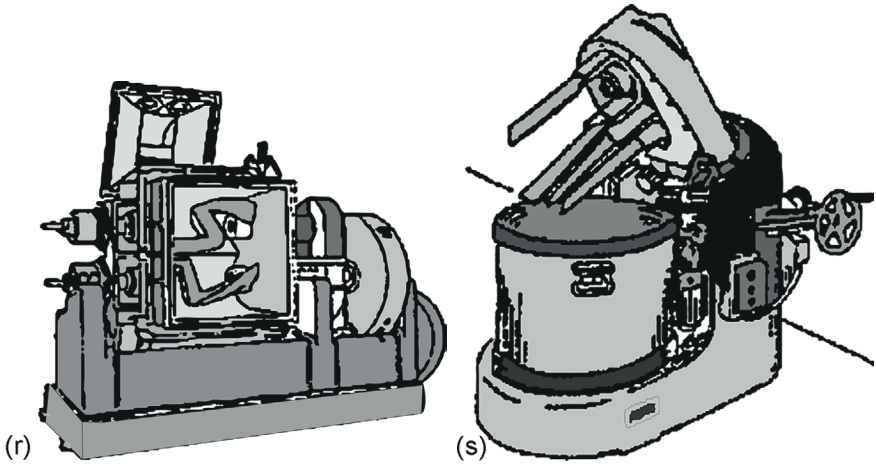


Figure 9.7, Cont'd (r) Kneader. (s) Horizontal kneader.

Radial flow propellers as shown in Figure 9.7g–j have blades parallel to the propeller shaft axis. On the other hand, turbine propellers as shown in Figure 9.7g–h rotate the mixing tank contents in a circular motion in both vertical and axial directions. The diameter of paddle propellers shown in Figure 9.7i reaches 60% of the mixing tank diameter and rotates with relatively low speeds.

Paddle stirrers are used in mixing high viscosity liquids or pastes, whereas anchor stirrers are used for extremely high viscosity liquids or pastes, as shown in Figure 9.7k–m. This type has a small clearance between the mixing propeller and mixing tank walls. Figure 9.7n shows the multiple vane stirrers, and Figure 9.7o–p[3] shows the motion of the inclined propellers.

Figure 9.7q[3] shows typical kneaders used in the production of putties. The kneader consists of a separate tank that can be fixed in the mixer or transferred with its contents to the packing unit. This system helps in weighing the tank content before mixing and to clean the mixing vessel in the cleaning unit. In this system, the mixers can be elevated vertically or laterally as shown in Figure 9.7r.[3]

A horizontal kneader composed of a U-shaped vessel in two mixers with unique shape rotate in different directions with small clearance between them, as shown in Figure 9.7s.[3] There are other types of kneaders including one that can be heated by steam or cooled by water in order to control the viscosity of the mixture.

A few essential types of mixers are described below:

(a) *Twin Shaft Disperser (TSD)*: It is mild steel-made processing vessel fitted with two shafts at the top. The central shaft is referred to as the slow speed shaft and is connected to a cage having scrappers and is rotated at the rpm of about 30 to 40. It is designed to scrape the mill base material, which is stuck to the inner

wall of the vessel during the mixing process. The other shaft, which is fitted at an inclination to the central axis, the cylindrical vessel, rotates at an exceedingly high speed of about 1400 rpm. This shaft is fitted with a circular saw-blade type impeller disc at the bottom that is known as a cowl disc. The saw-blade type impeller is designed and placed inside the vessel in such a manner that the mixture of powder, medium, and the solvent is subjected to proper shear flow patterns in order to achieve the dispersion.

(b) *Overhead Mixture (OHM)*: The main task of this machine is to grind the batch that comes from TSD. Normally this machine is fitted just next to TSD.

(c) *High-Speed Disperser (HSM)*: This equipment is used when the pigment is lesser in compared to the solvent to achieve homogenous dispersion.

9.6.2 Mills

The paint and coating industry uses different types of mills, such as roller mills and ball mills. A three-roller mill is shown in Figure 9.8,[3] in which each roller rotates in the opposite direction of others and with different speeds with a 1:3:9 ratio. The clearance between each two rollers is the key factor to maintain the desired finesse of dyes that leads to the desired homogeneity. This type of mills is open and, therefore, cannot be used in grinding of paints that contain high volatility solvents because emissions may lead to SHE-related issues.

Another relevant class is the ball mills. This type consists of a cylinder rotating about its horizontal axis and containing the grinding balls that may be made of steel or pebbles. If steel balls are used, the cylinder lining will be also made of steel and is used only with dark color paints and coatings. But if the balls are made of pebbles or ceramics the cylinder lining will be made of ceramic or silica and can be used with white or light color. The grinding efficiency and fineness of particles are dependent on the dimensions of the cylinder, speed of rotation, balls size, and balls density. Some mills have the length of the cylinder equal to its diameter, but to maintain a higher degree of fineness mills with a length larger than their diameter are used. Other types of mills include one in which the grinding operation is made in steps inside the mill as the cylinder is separated

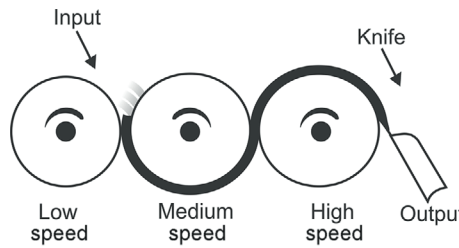


Figure 9.8 Three roller mills.

into sections with screens with suitable sizes separating the sections wherein the initial grinding is done in the first section and the finishing is done in the final section. A bars mill is used instead of balls in order to obtain particles with slightly different sizes that are suitable for dry grinding and/or grinding of colloidal particles.

Presently, the most commonly used mills, in large modern factories, are sand mills (vertical or horizontal) and dyno mills. The relations between the internal diameter of balls mills and the diameter of balls are shown in Table 9.3[3] and Figure 9.9.[3]

CVRD's research center has conducted pilot tests to discover new technologies of improving ball milling efficiency on grinding mill feed. It was noticed that with a mill feed having particle finesse below 170 µm, millpebs when mixed at 30% by weight with grinding balls improves ball milling efficiency by 15%. The results of pilot plant trials proved that millpebs breakage rate exceeds that for 25 mm grinding balls from 209 to 44 µm; however, performance is similar below 44 µm. Somehow, at 80% slurry density, millpebs were escaping the mill.[4]

Some of the primarily used mills are described below:

(a) Sand Mill (SM)

The sand mill is equipment used for size reduction of powder particles uniformly dispersed in the premixed millbase. The premixed millbase is passed

TABLE 9.3 Relations Between the Internal Diameter of Ball Mills and the Ball Diameter

Internal Diameter	Ball Diameter (cm) and Their Percentage
30-60	1.5 (70%), 2.5 (30%)
90-120	1.5 (30%), 2.5-4 (60%), 4-5 (10%)
120-150	2-2.5 (85%), 5-6.5 (15%)

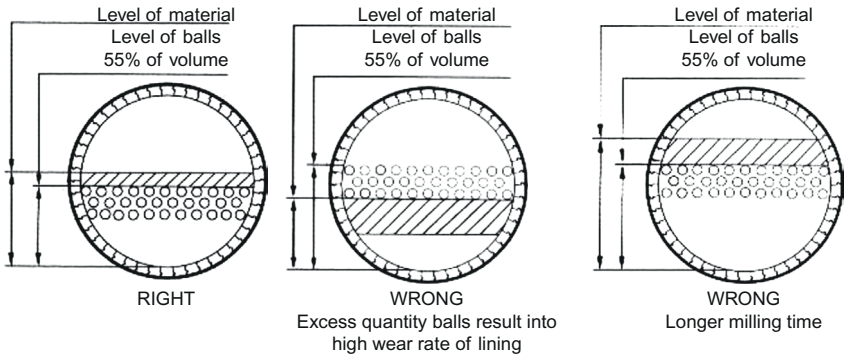


Figure 9.9 The relations between the internal diameter of ball mills and the diameter of balls.

through a cylinder bank of sand, which is being subjected to intense agitation. During passage upward through the agitated sand zone, the millbase is caught and ground between the sand particles—a strong shearing action that affects the dispersion of the pigment into the vehicle and also reduces the particle size of the pigment. On emerging from the active sand zone, the dispersed millbase overflows through an exit screen having size enough to permit free flow of the millbase while holding the sand particles.

The agitation of the sand particles is produced by flat disk impellers, which revolve at extremely high speed (peripheral velocity of 2000 ft/min) inside the shell of the sand mill. Sand particles and millbase adjacent to the impeller surfaces pick up the impeller motion through viscous resistance and, as a result, are slung outward against the confining walls of the shell. The shell is fitted with a jacket to allow cooling water circulation in order to dissipate the heat generated during the grinding process. The critical process parameter in this process is the flow rate of millbase coming out of the sand mill. This is crucial for achieving the desired dispersion and grinding. Generally the grinding media used are glass beads of size 0.6 to 1.4 mm. And the amount of grinding media filled in the shell of the sand mill is about half of the shell volume.

(b) Ball Mill

This equipment is mostly used for paints and coatings consisting of extremely hard pigments. Unlike the sand mill route, both premixing and grinding operation are carried out in single equipment.

A ball mill consists of a cylinder container mounted horizontally and partially filled with either pebbles or ceramic or metallic balls, known as grinding media. The entire quantity of powders (pigments and extenders), part of the medium and solvent, along with dispersing agents are charged to the ball mill. Grinding (dispersion) of the millbase is accomplished by rotating the ball mill and its constituents about the horizontal axis of the mill at a rate sufficient to lift the pebbles or balls to one side and then cause them to roll, slide, and tumble to the lower side. Because of this cascading action pigment particles are caught between the tumbling balls and are subjected to both impact and intensive shear. This highly turbulent mixing action on the millbase trapped in the ball interstices imparts the required dispersion effect. Some of the decisive factors that need to be monitored for achieving effective dispersion are:

- Speed of rotating of the ball mill
- Ball charge
- Millbase viscosity

(c) Attritor

An attritor is similar to the ball mill in operation. The only difference between an attritor and a ball mill is that the ball mill rotates around a horizontal axis whereas the attritor rotates vertically.

9.6.3 Filters

During the manufacturing in paints and coatings industry or during the oil heating process the liquids are contaminated by foreign matters. Moreover, the paint and coating may contain particles that were not properly ground or some polymers that remain undissolved. Some surface hardness may also contribute to the contamination. Figure 9.10[5] shows a type of filter.

For all such reasons, paints and coatings in liquid form must be purified by either of the following methods:

- Using single cylinder mill
- Using filter press
- Using centrifugal separator
- Using fine screens
- Using settling techniques

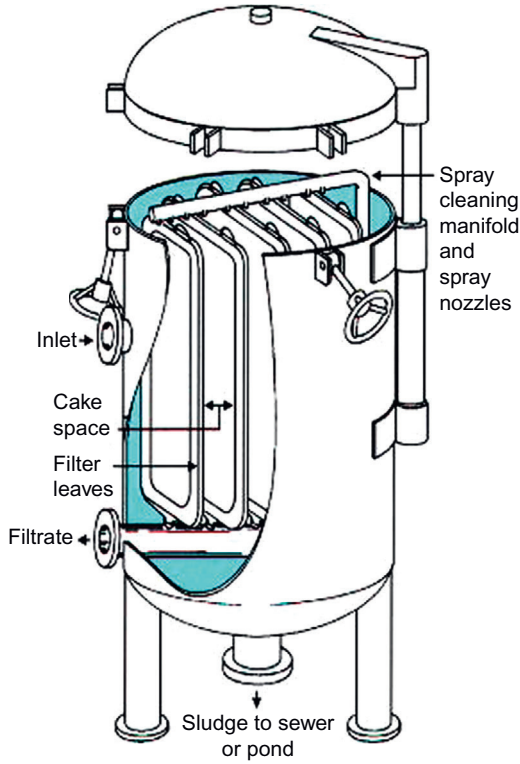


Figure 9.10 Filter.

Centrifuges, screens, or pressure filters are used to remove nondispersed pigments. The finished paint or coating produced from pilot plant is poured into small can, labeled, packed, and moved to storage area/shelf.

9.7 General Checkpoints for a Paint and Coating Pilot Plant

For the smooth start-up of a pilot plant for paints and coatings, there are certain routine checks that should be carried out. Normally this covers cleanliness of reactor, and working of accessories including safety devices and process control systems. Table 9.4 shows typical checkpoints:

9.8 General Safety Precautions in Paint and Coating Pilot Plant

Because most of the ingredients in the trials are volatile and explosive, it is of utmost importance to augment pilot plant with suitable and proper safety devices such as safety valves and rupture discs. Listed in Table 9.5 are some common safety checkpoints that are normally taken care of prior to charging in the pilot reactors.

TABLE 9.4 Checkpoints for a Typical Paint and Coating Pilot Plant Manufacturing

Reactor condition	Clean reactor/no residue/valve function/periodical testing of pressure/periodical testing of coil pressure/ultrasonic thickness measurement/periodical external inspection/testing of safety devices
Separator	Drain line ok/view glass clear
Condenser	Vent open cooling pressure ok
Cooling tower	Proper pressure standby the pump in operating condition
Nitrogen pressure	Inert atmosphere, reflux rate

TABLE 9.5 Safety Precautions While Handling Pilot Reactor

Heating Fluid Leakage	Potential Fire Hazard
Water contamination in heating fluid	• Pressurization of lines • Rupture of flange packing • Expansion tank over flow (flash over)
Hytherm flash point low	Fire hazard

9.9 Typical Example of Pilot Scale Trial and Scale-Up of Acrylic Latex for Coating Applications

Tables 9.6 and 9.7 show a typical recipe for latex used in coating applications; processing parameters; a temperature profile; and typical finished latex properties.

9.9.1 General process of charging

- Charge the initial aqueous charge in the reactor.
- Raise the temperature of reactor to 80 °C with nitrogen purging. Nitrogen blanketing should be maintained throughout the reaction.
- Charge 10% of monomer mixture and surfactant solution and 20% catalyst solution within 10 min into the reactor. Hold all the feeds for 15 min at this stage.
- Thereafter feed the remaining parts of monomer mixture, surfactant solution, and catalyst solution with controlled feed rate in 4 h. Maintain the temperature at 80 °C throughout the run.
- After addition of all the feeds is complete, hold the reactor at 80 °C for 30 min.
- Cool the reactor to 30 °C or to ambient temperature and adjust the pH of finished latex to 7.0 using ammonia.

TABLE 9.6 Typical Recipe of Styrene Butylacrylate Latex for Coating Application

Ingredient	Recipe Parts Bom[a]
Initial aqueous charge	
Process water	61.5
Anionic emulsifier	0.17
Feed into reactor	
Monomer mixture	
Butylacrylate	85.0
Methylmethacrylate	13.0
Methacrylic acid	2.0
Surfactant solution	
Anionic emulsifier	1.35
Process water	20.0
Catalyst solution	
Process water	25.0
Potassium persulfate	0.45

[a]Bill of material.

TABLE 9.7 Typical Properties of the Latex (Before pH Make-Up)

Parameters	Value
Total solids	47.5%
pH	2.5
Conversion	99.7%
Grit content	Nil
Particle size	1000 A°
Brookfield viscosity RV # 50, rpm @25 °C	45 cps
Surface tension @25 °C	45 dynes/cm
Mechanical stability	Medium

9.9.2 Pilot plant setup

In general, pilot plant of aqueous emulsion R&D consists of a reactor, facility for nitrogen blanketing, intermediate vessels for making different solutions, agitators, jacket for circulating temperature maintaining fluid, flow meters to maintain desired flow rate, and so on. Last but not least it should have a proper safety device such as a safety valve and rupture disc. For precise control it normally should have a sophisticated control system to maintain temperature profile and automatic charging of ingredients in a stipulated time period. Series of experiments are conducted in the pilot reactor to optimize recipe that is screened initially on a lab reactor, and subsequently in a similar way the recipe is further optimized with respect to thermochemical data and finished product quality.

For further scale-up to the commercial production, the following engineering calculations as shown in Tables 9.8–9.10 are of utmost significance to get the desired finished product with targeted properties and quality in line with what was obtained at pilot scale.

TABLE 9.8 Geometric Proportions for a Standard Agitation System

$D_A:D_T = 1:3$	$H:D_T = 1$	$J:D_T = 1:12$
$E:D_A = 1$	$W:D_A = 1:5$	$L:D_A = 1:4$

B = Number of blades on impeller
R = Number of baffles
D_A = Agitator diameter
H = Liquid height
D_T = Tank diameter
E = Height of the agitator from the bottom of the tank
L = Baffle width
J = Agitator blade length
W = Agitator blade width

TABLE 9.9 Impeller Selection Guide

Type of Impeller	Range of Liquid (cP)	Viscosity (kg/m s)
Anchor	10^2-2×10^3	10^{-1}-2
Propeller	10^0-10^4	10^{-3}-10^1
Flat-blade turbine	10^0-3×10^4	10^{-3}-3×10^1
Paddle	10^2-3×10^1	10^{-1}-2×10^1
Gate	10^3-10^5	10^0-10^2
Helical screw	3×10^3-3×10^5	3-3×10^2
Helical Ribbon	10^4-2×10^6	10^1-2×10^3
Extruders	$>10^6$	$>10^3$

TABLE 9.10 Important Engineering Parameters for Mixing[6]

$\boldsymbol{NRe} = 10.75Nd^2S/\mu$, *Reynolds number*
$\boldsymbol{Np} = 1.523(10^{13})P/N^3d^5S$, *Power number*
$\boldsymbol{NQ} = 1.037(10^5)Q/Nd^3$, *Flow number*
tbN = *Dimensionless blend time*
$\mathbf{NFr} = 7.454(10^{-4})\ N^2d$, *Froude number*

d = impeller diameter (in.)
D = vessel diameter (in.)
N = rpm of impeller shaft
P = horsepower input
Q = volumetric pumping rate (cuft/s)
S = specific gravity
tb = blend time (min)
p = viscosity (cP)

9.10 Conclusion

Pilot plants still play a key role in the modern paints and coating industry and give firsthand information about processing parameters, product quality, and any associated safety, health, and environment-related aspects. This especially helps create a timely and hassle-free scale-up of the desired paint and coating and one that is of high and consistent quality. Pilot plants play major roles in FMCG products such as paints and coatings, where entering into the market and reaching the masses and meeting customer satisfaction is the topmost priority.

References

1. Anderson CD, Daniels ES. Rapra Review Reports, Report 160 2003; 14(4).
2. Liu K, Neeld K. Simulation of mixing and heat transfer in stirred tanks with VisiMix®. In: AIChE: Proceeding from annual meeting topical conference on process development from research to manufacturing, industrial mixing and scale-up; 1999.
3. Environics. *Paints industry—self—monitoring manual*; 2002.
4. Alives VK, Lacaoste-Bouchet P. Comparative Grinding pilot test of grinding balls vs balls/ mill pebs blend: a report of CVRD Research Centre, January 17, 2004.
5. http://www.dicalite-europe.com/filtrat.htm.
6. http://www.pacontrol.com/process-information book/MixingandAgitation2093851_10.pdf.

Chapter 10

Sol-Gel Route for the Development of Smart Green Conversion Coatings for Corrosion Protection of Metal Alloys

Atul Tiwari, L.H. Hihara
Department of Mechanical Engineering, University of Hawaii at Manoa, Honolulu, Hawaii, USA

10.1 Introduction

Coatings constitute an indispensable class of materials that have enjoyed high commercial success. A wide variety of coatings is available to meet the demands of consumers. The global coating market is forecasted to increase at a compound annual growth rate of 5.46% and will reach an estimated value of $107 billion in year 2017.[1] Most coatings compositions are developed with chemical ingredients that are relatively nontoxic. However, recent regulations posted by Environmental Protection Agency (EPA) in the United States and Registration, Evaluation, Authorization and Restriction of Chemicals (REACH) in Europe, have forced coating formulators to adopt alternate development methodologies using nonregulated environmentally

Intelligent Coatings for Corrosion Control
Copyright © 2015 Elsevier Inc. All rights reserved.

benign chemicals.[2–4] Current developments in eco-friendly coatings (also known as green coatings) have gained significant attention.[5] The word "green chemistry" was coined by Paul Anastas in 1991 and has now become a synonym for environmental friendly chemical synthesis. The development of green coating compositions can be achieved by following the principles of green chemistry[6]:

- Use of less toxic chemical monomers
- Synthesis of less hazardous chemicals
- Synthetic routes to prevent waste
- Use of safer solvents
- Reduction of chemical derivates
- Limited utilization of auxiliary substances
- Optimization of the process for energy efficiency
- Use of catalysts
- Incorporation of renewable materials
- Biodegradable without release of hostile byproducts
- Safer chemical routes to prevent hazardous accidents
- Development of analytical methodologies to allow the real-time-in process monitoring

The practice of green chemistry and development of green coatings is still in its infancy. Academic institutions and the industrial sector are working on developing new synthetic routes for the creation of safer environmental friendly coatings. This chapter describes a coating composition that embraces the above stated 12 principles of green chemistry. The composition was developed through the sol-gel route with chemical components that were carefully selected to synthesize a thin impervious barrier on a metal surface. The first section of this chapter describes the smart green chemistry that is adopted to develop the Green Conversion Coating (GCC). In the second section, the GCC material has been characterized using various analytical techniques to insure the integrity of the chemical structure. Finally, in the third section, the corrosion barrier properties of a GCC layer ~5 μm applied to various aluminum alloys have been examined and compared with two other commercial conversion coatings.

10.2 Development of Smart Chemistry

The green quasi-ceramic coating was prepared by following a patented method briefly described as follows[7]: A mixture of silanes was prepared by reacting calculated quantities of methyltriacetoxysilane (MTAS), methyltrimethoxysilane (MTMS), and tetramethoxysilane (TMS) in a reactor vessel followed by sonication and an addition of isopropanol. In a second reactor, a calculated quantity of sodium bicarbonate was dissolved in a known volume of water. The water was constantly stirred while sodium salt

was added and then stirred every 2 h. The content of the second reactor was added to the content of the first and then sonicated for 30 min. In a third reactor, the calculated quantity of tetraethoxy titanium (TET) was sonicated in isopropanol for 30 min and added to the solution obtained in the above steps. A known quantity of isopropanol (IPA), diethyl ether, and dibutyltindilaurate (DBTDL) were mixed separately in a reaction vessel and added to the solution obtained in the above steps. The entire solution was left for 30 min in ambient conditions before using it as a green coating precursor material.

It is well known that one or mixture of more than one alkoxysilane when dried on a surface could form a coating-like structure.[8] However, proper selection of chemical components is crucial to meet the desired properties. In the GCC composition, the first added silane was MTAS, which was selected for the following reasons: In order for a material to form stable coating on metal surface such as aluminum, permanent covalent bond formation with the available hydroxyl functionalities is critical. However, the hydroxyl functionality is not always readily available on the materials surface. The inert oxide layer over the metal surface does not allow the formation of permanent covalent bonding between the silicones and metal. It was, therefore, necessary to remove the inert oxide layer and expose the hydroxyl functionality for the covalent bond formation. However, the removal of the inert oxide layer and coating the metallic surface thereafter to construct permanent covalent bonds is nearly impossible as the rate of formation of the inert oxide layer is practically instantaneous.[9] For GCC development, the advantage of the availability of hydrolysable acetate groups in MTAS was considered. Moreover, the methyl group in MTAS could play a pivotal role in promoting the facile release of acetate as acetic acid that could act as a catalyst during the hydrolysis of silanes as well as etching agent to remove the inert oxide layer. Therefore, acetate group could performs *three functions*; that is, catalyst, etching agent and buffering agent (discussed later).

The second added silane in the GCC was TMS which is a highly reactive silicone where the methoxy group can readily react and form covalent bonds with the hydroxyl functionalities that become available after the inert oxide layer is etched. Moreover, it can create a template for new crosslinking reactions. Therefore, TMS performs *two functions*; that is, attaching the exposed hydroxyl functionalities on the metal substrate and generation of template for the new crosslinking reactions.

The third added silane in GCC composition was MTMS, which has a $-CH_3$ hydrocarbon group in the coating composition to promote the release of $-OCH_3$. Moreover, it was beneficial to have the hydrocarbon attached as pendant to silane and not in the backbone structure. The hydrocarbons are prone to UV-light degradation and, therefore, could affect the backbone chemistry upon UV light exposure. The methyl group used as pendant may effectively work as an "umbrella-shield" against the attack of water molecules. MTMS presumably could perform *two functions*; that is, supply enough pendant hydrocarbons to impart desired flexibility to the coating and act as a shield against water molecules.

It should be clarified that while MTAS could supply all of the desired hydrocarbon content to the coating; its sole use would generate high amounts of acetic acid that could decrease the pH of the medium and corrode the metal surface during the coating application process. Hence, the use of MTMS was necessary to reduce the formation of excess acetic acid and to regulate the amount of hydrocarbon that remained in the coating. Too much hydrocarbon could lead to the formation of a semiporous network structure reducing the coating hardness (higher the hydrogen content less the hardness of the coating).[10]

It was discovered that an appropriate amount of three silanes was necessary to control the desired properties. Too much amount of *MTAS* will produce high amounts of acetic acid and could corrode the metal surface while too little amounts may not be sufficient to perform all three actions simultaneously as mentioned earlier. An abundance of *TMS* could lead to brittle coating structure due to elevated crosslinking density while low amounts may not be sufficient to capture the sufficient hydroxyl functionalities over the metal surface. High amounts of *MTMS* could increase the hydrocarbon content while, too little amount may not impart a sufficient amount of hydrocarbon.

Although the above three silanes were selected to perform specific functions to form a coating, there are more requirements to fulfill to ensure an impervious corrosion barrier coating will form. It is difficult to develop a coating formulation without knowing the characteristics of the metal substrate and its corrosion activity. Stated below is the brief chemistry that occurs when silanes are mixed in desired quantity in an appropriate nonanhydrous alcohol that contains traces of water molecules. When silanes are added to such a solvent and subjected to ultrasonic mixing, the energy from the ultrasonic treatment triggers the hydrolysis reaction of the silanes. However, there are not enough water molecules to complete the entire hydrolysis reaction, and activated sol is created.

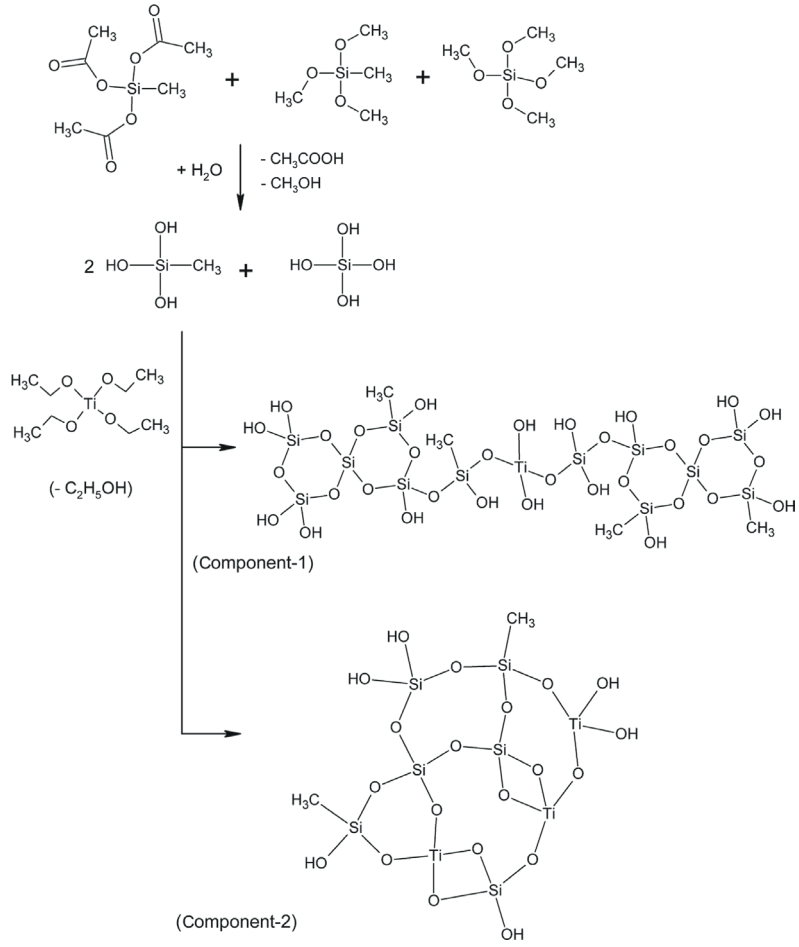
A saturated aqueous solution of sodium bicarbonate ($Na^+ HCO_3^-$) was added to the above-activated sol and ultrasonically agitated to trigger the hydrolysis reaction. The use of a saturated sodium bicarbonate solution was necessary to avoid the hydrolysis of entire acetoxy or alkoxy groups at this stage. In fact, it was vital to maximize the Na^+ concentration in the solution. The acetate (CH_3COO^-) and Na^+ ions in the solution along with the intermediate carbonic acid (H_2CO_3) perform a buffering action [(CH_3COONa)+CH_3COOH]. The presence of alcohol could facilitate the formation of carbonic acid intermediate. This in-situ generated buffer controls the pH of the solution when it's needed at the time of coating application to neutralize the metal surface when large amounts of acetic acid are generated as the activated sol is hydrolyzed upon the exposure to humid air during curing. Additionally, in-situ-generated sodium acetate in the barrier coating acts as a barrier against the attack of the hydronium ions. This salt remains in the network for the entire service life span of the coating.

The water used in this case serves *dual purposes*; that is, it facilitates the formation of ionic species (Na^+ HCO_3^-) and provides the medium for the extended hydrolysis reactions. TET was also used in the formulation to generate, on exposure to air in-situ, self-assembled nanoparticles of titanium dioxide (TiO_2). These titanium dioxide nanoparticles are likely to actively contribute to the formation of backbone structure of the coating. TET was added in the formulation with the intention of imparting UV-light degradation protection and contributing to the cohesion and hardening of the coating structure. Additionally, incorporation of TET may prevent phase separation and agglomeration which usually occurs with the addition of preformed TiO_2. TET was blended into alcohol (not anhydrous) to induce hydrolysis before adding to the silicone composition. TET, therefore, plays *two crucial roles*; that is, acting as a shield against UV-light and imparting hardness to the coating structure. However, an optimal amount of TET is required. Too much of TET adversely affected the curing and hardening process. The critical concentration of TET was determined after conducting a series of nanomechanical testing to determine the optimum hardness.

The DBTDL catalyst was dissolved in a mixture of alcohol and diethyl ether that was activated by ultrasonic mixing. The catalyst was necessary to induce the condensation reaction between different chemical moieties at ambient temperature. Diethyl ether was chosen as a cosolvent due to its extreme surface cleaning tendency.

The sequence of reacting chemical constituents discussed above is the deciding factor in achieving the desired barrier properties of the coating. The saturated aqueous solution of Na^+ HCO_3^- was thoroughly blended into the silicone solution until the water molecules were preferably mixed or consumed in the solution. In the next step, the TET solution was added to the above-activated silane composition. Contrary to this, if TET is added to the silane solution before the addition of saturated solution of Na^+ HCO_3^-, the entire solution will turn milky white and inferior coating properties will be obtained.

When coating formulation is applied to the metal surface, the free acetic acid etches the inert oxide layer. The inert oxide layer is solubilized in the coating formulation and acts as a component in the coating network. TMS attacks the hydroxyl functionalities that are made available on the metal surface as a result of etching the inert oxide layer. The methoxy group in TMS and MTMS hydrolyzes in the presence of acetic acid and reacts to form a three-dimensional network. Similarly, TET also hydrolyzes in the presence of ambient moisture and interacts with silanol in backbone formation. The generated acetic acid reacts with Na^+ to form sodium acetate. The sodium acetate, free acetic acid, and carbonic acid create buffering action that controls the pH of the solution. This buffering action should last for the duration of the coating life. The catalyst facilitates the formation of the coating network in ambient conditions (Scheme 10.1).



Scheme 10.1 Generalized mechanism showing major components of reactive gel, a precursor to GCC and reactions occurring during GCC gel formation.

10.3 Characterization Methodology

10.3.1 Spectroscopic analysis

The competing reactants with different activity coefficients could be possibly leading to an intermediate macromolecular mixture of varying chain lengths. However, the polymer chains in the mixture align during the curing/hardening stage, giving rise to a condensed three-dimensional network. The precursor monomers, the gel macromolecules, and crosslinked network should be studied at entire development stages to confirm the integrity of the desired structure. The following section describes various characterization studies conducted during the development of GCC.

10.3.1.1 FTIR analysis of cured coating and precursor to coatings

It is widely accepted that molecular packing arrangement in the hybrid material depends largely on the hardening kinetics.[11] Also, that fast and uncontrolled evaporation of the solvent does not provide enough time for the polymer strands to align in a confined manner. Such curing process leads to defects such as cavities, pinholes, or holidays in the coating network. Corrosive electrolytes tend to diffuse through these holidays and reach the surface of the metal, leading to delamination and failure of the coating. A rapid curing kinetics or in-situ observations of the hardening mechanism using FTIR could help in determining the volume collapse or hardening route in the complex chemical network.[12,13]

Figure 10.1a displays 3D FTIR absorbance spectra as a function of time. The 3D FTIR spectra shown in Figure 10.1a displays the in-situ hardening phenomenon observation on the GCC gels. Spectra were recorded on liquid precursor to coating that was aged (in a sealed container) in ambient conditions for 24 h. The sharp peaks (not shown) due to evaporation of the volatile solvent appeared during the initial stages of the run. The peaks that appeared at ~2900 cm^{-1} corresponded to the hydrocarbon portion in the coating formulation. More specifically, the peak that appeared in the spectra at 2920 cm^{-1} corresponds to symmetric −CH stretching while the peak that appeared at 2975 cm^{-1} corresponds to asymmetric −CH stretching. These peaks were found consistently and independent of time in each spectrum, indicating that the hydrocarbon portion of the composition did not take part during the initial phases of the reaction. The peak at 1600 cm^{-1} corresponds to the acid functionality[12] (as a result of acetic acid formation), which appeared during the initial phase of the reaction and disappeared after 15 min. Most of the peaks appearing in the range of 500-1500 cm^{-1} remained constant, except an additional peak that appeared at 1050 cm^{-1}, which corresponds to the SiOSi network formation.[14,15] A sharp peak appearing at ~915 cm^{-1} represented a combined contribution from TiOSi and silanol (SiOH) linkages.[16,17]

In Figure 10.1b, hump at 3400 cm^{-1} indicates the presence of hydrogen bonding in the molecular structure. The intensity of hump decreases as material solidifies. The strong, sharp peak at 1271 cm^{-1} is due to Si-OCH_3 vibrations.[18] The peak between 1000-1100 cm^{-1} is due to Si-O-Si vibrations. The peak at 911 cm^{-1} is due to an −OH group produced as a result of the hydrolysis of alkoxysilanes. The peak at 911 cm^{-1} was stronger in the gel stage but weaker in the solid stage, probably due to the consumption of the generated hydroxyl groups during the crosslinking and hardening phase. Another strong peak at 777 cm^{-1} is due to the contribution from hydrocarbons in the quasi-ceramic structure.

10.3.1.2 Raman analysis of cured coatings and precursor to coatings

To complement the FTIR analysis, Raman spectroscopy can be used to determine the organic as well as the inorganic components in the chemical structure. In gel stage (Figure 10.2), appearance of major peaks is due to hydrocarbon portion in the

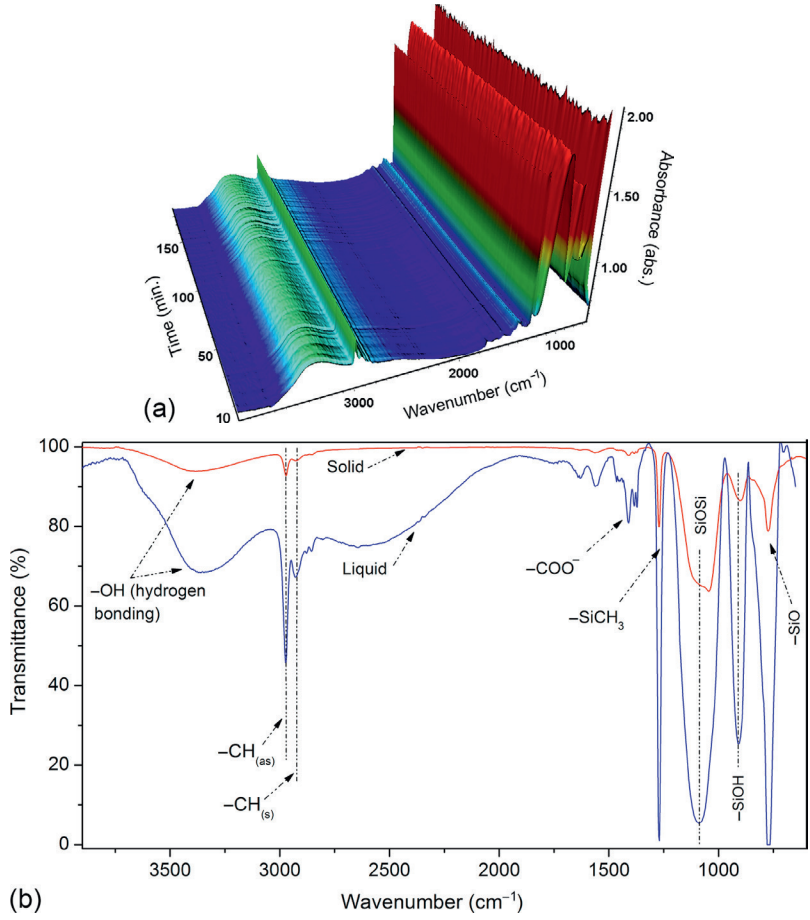


Figure 10.1 FTIR spectra acquired while curing of GCC. (a) 3D spectra assignment recorded during curing kinetics study of GCC; (b) spectrum of liquid precursor and solidified coating.

material. The contribution from carbonyl functionality at 1740 and 950 cm^{-1} due to silanol can be visualized. In the solid state, the Raman spectrum show four main peaks between 450 and 3100 cm^{-1}. Two sharp peaks appearing at 2936 and 2902 cm^{-1} correspond to the antisymmetric and symmetric CH_2 hydrocarbon portions of the spectra.[19,20] The relatively weak peak at 1400 cm^{-1} again corresponds to hydrocarbon (CH_2 bending/scissoring vibration)[21] and another strong peak at ~1100 cm^{-1} is due to the combined contribution from hydrocarbon and SiOSi backbone. A short hump was observed around 500 cm^{-1}, suggesting the presence of titanium in an amorphous phase.[22,23]

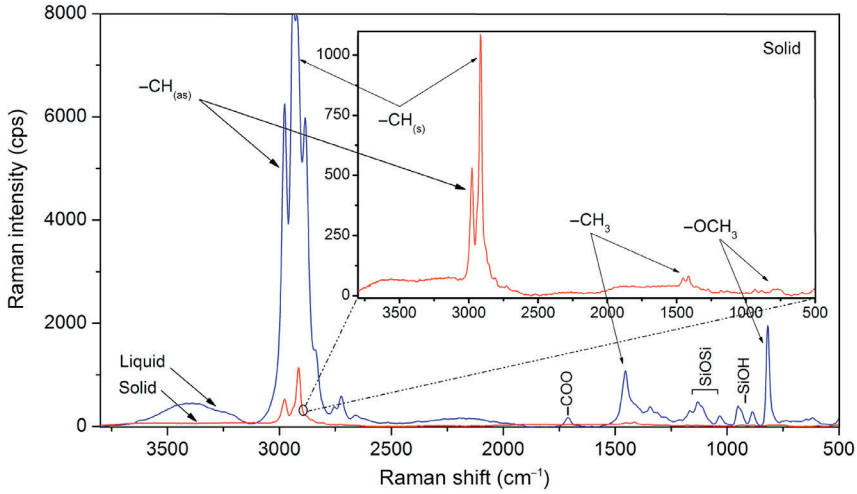


Figure 10.2 Raman spectra acquired on liquid precursor and solid GCC.

10.3.1.3 NMR analysis of cured coatings and precursor to coatings

NMR spectroscopy has been the backbone of organic materials characterization. It can precisely identify the reaction mechanism that may occur during the transition of liquid to gel to solid. Liquid precursor to GCC was analyzed with ^{13}C and ^{29}Si NMR. The ^{13}C NMR analysis in Figure 10.3a shows three major peaks at 3.63 ($-O\underline{C}H_3$), 25.26 ($-\underline{C}H_2$), 30.51 ($-CH_3$), and 65.52 ($-O\underline{C}H_2CH_3$) ppm.[24] Similarly, ^{29}Si spectrum (Figure 10.3b) displayed four peaks at −51.29 (D), −66.70 (T^3), 103.26 (Q^4), and 111.53 (Q^4) ppm.[25]

10.3.1.4 XPS analysis of cured coatings

The GCC-coated specimens were analyzed using XPS (Figure 10.4) to confirm the bonding chemistry with metal surface. Thin layer of GCC was coated on 7075 aluminum alloy (containing Al 87-91 wt.%, Cr 0.18-0.28 wt.%, Cu 1.2-2.0 wt.%, Fe 0.5 wt.%, Mg 2.1 wt.%, Mn 0.3 wt.%, Zn 5-6 wt.%, Si, Ti and others 0.8 wt.%) and dried for 30 days in ambient conditions. A surface survey scan in Figure 10.4a displays the presence of Si, O, Cu, Ti, Na, and Mg. Additionally, small concentrations of Mg (0.15 at.%) and Cu (0.03 at.%) were also seen in the spectrum that originate from the metal substrate. It is expected that coating may have been thin in the surveyed area, exposing the surface roughness peaks that contained copper in solid solution, in Guinier-Preston (GP) zones, or in precipitate. Another assumption is that a small amount of the alloy may have dissolved in the coating during the application process. Single peak occurred at 532 eV in the O1s deconvoluted spectra, which corresponds to oxygen attached to carbon. No peak was found for oxygen attached to silicone in

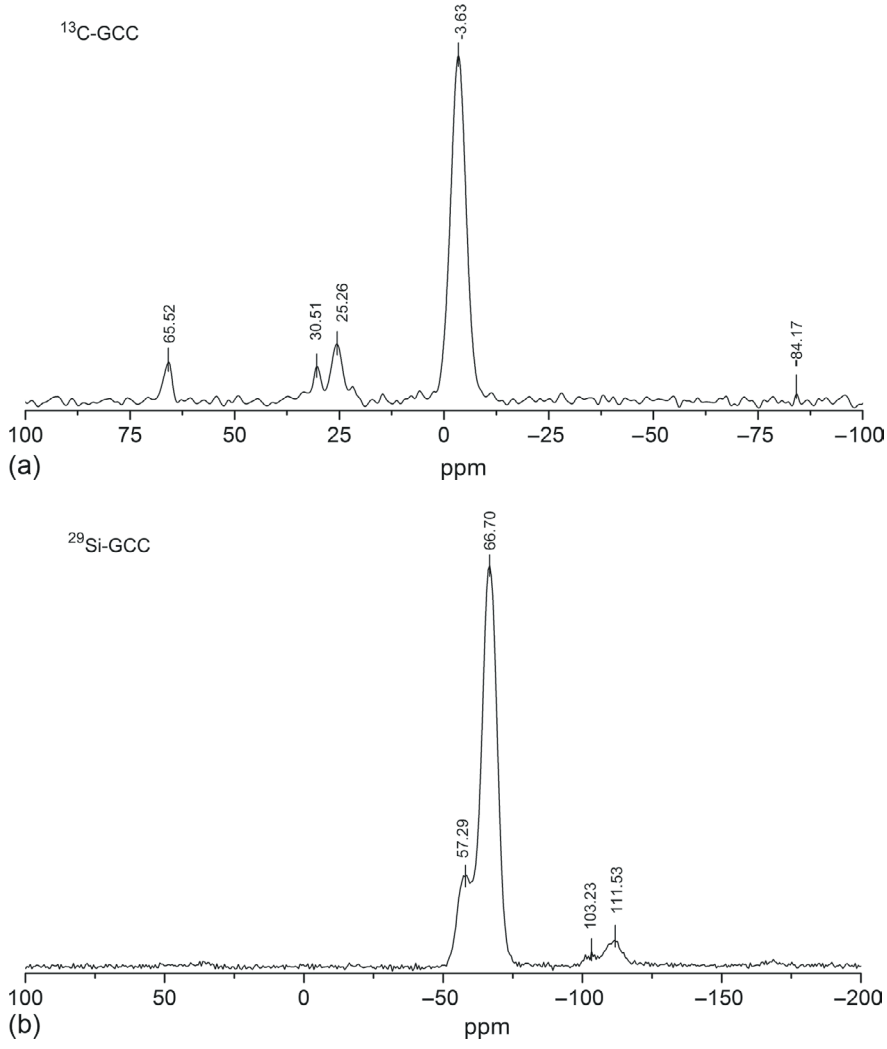


Figure 10.3 NMR analysis of the precursor to GCC. (a) ^{13}C NMR analysis; (b) ^{29}Si NMR analysis.

O1s deconvolution, though silicone attached to oxygen was seen in the Si2p deconvolution at 102.5 eV. It appears that the O-Si peak was totally masked by the C-O (siloxane) peak in the O1s deconvolution. The atomic percentage of carbon was 31.84, a value higher than the atomic percentage of silicon (28.21 at.%). However, it was expected that the concentration of carbon in the final coat would be lower than that of silicon. A higher value of carbon suggested that a few of the alkyl groups on the silicones were still present after the hardening/curing process. This is similar to what was observed in FTIR spectrum.

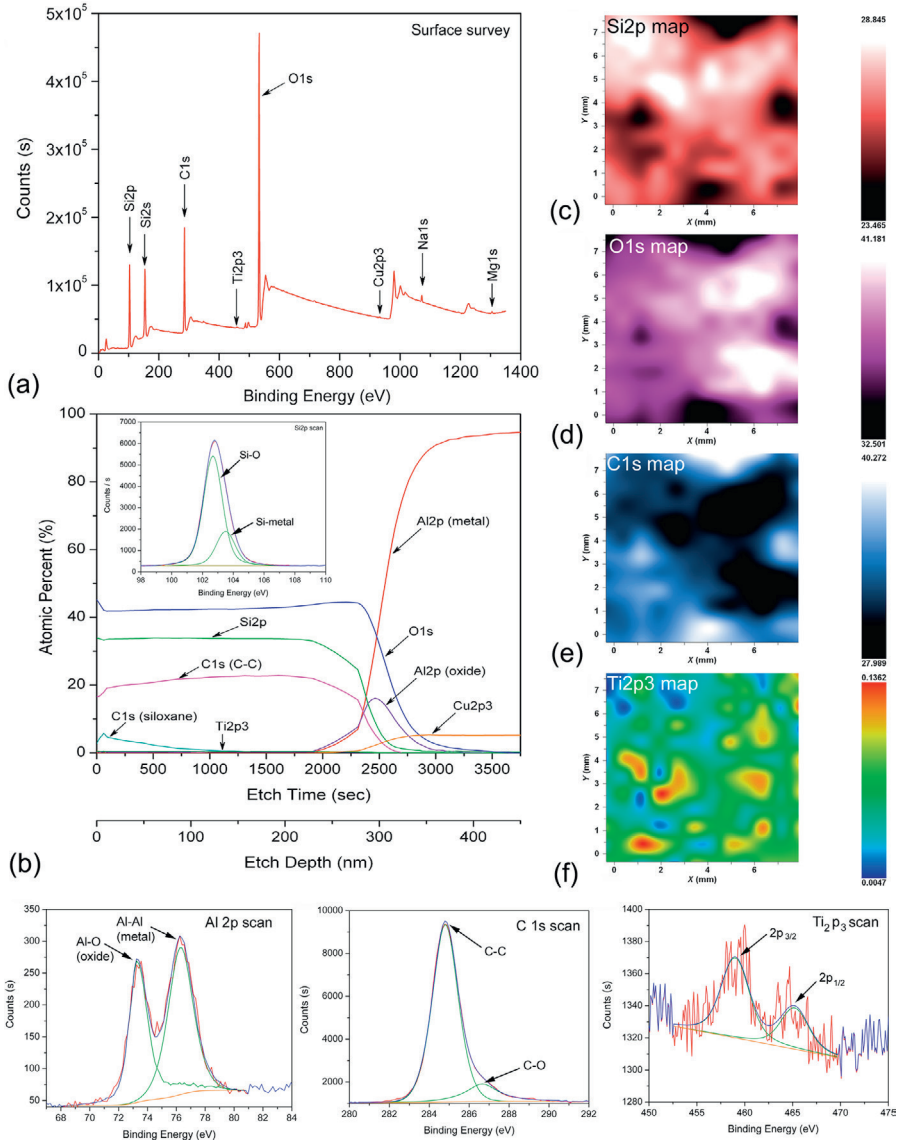


Figure 10.4 XPS spectra acquired on GCC cured over aluminum surface.

The depth profile (Figure 10.4b) and surface (Figure 10.4c–f) maps suggest that oxygen and silicone were uniformly distributed spatially and through the thickness of the coating. Carbon composition was not uniform in the coating, probably due to the presence of a small amount of unreacted alkoxysilanes. Results show that GCC can form stronger bonds with aluminum and its remnant oxide, but the bond strength

of GCC to copper/intermetallics in GP zones or other precipitates that exist in aluminum alloys is still not clear.

The C-O peak (Figure 10.4h) at 287 eV suggested the presence of unreacted methoxy groups in the coating structure while another peak at 285 eV is probably due to C-Si linkage due to surfaced methyl groups.[26] The deconvolution of Si2p curve shows two peaks (inset Figure 10.4b) in the deconvolution spectra. One peak occurred at 102.5 eV, corresponding to the SiOSi formation,peak which is generally found at 103 eV and has been shifted due to SiO_2 formation.[27] This peak at 103 eV suggested that some of the silicone macromolecules were detached from the backbone and had converted to silica.

Two different peaks of titanium were found in the Ti2p spectra (459.15 and 464.98 eV) obtained on the coating (Figure 10.4i). This Ti2p is a doublet separation between 2p1/2 and 2p3/2 peaks with a shift in 5.83 eV binding energy shift.[28] It appears that either the rutile or the anatase form of TiO_2 had formed as a result of hydrolysis and the subsequent conversion of the titanium compound.[29] There is evidence to support that peak at 459.15 eV could have a contribution from Ti-Si linkage.[30] This transformation suggests that a uniform distribution of TiO_2 nanoparticles can be achieved by sol-gel route of synthesis.

During depth profiling, sodium appeared at 1072.06 eV as one of its salts was added in the coating composition. Silicon was found up through the depth of 400 nm in the coating while the aluminum oxide value peaked at 340 nm. These results suggest that GCC penetrated the inert oxide layer of aluminum and reached the interface of aluminum and oxide to form a bond with the aluminum metal. A silicon peak (as shown in the inset of Figure 10.4b) was recorded after sputtering etch depth of 280 nm, at a point where silicon (Si2p), aluminum oxide (Al2p), and aluminum metal (Al2p) existed together in a narrow domain.

10.3.2 Thermal analysis

10.3.2.1 Thermal analysis of liquid precursor to GCC in inert and air atmosphere

Thermogravimetric analysis was performed on the solid and liquid precursor solution of GCC (Figure 10.5) that contained volatile solvents similar to those reported elsewhere.[31–33] The inset (Figure 10.5b) shows weight loss in liquid precursor to GCC as a function of temperature in inert and air atmosphere. The ordinate on the right axis shows derivatograms obtained in inert and air atmosphere.

In an inert atmosphere (flowing nitrogen gas) the coating precursor (after the solvent evaporated) decomposed to 13 wt.% at 110 °C and residue at ultimate decomposition was 8.7 wt.%. Similarly, in oxidative pyrolytic atmosphere (flowing air), the precursor decomposed to 13 wt.% at 148 °C, while the residue at ultimate

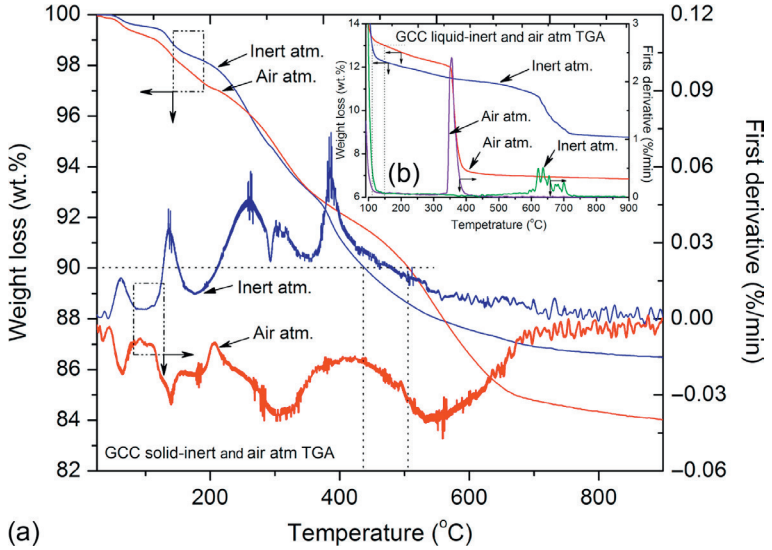


Figure 10.5 Thermogravimetric analysis of GCC. (a) TGA of solidified GCC; (b) TGA of precursor to GCC (in inset).

decomposition was 6.8 wt.%. The maximum rate of decomposition occurred at 630 °C in the inert atmosphere while at ~360 °C in the air atmosphere.

10.3.2.2 Thermal analysis of solid GCC in inert and air atmosphere

After heating to 100 °C, ~85% of volatile components including solvent and free and bound water evaporated from the precursor. After all the volatile components eluted, the precursor transformed to a solid mass and decomposed during the subsequent heating steps as the temperature increased. The left ordinate in Figure 10.5a shows weight loss in solid GCC as a function of temperature in inert and air atmosphere, while the right ordinate displays first derivative obtained as a result of decomposition of solid GCC in inert and air atmosphere. The 10 wt.% decomposition in an inert atmosphere occurred at 506 °C while at 438 °C in air atmosphere. The maximum rate of decomposition in air atmosphere occurred at ~205 °C with 16 wt.% residue at ultimate decomposition temperature while in an inert atmosphere, it occurred at 380 °C with 16.5 wt.% residue at ultimate decomposition temperature. Noticeable amounts of degradation incurred at ~350 °C in solid and liquid precursors to GCC both in the air and inert atmosphere. The FTIR-assisted evolved gas analysis suggested that at 350 °C crosslinked 3D backbone structure decomposes with the release of silane and associated methyl moiety. Multiple-step degradation patterns were observed in each case, suggesting that the coating network is composed of multicomponent structures.

10.3.3 Nanoindentation analysis

The GCC cures to form conversion coating on metal surfaces. Unlike traditional coatings, peeling of GCC out of substrate for mechanical analysis is not a viable option. The mechanical properties of GCC have to be determined using nanoindentation techniques.[34]

10.3.3.1 Estimation of hardness and modulus in GCC

The hardness (H) and modulus (E) were determined by nanoindenter using Berkovich tip. The loading and unloading curves shown in Figure 10.6a demonstrated the elastic recovery of the coatings with negligible plastic deformation.[35] A close observation of loading/unloading curves and standard deviation data suggests that the coating has a smooth surface morphology. The loading and unloading curves also indicated that residual deformation was low in each case, suggesting that the coating has elastic nature. There was no deviation or discontinuity in loading and unloading segments suggesting that coating did not delaminate during testing. The H and E values were plotted as a function of displacement into the coating on three different aluminum alloys in Figure 10.6b. The average H for GCC coated on 2024Al, 6061Al, and 7075Al were 0.42, 0.41, and 0.47 GPa, respectively, while the average E were 4.40, 4.51, and 5.45 GPa, respectively. These values are comparable to those obtained on other silicone ceramer coatings.[11,36] Similar measurements were recorded on the uncoated aluminum alloys polished to mirror finish to compare the results obtained

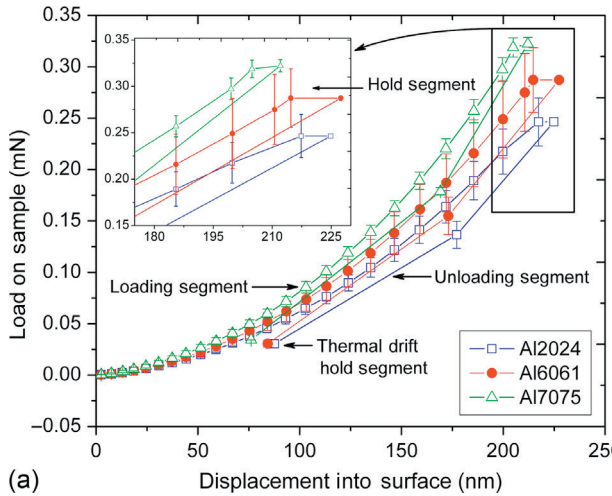


Figure 10.6 Nanoindentation analysis of GCC coated over aluminum surface. (a) Load vs displacement curve;

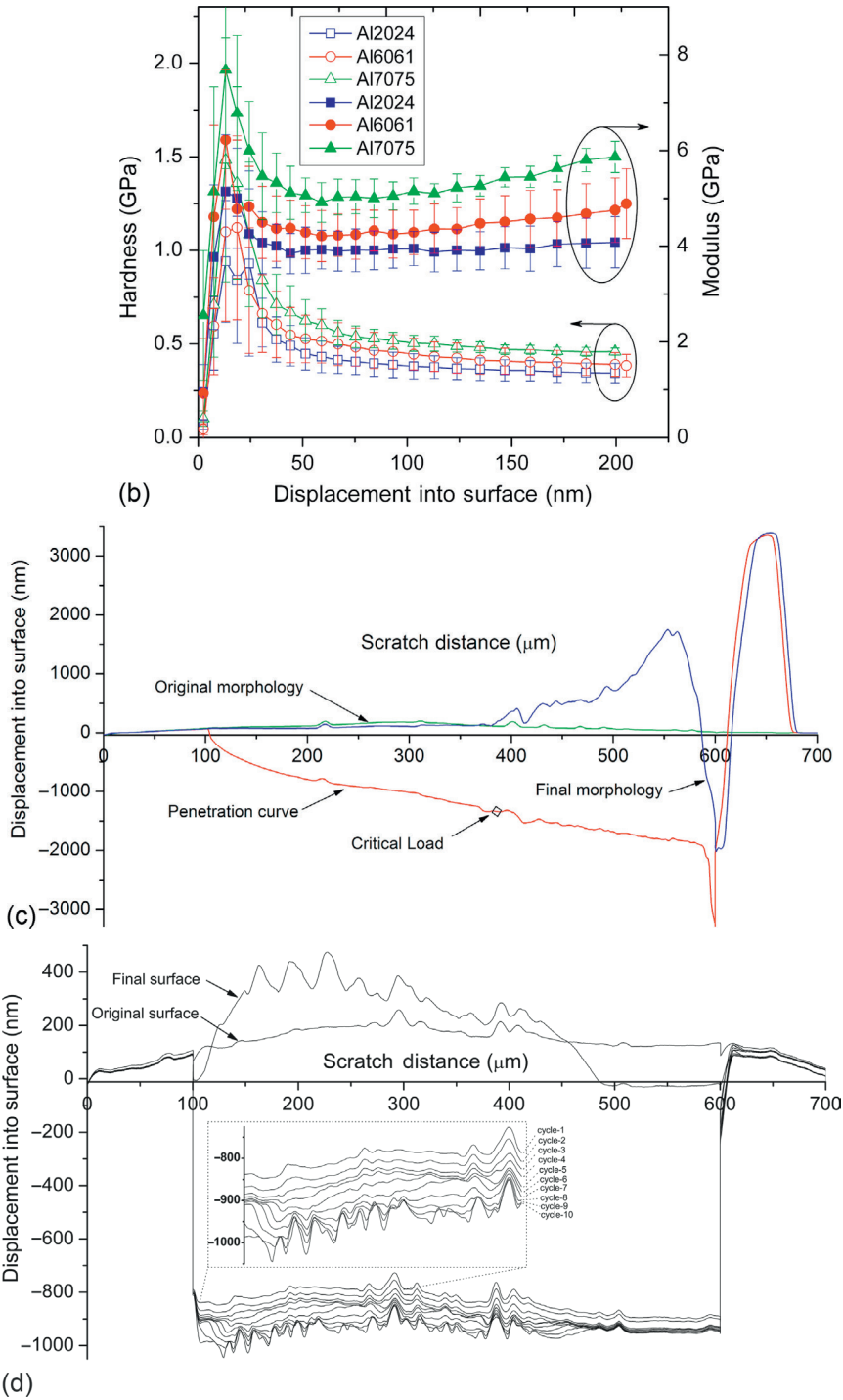


Figure 10.6, Cont'd (b) H and E as a function of displacement; (c) scratch profile; (d) wear analysis of solid GCC.

on the coating. The average H of 2024Al, 6061Al, and 7075Al were 1.87, 1.47, and 2.37 GPa, respectively, while the average E were 77, 76, and 78 GPa, respectively. The slight variation in mechanical properties of GCC shows that the coating may have been influenced by a small degree from the substrate mechanical properties or solubilized alloying elements from the substrate alloy. Note that mechanical properties of the coating are consistent with the substrate except in case of 6061Al where it showed higher standard deviation compared to the other two cases.

10.3.3.2 Estimation of adhesion through nanoscratch

Nanoscratch test using nanoindenter can help in determining the cohesive, as well as adhesive, modes of failure in coatings. The nanoscratch analysis using a nanoindenter could give an insight on adhesion, fracture, and wear characteristics of the material. Moreover, nanoscratch testing could also help in understating the near-surface strength of a material.[37,38] When a coating is subjected to a scratch test, the indenter can pass through three key regimes in the material: elastic, plastic, and fracture. The fracture is followed by delamination and chipping off the coated surface. The estimation and application of the correct load required to study the above-mentioned deformations is extremely beneficial. The high load can fracture the coating upon contact, eliminating the appearance of the other two regimes. Therefore, maximum applied load, scratch velocity, and scratch distance are critical in determining the true parameters.

In a typical nanoscratch test, the indenter tip approaches the surface of the test sample at a rate of 30 nm/s. Surface contact was set according to a predetermined increase in measured stiffness, S. The load applied to the indenter was then increased to a small profiling load of 20 μN, and the original surface topography was scanned over the entire scratch path. When the indenter returned to the origin after the initial profiling scan, a preprofile was performed up to the location of the desired scratch position. The indenter was then ramp loaded while the translation stages moved the sample along the scratch path at a rate of 10 μm/s. When the scratch length criteria were met, the indenter was unloaded to the profiling load and a postprofile scan was performed to the same length as the preprofile scan. The pre- and postprofile segments were used to level the scratch cycle data. Once the postprofile was completed, the stages moved into position for the cross-profile segment and the cross-profile was initiated. The indenter was then withdrawn from the sample completely, and the sample was moved into position for the next experiment.

Figure 10.6c shows the penetration curve along with residual surface morphology as a function of the scratch distance on GCC. In this case, sample was scratched using Berkovich tip (face forward) with maximum load of 30 mN with scratch velocity

of 10 μm/s until scratch distance of 500 μm. The original morphology of the coating was smooth with average roughness of ~40 nm. It appears from the penetration curve that the progressing load bearing the indenter tip pushed the coating and fractured at a critical load of ~17 mN after traveling a scratch distance of 385 μm. The depth at critical load was 1450 nm. Moreover, at critical load, the lateral force was 5.72 mN with a coefficient of friction of 0.34. Insignificant plastic deformation (3.6%) was observed in coating with pile-up height of 15 nm.

10.3.3.3 Wear analysis of GCC

Conventional wear analysis involves rubbing spherical head over coated surface and observing the damage after a predefined number of cycles. Nanoindenter head can be used alternatively to gain precise and in-depth information on the removal of material at the end of a predefined number of wear cycles. In a typical nanoindenter assisted wear test, the indenter tip approached the surface of the test sample at a rate of 10 nm/s. Surface contact was set according to a predetermined increase in measured stiffness, *S*. The load applied to the indenter was then increased to a small profiling load of 50 μm, and the original surface topography was scanned over the entire scratch path. When the indenter returned to the origin after the initial profiling scan, a preprofile was performed up to the location of the desired scratch position. The indenter was then loaded to 8 mN. This load was held constant while the translation stages moved the sample along the scratch path at a rate of 50 μm/s. When the scratch length criteria were met the indenter was unloaded to the profiling load and a postprofile scan was performed to the same length as the preprofile scan. The pre- and postprofile segments were used to level the scratch cycle data. Once the postprofile was completed the stages moved the sample back to the origin (location of preprofile). The indenter was loaded to the profiling load, and the residual topography of the wear track was recorded. This combination of wear cycle and profiling was repeated for 10 cycles. After the completion of the wear cycles, a cross-profile was performed. The indenter was then withdrawn entirely, and the sample was moved into position for the next experiment.

Figure 10.6d shows wear analysis on GCC coated over 6061Al surface. The original surface morphology displayed surface roughness of ~250 nm, while after the end of wear cycles surface roughness was ~450 nm. On observing average friction coefficient and average lateral force in each cycle, it was apparent that coating failure occurred after seven wear cycles, or the indenter head slides for 4200 μm. The maximum wear track deformation was ~550 μm^2. The service lifetime of the coating can be predicted by selecting the appropriate testing indenter tip and test environment and approximate service load that the coating could experience.

10.3.4 Surface morphology

A quasi-ceramic or hybrid silicone coating with active hydroxyl functionalities condenses gradually over time, resulting in a dense three-dimensional structure. These high-density coating networks are difficult to study using conventional microscopic techniques.

10.3.4.1 Surface morphological analysis with FESEM

The GCC hardened in ambient conditions over 7075Al was examined with Field Emission Scanning Electron Microscopy (FESEM). Figure 10.7a shows condensed surface texture over GCC without any signs of defects or holidays in the area of the scan. Scratches were deliberately generated on the coated surface to visualize the morphology of the nanoparticles around the scratched regime. Certain regions

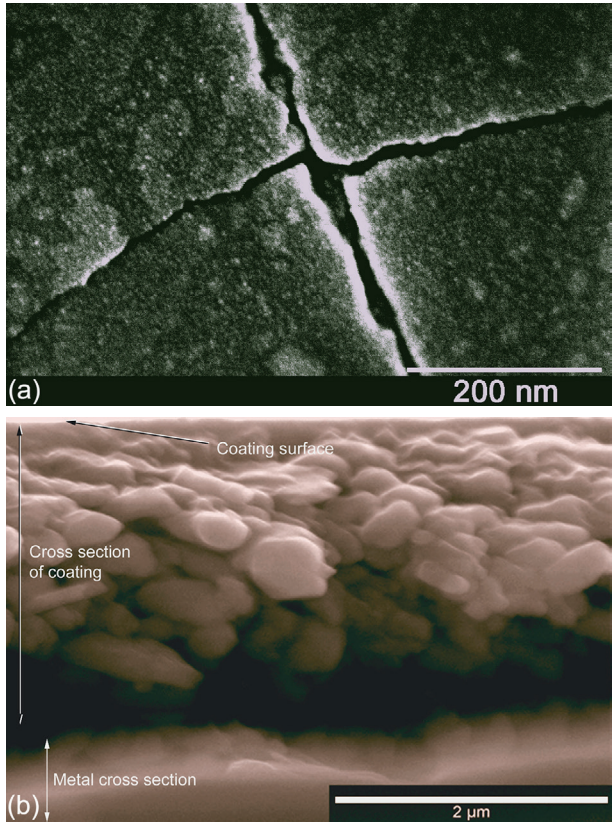
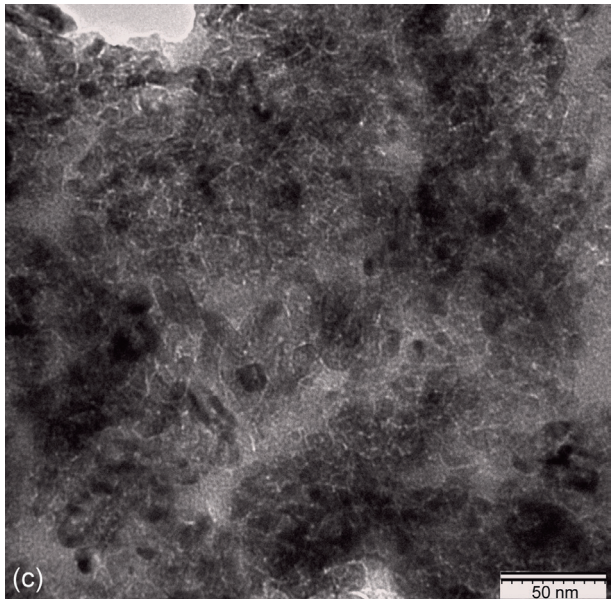


Figure 10.7 Microscopic analysis of GCC. (a) FESEM surface topography; (b) cross section FESEM of GCC coated surface;



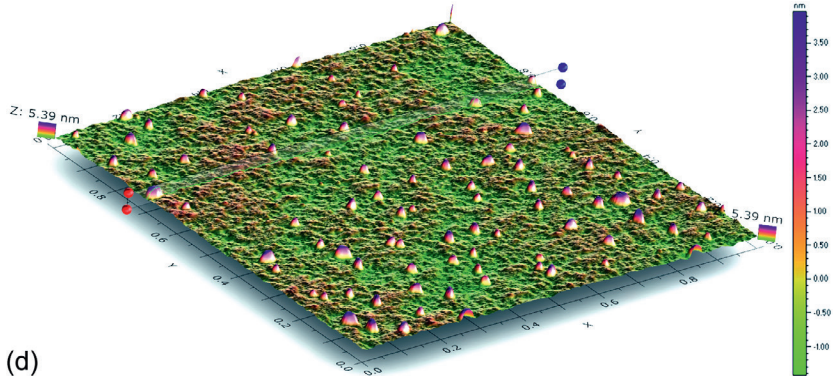


Figure 10.7, Cont'd (c) TEM of solid GCC showing dispersion of nanoparticles; (d) surface topography of GCC proved using AFM.

in the coating were chipped off around the deliberate defect. Little phase contrast observed on the surface was probably due to the nonuniform distribution of the condensed quasi-ceramic sol particulates. An attempt to focus on individual quasi-ceramic particles returned with limited success due to the charging of the sample at an ultrahigh resolution.

To understand the assembly of these nanoparticulates, a cross-sectional FESEM analysis was conducted over ambient condition dried GCC-coated 7075Al surface. The FESEM image in Figure 10.7b shows two distinct layers of GCC. The estimated total thickness of GCC layer was 3 µm. The top layer was dense while the succeeding

layers showed bundles—clusters of sol particulates. It appeared that these sol bundles condensed over time to result in dense surface morphology.

10.3.4.2 Surface morphological analysis with TEM

To visualize the bulk of GCC, Transmission Electron Microscopy (TEM) was conducted on solidified coating. The TEM image in Figure 10.7c displays the distribution of in-situ-generated titanium compound nanoparticulates in the GCC matrix. The average diameter of nanoparticles was ~15 nm and substantial agglomeration was observed in certain areas. At a higher magnification, a prominent sharp interface appeared between the nanoparticles.[36] It is assumed that these nanoparticles were formed as a result of either the conversion of titanium ethoxide into TiO_2[39] or the condensation into TiOTi macromers.[40]

10.3.4.3 Surface morphological analysis with AFM

As mentioned earlier, thin transparent films and coatings are difficult to analyze with conventional microscopic techniques. The Atomic Force Microscopy (AFM) technique was adopted to investigate the surface morphology of the GCC hardened over a mirror shine polished 6061Al surface. A 3D AFM image of the surface roughness is shown in Figure 10.7d. The average particle size was ~70 nm while the average height of the heap (formed as a result of sol particulate confinement) was on the order of 225 nm. It is worth mentioning that titanium nanoparticles *were* in-situ generated during the reaction and drying processes in GCC. The titanium compound chemically bound with the organic functionalities available in the hybrid material. However, domains that contained titanium nanoparticles could be distinctly visualized in AFM. Notice that the surface roughness indicated here includes the roughness that already existed on the bare polished aluminum surface.[11] A dense coating network without any signs of holidays was seen in the area under the scan.

10.4 Evaluation of Coating

The corrosion barrier properties of the coatings need to be tested in various simulated and natural corrosive environments. Moreover, the impervious barrier coatings should be tested along with the similar commercially available coatings. In most cases, for simulated corrosive environment tests, ASTM or other industry standards are adopted. In case of natural outdoor atmosphere exposure, results may vary from one place to another. Therefore, results from standard coating should be compared to the new coating. The following sections describe the studies on barrier properties of GCC compared to the other two industrial coatings, chro-

mated (ADC) and nonchromated (ADNC). Due to the proprietary issues with the commercial coatings, these will be designated here with generic designations (i.e., ADC and ADNC).

To visualize the corrosion activity, specimens were imaged using either Video Image Enhanced Evaluation of Weathering (VIEEW) surface analyzer or optical photography. SEM was utilized for in-depth analysis of corroded areas. The scanning procedure was conducted prior to exposure to document the initial specimen condition, and after exposure to document subsequent damage resulting from exposure. The VIEEW system captures digital images of samples under direct and diffuse lighting schemes optimized by the user to highlight and enhance surface defects. Software is then used to process images and quantify damaged areas.

10.4.1 Laboratory experiments

10.4.1.1 Immersion tests

The metals coupons were pin-stamped, surface prepared, and dip-coated with GCC in the lab facilities (Figure 10.8) while the commercial coatings were applied by the third-party vendor in accordance with the coating manufacturer's standard procedures. Coatings were cured in ambient conditions for at least two weeks.

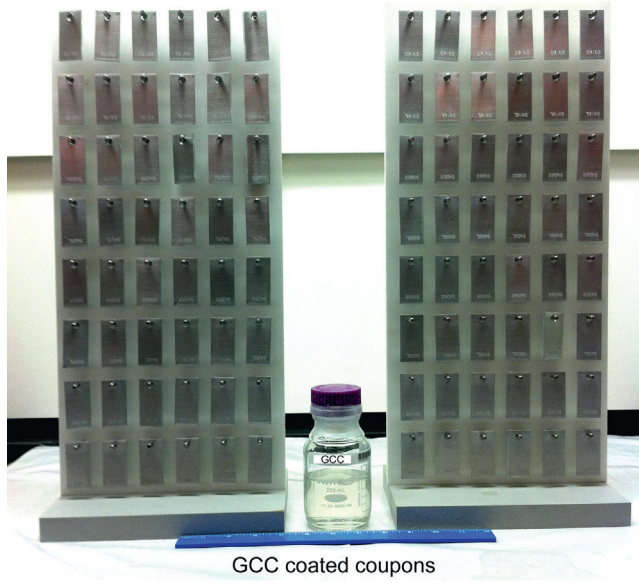


Figure 10.8 Setup for GCC application over metal alloys.

10.4.1.1.1 Immersion in ASTM seawater and sodium sulfate solution

The immersion test was performed in simulated seawater as per ASTM. Aluminum alloys 2024, 5086, 6061, and 7075 were treated with GCC, ADC, and ADNC coatings. Coupons were scribed to test the corrosion behavior at the coating and scratch interface. Coupons were immersed in air-exposed electrolytes at 30 °C. Each beaker contained three similar coupons that were mounted on plastic holders. Figure 10.9a shows immersion setup for ASTM seawater and 0.5 M Na_2SO_4 solution. Figure 10.9b shows the coupons mounted on the plastic sample holders that were retrieved after the immersion experiment.

In general, uncoated coupons showed more severe corrosion damage than did coated coupons. The corrosion was severe on the back side of coated coupons compared to the front side, probably due to coating damage during the application and drying process. Figure 10.10a–d shows corrosion damage calculated from VIEEW image analysis for uncoated and coated coupons after 2 months and 6 months of immersion test in ASTM seawater and 0.5 M Na_2SO_4 solution respectively. In the

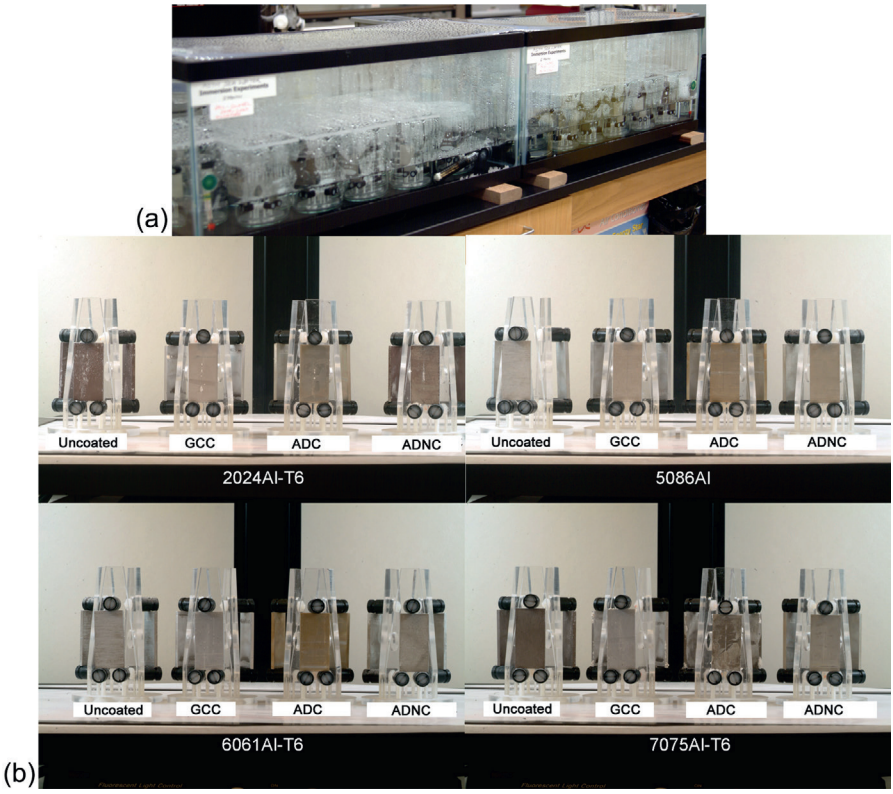


Figure 10.9 Setup for the immersion experiments. (a) Immersion chamber; (b) coupons on triangular plastic holders.

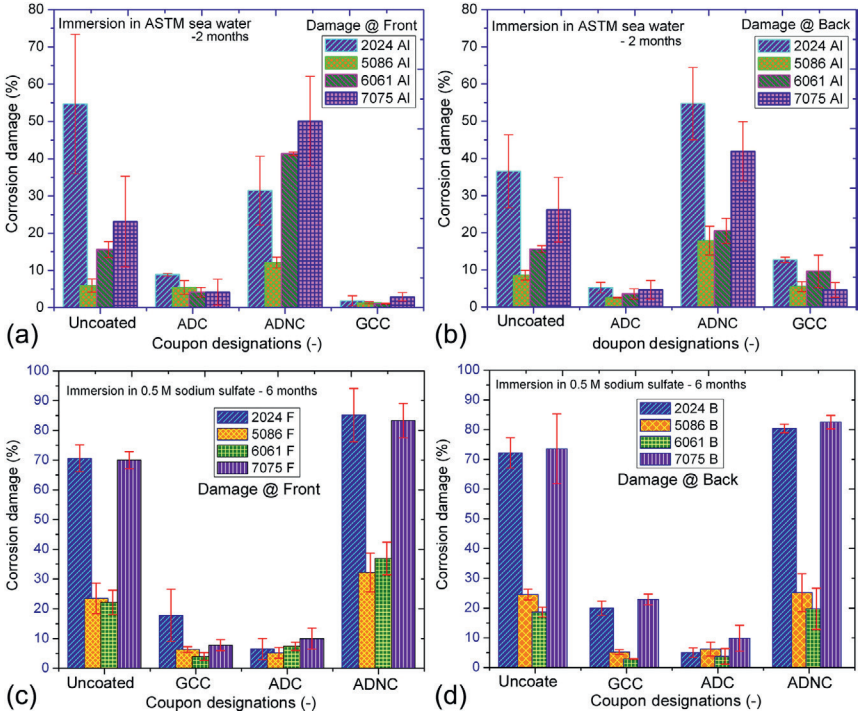


Figure 10.10 VIEEW assisted corrosion damage assesment on coupons. (a) Front face of the coupons after 2 months immersion in ASTM sea-water; (b) back face of the coupons after 2 months immersion in ASTM sea-water; (c) front face of the coupons after 6 months immersion in sodium sulfate solution; (d) back face of the coupons after 6 months immersion in sodium sulfate solution..

case of coupons retrieved from ASTM seawater immersion, GCC displayed similar corrosion protection as ADC and outperformed ADNC-coated coupons. Also, 5086Al-coated coupons were better protected than the others. Similarly, in the case of coupons retrieved from Na_2SO_4 immersion, the GCC displayed comparable corrosion protection as ADC and outperformed ADNC-coated coupons. Moreover, 6061Al-coated coupons were significantly protected compared to other coupons.

10.4.1.2 Surface appearance investigations

10.4.1.2.1 Appearance after immersion in ASTM seawater

The uncoated and coated coupons were immersed in ASTM seawater and retrieved after the predetermined exposure period. The corroded coupons were cleaned and analyzed using VIEEW image analyzer. Figure 10.11a shows VIEEW scans of uncoated coupons. Three coupons for each alloy were scanned, but only one coupon from each set is shown here. The red color over the image represents the damage due to corrosion.

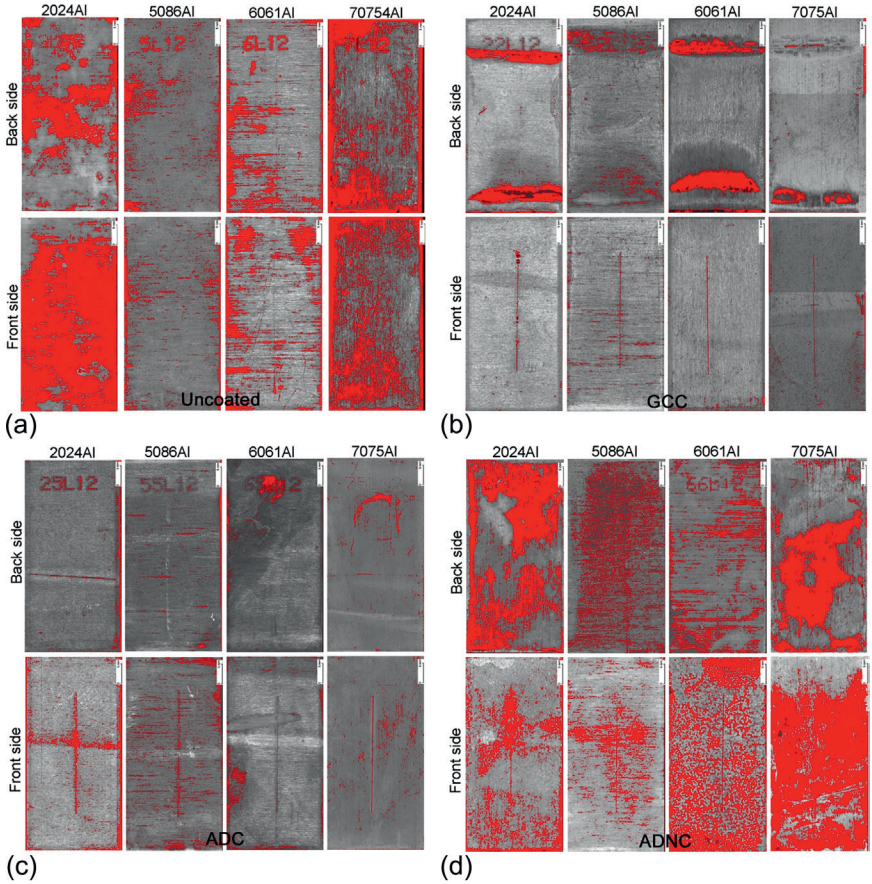


Figure 10.11 VIEEW images of corrosion damages on coupons after two months immersion in ASTM sea water. (a) Uncoated coupons; (b) GCC coated coupons; (c) ADC coated coupons; (d) ADNC coated coupons.

The severe corrosion could be seen on the uncoated 2024Al and 7075Al coupons. Moderate corrosion was observed over the 5086Al and 6061Al coupons. Figure 10.11b shows VIEEW scans of GCC-coated coupons. The corrosion damage on the back side of the coupon is probably due to the loss of coating during the application and drying process. The coated coupons were generally protected from corrosion. The corrosion was observed in the region of deliberate scratch. No coating delamination was observed near the scribed regime.

Figure 10.11c shows VIEEW scans of ADC-coated coupons. In this case, both the back and front sides of the coupon showed superior corrosion protection. However, corrosion was observed in the region of the deliberate scratch. Figure 10.11d shows VIEEW scans of ADNC-coated coupons. The back as well as front sides of the

coupons were severely damaged due to corrosion, suggesting that the coating was not impervious and did not provide adequate protection to the metal surface.

10.4.1.2.2 Appearance after immersion in sodium sulfate solution

The uncoated and coated coupons were immersed in 0.5 M sodium sulfate solution and retrieved after the predetermined exposure period. The corroded coupons were cleaned and analyzed using the VIEEW image analyzer. Figure 10.12a shows VIEEW scans of uncoated coupons. A high degree of corrosion damage was observed on the back and front sides of the coupons. The severe corrosion could be seen on the uncoated 2024Al and 7075Al coupons. Moderate corrosion was observed on the 5086Al and 6061Al coupons. Figure 10.12b shows a VIEEW scan of the

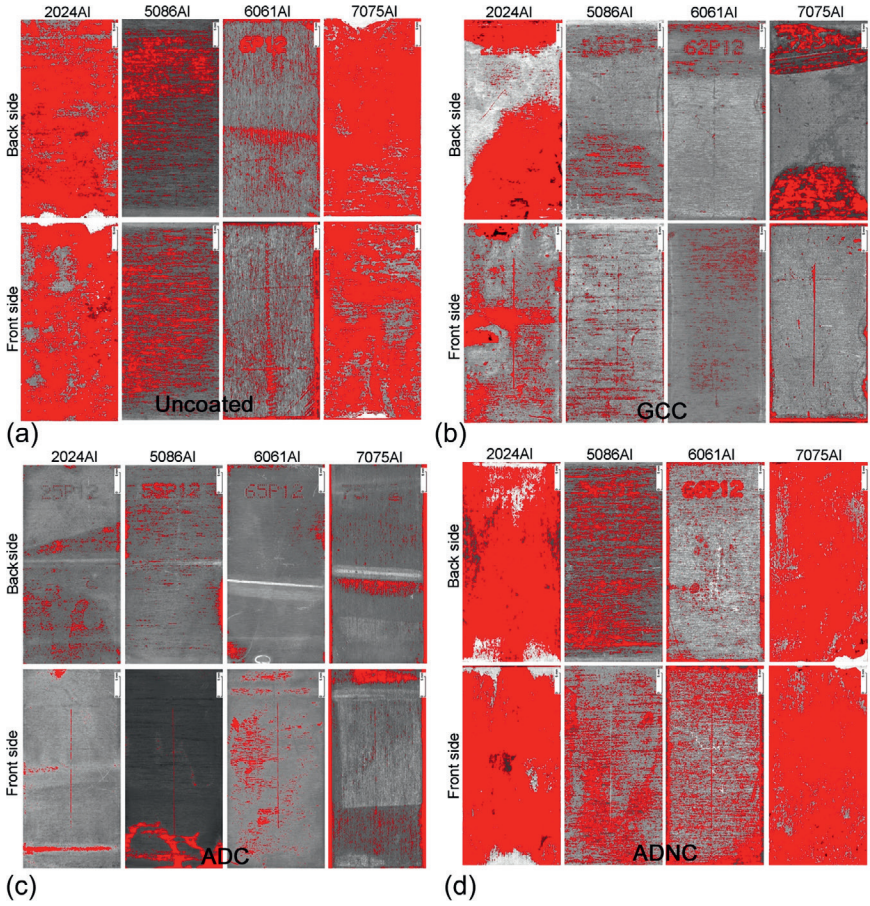


Figure 10.12 VIEEW images of corrosion damages on coupons after six months immersion in 0.5M sodium sulfate solution. (a) Uncoated coupons; (b) GCC coated coupons; (c) ADC coated coupons; (d) ADNC coated coupons..

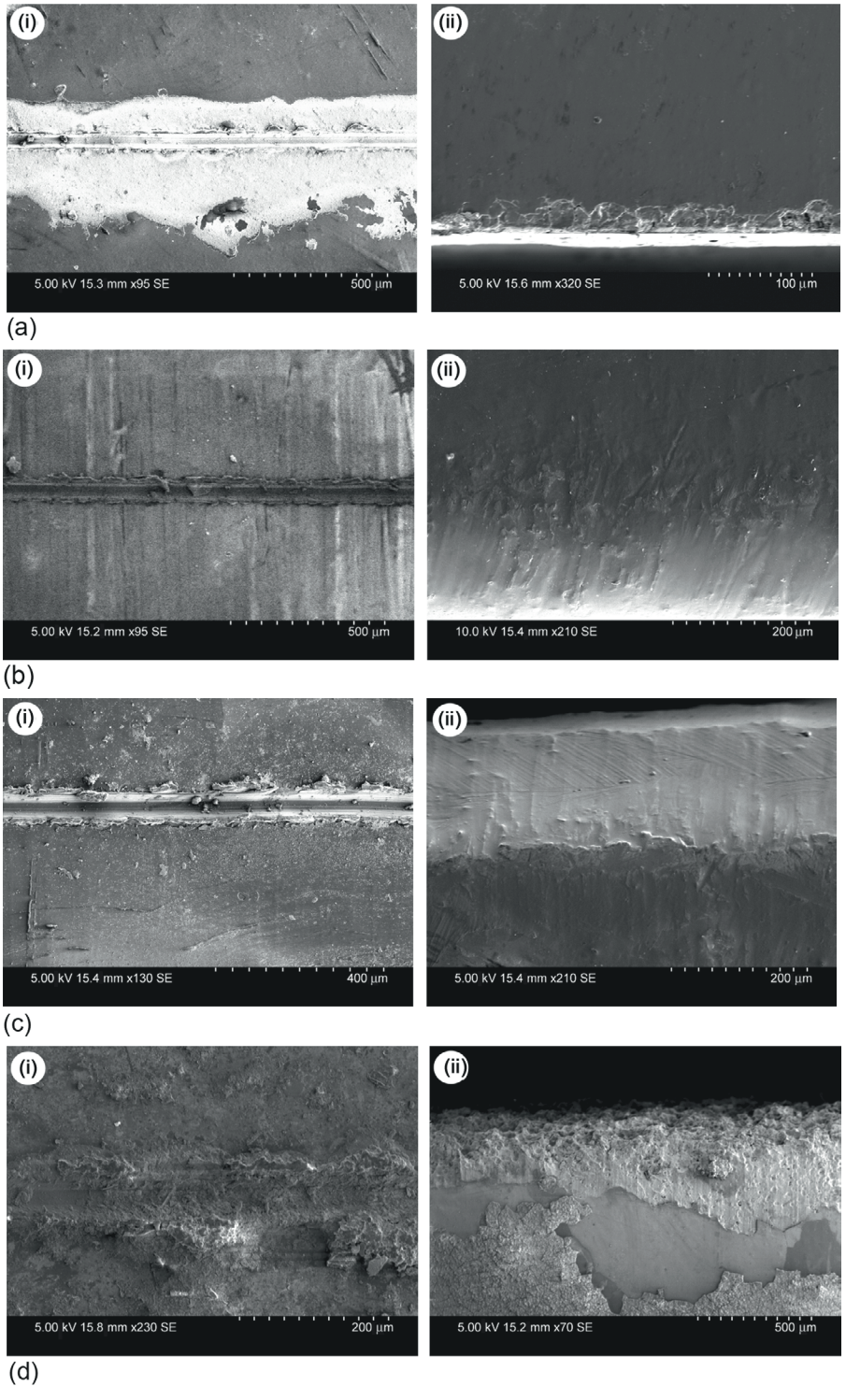


Figure 10.13 SEM analysis on GCC coated aluminum coupons that were immersed in 0.5M Na_2SO_4 solution for 6 months. (a) coated 2024 Al coupons; (b) coated 5086 Al; (c) coated 6061 Al coupons; (d) coated 7075 Al coupons .

GCC-coated coupons. The back side of the coupon suffered severe corrosion damage while the front side of 5086Al and 6061Al were significantly protected. The front side of 2024Al and 7075Al coupons displayed moderate corrosion. The corrosion was observed in the region of the scribe, but no coating-substrate delamination was observed. Figure 10.12c shows VIEEW scans of ADC-coated coupons. The back side of the coupon displayed moderate corrosion while the front side of the coupons displayed superior corrosion protection except in few cases where the coating might have been damaged during the application process. Figure 10.12d shows VIEEW scans of ADNC-coated coupons. The backs as well as the front sides of the coupons were severely damaged due to corrosion, suggesting that the coating was not impervious enough to provide adequate protection to the metal surface.

10.4.1.2.3 Analysis of coupons retrieved after immersion test

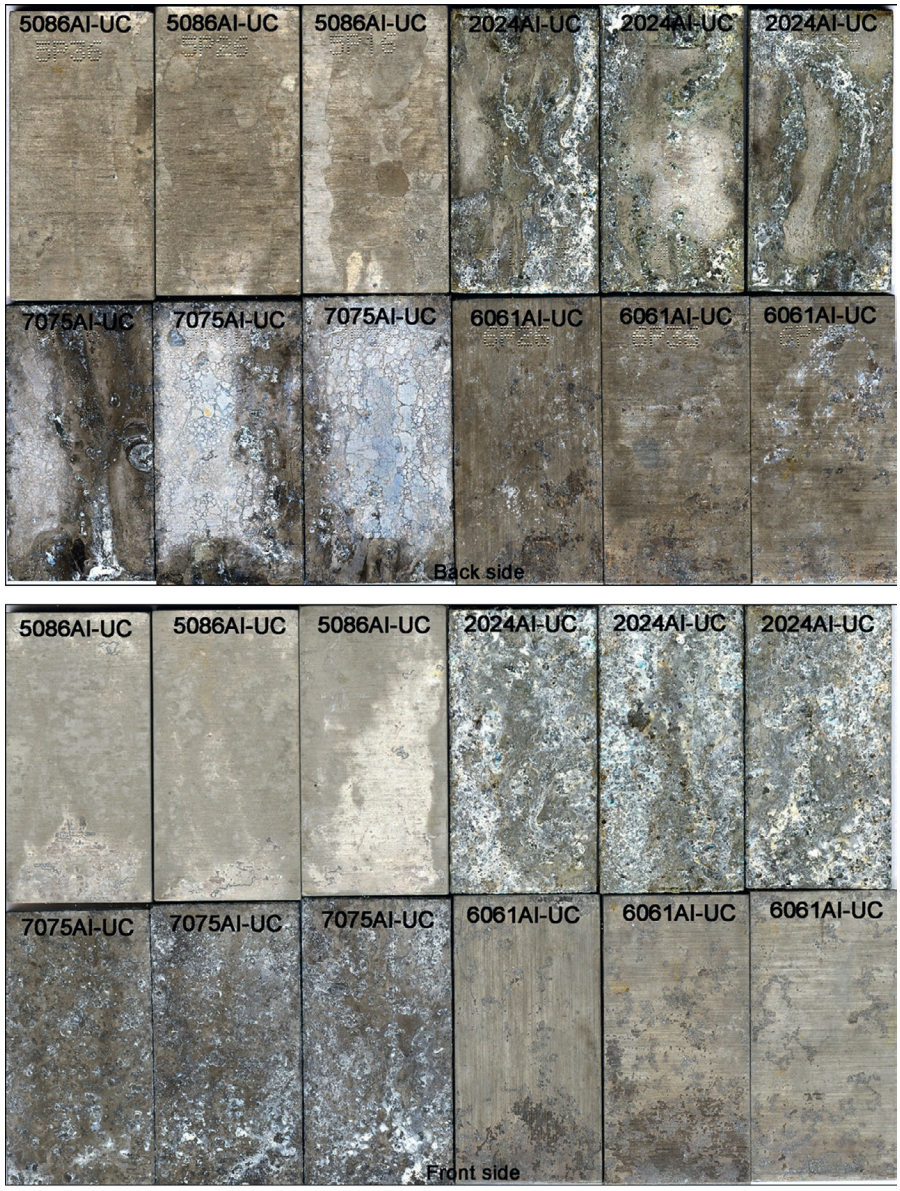
The corroded coupons that were retrieved after immersion test were studied under the SEM to understand the corrosion process in GCC-coated coupons. Figure 10.13a–d display the SEM images acquired over four different aluminum alloys.

In the case of GCC-coated 2024Al coupons (Figure 10.13a), the coating was moderately effective in preventing the corrosion on the substrate. Though scattered pinholes were observed, most of the surface was protected. No sign of coating delamination was observed in the area around the scratch. The corrosion products precipitated and crept out of the scratched region; the edges and corners of the coupons were not protected by the coating. In the case of GCC-coated 5086Al coupons (Figure 10.13b), the coating was impervious and protected the substrate. Little to no corrosion damage was observed in the region of the scan. Moderate corrosion activity was observed in the scratch, but no sign of coating delamination was seen. The edges and corners were significantly protected, and coating was well adhered to the metal surface.

In the case of GCC-coated 6061Al coupons (Figure 10.13c), the coating was effective in protecting the surface. Little to no corrosion activity was seen on the coated surface; however, white precipitate was scattered all around the surface. No sign of coating delamination was observed near the scratched region. Moreover, the edges and corners were protected. In the case of GCC-coated 7075Al coupons (Figure 10.13d), the coating was effective in protecting ~80-90% of the substrate. Even so, severe corrosion activity was observed in some regions around the scratch, and some regions of the coating were thoroughly covered with the corrosion product. Also, the edges and corners were severely damaged.

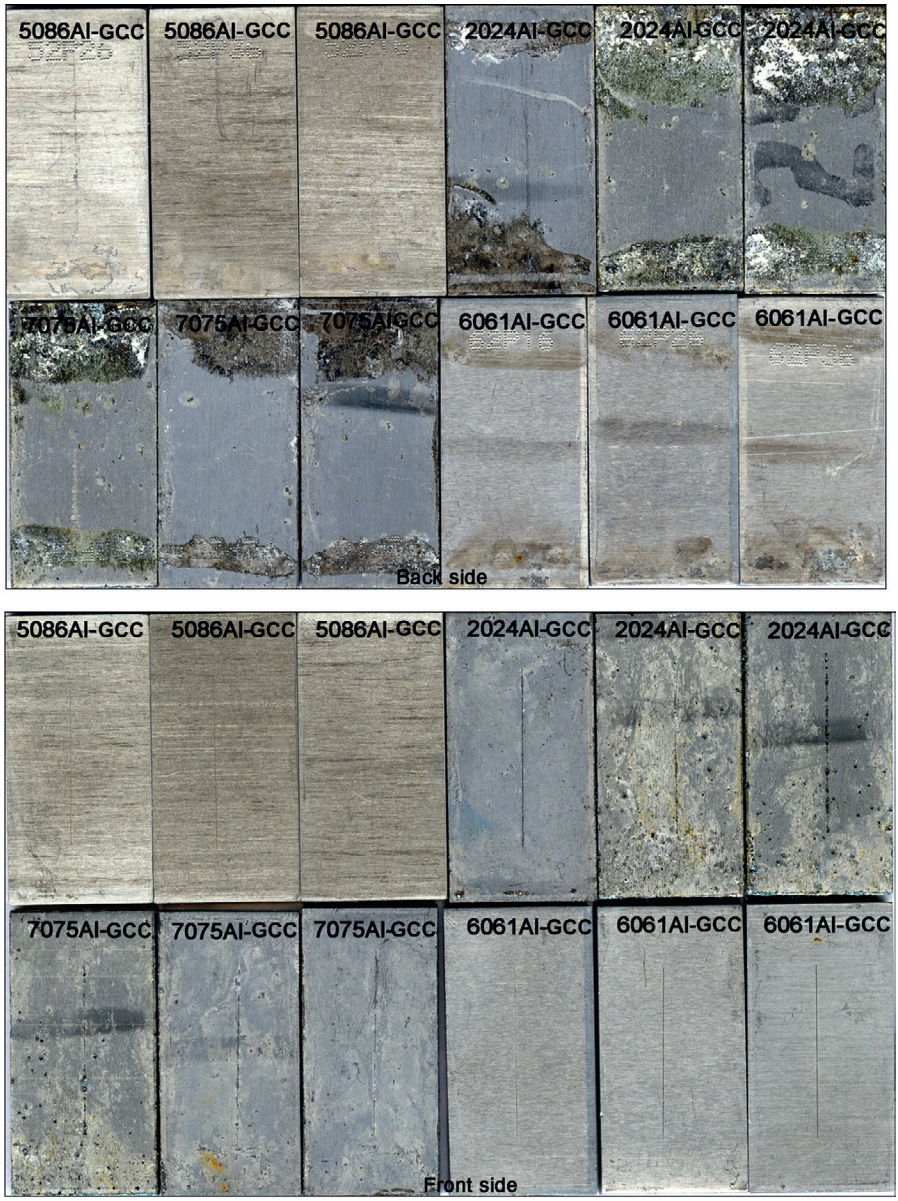
10.4.1.2.4 Surface appearance after accelerated weathering according to ASTM-B117 standard

The uncoated and coated coupons of 2024Al, 5086Al, 6061Al, and 7075Al were tested for 2688 hours as per ASTM standards. The coupons were scanned using a photo-scanner to visualize the corrosion damages over the surface of the coupons. Figure 10.14a–d illustrates the corrosion phenomenon over the uncoated and coated aluminum surfaces. In general, the uncoated coupons suffered severe corrosion



(a)

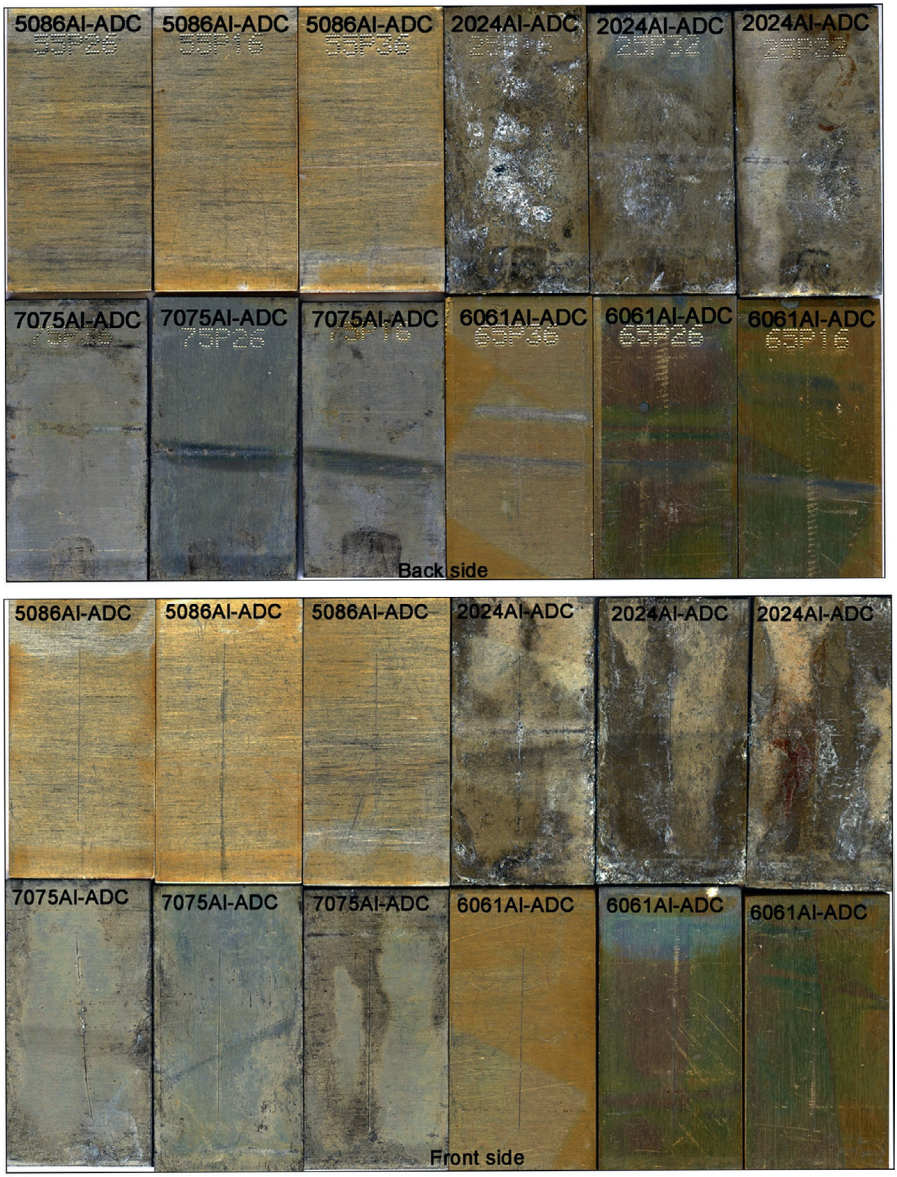
Figure 10.14 Optical light scans of coupons retrieved after 2,688 hours of exposure as per ASTM-B117. (a) Back side of the uncoated coupons (top); Front side of the uncoated coupons (bottom).



(b)

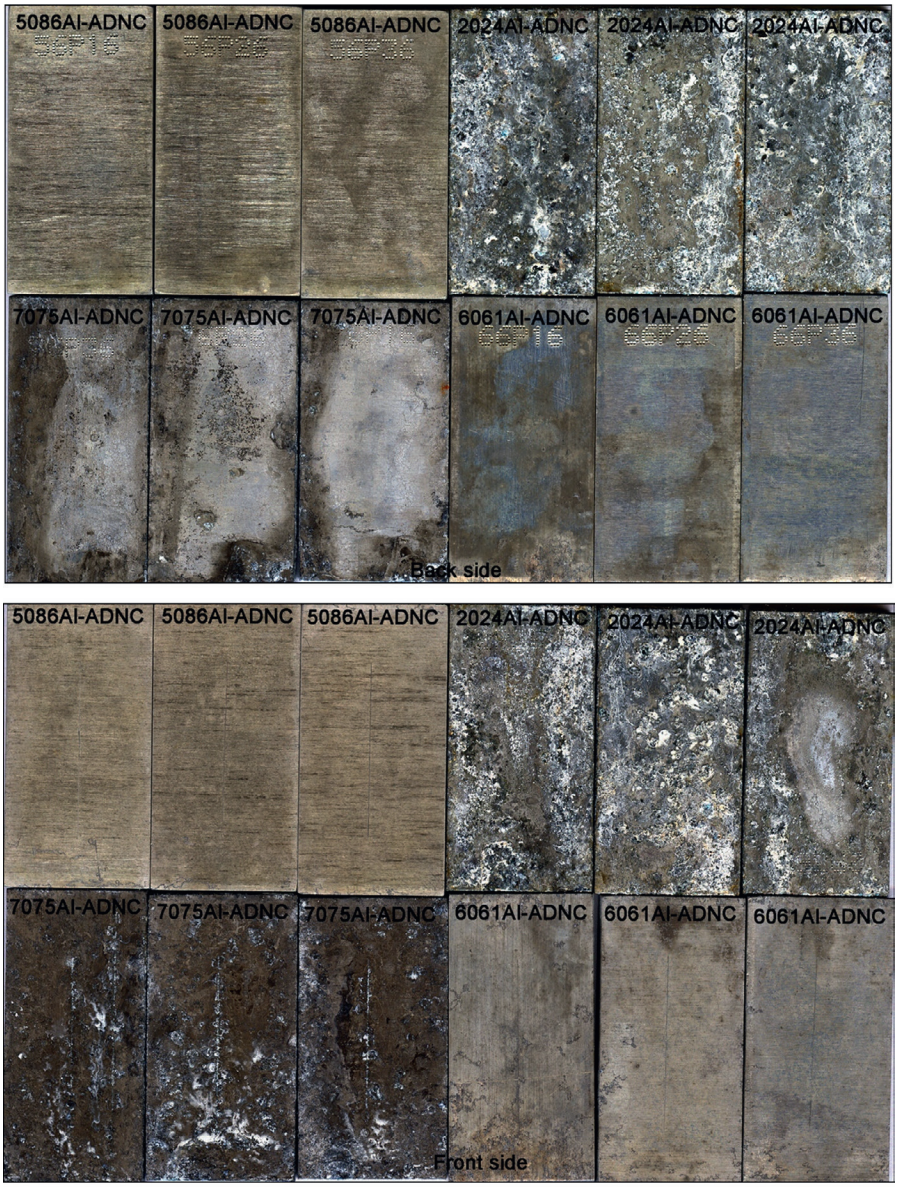
Figure 10.14, Cont'd (b) Back side of the GCC coated coupons (top); Front side of the GCC coated coupons (bottom).

(Continued)



(c)

Figure 10.14, Cont'd (c) Back side of the ADC coated coupons (top); Front side of the ADC coated coupons (bottom).



(d)

Figure 10.14, Cont'd (d) Back side of the ADNC coated coupons (top); Front side of the ADNC coated coupons (bottom).

damage compared to the coated coupons. The coated 5086Al and 6061Al coupons were significantly protected while coated 2024Al and 7075Al coupons were most affected by the corrosion. The GCC and ADC coatings provided comparable and better corrosion protection than did the ADNC coating.

10.4.1.2.5 Analysis of coupons retrieved after accelerated weathering

The coupons retrieved after accelerated corrosion experiments (ASTM B117) were studied under the SEM to understand the corrosion process in the GCC-coated coupons. Figure 10.15–10.18 displayed the SEM images acquired over four different aluminum alloys. Several deep pits were observed in certain regions of the 2024Al-coated surface. Figure 10.15 shows corrosion product over the scribed coating, but the coating was adhered to the metal surface. The end of the scribe displayed severe corrosion and pit formation.

In the case of GCC-coated 5086Al coupons (Figure 10.16), corrosion product was found near the scratched region. Moreover, no pit formation or coating delamination was observed. Severe degradation of the coated surface was seen at the edge of the specimens. Similarly, in case of GCC-coated 6061Al coupons (Figure 10.17), the corrosion product covered the scratched region of the coating. No coating delamination was observed in this case. The edges and corners of the specimens were

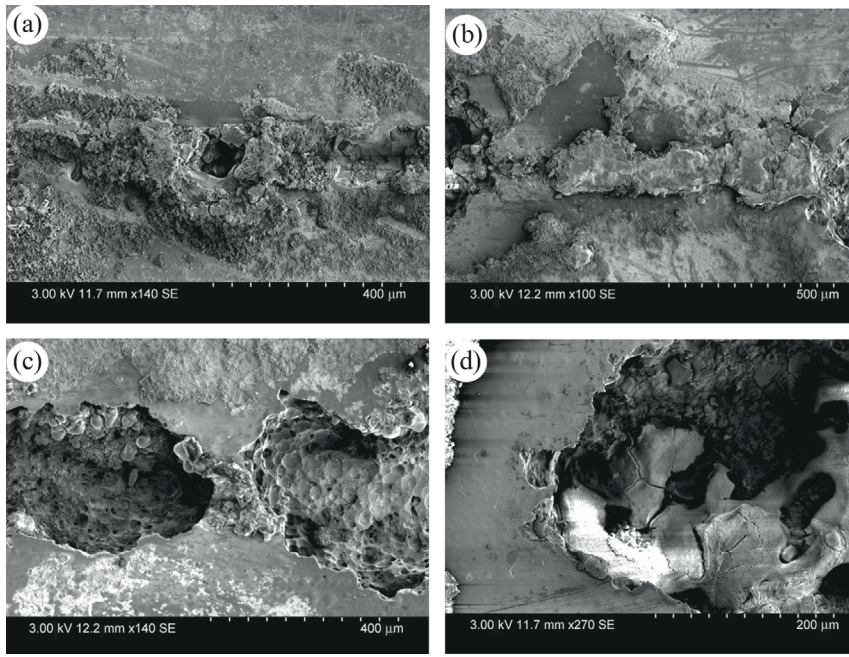


Figure 10.15 SEM analysis of GCC coated 2024Al after 456 hours of ASTM B117 exposure.

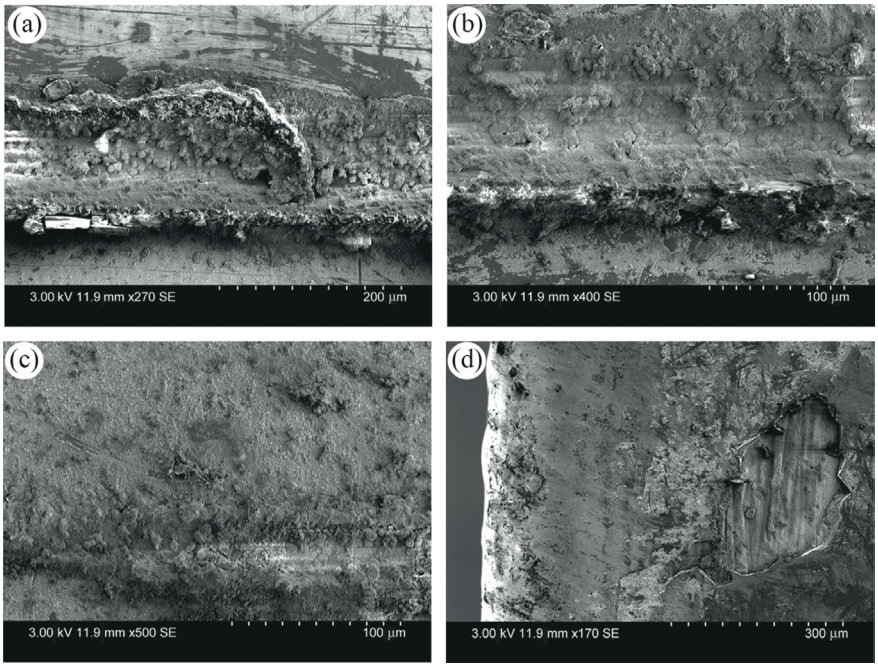


Figure 10.16 SEM analysis of GCC coated 5086Al after 456 hours of ASTM B117 exposure.

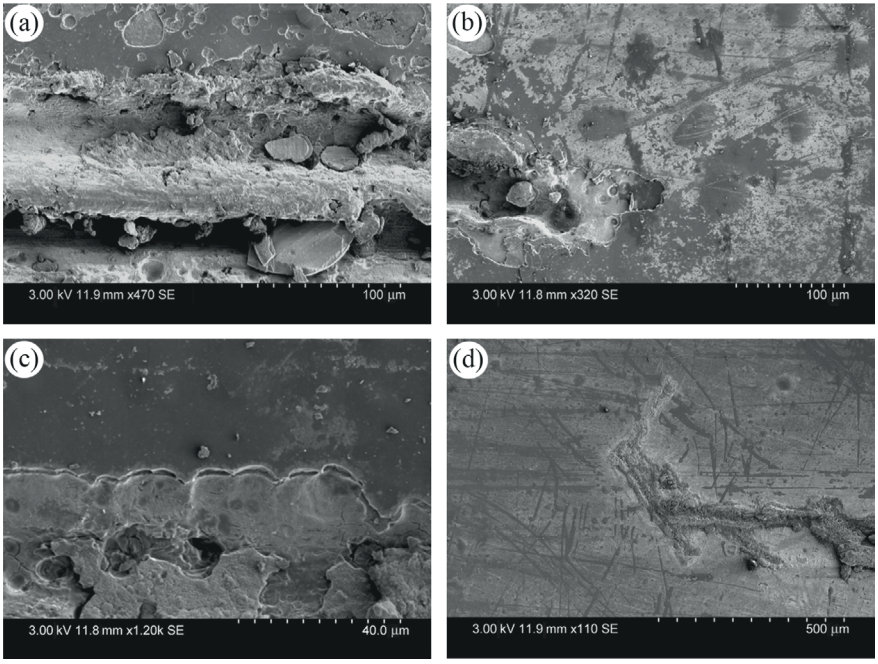


Figure 10.17 SEM analysis of GCC coated 6061Al after 456 hours of ASTM B117 exposure.

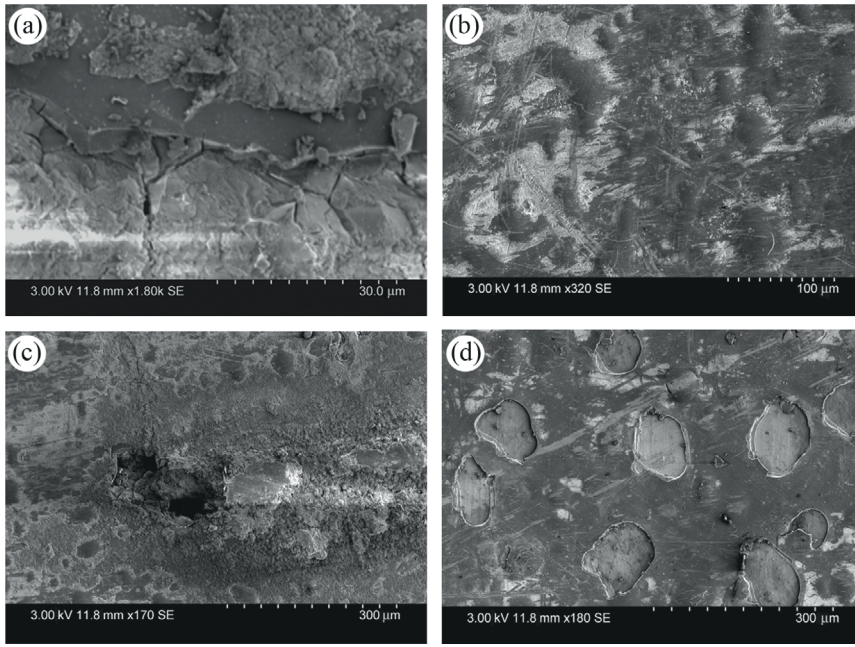


Figure 10.18 SEM analysis of GCC coated 7075Al after 456 hours of ASTM B117 exposure.

significantly protected. In contrast, GCC-coated 7075Al coupons (Figure 10.18) suffered severe damages due to corrosion. The coated surface chipped off, resulting in deep pit formations as well as edges and corners severely damaged.

10.4.2 Outdoor experiments

To accomplish this testing, four specimens of each coating condition were coated. One of the four specimens was subsequently scribed to study corrosion at a deliberate coating defect. After the virgin and coated coupons were analyzed and scanned, each coupon was mounted onto a faceplate using nonconductive Delrin® insulators and nylon fasteners (Figure 10.19). The uncoated coupons, coated coupons, and coated-and-scribed coupons were mounted alongside each other at the six test sites. Uncoated and coated coupons were exposed at the outdoor (natural weather) testing facilities (Figures 10.20–10.25) developed at Hawaiian Islands by the Hawaii Corrosion Laboratory in the University of Hawaii at Manoa. Coupons were exposed at Lyon Arboretum (LA), Coconut Island (CIL), Campbell Industrial Park (CIP), Kilauea (KLV), Marine Core Base Hawaii (MCBH), and Mauna Loa (MLO). These sites were selected because these represent the diverse corrosive climate conditions. The bare and coated coupons were mounted with the pin-stamped surfaces facing downward. The scribed specimens were mounted with the scratched surfaces facing

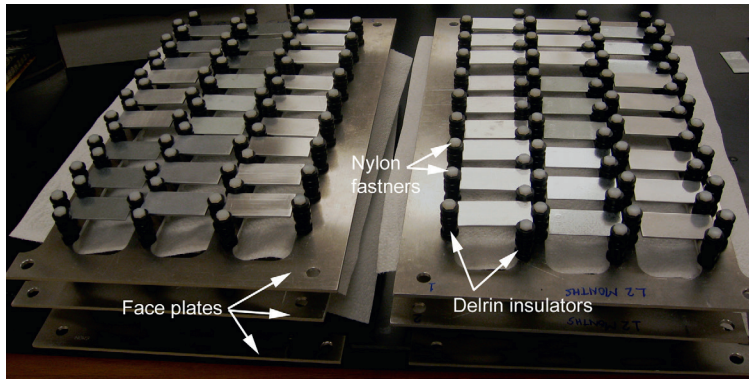


Figure 10.19 Coupons mounted on aluminum faceplates for outdoor natural atmosphere exposures. Insulator Delrin® spacers and nylon fasterns were used.



Figure 10.20 Coupons being exposed at Lyon Arboretum test site in Hawaii.

up. After retrieval from the outdoor exposure, the coupons were cleaned in an ultrasonic bath and wiped with ethanol.

10.4.2.1 Assessment of corrosion damages

Both sides of each coupon (uncoated and coated) were scanned prior to and after exposure using the VIEEW surface analyzer. Cleaned coupons were scanned using the preset imaging procedure in the VIEEW image analyzer. Both top and bottom surfaces of the uncoated and coated coupons were scanned to visualize and quantitatively

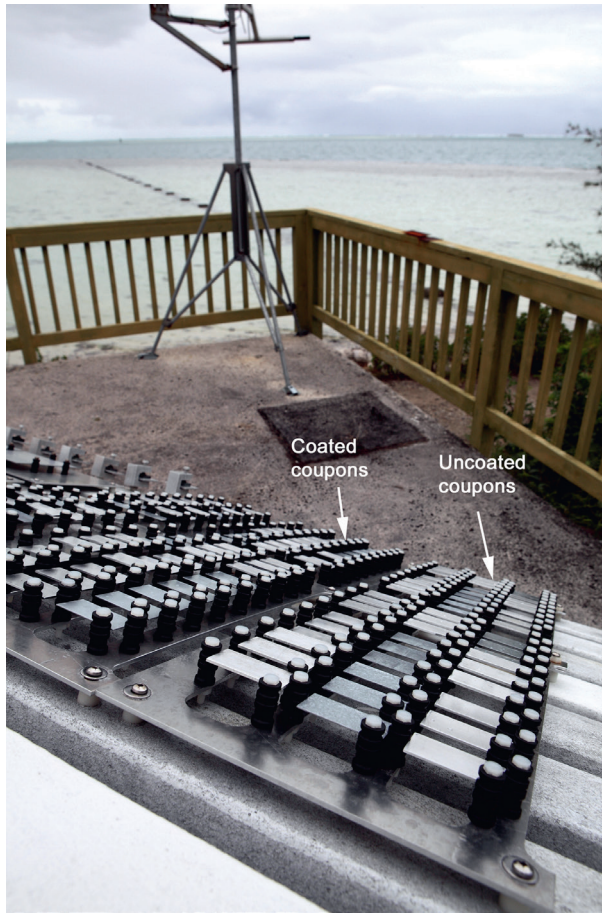


Figure 10.21 Coupons being exposed at Coconut Island test site in Hawaii.

determine the amount of damage caused due to corrosion. Damage caused to the coated surface was compared to that on the uncoated surface of the same metal alloy.

Figures 10.26–10.28 show the percentage of corroded surface area for each alloy as a result of 12 months of exposure at LA, CIL, and CIP. In these bar diagrams, the percent corrosion damage (average value reported) and standard deviation bars are based on three specimens for each condition. The LA test site receives a high amount of rainfall with a negligible amount of chloride content. At this site (Figure 10.26), 2024Al and 6061Al were significantly protected by GCC and ADC. Significantly less corrosion damage was observed on 7075Al coupons coated with both GC and ADC. The CIL is a marine test site and receives a high amount of chloride content deposition on the exposed metals. Similar to LA, coupons at this site (Figure 10.27)



Figure 10.22 Coupons being exposed at Cambell industrial park test site in Hawaii.



Figure 10.23 Coupons being exposed at Kilauea test site in Hawaii.

displayed similar corrosion trends. Corrosion was severe over uncoated and coated 7075Al while 2024Al and 6061Al remained protected. The corrosion on GCC-coated 7075Al was less than ADC-coated 7075Al coupons. The CIP test site receives high amount of corrosive industrial gases, but not the significant chloride ions. At this site (Figure 10.28) corrosion activity was higher on the coated 2024Al and 6061Al

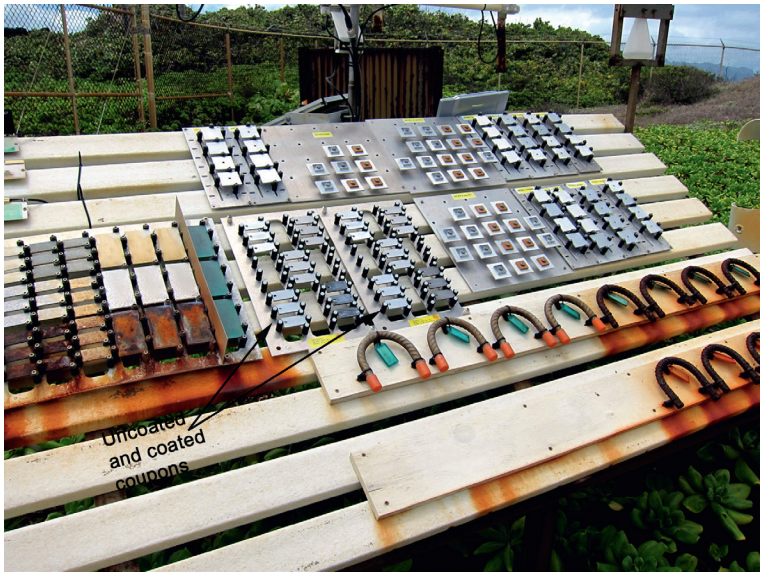


Figure 10.24 Coupons being exposed at MCBH test site in Hawaii.



Figure 10.25 Coupons being exposed at Mauna Loa test site in Hawaii.

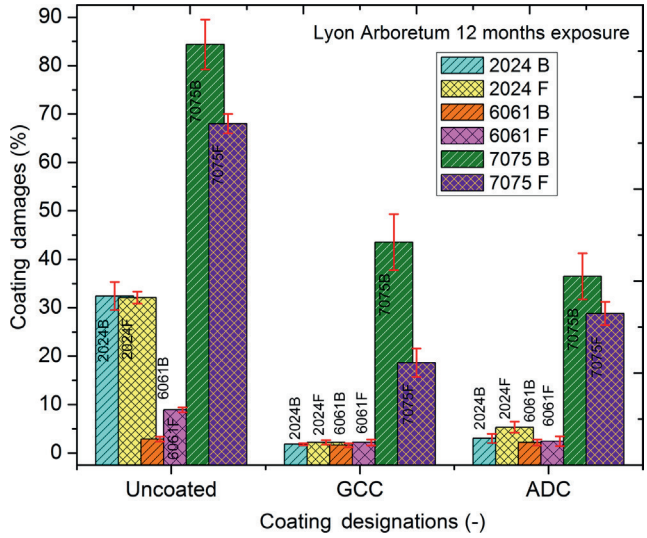


Figure 10.26 VIEEW assisted corrosion damage assesment on coupons after 12 months expsore at Lyon Arboretum test site.

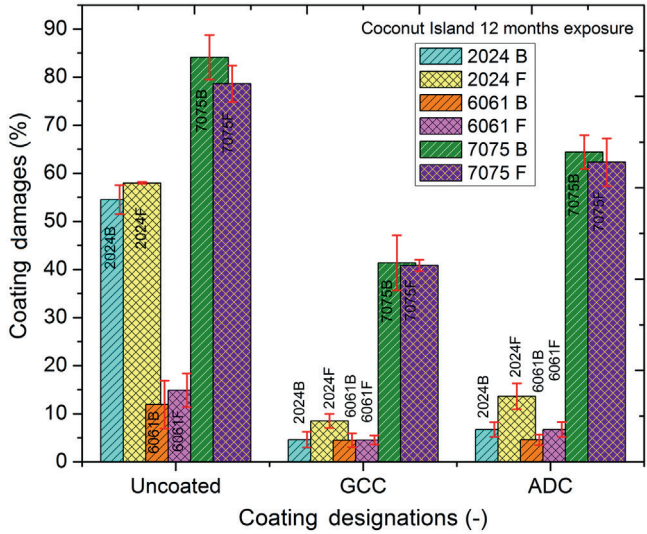


Figure 10.27 VIEEW assisted corrosion damage assesment on coupons after 12 months expsore at Coconut Island test site.

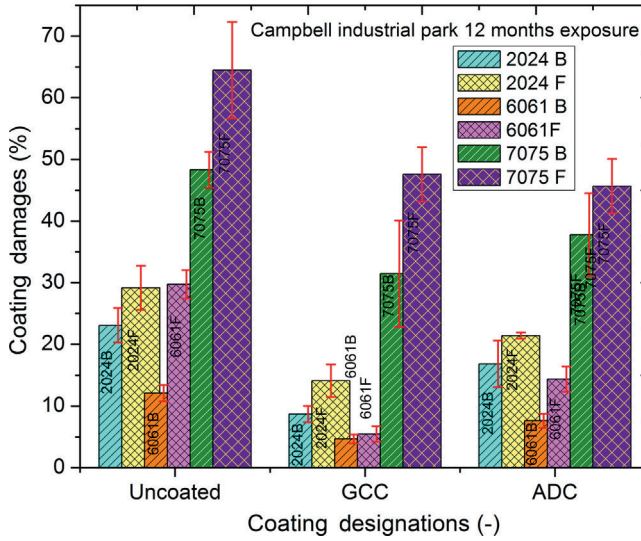


Figure 10.28 VIEEW assisted corrosion damage assesment on coupons after 12 months expsore at Campbell Industrial Park test site.

test coupons while corrosion on coated 7075Al was similar to those on other two test sites (i.e., LA and CIL). In general, the GCC-coated coupons displayed better corrosion protection compared to ADC-coated coupons. Results from the three test sites suggested that GCC and ADC provided corrosion protection over 2024Al and 6061Al. Also, GCC provided better corrosion protection than ADC. However, no significant corrosion protection was imparted to 7075Al by either GCC or ADC.

Figure 10.29 shows a picture of the coupons mounted on the faceplate that were exposed for 12 months period at KLV test sites. Severe corrosion was observed on the uncoated and coated coupons. An attempt to scan the coupons using VIEEW did not succeed due to poor surface contrast on the coupons as a result of severe corrosion. Visual inspection suggested that similar corrosion damages were observed on GCC- and ADC-coated coupons.

10.4.2.2 Analysis after UV light exposure test

Uncoated and coated coupons were mounted on face plates and exposed for 6-month periods at MLO test site in Hawaii situated at 110,000 feet elevation (Figure 10.25). After the exposure periods, no visual damage was observed on the coated specimens. To check the structural integrity, coated coupons were analyzed using Raman spectroscopy. Figure 10.30a,b shows Raman spectra that were collected before and after 6 months of exposure of the coated aluminum alloys. No significant difference was observed in the Raman spectra before and after the exposure, suggesting that the coating remained unaffected by the solar radiation.

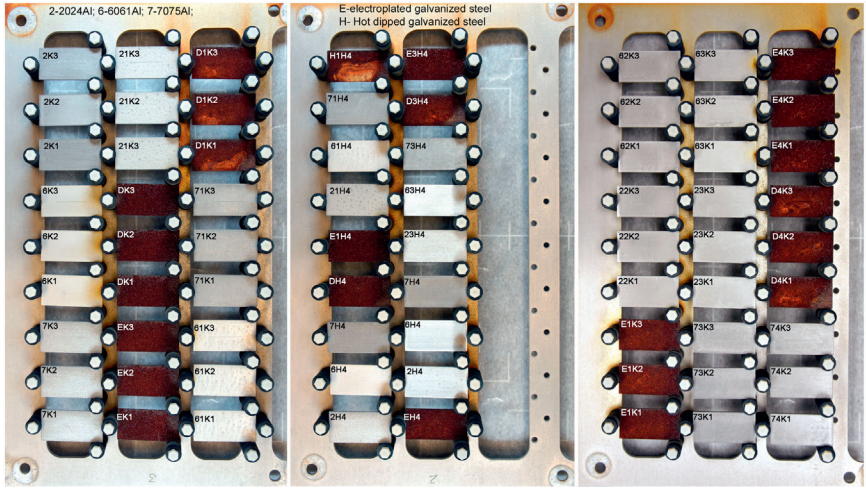


Figure 10.29 Visual inspection of coupons retrieved from Kilauea test site after 12 months of exposure.

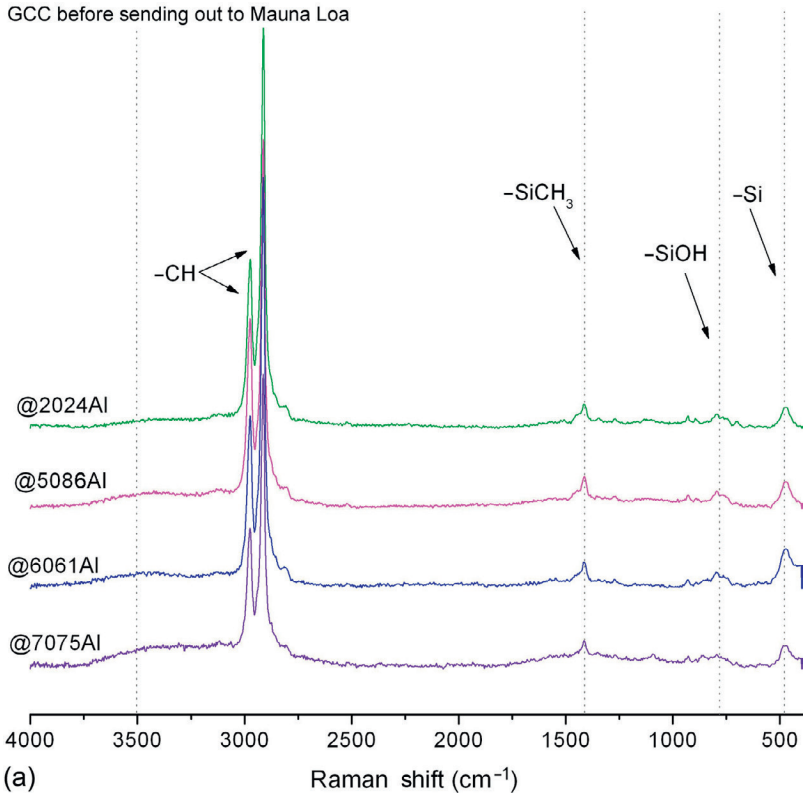


Figure 10.30 Raman analysis of coated coupons. (a) Before exposure;

(Continued)

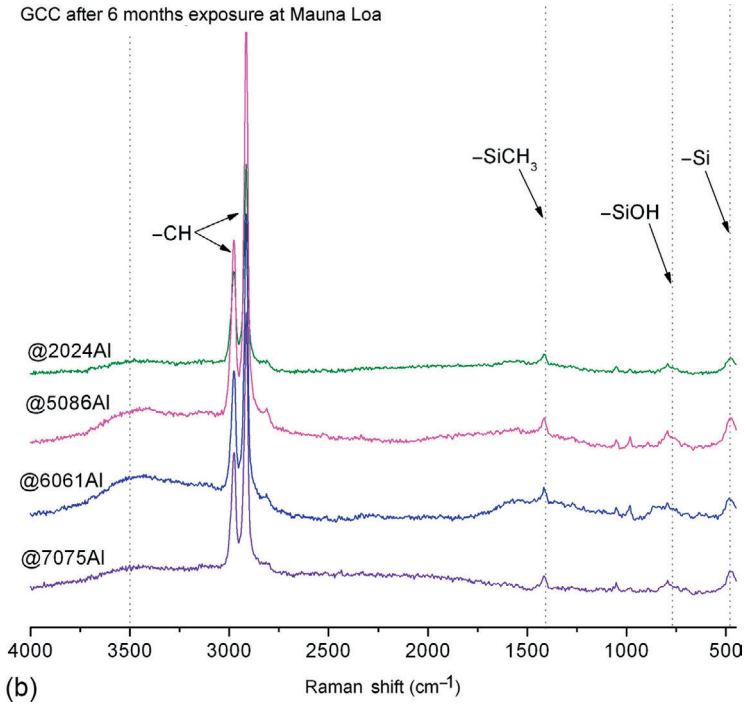


Figure 10.30, Cont'd (b) after 6 months expsoure at Mauna Loa test site.

10.5 Conclusion

Synthesis of GCC through sol-gel route has been achieved. The role of each chemical entity and chemistry behind the smart composition has been described in detail. The liquid precursor to the coating and solidified coating has been characterized with FTIR, Raman, NMR, and X-ray photoelectron spectroscopy. The XPS peak assignments confirmed that the coating composition penetrated the inert oxide layer of the metal and formed covalent bonds with available active functionalities over the metal surface. Thermal studies performed on the liquid precursor and solid material helped in the understanding of the presence of multiple chemical entities in the material, and their degradation patterns confirmed the absence of environmentally hostile chemical constituents. The nanomechanical analysis using nanoindentation helped in analyzing the strength of the coating over the metal surface. The nanoindentation results and morphological studies confirmed that the GCC formed a condensed barrier film over the metal surface. The corrosion barrier strength was evaluated by conducting a series of laboratory and outdoor experiments. The anticorrosion properties of the GCC were compared with the two commercially

available conversion coatings. Based on results from the laboratory and outdoor exposure experiments, it was concluded that the GCC acted as impervious barrier against corrosion similar to the commercial chromate conversion coating and outperformed the commercial nonchromate conversion coating.

Acknowledgment

The patented SiloXel coating (GCC) was developed under US Army sponsored project (DAAE30-03-C-1071). Later, this project was supported by the Office of Naval Research (N00014-09-1-1056) and Office of Secretary of Defense (FA8501-HAW-001 and W9132T-09-2-0022). The authors are grateful for the support from the US Marine Corps (USMC) Corrosion Prevention and Control Program, and the Department of Energy, Oak Ridge National Laboratory (Contract #4000106469) for the project entitled "Pacific Rim Corrosion Assessment and Mitigation Program (PacRimCAMP)." The authors are particularly grateful to Matthew Koch of the USMC; Andrew Sheetz and Forrest Pilgrim of the Naval Surface Warfare Center, Carderock Division; and J. Allen Haynes, Timothy Vane, and Steven Pawel of ORNL.

References

1. Gagro D. Global coatings market to reach USD 107 billion by 2017. Eur Coating J 2012;12:6.
2. Warnon J. The REACH regulation and its impact on the coatings industry. Paint Coat Ind 2005;21(7):106–12.
3. Mikan J. Is the coatings industry heading towards increased chemical regulation in the wake of the EU's REACH regulation? JCT Coat Tech 2009;6(1):26–9.
4. Roth-Evans B. The advantages & drawbacks of the EPS's coating & composites coordinate rule development. In: AESF SUR/FIN conference, Chicago, IL, June 25–29, 2000. http://www.trinityconsultants.com/TechnicalPapers/.
5. de Sousa MPeS C, Oliveira RLF, Mandarino LC. Green chemistry principles and applications in the paint industry. Paint Coat Ind 2014;3:72–84.
6. Anastas PT, Warner JC. Green chemistry theory and practice. New York: Oxford University Press; 1998 p. 129.
7. Hihara LH, Tiwari A. Corrosion protection coatings and methods of making the same. USA Patent US 8,480,929; 2013.
8. Brinker CJ, Hurd AJ, Schunk PR, et al. Review of sol-gel thin film formation. J Non-Cryst Solids 1992;147–148:424–36.
9. Foley RT, Nguyen TH. The chemical nature of aluminum corrosion. J Electrochem Soc 1982;129(3):464–7.
10. Qi Y, Prenzel T, Harriman TA, et al. Investigation of hydrogen concentration and hardness of ion irradiated organically modified silicate thin films. Nucl Instr Meth Phys Res Sec B-Beam Inter Mat 2010;268(11–12):1997–2000.
11. Tiwari A, Zhu J, Hihara LH. The development of low-temperature hardening silicone ceramer coatings for the corrosion protection of metals. Surf Coat Technol 2008;202(19):4620–35.
12. Saure R, Wagner GR, Schlünder EU. Drying of solvent-borne polymeric coatings: II. Experimental results using FTIR spectroscopy. Surf Coat Technol 1998;99(3):257–65.
13. Tejedor-Tejedor MI, Paredes L, Anderson MA. Evaluation of ATR–FTIR spectroscopy as an "in situ" tool for following the hydrolysis and condensation of alkoxysilanes under rich H_2O conditions. Chem Mater 1998;10(11):3410–21.

14. Innocenzi P. Infrared spectroscopy of sol-gel derived silica-based films: a spectra-microstructure overview. J Non-Cryst Solids 2003;316(2–3):309–19.
15. Jiang H, Zheng Z, Wang X. Kinetic study of methyltriethoxysilane (MTES) hydrolysis by FTIR spectroscopy under different temperatures and solvents. Vib Spectrosc 2008;46(1):1–7.
16. Launer PJ. Infra-red analysis of organosilicon compounds: spectra-structure correlations. In: Arkles B, editor. Silicon compounds: register and review. 1987. p. 323, Bristol:Petrarch Systems.
17. Zeitler VA, Brown CA. The infrared spectra of some Ti-O-Si, Ti-O-Ti and Si-O-Si compounds. J Phys Chem 1957;61(9):1174–7.
18. Tiwari A. Applications of some spectroscopic techniques on silicones and precursor to silicones. In: Tiwari A, Soucek MD, editors. Concise encyclopedia of high performance silicones. New Jersey: Wiley Scrivener Press; 2014, p. 177–89.
19. Bersani D, Lottici PP, Casalboni M, et al. Structural changes induced by the catalyst in hybrid sol-gel films: a micro-Raman investigation. Mater Lett 2001;51(3):208–12.
20. Gumula T, Paluszkiewicz C, Blazewicz M. Structural characterization of polysiloxane-derived phases produced during heat treatment. J Mol Struct 2004;704(1–3):259–62.
21. Bantignies J-L, Vellutini L, Maurin D, et al. Insights into the self-directed structuring of hybrid organic–inorganic silicas through infrared studies. J Phys Chem B 2006;110(32):15797–802.
22. Balachandran U, Eror NG. Raman spectra of titanium dioxide. J Solid State Chem 1982;42(3):276–82.
23. Frank O, Zukalova M, Laskova B, et al. Raman spectra of titanium dioxide (anatase, rutile) with identified oxygen isotopes (16, 17, 18). Phys Chem Chem Phys 2012;14(42):14567–72.
24. El Rassy H, Pierre AC. NMR and IR spectroscopy of silica aerogels with different hydrophobic characteristics. J Non-Cryst Solids 2005;351(19–20):1603–10.
25. Taylor RB, Parbhoo B, Fillmore DM. Nuclear Magnetic Resonance Spectroscopy. In: Lee Smith A, editor. The analytical chemistry of silicones, vol. 112. New York: John Wiley & Sons; 1991.
26. O'Hare L-A, Hynes A, Alexander MR. A methodology for curve-fitting of the XPS Si 2p core level from thin siloxane coatings. Surf Interface Anal 2007;39(12–13):926–36.
27. Hanley L, Fuoco E, Wijesundara MBJ, et al. Chemistry and aging of organosiloxane and fluorocarbon films grown from hyperthermal polyatomic ions. 4th ed. Boston, Massachusetts, USA: AVS; 2001, p. 1531–6.
28. Vitanov P, Stefanov P, Harizanova A, et al. XPS characterization of thin $(Al_2O_3)_x(TiO_2)_{1-x}$ films deposited on silicon. J Phys Conf Ser 2008;113(012036):1–4.
29. Saini KK, Sharma SD, Chanderkant M, et al. Structural and optical properties of TiO_2 thin films derived by sol-gel dip coating process. J Non-Cryst Solids 2007;353(24–25):2469–73.
30. Yang WY, Iwakuro H, Yagi H, et al. Study of oxidation of $TiSi_2$ thin film by XPS. Jpn J Appl Phys 1984;23:1560.
31. Tiwari A, Hihara LH. Thermal stability and thermokinetics studies on silicone ceramer coatings: part 1—inert atmosphere parameters. Polym Degrad Stab 2009;94(10):1754–71.
32. Wu KH, Chao CM, Yeh TF, et al. Thermal stability and corrosion resistance of polysiloxane coatings on 2024-T3 and 6061-T6 aluminum alloy. Surf Coat Technol 2007;201(12):5782–8.
33. Marrone M, Montanari T, Busca G, et al. A Fourier transform infrared (FTIR) study of the reaction of triethoxysilane (TES) and bis[3-triethoxysilylpropyl]tetrasulfane (TESPT) with the surface of amorphous silica. J Phys Chem B 2004;108(11):3563–72.
34. Tiwari A, Agee P. Nanoindentation, nanoscratch and dynamic mechanical analysis of high performance silicones. In: Tiwari A, editor. Nanomechanical analysis of high performance materials. New York: Springer; 2014. p. 103–19.
35. Tiwari A, Hihara LH. High performance reaction-induced quasi-ceramic silicone conversion coating for corrosion protection of aluminium alloys. Prog Org Coat 2010;69(1):16–25.

36. Tiwari A, Hihara LH. Nanoindentation and morphological analysis of novel green quasi-ceramic nanocoating materials. Prog Org Coat 2014;77(7):1200–7.
37. Zhang X, Hu L, Sun D. Nanoindentation and nanoscratch profiles of hybrid films based on ([gamma]-methacrylpropyl)trimethoxysilane and tetraethoxysilane. Acta Mater 2006;54(20):5469–75.
38. Etienne-Calas S, Duri A, Etienne P. Fracture study of organic-inorganic coatings using nanoindentation technique. J Non-Cryst Solids 2004;344(1–2):60–5.
39. Aarik J, Aidla A, Sammelselg V, et al. Characterization of titanium dioxide atomic layer growth from titanium ethoxide and water. Thin Solid Films 2000;370:163–72.
40. Chappell JS, Procopio LJ, Birchall JD. Observations on modifying particle formation in the hydrolysis of titanium(IV) tetra-ethoxide. J Mater Sci Lett 1990;9(11):1329–31.

Chapter 11

Conducting Polymers with Superhydrophobic Effects as Anticorrosion Coating

Al de Leon, Rigoberto C. Advincula
Department of Macromolecular Science and Engineering, Case Western Reserve University, 2100 Adelbert Rd., Cleveland, OH, USA

11.1 Introduction

It is practically impossible to prevent corrosion. Thermodynamically, corrosion is an energetically favorable process that converts a high-energy metal into its low-energy oxide form. Corrosion not only poses serious problems economically and industrially, but also endangers human life. While there is no way to stop corrosion activity, the only option is to slow down its growth rate by preventing the aggressive species from reaching the metal surface, or by having a sacrificial material that preferentially reacts in place of the metal.

Intelligent Coatings for Corrosion Control
Copyright © 2015 Elsevier Inc. All rights reserved.

11.2 Corrosion Protection

The natural defense of the metal against corrosion is its oxide layer (or rust, in the case of iron). The oxide layer is formed when the metal reacts with the aggressive species from the electrolyte solution. However, most of the time, the oxide layer is not dense enough to prevent further diffusion of aggressive species into the metal surface. Some corrosion protection methods focus on improving the property of the oxide layer. It has been shown that alloying can drastically increase the density and reduce the porosity of the oxide layer.[1] However, alloying is very expensive and can significantly affect the mechanical properties of the metal. Another approach is to use a coating to separate the metal and the corrosive environment. Coatings can be divided into two general areas: conversion coatings and organic coatings.[2]

11.2.1 Conversion coatings

Conversion coatings are formed by chemically or electrochemically transforming the elemental composition of the metal surface. This coating can function as a stand-alone corrosion protection coating and/or as an adhesion layer for the succeeding organic coating. Two of the most used conversion coatings, especially for iron, are phosphate-based and chromate-based. Phosphate-based coatings involve the immersion of the metal surface in a solution of Ti colloids, and subsequently into a solution containing either zinc phosphate or iron phosphate.[3] The colloids act as nucleation sites for the growth of the phosphate crystals. In the case of zinc phosphate, the immediate metal surface is dissolved into the solution, which decreases the local pH. The decrease in pH drives the equilibrium towards the deposition of $Zn(H_2PO_4)_2$ on the metal surface. In the case of iron phosphate, the iron is first converted into iron oxide and eventually into iron phosphate.[4] Chromate-based coatings, on the other hand, protect the metal by functioning as a physical barrier against aggressive species.[1] They also effectively prevent the transport of ions because they form bipolar membranes with negatively charged outer layers and positively charged inner layers. Chromate-based coatings can also heal themselves when damaged. Electrolytes that fill the defect produce Cr(IV) from the hydrolysis of Cr(III)-O-Cr(IV) from the porous $Cr(OH)_3$ networks. The Cr(IV) is then reduced to Cr(III) hydroxide and adsorbs on the defect sites. However, the problem with chromate-based coatings is that they are highly toxic and carcinogenic to human.[5]

11.2.2 Organic coatings

Organic coatings, on the other hand, can be subdivided into conducting and nonconducting. The basic function of the organic coating is to separate the metal surface from the corrosive environment and to act as a barrier that prevents or slows down

the diffusion of aggressive chemicals and corrosion products. Organic coating can be designed to prevent selectively the diffusion of water, oxygen, ions, or its combination. For the case of nonconducting polymer, the coating itself also functions as an insulating layer that prevents the transfer of electrons from the metal surface into the aggressive species, which is necessary for the formation of the metal oxide or rust. Barrier coatings, such as epoxy, are employed extensively and have been proven to prevent corrosion effectively until coating defects are introduced.[6] Failure starts when pits or holes are formed, usually from mechanical shocks or aging, in the coating. The corrosive species attacks the underlying metal through the defects, increases the exposed surface, and thereby accelerates the corrosion process.[7] The reaction happens not only on the exposed metal surface, but also on the metal underneath the coating. The aggressive species can react with the coating or the metal substrate, which eventually causes cathodic or anodic delamination, respectively. To prevent the delamination of the coating, one can coat the metal with a conducting polymer.

11.3 Conducting Polymer as an Anticorrosion Coating

Conducting (or electro-active) polymers are a special type of polymer with extensive π-electron delocalization along their backbones that give rise to interesting optical properties and allows them to become good electrical conductors (typically when oxidized or reduced).[8] Conducting polymers have been utilized in a wide range of applications because they possess both the electronic properties of semiconductors and the processability of conventional polymers.[2] Having a conjugated backbone and/or a backbone that has low oxidation potential is necessary, but not sufficient for the polymer to be conductive.[9] Conjugation provides the orbital system that allows the charge carriers to move because of the continuous overlapping of the pi-orbitals along the backbone. Most organic polymers, including some conjugated polymers, do not have intrinsic charge carriers. Charge carriers can be introduced by partial oxidation (p-doping) of the polymer chain with electron acceptors or by partial reduction (n-doping) with electron donors.[10] Such doping processes mostly introduce charged defects (e.g., polaron, bipolaron, and soliton) along the polymer backbone.

There are several ways to introduce charge carriers or to dope the conjugated polymer to become conducting, but the most widely used are electrochemical and chemical oxidation/reduction. Electrochemical doping offers advantages over other doping techniques: doping level can be precisely controlled by controlling the amount of current passed, and doping and dedoping processes can be done simply by changing the applied potential.[11] Partial oxidation of the conjugated polymer converts the polymer into its cationic salt form, while partial reduction yields the anionic salt form. Both forms are conducting; however, cationic salt form is more stable.[9]

11.3.1 Coating procedure

Successful use of conducting polymer as an anticorrosion coating depends heavily on how well it can coat the metal substrate. These coatings should have a very good barrier property, are free from any defects where aggressive species can diffuse through, and are strongly adhered on the metal surface to be effective. Next are some of the coating procedures used widely in the industry and in research.

11.3.1.1 Casting-Based Methods

The process of casting involves dissolution of the conducting polymer in a suitable solvent, usually volatile organic solvent or water, and then spreading of the solution over the substrate. Examples include, but are not limited to, dip-coating, drop-casting, spray-coating, and spin-coating. The film of polymer can be obtained after the evaporation of the solvent. This step is commonly followed by an annealing step to make sure that the coating is free of solvent and that the polymer homogenously coats the metal substrate. Coating thickness depends on the polymer concentration, spin speed (for spin-coating), or dipping speed (for dip-coating). One major disadvantage of this technique is that it is hard to find a suitable solvent that can dissolve the conducting polymer.

11.3.1.2 Paint/Resin-Blended Coatings

Alternatives to casting-based methods is to disperse the conducting polymer into a paint or into epoxy or acrylic resins. With this approach, finding a suitable solvent can be bypassed since the conducting polymer can be dispersed in its solid form. In addition, it is possible with this approach to achieve the synergistic effect of the mechanical properties of the paint or resins and the electrical properties of the conducting polymers. This is also the method of choice in expanding the application of conducting polymer to the industrial level, especially in coating large structures.

11.3.1.3 Electropolymerization/Electrodeposition

Electropolymerization is another coating procedure wherein the conducting polymer is formed and deposited from a monomer solution onto a conducting substrate. This is usually the method of choice in coating relatively small areas. Care must be taken in choosing the electropolymerization condition, especially the applied potential and current. The applied potential should be high enough to oxidize the monomer and polymerize it, but low enough not to dissolve the metal or induce corrosion. The electrochemical coating is usually done in an electrochemical cell composed of the substrate to be coated as the working electrode and two inert materials as the counter

electrode (usually platinum) and the reference electrode (usually Ag/AgCl or SCE). The polymerization solution contains the monomer, solvent, and the supporting electrolyte. This method can be further divided into potentiodynamic, galvanostatic, and potentiostatic electropolymerization.

11.3.1.3.1 Potentiodynamic Electropolymerization

Potentiodynamic electropolymerization is characterized by a cyclic regular sweep of potential between the limits of the monomer oxidation and the reduction of the polymerized conducting polymer.[12] The growing polymer film continuously changes from its neutral state to its doped (or conducting) state as the potential is swept back and forth. This process is accompanied by the continuous absorption and desorption of the electrolyte and the solvent to stabilize the growing film.

11.3.1.3.2 Galvanostatic Electropolymerization

Galvanostatic electropolymerization involves the application of constant current to polymerize the conducting polymer at a constant rate. At the beginning of the electropolymerization, the potential rises for a short period and then decreases after a while. It has been explained that the sudden increase in potential is brought about by the formation of the redox-active charged oligomers in front of the electrode. The subsequent decrease in the potential is brought about by the catalytic effect of the charged oligomers to oxidize the monomers. The measured potential also depends on the temperature—the measured potential decreases with decrease in temperature. This can be explained by the decrease of the volume of the solvent, which consequently increases the concentration of the monomer as the temperature decreases.[13]

11.3.1.3.3 Potentiostatic Electropolymerization

Potentiostatic electropolymerization involves the application of constant potential. The rate of polymerization can be controlled depending on the applied potential. This method is similar to the galvanostatic electropolymerization and is different to potentiodynamic electropolymerization because no material is discharged from the deposited film during the coating procedure.

Polypyrrole films polymerized using potentiostatic electropolymerization (and also by galvanostatic electropolymerization) are of dendritic type and have low adhesion strength on the substrate. In contrast, when the polypyrrole is polymerized potentiodynamically, the resulting film is shiny black, adheres strongly on the substrate, and has a smooth and homogenous surface morphology. This has been explained as due to the formation of a large number of equivalent nucleation sites during the growth process.[14] Poly(3-methylthiophene) films, on the other hand, showed better electrical properties (conductivity, charge mobility, number of free carriers, and band gap) when polymerized potentiostatically than when polymerized potentiodynamically.[15]

11.3.2 Mechanism of protection

There are several proposed reasons why conducting polymer effectively prevents corrosion. Next some of established protection mechanisms are discussed.

11.3.2.1 Barrier Protection

Conducting polymer, when coated properly, can separate the metal substrate and the corrosive environment. The absence of pinholes, cracks, and other coating defects guarantees effective protection. Conducting polymer can also be tuned to prevent diffusion of ions, water, and other aggressive species selectively. This protection mechanism is not unique to conducting polymers; that is, even nonconducting polymer can act as a barrier. The coating blocks the diffusion of the ions and corrosion products, thus preventing the establishment of galvanic coupling between the local anodes and cathodes.

11.3.2.2 Ennobling Mechanism

What differentiates conducting polymer from nonconducting polymer is that the conducting polymer can induce the oxidation of metal surface to form its metal oxide and maintain the metal in its passive or "noble" form. In order for this to happen, the polymer should have lower oxidation potential than the metal it is protecting.[16] The formed oxide layer, sometimes called the passive layer, prevents further corrosion by functioning as another layer of barrier against diffusion of aggressive species and as an insulating layer that prevents the flow of electrons. Conducting polymer also improves the passivity of the oxide layer and inhibits the cathodic and anodic delamination of the coating.[17]

11.3.2.3 Polymer is Preferentially Oxidized

This mechanism is similar to the protection mechanism of zinc to iron. Polymer has lower oxidation potential than the metal and therefore the polymer is preferentially oxidized. However, unlike zinc, the oxidized form of the polymer remains insoluble to the corrosive environment and remains intact on the metal surface. The polymer does not dissolve away and therefore protects the metal for a longer time.

11.3.2.4 Self-Healing

The self-healing mechanism was based on the assumption that the conducting polymer releases the doping anions, stored inside the conducting polymer matrix, when a coating defect appears. The doping anions diffuse into the defect site and decrease the

corrosion rate. The passive oxide layer then re-forms between the metal and the conducting polymer brought about by the oxidative capability of the conducting polymer.[16]

11.3.3 Examples of conducting polymers

Interest in conducting polymer research began in the 1970s when films of polyacetylene were found to have semiconductive properties in their reduced form and high electrical conductivity when exposed to iodine vapor.[8,18] Exposure to iodine increased conductivity by more than fifteen orders of magnitude and reached a value in the range of 10^4-10^6 S/cm^2, which is comparable to that of the metals. For anticorrosion applications, however, polyacetylene is rarely used because it degrades in air. Next some of the conducting polymers that have been used as anticorrosion coatings are examined.

11.3.3.1 Polyaniline

Polyaniline (PANI) is considered one of the conducting polymers most used as an anticorrosion coating. It has the following advantages over other conducting polymers: (1) it can be synthesized easily via chemical or electrochemical means, (2) it can be doped and dedoped easily by treatment with aqueous acid and base, (3) it cannot be degraded easily, and (4) the aniline monomer is relatively cheap.[19] First report of its synthesis dates back to 1862[20] and its primary application was as textile dye. It was only during the 1960s that the electrical property of PANI was realized.[21]

PANI can be synthesized either chemically or electrochemically. Chemical synthesis of PANI involves the oxidation of aniline in acidic medium with an oxidizing agent such as ammonium persulfate and tetrabutyl ammonium periodate. [22,23] First report of electrochemical oxidation of aniline was done by Letheby and was later extended to polymerize alkyl, alkoxy, and dimethoxy-substituted aniline.[20] It has been proven that chemical oxidation of aniline yields linear PANI, while electrochemical oxidation of aniline yields a cross-linked polymer network.[24,25] PANI can exist in a number of well-defined oxidation states.[26] PANI can either be fully reduced (leucoemeraldine), fully oxidized (pernigraniline), or partially oxidized (protoemeraldine, emeraldine, nigraniline). None of these are conducting. PANI becomes moderately conducting when the partially oxidized states, specifically the emeraldine base, are protonated by adding an aqueous acid solution.

Recently, Sakhri et al.[27] compared the efficacy of PANI to zinc phosphate as an anticorrosion pigment by mixing each into a chlorinated rubber paint and applying the composite paint onto the carbon steel substrates. They found out that PANI performs better even with a very low loading of 1.5 wt.% compared to zinc phosphate. They also reported that although the coating with PANI pigment absorbs more water, the high electroactivity of PANI increases the alkalinity at the polymer/metal interface, which increases the stability against cathodic disbondment of the coating.

Adhesion of PANI on the metal substrate can easily be improved by combining it with silica sol-gel as demonstrated by Akid et al.[28] The PANI/silica sol-gel composite coating offers both the anticorrosion resistance of PANI and the mechanical property of the silica sol-gel. Even with low PANI/sol-gel ratio, the composite passed the 500 h in the salt spray testing without any visible sign of corrosion or any undercutting (see Figure 11.1). Scanning vibrating electrode technique (SVET) also confirms the self-healing capability of the PANI/sol-gel composite due to the ability of the

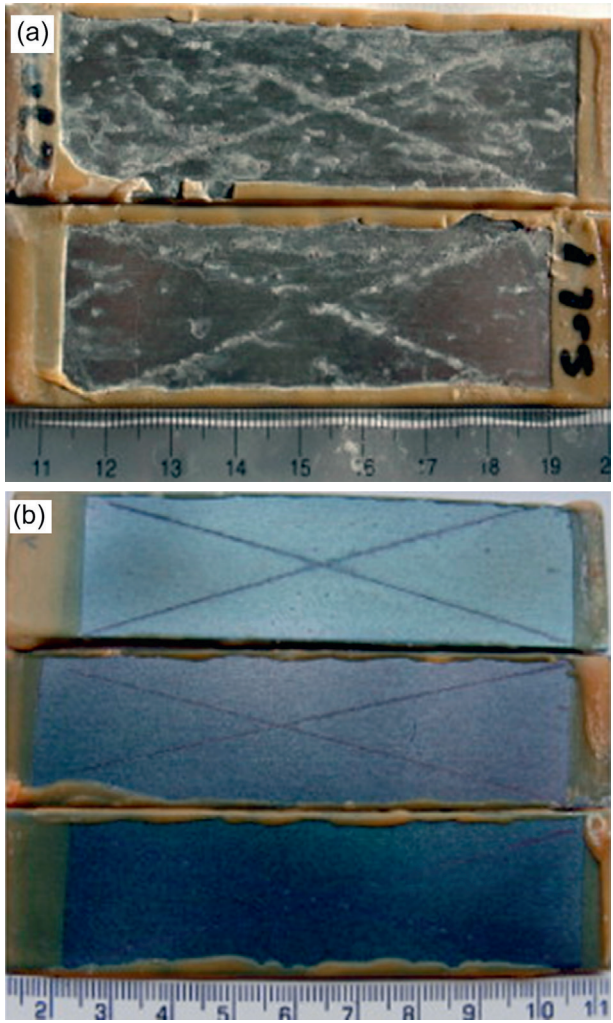


Figure 11.1 Images of the scribed aluminum substrate coated with sol-gel only (a), and PANI/sol-gel (b).[28]

PANI to undergo oxidation-reduction reaction. Finally, they reported that high PANI content (more than 2.5%) could greatly reduce both the corrosion protection and the adhesion of the composite coating.

Titania/PANI/polyvinyl butyral hybrid coating has also been proven to provide superior anticorrosion performance.[29] Radhakrishnan et al. claimed that the effectiveness of this hybrid coating is brought about by (1) the improvement of its barrier properties, (2) the redox capability of PANI, and (3) the formation of p-n junction that prevents the charge transport when the coating is damaged. The developed hybrid coating can release the PANI to heal the defects and prevent catastrophic failure.

11.3.3.2 Polypyrrole

Polypyrrole is an example of heterocyclic conductive polymer. The earliest report of its synthesis was in 1968.[30] Electrochemical synthesis of polypyrrole in sulfuric acid yielded a black conducting film, which is stable under ambient conditions and even at temperatures above 200 °C.[8] Electrical and mechanical properties of the electropolymerized polypyrrole film depend heavily on the counter-ion used. Using perchlorate instead of oxalate can increase its conductivity by 10 times.[31,32] Commercially available polypyrrole films with tosylate counter-ions are highly conductive (15 S/cm) and are very stable under ambient conditions (conductivity only decreased by 15% after 1 year).[33]

To increase the processability of polypyrrole, soluble forms were synthesized by adding flexible side chains along the ring. Addition of various functionalities at the nitrogen can also improve its solubility; however, the conductivity of the resulting film can be reduced drastically because of the strong steric interactions of the substituent at the nitrogen and the hydrogens at the 3- and 4-positions of the adjacent pyrrole rings. The adjacent rings are forced out of the plane, which results in loss of conjugation and ultimately drastic reduction of its conductivity.[34,35]

Recently, Gonzalez et al. studied the electropolymerization of pyrrole in the presence of nitrate and molybdate anions and evaluated the anticorrosion property of the resulting film.[36] They reported that only the film electropolymerized potentiostatically has the strong adhesion on the stainless steel substrate and can completely prevent the pitting corrosion in chloride solution. There are no observable pits or defects on the coating as seen in Figure 11.2 after 12 h of polarization at 0.60 V versus Ag/AgCl in 0.15 M NaCl. It has also been suggested that the presence of nitrate and molybdate provided the polymer coating with fixed negative charge, which prevents the diffusion of the negative chloride ions through the polymer matrix.

Mrad et al. found out that addition of hydroxyquinoline or molybdate anions drastically changes the morphology and the thickness of the electropolymerized

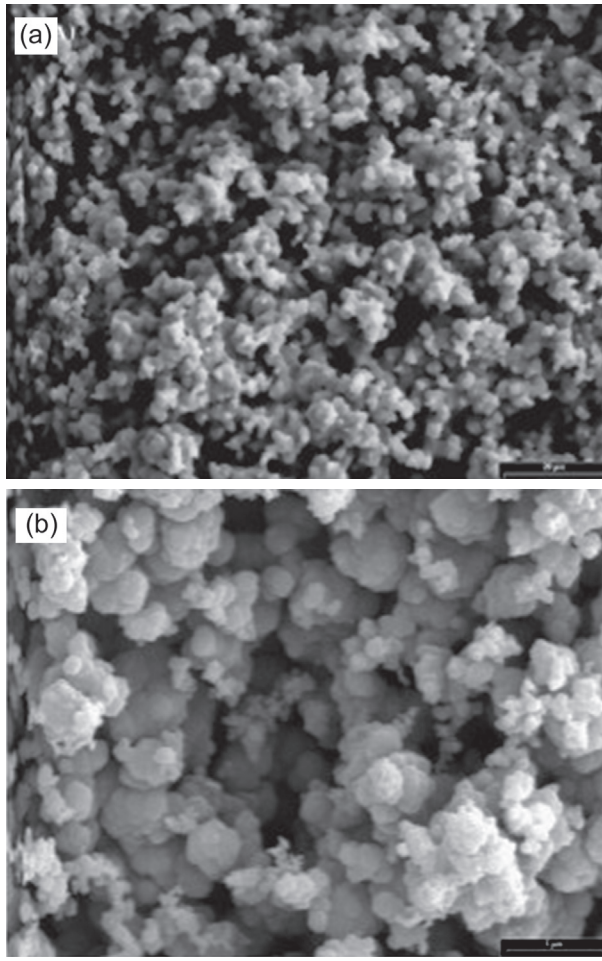


Figure 11.2 SEM images of the surface of the PPy-coated steel electrode after 12 h of polarization at 0.60 V versus Ag/AgCl.[36]

polypyrrole and moderates the resistance of the coating against pitting corrosion of the aluminum alloy.[37] Hybrid coating comprising polypyrrole and titania nanotubes has been recently studied by Herrasti et al.[38] They reported that addition of titania nanotubes increases the polymerization rate of pyrrole because the nanotubes act as nucleation sites. Also, the hybrid coating improved the corrosion resistance of stainless steel by 400 times as compared to the uncoated steel, and by twice as compared to the stainless steel coated with just polypyrrole.

11.3.3.3 Polythiophene

Polythiophene is similar to polypyrrole, but with sulfur in place of the nitrogen in the aromatic ring. Chemical synthesis of polythiophene can be performed by mixing thiophene monomer and sulfuric acid to yield a dark insoluble material or by using a Grignard-type coupling of 2,5-dibromothiophene.[39–41] A highly conducting form of polythiophene is composed of monomers linked at the 2- and 5-positions. Defects like 2,4- and 2,3-linkages reduce the degree of conjugation and, in effect, reduce the conductivity of the resulting film [42] In terms of processability, addition of flexible side chains at the 3- and/or 4-position can improve the solubility of polythiophene. Electropolymerization of thiophene monomer is rarely done because it requires high oxidation potential (2.07 vs. SCE). Instead, thiophene oligomers, such as bithiophenes and terthiophenes with oxidation potentials of 1.05 and 1.31 V versus SCE, respectively, are used.[43]

In terms of anticorrosion property, poly(thiophene) was recently used as part of a polymer alloy that was used as a coating on mild steel.[44] It has been shown that the resulting polymer alloy coating has very high heat resistance and is stable at 380 °C. Also, impedance spectroscopy measurement was used to prove that the coatings were initially capacitance in nature with very high resistance (10^7-$10^8\,\Omega\,cm^2$). These resistances decreased only by two- to threefold after immersion in 3 wt.% NaCl. Leon-Silva et al. recently reported that thermal annealing of poly(3-octylthiophene) can drastically improve its anticorrosion property.[45] This was due to the densification of the conducting polymer coating, through which the diffusion resistance of aggressive species becomes a lot higher.

11.4 Superhydrophobic Coating as an Anticorrosion Coating

Interest in using superhydrophobic coatings developed from its application as a self-cleaning surface and as an antisticking, anticontamination, and anticorrosion coating.[46] A direct measure of the wettability of the surface is the contact angle. Surfaces with a water contact angle of >150° are superhydrophobic, while surfaces with a water contact angle of about 0° are superhydrophilic. In nature, there are many species that exhibit superhydrophobicity, such as leaves of a lotus plant, legs of a water strider, and wings of a cicada.[47]

11.4.1 Theoretical background

In-depth understanding of superhydrophobicity requires the examination of the relationship between the surface energy and the surface roughness and the wettability of the surface. The most basic equation is the Young's equation. Derivation of the

Young's equation starts with the consideration of the sessile drop on an ideal, rigid, homogeneous, flat and inert surface.[47] When a liquid is dropped on a solid substrate, there exists a three-phase contact line where the air, liquid, and solid contacts each other. Young's equation is given by

$$\cos\theta = \frac{\gamma_{SV} - \gamma_{SL}}{\gamma_{LV}}$$

where γ_{SV}, γ_{SL}, and γ_{LV} refer to the interfacial surface tensions between the solid and the gas, the solid and the liquid, and the liquid and the gas, respectively. The θ is called the Young's contact angle (or just contact angle). The value of the contact angle is the result of the thermodynamic equilibrium of the free energies at the solid-liquid-gas phase. If water is used as the liquid, then the surfaces with $\theta < 90°$ are hydrophilic, while surfaces with $\theta > 90°$ are hydrophobic.

Real surfaces are most of the time neither perfectly flat nor homogeneous (see Figure 11.3). Wenzel proposed an equation that considers both the surface roughness and surface energies.[48] The Wenzel equation (11.1) is given as

$$\cos\theta^{W} = r\cos\theta \tag{11.1}$$

where θ^{W} corresponds to the apparent (Wenzel) contact angle, r represents the roughness factor, and θ refers to the Young's contact angle. The basic assumption of the Wenzel's theory is that the liquid follows the roughness of the surface by permeating into the grooves. The roughness factor (r) is defined as the ratio of the actual surface area and the projected surface area. Therefore, for perfectly flat surfaces, the value of $r = 1$, while for rough surfaces the value of $r > 1$. As can be seen from the Wenzel's equation, roughness can enhance the hydrophobicity and hydrophilicity of the surface depending on its surface energy. It has been demonstrated that the apparent contact angle increases as the roughness factor increases, until it exceeds $r = 1.7$, wherein deviations from the Wenzel's theory become apparent.[49] As the surface becomes rougher, it becomes hard for the water to permeate through the grooves mostly because of the packets of air that are trapped. As a result, the liquid droplet rests on a "composite" surface comprising the trapped air and the tip of the surface. Cassie-Baxter proposed that the apparent contact angle is related to the fraction of the surface that is in contact with the liquid as shown in the following equation.

$$\cos\theta^{CB} = f\left(1 + \cos\theta\right) - 1$$

where θ^{CB} corresponds to the apparent (Cassie-Baxter) contact angle, f is the fraction of the solid surface that is in contact with the liquid, and θ refers to the Young's contact angle.[47] Following the Cassie-Baxter equation, we can see that to have a superhydrophobic surface, f should be as small as possible or the surface is comprised of a solid material with very high contact angle.

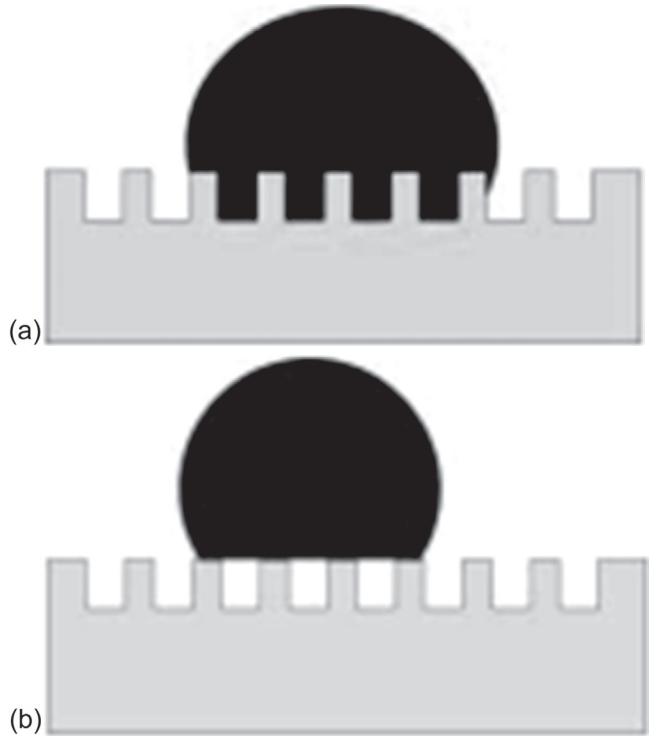


Figure 11.3 Behavior of liquid drop on a rough surface: (a) liquid follows the surface roughness (Wenzel); (b) liquid is suspended on the tip of the surface (Cassie-Baxter).[46]

11.4.2 Fabrication procedures

Most of the procedures in fabricating superhydrophobic surfaces involve either roughening the surface (to make *f* as small as possible) followed by hydrophobization (to make θ as high as possible) or roughening the low-surface energy materials. Next some of the methods that have been used in fabricating superhydrophobic coatings for anticorrosion applications are presented.

11.4.2.1 Chemical Deposition

Chemical deposition involves a reaction wherein the product self-assembles and coats the substrate. It can be further divided into chemical vapor deposition, chemical bath deposition, and electrochemical deposition. Recently, Wang et al. deposited zinc

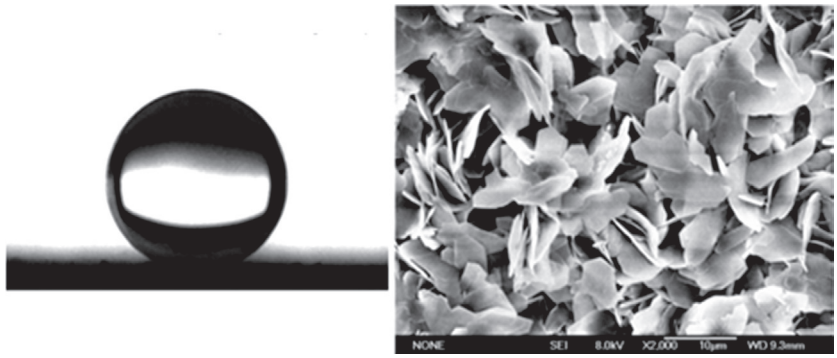


Figure 11.4 Contact angle photographs of zinc coated with superhydrophobic film (left) and surface morphology of the superhydrophobic coating (right).[50]

tetradecanoate film via potentiostatic electrolysis of tetradecanoic acid using zinc as the working electrode.[50] Deposition of $Zn(CH_3(CH_2)_{12}(COO)_2)$ on the zinc surface caused its contact angle to change from 62°±3° for bare zinc to 152.5°±3°. The petal structures (see Figure 11.4) with low surface energy found on the zinc surface caused the superhydrophobicity. They observed a five orders of magnitude decrease in capacitance and dramatic increase in the resistance because of the air trapped between these structures.

Zhang et al. deposited 1*H*,1*H*,2*H*,2*H*-perfluorooctyltriethoxysilane (PTES) onto the roughened surface of titanium to render it superhydrophobic.[51] The rough surface of the titanium was brought about by the formation of anodic titania films grown by potentiostatic anodization. The contact angle before and after the deposition of the fluorinated silane is about 10° and as high as 160°, respectively. The superhydrophobic film prevented the corrosion of the underlying titanium metal even after 90 days of immersion in 3.5 wt.% NaCl. The excellence corrosion resistance was attributed to the trapped air in between the nanopores that limits the water accessibility and the diffusion of Cl^- ions. Carbon fiber can also be used to fabricate superhydrophobic coating on zinc, as demonstrated by Qiu et al.[52] The surface of the zinc substrate was roughened by immersing it into 0.1 M $CuCl_2$ solution. Metallic copper dendritic structure was formed on the zinc surface and became the catalyst for the deposition of the carbon fiber on it. Polarization scans revealed that the current density for the Zn coated with superhydrophobic carbon fiber is 2.83×10^{-11} A/cm^2, while the current density for bare Zn is 3.05×10^{-5} A/cm^2. Similar to previous cases, the trapped air is the one responsible for the six orders of magnitude decrease of current density. Liu et al. showed that coating zinc foil with superhydrophobic coating could decrease the corrosion current to 1.62×10^{-7} versus 1.09×10^{-5} A/cm^2 for the uncoated zinc.[53] The superhydrophobic coating was fabricated by immersing the zinc foil into the hydrolyzed solution of 1*H*,1*H*,2*H*,2*H*-perfluorooctyltrichlorosilane for 5 days. The contact

angle increased from 64° to 151°. SEM image of the zinc surface after immersion in 3% NaCl for 1 day shows the formation of dense film of ZnO structures all over the surface. On the other hand, similar structures are visible only on some areas on the SH-coated zinc immersed in the same solution for 29 days.

11.4.2.2 Colloidal Assemblies

Micro- and nanoparticles can provide surface roughness when deposited on the metal surface. Further treatment of these particles to decrease their surface energy can render the surface with superhydrophobicity. Recently, Weng et al. employed the use of organic fluorinated polyacrylate and methyltriethoxysilane (MTES)-based silsesquioxanes particles to fabricate superhydrophobic coating on cold-rolled steel.[54] Because of the surface roughness provided by the particles (about 400 nm in diameter) and the low surface energy provided by the fluorinated polyacrylate, the contact angle increased from 74.1° for bare steel to 153.2° (Figure 11.5). Potentiodynamic

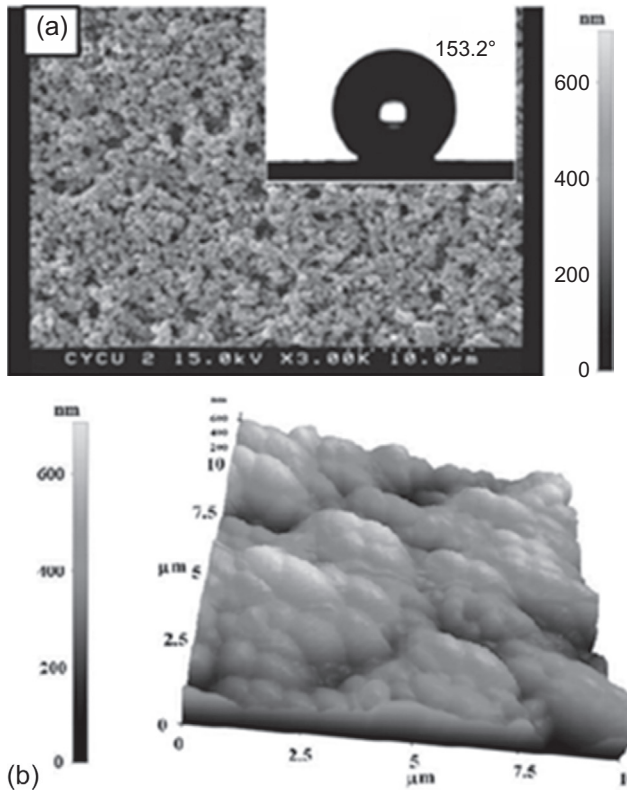


Figure 11.5 SEM image (a) and AFM image (b) of the superhydrophobic coating on CRS. Contact angle photograph in the inset.[54]

measurements revealed that the corrosion rate was decreased from 12.77 mm/year for bare steel to 0.02 mm/year for the coated steel.

Silica colloids can also be used to fabricate superhydrophobic coating on aluminum foil, as demonstrated by Xu et al.[55] They dip-coated the cleaned aluminum substrate with a sol-gel containing 2.5 wt.% silica colloid particles and 0.2 wt.% polystyrene microspheres. The polystyrene microspheres were used as a removable template to control the surface roughness of the coating. After the removal of the polystyrene microspheres by heating the coating at 550 °C, the surface energy of the coating was lowered by chemical vapor deposition of perfluoroalkylsilane. The resulting coating can protect the underlying aluminum foil from acid attack for at least 5 h. Rao et al. coated the copper substrate with a superhydrophobic coating by immersing the substrate into solution containing MTES, methanol, water, and ammonium hydroxide. [56] The gel network was then densified by sintering at 250 °C for 3 h. To test the long term stability of the coating, the coated substrate was immersed in 50% HCl solution. No change in wettability was observed after 100 h of immersion, however, the contact angle decreased from 158° to 146° after 120 h of immersion.

11.4.2.3 Other Methods

Yuan et al. demonstrated that surface energy can be effectively lowered by growing a polymer brush on the roughened surface of copper.[57] A copper surface was roughened by etching in solution of nitric acid and hydrogen peroxide. The vinyl-terminated silane was then self-assembled on the surface and subsequently, fluorinated polymer brush was grown from it. Polymerization for 6 h resulted in very rough surface with contact angle value of 159° (Figure 11.6). The superhydrophobic coating shows 95.3% corrosion inhibition efficiency after immersion in 3.5 wt.% NaCl for 1 day and 91.3% after immersion for 21 days.

Electrospun nanofibers can also be used to fabricate superhydrophobic anticorrosion coating.[58] They showed that superhydrophobic coating can be fabricated by using (heptadecafluorodecylacrylate-co-acrylic acid)-*b*-poly(acrylonitrile) nanofiber. Acetic acid salt spray test was used to test the adhesion of the coating. After the accelerated corrosion test, they saw that the contact angle of the substrate coated with thick nanofiber mat remained unchanged.

11.5 Superhydrophobic Conducting Polymers as Anticorrosion Coatings

Conducting polymer protects the metal from corrosion because aside from being a barrier against aggressive species, it also induces the formation of the passive oxide layer at the metal and coating interface. On the other hand, superhydrophobic

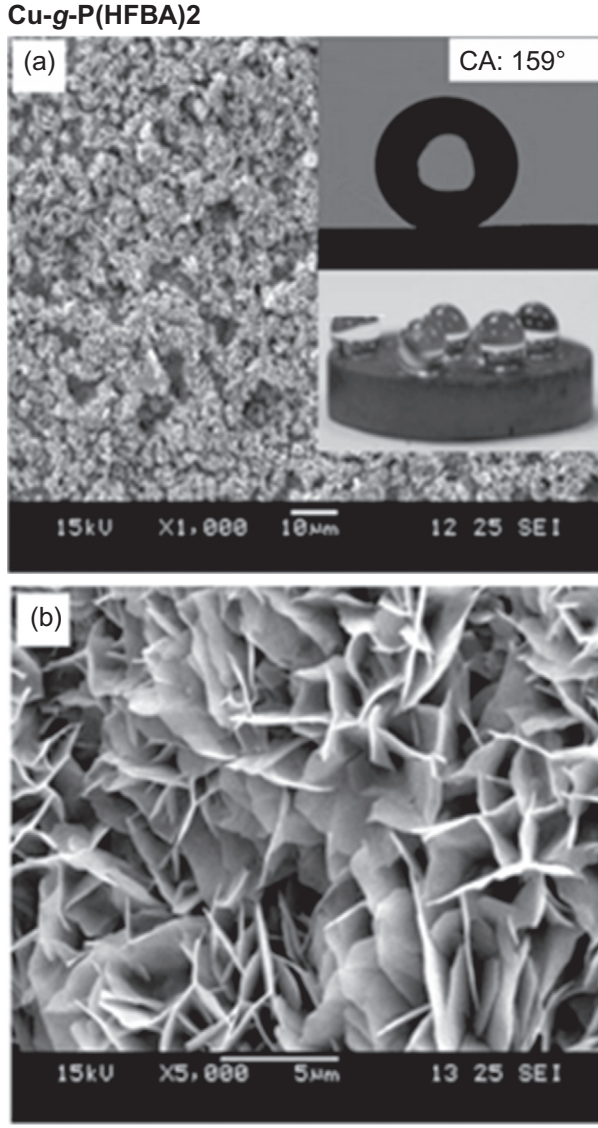


Figure 11.6 SEM images of the coating after the growth of the polymer brush: low magnification (a) and high magnification (b). Insets are the contact angle photographs and optical image of water on the Cu substrate.[57]

coatings protect the underlying substrate by preventing the diffusion of water that acts as a medium for diffusion of aggressive species towards the metal. It is therefore reasonable to think that by making a superhydrophobic coating from a conducting polymer, one can have a coating with enhanced corrosion protection ability.

The fabrication of superhydrophobic coating from conducting polymer has been the focus of interest of some research. Qu et al. demonstrated that superhydrophobic PANI nanowires can be prepared by adsorbing low-surface energy molecules on it.[59] PANI nanowire film was prepared by electropolymerization of aniline in sulfuric acid on titanium-coated silicon wafer with anodized aluminum as the hard template. The resulting PANI was then immersed in solution containing perfluorooctanoic acid and *N*,*N*′-dicyclohexylcarbodiimide in methanol for 2 h. The resulting film has contact angle of 160° ± 1°. Alternative procedure in fabricating superhydrophobic PANI was developed by Zhu et al.[60] They reported a template-free approach to synthesize 3D box-like microstructures of PANI by self-assembly of PANI nanofibers in the presence of perfluorosebacic acid with contact angle of 151.7°. They proposed that the self-assembly of PANI nanofibers to box-like structures was brought about by the cooperation between the perfluorosebacic acid and aniline. Hydrogen bonding and hydrophobic interactions hold the nanofiber together to form the box.

Xu et al. demonstrated that the wettability of rough PPy film can be effectively controlled by applying potential in the presence of fluorinated dopant. [61] Superhydrophobic PPy was fabricated by galvanostatic electropolymerization of pyrrole with perfluorooctanesulfonate as the dopant. The resulting film has contact angle of 152° ± 2°. Applying −0.6 V versus SCE converts the superhydrophobic into its superhydrophilic neutral form. Applying 1.0 V in the presence of perfluorooctanesulfonate converts it back to being superhydrophobic (Figure 11.7).

The number of studies on application of superhydrophobic conducting coating to corrosion is still limited. Weng et al. used nanocasting technique to mold an electroactive epoxy to have morphology derived from *Xanthosoma sagittifolium* leaves.[62] The resulting coating has contact angle of about 155°. Immersion of the coated cold-rolled steel to neutral 3.5% aqueous NaCl for one day shows 86.77% protection efficiency. Increasing the acidity of the NaCl solution reduces the protection efficiency by a minimal amount, with the lowest at 84.66% for pH = 1. Immersion for 7 days in neutral NaCl solution caused the protection efficiency to drop to 86.31%. They also compared the anticorrosion performance of the superhydrophobic electroactive coating to the flat (hydrophobic) electroactive coating. The protection efficiency of the flat (hydrophobic) electroactive coating is just 69.1% and 52.3% after immersion in neutral NaCl solution for 1 and 7 days, respectively. Alternative approach in fabricating superhydrophobic conducting coating involves the combined colloidal assembly and electropolymerization.[63] Monolayer of polystyrene nanospheres ($d = 500$ nm) was deposited by Langmuir-Blodgett-like technique onto the stainless steel. The polystyrene nanoparticles provide the microscale roughness and also act as another layer of barrier against diffusion of aggressive chemicals. Terthiophene-derivative monomer was then electropolymerized on top of it. This provides the low surface energy coating, additional nanometer scale roughness, and anodic protection of the underlying stainless steel substrate. The resulting film has contact angle of 152° ± 1°. Corrosion protection of the resulting film was

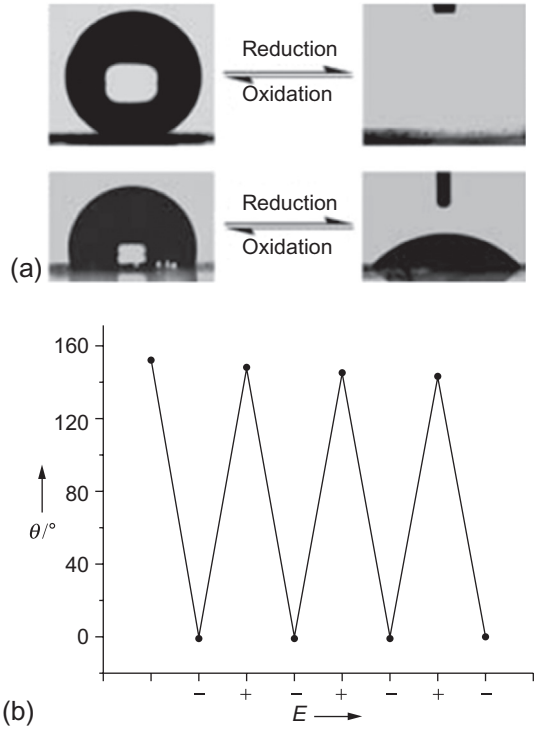


Figure 11.7 Electrical-potential-induced wettability conversion between the doped (oxidized) PPy films and the dedoped (neutral) PPy films (a) and reversible switching between superhydrophobicity and superhydrophilicity (b).[61]

tested by immersing the coated steel in 3.5 M NaCl solution of varying pH and temperature. Potentiodynamic measurements reveal that the superhydrophobic coatings have protection efficiency of 96.6%, 96.9%, 96.2%, and 95.8% for pH1, 7, 14, and $T = 60\,^{\circ}C$, respectively, after immersion for 1 day. Immersion for 7 days reduced the protection efficiency minimally. The superior corrosion protection is brought about by the redox catalytic ability of the conducting polymer and the water-repellant property of the superhydrophobic coating acting synergistically.

11.6 Conclusion

In summary, enhanced corrosion protection can be derived by combining the outstanding redox capability of conducting polymer and water-repellant property of superhydrophobic coatings. The superior performance can be attributed to the high water repellency of the polymer coating combined with its capability to protect the

substrate anodically. The ability of the coating to prevent the adhesion of water is important to its anticorrosion property as water serves as the medium for diffusion of aggressive chemicals and corrosion products, from being absorbed by the coating.

Acknowledgments

The authors gratefully acknowledge funding from the NSF DMR-1304214 and NSF CHE-1247438. Technical support from KSV Instruments (Attension/Biolin Scientific), INFICON Inc, Agilent Technologies, Park Systems, and Optrel GbR is also acknowledged.

References

1. Kendig M, Davenport A, Isaac H. The mechanism of corrosion inhibition by chromate conversion coatings from x-ray absorption near edge spectroscopy (Xanes). Corros Sci 1993;34(1):41–9.
2. Satoh M, Kaneto K, Yoshino K. Electrochemistry preparation of high quality poly(p-phenylene) film. J Chem Soc Chem Commun 1985;22:1629–30.
3. Niu L, Jiang Z, Li G, et al. A study and application of zinc phosphate coating on AZ91D magnesium alloy. Surf Coat Technol 2006;200(9):3021–6.
4. Gorecki G. Iron phosphate coatings—composition and corrosion resistance. Corrosion 1992;48(7):613–6.
5. Balaraju J, Rajam K. Electroless deposition and characterization of high phosphorus Ni-P-Si_3N_4 composite coatings. Int J Electrochem Sci 2007;2:747–61.
6. Talo A, Passiniemi P, Forsen O, et al. Polyaniline/epoxy coatings with good anti-corrosion properties. Synth Met 1997;85:1333–4.
7. Mansfeld F, Kendig M, Tsai S. Evaluation of corrosion behavior of coated metals with AC impedance measurements. Corrosion 1982;38(9):478–85.
8. Chiang C, Fincher C, Park Y, et al. Electrical conductivity in doped polyacetylene. Phys Rev Lett 1977;39:1098.
9. Searson P, Moffat T. Photoelectrochemical systems. Crit Rev Surf Chem 1994;3:29.
10. Macdiarmid A, Chiang J, Richter A. Polyaniline: a new concept in conducting polymers. Synth Met 1987;18:285–90.
11. Kaufman J, Kanazawa K, Street G. Gravimetric electrochemical voltage spectroscopy: in situ mass measurements during electrochemical doping of the conducting polymer polypyrrole. Phys Rev Lett 1984;53:2461–4.
12. Anand J, Palaniapan S, Sathyanarayana D. Conducting polyaniline blends and composites. Prog Polym Sci 1998;23:993–1018.
13. Heinze J, Rasche A, Pagels M, et al. On the origin of the so-called nucleation loop during electropolymerization of conducting polymers. J Phys Chem B 2007;111:989.
14. Otero T, DeLaretta E. Electrochemical control of the morphology, adherence, appearance and growth of polypyrrole films. Synth Met 1988;26:79.
15. Sanchez D, Dıaz R, Herrasti P, et al. Electrogeneration and characterization of poly(3-methylthiophene). Polym J 2001;33:514.
16. Wessling B. Passivation of metals by coating with polyaniline: corrosion potential shift and morphological changes. Adv Mater 1994;6(3):226.
17. Wessling B. Corrosion prevention with an organic metal (polyaniline): surface ennobling, passivation, corrosion test results. Mater Corrosion 1996;47:439.

18. Shirakawa H, Louis E, MacDiarmid A, et al. Synthesis of electrically conducting organic polymers: halogen derivatives of polyacetylene, (CH)*x*. J Chem Soc Chem Commun 1977;16:578–80.
19. Iroh J, Rajagopalan R. Electrochemical polymerization of aniline on carbon fibers in aqueous toluene sulfonate solution. J Appl Polym Sci 2000;76(10):1503–9.
20. Letheby H. On the production of a blue substance by the electrolysis of sulphate of aniline. J Chem Soc 1862;15:161.
21. Mohilner D, Adams R, Argersinger W. Investigations of the kinetics and mechanism of the anodic oxidation of aniline in aqueous sulfuric acid solution at a platinum electrode. J Am Chem Soc 1962;84:3618–22.
22. Scherr E, MacDiarmid A, Manohar S, et al. Polyaniline: oriented films and fibers. Synth Met 1991;41(1):735–8.
23. Epstein A, Ginder J, Zuo F, et al. Insulator-to-metal transition in polyaniline. Synth Met 1987;18:303.
24. Kitani A, Kaya M, Yano J, et al. "Polyaniline": formation reaction and structure. Synth Met 1987;18:341.
25. Vachon D, Angus Jr R, Lu F, et al. Polyaniline is poly-para-phenyleneamineimine: proof of structure by synthesis. Synth Met 1987;18:297.
26. Green A, Woodhead A. Aniline-black and allied compounds. J Chem Soc, Trans 1910;97:2388–403.
27. Sakhri A, Perrin F, Aragon E, et al. Chlorinated rubber paints for corrosion prevention of mild steel: a comparison between zinc phosphate and polyaniline pigments. Corros Sci 2010;52:901–9.
28. Akid R, Gobara M, Wang H. Corrosion protection performance of novel hybrid polyaniline/sol–gel coatings on an aluminium 2024 alloy in neutral, alkaline and acidic solutions. Electrochim Acta 2011;56(5):2483–92.
29. Radhakrishnan S, Siju C, Mahanta D, et al. Conducting polyaniline–nano-TiO_2 composites for smart corrosion resistant coatings. Electrochim Acta 2009;54:1249–54.
30. Dall'Olio A, Dascola G, Varacca V, et al. Electron paramagnetic resonance and conductivity of an electrolytic oxypyrrole [(pyrrole polymer)] black C R Acad Sci Ser. IIc: Chim. 1968;C267:433.
31. Jen K, Miller G, Elsenbaumer R. Highly conducting, soluble, and environmentally-stable poly(3-alkylthiophenes). J Chem Soc Chem Commun 1986;17:1346–7.
32. Yamamoto T, Morita A, Miyazaki Y, et al. Preparation of π-conjugated poly(thiophene-2,5-diyl), poly(*p*-phenylene), and related polymers using zerovalent nickel complexes. Linear structure and properties of the π-conjugated polymers. Macromolecules 1992;25:1214.
33. Naegele D, Bittihn R. Electrically conductive polymers as rechargeable battery electrodes. Solid State Ionics 1988;983:28.
34. Sato M, Tanaka S, Kaeriyama K. Poly(3-dodecyl-2,5-thiophenediyl), a soluble and conducting polythiophene. Makromol Chem 1987;188:1763.
35. Kanazawa K, Diaz A, Geiss R, et al. 'Organic metals': polypyrrole, a stable synthetic 'metallic' polymer. J Chem Soc Chem Commun 1979;19:854–5.
36. Gonzalez M, Saidman S. Electrodeposition of polypyrrole on 316L stainless steel for corrosion prevention. Corros Sci 2011;53:276–82.
37. Mrad M, Dhouibi L, Montemor M, et al. Effect of doping by corrosion inhibitors on the morphological properties and the performance against corrosion of polypyrrole electrodeposited on AA6061-T6. Prog Org Coat 2011;72:511–6.
38. Herrasti P, Kulak A, Bavykin D, et al. Electrodeposition of polypyrrole–titanate nanotube composites coatings and their corrosion resistance. Electrochim Acta 2011;56:1323–8.
39. Meyer V. Ueber den Begleiter des Benzols im Steinkohlentheer. Chem Ber 1883;16(1):1465.
40. Yamamoto T, Sanechika K, Yamamoto A. Preparation of thermostable and electric-conducting poly(2,5-thienylene). J Polym Sci Polym Lett Ed 1980;18:9–12.
41. Lin J, Dudek L. Synthesis and properties of poly(2,5-thienylene). J Polym Sci Polym Lett Ed 1980;18:2869.

42. Roncali J, Lemaire M, Garreau R, et al. Enhancement of the mean conjugation length in conducting polythiophenes. Synth Met 1987;18:139.
43. Diaz A, Crowley J, Bargon J, et al. Electrooxidation of aromatic oligomers and conducting polymers. J Electroanal Chem 1981;121:355–61.
44. Palraj S, Selvaraj M, Vidhya M, et al. Synthesis and characterization of epoxy–silicone–polythiophene interpenetrating polymer network for corrosion protection of steel. Prog Org Coat 2012;75:356–63.
45. Leon-Silva U, Nicho M, Gonzalez-Rodriguez J, et al. Effect of thermal annealing of poly(3-octylthiophene) films covered stainless steel on corrosion properties. J Solid State Electrochem 2010;14(6):1089–100.
46. Li X, Reinhoudt D, Crego-Calama M. What do we need for a superhydrophobic surface? A review on the recent progress in the preparation of superhydrophobic surfaces. Chem Soc Rev 2007;36:1350–68.
47. Yan Y, Gao N, Barthlott W. Mimicking natural superhydrophobic surfaces and grasping the wetting process: A review on recent progress in preparing superhydrophobic surfaces. Adv Colloid Interface Sci 2011;169:80–105.
48. Wenzel R. Resistance of solid surfaces to wetting by water. Ind Eng Chem Res 1936;28:988–94.
49. Jopp J, Grull H, Yerushalmi-Rozen R. Wetting behavior of water droplets on hydrophobic microtextures of comparable size. Langmuir 2004;20:10015.
50. Wang P, Zhang D, Qiu R, et al. Super-hydrophobic film prepared on zinc as corrosion barrier. Corros Sci 2011;53:2080–6.
51. Zhang F, Chen S, Dong L, et al. Preparation of superhydrophobic films on titanium as effective corrosion barriers. Appl Surf Sci 2011;257:2587–91.
52. Qiu R, Zhang D, Wang P. Superhydrophobic-carbon fibre growth on a zinc surface for corrosion inhibition. Corros Sci 2013;66:350–9.
53. Liu H, Szunerits S, Xu W, et al. Preparation of superhydrophobic coatings on zinc as effective corrosion barriers. ACS Appl Mater Interfaces 2009;1:1150–3.
54. Weng C, Peng C, Chang C, et al. Corrosion resistance conferred by superhydrophobic fluorinated polyacrylate–silica composite coatings on cold-rolled steel. J Appl Polym Sci 2012;126:E48–55.
55. Xu Q, Wang J. A superhydrophobic coating on aluminium foil with an anti-corrosive property. New J Chem 2009;33:734–8.
56. Rao A, Latthe S, Mahadik S, et al. Mechanically stable and corrosion resistant superhydrophobic sol–gel coatings on copper substrate. Appl Surf Sci 2011;257:5772–6.
57. Yuan S, Pehkonen S, Liang B, et al. Superhydrophobic fluoropolymer-modified copper surface via surface graft polymerisation for corrosion protection. Corros Sci 2011;53:2738–47.
58. Grignard B, Vaillant A, de Coninck J, et al. Electrospinning of a functional perfluorinated block copolymer as a powerful route for imparting superhydrophobicity and corrosion resistance to aluminum substrates. Langmuir 2011;27:335–42.
59. Qu M, Zhao G, Cao X, et al. Biomimetic fabrication of lotus-leaf-like structured polyaniline film with stable superhydrophobic and conductive properties. Langmuir 2008;24:4185–9.
60. Zhu Y, Li J, Wan M, et al. 3D-boxlike polyaniline microstructures with super-hydrophobic and high-crystalline properties. Polymer 2008;49:3419–23.
61. Xu L, Chen W, Mulchandani A, et al. Reversible conversion of conducting polymer films from superhydrophobic to superhydrophilic. Angew Chem Int Ed 2004;44:6009–12.
62. Weng C, Chang C, Peng C, et al. Advanced anticorrosive coatings prepared from the mimicked *Xanthosoma sagittifolium*-leaf-like electroactive epoxy with synergistic effects of superhydrophobicity and redox catalytic capability. Chem Mater 2011;23:2075–83.
63. de Leon A, Pernites R, Advincula A. Superhydrophobic colloidally textured polythiophene film as superior anticorrosion coating. ACS Appl Mater Interfaces 2012;4:3169–76.

Chapter 12

Smart Protection of Polymer-Inhibitor Doped Systems

Carmina Menchaca-Campos*, Jorge Uruchurtu*, Miguel Ángel Hernández-Gallegos†, Alba Covelo‡, Miguel Ángel García-Sánchez§

**Centro de Investigación en Ingeniería y Ciencias Aplicadas, Universidad Autónoma del Estado de Morelos, Av. Universidad 1001, Col. Chamilpa, 62209 Cuernavaca, Morelos, México*

†Facultad de Ingeniería, Universidad Nacional Autónoma de México, Av. Universidad 3000, Copilco Universidad, Coyoacán, 04510 Ciudad de México, D.F.

‡Facultad de Química, Universidad Nacional Autónoma de México, Av. Universidad 3000, Copilco Universidad, Coyoacán, 04510 Ciudad de México, D.F.

§Depto. Química, Universidad Autónoma Metropolitana, Av. San Rafael Atlixco No 186, Iztapalapa, Vicentina, 09340 Ciudad de México, D.F.

12.1 Introduction

Every corrosive protection effort may be lost or become more costly if the mechanisms are effective but not efficient and/or applied in an area ill-prepared or under nonideal conditions. Traditional coatings are designed to passively protect the substrate to which they are applied by providing a barrier between the surface and the environment. More advanced coatings contain a small percentage of a functional additive that enables the coatings to provide some increased functionality. Other coatings have some functionality incorporated into the resin itself. The functionality in these materials is constant and is determined solely by the initial coating formulation.[1]

Smart coatings go much further, and, in order to be considered intelligent, they must be able to sense a change in conditions in the environment and respond to that

Intelligent Coatings for Corrosion Control
Copyright © 2015 Elsevier Inc. All rights reserved.

change in a predictable and noticeable manner. Challener states that "smart coatings combine functionality with design to provide a system that offers simultaneous multifunctional and multidimensional beneficial effects. They offer over and above the normal functions of a coating, specifically protection and decoration, and also some unique, unusual functional properties which involve the intelligent selection between various types of responses to a given environmental stimulus."[1]

So it is necessary to develop new "avant-garde" design schemes to achieve effective protection. Currently, a smart coating applied using nanotechnology promises solutions to this problem and benefits everything from new applications to existing structures under more efficient solution. Storage of the inhibitor is based on the use of particles, which can play the role of storage devices for corrosion inhibitors, adsorbed inside.[2–5]

One of the most employed methods to mitigate corrosion is the use of inhibitor substances that, when added in small amounts to an aggressive media, reduce markedly the corrosion rate. In terms of corrosion, inhibitors occupy a special place because of their specific protection and widespread application. Most inhibitor applications are in aqueous medium (natural water, acid solutions for pickling) and partial water systems (primary and secondary processing of petroleum and refining plants), and protection from atmospheric corrosion.

When selecting inhibitors, it should be taken into account what metal is to be protected, in which environment it is to be exposed (temperature, pressure, flow, etc.), and also its efficiency, availability, toxicity, and cost-effectiveness. Various mechanisms of action are considered, such as interface inhibition, electrolyte layer inhibition, membrane inhibition, and passivation.

A new generation of anticorrosion coatings that respond to changes in the environment has sparked great interest from material scientists, because corrosion is one of the most important causes of destruction of structures that involves the loss of material, and prevention is paramount in protecting investments. This type of protection is intended to retard corrosion of the metal substrate and/or control it. These anticorrosion coatings possess both passive matrix functionality and active response to changes in the local environment. Corrosion involves metal loss, and active corrosion protection aims to restore material properties (functionality) when the passive coating matrix is broken and corrosion of substrate has started. The coating has to release the active and repairing material substance within a short time after the coating integrity has been breached. This acts as a local trigger for the mechanism that heals the defect.

The oldest types of self-repairing coatings are polymer-based coatings. The concept of these coatings is as follows. Micrometer-scale containers, filled with monomers similar in nature to the polymer matrix and an appropriate catalyst or ultraviolet (UV)-sensitive agent to initiate the polymerization of the monomer when released at the damaged spot of the polymer coating, are incorporated inside the coating matrix. When these microcontainers become mechanically deformed, they release the monomer and catalyst and thus seal the defect.[3,4] Repair of macroscopic adhesion defects

formed throughout the service life of composites, was carried out by filling hollow fibers with a polymer resin; these fibers would then fracture under excessive loading of the structure.[5,6] The sealing component could be different methyl compounds for fixing adhesion of the polypropylene matrix.[7,8] Polyelectrolyte-based aqueous poly-(L-lysine) poly-(ethylene glycol) was employed as the self-healing agent in an oxide-based tribo-system.[9] The barrier properties of a damaged coating can also be recuperated by a simple blocking of the defects with insoluble precipitates.

Another approach to hybrid self-healing coatings is based on the use of inhibitors that can be released from the coating system. However, the direct introduction of inhibitor components into protective coatings very often leads to the deactivation of a corrosion inhibitor and degradation of the polymer matrix.[8] To overcome this, several systems entrapping the inhibitor and preventing its direct interaction with the coating matrix have been developed. One quite simple approach to inhibitor entrapment is based on the complexation of organic molecules by cyclodextrin[9]; another is based on the use of oxide nanoparticles, which can play the role of nanocarriers for corrosion inhibitors adsorbed on their surface. Immobilization of Ce^{3+} ions on the surface of ZrO_2 nanoparticles was achieved during the synthesis of a nano-sol by the controlled hydrolyzation of the precursor with Ce ions in an aqueous solution.[10] The inhibition through inorganic ions can also be incorporated by exchangeable ions associated with cation and anion-exchange solids. Ca(II) and Ce(III) cation-exchanged bentonite anticorrosion pigments are prepared by the exhaustive exchange of naturally occurring bentonite.[11] For anion-exchange solids, the release of inhibitor anions can be provoked by aggressive corrosive chloride ions.[12,13]

The most important aspect in the design of new active coatings is to make nanocontainers that have good compatibility with the matrix components, that can encapsulate and maintain the active material, and that possess a shell with permeability properties that can be controlled by external stimuli. In order to develop functionalized micro- and nanocontainers, several properties in the shell structure and composition have to be combined.

Recently, the goal of coating technology is to formulate *smart* coatings as structured systems providing selective response to physical, physicochemical or biochemical external stimulus such as temperature, stress, strain, and corrosion. Their smart response is a combination of coating properties and the incorporation of unique nanotechnology material properties.[14] Ideally, a smart corrosion-inhibitor system coating will generate or release an inhibitor only when demanded and required by the corrosion initiation process. In this respect, different types of smart coatings have been proposed: paints (in particular waterborne without solvents detrimental to the environment) formulated with conductive polymers, self-healing coatings with ion exchange, and more.[1,10,14]

Depending on the nature of the "smart" materials (e.g., polymers, nanoparticles, or hybrids) introduced into the container shell, various stimuli can induce reversible

and irreversible shell modifications. The different responses that can be observed vary from fine effects like tunable permeability, to more profound ones like total rupture of the container shell.[13,14]

Several approaches have been developed so far to fabricate micro-, meso-, and nanocontainers.[11,13] One approach is based on the self-assembly of lipid molecules or block copolymers into spherically closed bilayer structures.[13–16] These relatively unstable structures then undergo cross-linking to stabilize the nanocontainer shell. A second approach is to use hyperbranched polymers as nanocontainers.[17–19] However, in this case the particle preparation is a rather costly and time-consuming procedure, limiting any possible applications and scaling up. A third procedure involves suspension and emulsion polymerization around latex particles to form a cross-linked polymer shell. This method allows the obtaining of hollow nanoshells from as small as 100 nm in a simple one-step procedure.[18,19]

The approaches described above provide the general route for shell formation. The next step in the fabrication of nanocontainers suitable for self-repairing anticorrosion coatings is to make the nanocontainer shell sensitive to the corrosion process itself. Nanocontainers with a shell that possesses controlled release properties can be used to fabricate a new family of active coatings that can respond quickly to changes in the coating environment or the coating's integrity.

The release of corrosion inhibitors encapsulated within nanocontainers is triggered by the corrosion process, which prevents the spontaneous leakage of the corrosion inhibitor out of the coating. Moreover, if different types of nanocontainers loaded with the corresponding active agents are incorporated simultaneously into a coating matrix, the coating can act in several different ways (e.g., antibacterial, anticorrosion, and antistatic).

This task can be achieved by employing the layer-by-layer (LbL) assembly approach in the formation of the nanocontainer shell.[19–21] These polyelectrolyte films are able to change their chemical composition with pH because the degree of dissociation of them is pH sensitive. The films can be made to be richer in one polymer than in the other by working in a pH regime in which one of the polymers is weakly charged, while the other is strongly charged. Active species deposited as a component of this kind of film are able to be released on demand. The shell of the resulting containers is semipermeable and sensitive to a variety of physical and chemical conditions (mechanical impact, change in pH) in the surrounding medium, enabling it to regulate the release of the entrapped inhibitor species. Nanocontainers able to regulate the storage/release of an inhibitor can thus be constructed with nanometer-scale precision.

Another novel and seldom reported[22,23] approach is to use polymer nylon pellets or electrospun fibers and its properties as storage/carriers in combination with inhibitors and conventional coatings as a possible corrosion protection smart coating system.

12.2 Rebar Concrete Application

A simple approach was attempted in rebar concrete to inhibit corrosion that happens when steel is in contact with the electrolytic medium that promotes their physical and chemical degradation, and also affecting its practical application. In rebar concrete for construction developments, steel used plays an important role as structural element of buildings and civil works. One way to inhibit the chemical degradation of steel in concrete consists in absorbing an inhibitor onto "activated" nylon particles acting as storage/carrier, which are added as aggregates in the concrete mixture.

Reinforced concrete is exposed during their lifetimes to aggressive environments and sometimes is subject to stress, which attacks concrete or steel reinforcement. Concrete is alkaline with a 12-14 pH, promoting a protective passive layer preventing corrosion from occurring. The passive film is not indestructible, and it can be damaged by chemical and/or mechanical breakdown. Proper design and preparation of concrete would guarantee long-term durability to the system. Nevertheless some damage may occur during the service life and preventive measures are often used to further protect the structures. These include the use of cathodic protection, chloride removal, penetrating sealers, preventive and curative inhibitors, and coatings to control rebar corrosion and the improvement of the mechanical properties of concrete. These will extend the service life of the structure.

In recent years, the use of inhibitors has increased significantly being these chemical substances that decrease the corrosion rate of rebar steel in the corrosion system. The inhibitors are chemical substances organic or inorganic, which act under different concentrations and mechanisms, diminishing corrosion. Organic inhibitors may form a barrier over the metal surfaces and can affect the anodic, the cathodic, or both reactions. Inorganic inhibitors promote oxidation and formation of a protective passive film. A good review on the subject has been presented recently.[24,25]

Concrete modification by using polymeric materials has been studied for the last four decades. Nevertheless, in certain applications these kinds of materials had failed, and it is necessary to use other complex and expensive technologies for specific applications. In general, the reinforcement with fibers or particles of brittle building materials has been known for long time, as well as, synthetic materials as polyvinyl alcohol, polypropylene, polyethylene and polyamides.[26–29]

Micro- or macro-synthetic nylon fibers have been in use since early 1980s for secondary temperature-shrinkage reinforcement in concrete. In the microcase monofilaments and fibrillated shapes are used. Because these fibers are very thin, their number per weight (fiber count) is in the range of millions per kilogram of concrete.[30]

Several improvements can occur when adding micro-synthetic nylon fibers to the concrete, typically at dosage rates of 0.6-0.9 kg/m^3 of mixture:

a) Reduction in cracking, plastic shrinkage cracking, and plastic settlement. The reduction in cracking and settlement prior to setting produces concrete with improved long-term durability.
b) Improvement in high impact resistance by lowering the extent of stretching and pull-out of the fibers which occurs at large strains, resulting in failure of the matrix at relatively low loads.
c) Creation of a 3-D network of reinforcement with superior fiber/mix bonding. The integration of fibers disperses stress evenly throughout the reinforcement network, modifies the micro-macro cracking mechanism and enhances durability.
d) Reduction the number of bleeding channels and thus the bleed, resulting in less water migration to the concrete surface. This action helps to control the water/cement ratio and produces a concrete with less permeability, greater strength, and improved toughness.

The materials used so far to reinforce the concrete matrix are adhering only by physical interactions and not by primary chemical bonds. Other procedures used such as chemical attack or thermal treatment, are costly and time consuming.

The aggregates in concrete take up 75% of the total volume: clay, lime, organic matter or chemical salts, and so on. ASTM standards define the shape and size of aggregates.[28] Concrete manufactured from Portland cement is the most utilized due to its range of applications (structures, blocks, pavement, etc.) and the resulting properties including durability and plasticity.

Generally, simple concrete shows high compressive but low tensile strength. Thus, it is necessary to add various aggregates. The problem of adhesion of added polymers has already noticed. The polymer is surrounded by sand and gravel, facilitating the development of cracks when subjected to mechanical stress. Formation of cracks along with alternative mechanisms of polymer response under load, have been thoroughly reviewed.[31]

Improvement of concrete by using polymeric materials has been attempted before, Given the properties of concrete without such a reinforcement, the main objectives of adding them are high compressive and tensile strength, high impact and abrasive resistance, service in adverse environments (wind, moisture, etc.), lower weight, and lower costs.[32,33]

The reinforced concrete structural element (embedded steel) is gradually facing electrolyte medium leakage due to contaminated water, which will foster corrosion and a long-term metal pulverization, mechanically unprotecting the structural element. Therefore, there is currently an arduous work for development

of new construction material, new coatings, or the use of new inhibitors, to monitor the corrosion in the different structural elements and thus avoid major economic losses.

The possibility of using construction materials that decrease the embedded steel corrosion and harmonize together with this particular structure without affecting it mechanically has set the pace to study the use of polymer aggregates as a "smart inhibitor storage/carrier system" (smart system). An alternative explored was to activate the polymer surface by the use of gamma radiation or chemical attack, to have at least a chance to make it compatible with the brittle concrete matrix, and to "pack" the inhibitor within the cavities formed.

The smart system will be able to release the corrosion inhibitor at the time when oxidation reactions do occur; the inhibitor will move due to capillary action or other through the porous structure till reaching the metal to be protected and electrochemically reduced or, alternatively, promoting oxidation and passive film formation. In both cases it is estimated that with the proper release of the inhibitor and timely transportation of it, the steel corrosion rate will be significantly reduced. Also the presence of polymeric material within the concrete mixture as an additive, improves the mechanical properties of the concrete.[32]

Figure 12.1 compares the compression resistance (%) as a function of concrete curing time, for concrete slabs without ($f_c = 219.91\,kg/cm^2$) and with nylon 6,6 pellets ($f_c = 225.40\,kg/cm^2$) as additives in the concrete matrix. An improvement of the mechanical properties of concrete was reached with the addition and compares favorably with reported results.[33]

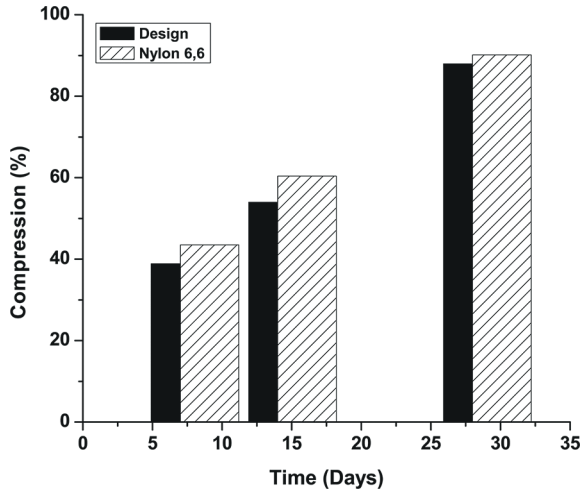


Figure 12.1 Concrete compression resistance with and without nylon 6,6 for the curing period.

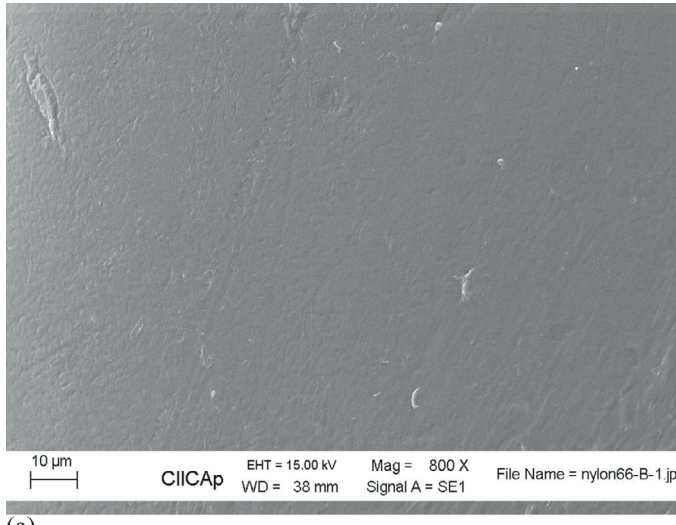
12.2.1 Polymer selection

The material additive used should not corrode, and it has to be able to store the inhibitor and should be compression resistant in order to harmonize with the concrete structure. With these considerations, the use of a polyamide such as nylon 6,6 is proposed. The commercial presentation of nylon may be fibers, blocks, bars, or pellets.

The polyamide has a smooth surface, for such reason the surface has to be exposed to chemical (different NaOH concentrations) or gamma irradiation (argon or air atmospheres) activation so it can be able to turn the surface porous or rugged to promote the adsorption of the corrosion inhibitor, as seen in Figure **12.2**. The effect of chemical treatment in a sodium hydroxide solution at 80 °C and gamma irradiation are clearly visible over the surface of nylon 6,6 pellets, rendering them active forming mesopores over the surface.[23] The detailed procedure has been reported elsewhere.[34–36]

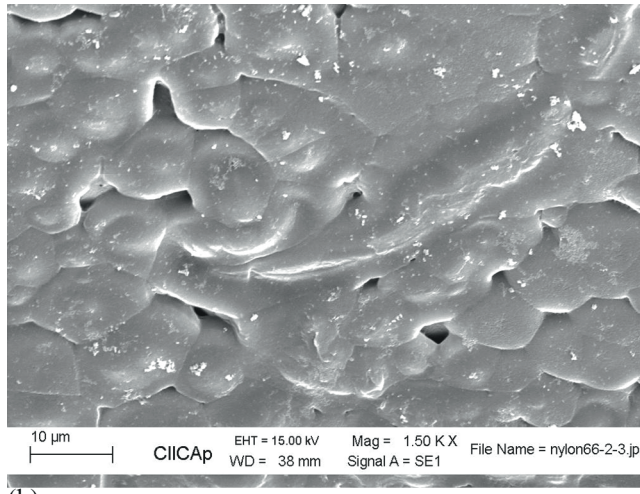
Adsorption of the passivation inhibitor onto the nylon 6,6 pellets active surface is obtained filling up the nylon pellets, in acetone with up to 8% (80 mg/ml) of ferric nitrate [$Fe(NO_3)_3$]. Activated nylon 6,6 pellets are immersed in cycles to achieve maximum particles weight gain by the presence of the inhibitor.[23] The formation of seals on the ends of the activated polymer is based on the reaction between the inhibitor loaded and the transition Fe metal ions that brings insoluble complexes of ferric nitrate distributed at the ends of the smart system acting as seals or stoppers, forming in this way the smart system.

Surface roughness of nylon 6,6 is determined after activation through image processing and fractal dimension analysis.[37–42] Figure **12.3** presents the fractal dimension

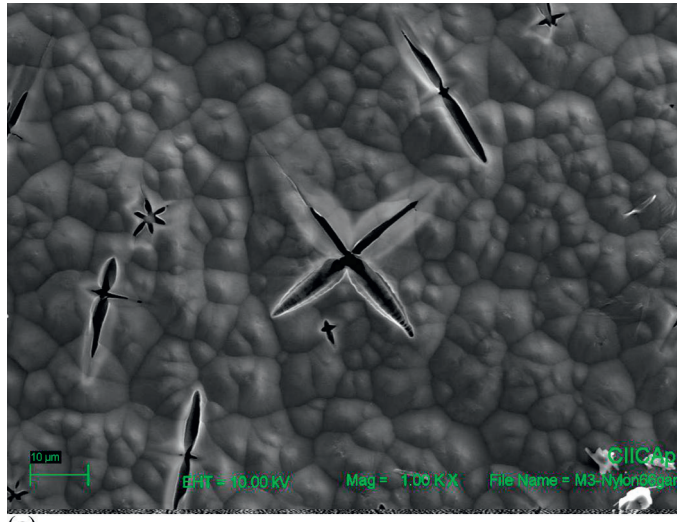


(a)

Figure 12.2 Active nylon 6,6 (a) blank, under



(b)



(c)

Figure 12.2, cont'd (b) chemical, and (c) gamma irradiated treatment.

for gamma irradiated as a function of dose and chemical treatment as a function of time of immersion samples, and the roughest surface conditions were obtained. Chemically treated pellets were selected for inhibitor adsorption and further rebar concrete additives.

The choice of the $Fe(NO_3)_3$ passivation inhibitor concentration is performed based on a combination of different parameters such as inhibitor activity for corrosion

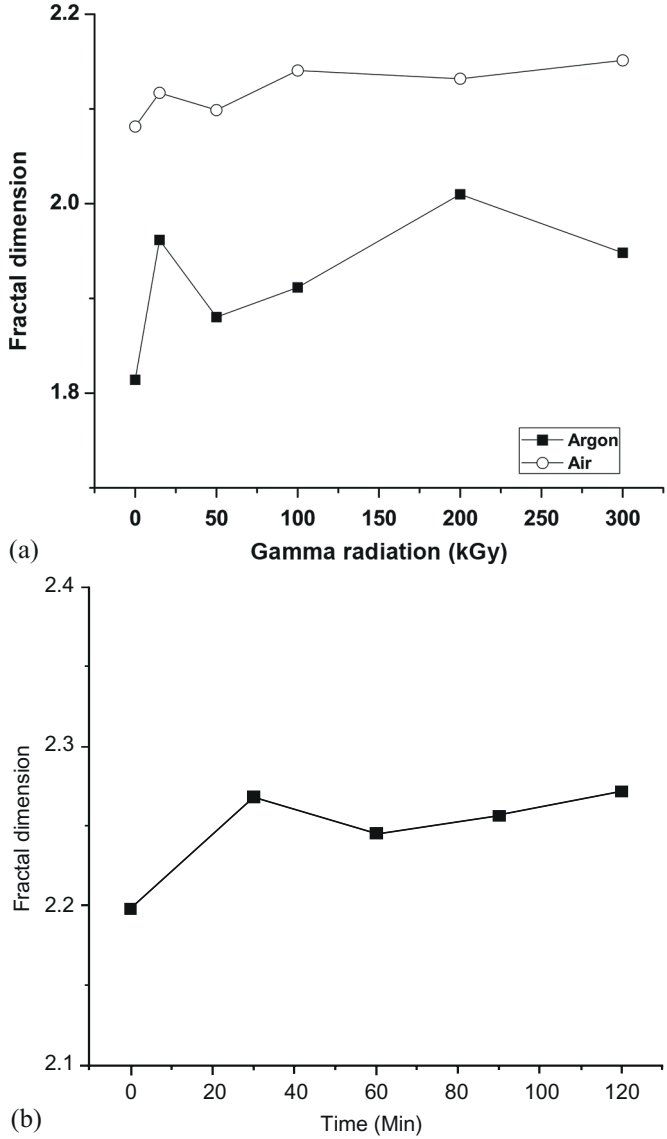


Figure 12.3 Fractal dimension of nylon 6,6 under (a) gamma irradiated as a function of dose and (b) chemical treatment as a function of time of immersion.

protection of the steel, corrosion potential, pitting potential, passivation current density obtained using potentiodynamic polarization measurements.[24] They are performed in a saturated basic $Ca(OH)_2$ and $CaCl_2$ 1:1 solution (pH 12) simulating the concrete in solution environment, in the absence and presence of nylon 6,6 pellets containing the

adsorbed inhibitor in different concentrations, as shown in Figure **12.4**. More positive corrosion potentials are obtained as a function of inhibitor concentration. Also, the passive current is smaller for lower overpolarization, but the pitting potential became more negative, as shown in Figure **12.4**a. The free corrosion potential and the noise current density as a function of time of immersion in chloride solution for rebar concrete, with and without the smart system as aggregates, are presented in Figure **12.4**b. Both potentials increased similarly to noble values as a function of time, but noise current densities observed for the two systems did not. These results demonstrate the effect of the inhibitor release and corrosion protection activity.

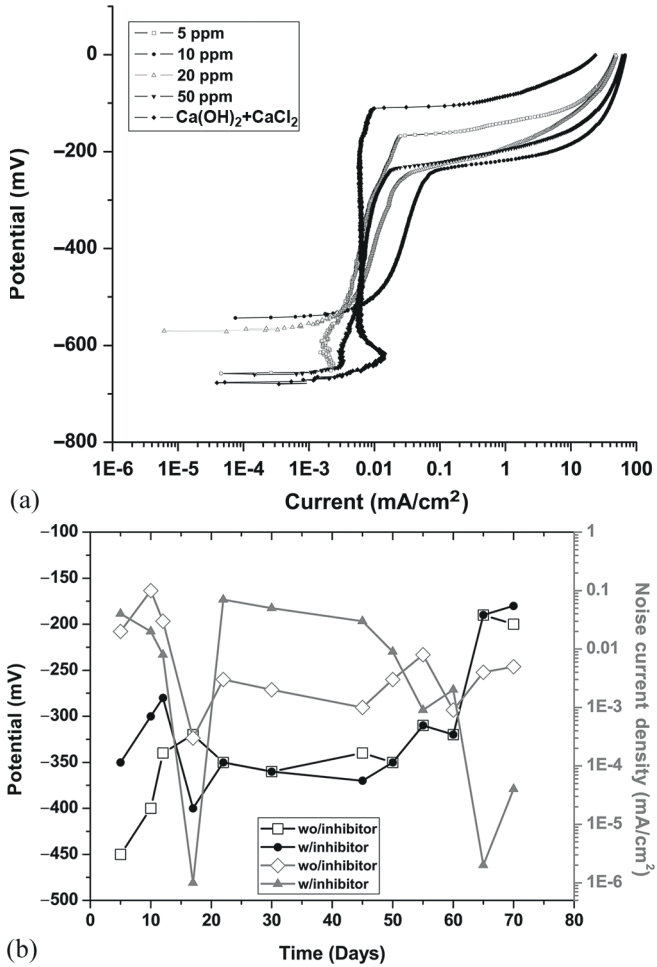


Figure 12.4 (a) Polarization curves in a simulated concrete environment and (b) concrete samples immersed in chloride solution as a function of time.

The release of the adsorbed corrosion inhibitor may be triggered by the corrosion process itself, which prevents the spontaneous leakage of such inhibitor or the slow release from the smart system providing a response to changes in the service environment.[43]

12.3 Electrospun Smart Coating

As far as metallic monuments, statues, and works of art are concerned, they account for the vast majority of existing and cultural heritage objects. Copper and its alloys play an important role as a base metallic material used by artists and architects. Corrosion processes is a complex phenomenon involving corrosion products or oxide film formation on copper and alloys. These products are formed by a number of brittle oxide and hydroxide surface layers, in many cases of different colors and textures, some of calcareous origin, including silicates, and all of them formed over the copper oxidation patina (typically cuprite).[44–48] Copper, commonly used in structures and sculptures, is usually covered with layers of corrosion products providing its aesthetic value and, at the same time, protecting the metallic substrate. Due to the increase in atmospheric pollution, these layers commonly dissolve when exposed to polluted environments.

Polymeric materials' efficiency as corrosion protection coatings for metals increases when polymeric ligands are modified using corrosion inhibitors.[49] Nanocarriers with storage properties, liberating inhibitors in a controlled way, can be used to manufacture a new family of hybrid coatings that respond to changes within the coating environment or its integrity. Liberation of encapsulated inhibitors within nanostorage/carriers is activated by the corrosion process itself, preventing spontaneous leaking out of the inhibitor from the coating. With this restriction, it is possible to reach the double goal of corrosion protection by a barrier and inhibitor mechanism of metallic elements.

Electrospinning is a recognized technique to create polymer fibers with diameters ranging from 40 to 2000 nm.[48] Fibers can be electrospun direct from solution or from the fused material state, controlling the diameter size through adjustment of the surface tension, solution concentration, conductivity, and so forth.[48,50,51] Electrospinning occurs when the electric force of the solution surface overcomes the surface tension and triggers an electric spark provoking the solution to be expelled from the containing device (syringe) and the jet flow impacts, deposits, and is collected in a metal screen. When the expelled material dries out or solidifies, it forms an electric charged fiber, and this could be directed or speeded up by electric forces.[44–52] As the jet stretches and dries, radial electrical forces cause it to splash repeatedly, and the fibers dry and solidify.[53–55] The improvements in the electrospinning technique allow production of liquid crystals or other tailored systems and even thinner fibers.[56] The

thermodynamic compatibility between polymers and corrosion inhibitors allows their combination as an integral material system, creating quasi-compatible compounds. This is the direction in which polymer-inhibitor materials science is progressing.[57]

Inhibitors are compounds capable of diminishing metal corrosion even at very low concentrations in aggressive media. They change the electrochemical reaction kinetics producing corrosion, and the rate is significantly slowed down.[49] Corrosion processes include, in most cases, water molecules, and inhibitors are used in aqueous systems and in atmospheric corrosion protection. Nowadays, corrosion inhibitors do exist such as chromates, nitrites, benzotriazole, and other organic and inorganic compounds. Benzotriazole (BTAH) is an organic compound of low molecular weight with metallic corrosion-inhibitor properties, for copper in particular.

The next step in the fabrication of nanostorage/carriers by the authors,[53,54] suitable for self-repairing anticorrosion coatings, is to make them sensitive to the corrosion process, or another external trigger, in order to activate the release of the stored inhibitor species. The mechanism of these storage/carriers is the *smart* self-healing process, being able to regulate the storage/release of an inhibitor.[19,21]

The direct introduction of components of the protective coating inhibitor often leads to the deactivation of the corrosion-inhibitor and polymer matrix degradation. An alternative approach is to produce a corrosion protection hybrid coating containing a commercial polymer varnish and electrospun nylon 6,6 nanofibers acting as a BTAH inhibitor storage/carrier and the whole as a "smart coating." The objective is the possible application of this corrosion protection system to statues or works of art of cultural value, commonly made of copper or its alloys and exposed to atmospheric corrosion conditions.

To achieve these, the authors studied several system conditions to electrospin and *trap* the inhibitor. The concept of this smart coating is as follows: the scale of the storage/carriers is of nanometer dimensions, so these are matched with the corrosion inhibitor. When these storage/carriers are, for instance, mechanically deformed or the metal surface is corroding, the inhibitor is released slowing it down as a passive layer formed over the surface as a consequence of the changes in the chemical environment. Also, the intricate electrospun nylon 6,6/benzotriazole (Ny-BTAH) inhibitor film formed in combination with a polymer coating acts as a smart coating and barrier and tortuous path for the eventual diffusion of aggressive species reaching the metal surface.[53,54]

Once coating films are elaborated, they have to be characterized by infrared spectroscopy (FTIR), where nylon 6,6, solid BTAH, and Ny-BTAH 20% electrospun fibers spectra are presented, as shown in Figure 12.5a. Absorption peaks for BTAH inhibitor and for nylon 6,6 are observed. The spectrum of Ny-BTAH 20%, presents peaks corresponding to the ones observed in the other spectra, indicative of the merging of nylon and BTAH in the film formed. The electrospun fibers were observed under SEM and the merged Ny-BTAH present a transparent quality, as observed in

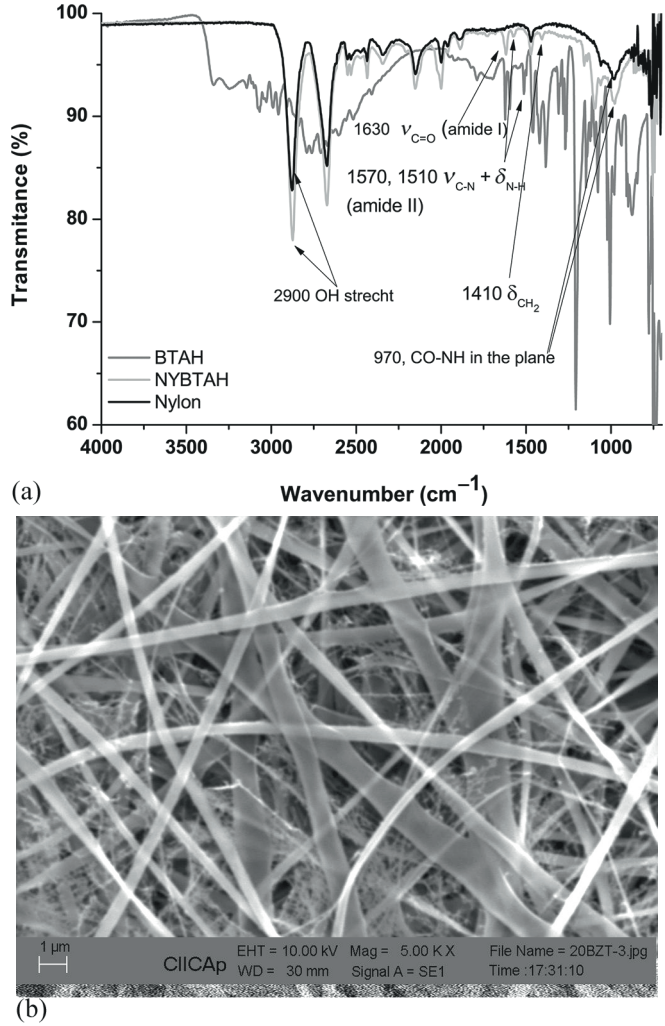


Figure 12.5 Electrospun nylon 6,6/BTAH fiber: (a) FTIR spectra and (b) SEM micrograph.

Figure 12.5b.[54] Afterwards, a waterborne alkyd varnish was painted over the electrospun nylon inhibitor (smart) coating, drying at ambient temperature for 24 h. Good adhesion properties are determined after testing.

Once coated copper electrodes are prepared, electrochemical evaluation is realized, and the results are presented below. Figure 12.6a shows the free corrosion potential as a function of time of immersion, comparing bare copper (blank), copper varnish coated, and copper smart coating immersed in a chloride-sulfate solution. The noblest potential is observed for copper smart coating, followed by the copper

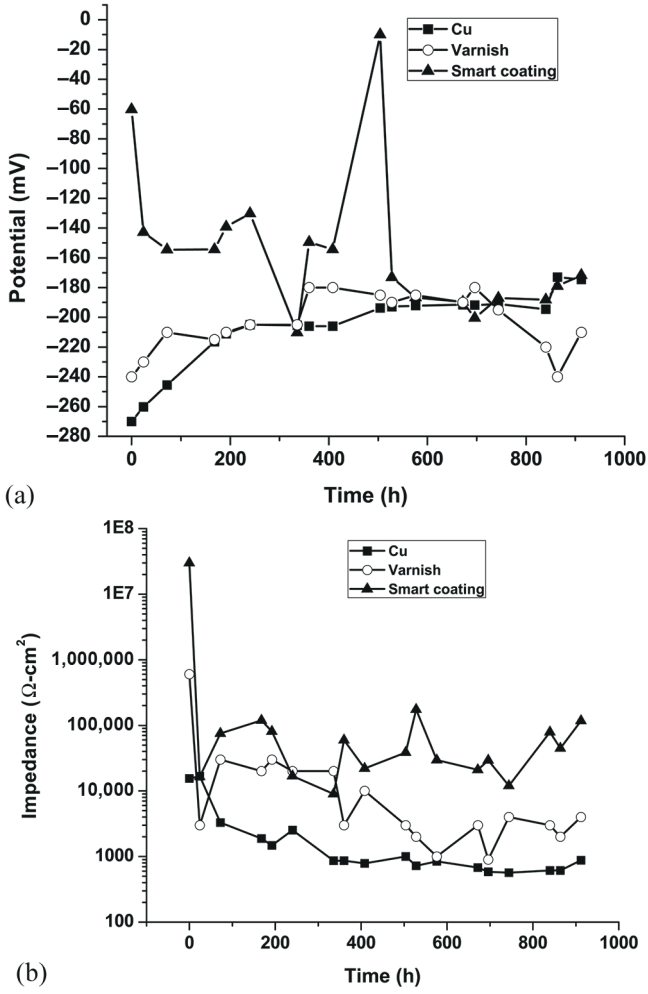


Figure 12.6 Comparison of bare copper and coatings behavior: (a) corrosion potential and (b) total impedance as a function of time of immersion.

varnish coated presenting similar behavior to the bare copper sample, as seen in Figure 12.6a. At about 350 h of immersion the decreasing potential of the smart coating sample reached the steady state values of the other two. This behavior could be ascribed to the difficulty of aggressive anions reaching the metal surface due to limitations in the diffusion path promoted by the nylon/inhibitor fibers and varnish coating action.

To test the "intelligence" of the smart coating produced after 500 h immersion, a mechanical coating simulating an in-service coating damage was produced scribing

the coating surface with the tip of a cutter. A change in the noble direction was registered, returning back to more active potential values but increasing again, therefore showing better anticorrosion performance. The total impedance value acts accordingly.

The averaged total electrochemical impedance modulus observed for bare copper, copper varnish, as well as for the copper smart coating samples as a function of immersion are presented in Figure 12.6b. Higher total impedance values are observed, for the smart coated, as compared to the bare copper and copper varnish samples. Bear in mind the scratch made after 500 h, where the impedance drops markedly for the smart coating sample, increasing again afterwards till the end of the time of immersion. The potential and total impedance change suggests that corrosion and oxide film formation is taking place over copper exposed by the damaged area and promoted by the action of the BTAH inhibitor release.[54] In general it can be said that the total impedance values remained higher because of the inhibitor action and are considered as good impedance coating after 900 h in the aggressive conditions, confirming the "intelligent" action of the smart coating.

To observe the damaged scribed surface morphology, SEM micrographs are obtained and presented in Figure 12.7a, and the elemental chemical analysis performed to the sample is shown in Figure 12.7b, presenting corrosion products with elements associated to the electrolyte such as sodium, chloride, and sulfate. Elements revealing

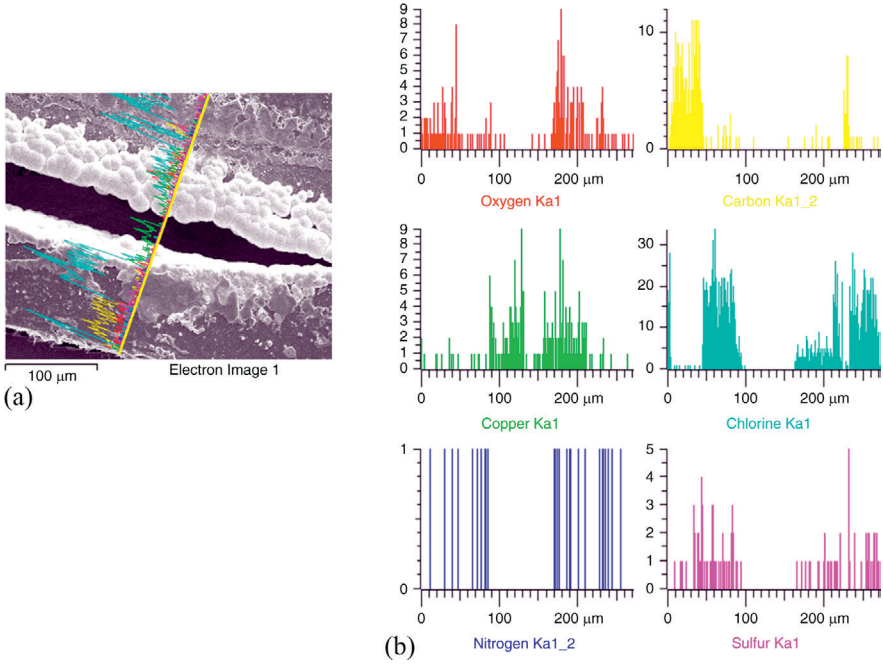


Figure 12.7 Coating scribed: (a) surface morphology and (b) chemical analysis.

the presence of the polymer and inhibitor like carbon, oxygen, and nitrogen are also present. Also copper as metallic substrate and particles of iron associated to the cutter used to cause the artificial damage over the polymer coating is observed. All these suggest the probable formation of a layer of a polymeric compound from the ligand action of BTAH inhibitor, as reported.[58,59]

The results obtained support the following mechanism for copper-BTAH inhibitor film formation in chloride solution[58]

$$4Cu + 8Cl^- + O_2 + 2H_2O \Rightarrow 4CuCl_2 + 4OH^-$$

$$CuCl_2 + n\text{BTAH} \Rightarrow \left[-\text{CuBTA}-\right]_n + nH^+ + 2nCl^-$$

The possible formation of this polymer will further protect the damaged area, passivating the surface with the help of the smart coating system proposed to act in aggressive atmospheric conditions.

12.4 Sol-Gel Coatings for Corrosion Control

The sol-gel route for processing inorganic materials can be tracked to the beginning of the twentieth century with studies based on silica gels carried out mainly by Graham and Ebelmen (1842).[60] These research results led to the conclusion that the use of tetraethyl-orthosilicate (TEOS) as a precursor in an acidic environment formed a glasslike material, which was a viscous gel with different applications (optical, ceramic) and considered a composite. These research results led to the conclusion that the hydrolysis and polycondensation of silicon precursors, such as the tetraethyl-orthosilicate (TEOS) in an acidic or basic environment. The growing of the inorganic network renders first a colloidal suspension or so and, the continuity of the condensation reactions increases the size and complexity of the network until a glasslike material or gel is formed. The gel consists of a solid network with remnant liquid trapped in its pores or a viscous gel (optical, ceramic) because this new material is considered a composite. Waterless gels present cracks, thus making them difficult for other applications.[61] However; the inorganic network is susceptible to different applications after the proper chemical, thermal, or physicochemical treatment. These procedures have been named the sol-gel method, and because the hydrolysis and polycondensation reactions occur under relative soft chemical and thermal conditions, it was considered a soft chemistry, or *chemi deuce*.[62,63]

In the 1970s the new formulations were synthesized because the former gels had presented defects. In 1971 the precursor TEOS was synthesized in conjunction with cationic surfactants, which led to the production process named low-bulk density silica sol-gel.[64] Since then, many scientists[65–68] have synthesized new formulations in order to enhance the sol-gel properties. From that moment, the synthesis of organic-inorganic hybrid sol-gels began to reveal wider applications than those observed with the former sol-gels.

Since that discovery, different applications in the form of coatings have been produced using this sol-gel route. The sol-gel coatings present numerous advantages as compared with other processing technologies, such as a high purity and homogeneous matrix, and low curing temperatures of processing (< 500 °C). Furthermore, the soft conditions usually employed in the sol-gel process allow the physical trapping of diverse inorganic, organic,[69–71] biochemical,[72,73] or biological[74,75] species inside the pores of the network.

This fact maintains the base substrate properties unaltered mainly in metallic materials. During the past two decades, the sol-gel route has extensively enhanced its applications because of its versatility in combination with other materials that lead to more uniform and more resistant coatings. Furthermore, this new synthesis route prepares a new family of ceramic glass coatings which are applicable mainly in electronics, optics, ceramics, automotive, biotechnology, and corrosion.[76,77]

Hybrid sol-gel coatings from the standpoint of corrosion resistance offer wide possibilities because brittleness and high temperatures are avoided. The single inorganic oxide sol-gel layers usually present cracks and voids after the curing treatment. Therefore, hybrid sol-gel coatings, which have low viscosity, allow easy casting into a mold during the deposition procedure regardless of the technique used for this purpose.[78–80] Dip-coating and spin-coating, which are the two most common deposition methods,[81,82] offer advantages as compared to spraying or electrodeposition procedures. These advantages are homogeneous thickness and low superficial defects such as pores (see below).

An example of the influence of the corrosion properties as a function of the deposition technique, (Figure 12.8a and b) shows an aluminum-coated sample immersed in NaCl 0.1 M after 48 h. As can be seen the best resistance properties is given by the spin-coating and the dip-coating techniques with final impedance (resistance) at low frequencies up to $10^5\,\Omega\text{-cm}^2$. The paint brush and the spray technique offered the lowest resistance properties. All samples had similar average thickness around 4-5 µm thus it is clear from these results that dip-coating and spray painting techniques increased the number of defects in the coating.

The hybrid sol-gel coatings also offer additional advantages after the coating deposition, which are the use of a low processing temperature and the final characteristics of a hydrophobic/hydrophilic matrix. The inorganic part generally controls brittleness, hardness, and a degree of transparency after the curing time process while the organic counterpart governs density, thermal stability, and superficial properties such as porosity.[83] If the organic part or molecules are solely entrenched within the inorganic matrix, weak bonds such as Van-der Walls forces or electrostatic bonds are formed. On the other hand, when the organic and inorganic parts establish strong interactions among all molecules, the formation of covalent bonds is the main bonding force.

From the early 1990s, some other materials have been synthesized from concentric nanoparticle multilayers to improve the properties of the final substrate. Thus, the synthesis of particles with useful dual properties, for instance magnetic and

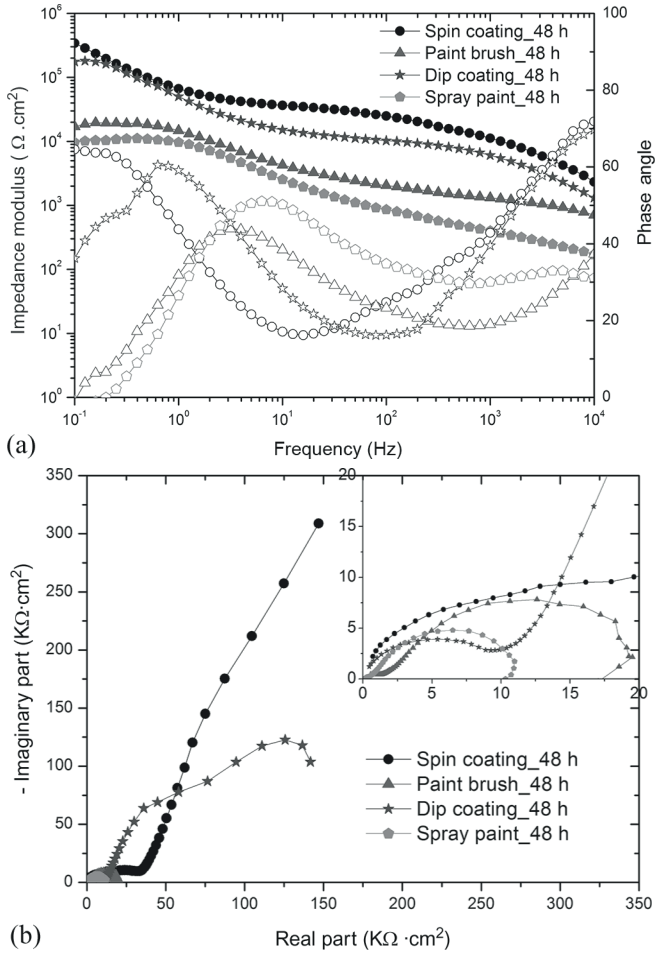


Figure 12.8 Evolution impedance: (a) Bode and (b) Nyquist diagrams of aluminum-coated samples with different deposition techniques, immersed in NaCl 0.1 M after 48 h.

luminescent, is a very attractive possibility. As a consequence new methodologies for the synthesis of nanoparticles composed of two or more materials, named core/shell nanoparticles, have been developed.[84–87] The sol-gel method allows the possible synthesis of a network of transition metals oxides such as TiO_2, ZrO_2, ZnO, and Al_2O_3.[61]

Additionally, these hybrid materials can also be employed when fibers, nanoparticles, or nanocontainers are incorporated into the network. Depending on the nature of the species in the coatings, different categories of components can be described according to their chemical bond with the inorganic/organic matrix.[88] In

order to obtain a gel, different basic steps are needed for this process[68,76]: mixing, gelation, aging, drying, and sintering. The application of the sol-gel process for the synthesis of new hybrid materials, and production of catalyst, biosensors, or hybrid materials for drug or anticorrosion delivery, are modern emerging interdisciplinary areas.

12.4.1 Corrosion applications

Sol-gel methodology intended to protect substrates against the corrosion process has grown in the last 15 years. The former inorganic coatings containing silica-oxides were evaluated as protective layers because of their high chemical stability and excellent wear-erosion resistance.[89] The SiO_2, ZrO_2, Al_2O_3, and TiO_2 based coatings are generally excellent layers for the prevention of oxygen diffusion in metal substrates.[90,91] Bi-ceramic coatings based on TiO_2-SiO_2 formulations have provided high resistance to metal oxidation for 15 h at 800 °C. However, their oxidation resistance in acidic conditions (H_2SO_4) was poor. The ZrO_2 coatings are improved with the incorporation of Y_2O_3 because the yttrium has a great affinity with oxygen to form a stable layer. Nevertheless, the corrosion resistance is a function of the internal or superficial defects formed after a high sintering temperature.[79] The differences between thermal expansion coefficients of the coating and the substrate impeded the formation of thicker layers without cracks. For this reason, hybrid sol-gel coatings are formulated in order to prevent high curing temperatures leading to thicker layers (micrometers from single layer deposition). Thus, superficial defect-free coatings with better adherence and flexibility properties can be achieved.[92,93]

As previously mentioned, the incorporation of TEOS has led to a less viscous gel with wider applications. The combined use of TEOS with an organo-modified alkoxide such as the methyl-triethoxysylane (MTES) in a molar ratio of 40/60 allows free-crack coatings up to 2 micrometers in thickness to be obtained from a single layer deposition.[94] The alkaline conditions in which the TEOS/MTES proceeds promote the formation of nanoparticles of diameter sizes below 20 nm, which behave as dense particulates. These conditions induced a high hydrolysis reaction rate, which needed water content in order to promote the slow formation and growth of the agglomerates within the gel network. This type of gel has successfully been employed in the corrosion protection of galvanized steel.[95] Other studies have demonstrated that the electrophoretic deposition of particulate *sols* with basic catalyst allows thickness coatings between 2 and 10 μm. This route promotes not only thicker coatings, but also denser layers because of the electric field that easily attracts the colloidal particles to the metal substrate, thus reducing the porosity of the coating and improving the corrosion resistance in stainless steel.[96]

However, despite all the modified routes, the synthesis of silica hybrid sol-gel coatings still persist as limitations for corrosion protection because these coatings do not provide good barrier properties in solutions of acidic or neutral pH. To overcome this limitation, the incorporation of other oxides such as zirconium, titanium, and aluminum has enhanced the corrosion applications from basic to neutral media. The development of ZrO_2/SiO_2 coatings through hydrolysis and polycondensation reactions of a zirconium tetrabutoxide solution with MTES at different molar ratios proved to be effective in the formation of Si-O-Zr bonds at sintering temperatures below 700 °C. Examples of low sintering temperatures (400 °C-500 °C) are those obtained from the TEOS/MTES synthesis and those synthesized by a polymethyl methacrylate (PMMA) dispersion in a zircon sol which sintered at 200 °C during a period of 30 min, thus improving the corrosion resistance of stainless steel. Nevertheless, these developments were dependent on the amount of organic phase during the synthesis process because high organic proportion could initiate segregation of phases and then coating delamination.

The 3-glycidyloxypropyl-trimethoxysilane (GPTMS), which belongs to organo-modified silicon precursors, $R–Si(OR)_3$, where R represents organic groups such as epoxy, vinyl, metacryl, in conjunction with SiO_2 solution and acid catalyst, has permitted the formulation of new coatings for aluminum alloys with sintering temperatures below 200 °C.[96–98] These coatings have had a nominal thickness between 5 and 10 μm. From this standpoint, numerous combinations have been proposed in order to improve the corrosion protection of aluminum alloys employing the sol-gel route. Our research group has made hybrid coatings of tetra-*n*-propoxyzirconium [$Zr(PrO^n)_4$ or TPOZ] and 3-glycidyloxypropyl-trimethoxysilane on an AA2024-T2 aluminum alloy.

Coating protection behavior is analyzed in a 0.1 M NaCl solution by means of electrochemical impedance spectroscopy at room temperature. The hybrid sol-gel coatings are doped by the incorporation of 1% or 5% cerium nitrate as a corrosion inhibitor. In addition, nanocontainers SBA15 (Santa Barbara Amorphous Material 15) saturated with a cerium compound are also loaded into the sol-gel formulation in order to compare their protection against corrosion with that obtained from the addition of free Ce^{3+} coatings. The cerium compounds that belong to the green inhibitors to enhance corrosion resistance combine barrier properties with an active inhibition mechanism in a damaged coating. According to Figure 12.9a and b, the sol-gel coatings loaded with saturated SBA nanocontainers exhibited the best dielectric properties after 48 h. Therefore, cerium containing coatings combined during the synthesis process do not provide better corrosion resistance on Al 2024-T3 alloy; hence, in order to provide a better inhibition effect against the corrosion process, the inorganic inhibitor works better when it is released slowly.

The sol-gel development has led to new protective coatings focused on new hybrid organic-inorganic systems incorporating not only modified alkoxides, but also nanostructured particles with the blocking effects of the aggressive species. Our

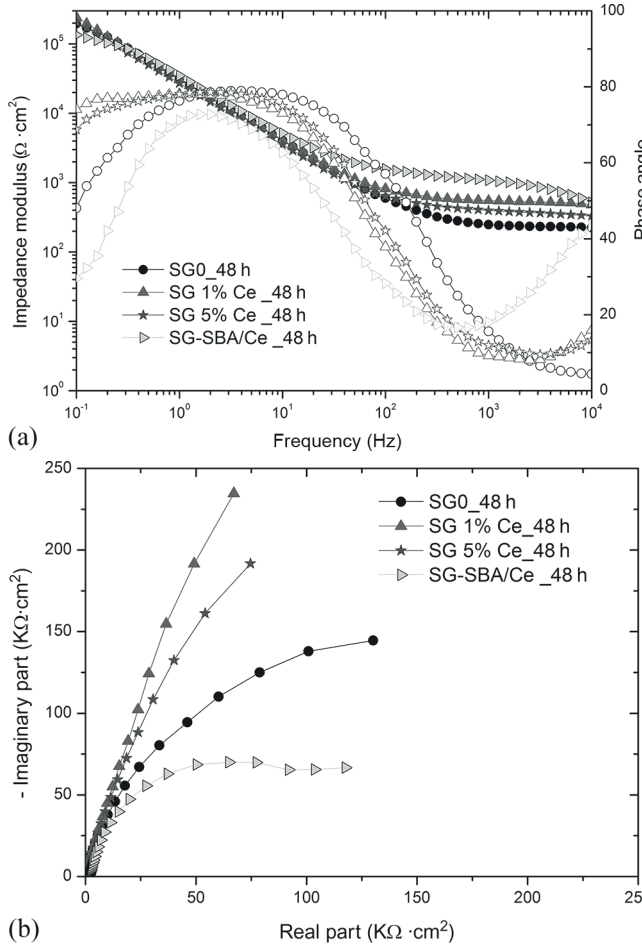


Figure 12.9 Impedance: (a) Bode and (b) Nyquist diagrams of cerium-doped sol-gel coatings after 48 h immersed in NaCl 0.1 M.

research group has also incorporated nylon fibers into the sol-gel system through the electrospinning technique. The results of the electrochemical properties carried out with the EIS technique are presented in Figure 12.10a and b, where the effect of the electrospinning time on the fiber density can be seen (Figure 12.11a and b). From the Bode plots it is noted that the highest dielectric properties are ascribed to electrospun nylon for 2.5 min with a low frequency impedance modulus, in the order of $10^5\,\Omega$-cm^2, which remains unchanged after 45 days of immersion. The average coating thickness is around 4 µm, and its micrograph corresponds to that presented in Figure 12.11a. As can be seen, the nylon fibers created a web completely covered by

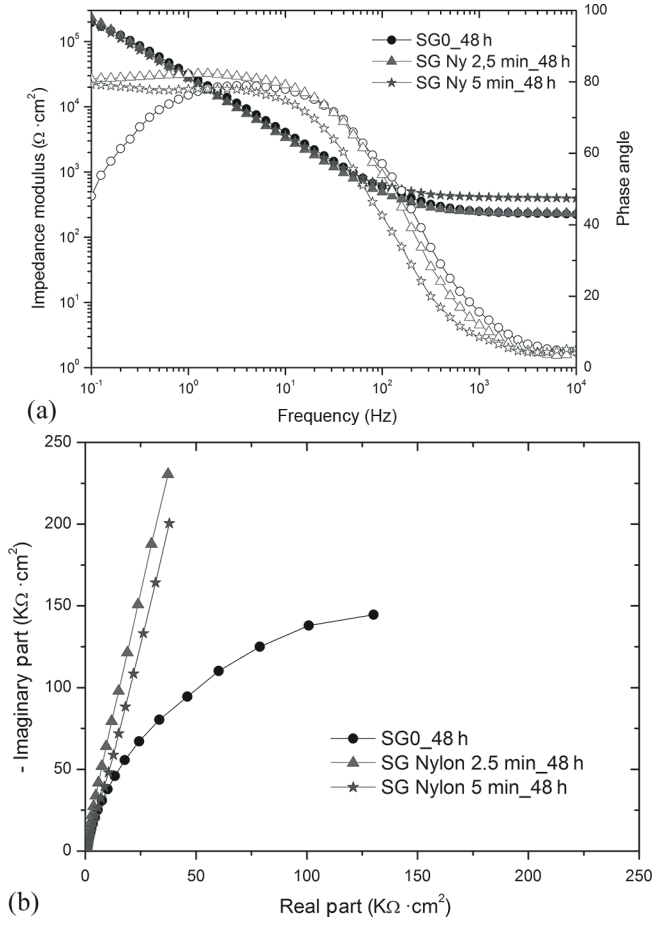
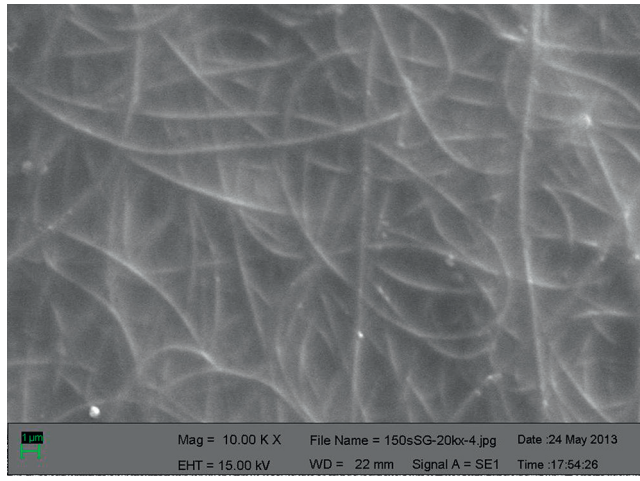


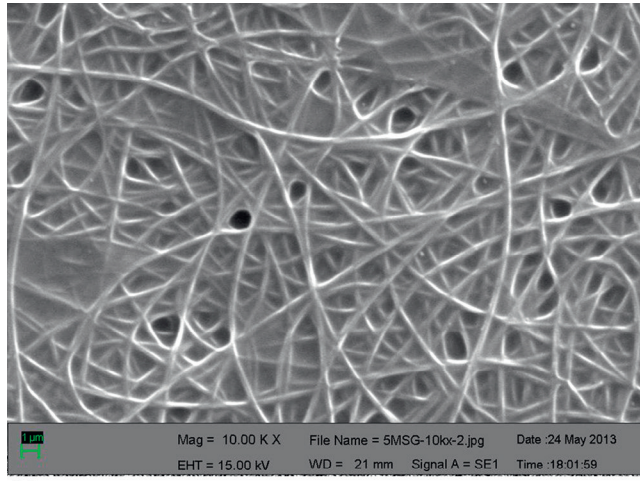
Figure 12.10 Evolution of impedance: (a) Bode and (b) Nyquist diagrams, after the incorporation of nylon fibers into the sol-gel system, immersed in NaCl 0.1 M after 48 h.

the sol-gel whereas the fibers shown in the micrograph ascribed to electrospun nylon for 5 min do not cover the entire surface. These results suggest that the sol-gel needed a specific anchorage profile to be deposited onto the nylon fibers. The high density of nylon fibers obtained at larger electrospin times seemed to decrease the adherence properties, thus decreasing the protective properties as well.

Consequently, the adequate selection of precursors, the molar ratio between organic/inorganic phases, a proper catalyst agent, and synthesis-condition parameters will allow denser and thicker coatings with low sintering temperatures capable of being used in other substrates such as the low-melting temperature alloys of aluminum and magnesium.[99,100]



(a)



(b)

Figure 12.11 Sol-gel coating micrographs (a) after electrospinning with nylon during 2.5 min and (b) after electrospinning with nylon during 5 min.

12.5 Conclusion

In this chapter, novel applications of nylon-activated particles or electrospun fibers in combination with inhibitors, polymer, and sol-gel coatings are presented. These examples form what are considered *smart* coatings and systems. Good promise can be envisage in these examples, as to the development of more efficient systems of this type.

Acknowledgments

The authors wish to thank to SEP-PROMEP for the support provided both to the Academic Body "Desarrollo y Análisis de Materiales Avanzados" (UAEMOR-CA-43) and to the Academic Network "Diseño Nanoscópico y Textural de Materiales Avanzados." Finally, the authors give thanks to CONACyT for the grants received during this work.

References

1. Challener C. The intelligence behind smart coatings. J Coat Tech 2006;3(January):50–5.
2. Andreeva D, Shchukin D. Smart self-repairing protective coatings. Mater Today 2008;11(10):24–30.
3. Feng W, Patel SH, Young MY, et al. Smart polymeric coatings—recent advances. Adv Polym Technol 2007;26(1):1–13.
4. Li W, Calle LM. Smart coating for corrosion sensing and protection In: *Proceedings of the US Army Corrosion Summit*. Clearwater Beach, FL: US Army Corrosion Summit; 2006.
5. Davis SJ, Watts JF. Organization of methoxysilane molecules on iron. Int J Adhes Adhes 1996;16(1):5–15.
6. Allsop NABM, Glass NFC, Harris AE, et al. Thermal analysis in the development of self validating adhesives. Thermochim Acta 1998;315(1):67–75.
7. Brown EN, White SR, Sottos NR. Microcapsule induced toughening in a self-healing polymer composite. J Mater Sci 2004;39:1703–10.
8. Abdullayev E, Lvov Y. Halloysite clay nanotubes for controlled release of protective agents. J Nanosci Nanotechnol 2011;11(11):10007–26.
9. Khramov AN, Voevodin NN, Balbyshev VN, et al. Hybrid organo-ceramic corrosion protection coatings with encapsulated organic corrosion inhibitors. Thin Solid Films 2004;447–448:549–57.
10. Zheludkevich ML, Serra R, Montemor MF, et al. Nanostructured sol–gel coatings doped with cerium nitrate as pre-treatments for AA2024-T3. Electrochim Acta 2005;51(2):208–17.
11. Buchheit RGMS, Schmutz P, Guan H. Active corrosion protection in Ce-modified hydrotalcite conversion coatings. Corros Sci 2002;58(1):3–14.
12. Leggat RBZW, Buchheit RG, Taylor SR. Performance of hydrotalcite conversion treatments on AA2024-T3 when used in coating systems. Corros Sci 2002;58(4):322–8.
13. Meier W. Polymer nanocapsules. Chem Soc Rev 2000;29(5):295–303.
14. Peyratout CSMH, Dähne L. Preparation of photosensitive dye aggregates and fluorescent nanocrystals in microreaction containers. Adv Mater 2003;15(20):1722–6.
15. Förster S, Plantenberg T. From self-organizing polymers to nanohybrid and biomaterials. Angewandte Chemie International Edition 2002;41(5):689–714.
16. Deyá C, Romagnoli R, Amo B. A new pigment for smart anticorrosive coatings. J Coat Technol Res 2007;4(2):167–75.
17. Manna AIT, Aoi K, Okada M, et al. Synthesis of dendrimer-passivated noble metal nanoparticles in a polar medium: comparison of size between silver and gold particle. Chem Mater 2001;13(5):1674–81.
18. Sunder AKM, Hanselmann R, Mülhaupt R, et al. Molecular nanocapsules based on amphiphilic hyperbranched polyglycerols. Angew Chem Int Ed 1999;38(23):3552–5.
19. Lu X, Xin Z. Preparation and characterization of micron-sized polystyrene/polysiloxane core/shell particles. Colloid Polym Sci 2006;284(9):1062–6.
20. Zoldesi CI, van Walree CA, Imhof A. Deformable hollow hybrid silica/siloxane colloids by emulsion templating. Langmuir 2006;22(9):4343–52.

21. Schneider G, Decher G. From functional core/shell nanoparticles prepared via layer-by-layer deposition to empty nanospheres. Nano Lett 2004;4(10):1833–9.
22. Menchaca EC, Hernández S, Tejeda A, et al. Adsorption of Fe(NO3)3 onto Activated Nylon-6,6 as a Container and a Possible "Smart" Corrosion Inhibitor-containing System. Adsorption Science & Technology 2011;29(5):507–517.
23. Menchaca EC, Hernández S, Tejeda A, Sarmiento E, Uruchurtu J, García MA. Adsorption of Fe $(NO_3)_3$ onto Activated Nylon-6,6 as a Container and a Possible "Smart"Corrosion Inhibitor-containing System. Adsorpt Sci Technol 2011;29(5):507–17.
24. Gece G. Drugs: a review of promising novel corrosion inhibitors. Corros Sci 2011;53(12):3873–98.
25. Abdulrahman AS, Mohammad I, Mohammad SH. Corrosion inhibitors for steel reinforcement in concrete: a review. Sci Res Essays 2011;6(20):4152–62.
26. Ramaswamy A, Reddy H. Time dependent deformations in concrete: a multi-scale approach. In: Dattaguru B, Gopalakrishnan S, Aatre VK, editors. IUTAM symposium on multi-functional material structures and systems, (vol. 19); Netherlands: Springer; 2010. p. 55–64.
27. Fowler D. Polymers in concrete: a vision for the 21st century. Cem Concr Res 1999;21(5–6):449–52.
28. Beaudoin JJ. Handbook of fiber-reinforced concrete, principles, properties developments and applications. Park Ridge, NJ, USA: Noyes Data Corporation; 1990. ISBN: 0815512368. http://worldcat.org/isbn/0815512368.
29. Hoult NA, Sherwood EG, Bentz EC, et al. Does the use of FRP reinforcement change the one-way shear behavior of reinforced concrete slabs? J Compos Constr 2008;12(2):125–33.
30. Zheng Z, Feldman D. Synthetic fibre-reinforced concrete. Prog Polym Sci 1995;20:185–210.
31. Pfeifer DW, McDonald DB, Krauss PD. The rapid chloride permeability test and its correlation to the 90-day chloride ponding test. PCI J 1994;39(1):38–47.
32. Martínez-Barrera G, Menchaca-Campos C, Vigueras-Santiago E, et al. Post-irradiation effects on Nylon-fibers reinforced concretes. e-Polymers 2013;10(1):457–469.
33. Martínez-Barrera G, Villarruel UT, Vigueras-Santiago E, et al. Compressive strength of gamma-irradiated polymer concrete. Polym Compos 2008;29(11):1210–7.
34. Martínez-Barrera G, Menchaca-Campos C, Hernández-López S, et al. Concrete reinforced with irradiated nylon fibers. J Mat Res 2006;21(02):484–91.
35. Menchaca C, Alvarez-Castillo A, Lopez-Valdivia H, et al. Radiation-induced morphological changes in polyamide fibers. Int J Polym Mater 2002;51(9):769–81.
36. Martínez-Barrera G, Campos CM, Ureña-Nuñez F. Gamma radiation as a novel technology for development of new generation concrete. In: Adrovic F, editor. Gamma radiation. Rijeka, Croatia: InTech; 2012. p. 320.
37. Menchaca C, Nava JC, Valdez S, et al. Gamma-irradiated nylon roughness as function of dose and time by the hurst and fractal dimension analysis. J Mat Sci Eng 2010;4(9):50–8.
38. Menchaca C, Demesa G, Santiaguillo A, et al. Gamma irradiation effect on nylon 6–12 modification under argon atmosphere. J Mat Sci Eng 2012;4(B2):247–54.
39. Hernández M, Genescá J, Uruchurtu J, et al. Correlation between electrochemical impedance and noise measurements of waterborne coatings. Corros Sci 2009;51(3):499–510.
40. Bahena D, Rosales I, Sarmiento O, et al. Electrochemical noise chaotic analysis of NiCoAg alloy in hank solution. Int J Corros 2011;2011:1–11.
41. González-Nuñez MA, Uruchurtu-Chavarín J. R/S fractal analysis of electrochemical noise signals of three organic coating samples under corrosion conditions. J Corros Sci Eng 2003;6:1–15.
42. Mayorga-Cruz D, Sarmiento-Martinez O, Uruchurtu-Chavarin J. Investigation of system dynamics in a corrosion process by optical and electrochemical methods. ECS Trans 2008;13(27):19–32.
43. Troconis de Rincón O, Sánchez M, Millano V, et al. Effect of the marine environment on reinforced concrete durability in Iberoamerican countries: DURACON project/CYTED. Corrosion Sci 2007;49(7):2832–2843.

44. Reneker DH, Chun I. Nanometre diameter fibres of polymer, produced by electrospinning. Nanotechnology 1996;7:216–23.
45. Yao Z. Corrosion and its control. Amsterdam: Elsevier; 1998.
46. Rozenfield IL. Corrosion Inhibitors, McGraw Hill Higher Education. December 1, 1981. 327 pages. ISBN-13: 978-0070541702.
47. Graedel TE, Nassau K, Franey JP. Copper patinas formed in the atmosphere—I. Introduction 1987; 27(7):639-657.
48. Yarin AL, Koombhongse S, Reneker DH. Taylor cone and jetting from liquid droplets in electrospinning of nanofibers. J Appl Phys 2001;90(9):4836.
49. Sørensen PA, Kiil S, Dam-Johansen K, et al. Anticorrosive coatings: a review. J Coat Technol Res 2009;6(2):135–76.
50. Shin YM, Hohman MM, Brenner MP, et al. Experimental characterization of electrospinning: the electrically forced jet and instabilities. Polymer 2001;42(25):9955–67.
51. Deitzel JM, Kleinmeyer JD, Hirvonen JK, et al. Controlled deposition of electrospun poly(ethylene oxide) fibers. Polymer 2001;42(19):8163–70.
52. Koombhongse S, Liu W, Reneker D. Flat polymer ribbons and other shapes by electrospinning. J Polym Sci B 2001;39:2598–606.
53. Soto-Quintero A, Uruchurtu-Chavarín J, Cruz-Silva R, et al. Electrospinning smart polymeric inhibitor nanocontainer system for copper corrosion. ECS Trans 2011;36(1):119–27.
54. Menchaca C, Castañeda I, Soto-Quintero A, et al. Characterization of a "Smart" hybrid varnish electrospun nylon benzotriazole copper corrosion protection coating. Int J Corros 2012;2012:1–10.
55. Ávila-Gonzalez C, Cruz-Silva R, Menchaca C, et al. Use of silica tubes as nanocontainers for corrosion inhibitor storage. J Nanotechnol 2011;2011:1–9.
56. Rinzler AG, Hafner JH, Nikolaev P, et al. Unraveling nanotubes: field emission from an atomic wire. Science 1995;269:1550–3.
57. Pinčuk LS. Melt blowing: equipment, technology, and polymer fibrous materials. New York: Springer; 2002.
58. Kosec T, Merl DK, Milošev I. Impedance and XPS study of benzotriazole films formed on copper, copper–zinc alloys and zinc in chloride solution. Corros Sci 2008;50(7):1987–97.
59. Finšgar M, Milošev I. Inhibition of copper corrosion by 1,2,3-benzotriazole: a review. Corros Sci 2010;52(9):2737–49.
60. Ebelmen JJ. Recherches sur quelques composés de l'urane. Ann Chim Phys 1842;5(3):189–193.
61. Hench LL, West JK. The sol-gel process. Chem Rev 1990;90:33–72.
62. Livage J. Chimie douce: from shake-and-bake processing to wet chemistry. New J Chem 2001;25(1):1.
63. Sanchez C, Rozes L, Ribot F, et al. "Chimie douce": a land of opportunities for the designed construction of functional inorganic and hybrid organic-inorganic nanomaterials. C R Chim 2010;13(1–2):3–39.
64. Chiola V, Ritsko JE,Vanderpool CD. Process for producing low-bulk density silica. USA patent 3,556,725 1971.
65. Huang HH, Orler B, Wilkes GL. Ceramers: hybrid materials incorporating polymeric/oligomeric species with inorganic glasses by a sol-gel process 2. Effect of acid content on the final properties. Polym Bull 1985;14(6):557–64.
66. Schmidt H, Seiferling B. Chemistry and applications of inorganic-organic polymers (organically modified silicates). In: Materials research society symposium proceedings. Materials Research Society; 1986. p. 739–50.
67. Philipp G, Schmidt H. New materials for contact lenses prepared from Si- and Ti-alkoxides by the sol-gel process. J Non Cryst Solids 1984;63:283–92.

68. Schmidt H, Scholze H, Kaiser A. Principles of hydrolysis and condensation reaction of alkoxysilanes. J Non Cryst Solids 1984;63(1–2):1–11.
69. Levy D, Reisfeld R, Avnir D. Fluorescence of europium(III) trapped in silica gel-glass as a probe for cation binding and for changes in cage symmetry during gel dehydration. Chem Phys Lett 1984;109(6):593–7.
70. Campostrini R, Carturan G, Ferrari M, et al. Luminescence of Eu3+ ions during thermal densification of SiO_2 gel. J Mater Res 1992;7(3):745–53.
71. Pouxviel JC, Dunn B, Zink JI. Fluorescence study of aluminosilicate sols and gels doped with hydroxyl trisulfonated pyrene. J Phys Chem 1989;93(5):2134–9.
72. Miller JM, Dunn B, Valentine JS, et al. Synthesis conditions for encapsulating cytochrome c and catalase in SiO_2 sol-gel materials. J Non Cryst Solids 1996;202(3):279–89.
73. Menaa B, Miyagawa Y, Takahashi M, et al. Bioencapsulation of apomyoglobin in nanoporous organosilica sol-gel glasses: influence of the siloxane network on the conformation and stability of a model protein. Biopolymers 2009;91(11):895–906.
74. Campostrini R, Carturan G, Caniato R, et al. Immobilization of plant cells in hybrid sol-gel materials. J Sol-Gel Sci Technol 1996;7:87–97.
75. Avnir D, Coradin T, Lev O, et al. Recent bio-applications of sol-gel materials. J Mater Chem 2006;16(11):1013–30.
76. Brinker CJ, Scherer GW. Sol-gel science: the physics and chemistry of sol-gel processing. Amsterdam: Elsevier; 1990.
77. de la Rosa-Fox N, Esquivias L, Piñero M. Organic-inorganic hybrid materials from sonogels. In: Handbook of organic-inorganic hybrid materials and nanocomposites. Volume 1: Hybrid Materials Edited by H. S. Nalwa. ISBN: 1-58883-011-X. American Scientific Publisher; 2003.
78. Flory PJ. Introductory lecture: levels of order in amorphous polymers. Faraday Discuss Chem Soc 1979;68:14–25.
79. Brook R. Sol-gel technology for thin films, fibers, preforms, electronics, and speciality shapes. [Klein LC, editor.]. New Jersey, USA: Noyes Publications; 1988 xxi, 407 p.
80. Schmidt H. New type of non-crystalline solids between inorganic and organic materials. J Non Cryst Solids 1985;73:681–91.
81. Coltrain BK, Sanchez C, Schaefer DW, et al. Better ceramics through chemistry 7: Organic/inorganic hybrid materials; Spring meeting of the Materials Research Society (MRS), San Francisco, CA (United States), 8-12 Apr. 1996. ISBN 1-55899-338-X.
82. Donley MS, Mantz RA, Khramov AN, et al. The self-assembled nanophase particle (SNAP) process: a nanoscience approach to coatings. Prog Org Coat 2003;47(3–4):401–15.
83. Castro Y, Ferrari B, Moreno R, et al. Coatings produced by electrophoretic deposition from nanoparticulate silica sol–gel suspensions. Surf Coat Technol 2004;182(2–3):199–203.
84. Kresge CTLM, Roth WJ, Vartuli JC, et al. Ordered mesoporous molecular sieves synthesized by a liquid crystal template mechanism. Nature 1992;359:710–2.
85. Naik B, Ghosh NN. A review on chemical methodologies for preparation of mesoporous silica and alumina based materials. Recent Pat Nanotechnol 2009;33(3):213–24.
86. Mizoshita N, Tani T, Inagaki S. Syntheses, properties and applications of periodic mesoporous organosilicas prepared from bridged organosilane precursors. Chem Soc Rev 2011;40(2):789–800.
87. Chaudhuri RG, Paria S. Core/shell nanoparticles: classes, properties, synthesis mechanisms, characterization, and applications. Chem Rev 2012;112(4):2373–433.
88. Schmidt H. Organic modification of glass structure new glasses or new polymers? J Non Cryst Solids 1989;112:419–23.
89. Mackenzie JD. Structures and properties of Ormosils. J Sol-Gel Sci Technol 1994;2(1–3):81–6.
90. Guglielmi M. Sol-gel coatings on metals. J Sol-Gel Sci Technol 1997;8(1–3):443–9.

91. Zhu M, Li M, Li Y, et al. Influence of sol–gel derived Al_2O_3 film on the oxidation behavior of a Ti_3Al based alloy. Mater Sci Eng A 2006;415(1–2):177–83.
92. Metroke TL, Kachurina O, Knobbe ET. Spectroscopic and corrosion resistance characterization of GLYMO–TEOS Ormosil coatings for aluminum alloy corrosion inhibition. Prog Org Coat 2002;44(4):295–305.
93. Atik M, Zarzycki J. Protective TiO_2-SiO_2 coatings on stainless steel sheets prepared by dip-coating. J Mat Sci Lett 1994;13(17):1301–4.
94. Chou TP, Chandrasekaran C, Limmer SJ, et al. Organic–inorganic hybrid coatings for corrosion protection. J Non-Cryst Solids 2001;290(2–3):153–62.
95. Chou TP, Chandrasekaran C, Cao GZ. Sol-gel-derived hybrid coatings for corrosion protection. J Sol-Gel Sci Technol 2003;26:321–7.
96. Vazquez-Vaamonde AJ, de Damborenea JJ, Damborenea-Gonzalez JJ. Ciencia e ingeniería de la superficie de los materiales metálicos Volume 31 of Textos universitarios. Madrid Spain: Editorial CSIC - CSIC Press, 2001. 632 pages.
97. Conde A, Damborenea J, Durán A, et al. Protective properties of a sol-gel coating on zinc coated steel. J Sol-Gel Sci Technol 2006;37(1):79–85.
98. Castro Y, Duran A, Damborenea JJ, et al. Electrochemical behaviour of silica basic hybrid coatings deposited on stainless steel by dipping and EPD. Electrochim Acta 2008;53(20):6008–17.
99. Schmidt H, Langenfeld S, Nab R. A new corrosion protection coating system for pressure-cast aluminium automotive parts. Mater Des 1997;18(4–6):309–13.
100. Collazo A, Hernández M, Nóvoa XR, et al. Effect of the addition of thermally activated hydrotalcite on the protective features of sol–gel coatings applied on AA2024 aluminium alloys. Electrochim Acta 2011;56(23):7805–14.

Chapter 13

Properties and Applications of Thermochromic Vanadium Dioxide Smart Coatings

Mohammed Soltani[*], **Anthony B. Kaye**[†]
[*]RSL-Tech, 9114 Descartes, Montreal, Quebec, Canada
[†]Department of Physics, Texas Tech University, Box 41051, Lubbock, Texas, USA

13.1 Introduction and Properties of VO_2

Since the work of Morin in 1959,[1] the thermochromic material vanadium dioxide (VO_2) has continued to interest researchers around the world, for both the scientific challenge to understand the complex mechanisms behind its ultrafast phase transition and the development of potential applications using VO_2 for innovative coatings, sensors, and devices.

VO_2 undergoes an ultrafast, reversible, solid-solid semiconductor-to-metallic phase transition (SMT) at the low temperature of $T_{trans} \sim 68\,°C$. This phase transition is accompanied by a structural change from a monoclinic crystalline structure (low temperature) to a tetragonal rutile crystalline structure (high-temperature); Figure 13.1 shows the crystalline structures of VO_2 in each of these states.

Intelligent Coatings for Corrosion Control
Copyright © 2015 Elsevier Inc. All rights reserved.

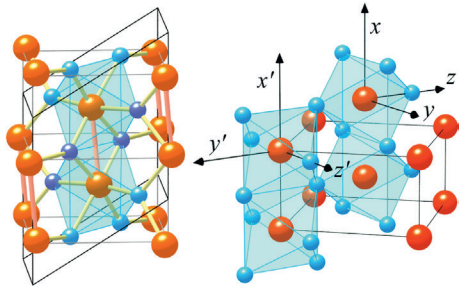


Figure 13.1 Crystalline structure of VO_2: monoclinic (low temperature; left) and tetragonal rutile (high temperature; right) structures are shown with orange/red spheres representing vanadium atoms and blue/purple spheres representing oxygen atoms. *Taken from Ref. [2], with permission.*

The SMT is also accompanied by a strong change of the electrical and optical properties: the electrical resistivity decreases by almost three orders of magnitude (see Figure 13.8, below), and the material changes from transparent to opaque (with the strongest difference in the large infrared [IR] region of the spectrum, between 1 and 25 μm) as the phase transition occurs. Figure 13.2 shows the IR transmittance of VO_2-coated quartz as a function of temperature; VO_2 is virtually transparent at low temperatures (i.e., in its semiconducting state) and becomes opaque and more reflective at high temperatures. The transmittance in the metallic state drops to zero in the same IR spectral range (Figure 13.2).

Crunteanu et al.[4] shows the temperature dependence of the DC conductivity and the THz transmittance of a 120-nm thick VO_2 film deposited on c-plane sapphire (Al_2O_3) substrates; the results are shown in Figure 13.3.

In Figure 13.3, we see that, as the temperature increases, the conductivity also increases, but less of the THz signal is transmitted through the VO_2 layer.[4] This THz transmissivity variation can be exploited in the fabrication of advanced, tuneable THz systems.

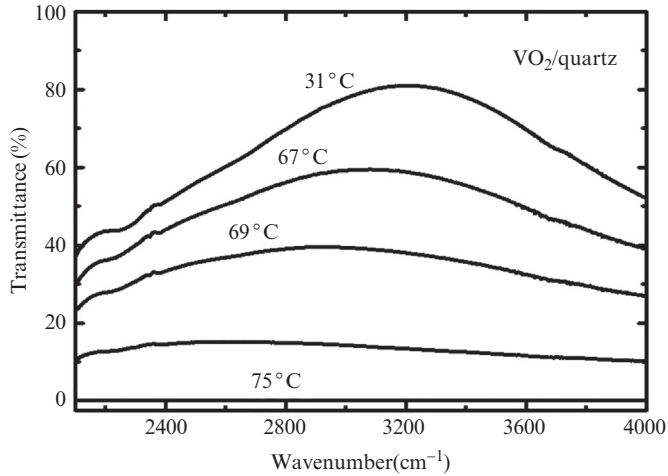


Figure 13.2 Infrared transmittance during the heating cycle for a VO_2-coated quartz substrate. *Taken from Ref. [3], with permission.*

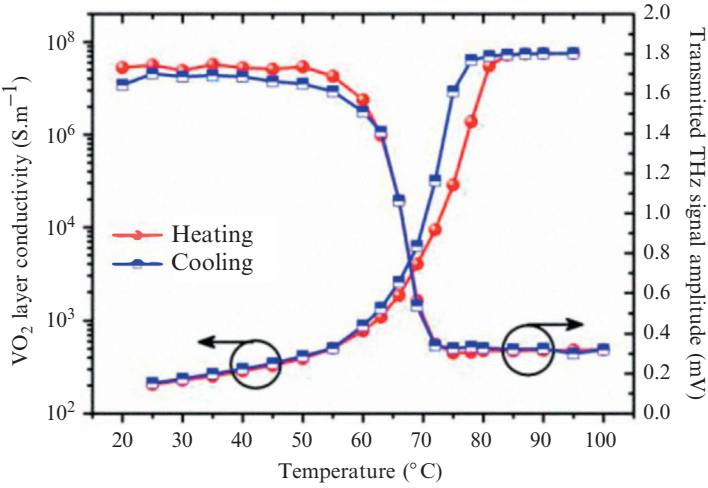


Figure 13.3 Temperature versus DC conductivity and transmitted THz signal amplitude. *Taken from Ref. [4], with permission.*

Figure 13.4 shows a sketch of the valence band diagrams for both the tetragonal rutile (i.e., metallic state; left) and monoclinic (M_1) (i.e., semiconducting state; right) phases of VO_2. In the tetragonal phase, VO_2 has one outer *d* electron per molecule and the two partially filled $d_{\|}$ and $d_{\|}^*$ valence bands overlap. At low temperatures, the vanadium π^* band is above the Fermi energy (E_F) and the *3d* band is split between one filled $d_{\|}$ band and one empty $d_{\|}^*$ band; the energy between these valence bands (i.e., the band gap energy) is 0.67 eV.[5] As a result, when sufficient energy is provided, the charge density increases and VO_2 switches to its metallic state (see also discussions in Refs. [6,7]).

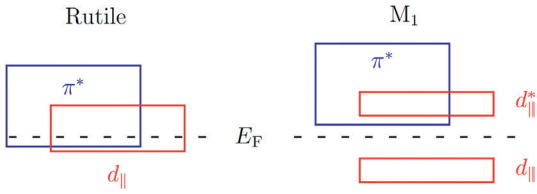


Figure 13.4 Valence band diagrams for metallic tetragonal (rutile) and semiconducting monoclinic (M_1) states of VO_2. *Taken from Ref. [2], with permission.*

13.1.1 VO_2 SYNTHESIS METHODS

A variety of methods can be used to synthesize VO_2; these methods include chemical vapor deposition, reactive electron-beam evaporation, reactive magnetron sputtering, pulsed-laser deposition, sol-gel methods, hydrothermal processes, physical vapor transport, and activated reactive evaporation (Table 13.1). In 2008, a comparison of various VO_2 fabrication methods was published by Nag & Haglund.[55] The

TABLE 13.1 Methods of VO_2 Synthesis

VO_2 Production Methodology	Example Reference(s)
Chemical vapor deposition	8–12
Reactive electron-beam deposition	13
Reactive magnetron sputtering	14–26
Pulsed laser deposition	27–38
Sol-gel	28,39–48
Hydrothermal process	49
Physical vapor transport	50–53
Activated reactive evaporation	54

thermochromic properties (i.e., transition temperature, switching contrast, hysteresis width) are extremely dependent on the various deposition parameters (e.g., temperature, composition of the deposition atmosphere, and atmospheric pressure) and upon the specific characteristics of the substrate (e.g., material, crystalline structure, and temperature during deposition).[56]

13.1.2 Switching Time of the Phase Transition of VO_2

Despite more than 50 years of research, the physical mechanism behind the ultrafast solid-solid SMT of VO_2 is still a topic of controversy. Generally speaking, there are two models that are used to describe the SMT:

(a) the Peierls model,[6,57–61] in which the SMT is described in terms of interactions between electrons and phonons and is structurally driven, and
(b) the Mott-Hubbard model,[57,62–65] which describes the SMT in terms of an electron-electron correlation and is therefore charge driven.

This controversy has been discussed in a number of places; excellent discussions can be found in the literature (e.g., Refs. [66–71]), but despite this research, the question remains: Which comes first: the structural change or the electronic transition?

At the same time, a collection of experiments enables us to understand the ultrafast SMT of VO_2; among other things, the measured transition time is dependent upon:

- the resolution of the experimental setup;
- the properties of the substrate;
- the thickness of the VO_2, the size and shape of the VO_2 particles, any structural defects present in the sample; and
- the properties of the dopants and/or impurities that are present in the sample.

Table 13.2 summarizes the measured switching time of VO_2 transitions using femtosecond pump-probe spectroscopy (in transmission and reflection), femtosecond X-ray spectroscopy, four-dimensional imaging, and ultrafast electron microscopy.

TABLE 13.2 Experimental Switching Time Measurements of the SMT of VO_2

VO_2 Thickness	Growth Substrate	Measurement Technique	Optical[a] t_{switch} (fs)	Reference
200 nm	Glass	Femtosecond pump-probe spectroscopy on transmission and reflection modes	500	25
200 nm	Glass	Femtosecond X-ray and pump-probe reflectivity spectroscopy	470	72
50 and 100 nm 50 nm 200 nm	SiO_2 Al_2O_3 MgO	Pump-probe transient reflectivity	10^4-10^5	73
25 nm 50 nm 70 nm 90 nm 100 nm 140 nm 160 nm	SiO_2	Pump-probe transient reflectivity	500 (but slower in deep layers of films thicker than 50 nm)	74
120 nm	BK7 glass	THz pump-probe transmission spectroscopy	6000	75
100 nm	Al_2O_3	THz pump-probe transmission spectroscopy	700	76
50-200 nm	Mica	Four-dimensional imaging; ultrafast electron microscopy	3100	48
5 nm single crystal	—	Four-dimensional imaging; ultrafast electron microscopy	307	77
100 nm nanoparticles	Silica	Pump-probe transmission spectroscopy	<120	78

[a]The typical switching time in SMTs that are electrically induced is on the order of one nanosecond slower than that reported in Table 13.1 (see Ref. [79]).

13.1.3 Effects of atomic oxygen irradiation on the properties of VO_2

Jiang et al.[80] investigated the effects of atomic oxygen (AO) irradiation on the thermochromic properties of VO_2-coated aluminum substrates. In this study, a space environment was simulated by irradiating VO_2/Al with AO doses equivalent to 6 months and 3 years in a typical low Earth orbital environment; results showed that the thermochromic properties of VO_2 were slightly affected by small doses of AO irradiation, but dramatically affected after longer exposures. Scanning electron microscopy (SEM) analysis showed mild erosion of the sample irradiated with high AO doses, and the X-ray photoelectron analysis showed that the oxygen-to-vanadium ratio in the VO_2 sample increased slightly (likely due to the high reactivity of the oxygen ions with the VO_2[80]). In addition, the IR emittance is temperature dependent; specifically, the IR emittance increased and the T_{trans} decreased slightly when VO_2 was irradiated with a high AO dose. Similar increased emittance was observed in the case of high quality of SiO_2 layers, which is currently used as a protective layer in the AO irradiation environment.[80]

The increasing of the IR emittance with the increase in temperature of the VO_2/Al was exploited in the fabrication of passive smart radiator devices to control the temperature of the spacecraft and then ensure a good operation of the on-board equipment.[80–83]

13.1.4 Doping effects on the phase transition of VO_2

The T_{trans} of VO_2 is relatively close to room temperature (~68 °C). However, for practical applications, T_{trans} must be modified to the specific temperature dictated by the requirements of the device and its operating environment. A wide range of dopants has been used to both increase and decrease the transition temperature of VO_2 (Table 13.3). In the following sections, we describe some of the most interesting results resulting from doping VO_2 with these dopants.

13.1.4.1 Mo dopant and sol-gel VO_2

Hanlon et al.[111] investigated the effect of Mo doping on the thermochromic properties of VO_2 synthesized on a glass substrate using a sol-gel method. Figure 13.5 compares the electrical conductivity of undoped VO_2 to that of Mo-doped VO_2 films. The conductivity of both undoped and doped VO_2 films increases with temperature. The Mo dopant reduces the hysteresis width and decreases the $T_{trans,}$ which reaches 24 °C for 7 at.% of Mo.

13.1.4.2 Co-doping VO_2 with W and F

Burkhardt et al.[86] studied the effects of doping VO_2 with W and F; Figure 13.6 shows the temperature dependence of the transmittance at a wavelength of 2 μm for

TABLE 13.3 Effects of Dopants on VO_2[6,55]

Dopant	Change in T_{trans} (°C/at.%)	Sample Reference
F	−35	84–86
Cr	+3	9,87–97
Fe	+3	9,87,93,95–97
Ga	+6.5	98
Al	+9.0	87,93,98,99
Ti	−0.5 to −0.7	88,89,96,97,100
Re	−4	88,101,102
Ir	−4	101
Os	−7	101
Ru	−10	101
Ge	+5	96,98,103,104
Nb	−7.8	40,88,92,93,96,105–109
Ta	−5 to −10	97,108
Mo	−5 to −10	88,105,110–113
W	−23 and −28	3,6,86,88,89,100,105,114–119
Ce	−4.5	120
Au	−6.4	121

undoped, W-doped, and F-doped VO_2 thin films deposited by RF sputtering from a vanadium target in background of O_2-Ar gas. In addition, Burkhardt et al. found that both dopants decrease T_{trans} and narrow the hysteresis at the cost of switching contrast (i.e., variation of the transmittance between the low-temperature and high-temperature states).[86]

13.1.4.3 Ce-doped VO_2

Recently, Song et al.[120] synthesized Ce-doped VO_2 films on a muscovite substrate using a sol-gel method. The transmittance switching measurements at a wavelength of 2.5 µm showed that Ce decreased T_{trans} by about 4.5 °C/at.%. In addition, Song et al.'s results indicate that Ce may be the only VO_2 dopant that reduces the gain size of the VO_2 films (see Figure 13.1 in Song et al.[120]).

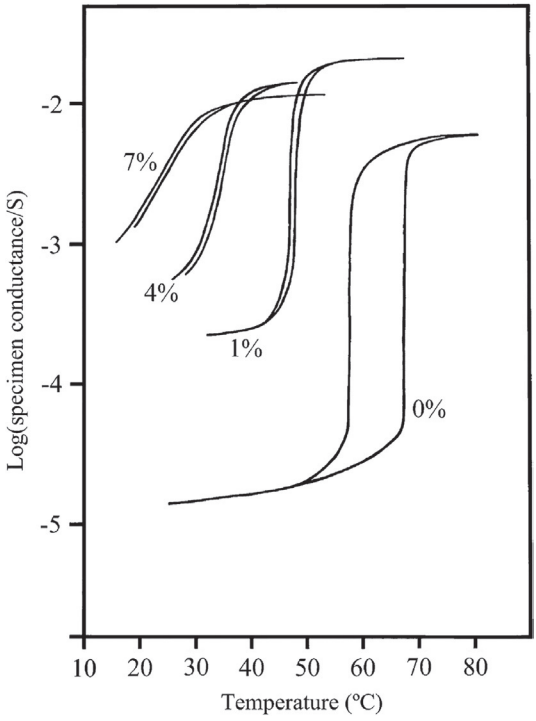


Figure 13.5 A comparison of the electrical conductivity of undoped, 1 at.%, 4 at.%, and 7 at.% Mo-doped VO_2 films on glass as a function of temperature. *Taken from Ref. [111], with permission.*

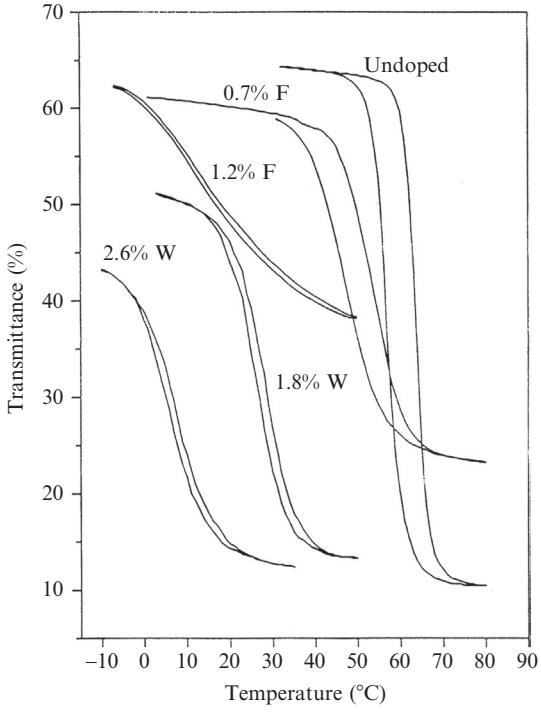


Figure 13.6 Comparison of the hysteresis loops in transmittance showing switching at 2 μm for undoped, W-doped, and F-doped VO_2 thin films. *Taken from Ref. [86], with permission.*

13.1.4.4 Comparing W-doped and W-Ti Co-doped VO_2

Soltani et al.[3] studied the effects of doping VO_2 with W and co-doping VO_2 with W and Ti. The results are shown in Figure 13.7, which compares the transmittance at a wavelength of 2.5 μm through both heating and cooling cycles of undoped, W(1.4 at.%)-doped, and W(1.4 at.%)-Ti(12 at.%) co-doped VO_2 thin films on quartz substrates. In this figure, we see that the transmittance drops (i.e., the samples become more opaque) with increasing temperature for undoped and metal-doped VO_2, but both W and Ti significantly affect the transmittance of the semiconducting state: the transmittance drops from 50% for the undoped film to about 40% for the W-Ti co-doped VO_2 film and to about 30% for W-doped VO_2. In the metallic state, all of the films are completely opaque. The hysteresis width (about 5 °C) of W-doped VO_2 remains identical to that of undoped VO_2, but co-doping VO_2 with W and Ti almost completely suppresses the hysteresis—a fact that can be exploited in the fabrication of optical modulators. T_{trans} is significantly affected by W doping, dropping to ~36 °C for 1.4 at.% W-doped VO_2 (cf. 68 °C for an undoped VO_2 film of the same thickness) and corresponding to 22.85 °C per at.% W dopant.[3]

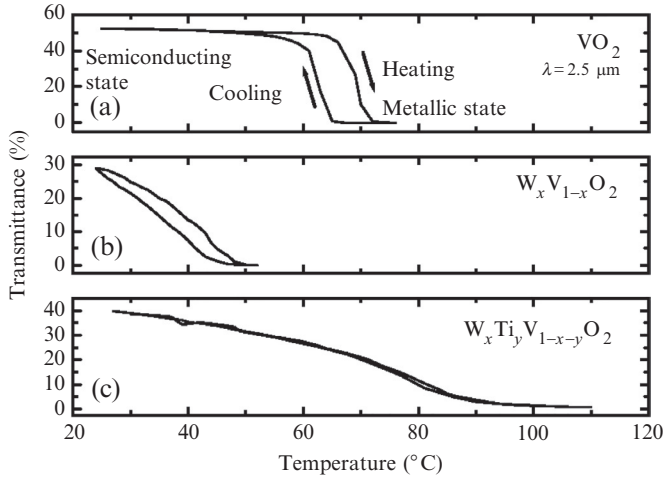


Figure 13.7 Comparison of the optical hysteresis loops at a wavelength of 2.5 μm obtained from the temperature dependence of the IR transmittance in both heating and cooling cycles of (a) undoped VO_2 (top), (b) W(1.4 at.%)-doped VO_2 (center), and (c) Ti(12 at.%)-W(1.4 at.%) co-doped VO_2 (bottom). *Taken from Ref. [3], with permission.*

In addition to the optical effects, doping VO_2 with W and Ti also affects electrical resistivity; Figure 13.8 shows the temperature dependence of the electrical resistivity of undoped, W(1.4 at.%)-doped, and Ti(12 at.%)-W(1.4 at.%) co-doped VO_2 thin films. Due to the SMT, the resistivity of all of the samples decreases as the

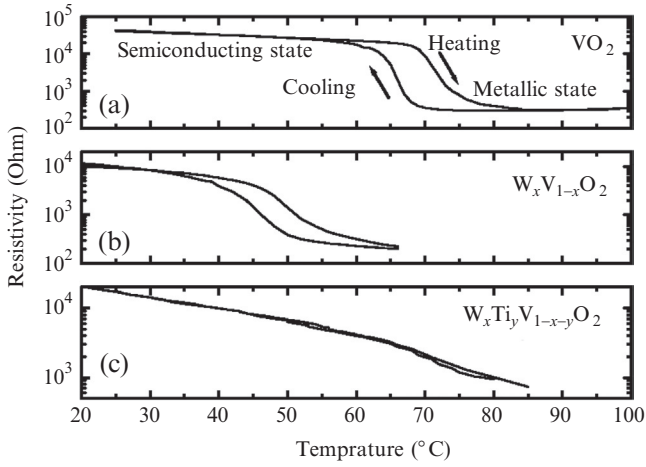


Figure 13.8 Comparison of the temperature dependence of the electrical resistivity of (a) undoped VO_2, (b) W(1.4 at.%)-doped VO_2, and (c) Ti(12 at.%)-W(1.4 at.%) co-doped VO_2. *Taken from Ref. [3], with permission.*

temperature of the sample increases (i.e., when the sample switches to its metallic state, it is a better conductor). W doping has relatively little effect on the resistivity of the metallic state, but decreases the resistivity of the semiconducting state (i.e., doping with metals makes the semiconducting state more metallic) due to the increase in the number of charge carriers in the film resulting from the presence of the W donor dopant.

Compared to the W-doped VO_2, the electrical resistivity of W-Ti co-doped VO_2 is enhanced in both states. In the W-Ti co-doped film, the Ti concentration (12 at.%) is much higher than that of W dopant (1.4 at.%). As a result, the Ti acceptors compensate for the W donors, causing a decrease in the overall carrier charge and enhancing the resistivity in both states.

The change in resistivity as a function of temperature is exploited in IR bolometers that utilize the change resistivity to measure heating by IR radiation. The principal property that must be maximized in order to achieve maximum sensitivity for IR bolometers is the temperature coefficient of resistance (*TCR*), defined as the slope of the log of electrical resistivity *R* of the semiconducting state:

$$\mathrm{TCR} = \frac{\mathrm{d}R}{R\mathrm{d}T} \tag{13.1}$$

The TCR values for VO_2 (−1.76%/°C) and W-doped VO_2 (−1.76%/°C) are comparable to that of VO_x (−2%/°C) (which is currently used in commercially available uncooled IR micro-bolometers).[122] Raytheon recently patented a neutron detector

system combining a microbolometric sensitive VO_x layer with a neutron sensitive reaction layer (e.g., ^{10}B or ^{6}Li).[123]

The results of Soltani et al.[3] demonstrate that the Ti-W co-doped VO_2 results in a much higher TCR (–5.12%/°C)—a value comparable to that of a single VO_2 crystal (–6%/°C). The suppression of both the optical and electrical hysteresis combined with the higher TCR of Ti-W co-doped VO_2 films will open the way for development of innovative IR sensors based on these characteristics.

13.2 Applications

As discussed in Section 13.1.4, the T_{trans} of VO_2 can be tailored to almost any desirable temperature by controlling the concentration levels of dopants. In addition, the SMT of VO_2 can be initiated by external stimuli such as temperature, pressure, photo-carrier injection, photo-excitation, or an electric field. Indeed, in some cases, these external environments can be constructed in such a way that only a minimum change in the environment is required to initiate the SMT (i.e., a VO_2 film could be held at a specific voltage potential so that the film required a small amount of thermal energy to initiate the SMT). These characteristics make VO_2 very attractive for a wide variety of applications. In the following sections, we describe a few of the VO_2-enabled applications, including optical and electrical switches, RF-microwave switches, tuneable plasmonic and metamaterial systems, and smart windows.

13.2.1 All-optical switches

All-optical switches are highly desirable for a large number of industrial applications in the communications and computing industries (among others). As we continue to watch Moore's Law being enacted,[124] the issue for integrated circuit manufacturers is no longer the size of the transistors, but the space occupied by interconnects. New paradigms of device performance could become available if we begin to take advantage of the ultrafast switching properties of VO_2.

Soltani et al.[37] investigated all-optical switching of undoped and W(1.4 at.%)-doped VO_2 films using a fiber-fed pump-probe technique in which a continuous wave diode laser ($\lambda = 980$ nm) with controllable power ($P_{max} = 60$ mW) was used to induce the SMT in the VO_2 (100-250 nm thick on quartz substrates), while another laser ($\lambda = 1550$ nm) was used to probe the transmittance switching of VO_2. Both beams were coupled into a single-mode optical fiber using a "Y" coupler and excited the sample at normal incidence. The transmitted light was collected by a single-mode optical fiber, and the results were recorded as a function of the pump laser power. Figure 13.9 compares the transmittance switching at 1550 nm as a function of increasing pump laser power for VO_2 and for W-doped VO_2 films, and shows that

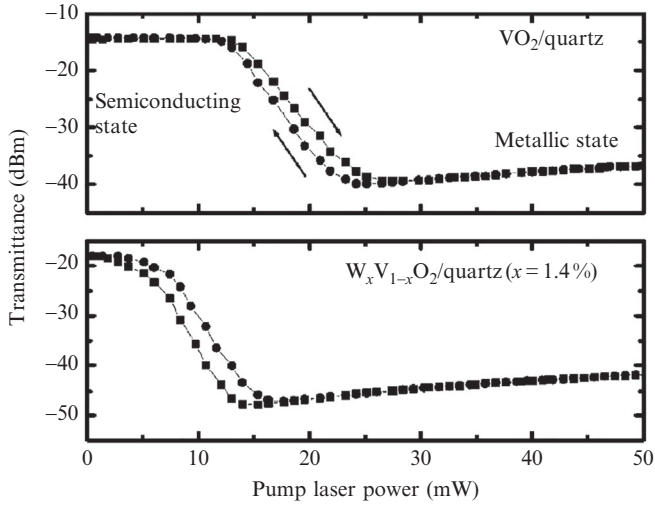


Figure 13.9 Transmittance switching driven at 980 nm and measured at 1550 nm for VO_2 and W-doped VO_2 thin films on quartz substrates. *Taken from Ref. [37], with permission.*

TABLE 13.4 Summary of Pump-Probe Results for Undoped and W-Doped VO_2[37]

Sample	Pump (980-nm) Power Required for Switching (mW)	Optical Hysteresis Width (mW)	Optical Contrast (dB)
Undoped VO_2	18	1.3	25
W-doped VO_2	10	1.95	28

both films switch from their semiconducting to their metallic states under the photo-excitation by the laser. Table 13.4 summarizes the results.

The switching mechanism in this experiment is due to the change in the band gap energy of VO_2 from photo-excitation by the pump laser.[125] Since the photon energy used in this experiment ($h\nu = 1.265$ eV) is higher than that of the valence band gap energy of VO_2 (0.67 eV[5]), increasing the pump laser power induces photo-excitation of the electrons from the filled $d_{\|}$ band into the empty $d_{\|}^*$ band. This creation of electron-hole pairs (i.e., excitons) in the VO_2 film causes overlapping of the $d_{\|}$ and $d_{\|}^*$ valence bands with the one-half filled valence d band (see Figure 13.4, above). As a result, the charge density increases, and the VO_2 switches to its metallic state.

Other studies (e.g., Rini et al.[5]) have shown that VO_2 can be switched well below the band gap energy of 0.67 eV. Although the highest contrast switching observed for

VO_2 is in the infrared, other experiments conclude that excitation can be driven by wavelengths in the optical region (even at very low power), although the observed contrast is very small and was assisted by localized surface plasmon resonances (LSPRs) from Au nanoparticles (NPs) (see Section 13.2.4).[126]

13.2.2 Electrical switches

Soltani et al. excited the VO_2 SMT by applying up to 20 DC volts and simultaneously measuring the reflectance and transmittance of a VO_2/TiO_2/ITO/glass structure at a wavelength of 1550 nm.[125]

In this structure (i.e., VO_2/TiO_2/ITO/glass), TiO_2 was used as a buffer layer to improve the crystallinity of the VO_2, and ITO was used as transparent electrode. The DC voltage was applied between the ITO (bottom electrode) and the VO_2 layer (top electrode). The entire structure was probed at incidence angle of 45° by an IR laser beam ($\lambda = 1550$ nm) from a tunable fiber laser source. The reflected and transmitted light was collected by two single-mode optical fibers and recorded by two photodetectors. Figure 7 of Soltani et al.[125] shows results from this experiment in which we see that the transmittance decreases and the reflectance increases with increasing the applied voltage (i.e., the material becomes more opaque and more metallic as the voltage is applied). The extinction ratio between the semiconducting and the metallic states is 12 dB in the transmittance mode and 5 dB in the reflectance mode at a switching voltage of 11.5 V.

The switching mechanism in this case is due to the charge transfer from the TiO_2 into the VO_2 layer under voltage.[125] When the applied voltage increases, the carrier charges are injected into VO_2, and as a result, the charge density increases and the VO_2 band gap vanishes (see Figure 13.4, above), resulting in the VO_2 switching to its metallic state.

13.2.3 VO_2-based hybrid metamaterial devices

Metamaterials are engineered materials that are designed to have physical properties that cannot be found in nature and allow the realization of new exciting devices that include (but are not limited to): cloaking, ultrafast optoelectronic switches, high-resolution imaging, transformation optics, radio frequency communications, and millimeter radar. Generally speaking, metamaterial devices consist of a dielectric substrate on which a periodic metallic structure (e.g., sub-wavelength resonator) is placed. The metamaterial's unit cell is designed in such a way that a specific resonant frequency is generated in response to an incident electromagnetic wave. Metamaterial-based systems have been designed to operate in the spectral range from the microwave through the THz to near-visible wavelengths (i.e., a portion of the electromagnetic spectrum ranging from a few mm to 400 nm). Recently, more research efforts have

been concentrated on the realization of tuneable metamaterials with nonlinear properties, and many of these take advantage of VO_2 to accomplish their goals. Incorporating VO_2 enables the devices to be tuneable by modulating the SMT of VO_2 with an external stimulus (e.g., temperature, photo-excitation, and electric fields).

13.2.3.1 Tuneable metamaterial devices

Crunteanu et al.[4] exploited the phase transition of VO_2 in the fabrication of thermally tuneable metamaterial devices operating between 0.1 and 1 THz; a sketch of the unit cell and an optical micrograph of their device are shown in the left and right panels of Figure 13.10, respectively.

The VO_2 hybrid metamaterial fabricated by Crunteanu et al. consists of a 500-µm thick c-cut sapphire substrate, a 120-nm thick active layer of VO_2, and a series of Au (200 nm)/Ti (10 nm) periodic resonator cells assembled using an electron-beam evaporation and lift-off process.[4] This device exploits the thermally controllable THz signal transmitted through the active VO_2 layer.

Crunteanu et al.[4] used THz time-domain spectroscopy to investigate the temperature dependence of the metamaterial devices. The normalized transmitted signals of the incident THz electric field were extracted from the ratio of the Fourier transform time traces of the transmitted THz signals through the device using the c-cut sapphire substrate as a reference; the results are shown in Figure 13.11.

In Figure 13.11, the two different configurations show that the THz transmitted signals are considerably attenuated when the VO_2 active layer switches to its metallic state at 100 °C (red curves exhibiting plateau). In the semiconducting state (at 20 °C; blue curves exhibiting resonant peaks), a resonant frequency of 0.65 THz is observed in the perpendicular configuration (left panel of Figure 13.11); this resonance is red-shifted to 0.45 THz and a second resonant frequency at 0.8 THz (due to the coupling

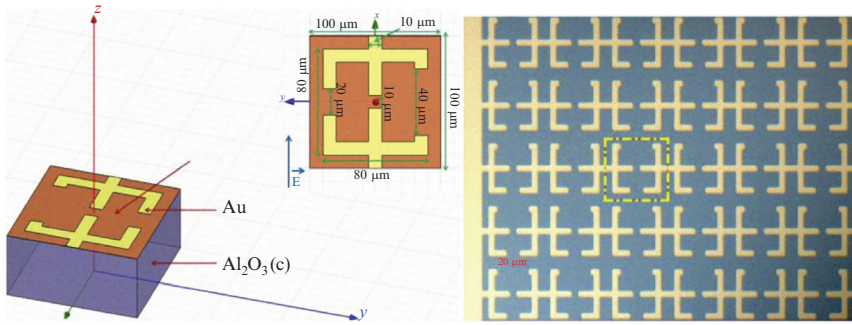


Figure 13.10 Unit cell of a THz metamaterial (left) and an optical micrograph of the device based upon the sketch. *Taken from Ref. [4], with permission.*

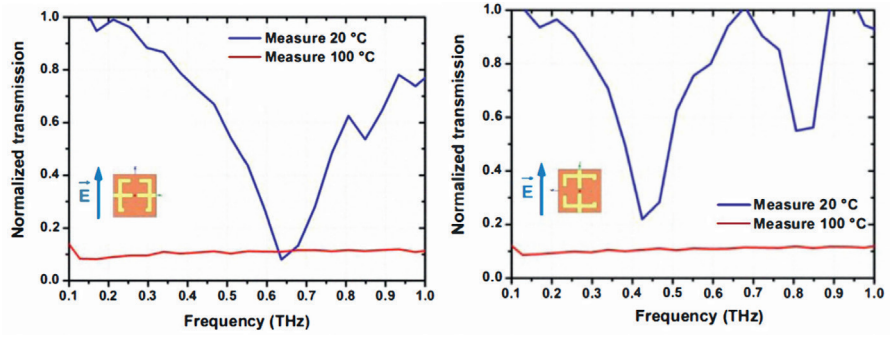


Figure 13.11 THz transmission through the VO_2 hybrid metamaterial in the semiconducting (blue) and metallic (red) phases when the incident electric field is perpendicular (left) and parallel (right) to the gap. *Taken from Ref. [4], with permission.*

of the different branches of the metamaterial's unit cell) is observed in the parallel orientation (right panel of Figure 13.11). These results show that simply rotating the device around the direction of the incident THz electric field can vary the resonant frequency at room temperature.

The fact that we can electronically stimulate the SMT of VO_2 implies that we can also fabricate VO_2-hybrid metamaterial devices that can be electrically tuned. Driscoll et al.[127] fabricated such a device by incorporating a patterned single layer of gold split-ring resonator (SRR) arrays onto 90-nm-thick VO_2 films deposited on a sapphire substrate using a sol-gel method (see panel A of Figure 1 in Driscoll et al.[127]). This device exploits the memory effect of the wide hysteresis loop of the SMT of VO_2 (see panel B of Figure 1 in Driscoll et al.[127]): the induced phase transition in VO_2 layer creates a large change in the permitivity of VO_2 that then increases the capacitance of the SRR. As a result, the resonant frequency decreases as the temperature increases (see panel C of Figure 1 in Driscoll et al.[127]). In the semiconducting state, the resonance frequency is 1.65 THz; this frequency redshifts by ~20% as the temperature increases and induces the phase transition of VO_2.

The device's electronic response control was demonstrated by maintaining its temperature at 338.6 K where the hysteresis is more pronounced (see the vertical dotted line in panel B of Figure 1 in Driscoll et al.[127]), and by then applying a series of electric pulses to the device. Figure 2 of Driscoll et al.[127] shows the effects on the resonant frequency of the device due to the 1-s electric pulses with increasing power. In that figure, we see that the resonant frequency redshifts and the capacitance increases as the power of the electric pulses increases. The frequency remained redshifted even after stopping the electric pulses, thereby demonstrating the persistent change in the VO_2-hybrid metamaterial device.

Several groups have modeled these devices using a circuit model, in which each SRR array is modeled by an RLC circuit element with a resonance frequency

$\omega=(LC)^{-1/2}$.[127] The inductance L is constant, and the capacitance of the SRR array changes with the frequency $C/C_0=(\omega/\omega_0)^2$. The increase in conductivity introduces a memory capacitance C_m and a memory resistance R_m, which reduce the quality factor of the device. The total capacitance $C_{tot}=C_0+C_m$ increases since each electric pulse (V_{ext}) causes the conductivity of the VO_2 layer to increase.

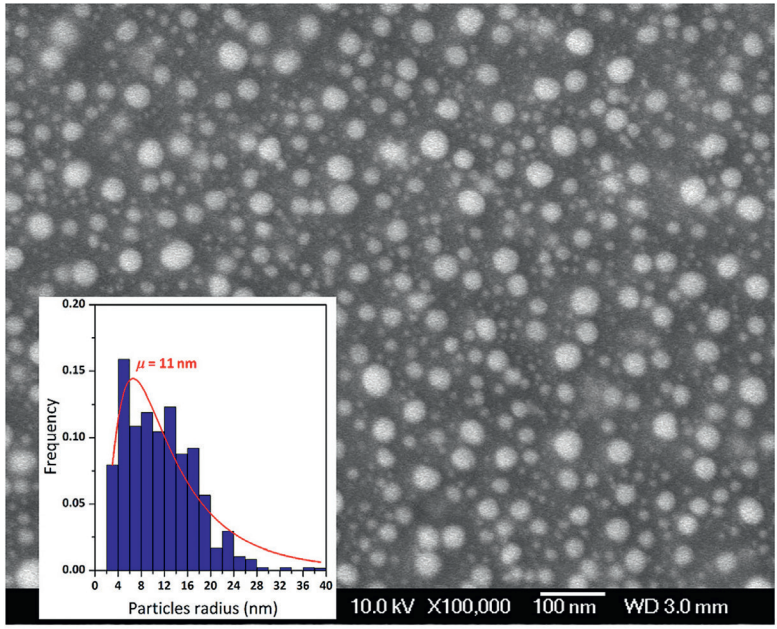


Figure 13.12 An SEM image of VO_2-Au composite material; the inset shows the size distribution of the Au NPs on the surface. *Taken from Ref. [128], with permission.*

13.2.4 VO_2 PLASMONIC DEVICES

Another fascinating application of VO_2 is the possibility of creating systems in which a LSPR can be generated and tuned by combining VO_2 with noble metal structures. By selecting the correct material, size, shape, pattern, and surrounding dielectric medium, devices can be finely tuned. Below, we describe three approaches used to fabricate such plasmonic systems: using composites, bilayer structures, and nano-arrays.

13.2.4.1 VO_2-Au nanoparticle composite

Orlianges et al.[128] investigated the electrical resistivity and optical properties of VO_2 thin films containing Au nanoparticles (NPs). The VO_2-Au nanocomposite had a thickness

of 200 nm that was synthetized by PLD onto c-cut sapphire substrates and alternatively ablating Au and vanadium targets using a KrF laser in an O_2 reactive gas atmosphere at a temperature of 920 K; an image of the resulting material is shown in Figure 13.12.

The temperature dependence of the electrical resistivity measurements showed the normal behavior of the SMT of VO_2: the resistivity decreased inversely with the temperature for both pure VO_2 films and the VO_2-Au composite. However, the VO_2-Au NP composite showed slightly less switching contrast (but within the same order of magnitude of plain VO_2 film) and had a slightly lower T_{trans} (341.85 K for VO_2-Au NPs compared to 345.34 K for the plain VO_2 film). Figure 13.13 shows the transmittance between 300 and 1500 nm for the VO_2-Au NPs composite, where we see that the transmittance in the NIR decreases with increasing temperature. This behavior is due to the thermally induced increase in free-carrier charge within the VO_2. The absorption peak near 650 nm is attributed to the LSPR of the Au NPs, and the position of the peak blueshifts as the temperature increases due to the variation of the dielectric properties of VO_2 at high temperatures (see, e.g., Verleur et al.[129]). The transmittance hysteresis loops (see the inset in Figure 13.13) indicate that as the temperature increases, the transmittance at 750 nm increases, but the transmittance at longer wavelengths (e.g., 1550 nm) decreases.

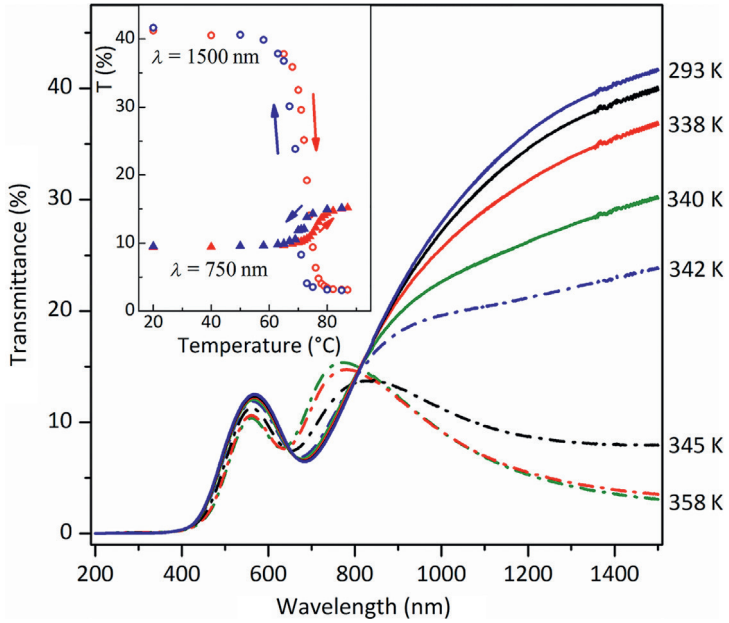


Figure 13.13 Transmittance spectra of VO_2 film containing Au NPs at selected temperatures during the heating process and thermal hysteresis loops of optical transmittance for 750 and 1500 nm (inset). *Taken from Ref. [128], with permission.*

13.2.4.2 Bilayer structure: Au-nanoparticles/VO_2 thin films

Xu et al.[130] created a bilayered system of Au NPs deposited directly on top of 25 nm of VO_2 on c-cut sapphire substrates (i.e., Au-NPs/VO_2/Al_2O_3). The VO_2 and Au NPs with equivalent mass thickness (d_m = 1, 2, 4, and 6 nm) were created using an RF magnetron sputtering process.

The bilayer structure was significantly more opaque in the NIR than the VO_2 reference material. As expected, both the VO_2 and bilayer composite samples were transparent in the infrared in the semiconducting state (at 30 °C), but the two samples were quite different once the VO_2 became metallic (at 80 °C). This difference was caused by the addition of the Au NPs and was very sensitive to the amount of Au in the sample. In addition, as more Au was added, the peak position of the LSPR continously redshifted (both as a function of the amount of Au and temperature). Figure 13.14 shows the absorption switching of the Au (6 nm)/VO_2(25 nm)/sapphire composite with its corresponding LSPR peak position: the redshift of this sample is 200 nm. Note that the LSPR of Au (6 nm)/quartz reference (without VO_2) is unaffected by the temperature increase, showing that this effect must be due to the interaction of the Au with the VO_2.

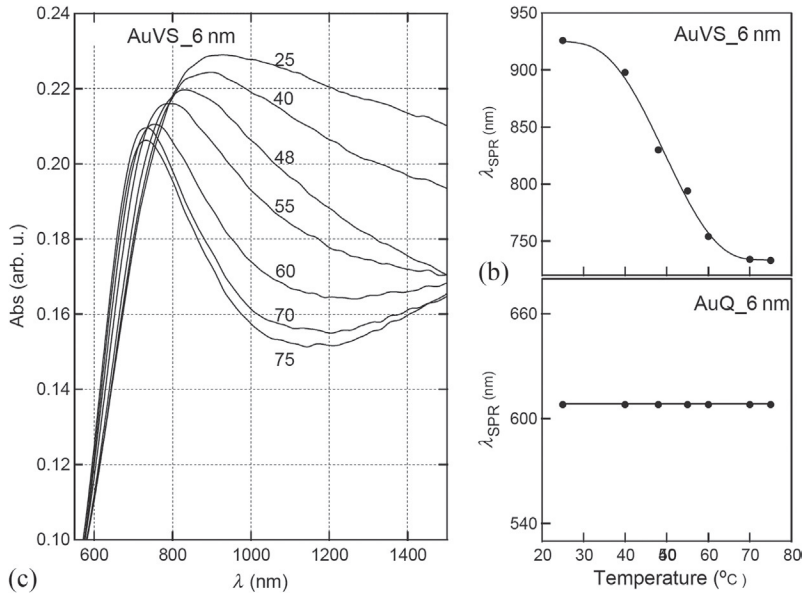


Figure 13.14 (a) Absorption switching (from 25 up to 75 °C) of Au (6 nm)/VO_2 (25 nm)/sapphire, (b) the corresponding temperature-dependent of the LSPR wavelength λ_{LSPR} compared to that of (b) the Au (d_m = 6 nm)/quartz reference without VO_2. *Taken from Ref. [130], with permission.*

13.2.4.3 Au::VO_2 nano-arrays

Ferrara et al.[126] compared the optically induced SMT of VO_2 film with that of the plasmonic response of Au::VO_2 nanocomposites. In this case, the nanocomposites consisted of 60 nm of VO_2 on top of 140-nm diameter, 20-nm thick Au arrays. The Au was patterned onto a c-cut sapphire substrate using standard electron-beam lithography techniques, and the VO_2 layer was deposited onto the fabricated Au arrays with PLD. Figure 13.15a shows the SEM image of the fabricated Au array before deposition of the VO_2 layer. Figure 13.15b compares the extinction efficiency of the Au::VO_2 structure when the VO_2 switches from its semiconducting state at 22 °C to its metallic state at 100 °C. Similar to the prior examples, the LSPR redshifts with increasing temperature, but shifts as much as 250 nm using this construction. Figure 13.15c compares the temperature dependence of the absorption at 785 nm for Au::VO_2 structure and VO_2 film. In the semiconducting state, both samples are

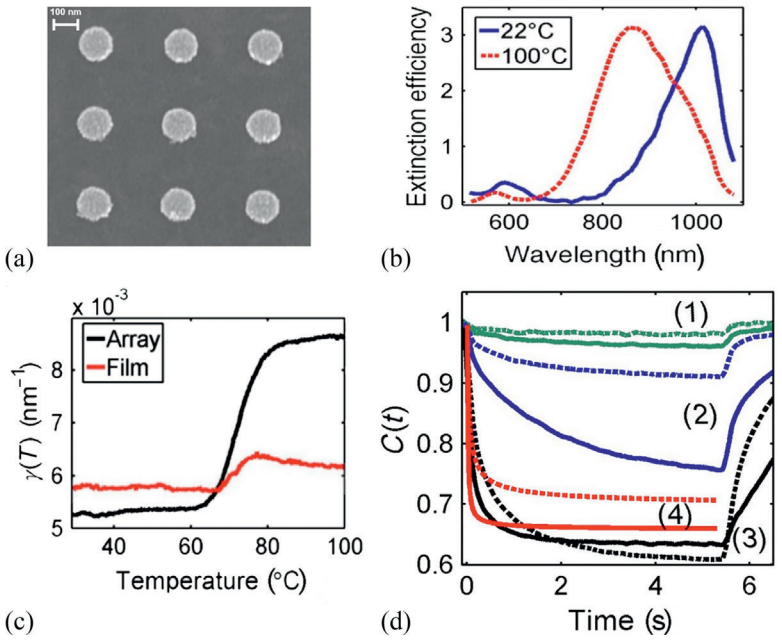


Figure 13.15 (a) An SEM image of the 140-nm Au array before deposition of the VO_2 film, (b) extinction spectra of 140 nm Au::VO_2 arrays in the semiconducting (blue) and metallic (red) states of VO_2, (c) absorption coefficient $\gamma(T)$ taken at $\lambda = 785$ nm and calculated from transmission measurements, (d) typical $C(t)$ measurements for the VO_2 film (dashed) and for the Au::VO_2 structure (solid) for 33 (1), 76 (2), and 163 W cm^2 (3); the theoretical prediction from Equation (13.2) for 76 W cm^2 is shown as the pair of curves labeled (4). *Taken from Ref. [126], with permission.*

relatively transparent, but in the metallic state, the Au::VO_2 is significantly more opaque than plain VO_2 film.

Ferrara et al.[126] also investigated the effects on switching due to optically induced LPSRs using a standard pump-probe experiment. The pump beam (785 nm) with variable intensity I was used to induce the SMT, while the transmittance of the Au::VO_2 structure was probed by an 18 W/cm^2 diode laser ($\lambda = 1550$ nm). The temperature of the structure was maintained in the semiconducting state at 55 °C [i.e., $T < T_{trans}(VO_2)$], and for each measurement, the Au::VO_2 nanostructured array was irradiated by the pump beam for 5.3 s. Figure 13.15d shows the contrast of the switching $C(t)$ (defined as the transmittance at 1550 nm normalized to that of the semiconducting VO_2 for both the Au::VO_2 nanostructured array and the VO_2 film), and as expected, the material becomes opaque when the VO_2 changes phase and the contrast is more dramatic as the laser power is increased.

The Au::VO_2 structure switches to the metallic state faster than plain VO_2 film; at the maximum intensity, the Au::VO_2 structure reaches 85 °C in ~1 s (cf. equilibrium of 5.3 s for the plain VO_2 film). Using first-principles thermodynamics,[126] Ferrara et al. show that the temperature increase ΔT of the interface between the substrate and the sample (either plain VO_2 film or a Au::VO_2 nanostructured array) can be described by:

$$\Delta T = \frac{2q\sqrt{\alpha t}}{\kappa}\left[\frac{1}{\sqrt{\pi}} - i\ \mathrm{erfc}\left(\frac{a}{2\sqrt{\alpha t}}\right)\right] \tag{13.2}$$

in which $q = I(1-R)[1-\exp(-\gamma_{eff} z_0)]$ is the energy absorbed in the sample, and $\alpha = 5.3\times10^{-3}$ cm^2/s and $\kappa = 9.6$ mW/(cm °C) are the thermal diffusivity and conductivity of the glass substrate, respectively. In Equation (13.2), R is the reflectivity at the VO_2-air interface, γ_{eff} is the effective laser absorption coefficient, and z_0 is the thickness of the film.

This basic model has a few flaws. It predicts that $C(t)$ decreases more quickly and C_{max} increases more quickly than were experimentally observed. These discrepancies can be explained once we understand that this model overestimates the absorption in the metallic state, which then results in an overestimation of C_{max}. The model also ignores the fact that the granular nature of the VO_2 tends to preclude lateral heat diffusion out of the laser focal spot. Despite its shortcomings and relative simplicity, the model does support the main experimental results: the Au::VO_2 reaches a higher VO_2 metallic fraction and a higher C_{max} faster than the VO_2 film without the Au nanostructure (Figure 13.15d).

The dynamics of Au::VO_2 structure and VO_2 film were analyzed by fitting $\boldsymbol{C_{max}(I)}$ with a three-parameter sigmoid given by:

$$C(I) = 1 - \frac{1 - C_H}{1 + \exp\left(\dfrac{I - I_c}{I_w}\right)} \tag{13.3}$$

in which I_c is the critical switching intensity defined at the midpoint of the transition, I_w is the width of the transition, and C_H is the high-temperature contrast. [126] The fit to the experimental data (shown in Figure 13.16) indicates that both the I_c and I_w decrease by approximately a factor of 1.5 in the case of the Au::VO_2 structure, demonstrating that less pump laser power is required to drive the phase transition of the Au::VO_2 nanostructure than that of plain VO_2.

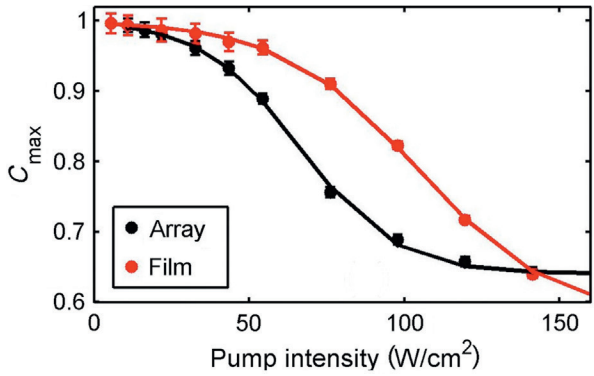


Figure 13.16 Maximum contrast as a function of the pump intensity for 140 nm Au::VO_2 (black) and VO_2 film (red) at $t = 5.3$ s. *Taken from Ref. [126], with permission.*

13.2.5 VO_2-BASED RF-MICROWAVE SWITCHES

Dumas-Bouchiat et al.[131] exploited the SMT of VO_2 in order to fabricate RF-microwave switches that operate between 560 MHz and 35 GHz. The design was based on a microwave coplanar waveguide (CPW), and integrated 200 nm of VO_2 as an active layer in two configurations: a shunt configuration (Figure 13.17, top) and a series configuration (Figure 13.17, bottom).

Each device was assembled as follows: (1) the substrate material was selected (either SiO_2/Si or c-cut sapphire); (2) ~200 nm of evaporated gold was placed onto the substrates; (3) the coplanar waveguides were patterned using lithography and wet etching; (4) a 200-nm thick film of VO_2 was deposited by PLD; and, (5) to minimize propagation losses, the Au lines were thickened by up to ~800 nm.[131] The temperature dependence of the transmittance through the CPW lines was recorded by means of a RF-microwave test bench; Figure 13.18 shows the evolution of the S_{21} parameters for the shunt configuration (a; top) and the series configuration (b; bottom) as the VO_2 switches from its semiconducting state at 300 K to its metallic state at 400 K.

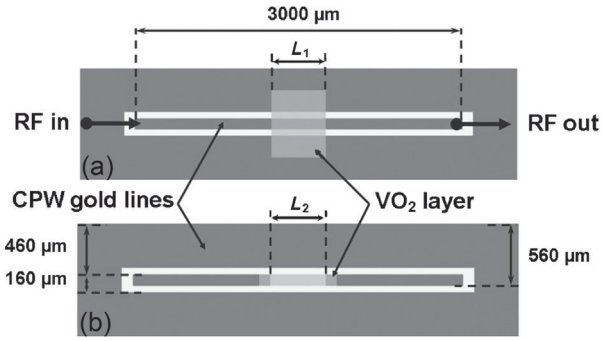


Figure 13.17 Basic microwave switch design based on VO_2. Shunt and series configurations are shown on the top and bottom, respectively. *Taken from Ref. [131], with permission.*

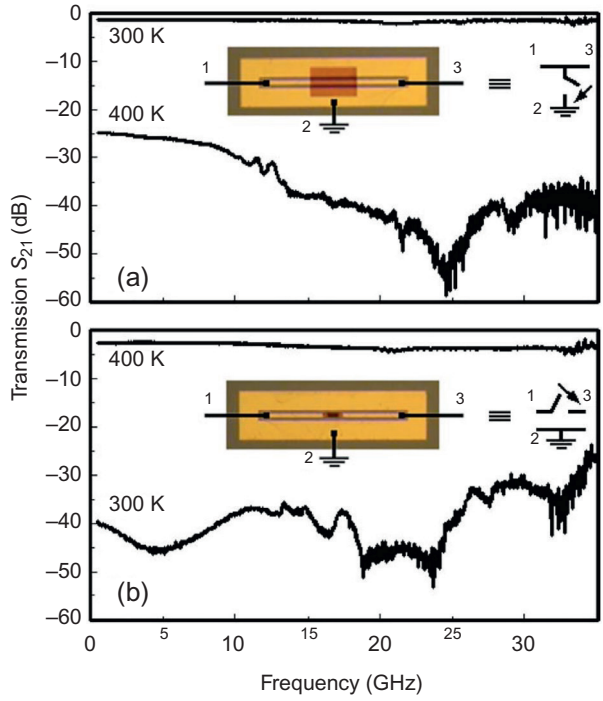


Figure 13.18 Transmission switching S_{21} of coplanar waveguide lines deposited on c-cut sapphire in two configurations: (a) shunt (top) and (b) series (bottom). *Taken from Ref. [131], with permission.*

At 300 K, the shunt switch loses very little signal (about 0.8 dB), but at 400 K, the VO_2 short-circuits the signal to the ground and strongly attenuates the signal (see Figure 13.18a).[131] The series configuration behaves oppositely to the shunt switch: at 300 K, the signal is largely attenuated due to the presence of the VO_2 layer, and at 400 K the signal is transmitted through the metallic state of VO_2 with insertion losses as low as 2.5 dB (see Figure 13.18b).[131]

Despite the differences in electrical resistivity between the VO_2:Al_2O_3(c) and VO_2:Si/SiO_2 systems, both configurations displayed similar performance, demonstrating that VO_2 is a very promising active material that can be used to fabricate active, high-contrast, high-isolation RF-microwave switches operating over a large frequency range.

13.2.6 Smart windows

As discussed in Section 13.1, as a result of the solid-solid phase transition, the IR transmittance of VO_2 changes considerably as a function of temperature, but the visible transmittance remains unchanged. This characteristic can be exploited in "smart windows" applications, in which the external temperature affects the IR thermochromic properties of VO_2 and thereby enables the interior temperature of the building to remain regulated (cooler) with less need for costly air-conditioning systems (for a recent review of this technology, please see the recent review by Kamalisarvestani et al.[132]).

Since the natural T_{trans} of VO_2 is higher than that the typical environmental temperature, this application requires the use of doped VO_2 with a tailored T_{trans}. Various dopant elements have been used to alter the T_{trans} of VO_2 (see Section 13.1.4, above), but these dopants can also degrade the optical and thermochromic properties of VO_2. Several approaches have been proposed to improve these properties, including those of Li et al.,[133] who proposed using a combination of VO_2 and TiO_2 manufactured as core-shell nanoparticles, which could then be formed into flexible foils and used as a component in these smart windows. The VO_2/TiO_2 structure integrates the thermochromic properties of VO_2 nanorod cores with the photocatalytic properties of TiO_2 anatase shells. Li et al.[133] also observed that plain VO_2 films are dark yellow (even when quite thin), but the use of VO_2/TiO_2 core-shell particles to create a film increased the luminous transmittance and changed the color of the films to light blue (see Figure 13.19).

Min et al.[134] developed a VO_2-based porous structure exhibiting high luminous transmittance and excellent solar modulation efficiency, and recently, Mg-doped VO_2 NPs[135], F-doped VO_2 NPs,[136] and W-, Mo-, and W-doped VO_2 films were all proposed as potential ways to improve the luminous transmittance of the VO_2-based smart windows.

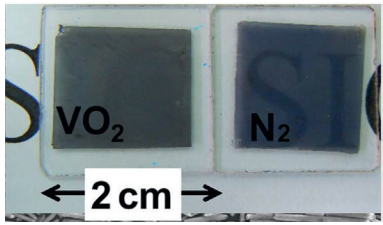


Figure 13.19 20-nm VO_2/TiO_2 core/shell particle film on glass (left) and 70-nm VO_2/TiO_2 core-shell particle film on glass (right). Notice the strong color change from yellow/brown to blue and the transparency difference between the two samples. *Taken from Ref. [133], with permission.*

13.3 Conclusion

In this brief review, we have presented some of the fascinating smart coatings and interesting applications that can only be created using the thermochromic properties and ultrafast SMT of VO_2. In addition, it is clear that progress towards commercial "smart windows" continues to be made in leaps and bounds with the improvement of their transmittance in the visible portion of the spectrum and in solar modulation efficiency[132,137,138] Finally, we can all look forward to the use of VO_2 in combination with noble metals in the fabrication of plasmonic- and metamaterial-based devices that can be used in a wide variety of applications including (but not limited to) optical modulators,[139] negative capacitors,[140] field effect transistors,[141] active shutters,[142] optical limiting devices,[143] sunshields for spacecraft,[144] and photonic resonators.[145] Many other applications that take advantage of the unique properties of VO_2 are sure to arise in the near future.

References

1. Morin F. Oxides which show a metal-to-insulator transition at the Neel temperature. Phys Rev Lett 1959;3(1):34–6.
2. Eyert V. The metal insulator transitions of VO_2: a band theoretical approach. Ann Phys 2002;11(9):650–704.
3. Soltani M, Chaker M, Haddad E, et al. Effects of Ti–W codoping on the optical and electrical switching of vanadium dioxide thin films grown by a reactive pulsed laser deposition. Appl Phys Lett 2004;85(11):1958–60.
4. Crunteanu A, Leroy J, Humbert G, et al. Tunable terahertz metamaterials based on metal-insulator phase transition of VO_2 layers. In: Microwave symposium digest (MTT), 2012 IEEE MTT-S international; IEEE; 2012. p. 1–3.
5. Rini M, Hao Z, Schoenlein R, et al. Optical switching in VO_2 films by below-gap excitation. Appl Phys Lett 2008;92(18):181904.
6. Goodenough JB. The two components of the crystallographic transition in VO_2. J Solid State Chem 1971;3:490–500.
7. Goodenough JB. Metallic oxides. Prog Solid State Chem 1971;5:145–399.
8. Koide S, Takei H. Epitaxial growth of VO_2 single crystals and their anisotropic properties in electrical resistivities. J Physical Soc Japan 1967;22(3):946–7.

9. Everhart C, MacChesney J. Anisotropy in the electrical resistivity of vanadium dioxide single crystals. J Appl Phys 1968;39(6):2872–4.
10. Maruyama T, Ikuta Y. Vanadium dioxide thin films prepared by chemical vapour deposition from vanadium (III) acetylacetonate. J Mater Sci 1993;28(18):5073–8.
11. Ryabova L, Serbinov I, Darevsky A. Preparation and properties of pyrolysis of vanadium oxide films. J Electrochem Soc 1972;119(4):427–9.
12. Ibisate M, Golmayo D, López C. Vanadium dioxide thermochromic opals grown by chemical vapour deposition. J Opt A-Pure Appl Opt 2008;10(12):125202.
13. Marvel R, Appavoo K, Choi B, et al. Electron-beam deposition of vanadium dioxide thin films. Appl Phys A: Mater Sci Process 2013;111:975–81.
14. Chain E. Effects of oxygen in ion-beam sputter deposition of vanadium oxide. J Vac Sci Technol A 1987;5(4):1836–9.
15. Fuls E, Hensler D, Ross A. Reactively sputtered vanadium dioxide thin films. Appl Phys Lett 1967;10(7):199–201.
16. Guinneton F, Sauques L, Valmalette J-C, et al. Optimized infrared switching properties in thermochromic vanadium dioxide thin films: role of deposition process and microstructure. Thin Solid Films 2004;446(2):287–95.
17. Rozgonyi G, Hensler D. Structural and electrical properties of vanadium dioxide thin films. J Vac Sci Technol 1968;5(6):194–9.
18. Thornton JA. Plasma-assisted deposition processes: theory, mechanisms and applications. Thin Solid Films 1983;107(1):3–19.
19. Duchene J, Terraillon M, Pailly M. RF and DC reactive sputtering for crystalline and amorphous VO_2 thin film deposition. Thin Solid Films 1972;12(2):231–4.
20. Mahan JE. Physical vapor deposition of thin films, by John E. Mahan. Wiley-VCH; 2000, ISBN: 0-471-33001-9, pp. 336.
21. Wasa K, Kitabake M, Adachi H. Thin films materials technology: sputtering of compound materials. New York: William Andrew, Inc.; 2004.
22. Jin P, Yoshimura K, Tanemura S. Dependence of microstructure and thermochromism on substrate temperature for sputter-deposited VO_2 epitaxial films. J Vac Sci Technol A 1997;15(3):1113–7.
23. Rozgonyi G, Polito W. Preparation of thin films of vanadium (di-, sesqui-, and pent-) oxide. J Electrochem Soc 1968;115(1):56–7.
24. Lim S, Long J, Xu S, et al. Nanocrystalline vanadium oxide films synthesized by plasma-assisted reactive RF sputtering deposition. J Phys D Appl Phys 2007;40(4):1085–90.
25. Becker MF, Buckman AB, Walser RM, et al. Femtosecond laser excitation of the semiconductor-metal phase transition in VO_2. Appl Phys Lett 1994;65(12):1507–9.
26. Chen X, Li J, Lv Q. Thermoelectrical and optical characteristics research on novel nanostructured VO_2 thin film. Optik Int J Light Electron Opt 2013;124(15):2041–4.
27. Borek M, Qian F, Nagabushnam V, et al. Pulsed laser deposition of oriented VO_2 thin films on R-cut sapphire substrates. Appl Phys Lett 1993;63(24):3288–90.
28. Chae B, Youn D, Kim H, et al. Fabrication and electrical properties of pure VO_2 phase films. J Korean Phys Soc 2004;44(4):884–8.
29. Chrisey DB, Hubler GK. Pulsed laser deposition of thin films. In: Chrisey DB, Hubler GK, editors. Pulsed laser deposition of thin films. Wiley-VCH; May 2003. p. 648, ISBN: 0-471-59218-8.
30. Eason R. Pulsed laser deposition of thin films: applications-led growth of functional materials. New York: John Wiley & Sons; 2007.
31. Aguadero A, de la Calle C, Pérez-Coll D, et al. Study of the crystal structure, thermal stability and conductivity of $Sr(V0.5Mo0.5)O_3+\delta$ as SOFC material. Fuel Cells 2011;11(1):44–50.
32. Kim D, Kwok H. Pulsed laser deposition of VO_2 thin films. Appl Phys Lett 1994;65(25):3188–90.

33. Kana Kana JB, Ndjaka JM, Ngom BD, et al. High substrate temperature induced anomalous phase transition temperature shift in sputtered VO_2 thin films. Opt Mater 2010;32(7):739–42.
34. Pauli S, Herger R, Willmott P, et al. X-ray diffraction studies of the growth of vanadium dioxide nanoparticles. J Appl Phys 2007;102(7):073527.
35. Donev EU, Suh JY, Lopez R, et al. Using a semiconductor-to-metal transition to control optical transmission through subwavelength hole arrays. Adv Optoelectron 2008;2008:1–10.
36. Akiyama M, Oki Y, Nagai M. Steam reforming of ethanol over carburized alkali-doped nickel on zirconia and various supports for hydrogen production. Catal Today 2012;181(1):4–13.
37. Soltani M, Chaker M, Haddad E, et al. Optical switching of vanadium dioxide thin films deposited by reactive pulsed laser deposition. J Vac Sci Technol A 2004;22(3):859–64.
38. Rúa A, Cabrera R, Coy H, et al. Phase transition behavior in microcantilevers coated with M_1-phase VO_2 and M_2-phase VO_2:Cr thin films. J Appl Phys 2012;111(10):104502.
39. Beteille F, Livage J. Optical switching in VO_2 thin films. J Sol-Gel Sci Technol 1998;13(1–3):915–21.
40. Guzman G, Beteille F, Morineau R, et al. Thermochromic $V1-xNb_xO_2$ sol-gel thin films. Eur J Solid State Inorg Chem 1995;32(7–8):851–61.
41. Chen H-K, Hung H-C, Yang TC-K, et al. The preparation and characterization of transparent nano-sized thermochromic VO_2–SiO_2 films from the sol–gel process. J Non-Cryst Solids 2004;347(1):138–43.
42. Dachuan Y, Niankan X, Jingyu Z, et al. Vanadium dioxide films with good electrical switching property. J Phys D Appl Phys 1996;29(4):1051–7.
43. Guzman G, Beteille F, Morineau R, et al. Electrical switching in VO_2 sol–gel films. J Mater Chem 1996;6(3):505–6.
44. Livage J. Sol-gel chemistry and electrochemical properties of vanadium oxide gels. Solid State Ionics 1996;86–88:935–42.
45. Appavoo K, Lei DY, Sonnefraud Y, et al. Role of defects in the phase transition of VO_2 nanoparticles probed by plasmon resonance spectroscopy. Nano Lett 2012;12(2):780–6.
46. Partlow D, Gurkovich S, Radford K, et al. Switchable vanadium oxide films by a sol-gel process. J Appl Phys 1991;70(1):443–52.
47. Wu YF, Fan LL, Chen SM, et al. Spectroscopic analysis of phase constitution of high quality VO_2 thin film prepared by facile sol-gel method. API Adv 2013;3(4):042132.
48. Grinolds MS, Lobastov VA, Weissenrieder J, et al. Four-dimensional ultrafast electron microscopy of phase transitions. Proc Natl Acad Sci 2006;103(49):18427–31.
49. Popuri SR, Miclau M, Artemenko A, et al. Rapid hydrothermal synthesis of VO_2 (B) and its conversion to thermochromic VO_2 (M_1). Inorg Chem 2013;52(9):4780–5.
50. Guiton BS, Gu Q, Prieto AL, et al. Single-crystalline vanadium dioxide nanowires with rectangular cross sections. J Am Chem Soc 2005;127(2):498–9.
51. Bassim ND, Schenck PK, Donev EU, et al. Effects of temperature and oxygen pressure on binary oxide growth using aperture-controlled combinatorial pulsed-laser deposition. Appl Surf Sci 2007;254(3):785–8.
52. Wu J, Gu Q, Guiton BS, et al. Strain-induced self organization of metal-insulator domains in single-crystalline VO_2 nanobeams. Nano Letters 2006;6(10):2313–7.
53. Tselev A, Luk'yanchuk I, Ivanov I, et al. Symmetry relationship and strain-induced transitions between insulating M_1 and M_2 and metallic R phases of vanadium dioxide. Nano Letters 2010;10(11):4409–16.
54. Case FC. Influence of ion beam parameters on the electrical and optical properties of ion assisted reactively evaporated vanadium dioxide thin films. J Vac Sci Technol A 1987;5(4):1762–6.
55. Nag J, Haglund Jr. R. Synthesis of vanadium dioxide thin films and nanoparticles. J Phys Condens Matter 2008;20(26):264016.
56. Jeong J, Aetukuri N, Graf T, et al. Suppression of metal-insulator transition in VO_2 by electric field-induced oxygen vacancy formation. Science 2013;339(6126):1402–5.
57. Zylbersztejn A, Mott N. Metal-insulator transition in vanadium dioxide. Phys Rev B 1975;11(11):4383.

58. Peierls RE. Quantum theory of solids. Oxford: Oxford University Press; 1955.
59. Wentzcovitch RM, Schulz WW, Allen PB. VO_2: Peierls or Mott-Hubbard? A view from band theory. Phys Rev Lett 1994;72(21):3389–92.
60. Paquet D, Leroux-Hugon P. Electron correlations and electron-lattice interactions in the metal-insulator, ferroelastic transition in VO_2: a thermodynamical study. Phys Rev B 1980;22(11):5284–301.
61. Cavalleri A, Dekorsy T, Chong HH, et al. Evidence for a structurally-driven insulator-to-metal transition in VO_2: a view from the ultrafast timescale. Phys Rev B 2004;70(16):161102.
62. Hubbard J. Electron correlations in narrow energy bands. Proc R Soc Lond A Math Phys Sci 1963;276(1365):238–57.
63. Hubbard J. Electron correlations in narrow energy bands. II. The degenerate band case. Proc R Soc London, Ser A 1964;277(1369):237–59.
64. Hubbard J. Electron correlations in narrow energy bands. III. An improved solution. Proc R Soc London, Ser A 1964;281(1386):401–19.
65. Rice T, Launois H, Pouget J. Comment on "VO_2: Peierls or mott-hubbard? A view from band theory". Phys Rev Lett 1994;73(22):3042.
66. Cavalleri A, Rini M, Chong H, et al. Band-selective measurements of electron dynamics in VO_2 using femtosecond near-edge X-ray absorption. Phys Rev Lett 2005;95(6):067405.
67. Qazilbash MM, Brehm M, Chae B-G, et al. Mott transition in VO_2 revealed by infrared spectroscopy and nano-imaging. Science 2007;318(5857):1750–3.
68. Kübler C, Ehrke H, Huber R, et al. Coherent structural dynamics and electronic correlations during an ultrafast insulator-to-metal phase transition in VO_2. Phys Rev Lett 2007;99(11):116401.
69. Biermann S, Poteryaev A, Lichtenstein A, et al. Dynamical singlets and correlation-assisted peierls transition in VO_2. Phys Rev Lett 2005;94(2):026404.
70. Tomczak JM, Biermann S. Effective band structure of correlated materials: the case of VO_2. J Phys Condens Matter 2007;19(36):365206.
71. Haverkort M, Hu Z, Tanaka A, et al. Orbital-assisted metal-insulator transition in VO_2. Phys Rev Lett 2005;95(19):196404.
72. Cavalleri A, Tóth C, Siders C, et al. Femtosecond structural dynamics in VO_2 during an ultrafast solid-solid phase transition. Phys Rev Lett 2001;87(23):237401.
73. Lysenko S, Vikhnin V, Zhang G, et al. Insulator-to-metal phase transformation of VO_2 films upon femtosecond laser excitation. J Electron Mater 2006;35(10):1866–72.
74. Lysenko S, Rua A, Vikhnin V, et al. Light-induced ultrafast phase transitions in VO_2 thin film. Appl Surf Sci 2006;252(15):5512–5.
75. Zhi C, Qi-Ye W, Kai D, et al. Ultrafast and broadband terahertz switching based on photo-induced phase transition in vanadium dioxide films. Chin Phys Lett 2013;30(1):017102.
76. Nakajima M, Takubo N, Hiroi Z, et al. Study of photo-induced phenomena in VO_2 by terahertz pump-probe spectroscopy. J Lumin 2009;129(12):1802–5.
77. Baum P, Yang D-S, Zewail AH. 4D visualization of transitional structures in phase transformations by electron diffraction. Science 2007;318(5851):788–92.
78. Rini M, Cavalleri A, Schoenlein R, et al. Giant, ultrafast optical switching based on an insulator-to-Metaltransition in VO_2 nano-particles: photo-activation of shape-controlledplasmons at 1.55 µm. Berkeley, CA (US): Ernest Orlando Lawrence Berkeley National Laboratory; 2004.
79. Hormoz S, Ramanathan S. Limits on vanadium oxide Mott metal–insulator transition field-effect transistors. Solid-State Electron 2010;54(6):654–9.
80. Jiang X, Soltani M, Haddad E, et al. Effects of atomic oxygen on the thermochromic characteristics of VO_2 coating. J Spacecraft Rockets 2006;43(3):497–500.
81. http://www.mpb-space.com/web/smart_structures/radiator.html.
82. Kruzelecky RV, Haddad E, Wong B, et al. Variable emittance thermochromic material and satellite system. *US patent 7761053 B2*; 2010.

83. Soltani M, Chaker M, Haddad E, et al. Thermochromic vanadium dioxide (VO_2) smart coatings for switching applications. In: Chen X, editor. Applied physics in the 21st century. Research Signpost; Kerala, India; 2008. ISBN: 978-81-7895-313-7.
84. Bayard M, Reynolds T, Vlasse M, et al. Preparation and properties of the oxyfluoride systems V2O5F and VO_2-xFx. J Solid State Chem 1971;3(4):484–9.
85. Bayard M, Pouchard M, Hagenmuller P, et al. Propriétés magnétiques et electriques de l'oxyfluorure de formule $VO_2 - xFx$. J Solid State Chem 1975;12(1):41–50.
86. Burkhardt W, Christmann T, Meyer B, et al. W-and F-doped VO_2 films studied by photoelectron spectrometry. Thin Solid Films 1999;345(2):229–35.
87. Galy J, Casalot A, Darriet J, et al. Some new phases with non-stoichiometric character in V2O5-VO2-M2O3 systems (M = Al Cr and Fe). Bull Soc Chim Fr 1967;1:227–34.
88. Marinder B-O, Magneli A. Metal-metal bonding in some transition metal dioxides. Acta Chem Scand 1957;11(10):1635–40.
89. MacChesney J, Guggenheim H. Growth and electrical properties of vanadium dioxide single crystals containing selected impurity ions. J Phys Chem Solid 1969;30(2):225–34.
90. Marezio M, McWhan DB, Remeika J, et al. Structural aspects of the metal-insulator transitions in Cr-Doped VO_2. Phys Rev B 1972;5(7):2541–51.
91. Pierce J, Goodenough J. Structure of orthorhombic V0.95Cr0.05O2. Phys Rev B 1972;5(10): 4104–11.
92. Pouget J, Lederer P, Schreiber D, et al. Contribution to the study of the metal-insulator transition in the V1-xNbxO_2 system—II magnetic properties. J Phys Chem Solid 1972;33(10):1961–7.
93. Villeneuve G, Bordet A, Casalot A, et al. Proprietes physiques et structurales de la phase Crx$V1-xO2$. Mater Res Bull 1971;6(2):119–30.
94. Villeneuve G, Drillon M, Hagenmuller P. Contribution a l'etude structurale des phases V1-xCrxO2. Mater Res Bull 1973;8(9):1111–21.
95. Kosuge K. The phase transition in VO_2. J Physical Soc Japan 1967;22:551–7.
96. Mitsuishi T. On the phase transformation of V02. Jpn J Appl Phys 1967;6(9):1060–71.
97. Futaki H, Kobayashi K, et al. Thermistor composition containing vanadium dioxide. *U.S. patent 3,402,131*; September17, 1968.
98. Kitahiro I, Watanabe A. Shift of transition temperature of vanadium dioxide crystals. Jpn J Appl Phys 1967;6(8):1023–4.
99. Longo JM, Kierkegaard P. A refinement of the structure of V02. Acta Chem Scand 1970;24(2):420–6.
100. Walter Rüdorff H. Kornelson. Angew Chem 1968;7:229.
101. Chamberland BL, Rogers DB. Temperature sensitive conductive metal oxide modified vanadium dioxides. *U.S. patent 3,542,697*; November. 24, 1970.
102. Sävborg Ö, Nygren M. Magnetic, electrical, and thermal studies of the V1-x$RexO_2$ system with $0 \leqq x \leqq 0.15$. Phys Status Solidi A 1977;43(2):645–52.
103. Aoki M, Kobayashi K, Futaki H. Abstract of the fall meeting of the Applied Physical Society of Japan 1965;59. (in Japanese); see also Futaki H, Aoki M. Effects of various doping elements on the transition temperature of vanadium oxide semiconductors. Jpn J Appl Phys 1969;8:1008.
104. Neuman C, Lawson A, Brown R. Pressure dependence of the resistance of VO_2. J Chem Phys 1964;41:1591–5.
105. Batista C, Ribeiro RM, Teixeira V. Synthesis and characterization of VO_2-based thermochromic thin films for energy-efficient windows. Nanoscale Res Lett 2011;6(1):1–7.
106. Jorgenson G, Lee J. Doped vanadium oxide for optical switching films. Sol Energy Mater 1986;14(3):205–14.
107. Rüdorff W, Märklin J. Untersuchungen an ternären Oxiden der Übergangsmetalle. III. Die Rutilphase (V1-xNbx) O2. Z Anorg Allg Chem 1964;334(3–4):142–9.
108. Trarieux H, Bernier JC, Michel A. Ann Chim 1969;4:183–94.

109. Villeneuve G, Launay J-C, Hagenmuller P. Proprietes electriques du systeme V1-xNbxO2. Solid State Commun 1974;15(10):1683–7.
110. Kierkegaard P, Axrup S, Israesson M, et al. Studies on structural relations in crystalline and vitreous compounds. [Stockholm Univ (Sweden) Inst of Inorganic and Physical Chemistry], DTIC Document, DIS No. 31; 1968.
111. Hanlon T, Coath J, Richardson M. Molybdenum-doped vanadium dioxide coatings on glass produced by the aqueous sol–gel method. Thin Solid Films 2003;436(2):269–72.
112. Jin P, Tanemura S. V1-xMo_xO_2 thermochromic films deposited by reactive magnetron sputtering. Thin Solid Films 1996;281:239–42.
113. Wu Z, Miyashita A, Yamamoto S, et al. Molybdenum substitutional doping and its effects on phase transition properties in single crystalline vanadium dioxide thin film. J Appl Phys 1999;86(9):5311–3.
114. Jin P, Tanemura S. Relationship between transition temperature and x in V1-xWxO2 films deposited by dual-target magnetron sputtering. Jpn J Appl Phys 1995;34(5A):2459–60.
115. Lee M-H, Kim M-G. RTA and stoichiometry effect on the thermochromism of VO_2 thin films. Thin Solid Films 1996;286(1):219–22.
116. Nygren M, Israelsson M. A DTA study of the semiconductor-metallic transition temperature in V1-xWxO2, 0≤ x≤ 0.067. Mater Res Bull 1969;4(12):881–6.
117. Reyes J, Sayer M, Chen R. Transport properties of tungsten-doped VO_2. Can J Phys 1976;54(4):408–12.
118. Tang C, Georgopoulos P, Fine M, et al. Local atomic and electronic arrangements in WxV1-xO2. Phys Rev B 1985;31(2):1000–11.
119. Tazawa M, Jin P, Tanemura S. Optical constants of V(1-x)W(x)O2 Films. Appl Opt 1998;37(10):1858–61.
120. Song L, Zhang Y, Huang W, et al. Preparation and thermochromic properties of Ce-doped VO_2 films. Mater Res Bull 2013;48(6):2268–71.
121. Cavanna E, Segaud J, Livage J. Optical switching of au-doped VO_2 sol-gel films. Mater Res Bull 1999;34(2):167–77.
122. Uncooled detectors for thermal imaging cameras. http://www.flir.com/uploadedfiles/Eurasia/MMC/Appl_Stories/AS_0015_EN.pdf.
123. Rhiger DR, Harris B. Neutron detection system. *US Patent 8183537*; 2012.
124. Moore GE. Cramming more components onto integrated circuits. Electronics 1965;Volume 38:114–7, See also: Moore GE. Cramming more components onto integrated circuits. *Proc IEEE* 1998; **Volume 86**(1):82–5.
125. Soltani M, Chaker M, Haddad E, et al. 1 × 2 optical switch devices based on semiconductor-to-metallic phase transition characteristics of VO_2 smart coatings. Meas Sci Technol 2006;17(5):1052–6.
126. Ferrara DW, MacQuarrie ER, Nag J, et al. Plasmon-enhanced low-intensity laser switching of gold::vanadium dioxide nanocomposites. Appl Phys Lett 2011;98(24):241112.
127. Driscoll T, Kim H-T, Chae B-G, et al. Memory metamaterials. Science 2009;325(5947):1518–21.
128. Orlianges JC, Leroy J, Crunteanu A, et al. Electrical and optical properties of vanadium dioxide containing gold nanoparticles deposited by pulsed laser deposition. Appl Phys Lett 2012;101(13):133102.
129. Verleur HW, Barker Jr. AS, Berglund CN. Optical properties of VO_2 between 0.25 and 5 eV. Phys Rev 1968;172(3):788–98.
130. Xu G, Huang C-M, Tazawa M, et al. Tunable optical properties of nano-Au on vanadium dioxide. Opt Commun 2009;282(5):896–902.
131. Dumas-Bouchiat F, Champeaux C, Catherinot A, et al. rf-microwave switches based on reversible semiconductor-metal transition of VO_2 thin films synthesized by pulsed-laser deposition. Appl Phys Lett 2007;91(22):223505.

132. Kamalisarvestani M, Saidur R, Mekhilef S, et al. Performance, materials and coating technologies of thermochromic thin films on smart windows. Renew Sustain Energy Rev 2013;26:353–64.
133. Li Y, Ji S, Gao Y, et al. Core-shell VO_2@TiO_2 nanorods that combine thermochromic and photocatalytic properties for application as energy-saving smart coatings. Sci Rep 2013;3:1370.
134. Min Zhou JB. Minshan Tao, Rui Zhu, Yingting Lin, Xiaodong Zhanga, and Yi Xie. Periodic porous thermochromic VO_2(M) films with enhanced visible transmittance. Chem Commun 2013;49:6021–3.
135. Zhou J, Gao Y, Liu X, et al. Mg-doped VO_2 nanoparticles: hydrothermal synthesis, enhanced visible transmittance and decreased metal–insulator transition temperature. Phys Chem Chem Phys 2013;15(20):7505–11.
136. Gao YF, Zhou J, Dai L, et al. F-doped VO_2 nanoparticles for thermochromic energy-saving foils with modified color and enhanced solar-heat shielding ability. Phys Chem Chem Phys 2013;15:11723–9.
137. Roberts PMS. Smart window. *Patent application US 20120301642 A1*; 2012.
138. Kim H, Kim Y, Kim KS, et al. Flexible thermochromic films based on hybridized VO_2/graphene. ACS Nano 2013;7(7):5769–76.
139. Jiang L, Carr WN. Design, fabrication and testing of a micromachined thermo-optical light modulator based on a vanadium dioxide array. J Micromech Microeng 2004;14(7):833.
140. Soltani M, Chaker M. System and method for generating a negative capacitance. *Patent application US20120286743*; 2012.
141. Byung Gyu CHAE, Hyun Tak KIM, Doo Hyeb YOUN. Field effect transistor using vanadium dioxide layer as channel material and method of manufacturing the field effect transistor. *US patent 6933553 B2*; 2005.
142. Jeffrey De Natale F. Vanadium-dioxide front-end advanced shutter technology. *US patent 8067996 B2*; 2011.
143. Kaye AB, Richard Forsberg HJ. Phase-change materials and optical limiting devices utilizing phase-change materials. *US patent 8259381 B2*; 2012.
144. Soltani M, Chaker M, Haddad E, et al. Thermochromic vanadium dioxide smart coatings grown on Kapton substrates by reactive pulsed laser deposition. J Vac Sci Technol A 2006;24(3):612.
145. Bryan L, Jackson LVJ, Zhiyong Li. Photonic device including at least one electromagnetic resonator operably coupled to a state-change material. *US patent 7446929 B1*; 2008.

Chapter 14

One-Part Self-Healing Anticorrosive Coatings: Design Strategy and Examples

Jinglei Yang, Mingxing Huang
School of Mechanical and Aerospace Engineering, Nanyang Technological University, Singapore

14.1 Introduction

Corrosion of metal is one of the most destructive processes that results in material failure, and it causes huge economic loss annually. Corrosion is a destructive attack of a metal by chemical or electrochemical reaction with the environment, and it is an electrochemical process that involves anodic reaction and cathodic reaction.[1,2] Reduction reactions and oxidation reaction occur at the cathodic area and anodic area, respectively, while the corrosion of metal usually occurs at the anodic area.

As an example, the corrosion of iron is demonstrated in Figure 14.1. It can be seen that, when an iron panel is immersed in corrosive electrolyte solution, the cathodic reaction consists of the reduction of dissolved oxygen, hydrogen ion, and water, while the oxidation reaction at the anodic area dissolves iron to produce Fe^{2+},

Intelligent Coatings for Corrosion Control
Copyright © 2015 Elsevier Inc. All rights reserved.

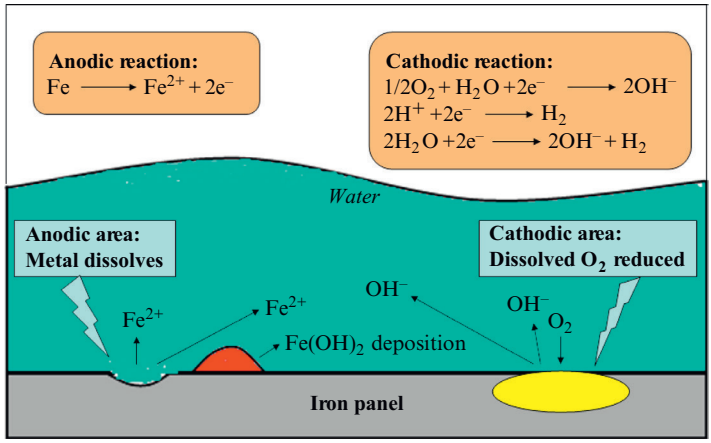


Figure 14.1 Mechanism of iron corrosion in water.

leaving voids in the iron panel. Usually Fe^{2+} will react with OH^- in the solution to yield $Fe(OH)_2$, and after a serial of further reactions, finally Fe_2O_3 will be produced, and this is the rust that one usually sees on a corroded iron.

Corrosion control is one of the most important issues when people use metals. To date many strategies have been developed to alleviate corrosion damage, and traditional approaches include material selection, cathodic protection, addition of corrosion inhibitor, engineering design, and so forth.[2–4] Nevertheless, among the variety of approaches for corrosion control, applying coating on an object is the most straightforward one to provide corrosion protection function to metal substrates. Coating provides a direct barrier layer to separate the underneath metal from external corrosive environment. In addition, corrosion inhibitor can be loaded into the coating layer to provide further corrosion suppression function. However, the degradation of coating is always a problematic issue. If coating degradation and failure are not detected in a timely manner, the underlying metal will be directly exposed to the corrosive environment and may suffer from severe and rapid corrosion. In this case, if the coating can autonomously respond to the degradation and failure to recover its integrity or other function, its service life will be dramatically extended, and the corrosion protection function will be prolonged as well. Materials that possess the autonomous recovery ability are self-healing materials.

Self-healing behavior is a ubiquitous phenomenon in nature. For example, animals are able to self-heal via a "bleeding" mechanism when their skin experiences injury or scratches.[5] In such a process, the biological system responds to external stimuli, injury for example, and transfers healing species to the injured location to heal the injury. Inspired by nature, modern self-healing materials are also able to sense damage and release healing agents to realize self-healing

function. Self-healing is advantageous over traditional techniques including welding, patching, and *in situ* curing of resin for repairing materials because it is much more time and cost efficient.[6]

Due to their great importance, self-healing materials have been the focus of researchers since the last century, and many approaches have been developed for their manufacturing. However, most of early self-healing materials require manual intervention such as heating and irradiation. For example, Jud et al.[7] reported the self-healing performance of a thermoplastic polymer, but the healing was realized at elevated temperature that allowed for molecular interdiffusion. Chung et al.[8] reported the self-healing behavior of a poly(methoxy methylacrylate) coating, but light irradiation was necessary to trigger the cyclo-addition reaction of cinnamoyl groups to achieve the healing purpose.

In an ideal self-healing system, the healing behavior should be completely autonomous without any manual intervention. In this sense, the first self-healing material was developed by White et al.[9] in 2001. Dicyclopentadiene (DCPD) monomer was stored in poly(urea-formaldehyde) (PUF) microcapsules, which were evenly distributed in a polymer matrix. The self-healing function was realized via the polymerization of DCPD when the monomer contacted predispersed Grubbs' catalyst particles. The whole process did not require any detection or manual intervention to initiate the repairing behavior and thus was deemed as self-healing. To date, a number of self-healing materials have appeared, and the progress on this topic can be found on many review papers.[5,10–13]

The concept of self-healing has been recently proposed for anticorrosion applications, and this novel approach has become a promising direction to develop anticorrosive coatings. Usually degradation of coating starts from the formation of microcracks. Microcracks will rupture embedded reservoir where healing agents are stored, and the healing agents flow into the crack plane, undergoing healing reaction to rebond the cracks of the self-healing coating. In principle, capsules, hollow tubes and microvascular network can be used as reservoirs to store the healant in the development of self-healing coatings, but considering the restriction of the small thickness of coating, only microcapsules can be employed in a coating system. For example, Sauvant-Moynot et al.[14] fabricated a self-healing anticorrosive coating-based on the microencapsulation of a water-soluble and self-curable epoxy eletrodepositable adduct. When the adduct came into contact with water, it would cure and deposit in the cracks to exhibit self-healing capabilities. When an electrochemical impedance spectroscopy (EIS) test was performed on a steel panel treated with such a coating, it was revealed that the self-healing coating greatly improved its anticorrosion ability. Suryanarayana et al.,[15] Samadzadeh et al.,[16] and García et al.[17] also developed different self-healing anticorrosive coatings with different chemistry.

When microcapsules are incorporated into polymer to create self-healing anticorrosion function, the capsules should fulfill some strict requirement. For example, the

capsules should be mechanically robust enough to remain intact during processing and transportation, but on the other hand, they should be able to be ruptured on demand.[18] In addition, they should be stable and compatible with the healing species, host coating matrix, and practical environment where the final coating will be exposed to.

14.2 Design Strategies of One-Part Self-Healing Anticorrosive Coatings

14.2.1 Preparation of conventional self-healing materials

Self-healing materials can be generally classified into intrinsic and extrinsic systems based on their self-healing mechanism. Intrinsic self-healing materials usually take use of the reversible reaction of some functional groups of the materials. However, for intrinsic systems, usually external stimulus such as heat or light irradiation is required to trigger the healing reaction. For example, an oxetane-substituted chitosan precursor incorporating polyurethane (PU) was reported to exhibit good self-healing performance,[19] but UV radiation was necessary to trigger the healing reaction. Extrinsic self-healing materials, on the other hand, realize the self-healing function by prestored healing agents. Healing agents are stored in reservoir that is distributed in the host polymer, and they will be released in response to external stimuli. Based on the reservoirs used, self-healing materials can be generally divided into three groups: microcapsule-based,[20,21] hollow tube-based,[4] and microvascular-based.[22,23]

Preparation of microcapsules-based self-healing materials involves microencapsulation, a technique of encapsulating core material into microcapsules. Microencapsulation has been applied in various fields such as agriculture, pharmaceuticals, foods, textiles, coatings, flavoring and fragrances, and adhesives for a long time,[24] and it has also become one of the most important methods to design self-healing materials because it can be used for both bulk polymer composites and thin polymer coatings and the amount of healing agent can be monitored by tuning the microcapsules diameter. The healing function is usually realized by the polymerization reaction of a healing agent that is stored in microcapsules, and in most cases, a catalyst is necessary for triggering such a reaction. In a typical microcapsule-based system, the microcapsules containing healing agents are ruptured when cracks form in the host polymer matrix, and the encapsulated healing agents are hence released. Upon contact with catalyst, the healing agents undergo polymerization, forming a film to heal the cracks, as illustrated in Figure 14.2.[10] The self-healing polymer may be based on a monocapsules basis, in which the healing agent is encapsulated and the catalyst is directly distributed in a host matrix. Alternatively, self-healing polymer may be based on a dual capsules basis, in which the healing agent and catalyst

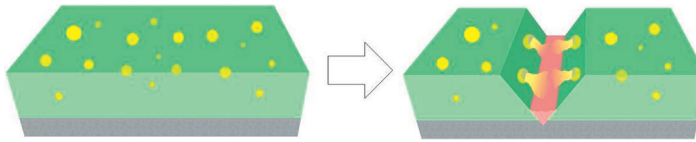


Figure 14.2 Mechanism of healing in a microcapsule-based system.

are both encapsulated in discrete capsules and the capsules are then randomly distributed in the host polymer matrix. Samadzadeh et al. reviewed the recent progress of microcapsules-based self-healing materials.[25]

Microencapsulation can be reached via a number of methods such as coacervation[26,27] and interfacial polymerization, spray drying.[28,29] Among the numerous methods for microencapsulation, interfacial polymerization and *in situ* polymerization are most common for self-healing materials development.

Interfacial polymerization usually takes place in a normal oil-in-water emulsion system, which is prepared by dispersing a water immiscible organic liquid (oil phase) into an aqueous continuous phase with the assistance of surfactant. In a typical interfacial polymerization reaction, one reactant of the polymerization and target core materials are contained in the oil phase, while the second reactant is in the aqueous phase. Polymerization reaction between the two reactants from different phases occurs to generate a polymer wall at the interface between the aqueous and organic phases, with core material being encapsulated.[25,30–32] For example, Yang et al.[33] reported the microencapsulation of isophorone diisocyanate (IPDI) by PU microcapsules via an interfacial polymerization. In this study, a toluene diisocyanate (TDI)-based PU prepolymer was prepared at first, which was mixed well with IPDI, the target core material, to form the oil phase. After the generation of oil-in-water emulsion system by adding the oil phase into aqueous continuous phase, addition of chain extender 1,4-butanediol initiated its polymerization reaction with the more reactive TDI prepolymer from the oil phase, while the less reactive IPDI was encapsulated as core material.

The IPDI-filled PU microcapsules had smooth surface as shown in Figure 14.3a. From Figure 14.3b, it is seen that the diameter and shell thickness of the obtained microcapsules were highly dependent on agitation rate during the reaction. When the agitation rate was 500 RPM, the prepared capsules had a diameter of about 413 µm. This is the first successful encapsulation of liquid-state reactive isocyanate monomer, whose high reactivity with water shows the potential for the development of one-part and catalyst-free self-healing system.

In situ polymerization has been one of the most popular methods to encapsulate active agents for self-healing application. Similar to interfacial polymerization, *in situ* polymerization also takes place in an emulsion system, but the reactants for the polymerization are from the same phase. The most well-known example of

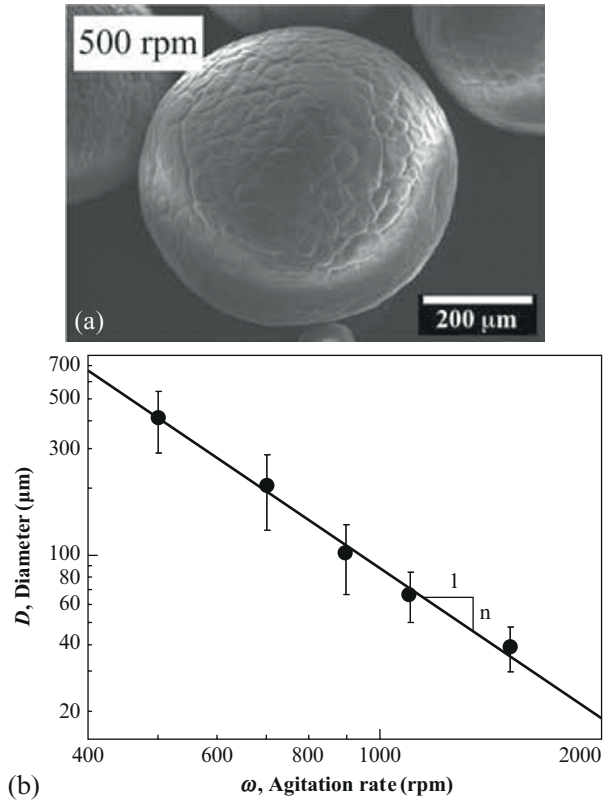


Figure 14.3 (a) Morphology of IPDI-filled PU microcapsules and (b) average diameter of microcapsules as a function of agitation rate.[33]

in situ polymerization for self-healing materials development is the synthesis of PUF microcapsules.

PUF is an excellent material that has been widely used in self-healing material. Microcapsules made from PUF are robust enough to withstand processing for self-healing materials manufacturing, and they can also be ruptured easily by propagating microcracks.[34] Yuan et al.[35,36] reported the preparation of PUF microcapsules containing epoxy resin through a two-step reaction. In the first step, urea-formaldehyde prepolymer was synthesized in aqueous phase, and in the second step, epoxy resin, the target core materials, was added into the obtained prepolymer solution to create an oil-in-water emulsion. The *in situ* polymerization of the urea-formaldehyde prepolymer yielded PUF microcapsules with epoxy resin encapsulated inside.

Brown et al.[20] reported a single-step reaction for the preparation of PUF microcapsules through *in situ* polymerization. In the synthesis, urea, ammonium chloride,

and resorcinol were added to ethylene maleic anhydride surfactant solution. After dissolution of these chemicals, the pH value of the solution was adjusted to 3.5 by adding sodium hydroxide and hydrochloric acid. DCPD liquid was added into the aqueous solution under stirring to create an oil-in-water emulsion system. A 37 wt.% formaldehyde solution was then introduced into the system. The *in situ* polymerization between urea and formaldehyde in the aqueous phase produced PUF microcapsules surrounding the DCPD oil droplets.

SEM images of the shell structure of the prepared PUF microcapsules as shown in Figure 14.4 revealed that the capsule shell was comprised of a smooth inner surface and a rough outer surface. The thickness of the inner surface was between 160 and 220 nm, and it was largely independent on synthesis parameters. The outer surface was an agglomeration of PUF nanoparticles. The microcapsules as prepared contained 83-92 wt.% DCPD, and the capsules diameter ranged from 10 to 1000 µm depending on agitation rate.

The method as described above has been used as a standard method to prepare PUF microcapsules. For example, Suryanarayana et al.[15] reported the microencapsulation of linseed oil by PUF microcapsules via an *in situ* polymerization following a very similar procedure, and García et al.[17] also similarly encapsulated a water reactive silyl ester for self-healing purposes.

Poly(melamine-formaldehyde) (PMF) microcapsules are also extensively used for self-healing application, and they are advantageous over PUF microcapsules in their mechanical properties, stability, and chemical resistance.[37–39] PMF microcapsules can also be prepared via *in situ* polymerization following a procedure similar to that for PUF microcapsules.[37,38]

Interfacial and *in situ* polymerization reactions have been extensively explored to synthesize single-component capsules. However, when microencapsulation is applied to develop self-healing materials, microcapsules made from single component

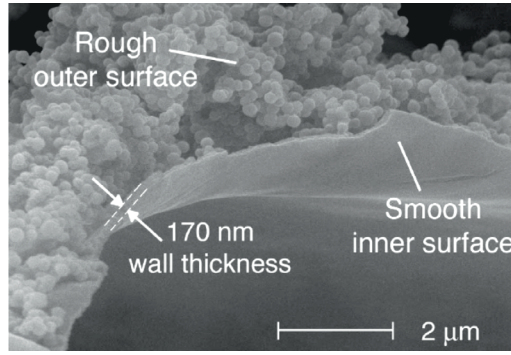


Figure 14.4 SEM image of shell structure of PUF microcapsules prepared via *in situ* polymerization.[20]

may not meet the complicated and strict requirement in practical application.[40] For example, PU microcapsules possess excellent mechanical and thermal property, but they are likely to agglomerate due to the cross-linking of residual isocyanate functional groups, and hence the distribution into host matrix may be problematic.[41] PUF microcapsules also have good mechanical property, and they can be easily distributed into host polymer, but they are unable to withstand high temperature, which is usually required in materials processing. To overcome these limitations, researchers developed techniques to prepare multilayered microcapsules to encapsulate active agents for self-healing applications. Microcapsules composed of two or more materials possess the combined advantage while avoiding the disadvantage of each single material, and hence they are superior.

Multilayered microcapsules can be prepared via a procedure combining interfacial polymerization and *in situ* polymerization. For example, Caruso et al.[42] demonstrated the microencapsulation of ethyl phenylacetate by PU-PUF double-layered microcapsules by combining interfacial and *in situ* polymerization in a single batch process. Compared with the normal *in situ* polymerization approach as described elsewhere for making PUF capsules,[20] herein after the addition of urea, ammonium chloride, and resorcinol into the surfactant solution and pH adjustment, a mixture of the core material and a PU prepolymer, rather than the core material alone, was added into the above aqueous solution to generate an oil-in-water emulsion system. The rest of the operation including the further addition of formaldehyde solution, temperature control, and product collection were all carried out the same as those for normal *in situ* polymerization. As shown in Figure 14.5, two distinct phases were observed on the atomic force microscopy images of the prepared microcapsules, and the shell consists of a PU inner shell and a PUF outer shell. As a control, a single-layered PUF capsule was also examined for comparison. Thermogravimetric analysis (TGA) of the prepared capsules revealed that the PU-UF capsules exhibited much better protection to the core materials compared with single-layered PUF capsules.

Aside from the microcapsules-based system as discussed above, a hollow tube-based system is another important type of self-healing material. Healing agents are stored in hollow tubes, which are embedded into polymeric host matrix to induce the desired self-healing function.[43–49] For self-healing polymer composite based on hollow tubes, the embedded tubes serve both as the reservoir for healing agent storage and as reinforcement fillers.[50]

Compared with microcapsules, hollow tubes can store more healing agents and hence the healing performance will be better.[12] The mechanism of self-healing behavior of hollow tube-based self-healing materials can be illustrated in Figure 14.6. Once cracks form in a polymer composite, the embedded hollow tubes will be ruptured to release the stored healing agents into the cracks site. The polymerization reaction of the healing agents will rebond the cracks and therefore realize the self-healing function.

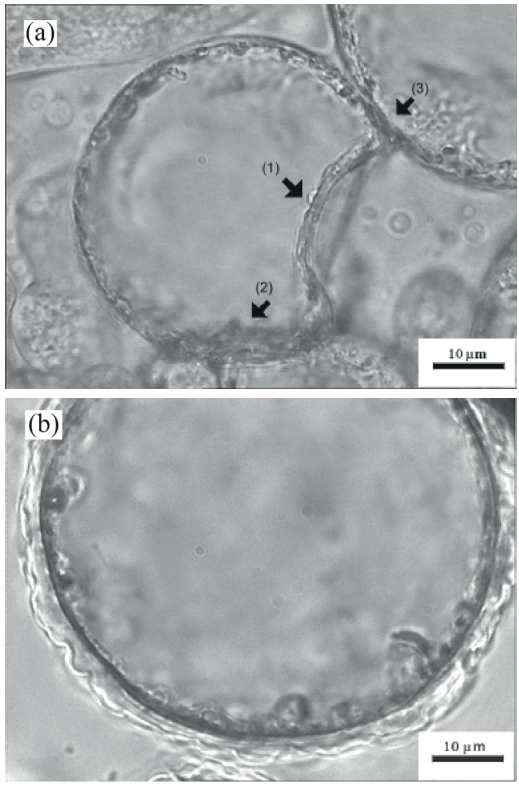


Figure 14.5 Atomic force microscopy images of (a) PUF single-layer microcapsules and (b) PU-PUF double-layered microcapsules.[42]

Glass fibers are the most important material used as hollow tubes for self-healing materials. It is primarily due to the fact that glass fibers are inert to most healing agents and host polymer matrix. In addition, they can be broken easily by cracks formed in the host matrix to release the containing healing agents.[51] On the contrary, it may be difficult to sense the crack in tubes made from other materials such as copper or aluminum, and therefore the healing behavior will not be triggered.[6] Compared with microcapsules-based self-healing system, a hollow tube-based system requires special attention to the compatibility of the healing agents with the hollow tubes, and hence various properties of the healing agents, such as their surface wettability, viscosity, chemical reactivity, and so on, should be comprehensively considered.[11] For example, healing agents that are too viscous may be unable to be introduced into the tubes, and even after the self-healing system is eventually developed, the healing agents are less likely to flow into the cracking sites where healing behavior is desired. In addition, the wettability of the healing species in the tubes is also a critical concern.

The research on microcapsule and hollow tube-based self-healing materials has achieved great advancement. Nevertheless, neither of these materials is able to repair

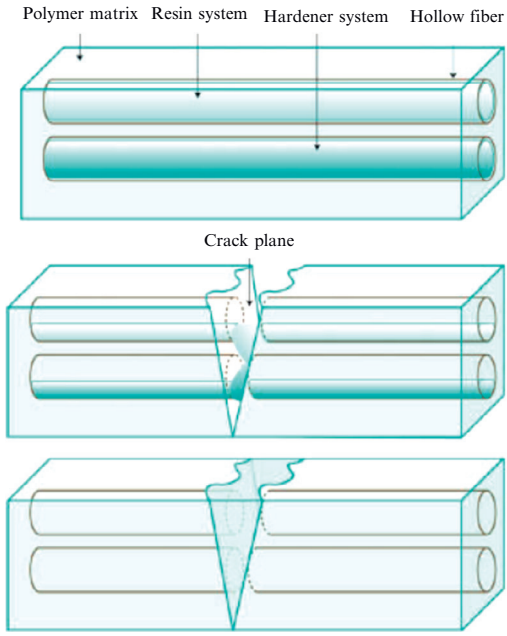


Figure 14.6 Mechanism of self-healing in a hollow tube-based system.[49]

the same location more than once.[12] For example, in a microcapsule-based materials, when the healing process is triggered due to the capsules rupture, the healing agent will be depleted, leaving voids in the host matrix. Then when another healing is desired at the same location, no healing agent will be available to meet the purpose. The same result will happen to a hollow tube-based self-healing system, because the healing agents stored are still finite even though they are in larger volume compared with those in microcapsules. Moreover, in most cases the second fracture will tend to occur at the same location as the initial one, because it is hard for the materials to reach a complete recovery in either the material integrity or the mechanical property. To overcome this problem, microvascular was proposed as an alternative approach for self-healing materials development.[52–55]

In a microvascular-based self-healing system, a three-dimensional vascular network is embedded into the polymer host matrix, and healing agents are stored in the network. Once damage or cracks in the host matrix rupture the vascular, the healing agents will be transported to the damaged site via the vascular network. Figure 14.7 illustrates the mechanism of the healing process in skin and in a microvascular-based self-healing system. It can be seen that in such a self-healing system, the healing process is a better imitation to the nature.[5] The healing agents can be supplied from other places via the interconnected network, and their supply will not be exhausted at one location, hence the microvascular-based system can achieve multiple healing.[56]

Toohey et al.[23] demonstrated the self-healing performance of a microvascular-based self-healing material. In such as system, a rectangular three-dimensional microvascular network was integrated throughout a polymer substrate via a direct-write assembly of a fugitive organic ink,[57] and an epoxy layer modified by different percentage of Grubbs' catalyst particles was then deposited on the substrate. The interconnected microvascular channels ($d = 200\,\mu m$) were filled with DCPD as healing agents. Once crack formed on the top epoxy layer, the underneath channels were broken, and the stored DCPD was released from the vertical channels to the crack sites. Upon contact with the embedded Grubbs' catalyst, the polymerization of DCPD formed a film to repair the crack. In the healing process, the horizontal channels severed the passage through which DCPD could be transported throughout the whole network to ensure the system was always filled with healing agents, and therefore enabled the multiple healing. The healing efficiency of the manufactured system was assessed, and the test showed as high as 70% recovery of the fracture toughness after damage in a four-point bending protocol.

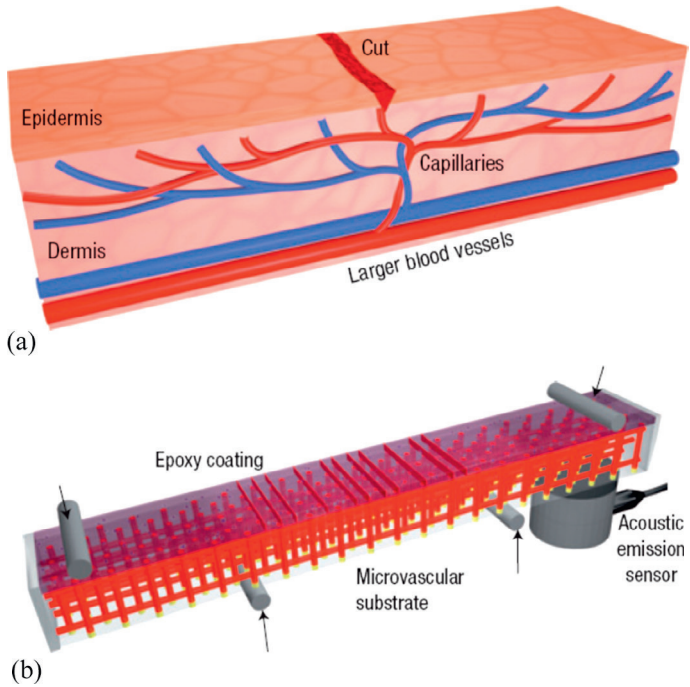


Figure 14.7 (a) Schematic diagram of a capillary network in the dermis layer of skin with a cut in the epidermis layer and (b) schematic diagram of a microvascular-based self-healing structure with a microvascular substrate and a brittle epoxy coating.[52]

14.2.2 Design of one-part self-healing anticorrosive coatings

In most existing self-healing materials, the healing reaction is based on a two-part reaction. For example, Toohey et al.[54] reported a self-healing material that is based on the two-part reaction between epoxy resin and hardener. Otherwise, the healing reaction is based on the polymerization reaction of a single component, but it requires the presence of a catalyst[9,23] or other external intervention such as heat or UV irradiation.[19] From the mechanism of corrosion as discussed above, it is seen that the corrosion of metal always involves moisture or water, and this is a feature that can be employed to develop one-part self-healing anticorrosive coatings. In this case, the prestored healant is able to react with moisture to realize the self-healing anticorrosive function.

In principle, the approaches for the self-healing materials development as discussed above are also valid for the preparation of one-part self-healing anticorrosive coatings. Nevertheless, if the constraint of the small thickness of the coating is taken into consideration, microencapsulation is the most suitable method. For the development of one-part self-healing anticorrosive coatings, selection of the healing agent is a crucial issue. First of all, the healing agent should be curable under the circumstance that the materials are exposed to when the healing behavior is expected. Secondly, the healing agent should have good flowability so that it is able to easily flow into the cracks once microcracks are formed in a coating.

Isocyanate monomer, for example, is a good candidate for one-part self-healing anticorrosive coatings. Isocyanates are reactive with water or moisture to produce carbamic acid, which is unstable and tends to decompose to an amine which in turn reacts with isocyanate to form urea or biuret or other polymeric products, as demonstrated in Figure 14.8.

Organic silane is another example that has potential as a one-part self-healing anticorrosive coating. Upon contact with moisture, organic silane will undergo polycondensation to form a silane film as shown in Figure 14.9.

One-part self-healing anticorrosive coatings are advantageous over conventional self-healing systems. The preparation of the one-part coatings is much simpler and more time efficient. Meanwhile, only one set of microcapsules is synthesized and incorporated to develop the coatings, so the impact of microcapsules to the host polymer matrix is minimized. In addition, the use of catalyst becomes unnecessary due to the self-curable property of the healant in such coatings, which is of considerable economic importance. In the next section, the design and advantage of one-part self-healing corrosive coatings will be illustrated by two examples.

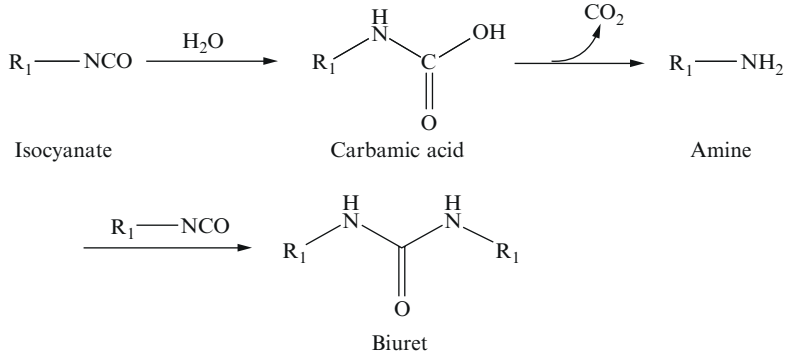


Figure 14.8 Mechanism of the reaction of isocyanate with water.

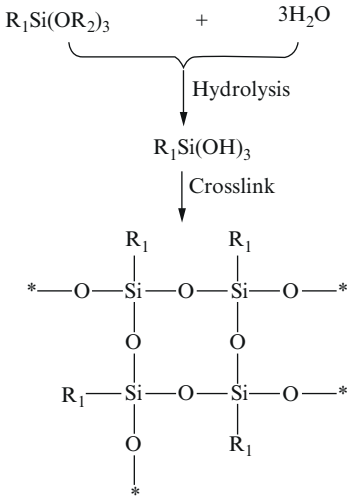


Figure 14.9 Hydrolysis and polycondensation of organic silane.

14.3 Examples of One-Part Self-Healing Anticorrosive Coatings

14.3.1 Diisocyanate-based one-part self-healing anticorrosive coating

14.3.1.1 Microencapsulation of diisocyanate via interfacial polymerization

Isocyanates are potential candidates for the development of one-part self-healing anticorrosive coatings because of their self-curable properties. Nevertheless, the high reactivity of isocyanates brings difficulty for their processing and encapsulation. Previous research on the encapsulation of isocyanate has been mainly

restricted to its solid state or blocked form. For example, Yang et al. and Rawlins et al. reported the encapsulation of a blocked form of polyisocyanate by polystyrene nanocapsules via emulsion polymerization,[58–60] and Walther et al. demonstrated that the microencapsulation of a solid-state naphthylene-1,5-diisocyanate by protective materials such as polystyrene, chlorinated rubber, and polyvinyl butyl ether that were inert to the encapsulated isocyanate.[61] To date, very few public documents have appeared related to the encapsulation of liquid-state isocyanate monomers.

Yang et al.[33] for the first time reported the microencapsulation of a liquid-state isocyanate monomer. The IPDI monomer was encapsulated by PU microcapsules via an interfacial polymerization approach in an oil-in-water emulsion system. As illustrated in Figure 14.10, the interfacial polymerization reaction between the TDI prepolymer and 1,4-butanediol produced the PU shell structure of the final microcapsules. However, the synthesis was based on a self-prepared urethane prepolymer, and thus the preparation would be quite tedious. In addition, the reactivity of IPDI is not very high, which is unfavorable for the self-healing coating because it is desirable that the healing reaction occurs in a short period of time to ensure the instant healing function.

Following a similar method, a more reactive liquid-state diisocyanate monomer, hexamethylene diisocyanate (HDI), is also successfully encapsulated into PU microcapsules through an interfacial polymerization process shown in Figure 14.11. In this synthesis, a commercial MDI prepolymer was employed as the reactant to construct the shell.

In the synthesis, the MDI prepolymer Suprasec 2644 was dissolved in HDI to yield an oil phase, which was dispersed into gum arabic surfactant solution to create an oil-in-water emulsion. When 1,4-butanediol was introduced, the reaction between

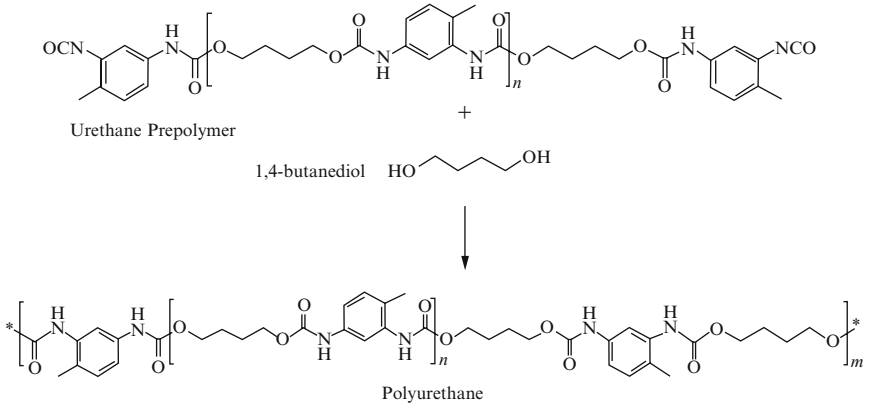


Figure 14.10 Scheme of the microencapsulation of IPDI by PU microcapsules.[33]

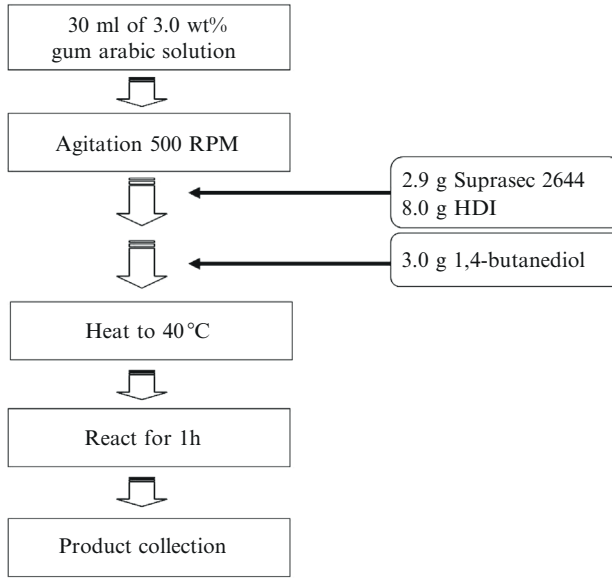


Figure 14.11 Procedure for the synthesis of HDI-filled PU microcapsule.

the hydroxyl functional group from the aqueous phase and the isocyanate functional group from the oil phase occurred to create a PU membrane surrounding the oil droplets. The reaction mechanism of PU formation is very similar to that shown in Figure 14.10, while the only difference is that the TDI prepolymer is replaced by an MDI prepolymer. The diol in the aqueous phase diffused across the initial membrane to further react with the isocyanates and resulted in the membrane increment.[62] The MDI prepolymer was much more reactive than HDI, and hence the primary reaction was between 1,4-butanediol and the MDI prepolymer to form the shell structure, while the relatively less reactive HDI liquid was encapsulated as core material to produce the final microcapsules. All of the materials used in the synthesis were commercially available, so it was seen that the microencapsulation of HDI was realized in a much more simplified procedure compared with the encapsulation of IPDI, as reported before.[33] In a typical run of synthesis, the oil phase was composed of 2.9 g MDI prepolymer and 8.0 g HDI, the concentration of the gum arabic surfactant solution was 3 wt.%, the agitation rate was 500 RPM, and the temperature of reaction was 40 °C. At such a condition, the yield of the capsules was about 70%, and the resultant microcapsules had an average diameter of 86.5 µm and a shell thickness of about 6.5 µm.

Given that the synthesis of the capsule shell wall was not a strict stoichiometric reaction, excess 1,4-butanediol was used to ensure the Suprasec 2644 was completely consumed. The yield of the synthesis is calculated simply as below:

$$\text{Yield}(\%) = \frac{W_{cap}}{W_{pre\text{-}p} + W_{diol} + W_{HDI}} \times 100\% \tag{14.1}$$

where W_{cap} is the mass of the collected microcapsules after drying, and $W_{pre\text{-}p}$, W_{diol}, W_{HDI} are the masses of the MDI prepolymer, 1,4-butanediol, and HDI, respectively. This is a rough method for estimating the yield of the synthesis.

Based on the calculation described above, at a 500-RPM agitation rate, the typical yield was calculated to be 65-74% and slightly varied with reaction parameters. It was found that the yield was lower at higher agitation rates, and it declined to ~54% when the agitation rate was raised to 2000 RPM.

The formation of microcapsules is quite fast in the synthesis due to the high reactivity of the MDI prepolymer. Optical microscopy examination during the reaction course showed that microcapsules formed within 15 min after the addition of 1,4-butanediol. However, a minimum reaction time (MRT) was necessary to ensure the shell of the capsules was mechanically strong enough to withstand the following filtration and further processing. Finding the MRT of the synthesis is very important both for saving time and for quality control of the microcapsules shell. To determine the MRT, products were sampled from the emulsion solution at 10-min intervals until dispersed dry microcapsules could be collected by filtration. Although microcapsules were observed at quite an early stage, the capsules formed before MRT were found to collapse to yield viscous bulk polymer during the filtration. As shown in the Table 14.1, the required MRT reduced steadily with the increase of reaction temperature. It meant that the capsule shell growth was more rapid at a higher temperature, and this is consistent with the fact that the rate of polymerization reaction for PU formation is positively dependent on temperature.

14.3.1.2 Chemical constituent of microcapsules

The chemical constituent of the resultant microcapsules was characterized by FTIR. As a comparison, complete capsules together with pure grades of HDI, MDI prepolymer, shell, and core materials were investigated. As illustrated in Figure 14.12, the characteristic signals at 2267.6 cm^{-1} (–NCO stretch) and 2929.5 cm^{-1} (CH_2 stretch) from the full microcapsule reveal that the resultant capsules contained large amounts

TABLE 14.1 Minimum Reaction Time (MRT) and Fill Content of Microcapsules Prepared at Different Temperatures

Temperature (°C)	30	40	50	60
MRT (min)	150	60	45	30
HDI content (wt.%)	65	62	35	18

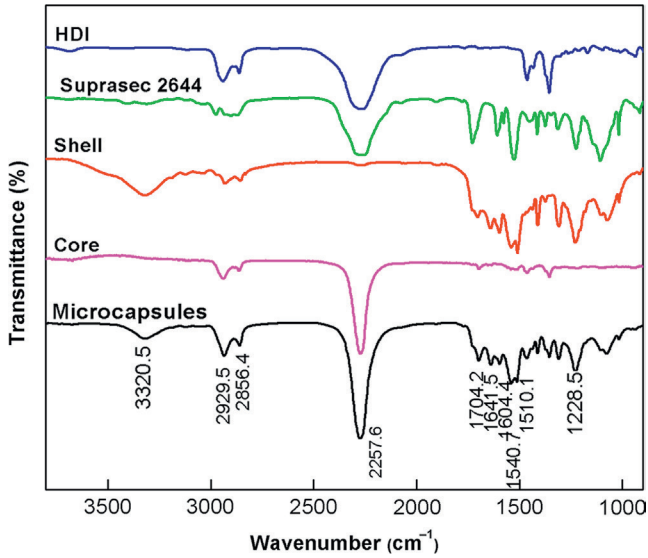


Figure 14.12 FTIR spectra of HDI, Suprasec 2644, prepared PU microcapsule, capsule shell and capsule core material.[77]

of HDI. Meanwhile, the NCO signal (2267.6 cm^{-1}) is not observed from the spectrum of capsule shell. It means that the HDI was not absorbed in the microcapsule shell. In addition, it is seen that the spectrum of core materials is almost the same as that of pure HDI, indicating that the core material was mainly composed of pure HDI. Therefore, it can be concluded that the HDI was successfully encapsulated into the PU microcapsules. In addition, the absence of the NCO signal in the spectrum of the pure shell indicates that the prepolymer chains were extended to form the PU bulk shell. Based on these observations, it is logical to conclude that polymerization of the MDI prepolymer produced the PU microcapsules shell, and HDI was encapsulated as a core material in the synthesis.

14.3.1.3 Morphology and diameter of microcapsules

The synthesized microcapsules have a spherical shape with a smooth surface as shown in Figure 14.13. It was found that the inner surface of the capsules was not as smooth as the outer surface. Meanwhile, the coarse cross-section of the capsules indicates that the capsules shell may contain some voids. The average shell thickness of capsules was in the range of 1.1-12.48 µm when the agitation rate varied in the range of 300-2000 RPM.

In the development of self-healing materials through microencapsulation, control of capsule diameter is critical because the diameter greatly influences the self-healing

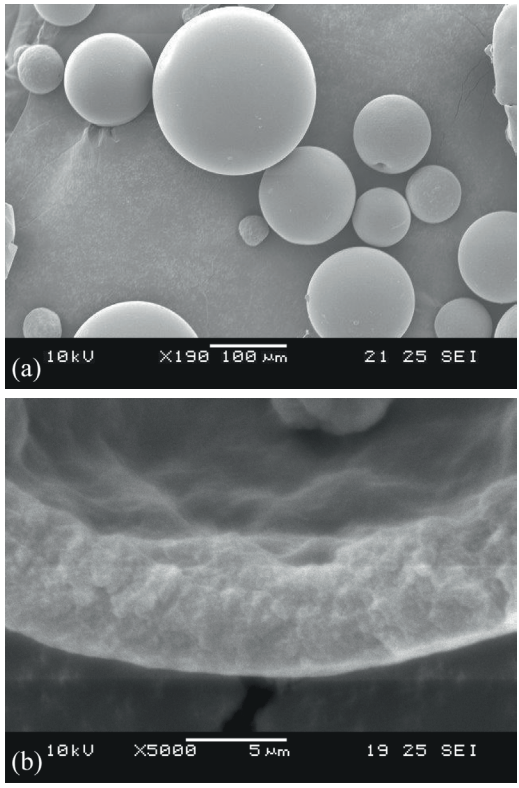


Figure 14.13 Morphology of HDI-filled PU microcapsules. (a) Spherical shaped microcapsules; (b) shell structure of microcapsules.[77]

performance,[63] and in some conditions, only the capsules with a certain range of diameter are suitable. The microcapsules diameter is influenced by a combination of several factors, including the geometry of the mixing device, viscosity of the reaction media, surfactant concentration, agitation rate, temperature, and so on, while the agitation rate is the most important one. As illustrated in Figure 14.14, when all other variables remained the same during microcapsules synthesis, higher agitation speed resulted in smaller microcapsule size, and the average diameter possessed a linear relationship with the agitation rate in double-logarithm coordinates. This result is also found in previous studies.[20,33]

14.3.1.4 Thermal property and core fraction of microcapsules

The TGA weight loss curves of microcapsules synthesized at 500 RPM along with pure HDI and capsule shell materials as a function of temperature are shown in Figure 14.15. It can be observed that microcapsules experienced significant weight loss by 180 °C. This weight loss is in good agreement with that of HDI and reveals the successful encapsulation of HDI within the microcapsules. The decomposition of

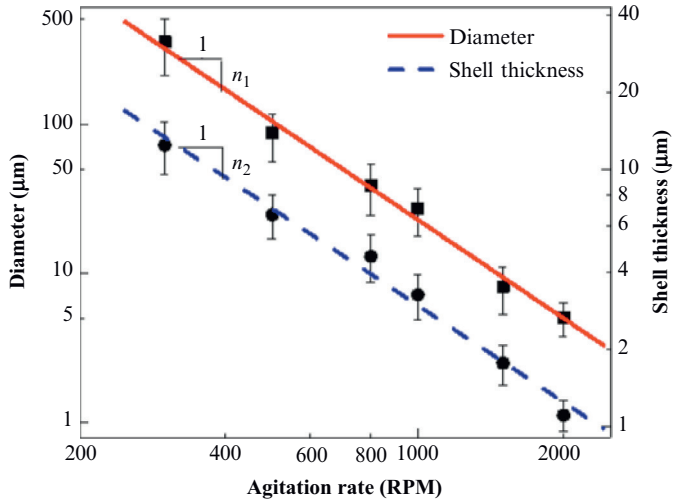


Figure 14.14 Average diameter and shell thickness of prepared microcapsules prepared at different agitation rate ($n_1 = 2.18$; $n_2 = 1.25$).[77]

shell materials started from about 240 °C. Figure 14.15 also illustrated the derivative of the weight loss curve of microcapsule. The evaporation process of HDI in the first peak and decomposition process of shell in the peaks after 240 °C are apparent on the curve of the full microcapsules.

The HDI content or the core fraction in the prepared microcapsules was determined from the peak width of the derivative curve of full microcapsules. From Figure 14.15 it is seen that the HDI content of the microcapsules was about 62 wt.% at 500 RPM based on the weight loss of HDI.

14.3.1.5 Preparation of HDI-based self-healing anticorrosive coating

Diisocyanate-based one-part self-healing anticorrosive epoxy coating was prepared by dispersing a certain weight percentage of the synthesized HDI microcapsules into epoxy resin EPOLAM 5015 at ambient temperature, followed by mixing hardener EPOLAM 5014. The mixture was degassed for 20 min and then applied on the pretreated substrates by an adjustable film applicator. The coating was cured at ambient temperature in open air for 24 h.

14.3.1.6 Accelerated salt immersion corrosion test

An accelerated salt immersion test was performed to the HDI microcapsules-based epoxy coating. In this test, the average diameter of the microcapsules was about 100 μm,

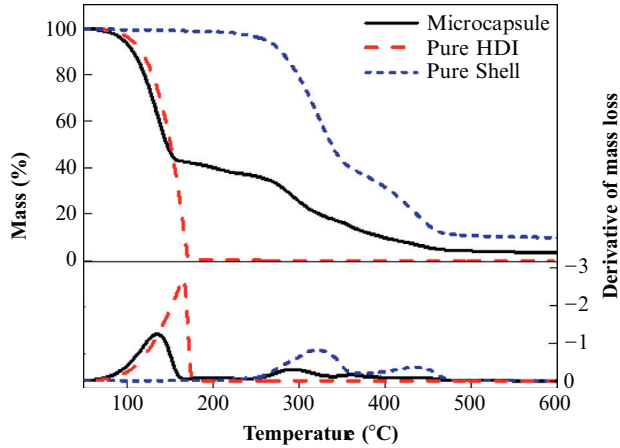


Figure 14.15 TGA weight loss of pure HDI, full microcapsule and microcapsule shell, and the derivative of TGA curve of microcapsules.[77]

and 10 wt.% of microcapsule were mixed into the epoxy resin to yield the final coating. The prepared HDI-based coating was manually scribed following the standard method of ASTM D1654 and then exposed to 10 wt.% NaCl aqueous solution for 48 h. As shown in Figure 14.16, when the scribed specimen coated with the neat epoxy coating was immersed in salt solution, severe corrosion was observed at the scribed area. On the contrary, the specimen coated with the self-healing coating was free of corrosion after immersion. Such a difference clearly demonstrates that the epoxy coating modified by HDI-filled microcapsules exhibited excellent anticorrosion property.

In order to reveal the mechanism of the anticorrosion function of the microcapsules-based coating, the scribed area of the coating was examined by SEM after immersion. Figure 14.17 illustrates the scribed locations of the HDI-based coating and the blank epoxy coating when the coatings were immersed in salt solution for two days. After the application of scratches on the coatings, the underlying steel substrate was exposed to corrosive salt solution and would be corroded. Comparing Figure 14.17a with b, it is clearly seen that some new materials were created in the scribes of the HDI-based epoxy coating after immersion. It means that the crack on this coating was healed autonomously. This is self-healing because such a healing process did not involve any manual intervention. Due to such a self-healing activity, the scribes were sealed and the underneath steel was separated again from external corrosive environment to display corrosion protection function. The materials generated in the crack should be the product between HDI, released from ruptured microcapsules, and water from the environment. As a comparison, it could be seen from Figure 14.17c and d that the crack of the control specimen was not sealed, and therefore the corrosive salt solution can still directly attack the steel.

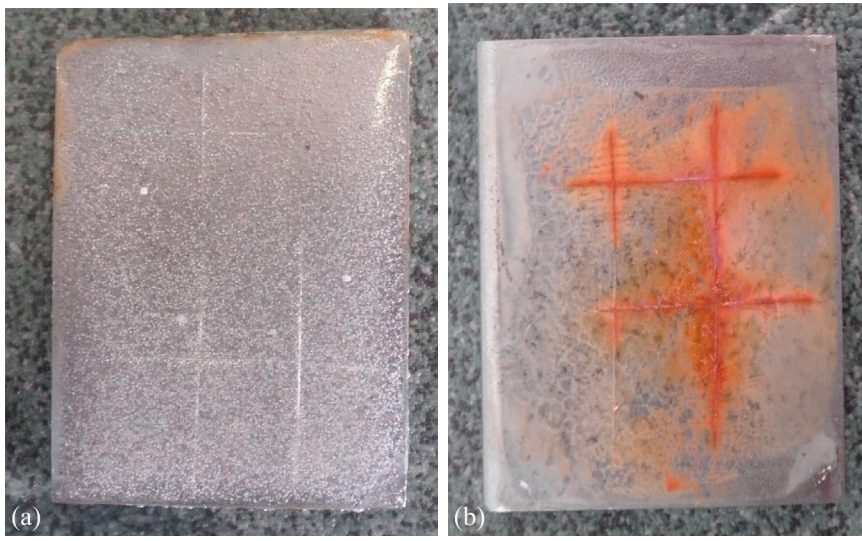


Figure 14.16 Coated steel panel after immersion in 10 wt.% NaCl solution for 48 h: (a) coated with HDI-based self-healing coating and (b) coated with blank coating.[77]

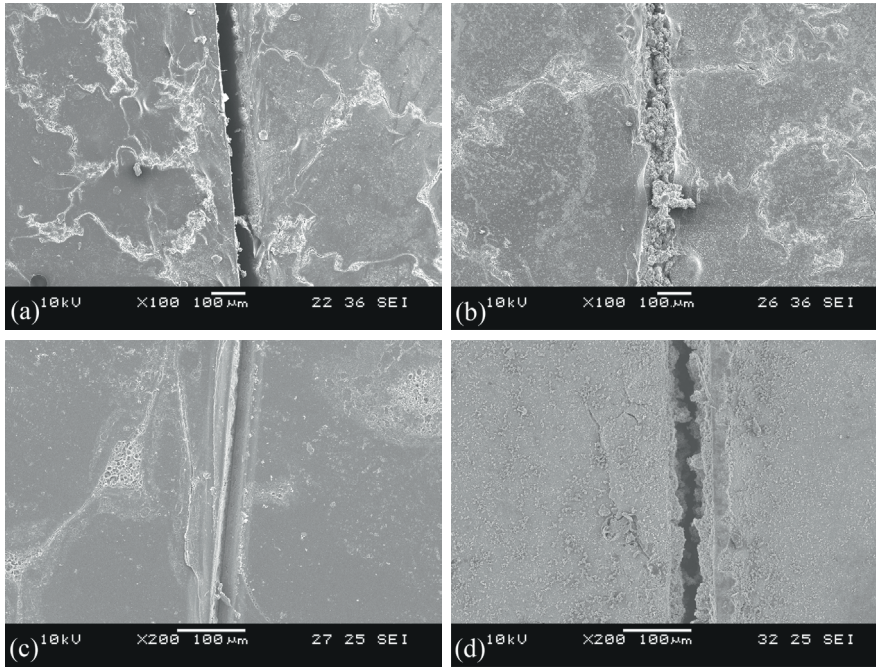


Figure 14.17 SEM images of the scribed regions of HDI-based epoxy coating (a) before immersion; (b) after immersion and control epoxy coating; (c) before immersion; (d) after immersion. The coated specimens were immersed in 10 wt.% NaCl solution for 48 h.[77]

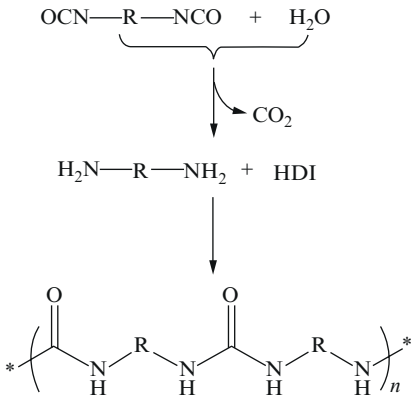


Figure 14.18 Healing reaction of HDI with water.

From the discussion for the HDI-based anticorrosive coatings as described above, it is seen that the excellent corrosion protection function of the microcapsules-based coating was realized through a self-healing/sealing mechanism. When the microcapsules modified coatings were scratched, the healing species HDI would flow from the ruptured microcapsules into the cracks. Upon contact with water or moisture, the healing species would then undergo a healing reaction in the form of polymerization, crosslink, or condensation to create a film within the scribes, separating the metal substrate from the corrosive external environment. As a result, the corrosion of the substrate was hindered. On the contrary, for the control sample, the underlying metal substrate would be severely corroded because it was directly exposed to corrosive salt solution once the coating was scratched. The healing reactions of the HDI-based self-healing anticorrosive coatings are demonstrated in Figure 14.18. HDI monomer will react with water to produce an amine, which further reacts with HDI to form a polyurea film. However, it is noteworthy that in a real situation, the actual healing reaction and the chemical constituent of the newly formed film may be much more complicated than those proposed here.

14.3.1.7 Salt spray test

In order to better assess the anticorrosive performance of the HDI microcapsules incorporated epoxy coating, a comprehensive salt spray test was performed following the standard test method of ASTM B117.

The HDI microcapsules-based epoxy coatings were manually scribed following the standard method of ASTM D1654 and placed in a salt spray chamber, while the corrosion behavior of the specimens was monitored. The influences of three parameters, the average diameter of HDI microcapsules, weight fraction of microcapsules in coating, and the thickness of final coating, to the corrosion protection ability of the coatings were investigated. For each parameter three values were taken, so overall 27

TABLE 14.2 Formulations of HDI Microcapsules-Based Epoxy Coating

D (μm)	*Φ* (wt.%)	*H* (μm)	Name of Samples
100±31.6	10	400, 300, 200	SP-100-10-400; SP-100-10-300; SP-100-10-200
	5		SP-100-5-400; SP-100-5-300; SP-100-5-200
	2		SP-100-2-400; SP-100-2-300; SP-100-2-200
50±17.2	10		SP-50-10-400; SP-50-10-300; SP-50-10-200
	5		SP-50-5-400; SP-50-5-300; SP-50-5-200
	2		SP-50-2-400; SP-50-2-300; SP-50-2-200
30±9.4	10		SP-30-10-400; SP-30-10-300; SP-30-10-200
	5		SP-30-5-400; SP-30-5-300; SP-30-5-200
	2		SP-30-2-400; SP-30-2-300; SP-30-2-200
Control (pure epoxy)	0		SP-Blk-400; SP-Blk-300; SP-Blk-200

Note: Naming policy of samples is used as SP-*D*-*Φ*-*H* where SP means salt spray test, *D* is average diameter of microcapsules, *Φ* is weight fraction of microcapsules in coating, and *H* is thickness of coating.

formulations of coatings were prepared for the test. In addition, three blank epoxy coatings were prepared at different coating thicknesses as control. All the formulations of the coatings for the salt spray test are summarized in Table 14.2, and they are labeled in the format of SP-*D*-*Φ*-*H*, while the three control samples were labeled as SP-Blk-*H*.

The specimens were exposed to salt fog for two months in a monitored salt spray chamber. As shown in Figure 14.19, it is seen that after exposure, the blank epoxy coatings (SP-Blk-400, SP-Blk-300, SP-Blk-200) with three different thicknesses developed corrosion along the scribes. Among the other 27 microcapsules modified coatings, coatings SP-100-10-400 and SP-100-10-300 showed no corrosion, indicating their excellent corrosion protection property. In the meantime, slight corrosion was also observed on coatings SP-100-10-200, SP-100-5-400, SP-100-5-300, and SP-100-5-200. It means that these four formulations could provide some corrosion protection, but the performance was slightly worse compared with formulations SP-100-10-400 and SP-100-10-300. For the other formulations, severe corrosion was observed along the scribes, indicating that the protection of these coatings to steel substrates was quite poor. The results reveal that the HDI microcapsules-based epoxy coatings exhibit good corrosion protection function to metal substrate if they are properly formulated.

It was found from the salt spray test that the growth of corrosion was related to exposure time. Figure 14.20 demonstrated the process that corrosion developed on three coatings (SP-100-10-400, SP-50-10-400, and SP-30-10-400) when the salt spray test proceeded. It is seen that corrosion started to appear on SP-50-10-400 and

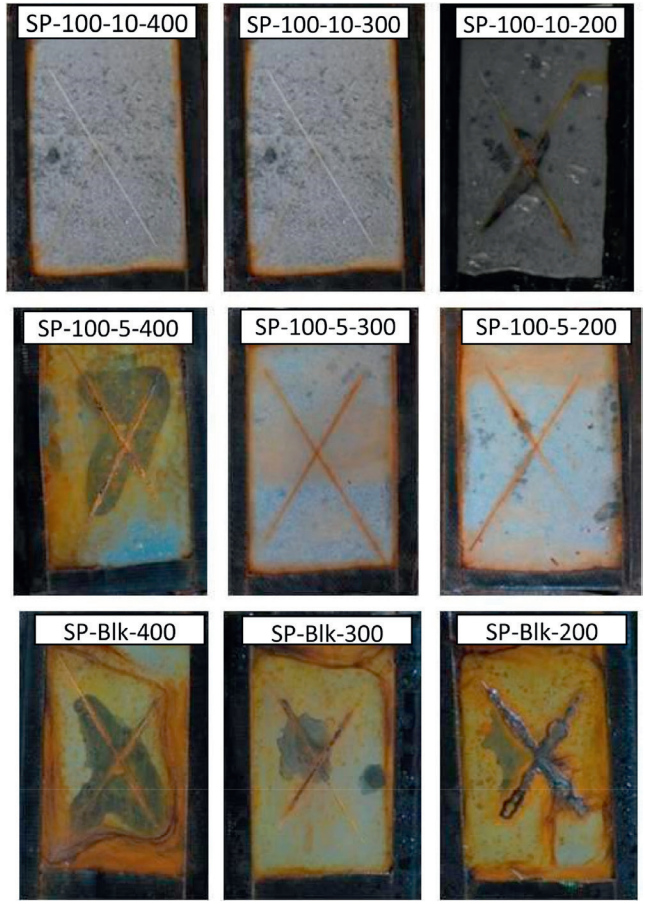


Figure 14.19 HDI-based one-part self-healing coatings after exposure to salt spray for 2 months.[78]

SP-30-10-400 from the first week, and more and more rust was observed when the exposure time of the specimens in salt fog increased. This is a reasonable result because corrosion is an electrochemical process, and it proceeds with time.

Figure 14.20 also revealed the influence of microcapsules size on the corrosion protection ability of the microcapsules-based coating. The three formulations, SP-100-10-400, SP-50-10-400, and SP-30-10-400, differed only in the average diameter of the HDI microcapsules, while the other two parameters of self-healing coatings remained the same. It is seen that specimen SP-100-10-400, in which the diameter of HDI microcapsules was 100 μm, was almost free from rust, while specimen

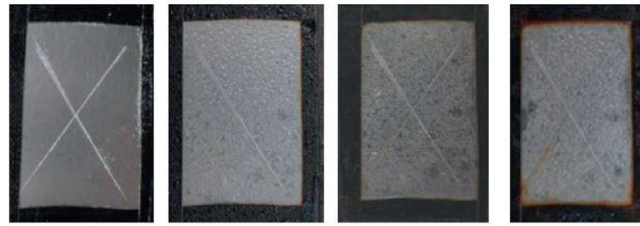
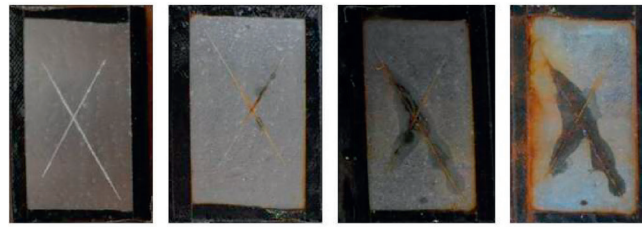
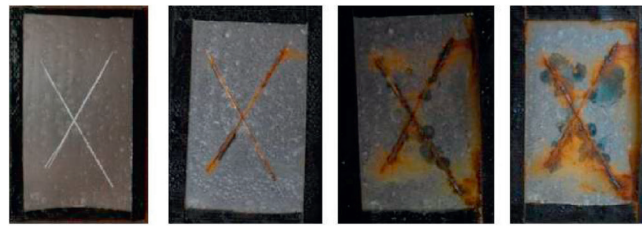
Formulations	Exposure Time in Salt Fog			
	0 week	1 week	1 month	2 months
SP-100-10-400: $D = 100 \pm 31.6$ μm $\Phi = 10$ wt.% $H = 400$ μm				
SP-50-10-400: $D = 50 \pm 17.2$ μm $\Phi = 10$ wt.% $H = 400$ μm				
SP-30-10-400: $D = 30 \pm 9.4$ μm $\Phi = 10$ wt.% $H = 400$ μm				

Figure 14.20 Influence of exposure time and capsules diameter on the anticorrosive performance of HDI-based self-healing coatings.[78]

SP-30-10-400, in which the diameter of microcapsules was 30 μm, showed most serious corrosion. The extent of corrosion of specimen SP-50-10-400 was between that of these two specimens. Actually the comparison of other specimens also showed a similar trend, in which the coatings exhibited best corrosion resistance performance when the diameter of incorporated microcapsules was 100 μm, followed by the 50 μm specimens and the 30 μm specimens showed worst corrosion protection. This results indicate that the HDI microcapsules-based epoxy coating afforded better corrosion protection towards a steel substrate when the diameter of microcapsules was bigger, given other parameters of the coating remained. This result is in good agreement with that reported in another publication.[63]

The corrosion protection performance of the HDI-based coating was also affected by the weight fraction of microcapsules in the coating and the coating thickness. Figure 14.21 shows nine specimens after exposed to salt fog for two months. The diameter of the HDI microcapsules was at 100 μm for the nine specimens, while the weight fraction of microcapsules and coating thickness varied for each formulation. If we compare the specimens in each row, in which the weight fraction of microcapsules was constant, it is seen that, generally, more rust was observed on the specimens with smaller coating thicknesses. If the specimens in each column, in which the

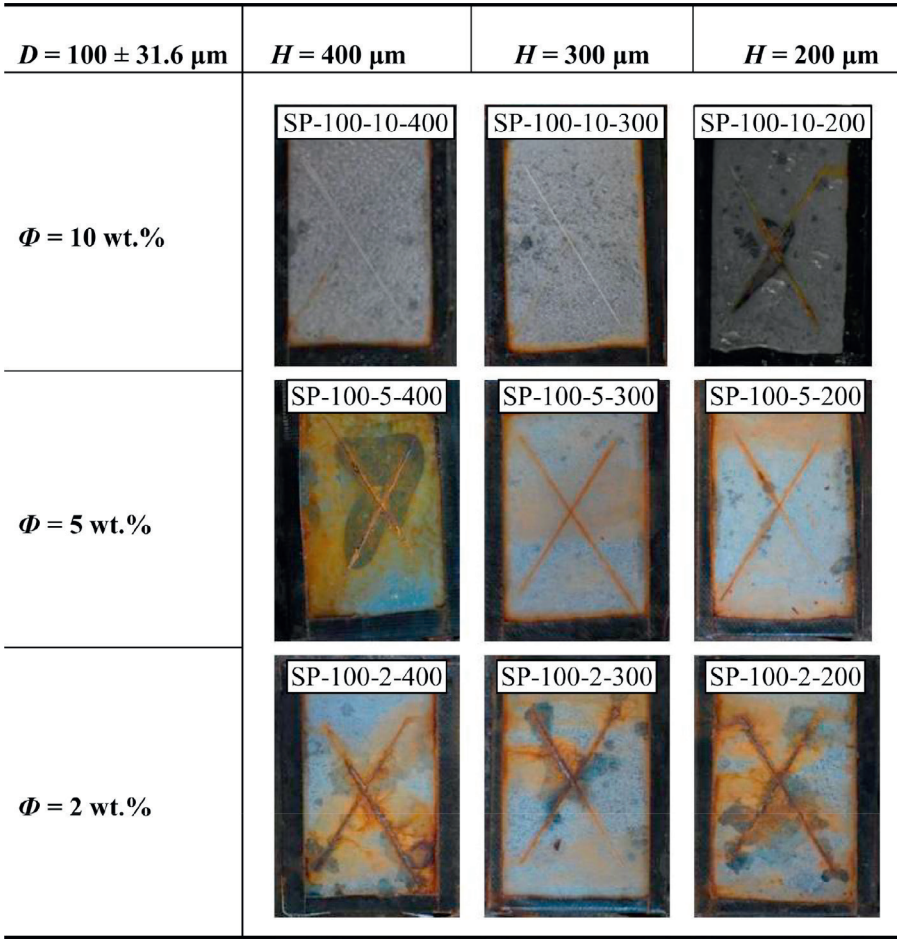


Figure 14.21 Influence of weight fraction of microcapsules (Φ) and coating thickness (H) on the anticorrosive performance of HDI-based self-healing coatings.[78]

coating thickness was the same, were compared, it could be found that the corrosion was more severe when the weight fraction of capsules declined. A similar trend can also be found from other specimens. The results imply that higher microcapsule content in the coating as well as larger coating thickness is favorable for the HDI-based self-healing anticorrosive coating. It should be pointed out that although the edge and backside of the substrate was protected by water-resistant tape during the salt spray test, some corrosion still occurred at the noncoated part. That is why much of yellowish rust was seen on the specimen although the real corrosion was much less as for specimen SP-100-5-200 in Figure 14.21.

14.3.1.8 Influence of parameters on anticorrosive performance

The salt spray test of the HDI-based self-healing anticorrosive coating reveals that the microcapsules size, weight fraction of microcapsules in coating, and the coating thickness all significantly influenced the anticorrosion performance of the prepared coating. Generally, larger microcapsules size, higher microcapsules content, and thicker coating would afford better corrosion protection. For microcapsules-based self-healing polymer materials, the self-healing performance is influenced by factors such as the content of microcapsules in the polymer and diameter of microcapsules.[64] Rule et al. pointed out that for a scratched self-healing material, the self-healing performance was directly related to the amount of healing agents that were available for delivery per unit scratch area.[63] Based on a simplified model, an equation was proposed to explain the proportional effect of the microcapsules weight fraction and diameter on the self-healing performance of a microcapsules-based self-healing material. Mookhoek et al.[65] also developed a model to predict influences of capsule diameter, aspect ratio, and concentration, as well as the crack opening distance on the self-healing performance. It has been revealed that the anticorrosive function of the scribed HDI-based coating was mainly realized through a self-sealing mechanism. Hence, the influences of these three factors on the anticorrosive property of the coating are discussed in terms of the self-healing behavior.

The discussion below is based on several assumptions: (1) the microcapsules with uniform diameter are evenly distributed in the coating matrix; (2) the fill content of each microcapsule is the same; (3) the shell of the microcapsules is negligible; (4) when a scratch forms in the coating, all of the microcapsules located at the scratch plane are ruptured; (5) all of the encapsulated healing agents of ruptured microcapsules will freely flow into the scratch; and (6) the healing species will spread within the scratch.

Consider a rectangle microcapsules-based coating is penetrated by a planar scratch as shown in Figure 14.22. Microcapsules with uniform diameter (d) are randomly distributed in the coating matrix. When a planar scratch penetrates the

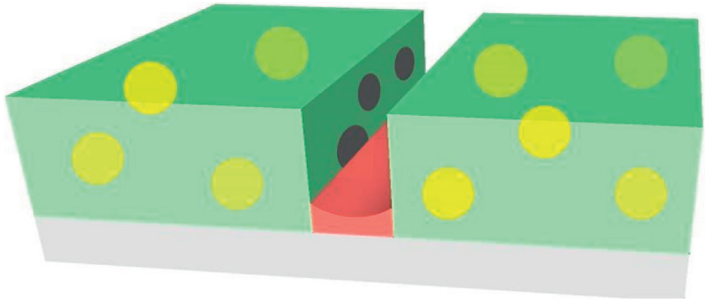


Figure 14.22 Schematic diagram of a scratched microcapsules-based coating.

coating, all of the microcapsules lying in the scratch will be ruptured to release the healing species.

The number of microcapsules that are ruptured (n) is:

$$n = NP \tag{14.2}$$

where N is the total number of microcapsules in the coating; P is the probability that the center of a microcapsule lies within the rupture zone of the scratch plane.

Because the microcapsules were assumed to be distributed evenly in the coating, the probability is:

$$P = \frac{Ad}{M/\rho} = \frac{\rho Ad}{M} \tag{14.3}$$

where A is the area of the scratch plane; d is the diameter of the microcapsules; M is the mass of the coating; ρ is the density of the coating.

The total number of microcapsules in the coating can be calculated as:

$$N = \frac{\Phi M}{m} \tag{14.4}$$

and the area of the scratch plane is:

$$A = HL \tag{14.5}$$

where Φ is the weight fraction of microcapsules in the coating; m is the mass of one microcapsule; H is the thickness of coating; L is the length of the scratch.

Combine Equations (14.2)–(14.5), the number of microcapsules ruptured by the scratch is calculated as:

$$n = \frac{\rho \Phi H Ld}{m} \tag{14.6}$$

In a typical self-healing material, the amount of the delivered healing agents has to be normalized by the area of the scratch plane because it is expected that the entire scratch plane is reconnected and rebonded.[63] Nevertheless, for corrosion

protection purpose, the basic requirement is that the exposed substrate is covered by the healing agents in the whole length of the scratch with a certain width, while the agents do not have to completely fill the entire scratch depth. Therefore, the amount of the delivered healing agents is normalized by the scratch projection area as below:

$$m_0 = \frac{nm}{tL} = \frac{\rho \Phi H d}{t} \tag{14.7}$$

where t is the width of the scratch.

For a given microcapsules-based coating, the density of the coating (ρ) is basically determined by the coating matrix itself if the fraction of microcapsules is not too high, and hence it can be considered as a constant. From Equation (14.7), it is seen that the amount of healing species available at the scratched sites is proportional to the weight fraction of microcapsules (Φ), diameter of microcapsules (d), and thickness of coating (H). In addition, according to the discussion in last section, the anticorrosion function is realized through a self-healing mechanism, and better self-healing property indicates better anticorrosion property. Therefore, the corrosion protection performance is accordingly also positively related to the microcapsules diameter, microcapsules weight fraction, and coating thickness. This conclusion is consistent with the results as observed in the salt spray test. Furthermore, although the effect of the scratch width to the corrosion protection function of the coating was not investigated in our study, it is seen from Equation (14.7) that the corrosion protection function of the microcapsules-based coating should be inversely related to the width of the scratch (t). It suggests that a wider scratch is more difficult to be self-repaired by the coating itself.

14.3.2 Organic silane-based one-part self-healing anticorrosive coating

14.3.2.1 Microencapsulation of perfluorooctyl triethoxysilane via in situ *polymerization*

Inorganic silicates have been used for self-healing and corrosion protection applications for many years.[66–68] For example, Aramaki et al. used sodium silicate in the preparation of a highly protective and self-healing film, which displayed good corrosion suppression effect to the zinc surface.[67] The inorganic silicate-based corrosion-resistant coating mainly makes use of the deposition of silicates to realize the corrosion suppression function. But inorganic silicates are usually directly mixed into the coating matrix, and hence they may be susceptible to interaction with environment leading to problems in corrosion protection during long-term service. Organic silane molecules tend to hydrolyze in wet environments and crosslink to form a solid film, and such a property indicates their potential as a novel healing agent for a one-part and catalyst-free self-healing additive

to corrosion-resistant coatings. To date, the research on organic silanes for self-healing materials remains largely unexplored, and only a few publications have appeared.[17,31,32] Braun and coworkers reported the polydimethylsiloxane-based microcapsules applied for self-healing coatings.[31,32] A mixture of hydroxyl end-functionalized polydimethylsiloxane and polydiethoxysiloxane was directly phase-separated or encapsulated and then dispersed in epoxy matrix, and the yielding coating exhibited good self-healing ability for corrosion protection. However, organo-tin catalyst was necessary for such self-healing systems. Another study examined microencapsulation of self-synthesized silyl ester for self-healing coatings.[17] Octyldimethylsilyloleate, a silyl ester, was synthesized and encapsulated into PUF microcapsules, which were then incorporated into epoxy to produce a self-healing coating, and the excellent corrosion-resistant property of the prepared coating was demonstrated via self-healing. But the synthesis of silyl ester increased the complexity and cost to the procedure.

A novel one-part self-healing anticorrosive polymer coating is fabricated based on the microencapsulated an organic silane, that is, *1H*,*1H′*,*2H*,*2H′*-perfluorooctyl triethoxysilane (POTS). There are several advantages of this coating system over the existing self-healing materials: (1) POTS is able to hydrolyze in wet environment to form a silane-based film and, as mentioned, such ability indicates that the use of catalyst can be avoided in the end self-healing product. (2) The newly formed film from hydrolysis and polycondensation of POTS and water is hydrophobic.[69] Such a special wetting property will serve to repel aqueous electrolyte solution away from metal and hence provides further corrosion protection to metal substrate.[17] (3) POTS is commercially available and hence the preparation of self-healing coating will be more convenient and time efficient for mass production.

PUF microcapsules containing POTS as core materials were synthesized through an *in situ* polymerization reaction in an oil-in-water emulsion system.[20] At ambient temperature, 50 ml of deionized water and 12.5 ml of 2.5 wt.% aqueous solution of ethyl maleic anhydride copolymer were mixed in a 500 ml beaker. Under mechanical agitation, 1.25 g urea, 0.125 g ammonium chloride and 0.125 g resorcinol were dissolved in the solution. The pH of solution was raised from ~2.60 to 3.50 by dropwise addition of 1 M sodium hydroxide solution. One drop of 1-octanol was added to eliminate surface bubbles. 10 g of POTS liquid was dissolved in 5 g of toluene to form the oil phase, which was then slowly added into the above aqueous solution to generate emulsion. After stabilization for 10 min, 3.17 g of 37 wt.% aqueous solution of formaldehyde was added. The emulsion was covered and heated to 55 °C at a heating rate of 1 °C/min. After 4 h of continuous agitation, the stirrer and hot plate were switched off. The resultant microcapsules were filtered and washed with distilled water for several times. Microcapsules were collected for air-drying at ambient temperature for 48 h before further analysis. A typical procedure for the synthesis is outlined in Figure 14.23.

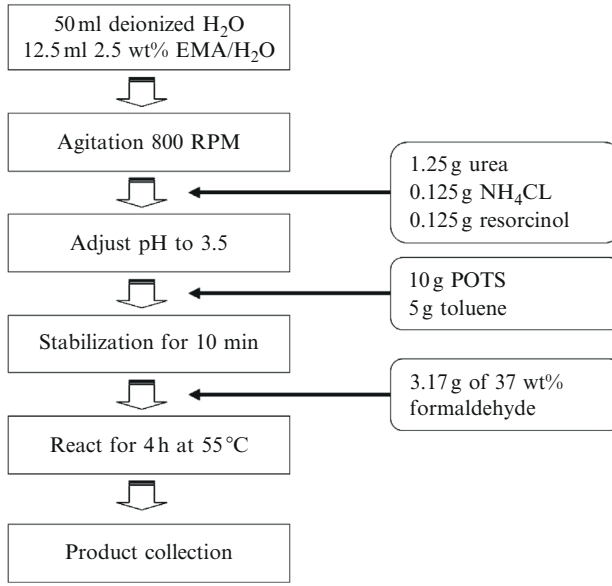


Figure 14.23 Procedure for the synthesis of POTS-filled PUF microcapsules.

In the synthesis, ethylene maleic anhydride copolymer was surfactant, urea and formaldehyde were the monomers contributing to the microcapsule shell, and POTS was the encapsulated core material. Ammonium chloride served as hardeners while resorcinol was a further brancher involved in the polymerization reaction with urea and formaldehyde.[70] Resorcinol also behaved to improve the resistance of PUF bonds to the influence of water in the synthesis.[71] When the oil phase comprised of POTS and toluene was added into the aqueous solution containing surfactant, urea, ammonium chloride, and resorcinol, an oil-in-water emulsion was created. After the addition of formaldehyde solution, polymerization reaction between urea and formaldehyde occurred in the acidic aqueous phase to form a PUF membrane surrounding the oil phase, as illustrated in Figure 14.24. Further polymerization reaction produced PUF nanoparticles depositing on the initial membrane, leading to the shell increment to form the final microcapsules shell. The encapsulation was achieved at elevated temperature, and therefore most of toluene will evaporate away during the synthesis, leaving POTS as the main component of core materials in the final microcapsules, which will be illustrated by FTIR analysis in a later section.

The synthesis of the capsule was not a strict stoichiometric reaction, and most of the toluene would evaporate during the heated reaction process. The yield of the synthesis is therefore simply calculated by the ratio of the mass of collected microcapsules to the total mass of POTS, urea, ammonium chloride, and resorcinol, while the mass of toluene was ignored. Based on this calculation, the yield was around

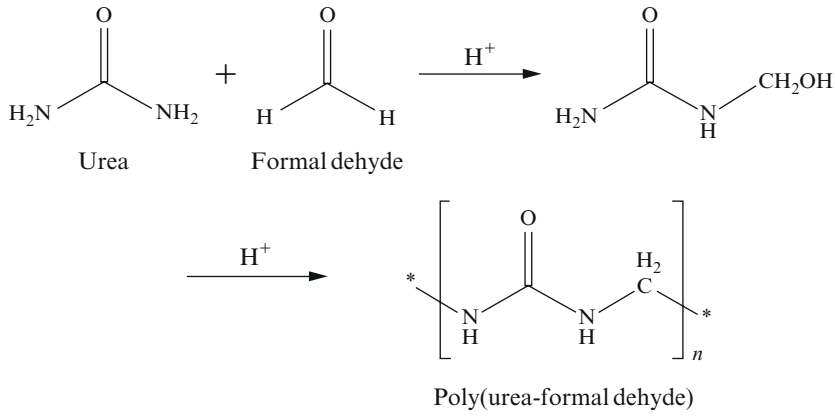


Figure 14.24 Mechanism of the PUF microcapsules synthesis.

67% in a typical synthesis, in which the agitation rate was 800 RPM. The yield of the synthesis is also dependent on the agitation rate during the synthesis, and it reduced to about 52% when the agitation rate was increased to 1500 RPM.

14.3.2.2 Chemical constituent of microcapsules

The chemical constituent of prepared microcapsules was determined from FTIR analysis. The FTIR spectra of complete capsules together with pure grades of POTS, shell, and core materials were shown in Figure 14.25. It is seen that the full capsules contained signals at 3330 cm^{-1} (O–H and N–H stretching), 1620 cm^{-1} (C=O stretching), and 1540 cm^{-1} (N–H bending),[36,72] indicating the formation of PUF from the polymerization reaction between urea and formaldehyde. In addition, the signals at 1240 cm^{-1} and 1190 cm^{-1} (C–F stretching) as well as the signals at 1100 cm^{-1} and 1080 cm^{-1} (Si–O–C stretching) implie the presence of POTS within the synthesized microcapsules. A simple comparison between the spectrum of full microcapsule and capsule shell clear shows that the POTS was absent in the shell part. In the meantime, it can be seen that the spectrum of capsule core is identical to that of pure POTS. Therefore, it is logical to conclude that POTS is not absorbed on the PUF microcapsules; instead, it is indeed encapsulated into the microcapsules as core materials. In other words, the synthesis successfully produced PUF microcapsules containing POTS liquid as the core material.

14.3.2.3 Morphology and diameter of microcapsules

The synthesized microcapsules were analyzed under SEM. As shown in Figure 14.26a, the produced microcapsules have a spherical shape. In addition, it is

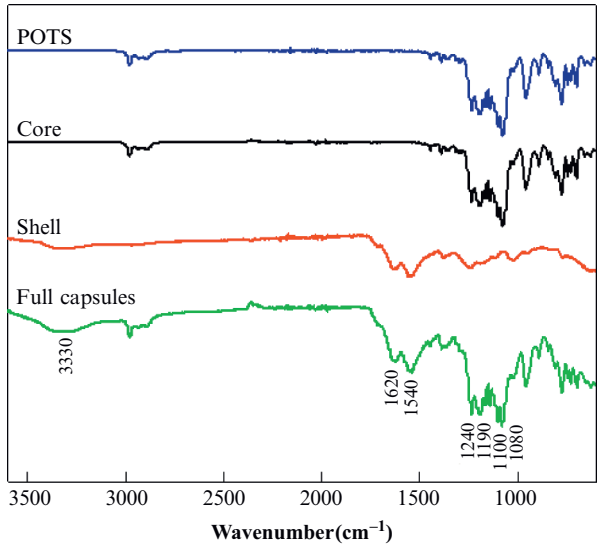


Figure 14.25 FTIR spectra of POTS, capsule core, capsule shell, and full PUF microcapsules.[80]

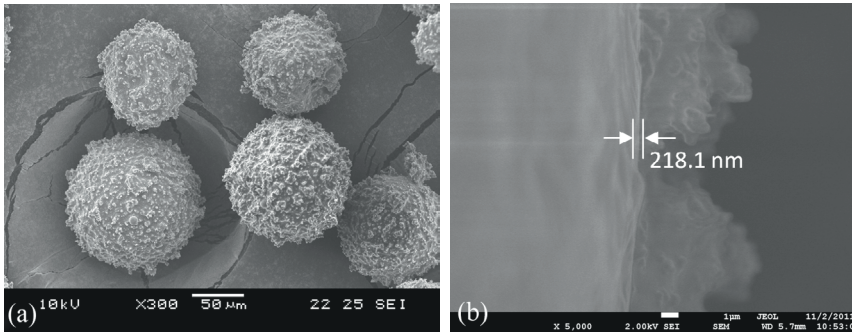


Figure 14.26 SEM images of (a) POTS-filled PUF microcapsules and (b) cross-section of microcapsule shell.[80]

seen from Figure 14.26b that the microcapsule is composed of a rough outer surface and a relatively smooth inner surface. The inner surface is an impervious PUF shell, and the outer surface is the deposition of a large number of PUF nanoparticles.[20] The cross-section of the capsule wall reveals that the thickness of the smooth inner shell is around 218 nm. The shell structure of the synthesized microcapsules is in good agreement with those described in other publications.[16,20]

The average diameter of the POTS microcapsule is dependent on the agitation rate during the synthesis. As illustrated in Figure 14.27, the average diameter of

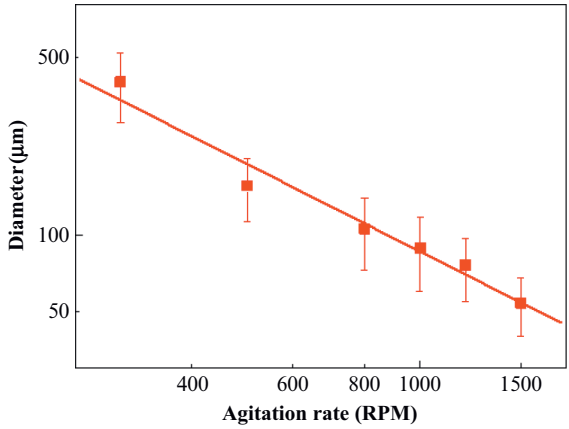


Figure 14.27 Average diameter of POTS-filled PUF microcapsules as a function of agitation rate.[80]

microcapsule would reduce from about 400 to about 40 μm when the agitation rate was raised from 300 to 1500 RPM. This observation demonstrates that the increase of agitation rate will result in smaller microcapsules. The main reason for such a correlation is that at higher agitation rate, finer oil droplets would form in the emulsion system due to the stronger shear force. Because the diameter of the final microcapsules was highly dependent on the oil droplet size in an *in situ* polymerization,[73] in this case, the final microcapsules were accordingly smaller. Actually, as shown in Figure 14.27, the mean diameter of resultant microcapsules exhibits a linear relationship to the agitation rate in double-logarithm coordinates, and this result is consistent with other research.[20,33]

14.3.2.4 Thermal property and core fraction of microcapsules

The thermal property and core fraction of microcapsules were characterized by TGA analysis. The TGA weight loss curves of microcapsules synthesized at 800 RPM along with pure POTS and capsule shell material as a function of temperature are shown in Figure 14.28. It can be seen that microcapsules experienced significant weight loss from ~100 °C, which is in good agreement with that of pure POTS, revealing the successful encapsulation of POTS within the microcapsules. The decomposition of shell materials started from about 200 °C.

The derivative of the weight loss curve of microcapsules was also plotted in Figure 14.28. It clearly shows the evaporation process of POTS in the first peak and decomposition process of capsules shell in the peaks after 200 °C. From the peak width of the derivative curve, the core fraction of the microcapsules was determined to be around 60 wt.% at 800 RPM. The core fraction of the produced microcapsules

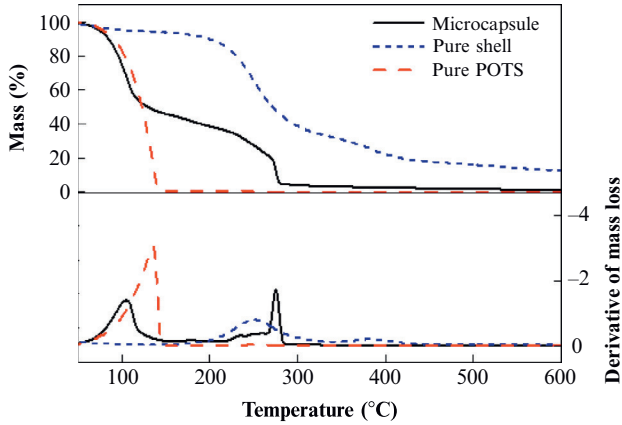


Figure 14.28 TGA weight loss curve of pure POTS, prepared PUF microcapsules, and capsule shell, and the derivative of these TGA curves.[80]

could be increased by raising the content of POTS in the oil phase, but as will be discussed in a later section, the quality of microcapsules would be compromised.

14.3.2.5 Preparation of POTS-based self-healing anticorrosive coating

POTS-based self-healing anticorrosive epoxy coatings were prepared by dispersing a certain amount of synthesized POTS-filled PUF microcapsules into epoxy resin. During the synthesis, the agitation rate was carefully tuned so that the produced microcapsules had expected diameter. The synthesized microcapsules were mixed into epoxy resin EPOLAM 5015 at ambient temperature, followed by mixing hardener EPOLAM 5014. The mixture was degassed for 20 min and then applied on the pretreated substrates by an applicator. The epoxy resin was cured at ambient temperature in open air for 24 h.

Self-healing anticorrosive silicon elastomer was also prepared in a similar manner by dispersing a certain amount of the synthesized microcapsules into silicon resin Sylgard 184 at ambient temperature, followed by mixing hardener. The mixture was then degassed for 20 min and then applied on a pretreated substrate. The silicone elastomer was cured at ambient temperature in open air for 24 h.

14.3.2.6 Accelerated salt immersion corrosion test

An accelerated salt immersion test was performed to the POTS microcapsules-based epoxy coating to demonstrate the self-healing anticorrosive property. The prepared coating was manually scratched and then immersed into 10 wt.% NaCl aqueous solution to evaluate the anticorrosion performance. It can be seen from Figure 14.29

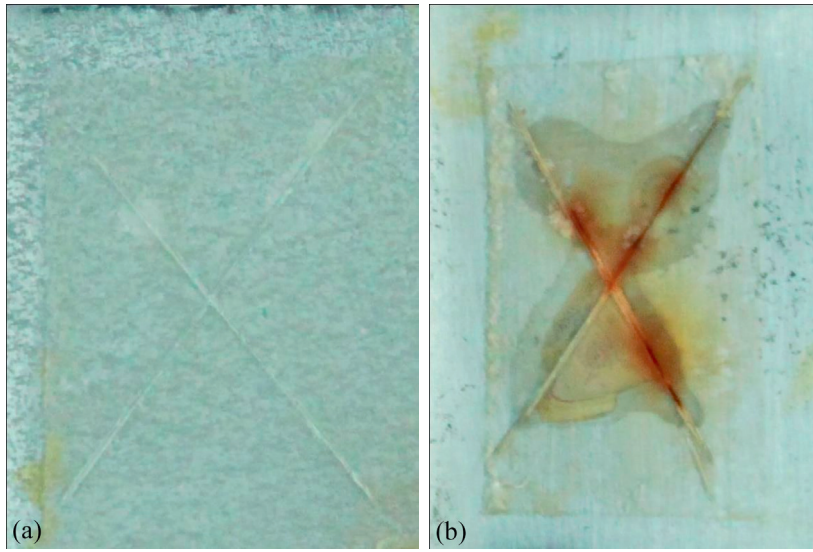


Figure 14.29 Coated steel panel after immersion in 10 wt.% NaCl solution for 48 h: (a) coated with POTS-based self-healing coating and (b) coated with blank coating.[80]

that the scratched area of the steel panel coated with self-healing coating was nearly fully free of corrosion after 48 h immersion in salt solution, while severe corrosion was seen in the control specimen. This considerable difference clearly demonstrates the excellent corrosion protection of the prepared coating towards steel panel.

The scratched areas of both the POTS-based epoxy coating and the control coating were inspected with SEM after the accelerated salt immersion corrosion test was completed, as shown in Figure 14.30. Comparing Figure 14.30a and b, it is obvious that the crack of the POTS-based coating was filled with newly formed materials after the immersion. The crack was in this way resealed to retard the diffusion of salt solution and thus protected the substrate from corrosion. On the contrary, from Figure 14.30c and d, it is seen that the crack of the control specimen was still open. Therefore, it could be concluded that the anticorrosion function of the coating originated from its sealing/self-healing property. However, as shown in Figure 14.30b, it is also observed that the sealing material of the POTS-based coating is not very dense and even, which may influence the corrosion protection performance of the coating, especially when a long-term effect is considered.

14.3.2.7 Corrosion protection performance of intact coating in HCl solution

The anticorrosion property of an intact POTS-based coating was demonstrated by a long-time corrosion test. POTS microcapsules-based silicone elastomer was coated

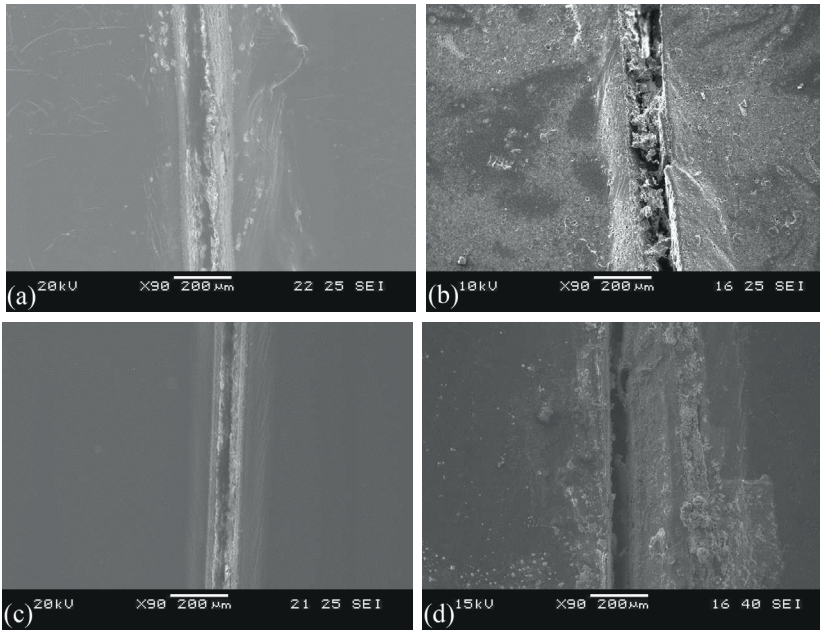


Figure 14.30 SEM images of the scribed regions of POTS-based epoxy coating (a) before immersion; (b) after immersion and control epoxy coating (c) before immersion; (d) after immersion). The coated specimens were immersed in 10 wt.% NaCl solution for 48 h.[80]

on pretreated steel substrate and then exposed to 1 M hydrochloric acid solution for one month. As shown in Figure 14.31, apparently the POTS-based anticorrosive silicon elastomer shows much less corrosion than the control specimen after exposure.

When the coating was peeled off, the underlying steel substrate was examined under SEM, as shown in Figure 14.32. It is seen that prior to exposure to the HCl solution, both steel substrates have a smooth surface (Figure 14.32a and c). Nevertheless, after exposure, the surface of the anticorrosive specimen (Figure 14.32b) was much smoother than the control sample (Figure 14.32d). Given that the corrosion of metal will create rust and destroy the smooth substrate surface, this considerable difference indicates that the steel substrate coated with POTS-based anticorrosive coating was much less corroded during the exposure to corrosive HCl acid solution.

The corrosion-resistant property of the POTS-based coating was further demonstrated by EDX analysis. It is known that corrosion of steel will convert iron (Fe) into rust (Fe_2O_3). Hence, for a steel panel, within a given area, the ratio of element O to Fe (O/Fe) will increase when corrosion occurs, and a higher O/Fe value in turn implies more corrosion. To compare the extent of corrosion on the steel substrate that was coated with POTS-based anticorrosive elastomer or control elastomer during exposure to 1 M HCl solution, the steel substrates were analyzed by EDX to determine the

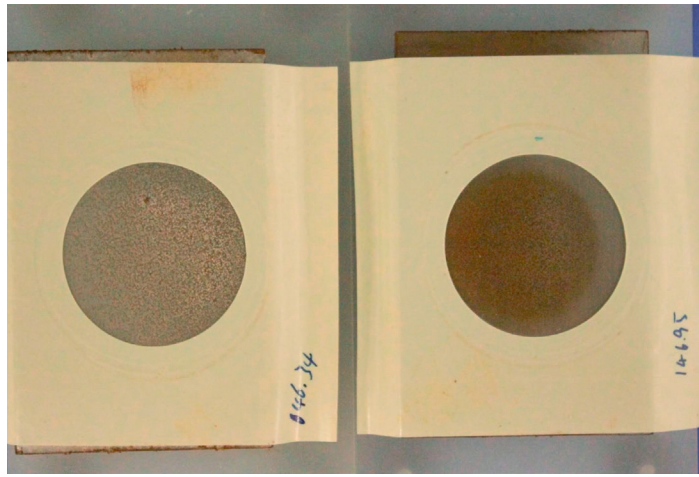


Figure 14.31 POTS-based anticorrosive silicon elastomer (left) and control (right) elastomer coatings after exposure to 1 M HCl solution for 1 month.[79]

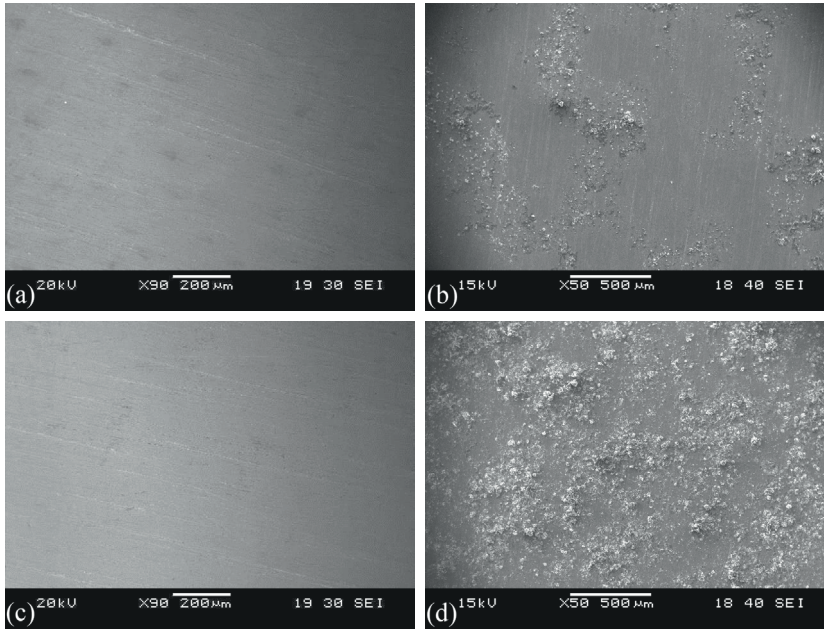


Figure 14.32 SEM images of steel substrate of (a) anticorrosive specimen before exposure; (b) anticorrosive specimen after exposure; (c) control specimen before exposure; and (d) control specimen after exposure.[79]

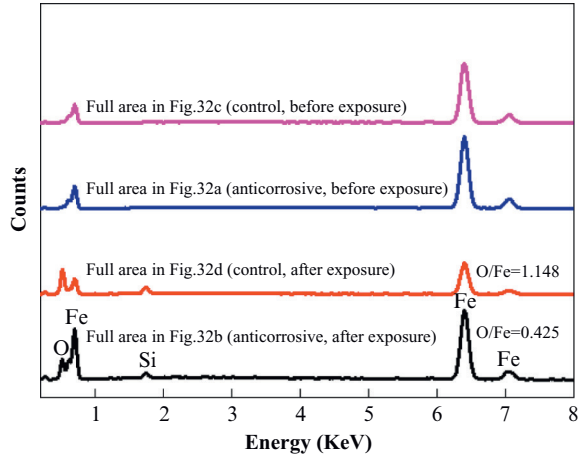


Figure 14.33 EDX analysis of POTS-based anticorrosive coating and control coating. The specimen and analyzed area are the same as those shown in Figure 14.32.[79]

O/Fe ratio of the substrate. As shown in Figure 14.33, prior to exposure to HCl solution, the steel substrates of both anticorrosive specimen and control specimen afforded only element Fe. It means that the substrates were nearly totally free of corrosion. After exposure, elements O, Fe, and Si were detected on both specimens, but it can be seen that the O/Fe value was dramatically different between two specimens. The O/Fe of the substrate coated with anticorrosive elastomer is 0.425 while that of the control sample is 1.148. It is admitted that the O/Fe difference between these two specimens alone is not very conclusive because the corrosion product may be quite complicated, and in the meantime, element O may come from other sources such as open air and silicone elastomer. Nevertheless, if the influence of other factors is assumed to be at the same level for the two specimens in the test, which is a reasonable assumption, the apparently smaller O/Fe value of the anticorrosive specimen from another aspect supports the conclusion above that the corrosion of substrate coated with the POTS-based anticorrosive coating is less compared with that of the control specimen. From the SEM and EDX analysis, it can be concluded that the integration of POTS microcapsules enhanced the corrosion protection performance of the silicon elastomer coating.

The anticorrosive property of the unscratched microcapsules-based one-part self-healing coating can also be explained by the healing reaction of the healing agents, that is, POTS that were prestored in the coating systems. Corrosion is an electrochemical process that requires the involvement of water. When metal is protected by a coating layer, although intact coating is able to effectively separate the substrate from a corrosive environment, corrosion is still inevitable in terms of long-term effect because water may penetrate the coating via diffusion to corrode the substrate. For the microcapsules-based coating, the prestored healing agents were reactive with

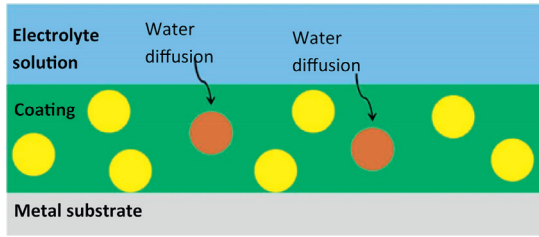


Figure 14.34 Schematic diagram of the corrosion retardant effect of microcapsules in an intact microcapsules-based coating.

water, so the water molecules may be trapped by healing species that are stored in the capsules during the diffusion process, as illustrated in Figure 14.34. It means that the rate that the water passing though the coating layer will be retarded, and as a result, the corrosion of the underlying metal substrate will accordingly be retarded.

14.4 Concluding Remarks and Perspectives

The past decade has witnessed great progress in the field of self-healing materials, and the concept of self-healing has been employed for corrosion control. Nevertheless, most existing self-healing anticorrosive coatings are two-part systems, or require catalyst or external intervention in order to trigger the self-healing process. One-part self-healing anticorrosive coatings can be prepared by incorporating one set of microcapsules containing suitable healing agents into a host coating matrix. Once the coating is scratched to rupture the incorporated microcapsules, the encapsulated healing agents will flow to the scratches. Upon contact with environment, the healing agents will undergo an autonomous self-healing reaction without any manual intervention. In this system, only one type of microcapsules was integrated into the coating matrix, making the fabrication of the self-healing coating much more time efficient. In addition, the self-healing function was realized from the reaction of the encapsulated healing species with its environment. Therefore, the use of a catalyst becomes unnecessary, which is of considerable economic importance.

The design of one-part self-healing anticorrosive is further demonstrated by two examples. A diisocyanate monomer and an organic silane were used as healants to develop separate one-part self-healing anticorrosive coatings, respectively. The excellent corrosion protection function of the created coatings was demonstrated by an accelerated salt immersion corrosion test and salt spray test. The anticorrosion function was realized through a self-healing mechanism, and the good self-healing performance of the coatings was quantitatively demonstrated by both DC electrochemical test and EIS measurements. The self-healing anticorrosive performance

of the prepared coating was found to be related to the microcapsules diameter, microcapsules weight fraction in the coating and the coating thickness. Generally, larger microcapsules size, higher microcapsule weight fraction, and larger coating thickness are favorable to achieve better self-healing anticorrosive performance. The influences of the coating variables on the anticorrosive performance of the coating were explained based on a simplified model. It is revealed that the self-sealing behavior of the coating does not require manual intervention. In addition, in both self-sealing coatings only one healing agent is used without catalyst, so they are one-part and catalyst-free self-healing coating systems.

Although tremendous endeavors have been invested in the research of one-part self-healing anticorrosive coatings, and some products have been successfully fabricated, there are still a number of challenges to be addressed. For example, some healing agents such as diisocyanate monomers have shown great potential for the development of one-part self-healing anticorrosive coatings, but they may impose some environmental hazard, especially when long-term effect is considered. In addition, the one-part self-healing anticorrosive coating makes use of the reaction of the prestored healing species with its environment, but the high reactivity of the healant may cause some problem in the stability of the microcapsules as well as of the prepared coating.

The techniques for the development of one-part self-healing anticorrosive are not sufficiently mature for practical applications, and the research on this topic has drawn considerable attention. Here we propose our own perspectives on the research of one-part self-healing anticorrosive coatings, but the whole future picture of this field will definitely not be restrained in these aspects.

1. Microencapsulation of new healing species for self-healing anticorrosive applications. Finding new healing species with higher efficiency but lower environmental toxicity is always a very important part in the field of self-healing materials.
2. To improve the durability of the one-part self-healing anticorrosive coating. Durability is one of the most important requirements when a coating is developed for practical applications. In order to achieve high durability, the microcapsules have to be both chemically and mechanically stable. In addition, they should be able to provide good protection to the active healing agents so that the reactivity of the healing agents is maintained, and the capsules should also be compatible with the host coating matrix. Unfortunately, the durability of some one-part self-healing anticorrosive coatings is yet to be improved. For example, although the HDI-based coating exhibits excellent self-healing anticorrosive properties, it is found that the prepared microcapsule has a high permeability, and the stability of the microcapsules in organic solvents is still far from satisfactory. Hence, more efforts should be made to improve the barrier property of the microcapsules. PUF microcapsules have shown much better barrier property, so we may try to

synthesize two-layer microcapsules to store the healing species. The synthesis may be realized through a two-step procedure.[74] HDI-filled PU microcapsules are prepared first, which are then used as the template to synthesize the second layer of PUF microcapsules. In addition, it has been reported that the barrier property of microcapsules could be improved by adding nanoclays in the wall.[75] We also can try to modify the current PU microcapsules with some nanoclays or other fillers to improve the stability of the microcapsules for filed applications. In addition, the permeability of the PU microcapsules is also determined by the chemical composition of the shell materials themselves. For example, it has been reported that the PU microcapsules made from MDI are more permeable than those made from TDI.[76] Hence, we can try to redesign the synthesis by using different starting materials in order to improve the barrier property and stability of the microcapsules.

3. Different self-healing and corrosion tests have been performed to evaluate the quality of the prepared self-healing coating in the present study. But some of the test methods are only qualitative, while more quantitative results may be necessary to characterize the self-healing anticorrosive performance of the developed coating. In addition, the conditions under which these tests were conducted are still different from the real environment that the coatings may be exposed to. Hence, larger scale field tests are necessary before the coatings are considered for practical applications.

References

1. Revie RW, Uhlig HH. Corrosion and corrosion control. Hoboken, New Jersey: John Wiley & Sons; 2008.
2. Marcus P. Corrosion mechanisms in theory and practice. 2nd ed. Boca Raton, Florida: CRC Press; 2002.
3. Koch GH. Corrosion cost and preventive strategies in the United States. Mclean, Virginia: Turner-Fairbank Highway Research Center; 2002.
4. Uligh HH. Corrosion and corrosion control: an introduction to corrosion science and engineering. Hoboken, New Jersey: John Wiley & Sons; 1971.
5. Trask RS, Williams HR, Bond IP. Self-healing polymer composites: mimicking nature to enhance performance. Bioinspir Biomim 2007;2(1):9.
6. Wu DY, Meure S, Solomon D. Self-healing polymeric materials: a review of recent developments. Prog Polym Sci 2008;33(5):479–522.
7. Jud K, Kausch HH. Load transfer through chain molecules after interpenetration at interfaces. Polym Bull 1979;1(10):697–707.
8. Chung CM, Roh YS, Cho SY, et al. Crack healing in polymeric materials via photochemical [2+2] cycloaddition. Chem Mater 2004;16(21):3982–4.
9. White SR, Sottos NR, Geubelle PH, et al. Autonomic healing of polymer composites. Nature 2001;409(6822):794–7.
10. Wool RP. Self-healing materials: a review. Soft Matter 2008;4(3):400–18.
11. Blaiszik BJ, Kramer SLB, Olugebefola SC, et al. Self-healing polymers and composites. Annu Rev Mater Res 2010;40(1):179–211.

12. Murphy EB, Wudl F. The world of smart healable materials. Prog Polym Sci 2010;35(1–2):223–51.
13. Syrett J, Becer C, Haddleton D. Self-healing and self-mendable polymers. Polym Chem 2010;1(7): 978–87.
14. Sauvant-Moynot V, Gonzalez S, Kittel J. Self-healing coatings: an alternative route for anticorrosion protection. Prog Org Coat 2008;63(3):307–15.
15. Suryanarayana C, Rao KC, Kumar D. Preparation and characterization of microcapsules containing linseed oil and its use in self-healing coatings. Prog Org Coat 2008;63(1):72–8.
16. Samadzadeh M, Boura SH, Peikari M, et al. Tung oil: an autonomous repairing agent for self-healing epoxy coatings. Prog Org Coat 2011;70(4):383–7.
17. García SJ, Fischer HR, White PA, et al. Self-healing anticorrosive organic coating-based on an encapsulated water reactive silyl ester: Synthesis and proof of concept. Prog Org Coat 2011;70(2–3):142–9.
18. Nesterova T, Dam-Johansen K, Kiil S. Synthesis of durable microcapsules for self-healing anticorrosive coatings: a comparison of selected methods. Prog Org Coat 2011;70(4):342–52.
19. Ghosh B, Urban M. Self-repairing oxetane-substituted chitosan polyurethane networks. Science 2009;323(5920):1458.
20. Brown E, Kessler M, Sottos N, et al. In situ poly (urea-formaldehyde) microencapsulation of dicyclopentadiene. J Microencapsul 2003;20(6):719–30.
21. Kessler MR, Sottos NR, White SR. Self-healing structural composite materials. Compos A Appl Sci Manuf 2003;34(8):743–53.
22. Bejan A, Lorente S, Wang KM. Networks of channels for self-healing composite materials. J Appl Phys 2006;100(3), 033528-6.
23. Toohey K, Sottos N, Lewis J, et al. Self-healing materials with microvascular networks. Nat Mater 2007;6(8):581–5.
24. Simon B. Microencapsulation: methods and industrial applications. 2nd ed. New York: Taylor & Francis; 2006.
25. Samadzadeh M, Boura SH, Peikari M, et al. A review on self-healing coatings-based on micro/nanocapsules. Prog Org Coat 2010;68(3):159–64.
26. Hawlader MNA, Uddin MS, Khin MM. Microencapsulated PCM thermal-energy storage system. Appl Energ 2003;74(1–2):195–202.
27. Mayya KS, Bhattacharyya A, Argillier J. Microencapsulation by complex coacervation: influence of surfactant. Polym Int 2003;52(4):644–7.
28. Gharsallaoui A, Roudaut G, Chambin O, et al. Applications of spray-drying in microencapsulation of food ingredents: an overview. Food Res Int 2007;40(9):1107–21.
29. Shu B, Yu W, Zhao Y, et al. Study on microencapsulation of lycopene by spray-drying. J Food Eng 2006;76(4):664–9.
30. Cho J, Kwon A, Cho C. Microencapsulation of octadecane as a phase-change material by interfacial polymerization in an emulsion system. Colloid Polym Sci 2002;280(3):260–6.
31. Cho S, Andersson H, White S, et al. Polydimethylsiloxane-based self-healing materials. Adv Mater 2006;18(8):997–1000.
32. Cho SH, White SR, Braun PV. Self-healing polymer coatings. Adv Mater 2009;21(6):645–9.
33. Yang J, Keller MW, Moore JS, et al. Microencapsulation of isocyanates for self-healing polymers. Macromolecules 2008;41(24):9650–5.
34. Keller M, Sottos N. Mechanical properties of microcapsules used in a self-healing polymer. Exp Mech 2006;46(6):725–33.
35. Yuan L, Gu A, Liang G. Preparation and properties of poly(urea-formaldehyde) microcapsules filled with epoxy resins. Mater Chem Phys 2008;110(2–3):417–25.
36. Yuan L, Liang G, Xie J, et al. Preparation and characterization of poly(urea-formaldehyde) microcapsules filled with epoxy resins. Polymer 2006;47(15):5338–49.

37. Yuan Y, Rong M, Zhang M. Preparation and characterization of microencapsulated polythiol. Polymer 2008;49(10):2531–41.
38. Yuan L, Liang G, Xie J, et al. Synthesis and characterization of microencapsulated dicyclopentadiene with melamine–formaldehyde resins. Colloid Polym Sci 2007;285(7):781–91.
39. Dunky M. Urea-formaldehyde (UF) adhesive resins for wood. Int J Adhes Adhes 1998;18(2):95–107.
40. Caruso MM, Davis DA, Shen Q, et al. Mechanically-induced chemical changes in polymeric materials. Chem Rev 2009;109(11):5755–98.
41. Chu LY, Park SH, Yamaguchi T, et al. Preparation of micron-sized monodispersed thermoresponsive core−shell microcapsules. Langmuir 2002;18(5):1856–64.
42. Caruso MM, Blaiszik BJ, Jin H, et al. Robust, double-walled microcapsules for self-healing polymeric materials. ACS Appl Mater Interfaces 2010;2(4):1195–9.
43. Motuku M, Vaidya U, Janowski G. Parametric studies on self-repairing approaches for resin infused composites subjected to low velocity impact. Smart Mater Struct 1999;8:623–8.
44. Pang J, Bond I. Bleeding composites'—damage detection and self-repair using a biomimetic approach. Compos A Appl Sci Manuf 2005;36(2):183–8.
45. Hayes S, Zhang W, Branthwaite M, et al. Self-healing of damage in fibre-reinforced polymer-matrix composites. J R Soc Interface 2007;4(13):381.
46. Dry C. Passive tuneable fibers and matrices. Int J Mod Phys B 1992;6:2763–71.
47. Dry C. Procedures developed for self-repair of polymer matrix composite materials. Compos Struct 1996;35(3):263–9.
48. Li VC, Lim YM, Chan YW. Feasibility study of a passive smart self-healing cementitious composite. Compos Part B-Eng 1998;29(6):819–27.
49. Mauldin T, Kessler M. Self-healing polymers and composites. Int Mater Rev 2010;55(6):317–46.
50. Brown EN, Sottos NR, White SR. Fracture testing of a self-healing polymer composite. Exp Mech 2002;42(4):372–9.
51. Yin T, Zhou L, Rong MZ, et al. Self-healing woven glass fabric/epoxy composites with the healant consisting of micro-encapsulated epoxy and latent curing agent. Smart Mater Struct 2008;17:015019.
52. Toohey K, Sottos N, White S. Characterization of microvascular-based self-healing coatings. Exp Mech 2009;49(5):707–17.
53. Williams H, Trask R, Knights A, et al. Biomimetic reliability strategies for self-healing vascular networks in engineering materials. J R Soc Interface 2008;5(24):735–47.
54. Toohey KS, Hansen CJ, Lewis JA, et al. Delivery of two part self healing chemistry via microvascular networks. Adv Funct Mater 2009;19(9):1399–405.
55. Williams H, Trask R, Bond I. Self-healing composite sandwich structures. Smart Mater Struct 2007;16:1198.
56. Hansen CJ, Wu W, Toohey KS, et al. Self healing materials with interpenetrating microvascular networks. Adv Mater 2009;21(41):4143–7.
57. Therriault D, White SR, Lewis JA. Chaotic mixing in three-dimensional microvascular networks fabricated by direct-write assembly. Nat Mater 2003;2(4):265–71.
58. Yang H, Mendon S, Rawlins J. Nanoencapsulation of blocked isocyanates through aqueous emulsion polymerization. Express Polym Lett 2008;2(5):349–56.
59. Rawlins J, Yang H, Mendon S. Nanoencapsulation of isocyanates via aqueous media. *US Patents*; 2008.
60. Cheong IW, Kim JH. Synthesis of core-shell polyurethane-urea nanoparticles containing 4,4[prime or minute]-methylenedi-p-phenyl diisocyanate and isophorone diisocyanate by self-assembled neutralization emulsification. Chem Commun 2004;21:2484–5.
61. Walther, M., Rudolf T, Rudolf Z. Process for the manufacture of an encapsulated isocyanate. *US Patent: United States*; 1968.

62. Ni P, Zhang M, Yan N. Effect of operating variables and monomers on the formation of polyurea microcapsules. J Membr Sci 1995;103(1–2):51–5.
63. Rule J, Sottos N, White S. Effect of microcapsule size on the performance of self-healing polymers. Polymer 2007;48(12):3520–9.
64. Brown EN, White SR, Sottos NR. Microcapsule induced toughening in a self-healing polymer composite. J Mater Sci 2004;39(5):1703–10.
65. Mookhoek SD, Fischer HR, van der Zwaag S. A numerical study into the effects of elongated capsules on the healing efficiency of liquid-based systems. Comput Mater Sci 2009;47(2):506–11.
66. Gao H, Li Q, Chen FN, et al. Study of the corrosion inhibition effect of sodium silicate on AZ91D magnesium alloy. Corros Sci 2011;53(4):1401–7.
67. Kartsonakis I, Daniilidis I, Kordas G. Encapsulation of the corrosion inhibitor 8-hydroxyquinoline into ceria nanocontainers. J Sol-Gel Sci Technol 2008;48(1):24–31.
68. Kartsonakis IA, Balaskas AC, Koumoulos EP, et al. Incorporation of ceramic nanocontainers into epoxy coatings for the corrosion protection of hot dip galvanized steel. Corros Sci 2012;57:30–41.
69. Li Y, Li L, Sun J. Bioinspired self-healing superhydrophobic coatings. Angew Chem Int Ed 2010;49(35):6129–33.
70. Scopelitis E, Pizzi A. Urea–resorcinol–formaldehyde adhesives of low resorcinol content. J Appl Polym Sci 1993;48(12):2135–46.
71. Cosco S, Ambrogi V, Musto P, et al. Urea formaldehyde microcapsules containing an epoxy resin: influence of reaction parameters on the encapsulation yield. Macromol Symp 2006;234(1):184–92.
72. Liao L, Zhang W, Zhao Y, et al. Preparation and characterization of microcapsules for self-healing materials. Chem Res Chin Univ 2010;26(3):496–500.
73. Ovez B, Citak B, Oztemel D, et al. Variation of droplet sizes during the formation of microspheres from emulsion. J Microencapsul 1997;14:489–99.
74. Li G, Feng Y, Gao P, et al. Preparation of mono-dispersed polyurea-urea formaldehyde double layered microcapsules. Polym Bull 2008;60(5):725–31.
75. Fan C, Zhou X. Preparation and barrier properties of the microcapsules added nanoclays in the wall. Polym Adv Technol 2009;20(12):934–9.
76. Jabbari E. Morphology and structure of microcapsules prepared by interfacial polycondensation of methylene bis(phenyl isocyanate) with hexamethylene diamine. J Microencapsul 2001;18(6):801–9.
77. Huang MX, Yang JL. Facile microencapsulation of HDI for self-healing anticorrosion coating. J Mater Chem 2011;21(30):11123–30.
78. Huang MX, Yang JL. Salt spray and EIS studies on HDI microcapsule-based self-healing anticorrosive coatings. Progr Org Coating 2014;77(12):168–75.
79. Huang MX, Yang JL. Long-term performance of *1H,1H',2H,2H'*-perfluorooctyl triethoxysilane (POTS) microcapsule-based self-healing anticorrosive coatings. J Intel Mater Sys Struct 2014;25(1):98–106.
80 Huang MX, Zhang H, Yang JL. Synthesis of organic silane microcapsules for self-healing corrosion resistant polymer coatings. Corros Sci 2012;65:561–6.

Chapter 15

Intelligent Stannate-Based Coatings of Self-Healing Functionality for Magnesium Alloys

Abdel Salam Hamdy Makhlouf
Department of Manufacturing Engineering, College of Engineering and Computer Science, University of Texas Pan-American, 1201 West University Dr., Edinburg, Texas, USA

15.1 Introduction

Magnesium alloys are emerging as lightweight structural materials for many innovative applications and, in particular, automotive and aerospace industries. This chapter highlights the common types of magnesium alloys and possible forms of corrosion that can be occulated on magnesium. Additionally, the possibility of using stannate conversion coating treatment as inexpensive, clean, and simple coating technology of self-healing characteristics for corrosion protection is also described.

Intelligent Coatings for Corrosion Control
Copyright © 2015 Elsevier Inc. All rights reserved.

15.2 Types of Magnesium Alloys

Magnesium alloys can be classified into two main categories: cast and wrought alloys. Magnesium alloys are typically used as cast alloys; however, research on wrought alloys has shown tremendous growth during the last decade. Cast magnesium alloys have been extensively used for many industrial applications, namely automotive, electronics, and aerospace. The most common cast magnesium alloys are: AZ63, AZ81, AZ91, AM50, ZK51, ZK61, ZE41, ZC63, HK31, HZ32, QE22, QH21, WE54, WE43, and Elektron 21. The most common wrought magnesium alloys are: AZ31, AZ61, AZ80, Elektron 675, ZK60, M1A, HK31, HM21, ZE41, and ZC71. Here, the prefix letters designate two principal alloying metals in magnesium alloys that were developed according to ASTM B275 where: A: Aluminum; C: Copper; E: Rare earths; H: Thorium; K: Zirconium; L: Lithium; M: Manganese; O: Silver; S: Silicon; T: Tin; W: Yttrium; Z: Zinc; B: Bismuth; R: Chromium; D: Cadmium; N: Nickel; F: Iron.

Generally, magnesium alloys are highly susceptible to corrosion, especially when chloride ions are present in the surrounding environment. The potential-pH diagram of magnesium shows possible protection of Mg at high pH values, which may result from $Mg(OH)_2$ formation during the corrosion reaction. However, in contact with aqueous solutions the formation of MgH_2 and Mg^+ cannot exist due to thermodynamic nonequilibrium for Mg alloys.[1] Many schemes have been proposed to improve the corrosion protection of magnesium alloys in chloride-containing solutions. However, most of the available technologies are toxic, expensive, or based on sophisticated multistep processes that make them industrially unattractive.

Over the last decade, the author's research group identified that the issue of designing a simple eco-friendly coating technology for magnesium alloys is of prime concern for industry and academia. The corrosion protection performance of different magnesium alloys was investigated using several environmentally friendly coating systems based on cerate, stannate, zirconate, vanadate, or permanganate. Such coatings have been engineered to provide a maximum localized corrosion protection to different types of magnesium alloys such as AZ91D, AZ31D, AZ91E, and Elektron ZE41 Mg-Zn-rare earth alloy in chloride-containing environments.[2–13] Among the coatings that have been designed in the author's group, stannate conversion coating treatment has proven to provide unique corrosion protection along with self-healing characteristics.[8,14–17] This chapter discusses the detail of synthesis of a simple, inexpensive conversion coating treatment approach based on nontoxic stannate.

15.3 Common Forms of Magnesium Corrosion

Corrosion is a naturally occurring process, which has been defined by the National Association for Corrosion Engineers (NACE) as "the deterioration of a substance

(usually a metal) or its properties because of a reaction with its environment." During the corrosion process, the metal has a natural tendency to shift toward the lowest possible energy state through a reaction with the surrounding oxygen, moisture, and water to form (hydro)oxides as corrosion products.

There are several forms of corrosion in aqueous media. The following section highlights some of the most common corrosion forms with a special emphasis on those that can occur on magnesium alloys.

15.3.1 General corrosion

General corrosion is the most common form of corrosion and is also called uniform corrosion where the electrochemical reactions (in aqueous or atmospheric media) proceed uniformly over the entire exposed metal surface over a large area. As such, general corrosion represents the greatest destruction of metal on a tonnage basis. As a result, the metallic surface becomes rough and possibly frosted in appearance (Figure 15.1). However, general corrosion is less dangerous than the other corrosion forms because the life of equipment or structures can be accurately estimated from simple corrosion tests and sometimes by visual inspection.

The occurrence of general corrosion in magnesium alloys is quite common. Figure 15.2 shows an example of general corrosion for AZ31D after 1 week of immersion in NaCl solution. Using more corrosion-resistant materials or protective coatings is the most effective approach to control such corrosion.



Figure 15.1 Schematic representation showing the uniform attack due to general corrosion.

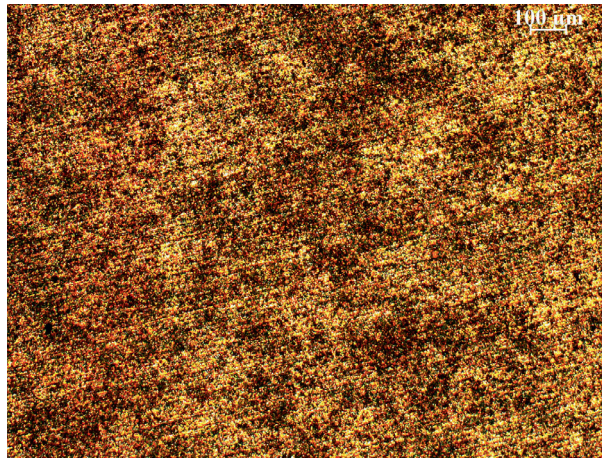


Figure 15.2 An example of general corrosion for magnesium alloy.

15.3.2 Pitting corrosion

Pitting corrosion is more destructive than uniform attack is because it is difficult to predict and leads to unexpected failure. The naturally occurring passive films formed over many metallic substrates (such as aluminum, copper, stainless steel, etc.) can provide a considerable corrosion resistance over a long time in corrosive media. However, if corrosion occurs (due to material defects or changes in the surrounding environment), some pits could form. Pitting is most likely to occur in a halide ion containing media (mostly chloride) in the presence of oxygen or oxidizing agents.

Figure 15.3 shows a schematic representation of pitting corrosion. Pitting corrosion can occur at free corrosion potential of magnesium, when exposed to chloride ions in a nonoxidizing medium[18] as a result of the passivity breakdown.[18,19] This is followed by the formation of an electrolytic cell (Figure 15.4) in which the secondary

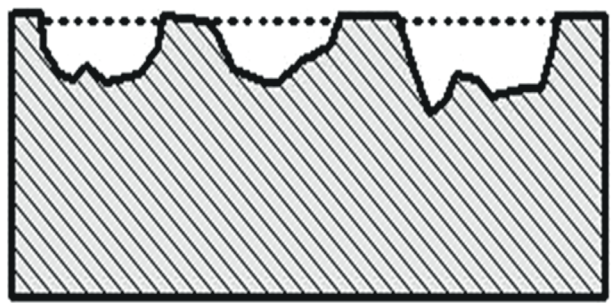


Figure 15.3 Schematic representation of pitting corrosion.

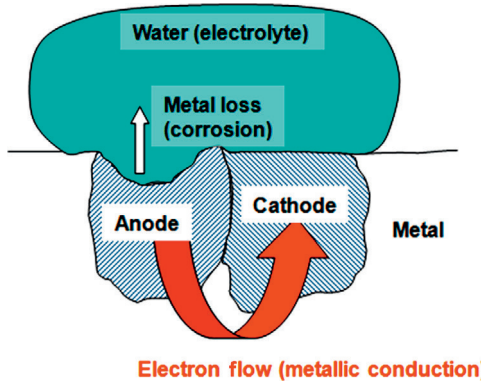


Figure 15.4 Schematic representation of an electrolytic cell.

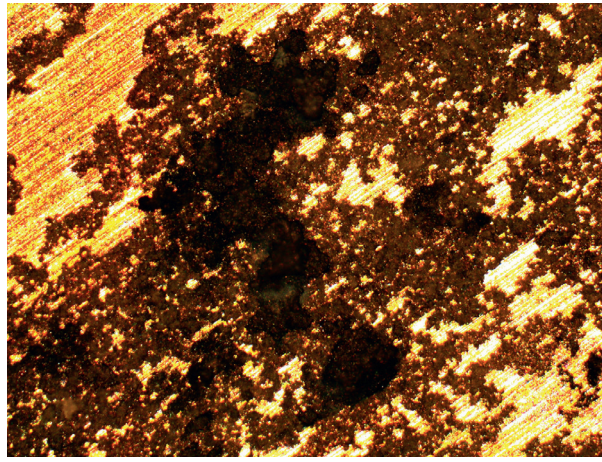


Figure 15.5 An example of pitting corrosion on AZ91D magnesium alloy after 7 days of immersion in 3.5 wt.% NaCl solution.

phase of AlMn, AlMnFe, and so on, acts as a cathode and the surrounding Mg matrix acts as an anode. Figure 15.5 is an example of pitting corrosion in a AZ91D magnesium alloy immersed for a week in corrosive 3.5 wt.% NaCl solution.

15.3.3 Crevice (under deposit) corrosion

Crevice corrosion is another destructive form of localized corrosion. It usually occurs in the areas under deposits where free access to the surrounding environment is restricted. Crevice corrosion is caused on contact of metals with metals or metals with nonmetals, for example, gaskets, couplings, and joints. It may occur also at washers,

under barnacles, at sand grains, under applied protective films, and at pockets formed by threaded joints.

There is a large debate in the literature about the possibility of occurrence of crevice corrosion in magnesium alloys. Some researchers reported that crevice corrosion could not occur in magnesium alloys.[18,20] Although a form of attack that occurs at narrow gaps ("crevice") appears similar to crevice corrosion, it is not a true crevice corrosion (Figures 15.6 and 15.7). The justification for this observation is that the corrosion is caused by the retention of moisture in the crevice which, being unable to evaporate, promotes the corrosion of metal in the narrow to recess over extended periods. In fact, this is typically called "filiform corrosion," which is a peculiar type

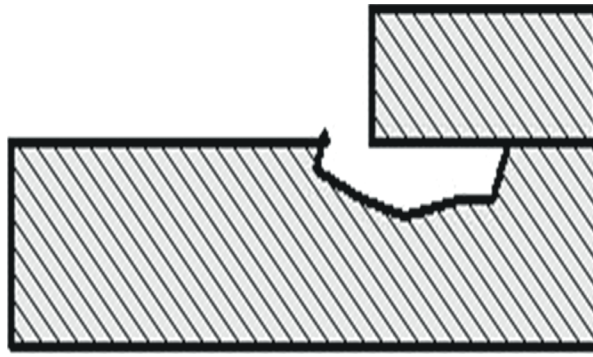


Figure 15.6 Schematic representation of crevice corrosion.

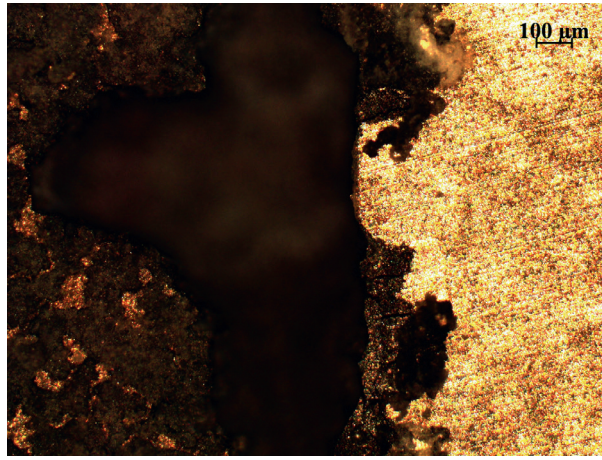


Figure 15.7 An example of crevice corrosion on AZ91D magnesium alloy coated with stannate (under specific conditions) after 7 days of immersion in 3.5% NaCl solution.

of crevice corrosion. As such, it is deduced that crevice corrosion could possibly occur in magnesium alloys.

In contrast, other researchers[21] proposed a mechanism for the possible occurrence of crevice corrosion in magnesium alloys in which crevice corrosion could be initiated due to the hydrolysis reaction when oxygen does not play a major role in the corrosion mechanism. The formation of Mg hydroxide should influence the properties of the interface between the Mg and the solution in the crevice.

Based on the author's previous studies with different magnesium alloys in chloride-containing solution,[2–17] typical filiform and crevice corrosion have been identified (Figures 15.7 and 15.8). It is believed the occurrence of crevice or filiform corrosion could be initiated under certain conditions. For example, in case of imperfect chemical conversion coating treatments using salts such as cerium, vanadium, zirconium, tin, or manganese to protect magnesium alloys. The crevice or filiform corrosion is caused by active galvanic cells that originate across the metal surface due to the formation of oxide thin-film of the salts of irregular surface morphology. The metal parts covered by oxide act as cathodes, whereas the uncovered Mg parts act as anodes.

15.3.4 Filiform corrosion

As mentioned above, filiform corrosion is a particular form of crevice corrosion. This type of corrosion typically occurs on coated surfaces when moisture or a corrosive solution penetrates through the defective coatings. It is caused by active galvanic cells across the metal surface. Its head is anodic, whereas the tail is cathodic (Figure 15.8).

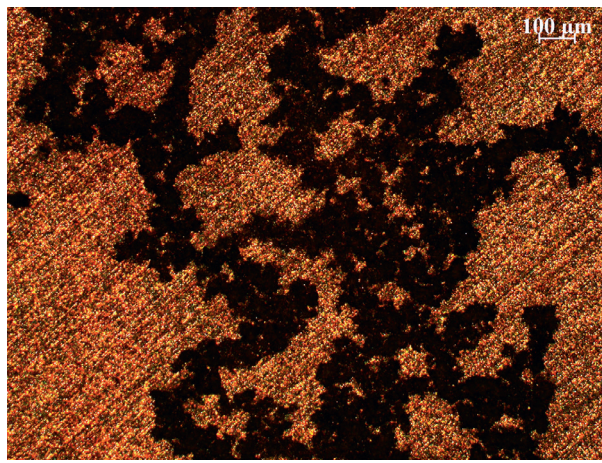


Figure 15.8 An example of filiform corrosion on AZ91D magnesium alloy coated with stannate (under specific conditions) after 7 days of immersion in 3.5% NaCl solution.

Lacquers and "quick-dry" paints are most susceptible to filiform corrosion. Thus, an ideal coating should exhibit low water vapor transmission characteristics and excellent adhesion. The occurrence of pitting and filiform corrosion for magnesium alloy AZ91 was identified by some researchers.[22] Dexter[23] proposed a model of filiform corrosion for magnesium that is driven by oxygen concentration between the head and tail. However, the proposed model is in contradiction with the theory that magnesium corrosion is relatively insensitive to oxygen concentration differences.

To avoid filiform corrosion, a suitable surface preparation or treatment prior to coating should be applied. In addition, a proper inspection of coatings to ensure the absence of coatings defects, such as holidays, or holes, should be used.

15.3.5 Galvanic corrosion

Galvanic corrosion is an electrochemical action of two dissimilar metals in the presence of an electrolyte and an electron conductive path (Figure 15.9). A potential difference usually exists when two dissimilar metals are in contact. In such case, corrosion of less resistant metal is increased while corrosion for more resistant metal is reduced; whereas, more active metal acts as an anode (the one that will corrode) and more resistant metal acts as a cathode. The further apart the metals in the galvanic series are (Figure 15.10), the higher the rate of galvanic corrosion there is. Magnesium alloys have high susceptibility to galvanic corrosion due to excessive levels of heavy metal or flux contamination. Severe galvanic corrosion takes place when magnesium is in contact with less active metals such as Fe, Ni, or Cu (they have low hydrogen overpotential and act as efficient cathodes). On the contrary, metals that combine an active corrosion potential with high hydrogen overpotential such as Al, Zn, Cd, and Sn, are much less damaging, and, therefore, they are favorable as alloying elements for magnesium alloys.

There are several factors affecting the rate of galvanic corrosion: (1) the degree of potential difference between the two metals; (2) the distance effect, with the greatest attack usually being near the junction; (3) the area effect, where it is better to have large anodes and small cathodes; and (4) the corrosiveness of the surrounding media.

The author's recent research studies on some rare-earth-containing magnesium alloys such as AZ91E, EV31A-T6, and Elektron ZE41 Mg-Zn-rare earth revealed the

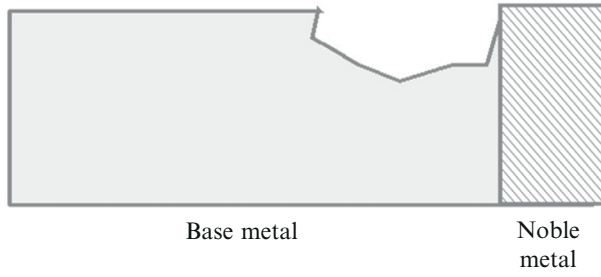


Figure 15.9 Schematic representation of galvanic corrosion.



Figure 15.10 Galvanic series in seawater.

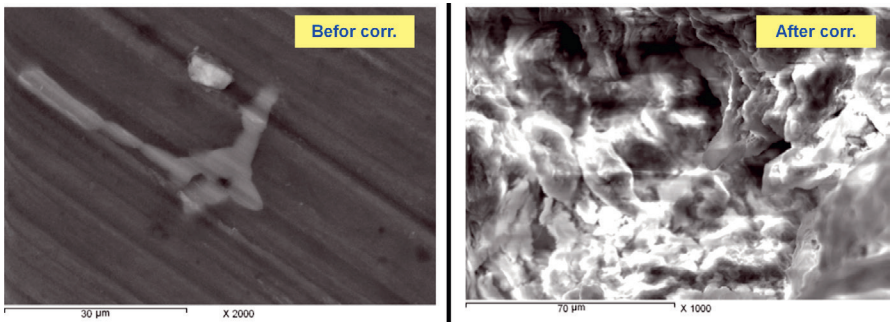


Figure 15.11 An example of galvanic corrosion (due to the potential difference between the rare-earth phase and Mg matrix) on Mg-Zn-rare earth (DF9690) magnesium alloy before (left) and after (right) 7 days of immersion in.5 wt.% NaCl solution.

occurrence of galvanic corrosion between the inert phase associated with rare-earth metals and active magnesium matrix.[6,9–12,15] Figure 15.11 shows the formation for rare-earth phases in Mg matrix and the occurrence of galvanic corrosion at the interface.

15.3.6 Stress corrosion cracking

Stress corrosion cracking (SCC) is an extremely destructive type of corrosion damage in engineering equipment and structures. SCC is caused by the effects of tensile stress in corrosive environments. Stresses may be due to applied loads, residual stresses from the manufacturing process, or a combination of both.

Most of the SCC cases reported for magnesium alloys have focused on extruded or rolled Mg alloys.[24] Die-cast magnesium alloys are more susceptible to SCC than

rapidly solidified and semisolid cast alloys. Magnesium alloys containing A1 are more susceptible to SCC in air, distilled water, and chloride-containing solutions. Two mechanisms have been proposed for SCC in Mg alloys[25]:

1. Continuous crack propagation by anodic dissolution at the crack tip (commonly called the dissolution model), where it includes a preferential attack model, film rupture model, tunneling theory, and so on
2. Discontinuous crack propagation by a series of mechanical fractures at the crack tip (commonly called the brittle fracture models), where it involves cleavage processes and hydrogen embrittlement theory

According to the fracture morphology of the crack, SCC can be divided into two types:

1. Transgranular SCC: This is the common form in magnesium alloys where it, mostly, has HCP crystal structures that are susceptible to cleavage due to the less slip systems available. In general, the occurrence of SCC in magnesium alloys is always linked with hydrogen evolution. Such observation has been evidenced by other authors.[24,26]
2. Intergranular SCC: This is a minor form of SCC in magnesium and is mainly related to localized galvanic attack of the matrix when coupled with cathodic grain-boundary precipitates.[26]

15.3.7 Intergranular corrosion

Intergranular corrosion is an attack that occurs at the grain boundaries of a metal or alloy due to the precipitation of secondary phase. A highly magnified cross-section can show the granular structure with a clearly defined boundary that chemically differs from the grain.

There is a large debate between the researchers whether magnesium alloys suffer intergranular corrosion or not. It has been taken for granted that true intergranular corrosion could not occur in Mg alloys because the phases at the grain boundaries are almost cathodic to the grains.[27] Corrosion tends to be concentrated in the area adjacent to the grain boundary until eventually the grain may be undercut and fall out.[18,20] However, some researchers recently showed that intergranular corrosion can occur on some magnesium alloys such as WE43.[28] In another work, researchers claimed that in the early stages of immersion, a localized attack of AE81 can be formed at the grain boundaries,[21] which can be considered intergranular (intercrystalline) corrosion. The reason for such a tendency is still unclear. Generally, magnesium alloys containing low Al concentration corrode at a faster rate than those containing Al-rich regions.

15.3.8 Corrosion fatigue

Corrosion fatigue is a special kind of SCC caused by a synergistic effect between cyclic stress and corrosion. Corrosion fatigue represents the most destructive attacks that can occur on metallic structures without exception. Damage from corrosion fatigue is greater than the sum of the damage from both cyclic stresses and corrosion.

15.4 Mitigation of Magnesium Corrosion Using Stannate Conversion Coatings

15.4.1 Synthesis and testing of stannate coatings

Magnesium alloys AZ91E and AZ91D specimens were supplied by Magnesium Elektron, UK. The specimens used are in the form of 60×30×3 mm, were abraded to an 800 finish, degreased, washed with distilled water, and dried for 5 min in hot air.

The stannate coating used in this study was prepared from potassium stannate, $K_2SnO_3{\cdot}3H_2O$ + 10 g/l NaOH for 30 min at pH 12.9. The coated samples were tested in 3.5 wt.% NaCl solution. The solutions were prepared from laboratory grade chemicals and nanopure distilled water. A series of samples were prepared under different conditions prior to applying stannate coating treatment. The samples were subjected to different kinds of surface modifications. Each condition is specified under its related figure.

Several electrochemical techniques such as hydrogen evolution and potentiodynamic and salt spray chamber tests, have been used for evaluating the performance of the stannate coatings over magnesium substrate. Hydrogen evolution method (Figure 15.12) was used to determine the hydrogen evolution rate of stannate-coated AZ91D and AZ91E alloys in NaCl. The calculation of hydrogen evolved due to the reaction of a metal of high corrosion susceptibility such as magnesium immersed in a corrosive solution (such as chloride) is proven to be an accurate technique for evaluating the corrosion resistance of Mg and its alloys. The reaction can be expressed as follows:

$$Mg + 2H_2O \rightarrow Mg(OH)_2 + H_2 \tag{15.1}$$

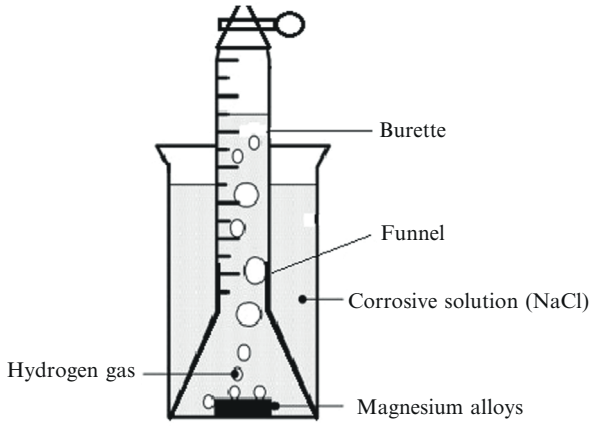


Figure 15.12 Experimental setup for measuring the hydrogen evolution rates.

The basic principle of hydrogen evolution technique can be understood from the electrochemical Equation (15.1), where the dissolution of one Mg atom generates one H_2 gas molecule. In other words, the evolution of 1 mole of H_2 gas corresponds to the dissolution of 1 mole of Mg. Therefore, measuring the volume of H_2 evolved is equivalent to measuring the weight loss of Mg dissolved, and the measured H_2 evolution rate is equal to the weight-loss rate. Interestingly, the anodic reaction is the dissolution of Mg and the cathodic reaction is the H_2 evolution, and there is no contribution of oxygen reduction to the cathodic process which is one of the main advantages for this technique.

The evolved hydrogen gas due to the chemical reaction of AZ91D and AZ91E magnesium alloys specimens with the electrolyte 3.5 wt.% NaCl solution was collected by a funnel just above the specimen and then went into a burette and gradually displaced the test solution in the burette. In this way, the kinetics of the evolved hydrogen gas can be determined by reading the height of the test solution level in the burette.

The durability of the stannate coating systems was measured according to ASTM B117 test[29] in which the corrosion resistance of coated and uncoated materials can be evaluated through exposure to a continuous indirect spray of a neutral (pH 6.5-7.2) salt water solution at an elevated temperature.

Cyclic voltammetry measurements of specimens previously immersed for 7 days in 3.5 wt.% NaCl solution were accomplished at a scan rate of 0.07 mV/s using an Autolab PGSTAT 30 galvanostat/potentiostat, Metrohm.

SEM and EDS were used to examine the microstructure of the coated samples before and after the immersion in NaCl solution. SEM images of the samples that were immersed in 3.5 wt.% NaCl for 7 days, washed with nanopure deionized water, and then dried, were obtained using a digital scanning electron microscope Model JEOL JSM 5410, Oxford Instruments, Japan. Microprobe analysis was performed using energy dispersive spectrometry, EDS, Model 6587, Pentafet Link, Oxford microanalysis group, UK.

Corrosion morphology was examined with a metallographic microscope (LEICA DMR) with a Quips programming window, LEICA Imaging Systems Ltd., Cambridge, UK, to investigate the types of corrosion produced on the substrate surfaces before and after immersion in 3.5 wt.% NaCl solution.

15.4.2 The performance of stannate-based coatings

Surface examination of as-abraded and stannate-coated samples was performed using optical microscope, visual inspection, and SEM-EDS (Figures 15.13–15.17). Generally, the stannate-coated samples showed better resistance to localized corrosion (pitting, crevice, filiform, etc.) after 7 days of immersion in NaCl solution compared to the as-abraded sample that showed severe corrosion. Interestingly, stannate-coated samples, under particular conditions, showed self-healing characteristics (see Figures 15.15 and 15.16). The pitting density of as-abraded AZ91E

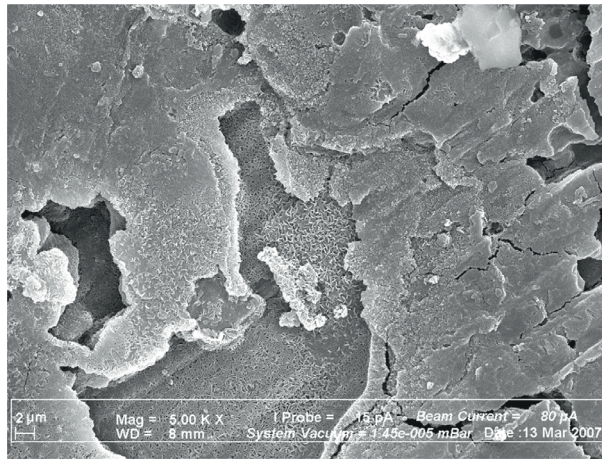


Figure 15.13 SEM of as-abraded AZ91E samples (without stannate coating) after 1 week of immersion in 3.5 wt.% NaCl solution. The image shows severe localized corrosion.

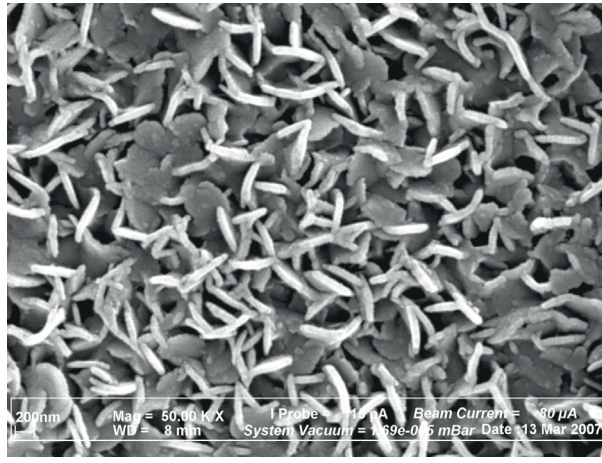


Figure 15.14 SEM of AZ91E samples that were subjected to acidic pickling surface modification followed by stannate coating treatment after 1 week of immersion in 3.5 wt.% NaCl solution. The image shows the formation of porous nonprotective coatings.

samples was 12 pit/cm^2 and decreased to be 5 pit/cm^2 for the samples that were directly treated with stannate without any surface modification. This observation points to the important role of stannate coatings over magnesium substrate that acts as a barrier for diffusion of aggressive ions and oxygen, besides their ability to reject the chloride ions from the surface by forming a uniformly distributed magnesium (hydro)oxide layer enriched with tin oxide (Figures 15.13 and 15.16).

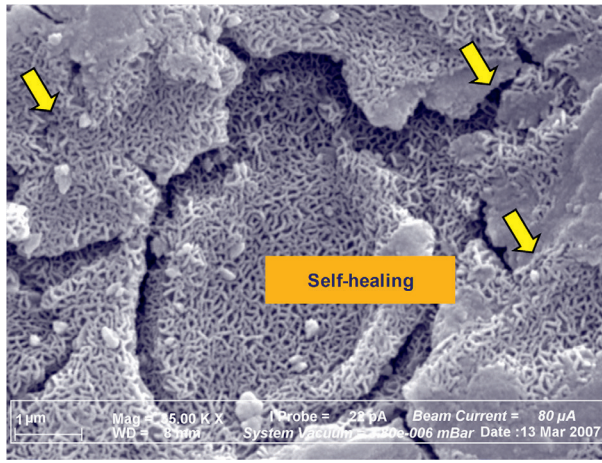


Figure 15.15 SEM of AZ91E samples that were subjected to alkaline etching surface modification followed by stannate coating treatment after 1 week of immersion in 3.5 wt.% NaCl solution. The image shows the formation of imperfect protective coatings with a limited self-healing ability to repair the defected areas.

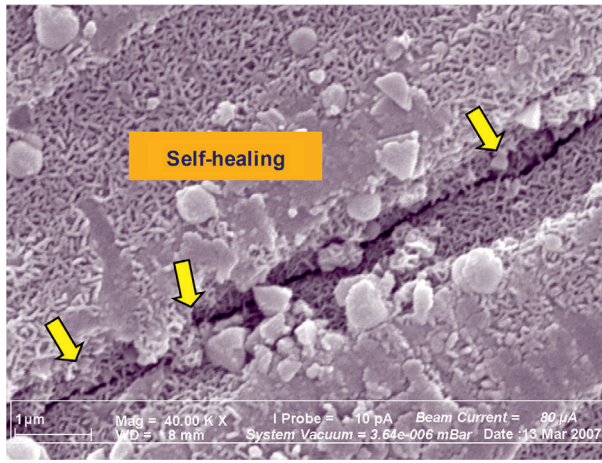


Figure 15.16 SEM of AZ91E samples that were directly treated in stannate coating treatment (without any surface modification) after 1 week of immersion in 3.5 wt.% NaCl solution. The image shows the formation of compact protective coatings of self-healing ability to repair the defected areas.

Table 15.1 shows the average amount of hydrogen evolution collected per hour for the as-abraded and stannate-coated AZ91E and AZ91D alloys over 270 h of immersion in a 3.5 wt.% NaCl solution. It was evidenced that the rate of hydrogen evolution increased as a function of time. The amount of hydrogen gas collected from the as-abraded AZ91E and AZ91D samples after 270 h of immersion in NaCl is comparable

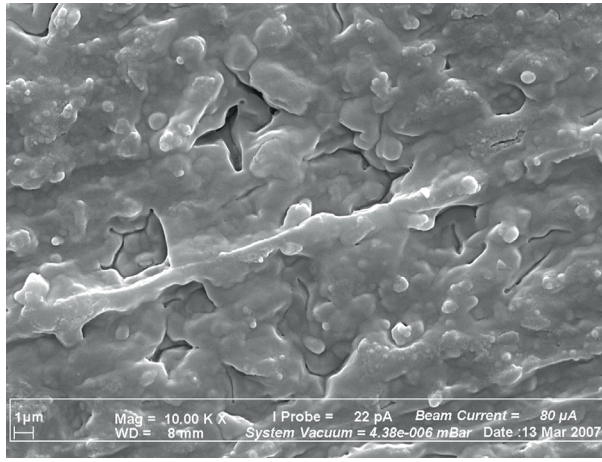


Figure 15.17 SEM of AZ91E samples that were subjected to surface modification using alkaline etching followed by acidic pickling followed by stannate coating treatment after 1 week of immersion in 3.5 wt.% NaCl solution. The image shows the formation of compact protective coatings.

TABLE 15.1 The Average Amount of Hydrogen Evolution Collected per Hour for the As-Abraded and Stannate Coated AZ91E and AZ91D Alloys over 270 h of Immersion in NaCl Solution

Sample	Amount of H_2 Evolution ml/h
AZ91D	0.013440
AZ91E	0.013985
AZ91D+stannate	0.005040
AZ91E+stannate	0.007051

to each other. The measured amount of hydrogen gas collected after stannate coatings was less than half of those measured for as-abraded samples. AZ91D showed a better corrosion resistance than AZ91E. The results indicate that stannate conversion coatings play a crucial role in the corrosion protection process of Mg substrate by forming a tin oxide-rich magnesium hydroxide layer that acts as a barrier for oxygen diffusion in metal surface, and hence, improves the corrosion resistance.[8,14–17]

The corrosion rates of as-abraded and stannate-coated AZ91E and AZ91D were measured by a salt spray chamber test according to standard ASTM B117.[29] The corrosion rate of as-abraded AZ91E was measured to be 296 µm/year, which is higher than that measured for AZ91D (254 µm/year) and confirms that the corrosion resistance of AZ91D is higher than AZ91E, as shown in Table 15.2. It was confirmed that stannate coating improves the corrosion resistances of both alloys. The measured

TABLE 15.2 The Corrosion Rates of the As-Abraded and Stannate-Coated AZ91E and AZ91D Alloys Measured According ASTM B117[29]

Sample	Corrosion Rate (μm/year)
AZ91D	254
AZ91E	296
AZ91D+stannate	160
AZ91E+stannate	184

corrosion rates of stannate-coated AZ91E and AZ91D samples (directly coated with stannate without any surface modification) are 184 and 160 μm/year, respectively. Such finding confirms the positive effect of stannate coatings in improving the corrosion protection of magnesium alloys.[8,14–17]

Localized corrosion is the most dangerous corrosion phenomenon in degradation of materials intended for long-term use in industry. Pitting is of particular concern because it may lead to premature breaching of the materials through electrochemical dissolution processes that can accelerate with time. Cyclic voltammetry technique was used to compare between the pitting corrosion resistance of as-abraded AZ91E and AZ91D after 7 days of immersion in a 3.5 wt.% NaCl solution. Cyclic voltammetry (Figure 15.18) showed a shift of about 200 μA in the cathodic current in the passive direction for AZ91E samples compared with the AZ91D specimens. However, the corrosion potential, E_{Corr}, and the pitting potential, E_{pit}, of the AZ91D

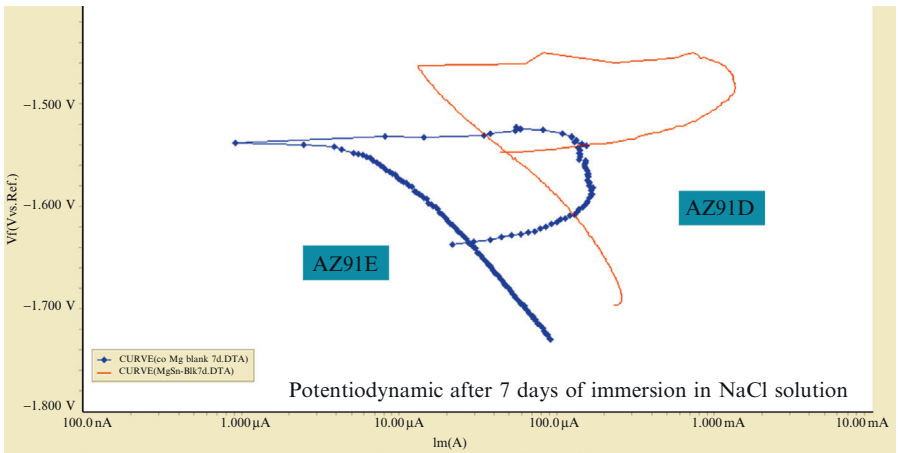


Figure 15.18 Potentiodynamic of AZ91D and AZ91E after 7 days of immersion in 3.5% NaCl solution.

samples were 80 mV nobler than AZ91E samples. These results are in agreement with the data obtained from the hydrogen gas collection, salt spray chamber test, visual inspection, and macro- and microscopic examinations.

15.4.3 Self-healing functionality of stannate coatings

Self-healing action can be defined as the ability of the coatings to repair any possible surface defects/damages that can occur at the coated substrates due to mechanical wear or chemical attack.[14] The healing process usually takes place through a chemical reaction between the coating materials and the surrounding environments to form chemical products (mainly oxides) that block the defected/damaged areas from further attack. The author's previous work on stannate coatings[8,14–17] showed that corrosion resistances of stannate-coated magnesium samples increase with increasing the immersion time in corrosive solution. This finding contradicts the known fact that corrosion resistance of a metal or alloy is decreased when immersed in a corrosive solution over a range of time. Such behavior was attributed to the conversion of the tin-oxide film formation from a less protective form (II) to a more stable tin-oxide form (VI).

The chemistry behind the self-healing functionality due to stannate coatings lies in changing the oxidation states of tin from (II) to (VI) oxide. According to the periodic table, tin, as a member of Group 4 elements, has increasing tendency to form compounds of a +2 oxidation state. Tin(IV) is a more stable oxidation state, which means that tin(II) compounds have a strong tendency to convert into tin(IV). This explains that Sn^{2+} ions in solution are good reducing agents.

Surprisingly, the author's previous work on stannate coatings for magnesium alloys showed that the self-healing functionality is linked to the type of magnesium alloys. In other words, the chemical composition of the magnesium alloy seems to have a direct influence on the ability of stannate coatings to practice the self-healing capability. For example, stannate coatings over AZ91D showed a perfect self-healing functionality.[14,16,17]. Conversely, stannate coatings lose their self-healing characteristics over rare-earth containing magnesium alloy such as EV31A-T6.[15] The reason for such an unexpected behavior is still not clear. However, it appears that the presence of certain alloying elements (such as rare-earth elements) might have an adverse catalytic effect on the conversion of tin(II) compounds to tin(IV), which is essential for self-healing ability.

15.5 Conclusion and Future Remarks

Stannate conversion coatings have been engineered as a promising chrome-free alternative for the corrosion protection of magnesium alloys. The stannate coatings approach is based on a simple free immersion in a diluted stannate solution to form a stannate chemical conversion coating over an Mg surface. Stannate conversion coatings act as

a barrier for corrosive ions and oxygen. Such coating decreases the corrosion rates of magnesium alloys and displays noticeble self-healing characteristics. The self-healing functionality due to stannate coatings, however, depends on the type of magnesium alloys. The chemical composition of the magnesium alloy seems to have a direct influence on the ability of stannate coatings to show the self-healing capability. Surface modification prior to stannate coating seems to have an improper effect on the corrosion protection of magnesium alloys. The best protection was obtained from the samples that were directly treated in stannate without any surface modification. The optimum conditions for stannate coatings that can offer a pitting auto-repair functionality to magnesium substrate in chloride solution have been determined. Future work should be directed toward designing a complete coating system based on stannate. A top coating such as epoxy, polyurethane, flouroploymer, or polyaniline might be a candid choice.

Acknowledgments

The authors wish to thank Dr. David Tawil, Magnesium Elektron, for providing the magnesium specimens.

References

1. Perrault GG. Magnesium. In: Bard AJ, editor. Encyclopedia of electrochemistry of the elements, vol. VIII. NY: Marcel Dekker; 1978. p. 262–318 Chapter, VIII-4.
2. Hamdy AS. Enhancing corrosion resistance of magnesium alloy AZ91D in 3.5% NaCl solution by cerate conversion coatings. J Anti-Corros Meth Mater 2006;53(6):367–73.
3. Hamdy AS. Alkaline based surface modification prior to ceramic based cerate conversion coatings for magnesium AZ91D. J Electrochem Solid State Lett 2007;10(3):C21–5.
4. Hamdy AS. A novel approach in designing chrome-free chemical conversion coatings for automotive and aerospace materials. Eur Coating J 2008;86(3):43–50.
5. Hamdy AS, Farahat M. Chrome-free zirconia-based protective coatings for magnesium alloys. J Surf Coat Technol 2010;204(16):2834–40.
6. Hamdy AS, Doench I, Möhwald H. Assessment of a one-step intelligent self-healing vanadia protective coatings for magnesium alloys in corrosive media. J Electrochim Acta 2011;56(5):2493–502.
7. Hamdy AS, Doench I, Möhwald H. Smart self-healing anti-corrosion vanadia coating for magnesium alloys. Prog Org Coat 2011;72(3):387–93.
8. Hamdy AS. Casting out chromium: nontoxic pre-treatments protect magnesium and aluminium alloys. Eur Coating J 2012;3(3):16–20.
9. Hamdy AS, Doench I, Möhwald H. Vanadia-based coatings of self-repairing functionality for advanced magnesium Elektron ZE41 Mg–Zn-rare earth alloy. Surf Coat Tech 2012;206(17):3686–92.
10. Hamdy AS, Doench I, Möhwald H. The effect of vanadia surface treatment on the corrosion inhibition characteristics of advanced magnesium Elektron 21 alloy in chloride media. Int J Electrochem Sci 2012;7(9):7751–61.

11. Hamdy AS, Hussien H. Deposition, characterization and electrochemical properties of permanganate-based coating treatments over ZE41 Mg-Zn-rare earth alloy. Int J Electrochem Sci 2013;8(8):11386–402.
12. Hamdy AS, Hussien H. "The effect of solution pH of permanganate coating on the electrochemical characteristics of ZE41 magnesium alloy in chloride media". Int'l J. Electrochemical Sci 2014;9:2682–2695.
13. Hamdy AS, Doench I, Möhwald H. "Intelligent self-healing corrosion resistant vanadia coating of flower-like morphology for AA2024 and novel magnesium alloys", Proceedings of 38th Int'l Conference on Metallurgical Coatings and Thin Films, 2-6 May 2011, San Diego, USA.
14. Hamdy Makhlouf AS, editor. Handbook of smart coatings for materials protection. Cambridge, UK: Woodhead Publishing Limited; 2014; 9780857096807, 656 pages.
15. Hamdy AS, Butt D. Corrosion mitigation of rare-earth containing magnesium EV31A-T6 alloy via chrome-free conversion coating treatment. J Electrochim Acta 2013;108(10):852–9.
16. Hamdy AS, Butt D. Novel smart stannate based coatings of self-healing functionality for AZ91D magnesium alloy. J Electrochim Acta 2013;97(5):296–303.
17. Hamdy AS. Effect of surface modification and stannate concentration on the corrosion protection performance of magnesium alloys. J Surf Coat Technol 2008;203(3):240–9.
18. Song G, Atrens A. Corrosion mechanisms of magnesium alloys. Adv Eng Mater 1999;1:11–33.
19. Rong-chang Z, Wangqiu Z, En-hou H, et al. Effect of pH value on corrosion of as-extruded AM60 magnesium alloy. Acta Metall Sin 2005;44(3):307–11 (in Chinese).
20. Maker GL, Kruger J. Corrosion of magnesium. Int Mater Rev 1993;38(3):138–53.
21. Ghali E, Dietzel W, Kainer KU. General and localized corrosion of magnesium alloys: a critical review. J Mater Eng Perform 2004;13(1):7–23.
22. Lunder O, Lein JE, Hesjevik SM, et al. Corrosion morphologies on magnesium alloy A291. J Werkstoffe und Korrosion 1994;45(2):331–40.
23. Dexter SC. Metals handbook (vol. 13). 9th ed. Ohio: ASM International; 1987, p. 106.
24. Miller WK. Stress-corrosion cracking. Ohio: ASM; 1993, p. 251.
25. Wmzer N, Atrens A, Song C, et al. A critical review of the stress corrosion cracking (SCC) of magnesium alloys. J Adv Eng Mater 2005;7(8):659–93.
26. Song R, Blawert C, Dietzel W, et al. A study on stress corrosion cracking and hydrogen embrittlement of AZ31 magnesium alloy. J Mater Sci Eng A 2005;A399:308–17.
27. Zhen-song T, Wei Z, Jiu-qing L, et al. Initial laws of atmospheric galvanic corrosion for magnesium alloys. Chin J Nonferr Metals 2004;14(4):554–61 (in Chinese).
28. Valente T. Grain boundary effects on the behavior of WE43 magnesium castings in simulated marine environment. J Mater Sci Lett 2001;20(1):67–9.
29. ASTM B117. Standard practice for operating salt spray (fog) apparatus. Conshohocken, PA: ASTM International; 1997.

Chapter 16

Electroactive Polymer-Based Anticorrosive Coatings

Kung-Chin Chang, Jui-Ming Yeh
Department of Chemistry, Center for Nanotechnology and Biomedical Technology at Chung-Yuan Christian University (CYCU), Chung Li, Taiwan, ROC

16.1 Introduction

Traditionally, polymeric materials have been used as insulators. However, in the early 1960s, Pohl and Katon et al. synthesized and characterized some conjugated polymers with conductivities in the semiconductor range.[1,2] Until 1977, the first polymer shown to conduct electricity was iodine-doped poly(acetylene). This discovery was published by Hideki Shirakawa et al. As a result of this pioneering work,[3,4] they received the 2000 Nobel Prize in Chemistry. The development of this new class of polymeric materials continues to offer the promise of a wide range of novel applications, including molecular electronics, actuators, electrochromic windows/displays, supercapacitors, transistors, photovoltaics, and corrosion protection. This discovery opened up new areas of research, with many commercial products now incorporating polymers as electrical conductors.

Intelligent Coatings for Corrosion Control
Copyright © 2015 Elsevier Inc. All rights reserved.

For application of the conducting polymer to corrosion protection, DeBerry in 1985 was first to report that stainless steel covered by polyaniline (PANI) remained in the passive state for a relatively long period in sulfuric acid solution.[5] Wessling then pointed out that the conducting polymer coating of PANI and polypyrrole (PPy) possibly possessed self-healing properties, in which the passive oxide between the substrate metal and the conducting polymer could be spontaneously reformed at a flawed site by oxidative capability of the conducting polymer.[6]

Electroactive polymers (EAPs) are composed of conjugated chains containing π-electrons delocalized along the polymer backbone. They are a new class of materials that received recent attention from academia and industry due to their potential for applications such as biosensors, artificial muscles, actuators, corrosion protection, electronic shield shielding, environmentally sensitive membranes, visual displays, solar materials, and components in high-energy batteries.

In this chapter, we present the EAP-based materials composed of conjugated oligoaniline into the polymer backbones (including EAP, electroactive polymer nanocomposites (EAPNs), and electroactive polymer with hydrophobic/superhydrophobic surfaces (HEAPs/SEAPs)) as model coatings to demonstrate the advanced anticorrosive properties by performing a series of electrochemical corrosion measurements.

16.2 Corrosion

Corrosion is the deterioration of materials by chemical interaction with their surrounding environment. The consequences of corrosion are many and varied and the effects of these on the safe, reliable, and efficient operation of equipment or structures are often more serious than simple loss of a mass of a metal. Failures of various kinds and the need for expensive replacements may occur even though the amount of metal destroyed is quite small. Some of the disastrous effects of corrosion can be summarized below:

(1) Hazards or injuries to people arising from structural failure or breakdown (e.g., bridges, cars, aircrafts)
(2) Reduced value of goods due to deterioration of appearance
(3) Contamination of fluids in vessels and pipes (for instance, beer goes cloudy when small quantities of heavy metals are released by corrosion)
(4) Loss of technically important surface properties of a metallic component. These could include frictional and bearing properties, ease of fluid flow over a pipe surface, electrical conductivity of contacts, surface reflectivity, or heat transfer across a surface
(5) Perforation of vessel and pipes allowing escape of their contents and possible harm to the surroundings

(6) Loss of time availability of profile-making industrial equipment
(7) Reduction of metal thickness leading to loss of mechanical strength and structural failure or breakdown. When the metal is lost in localized zones so as to present a cracklike structure, very considerable weakening may result from quite a small amount of metal loss
(8) Added complexity and expense of equipment that needs to be designed to withstand a certain amount of corrosion and to allow corroded components to be conveniently replaced
(9) Mechanical damage to valves, pumps, and so on, or blockage of pipes by solid corrosion products

16.3 Measures of Corrosion Prevention

There are several methods of corrosion control, such as inhibitors, cathodic protection,[7] anodic protection,[8] coating[9] and alloying. The next section briefly describes a few of these methods.

16.3.1 Inhibitors

An inhibitor is a substance that, when added in small concentrations to an environment, decreases the corrosion rate. In a sense, an inhibitor can be considered as a retarding catalyst. There are numerous inhibitor types and compositions. Most inhibitors have been developed by empirical experimentation, and many inhibitors are proprietary in nature and thus their composition is not disclosed. Inhibition is not completely understood because of these reasons, but it is possible to classify inhibitors according to their mechanism and composition.[10,11] Figure 16.1 is the schematic diagram of adsorption inhibitors. Adsorption inhibitors form a chemisorptive bond with the metal surface and impede ongoing electrochemical dissolution reactions.[12]

16.3.2 Cathodic protection

Cathodic protection was employed before electrochemistry had been developed. Humphrey Davy used cathodic protection on British naval ships in 1824. The principles of cathodic protection may be explained by considering the corrosion of a typical metal in an acid environment. Electrochemical reactions occurring are the dissolution of the metal and the evolution of hydrogen gas:

$$M \rightarrow M^{n+} + ne$$

$$2H^{+} + 2e \rightarrow H_2$$

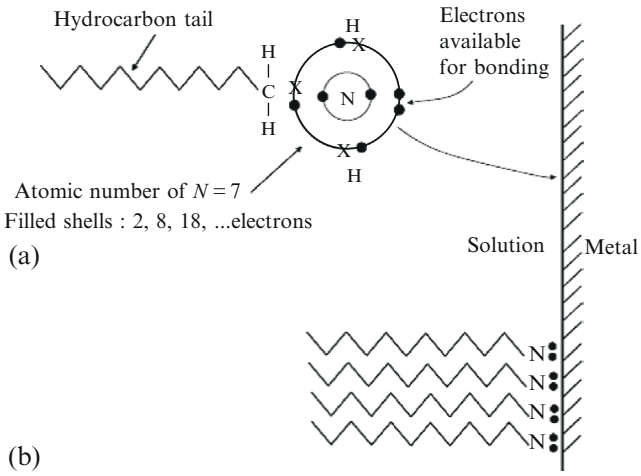


Figure 16.1 (a) Chemisorption of amines at a metal surface. The solid black dots denote electrons belonging to the N atom, whereas the Xs refer to electrons from H or C atoms. (The size of the nitrogen atom is exaggerated relative to the rest of the molecule.) (b) Formation of a close-packed monolayer on the metal surface.[12]

16.3.3 Anodic protection

In contrast to cathodic protection, anodic protection is relatively new; it was first suggested by Edeleanu in 1954. This technique was developed using electrode kinetics principles and is somewhat difficult to describe without introducing advanced concepts of electrochemical theory. Simply, anodic protection is based on the formation of a protective film on metals by externally applied anodic currents.[13]

16.3.4 Coatings

16.3.4.1 Metallic and other inorganic coatings

Relatively thin coatings of metallic and inorganic materials can provide a satisfactory barrier between metal and its environment. The chief function of such coating (aside from sacrificial coatings such as zinc) is to provide an effective barrier. Metal coatings are applied by electrodeposition, flame spraying, cladding hot dipping, and vapor deposition. Inorganics are applied or formed by spraying, diffusion, or chemical conversion. Spraying is usually followed by baking or firing at elevated temperatures. Metal coatings usually exhibit some formability, whereas the inorganics are brittle. In both cases a complete barrier must be provided. Porosity or other defects can result in accelerated localized attack on the basic metal because of two-metal effects.[14] There are two types of metallic coatings used to protect underlying metal substrates. These are sacrificial and noble metal coatings. The first of these types,

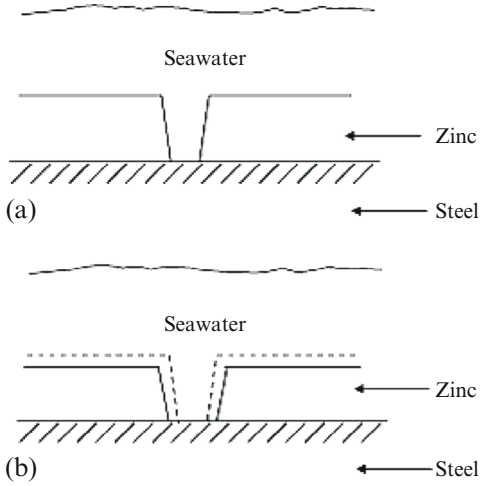


Figure 16.2 A sacrificial protective coating. When a break or an imperfection develops in the coating and extends down to the substrate, as shown in (a), the zinc coating will galvanically corrode to protect the underlying substrate, as shown in (b).[12]

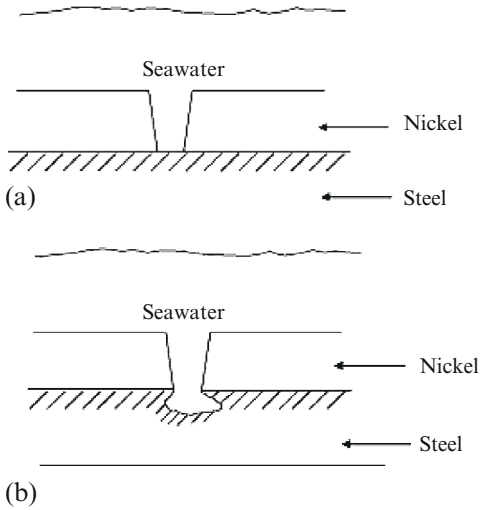


Figure 16.3 A noble metal protective coating. When a break or an imperfection develops in the nickel coating and extends down to the substrate, as shown in (a), the underlying steel substrate will galvanically corrode, as shown in (b).[12]

sacrificial coatings, functions by cathodic protection of the substrate. Figure 16.2 is the schematic diagram of sacrificial coating. The second type of metallic coating, the noble metal coating, is illustrated by a coating of nickel on steel. Figure 16.3 is the schematic diagram of noble metal coating.[12]

16.3.4.2 Organic coatings

These involve a relatively thin barrier between substrate material and the environment. Paints, varnishes, lacquers, and similar coatings doubtless protect more metal on a tonnage basis than any other method for combating corrosion. Exterior surfaces are most familiar, but inner coatings or linings are also widely utilized. Approximately

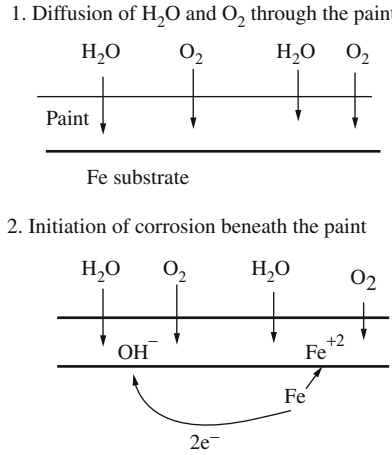


Figure 16.4 The first two steps in the deterioration of an organic coating.[16]

$2 billion per year are expended in the United States on organic coatings. A myriad of types and products are involved, and some are accompanied by outlandish claims. Substantial knowledge of this complex field is required for successful performance. The best procedure for the uninitiated is to consult with a reputable producer of organic coatings. As a general rule, these coatings should not be used where the environment would rapidly attack the substrate material.[15] Figure 16.4 is the schematic diagram of the deterioration of an organic coating. The sequence of events which occurs in the breakdown of an organic coating in the subcoating microenvironment is illustrated by the work of Ritter and Rodriguez.[16] The sequence of events is as follows[12]:

(a) The organic coating first becomes penetrated by water and oxygen molecules, as discussed above.
(b) Corrosion is initiated due to several possible causes, such as defects in the coating, mechanical rupture of the coating, or chemical rupture through generation of osmotic pressure at sites containing soluble salts.
(c) The substrate iron then goes into a solution at a local anodic site:

$$Fe \rightarrow Fe^{2+} + 2e^-$$

16.4 Polymer Coatings

Polymeric (or organic) coatings have been employed to protect metals against corrosion for a long time. The primary effect of a polymeric coating is to function as a physical barrier against aggressive species such as O^2 and H^+. However, all polymeric coatings are not permanently impenetrable, and once there are defects in the coatings, pathways will be formed for the corrosive species to attack the metallic

substrate, and localized corrosion will occur. Therefore, as a second line of defense against corrosion, various pigments with a lamellar or platelike shape such as micaceous iron oxide and aluminum flakes have been introduced into the polymeric coating to effectively increase the length of the diffusion pathways for oxygen and water, as well as to decrease the permeability of the coatings. A number of electrochemical measurements have been used as a tool to evaluate the anticorrosion performance of polymeric coatings, including electroactive (e.g., polyaniline) or nonelectroactive (e.g., polystyrene) polymers. Wei et al.[17] demonstrated the anticorrosive performance of electroactive polyaniline and nonelectroactive polystyrene by performing a series of electrochemical measurements of corrosion potential and corrosion current on the sample-coated cold-rolled steel (CRS) electrode under various conditions. Lee and coworkers[18] investigated the corrosion-resistance properties of PANI-coated mild steel in saline and acid by electrochemical impedance spectroscopy (EIS).

Recently, EAPs, EAPNs, and HEAPs/SEAPs used as enhanced anticorrosion coatings have been reported by Yeh et al.[19–30] For example, EAPs (e.g., polyimide,[19] epoxy,[20] polyurethane,[21] polyamide,[22] and polyurea[23]), EAPNs (e.g., polyimide-clay,[24] polyimide-TiO_2,[25] epoxy-SiO_2,[26] and polyanilie-graphene[27]), and HEAPs/SEAPs (e.g., epoxy,[28–30] PANI,[31] and polyimide[32]) for making a series of novel advanced anticorrosion coatings based on a series of electrochemical corrosion parameter measurements of corrosion potential, polarization resistance, corrosion current, and EIS at room temperature.

16.4.1 EAP-based coatings

Corrosion protection using EAPs was first suggested by MacDiarmid in 1985.[33] EAPs can be synthesized both chemically and electrochemically. It has been observed that most EAPs can be electrochemically produced by anodic oxidation, enabling one to obtain a conducting film directly on a surface. EAPs can go from the insulating to the conducting state through several doping techniques, such as (1) chemical doping by charge transfer, (2) electrochemical doping, (3) doping by acid-base chemistry (only PANI undergoes this form of doping), (4) photodoping, and (5) charge injection at a metal-semiconducting polymer interface.[34]

Among those EAPs, PANI is a potential material for commercial applications due to its environmental stability, good processability, and relatively low cost.[35,36] However, PANI prepared by chemical and/or electrochemical means usually exhibits structural defects and has limited solubility in many solvents. These shortcomings would impede the better understanding of the structure-property correlations and the conducting mechanism and also restrict the practical applications of PANI. One possible approach to alleviate the problems is the incorporation of well-defined and conjugated oligoaniline[37,38] into the copolymer backbones, which could combine the properties of the specific oligoaniline and desirable polymer properties such as mechanical strength and film-forming ability.

In 2009 and 2012, Yeh et al.[19–21] described the first evaluations for the effect of amine-capped aniline trimer (AT) on the corrosion protection efficiency of as-prepared electroactive polyimide, epoxy, and polyurethane. First of all, the amine-capped ATs were synthesized by a one-step method from the oxidative coupling reactions of *p*-phenylenediamine with aniline in an acidic aqueous medium. Subsequently, a series of polyimides, epoxy, and polyurethane with different content of AT molecules were obtained by thermal imidization, thermal curing, and prepolymerization. The synthesis procedure of electroactive polyimide, epoxy, and polyurethane is depicted in Figures 16.5–16.8. The as-prepared electroactive polyimide, epoxy, and polyurethane were further identified by a series of electrochemical measurements, such as corrosion potential (E_{corr}), polarization resistance (R_p), corrosion current (I_{corr}), and EIS studied in 5 wt.% NaCl electrolyte.

Figures 16.8–16.10 and Table 16.1 represent the results of electrochemical measurements of potentiodynamic (e.g., Tafel plots) and EIS (e.g., Nyquist and Bode plots) of electroactive polyimide at room temperature.

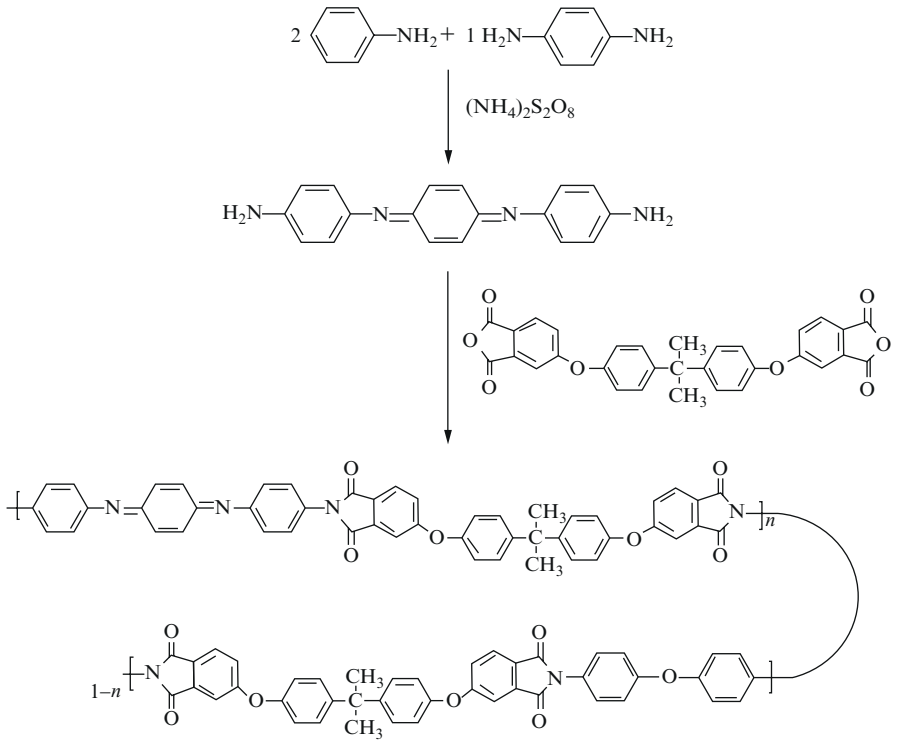


Figure 16.5 Schematic representation of the synthesis of aniline trimers and polyimides.[19]

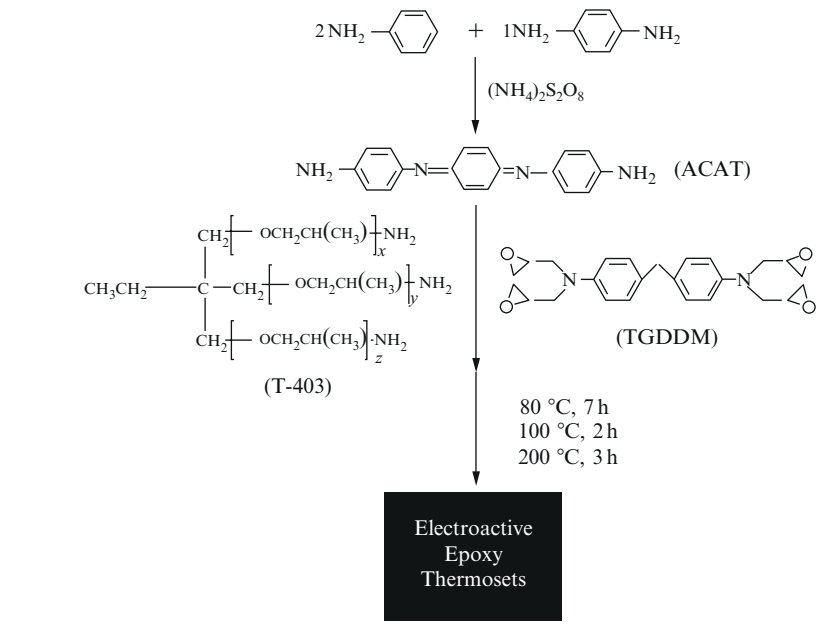


Figure 16.6 Flow chart for the synthesis of electroactive epoxy thermosets.[20]

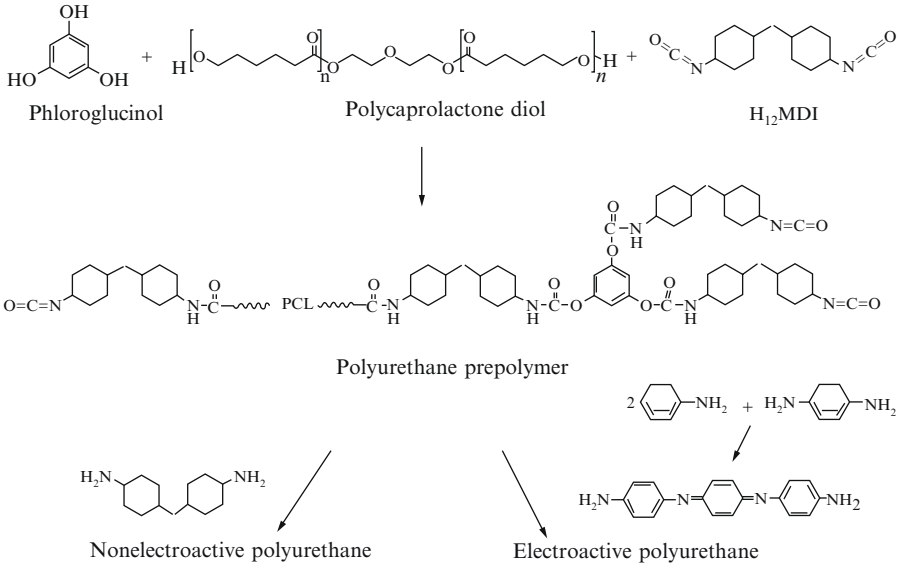


Figure 16.7 Schematic representation of the synthesis of EPU and NEPU.[21]

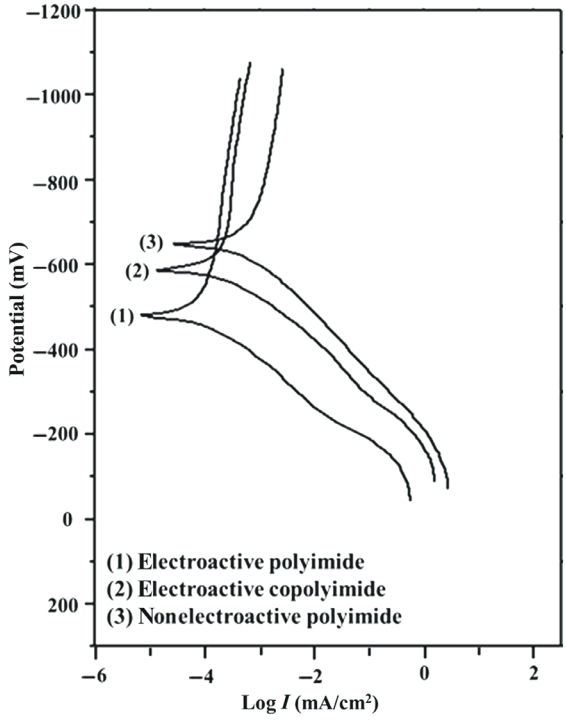


Figure 16.8 Tafel plots for (1) electroactive polyimide, (2) electroactive copolyimide, and (3) non-electroactive polyimide, measured in 5 wt.% aqueous NaCl solution.[19]

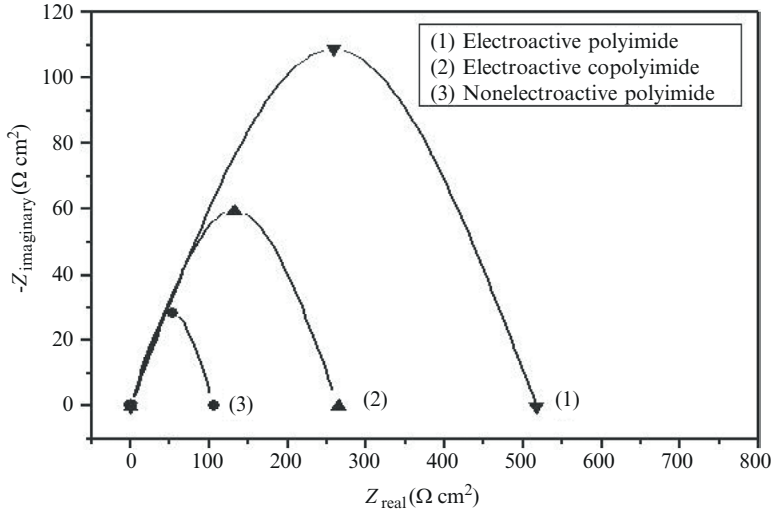


Figure 16.9 Nyquist plots for (1) electroactive polyimide, (2) electroactive copolyimide, and (3) non-electroactive polyimide-coated CRS electrode, measured in 5 wt.% aqueous NaCl solution.[19]

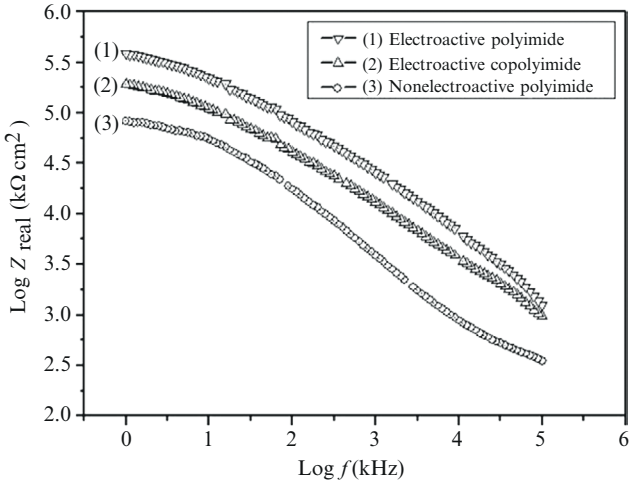


Figure 16.10 Bode plots for (1) electroactive polyimide, (2) electroactive copolyimide, and (3) non-electroactive polyimide-coated CRS electrode, measured in 5 wt.% aqueous NaCl solution.[19]

The as-prepared polyimide with higher content of ATs exhibited obviously enhanced corrosion protection efficiency on CRS electrodes. The significant enhancement of corrosion protection on CRS electrodes probably is attributed to the redox catalytic property of electroactive aniline trimer in the formation of a passive layer of metal oxide, which was investigated by SEM and ESCA and is shown in Figures 16.11 and 16.12. The iron oxide of the CRS surfaces were studied and found to have a thin layer containing Fe_2O_3 and Fe_3O_4. The passivation mechanism of electroactive polyimide on the CRS surface is similar to that of PANI. The ATs show the excellent corrosion inhibition and act as a redox catalyst to increase the corrosion protecting ability.

16.4.2 EAP-based nanocomposite coatings

In the past 20 years, polymer nanocomposites used as enhanced anticorrosion coatings have been reported by Yeh et al.,[39–47] for example, polymer-clay nanocomposites[39–45] and polymer-silica/titanium nanocomposites[46,47] through different preparative routes such as in situ polymerization or a solution dispersion approach for making a series of advanced anticorrosion coatings based on a series of electrochemical corrosion parameter measurements at room temperature. Enhanced corrosion protection effect of polymer nanocomposites compared to bulk polymer might be a result from dispersing silicate nanolayers of clay and silica/titanium nanoparticles in polymer matrix to increase the tortousity of diffusion pathway of oxygen gas.[48,49]

Currently, the research interests on developing EAPNs as anticorrosion coatings, and polymers with different types of inorganic fillers, were employed and listed as follows:

TABLE 16.1 Feed composition ratio of electroactive polyimide, electroactive copolyimide, and non-electroactive polyimide with the E_{corr}, R_p, I_{corr}, and R_{corr} measured with electrochemical method.[19]

	Feed Composition (M)								
	Diamine		Dianhydride	Electrochemical Corrosion Measurements					
Compound Code	ODA	ATs	BSAA	E_{corr} (mV)	R_p (kΩ cm^2)	I_{corr} (μA/cm^2)	R_{corr} (MPY)	Thickness (μm)	P_{EF} (%)
Bare[a]	-	-	-	–720	0.018	18.900	8.820	-	
Electroactive polyimide	0	1	1	–486.5	0.560	0.103	0.048	22	30.0
Electroactive copolyimide	0.5	0.5	1	–592.2	0.246	0.400	0.187	20	12.6
Nonelectroactive polyimide	1	0	1	–647.8	0.074	0.700	0.327	19	3.1

[a]Pristine CRS used for test.

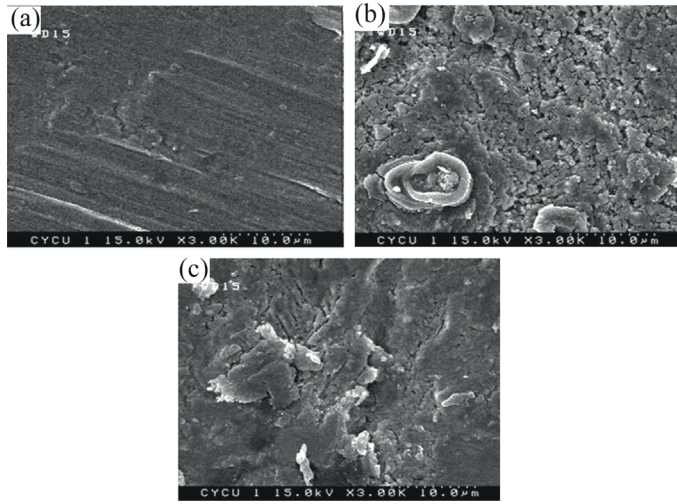


Figure 16.11 SEM image for (a) polished, (b) electroactive copolyimide-coated, (c) electroactive polyimide-coated CRS surface.[19]

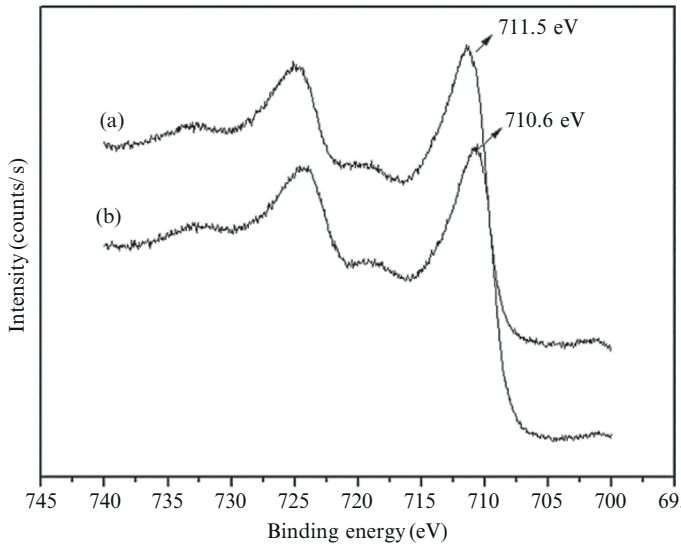


Figure 16.12 ESCA Fe 2p core level spectra of (a) electroactive copolyimide, (b) electroactive polyimide.[19]

16.4.2.1 EAP/silicate nanolayer (clay) nanocomposites

Yeh et al. investigated the effect of organophilic-MMT clay on the anticorrosive properties of EAPNs (e.g., polyimide-clay[24]). The electroactive PI-clay (EAC) nanocomposite materials were prepared by performing the chemical imidization

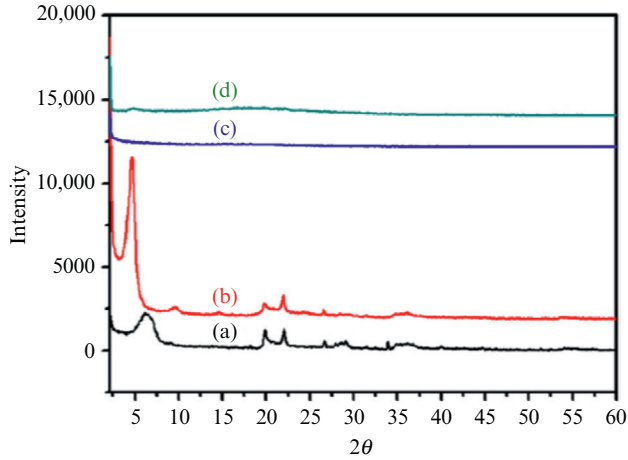


Figure 16.13 Wide-angle power X-ray diffraction patterns of (a) MMT, (b) organophilic-MMT clay, (c) EPC01, (d) EPC03 nanocomposite material.[24]

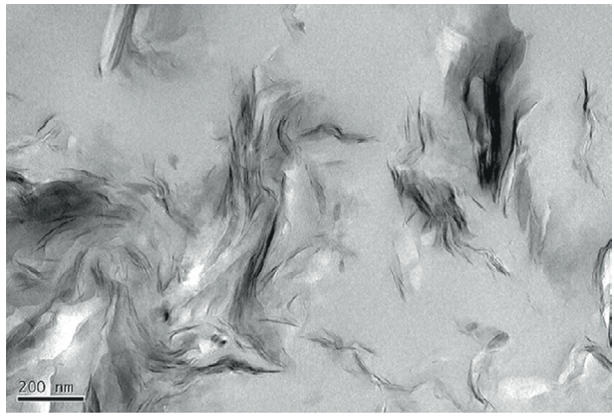


Figure 16.14 TEM micrographs of (a) EPC01 × 20 K (b) EPC03 × 20 K.[24]

of EPI in the presence of organophilic clay platelets. Dispersion capability of organophilic clay in EPI matrix was further identified by wide-angle powder X-ray diffraction (WAXRD; Figure 16.13) pattern and transmission electron microscopy (TEM; Figure 16.14). To study the effect of organophilic clay on the anticorrosive properties of EAC nanocomposite coatings, a series of electrochemical (e.g., corrosion potential, polarization resistance, corrosion current, corrosion rate, and protection efficiency) measurements were studied; the results are shown in Figure 16.15 and Table 16.2. The as-prepared EAC nanocomposite coatings were found to exhibit advanced corrosion protection efficiency as compared to that of NEPI, EPI, and bare CRS electrodes based on the sequential electrochemical

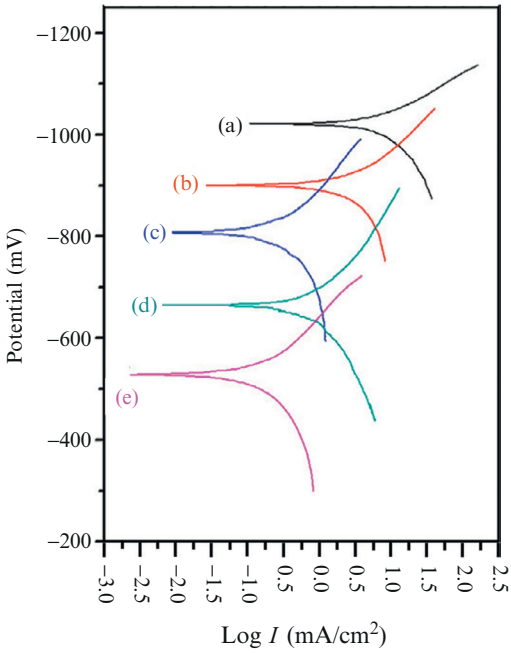


Figure 16.15 Tafel plots for (a) Bare (b) NEPI (c) EPI (d) EPC01 (e) EPC03 measured in 5 wt.% aqueous NaCl solution.[24]

corrosion measurements in saline condition. The significant enhancement in corrosion protection of EACN coatings on CRS electrodes might probably be attributed to the redox catalytic property of organic EPI inducing the formation of a passive metal oxide layer and to the fact that the barrier property of well-dispersed organophilic clay platelets existed in EPI matrix, as evidenced by the investigations by the SEM/ESCA and GPA studies, respectively. The analytical results of SEM and ESCA were similar to Figures 16.11 and 16.12, and the results of gas barrier properties are shown in Figure 16.16.

16.4.2.2 EAP/nanoparticle (TiO_2, SiO_2) nanocomposites

Yeh et al. described the anticorrosive properties of a series of EAP-TiO_2/SiO_2 nanocomposites (e.g., polyimide-TiO_2[25] and epoxy-SiO_2[26]). The electroactive PI-TiO_2 (EPT) nanocomposite materials were prepared by performing the chemical imidization. The dispersion capability of TiO_2 nanoparticles in EPI matrix was further observed by TEM studies (Figure 16.17). It should be noted that the EPT even adding 10% content of TiO_2 still revealed a redox current as compared to that of EPI. According to electrochemical measurement, EPT exhibited a good anticorrosion property; the results are shown in Figures 16.18–16.20 and Table 16.3. The mechanism of anticorrosion property for EPT could be attributed the a synergistic effect of formation of passive metal oxide layers induced from redox catalytic capabilities of ACAT units, and a gas barrier property induced from well-dispersed TiO_2 nanoparticles in its matrix. The analytical

TABLE 16.2 Feed composition ratio and electrochemical corrosion measurements of the prepared materials.[24]

	Feed Composition (g)				Electrochemical Corrosion Measurements					
Sample Code	ODA	ACAT	BSAA	Organophilic clay	E_{corr} (mV)	R_p (kΩ cm^2)	I_{corr} (μA/cm)^2	R_{corr} (mm/year)	Thickness (μm)	P_{EF} (%)
Bare[a]	-	-	-	-	−1020.9	2.47	9.14	1.07×10^{-1}	-	-
NEPI	0.1	-	0.26	-	−900.2	5.09	4.02	4.71×10^{-2}	25	1.06
EPI	-	0.145	0.26	-	−807.7	17.30	2.53	2.96×10^{-2}	25	6.00
EPC01	-	0.145	0.26	0.004	−664.9	36.67	1.89	2.21×10^{-2}	24	13.85
EPC03	-	0.145	0.26	0.012	−528.5	69.99	1.09	1.28×10^{-2}	27	27.34

[a]Pristine CRS used for test.

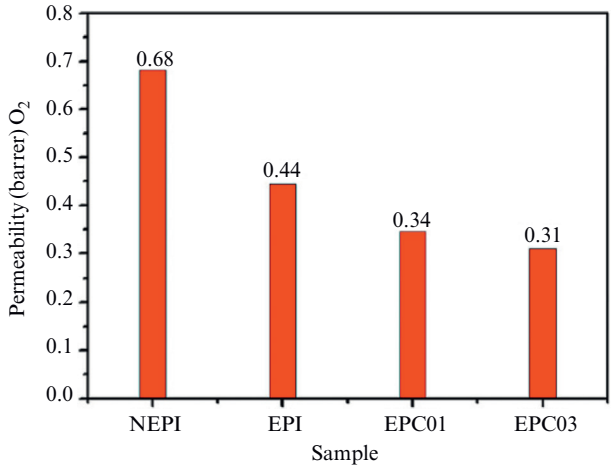


Figure 16.16 Permeability of O_2 as a function of clay content in EPC nanocomposite materials.[24]

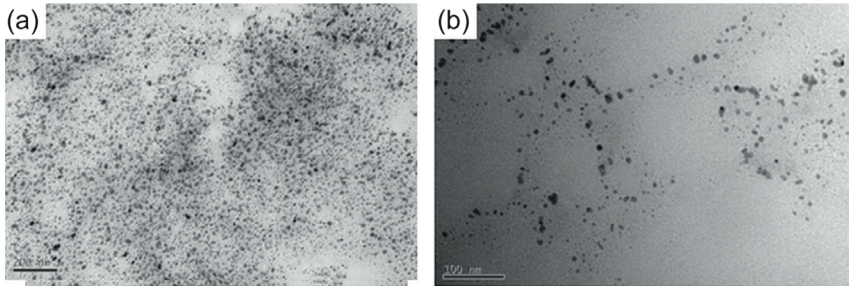


Figure 16.17 TEM images of EPT10 (a) × 20 K (b) × 50 K.[25]

results of passive metal oxide layers were similar to Figure 16.11, and the results of gas barrier properties were shown in Figure 16.21. The synergistic effects cause the EPT coatings to reveal advanced corrosion protection efficiency as compared to that of NEPI, EPI, and bare CRS electrodes based on the sequential electrochemical corrosion measurements in saline condition.

16.4.2.3 EAP/graphene nanocomposites

Yeh et al. reported the anticorrosive properties of EAP-graphene nanocomposites (e.g., polyaniline-graphene[27]). The polyaniline/graphene composites (PAGCs) were prepared by *in situ* oxidative polymerization. The as-prepared PAGCs were subsequently characterized by TEM (Figure 16.22). From the results of electrochemical measurements, gas permeability, and vapor permeability rates (Figures 16.23 and 16.24), the PAGCs

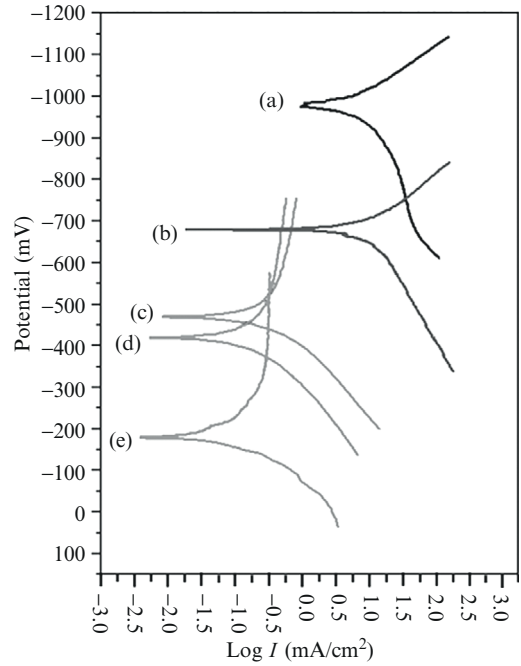


Figure 16.18 Tafel plots for (a) NEPI, (b) EPI, (c) EPT05, and (d) EPT10 measured in 5 wt.% aqueous NaCl solution.[25]

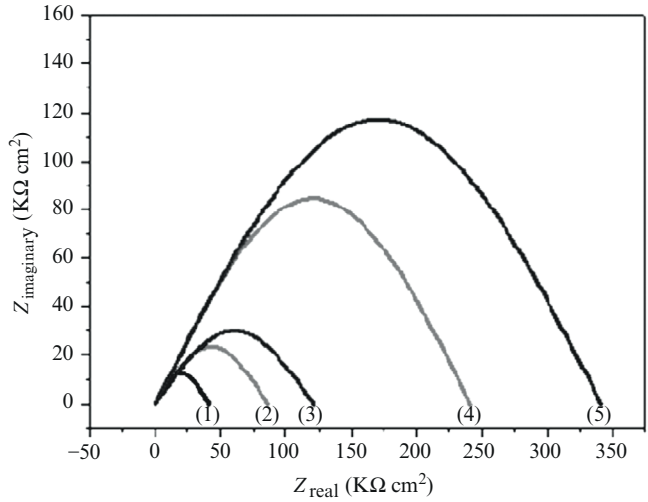


Figure 16.19 Nyquist plots for (1) neat CRS, (2) NEPI, (3) EPI, (4) EPT05 and (5) EPT10-coated CRS electrode, measured in 5 wt.% aqueous NaCl solution.[25]

coatings were shown to effectively protect steel because of the good O_2 and H_2O gas barrier. Well-dispersed graphene, with a relatively high aspect ratio compared with clay, in a polymer matrix enhances the gas barrier and is responsible for the highly desirable anticorrosion properties that make PAGCs coatings much more effective than polyaniline-clay composite (PACCs) coatings.

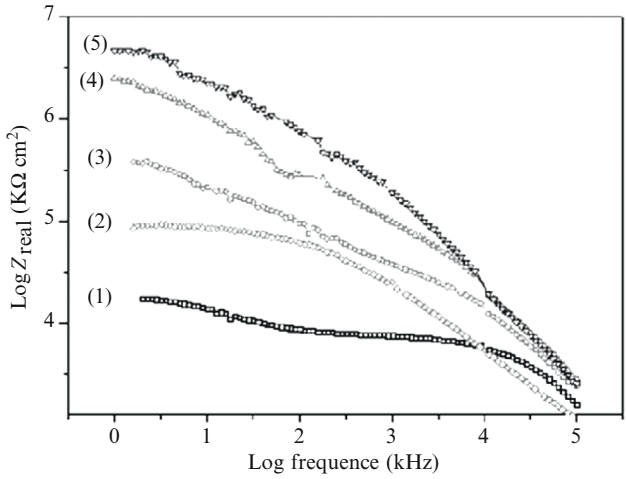


Figure 16.20 Bode plots for (1) neat CRS, (2) NEPI, (3) EPI, (4) EPT05 and (5) EPT10-coated CRS electrode, measured in 5 wt.% aqueous NaCl solution.[25]

16.4.2.4 EAP-based hydrophobic/superhydrophobic coatings

Over the past few years, the remarkable surface structures of superhydrophobic plant leaves, characterized by the so-called lotus effect, have attracted the attention of many researchers. In particular, the superhydrophobic property induced by these structures has become quite an important issue because there are a variety of practical applications utilizing their self-cleaning, drag reduction, antifogging and anticorrosion effects, and so on. However, reports on the corrosion protection studies associated with hydrophobic/superhydrophobic surfaces using EAP coatings are limited. Recently, Yeh et al. demonstrated a feasible strategy to develop advanced anticorrosion coatings by combining the crucial benefits of electroactivity and hydrophobicity/superhydrophobicity in corrosion protection.

A photograph of natural, fresh *Xanthosoma sagittifolium* leaves is shown in Figure 16.25a. Figure 16.25b is the high magnification SEM image of the *X. sagittifolium* leaf. The average contact angle formed on the fresh *X. sagittifolium* leaves is *ca*. 146°, as shown in the illustration in Figure 16.25b. From Figure 16.25b, many small papillary hills are clearly visible on the natural *X. sagittifolium* leaf. The diameters of the small papillary hills are between 7 and 9 μm.

The hydrophobic/superhydrophobic polymer coating was fabricated through a nanocasting technique using the PDMS templates. Figures 16.26 and 16.27 shows the structures on the surfaces of the nanocasted layers on the CRS slides observed using SEM. Numerous papillary microstructures whose average diameter is about 7-9 μm are formed on the surfaces. The papillary microstructures are replicas of the surface patterns of the *X. sagittifolium* leaves.

Figure 16.28 shows the schematic diagram for the fabrication of hydrophobic/superhydrophobic electroactive polymer coating materials. First, a PDMS prepolymer is

TABLE 16.3 Feed composition ratio and electrochemical corrosion measurements of the prepared materials.[25]

	Feed Composition (g)				Electrochemical Corrosion Measurements					
Sample Code	ODA	ATs	BSAA	$Ti(OBu)_4$	E_{corr} (mV)	R_p (kΩ cm²)	I_{corr} (μA/cm²)	R_{corr} (mm/year)	Thickness (μm)	P_{EF} (%)
Bare[a]	-	-	-	-	−976.9	0.011	5.275	6.2×10^{-2}	-	-
NEPI	0.1	-	0.26	-	−647.8	0.074	0.700	8.2×10^{-3}	20	5.98
EPI	-	0.145	0.26	-	−469.5	0.112	0.598	7.0×10^{-3}	20	9.56
EPT05	-	0.145	0.26	0.203	−330.4	0.271	0.333	3.9×10^{-3}	22	24.56
EPT10	-	0.145	0.26	0.405	−179.0	0.439	0.164	1.9×10^{-3}	21	40.37

[a]Pristine CRS used for test.

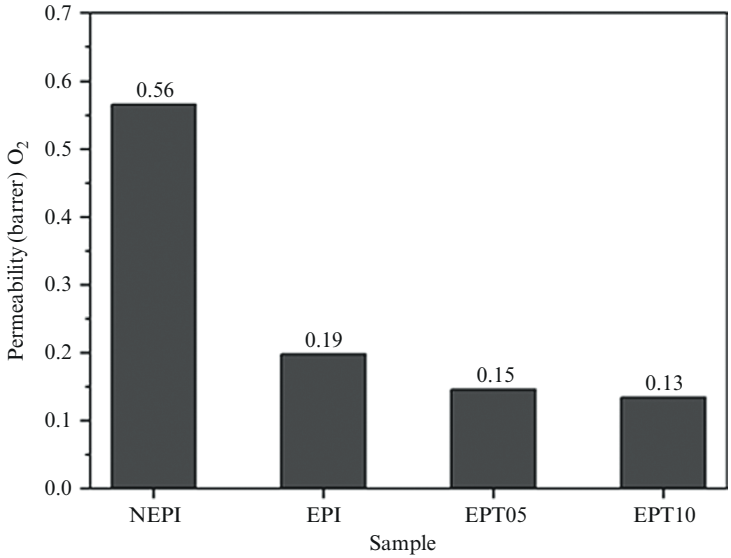


Figure 16.21 Permeability of O_2 as a function of the TiO_2 content in the EPTs nanocomposite materials.[25]

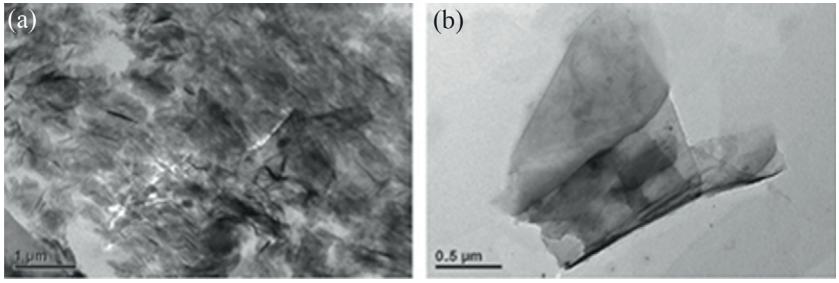


Figure 16.22 TEM images of PAGCs05 at (a) low magnification and (b) high magnification.[27]

cast against a fresh *X. sagittifolium* leaf surface and then cured under proper conditions. The PDMS template prepared has negative *X. sagittifolium* leaf surface structures and is obtained after peeling the leaf off. Second, the substrate is covered with the EAP solution, and the template is pressed against the CRS. After the process and peeling off the PDMS template, a *X. sagittifolium* leaflike surface is formed on the CRS.

The resulting hydrophobic electroactive epoxy (HEE)[29], superhydrophobic electroactive epoxy (SEE),[28,30] polyaniline (SH-PANI),[31] and polyimide (SEPI)[32] with the replicated nanostructured surface showed a hydrophobic and superhydrophobic characteristic with a water contact angle of ~120° and ~155°. The significant increase in the contact angle indicated that the biomimetic morphology effectively

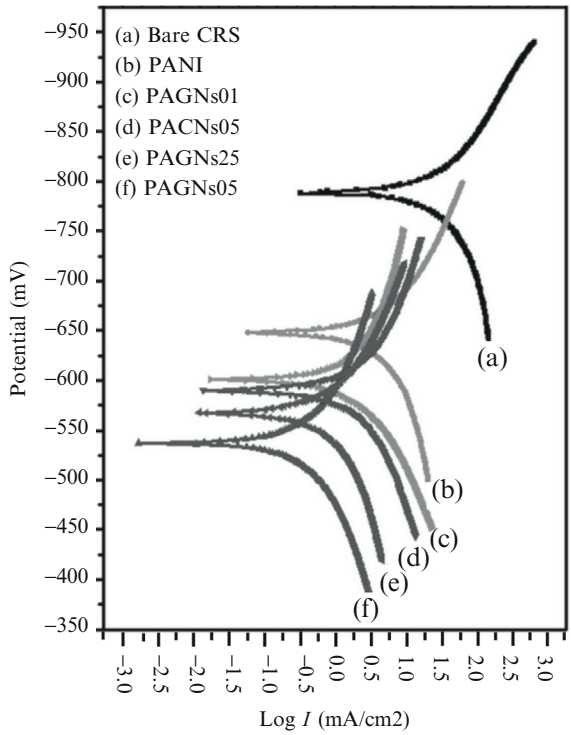


Figure 16.23 Tafel plots for (a) bare steel, (b) PANI-coated, (c) PAGCs01-coated, (d) PACCs05-coated, (e) PAGCs025-coated, and (f) PAGCs05-coated electrodes measured in 3.5 wt.% aqueous NaCl solution.[27]

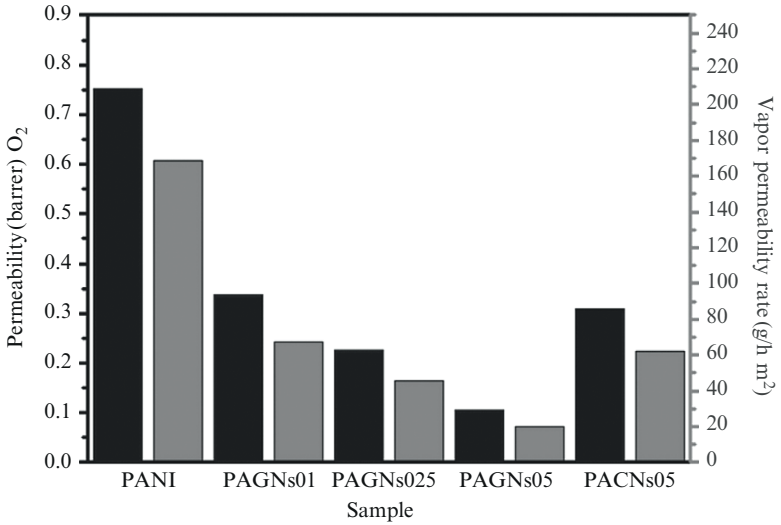


Figure 16.24 Permeability and vapor permeability rates of PANI, PAGCs (PAGCs01, PAGCs025, PAGCs05), and PACCs05.[27]

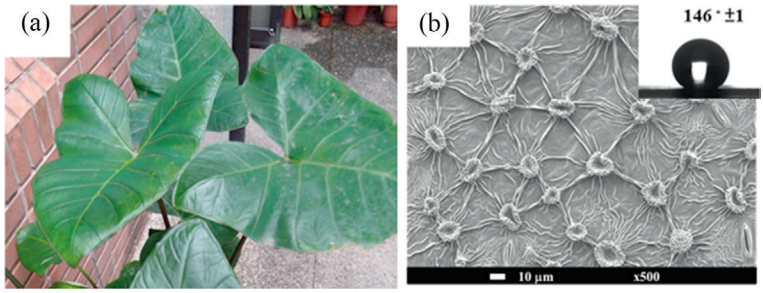


Figure 16.25 (a) Photograph of Xanthosoma sagittifolium leaves. (b) SEM image of fresh, natural leaf. Illustration is water contact angle of Xanthosoma sagittifolium leaf.[32]

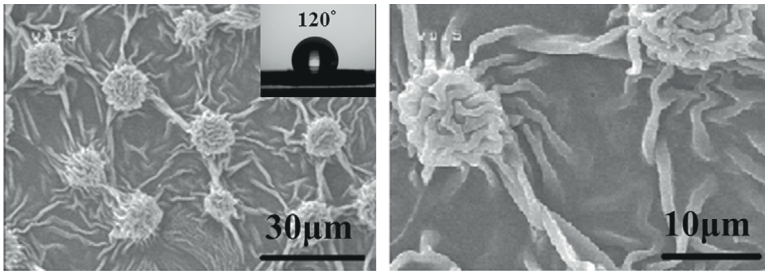


Figure 16.26 SEM images of the electroactive epoxy (EE) surface with the replicated structure from the Xanthosoma sagittifolium leaf. Inset shows contact angle of polymeric surface.[29]

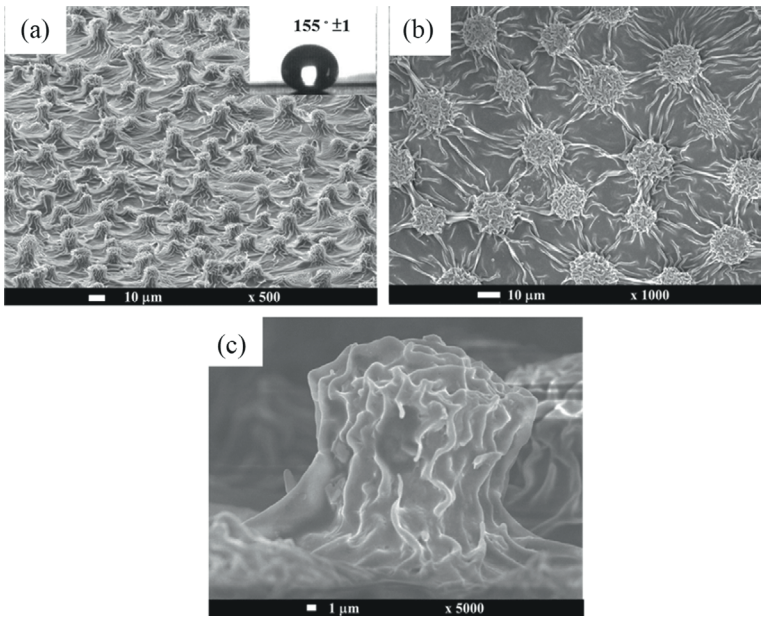


Figure 16.27 SEM images of (a) Xanthosoma-sagittifolium-leaf-like super-hydrophobic polymeric surface. Inset shows contact angle of polymeric surface. (b) Topview of polymeric surface. (c) Cross-sectional view of polymeric surface.[32]

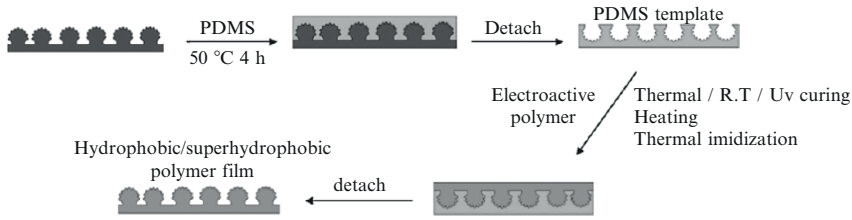


Figure 16.28 Scheme for preparing the biomimetic hydrophobic/superhydrophobic electroactive polymer film by using the nanocasting technique.

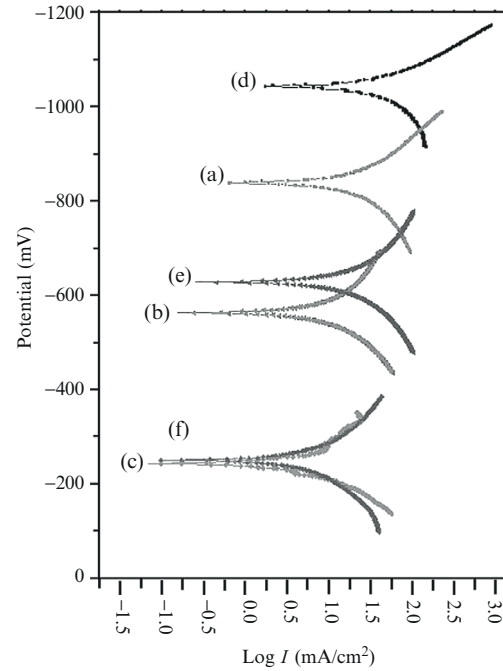


Figure 16.29 Tafel plots for (a) bare CRS, (b) EE-coated, and (c) SEE-coated electrodes measured in 3.5 wt.% aqueous NaCl solution; (d) bare CRS, (e) EE-coated, and (f) SEE-coated electrodes measured after immersion in 3.5 wt.% aqueous NaCl solution for 7 days.[28]

repelled water. The results of potentiodynamic and electrochemical impedance spectroscopic measurements in saline conditions (Figure 16.29 and Table 16.4) indicated that the electroactive epoxy coating with superhydrophobic surfaces (SEE) offered better protection against corrosion than the electroactive epoxy (EE) coating did.

16.5 Conclusions

EAPs have been shown to offer many potential advantages as corrosion protection coatings. This chapter is intended to provide the reader with an understanding of synthesis and mechanism of corrosion in metal with protective EAP-based coatings.

TABLE 16.4 Electrochemical corrosion measurements for EE and SEE.[28]

			Electrochemical Corrosion Measurements			
Sample Code	Immersion Period[a] (day)	pH values[b]	E_{corr} (mV)	I_{corr} (μA/cm²)	Protection Efficiency (%)	Coating Thickness (μm)
Bare[c]	0	7	−839	32.73		
EE	0	7	−564	10.11	69.11	31
SEE	0	7	−244	4.33	86.77	30
SEE	0	5	−246	4.39	86.58	30
SEE	0	3	−253	4.60	85.94	29
SEE	0	1	−259	5.02	84.66	32
bare	7	7	−1047	46.88	−43.23	-
EE	7	7	−628	15.58	52.39	31
SEE	7	7	−253	4.48	86.31	31

[a]3.5% aqueous NaCl electrolyte as an immersion solution.
[b]pH values control by 1 M HCl (aq).
[c]Pristine CRS used for test.

Enhancement of corrosion protection using EAP-based coatings might be attributed to the following three reasons: (1) the redox catalytic capabilities of oligoaniline units in EAP may induce the formation of passive metal oxide layers on CRS electrode, (2) the well-dispersed inorganic fillers embedded in EAP matrix could function as an impervious layer to effectively enhance the oxygen barrier property, and (3) the hydrophobicity/superhydrophobicity of the coating repelled the moisture and further reduced the water/corrosive media adsorption on the EAP surface, preventing the underlying metals from corrosion attack.

References

1. Pohl HA. The organic semiconductor challenge. Chem Eng 1961;68(22):105–10.
2. Katon JE, Wildi BS. Semiconducting organic polymers derived from nitriles. Thermoelectric power and thermal conductivity measurements. J Chem Phys 1964;40(10):2977–83.
3. Shirakawa H, MacDiarmid AG, Heeger AJ, et al. Synthesis of electrically conducting organic polymers: halogen derivatives of polyacetylene, (CH)x. J Chem Soc, Chem Commun 1977;16:578–80.
4. Heeger AJ, MacDiarmid AG, Shirakawa H, et al. Anisotropic optical properties of pure and doped polyacetylene. *Report*, 1978; Issue LRSM-TR-78-6, Order No. AD-A058374, 22 pp.
5. DeBerry DW. Modification of the electrochemical and corrosion behavior of stainless steels with an electroactive coating. J Electrochem Soc 1985;132(5):1022–6.

6. Wessling B. Passivation of metals by coating with polyaniline: corrosion potential shift and morphological changes. Adv Mater 1994;6(3):226–8.
7. Kim DK, Muralidharan S, Ha TH, et al. Electrochemical studies on the alternating current corrosion of mild steel under cathodic protection condition in marine environments. Electrochim Acta 2006;51(25):5259–67.
8. Cecchetto L, Delabouglise D, Petit P. On the mechanism of the anodic protection of aluminium alloy AA5182 by emeraldine base coatings: evidences of a galvanic coupling. Electrochim Acta 2007;52(11):3485–92.
9. Praveen BM, Venkatesha TV, Naik YA, et al. Corrosion studies of carbon nanotubes–Zn composite coating. Surf Coat Tech 2007;201(12):5836–42.
10. Alquist FN, Wasco J. Inhibition of sodium trichloroacetate weed killer solutions. Corrosion 1952;8:410–1.
11. Rosenfeld IL. New data on the mechanism of metals protection with inhibitors. Corrosion 1981;37(7):371–7.
12. McCafferty E. Introduction to corrosion science. New York: Springer; 2010 p. 357–402.
13. Acello SJ, Greene ND. Anodic protection of austenitic stainless steels in sulfuric acid-chloride media. Corrosion 1962;18:286t–90t.
14. McCafferty E, Moore PG, Pease GT. Effect of laser-surface melting on the electrochemical behavior of an aluminum-1% manganese alloy. J Electrochem Soc 1982;129(1):9–17.
15. Fisher AO. Laboratory study of corrosion control for a once-through cooling water system. Mater Prot 1964;3(10):8–13.
16. Ritter JJ, Rodriguez MJ. Corrosion phenomena for iron covered with a cellulose nitrate coating. Corrosion 1982;38(4):223–5.
17. Wei Y, Wang J, Jia X, et al. Polyaniline as corrosion protection coatings on cold rolled steel. Polymer 1995;36(23):4535–7.
18. Li P, Tan TC, Lee JY. Corrosion protection of mild steel by electroactive polyaniline coatings. Synthetic Met 1997;88(3):237–42.
19. Huang KY, Jhuo YS, Yeh JM, et al. Electrochemical studies for the electroactivity of amine-capped aniline trimer on the anticorrosion effect of as-prepared polyimide coatings. Eur Polym J 2009;45(2):485–93.
20. Huang KY, Shiu CL, Yeh JM, et al. Effect of amino-capped aniline trimer on corrosion protection and physical properties for electroactive epoxy thermosets. Electrochim Acta 2009;54(23):5400–7.
21. Peng CW, Hsu CH, Yeh JM, et al. Electrochemical corrosion protection studies of aniline-capped aniline trimer-based electroactive polyurethane coatings. Electrochim Acta 2011;58:614–20.
22. Huang TC, Yeh TC, Yeh JM, et al. Electrochemical investigations of the anticorrosive and electrochromic properties of electroactive polyamide. Electrochim Acta 2012;63:185–91.
23. Yeh TC, Huang TC, Yeh JM, et al. Electrochemical investigations on anticorrosive and electrochromic properties of electroactive polyuria. Polym Chem 2012;3(8):2209–16.
24. Huang HY, Lai CL, Yeh JM, et al. Advanced anticorrosive materials prepared from amine-capped aniline trimer-based electroactive polyimide-clay nanocomposite materials with synergistic effects of redox catalytic capability and gas barrier properties. Polymer 2011;52(11):2391–400.
25. Weng CJ, Huang JY, Yeh JM, et al. Advanced anticorrosive coatings prepared from electroactive polyimide-TiO_2 hybrid nanocomposite materials. Electrochim Acta 2010;55(28):8430–8.
26. Huang TC, Su YA, Yeh JM, et al. Advanced anticorrosive coatings prepared from electroactive epoxy-SiO_2 hybrid nanocomposite materials. Electrochim Acta 2011;56(17):6142–9.
27. Chang CH, Huang TC, Yeh JM, et al. Novel anticorrosion coatings prepared from polyaniline/graphene composites. Carbon 2012;50(14):5044–51.
28. Weng CJ, Chang CH, Yeh JM, et al. Advanced anticorrosive coatings prepared from the mimicked *Xanthosoma sagittifolium*-leaf-like electroactive epoxy with synergistic effects of superhydrophobicity and redox catalytic capability. Chem Mater 2011;23(8):2075–83.

29. Yang TI, Peng CW, Yeh JM, et al. Synergistic effect of electroactivity and hydrophobicity on the anti-corrosion property of room-temperature-cured epoxy coatings with multi-scale structures mimicking the surface of *Xanthosoma sagittifolium* leaf. J Mater Chem 2012;22(31):15845–52.
30. Peng CW, Chang KC, Yeh JM, et al. UV-curable nanocasting technique to prepare bio-mimetic super-hydrophobic non-fluorinated polymeric surfaces for advanced anticorrosive coatings. Polym Chem 2013;4(4):926–32.
31. Peng CW, Chang KC, Yeh JM, et al. Nano-casting technique to prepare polyaniline surface with bio-mimetic superhydrophobic structures for anticorrosion application. Electrochim Acta 2013;95:192–9.
32. Chang KC, Lu HI, Yeh JM, et al. Nanocasting technique to prepare lotus-leaf-like superhydrophobic electroactive polyimide as advanced anticorrosive coatings. ACS Appl Mater Inter 2013;5(4):1460–7.
33. MacDiarmid AG. Short course on electrically conductive polymers. New York: New Platz; 1985.
34. Heeger AJ. Semiconducting and metallic polymers: the fourth generation of polymeric materials. J Phys Chem B 2001;105(36):8475–91.
35. Kohlman RS, Joo J, Epstein AJ. In: Mark J, editor. Physical properties of polymers handbook. New York: American Institute of Physics; 1996.
36. Trivedi DC. Handbook of organic conductive molecules and polymers. New York: John Wiley & Sons; 1997.
37. Martin RE, Diederich F. Linear monodisperse π-conjugated oligomers: model compounds for polymers and more. Angew Chem Int Ed 1999;38(10):1351–77.
38. Zhou YC, Geng JX, Zhou E, et al. Crystal structure and morphology of phenyl-capped tetraaniline in the leucoemeraldine oxidation state. J Polym Sci Pol Phys 2006;44(4):764–9.
39. Yeh JM, Liou SJ, Lai CY, et al. Enhancement of corrosion protection effect in polyaniline via the formation of polyaniline-clay nanocomposite materials. Chem Mater 2001;13(3):1131–6.
40. Yeh JM, Chen CL, Chen YC, et al. Enhancement of corrosion protection effect of poly(o-ethoxyaniline) via the formation of poly(o-ethoxyaniline)-clay nanocomposite materials. Polymer 2002;43(9):2729–36.
41. Chang KC, Jang GW, Yeh JM, et al. Comparatively electrochemical studies at different operational temperatures for the effect of nanoclay platelets on the anticorrosion efficiency of DBSA-doped polyaniline/Na^+-MMT clay nanocomposite coatings. Electrochim Acta 2007;52:5191–200.
42. Yeh JM, Liou SJ, Lin CY, et al. Anticorrosively enhanced PMMA-clay nanocomposite materials with quaternary alkylphosphonium salt as an intercalating agent. Chem Mater 2002;14(1):154–61.
43. Yu YH, Yeh JM, Liou SJ, et al. Organo-soluble polyimide (TBAPP-OPDA)/clay nanocomposite materials with advanced anticorrosive properties prepared from solution dispersion technique. Acta Mater 2004;52(2):475–86.
44. Chang KC, Chen ST, Yeh JM, et al. Effect of clay on the corrosion protection efficiency of PMMA/Na^+-MMT clay nanocomposite coatings evaluated by electrochemical measurements. Eur Polym J 2008;44(1):13–23.
45. Yeh JM, Huang HY, Chen CL, et al. Siloxane-modified epoxy resin-clay nanocomposite coatings with advanced anticorrosive properties prepared by a solution dispersion approach. Surf Coat Tech 2006;200(8):2753–63.
46. Yeh JM, Weng CJ, Liao WJ, et al. Anticorrosively enhanced polymethyl methacrylate-SiO_2 hybrid coatings prepared from the sol-gel approach with MSMA as the coupling agent. Surf Coat Tech 2006;201(3–4):1788–95.
47. Huang KY, Weng CJ, Yeh JM, et al. Preparation and anticorrosive properties of hybrid coatings based on epoxy-silica hybrid materials. J Appl Polym Sci 2009;112(4):1933–42.
48. Yano K, Usuki A, Okada A, et al. Synthesis and properties of polyimide-clay hybrid. J Polym Sci Pol Chem 1993;31(10):2493–8.
49. Bharadwaj RK. Modeling the barrier properties of polymer-layered silicate nanocomposites. Macromolecules 2001;34(26):9189–92.

Chapter 17

Corrosion Protective Coatings for Ti and Ti Alloys Used for Biomedical Implants

Liana Maria Muresan
"Babes-Bolyai" University, Faculty of Chemistry and Chemical Engineering, Cluj-Napoca, Romania

17.1 Introduction

Titanium and its alloys are biologically inert materials widely used in the production of biomedical implants due to their high tensile and fatigue strength, low Young modulus, and superior corrosion and wear resistance.[1] Moreover, they are biocompatible, providing direct bonding with bone surface in orthopedic and dental surgery, and are inert in physiological environments.[2]

Titanium is a material with a high superficial energy and after implantation it provides a favorable body reaction that leads to direct deposition of minerals on the bone-titanium interface and titanium osseointegration.[3] This is due mainly to the thin

Intelligent Coatings for Corrosion Control
Copyright © 2015 Elsevier Inc. All rights reserved.

TiO_2 film naturally formed on its surface, which is very stable and chemically inert. Nevertheless, bulk titanium used in implants presents three main problems[4]:

- high processing energy due to melting and casting difficulties
- slow reaction with the human tissues resulting in difficulties in bone attachment
- higher elastic modulus compared to bone

One of the ways to reduce the problems associated with stress generated by the incompatibility between the elastic modulus of Ti implant and that of the bone is to fabricate titanium implants with controlled porosity.[5] Recently, porous Ti scaffolds with good mechanical properties (particularly, elastic modulus and stiffness) that provide a favorable environment for bone growth and a significant enhancement in the osteoblastic activity were produced.[6]

Although "commercially pure" titanium has acceptable mechanical properties and has been used for different implants, presently, for most biomedical applications, titanium is alloyed with nickel or with small amounts of aluminum, vanadium, or niobium. These elements improve some of the Ti characteristics such as strength, mechanical properties, corrosion resistance, and so on. Titanium alloys most frequently used in dental and orthopedic implantations are NiTi (Nitinol), Ti-6Al-4V, and Ti-6Al-7Nb.

NiTi is a material with excellent shape memory effect and super elasticity and damping capacity suitable for use in orthopedic implants. In dentistry, the material is used in orthodontics for brackets and wires connecting the teeth. However, it should be mentioned that its high Ni content constitutes a potential threat to its safe use *in vivo*.[7]

Ti-6Al-4V is the material used for ~20-30% of commercially available medical devices. It contains 6% Al and 4% V by weight and is by far the most common Ti alloy. As in the case of NiTi, during the Ti-6Al-4V use for implants the release of metallic ions in the physiological environment could be harmful to the health. Thus, Al and V may cause neurological disorders and bone diseases when they are released in the human body.[8]

Ti-6Al-7Nb is another titanium alloy with excellent strength and biocompatibility dedicated for surgical implants, used especially for replacement hip joints. It is a typical $\alpha+\beta$ alloy, with Al as stabilizer for the α phase and Nb as stabilizer for the β phase.[2] It is usually stable in neutral halide solutions, but in acidic media is prone to accelerated dissolution.[9]

Irrespective of the material nature, the most important requirement for the long-term success of implants is the stable interface between the biomaterial and the surrounding tissue.[10] Hence, an improvement of all Ti-based materials corrosion resistance is of particular importance. In this regard, TiO_2 naturally formed on the surface is one of the main candidates for protective coatings on Ti and Ti alloys substrates due to its thermodynamic stability, chemical inertia, and low solubility in body fluids.[11] Titania with specific structures of anatase and rutile was found to stimulate apatite formation[12] and were proved to be much more beneficial for bone growth

than the amorphous TiO_2.[13] However, the native TiO_2 layer is very thin, irregular, and porous and there is also the risk of viruses being carried by this layer. Moreover, the TiO_2 naturally formed on Ti surface is not sufficient to ensure a strong chemical bond with bone tissue and a safe, long lifetime of the implants. Consequently efforts are made for thickening the oxide layer along with an improvement of its surface ability to promote osteosynthesis and to increase its corrosion and wear resistance.

The development of nanostructures has allowed unprecedented access to an intimate interaction with the biological environment. For bone regeneration and repair, re-creating substrates on a nanoscale allows scientists to probe the first level of the bone structural hierarchy.[14] Studies have shown that TiO_2 films consisting of nanostructures (nanotubes, nanorods, nanosheets, etc.) exhibit high hydrophilicity, improving thus the bioactivity and bone-bonding behavior of materials for implants.[15,16] However, there is still a lot to do in the direction of improving the behavior of implant biomaterials. Some of the most widely used methods to modify the characteristics of materials surface are presented below.

17.2 Surface Modification Methods

As already mentioned, optimization of the biomaterial surface is necessary in order to trigger osseointegration, to minimize metallic ion release, and to ensure a longer lifetime of an implant. There are several possible ways to form a surface layer on the implant materials[17]:

(i) materials deposition on the substrate (e.g., by sol-gel method, spray method, or electrolytic deposition)
(ii) material removal from the substrate (e.g., by etching)
(iii) substrate surface transformation (e.g., by anodic oxidation)

Some of the most used methods to modify the surface of Ti and Ti alloys are presented below.

17.3 Sol-Gel Method

Sol-gel process is a method for producing solid materials from small molecules that is suitable for preparing different coatings (e.g., silicium and titanium oxides) on the surface of Ti-based materials. It involves conversion of small molecules (precursors) into a colloidal solution (sol) and then into an integrated network (gel) consisting of either discrete particles or network polymers.

The main advantages of the sol-gel method are[18]: (1) low processing temperature (avoiding volatilization of entrapped species), (2) the possibility to cast coatings in complex shapes, and (3) the use of compounds that do not introduce impurities into

the end product. Among the disadvantages of this method one can count the relatively long period of time for processing flow and the difficulties related to phase separation occurring especially in hybrid coating synthesis.

The sol-gel process involves four stages: (1) hydrolysis, (2) condensation/polymerization of monomers, (3) growth of particles, and (4) gel formation.[18] These processes are influenced by several experimental parameters such as pH, temperature, concentration of the reactants, and presence of additives.

Traditional precursors for sol-gel coatings are alkoxysilanes such as tetraethyl orthosilicate (TEOS) and tetramethyl orthosilicate (TMOS), but efforts are made in order to find less toxic and more environmental friendly precursors.

TiO_2 can be prepared, for example, starting from precursor solutions containing an alkoxide (e.g., tetrabutylorthotitanate) and diethanolamine dissolved in ethanol[16] and mixing them with water (with or without additives) in a certain ratio.

SiO_2 coatings can be prepared starting from a precursor solution consisting of tetraethylorthosilicate $Si(OC_2H_5)_4$, H_2O, C_2H_5OH, and HCl, mixed at a certain molar ratio.[19] Different compounds (inhibitors, pigments, etc.) can be added in order to improve the physicochemical properties of the coating.

Irrespective of the nature of the film, the two main techniques used to apply a sol-gel coating on the surface of a metallic substrate are dip-coating and spin-coating.

17.3.1 Dip-coating

By this technique, the material from which the film is produced is put into solution, and then the substrate is progressively dipped into and is extracted from the solution at a controlled rate (Figure 17.1). After the solvent evaporates, a thin and

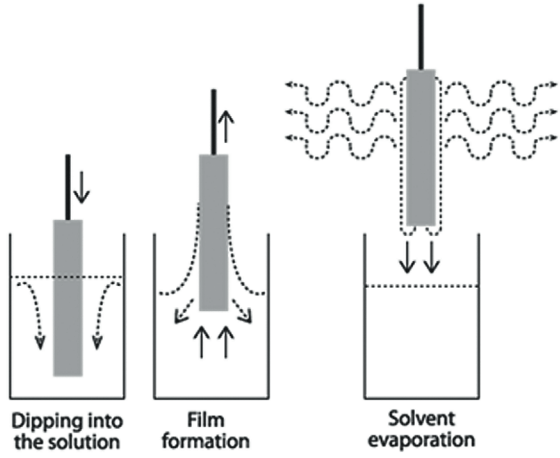


Figure 17.1 Schematics of a dip-coating process.[20]

homogeneous film is produced. The thickness of deposited liquid film coatings depends on the coating solution properties such as density, viscosity, and surface tension, as well as surface withdrawal speed from the coating solution. The thickness of the film is generally bigger than that prepared by spin-coating with the same solutions.

Dip-coating was successfully used, for example, to prepare sol-gel-derived Al_2O_3 films on γ-TiAl-based alloys,[21] porous TiO_2 films,[16] hydroxyapatite (HA) coatings,[22] and SrO-SiO_2-TiO_2 on NiTi,[23] and so on.

17.3.2 Spin-coating

In the case of spin-coating, an amount of solution is placed on the substrate that is rotated at high speed in order to spread the fluid by centrifugal force (Figure 17.2). After the evaporation of the solvent, a thin, homogeneous film is formed. As in the case of dip-coating, final film thickness and other properties will depend on the nature of the sol-gel coating (viscosity, drying rate, surface tension, etc.) and on the parameters chosen for the spin process. Higher spin speeds and longer spin times give birth to thinner films.[25] Generally, a moderate spinning speed is recommended. The drying rate should also be slow in order to ensure film uniformity. A supplementary drying step is sometimes necessary after the high-speed spin step to further dry the film without substantially thinning it.

By using spin-coating, SiO_2 films were deposited on Ti-48Al alloy,[19] sphene ($CaTiSiO_3$) ceramics on Ti-6Al-4V[26] alkoxide-based HA nanocoatings on Ti and Ti-6Al-4V substrates,[27] HA[28] and HA/polymer coatings on Ti,[29] TiO_2 on Ti-6Al-4V,[30] and many others.

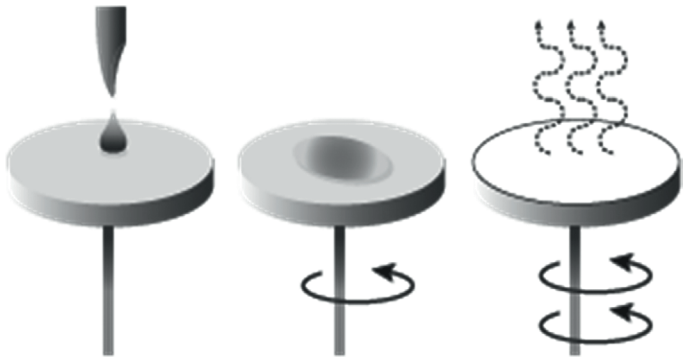


Figure 17.2 Schematics of a spin-coating process.[24]

17.4 Laser Oxidation

Laser surface treatment is a thermal process that has an advantage over conventional furnace treatment. It is based on the heating caused by the light adsorption of the surface layer and the cooling ensured by the high conductivity of the material.[31] The adsorbed laser energy results in a thin surface layer with desired properties while the bulk of the material is unaffected.

By using laser treatments followed by AFM investigations, it was proved that the morphological modifications of Ti-based alloys play a key role in cell adherence and proliferation by influencing cell-material interactions.[32]

Porous Ti samples were fabricated by using laser power in an attempt to improve the osteoconductivity and reduce the problems associated with stress shielding.[5]

NiTi were treated with a pulsed Nd:YAG laser in air, by using selected parameters aiming to obtain uniform oxide films of controlled thickness.[7] The corrosion resistance of the so-treated NiTi samples increased about 15 times, while the surface Ni/Ti ratio was reduced. The last feature is important as the high Ni content in NiTi constitutes a potential threat to its safe use *in vivo*.

17.5 Anodic Oxidation

Anodic oxidation is a traditional surface modification method of Ti and its alloys that allows the obtaining of the desired properties of oxide layer by controlling the electrochemical parameters, such as electrolyte composition and concentration, applied potential or current, temperature, and so on.

Anodic oxidation can be performed potentiostatically[33] or galvanostatically[34] in different electrolytes. The most common electrolyte solutions used for anodization are H_2SO_4,[12,33] Na_2SO_4,[33] CH_3COOH,[33,35,36] H_3PO_4,[33] and HF.[13,14] Mixture of inorganic substances or hybrid inorganic-organic solutions could be also used.[2,37,38] It was reported that porous anodic films consisting of and/or anatase are produced by anodizing in H_2SO_4 and Na_2SO_4 solutions, while amorphous TiO_2 films are produced in CH_3COOH and H_3PO_4.[33] Self-organized TiO_2 nanotubes can be generated from viscous electrolytes consisting of glycerol or ethylene glycol with addition of ammonium fluoride.[38] Viscosity of the electrolyte plays a key role in the nanotubes growth process.

The oxidation potentials are usually determined before the anodic oxidation step from potentiodynamic polarization experiments.[35]

Oxide layers formed by anodization differ according to the substrate, for example, oxidation in chromic acid produced a TiO_2 layer on titanium substrate, but layers consisting of TiO_2 and Al_2O_3 oxides on a Ti-6Al-4V substrate.[39] The minor oxides formed by anodic oxidation in the TiO_2 layer on the Ti-6Al-7Nb alloy are Al_2O_3 and Nb_2O_5.[35]

In order to prepare layers with high apatite-forming ability, anodic oxidation can be carried out in complex solutions containing calcium and/or phosphate ions.[40]

17.6 Plasma Electrolytic Oxidation

Plasma electrolytic oxidation is a relatively inexpensive and simple method used for increasing surface roughness of the materials, allowing also the synthesis of ceramiclike oxide films on some metals.[41] It is similar to anodizing, but it employs higher potentials so that the resulting plasma modifies the structure of the oxide layer. Thus, the method combines electrochemical oxidation with a spark treatment in the plating bath. If this contains aluminate, phosphate, silicate, and sulfate anions or some of their combinations, bioactive layers enriched in these elements are formed.[42] The incorporation of Ca and P into an oxide film formed *via* anodic oxidation on Ti-15Mo alloy[41] or Ti-6Al-7Nb,[43] as well as the formation of a bioactive film on Ti-6Al-4V[8] after the application of a voltage higher than the breakdown voltage of the oxide layer, were also reported. Plasma electrolytic oxide coatings are generally recognized for high hardness, wear, and corrosion resistance.

17.7 Electrolytic Deposition

A promising route for deposition of thin oxide films from aqueous solutions is the electrolytic deposition method using $TiCl_4$ or $TiOSO_4$ as starting materials in the presence of hydrogen peroxide.[44] The procedure consists in galvanostatic electrodeposition at 0 °C from a solution obtained by slow addition of $TiCl_4$ and H_2O_2 and subsequent adjustment of the solution volume. The resulting films are uniform, of high purity, present excellent adhesion to the substrate, and have good mechanical properties. The electrolytic deposition can be followed by annealing.

A possible mechanism for TiO_2 electrodeposition is based on hydrolysis of the peroxo-complex of Ti in the presence of OH^- ions generated at the cathode.[45]

$$TiCl_4 \rightarrow Ti^{4+} + 4Cl^-$$

$$Ti^{4+} + H_2O_2 + (n-2)H_2O \rightarrow \left[Ti(O_2)(OH)_{n-2}\right]^{(4-n)+} + nH^+$$

$$\left[Ti(O_2)(OH)_{n-2}\right]^{(4-n)+} + mOH^- + kH_2O \rightarrow TiO_3(H_2O)_x$$

$$2TiO_3(H_2O)_x \rightarrow 2TiO_2 + O_2 + 2xH_2O$$

A fluorine-doped HA/ZrO_2 two-layer coating was prepared by electrodeposition on titanium in $ZrO(NO_3)_2$ aqueous solution and subsequently in a mixed solution of $Ca(NO_3)_2$, $NH_4H_2PO_4$, and NaF. The adherence of the two-layer coating was found to be significantly higher than that of the pure HA coating.[46]

17.8 Combined Methods

Sometimes, the combination of two or more methods is used in order to improve surface layer properties and to attain the desired characteristics. Thus, the combined laser/sol-gel synthesis of calcium silicate coating was produced on Ti-6Al-4V substrates for improved cell integration.[47]

Anodic oxidation treatment applied on laser-processed porous Ti samples was used to produce bioactive TiO_2 nanotube arrays that significantly changed the surface properties and enhanced the apatite-forming ability of porous TiO_2 samples in simulating body fluid.[5] By creating the nanotube arrays, the healing time due to increased biocompatibility can be significantly reduced.

The polymeric sponge replication method followed by microarc oxidation (MAO) was used to prepare HA/TiO_2 hybrid coatings on highly porous Ti scaffolds.[6] For this purpose, a polyurethane sponge was covered with titanium hydride slurry (consisting of TiH_2 dispersed in ethanol containing triethyl phosphate and polyvinylbutyl), and then heated at 800 °C to convert TiH_2 to Ti. The surface was then coated with a hybrid, bioactive, microporous HA/TiO_2 layer using MAO.

17.9 Protective Films

The protective layers produced on the surface of Ti and Ti-based alloys for enhancing their corrosion resistance, as well as their biocompatibility, are of different natures: oxides, composites, HA, hybrid organic-anorganic, ceramic, and so on.

17.9.1 Oxides

Oxide-based films are the most frequently produced on the Ti substrates. The most important factors deciding their corrosion resistance are the oxide thickness, and its evenness and compactness. The main oxide formed on the surface of Ti alloys is TiO_2, but minor oxides of the alloying elements (Al_2O_3, Nb_2O_5, NiO, etc.) are also produced.

TiO_2 can be produced in different crystallographic forms (anatase, rutile, brookite; see Figure 17.3), depending on the substrate nature and the preparation conditions.

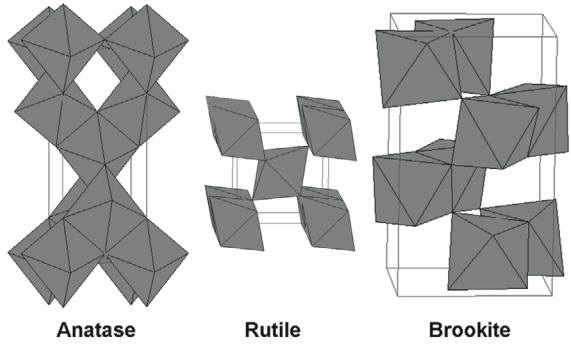


Figure 17.3 Crystallographic forms of TiO_2.

From the point of view of osseointegration abilities, crystalline forms are superior to amorphous ones and nanostructured layers are superior to microstructured ones. For example, rutile can induce apatite formation, especially when it has a crystal orientation in the (101) plane, because the matching structure with apatite (002) promotes the nuclei formation for epitaxial crystal growth. On the contrary, amorphous titania layers are not able to induce apatite formation.[33]

Osteoblasts are very sensitive to the different materials' topographies and respond differently on submicron- and nanometer-sized surfaces. This is why nanostructured TiO_2 are preferred and are often generated on the top of the thin TiO_2 naturally formed on the Ti surface, aiming to accelerate osteogenesis. Besides, the systems based on nanotubes are very hydrophilic and promote greater cell adhesion and increased channeling for fluid exchange that contributes to bone remodeling.[14]

The adhesion/propagation of the osteoblasts is substantially improved on vertically aligned and laterally spaced TiO_2 nanotubes.[15] This type of nanotube can be obtained by anodic oxidation of Ti in diluted HF acid[13,14] and confer to the substrate increased surface area, porous structure, and superior osteoblast cell growth.

Anodization of the same material in different electrolytes leads to the formation of different oxidic nanostructures. For example, oxide layers obtained by anodic oxidation of Ti_6Al_7Nb alloy in $(NH_4)_2SO_4 + NH_4F$ solution are more homogeneous than those obtained in a solution containing glycerol and NH_4F and water.[2] The concentration of F^- in the electrolytes ions is also important: the larger its concentration, the higher the diameters of pores and the surface roughness. It should be also noticed that, as the electrolytes used for anodization are fluoride-based, the nanotubes always contain a certain amount of incorporated fluorine,[48] which could be useful for the enhancement of antibacterial properties of the surface.

17.9.2 Hydroxyapatite

Hydroxyapatite, with the formula $Ca_{10}(PO_4)_6(OH)_2$, is the major inorganic component of bones that is able to accelerate bone ingrowths onto the surface of a biomedical implant. HA has excellent biocompatibility and bioactivity, but bad mechanical properties; therefore, HA is usually deposited on the Ti-based implants in order to obtain materials that possess both bioactivity and mechanical resistance.

HA can be deposited on titanium-based surfaces by using different methods, such as electrochemical deposition,[49] plasma spraying,[50,51] and sol-gel method.[52] Sometimes, an intermediate TiO_2 layer is produced between the Ti and HA layer for improving the bonding capacity of HA on the Ti substrate and, thus, improving the integrity of the coating.[27,53] Composite materials with improved bioactivity and corrosion resistance can be obtained by embedding HA particles in titania gel, depositing this mixture by spin-coating onto substrates and then calcinating it.[52]

17.9.3 Composites

Different composite layers can also be deposited on Ti-based biomaterials in order to improve the physicochemical properties and the bioactivity of the surface.

Knowing the beneficial effect of strontium on bone formation, $SrO\text{-}SiO_2\text{-}TiO_2$ composite coatings were produced by sol-gel-method on NiTi substrates aimed at increasing its corrosion resistance and cytocompatibility.[23] The coating significantly decreased the release of nickel ions and exhibited enhanced adhesion of osteoblastlike cells. Biphasic fluorine-doped HA/Sr-substituted HA (FHA/SrHA) were prepared on Ti substrates by sol-gel and dip-coating methods with the intention to induce rapid cellular responses after implantation and long lifetime.[54] The dispersion of SrHA in FHA has promoted growth and attachment of osteoblast cells. In the same time, an increase of SrHA content determined an increase of surface roughness.

To accelerate the formation of HA on TiO_2 modified surfaces, a simulated body fluid with high ionic strength can be used for a biomimetic apatite deposition process.[55]

A class of composites of particular importance is represented by Ag/TiO_2 coatings. Starting from the fact that silver is one of the most interesting antibacterial materials and that TiO_2 is an excellent support material, different Ag/TiO_2 composites were prepared by using various methods. Some of them are summarized in Table 17.1.

17.9.4 Hybrid coatings

Hybrid inorganic-organic coatings have drawn a lot of attention due to their unique properties determined by the synergetic combination of inorganic and organic

TABLE 17.1 Composite Ag/TiO_2 Coatings

Substrate	Composite Coatings	Preparation Method	Properties	Reference
Rutile-structured TiO_2 particles	**Ag/TiO_2**	Micellar layer-by-layer deposition	Antibacterian activity against gram-negative *E. coli*	56
Ti	**Ag/TiO_2**	Electrochemical deposition	Catalytic activity towards oxygen reduction	57
Ti	**Ag/TiO_2**	Sol-gel spin coating	Antibacterian activity against gram-negative *E. coli*	58
Ti foil	**Ag/TiO_2**-nanotubes	Anodization of Ti followed by sputter-deposition of Ag	Enhanced SERS activity	59
Ti	**AgHA/TiO_2**	Plasma electrolytic processing	Corrosion resistance	60

components. When hybrid coatings are deposited on the surface of biomaterials, they significantly improve their characteristics.

HA/TiO_2/poly(lactide-co-glycolide) coatings were prepared by sol-gel method on titanium substrates[29] and compared with HA layers obtained by plasma spraying. The composite layers possessed no cracks, demonstrated increased adhesion of osteoblasts, and presented micron surface roughness.

Apatite/collagen hybrid coatings were prepared on NiTi alloy through electrochemical deposition[61,62] from an electrolyte containing 0.1 mg/ml collagen dissolved in a double-strength simulated body fluid. Apatite/collagen-coated NiTi samples possessed higher wettability and corrosion resistance than either uncoated or apatite-coated samples.

17.9.5 Ceramic coatings

Glass-ceramics, such as hardystonite ($Ca_2ZnSi_2O_7$) and sphene ($CaTiSiO_5$), have attracted much attention in the biomedical field because they provide great possibilities to manipulate their properties by posttreatments, including strength, degradation rate, and coefficient of thermal expansion.

Nanostructured glass-ceramics prepared by a plasma spray technique on Ti-6Al-4V alloys using conventional powders exhibited enhanced capacity for osteoblasts attachment,

which has been ascribed to the Ca and Si ions released from the coatings.[26,63] Ceramic coatings consisting of TiO_2 rutile and $TiAl_2O_5$ were produced on Ti-6Al-4V alloy by an alternating-current, microarc oxidation in aluminate solution.[64] Calcium phosphate ceramic (CPC) coatings were electrophoretically deposited and sintered on titanium or its alloys.[65] Other ceramic coatings such as $CaO\text{-}P_2O_5\text{-}TiO_2\text{-}Na_2O$ exhibiting excellent adhesion to the substrate during the tensile and fatigue tests were deposited on Ti-29Nb-13Ta-4.6Zr.[66] Ceramic layers consisting of Al_2TiO_5, $-\alpha$ Al_2O, and rutile TiO_2 were prepared on Ti-6Al-4V alloy by pulsed bipolar microplasma oxidation (MPO) in $NaAlO_2$ solution.[67] Extending the MPO time, the surface roughness of the coatings increased whereas the thickness and the compactness of the coatings were improved.

17.10 Corrosion Studies

The most important requirement for a biomaterial is its compatibility with the human body. The bioimplants should not cause adverse effects such as allergies or inflammations and should not be toxic. Other important requirements for a successful implant material are very high mechanical, corrosion, and wear resistance in order to ensure a long service period (over 15 years).

In the physiological environment, biomedical implants are subjected to corrosion, especially to mechanically accelerated electrochemical processes such as stress corrosion, corrosion fatigue, and fretting corrosion. Fretting corrosion, alone or in combination with crevice corrosion, has been identified as one of the most important modes of corrosion of Ti-based implants such as hip, knee, and shoulder replacements.[9,68]

Due to corrosion processes, even the most resistant materials undergo electrochemical exchange and release metal ions in the physiological environment, producing different inconvenient or even implant failure.[69] For Ti-based alloys, mostly Ti is released, but also Al and V were detected in the case of Ti-Al-V alloy.[9] It is accepted that the tolerable corrosion rate for metallic implants should be about 2.5×10^{-4} mm/year.[70] In this context, the failure due to corrosion remains one of the challenging clinical problems and all the implantable materials should be tested from a corrosion behavior point of view, apart from other properties. Moreover, different approaches should be used in order to enhance the corrosion resistance.

A way to stabilize the passive film formed on Ti-based surfaces is Ti alloying with selected elements that stabilize either the α-phase (Al) or the β-phase (Mo, V, Fe) of the alloy and enlarge its passive range.[71,72] Other methods consist, as already mentioned, in modifying the surface of the implant materials in a convenient way.

In order to investigate the corrosion behavior of Ti-based biomaterials, different artificial physiological solutions can be used simulating plasmatic serum (Ringer's and Hank's solution), saliva, or sweat. The composition of some of these artificial physiological solutions is presented in Tables 17.2–17.4.

TABLE 17.2 Chemical Composition of Simulated Physiological Solutions[73]

Physiological Solution	Substance	Concentration (g/l)	pH
Hank	NaCl	8.0	6.9
	KCl	0.4	
	$NaHCO_3$	0.35	
	$NaH_2PO_4 \cdot H_2O$	0.25	
	$Na_2HPO_4 \cdot 2H_2O$	0.06	
	$CaCl_2 \cdot 2H_2O$	0.19	
	$MgCl_2$	0.19	
	$MgSO_4 \cdot 7H_2O$	0.06	
	Glucose	1.0	
Ringer	NaCl	8.69	6.4
	KCl	0.30	
	$CaCl_2$	0.48	

TABLE 17.3 Chemical Composition of Artificial Saliva (pH 6.75)[74]

Compound	Concentration (g/l)
Methyl-*p*-hydroxybenzoate	2.00
Na Carboxymethylecellulose	10.0
$MgCl_2 \cdot 6H_2O$	0.059
$CaCl_2 \cdot 2H_2O$	0.166
K_2HPO_4	0.804
KCl	0.625
KH_2PO_4	0.326

The *in vitro* evaluation of the corrosion behavior is an important step in the elaboration of new biomaterials. The corrosion resistance of biomaterials used for implants is usually tested by electrochemical methods because they are accelerated tests that allow evaluating rapidly the performance of materials and predicting their long-time behavior. The most common electrochemical methods are open circuit potential measurements, cyclic voltammetry, potentiodynamic polarization measurements, and electrochemical impedance spectroscopy.

By comparing three titanium-based materials (Ti, NiTi, and Ti-6Al-7Nb), it was reported that Ti-6Al-7Nb alloy possesses the greatest corrosion resistance in simulated

TABLE 17.4 Chemical Composition of Artificial Sweat[75]

	Concentration (% (w/v))			
	AATCC	ISO	ISO	EN
Chemical Composition	**pH 4.3**	**pH 5.5**	**pH 8.0**	**pH 6.5**
L-histidine monohydrochloride monohydrate ($C_6H_9O_2N_3 \cdot HCl \cdot H_2O$)	0.025	0.05	0.05	—
Sodium chloride (NaCl)	1.00	0.50	0.50	1.08
Disodium hydrogen orthophosphate dodecahydrate ($Na_2HPO_4 \cdot 12H_2O$)	—	—	0.50	—
Sodium dihydrogen orthophosphate dihydrate ($NaH_2PO_4 \cdot 2H_2O$)	—	0.22	—	—
Disodium hydrogen orthophosphate anhydrous (Na_2HPO_4)	0.10	—	—	—
Lactic acid (88%)	0.097	—	—	0.12
Urea	—	—	—	0.13

Hanks physiological solution at pH 7.4 and 37 °C, this behavior being valid for the untreated samples as well as for the samples anodically oxidized at 3.0V in acetic acid.[35] The polarization resistance values, determined from EIS measurements for the oxidized Ti-6Al-7Nb alloy during the later stages of immersion in Hank's solution, are one order of magnitude higher than those determined for the untreated alloy. Thus, the anodized samples possess a much higher corrosion resistance than the untreated ones.

A two-layer model was proposed to accurately describe the corrosion behavior of the oxidized Ti alloys. Thus, it is generally accepted that the surface film consists of a two-layer oxide, composed of a dense inner layer and a porous outer layer[76] (Figure 17.4).

The high corrosion resistance is due to the thin barrier-type inner layer, while its osseointegration ability is attributed to the porous outer layer. The significant enhancement of the polarization resistance values at longer immersion time in the physiological solution could be due to the stabilization of the barrier layer (e.g., by some sealing processes inside pores of the oxide film[77]), which might diminish the tendency of the alloy to corrosion. The nature of the porous layer depends on the nature of the alloy and the anions present in the solution.[78] The two-layer model accurately describes also the electrochemical behavior of HA coatings on Ti-6Al-4V in Ringer's physiological solution.[79]



Figure 17.4 Scheme of the two-layer model proposed for oxidized Ti alloys.

17.11 Conclusions

Surface modification is one of the ways to significantly improve the corrosion and wear resistance of Ti-based materials along with their surface texture and biocompatibility. Protective layers of different natures (oxides, HA, composites, hybrid layers, etc.) can be generated on the materials' surface by various methods such as electrooxidation, laser oxidation, and sol-gel spin coating technique.

The performance of biomaterials used for implants should be evaluated by determining their physical, chemical, and biological properties. As the materials behavior *in vivo* is a complex one, the understanding of the implant materials behavior requires joint efforts of materials science, medicine, biology, and engineering. The *in vitro* experiments should be considered only as screening tests.

References

1. Milosev I. Metallic materials for biomedical applications: laboratory and clinical studies. Pure Appl Chem 2011;83(2):309–24.
2. Mindroiu M, Pirvu C, Ion R, et al. Comparing performance of nanoarchitectures fabricated by Ti_6Al_7Nb anodizing in two kinds of electrolytes. Electrochim Acta 2010;56:193–202.
3. Acero J, Calderón J, Salmeron J, et al. The behaviour of titanium as a biomaterial: microscopy study of plates and surrounding tissues in facial osteosynthesis. J Cranio Maxill Surg 1999;27:117–23.
4. Oldani C, Dominguez Al. Titanium as a biomaterial for implants. In: Fokter S, editor. Recent advances in arthroplasty. Rijeka, Croatia: InTech; 2012; Available from: http://www.intechopen.com/books/recent-advances-in-arthroplasty/titanium-as-a-biomaterial-for-implants.
5. Das K, Balla VK, Bandyopahyay A, et al. Surface modification of laser-processed porous titanium for load-bearing implants. Scr Mater 2008;59:822–5.
6. Lee J-H, Kim H-E, Koh Y-H. Highly porous titanium (Ti) scaffolds with bioactive microporous hydroxyapatite TiO_2 hybrid coating layer. Mater Lett 2009;63:1995–8.
7. Wong MH, Cheng FT, Man HC. Laser oxidation of NiTi for improving corrosion resistance in Hank's solution. Mater Lett 2007;61:3391–4.
8. Krzakala A, Sluzalska K, Dercz G, et al. Characterization of bioactive films on a Ti-6Al-7Nb alloy. Electrochim Acta 2013;104:425–38.
9. Virtanen S, Milosev I, Gomez-Barrena E, et al. Special modes of corrosion under physiological and simulated physiological conditions. Acta Biomater 2008;4:468–76.
10. Ochsenbein A, Chai F, Winter S, et al. Osteoblast responses to different oxide coatings produced by the sol-gel process on titanium substrates. Acta Biomater 2008;4:1506–17.
11. Breme J. Titanium and titanium alloys, biomaterials of preference. Rev Metall 1989;10:625–37.
12. Yang B, Uchida M, Kim H-M, et al. Preparation of bioactive titanium metal *via* anodic oxidation treatment. Biomaterials 2004;25:1003–10.
13. W-q Yu, Qiu J, Xu L, et al. Corrosion behaviors of TiO_2 nanotube layers on titanium in Hank's solution. Biomed Mater 2009;4:1–6.
14. Brammer KS, Frandsen CJ, Jin S. TiO_2 nanotubes for bone regeneration. Trends Biotechnol 2012;30(5):315–22.
15. Oh S, Daraio C, Chen L-H, et al. Significantly accelerated osteoblast cell growth on aligned TiO_2 nanotubes. J Biomed Mater Res A 2006;78:97–103.

16. Fu T, Wu X-ming, Wu F, et al. Surface modification of NiTi alloy by sol-gel derived porous TiO_2 film. Trans Nonferrous Met Soc China 2012;22:1661–6.
17. Toth C, Szabo G, Kovacs L, et al. Titanium implants with oxidized surfaces: the background and long-term results. Smart Mater Struct 2002;11:813–8.
18. Wang D, Bierwagen GP. Sol-gel coatings for corrosion protection. Prog Org Coat 2009;64:327–38.
19. Teng S, Liang W, Li Zh, et al. Improvement of high-temperature oxidation resistance of Ti-Al-based alloy by sol-gel method. J Alloys Compd 2008;464:452–6.
20. http://hosting.umons.ac.be/php/lpsi/Dip.
21. Zhang XJ, Li Q, Zhao SY, et al. Improvement in the oxidation of γ-TiAl-based alloy by sol-gel derived Al_2O_3 film. Appl Surf Sci 2008;255:1860–4.
22. Zhang JX, Guan RF, Zhang XP. Synthesis and characterization of sol-gel hydroxyapatite coatings deposited on porous NiTi alloys. J Alloys Compd 2011;509:4643–8.
23. Zheng CY, Nie FL, Zheng YF, et al. Enhanced corrosion resistance and cellular behavior of ultrafine-grained biomedical NiTi alloy with a novel SrO-SiO_2-TiO_2 sol-gel coating. Appl Surf Sci 2011;257:5913–8.
24. http://hosting.umons.ac.be/php/lpsi/Spin.
25. Tredwin CJ, Georgiou G, Kim H-W, et al. Hydroxyapatite, fluor-hydroxyapatite and fluorapatite produced *via* the sol-gel method: bonding to titanium and scanning electron microscopy. Dent Mater 2013;29(5):521–9.
26. Wu C, Ramaswamy Y, Gale D, et al. Novel sphene coatings on Ti-6Al-4V for orthopedic implants using sol-gel method. Acta Biomater 2008;4:569–76.
27. Roest R, Latella BA, Heness G, et al. Adhesion of sol-gel derived hydroxyapatite nanocoatings on anodized pure titanium amd titanium (Ti6Al4V) alloy substrates. Surf Coat Technol 2011;205:3520–9.
28. Carrado A, Viart N. Nanocrystalline spin coated sol-gel hydroxyapatite thin films on Ti substrate: towards potential applications for implants. Solid State Sci 2010;12:1047–50.
29. Sato M, Slamovich EB, Webster TJ. Enhanced osteoblast adhesion on hydrothermally treated hydroxyapatite/titania/polya(lactide-co-glycolide) sol-gel titanium coatings. Biomaterials 2005;26:1349–57.
30. Zaveri N, McEwen GD, Karpagavalli R, et al. Biocorrosion studies of TiO_2 nanoparticle-coated Ti-6Al-4V implant in simulated biofluids. J Nanopart Res 2010;12:1609–23.
31. Montealegre MA, Castro G, Rey P, et al. Surface treatments by laser technology. Contemp Mater 2010;I–1:19–30.
32. Guillemot F, Prima F, Tokarev V, et al. Sur la biofonctionnalisation d'alliages de titane par traitement laser: Résultats et perspectives. Appl Phys A 2003;77:899–904.
33. Cui X, Kim H-M, Kawashita M, et al. Preparation of bioactive titania films on titanium metal via anodic oxidation. Dent Mater 2009;25:80–6.
34. Bayat N, Sanjabi S, Barber ZH. Improvement of corrosion resistance of NiTi sputtered thin films by anodization. Appl Surf Sci 2011;257:8493–9.
35. Milosev I, Blejan D, Varvara S, et al. Effect of anodic oxidation on the corrosion behavior of Ti-based materials in simulated physiological solution. J Appl Electrochem 2013;43:645–58.
36. Shi P, Cheng FT, Man HC. Improvement in corrosion resistance of NiTi by anodization in acetic acid. Mater Lett 2007;61:2385–8.
37. Dey T, Roy P, Fabry B, et al. Anodic mesoporous TiO_2 layer on Ti for enhanced formation of biomimetic hydroxyapatite. Acta Biomater 2011;7:1873–9.
38. Macak JM, Schmuki P. Anodic growth of self-organized anodic TiO_2 nanotubes in viscous electrolytes. Electrochim Acta 2006;52:1258–64.
39. Zwilling V, Darque-Ceretti E, Boutry-Forveille A, et al. Structure and physicochemistry of anodic oxide films on TA6V alloy. Surf Interface Anal 1999;27:629–37.

40. Ishizawa H, Ogino M. Formation and characterization of anodic titanium oxide films containing Ca and P. J Biomed Mater Res 1995;29:65–72.
41. Simka W, Krzakala A, Korotin DM, et al. Modification of a Ti-Mo alloy surface via plasma electrolytic oxidation in a solution containing calcium and phosphorus. Electrochim Acta 2013;96:180–90.
42. Yerokhin AL, Nie X, Leyland A, et al. Characterisation of oxide films produced by plasma electrolytic oxidation of a Ti–6Al–4V alloy. Surf Coat Technol 2000;130:195–206.
43. Krzakala A, Sluzalska K, Widziolek M, et al. Formation of bioactive coatings on a Ti-6Al-7Nb alloy by plasma electrolytic oxidation. Electrochim Acta 2013;104:407–24.
44. Kern P, Schwaller P, Michler J. Electrolytic deposition of titania films as interference coatings on biomedical implants: microstructure, chemistry and nano-mechanical properties. Thin Solid Films 2006;494:279–86.
45. Zhitomirski I, Gal-Or L, Kohn A, et al. Electrodeposition of Ceramic Films from Non-Aqueous and Mixed Solutions. J Mater Sci 1995;30:5307–12.
46. Huang Y, Yan Y, Pang X. Electrolytic deposition of fluorine-doped hydroxyapatite/ZrO_2 films on titanium for biomedical applications. Ceram Int 2013;39:245–53.
47. Mirhosseini N, Crouse PL, Li L, et al. Combined laser/sol-gel synthesis of calcium silicate coating were produced on Ti-6Al-4V substrates for improved cell integration. Appl Surf Sci 2007;253:7998–8002.
48. Matykina E, Hernandez-Lopez JM, Conde A, et al. Morphologies of nanostructured TiO_2 doped with F on Ti–6Al–4V alloy. Electrochim Acta 2011;56:2221–9.
49. Y-y Zhang. Tao J, Pang Y-c, Wang W, Wang T. Electrochemical deposition of hydroxyapatite coatings on titanium. Trans Nonferrous Met Soc China 2006;16:633–7.
50. Demnati I, Parco M, Grossin D, et al. Hydroxyapatite coating on titanium by a low energy plasma spraying mini-gun. Surf Coat Technol 2012;206:2346–53.
51. Quek CH, Khor KA, Cheang P. Influence of processing parameters in the plasma spraying of hydroxyapatite/Ti–6Al–4V composite coatings. J Mater Process Tech 1999;89–90:550–5.
52. Su B, Yu Zhang G, X, Wang C.. Sol-gel derived bioactive hydroxyapatite/titania composite films on Ti6A14V. J Univ Sci Technol Beijing 2006;13:469–75.
53. Kim HW, Koh YH, Li LH, et al. Hydroxyapatyte film on titanium substrate with titania buffer layer processed by sol-gel method. Biomaterials 2004;25:2533–8.
54. Yin P, Feng FF, Lei T, et al. Colloidal-sol gel derived biphasic FHA/SrHA coatings. Surf Coat Tech 2012;207:608–13.
55. Sun T, Wang M. Low temperature biomimetic formation of apatite/TiO_2 composite coatings on Ti and NiTi shape memory alloy and their characterization. Appl Surf Sci 2008;255:396–400.
56. Lin W-C, Chen C-N, Tseng T-T, et al. Micellar layer-by-layer synthesis of TiO2/Ag hybrid particles for bactericidal and photocatalytic activities. J Eur Ceram Soc 2010;30:2849–57.
57. Mentus SV, Boskovic I, Pjesic JM, et al. Tailoring the morphology and electrocatalytic properties of electrochemically formed Ag/TiO_2 composite deposits on titanium surfaces. J Serb Chem Soc 2007;72:1403–18.
58. Mai L, Wang D, Zhang S, et al. Synthesis and bactericidal ability of Ag/TiO2 composite films deposited on titanium plate. Appl Surf Sci 2010;257:974–8.
59. Roguska A, Kudelski A, Pisare MK, et al. *In situ* spectroelectrochemical SERS investigations on composite Ag/TiO2 nanotubes/Ti substrates. Surf Sci 2009;603:2820–4.
60. Kotharu V, Ngumothu R, Arumugam CB, et al. Fabrication of corrosion resistant, bioactive and antibacterial silver subtituted hydroxyapatite/titania composite coating on Cp Ti. Ceram Int 2012;38:731–40.
61. Sun T, Lee W-C, Wang M. A comparative study of apatite coating and apatite/collagen composite coating fabricated on NiTi shape memory alloy through electrochemical deposition. Mater Lett 2011;65:2575–7.

62. Hu K, Yang X-J, Cai YL, et al. Prepartion of bone-like composite coating using a modified simulated body fluid with high Ca and P concentrations. Surf Coat Technol 2006;201:1902–6.
63. Wang G, Lu Z, Liu X, et al. Nanostructured glass–ceramic coatings for orthopaedic applications. J R Soc Interface 2011;8(61):1192–204.
64. Wang C, Chen R, Deng Z, et al. Structure and properties characterization of ceramic coatings produced on Ti–6Al–4V alloy by microarc oxidation in aluminate solution. Mater Lett 2002;52:435–44.
65. Kim CS, Ducheyne P. Compositional variations in the surface and interface of calcium phosphate ceramic coatings on Ti and Ti-6Al-4V due to sintering and immersion. Biomaterials 1991;12:461–9.
66. Li SJ, Niinomi M, Akahori T, et al. Fatigue characteristics of bioactive glass-ceramic-coated Ti-29Nb-13Ta-4.6Zr for biomedical application. Biomaterials 2004;25(17):3369–78.
67. Yao Z, Jiang Z, Xin S, et al. Electrochemical impedance spectroscopy of ceramic coatings on Ti–6Al–4V by micro-plasma oxidation. Electrochim Acta 2005;50:3273–9.
68. Khan MA, Williams RL, Williams DF. Conjoint corrosion and wear in titanium alloys. Biomaterials 1999;20:765–72.
69. Kohn DH. Metals in medical applications. Curr Opin Solid State Mater Sci 1998;3:309–16.
70. Manivasagam G, Dhinasekaran D, Rajamanickam A. Biomedical implants: corrosion and its prevention-A review. Recent Patents Corr Sci 2010;2:40–54.
71. Gonzalez JEG, Mirza-Rosca JC. Study of the corrosion behavior of titanium and some of its alloys for biomedical and dental implant applications. J Electroanal Chem 1999;471:109–15.
72. Gad MMA, Mohamed KE, El-Sayed AA. Effect of molybdate ions on the corrosion behavior of Ti alloys. J Mater Sci Tech 2000;16:45–9.
73. Bundy KJ. Corrosion and other electrochemical aspects of biomaterials. Crit Rev Biomed Eng 1994;22:139–251.
74. McKnight-Hanes C, Whitford GM. Fluoride release from three glass ionomer materials and the effects of varnishing with or without finishing. Caries Res 1992;26:345–50.
75. Kulthong K, Srisung S, Boonpavanitchakul K, et al. Determination of silver nanoparticle release from antibacterial fabrics into artificial sweat. Part Fibre Toxicol 2010;7:1–8.
76. Lavos-Valereto IC, Wolynec S, Ramires I, et al. Electrochemical impedance spectroscopy characterization of passive film formed on implant Ti-6Al-7Nb alloy in Hank's solution. J Mater Sci Mater Med 2004;15:55–9.
77. Pan J, Thierry D, Leygraf C. Electrochemical impedance spectroscopy study of the passive oxide film on titanium for implant application. Electrochim Acta 1996;41:1143–53.
78. Aziz-Kerzo M, Conroy KG, Fenelon AM, et al. Electrochemical studies on the stability and corrosion resistance of titanium-based implant materials. Biomaterials 2001;22:1531–9.
79. Souto RM, Laz MM, Reis RL. Degradation characteristics of hydroxyapatite coatings on orthopaedic TiAlV in simulated physiological media investigated by electrochemical impedance spectroscopy. Biomaterials 2003;24:4213–21.

Chapter 18

Optical Sensors for Corrosion Monitoring

C.R. Zamarreño, P.J. Rivero, M. Hernaez, J. Goicoechea, I.R. Matías, F.J. Arregui

Sensor Research Laboratory, Electrical and Electronic Engineering Department, Universidad Pública de Navarra, Edif. Los Tejos, Campus Arrosadia, Pamplona, Spain

18.1 Introduction

From the carved caves in the rocks and straw huts to the high skyscrapers and offshore windmills of the last century, human beings have shaped the world for their own convenience. Although made to last, all of these structures and facilities have deteriorated in the course of the years, either damaged severely or even collapsed by adversities, sometimes unpredictable, which affect their expected lifetime severely.

The term structural health monitoring (SHM) refers to the technology developed in order to provide a way to evaluate the properties of these structures and ensure their safety, durability, serviceability, and sustainability. Therefore, SHM systems can consist of a wide number of sensors and transmission systems for an adequate data management and health diagnosis. A big effort is being done by the scientific community as well as companies attracted by the growing market in the development of

Intelligent Coatings for Corrosion Control
Copyright © 2015 Elsevier Inc. All rights reserved.

advanced sensors with high performance to monitor loads, environmental factors, and deterioration of structures for SHM.[1–4] Some of the key parameters to be monitored for SHM are temperature, humidity, acidity, salinity, UV radiation, carbonization, deformation, strain, fatigue damage, and corrosion. Among them, corrosion is one of the main problems in structures such as industrial plants as well as other types of metallic assemblies, especially those exposed to harsh environments such as oil ducts and aircrafts. Corrosion has become a main concern in the last years owing to the high repairing costs and the risks associated to the possible failure or collapse of civil structures. Given that corrosion can cause serious deterioration in structural performance, early detection and monitoring of the corrosion damage of a structure is critical.[5,6]

Concerning the important role of corrosion in SHM there is a great demand for developing nondestructive, real time, and low-cost techniques to give an early indication of corrosion in new and existing constructions with the aim of reducing both the maintenance and the risks associated with corrosion problems.[7] Optical fiber sensors (OFSs) are emerging as a superior technology capable of carrying out this purpose as well as offering other attractive performances derived from the particular characteristics of the silica, such as small size, light weight, large durability, immunity to electromagnetic fields, low losses at optical frequencies, large bandwidth, easy integration in existing and new structures, and resistance to high temperature and corrosive and hazardous environments. Besides, the easy multiplexation in wavelength and the compatibility with large distance optical communication systems enable it to perform multiple point remote measurements as well as fully distributed measures with good spatial resolution using a single optical fiber.[3,5,8–11] Because of the intrinsic interdisciplinary field of SHM, optical fibers and corrosion sensing mechanisms, researchers from a wide spectrum of disciplines, such as civil engineering, chemistry, optoelectronics, and physics, have been attracted to the study and development of OFS for corrosion detection.

This chapter examines the more recent findings in OFS for corrosion detection, highlighting some of the achievements and describing some of the challenges that remain. Some of the most typical optical fiber detection techniques are described in Section **18.2** while Section **18.3** describes some interesting applications of optical fiber sensing devices for corrosion detection in reinforced concrete structures, aircrafts, or oil pipes, among many others.

18.2 Optical Fiber Interrogation Principles

OFS consist basically of amplitude, phase, frequency, or polarization state modulations induced by the selected measure and in the light traveling through the optical fiber. OFS systems consist of a transducer, a communication channel, and an associated subsystem for generating and/or detecting, processing, and conditioning the signal. It is usually distinguished from intrinsic when the fiber acts both as

transducer and communication channel, or from extrinsic OFS when the fiber simply operates as the communication channel. Attending to the application of OFS in real-life applications, it is also possible to distinguish three different types of arrangements: localized, multiplexed, and distributed sensor systems. Some of the main optical fiber sensing configurations are reviewed in the next few paragraphs.

18.2.1 Fiber Bragg gratings

Fiber Bragg gratings (FBGs) are optical filters that allow the transmission of some wavelengths and reflect others; this is achieved by introducing a variation in the refractive index of the core of the fiber periodically along a certain length. FBGs are generally fabricated with the help of a laser by writing a periodic pattern at the core of the fiber for a short length (close to 1 cm). The reflections originated at the core due to refractive index changes in the pattern produce a back reflection at a certain wavelength known as resonant frequency.[12] Resonant wavelength can be obtained by Bragg's law from Equation (18.1):

$$\lambda B = 2 n_{\text{eff}} \Lambda \tag{18.1}$$

where λB is the resonant wavelength, n_{eff} is the effective refractive index of the fiber core, and Λ is the pitch length of the grating or period of the grating.

Thus, any change in the pitch length or refractive index will induce a shift in the resonant wavelength. Consequently, temperature, strain, cracks, or deformations of the fiber can be monitored by the corresponding resonant wavelength shift.[13]

A strong point of FBGs are their capability of multiplexing in wavelength that enable multiple point or quasi-distributed sensing. FBG sensors have been successfully developed by different companies (www.hbm.com, www.technicasa.com, www.fbgs.com), as represented in Figure 18.1, and are extensively applied in real-life applications.[3]

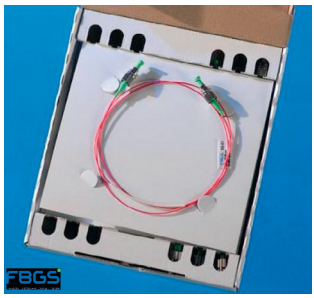


Figure 18.1 Commercial FBG sensors for strain measurements. *Courtesy of FBGS (www.fbgs.com).*

FBG sensors are usually embedded into a fiber-reinforced polymer (FRP) composite or welded to steel structures to protect the brittle optic fiber against breakage.[1] Here embedded FBG sensors should be correctly matched with the stiffness of the structural matrix in order to obtain consistent information from civil structures.

18.2.2 Interferometers

Interferometric sensors rely on phase change detections produced by the selected measurand on the light traveling through the optical waveguide. Interferometric sensors can be used in corrosion sensing applications as well. In the case of an optical fiber, the light launched into the fiber is reflected back at two different interfaces forming an interferometric cavity or etalon, as schematically represented in Figure 18.2.

The variation of the transmitted power is originated by interference between the multiple reflections of light between the two reflecting surfaces. Interference can be constructive or destructive when the transmitted beams are in-phase or out-of-phase, respectively. The phase difference (δ) for each reflection is given in Equation (18.2):

$$\delta = \frac{2\pi}{\lambda} 2n\ell \cos\theta \tag{18.2}$$

where λ is the wavelength of the light in vacuum, θ is the angle of the light traveling through the etalon, l is the thickness of the etalon, and n is the refractive index of the material that forms the cavity.[14] From Equation (18.1) phase changes in general can be given by changes either in the length, index, or geometry of the etalon. Thus, changes of the cavity parameters, which can be either passive or active, induced by the measurand modify the interference pattern and can serve as the transducer mechanism. The interference pattern can be originated using both coherent and low-coherence techniques depending on the cavity size.

Multiple groups and companies (www.roctest.com and www.fiso.com) have exploited this structure for strain, pressure, displacement, vibration, chemical, and humidity sensing, and some of their commercial devices are represented in Figure 18.2.

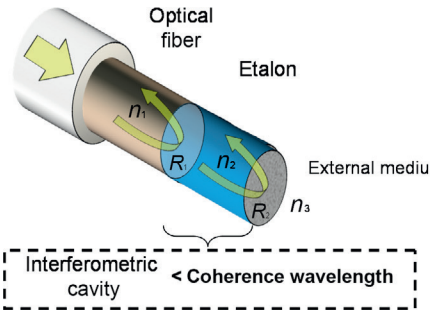


Figure 18.2 Schematic representation of an interferometric cavity at the distal end of the optical fiber where n is the refractive index of each material and R is the reflectivity of the interface between the materials.

18.2.3 Distributed sensing

Distributed measurements exploit the optical fiber as the sensing. Here, an optical pulse is launched into the fiber. Then, the light power that emerges at the launch end as a result of the linear or nonlinear effects in the fiber is time resolved in order to provide information about the state of the fiber. The collected information can be correlated with the spatial position by means of the speed of the light in the fiber as a function of distance and light. Whithin optical fiber distributed sensors, we can include from the traditional optical time domain reflectometry (OTDR) and signal processing techniques that enable to measure optical power attenuations associated with cracks, micro, and macrobends to the more recent as well as more complex nonlinear phenomena based on Raman and Brillouin scattering effects and their corresponding measurement techniques, such as Raman optical time domain reflectometry (ROTDR) or Brillouin optical time domain reflectometry (BOTDR, setup represented schematically in Figure 18.3), which are both temperature and strain dependent.[15–17]

18.2.4 Optical intensity modulations

Light intensity modulations based on the direct interaction of the measurand are a conventional method for the fabrication of OFSs. These sensors are based on the contour conditions of the total internal reflection phenomenon that occurs at the interface between two mediums, the first with high refractive index (guiding medium) and the latter with lower refractive index (reflecting medium). In the boundary of these mediums the light is totally reflected, but some part will enter through the

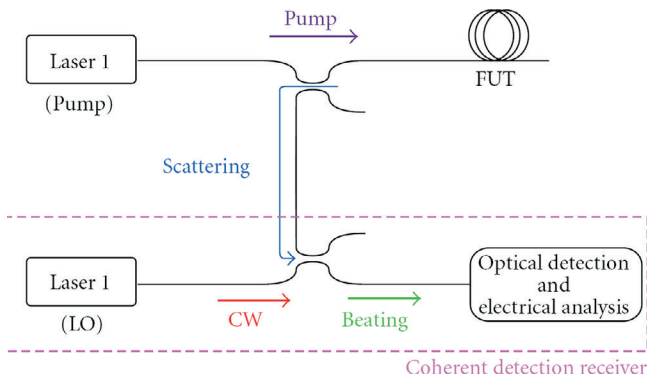


Figure 18.3 Typical configuration for a BOTDR system. FUT is the fiber under test or distributed transducer, LO is the local oscillator, and CW is the continuous wave. *Reprinted from Ref. [17] under Creative Commons License.*

low refractive index medium, which is called evanescent field. The main problem of these devices is that the light entering in the low refractive index medium will decay exponentially as a function of the penetration depth, making it paramount to come as close as possible to the guiding part in order to obtain good sensitivity. In the case of optical fibers the interaction of the evanescent field and the measurand is related to the opto-geometrical parameters of the fiber. Different configurations have been proposed in order to enhance evanescent field interaction by means of the modification of the optical fiber geometry, such as polished fibers, cladding removed fibers, chemically etched fibers, stretched fibers, microstructured fibers or D-shape fibers. Then, the detection will just resort on direct or indirect interactions of the evanescent field with the selected measurand. An example of evanescent field based OFS for pH sensing is shown in Figure 18.4.

18.2.5 Surface plasmon resonances

Surface plasmon resonance (SPR) refers to the excitation of surface plasmons (SPs), which are electromagnetic waves coupled on the surface between a metal and a dielectric medium (or air) propagated along the interface of the metal and dielectric material (or air) as it is schematically represented in Figure 18.5.

SPR devices are fabricated typically by adding a thin-metal layer (normally gold or silver) close to the optical fiber core. Consequently the evanescent field excites the SPs at the fiber core-metal layer interface. The correct coupling and SP generation strongly depend upon light wavelength, fiber parameters, fiber geometry, and metal layer properties.[18–20]

Many optical sensing systems have been developed using the SPR phenomenon thanks to the high sensitivity of the resonant wavelength to changes of refractive

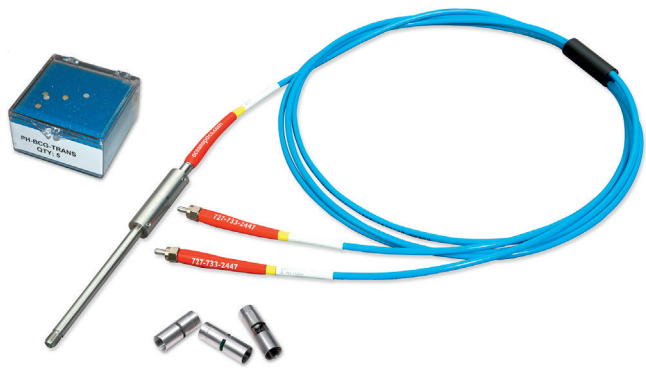


Figure 18.4 Evanescent field optical fiber pH sensor. *Courtesy of Ocean Optics (www.oceanopticssensors.com).*

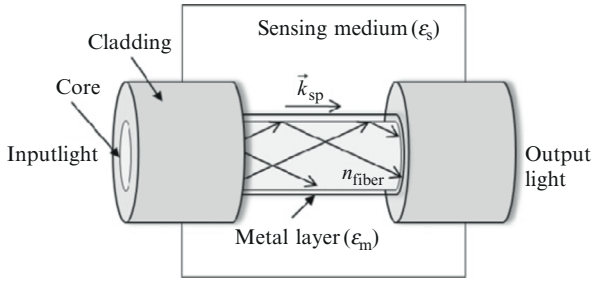


Figure 18.5 Basic structure of an optical fiber surface plasmon resonance sensor. *Reprinted from Ref. [21] with permission from Elsevier.*

index of both the metal layer and the sensing medium as well as thanks to the thickness of the metal layer and overlayer. Thus, the proper selection of sensitive thin-films enables researchers to easily obtain SPR-based devices for a wide range of applications including corrosion detection.[21,22]

18.3 Corrosion Measurements

The potential application of OFS for corrosion monitoring includes a vast field of areas, such as renewable energies, transportation, civil engineering, and oil and gas, among many others, which will be reviewed in this section.

Four basic approaches to corrosion sensing can be distinguished: direct measurement of corrosion degradation effects, measurement of corrosivity by relating the degradation of the sensor itself to the degradation of an adjacent structure, measurement of corrosion products or precursors, and measurement of environmental parameters in order to predict corrosive effects.[8,9]

18.3.1 Direct measurements of corrosion

Strain and deformation of a structure at an early stage can give valuable information about its mechanical properties and particularly the corrosion of the same. Optical fibers fully integrated into structures are able to monitor directly the initiation and progress of corrosion-induced mechanical degradation. The sensors are commonly embedded into a structure to form a novel self-strain and temperature monitoring system. The embedded sensor, due to its extremely small physical size, can provide the information at a high accuracy and resolution without influencing the dimension and mechanical properties of the structure. A common application consists of temperature and strain detection in reinforced concrete structures where cracks can be developed and propagated as a result of corrosion originating strain,

deformation, or displacements. A few works have studied FBGs strain sensors to monitor the corrosion rate in civil engineering structures at single or multiple points.[23–27] In Ref. [26] it is presented and experimentally demonstrated the utilization of a new fiber glass-reinforced polymer (FGRP) optical fiber Bragg gratings (OFBG), which is merged within the stay cable (see Figure 18.6) in bridges for corrosion detection. This work shows the importance of the optical fiber embodiment and armor in order to withstand the harsh working conditions and obtain large durability of the sensor.

Strain and deformation sensing in reinforced concrete structures has been also addressed by means of optical fiber interferometers.[28–32] In particular, the location of the sensor in Ref. [29] enables the detection of tensile strain perpendicularly to the plane of the reinforced steel bars. This configuration enables to monitor the strain or delamination associated to the longitudinal cracks along the reinforcing bars resulting from the radial expansion of the corroding rebars, particularly in those places where visual inspection is not possible. In Ref. [28] the strain response of an OFS based on white light interferometry (WLI) and FBGs is compared showing the feasibility of obtaining low-cost and stable sensors for corrosion detection. Additionally, WLI corrosion sensors (WLI-CS) were embedded in concrete and subjected to corrosion tests showing good agreements with other sensing technologies.

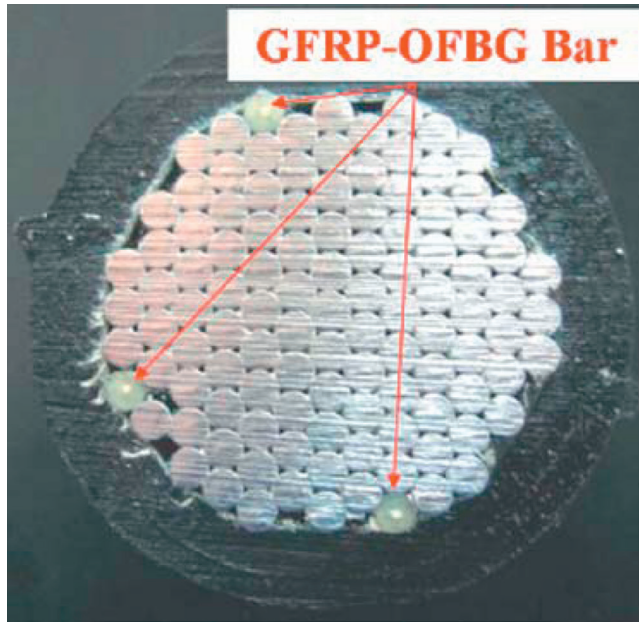


Figure 18.6 Cross-section of cable with FGRP-OFBG bars. *Reprinted from Ref. [26] with permission from Elsevier.*

OTDR techniques enable distributed sensing in order to monitor optical fiber bents associated to corrosion in structures and can be a cost-effective solution.[33] Cutting-edge detection techniques based on BOTDR enable distributed sensing of strain in steel-reinforced concrete in long-distance applications and with high spatial resolution.[34–37] A novel arrangement based on Brillouin scattering, known as fiber optic coil winding, is described in Ref. [36]. Here, the authors exploit the distributed sensing ability of the technique to directly measure the expansion strain caused by corrosion. The sensing element is quite simple and consists of winding the optical fiber around the steel rebar, as in Figure 18.7. Thus, the fiber optic will be stretched when the steel rebar expands due to corrosion and will be monitored using the BOTDR analyzer.

In Ref. [35], the authors describe a novel method in order to overcome some of the challenges of long-distance embedded optical fiber sensor (LEOFS), such as the fragility of the optical fiber or interference with construction techniques. This method employ air-blowing in order to lay the optical fiber into the preinstalled tubes and uses the vacuum grouting technique to fix the optical fiber tightly inside the tubes. Given that this technique enables LEOFS to be installed into the tubes separately, it has no interference in the construction and the sensors can be easily replaced and repaired if necessary.

Moving out from reinforced concrete structures, the degradation of civil and military airframes is a main concern because they are operating in many cases far beyond their original expected lifetime. Here, corrosion is also an important factor that can lead to material loss and cracks, which can be costly to support in terms of reparations and human lives. The role of OFS and the accurate interpretation of their signals can be crucial in order to proceed with the correct maintenance.[7] For example, in Ref. [38] it is shown the utilization of a LPG sensor to measure corrosion in aging structures as well as to avoid the temperature dependence of FGB sensors with the same characteristics, while in Ref. [39] the detection of the delamination of metals using a FGB sensor is simulated. A different application consists of corrosion monitoring in marine environments.[31] Here, the authors employ a metal-coated optical fiber that acts as a corrosion fuse that interrupts the optical fiber transmission when it is corroded, as is schematically represented in Figure 18.8.

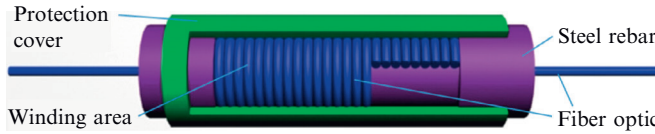


Figure 18.7 Basic packaging structure of the Brillouin corrosion expansion sensor. *Reprinted from Ref. [36] under Open Access License.*

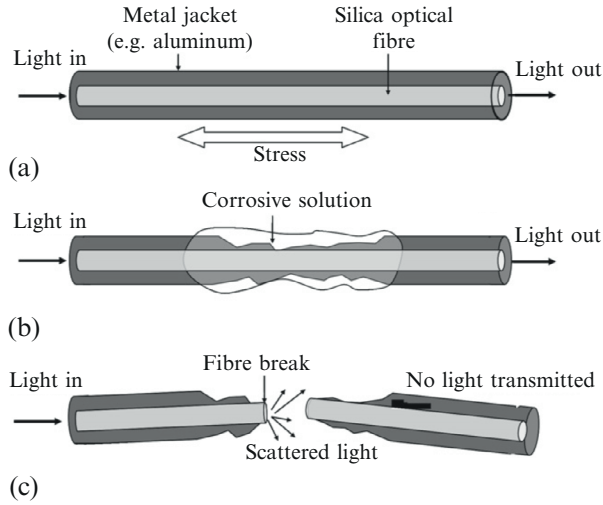


Figure 18.8 Sensing principle of stressed aluminum-coated optical fiber corrosion sensor: (a) sensor prior to exposure to corrosive solution, (b) aluminum jacket corrodes in the presence of a corrosive solution, and (c) silica fiber is exposed and sensor fiber breaks.

Apart from the mentioned continuous *in situ* corrosion monitoring structures, also described can be other devices, handhold devices, intended for discrete study and characterization of corrosion as a function of the color[40] or roughness[41–43] of the samples. Table 18.1 summarizes the characteristics and main features of the sensors described in this section.

18.3.2 Corrosivity direct measurements using metallic sacrificial layers

The sensors proposed here do not detect the corrosion of the material in a direct way. Instead, a layer made of a material similar to that which degradation is going to be monitored coats the chosen optical fiber architecture. In other words, the corrosion of the structure of interest is estimated by monitoring the corrosion of a similar material deposited onto an optical fiber. The sensors are placed near the structure that needs to be preserved. Most commonly, degradation is detected on metals using this strategy. Some examples are aluminum, steel, copper, and nickel and are of special importance in construction, civil engineering, and aeronautics. Nevertheless, some of these structures can be also applied to detect the degradation of other materials such as paintings or protective coatings.

Different optical fiber topologies have been used as corrosion detectors, from typical transmission configurations to FBGs or sensors based on SPRs. Obviously, the dynamical range of these sensors strongly depends on the thickness of the deposited

TABLE 18.1 Summary and Characteristics of OFS for Corrosion Sensing Based on Direct Measurements

Sensing Technology	Measurand	Main Features	Application	Ref.
FBG/LPG	Strain/refractive index	66/101 nm/RIU	Aircrafts	38
FBG	Disbond/ delamination	Simulations	Aircrafts	39
Etched cladding FBG	Refractive index	1 nm shift after 70 days	Steel rebars	27
FBG	Strain	Mass loss per time model	Structures	23
		Integration of fibers with steel bars	Stay cables in bridges	26
		Prestrained FBG with 3.2 nm shift range	Civil engineering	24
LPG		Corrosion rate of reinforcement steel rebar	Structures	25
Brillouin		Coil winding method	Steel-reinforced concrete	36
		Fiber-reinforced polymer cables	Stay cables in bridges	34
		Novel embedding method in concrete	Reinforced concrete	35
		Detection and location of initial cracks	Prestressed steel in reinforced concrete	37
White light interferometry	Deformation	1/100 mm resolution	Concrete structures	32
Fabry-Perot interferometer	Strain	Corrosion induced strain perpendicularly to the plane of reinforced steel bars	Reinforced concrete	29
White light interferometry		Low cost	Reinforced concrete	28
Interferometry		Distributed sensing of echoed acoustic signals	Reinforced concrete in bridges	30
Transmission		Stressed metal-coated optical fibers/corrosion fuse	Oil pipes	31

Continued

TABLE 18.1 Summary and Characteristics of OFS for Corrosion Sensing Based on Direct Measurements—cont'd

Sensing Technology	Measurand	Main Features	Application	Ref.
Optical time Domain reflectometry	Optical fiber bents	Low cost	Structures	33
Reflectometry	Color	Simple and low cost	Structures	40
Scattering	Roughness	Spatially resolved profiles	Corroded metals	42
Reflectance		Resolution of 0.1 mm	Pipe inspection	41
		Low cost device based on plastic optical fiber	Pipe inspection	43

coating. For this reason, this parameter has a crucial importance, and it has to be chosen according to the concrete application of the sensor.

One of the simplest sensing architectures applied to this kind of sensor is based on a reflection setup. The sensing device consists of an optical fiber tip perpendicularly cleaved coated by a layer of the material to be monitored. If the reflectivity of this material is high enough, most of the light sent through the fiber will be reflected and the reflected optical power will present its maximum value. As long as the coating is suffering from degradation, its thickness and the value of the reflected optical power will decrease. This way, when the coating has been completely removed from the optical fiber tip, the reflected optical power will reach its minimum value.

Some examples of this configuration can be found in Refs. [44–47] where the authors use this simple configuration to develop OTDR multipoint sensing systems devoted to the detection of aluminum and steel degradation, respectively. As an example, in Figure 18.9 the response of an array of optical fiber corrosion sensors is shown. A 200 nm-thick iron coating was sputtered onto each sensor. The sensing devices were placed at variable distances from seawater, which explains the differences in the output signal of each sensor.

Another topology widely applied in corrosion sensing is the absorption configuration. The cladding of a portion of optical fiber is replaced by a high-reflecting coating of the same material to be monitored. This way, a significant attenuation of the higher order modes is produced in this coated zone. For this reason, the transmitted optical power will be significantly lower. As the coating corrodes, the cladding around the core is removed, the absorption losses decrease, and the transmitted optical power increases.[48]

Sensors used to detect corrosion on aluminum,[49,51] copper,[52] nickel,[53,54] or steel[55,56] are present in the bibliography. These examples apply different deposition methods to create the sensitive coatings, such as sputtering, thermal evaporation, or electrodeposition, depending on the material to be deposited.

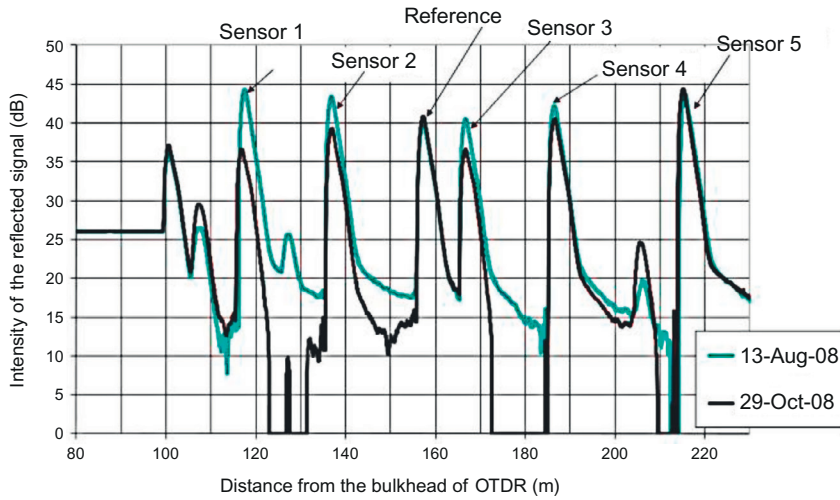


Figure 18.9 Response of an OTDR array of optical fiber steel corrosion sensors based on reflection. *Reprinted from Ref. [47] under Creative Commons License.*

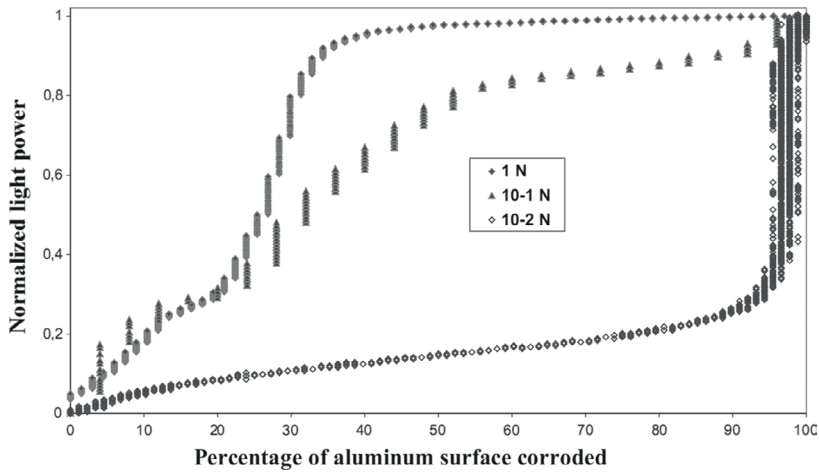


Figure 18.10 Response of an aluminum corrosion sensor based on absorption when it is subjected to different concentrations of nitric acid. *Reprinted from Ref. [49] with permission from Elsevier.*

In Ref. [49] the authors develop and characterize transmission sensors for detecting aluminum corrosion. Aluminum coatings were deposited via thermal evaporation onto the optical fiber core. For a coating thickness of 2 µm, the response of the output optical power when the sensitive zone is immersed in nitric acid (1 N, 10-1 N, and 10-2 N) is shown in Figure 18.10. It can be clearly appreciated how the transmitted

power rises as far as the aluminum layer corrodes. This rise is faster if the concentration of nitric acid is higher.

SPR OFSs have been also used to detect the corrosion of metals. Abdelmalek studied the optical properties of gold-aluminum films, using a sensor based on this phenomenon.[57] When the sensitive region is immersed in water, the SPR peak shifts slightly to higher angles of incidence due to the difference between the refractive index of water and air. After 3.5 h, the corrosion of aluminum produces an important shift of the peak and a change in its shape, as can be seen in Figure 18.11. A deeper study of this phenomenon where a combination of SPR and FBGs is applied to the fabrication of corrosion sensors can be found in Ref. [58].

Some other authors have taken advantage of the sensitivity of FBGs to strain by developing optical fiber corrosion sensors.[59,60] In 1996, Green et al. proposed corrosion sensors based on prestrained short-period gratings and LPGs.[61]

Decades later, Hu et al. developed an FBG sensor for steel corrosion monitoring.[62] In particular, a steel sensing film of 12-15 µm thick is electroplated on the surface of the FBG. When this film is corroded, it suffers a longitudinal change that causes the strain of the FBG. Consequently, the optical output of the FBG will experience a wavelength shift that can be detected with a spectrometer. As FBG are also sensitive to temperature, an FBG without steel coating is used as reference. In order to induce accelerated corrosion of the film, sensors are immersed into NaCl solutions (0.5 M). In Figure 18.12, the shift of the FBG peak during an 18-day experiment is shown.

One main peak can be observed in the spectrum of the sensor before being introduced into the NaCl solution. This peak shifts to a higher wavelength 4 days later. Eight days after the immersion, multiple peaks are observed, and, finally, after 18 days in the cabinet, they merge into one major peak. The authors conclude that

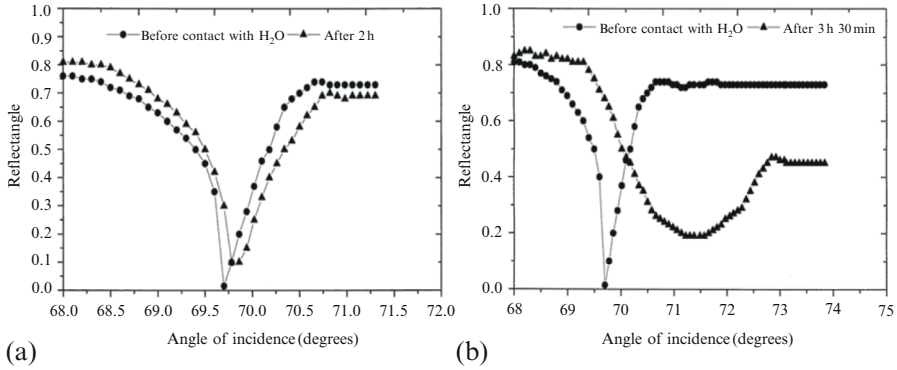


Figure 18.11 Shift and shape change of the SPR when the aluminum layer is corroded after (a) 2 h and (b) 3 h 30 min. *Reprinted from Ref. [57] with permission from Elsevier.*

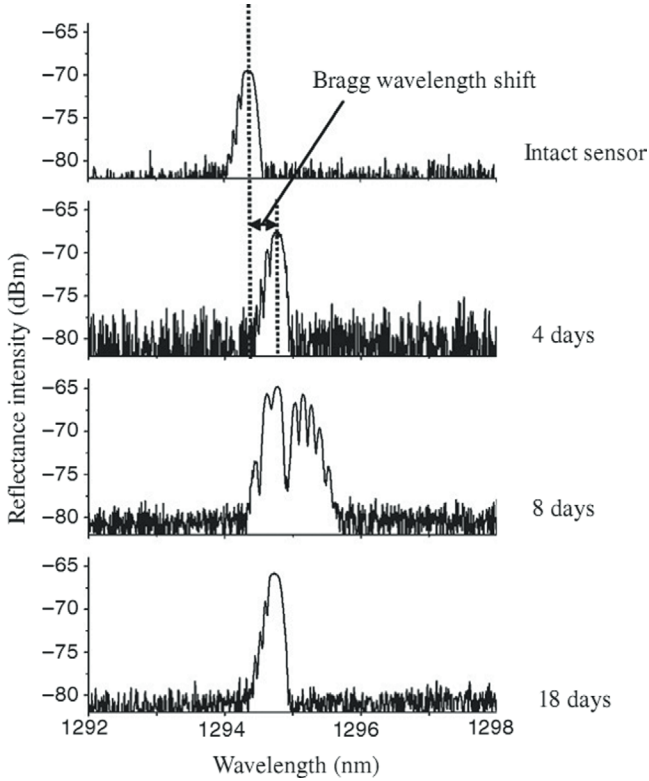


Figure 18.12 Bragg wavelength shift at different moments during an 18-day experiment. *Reprinted from Ref. [62] with permission from Elsevier.*

the multiple peaks are related to nonuniform strain and, consequently, can be used as a critical signal of the intense corrosion of the steel.

There are other examples of OFSs for indirect corrosion monitoring, but those presented here are the most representative. A summary with the main features of the approaches reviewed in this section is given in Table 18.2.

18.3.3 Measurement of Corrosion Products and Precursors

The detection of corrosion precursors and by-products derived from progressive deterioration can be perfectly monitored when a proper coating is deposited onto an optical fiber. The results obtained can help the engineer to make a final decision about the need for preventive maintenance or premature replacement of the structure. In Figure 18.13, a scheme about the chemical elements of analysis (precursors and by-products) is shown using embedded optical fibers in order to help ensure the safety of the structure.

TABLE 18.2 Summary and Characteristics of OFS for Corrosion Sensing Based on Indirect Measurements

Sensing Technology	Sensing Material	Coating Fabrication Method	Ref.
Reflection+OTDR	Al	Evaporation	44,45
Intensity		Thermal evaporation	48,49
		Sputtering	50,51,63
SPR	Au-Al	PVD/Evaporation	57,58
Reflection	Ni	Evaporation	64
Transmission Attenuation		Electroless	53,54,65
OTDR	Steel	Sputtering	47,66,67
Intensity		Evaporation	55,56
FBG		Electroplating	55,56,65,68
			62
		Sputtering	59,60
Intensity	Cu	Electroless	49,52
FBG		Evaporation	62

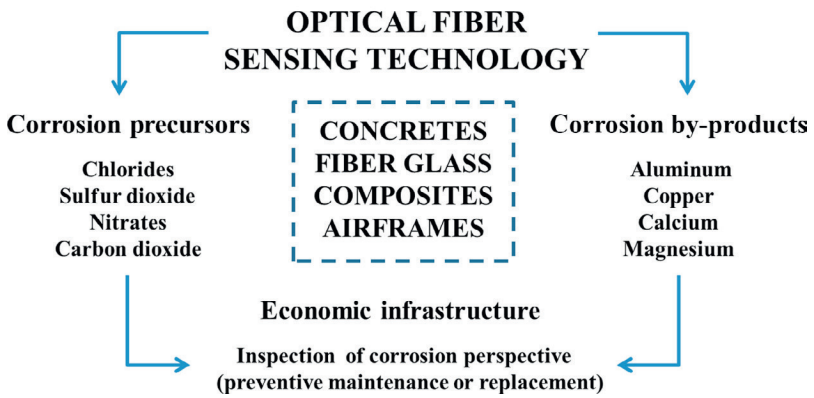


Figure 18.13 Scope of the optical fiber technology to detect corrosion precursors and by-products derived in terms of chemical analysis.

18.3.3.1 Detection of corrosion precursors

The ingress of harmful ions such as carbon dioxide, nitrate, sulfur dioxide, or chloride has a deteriorating impact on the performance of engineering materials because the ions are capable of inducing a higher corrosion rate, compromising the integrity of the structure.[6] However, not only these ions can accelerate the corrosion process, but also the presence of microorganisms, such as sulfate-reducing bacteria (SRB), which can have an important role in localized corrosion.[69] Of all these, the waterborne chlorides are one of the most influential factors in the rapid development of the corrosion. Their presence can be due to the use of deicing salts on roadways or bridges to lower the melting point of the ice, during which process some of these salts react with the H_2O that transports the chloride into cracks near metal.[70,71] Several studies have reported that the rate of corrosion strongly depends on the amount of chlorides present within the structure. Once chloride ion penetration occurs, active corrosion is initiated with a sequence of events such as cracking and spalling.[72] The process is slow and complex as a function of the involved materials and environmental variables. An interesting aspect is that the corrosion process is accelerated in marine places in comparison with other environments such as inland structures due to the higher presence of chloride ions in coastal areas.

In order to detect chloride ion penetration in concretes, the usual methods are based on a chemical analysis in an external laboratory. However, this analysis shows inherent limitations, such as being destructive and expensive, and do not provide continuous information in real time because it is necessary to collect the sample and a further analysis to know the chloride content. To overcome these limitations, the use of optical fiber as a nondestructive technique allows us to obtain the information *in situ* with high accuracy through remote measurements and to control the state of the structure.[3] Once optical fibers are embedded in a concrete structure, most of the sensing schemes to detect corrosion are based on a spectroscopic analysis of the surface of the material in which light signals are reflected from both corroded and uncorroded areas. A relevant study is reported in Refs. [11,10], where the use of a twin-fiber technique (separate transmit and receive fibers) can determine the presence of corrosion via color modulation of the broadband input signal. However, this spectroscopic technique is based on a local inspection of the corrosion area due to a color shift, but it is not possible to estimate the chloride ion concentration present in the final structure.

An interesting approach is proposed in Ref. [73], where an absorbance-based sensor is developed to monitor the chemical interaction of silver nitrate-fluorescein-chloride mixture, which results in a red coloration. The end of an optical fiber is coated by a solid net that contains the mixture of fluorescein and silver nitrate. If the chloride ions penetrate this net, a colorimetric change is immediately observed. The range of chloride detection is from 0 to 40 mM, and higher values of absorbance

correspond to the higher values of chloride concentration. However, all the measurements are made in a short period of time after the addition of chloride, a critical parameter in the development of the sensor. The absorption peak is located in the 500 nm region and can be perfectly measured with blue or green laser diodes. The signal remains stable for the first 10 minutes, but a higher period of time results in a total precipitation. In addition, once the chemical interaction has occurred, the process is completely irreversible.

According to the previous results, it is necessary to implement an optical sensor more attractive in terms of reversibility and time dependence in order to detect the chloride concentration. The use of a fluorescence-based sensor combined with optical fiber is one of the most promising alternatives.[74,75] In these cases, the sensors are based on fluorescence quenching, by which the excited reagent is deenergized by nonradioactive collision with the molecules of the analyte (halide ions). The collisional quenching is a reversible process whereby the emitted fluorescence intensity decreases linearly when the quencher concentration is increased. This process can be described by the Stern-Volmer equation:

$$\frac{I_F^o}{I_F} = 1 + K_{SV}[Q]$$

I_F^o, fluorescence intensity in the absence of quencher; I_F, fluorescence intensity in the presence of quencher; $[Q]$, quencher concentration; K_{SV}, diffusion dependent Stern-Volmer constant.

The extinction mechanism is composed of a contact between the excited state of the fluorescent specie (dye) and the quencher (chloride), as can be observed in Figure 18.14.

First experiments with fluorescence-based sensors to detect chloride concentration were reported in Refs. [73,74], where the use of two different quinoline derivatives dyes (ABQ and MEQ) is presented. The results indicate that ABQ displays higher fluorescence efficiency than MEQ. The next steps were a further immobilization of both dyes in a microporous silica coating using the sol-gel technique, and then the coating of a declad optical fiber. The desired configuration for *in situ* chloride detection was an evanescent wave excited coating. However, once the sol-gel coating was applied onto the optical fiber, no fluorescence signal was detected. The main reason could be because smaller analyte molecules (chloride) can penetrate the microenvironment of the sol-gel matrix; as a result, no interaction between anlayte and dye was observed. Different sol-gel formulations at different pH values were investigated, but none was successfully proved as an evanescent-wave sensor.

An interesting approach using an optical fiber combined with luminescence measurements for free chloride ion detection in concrete is presented in Ref. [75]. In this case, the use of a new fluorophore, known as lucigenin, is of great interest because it has a higher quenching sensitivity than other products and its Stern-Volmer's

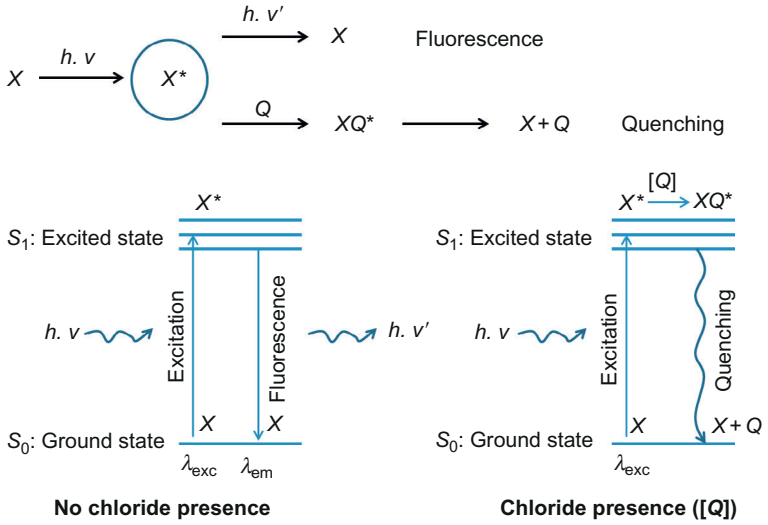


Figure 18.14 Scheme of both fluorescence and fluorescence quenching mechanisms as a function of the presence of chloride ions (analyte).

constant (K_{SV}) is the highest for chlorine indicators. Here, a sol-gel method was also chosen to encapsulate the dye into a polymeric matrix at the end of the optode. The term optode refers to detectors that are transducers between the measured quantity and optical fibers. The optical design of the sensor is shown in Figure 18.15, where the four elements of the fluorescence system are present (an excitation source, indicator for the analyte detection, wavelength filters, and the detector). In addition, multimode optical fibers are used to connect the emission module to the optical probe (optode).Two experimental tests, hot maritime climate and cold continental climate, were performed in a controlled environment to determine the chloride content. The results can detect free chloride concentration between 30 and 350 mM with a good reproducibility and a good stability.

Other optical fiber based techniques have also been reported[76,78] for chloride detection, which do not require expensive optical sources or detection systems as was previously thought in the fluorescence-based sensors. Of these, the use of long period grating pair (LPGP)[79] is of great interest because small quantities of chloride ions in NaCl solutions can be detected (10 ppm). In addition, the results reveal that through monitoring the induced wavelength shift, the LPGP could reach a better precision (over six times) than single LPG when changes in the refractive index of the surrounding medium were monitored. This high sensitivity makes possible the use of LPGP in early stage monitoring for corrosion of materials in both the marine environment and for salt sprays used for deicing road surfaces in cold climates.

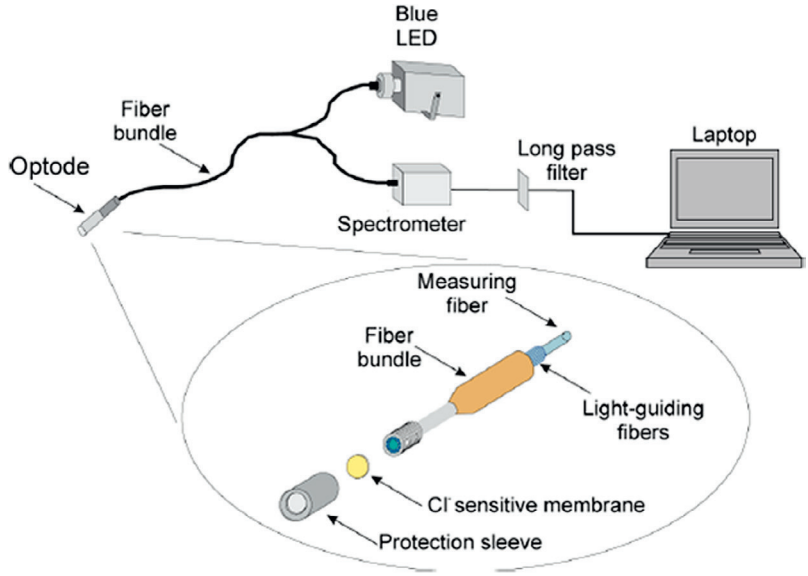


Figure 18.15 Instrumental setup to determine ion chloride. *Reprinted from Ref. [75] with permission from © IOP Publishing. All rights reserved.*

18.3.3.2 Detection of corrosion by-products

In this section, the design of OFSs to detect the presence of corrosion by-products is shown. More specifically, different optical fiber approaches are presented to detect the release of metal ions when the corrosion process is active. This release corresponds to divalent (Ca^{2+}, Cu^{2+}, Mg^{2+}) as well as trivalent (Al^{3+}) ions that are the most used in alloys and whose monitoring can determine the health status of the structure.

The mostly optical fiber corrosion sensors are based on the variation of an optical signal when a metalized optical fiber core is immersed in corrosive solutions. Different techniques are used to metalize the fiber core, and a change in the light transmission of the waveguide is observed when the metal is corroded.[49,52,54,55] The degradation of this metallic film is correlated with the degradation of the final structure. An interesting approach is presented by Refs. [80,81] in where an optical fiber Fourier transform infrared (FT-IR) evanescent wave absorption spectroscopy is used to detect aluminum hydroxide $Al(OH)_3$, one of the most principal corrosion products of the aluminum alloys. However, no information about concentration of this corrosion product is shown.

The first studies to determine the presence and concentration of corrosion by-products are based on the use of LPG chemical sensors in inaccessible regions of aircraft.[82,83] A chelating polymer coating is deposited onto the surface of the LPG, which has an affinity to divalent metal ions (Cu^{2+}). Once metal ions are present, a

chemical crosslink between the metallic ions and the chelating polymer is observed, forming an increase of the polymer density that results in an increase in the refractive index at the surface of the fiber. The principle of the sensor operation is that light traveling through the optical fiber will be scattered out of the grating at different optical wavelengths when the refractive index of the coating is changed due to the presence of the target molecule absorption (metal ions). In fact, a shift in the wavelength of the spectral loss peak is observed when the LPG metal ion sensor is exposed to $CuSO_4$ solution, and then, after washing with DI water, this shift do not come back to the original wavelength position, indicating that a chemical crosslink between the ions and the chelating polymer has been observed. In addition, the response of this LPG sensor is a function of the cation concentration (Cu^{2+}) where a shift in the spectral loss peak wavelength is increased with Cu^{2+} concentration in a range of 0.5-5 mM. The minimum detection level of the LPG metal ion sensor corresponds to 32 ppm.

The use of fluorescent fiber optic sensors as it was used to detect chloride ions also makes possible the detection of aluminum cations from an early stage of the corrosion process. However, the sensing mechanism used in the detection of these specific ions is based on fluorescence emission and not the quenching process. A novel method for sensing the corrosion of aluminum alloys is reported in Ref. [84], where an indicator, known as 8-hydroxyquinoline (8-HQ), forms a fluorescent metal-ion complex with aluminum, known as Tris(8-hydroxyquinolyl) aluminum (Alq3).[85] In addition, 8-HQ is insoluble in water with the advantage of eliminating the problem of leaching of the fluorophore by water. The end of an optical fiber was coated with a polymeric porous matrix (3-PEG/PU) that contains the indicator, and a fluorescent signal was detected when aluminum ions were in contact with the dye. However, several limitations of the 3-PEG/PU polymeric system, including swelling or health hazards associated to the cross-linker used (isocyanate), indicate the need of exploring safer alternatives to encapsulate the dye.

An interesting approach focused on the detection of by-products of the corrosion aluminum alloys is presented in Ref. [86], using both 8-HQ and MNIP (molecularly non-imprinted polymer), which is a polymer with a chemical affinity for the ions without the need of being previously synthesized in the presence of the mentioned ion. The results show that the optical sensor has an adequate sensitivity to the aluminum ions and its detection is not influenced by the presence of other by-products of the corrosion process, such as Ca^{2+}, Na^{+}, Mg^{2+}, and Cu^{2+}. More specifically, Ca^{2+} and Mg^{2+} induce fluorescence of the MNIP, whereas Na^{+} and Cu^{2+} ions do not show fluorescence behavior. In addition, the higher intensity of the Al^{3+} fluorescence peak allows its detection and the separation of the contribution from other ions (Ca^{2+} or Mg^{2+}). An important consideration is that the MNIP should have enough available sites for the bonding of Al^{3+} ions for a successful detection, and these sites should not be fully occupied by other sensitivity fluorescence ions (Ca^{2+} or Mg^{2+}). However, emission spectra evolution indicates that the presence of Al^{3+} ions can be perfectly

detected, even if the MNIP was exposed to the other by-products. The limit of aluminum ion concentration is 10-4 M, showing an increase of the fluorescence intensity with higher aluminum concentrations. Similar results are presented in Ref. [87] with a linear concentration range of Al^{3+} between 0.5 and 5.0 mM, using a fluorescent dye morin immobilized on the fiber's distal end.

In all the previous experiments, the optical sensor has to be in close proximity to the corrosion affected area in order to detect the presence of corrosion by-products. To overcome this limitation, the development of a novel method to measure aluminum ions released in aluminum alloy corrosion is presented.[88] Here, an exposed-core microstructured optical fiber (MOF) is reported that has a micron-scaled core and several holes in the transverse cross-section to confine light by reducing the effective refractive index of the cladding. The sensor is fabricated using a glass extrusion process and chemical etching, respectively. This specific design allows a better evanescent field interaction and greater fluorescence than can be achieved with other conventional fibers. In this case, the selection of a fluorophore, known as lumogallion, which acts in acidic conditions, is of great interest because corrosive environments tends to reduce the pH of the surrounding medium. The results indicate that the detection limit is ~200 nM with a linear response from 500 nM to 20 μM to aluminum ions.

To conclude this section, Table 18.3 summarizes the published works on corrosion precursors or by-products sensors with their respective sensing mechanisms and interesting observations for each one.

18.3.4 Relative humidity monitoring for corrosion control

Presence of water is one of the most frequent causes of infrastructure deterioration. Water acts as a transporter for aggressive agents, such as chloride or sulfate ions. In addition, water is a reaction medium in some destructive chemical processes. In general, water plays a key role in the processes of corrosion. For this reason, it is of great importance to implement sensing tools to allow the early detection of the humidity in order to avoid the structures damage and the presence of water, which will remediate the situation before the damage to the structures is produced.

A huge number of optical fiber humidity sensors can be found in the bibliography.[89,90] Several optical fiber topologies have been applied for the fabrication of these devices, such LPGs, FBGs, sensors based on evanescent field, sensors based on lossy mode resonances (LMR), and interferometers.[91–99] An important part of these devices have been specifically designed for early corrosion detection.[100–106] Some examples are presented in this section.

Mendoza et al. developed a distributed optical system for detecting humidity and pH changes in aircraft joints.[102,103] This system consists of optical fiber pH and humidity sensors based on the evanescent field. The fabrication of the humidity sensors involved the doping of the optical fiber permeable polymer cladding with a solvatochromic reagent. The color of this indicator strongly depends on the presence of

TABLE 18.3 Summary and Main Characteristics of Optical Fiber Corrosion Sensors Based on the Detection of Corrosion Precursors and By-Products

Sensing Technology	Analyte	Main Features	Ref.
Absorbance	Chloride	Formation of a red precipitate	73
		Irreversible process	
		Precipitation	
Fluorescence quenching		Dye: Quinoline derivatives (ABQ, MEQ)	74
		No measurements	
		pH dependence sol-gel matrix	
		Dye: Lucigenin	75
		Detection: 30-350 mM	
		Simulation tests (hot maritime and cold continental climate)	
LPGP transmission		Monitoring refractive index	76–78
		Detection of small quantities of chloride ions (10 ppm)	
	Copper	Monitoring refractive index	82,83
		Range detection: 0.5-5 mM	
		Minimum detection level: 32 ppm	
Fluorescence emission	Aluminum	Dye: 8-hydroxyquinoline (8-HQ)	86
	Calcium	Polymeric matrix: MNIP	
	Magnesium	Detection limit of 10^{-4} M	
	Aluminum	Dye: 8-hydroxyquinoline (8-HQ)	84
		Limitations of matrix 3-PEG/PU	
		Dye: Morin	87
		Linear range: 0.5-5.0 mM	
		Dye: Lumogallion	88
		Linear range: 500 nM-20 µM	
		Detection limit: 200 nM	

humidity in the ambient. When the humidity increase, the dye absorbs at a different wavelength, and, consequently, the fiber loss will depend on the humidity percentage. This way, a difference of more than 1 dB (at a wavelength of 1300 nm) can be appreciated between the attenuation due to the evanescent field when the sensor is placed in a wet medium and the same magnitude when it is in a dry medium.

In Ref. [106], the authors fabricate an OFS based on a LPG. First of all, they inscribed the gratings by focused beam of CO_2 laser onto single mode fibers with core and cladding diameters of 8.2 and 125 μm, respectively. Once the LPG was ready, they deposited a nanocoating made of polyallylamine hydrochloride (PAH), polyacrylic acid (PAA) poly-sodium 4-stirenesulfonate (PSS), and alumina (Al_2O_3) by using the LbL technique. According to the authors, the purpose of the PAH/PAA nanofilm is to increase the sensitivity of the sensor, while the Al_2O_3/PSS nanofilm increases the water absorption. The response of the coated LPG when it is subjected to relative humidity variations from 20% to 90% is shown in Figure 18.16a. A double effect can be distinguished. On one hand, the resonance shifts to the left, showing a change of 3.6 nm. On the other hand, an intensity variation of 6.978 dBm is appreciated. Both responses are more clearly shown in Figure 18.16b.

These data suppose a wavelength sensitivity of 0.051 nm/%RH and an intensity sensitivity of 0.099 dBm/%RH. In addition, this optical fiber humidity sensor showed a small dependence to temperature changes, what make it suitable for implementation of concrete structures health monitoring.

Other optical fiber humidity sensors designed for corrosion control are summarized in Table 18.4.

18.3.5 Optical pH sensors for corrosion control

Among other physical and chemical conditions, such as moisture (see Section 18.3.4) or chloride ions concentration (see Section **18.3.3**), the pH of a medium is a parameter that is altered when corrosion occurs. Therefore it is very important to have information about the stability of the pH of the medium in which corrosion may occur as long as it can provide an early warning signal prior to the massive degradation of the metallic structure, and it may be possible to take predictive maintenance actions.

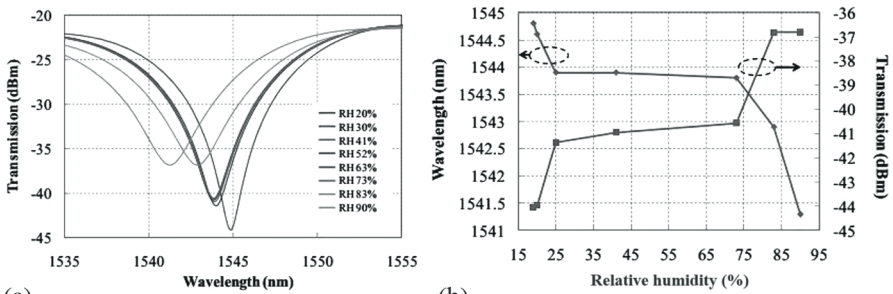


Figure 18.16 (a) Transmission spectra of the coated LPG for a RH variation from 20% to 90%, and (b) dependence of LPG resonance wavelength and intensity on RH. *Reprinted from Ref. [106] with permission from SPIE.*

TABLE 18.4 Summary and Main Characteristics of Optical Fiber Corrosion Sensors Based on the Detection of Humidity

Sensing Technology	Sensing Material	Coating Fabrication Method	Ref.
LPG	PAH/PAA+Al_2O_3/PSS	LbL	106
	PEO	Polymerization	38,61,82
FBG	Hydrophilic medium	-	93
Evanescent field	Solvatochromic reagent	Diffusion	102,103
Evanescent field (POF)	HEC/PVDF	Dip-coating	107
	$CoCl_2$/PVA—pullulan	-	108

It has been demonstrated that acidic pH conditions below pH 9 can damage the steel structures, and therefore long-term monitoring of pH values in the range of 9-13 with a resolution of about 0.5 pH units can be very useful for early detection of potential corrosion condition.[8]

The most common approaches to optical pH sensing are based on a primary transducting material which transforms the pH of the analyzed medium into a useable optical signal that can be collected using an optical fiber. Basically it is possible to differentiate two main approaches regarding the optical phenomena underneath the chemical-optical transduction: fluorescence-based sensors and colorimetric sensors.

This last group involves probably the most straightforward method to get optical information from the pH of a medium because there are many pH indicators traditionally used in acid-base titration. Nevertheless, other fluorescence-based approaches for optical fiber pH sensing for corrosion detection can be found. In a basic OFS configuration, the colorimetric or the fluorescent dyes are immobilized into a proton permeable membrane and the changes of their UV-VIS spectra or fluorescence emission can be monitorized using an optical fiber or an optical fiber bundle. Some authors have reported different immobilization media for creating the sensitive areas such as polyurethanes,[109–111] hydrogels,[112,113] and celluloses.[114–116] But one of the most used immobilization media are the sol-gel matrices [117–120] because they are fully inorganic matrices, mechanically robust, optically transparent, and permeable to H^+ and OH^- ions.[117]

All those matrix materials can be used to place the pH indicators or fluorophores within the light path of a measuring optical system, and therefore any optical change in the indicators can be registered. This region where the indicators interact with the external medium and at the same time with the light conducted by the optical fiber is often called sensitive region, or sensitive coating (or chamber), depending on the particular application. The configuration of this sensitive region is not always the

same, and it strongly depends on the nature of the indicator (colorimetric or fluorescent). When fluorescent indicators are used it is very important to maximize the collection of the emitted fluorescent signal and at the same time minimize coupling of the excitation light as it can mask the fluorescence signal at the detector. This is shown in Figure 18.17a and B, where the excitation light interacts with the fluorescent material, and passes through it, reflecting back only in a small proportion. The emitted fluorescent light is emitted in all directions, and some of this emission will be collected by the optical fiber and further analyzed. Figure 18.17C shows an alternative transmission setup arranged in a U-bend typically used with colorimetric indicators. In such configuration white light can be used as excitation for the sensor, and the transmitted light is guided towards the detector (spectrometer). Changes in the UV-VIS absorption spectrum will give information about the pH of the colorimetric indicator immobilized into the sample chamber. Other simpler approaches can be used replacing the white light source and the spectrometer by LEDs and simple photodetectors [121] to achieve information only at the sensitive bands of the colorimetric indicators.

One of the most robust optical approaches for civil engineering applications is a reflection setup using a multiple fiber optode.[122] As it is shown in Figure 18.18, those fiber bundles use a complex structure of peripheral optical fibers to maximize

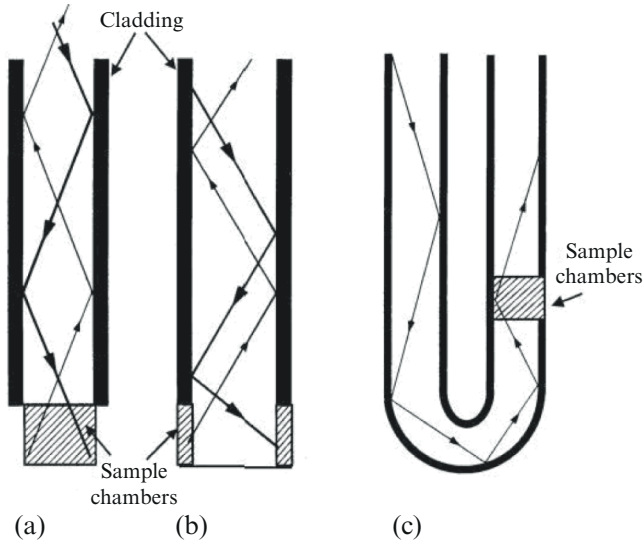


Figure 18.17 Schematic representation of various sample chamber locations on the optical fibers. The probe cladding is indicated by the darkened area. (a) and (b) show a typical fluorescent probe while (c) shows a typical absorbance sensor located within the path of the fiber at the side of the probe. Fluorescent sensors may also be located in this position because fluorescent light is emitted in all directions. *Reprinted from Ref. [138] with permission from Elsevier.*

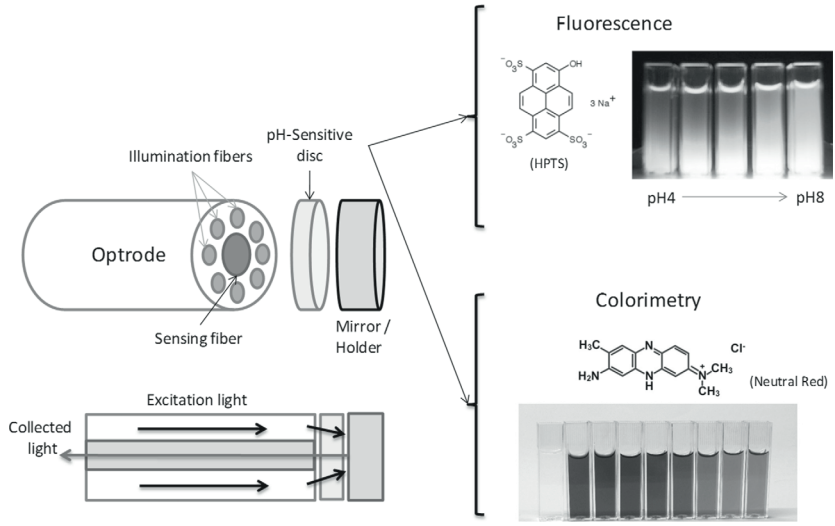


Figure 18.18 pH multiple fiber optode. Depending on which indicator is immobilized into the pH-sensitive disc, it is possible to make fluorescence or colorimetric-based measurements.

the amount of illumination light (excitation), and a central optical fiber to collect the reflected optical spectrum.

Habel and coworkers have developed colorimetric dye-based pH optodes and have successfully measured pH *in situ* a steel-reinforced concrete structure for more than 6 years installed in cooling towers of a power plant.[8] They have used multi-wavelength measurements that give ratiometric information about the acid-basic state of the pH indicator, which is more robust to optical power fluctuations or even signals to the detector. The colorimetric or fluorescent indicator is immobilized into a disc-shaped matrix (polymeric, sol-gel, etc.), where optical properties are altered by the pH of the external medium. When fluorescent indicators are used the peripheral optical fibers excite the fluorescence in the sensitive disc and only a small portion of this excitation optical power is collected by the central interrogation fiber. As the fluorescence is emitted omnidirectionally, this signal can be collected and analyzed at the detector. When colorimetric indicators are used, the optode ends with a mirror that focuses back the transmitted light into the central sensing fiber, keeping the information of the optical absorption of the dyed disc. Such optical fiber bundles have become a very robust choice for pH optical sensing[8] and some of them are commercially available.[123] It has been observed than the most serious attacks concerning stability of pH-sensitive membrane occurred in the first few months.[8] In Figure 18.19 a real application of pH colorimetric optodes is shown. The optical pH sensors are



Figure 18.19 Picture of a real application of pH optodes into a steel-reinforced concrete. These sensors use a colorimetric approach, and they were embedded into a cooling tower in a power plant. *Reprinted from Ref. [8] with permission from Springer.*

immobilized close to the steel structure prior to the concrete pouring during the construction of a cooling tower of a power plant. The color (pH) of the sensitive elements could be monitored remotely for more than 6 years.

Other researchers have proposed alternative colorimetric pH-sensitive dyed matrices. For example, Carmona and coworkers have proposed a colorimetric approach for monitoring the acidity in historic monuments and prevent the stone degradation.[119] In their work they propose a sensitive coating using Chlorophenol Red integrated into an inorganic silica matrix fabricated using the sol-gel technique. Figure 18.20 shows the chemical change in the pH colorimetric indicator, and the change in the absorption spectrum of the sensitive coating as pH is varied in a Kesternich chamber.

Alternatively use of fluorescence-based optical pH sensors is commonplace because fluorescent labeling is a widely used tool in biology and medicine to study tissues of even intracellular mechanisms. Consequently there is very wide knowledge of the fluorophores and the techniques for immobilizing them into substrates, and it is possible to find in the literature a lot of fluorescent-based optical fiber pH sensors[124,125] for applications such as ammonia sensing,[126,127] CO_2 monitoring,[128–131] or oxygen detection.[132,133] Nevertheless the implementation of fluorescent OFSs in civil engineering has fewer applications than do other scientific disciplines. The main drawbacks of fluorescence-based pH sensors in civil or industrial engineering

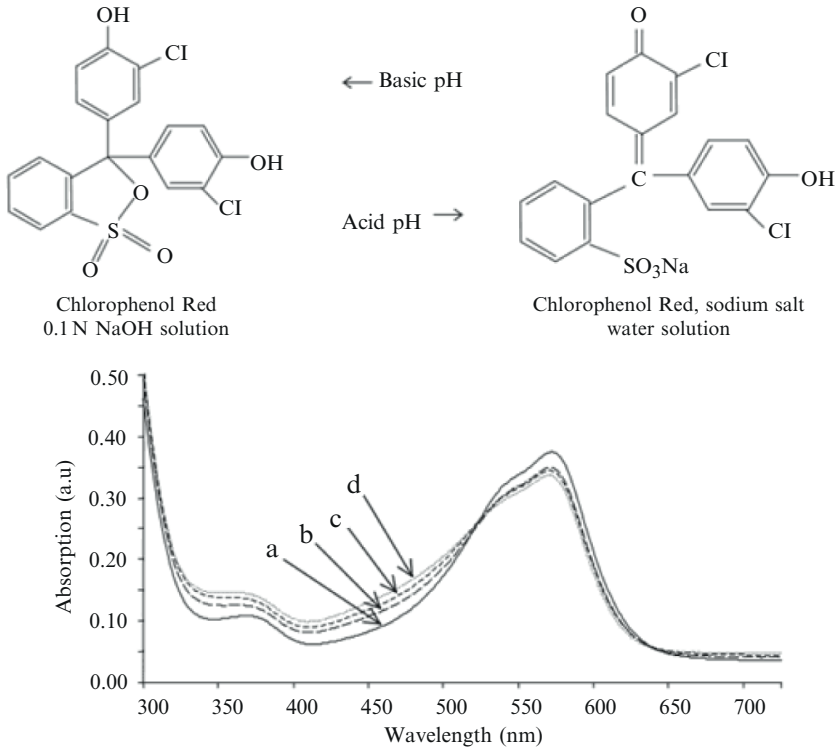


Figure 18.20 Evolution of the optical absorption of the Chlorophenol Red dye as the pH is decreased into a Kesternich chamber. All coatings were initially submitted to basic buffered solution (pH 10), exposed to different SO_2 concentrations: (a) 0 ppm, (b) 10 ppm, (c) 20 ppm, and (d) 50 ppm. *Reprinted from Ref. [119] with permission from Elsevier.*

environments are the higher degradation rates in fluorescence dyes compared to colorimetric ones in harsh environments and the high attenuation of the optical fiber at the typical excitation wavelengths that strongly limits the distance of the optode from the excitation light source.

Nevertheless, some authors have proposed alternative approaches for metal corrosion detection and characterization using the variation of fluorescence to detect the local changes in pH. Some researchers have used fluorescence microscopy to study and characterize the corrosion mechanisms in the surface or interfaces of metals.[134–136] Alternatively Walt and coworkers present an interesting fiber optic sensor tip that can easily get images from a surface.[137] In this case an optical fiber bundle is placed very close to the observed surface (see Figure 18.21). Each optical fiber collects the emitted light of a small portion of surface, acting as a single pixel of an image, so it is possible to reconstruct the fluorescence of the emitted surface with

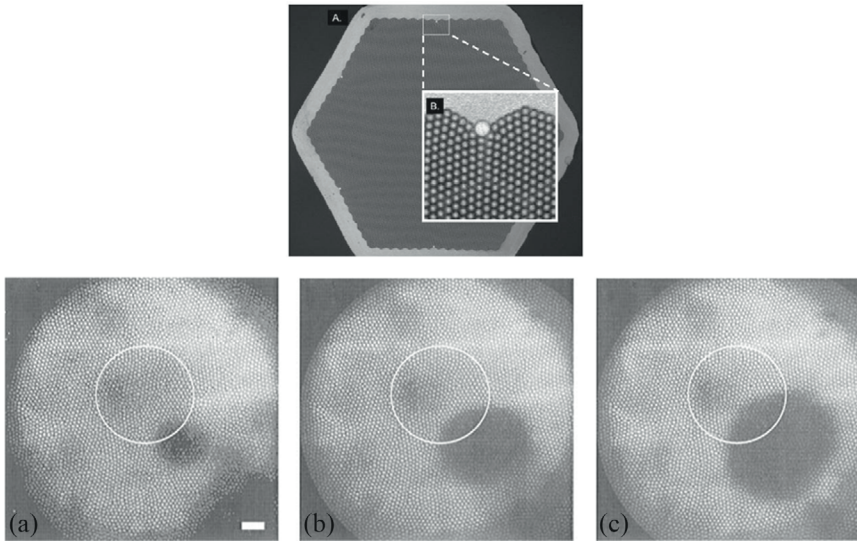


Figure 18.21 In the upper image there is a view of the multifiber optode used for imaging. Reprinted with permission from Ref. [139]. Copyright (1997) American Chemical Society. In the bottom pictures, it is possible to see three different stages of the corrosion of an aluminum-clad copper wire. (a) 30 s, (b) 7 min, and (c) 17 min of exposure to a phosphate buffer solution (pH 6.2, 0.1 M KCl). The dark region denotes that the fluorescence is being quenched due to local pH decreasing as corrosion occurs. *Reproduced from Ref. [137] with permission from The Royal Society of Chemistry (RSC).*

some spatial resolution, having an image. Using this approach they have been capable of visualizing corrosion sites and measuring local chemical concentrations in a real-time corrosion monitorization process. Figure 18.21 (bottom) shows the apparition of a corroded region denoted by a dark region where the pH locally decreases and this results in a fluorescence quenching.

18.4 Conclusion and Future Trends

The potential application of OFS for corrosion monitoring includes a vast field of areas of interest such as renewable energies, transportation, civil engineering, and oil and gas, which have been mentioned in this chapter. Optical fiber sensing devices for corrosion monitoring have been demonstrated as an attractive approach that can equal or even overcome other conventional sensors providing remote and distributed measurements, large durability, easy integration and installation, or enhanced reliability.

A complete review of optical fiber corrosion detection techniques has been presented in this chapter. The reviewed techniques include direct methods to detect the degradation of materials and to detect the consequences of this degradation (i.e., strain or deformations in different structures), indirect measurements to detect the corrosion of a material similar to that which degradation is going to be monitored, sensing of different corrosive agents or products of corrosion (i.e., the presence of chloride or oxygen ions), or environmental parameters such as humidity, as well as the detection of pH variations.

Furthermore, a brief illustration of OFS sensing techniques, such as FBG, FP, SPR, and other intensity approaches, already demonstrated for corrosion sensing, as well as their main technical characteristics, their principal measurands, and some of the manufacturers and commercial distributors have been also given in this chapter.

Many successful applications of optical fiber corrosion sensors have been reported in the recent years, and some of them have been presented in this chapter. However, the continuous advance in civil engineering and the utilization of both existing and novel structures in harsh and hostile environments still needs more research in order to use this sensor technology in practical, real-life applications and to solve the practical problems associated with these sensors, such as durability, robustness, low cost, distributed sensing, or easy replaceable. Consequently the demand of novel and improved techniques for corrosion monitoring will continue to be a hot topic for researchers and companies in the future.

Acknowledgments

This work was supported by the Spanish Ministry of Science and Innovation TEC2010-17805.

References

1. Ou J, Li H. Structural health monitoring in mainland china: review and future trends. Struct Health Monit 2010;9:219–31.
2. Inaudi D, Udd E, editors. Health monitoring of the Saint-Jean Bridge of Bordeaux, France using fiber Bragg grating extensometers. Proceedings of SPIE – the International Society for optical engineering: smart structures and materials 2003 smart sensor technology and measurement system, 3 March 2003–5 March 2003; 2003.
3. López-Higuera JM, Cobo LR, Incera AQ, et al. Fiber optic sensors in structural health monitoring. J Lightwave Technol 2011;29:587–608.
4 Udd E. Fiber grating sensors for structural health monitoring of aerospace structures. In: Inaudi D, Ecke W, Culshaw B, Peters KJ, Udd E, editors. Proc. SPIE 6167, Smart structures and materials 2006: smart sensor monitoring systems and applications, 61670C. March 30, 2006. http://dx.doi.org/10.1117/12.659048.

5. Wheat HG, Liu G. Fiber optic sensors for corrosion detection in reinforced concretea state of the art review. In: Wheat HG, editor. 17th international corrosion congress 2008: corrosion control in the service of society, vol. 5. Las Vegas, NV, United States; 2008. p. 2752–2759. 6 October 2008-10 October 2008.
6. Kumar V. Protection of steel reinforcement for concrete – a review. Corr Rev 1998;16:317–58.
7. Hughes AE, Hinton B, Furman SA, et al. Airlife – towards a fleet management tool for corrosion damage. Corr Rev 2007;25:275–93.
8. Habel WR, Krebber K. Fiber-optic sensor applications in civil and geotechnical engineering. Photonic Sens 2011;1:268–80.
9. Casas JR, Cruz PJS. Fiber optic sensors for bridge monitoring. J Bridge Eng 2003;8:362–73.
10. Fuhr PL, Huston DR. Corrosion detection in reinforced concrete roadways and bridges via embedded fiber optic sensors. Smart Mater Struct 1998;7:217–28.
11. Fuhr PL, Ambrose TP, Huston DR, McPadden AP. Fiber optic corrosion sensing for bridges and roadway surfaces. In: Matthews LK, editor. Proc. SPIE 2446, Smart structures and materials 1995: smart systems for bridges, structures, and highways, 2. April 20, 1995. http://dx.doi.org/10.1117/12.207716.
12. Poloso T. Fibre Bragg gratings optical sensing technology. Smart Mater Bull 2001;2001:7–10.
13. Udd E. Review of multi-parameter fiber grating sensors. In: Udd E, editor. Proc. SPIE 6770, Fiber optic sensors and applications V, 677002. October 11, 2007. http://dx.doi.org/10.1117/12.753525.
14. Goicoechea J, Zamarreño CR, Matias IR, et al. Utilization of white light interferometry in pH sensing applications by mean of the fabrication of nanostructured cavities. Sens Actuators, B Chem 2009;138:613–8.
15. Loayssa A. Optical fiber sensors for structural health monitoring. Lect Notes Electr Eng 2011;96:335–58.
16. Bao X, Chen L. Recent progress in Brillouin scattering based fiber sensors. Sensors 2011;11:4152–87.
17. Galindez-Jamioy CA, López-Higuera JM. Brillouin distributed fiber sensors: an overview and applications. J Sensors 2012;2012:204121(14pp).
18. Jorgenson RC, Yee SS. A fiber-optic chemical sensor based on surface plasmon resonance. Sens Actuators, B Chem 1993;12:213–20.
19. Homola J, Yee SS, Gauglitz G. Surface plasmon resonance sensors: review. Sens Actuators, B Chem 1999;54:3–15.
20. Sharma AK, Jha R, Gupta BD. Fiber-optic sensors based on surface plasmon resonance: a comprehensive review. IEEE Sensors J 2007;7:1118–29.
21. Lee B, Roh S, Park J. Current status of micro- and nano-structured optical fiber sensors. Opt Fiber Technol 2009;15:209–21.
22. Zamarreño CR, Hernaez M, Del Villar I, et al. Thin-film resonance supporting coatings deposited onto optical waveguides towards the fabrication of sensing devices. Recent Pat Mater Sci 2011;4:28–34.
23. Lee J, Yun C, Yoon D. A structural corrosion-monitoring sensor based on a pair of prestrained fiber Bragg gratings. Meas Sci Technol 2010;21:017002(7pp).
24. Yang S, Geng J, Ye Q, et al. Application of fiber Bragg gratings in monitoring metal corrosion. Zhongguo Jiguang 2006;33:641–4.
25. Liu H, Liang D, Han X, et al. Long period fiber grating transverse load effect-based sensor for the omnidirectional monitoring of rebar corrosion in concrete. Appl Opt 2013;52:3246–52.
26. Li H, Ou J, Zhou Z. Applications of optical fibre Bragg gratings sensing technology-based smart stay cables. Opt Lasers Eng 2009;47:1077–84.
27. Hassan MRA, Bakar MHA, Dambul K, et al. Optical-based sensors for monitoring corrosion of reinforcement rebar via an etched Cladding Bragg grating. Sensors (Switzerland) 2012;12:15820–6.

28. Zhao X, Cui Y, Wei H, et al. Research on corrosion detection for steel reinforced concrete structures using the fiber optical white light interferometer sensing technique. Smart Mater Struct 2013;22:065014(7pp).
29. Maalej M, Ahmed SFU, Kuang KSC, et al. Fiber optic sensing for monitoring corrosion-induced damage. Struct Health Monit 2004;3:165–76.
30. Chen X, Ansari F. Fiber optic stress wave sensor for detection of internal flaws in concrete structures. J Intell Mater Syst Struct 2000;10:274–9.
31. Wade SA, Wallbrink CD, McAdam G, et al. A fibre optic corrosion fuse sensor using stressed metal-coated optical fibres. Sens Actuators, B Chem 2008;131:602–8.
32. Robert CC, editor. Development and field test of deformation sensors for concrete embedding. Smart structures and materials 1996: industrial and commercial applications of smart structures technologies, 27 February 1996–29 February 1996; 1996.
33. Matthews LK, editor. Monitoring of corrosion in steel structures using optical fiber sensors. In: Smart structures and materials 1995: smart systems for bridges, structures, and, highways, 28 February 1995–3 March 1995.
34. Meyendorf NG, Peters KJ, Ecke W, editors. A new kind of smart cable with functionality of full-scale monitoring using BOTDR technique. Proceedings of SPIE – the International Society for Optical Engineering 2009.
35. Mao JH, Jin WL, He Y, et al. A novel method of embedding distributed optical fiber sensors for structural health monitoring. Smart Mater Struct 2011;20.
36. Zhao X, Gong P, Qiao G, et al. Brillouin corrosion expansion sensors for steel reinforced concrete structures using a fiber optic coil winding method. Sensors 2011;11:10798–819.
37. Shull PJ, Diaz AA, Felix Wu H, editors. Structural health monitoring of PC structures with novel types of distributed sensors. In: Nondestructive characterization for composite materials, aerospace engineering, civil infrastructure, and homeland security 2010, 8 March 2010–11 March 2010. 2010.
38. Bossi RH, Moran T, editors. Optical fiber grating-based strain and corrosion sensors. In: Nondestructive evaluation for process control in manufacturing, 3 December 1996–3 December 1996. 1996.
39. Wilson AR, Varadan VV, editors. Finite element modeling to determine thermal residual strain distribution of bonded composite repairs for structural health monitoring design. Smart materials II, 16 December 2002–18 December 2002; 2002.
40. Singh N, Jain SC, Aulakh NS, et al. Fiber optic colorimetry technique for in-situ measurement of corrosion in civil structures. Exp Tech 2004;28:23–6.
41. Inari T, Takashima K, Watanabe M, et al. Optical inspection system for the inner surface of a pipe using detection of circular images projected by a laser source. Meas J Int Meas Confed 1994;13:99–106.
42. Gobi G, Sastikumar D, Balaji Ganesh A, et al. Fiber-optic sensor to estimate surface roughness of corroded metals. Opt Appl 2009;39:5–11.
43. Guillaume F, Greden K, Smyrl WH. Optical sensors for corrosion systems: I. Oxygen sensing. J Electrochem Soc 2008;155:J213–9.
44. Mizaikoff B, editor. Fiber-optic-based corrosion sensor using OTDR. In: 6th IEEE conference on sensors, IEEE sensors 2007, 28 October 2007 -31 October 2007. 2007.
45. Sampson DD, editor. Multipoint fiber-optic-based corrosion sensor. In: 19th international conference on optical fibre sensors, 15 April 2008–18 April 2008. 2008.
46. Nascimento JF, Silva MJ, Coêlho IJS, et al. Amplified OTDR systems for multipoint corrosion monitoring. Sensors 2012;12:3438–48.
47. Wan KT, Leung CKY. Durability tests of a fiber optic corrosion sensor. Sensors 2012;12:3656–68.

48. Murphy Kent A, Huston Dryver R, editors. Novel NDE fiber optic corrosion sensor. Smart structures and materials 1996: smart sensing, processing, and instrumentation, 26 February 1996–28 February 1996; 1996.
49. Benounis M, Jaffrezic-Renault N. Elaboration of an optical fibre corrosion sensor for aircraft applications. Sens Actuators, B Chem 2004;100:1–8.
50. Dong S, Liao Y, Tian Q. Sensing of corrosion on aluminum surfaces by use of metallic optical fiber. Appl Opt 2005;44:6334–7.
51. Dong S, Liao Y, Tian Q. Intensity-based optical fiber sensor for monitoring corrosion of aluminum alloys. Appl Opt 2005;44:5773–7.
52. Benounis M, Jaffrezic-Renault N, Stremsdoerfer G, et al. Elaboration and standardization of an optical fibre corrosion sensor based on an electroless deposit of copper. Sens Actuators, B Chem 2003;90:90–7.
53. Cardenas-Valencia AM, Byrne RH, Calves M, et al. Development of stripped-cladding optical fiber sensors for continuous monitoring. II: referencing method for spectral sensing of environmental corrosion. Sens Actuators, B Chem 2007;122:410–8.
54. Abderrahmane S, Himour A, Kherrat R, et al. An optical fibre corrosion sensor with an electroless deposit of Ni-P. Sens Actuators, B Chem 2001;75:1–4.
55. Dong S, Liao Y, Tian Q, et al. Optical and electrochemical measurements for optical fibre corrosion sensing techniques. Corros Sci 2006;48:1746–56.
56. Luo Y, Qiu Z, Song S, et al. Study on the sensing capability of Fe-C alloy corrosion sensing film. Mater Corros 2007;58:198–201.
57. Abdelmalek F. Study of the optical properties of corroded gold-aluminum films using surface plasmon resonances. Thin Solid Films 2001;389:296–300.
58. Abdelmalek F. Surface plasmon resonance based on Bragg gratings to test the durability of Au-Al films. Mater Lett 2002;57:213–8.
59. Cai H-L, Hu W-B, Zhang X-X, et al. A fiber Bragg grating sensor of steel corrosion at different humidities. Guangzi Xuebao 2011;40:690–3.
60. Cai LH, Li W, Fang HF. Characterization of Fe-C alloy film optical fiber corrosion sensors by fractal. Adv Mater Res 2011;239–242:976–80.
61. Murphy Kent A, Huston Dryver R, editors. Grating-based optical-fiber-based corrosion sensors. Smart structures and materials 1996: smart sensing, processing, and instrumentation, 26 February 1996–28 February 1996; 1996.
62. Hu W, Cai H, Yang M, et al. Fe-C-coated fibre Bragg grating sensor for steel corrosion monitoring. Corros Sci 2011;53:1933–8.
63. Qiu Z, Luo Y, Song S. The formation of pure aluminium corrosion sensing film on fiber and its electrochemical performance. Mater Corros 2007;58:109–12.
64. Butler MA, Ricco AJ. Reflectivity changes of optically-thin nickel films exposed to oxygen. Sens Actuators 1989;19:249–57.
65. Himour A, Abderrahmane S, Beliardouh NE, et al. Optical-fiber corrosion sensor based on deposit of Au/Ni-P. Jpn J Appl Phys Part 1: Regul Pap Short Notes Rev Pap 2005;44:6709–13.
66. Wan KT, Leung CKY, Chen L. A novel optical fiber sensor for steel corrosion in concrete structures. Sensors 2008;8:1960–76.
67. Wang Y, Huang H. Optical fiber corrosion sensor based on laser light reflection. Smart Mater Struct 2011;20:085003(7pp).
68. Luo Y, Qiu Z, Song S, et al. PVD and its incorporation with electroplating to fabricate Fe-C alloy film of fiber optical corrosion sensor. Huagong Xuebao 2004;55:947–51.
69. Javaherdashti R, Singh Raman RK, Panter C, et al. Microbiologically assisted stress corrosion cracking of carbon steel in mixed and pure cultures of sulfate reducing bacteria. Intern Biodeterior Biodegrad 2006;58:27–35.

70. Montemor MF, Simões AMP, Ferreira MGS. Chloride-induced corrosion on reinforcing steel: from the fundamentals to the monitoring techniques. Cem Concr Compos 2003;25:491–502.
71. Hime WG. Chloride-caused corrosion of steel in concrete. A new historical perspective. Concr Int 1994;16:56–60.
72. Matthews LK, editor. Embedded chloride detectors for roadways and bridges. Proceedings of SPIE – the International Society for Optical Engineering 1996.
73. Fuhr PL, MacCraith BD, Huston DR, Guerrina M, Nelson M, editors. Fiber optic chloride sensing: if corrosion's the problem, chloride sensing is the key. Proceedings of SPIE – the International Society for Optical Engineering 1997.
74. Fuhr PL, Huston DR, MacCraith B. Embedded fiber optic sensors for bridge deck chloride penetration measurement. Opt Eng 1998;37:1221–8.
75. Laferrière F, Inaudi D, Kronenberg P, et al. A new system for early chloride detection in concrete. Smart Mater Struct 2008;17:045017(7pp).
76. Tang J, Wang J. Measurement of chloride-ion concentration with long-period grating technology. Smart Mater Struct 2007;16:665–72.
77. Tomizuka M, Yun C-B, Giurgiutiu V, editors. Studies on measurement of chloride ion concentration in concrete structures with long-period grating sensors. Proceedings of SPIE – the International Society for Optical Engineering 2006.
78. Abi Kaed Bey SK, Chun Lam CC, Sun T, et al. Chloride ion optical sensing using a long period grating pair. Sens Actuators, A Phys 2008;141:390–5.
79. Wilson AR, Varadan VV, editors. In situ health monitoring of bonded composite repairs using a novel fibre Bragg grating sensing arrangement. Smart materials II, 16 December 2002–18 December 2002; 2002.
80. Spillman Jr WB, editor. Detection of aluminum corrosion by evanescent wave absorption spectroscopy with optical fibers. Proceedings of SPIE – the International Society for Optical Engineering 1995.
81. Kazemi AA, Kress BC, Chan EY, editors. Evanescent wave absorption measurements of corroded materials using optical fibers as remote probes. Proceedings of SPIE – the International Society for Optical Engineering 2010.
82. Cooper KR, Elster J, Jones M, Kelly RG, editors. Optical fiber-based corrosion sensor systems for health monitoring of aging aircraft. In: AUTOTESTCON (Proceedings). 2001.
83. Elster J, Greene J, Jones M, et al. Optical fiber-based chemical sensors for detection of corrosion precursors and by-products. Proc SPIE Int Soc Opt Eng 1999;3540:251–7.
84. Sinchenko E, McAdam G, Davis C, McDonald S, McKenzie I, Newman PJ, et al. Optical fibre techniques for distributed corrosion sensing. In: ACOFT/AOS 2006 – Australian conference on optical fibre technology/Australian Optical Society. 2006.
85. Ravi Kishore VVN, Aziz A, Narasimhan KL, et al. On the assignment of the absorption bands in the optical spectrum of Alq3. Synth Met 2002;126:199–205.
86. Venancio PG, Cottis RA, Narayanaswamy R, et al. Optical sensors for corrosion detection in airframes. Sens Actuators, B Chem 2013;182:774–81.
87. Szunerits S, Walt DR. Aluminum surface corrosion and the mechanism of inhibitors using pH and metal ion selective imaging fiber bundles. Anal Chem 2002;74:886–94.
88. Warren-Smith SC, Ebendorff-Heidepriem H, Afshar SV, et al. Corrosion sensing of aluminium alloys using exposed-core microstructured optical fibres. Mater Forum 2008;33:110–21.
89. Corres JM, Matias IR, Arregui FJ. Optical fibre humidity sensors using nano-films. Lect Notes Electr Eng 2008;21:153–77.
90. Yeo TL, Sun T, Grattan KTV. Fibre-optic sensor technologies for humidity and moisture measurement. Sens Actuators, A Phys 2008;144:280–95.

91. An J, Zhao Y, Jin Y, Shen C. Relative humidity sensor based on SMS fiber structure with polyvinyl alcohol coating. Optik 2013.
92. Correia SFH, Antunes P, Pecoraro E, et al. Optical fiber relative humidity sensor based on a FBG with a di-ureasil coating. Sensors (Switzerland) 2012;12:8847–60.
93. Inaudi D, Udd E, editors. Fiber optic grating moisture and humidity sensors. Smart structures and materials 2002 smart sensor technology and measurement systems, 18 March 2002–19 March 2002; 2002.
94. Wang J, Liang H, Dong X, et al. A temperature-insensitive relative humidity sensor by using polarization maintaining fiber-based Sagnac interferometer. Microwave Opt Technol Lett 2013;55:2305–7.
95. Liao Y, Jin W, Sampson DD, Yamauchi R, Chung Y, Nakamura K, Rao Y, editors. Miniature photonic crystal optical fiber humidity sensor based on polyvinyl alcohol. Proceedings of SPIE – the International Society for Optical Engineering 2012.
96. Yao J, Zhu T, Deng M, et al. A humidity sensor based on all-fiber Fabry-Perot interferometer formed by large offset splicing. Zhongguo Jiguang/Chinese J Lasers 2012;39.
97. Culshaw B, Liao YB, Wang A, Bao X, Fan X, editors. Optical fiber relative humidity sensor based on a hydrogel coated long period grating. Proceedings of SPIE – the International Society for Optical Engineering 2011.
98. Zamarreño CR, Hernaez M, Sanchez P, Del Villar I, Matias IR, Arregui FJ. Optical fiber humidity sensor based on lossy mode resonances supported by TiO2/PSS coatings. Procedia Engineering 2011.
99. Zhang S, Dong X, Li T, et al. Simultaneous measurement of relative humidity and temperature with PCF-MZI cascaded by fiber Bragg grating. Opt Commun 2013;303:42–5.
100. Bossi RH, Pepper DM, editors. Optical fiber corrosion sensors for aging aircraft. Process control and sensors for manufacturing, 31 March 1998–1 April 1998; 1998.
101. Udd E, Inaudi D, editors. Implementing fiber optic sensors to monitor humidity and moisture. Smart structures and materials 2004 – smart sensor technology and measurement systems, 15 March 2004–17 March 2004; 2004.
102. Reuter WG, editor. Distributed fiber optic chemical sensors for detection of corrosion in pipelines and structural components. Nondestructive evaluation of utilities and pipelines II, 1 April 1998–1 April 1998; 1998.
103. Cordell TM, Rempt RD, editors. Embeddable distributed moisture and pH sensors for nondestructive inspection of aircraft lap joints. In: Nondestructive evaluation of aging aircraft, airports, aerospace hardware, and materials, 6 June 1995–8 June 1995. Bellingham, WA, United States: Society of Photo-Optical Instrumentation Engineers; 1995.
104. Pirrotta S, Guglielmino E. Optical psychrometer for relative humidity measurement in non-conventional environments. In: Proc. SPIE 6619, Third European workshop on optical fibre sensors, 661920. July 02, 2007. http://dx.doi.org/:10.1117/12.738595. http://proceedings.spiedigitallibrary.org/proceeding.aspx?articleid=1304741.
105. Sun T, Grattan KTV, Srinivasan S, et al. Building stone condition monitoring using specially designed compensated optical fiber humidity sensors. IEEE Sens J 2012;12:1011–7.
106. Zheng S, Zhu Y, Krishnaswamy S. Nanofilm-coated long-period fiber grating humidity sensors for corrosion detection in structural health monitoring. In: Nondestructive characterization for composite materials, aerospace engineering, civil infrastructure, and homeland security 2011, 7 March 2011–10 March 2011. 2011.
107. Muto S, Suzuki O, Amano T, et al. A plastic optical fibre sensor for real-time humidity monitoring. Meas Sci Technol 2003;14:746–50.
108. Cho H, Tamura Y, Matsuo T. Monitoring of corrosion under insulations by acoustic emission and humidity measurement. J Nondestr Eval 2011;30:59–63.

109. Zhang S, Tanaka S, Wickramasinghe YABD, et al. Fibre-optical sensor based on fluorescent indicator for monitoring physiological pH values. Med Biol Eng Comput 1995;33:152–6.
110. Moreno J, Arregui FJ, Matias IR. Fiber optic ammonia sensing employing novel thermoplastic polyurethane membranes. Sens Actuators, B Chem 2005;105:419–24.
111. Yanaz Z, Filik H, Apak R. Development of an optical fibre reflectance sensor for lead detection based on immobilised arsenazo III. Sens Actuators, B Chem 2010;147:15–22.
112. Ng SM, Narayanaswamy R. Fluorescence sensor using a molecularly imprinted polymer as a recognition receptor for the detection of aluminium ions in aqueous media. Anal Bioanal Chem 2006;386:1235–44.
113. Perelman LA, Moore T, Singelyn J, et al. Preparation and characterization of a pH- and thermally responsive poly(*N*-isopropylacrylamide-coacrylic acid)/porous SiO_2 hybrid. Adv Funct Mater 2010;20:826–33.
114. Jones TP, Porter MD. Optical pH sensor based on the chemical modification of a porous polymer film. Anal Chem 1988;60:404–6.
115. Arregui FJ, Fernandez-Valdivielso C, Ilundain I, Matias IR. pH sensor made using cellulosic coating on a biconically tapered singlemode optical fiber. Proceedings of SPIE –the International Society for Optical Engineering 2000.
116. Oter O, Ertekin K, Kirilmis C, et al. Characterization of a newly synthesized fluorescent benzofuran derivative and usage as a selective fiber optic sensor for Fe(III). Sens Actuators, B Chem 2007;122:450–6.
117. MacCraith BD, McDonagh CM, O'Keeffe G, et al. Sol-gel coatings for optical chemical sensors and biosensors. Sens Actuators, B Chem 1995;29:51–7.
118. Grant SA, Glass RS. A sol-gel based fiber optic sensor for local blood pH measurements. Sens Actuators, B Chem 1997;45:35–42.
119. Carmona N, Villegas MA, Navarro JMF. Optical sensors for evaluating environmental acidity in the preventive conservation of historical objects. Sens Actuators, A Phys 2004;116:398–404.
120. Singh S, Gupta BD. Fabrication and characterization of a surface plasmon resonance based fiber optic sensor using gel entrapment technique for the detection of low glucose concentration. Sens Actuators, B Chem 2013;177:589–95.
121. Lau KT, Baldwin S, Shepherd RL, et al. Novel fused-LEDs devices as optical sensors for colorimetric analysis. Talanta 2004;63:167–73.
122. Munzke D, Saunders J, Omrani H, et al. Modeling of fiber-optic fluorescence probes for strongly absorbing samples. Appl Opt 2012;51:6343–51.
123. Oceanoptics Inc. *Products: optical pH sensor probes*. Available at: http://www.oceanoptics.com/Products/phsensor.asp; 2013 [accessed 07.07.2013].
124. Lobnik A, Oehme I, Murkovic I, et al. pH optical sensors based on sol-gels: chemical doping versus covalent immobilization. Anal Chim Acta 1998;367:159–65.
125. Wolfbeis OS. Materials for fluorescence-based optical chemical sensors. J Mater Chem 2005;15:2657–69.
126. Wolfbeis OS, Posch HE. Fibre-optic fluorescing sensor for ammonia. Anal Chim Acta 1986;185:321–7.
127. Xie Z, Guo L, Zheng X, et al. A new porous plastic fiber probe for ammonia monitoring. Sens Actuators, B Chem 2005;104:173–8.
128. Müller B, Hauser PC. Fluorescence optical sensor for low concentrations of dissolved carbon dioxide. Analyst 1996;121:339–43.
129. Ferguson JA, Healey BG, Bronk KS, et al. Simultaneous monitoring of pH, CO_2 and O_2 using an optical imaging fiber. Anal Chim Acta 1997;340:123–31.
130. Chu C, Lo Y. Fiber-optic carbon dioxide sensor based on fluorinated xerogels doped with HPTS. Sens Actuators, B Chem 2008;129:120–5.

131. Contreras-Gutierrez PK, Medina-Rodríguez S, Medina-Castillo AL, et al. A new highly sensitive and versatile optical sensing film for controlling CO_2 in gaseous and aqueous media. Sens Actuators, B Chem 2013;184:281–7.
132. Moreno-Bondi MC, Wolfbeis OS, Leiner MJP, et al. Oxygen optrode for use in a fiber-optic glucose biosensor. Anal Chem 1990;62:2377–80.
133. Jiang J, Gao L, Zhong W, et al. Development of fiber optic fluorescence oxygen sensor in both in vitro and in vivo systems. Respir Physiol Neurobiol 2008;161:160–6.
134. Alodan MA, Smyrl WH. Detection of localized corrosion of aluminum alloys using fluorescence microscopy. J Electrochem Soc 1998;145:1571–7.
135. Lee W, Guillaume F, Knutson TL, et al. Analysis of products at reaction sites by fluorescence microspectroscopy using the f-NSOM technique. J Electrochem Soc 2005;152:B111–5.
136. Loete F, Vuillemin B, Oltra R. pH mapping of localized corrosion in confined electrolytes by total internal reflection fluorescence microscopy. ECS Trans 2007;3(31):23–8; Cancun; Mexico; 29 October 2006 through 3 November 2006; Code 72279.
137. Epstein JR, Walt DR. Fluorescence-based fibre optic arrays: a universal platform for sensing. Chem Soc Rev 2003;32:203–14.
138. Mahutte CK. On-line arterial blood gas analysis with optodes: current status. Clin Biochem 1998;31:119–30.
139. Panova AA, Pantano P, Walt DR. In situ fluorescence imaging of localized corrosion with a pH-sensitive imaging fiber. Anal Chem 1997;69:1635–41.

Chapter 19

Characterization of High Performance Protective Coatings for Use on Culturally Significant Works

Tami Lasseter Clare, Natasja A. Swartz
Department of Chemistry, Portland State University, Portland, OR 97207, USA

19.1 Introduction

19.1.1 Protective coatings for the conservation of material cultural heritage

Artwork, archeological materials, and ethnographic objects often require the use of protective coatings to stabilize them against degradation. For indoor storage conditions (i.e., within a museum), stabilization is often achieved through effective climate control, such as humidity and temperature control of the microenvironment within a transparent vitrine. For pieces that are displayed outdoors or are monumental in scale, the challenge of providing a stable noncorrosive environment is nontrivial; and it is often necessary to apply protective coatings that act as chemical and physical

Intelligent Coatings for Corrosion Control
Copyright © 2015 Elsevier Inc. All rights reserved.

barriers. The types of materials used as coatings vary widely, and there are several critical features that must be considered to select an appropriate coating. First, the interaction between the substrate and the coating must be thoroughly understood. Adhesion at the substrate-coating interface often limits the effectiveness of the coating, where delamination provides a region for water/electrolyte accumulation and subsequent damage. Second, the material properties of the substrate must bear on coating selection. In the case of porous materials, such as stone or concrete, water vapor is drawn into or expelled from the material due to capillary action, and the coating should allow water vapor to pass or the damaging effects of efflorescence usually result. In the case of metals (e.g., bronze, brass, mild steel, Cor-Ten, and aluminum), impenetrable barrier films are thought to be the most effective means of achieving corrosion control. Third, the effects from the environment: ultraviolet light, daily and seasonal temperature and humidity fluctuations, pollutants, and physical abrasion (from windborne particulates or vandalism) should be considered. While numerous scientific studies exist that demonstrate the efficacy of a coating or groups of coatings on specific substrate(s), the sensitivity of cultural heritage objects necessitate that collections care personnel undertake their own testing to demonstrate compatibility between a specific substrate and coating.

Within the considerations of pairing an appropriate substrate and coating there exists additional constraints that affect the design of intelligent coatings for corrosion control for the conservation of material cultural heritage. The coating must be optically *T*ransparent; it must be *R*eversible (removable) without harming the underlying artwork; and it should be easily *A*pplied, requiring only a brush or pressurized air sprayer. Practically speaking, the coating must be *commercially* available, which typically requires that the price per gallon is acceptable for other applications where cost of materials is a critical deciding factor. The impact on the *E*nvironment and health of those applying the coating should be minimized. Taking account these five issues (TRACE) reduces the coatings options that otherwise would be acceptable in other fields when selecting coatings for conserving objects of cultural heritage. For example, curing coatings or those that require melting in an oven are not viable coatings for material cultural heritage.

Intelligence of protective coatings for use on material cultural heritage is therefore defined having at least one advanced chemical or physical property in addition to meeting the basic TRACE criteria. Advanced chemical or physical properties include the rational design of the polymer to achieve a specific improvement or the addition of components into the formulation to achieve marked increases in performance. Described below is our investigation of both chemical and physical modifications to coatings compatible with the TRACE requirements that are expected to improve the weatherability and water barrier properties of coatings, with the goal of increasing their working lifetime and corrosion protection for use in the conservation of material cultural heritage.

19.1.2 Defining intelligence: chemical and physical

Generally speaking, coatings having chemical intelligence will be able to be responsive to applied chemical stress (such as that produced by oxygen or radicals). Likewise, systems that can reduce physical stress by an induced response are considered to have physical intelligence. There are three broad categories of methods for conferring intelligence: (1) in resin, (2) in formulation, and (3) in encapsulation. First, the in resin approach involves incorporating intelligence into the polymer chain targeting specific functional groups that may respond to stresses. For example, incorporating fluorine groups close to the polymer chain backbone, such as in polyvinylidene fluoride (PVDF) and polytetrafluoroethylene (PTFE), will reduce chain-scission by re-forming homolytically cleaved bonds.[1–4] Or through the use of copolymers, functionalities having a range of glass transition temperatures (T_g) may confer flexibility to the polymer under a wider thermal range,[5] or monomers that may act as corrosion inhibitors may be copolymerized with those that act as barriers.[6] Second, the in formulation approach involves two differently functioning parts of a single mixture. For example, ultraviolet absorbers may be incorporated into the formulation of a polymeric suspension, allowing the polymer to act as a chemical and physical barrier against corrosion, while the UV absorber reacts with radicals formed to prevent chain-scission or side-group cleavage.[7] Third, rather than uniformly distributing intelligence throughout the polymer or dispersion, others cleverly encapsulate moieties that are released by a stressor and upon release act to mitigate that stress. An example of this approach is in self-healing coatings that, ideally, would fill-in cracks by the release of encapsulated chemicals due to an external stimulus such as pH, chloride ions, water, light, temperature, or other mechanical or physical changes.[8–12] Combinations of any of the three approaches and layering different coatings are commonly done.[13] In developing intelligent coatings for the prevention of corrosion on material cultural heritage, usually the simplest approach is preferred because that is expected to have the fewest unanticipated side-reactions over its lifetime, which reduces the risk of the coating damaging the very work being protected.

19.1.3 Commonly used coatings in the conservation of cultural heritage

It is useful to consider the history of protective coatings on material cultural heritage before discussing how improvements may be made. Since the Roman times, oils and resins were used as protective coatings on top of naturally formed metal oxides. In the first century, Pliny the Elder noted: “Things made of copper or bronze get covered with copper-rust more quickly when they are kept rubbed clean than when they are neglected, unless they are well greased with oil. It is said that the best way of preserving them is to give them a coating of liquid vegetable pitch.”[14] Starting in the nineteenth century plant oils, oil lacquers, and paraffinic waxes were used

to protect outdoor metals.[15] In the 1960s, a specialized lacquer (polymer dissolved in solvent) was developed to prevent copper corrosion by the International Copper Research Association (INCRA), which was called Incralac.[16] In 2008, we conducted an online survey sent to material cultural heritage conservators (with ~120 respondents) to learn more about how coatings are used in conservation today. To protect iron from corrosion, 47 respondents had used waxes, 23 had used solvent-borne acrylics, 45 had used pigmented coatings, 15 had used other polymeric coatings and only three had used acrylic emulsions (see Figure 19.1a). On bronze and brass, 84 had used waxes, 58 had used acrylic lacquers, 35 had used pigmented coatings, and only two used acrylic emulsions (see Figure 19.1b). These responses indicated that wax and paint are the most commonly used coatings for iron substrates and wax and acrylic lacquers are the most common for bronze protection. Despite the fact that conservators expected nonwax coatings, such as acrylic lacquers, to last longer, some even indicating that they expected a lifetime of up to 20 years, their use trailed that of the wax. Acrylic emulsions were rarely used by conservators. For acrylic lacquers, three specific resins are commonly used: Paraloid™ B-44, B-48, and B-72. Conservators reported having used one of those acrylic lacquers and benzotriazole (BTA), a corrosion inhibitor,[17] with 18 reporting having mixed BTA into Incralac (which is composed of Paraloid™ B-44), eight having used BTA as a pretreatment and 12 having used it as both a pretreatment and as a mix into the coating. In the survey we also asked conservators what was the expected lifetime of protective coatings (see Figure 19.1c). Fifty-four percent of respondents expected waxes to have a brief lifetime of 1 year or less. For nonwaxes, the lifetime expectancy was longer: with 39% expecting a lifetime of 3-5 years (see Figure 19.1d). The responses from the survey clearly indicated that although chemical advances in the past 100+ years have provided alternatives, wax is preferred by the conservation community as a protective coating and is expected to have a lifetime of 5 years or less.

19.1.4 Weathering studies of common coatings used in conservation

To obtain a quantitative understanding of the performance of some of the commonly used protective coatings in the conservation of material cultural heritage, a 4-year study was undertaken in 2009 during which bronze panels were coated and weathered under different conditions: 18 months in southern Florida exposure, under QUV-B light for 1000 h and outdoors for 18 months in Portland, Oregon. Tables 19.1–19.3 show the 60° gloss and film thickness changes of various coatings on bronze panels as measured using a Gardco TRI-gloss meter for each of the three different exposure situations. Notably, all panels reflected significant decreases in gloss, with losses ranging from 88% to 11%. Over time, the wax coated panels showed the greatest change in gloss, however gloss of waxed panels was the lowest at the start, having only 4-5% reflectance. During outdoor weathering waxed panels lost the most film thickness

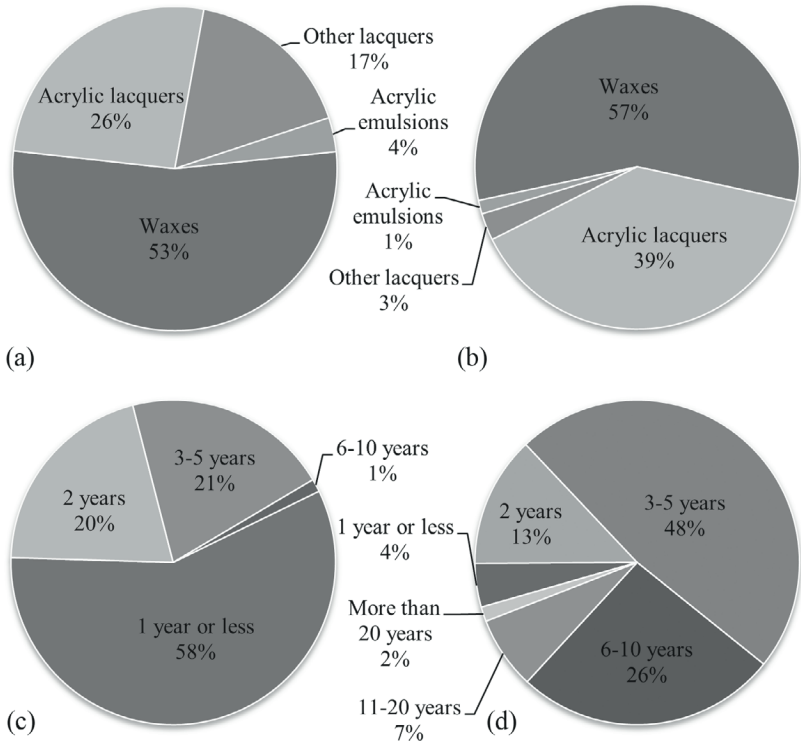


Figure 19.1 Results from a 2009 online survey. The questions asked were: (a) "Which coatings have you used to coat iron?" (b) "Which coatings have you used to coat bronze?" (c) "In your experience, what is the expected lifetime of wax coatings?" (d) "In your experience, what is the expected lifetime of nonwax coatings?."

TABLE 19.1 Gloss, Change in Gloss, Thickness, and Change in Thickness Measurements of Coated Bronze Substrates Taken Before and After 18 Months Weathering Outdoors in South Florida

Coating	Gloss 60° (%*R*)	Δ% Gloss 60°±S.D. (%*R*)	Thickness (mm)	Δ Thickness±S.D.
Wax (Butchers)	4	−88±9%	30.5	−5.8±0.3
Incralac	13	−33±4%	24.3	−1.2±0.1
B-44	11	−34±3%	25.9	−2.3±0.1
B-44 and BTA	13	−19±1%	25.5	−2.9±0.1
B-44 and Tinuvin	12	−39±5%	24.8	−2.6±0.1
B-44, Tinuvin and BTA	13	−55±5%	27.4	−0.6±0.1
Incralac (WB)	11	−23±2%	37.4	−4.5±0.2

TABLE 19.2 Gloss, Change in Gloss, Thickness, and Change in Thickness Measurements of Coated Bronze Substrates Taken Before and After 1000 h Weathering in a QUV-B Chamber

Coating	Gloss 60° (%*R*)	Δ% Gloss 60°±S.D. (%*R*)	Thickness (mm)	Δ Thickness±S.D.
Wax (Microcrystalline)	5	−57±3%	28.9	0.6±0.2
Incralac	17	−24±2%	27.6	−4.0±0.2
B-44	10	−23±1%	25.7	−1.2±0.1
B-44 and BTA	14	−13±1%	24.7	−0.2±0.1
B-44 and Tinuvin	16	−88±7%	26.6	−6.5±0.2
B-44, Tinuvin and BTA	15	−84±8%	22.8	−3.1±0.1

TABLE 19.3 Gloss, Change in Gloss, Thickness, and Change in Thickness Measurements of Coated Bronze Substrates Taken Before and After 18 Months Weathering Outdoors in Portland, Oregon

Coating	Gloss 60° (%*R*)	Δ% Gloss 60°±S.D. (%*R*)	Thickness (mm)	Δ Thickness±S.D.
Wax (Butchers)	4	−83±6%	24.1	−5.3±0.5
Incralac	20	−18±2%	21.1	−1.4±0.7
B-44	10	−11±1%	24.7	−0.6±0.6
B-44 & BTA	18	−12±1%	27.4	4.3±0.4

(−5.8 μm in South Florida and −5.3 μm in Portland), and significant corrosion/substrate darkening was observed. However likely because of the absence of ablative particulates within of the QUV chamber, weathered wax panels only lost 0.6 μm of film thickness. The coatings made from solvent-based resins, Incralac and Paraloid™ B-44, also showed overall losses in gloss and thickness upon exposure in each of the three weathering environments, and the addition of corrosion inhibitors and/or a light stabilizer (Tinuvin, added at 1% w/w) did not improve gloss or thickness retention over time. The resin in waterborne Incralac contains both acrylic and urethane, which is different from the acrylic-only solvent-based version; the performance of the waterborne coating was significantly different: it cracked and yellowed, corrosion formed underneath and, aside from the wax, showed the most film loss under South Florida exposure. For its poor initial performance, waterborne Incralac was omitted from further study along with a number of commercially available materials marketed

for conservation use. These results demonstrate that although the coatings included in this study were commonly used by conservators in our 2009 survey, they noticeably aged in every one of the conditions to which they were exposed. The results point to the need to develop higher-performing coatings with long working lifetimes that are also compatible with the TRACE requirements described in Section 19.1.1.

19.1.5 Our method of approach in developing intelligent coatings for material cultural heritage

We aim to confer both chemical and physical intelligence to coatings for the conservation of material cultural heritage by using a highly weatherable resin and incorporating nanoclays into the coating formulation. In the work that follows we describe separate studies, testing first chemically intelligent coatings then coatings having both physical and chemical intelligence. We utilize a waterborne resin that contains PVDF and polyacrylic acid in a 70:30 wt. ratio, which is available commercially as Kynar Aquatec® RC-10206 or as a 50:50 ratio, available as Kynar Aquatec® FMA 12 (Arkema Inc.). Being hydrophobic, PVDF is copolymerized with polyacrylic acid to improve its dispersibilty in water (yielding waterborne latex suspensions having a lower environmental impact than solvent-based coatings). PVDF-containing coatings are known to be highly resistant to degradation by UV light, having protective properties lasting for 30 years and longer.[3,18–20] Their long lifetime is due to their chemically inert structure, which in turn has the undesirable consequence of having poor adhesion to metals. A solvent-based coating of the highly UV transparent resin Paraloid™ B-44 (Dow Inc.) was used as a basecoat to adhere strongly to the metal substrate and to provide good interlayer adhesion to the weatherable topcoat of Kynar Aquatec® RC-10206. With the goal of conferring additional resistance to hygroscopic swelling, silicate nanoclays (Laponite RD, Rockwood Inc.) have been incorporated into the topcoat. An overview of our method of approach is shown in Figure 19.2. This coating system meets the TRACE requirements: (1) the coating is transparent—even with the inclusion of the nanoclays, their size is too small to cause

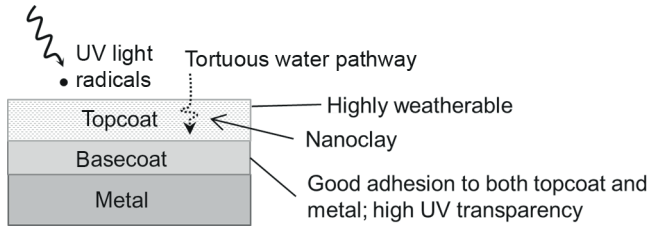


Figure 19.2 Overview of our method of approach for the design of intelligent coatings for use as protective layers for the conservation of material cultural heritage.

visible light scatter; (2) the coatings are reversible—both the solvent-based primer and waterborne topcoat are removable with acetone (and many other solvents); (3) the coatings may be applied by brush or spray gun (with the basecoat thinned to 20% wt. and the topcoat to ~35% wt.); (4) the resins are commercially available through Dow and Arkema Inc.; and (5) the coating system has a reduced environmental impact because it includes a waterborne component (Kynar Aquatec® RC-10206).

19.1.6 Anticipated challenges with this coating system

This coating could be further improved if the adhesion of the topcoat to the metal was increased so that the use of a basecoat was not required. Increasing the adhesion of the topcoat might be achieved by the incorporation of monomers known to interact with metals, such as ureido methacrylate,[21] or through modification of the resin to reduce its minimum film formation temperature (MFFT). (Kynar Aquatec® FMA 12 has a lower MFFT than Kynar Aquatec® RC-10205, at 12 °C compared to 22 °C, and has increased adhesion, although not sufficiently high to exclude the need for a basecoat.) An additional complication of the use of waterborne coatings comes from the differences in the mechanism of film formation from a latex suspension, which is considerably more complex and prone to film defects than the same process from solvent-based polymeric coatings. We have characterized these processes for our selected coating system[22] and have determined that coalescent migration is responsible for whitening films of Kynar Aquatec® RC-10206 if they are exposed to water before the film has completely formed.[23] In our previous work we determined that annealing of Kynar Aquatec® RC-10206 by an infrared heating lamp for 4 h reduced the whitening from 25% to 5%, which is comparable to controls of visually transparent sprayed films (where 0% is completely transparent and 100% is white).

19.1.7 Using electrochemical impedance spectroscopy to characterize barrier properties of protective films

Perhaps more important than monitoring visual changes (gloss, thickness, color, adhesion, whitening, etc.) of coated substrates during weathering is characterizing and monitoring their barrier properties: the ability of the protective coating to block the passage of corrosive ions and water. Measurements of films' barrier properties are assessed by numerous methods, such as voltammetry and potentiometry; however, those are generally not amenable to making measurements on sculptures or architectural elements as the measurement method itself must be nondestructive and noninvasive, methods that generally require applied voltages or current flow to induce electrochemical reactions.[24] Electrochemical impedance spectroscopy (EIS) has emerged as a useful method for coating analysis that, depending on the exact configuration of the setup, may be nondestructive because there is no net current applied

and measurements can be made at the open circuit potential.[20,25–28] EIS can be operated as a two-electrode measurement system where a small AC signal (~10-30 mV) is applied to the working electrode and the magnitude and phase of the current is measured at the counter electrode. Measurements are made as the frequency is varied in a range from ~1 to 1 MHz, with high frequencies limited by instrumental capabilities and noise limiting low-frequency measurements. Changes in either magnitude (Z) or phase measured at the counter compared to the working electrode are associated with resistive and/or capacitive characteristics of the system, because capacitors give rise to a –90° phase and their impedance is frequency dependent while resistors are in phase and are frequency independent, as shown in Equation (19.1).

$$Z_R = R;\ Z_C = \frac{1}{j\omega C} \tag{19.1}$$

R is the resistance, C is the capacitance, ω is the angular frequency, j is the complex number.

For a coated metal substrate exposed to electrolyte there are several circuit elements present, such as the bulk electrolyte, the capacitance of the protective coating, the resistance of the protective coating, and the resistance at each material interface. When there is a coating defect other circuit elements then present, such as the charge transfer resistance and double-layer capacitance. The values of each of these circuit elements can be determined by fitting the experimental data to equivalent circuit models. When monitored for change over time, the values of the individual elements give insight into how protective coatings change and eventually fail. Actual coated systems often do not behave like ideal capacitors and so constant phase elements (represented in Equation 19.2) are used to more accurately describe the observed data.

$$Z_{\mathrm{CPE}} = \frac{1}{(j\omega)^{\alpha} C} \tag{19.2}$$

α is an integer that varies between 1 and 0.5 (however α is usually between 1 and 0.9 for a dry/intact film).

19.2 Experimental Details

19.2.1 Experimental details for coating substrates

Bronze substrates (2.54×7.62 cm; 90% Cu 10% Sn, TB Hagstoz & Son Inc.) were treated to prevent flash rust with a 24 h immersion of 17 mM BTA (Alfa-Aesar) in ethanol. Basecoat primers were either resin dissolved in solvent [Paraloid™ B-44 resin, principally composed of poly(methyl methacrylate-co-ethyl acrylate), referred

to as SB Acrylic, in 20% (w%/w toluene), Dow, Inc.]. The topcoat used was water-borne Kynar Aquatec® RC-10206 latex, a poly(vinylidene fluoride) and poly(methyl methacrylate) blend, Arkema, Inc. Substrates were spray-coated with a Fuji HVLP Super 4 XPC™ for a dry film thickness of ~10-15 μm for each layer (i.e., primer base coats or WB PVDF topcoat) for a total dry film thickness of ~30 μm. Samples were annealed (heated) in an oven for 12 h at 60 °C.

19.2.2 Experimental details for weathering studies of coated panels

The Florida exposures of coated panels were conducted according to ASTM D6675 with salt spray exposure at Q-Labs in southern Florida at a 45° incline facing South with evaluation after hand washing with water every three months. The conditions for exposure to ultraviolet light were established according to ASTM G154 Cycle 2: a 500 h cycle consisting of 4 h of UV-B exposure at 60 °C, irradiance = 0.78 and 4 h of condensation at 50 °C. The coatings' thicknesses ranged between 25 and 30 μm for each panel and were applied by spray-coating or, for waxes, applied using a cloth and remelting under low, evenly applied heat.

19.2.3 Experimental details for characterizing substrates

Gloss and thickness measurements were acquired as an average of five trials with a Gardco μ-Tri-Gloss meter. EIS measurements were collected with Gamry Reference 600 Potentiostat and Gamry Framework software. EIS measurements were performed with a standard three-electrode Gamry Paint cell setup: a glass cell filled with 3% NaCl was clamped to a coated bronze panel acting as the working electrode, and the Ag/AgCl reference electrode and graphite counter electrode were immersed in the electrode solution with a 4-cm distance between the counter and working electrodes. An area of exposure of the working electrode equal to 14.6 cm^2 was used for analysis from 1 MHz to 0.1 Hz with AC voltage 20 mV rms, and DC voltage 0.0 V versus open circuit potential 0 ± 200 mV. Spectra were interpreted and modeled against equivalent electrical circuits (EECs) with Scribner Associates ZView. Errors in fit between EEC models and the data were calculated as the sum of residual error where the fit differed from the experimental data. Average potentiostat instrument error ranged from 10% at 0.1 Hz to <0.5% at 1 MHz.

Fourier transform infrared microspectroscopy (FTIR-m) measurements were made using a ThermoScientific iS10 infrared spectrometer with a Nicolet Continuμm FTIR microscope, and a 50-μm MCT (mercury telluride/cadmium telluride) detector was used to acquire each spectrum from 4000 to 650 cm^{-1} with 4 cm^{-1} resolution using Omnic software. Spectra of microsampled cross-sections were acquired in transmission mode for 128 scans on a diamond slide. Data was transformed using an N-B strong apodization function and Mertz phase correction. All X-ray studies were

acquired with a Rigaku Ultima IV Multipurpose X-ray diffractometer with a Cu-kα radiation source (λ = 1.542 Å) and step size = 0.002° for 12 s. Powder samples were ground finely with an agate motor and pestle and pressed into a random orientation on a mirrored slide. For scattering studies in transmission mode, thin-walled glass capillary tubes (1.5 mm, Charles-Supper, Co.) were filled with either the aqueous clay dispersions or wet resin and attached to a 20-mm sample window fixed in place adjacent to the vacuum path window.

19.3 Testing and Characterizing the Performance of Chemically Intelligent Coatings

19.3.1 Weathering studies of chemically intelligent coatings for outdoor metalwork

To test the weatherability of chemically intelligent coatings compared to common acrylic coatings, bronze or brass substrates coated with a primer of Paraloid™ B-44 and a topcoat of Kynar Aquatec® RC-10206 or just layers of Paraloid™ B-44 were prepared and weathered in South Florida for 18 months and in a QUV-B chamber for up to 2750 h. The changes in their barrier properties were monitored by EIS and changes in chemistry monitored by FTIR-m.

19.3.2 Characterization of weathered coated substrates by EIS

Before weathering, a simple model best fit both types of coatings, which can be seen in Figure 19.3, where R_b describes the bulk solution resistance and the remaining resistor and capacitor describe the coating. The simplicity of the circuit model implied that there was only a single pathway for current to travel along, due to the resistance of the coating and capacitance of the coating. However, after extensive weathering, the equivalent circuit model best fitting the data became more complex with the addition of either one or two pairs of parallel resistor and constant phase element. We observed that QUV-B films of Paraloid™ B-44 weathered for 2250 h were the most degraded because they required the complete set of three time constants, which are due to (1) the regions of dry/intact coating, (2) the water-swollen/defective layer of the coating, and (3) the exposed metal substrate (having an electrical double-layer capacitance and charge transfer resistance from the growing oxide layer). We attributed R_1 to the resistance of the coating itself, which was $4.2 \times 10^9\,\Omega$ before weathering. After weathering in the QUV-B chamber, the value of R_1 decreased to $1.21 \times 10^5\,\Omega$, and after weathering in Florida, it decreased to $3.12 \times 10^5\,\Omega$, making the reduction in resistance over four orders of magnitude. Comparatively, after weathering for 2750 h in the QUV-B chamber, the films with Kynar Aquatec® RC-10206

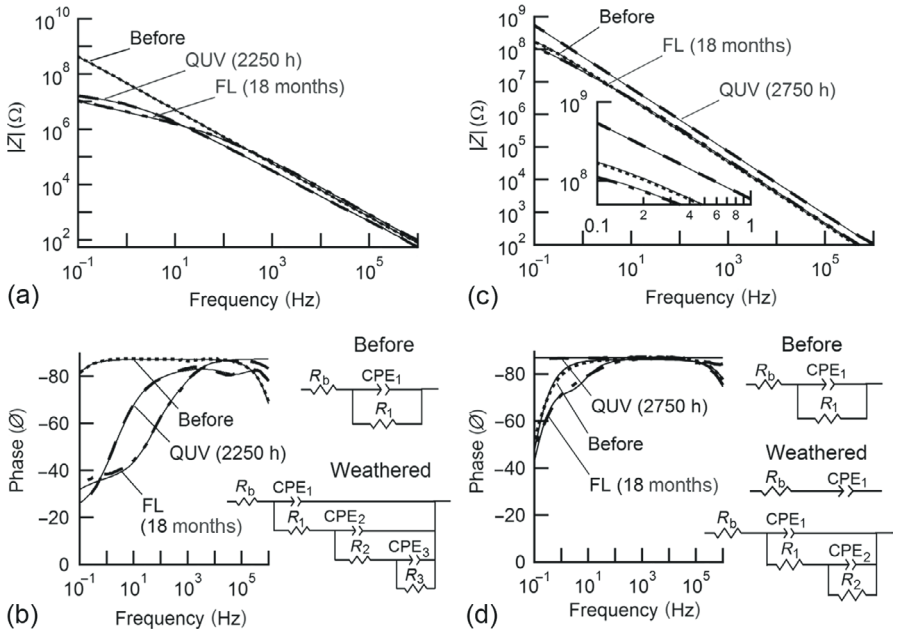
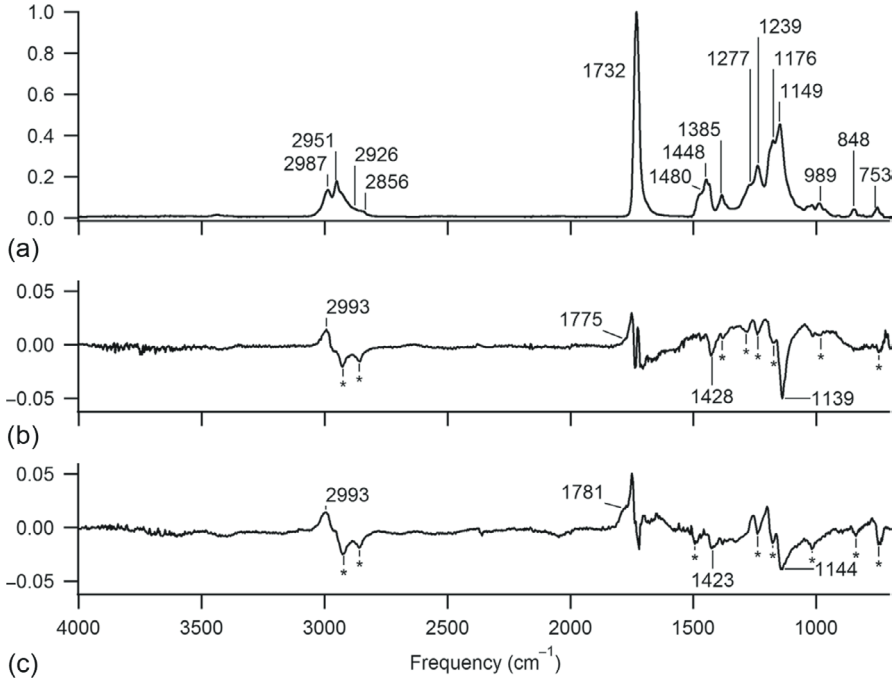


Figure 19.3 Electrochemical impedance spectra of coated bronze substrates before and after weathering in a QUV-B chamber or in Florida. (a) impedance (Z) and (b) phase (ϕ) versus frequency of a substrate coated with Paraloid™ B-44; (c) impedance (Z) and (d) phase (ϕ) versus frequency of a substrate coated with Paraloid™ B-44 basecoat and Kynar Aquatec® RC-10206 topcoat.

showed an increase in the total impedance at frequencies between 10 and 0.1 Hz, likely due to the completion of film formation assisted by the gentle heating (annealing) in the QUV-B weathering cycles. After the initial annealing increase (which actually improved the barrier properties of that coating), the film showed no measurable change in impedance. Before weathering, R_1 had a value of $2.76\times10^8\,\Omega$, and after weathering in Florida, that value decreased to $2.02\times10^7\,\Omega$. These data suggest that coatings with Kynar Aquatec® RC-10206 have longer working lifetimes both in South Florida and in accelerated weathering than do films of Paraloid™ B-44 alone.

19.3.3 Characterization of weathered coated substrates by FTIR

During weathering, coatings may undergo a variety of chemical changes that should be detectable. We monitored changes in chemistry of weathered films using FTIR-m. Shown in Figure 19.4 is the IR spectrum for a solid film of Paraloid™ B-44 before weathering, as well as the subtraction results after weathering in Florida for 18 months and after weathering in a QUV-B chamber for 2250 h. The spectra were



Wavenumber (cm^{-1})	Assignment
2850-2998	CH_3 asym stretch
1732	C=O stretch
1425, (1448)	CH_2 (scissor) def.
(1385), 1480	CH_3 (umbrella) def.
1149, 1176, 1239, 1277	C-O stretch
989	C-O-C stretch
848	CH_2 rocking + C-CH_3 stretch
753	CH_2 in-plane rocking

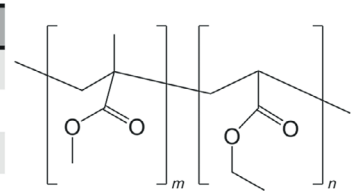


Figure 19.4 (a) FTIR spectra of Paraloid™ B-44 before (b) subtraction spectrum obtained after weathering in Florida for 18 months and (c) subtraction spectrum obtained after weathering in a QUV chamber for 2250 h. Asterisks were used to identify the same peaks as those labeled in the before weathering spectrum in (a). Table indicates functional group assignments for the polymer, an approximated structure of which is shown in the inset.

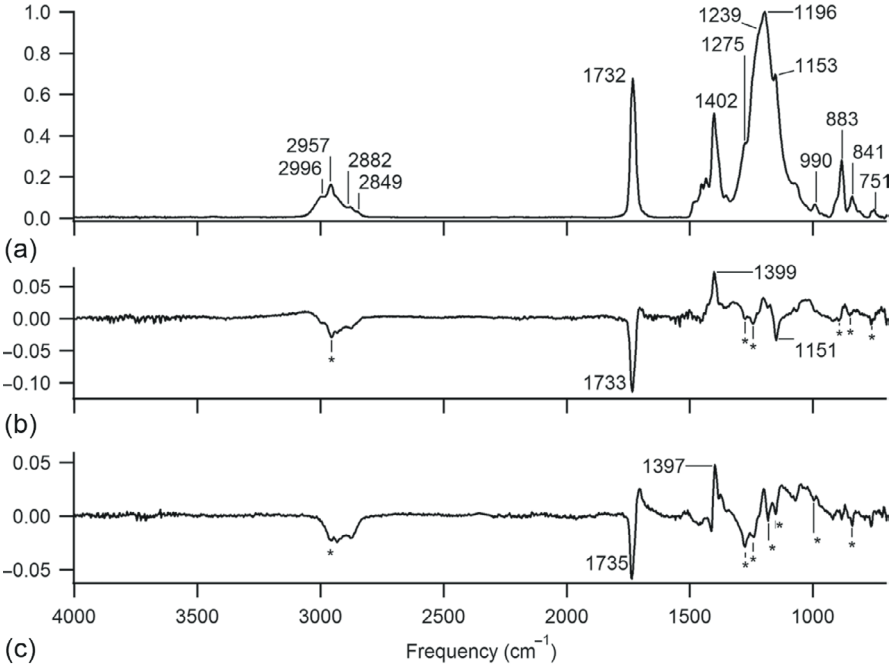
normalized to the most intense peak (the carbonyl peak at 1732 cm^{-1} before subtraction). A partial structure of Paraloid™ B-44 is also shown as a reference aid in correlating the IR band and chemical changes during weathering. Relative to the intensity of the carbonyl peak, the subtraction spectra after both types of weathering show decreases in bands associated with C–O–C stretching, C–O bond motions, CH_2 and CH_3 deformation, and rocking and stretching motions as can be seen in the spectra by the negative peaks. For example, the intense broad collection of peaks between 1140 and 1430 cm^{-1} that are associated with C–O bond motions decreased in intensity after weathering, as can be seen by the negative peaks in that region. The spectral changes indicated that one of the primary chemical changes associated with weathering is loss of the pendant methoxy ($-OCH_3$) or ethoxy ($-OCH_2CH_3$) groups. It is interesting to note that the intensity of the observed band decrease was not large. It has been observed that polymer degradation can lead to the loss of low molecular weight/volatile compounds that are not detected after weathering.[29] Similarly, while large peak decreases were not observed in our data, it is likely that volatile material was lost and thus not observable in our spectra (given that intensity normalization was necessary). Upon coating failure after QUV-B weathering, visual inspection of the panel showed puckering and shrinking of the film, suggestive of significant chemical and physical property changes in the film due to weathering.

Because Kynar Aquatec® RC-10206 contains PVDF and acrylic, preferential loss of the acrylic over the more weatherable PVDF components was expected and was observed in the data shown in Figure 19.5. The spectra were normalized to the most intense peak in the spectrum, which was the C–O stretch at 1149 cm^{-1}. Relative to that peak a decrease was observed in the carbonyl band, which is consistent with the loss of acrylic components. Although it is likely that C–O bond intensities decreased with the loss of carbonyl groups, interpretation of the 1140-1430 cm^{-1} region was complicated by the spectral overlap of the CF_2 and C–O bond motions. The films of Kynar Aquatec® RC-10206 remained flexible without cracks or puckers after weathering.

19.4 Characterizing Physically Intelligent Coatings

19.4.1 Use of synthetic nanoclay in waterborne nanocomposites coatings

The studies described above effectively incorporated chemical intelligence into coatings for outdoor metals and demonstrated longer working lifetimes than commonly used coatings to protect material cultural heritage. But, those studies did not take advantage of strategies to confer physical intelligence. We focus on incorporating optically transparent inorganic materials, such as the synthetic clay, Laponite, to produce films having reduced susceptibility to hygroscopic swelling. Large aspect



Wavenumber (cm^{-1})	Assignment
2850-2998	CH_3 asym stretch
1732	C=O stretch
1448	CH_2 (scissor) def.
1385	CH_3 (umbrella) def.
1240	CF_2 asym stretch
1150, 1210	CF_2 sym stretch, bend
1153, 1195, 1239, 1275	C-O stretch
990	C-O-C stretch
841	CH_2 rocking + C-CH_3 stretch
751, 883	CH_2 rocking

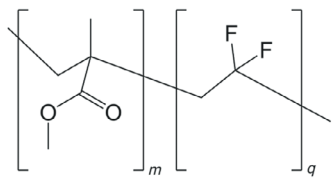


Figure 19.5 FTIR spectra of (a) Paraloid™ B-44 basecoat and Kynar Aquatec® RC-10206 topcoat before (b) subtraction spectrum obtained after weathering in Florida for 18 months and (c) subtraction spectrum obtained after weathering in a QUV chamber for 2250 h. Table indicates functional group assignments for the polymer, an approximated structure of which is shown in the inset.

ratio particles, such as clays, accomplish this by forcing water molecules to travel a tortuous path around them. Laponite is a synthetic silicate in the smectite family whose chemical formula $Na_{0.7}[(Si_8\ Mg_{5.5}Li_{0.3})O_{20}(OH)_4]$ creates a 2:1 particle with one octahedrally coordinated magnesium/lithium oxide sheet sandwiched between two tetrahedrally coordinated silica sheets and one interlayer cationic sheet of Na^+ ions and water molecules for charge balance. Laponite has discoid single crystals with a high aspect ratio of 25, specific surface area (350 m^2/g), and charged surfaces, where the face has an induced negative charge from the expansion of sodium cations out of the interlayer space, and the edge of the platelet is positively charged at near-neutral pH due to protonated hydroxyl groups along the magnesium-lithium octahedral sheet, as illustrated in Figure 19.6a.[30] Like many clays, Laponite is able to undergo chemical and exchange reactions because it has accessible hydroxyl groups available for silanation on the sheet's broken edge and exchangeable sodium cations connecting the face of particle-to-particle.[31–34] And like most clays, Laponite forms multilayered stacks of clay sheets that may be hundreds of nanometers in thickness, which, if left intact, are large enough to be visible to the eye and to cause significant disruptions in film formation when incorporated into coatings. An idealized picture of Laponite is shown in Figure 19.6a with a layer thickness of 1.08 nm and diameter of 25 nm. The size and shape of the individual platelet has been well characterized by powder diffraction as a disc shaped with a thickness of 1.29 nm in ambient conditions, a dis-

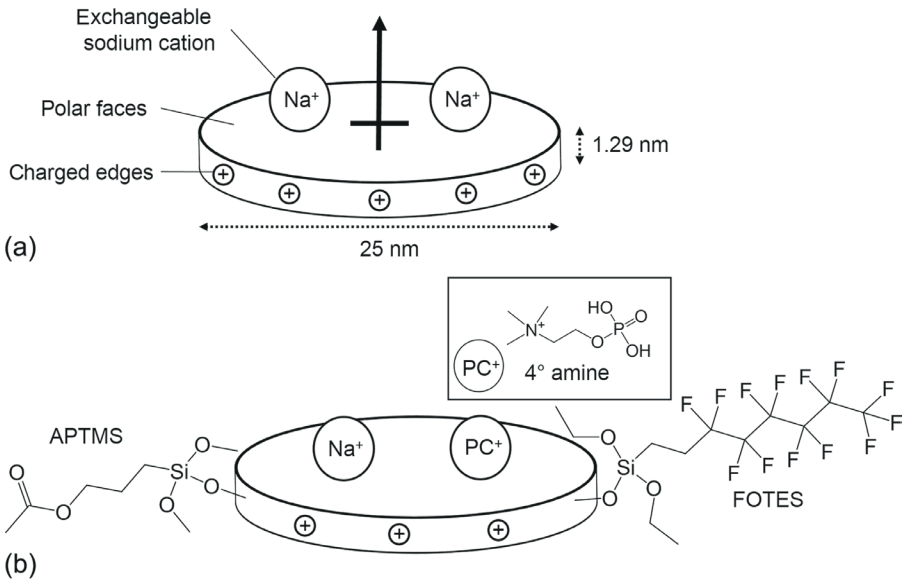


Figure 19.6 Overview of Laponite's properties (a) Laponite modification schemes used in this work (b).

crepancy with the smaller chemical structure that is caused by water sorption within the clay.[35] The swelling ability of Laponite aids in exfoliation, that is, separating the layers and stabilizing the individual platelets in solution, which can be a significant hurdle in successfully incorporating these nanoparticles into coatings. Once exfoliated, the platelets must be stable in solution so that they do not aggregate nor induce coagulation of the latex particles in the wet coating suspension. Stabilization of these anisotropically charged particles can be achieved in a number of ways including balancing the positive charges on the rim with a peptizing agent, inducing an inverse double-layer formation through cation exchange with surfactants, or covalently attaching any number of siloxane molecules. The selection of which method or combination thereof is based mostly on the specifics of the system and can also be used to confer specific chemical properties.

19.4.2 Modification of nanoclays to increase compatibility with the coating

To exfoliate and stabilize Laponite platelets and produce dispersed colloidal suspensions in Kynar Aquatec® RC-10206, two basic strategies were used: (1) covalent modification and (2) cation exchange. To accomplish that and to increase compatibility between the nanoclay and latex binder, Laponite was covalently modified by a silanation reaction with the accessible hydroxyl groups on the edge of the clay sheet. Two different silane molecules were used: 3-acetoxypropyltrimethoxysilane (Lap-APTMS), where its polar groups were expected to interact with the acrylic portion of the resin, or tridecafluoro-1,1,2,2-tetrahydrooctyl triethoxysilane (Lap-FOTES), where its hydrophobic, fluorinated groups were expected to interact with the PVDF portion of the resin. To encourage exfoliation after covalent modification, cation exchange of sodium atoms at the clay surface was conducted using phosphorylcholine tetrahydrate (PC), thus producing nanoclays that were both covalently and charge exchanged, referred to as Lap-APTMS + PC and Lap-FOTES + PC. The types of modification are shown in Figure 19.6b.

19.4.3 Experimental procedures for modification of the nanoclay

Laponite (RD, Southern Clay Products, Inc.) and silylating agents 3-acetoxypropyltrimethoxysilane (APTMS, Gelest, Inc.) and (tridecafluoro-1,1,2,2-tetrahydrooctyl) triethoxysilane (FOTES, Gelest, Inc.) were used as supplied without further drying or purification. Toluene was distilled directly into a flask containing Laponite RD (1 g nanoclay/100 mL solvent) under anhydrous conditions in a closed system (δ^+ N_2 flow). After 30 min of heating with stirring at 35 °C, the siloxane was added to the toluene clay mixture (1 mmol/g clay) and the contents in the flask were left to stir an additional 4 h at the same temperature. The covalently modified Laponite was

isolated for diffraction analysis by vacuum filtration with a 0.2 µm Nylon membrane, washed extensively with toluene, and dried overnight at 65 °C. The aqueous dispersions of modified Laponite were obtained by quenching the grafting reaction with 50 mL of water and isolating the water-stable nanoclay by liquid-liquid extraction in a separatory funnel, the final percent solids being ~2.5% (w clay/%w H_2O). The dispersions were then either sonicated with tetrasodium phyrophosphate (TSPP) for post-let down addition to the resin or prepared for further modification. For cation exchange the modified nanoclay (LR-APTMS and LR-FOTES) was diluted to 100 mL and heated to 50 °C after which one equivalent (CEC_{LR} = 0.75 mmol/g clay) of phosphorylcholine chloride calcium salt tetrahydrate (PC) was added and stirred for 12 h. The exchanged/grafted clay was vacuum filtered, washed with ethanol, and immediately redispersed in DI water for post-let down addition to the resin, as detailed in the formulation.

19.4.4 Characterization of modified Laponite by FTIR

Fourier transform infrared spectra of Lap-APTMS with and without PC were collected and shown in Figure 19.7. With Laponite present, a number of IR bands were produced by the hydroxyl groups and sorbed water in the clay, where O–H stretching peaks appeared from 3600 to 3400 cm^{-1} and an H–O–H deformation peak was visible near 1632 cm^{-1}, as can be seen in the spectrum of unmodified Laponite (Figure 19.7e). After grafting with APTMS additional peaks were observed: aliphatic C–H stretching (3000-2800 cm^{-1} region), carbonyl stretching at 1709 cm^{-1}, and C–H rocking at 1285 and 1259 cm^{-1}. No increase in the Si–O stretch (1012 cm^{-1}) was observed postmodification because the vast majority of the band's intensity was produced by Laponite itself and the silane functionalization contributed only slightly. The Lap-APTMS spectrum (Figure 19.7d) was subtracted from the Lap-APTMS + PC (Figure 19.7c) spectrum to observe small changes in the spectrum after cation exchange with PC and is shown in Figure 19.7b. A reference spectrum of PC only is shown in Figure 19.7a. Apparent in the subtraction spectrum are asymmetric and symmetric stretching $P–O_3$ bands at 1151 and 1092 cm^{-1}, respectively, the C–O–P stretching band at 967 cm^{-1}, and an additional C–H bending peak (δ C–H) near 1478 cm^{-1}; all are spectral features of the negatively charged phosphate head group because the quaternary amine is not infrared active. Given the relatively small amount of both phosphoryl choline on the surface and APTMS covalently bound to the edge compared to intense vibration of the nanoclay lattice structure, it is not surprising that the peaks corresponding to modification were of low intensity, as depicted in Figure 19.7c. Presence of the expected IR bands after each modification step in the production of Lap-FOTES and Lap-FOTES + PC were also verified by infrared analysis although the data is not shown. Negative peaks from the subtraction of Lap-APTMS from the Lap-APTMS + PC spectrum occur near the C=O and C–H

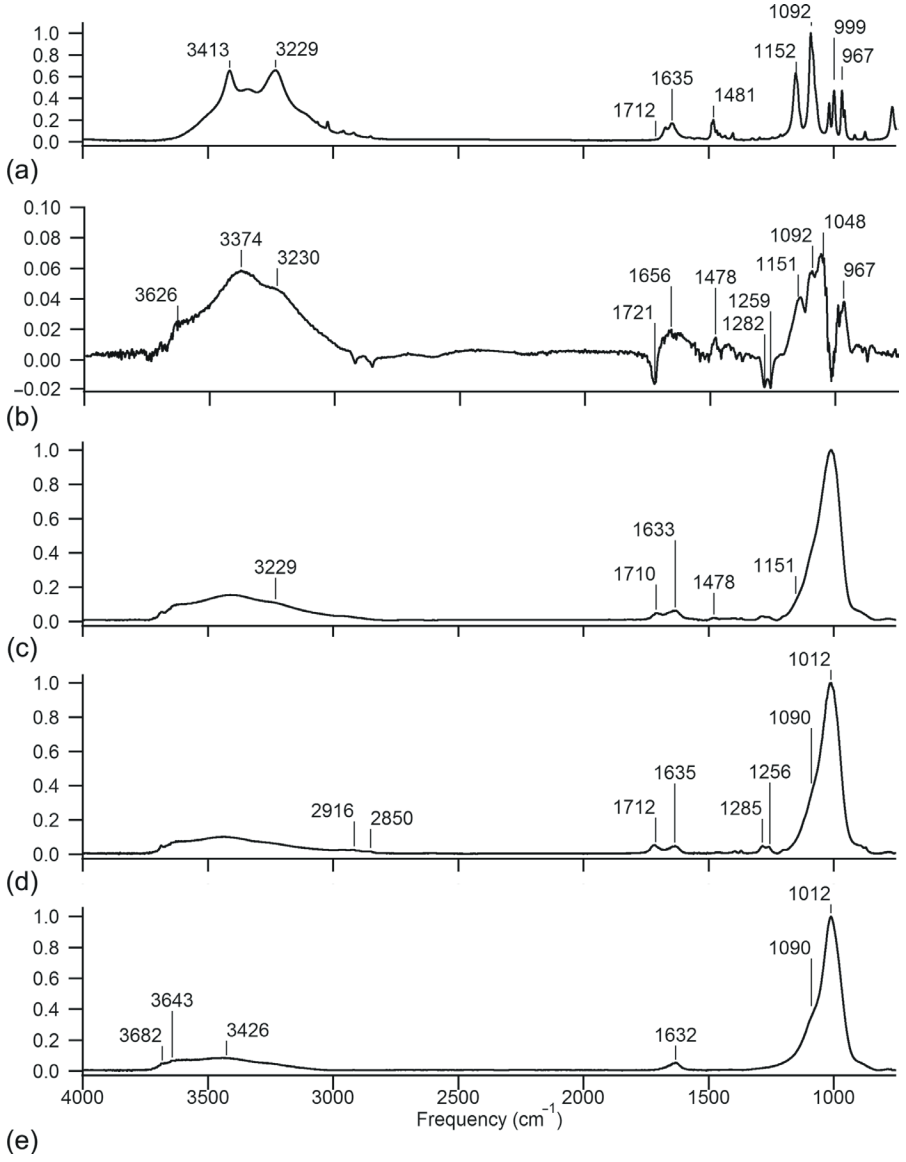


Figure 19.7 FTIR spectra of (a) phosphorylcholine chloride tetrahydrate (PC), (b) the subtraction result obtained by subtracting the spectrum of Lap-APTMS+PC (shown in (c)) from Lap-APTMS (shown in (d)). The spectrum of unmodified Laponite (Na-Lap) is shown in (e).

bending regions of the spectrum, indicating a slight loss of the silane after cation exchange, likely due to loss of adsorbed silane.

19.4.5 Characterization of modified Laponite by X-ray methods

Both wide angle X-ray diffraction (WAXD) and small angle X-ray scattering (SAXS) were utilized in characterizing particle sizes and inter- and intraparticle spacing in the sub-500 nanometer range. In general, the sharpening of a diffraction peak indicates an increase in short- or long-range order in the material. The WAXD patterns of Laponite before and after modification are shown in Figure 19.8. The most significant difference between spectra occurs at low angles and is the interlayer spacing (d_{001}) of the clay, that is, the distance from one cationic sheet to the next. Full characterization of the diffractogram of the unmodified sodium Laponite (labeled Na-Lap in Figure 19.8) indicated the basal spacing was 1.23 nm, calculated by Bragg's law from a broad peak occurring at 7.1 2θ, with additional peaks at 20.0 2θ ($d_{02,11}$ = 0.44 nm), 27.8 2θ (d_{005} = 0.32 nm), and 35.3 2θ ($d_{20,13}$ = 0.25 nm).[36] When covalently modified by APTMS the basal spacing increased: the d_{001} peak shifted to 5.6 2θ (d_{001} = 1.57 nm). Laponite modified with FOTES produced a broader peak with its maximum at 6.38 2θ, corresponding to a 001 spacing of 1.38 nm. Cation exchange did not appreciably change the basal plane spacing in either case, with a Lap-APTMS + PC peak at 5.59 2θ (d_{001} = 1.58 nm) and a Lap-FOTES + PC peak at 6.33 2θ (d_{001} = 1.39 nm), respectively (data not shown). These correspond well to established literature values where diffraction analysis of dry Laponite in ambient conditions provided a d_{001} peak occurring near 6.7° 2θ that corresponds to an interlayer spacing of 1.29 nm, where upon edge modification of the interlayer space increased to 1.41 nm.[37]

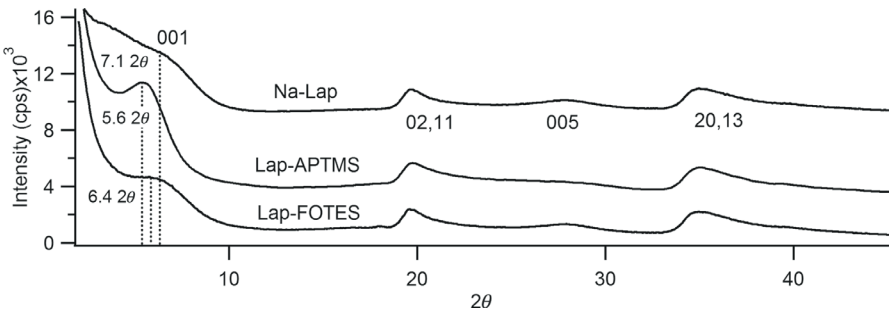


Figure 19.8 WAXD spectra of unmodified Laponite (Na-Lap) (top spectrum); Laponite covalently modified with APTMS (middle spectrum); and Laponite covalently modified with FOTES (bottom spectrum).

Further inspection of the undiluted aqueous dispersion of only covalently modified clays by SAXS suggested that two distinct sizes were present in the Laponite dispersions, with one corresponding to single, completely exfoliated platelets having thicknesses between 1.26 and 1.45 nm after covalent modification (1.11 nm before modification) and diameters between 25.22 and 28.92 nm (22.11 nm before modification); see Table 19.4 for a complete list of the values. These measurements show that on average with covalent modification, particle diameter increased, which is consistent with clay edge modification rather than random or face modification.

19.4.6 Fitting SAXS data

The SAXS curve of Lap-APTMS+PC was fit with two different particle geometries in Figure 19.9: spheroid (left) and cylindrical (middle). A platelet model, which might be the most suitable for Laponite, has not yet been developed. The spectrum fit with a spheroid model in neutral deionized water showed two distinct populations, one with an average platelet thickness of 1.75 nm and diameter of 34.98 nm and a second, more symmetric particle with average thickness and diameter of 36.91 nm (diameters were determined by geometrical calculations based on the spheroid and particle aspect shape). The 1.75 nm population consists of an estimated 96.6% of the scattering solids and likely represents disperse but intercalated platelets due to an estimated nearest neighbor value of 1.26 nm. The second set of particles, while larger and more uniform in shape, compose only 3.4% of the solids in the aqueous suspension, but are still involved with particle-particle interactions at a distance of 22.73 nm. For comparison, the SAXS curves of Lap-APTMS+PC were fit with a cylindrical model that yielded one population with an average diameter of 35.42 nm and a layer thickness of 1.77 nm. Other variables in the model assigned a nearest neighbor value equal to 1.78 nm, indicating that in both models the closest platelet was within the thickness of perpendicular travel through one hydrated particle. While both models provided good fits to the data, the results were slightly different, and AFM was utilized to provide an additional means for measuring particle sizes and to monitor the uniformity of the hydrated particles.

19.4.7 Characterization of modified Laponite by AFM

To provide a direct method of measuring particle sizes, a droplet of Lap-APTMS at a concentration of 0.025% w/w in water was allowed to dry on a freshly cleaved mica substrate and characterized by tapping mode atomic force microscopy (AFM). Shown in Figure 19.10 is a 500×500 nm height image. Many completely exfoliated Laponite platelets, having approximate dimensions of 35×1.5 nm, can be observed. The line sections of the image were taken to obtain particle height measurements. Particles 1 and 2 showed heights of ~1.5 nm, which are similar to thickness measurements

TABLE 19.4 WAXD and SAXS Characterization Data Table of Unmodified (Na-Lap) and Modified Laponite

	WAXD $T_{d_{001}}$ (nm)	SAXS D (nm) in H_2O Cylinder	SAXS T (nm) in H_2O Cylinder	SAXS T (nm) in H_2O Spheroid		SAXS D (nm) in H_2O Spheroid	SAXS T (nm) in FMA 12 Spheroid		SAXS D (nm) in FMA 12 Spheroid	
Na-Lap	1.23	22.11	1.11	A	1.84	27.59	A	1.66	A	24.84
				B	22.84	22.84	B	158.20	B	158.20
Lap-APTMS	1.57	25.22	1.26	A	1.18	23.50	A	1.29	A	25.86
				B	45.84	45.84	B	158.20	B	158.20
Lap-APTMS+PC	1.58	35.42	1.77	A	1.75	34.98	A	1.33	A	26.58
				B	36.91	36.91	B	158.20	B	158.20
Lap-FOTES	1.38	28.92	1.45	A	1.59	23.87	A	1.56	A	23.34
				B	104.59	104.59	B	152.44	B	152.44
Lap-FOTES+PC	1.39	35.56	1.78	A	2.00	29.94	A	1.55	A	23.19
		73.30	73.30	B	105.83	105.83	B	153.26	B	153.26

	Near Neighbor (nm) in H_2O Cylinder	Volume Fract. (%) in H_2O Cylinder	Near Neighbor (nm) in H_2O Spheroid		Near Neighbor (nm) in FMA 12 Spheroid		Volume Frac. (%) in H_2O Spheroid		Volume Frac. (%) FMA 12 Spheroid	
Na-Lap	15.28	100.00	A	1.06	A	1.93	A	95.27	A	13.59
			B	12.30	B	10.99	B	4.73	B	86.41
Lap-APTMS	1.82	100.00	A	1.33	A	1.33	A	98.30	A	22.33
			B	10.02	B	12.73	B	1.70	B	77.67
Lap-APTMS+PC	1.78	100.00	A	1.26	A	1.32	A	96.60	A	20.00
			B	22.73	B	12.62	B	3.40	B	80.00
Lap-FOTES	1.55	100.00	A	1.39	A	1.37	A	96.83	A	40.89
			B	24.68	B	13.79	B	3.17	B	59.11
Lap-FOTES+PC	2.19	93.58	A	1.94	A	1.51	A	92.41	A	25.05
	65.22	6.42	B	68.55	B	13.53	B	7.59	B	74.95

SAXS data was taken in both aqueous solution and in Kynar Aquatec® FMA 12 and fit using either or both cylinder or spheroid models, as labeled in the column headings. Nearest neighbor and volume fraction estimations were calculated by fitting SAXS data. Spheroid data fitting allowed two distributions to be fit, which are labeled as A and B within the data table.

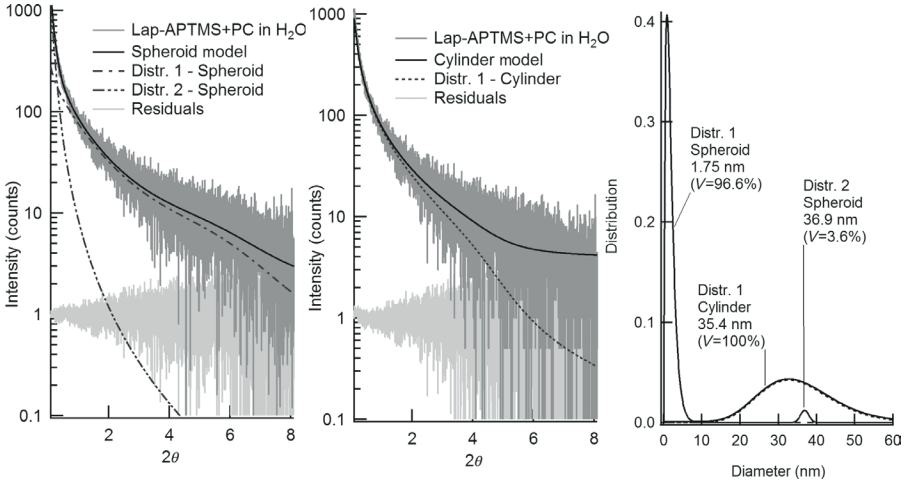


Figure 19.9 SAXS spectrum of Lap-APTMS+PC in water fit using a spheroid model (left), cylindrical model (middle), and the resulting particle diameters shown (right).

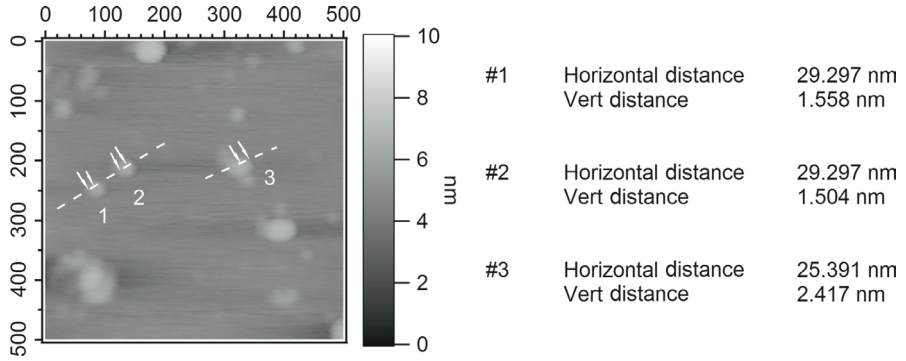


Figure 19.10 AFM height image (left) of Lap-APTMS+PC dried on a freshly cleaved mica substrate. Data table from line profiles of the height image is shown (right).

obtained by cylindrical fitting of SAXS data. Particle 3 appears to be larger and thicker, with a height of ~2.4 nm and diameter of ~55 nm. While small platelets were commonly observed, there were also aggregations of a few platelets (having dimensions of 125×7 nm), one of which can be seen in the lower left quadrant of Figure 19.10. Our observations by AFM, which compare well to other's,[38] and our values obtained by SAXS-fitting showed a small range of diameters that are comparable in size to the theoretical crystal model of Laponite. Observation of correctly sized particles provided confirmation that our analytical tools and data analysis were sensitive to Laponite dispersed in aqueous solutions or as a dry film or powder.

19.4.8 Incorporating modified Laponite into coatings

After having ensured that the platelets existed as mostly exfoliated small particles in aqueous dispersions as characterized by AFM, SAXS and having observed the optical clarity of the solutions, the stability of the clay in the waterborne PVDF resin was explored with the goal of limiting particle aggregation. It was found that at even low loading levels (<0.1% Laponite w/w% Kynar ARC) upon drying, the normally flexible film showed small cracks after spray-coating on bronze that may have been induced by aggregation of clay particles during drying. Control over platelet motion and charge was tuned by adjusting the rheology of the bulk matrix, and subsequently, a more viscous coating, Kynar Aquatec® FMA 12 was used. Films of that coating did not crack after drying, possibly because limiting particle diffusion may reduce nanoclay aggregation. The undiluted wet Kynar Aquatec® FMA 12 with Lap-APTMS+PC nanocomposite resin was analyzed by SAXS and fit to a two-dispersion spheroid model shown in Figure 19.11 in an effort to determine if either particle shape or interactions changed in the aqueous latex suspension compared to water alone (as shown in Figure 19.9). While the aqueous dispersions fit with a cylinder geometry model were found to give the most accurate data when compared with AFM data, spheroid fits allow for multiple populations with slightly different shapes in the dispersion, which certainly exist for Laponite (one distribution) in a polymer latex (the second distribution) suspension. Fitting the scattering curves obtained by SAXS to the spheroid model, one distribution had a size similar

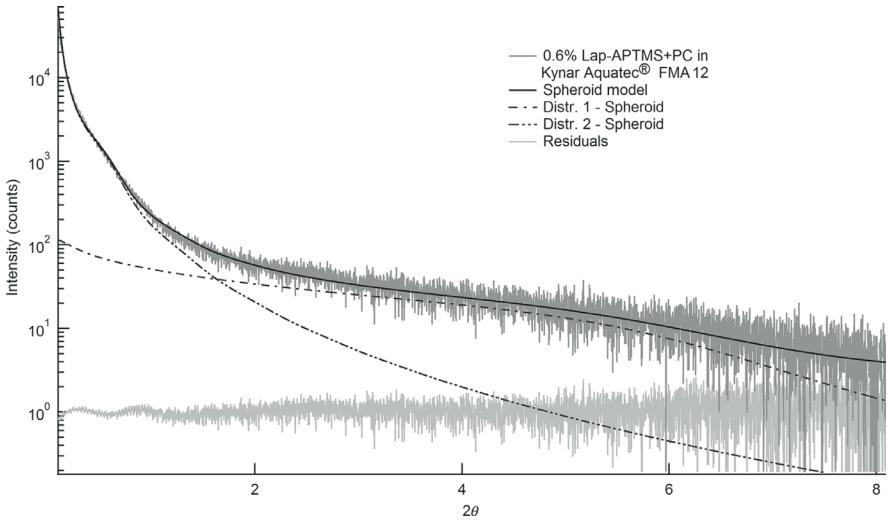


Figure 19.11 SAXS spectrum of Lap-APTMS+PC in Kynar Aquatec® FMA 12 fit with a spheroid model.

to that obtained in the aqueous SAXS data, having a diameter of 26.6 nm, 1.33 nm in thickness and a nearest neighbor at 1.32 nm, which likely corresponded to the Lap-APTMS+PC particle itself (labeled A in Table 19.4). A second distribution existed and was assigned to the blended PVDF/acrylic latex resin having a median size near 158.2 nm with a nearest neighbor of 12.6 nm (labeled B in Table 19.4). The small and broad diffraction peak occurring at 5.9 2θ (d_{001}) is an indication of low crystallinity, suggesting that there may be very short scale ordering in both distance and time in the suspension.

19.5 Testing the Performance of Physically Intelligent Coatings

19.5.1 Investigating the Barrier Properties of Waterborne PVDF-Clay Nanocomposites by EIS: Effects of Annealing

In our previous work we have shown that the barrier properties of the waterborne PVDF resin improved after exposure to QUV-B weathering cycles, due to the annealing effects of those cycles,[23] and we again investigated that effect for the nanocomposite films. Shown in Figure 19.12a and b are EIS spectra of films with the fluorinated nanoclay, Lap-FOTES+PC, incorporated into Kynar Aquatec FMA 12 as a topcoat with a solvent-based Paraloid™ B-44 primer on bronze before

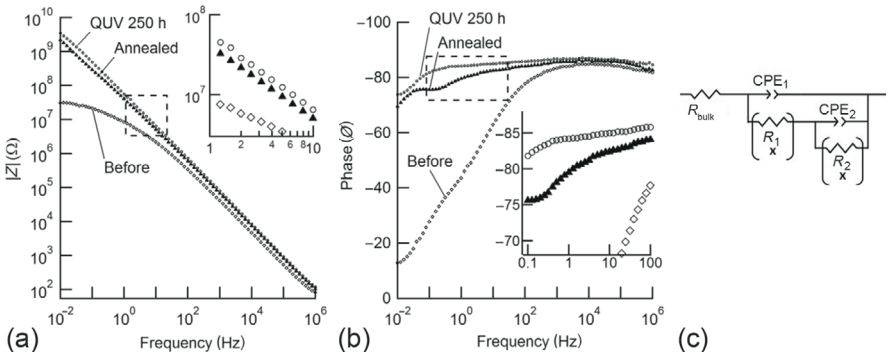


Figure 19.12 EIS spectra of films of Kynar Aquatec® FMA 12 with Lap-FOTES+PC incorporated on Paraloid™ B-44 primed bronze substrates. Impedance (a) or phase (b) versus frequency plots are shown. Equivalent circuit used to describe the system is shown (c). Based on the fits, it was determined that neither R_1 nor R_2 dominated the circuit at any frequency, and so the model was simplified to exclude those elements (although we included them in the illustration to acknowledge their physical presence and used parentheses to indicate that they were excluded from the fit).

annealing, after annealing, and after weathering in a QUV-B chamber for 250 h. There are two major changes in the EIS spectrum after annealing: (1) the total impedance of the system increased by approximately two orders of magnitude at low frequencies and (2) because the phase angle was close to –90° at all frequencies, capacitive properties of the system became dominant. After 12 h of annealing at 65 °C, every coated substrate with covalently modified Laponite (including those having undergone the additional cation exchange step) incorporated into the topcoat displayed a total impedance greater than 100 MΩ at 0.1 Hz, as well as a phase angle higher than –70° at all frequencies (one example data set is shown in Figure 19.12). Using the same method outlined in a previous publication,[23] the EEC shown in Figure 19.12c was fit to EIS data taken before and after films of Kynar Aquatec® FMA 12 with Lap-FOTES + PC incorporated were soaked in water for 4 h in a standard electrolyte. The three elements in the model fit to the data were assigned: R_{bulk} corresponded to the bulk electrolyte resistance, CPE_{Layer2} and CPE_{Layer1} corresponded to the electrolyte swollen (more permeable) portion of the coating and dry (less permeable, more protective, higher impedance, lower capacitance) layer of the coated bronze. As the CPE_{Layer1} was fit with a phase parameter nearly 0.95 in all cases, it is most likely associated with the drier portion of the topcoat due to its low capacitance and nearly ideal phase. In contrast, CPE_{Layer2} was assigned a phase parameter (ϕ) close to 0.85 in all cases, indicating that layer of the coating exhibited more water transport through the film.

In general, the permeability of a coating to electrolyte causes an increase in capacitance, which is not a desirable feature of protective coatings as it may precede corrosion. Capacitance can be determined from a constant phase element value and those values for films with and without nanoclays incorporated are shown in Table 19.5. Circuit model fitting provided an initial capacitance of 3.49 and 3.62 nF for Lap-FOTES + PC nanocomposites, which were higher than the 3.31 nF for Layer 1 and 2.14 nF for Layer 2 for the film containing Lap-APTMS + PC. The noncation exchanged Lap-FOTES was extremely difficult to disperse in a homogenous mixture and also had the highest modeled capacitance of 8.65 and 4.53 nF for the first and second layers, respectively.

19.5.2 Calculating capacitances and volume fractions of water in electrolyte swollen films

The resistance of films with and without having nanoclays incorporated was challenged by immersing coated metal substrates in water. Because water/electrolyte ingress causes capacitance to increase, calculated capacitance values may be used to determine volume fraction of water using the Brasher-Kingsbury equation.[39] Capacitance values and volume fractions of water occupying the coating before and after soaking in electrolyte were determined and are listed in Table 19.5. Films with

TABLE 19.5 Capacitance and Volume Fractions of Polymer Nanoclay Films

	Capacitance (nF) Before	Capacitance (nF) After	VF_{H_2O} (%V/V)	Total VF_{H_2O} (%V/V)
Kynar Aquatec ARC*	C1: 3.86	C1: 5.80	9.22	9.22
Kynar Aquatec FMA-12*	C1: 3.43	C1: 5.33	10.1	10.1
Na-Lap in FMA-12	C1: 1.57	C1: 1.89	4.21	8.90
	C2: 5.66	C2: 6.95	4.69	
Lap-APTMS in FMA-12	C1: 0.723	C1: 0.76	1.20	7.33
	C2: 2.50	C2: 3.28	6.13	
Lap-APTMS+PC in FMA-12	C1: 3.31	C1: 6.97	16.9	18.0
	C2: 2.14	C2: 2.24	1.06	
Lap-FOTES in FMA-12	C1: 8.65	C1: 1.06	4.55	7.02
	C2: 4.53	C2: 5.05	2.47	
Lap-FOTES+PC in FMA-12	C1: 3.49	C1: 3.96	2.90	3.45
	C2: 3.62	C2: 3.71	0.55	

C1 and C2 were calculated using fit values from circuit modeling. Because resistors did not fit the EIS data, capacitance values of films containing Laponite were calculated using $C = \text{CPE} \times \omega^{a-1}$, while capacitance values from circuit models where resistors fit data (films denoted by * where no nanoadditive was used) were calculated using $C = (\text{CPE} \times R)^{1/a}/R$ The values of C1 and C2 were then used to calculate volume fractions using: $\text{VF} = \log(C_t / C_0) / \log \varepsilon_{H_2O} \times 100\%$ where VF is the volume of water uptake in percent, C_t is the capacitance after soaking, C_0 is the initial dry capacitance, and ε_{H_2O} dielectric constant of water (80.1 at 20 °C).

not only the lowest volume fraction, but also the lowest initial capacitance should offer the best barriers to water transport through films and best corrosion protection. Kynar Aquatec® RC-10206 and FMA-12 films without nanoclay additives absorbed the most water (nearly 10% volume fraction of water) as calculated by their changes in capacitance after immersion. The Lap-APTMS film in FMA-12 absorbed 7.33% total volume fraction of water, while the film containing Lap-APTMS+PC absorbed 18.0%. For comparison, unmodified Laponite was also incorporated into films and found to uptake a total volume of water of 8.90%. The Lap-FOTES+PC dispersed easily in water, and showed the least total volume fraction uptake of 3.45%.

19.5.3 Assessment of the effect of intelligent coating

Comparing the performance of these intelligent coatings to our prior work on common waterborne and solvent-based acrylic coatings provides a useful metric for evaluating the effect of our method of approach. We previously determined that

waterborne coatings of Rhoplex™ WL-81 adsorbed a water volume fraction of ~14% and solvent-based coatings of Paraloid™ B-44 absorbed ~5%.[22] In the studies described here, we observed that waterborne films having only chemical intelligence had a water volume fraction of ~10%, considerably less than traditional waterborne coatings previously measured. Most interestingly, the best-performing films had both chemical and physical intelligence and resulted in a water volume fraction of ~3.5%, lower than solvent-based coatings and, in fact, were the lowest water volume fraction for protective coatings for corrosion control that we have measured to date.

19.6 Conclusions and Future Directions

Coatings commonly used in material cultural heritage conservation rely upon decades-old technologies because conservators have experience with the working properties of those coatings and issues associated with weathering, reversibility, and cross-reactivity have mostly been encountered with known work-arounds. However, as conservation professionals indicated (as reported in our survey) and as our weathering studies described above have shown, the protective lifetime of the commonly used coatings is limited. We have demonstrated that using chemically intelligent coatings based on the waterborne coating Kynar Aquatec® is an effective route to producing coatings with improved weatherability and extended working lifetimes. The estimated working lifetime is unknown as films of Kynar Aquatec® have not yet failed, while solvent-based acrylics have failed both in outdoor South Florida and in accelerated QUV-B weathering cycles. We have demonstrated that it is possible to build another aspect of intelligence into coatings by incorporating nanoclays, which provide a physical barrier for water. By chemically modifying nanoclays of Laponite with silane groups, we showed that stable suspensions in Kynar Aquatec® coatings may be produced. Using EIS, we showed that dry films containing Laponite have excellent barrier properties and maintain their protective properties during accelerated weathering, showing film capacitance values as low as 0.127 nF after weathering for 250 h in a QUV-B chamber. Lap-APTMS had higher performance before cation exchange based on its larger water fraction values and particle size estimates by SAXS that were observed after exchange. In contrast, the cation exchange step improved the dispersibility of Lap-FOTES and resulted in a most dramatic reduction in water uptake, with the lowest value that we have measured to date.

We aim to study the performance of the films with nanoclays incorporated to understand their long-term performance. Our goal is to provide higher-performing coatings that have been thoroughly tested and that meet the unique requirements for use in the conservation of material cultural heritage, so that they may be used in practice.

Acknowledgments

We gratefully acknowledge the support of the National Science Foundation, CHE 0936752 and the Institute for Museum and Library Services, LG 5-080071-08.

References

1. Baumberg I, Berezin O, Drabkin A, et al. Effect of polymer matrix on photo-stability of photo-luminescent dyes in multi-layer polymeric structures. Polym Degrad Stab 2001;73(3):403–10.
2. Botelho G, Silva MM, Goncalves AM, et al. Performance of electroactive poly(vinylidene fluoride) against UV radiation. Polymer Testing 2008;27(7):818–22.
3. Iezzi RA, Gaboury S, Wood K. Acrylic-fluoropolymer mixtures and their use in coatings. Prog Org Coat 2000;40(1–4):55–60.
4. Wood KA. Optimizing the exterior durability of new fluoropolymer coatings. Prog Org Coat 2001;43(1–3):207–13.
5. Alvial G, Matencio T, Neves BRA, et al. Blends of poly(2,5-dimethoxy aniline) and fluoropolymers as protective coatings. Electrochim Acta 2004;49(21):3507–16.
6. Bressy-Brondino C, Boutevin B, Hervaud Y, et al. Adhesive and anticorrosive properties of poly(vinylidene fluoride) powders blended with phosphonated copolymers on galvanized steel plates. J Appl Polym Sci 2002;83(11):2277–87.
7. Curkovic HO, Kosec T, Legat A, et al. Improvement of corrosion stability of patinated bronze. Corros Eng Sci Technol 2010;45(5):327–33.
8. Selvakumar N, Jeyasubramanian K, Sharmila R. Smart coating for corrosion protection by adopting nano particles. Prog Org Coat 2012;74(3):461–9.
9. Huang MX, Zhang H, Yang JL. Synthesis of organic silane microcapsules for self-healing corrosion resistant polymer coatings. Corrosion Sci 2012;65:561–6.
10. Jackson AC, Bartelt JA, Braun PV. Transparent self-healing polymers based on encapsulated plasticizers in a thermoplastic matrix. Adv Funct Mater 2011;21(24):4705–11.
11. Garcia SJ, Fischer HR, White PA, et al. Self-healing anticorrosive organic coating based on an encapsulated water reactive silyl ester: synthesis and proof of concept. Prog Org Coat 2011;70(2–3):142–9.
12. Shchukin DG, Mohwald H. Self-repairing coatings containing active nanoreservoirs. Small 2007;3(6):926–43.
13. Hughes AE, Cole IS, Muster TH, et al. Designing green, self-healing coatings for metal protection. NPG Asia Mater 2010;2(4):143–51.
14. Pliny (the Elder). Naturalis historia, Book XXI, C.E. 77–79.
15. Toch M. The chemistry and technology of paints. 2nd ed. New York: D. Van Nostrand Co; 1916.
16. Bharucha NR, Baker MT. Clear lacquers for copper and copper alloys: a summary of research carried out by B.N.F.M.R.A. for I.N.C.R.A. British Non-Ferrous Metals Research Association; 1965.
17. Walker R. Use of benzotriazole as a corrosion inhibitor for copper. Anti-Corros Methods Mater 1970;17(9):9–15.
18. Wood KA, Cypcar C, Hedhli L. Predicting the exterior durability of new fluoropolymer coatings. J Fluor Chem 2000;104(1):63–71.
19. Deflorian F, Fedrizzi L, Lenti D, et al. On the corrosion protection properties of fluoropolymer coatinGS. Prog Org Coat 1993;22(1–4):39–53.
20. Clare TL, Lins PA. Evaluation of fluorinated protective coatings for outdoor metals. In: Proceedings of the ICOM-CC metal 07 WG, protection of metal artifacts; 2007. p. 83–7.
21. Puomi P, Fagerholm HM. Characterization of hot-dip galvanized (HDG) steel treated with gamma-UPS, VS, and tetrasulfide. J Adhes Sci Technol 2001;15(5):509–33.

22. Swartz NA, Clare TL. Understanding the differences in film formation mechanisms of two comparable solvent based and water-borne coatings on bronze substrates by electrochemical impedance spectroscopy. Electrochim Acta 2012;62:199–206.
23. Swartz NA, Wood KA, Clare TL. Characterizing and improving performance properties of thin solid films produced by weatherable water-borne colloidal suspensions on bronze substrates. Prog Org Coat 2012;75(3):215–23.
24. Taryba M, Lamaka SV, Snihirova D, et al. The combined use of scanning vibrating electrode technique and micro-potentiometry to assess the self-repair processes in defects on "smart" coatings applied to galvanized steel. Electrochim Acta 2011;56(12):4475–88.
25. Bierwagen G. The physical chemistry of organic coatings revisited – viewing coatings as a materials scientist. J Coat Technol Res 2008;5(2):133–55.
26. Ellingson LA, Shedlosky TJ, Bierwagen GP, et al. The use of electrochemical impedance spectroscopy in the evaluation of coatings for outdoor bronze. Stud Conserv 2004;49(1):53–62.
27. Cano E, Lafuente D, Bastidas DM. Use of EIS for the evaluation of the protective properties of coatings for metallic cultural heritage: a review. J Solid State Electrochem 2010;14(3):381–91.
28. Cano E, Bastidas DM, Argyropoulos V, et al. Electrochemical characterization of organic coatings for protection of historic steel artefacts. J Solid State Electrochem 2010;14(3):453–63.
29. Lazzari M, Chiantore O. Thermal-ageing of paraloid acrylic protective polymers. Polymer 2000;41(17):6447–55.
30. Tawari SL, Koch DL, Cohen C. Electrical double-layer effects on the Brownian diffusivity and aggregation rate of laponite clay particles. J Colloid Interface Sci 2001;240(1):54–66.
31. Herrera NN, Letoffe JM, Reymond JP, et al. Silylation of laponite clay particles with monofunctional and trifunctional vinyl alkoxysilanes. J Mater Chem 2005;15(8):863–71.
32. Herrera NN, Letoffe J-M, Putaux J-L, et al. Aqueous dispersions of silane-functionalized laponite clay platelets. A first step toward the elaboration of water-based polymer/clay nanocomposites. Langmuir 2004;20(5):1564–71.
33. Herrera NN, Putaux J-L, Bourgeat-Lami E. Synthesis of polymer/laponite nanocomposite latex particles via emulsion polymerization using silylated and cation-exchanged laponite clay platelets. Prog Solid State Chem 2006;34(2–4):121–37.
34. Negrete-Herrera N, Putaux J-L, David L, et al. Polymer/laponite composite colloids through emulsion polymerization: influence of the clay modification level on particle morphology. Macromolecules 2006;39(26):9177–84.
35. Lezhnina MM, Grewe T, Stoehr H, et al. Laponite blue: dissolving the insoluble. Angew Chem Intern Ed 2012;51(42):10652–5.
36. Becerro AI, Mantovani M, Escudero A. Mineralogical stability of phyllosilicates in hyperalkaline fluids: influence of layer nature, octahedral occupation and presence of tetrahedral Al. Am Mineral 2009;94(8–9):1187–97.
37. Wang J, Wheeler PA, Jarrett WL, et al. Synthesis and characterization of dual-functionalized laponite clay for acrylic nanocomposites. J Appl Polym Sci 2007;106(3):1496–506.
38. Balnois E, Durand-Vidal S, Levitz P. Probing the morphology of laponite clay colloids by atomic force microscopy. Langmuir 2003;19(17):6633–7.
39. Brasher DM, Kingsbury AH. Electrical measurements in the study of immersed paint coatings on metal. I. Comparison between capacitance and gravimetric methods of estimating water-uptake. J Appl Chem 1954;4(2):62–72.

Chapter 20

Monitoring Corrosion Using Vibrational Spectroscopic Techniques

Shengxi Li
Hawaii Corrosion Laboratory, Department of Mechanical Engineering, University of Hawaii at Manoa, Honolulu, Hawaii, USA

20.1 Introduction

Spectroscopic techniques such as Raman spectroscopy and Fourier transform infrared spectroscopy (FTIR) have been widely used in corrosion research. Both *in situ* and *ex situ* experiments using these two vibrational techniques provide valuable information about the corrosion system. Extensive literature search resulted in a considerable number of papers published on corrosion studies using Raman and IR spectroscopy. However, only *in situ* applications of the two techniques in corrosion studies will be covered here due to their ability to acquire real-time information of the corrosion systems that allows monitoring the corrosion process.

In the following sections, the underlying theory of the two vibrational techniques will be first given. Then, the available techniques and instrumentation for *in situ* studies will be discussed. Finally, various examples of applications are presented to demonstrate the power of these two techniques for corrosion science and

Intelligent Coatings for Corrosion Control
Copyright © 2015 Elsevier Inc. All rights reserved.

related fields of research. The discussion of literature papers will be divided into four areas: general aqueous corrosion, atmospheric corrosion, corrosion inhibitors, and coatings.

20.2 Principles

20.2.1 Raman spectroscopy

When a monochromatic light is scattered from a molecule, most photons are elastically scattered with the same frequency (energy) as the incident photons. A small fraction of light is scattered at frequencies different from those of the incident photons, namely inelastic scattering. The elastic scattering is named Rayleigh scattering while the inelastic scattering is called Raman scattering, or Raman effect. The Raman effect was discovered in 1928 by V. C. Raman.

The Raman effect arises when incident photons interact with the electric dipole of a molecule. The photons excite the molecule from its ground state to a virtual energy state. The molecule emits a photon when it relaxes and returns to a different energy state. The energy difference between the two states results in the energy of the incident photons being shifted away from the excitation wavelength. If the final energy state of the molecule is higher than the initial state, then the emitted photon will be shifted to a lower frequency, which is designated as Stokes shift. If the final energy state is lower than the initial state, then the emitted photon will be shifted to a higher frequency, and this is designated as an anti-Stokes shift (Figure 20.1). The Stokes shift is what is usually observed in Raman spectroscopy.

The Raman effect is based on molecular deformations in the electric field (E) generated by the laser beam. Assuming that the laser is fluctuating at frequency ν, E can be written as a function of the amplitude, E_0, and the time, t:

$$E = E_0 \cos(2\pi\nu t) \tag{20.1}$$

The dipole moment (μ) of a molecule induced by this light is, therefore:

$$\mu = \alpha E = \alpha E_0 \cos(2\pi\nu t) \tag{20.2}$$

Here, the proportionality constant α is called the polarizability of the molecule. The polarizability represents the ease with which the electron cloud around a molecule can be deformed.

Similarly, if the molecule is also vibrating or rotating in sinusoidal fashion with frequency ν_m, the nuclear displacement Δr can be written as:

$$\Delta r = r_0 \cos(2\pi\nu_m t) \tag{20.3}$$

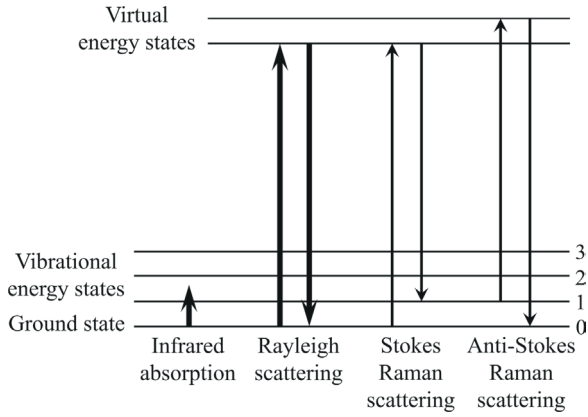


Figure 20.1 Schematic representation of the energy changes associated with Raman scattering, Rayleigh scattering, and IR absorption.

where r_0 is the vibrational amplitude.

When a molecule is at its equilibrium nuclear geometry, the polarizability of the molecule is α_0. While at some distance, the instantaneous polarization α is a linear function of the nuclear displacement, Δr:

$$a = a_0 + \left(\frac{\partial a}{\partial \mathrm{r}}\right)\Delta r \tag{20.4}$$

where the derivative $(\partial a/\partial r)$ represents the change in polarizability with change in position.

Combining Equations (20.2)–(20.4), we have:

$$\begin{aligned}\mu = \alpha E &= \alpha E_0 \cos\left(2\pi\nu t\right) \\ &= \alpha_0 E_0 \cos\left(2\pi\nu t\right) + \left(\frac{\partial a}{\partial \mathrm{r}}\right) r_0 E_0 \cos\left(2\pi\nu_{\mathrm{m}} t\right)\cos\left(2\pi\nu t\right) \\ &= \alpha_0 E_0 \cos\left(2\pi\nu t\right) + \frac{1}{2}\left(\frac{\partial a}{\partial \mathrm{r}}\right) r_0 E_0 \left\{\cos\left[2\pi t\left(\nu - \nu_{\mathrm{m}}\right)\right] + \cos\left[2\pi t\left(\nu + \nu_{\mathrm{m}}\right)\right]\right\}\end{aligned} \tag{20.5}$$

The first term relates to the scattered photon that has the same frequency as the incident photon, and thus explains Rayleigh scattering. The second term relates to the scattered photons with increased frequency $(\nu - \nu_{\mathrm{m}})$ and decreased frequency $(\nu + \nu_{\mathrm{m}})$ as compared to the incident photon, representing Stokes shift and anti-Stokes shift, respectively.

Equation (20.5) also gives a general selection rule that governs Raman scattering. Notice the derivative $(\partial a/\partial r)$ in the second term. If that derivative equals zero,

the entire second term will be zero, and there is no Raman scattering. Therefore, the selection rule for Raman scattering can be given as:

$$\left(\frac{\partial a}{\partial \mathrm{r}}\right) \neq 0 \tag{20.6}$$

that is, a molecular motion will be Raman-active only if the motion occurs with a change in polarizability. The amount of the polarizability change determines the Raman scattering intensity.

20.2.2 IR SPECTROSCOPY

Infrared radiation encompasses a section of the electromagnetic spectrum with wavenumbers ($\bar{\nu}$) from 12,800 to 10 cm^{-1} or wavelengths (λ) from 0.78 to 1000 μm. This infrared portion of the electromagnetic spectrum is usually divided into three subregions: near-IR region (12,800-4000 cm^{-1}), mid-IR region (4000-200 cm^{-1}), and far-IR region (200-10 cm^{-1}). The mid-IR region is the most commonly used region in IR spectroscopy.

Infrared spectroscopy is based on the interaction between IR radiation and molecules that results in the absorption of IR radiation by the molecules. At temperatures above absolute zero, all the atoms in molecules are in continuous vibration with respect to each other. When the frequency of a specific vibration equals the frequency of the incident IR radiation, the molecules absorb the radiation. The absorbed radiation matches the transition energy of the bond or group that vibrates in the molecule.

A molecule can vibrate in many ways, with each way called a vibrational mode. Simple diatomic molecules have only one bond and thus one vibrational mode that is not observed if the molecule is symmetrical. Polyatomic molecules have more bonds and correspondingly more vibrational modes. The total number of fundamental vibrational modes can be determined as follows. A polyatomic molecule with n atoms has $3n$ total degrees of freedom because each atom has three degrees of freedom. For a nonlinear molecule, 3 degrees of freedom are rotational and 3 are translational. Therefore, there are $3n-6$ degrees of freedom that are fundamental vibrations for nonlinear molecules. For linear molecules, because only 2 degrees are rotational, the total number of fundamental vibrations is $3n-5$. However, not all the vibrations can be observed in IR spectra. For a mode to be observed, changes must occur in the permanent dipole:

$$\left(\frac{\partial \mu}{\partial r}\right) \neq 0 \tag{20.7}$$

where μ is the dipole moment and r is the normal coordinate. In general, the larger the dipole change, the stronger the intensity (I) of the band in an IR spectrum:

TABLE 20.1 Comparison of Raman and IR Spectroscopy

Raman	IR
Originate from scattering of radiation	Originate from absorption of radiation
Require change in molecular polarizability	Require change in dipole moment
Water compatible	Water leads to intense absorption
Record by using a beam of monochromatic radiation	Record by using a beam of radiation having a large number of frequencies
Optics can be made of quartz or glass	Optics are usually made of salts (e.g., NaCl, KBr, and CsI)
Homonuclear diatomic molecules are Raman active	Homonuclear diatomic molecules are IR inactive

$$I = \left(\partial\mu / \partial r\right)^2 \tag{20.8}$$

A comparison of Raman and IR spectroscopy is shown in Table 20.1. The major difference between the two techniques lies in that Raman spectroscopy determines vibrations that cause a change in the polarizability of a molecule, while IR spectroscopy determines vibrations that cause a change in the dipole moment of a molecule. However, in theory, there are some vibrations that induce changes in both polarizability and dipole moment.

20.3 Methods and Equipment

20.3.1 Raman spectroscopy

There are many variations of Raman spectroscopy that have been developed to enhance the sensitivity (e.g., surface-enhanced Raman), to improve the spatial resolution (Raman microscopy), or to acquire very specific information (resonance Raman). For *in situ* studies in corrosion science, normal Raman spectroscopy is sufficient in most cases, but sometimes surface enhanced Raman spectroscopy (SERS) is necessary. Therefore, other techniques (e.g., resonance Raman) are not further covered here.

20.3.1.1 Normal Raman spectroscopy

In situ Raman spectroscopic studies of a corrosion system generally do not require specially designed equipment. Cells with or without flow configurations can be made using any material. When an enclosed cell is necessary, a quartz or even glass window can be used for passing the laser beam to the sample.

20.3.1.2 SERS

Surface-enhanced Raman spectroscopy is a technique that offers orders of magnitude increases in Raman scattering by molecules adsorbed on rough metal surfaces or nanostructures. Typical metals used for Raman scattering enhancement are Ag, Au, and Cu. To prepare the roughed surfaces, a conventional approach is to electrochemically rough the substrate through etching. Recently, surfaces are usually prepared by coating metallic nanoparticles on various substrates. There are two primary theories proposed for SERS: the electromagnetic theory and the chemical theory. The electromagnetic theory is based on the enhancement in the electric field provided by localized surface plasmons. The chemical theory proposes the formation of charge-transfer complexes and thus making it only applicable to chemisorbed species on metal surfaces.

20.3.2 IR SPECTROSCOPY

There are two primary experimental techniques in IR spectroscopy, transmission and reflection techniques. For *in situ* studies of corrosion phenomenon, reflectance spectroscopy is the commonly used technique. Among the various types of reflectance techniques, specular reflection, infrared reflection-absorption spectroscopy (IRAS), and attenuated total reflection (ATR) are well suitable for *in situ* studies.

20.3.2.1 Cells with optical windows for IR path

Because of the intense absorption of IR light by solvent (water), IR spectroscopy cannot be used as readily as Raman spectroscopy for *in situ* monitoring corrosion phenomenon in aqueous environments. Therefore, specific cells have to be designed with the aim of minimizing radiation losses by solvent absorption. One approach is by depositing very thin layers of electrolyte or small droplets on metal surfaces, which represents the common configuration for atmospheric corrosion studies. Figure 20.2 shows two typical experimental setups for *in situ* studies of atmospheric corrosion, with the one in Figure 20.2a for specular reflectance study and the one in Figure 20.2b for IRAS. For the IRAS studies, grazing angle incidence is usually used.

For studies in bulk solutions, IR reflectance spectra can still be obtained by reducing the distance between the sample and the IR window (Figure 20.2c). The IR transparent window is pressed against the sample, creating an extremely thin solution layer in between them. One problem with this configuration is the possible depletion of solution species due to electrochemical activities (e.g., corrosion) in the confined environment. To solve this problem, a flow cell can be designed to replenish solution species as reaction proceeds.

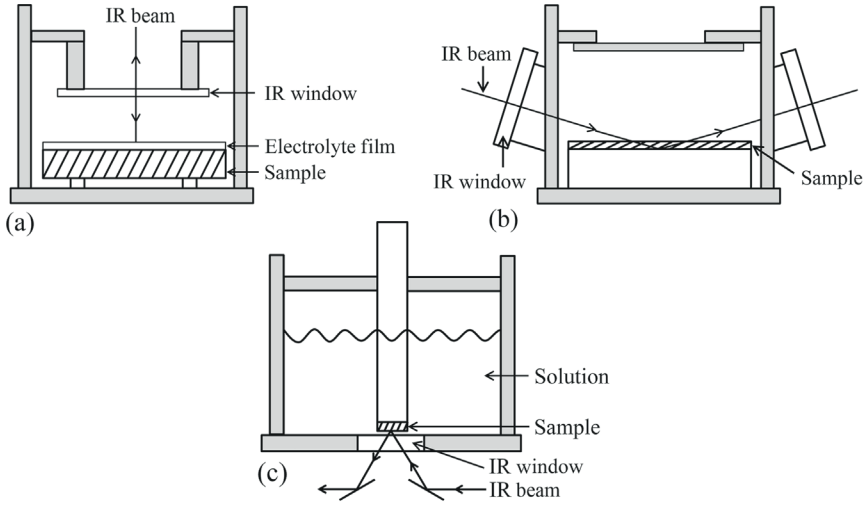


Figure 20.2 Experimental configurations for *in situ* IR spectroscopic studies: 1.

For all three configurations in Figure 20.2, the IR windows are in direct contact with liquid electrolyte or high-humid environment. Therefore, non-water-soluble IR window materials have to be used, such as zinc selenide (ZnSe) and calcium fluoride (CaF_2).

20.3.2.2 ATR

When an IR radiation enters from optically denser ATR crystals (refractive index n_1) to the optically rarer samples (refractive index n_2) at an angle exceeding the critical angle (θ_c), total internal reflection will occur inside the crystal. The critical angle is defined as:

$$\theta_c = \sin^{-1}\left(\frac{n_2}{n_1}\right) \tag{20.9}$$

This internal reflectance creates an evanescent wave that extends beyond the surface of the crystal into the sample that is in contact with the crystal. The evanescent wave protrudes only a few microns (0.5-5 µm) beyond the crystal surface and into the sample.

Some common ATR crystals are ZnSe, thallium bromide-thallium iodide (KRS-5), germanium (Ge), or silicon (Si). Prisms (Figure 20.3a) and hemispheres (Figure 20.3b) made of ATR crystals, for example, ZnSe, can be used for ATR-FTIR studies. In these configurations, IR beam is reflected once inside the crystal. Multiple internal reflection can be achieved by using the configuration shown in Figure 20.3c. In all three configurations, samples have to be in close contact with the crystals or can be plated on the crystals as thin films.

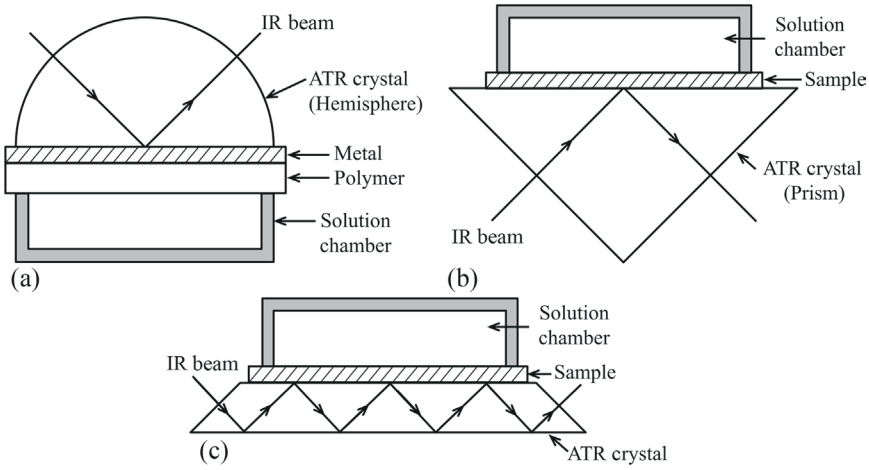


Figure 20.3 Experimental configurations for *in situ* IR spectroscopic studies: 2 ATR techniques.

20.4 Applications of *In Situ* Raman Spectroscopy in Corrosion Science

In situ Raman spectroscopy has several major advantages for corrosion studies especially in aqueous environments. First, water does not interfere with Raman acquisition in aqueous environments. Second, the laser beam does not perturb the corrosion system under the protection of water, that is, without altering the corrosion species. This enables the study of those unstable compounds such as green rust, which would have transformed to other phases in the ambient. Third, the high surface roughness caused by corrosion does not hinder Raman acquisition, but instead enhances Raman scattering.

20.4.1 Aqueous corrosion

The corrosion of metallic materials in aqueous environments is one of the most prevalent forms of corrosion and has been extensively studied over the past few decades. *In situ* Raman spectroscopy is well suited for monitoring the corrosion process in metal/liquid interface. A great number of *in situ* Raman spectroscopic studies have been conducted to characterize the anodic corrosion films or monitor the formation of corrosion products on metal surfaces in corrosive environments.

20.4.1.1 Anodic oxide film formation

The passive oxide films on metals enable the self-protection of metals against corrosion in aqueous environments. A series of work has focused on *in situ* Raman

spectroscopic identification of oxide films grown on various metal surfaces, including Fe, Ni, Co, Ag, Ti, Pb, and stainless steel. Most of the oxide films studied were either formed by anodic polarization[1–15] or by exposing the metals to hydrothermal environments.[16–20]

At anodic potentials, oxide films grow on metal surfaces; while at cathodic potentials, the oxide films dissolve. During this process, the formation, transformation (if any), and dissolution of the oxide films could be followed using *in situ* Raman spectroscopy. For example, according to *in situ* Raman data, the oxide film on Ni was found to be Ni_2O_3 (477 and 555 cm^{-1}) in 0.05 M NaOH solution[2] and NiO (500 and 555 cm^{-1}) in concentrated (1-10 M) H_2SO_4 solution.[3] On Cu in 0.1 M NaOH, Cu_2O was detected for potentials from 50 to about 500 mV during anodic sweeps, but was converted to $Cu(OH)_2$ at more anodic potentials (>637 mV), as evidenced by the appearance of the band at ~488 cm^{-1}.[6,7] The oxide film on Ti in acidic sulfuric solution was found to be anatase-type TiO_2 (145, 400, 515, and 640 cm^{-1}), which changed from amorphous to crystalline as the potential exceeded a particular value.[8] The protective oxide films also grow on Fe polarized in alkaline solutions and were determined to consist mainly of magnetite (Fe_3O_4) (550 and 670 cm^{-1}) in the inner layer.[11–13,15] An outer layer consisting of goethite (α-FeOOH) or lepidocrocite (γ-FeOOH) was also detected. The *in situ* capabilities of Raman spectroscopy were also extended to monitoring the surface films on iron and steel in high-temperature environments,[16–19] and various phases of iron oxides and oxyhydroxides were detected depending on the temperature.

20.4.1.2 General aqueous corrosion

Similar to monitoring the oxide film formation using *in situ* Raman spectroscopy, the general aqueous corrosion has been widely studied using this approach in order to identify the corrosion products formed during the corrosion process. Most of the work has been focused on iron and steel (e.g., galvanized steel, carbon steel, and stainless steel). Earlier work has characterized the corrosion products formed on galvanized steel during exposure to corrosive solutions.[21,22] Zinc hydroxycarbonates and hydroxychlorides were successfully identified as the two primary corrosion products. For the corrosion of iron and steel in corrosive media, especially chlorinated solutions, nonstable green rust has been detected as the corrosion products generated during pitting.[23–30] Two major Raman bands at ~433 and 507 cm^{-1} for the green rust were assigned to the Fe^{2+}–OH and Fe^{3+}–OH stretching modes, respectively. Depending on the corrosive media, the green rust can have different ions integrated in it, such as Cl^-, CO_3^{2-}, SO_4^{2-}, and $HCOO^-$. Other types of rust, such as Fe_3O_4 and γ-FeOOH, were also detected together with green rust. Siderite ($FeCO_3$) is another corrosion product that forms on steel in concentrated carbonate/bicarbonate solutions, simulating groundwater.[31,32]

Other corrosion phenomena of metals that have been investigated using *in situ* Raman spectroscopy include molybdenum[33] and tin[34] in NaCl and KOH solutions, zirconium-niobium alloy[35] and Ni-based alloy 600[36] under hydrothermal conditions, and Pt-Ni alloys in HCl solution.[37]

20.4.2 Atmospheric corrosion

Atmospheric corrosion proceeds under thin electrolyte layers or small droplets that form by condensation or absorption of water by airborne sea salt particles. The small amount of electrolyte facilitates the use of Raman spectroscopy to monitor the corrosion process *in situ*. Corrosion of zinc caused by predeposited NaCl particles with a density of ~0.4 μg/cm^2 serves as an example.[38] Zinc chloride ($ZnCl_2$) with a Raman band at 290 cm^{-1} was detected on the Zn surface 2 h after the sample was exposed to high humidity (84%). After 6 h exposure, when $ZnCl_2$ in the surface layer reached saturation, simonkollite ($ZnCl_2(Zn[OH]_2)_4$) with major Raman bands at 255 and 390 cm^{-1} was detected. The corrosion process under a single droplet was also studied for Zn[39] and carbon steel.[40–42] The Raman spectra from Zn under a seawater droplet showed the formation of ZnO, a sulfate-containing and a carbonate-containing compound.[39] The Raman spectra from carbon steel under single NaCl or Na_2SO_4 droplets indicated green rust and γ-FeOOH as the initial rust formation during sea salt droplets-induced marine atmospheric corrosion.[40–42] The spatial distribution of the corrosion reaction products was also revealed by *in situ* Raman spectroscopy, as shown in Figure 20.4.[41] Ferrous chloride ($FeCl_2$) and also possibly its chloride ions (245 and 286 cm^{-1}) were detected inside the corrosion initiation site or the corrosion pit, as the corrosion reaction products (Figure 20.4a). Green rust (GR1(Cl^-)) (425 and 501 cm^{-1}) was identified as the corrosion product formed in the vicinity immediately outside of the pit, while γ-FeOOH (246, 377, 525, and 645 cm^{-1}) was detected in regions outside of the GR region (Figure 20.4b and d). In the transitional region from GR to γ-FeOOH, Fe_3O_4 (666 cm^{-1}) also formed together with GR and γ-FeOOH (Figure 20.4c).

20.4.3 Corrosion inhibitors

Corrosion inhibitors are chemical compounds that are added to the surroundings (liquids or gases) of metallic materials to decrease their corrosion. Inhibitors work by the formation of a coating on metals, which prevents access of corrosive substance to the metal surfaces. The inhibitor molecules either attach to the metal or react with the surface to form a thin, adherent layer. In both cases, *in situ* Raman spectroscopy has been employed to study the adsorption mechanism and the film formation mechanism.

Benzotriazole (BTAH) has been used as an effective corrosion inhibitor for Cu and its alloys since the 1950s,[43] and was also extended to other metals. The high

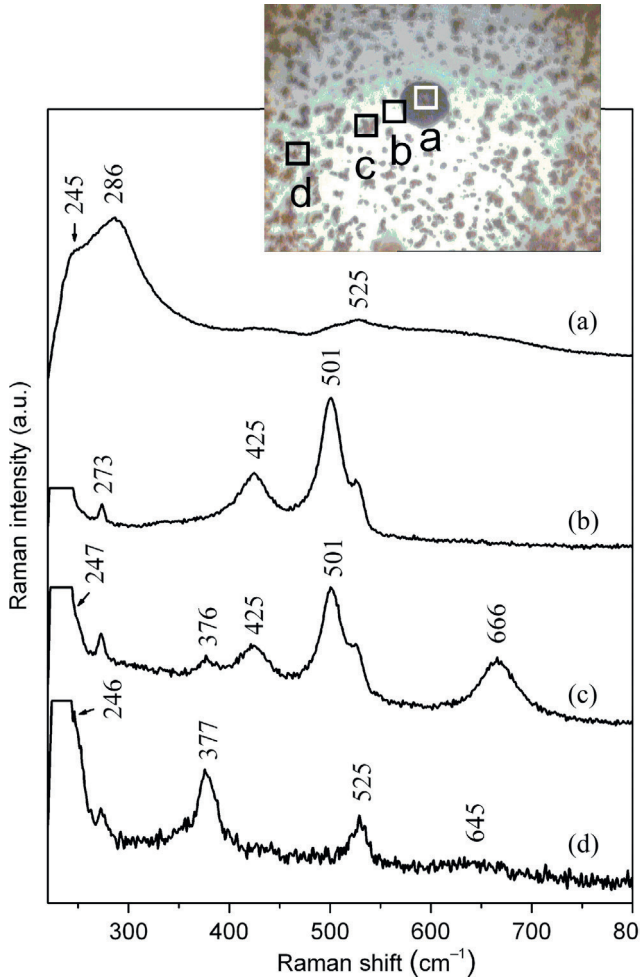


Figure 20.4 *In situ* Raman spectra from different locations on steel under the NaCl droplet after 30 min corrosion: (a) corrosion initiation site or the corrosion pit, (b) region surrounding the corrosion initiation site, (c) rust cluster formed in the transitional region from GR to lepidocrocite, and (d) yellowish rust cluster that formed far away from the corrosion initiation site. *Reproduced with permission from Ref. [41].*

corrosion inhibition efficiency of BTAH is attributed to the formation of a compact, polymerlike metal-BTAH complex on the metal surface.[44–46] The structure and composition of this complex can be revealed by *in situ* SERS, which provides information on even only a few monolayers of adsorbed species. Most of the *in situ* SERS studies on BTAH as corrosion inhibitors have been focused on Cu and Ag due to their strong Raman-enhancing effect. The inhibition effect of BTAH on Cu has been studied in

various environments, such as halide solutions,[44,46–48] sulfuric acid media,[49–52] organic solution,[53] and ionic liquids.[54]

Earlier studies showed that, in near neutral KCl solution, the complex formed by the reaction between Cu and BTAH was [Cu(I)BTA] according to *in situ* Raman data. In KCl/acid solution, the Raman spectra obtained at less negative potentials resembled that of [Cu(I)BTA] complex but, at more positive potentials the spectra were similar to that of $[Cu(I)\text{-}ClBTAH]_4$.[44] A recent study reported that, in neutral KCl solution, the initially formed complex was $[Cu^{I}(BTA)]_n$ and might have transformed to $[Cu^{I}(BTAH)]_4$ at more negative potentials. This was evidenced by the redshifts of the in-plane trigonal breathing mode from 1041 cm^{-1} at –0.5 V to 1021 cm^{-1} at –1.1 V and the increase in intensity of the NH in-plane bending mode (1144 cm^{-1}) at more negative potentials (Figure 20.5).[46] Therefore, it is probably necessary to take into

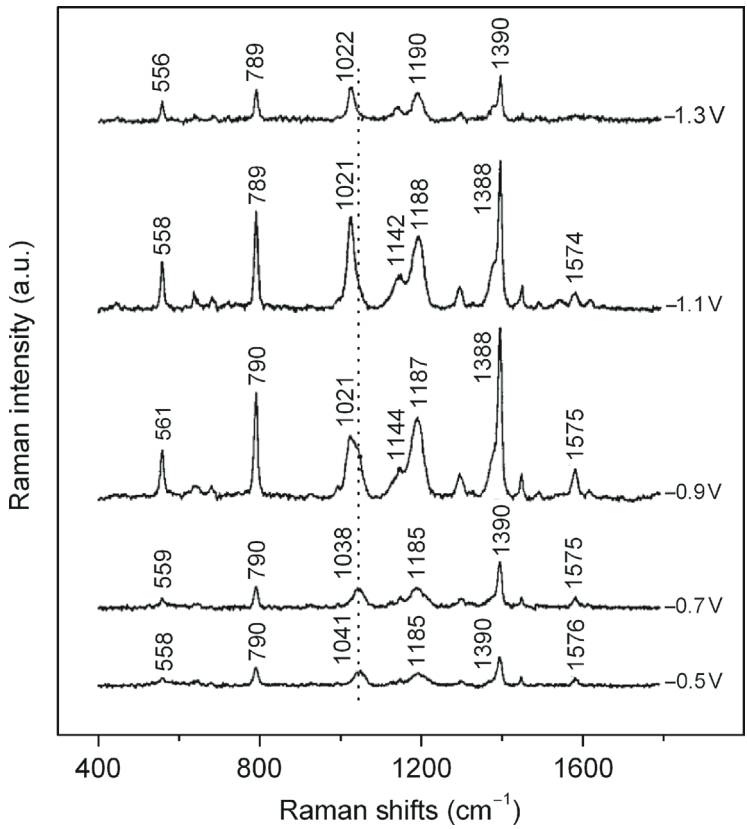


Figure 20.5 SERS spectra of Benzotriazole obtained from 0.1 M KCl at a Cu electrode at potentials indicated. Acquisition time, 10 s; accumulations, 2. *Reprinted with permission from Ref. [46]. Copyright 2002 American Chemical Society.*

account the effect of the presence of the $[Cu^{I}(BTAH)]_4$ or $[Cu(I)\text{-}ClBTAH]_4$ complexes in the corrosion inhibition of Cu in mild acidic KCl solution containing BTAH. In relatively strong acidic environment (e.g., H_2SO_4), $[Cu(I)BTA]_n$ complex was found as the film formed on the surface of Cu and its alloys.

Similar *in situ* SERS results were observed on Ag in either halide media or acetonitrile solution with BTAH.[45,55] In addition, *in situ* SERS studies were also extended to Fe, Ni, and Co by proper electrochemical roughing procedures.[46,56]

Other inhibitors that have been studied using *in situ* SERS include triethylstibine for Fe and Ni,[57] propargyl alcohol for Fe,[58] 2-mercaptobenzothiazole (MBT) for Cu,[59] phytic acid (IP6) for Ag,[60] volatile corrosion inhibitors for carbon steel,[61] salicylate for Cu,[62] and benzyldimethylphenylammonium chloride (BDMPAC) for low carbon steel,[63] methimazole (MMI) for Cu,[64] 2-amino-5-mercapto-1,3,4-thiadiazole (AMT) for Ag[65] and Co,[66] 3-amino-5-mercapto-1,2,4-triazole (AMTA) for Fe,[67] and 2-amino-5-(4-pyridinyl)-1,3,4-thiadiazole (4-APTD) for Cu.[68]

20.4.4 Coatings

Coatings including both organic and inorganic coatings are an effective approach to achieve corrosion protections for metals. *In situ* Raman spectroscopy is a powerful tool for the study of corrosion-protection coatings. First, the formation of coatings on metallic materials could be monitored using *in situ* Raman spectroscopy. Second, the changes and degradation of coatings especially organic coatings upon exposure to corrosive environments can be studied using *in situ* Raman spectroscopy. Last, the corrosion products underneath the coatings can be characterized through *in situ* Raman spectroscopy provided that the coatings are thin and transparent.

20.4.4.1 Conversion coatings

Conversion coatings refer to the coatings produced by a chemical or electrochemical treatment of the metallic surface using coating solutions. During the conversion process, part of the metal surface is converted into a protective surface layer. Examples of conversion coatings include chromate conversion coating (CCC), phosphate conversion coating (PCC), and black oxide coating.

In situ Raman spectroscopy was successfully used to study CCC on aluminium alloys. Given that the Raman scattering from water is quite week, Raman spectroscopy could be used to monitor the formation process of CCC in aqueous solution.[69] A band at approximately 858 cm^{-1} appeared following the addition of Alodine solution (or K_2CrO_4, $K_2Cr_2O_7$) to fresh $Cr(OH)_3$ precipitate, indicating the formation of CCC. By monitoring the change of the band intensity at 858 cm^{-1}, the growth rates of the CCC as well as their dependence on coating bath composition were studied.[70] It was found that the redox mediation action by $Fe(CN)_6^{-3/-4}$ is the mechanism for the acceleration of CCC formation.

In situ Raman spectroscopy was also used to monitor the release of chromate (CrO_4^{2-}) from CCC and its migration to neighboring regions of exposed alloy to protect them.[71–73] The chromate species redeposited as a film on fresh alloy surface, making the initially untreated alloy less active toward corrosion. The redeposition process occurred more rapidly in or near pits, showing the self-healing properties of CCC films.[74] Besides pitting corrosion, filiform corrosion was also effectively prevented by CCC films.[75]

PCC was also studied using *in situ* Raman spectroscopy. The dissolution of phosphate layers on zinc-coated steel in dilute NaOH solution was monitored by measuring the decay of the 996 cm^{-1} (PO_4^{3-}) band intensity, from which the rate of phosphate loss could be obtained.[76]

20.4.4.2 Polymeric coatings

Raman spectroscopy is especially suitable for studying polymers thanks to its high sensitivity towards the structure and conformation of the polymer backbone. Therefore, *in situ* Raman spectroscopy could be used to follow the growth of polymeric coatings on metals and their degradation in corrosive environments. In addition, this technique enables monitoring the corrosion product formation under the coatings provided that the coatings are very thin and transparent. The thin coating also reduces the time frame for corrosion to occur to match with that of Raman acquisition. Another requirement is the absence of fluorescence caused by the epoxy coating. Finally, it is better if the Raman bands of the coating do not interfere with those from the corrosion products.[77]

20.4.4.2.1 Epoxy coating

The earliest applications of *in situ* Raman spectroscopy in the study of polymer coatings were discussed in a series of papers on the corrosion of painted galvanized steel.[77–80] After being immersed in NaCl solutions for a certain time, the epoxy-polyamide (15-20 μm) coated galvanized steel developed two clearly different regions, with and without blisters. Two types of blisters were observed, black and large blisters and white and small blisters.[77] Raman spectra of the corrosion products inside the blisters could be obtained directly through the thin paint layer. The Raman spectra from the nonblistered regions corresponded to epoxy-polyamide resin coating with characteristic bands at 570 and 637 cm^{-1}. The Raman spectra from inside the black blisters showed the presence of zinc hydroxychloride with sharp bands at 260 and 390 cm^{-1}, while those from the white blisters indicated the existence of amorphous zinc oxide with a prominent band at 569 cm^{-1}.[78–80] It was believed that the black blisters correspond to the cathodic zones and the white blisters are anodic. This study was also extended to the case of zinc-coated steel samples with chromate or phosphate conversion layers.[79]

20.4.4.2.2 Electronically conducting polymer coating

Recently, there has been an increasing interest in the use of electronically conducting polymers (ECPs) for corrosion resistant coatings. Some of the ECPs that have been investigated for corrosion protection include polyaniline (PANI), polypyrrole (PPy), and polythiophene (PT).

The use of PANI for steel corrosion protection was first reported in the early 1980s.[81,82] Subsequently, a substantial amount of research has been devoted to the use of PANI for corrosion protection of various metals and alloys. The conventional approach to obtain the protective PANI layers was by electrochemical polymerization. *In situ* Raman spectroscopy has been extensively used to study the formation mechanisms of the PANI films,[83,84] normally on platinum electrodes. Even though not directly related to corrosion study, these studies laid the foundation for studying the protective PANI coating on metals using *in situ* Raman spectroscopy.

In situ Raman spectroscopy combined with cyclic voltammetry was employed to investigate the interaction between the passive layer on iron and PANI coating in sulfate medium.[85] The oxidation state of the PANI film on iron, which changed after voltammetric cycling, could be followed. After one redox cycle (0 to −1.0 V), the PANI film deprotonation was verified by the depletion of the band at 1330 cm^{-1} ($C–N^+$ stretching). Also, the depletion of benzenoid units was evident due to the decrease of the 1620 cm^{-1} band (C–C ring stretching) and the depletion of 1185 cm^{-1} band (quinine ring C–H bending).[85] After further cycling, the Raman spectra evolved toward a less oxidized form of PANI with a predominance of benzenoid rings (1185 and 1620 cm^{-1}). The reduced PANI on iron is no longer able to provide enough electrons to maintain iron in its passive state, and the passive layers break down. They also analyzed the PANI layer potentiostatically polymerized in phosphoric/metanilic solution as compared to the PANI layer grown in inorganic acid (HCl) by collecting Raman spectra at different polarization potentials (e.g., from 150 to −700 mV/SSE).[86] They found that the film prepared in metanilic acid had a more oxidized and less protonated state than that grown in inorganic acid solution, as evidenced by the strong Raman bands at 1330 cm^{-1} ($C–N^{+\cdot}$) and 1500 cm^{-1} ($C=N^{+\cdot}$) observed from the PANI film formed in metanilic acid. Therefore, the reduction of the PANI film is more difficult in the presence of metanilic acid, resulting in higher protective properties.

Another strategy for protecting metals using PANI is by forming epoxy and acrylic blends. The acrylic blend formed by PANI, poly(methyl methacrylate) (PMMA), and camphorsulfonic acid (CSA) is an example,[87–90] which had a low percolation threshold, a high conductivity, and enhanced mechanical properties as compared to PANI. Raman spectra of the PANI-PMMA-CSA blend indicated characteristic features of "secondary doped" PANI,[91] with a significant increase of the band at 1333 cm^{-1} corresponding to the $C=N^{+\cdot}$ mode. The ratio of the band at 1333 cm^{-1} and that at 1599 cm^{-1} corresponding to the aromatic C–C mode is equal to ~1, indicating that the film is in the emeraldine state. However, it diminished to ~0.7 after the coating

(on iron) was immersed in H_2SO_4 solution for 20 days, suggesting the reduction of the polymeric coating.[87] This ratio varies for different metal substrates, which indicates that the extent of the redox reaction in the film depends on the metals that have different reducing power (Figure 20.6).[88] Raman data also showed the presence of a second layer formed by counter ions released from PANI and various metal cations.

Another ECP that has been widely used for corrosion protection coatings is PPy. The formation or the electropolymerization of the PPy films on various metals could be followed by using *in situ* Raman spectroscopy.[92–96] Raman bands characteristic of the oxidized form of PPy at 927, 1086, 1238, 1368, and 1605 cm^{-1} were observed during the growth of PPy film, and those typical of the reduced form of PPy at 988, 1038, 1260, 1313, and 1564 cm^{-1} were detected during corrosion in corrosive medium.[94]

Take the thin PPy film on iron electrode and immersed in a 0.1 M K_2SO_4 solution (pH = 4) as an example.[97] Raman spectra were recorded during immersion and at different OCPs to monitor the redox states of the PPy and composite films. The Raman data revealed that the PPy film was in the oxidized form in the original state ($E_{oc} = 0$ V) and was protective to the iron substrate. Then, the OCP dropped to −0.4 V during protection and finally to −1.0 V after corrosion. During this process, the Raman bands at 1606 cm^{-1} (inter-ring C = C) and 1385 cm^{-1} (ring C = C) corresponding to the oxidized PPy both shifted towards lower wavenumbers, ~1570 and 1315 cm^{-1}, respectively, for the reduced form of PPy (Figure 20.7a). The bands for the defect modes at 929,

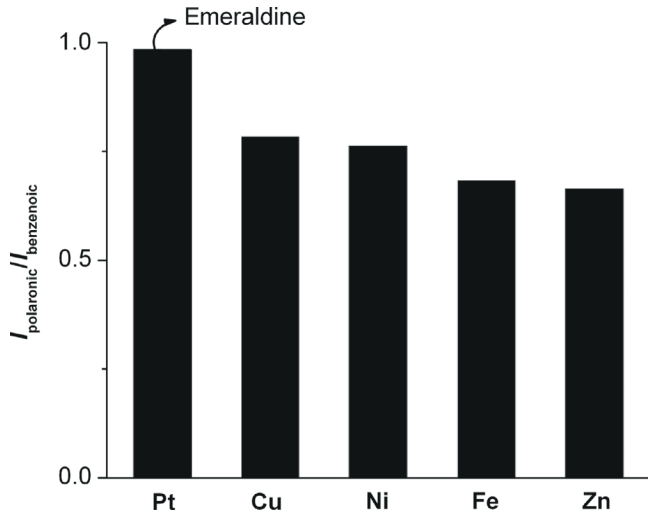


Figure 20.6 Intensity ratio of Raman bands located at 1333 and 1599 cm^{-1} for PMMA—20% PANI–CSA blend coating on different metals. Spectra were taken after 12 days in 1 mol L^{-1} H_2SO_4 electrolytic solution. *Reprinted from Ref. [88]. Copyright 2005, with permission from Elsevier.*

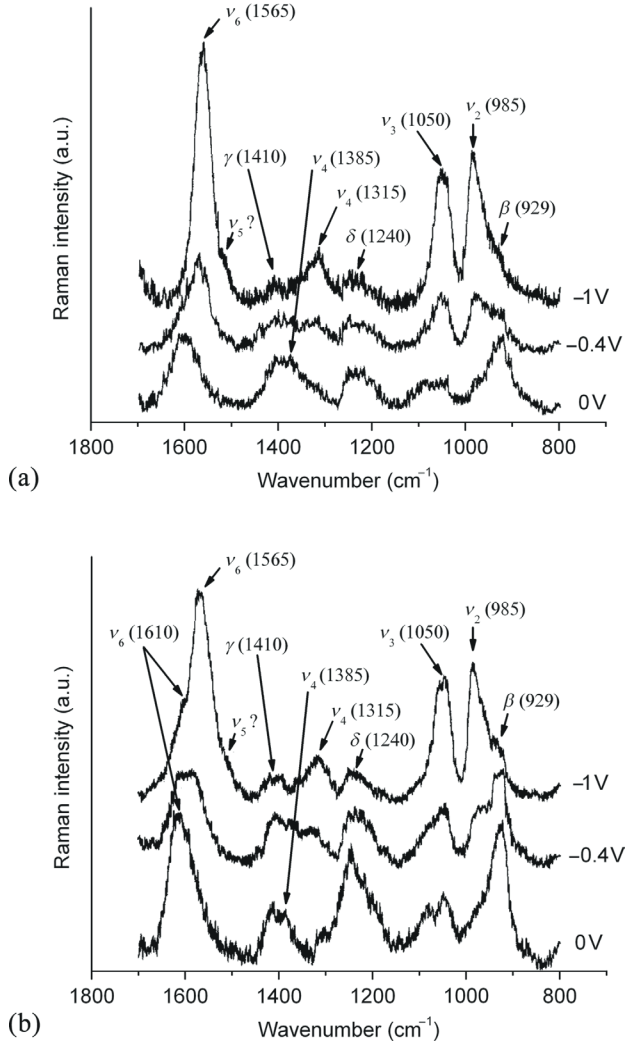


Figure 20.7 *In situ* Raman spectra of (a) PPy/Fe electrode, (b) composite/Fe electrode in 0.1 M K_2SO_4 (pH 4), recorded at different E_{oc}: 0, –0.4, and –1V. *Reproduced with permission from Ref. [97].*

1410, and 1240 cm^{-1} also decreased. The Raman bands which increased significantly during the OCP measurement are at 985 and 1050 cm^{-1}, which correspond to the reduced form of PPy. As compared to the PPy film alone, the PPy-PDAN composite film showed better ability to protect iron because the Raman bands that are typical of the oxidized form of PPy (929, 1240, 1410, and 1610 cm^{-1}) decreased more slowly upon reduction (Figure 20.7b).[97]

20.5 Applications of *In Situ* FTIR in Corrosion Science

FTIR has been widely used for corrosion studies, both *in situ* and *ex situ*. An extensive treatment of both *in situ* and *ex situ* application of FTIR in corrosion studies is found in Ref. [98] In this chapter, only *in situ* application of FTIR for corrosion studies will be covered.

20.5.1 Aqueous corrosion

It is difficult to probe corrosion phenomenon in bulk solutions using *in situ* FTIR due to intense absorption of IR radiation by water. However, by reducing the distance between the sample surface and the IR window, the corrosion process on the metal surface could be followed. The electrochemically controlled oxidation and reduction of lead in sulfuric acid was successfully monitored using *in situ* IRAS.[99] The growth and reduction of lead sulfate ($PbSO_4$) was followed by monitoring the band at 631 cm^{-1}, the integrated area of which showed a linear relationship with the consumed charge in the potential region where $PbSO_4$ forms. At more anodic potentials, the formation of lead dioxide (PbO_2) was observed as evidenced by an increased absorption band at 5200 cm^{-1}. Similar experiments were conducted to characterize the corrosion products formed on Ni electrodes in aqueous solutions containing pseudohalide ion series (OCN^-, SCN^-, and $SeCN^-$).[100] Ni corroded in all three solutions with the formation of Ni(II) cyanate complex, Ni(II) thiocyanate complex, and Ni(II) selenocyanate complex depending on the ion species in the solution. In the Ni/OCN^- system, the *in situ* data obtained using subtractively normalized interfacial Fourier transform infrared spectroscopy (SNIFTIRS) also showed the formation of CO_2 (2343 cm^{-1}), which was believed to be the ultimate product of electrolysis of the cyanate ion.

Other *in situ* FTIR studies of corrosion-related phenomena include anion adsorption on colloidal chromium (III) oxide hydroxide film simulating passive stainless steel surface,[101] characterization of the anodic film on iron in neutral phosphate solution ($Fe^{III}PO_4$),[102] and monitoring of the transport of corrosive species through the mortar layer.[103]

20.5.2 Atmospheric corrosion

Given that atmospheric corrosion occurs under extremely thin electrolyte layers, there is less absorption of IR radiation by water. Therefore, a great amount of work has been conducted to study atmospheric corrosion using *in situ* IRAS techniques. *In situ* IRAS has been developed to study the corrosion of metals (e.g., Cu, Zn, Al, and Mg) exposed to humid air[104] or humid air mixed with corrosive gases, such as SO_2,[104–110] NO_2,[107,109–111] O_3,[109] and SO_3.[112] The corrosive environments were generated

by passing air with humidity and certain levels of corrosive gases through the sample chamber. The interaction of metals with corrosive environments and the formation of corrosion products could be followed using *in situ* IRAS. For example, the initial corrosion products on Cu exposed to humid air (90% RH) were identified as copper(I) oxide while that formed in humid air containing SO_2 (0.23 ppm) was sulfite.[104] Similarly, the corrosion products formed on Ni,[105] Zn,[105] and Al[112] exposed to SO_2-containing humid air were also characterized using *in situ* IRAS. As complementary to *in situ* IRAS, quartz crystal microbalance (QCM)[106,109,111] and atomic force microscopy (AFM)[108,109] were the other two *in situ* techniques used for the study of humid air-induced atmospheric corrosion, to obtain the mass changes and morphological information, respectively.

The influence of organic constituents such as acetic acid, acetaldehyde, and formic acid on the atmospheric corrosion of metals, especially in indoor environments, was also studied using *in situ* IRAS.[113–117] Zinc acetate was detected as the major corrosion products in humid environments with sub-ppm concentration of acetic acid and acetaldehyde,[113,114] while zinc formate formed on zinc exposed to environments containing formic acid.[115]

Atmospheric corrosion of metals is greatly enhanced by NaCl deposition, which can originate from either airborne sea salt particles or deicing salts. NaCl particle-induced atmospheric corrosion has been studied using *in situ* IRAS for Zn,[118,119] Al,[120] Fe,[121] Cu,[122,123] and Mg.[124] For Zn with predeposited NaCl particles and then exposed to high humidity (>90%), a surface film containing ZnO, $Zn_5(OH)_8Cl_2{\cdot}H_2O$, and zinc $Zn_5(OH)_6(CO_3)_2$ was detected by *in situ* IRAS.[118] The rate of the corrosion process could also be evaluated from the rate of surface film formation obtained from the IRAS measurements. *In situ* IRAS also detected carbonate ions (1390 cm^{-1}) in the thin solution films in the secondary spreading region close to the original NaCl droplet.[119] Similar secondary spreading effects were observed on Cu and studied using *in situ* IRAS.[122,123] Another important application of *in situ* IRAS in atmospheric corrosion studies is the investigation of filiform corrosion of Al[120] and Fe.[121] The movement of the active filament head on coated Al surface could be followed with *in situ* FTIR microspectroscopy using the characteristic IR band at ~2500 cm^{-1} from $Al(H_2O)_6^{3+}$, the corrosion product in the filament.[120] Notice that the coating on Al must be thin and transparent in the spectral region of interest.

20.5.3 Corrosion inhibitors

In situ FTIR is a powerful tool for the investigation of the mechanism of corrosion inhibitors. In combination with electrochemical techniques, SNIFTIRS was used to study the formation of BTAH on Cu(100) surface.[125] The Cu(I)BTA complex was detected on Cu surface at potentials >–0.3 V as evidenced by the negative-going bands at 1119 and 1155 cm^{-1}. The bands assigned to BTAH in the solution were observed

as the positive-going bands at 1014, 1217, 1248, 1268, and 1308 cm^{-1}. The effects of anions (Cl^- and SO_4^{2-}) in the supporting electrolyte on the formation and decomposition of the Cu(I)BTA film on Cu were also investigated using *in situ* FTIR.[126] It was found that the Cu(I)BTA complex was formed more easily in Cl^--containing solution than in sulfate or bisulfate solutions. Other corrosion inhibitors that have been studied using *in situ* FTIR include BDMPAC, glutamic acid, triethylenetetramine (TETA), sodium tartrate, and sodium benzoate.[127]

20.5.4 Coatings

In situ FTIR studies of corrosion protection coating systems have been limited to polymeric coatings. Generally, two techniques can be used: FTIR-reflection spectroscopy and ATR-FTIR. While FTIR-reflection spectroscopy was employed to monitor the growth of organic coatings on metal surfaces, ATR was used mostly to study the transport of water and some ionic species through the organic coatings.

20.5.4.1 FTIR-reflection spectroscopy

Electrochemical cell with CaF_2 windows was designed to study the formation of polymer films on metal surfaces.[128,129] For the poly(thiophene-3-methanol) (PTOH) film on platinum electrodes, *in situ* FTIR spectra indicated that the perchlorate anions entered the PTOH film during the oxidation process as evidenced by the bands in the region of 1000-1500 cm^{-1}. When the film was reduced, the anions were expelled from the film because the band for the perchlorate anions decreased.[128] *In situ* FTIR was also used to study the growth of poly(*o*-phenylenediamine) (PPD) film on stainless steel, and the results suggested a ladder-type structure with alternating pyrazine and phenazine rings.[129] Similarly, *in situ* FTIR could be used to detect the solution species, that is, CO_2, during the formation of a semi-passivating layer on Cu.[62] The CO_2 was believed to be from the decarboxilation of the salicylate anion.

20.5.4.2 ATR-FTIR

The adhesion between the polymeric coating and the metal substrate plays an important role in the protective properties of the coatings. Water that transports through the coating to the metal/coating interfaces is a major cause of degradation and delamination of the coating. In addition, water also promotes corrosion of the metal substrate.

ATR-FTIR has been extensively used to study the transport of water and/or ionic species through polymer films to metal/polymer interfaces.[130–139] FTIR in the multiple internal reflection mode (FTIR-MIR) was used to obtain information on the water layer at the organic coating/substrate interface.[130–132] The effects of water evident in the 3000-3650 and 1625-1645 cm^{-1} regions were observed after the coating was exposed to water for a certain time. These features increased in intensity with

time while those for the coating decreased. The fact that the intensity change of 3400 cm^{-1} is proportionally related to the total amount of water in the coating enables a quantitative analysis of the water layer. By comparing the intensity changes of the water OH stretching band as a function of time, the rates at which water entered the coating/substrate interfacial region for three coating systems can be determined and compared.[132] Normal ATR-FTIR using ZnSe crystal as substrate was also employed to study the transport kinetics of both water and inhibitor anion (HPO_4^{2-}).[133,134]

In a series of papers, ATR-FTIR with the Kretschmann configuration was applied for *in situ* studies of the transport of water and ionic species (thiocyanate ions) through a polymer film to metal/polymer interfaces, such as aluminium/polymer interface and conversion coated-zinc/polymer interface. The fast increase of the stretching and bending vibrations of water at 3450 and 1650 cm^{-1} suggested a fast sorption of water in the coating and the aluminium/coating interface (Figure 20.8).[135] Another band at 950 cm^{-1} due to the vibrations of Al-O groups indicated the formation of corrosion products—aluminium oxide or hydroxide at the aluminium surface. In the thicyanate solution, a band at 2075 cm^{-1} due to the C=N vibration of the thicyanate ion was detected after prolonged exposure. As complementary to ATR-FTIR, which provided information about a specific region, electrochemical impedance spectroscopy (EIS) was employed to take into account the whole system.[137,138] The combination of ATR-FTIR and EIS was also extended to investigate the hidden interface between a conversion-coated zinc surface and a polymer coating upon exposure to an electrolyte.[139]

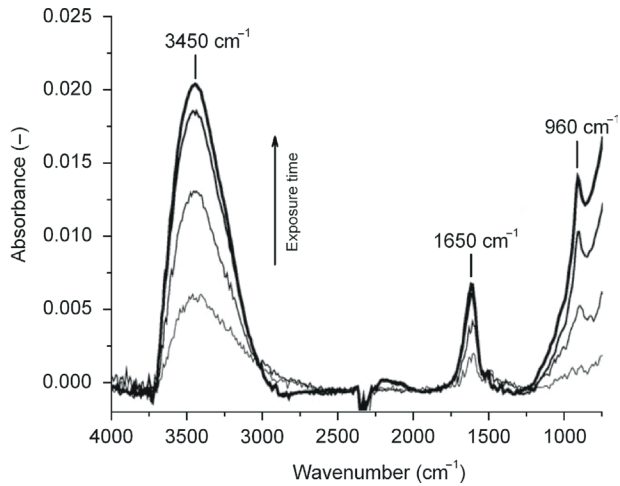


Figure 20.8 ATR-FTIR spectra of a ZnSe element coated with a thin aluminium film and a polymer film in contact with ultra pure deionized water. The exposure times were 40, 163 min, 26 and 50 h, respectively. *Reprinted from Ref. [135]. Copyright 2006, with permission from Elsevier.*

20.6 Conclusion

This chapter demonstrated the potential of Raman and IR spectroscopy for *in situ* studies of corrosion-related phenomena. Both techniques provide valuable real-time information on various corrosion systems. However, literature survey showed that more *in situ* studies were conducted using Raman spectroscopy than IR spectroscopy because of less interference from water for Raman acquisition. In addition, special sample preparation and experimental setup are required for *in situ* FTIR studies, especially in aqueous solutions. Therefore, challenges exist for IR spectroscopy to be applicable to more corrosion-related *in situ* studies.

Among the several applications discussed in this chapter, *in situ* study of corrosion protection coating systems is a prevalent subject, especially in recent years. The studies have been focused on all the important aspects in coating systems, which include *in situ* monitoring the growth of coatings, their degradation in corrosive environments, and characterization of the corrosion products underneath the coating if coating delamination occurs.

Acknowledgments

The author is grateful for the support from College of Engineering, University of Hawaii at Manoa. The author is particularly grateful to Prof. Lloyd Hihara, director of the Hawaii Corrosion Laboratory at the Department of Mechanical Engineering, University of Hawaii at Manoa.

References

1. Thibeau RJ, Brown CW, Goldfarb AZ, et al. Infrared and Raman spectroscopy of aqueous corrosion films on lead. J Electrochem Soc 1980;127(1):37–44.
2. Melendres CA, Xu S. In situ laser Raman spectroscopic study of anodic corrosion films on nickel and cobalt. J Electrochem Soc 1984;131(10):2239–43.
3. Delichere P, Hugot-Le Goff A, Yu N. Identification by in situ Raman spectroscopy of the films grown during the polarization of nickel in sulfuric solutions. J Electrochem Soc 1986;133(10):2106–7.
4. Hugot-Le Goff A, Pallotta C. In situ Raman spectroscopy for the study of iron passivity in relation to solution composition. J Electrochem Soc 1985;132(11):2805–6.
5. Thanos ICG. In situ Raman and other studies of electrochemically oxidized iron and iron-9% chromium alloy. Electrochim Acta 1986;31(7):811–20.
6. Hamilton JC, Farmer JC, Anderson RJ. In situ Raman spectroscopy of anodic films formed on copper and silver in sodium hydroxide solution. J Electrochem Soc 1986;133(4):739–45.
7. Smith JM, Wren JC, Odziemkowski M, et al. The electrochemical response of preoxidized copper in aqueous sulfide solutions. J Electrochem Soc 2007;154(8):C431–8.
8. Ohtsuka T, Guo J, Sato N. Raman spectra of the anodic oxide film on titanium in acidic sulfate and neutral phosphate solutions. J Electrochem Soc 1986;133(12):2473–6.
9. Thierry D, Persson D, Leygraf C, et al. In-situ Raman spectroscopy combined with x-ray photoelectron spectroscopy and nuclear microanalysis for studies of anodic corrosion film formation on iron-chromium single crystals. J Electrochem Soc 1988;135(2):305–10.

10. McMahon JJ, Ruther W, Melendres CA. In situ laser Raman spectroelectrochemical study of the corrosion of lead in dilute disodium sulfate solution at high temperature. J Electrochem Soc 1988;135(3):557–62.
11. Melendres CA, Camillone III N, Tipton T. Laser Raman spectroelectrochemical studies of anodic corrosion and film formation on iron in phosphate solutions. Electrochim Acta 1989;34(2):281–6.
12. Hugot-Le Goff A, Flis J, Boucherit N, et al. Use of Raman spectroscopy and rotating split ring disk electrode for identification of surface layers on iron in 1 M sodium hydroxide. J Electrochem Soc 1990;137(9):2684–90.
13. Johnston C. In situ laser Raman microprobe spectroscopy of corroding iron electrode surfaces. Vib Spectrosc 1990;1(1):87–96.
14. Baek WC, Kang T, Sohn HJ, et al. In situ surface enhanced Raman spectroscopic study on the effect of dissolved oxygen on the corrosion film on low carbon steel in 0.01 M NaCl solution. Electrochim Acta 2001;46(15):2321–5.
15. Joiret S, Keddam M, Novoa XR, et al. Use of EIS, ring-disk electrode, EQCM and Raman spectroscopy to study the film of oxides formed on iron in 1 M NaOH. Cem Concr Compos 2002;24(1):7–15.
16. Farrow RL, Nagelberg AS. Raman spectroscopy of surface oxides at elevated temperatures. Appl Phys Lett 1980;36(12):945–7.
17. Maslar JE, Hurst WS, Bowers WJ, et al. In situ Raman spectroscopic investigation of aqueous iron corrosion at elevated temperatures and pressures. J Electrochem Soc 2000;147(7):2532–42.
18. Maslar JE, Hurst WS, Bowers Jr. WJ, et al. In situ Raman spectroscopic investigation of stainless steel hydrothermal corrosion. Corrosion 2002;58(9):739–47.
19. Kumai CS, Devine TM. Oxidation of iron in 288°C, oxygen-containing water. Corrosion 2005;61(3):201–18.
20. Maslar JE, Hurst WS, Bowers Jr. WJ, et al. In situ Raman spectroscopic investigation of nickel hydrothermal corrosion. Corrosion 2002;58(3):225–31.
21. Bernard MC, Hugot-Le Goff A, Massinon D, et al. In situ Raman identification of corrosion products on galvanized steel sheets. Mater Sci Forum 1992;111–112:617–20.
22. Bernard MC, Hugot-Le Goff A, Phillips N. In situ Raman study of the corrosion of zinc-coated steel in the presence of chloride. I. Characterization and stability of zinc corrosion products. J Electrochem Soc 1995;142(7):2162–7.
23. Boucherit N, Hugot-Le Goff A, Joiret S. Raman studies of corrosion films grown on Fe and Fe-6Mo in pitting conditions. Corros Sci 1991;32(5–6):497–507.
24. Bocherit N, Hugot-Le Goff A, Joiret S. In situ Raman identification of stainless steels pitting corrosion films. Mater Sci Forum 1992;111–112:581–7.
25. Boucherit N, Hugot-Le Goff A. Localized corrosion processes in iron and steels studied by in situ Raman spectroscopy. Faraday Discuss 1992;94:137–47.
26. Bonin PML, Odziemkowski MS, Reardon EJ, et al. In situ identification of carbonate-containing green rust on iron electrodes in dolutions simulating groundwater. J Solution Chem 2000;29(10):1061–74.
27. Simard S, Odziemkowski M, Irish DE, et al. In situ micro-Raman spectroscopy to investigate pitting corrosion product of 1024 mild steel in phosphate and bicarbonate solutions containing chloride and sulfate ions. J Appl Electrochem 2001;31(8):913–20.
28. Reffass M, Sabot R, Jeannin M, et al. Effects of NO_2^- ions on localised corrosion of steel in $NaHCO_3$+NaCl electrolytes. Electrochim Acta 2007;52(27):7599–606.
29. Reffass M, Sabot R, Jeannin M, et al. Effects of phosphate species on localised corrosion of steel in $NaHCO_3$+NaCl electrolytes. Electrochim Acta 2009;54(18):4389–96.
30. Barchiche C, Sabot R, Jeannin M, et al. Corrosion of carbon steel in sodium methanoate solutions. Electrochim Acta 2010;55(6):1940–7.
31. Lee CT, Qin Z, Odziemkowski M, et al. The influence of groundwater anions on the impedance behaviour of carbon steel corroding under anoxic conditions. Electrochim Acta 2006;51(8–9):1558–68.

32. Lee CT, Odziemkowski MS, Shoesmith DW. An in situ Raman-electrochemical investigation of carbon steel corrosion in Na_2CO_3/$NaHCO_3$, Na_2SO_4, and NaCl solutions. J Electrochem Soc 2006;153(2):B33–41.
33. Wang K, Li Y-S, He P. In situ identification of surface species on molybdenum in different media. Electrochim Acta 1998;43(16–17):2459–67.
34. Huang BX, Tornatore P, Li Y-S. IR and Raman spectroelectrochemical studies of corrosion films on tin. Electrochim Acta 2000;46(5):671–9.
35. Maslar JE, Hurst WS, Bowers WJ, et al. In situ Raman spectroscopic investigation of zirconium-niobium alloy corrosion under hydrothermal conditions. J Nucl Mater 2001;298(3):239–47.
36. Maslar JE, Hurst WS, Bowers WJ, et al. Alloy 600 aqueous corrosion at elevated temperatures and pressures: an in situ Raman spectroscopic investigation. J Electrochem Soc 2009;156(3):C103–13.
37. Chen S, Wu S, Zheng J, et al. Spectroscopic and morphological studies on the electrooxidation of Pt–Ni alloys in HCl solution. J Electroanal Chem 2009;628(1–2):55–9.
38. Ohtsuka T, Matsuda M. In situ Raman spectroscopy for corrosion products of zinc in humidified atmosphere in the presence of sodium chloride precipitate. Corrosion 2003;59(5):407–13.
39. Cole IS, Muster TH, Lau D, et al. Products formed during the interaction of seawater droplets with zinc surfaces. J Electrochem Soc 2010;157(6):C213–22.
40. Li S. Marine atmospheric corrosion initiation and corrosion products characterization. In: Mechanical engineering. Honolulu: University of Hawai'i at Manoa; 2010. p. 205.
41. Li S, Hihara LH. In situ Raman spectroscopic study of NaCl particle-induced marine atmospheric corrosion of carbon steel. J Electrochem Soc 2012;159(4):C147–54.
42. Li S, Hihara LH. In situ Raman spectroscopic identification of rust formation in Evans' droplet experiments. Electrochem Commun 2012;18:48–50.
43. Allam N, Nazeer A, Ashour E. A review of the effects of benzotriazole on the corrosion of copper and copper alloys in clean and polluted environments. J Appl Electrochem 2009;39(7):961–9.
44. Rubim J, Gutz IGR, Sala O, et al. Surface enhanced Raman spectra of benzotriazole adsorbed on a copper electrode. J Mol Struct 1983;100:571–83.
45. Rubim JC, Gutz IGR, Sala O. Surface-enhanced Raman spectra of benzotriazole adsorbed on a silver electrode. J Mol Struct 1983;101:1–6.
46. Cao PG, Yao JL, Zheng JW, et al. Comparative study of inhibition effects of Benzotriazole for metals in neutral solutions as observed with surface-enhanced Raman spectroscopy. Langmuir 2002;18(1):100–4.
47. Kester JJ, Furtak TE, Bevolo AJ. Surface enhanced Raman scattering in corrosion science: benzotriazole on copper. J Electrochem Soc 1982;129(8):1716–9.
48. Thierry D, Leygraf C. Simultaneous Raman spectroscopy and electrochemical studies of corrosion inhibiting molecules on copper. J Electrochem Soc 1985;132(5):1009–14.
49. Da Costa SLFA, Agostinho SML, Chagas HC, et al. Study of the inhibiting action of benzotriazole on copper corrosion in deaerated sulfuric acid containing ferric ions by the rotating disc electrode, fluorescence, and Raman spectroscopies. Corrosion 1987;43(3):149–53.
50. Rubim JC. Surface enhanced Raman scattering (SERS) from benzotriazole adsorbed on brass electrodes. Chem Phys Lett 1990;167(3):209–14.
51. Villamil RFV, Corio P, Agostinho SML, et al. Effect of sodium dodecylsulfate on copper corrosion in sulfuric acid media in the absence and presence of benzotriazole. J Electroanal Chem 1999;472(2):112–9.
52. Maciel JM, Jaimes RFVV, Corio P, et al. The characterisation of the protective film formed by benzotriazole on the 90/10 copper–nickel alloy surface in H_2SO_4 media. Corros Sci 2008;50(3):879–86.

53. Yao J-L, Yuan Y-X, Gu R-A. Negative role of triphenylphosphine in the inhibition of benzotriazole at the Cu surface studied by surface-enhanced Raman spectroscopy. J Electroanal Chem 2004;573(2):255–61.
54. Costa LAF, Breyer HS, Rubim JC. Surface-enhanced Raman scattering (SERS) on copper electrodes in 1-*n*-butyl-3-methylimidazolium tetrafluoroborate (BMI.BF4): the adsorption of benzotriazole (BTAH). Vib Spectrosc 2010;54(2):103–6.
55. Yuan YX, Yang FZ, Morag CH, et al. The effect of triphenylphosphane on corrosion inhibition of benzotriazole at Ag electrode monitored by SERS in nonaqueous solution. Spectrochim Acta A Mol Biomol Spectrosc 2013;105:184–91.
56. Gallant D, Pézolet M, Simard S. Inhibition of cobalt active dissolution by benzotriazole in slightly alkaline bicarbonate aqueous media. Electrochim Acta 2007;52(15):4927–41.
57. Saito N, Nishihara H, Aramaki K. The mechanism for corrosion protective film formation on iron and nickel in acid solutions with organo-antimony compounds. Corros Sci 1992;33(8):1253–65.
58. Aramaki K, Fujioka E. Surface-enhanced Raman scattering spectroscopy studies on the inhibition mechanism of propargyl alcohol for iron corrosion in hydrochloric acid. Corrosion 1996;52(2):83–91.
59. Marconato JC, Bulhões LO, Temperini ML. A spectroelectrochemical study of the inhibition of the electrode process on copper by 2-mercaptobenzothiazole in ethanolic solutions. Electrochim Acta 1997;43(7):771–80.
60. Yang H-F, Feng J, Liu Y-L, et al. Electrochemical and surface enhanced Raman scattering spectroelectrochemical study of phytic acid on the silver electrode. J Phys Chem B 2004;108(45):17412–7.
61. Tormoen G, Burket J, Dante JF, et al. Monitoring the adsorption of volatile corrosion inhibitors in real time with surface-enhanced Raman spectroscopy. Corrosion 2006;62(12):1082–91.
62. Batista EA, Temperini MLA. An in situ SERS and FTIRAS study of salicylate interaction with copper electrode. J Solid State Electrochem 2007;11(11):1559–65.
63. Bozzini B, Romanello V, Mele C, et al. A SERS investigation of carbon steel in contact with aqueous solutions containing BenzylDiMethylPhenylAmmonium Chloride. Mater Corros 2007;58(1):20–4.
64. Pan Y-C, Wen Y, Xue L-Y, et al. Adsorption behavior of methimazole monolayers on a copper surface and its corrosion inhibition. J Phys Chem C 2012;116(5):3532–8.
65. Yang H, Sun X, Zhu J, et al. Surface enhanced Raman scattering, in situ spectro-electrochemical, and electrochemical impedance spectroscopic investigations of 2-amino-5-mercapto-1,3,4-thiadiazole monolayers at a silver electrode. J Phys Chem C 2007;111(22):7986–91.
66. Huo S-J, Zhu Q, Chu C-S, et al. Anticorrosive behavior of AMT on cobalt electrode: from electrochemical methods to surface-enhanced vibrational spectroscopy study. J Phys Chem C 2012;116(38):20269–80.
67. Sherif E-SM, Erasmus RM, Comins JD. In situ Raman spectroscopy and electrochemical techniques for studying corrosion and corrosion inhibition of iron in sodium chloride solutions. Electrochim Acta 2010;55(11):3657–63.
68. Pan Y-C, Wen Y, Guo X-Y, et al. 2-Amino-5-(4-pyridinyl)-1,3,4-thiadiazole monolayers on copper surface: observation of the relationship between its corrosion inhibition and adsorption structure. Corros Sci 2013;73:274–80.
69. Xia L, McCreery RL. Chemistry of a chromate conversion coating on aluminum alloy AA2024-T3 probed by vibrational spectroscopy. J Electrochem Soc 1998;145(9):3083–9.
70. Xia L, McCreery RL. Structure and function of ferricyanide in the formation of chromate conversion coatings on aluminum aircraft alloy. J Electrochem Soc 1999;146(10):3696–701.
71. Zhao J, Frankel G, McCreery RL. Corrosion protection of untreated AA-2024-T3 in chloride solution by a chromate conversion coating monitored with Raman spectroscopy. J Electrochem Soc 1998;145(7):2258–64.

72. Zhao J, Xia L, Sehgal A, et al. Effects of chromate and chromate conversion coatings on corrosion of aluminum alloy 2024-T3. Surf Coat Technol 2001;140(1):51–7.
73. Chidambaram D, Halada GP, Clayton CR. Spectroscopic elucidation of the repassivation of active sites on aluminum by chromate conversion coating. Electrochem Solid-State Lett 2004;7(9):B31–3.
74. Ramsey JD, McCreery RL. In situ Raman microscopy of chromate effects on corrosion pits in aluminum alloy. J Electrochem Soc 1999;146(11):4076–81.
75. Le BN, Joiret S, Thierry D, et al. The role of chromate conversion coating in the filiform corrosion of coated aluminum alloys. J Electrochem Soc 2003;150(12):B561–6.
76. Tomandl A, Wolpers M, Ogle K. The alkaline stability of phosphate coatings II: in situ Raman spectroscopy. Corros Sci 2004;46(4):997–1011.
77. Hugot-Le Goff A, Bernard MC, Phillips N, et al. Contributions of Raman spectroscopy and electrochemical impedance to the understanding of the underpaint corrosion process of zinc-coated steel sheets. Mater Sci Forum 1995;192–194:779–87.
78. Thierry D, Massinon D, Hugot-Le Goff A. In situ determination of corrosion products formed on painted galvanized steel by Raman spectroscopy. J Electrochem Soc 1991;138(3):879–80.
79. Bernard MC, Hugot-Le Goff A, Phillips N. In situ Raman study of the corrosion of zinc-coated steel in the presence of chloride. II Mechanisms of underpaint corrosion and role of the conversion layers. J Electrochem Soc 1995;142(7):2167–70.
80. Bernard MC, Hugot-Le Goff A, Massinon D, et al. Underpaint corrosion of zinc-coated steel sheet studied by in situ raman spectroscopy. Corros Sci 1993;35(5–8):1339–49.
81. Mengoli G, Munari MT, Bianco P, et al. Anodic synthesis of polyaniline coatings onto Fe sheets. J Appl Polym Sci 1981;26(12):4247–57.
82. DeBerry DW. Modification of the electrochemical and corrosion behavior of stainless steels with an electroactive coating. J Electrochem Soc 1985;132(5):1022–6.
83. Hugot-Le Goff A, Bernard MC. Protonation and oxidation processes in polyaniline thin films studied by optical multichannel analysis and in situ Raman spectroscopy. Synth Met 1993;60(2):115–31.
84. Quillard S, Berrada K, Louarn G, et al. In situ Raman spectroscopic studies of the electrochemical behavior of polyaniline. New J Chem 1995;19(4):365–74.
85. Bernard MC, Hugot-Le Goff A, Joiret S, et al. Polyaniline layer for iron protection in sulfate medium. J Electrochem Soc 1999;146(3):995–8.
86. Bernard MC, Joiret S, Hugot-Le Goff A, et al. Protection of iron against corrosion using a polyaniline layer II. Spectroscopic analysis of the layer grown in phosphoric/metanilic solution. J Electrochem Soc 2001;148(8):B299–303.
87. de Souza S, da Silva JEP, de Torresi SIC, et al. Polyaniline based acrylic blends for iron corrosion protection. Electrochem Solid-State Lett 2001;4(8):B27–30.
88. Torresi RM, de Souza S, da Silva JEP, et al. Galvanic coupling between metal substrate and polyaniline acrylic blends: corrosion protection mechanism. Electrochim Acta 2005;50(11):2213–8.
89. Seegmiller JC, Pereira da Silva JE, Buttry DA, et al. Mechanism of action of corrosion protection coating for AA2024-T3 based on poly(aniline)-poly(methylmethacrylate) blend. J Electrochem Soc 2005;152(2):B45–53.
90. da Silva JEP, de Torresi SIC, Torresi RM. Polyaniline/poly(methylmethacrylate) blends for corrosion protection: the effect of passivating dopants on different metals. Prog Org Coat 2007;58(1):33–9.
91. da Silva JEP, Temperini MLA, de Torresi SIC. Secondary doping of polyaniline studied by resonance Raman spectroscopy. Electrochim Acta 1999;44(12):1887–91.
92. Bukowska J, Jackowska K. In situ Raman studies of polypyrrole and polythiophene films on Pt electrodes. Synth Met 1990;35(1–2):143–50.
93. Ohtsuka T, Wakabayashi T, Einaga H. Optical characterization of polypyrrole-polytungstate anion composite films. Synth Met 1996;79(3):235–9.

94. Nguyen Thi Le H, Bernard MC, Garcia-Renaud B, et al. Raman spectroscopy analysis of polypyrrole films as protective coatings on iron. Synth Met 2004;140(2–3):287–93.
95. Van ST, Joiret S, Deslouis C, et al. In situ Raman spectroscopy and spectroscopic ellipsometry analysis of the iron/polypyrrole interface. J Phys Chem C 2007;111(39):14400–9.
96. Sheng N, Ueda M, Ohtsuka T. The formation of polypyrrole film on zinc-coated AZ91D alloy under constant current characterized by Raman spectroscopy. Prog Org Coat 2013;76(2–3):328–34.
97. Nguyen TD, Pham MC, Piro B, et al. Conducting polymers and corrosion PPy-PPy-PDAN composite films. J Electrochem Soc 2004;151(6):B325–30.
98. Leygraf C, Johnson M. Infrared spectroscopy. In: Marcus P, Mansfeld F, editors. Analytical methods in corrosion science and engineering. Boca Raton: CRC Press; 2006. p. 237–68.
99. Trettenhahn GLJ, Nauer GE, Neckel A. In situ external reflection absorption FTIR spectroscopy on lead electrodes in sulfuric acid. Electrochim Acta 1996;41(9):1435–41.
100. Mucalo MR, Li Q. In situ infrared spectroelectrochemical studies of the corrosion of a nickel electrode as a function of applied potential in cyanate, thiocyanate, and selenocyanate solutions. J Colloid Interface Sci 2004;269(2):370–80.
101. Degenhardt J, McQuillan AJ. In situ ATR-FTIR spectroscopic study of adsorption of perchlorate, sulfate, and thiosulfate ions onto chromium(III) oxide hydroxide thin films. Langmuir 1999;15(13):4595–602.
102. Borras CA, Romagnoli R, Lezna RO. In-situ spectroelectrochemistry (UV-visible and infrared) of anodic films on iron in neutral phosphate solutions. Electrochim Acta 2000;45(11):1717–25.
103. Lin J, Lin C, Lin Z, et al. In situ measurement of the transport processes of corrosive species through a mortar layer by FTIR-MIR. Cem Concr Res 2012;42(1):95–8.
104. Persson D, Leygraf C. In situ infrared reflection absorption spectroscopy for studies of atmospheric corrosion. J Electrochem Soc 1993;140(5):1256–60.
105. Persson D, Leygraf C. Initial interaction of sulfur dioxide with water covered metal surfaces: an in situ IRAS study. J Electrochem Soc 1995;142(5):1459–68.
106. Itoh J, Sasaki T, Seo M, et al. In situ simultaneous measurement with IR-RAS and QCM for investigation of corrosion of copper in a gaseous environment. Corros Sci 1997;39(1):193–7.
107. Faguy PW, Richmond WN, Jackson RS, et al. Real-time polarization modulation in situ infrared spectroscopy applied to the study of atmospheric corrosion. Appl Spectrosc 1998;52(4):557–64.
108. Wadsak M, Aastrup T, Odnevall WI, et al. Multianalytical in situ investigation of the initial atmospheric corrosion of bronze. Corros Sci 2002;44(4):791–802.
109. Aastrup T, Wadsak M, Leygraf C, et al. In situ studies of the initial atmospheric corrosion of copper. Influence of humidity, sulfur dioxide, ozone, and nitrogen dioxide. J Electrochem Soc 2000;147(7):2543–51.
110. Kleber C, Kattner J, Frank J, et al. Design and application of a new cell for in situ infrared reflection-absorption spectroscopy investigations of metal-atmosphere interfaces. Appl Spectrosc 2003;57(1):88–92.
111. Aastrup T, Leygraf C. Simultaneous infrared reflection absorption spectroscopy and quartz crystal microbalance measurements for in situ studies of the metal/atmosphere interface. J Electrochem Soc 1997;144(9):2986–90.
112. Dai Q, Freedman A, Robinson GN. Sulfuric acid-induced corrosion of aluminum surfaces. J Electrochem Soc 1995;142(12):4063–9.
113. Johnson CM, Tyrode E, Leygraf C. Atmospheric corrosion of zinc by organic constituents I. The role of zinc/water and water/air interfaces studied by infrared reflection/absorption spectroscopy and vibrational sum frequency spectroscopy. J Electrochem Soc 2006;153(3):B113–20.
114. Johnson CM, Leygraf C. Atmospheric corrosion of zinc by organic constituents. II. Reaction routes for zinc-acetate formation. J Electrochem Soc 2006;153(12):B542–6.

115. Johnson CM, Leygraf C. Atmospheric corrosion of zinc by organic constituents. III. An infrared reflection-absorption spectroscopy study of the influence of formic acid. J Electrochem Soc 2006;153(12):B547–50.
116. Hedberg J, Baldelli S, Leygraf C, et al. Molecular structural information of the atmospheric corrosion of zinc studied by vibrational spectroscopy techniques. Part I. Experimental approach. J Electrochem Soc 2010;157(10):C357–62.
117. Hedberg J, Baldelli S, Leygraf C. Molecular structural information of the atmospheric corrosion of zinc studied by vibrational spectroscopy techniques. II. Two and three-dimensional growth of reaction products induced by formic and acetic acid. J Electrochem Soc 2010;157(10):C363–73.
118. Persson D, Axelsen S, Zou F, et al. Simultaneous in situ infrared reflection absorption spectroscopy and Kelvin probe measurements during atmospheric corrosion. Electrochem Solid-State Lett 2001;4(2):B7–10.
119. Chen ZY, Persson D, Leygraf C. Initial NaCl-particle induced atmospheric corrosion of zinc—effect of CO_2 and SO_2. Corros Sci 2008;50(1):111–23.
120. LeBozec N, Persson D, Thierry D. In situ studies of the initiation and propagation of filiform corrosion on aluminum. J Electrochem Soc 2004;151(7):B440–5.
121. Weissenrieder J, Leygraf C. In situ studies of filiform corrosion of iron. J Electrochem Soc 2004;151(3):B165–71.
122. Chen ZY, Persson D, Nazarov A, et al. In situ studies of the effect of CO_2 on the initial NaCl-induced atmospheric corrosion of copper. J Electrochem Soc 2005;152(9):B342–51.
123. Chen ZY, Persson D, Leygraf C. In situ studies of the effect of SO_2 on the initial NaCl-induced atmospheric corrosion of copper. J Electrochem Soc 2005;152(12):B526–33.
124. Jönsson M, Persson D, Thierry D. Corrosion product formation during NaCl induced atmospheric corrosion of magnesium alloy AZ91D. Corros Sci 2007;49(3):1540–58.
125. Vogt MR, Nichols RJ, Magnussen OM, et al. Benzotriazole adsorption and inhibition of Cu(100) corrosion in HCl: a combined in-situ STM and in-situ FTIR spectroscopy study. J Phys Chem B 1998;102(30):5859–65.
126. Biggin ME, Gewirth AA. Infrared studies of benzotriazole on copper electrode surfaces. Role of chloride in promoting reversibility. J Electrochem Soc 2001;148(5):C339–47.
127. Bozzini B, Mele C, Romanello V. An in situ FT-IR evaluation of candidate organic corrosion inhibitors for carbon steel in contact with alkaline aqueous solutions. Mater Corros 2007;58(5):362–8.
128. Pohjakallio M, Sundholm G, Talonen P, et al. Characterization of the redox processes of poly (thiophene-3-methanol) by voltammetry, in situ optical beam deflection and Fourier transform IR techniques. J Electroanal Chem 1995;396(1–2):339–48.
129. D'Elia LF, Ortiz RL, Marquez OP, et al. Electrochemical deposition of poly(*o*-phenylenediamine) films on type 304 stainless steel. J Electrochem Soc 2001;148(4):C297–300.
130. Nguyen T, Byrd E, Lin C. A spectroscopic technique for in situ measurement of water at the coating/metal interface. J Adhes Sci Technol 1991;5(9):697–709.
131. Nguyen T, Bentz D, Byrd E. A study of water at the organic coating/substrate interface. J Coat Technol 1994;66(834):39–50.
132. Nguyen T, Byrd E, Bentz D, et al. In situ measurement of water at the organic coating/substrate interface. Prog Org Coat 1996;27(1–4):181–93.
133. Philippe L, Sammon C, Lyon SB, et al. An FTIR/ATR in situ study of sorption and transport in corrosion protective organic coatings: 1. Water sorption and the role of inhibitor anions. Prog Org Coat 2004;49(4):302–14.
134. Philippe L, Sammon C, Lyon SB, et al. An FTIR/ATR in situ study of sorption and transport in corrosion protective organic coatings: paper 2. The effects of temperature and isotopic dilution. Prog Org Coat 2004;49(4):315–23.

135. Öhman M, Persson D, Leygraf C. In situ ATR-FTIR studies of the aluminium/polymer interface upon exposure to water and electrolyte. Prog Org Coat 2006;57(1):78–88.
136. Wapner K, Stratmann M, Grundmeier G. In situ infrared spectroscopic and scanning Kelvin probe measurements of water and ion transport at polymer/metal interfaces. Electrochim Acta 2006;51(16):3303–15.
137. Öhman M, Persson D. An integrated in situ ATR-FTIR and EIS set-up to study buried metal–polymer interfaces exposed to an electrolyte solution. Electrochim Acta 2007;52(16):5159–71.
138. Öhman M, Persson D, Leygraf C. A spectroelectrochemical study of metal/polymer interfaces by simultaneous in situ ATR-FTIR and EIS. Electrochem Solid-State Lett 2007;10(4):C27–30.
139. Öhman M, Persson D, Jacobsson D. In situ studies of conversion coated zinc/polymer surfaces during exposure to corrosive conditions. Prog Org Coat 2011;70(1):16–22.

Index

Note: Page numbers followed by *f* indicate figures and *t* indicate tables.

A

AA2024 alloy, 25
Abdelmalek, F., 616
Abdullayev, E., 299–300
Absorption, 615*f*
Absorption switching, 478*f*
Accelerated salt immersion corrosion test, 509–512, 525–526
Accelerated weathering, 389–396
Acidic pickling surface modification, 549*f*, 551*f*
Acrylic latex pilot plant
  agitation system in, 359*t*
  charging process, 358
  impeller selection, 360*t*
  mixing engineering parameters, 360*t*
  setup, 359
Active agents, 318–321
Active feedback, 287–288, 301
Active-passive dissolution, 5*f*
Additives
  applications of, 337
  definition of, 337
  overview of, 337
Adhesion, 378–379
AFM. *See* Atomic Force Microscopy
Agitation system, 359*t*
Air atmosphere, 375
Air plasma spraying (APS), 45
Aircraft, corrosion in, 603–604, 622–623, 624–625
Akid, R., 416–417
Al. *See* Aluminum
Al-acetylacetonate, 107
ALD. *See* Atomic layer deposition
ALE. *See* Atomic layer deposition
Alkaline etching surface modification, 550*f*, 551*f*
Alkyd coatings, 318*f*
All-optical switches, 471–473
Alloys
  corrosion of
    costs of, 62–63
    definition of, 60–62
    overview of, 59–64, 79
    prevention of, 62–63
  in gas turbine engines, 32–33, 32*f*
  magnesium
    overview of, 537
    SCC mechanisms in, 545–546
    types of, 538
  in marine applications, 33
  pretreatment coating selection of, 64–65, 65*f*
  super-, 32–33, 32*f*
    chemical composition of, 39*t*
    Cr content influencing, 41
    hot corrosion of, 37
    nickel-based, 32–33, 32*f*, 48
    type-I corrosion conditions and, 37, 38*f*, 39*f*
    type-II corrosion conditions and, 38*f*
  titanium, 585–587
    oxidized, 598, 598*f*
    two-layer model for, 598, 598*f*
Alumina precursors
  Al-acetylacetonate, 107
  aluminum isopropoxide, 106
  overview of, 106–107
Alumina scales, 41, 53–55, 54*f*
Aluminide coatings, platinum incorporated into, 42
Aluminum (Al), 27–28
  corrosion sensor, 615*f*
  overlay coatings influenced by, 42–43, 43*f*
  precursors, 112–114
Aluminum isopropoxide, 106
Aluminum modified silica microparticles, 297*f*
Aluminum modified silica submicroparticles, 293*f*
American Society for Testing and Materials (ASTM) seawater, 384–387
Ammonium molybdate, 297*f*
Anastas, Paul, 363–364
Anchor stirrer, 349*f*
Annealing, 666–667
Anodic inhibitor, 10, 10*f*, 11*f*
Anodic oxidation, 590–591

Anodic oxide film formation, 680–681
Anodic protection, 560
Anodizing, 66–67
Anticorrosion coatings
  conducting polymer
    coating procedure in, 412–413
    examples, 415–419
    mechanism of protection, 414–415
    overview of, 411–419
  superhydrophobic coating
    fabrication procedures of, 421–424
    overview of, 419–424
    theoretical background of, 419–420
  superhydrophobic conducting polymers as, 424–427
Antipina, M. N., 307
APS. *See* Air plasma spraying
Aquence, 21–22, 22*f*
Aqueous corrosion
  anodic oxide film formation, 680–681
  general, 679
  in situ FTIR, 690
Aqueous emulsion based pilot plants
  buffers in, 344
  components involved in, 343–346
  emulsifiers in, 344
  emulsion feed process in, 344
  emulsion stabilizers in, 343
  initiators in, 344
  monomers in, 343, 344
  water in, 344
Arc spraying, 44–45
Army, U.S., 24
Artificial saliva, 597*t*
Artificial scratch, 271*f*
Artificial sweat, 598*t*
ASTM seawater. *See* American Society for Testing and Materials seawater
ASTM-B117 standard, 389–394
Atmospheric corrosion, 680–689, 690–691
Atomic Force Microscopy (AFM), 382, 423*f*, 661–664
Atomic layer deposition (ALD), 102–104, 103*f*
Atomic oxygen irradiation, 466
ATR. *See* Attenuated total reflectance
ATR-FTIR. *See* Attenuated total reflectance-Fourier-transform infrared spectroscopy
Attenuated total reflectance (ATR), 679
Attenuated total reflectance-Fourier-transform infrared spectroscopy (ATR-FTIR), 692–693
Attritor, 355
Au. *See* Gold
Au::VO_2 nano-arrays, 479–481
Avigal, Y., 117
Axial flow propellers, 349*f*, 350–351

B

Ball mills, 353–354, 354*t*, 355
BAM-PPV. *See* Poly(2,5-bis(*N*-methyl-*N*-hexylamino)phenylene vinylene)
Barrier
  coatings, 7–10
  properties, 648–649
  protection, 414
Bell, M. S., 99–100
Benzotriazole (BTA), 323*f*
Bilayer structure, 478
Biofilms, as pretreatment coatings, 78–79
Biomaterials, 586–587, 594–595, 596–598
Bisphenol A (BPA), 139–152
Bis(β-diketonate) silicon(IV) complexes, 111–112, 112*f*
Bones, 24
Boo, J.-H., 119
BOTDR. *See* Brillouin optical time domain reflectometry
BPA. *See* Bisphenol A
Bragg wavelength shift, 617*f*
Braun, P. V., 519–520
Bridges, corrosion in, 609–610, 619
Brillouin corrosion expansion sensor, 611*f*
Brillouin optical time domain reflectometry (BOTDR), 607, 607*f*, 611
Bronze, 643–647, 666–667, 666*f*
Brown, E., 496–497
BTA. *See* Benzotriazole
Buffers, 344
Burkhardt, W., 466–467
Burner rig test, 50
Buttry, D. A., 285–286

C

Capacitances, 667–668
Carbon nanotubes (CNTs), 197–198. *See also* Multiwalled carbon nanotube coatings
Carmona, N., 630
Caruso, M. M., 498
Cassie-Baxter equation, 420, 421*f*
Casting-based methods, 412
Cathodic inhibitor, 10, 11*f*
Cathodic protection, 28–29
  ICCP for
    advantages of, 30
    overview of, 30
  overview of, 29–30, 559
  sacrificial anodes for

advantages of, 29
disadvantages of, 30
overview of, 29–30
Cathodic-protection coatings, 12–14
CC Technologies Laboratories, Inc., 283–284
CCCs. *See* Chromate conversion coatings
(cod)Pt(Me)$_2$, 113*f*
Ce-doped VO_2, 467
Cells, 678–679
CeO_2 nanoparticles, 136, 152–160, 153*f*, 174–191
Ceramic coatings
overview of, 94
titanium, protective films as, 595–596
Ceramic cores, 292–297, 297*f*, 298–300
Ceramic matrix composites (CMCs), 94
Ceramic particles, 298*f*
Ceramics
nonoxide
Al, 112–114
Mo, 112–114
overview of, 112–121
Pt, 112–114
SiC, 116–121
TiCN, 114–115, 114*f*
W, 112–114
ZrCN, 114–115, 114*f*
oxide
alumina, 106–107
overview of, 106–112
silica, 107–112
titania, 107–112
zirconia, 107–112
Cerium (Ce), VO_2 doped with, 467
Cerium ions, 139–152
Cerium nitrate, 152–160, 297*f*
Cerium oxide, 152–160
Cerium salt, 174–191
Cerium-based conversion coatings, 70–71
Cerium-doped silane hybrid coatings. *See* Silane hybrid coatings
Chaddha, A. K., 119–120
Challener, C., 431–432
Chemical analysis, 618*f*
Chemical deposition, 421–423
Chemical intelligence, 643
Chemical vapor deposition (CVD)
ALE mode of, 102–104, 103*f*
electron beam, 101, 101*f*
fluidized bed, 99*f*, 102
focused ion-assisted, 104–105, 104*f*
laser-induced, 98–99
metalorganic
ALD, 102–104, 103*f*
EBCVD, 101, 101*f*
FBCVD, 99*f*, 102
IACVD, 104–105, 104*f*
LCVD, 98–99, 98*f*
overview of, 96–105, 97*f*
PECVD, 99–100, 99*f*, 100*f*
techniques of, 96–105
UVCVD, 99, 99*f*
organometallic, 96–97, 99
overview of, 94–95
plasma-enhanced, 99–100, 100*f*
precursors
as silica precursors, 110–112
as yttria precursors, 110–112
as zirconia precursors, 110–112
PVD compared with, 94–95
UV-induced, 99, 99*f*
variants, 96–105
Chemically intelligent coatings
characterizing, 651–654
EIS, 651–652
FTIR, 652–654
for outdoor metalwork, 651
performance of, 651–654
testing of, 651–654
weathered coated substrates, 651–654
weathering studies of, 651
China Lake, California, 75
Chloride ions, 619–621
Chlorophenol Red dye, 630, 631*f*
Chromate coatings, 135
Chromate conversion coatings (CCCs), 67–69
Chromia scale, 41, 53–55, 54*f*
Chromium (Cr), superalloys influenced by content of, 41
Chung, C. M., 493
Citric acid, 264*f*, 266*f*, 267*f*
Civil engineering, 609–610, 628–629, 630–631, 633
Clay, 569–571
CM 247 LC superalloy, 37, 38*f*, 39*f*, 53–55
CMCs. *See* Ceramic matrix composites
CNTs. *See* Carbon nanotubes
Co. *See* Cobalt
Coated bronze substrates, 644–647
Coating procedure
casting-based methods as, 412
electrodeposition, 412–413
electropolymerization
galvanostatic, 413
overview of, 412–413
potentiodynamic, 413
potentiostatic, 413
paint/resin-blended coatings, 412

Coating substrates, 649–650
Coating systems, 14
Coatings. *See also* Ceramic coatings; Conversion coatings; Nonmetallic-inorganic pretreatment coatings; Organic pretreatment coatings; Pretreatment coatings; Self-healing coatings
  ATR-FTIR, 692
  combinations of, 21
  for cultural heritage conservation, 643–647
  damage mechanisms, 126–128, 127*f*
  definition of, 336
  FTIR-reflection spectroscopy, 692
  functionality of, 20
  general process for
    overview of, 338–340
    sand mill route, 338–340
    thinning in, 339–340
  in situ FTIR, 692–693
  in situ Raman spectroscopy, 685–689
  inorganic, 560–561
  Laponite incorporated into, 665–666
  life of, 41
  metallic, 560–561
  microstructures of, 50
  outlook, 128–129
  precursor, 369–370, 371
  resistance, 275*f*
  survey, 645*f*
  thickness, 516*f*
  traditional, 20
  weathering studies of, 644–647
Cobalt (Co), nanocrystalline, 27, 27*f*, 28*f*
Cobalt/multiwalled carbon nanotube (Co/MWCNT) coatings, 27
Co-doping, 466–467, 468*f*, 469–471, 472*t*
Coefficient of thermal expansion (CTE), 94
Colloidal assemblies, 423–424
Composites, 594
Co/MWCNT coatings. *See* Cobalt/multiwalled carbon nanotube coatings
Concrete, compression resistance of, 437, 437*f*. *See also* Rebar concrete
Conducting polymer, 21
  anticorrosion coating
    coating procedure, 412–413
    examples, 415–419
    mechanism of protection, 414–415
    overview, 411–419
Conductive polymer coatings, 74–75
Container-based organic self-protecting coatings, 322–325
Containers. *See* Microcontainers; Nanocontainers
Continuous crack propagation, 546
Controlled release coatings
  with inhibitor-loaded nanocontainers, 78
  as organic pretreatment coating, 78
Convection, 6*f*
Conversion coatings
  cerium-based, 70–71
  chromate, 67–69
  corrosion protection, 410
  in situ Raman spectroscopy, 685–686
  lanthanide-based, 69–71
  miscellaneous-based, 71–72
  overview of, 67–72
  phosphate, 69
Copper, 444–447, 445*f*, 446*f*
Core fraction, 508–509, 524–525
Core microcontainers, 311*f*
Corrosion
  in aircraft, 603–604, 622–623, 624–625
  of alloys
    costs, 62–63
    definition, 60–62
    overview, 59–64, 79
    prevention, 62–63
  in bridges, 609–610, 619
  as challenge, 17
  combating, 284–287
  cost of, 18, 18*f*, 63–64, 63*t*, 283–284
  current density, 7*f*
  definition of, 538–539, 558
  under different environments, 61*f*
  as economic problem, 283–284
  effects of, 558
  in Europe, 283–284
  flow diagram, 62*f*
  forms of, 17, 61
  globe influenced by, 283–284
  iron, 491–492, 492*f*
  kinetics, 3–7
  loss percentage, 18*f*
  macroscopic forms of, 62*f*
  of metals
    costs, 62–63
    definition, 60–62
    overview, 59–64, 79
    prevention, 62–63
  methods for, 284–287
  microscopic forms of, 62*f*
  mitigation, with stannate conversion coatings, 547–553
  in other fluids, 60
  overview of, 2–7, 17–19, 283–287, 558–559
  potential, 7*f*, 217*f*

preventing, 409
sectors influenced by, 62
strategies, 63–64
tests, 205
thermodynamics, 2–3
in U.S., 283–284
Corrosion by-products, 622–624
Corrosion control
corrosion measurements and, 624–632
optical pH sensors for, 626–632
relative humidity monitoring for, 624–626, 627*t*
sol-gel coatings for
corrosion applications of, 450–453
overview of, 447–453
Corrosion damages, 397–402
Corrosion detector, turn-on, 27–28
Corrosion fatigue, 546
Corrosion inhibitors, 10–11
in situ FTIR, 691–692
in situ Raman spectroscopy, 682–685
microcontainers with, 315*f*, 316*f*
nanocontainers with, 313*f*, 315*f*, 316*f*
natural passibity synthesizing, 25–26
release of, 25
Corrosion measurements
corrosion control and, 624–632
of corrosion precursors, 617–624
of corrosion products, 617–624
direct
metallic sacrificial layers, 612–617
overview of, 609–612
indirect, 618*t*
optical pH sensors, 626–632
overview of, 609–632
relative humidity monitoring, 624–626, 627*t*
Corrosion monitoring. *See also In situ* Fourier-transform infrared spectroscopy; *In situ* Raman spectroscopy
equipment, 677–679
ATR, 679
IR spectroscopy, 678–679
Raman spectroscopy, 677–678
methods, 677–679
ATR, 679
IR spectroscopy, 678–679
Raman spectroscopy, 677–678
overview of, 673–674, 694
principles
IR spectroscopy, 676–677
Raman spectroscopy, 674–676
Corrosion precursors, 617–624
detection of, 619–621
optical fiber technology for, 618*f*, 625*t*
Corrosion prevention, measures of
anodic protection as, 560
cathodic protection as, 559
coatings as, 560–562
inhibitors as, 559
overview of, 559–562
Corrosion products, 617–624
detection of, 622–624
optical fiber technology for, 618*f*
Corrosion protection
conversion coatings, 410
organic coatings, 410–411
overview of, 409, 410–411
Corrosion sensing, 613*t*. *See also* Corrosion measurements
Corrosion studies, 596–598
Corrosion-control coatings. *See also* Corrosion inhibitors
barrier, 7–10
cathodic-protection, 12–14
electrochemical aspects of
corrosion, 2–7
overview of, 1, 7–14, 15
systems, 14
Coupons, 383–396
Cr. *See* Chromium
Creamers, 21
Creep strength, 32–33
Crevice corrosion
example of, 542*f*
overview of, 541–543
schematic representation of, 542*f*
"Criteria for a Recommended Standard: Occupational Exposure to Hexavalent Chromium" (NIOSH), 68–69
Cross-linking agent, 137
Crucible test, 51
Crunteanu, A., 462, 474
Cr(VI), 67–69
CTE. *See* Coefficient of thermal expansion
Culturally significant works
chemically intelligent coatings
characterization, 651–654
EIS, 651–652
FTIR, 652–654
for outdoor metalwork, 651
overview, 651–654
performance, 651–654
weathered coated substrates characterization, 651–654
weathering studies, 651
experimental details
for characterizing substrates, 650–651

Culturally significant works *(Continued)*
of coated panels, 650
for coating substrates, 649–650
overview, 649–651
for weathering studies, 650
overview of, 641–649, 669
barrier properties, 648–649
chemical intelligence, 643
commonly used coatings, 643–647
EIS, 648–649
intelligence, 643
material cultural heritage, 641–642, 647–648
physical intelligence, 643
protective coatings, 641–642
protective films, 648–649
weathering studies, 644–647
physically intelligent coatings
AFM, 661–664
annealing, 666–667
assessment, 668–669
barrier properties, 666–667
capacitances, 667–668
characterization, 654–666
EIS, 666–667
electrolyte swollen films, 667–668
modified Laponite, 658–660, 661–664, 665–666
performance testing, 666–669
SAXS data, 661
synthetic nanoclay, 654–658
volume fractions, 667–668
water, 667–668
waterborne nanocomposites coatings, 654–657
waterborne PVDF-clay nanocomposites, 666–667
x-ray methods, 660–661
Cured coatings, 369–370, 371–374
CVD. *See* Chemical vapor deposition
Cyclic voltammetry, 201, 205–216

D

Damage mechanisms, 126–128, 127*f*
Davy, Humphrey, 559
DCOIT. *See* 4,5-dichloro-2-*n*-octyl-4-isothiazolin-3-one
DCPD. *See* Dicyclopentadiene
Dean Test, 51
DeBerry, D. W., 74, 558
Dermer, O., 114–115
Detonation gun spraying, 45
Dexter, S. C., 543–544
D-Gun. *See* Detonation gun spraying
4,5-dichloro-2-*n*-octyl-4-isothiazolin-3-one (DCOIT), 320*f*, 323*f*
Dicyclopentadiene (DCPD), 24
Diffusion coatings, 42
Diisocyanate-based one-part self-healing anticorrosive coating
HDI-based
accelerated salt immersion corrosion test of, 509–512
anticorrosive performance of, 517–519
capsules diameter influencing, 515*f*
coating thickness influencing, 516*f*
exposure time influencing, 515*f*
healing reaction of, 512*f*
parameters influencing, 517–519
preparation of, 509
salt spray test, 512–517
scribed regions, 511*f*
water's reaction with, 512*f*
weight fraction of microcapsules influencing, 516*f*
microcapsules
chemical constituent, 506–507
diameter, 507–508
fill content, 506*t*
morphology, 507–508
MRT, 506*t*
thermal property, 508–509
microencapsulation of, 503–506
Dip-coating
overview of, 588–589
schematics of, 588*f*
of titanium, 588–589
Direct emulsion, 300–301
Direct measurements, corrosion
with metallic sacrificial layers, 612–617
OFS for, 613*t*
overview of, 609–612
Discontinuous crack propagation, 546
Dispersion
definition of, 337–338
factors influencing, 338
process
grinding, 338
liquid/solid, 338
overview, 337–338
separation, 338
stabilization, 338
stages, 338
wetting, 338
Distributed sensing, 607
DMS-4 superalloy, oxidation characteristics of, 40–41, 40*f*

Dopant concentration, 161
Doping effects, 466–471
Driscoll, T., 475
Drug release concept, 20
Dry corrosion, 61
Dufek, E. J., 285–286
Dumas-Bouchiat, F., 481–483

E

EAP-based anticorrosive coatings. *See* Electroactive polymer-based anticorrosive coatings
EBCVD. *See* Electron beam chemical vapor deposition
EB-PVD processes. *See* Electron beam physical vapor deposition processes
EDX analysis. *See* Energy-dispersive X-ray spectroscopy analysis
EIS. *See* Electrochemical impedance spectroscopy
Electrical circuits, 221*f*
Electrical switches, 473
Electrical-potential-induced wettability conversion, 427*f*
Electroactive polymer (EAP)-based anticorrosive coatings
  nanocomposite
    clay, 569–571
    graphene, 573–574
    hydrophobic, 575–580
    nanoparticle, 571–573
    overview of, 567–580
    silicate nanolayer, 569–571
    SiO_2, 571–573
    superhydrophobic, 575–580
    TiO_2, 571–573
  overview of, 557–558, 563–567, 580–581
Electro-active polymers. *See* Conducting polymer
Electrochemical corrosion measurements, 581*t*
Electrochemical impedance spectroscopy (EIS), 203–204, 216–229, 648–649, 651–652, 666–667
Electrochemical methods, 51, 52
Electrode, 60
Electrodeposition, 412–413
Electrokinetic potential, 201
Electrolyte, 60
Electrolyte swollen films, 667–668
Electrolytic cell, 541*f*
Electrolytic deposition, 591–592
Electron beam chemical vapor deposition (EBCVD), 101, 101*f*
Electron beam physical vapor deposition (EB-PVD) processes
  overview of, 45
  thermal spraying processes compared with, 46*t*
Electronically conducting polymer coating, 687–689
Electropolymerization
  galvanostatic, 413
  overview of, 412–413
  potentiodynamic, 413
  potentiostatic, 413
Electrospun smart coating, 442–447
Elemental analysis, 201
Emission spectra, 263*f*, 276*f*, 278*f*, 279*f*, 280*f*
Emulsifiers, 344
Emulsion droplets, 311–317
  interfacial polyaddition and, 311–315
  interfacial polycondensation and, 311–315
Emulsion feed process, 344–345
Emulsion polymerization, 315–317
Emulsion stabilizers, 343
Enamel. *See also* Porcelain enamel; Vitreous enamel
  coatings, 255–256
  definition of, 251
  experiment
    citric acid, 264*f*, 266*f*
    coating resistance, 275*f*
    color changes, 264*f*, 273*f*
    conclusion, 280–281
    cross-section, 270*f*, 274*f*
    discussion, 259–280
    emission spectra, 263*f*, 276*f*, 278*f*, 279*f*, 280*f*
    excitation spectra, 263*f*
    gloss change, 264*f*, 267*f*, 272*f*
    immersion, 264*f*, 266*f*, 267*f*
    main peak, 276*f*, 278*f*, 279*f*, 280*f*
    materials, 256–259
    overview, 280–281
    potassium pyrophosphate immersion, 267*f*, 268*f*, 269*f*, 270*f*
    procedures, 256–259
    results, 259–280
    roughness values, 265*f*, 268*f*
    salt spray exposure, 271*f*
    surface, 262*f*, 269*f*, 271*f*, 273*f*
    trend of intensity, 276*f*
    trend of luminescent properties, 275–280
    trend of protective properties, 261–275
  layers, 254*f*, 257*t*, 259–261, 263*f*
  overview of, 251–252, 255–256
  porosity, 254*f*
  properties, 261–280
  protection, 261–275

Energy-dispersive X-ray spectroscopy (EDX) analysis, 529*f*
Ennobling mechanism, 414
Environmental Protection Agency (EPA), 363–364
Epoxy coating, 686
Equipment
  corrosion monitoring, 677–679
    ATR, 679
    IR spectroscopy, 678–679
    Raman spectroscopy, 677–678
  paints and coating industry
    filters as, 356–357
    mills as, 353–355
    mixers as, 347–353
    overview of, 347–357
    propellers as, 349*f*
  pilot plant
    overview of, 342–343
    polymer emulsion, 345
    support units, 342–343
  spectroscopic techniques, 677–679
    ATR, 679
    IR spectroscopy, 678–679
    Raman spectroscopy, 677–678
Europe, 283–284
European Union (EU), 68–69
Evanescent field optical fiber pH sensor, 608*f*
Evans, U. R., 219–223, 228–229
Excitation spectra, 263*f*
Experiments
  culturally significant works
    characterizing substrates, 650–651
    coated panels, 650
    coating substrates, 649–650
    overview of, 649–651
    weathering studies, 650
  high performance protective coatings
    characterizing substrates, 650–651
    coated panels, 650
    coating substrates, 649–650
    overview, 649–651
    weathering studies, 650
  hydrogen evolution rates, 547*f*
  laboratory
    GCC, 383–396
    immersion tests, 383–385
    overview of, 383–396
    surface appearance investigations, 385–396
  luminescent enamel
    coating resistance, 275*f*
    color changes, 264*f*, 273*f*
    cross-section, 270*f*, 274*f*
    emission spectra, 263*f*, 276*f*, 278*f*, 279*f*, 280*f*
    excitation spectra, 263*f*
    gloss change, 264*f*, 267*f*, 272*f*
    immersion, 264*f*, 266*f*, 267*f*
    main peak, 276*f*, 278*f*, 279*f*, 280*f*
    materials, 256–259
    overview, 280–281
    potassium pyrophosphate immersion, 267*f*, 268*f*, 269*f*, 270*f*
    procedures of, 256–259
    results of, 259–280
    roughness values of, 265*f*, 268*f*
    salt spray exposure, 271*f*
    surface in, 262*f*, 269*f*, 271*f*, 273*f*
    trend of intensity in, 276*f*
    trend of luminescent properties in, 275–280
    trend of protective properties in, 261–275
  nanotube, 201–203
  outdoor, 396–402
  SHCs
    analytical methods in, 138–139
    composition of, 138*t*
    overview of, 137–139
    sample preparation in, 137–138
  steel substrates, 216–239
  substrates, 649–651
  vitreous enamel
    citric acid in, 264*f*, 266*f*
    coating resistance in, 275*f*
    color changes in, 264*f*, 273*f*
    conclusion of, 280–281
    cross-section of, 270*f*, 274*f*
    discussion of, 259–280
    emission spectra of, 263*f*, 276*f*, 278*f*, 279*f*, 280*f*
    excitation spectra in, 263*f*
    gloss change in, 264*f*, 267*f*, 272*f*
    immersion in, 264*f*, 266*f*, 267*f*
    main peak in, 276*f*, 278*f*, 279*f*, 280*f*
    materials in, 256–259
    overview of, 280–281
    potassium pyrophosphate immersion in, 267*f*, 268*f*, 269*f*, 270*f*
    procedures of, 256–259
    results of, 259–280
    roughness values of, 265*f*, 268*f*
    salt spray exposure in, 271*f*
    surface in, 262*f*, 269*f*, 271*f*, 273*f*
    trend of intensity in, 276*f*
    trend of luminescent properties in, 275–280
    trend of protective properties in, 261–275

ZRPs
low carbon steel substrates in, 203–205
materials in, 199–200
methods in, 201–205
nano-size particles in, 199, 201–203, 205–216
nanotubes in, 201–203
overview of, 199–205, 239–243
paint coatings in, 200, 203–205, 216–239
preparation of, 199, 200
results of, 205–243
steel substrates in, 216–239
synthesis in, 199–200

F

F. *See* Fluorine
Fabrication procedures
chemical deposition as, 421–423
colloidal assemblies, 423–424
other methods, 424
FBCVD. *See* Fluidized bed chemical vapor deposition
FBGs. *See* Fiber Bragg gratings
Federal Register, 68–69
Feed processes, 344–345
Fernelius, W., 114–115
Ferrara, D. W., 479–480
FESEM. *See* Field Emission Scanning Electron Microscopy
FGRP-OFBG bar. *See* Fiber glass-reinforced polymer-optical fiber Bragg gratings bar
Fiber Bragg gratings (FBGs), 605–606, 616–617
Fiber glass-reinforced polymer-optical fiber Bragg gratings (FGRP-OFBG) bar, 609–610, 610*f*
Field Emission Scanning Electron Microscopy (FESEM), 380–382
Filiform corrosion
example of, 543*f*
overview of, 543–544
Filiform corrosion test, 324*f*
Fill content, 506*t*
Film formation, 680–681
Filters, in paints and coating industry
overview of, 356–357
purification methods, 356
Flame spraying, 44
Florida, 644–647, 650. *See also* Culturally significant works
Fluidized bed chemical vapor deposition (FBCVD), 102, 102*f*
Fluorescence, scheme of, 621*f*
Fluorine (F), 466–467, 468*f*
Focused ion-assisted chemical vapor deposition (IACVD), 104–105, 104*f*
Fourier-transform infrared (FTIR) spectroscopy, 201–202, 207–208, 369, 652–654, 658–660
Fourier-transform infrared-reflection (FTIR-reflection) spectroscopy, 692
Frit, 251–252
FTIR spectroscopy. *See* Fourier-transform infrared spectroscopy
FTIR-reflection spectroscopy. *See* Fourier-transform infrared-reflection spectroscopy
Furnace test, 51

G

Galvanic corrosion
example of, 545*f*
overview of, 544–545
schematic representation of, 544*f*
seawater, 545*f*
Galvanized steel, 136. *See also* Hot-dip galvanized substrates
Galvanostatic electropolymerization, 413
García, S. J., 493, 497
Gas turbine engines
air, 33, 33*t*
alloys used in, 32–33, 32*f*
blades, 30–31, 31*f*, 32–33, 48
component lifetime, 30–31
contaminants, 33*t*
fuel, 33, 33*t*
hot corrosion of, 30–33
GCC. *See* Green coating compositions
GD OES. *See* Glow-discharge optical-emission spectroscopy
General aqueous corrosion, 679
General corrosion
example of, 540*f*
overview of, 539
schematic representation of, 539*f*
Glass fibers, 499
Glow discharge chemical vapor deposition. *See* Plasma-enhanced chemical vapor deposition
Glow-discharge optical-emission spectroscopy (GD OES), 204, 230–231
Gold (Au), 476–477, 478
Golecki, I., 116
Gonzalez, M., 417
Graphene nanocomposites, 573–574
Green chemistry, 363–364

Green coating compositions (GCC), 363–364. *See also* Smart chemistry, development of
  characterization methodology
    nanoindentation analysis, 376–379
    overview, 368–382
    spectroscopic analysis, 368–374
    surface morphology, 380–382
    thermal analysis, 374–375
  evaluation of
    laboratory experiments, 383–396
    overview of, 382–402
  overview of, 404–405
Grignard process, 118
Grinding, 338
Group IV metal coatings, 71
Growth mechanisms, nucleation and, 125–126, 125*f*
Grundmeier, G., 77
G2MT Laboratories, 63

H

[H]*1H*,*1H′*,*2H*,*2H′*-perfluorooctyl triethoxysilane (POTS). *See* Perfluorooctyl triethoxysilane
HA. *See* Hydroxyapatite
Haase, M. F., 308–309
Habel, W. R., 629–630
Hafnium, 47–48
Haglund, R., Jr., 463–464
Halloysite nanotubes, 293*f*, 298*f*
Halloysite-based containers, 320*f*, 323*f*
Halloysites, 297*f*
Hamdy, A., 25
Hanlon, T., 466
Hard anodization process, 66–67
HCl. *See* Hydrochloric acid
HDG substrates. *See* Hot-dip galvanized substrates
HDI-based self-healing anticorrosive coating. *See* Hexamethylene diisocyanate-based self-healing anticorrosive coating
Heller, D. K., 70–71
Herrasti, P., 417–418
Hexamethylene diisocyanate (HDI)-based self-healing anticorrosive coating
  accelerated salt immersion corrosion test, 509–512
  anticorrosive performance, 517–519
  capsules diameter influencing, 515*f*
  coating thickness influencing, 516*f*
  exposure time influencing, 515*f*
  formulations of, 513*t*
  healing reaction of, 512*f*
  parameters influencing, 517–519
  preparation of, 509
  salt spray test, 512–517
  scribed regions, 511*f*
  water's reaction with, 512*f*
  weight fraction of microcapsules influencing, 516*f*
Hexavalent chromium, 11
Hideki Shirakawa, 557
High performance protective coatings
  chemically intelligent
    EIS and, 651–652
    FTIR and, 652–654
    outdoor metalwork, 651
    overview of, 651–654
    performance of, 651–654
    testing of, 651–654
    weathered coated substrates characterization and, 651–652
    weathering studies of, 651
  experimental details
    for characterizing substrates, 650–651
    of coated panels, 650
    for coating substrates, 649–650
    overview, 649–651
    for weathering studies, 650
  overview of, 641–649, 669
    barrier properties, 648–649
    chemical intelligence, 643
    commonly used coatings, 643–647
    EIS, 648–649
    intelligence, 643
    material cultural heritage, 641–642, 647–648
    physical intelligence, 643
    protective films, 648–649
    weathering studies, 644–647
  physically intelligent
    AFM and, 661–664
    annealing of, 666–667
    assessment of, 668–669
    barrier properties of, 666–667
    capacitances of, 667–668
    characterizing, 654–666
    EIS, 666–667
    electrolyte swollen films, 667–668
    modified Laponite, 658–660, 661–664, 665–666
    performance testing of, 666–669
    SAXS data and, 661
    synthetic nanoclay and, 654–658
    volume fractions and, 667–668

water and, 667–668
waterborne nanocomposites coatings and, 654–657
waterborne PVDF-clay nanocomposites and, 666–667
x-ray methods for, 660–661
High temperature intelligent coatings, 30–33
High velocity oxy-fuel spraying (HVOF), 45
High-Speed Disperser (HSM), 353
High-speed mixer, 349*f*
Hinton, BRW, 70
Hollow tubes, 498, 499–500, 500*f*
Horizontal kneader, 349*f*, 352
Hot corrosion
comparison of techniques, 52*t*
definition of, 33
of gas turbine engines, 30–33
incubation period, 34–35
initiation stage, 35
mechanism of, 34–36
overview of, 33–41
oxides for resistance to, 36
propagation stage, 35–36
of superalloys, 37
types of, 34
Hot-dip galvanized (HDG) substrates, 161–173, 174–191
8-HQ. *See* 8-hydroxyquinoline
HSM. *See* High-Speed Disperser
Hu, W., 616
Humidity monitoring, 624–626, 627*t*
HVOF. *See* High velocity oxy-fuel spraying
Hybrid coatings, 21
sol-gel
overview of, 72–74
stages of, 73
titanium, protective films as, 594–595
Hybrid metamaterial devices, 473–476
Hydrochloric acid (HCl), 526–530
Hydrogen evolution, 551*t*
Hydrogen evolution rates experimental setup, 547*f*
Hydrophobic coatings, 575–580
Hydroxyapatite (HA), 594
8-hydroxyquinoline (8-HQ), 309*f*, 320*f*, 323*f*
Hysteresis loops, 468*f*, 469*f*

I

IACVD. *See* Focused ion-assisted chemical vapor deposition
ICCP system. *See* Impressed current cathodic protection system
Immersion tests, 205, 216–229
ASTM seawater, 384–387
of coupons, 383–396
overview of, 383–385
sodium sulfate solution, 384–385, 387–389
Impedance, 648–649, 651–652, 666–667
Impellers, 349*f*, 360*t*
Implants. *See* Titanium
Impressed current cathodic protection (ICCP) system, 29
advantages of, 30
overview of, 30
In situ emulsion polymerization, 315–317
In situ Fourier-transform infrared spectroscopy (*In situ* FTIR), applications of, 690–693
aqueous corrosion, 690
atmospheric corrosion, 690–691
coatings, 692–693
corrosion inhibitors, 691–692
In situ polymerization, 498, 519–522
In situ Raman spectroscopy, applications of, 680–689
aqueous corrosion, 680–682
atmospheric corrosion, 680–689
coatings, 685–689
corrosion inhibitors, 682–685
Inclined propeller, 349*f*
INCRA. *See* International Copper Research Association
Incralac, 643–647
Indirect measurements, 618*t*
Industrial sectors, 19*t*
Inert atmosphere, 375
Infrared (IR) path, 678–679
Infrared (IR) spectroscopy
cells, 678–679
IR path, 678–679
optical windows, 678–679
overview of, 676–677, 678–679
Inhibitor-loaded nanocontainers, 78
Inhibitors, 20, 297*f*, 559
Initiators, 344
Inorganic coatings, 560–561
IN 738 LC superalloy, 46*f*, 47*f*
In-situ polymerization, 24–25
Intelligence
chemical, 643
physical, 643
Intelligent coatings. *See also* Chemically intelligent coatings; High temperature intelligent coatings; Low temperature intelligent coatings; Physically intelligent coatings
benefits offered by, 20

Intelligent coatings *(Continued)*
burner rig test, 50
as commercially viable, 20
concept of, 48–55
crucible test, 51
definition of, 18–19
developed, 52–55
development of, 49, 647–648
electrochemical methods, 51, 52
furnace test, 51
for material cultural heritage, 647–648
microstructure of, 49*f*
outlook, 55–56
overview of, 18–19, 19*t*, 55–56
performance of, 52–55, 53*f*, 54*t*
techniques for assessment of, 50–52
thermogravimetric test, 51
zones, 50
Intensity, 276*f*, 278*f*, 279*f*, 280*f*
Interfacial physical phenomena, 301–310
irreversible interfacial attachment and, 307–310
L-b-L polyelectrolyte interfacial adsorption and, 305–307
Pickering emulsions and, 307–310
solvent induced interfacial precipitation and, 301–304
Interfacial polyaddition, 311–315
Interfacial polycondensation, 311–315
Interfacial polymerization, 498, 503–506
Interferometers, 606
Interferometric cavity, 606*f*
Intergranular corrosion, 546
Intergranular stress corrosion cracking (intergranular SCC), 546
International Copper Research Association (INCRA), 643–644
Interrogation principles, 604–609
Inverse emulsion, 300–301
Ion chloride, 622*f*
IR path. *See* Infrared path
IR spectroscopy. *See* Infrared spectroscopy
Iron corrosion, 491–492, 492*f*
Isocyanate monomer, 502, 503*f*

J

Jeong, S. H., 117–118
Jiang, X., 466
Jud, K., 493
Jung, I. N., 119

K

Kalck, P., 113–114
Kamalisarvestani, M., 483
Kaplan, M., 117
Katon, J. E., 557
Kawagishi, K., 48
Kendig, M., 203–204
Kilo lab, 341, 342*t*
Kim, Y., 118
Kinetics, 3–7
Kneaders, 349*f*, 352
Kumar, A., 24
Kuroda, S., 45

L

Laboratory experiments
immersion tests, 383–385
overview of, 383–396
surface appearance investigations, 385–396
Lanthanide-based conversion coatings
overview of, 69–71
properties of, 69
Laponite, 658–660, 661–664, 665–666
Larkin, D. J., 119–120
Laser oxidation, 590
Laser-induced chemical vapor deposition (LCVD), 98–99
Latex, properties of, 359*t*
Layer-by-layer (LbL) approach, 77–78
microcontainers prepared by, 305–307
nanocontainers prepared by, 305–307
polyelectrolyte interfacial adsorption, 305–307
Layered double hydroxides (LDHs)
microcontainers on basis of, 291–292
nanocontainers on basis of, 291–292
LbL approach. *See* Layer-by-layer approach
LCVD. *See* Laser-induced chemical vapor deposition
LDHs. *See* Layered double hydroxides
Leaves, 575–580
Lee, J. Y., 562–563
LEOFS. *See* Long-distance embedded optical fiber sensor
Leon-Silva, U., 419
Li, Y., 483
Liquid core, 309*f*
Liquid delivery systems, effect of solvent, 122–124
Liu, H., 422–423
Lomova, M. V., 307
Long period grating pair (LPGP), 621
Long-afterglow phosphors, 255
Long-distance embedded optical fiber sensor (LEOFS), 611
Low carbon steel substrates, 203–205
Low temperature intelligent coatings
categorizing, 20–21
overview of, 20–22

LPGP. *See* Long period grating pair
Luminescent effect, 257*t*, 270–271
Luminescent materials, properties of, 255
Luna Innovations, 24

M

MacDiarmid, A. G., 74, 563
Magnesium alloys
  overview, 537
  SCC mechanisms, 545–546
  types, 538
Magnesium corrosion, common forms of
  corrosion fatigue as, 546
  crevice corrosion as, 541–543
  filiform corrosion as, 543–544
  galvanic corrosion as, 544–545
  general corrosion as, 539
  intergranular corrosion as, 546
  overview of, 538–546
  pitting corrosion as, 540–541
  SCC as, 545–546
Main peak, 276*f*, 278*f*, 279*f*, 280*f*
Material cultural heritage, 641–642, 647–648. *See also* Culturally significant works
Maximum contrast, 481*f*
MBT. *See* Mercaptobenzothiazole
MCrAlY coatings. *See* Overlay coatings
MeBT. *See* Methylbenzothiazole
Mengoli, G., 74
Mercaptobenzothiazole (MBT), 297*f*, 313*f*
Mesoporous microparticles, 293*f*, 298*f*
Mesoporous nanoparticles, 293*f*
Metallic coatings, 12–13, 560–561
Metallic sacrificial layers, 612–617
Metalorganic chemical vapor deposition (MOCVD)
  ALD, 102–104, 103*f*
  EBCVD, 101, 101*f*
  FBCVD, 99*f*, 102
  IACVD, 104–105, 104*f*
  LCVD, 98–99, 98*f*
  overview of, 96–105, 97*f*
  PECVD, 99–100, 99*f*, 100*f*
  techniques, 96–105
  UVCVD, 99, 99*f*
Metal-organic precursors, 94–95
Metalorganics, 96–97
Metals
  active dissolution of, 4*f*
  corrosion of
    costs of, 62–63
    definition of, 60–62
    overview of, 59–64, 79
    preventing, 62–63
  passive dissolution of, 5*f*
Metalwork, 651
Metamaterial devices, 473–476
Methylbenzothiazole (MeBT), 316*f*
Microbial growths, 20
Microcapsules. *See also* Microencapsulation
  average diameter of, 509*f*
  diisocyanate-based one-part self-healing anticorrosive coating
    chemical constituent of, 506–507
    core fraction of, 508–509
    diameter of, 507–508
    fill content of, 506*t*
    morphology of, 507–508
    MRT of, 506*t*
    thermal property of, 508–509
  organic silane-based one-part self-healing anticorrosive coating
    accelerated salt immersion corrosion test of, 525–526
    chemical constituent of, 522
    core fraction of, 524–525
    corrosion protection performance of, 526–530
    corrosion retardant effect schematic diagram of, 530*f*
    diameter of, 522–524
    HCl solution and, 526–530
    morphology of, 522–524
    POTS-based self-healing anticorrosive coating with, 525
    thermal property of, 524–525
  polymers incorporated in, 23*f*
  scratched coating of, 517–519, 518*f*
  shell structure of, 508*f*
  shell thickness of, 509*f*
  spherical shaped, 508*f*
  TGA curve, 510*f*
  weight fraction of, 516*f*
Microcontainers
  active agents released from, 318–321
  assembly steps, 298*f*
  with ceramic core, 292–297, 297*f*, 298–300
  core, 311*f*
  with corrosion inhibitor, 315*f*, 316*f*
  with DCOIT, 323*f*
  on direct emulsion basis, 300–301
  distribution of, 321–322
  with 8-HQ, 309*f*
  emulsion polymerization and, 315–317
  interfacial physical phenomena, based on, 301–310
    on irreversible interfacial attachment basis, 307–310

Microcontainers *(Continued)*
L-b-L polyelectrolyte interfacial adsorption, 305–307
solvent induced interfacial precipitation, 301–304
on inverse emulsion basis, 300–301
on LDHs basis, 291–292
with liquid core, 309*f*
multilayered nanoparticulate shells of, 309*f*
with nanoparticle shells, 311*f*
in novel protective coating matrices, 321–322
organic self-protecting coatings based on, 322–325
overview of, 325–327
Pickering emulsion formation, 307–310
with polyelectrolyte shell, 292–297
polyepoxy, 316*f*
with polymeric shell, 292–297
with polystyrene shells, 304*f*
pores endings, 298–300
preparation
by bulk reactions, 311–317
by chemical reactions, 311–317
emulsion, based on, 302*f*
emulsion droplets, 311–317
via interfacial polyaddition, 311–315
via interfacial polycondensation, 311–315
by interfacial reactions, 311–317
methods, 291–317, 302*f*
through *in situ* emulsion polymerization, 315–317
steps, 298*f*
protective organic coatings approach, 287–291, 326*f*
PU, 323*f*
release kinetics, 320*f*
SEM images of, 312*f*, 318*f*
shell, 311*f*
with stimuli-responsive stoppers, 298–300
types of, 291–317
Microencapsulation, 494–498, 495*f*, 496*f*, 497*f*, 499–500, 499*f*, 503–506, 519–522
Microparticles
mesoporous, 293*f*, 298*f*
silica, 293*f*
cerium nitrate with, 297*f*
sodium hexafluorotitanate with, 297*f*
Microscopy
Atomic Force, 382, 423*f*, 661–664
Field Emission Scanning Electron, 380–382
Transmission Electron, 382
Microvascular-based self-healing system, 500, 501, 501*f*
Microwave switch design, 482*f*
Mills, 353–355
Minimum reaction time (MRT), 506*t*
Miscellaneous-based conversion coatings, 71–72
Mixers
high-speed, 349*f*
types of, 348
overview of, 338
TSD, 352–353
uses of, 347
Mixing engineering parameters, 360*t*
Mo. *See* Molybdenum
Mo dopant, 466, 468*f*
MOCVD. *See* Metalorganic chemical vapor deposition
Modified alkyd coatings, 318*f*
Modified Laponite, 658–660, 661–664, 665–666
Molybdates, 71
Molybdenum (Mo)
dopant, 466, 468*f*
precursors, 112–114
sol-gel VO_2 and, 466
Monomers, 343, 344
Montemor, M. E., 187, 190
Montemor, M. F., 70, 179–180
Mookhoek, S. D., 517
Morin, F., 461
Mott-Hubbard model, 464
Mrad, M., 417–418
MRT. *See* Minimum reaction time
Multifiber optode, 631–632, 632*f*
Multilayered nanoparticulate shells, 309*f*
Multiple fiber optode, 628–630, 629*f*
Multiple vane stirrer, 349*f*
Multiwalled carbon nanotube (MWCNT) coatings, 27, 28*f*

N

NACE. *See* National Association of Corrosion Engineers
NaCl. *See* Sodium chloride
Nag, J., 463–464
Nametkin, N. S., 119–120
Nanoclays, 654–664
Nanocomposite coatings
EAP-based, 567–580
clay, 569–571
graphene, 573–574
silicate nanolayer, 569–571

SiO_2, 571–573
TiO_2, 571–573
nanoparticle, 571–573
synthetic nanoclay in, 654–657
waterborne, 654–657
Nanocontainers, 78
active agents released from, 318–321
assembly steps, 298*f*
with ceramic core, 292–297, 297*f*, 298–300
with corrosion inhibitor, 313*f*, 315*f*, 316*f*
on direct emulsion basis, 300–301
distribution of, 321–322
with 8-HQ, 309*f*
emulsion polymerization and, 315–317
halloysite-based, 323*f*
interfacial physical phenomena, based on, 301–310
on irreversible interfacial attachment basis, 307–310
L-b-L polyelectrolyte interfacial adsorption, 305–307
solvent induced interfacial precipitation, 301–304
on inverse emulsion basis, 300–301
on LDHs basis, 291–292
with liquid core, 309*f*
with MBT, 313*f*
multilayered nanoparticulate shells of, 309*f*
in novel protective coating matrices, 321–322
organic self-protecting coatings based on, 322–325
overview of, 325–327
Pickering emulsion formation, 307–310
with polyelectrolyte shell, 292–297
polyepoxy, 316*f*
with polymeric shell, 292–297
with polystyrene shells, 304*f*
pores endings, 298–300
preparation
by bulk reactions, 311–317
by chemical reactions, 311–317
emulsion, based on, 302*f*
emulsion droplets, 311–317
via interfacial polyaddition, 311–315
via interfacial polycondensation, 311–315
by interfacial reactions, 311–317
methods, 291–317, 302*f*
through *in situ* emulsion polymerization, 315–317
steps, 298*f*
protective organic coatings approach, 287–291, 326*f*
release kinetics, 320*f*
SEM micrographs of, 318*f*
with silica shell, 313*f*
with stimuli-responsive stoppers, 298–300
types of, 291–317
Nanocrystalline cobalt, 27, 27*f*, 28*f*
Nanoindentation analysis
adhesion estimation, 378–379
hardness estimation, 376–378
modulus estimation, 376–378
nanoscratch, 378–379
wear analysis, 379
Nanoparticles, 152–160, 174–191
Au-, 478
mesoporous, 293*f*
nanocomposites, 571–573
shells, 311*f*
SHS, 293*f*
SMS, 293*f*
VO_2-Au composite, 476–477
in ZRPs
composition, 199*t*
cyclic voltammetry, 201, 205–207
elemental analysis, 201
FTIR spectroscopy, 201–202, 207–208
investigation, 205–216
preparation, 199
rheology, 202–203, 203*t*, 211–216
TEM, 202, 208–211
Nanoparticulate shells, 309*f*
Nanoscratch, 378–379
Nano-size additives. *See* Nanoparticles
Nanostructured materials engineering, 25–26
Nanotubes
halloysite, 293*f*
in ZRPs
electrokinetic potential, 201
experiment, 201–203
Natesan, K., 35–36
National Association of Corrosion Engineers (NACE), 63, 538–539
National economies, 63–64, 63*t*
National Institute for Occupational Safety and Health (NIOSH), 68–69
Natural passivity, 25–26
Naval Air Warfare Center Weapons Division, 75
Nickel-based superalloys, 32–33, 32*f*, 48
NiCoCrAlY coating, 52–55
NIOSH. *See* National Institute for Occupational Safety and Health
NMR spectroscopy. *See* Nuclear magnetic resonance spectroscopy

Nonmetallic-inorganic pretreatment coatings
conversion coatings
cerium-based, 70–71
chromate, 67–69
lanthanide-based, 69–71
miscellaneous-based, 71–72
overview of, 67–72
phosphate, 69
overview of, 66–72
Nonoxide ceramics
Al, 112–114
Mo, 112–114
overview of, 112–121
Pt, 112–114
SiC, 116–121
TiCN, 114–115, 114*f*
W, 112–114
ZrCN, 114–115, 114*f*
Normal Raman spectroscopy, 677
Novel protective coatings, 321–322, 326*f*
N-type semiconductor coatings, 13–14
Nuclear magnetic resonance (NMR) spectroscopy, 371
Nucleation, growth mechanisms and, 125–126, 125*f*
Nylon 6,6, 437, 437*f*, 438–442, 443–444, 444*f*

O

Occupational Safety and Health Administration (OSHA), 68–69
OFSs. *See* Optical fiber sensors
OHM. *See* Overhead mixture
OMCVD. *See* Organometallic chemical vapor deposition
One-part self-healing anticorrosive coatings
design strategies of
conventional self-healing materials, 494–501
overview of, 494–502
preparation, 494–501
examples of
diisocyanate-based, 503–519
organic silane-based, 519–530
overview of, 491–494, 530–532
perspectives, 530–532
remarks, 530–532
Online survey, 645*f*
Optical fiber sensors (OFSs)
characteristics of, 613*t*, 618*t*, 627*t*
for corrosion by-product detection, 618*f*, 625*t*
for corrosion precursor detection, 618*f*, 625*t*
for corrosion sensing, 613*t*, 618*t*
direct measurements and, 613*t*
evanescent field pH, 608*f*
humidity detection, based on, 627*t*
indirect measurements and, 618*t*
interrogation principles
distributed sensing, 607
FBGs, 605–606
interferometers, 606
optical intensity modulations, 607–608
overview, 604–609
SPRs, 608–609
overview, 604, 632–633
sample chamber location, 628*f*
steel corrosion, 615*f*
summary, 613*t*, 618*t*, 627*t*
Optical hysteresis loops, 469*f*
Optical intensity modulations, 607–608
Optical pH sensors, 626–632
Optical time domain reflectometry (OTDR), 607, 611, 615*f*
Optical windows, 678–679
Oregon, 644–647
Organic coatings, 410–411, 561–562
Organic pretreatment coatings
biofilms as, 78–79
conductive polymer, 74–75
controlled release coatings as, 78
hybrid sol-gel
overview of, 72–74
stages of, 73
inhibitor-loaded nanocontainers and, 78
overview of, 72–79
polyelectrolyte multilayer films as, 77–78, 77*f*
self-assembling, 76–77, 76*f*
Organic silane, 502, 503*f*
Organic silane-based one-part self-healing anticorrosive coating
microcapsules
accelerated salt immersion corrosion test, 525–526
chemical constituent, 522
core fraction, 524–525
corrosion protection performance, 526–530
corrosion retardant effect schematic diagram, 530*f*
diameter, 522–524
in HCl solution, 526–530
morphology, 522–524
in POTS-based self-healing anticorrosive coating, 525
thermal property, 524–525
microencapsulation and, 519–522

perfluorooctyl triethoxysilane and, 519–522
in situ polymerization and, 519–522
Organometallic chemical vapor deposition (OMCVD), 96–97, 99
Organometallic precursors
bulk synthesis, 105–121, 105*f*
chemistry, 124–125
nonoxide ceramics
Al, 112–114
Mo, 112–114
overview of, 112–121
Pt, 112–114
SiC, 116–121
TiCN, 114–115, 114*f*
W, 112–114
ZrCN, 114–115, 114*f*
oxide ceramics
alumina, 106–107
overview of, 106–112
silica, 107–112
titania, 107–112
zirconia, 107–112
Organometallics, 96–97
Orlianges, J. C., 476–477
OSHA. *See* Occupational Safety and Health Administration
OTDR. *See* Optical time domain reflectometry
Outdoor experiments, 396–402
Outdoor metalwork, 651
Overhead Mixture (OHM), 353
Overlay coatings
aluminum influencing, 42–43, 43*f*
major elements influencing, 47–48
overview of, 42–44
trace elements influencing, 47–48
Oxidation, 414
Oxide ceramics
alumina, 106–107
overview of, 106–112
silica, 107–112
titania, 107–112
zirconia, 107–112
Oxide film, 25–26
Oxides, 36, 592–593

P

Paddle propeller, 349*f*
Paddle stirrers, 349*f*, 352
Paint and coating pilot plant
general checkpoints for, 357, 357*t*
general safety precautions in, 357, 357*t*
Paint coatings
steel structures protected by, 28–29
in ZRPs
characterization, 203–205
composition, 200*t*
electrochemical impedance spectroscopy, 203–204
GD OES, 230–231
glow-discharge optical-emission spectroscopy, 204, 230–231
immersion test, 216–229
preparation, 200
salt-spray chamber test, 237–239
XPS, 232–237
x-ray photoelectron spectroscopy, 205
Paint/resin-blended coatings, 412
Paints
definition of, 336
general process for
overview of, 338–340
sand mill route, 338–340
thinning in, 339–340
Paints and coating industry, major equipment used in
filters as, 356–357
mills as, 353–355
mixers as, 347–353
overview of, 347–357
propellers as, 349*f*
PANI. *See* Polyaniline
Passive films, 25
PC. *See* Phosphorylcholine chloride tetrahydrate, FTIR spectra of
PE multilayer films. *See* Polyelectrolyte multilayer films
PECVD. *See* Plasma-enhanced chemical vapor deposition
Peierls model, 464
Perfluorooctyl triethoxysilane, 519–522. *See also* POTS-based self-healing anticorrosive coating
pH multiple fiber optode, 629–630, 629*f*
pH sensing, 607–608, 608*f*, 626–632
Phase transition, of vanadium dioxide
doping effects, 466–471
switching time, 464–465
Phosphate conversion coatings
overview of, 69
types of, 69
Phosphate-permanganate conversion coatings, 71
Phosphorylcholine chloride tetrahydrate (PC), FTIR spectra of, 659*f*
Physical intelligence, 643
Physical vapor deposition (PVD), 94–95

Physically intelligent coatings
AFM, 661–664
annealing, 666–667
assessment, 668–669
barrier properties, 666–667
capacitances, 667–668
characterizing, 654–666
EIS, 666–667
electrolyte swollen films, 667–668
modified Laponite, 658–660, 661–664, 665–666
performance testing of, 666–669
SAXS data, 661
synthetic nanoclay, 654–658
volume fractions, 667–668
water, 667–668
waterborne nanocomposites coatings, 654–657
waterborne PVDF-clay nanocomposites, 666–667
x-ray methods, 660–661
Physiological solutions, 597*t*
Pickering emulsions, 307–310
Pigments
definition of, 336
overview of, 336
properties of, 336
Pilot plants
acrylic latex
agitation system in, 359*t*
charging process in, 358
impeller selection for, 360*t*
mixing engineering parameters in, 360*t*
setup of, 359
aqueous emulsion based
buffers in, 344
components involved in, 343–346
emulsifiers in, 344
emulsion feed process in, 344
emulsion stabilizers in, 343
initiators in, 344
monomers in, 343, 344
water in, 344
for aqueous lattices, 346*f*
definition of, 340
kilo lab as different from, 341, 342*t*
layouts, 342, 342*f*
major issues, 342, 342*f*
overview of, 335–336, 340–347, 360
paint and coating
general checkpoints for, 357, 357*t*
general safety precautions in, 357
pilot reactor in, 357*t*
polymer emulsion, equipment in, 345
process equipment
overview, 342–343
support units, 342–343
for solvent-based polymers, 348*f*
solvent-based resin, 346–347
step by step scaling up
general steps involved in, 341
overview of, 340–341
reactors in, 340–341
types of, 343–347
uses of, 340
Pilot reactor, 357*t*
Pilot scale production, 335–336
Pipelines, 28–29
Pitting corrosion, 6*f*
example of, 541*f*
overview of, 540–541
schematic representation of, 540*f*
Plant technology, 21, 22*f*
Plasma electrolytic oxidation, 591
Plasma-enhanced chemical vapor deposition (PECVD), 99–100, 100*f*
Plasmonic devices, 476–481
Platinum (Pt)
in aluminide coatings, 42
precursors, 112–114
Pliny the Elder, 643–644
Pohl, H. A., 557
Poly(2,5-bis(*N*-methyl-*N*-hexylamino)phenylene vinylene) (BAM-PPV), 75, 75*f*
Polyamides, 435, 438–442
Polyaniline (PANI), 415–417
Polyelectrolyte interfacial adsorption, 305–307
Polyelectrolyte (PE) multilayer films, 77–78, 77*f*
Polyelectrolyte shell, 292–297, 320*f*
Polyepoxy microcontainers, 316*f*
Polyepoxy nanocontainers, 316*f*
Poly(melamine-formaldehyde) (PMF) microcapsules, 497
Polymer coatings
EAP-based
nanocomposite, 567–580
overview of, 563–580
in situ Raman spectroscopy, 686–689
electronically conducting, 687–689
epoxy coating, 686
overview of, 562–580
Polymer emulsion pilot plants, equipment in, 345
Polymeric shell, 292–297
Polymers
microcapsules incorporated in, 23*f*
self-healing coatings and, 23*f*
Polypyrrole, 417–418

Polystyrene shells, 304*f*
Polythiophene, 419
Poly(urea-formaldehyde) (PUF) microcapsules, 495–498, 497*f*. *See also* Perfluorooctyl triethoxysilane
Polyurethane (PU) microcapsules, 494, 495, 497–498, 504*f*, 505*f*, 508*f*
Polyurethane shells, 320*f*
Polyurethane-poly(urea formaldehyde) (PU-PUF) microcapsules, 498
Polyvinylidene fluoride (PVDF), 643
Porcelain enamel, 251–252. *See also* Vitreous enamel
Pores endings, 298–300
Porous nonprotective coatings, 549*f*
Portland, Oregon, 644–647
Potassium pyrophosphate, 267*f*, 268*f*, 269*f*, 270*f*
Potassium-permanganate conversion coatings, 71
Potentiodynamic electropolymerization, 413
Potentiostatic electropolymerization, 413
POTS. *See* Perfluorooctyl triethoxysilane
POTS-based self-healing anticorrosive coating
  accelerated salt immersion corrosion test, 525–526
  corrosion protection performance, 526–530
  EDX analysis of, 529*f*
  in HCl solution, 526–530
  preparation of, 525
  scribed regions of, 527*f*
PRC electrodeposition. *See* Pulse reverse current electrodeposition
Precursors
  alumina
    Al-acetylacetonate, 107
    aluminum isopropoxide, 106
    overview of, 106–107
  aluminum, 112–114
  coating, 369
    Raman spectroscopy of, 369–370
  corrosion, 617–624
    detection of, 619–621
    measurements of, 617–624
    OFSs for detection of, 618*f*
    optical fiber technology for, 618*f*, 625*t*
  CVD
    silica precursors, 110–112
    yttria precursors, 110–112
    zirconia precursors, 110–112
  metal-organic, 94–95
  molybdenum, 112–114
  organometallic
    Al nonoxide ceramics, 112–114
    alumina oxide ceramics, 106–107
    bulk synthesis, 105–121, 105*f*
    chemistry, 124–125
    Mo nonoxide ceramics, 112–114
    overview of nonoxide ceramics, 112–121
    overview of oxide ceramics, 106–112
    Pt nonoxide ceramics, 112–114
    SiC nonoxide ceramics, 116–121
    silica oxide ceramics, 107–112
    TiCN nonoxide ceramics, 114–115, 114*f*
    titania oxide ceramics, 107–112
    W nonoxide ceramics, 112–114
    zirconia oxide ceramics, 107–112
    ZrCN nonoxide ceramics, 114–115, 114*f*
  platinum, 112–114
  SiC, 122*f*
    applications of, 117*t*
    comparison of, 123*t*
    conventional, 117*t*
    overview of, 116–121
  silica
    CVD precursors as, 110–112
    overview of, 107–112
    sol-gel as, 109
  TiCN, 114–115, 114*f*
  titania
    overview of, 107–112
    sol-gel as, 108–109
  tungsten, 112–114
  yttria, 110–112
  zirconia
    CVD precursors as, 110–112
    overview of, 107–112
    sol-gel as, 109–110
  ZrCN, 114–115, 114*f*
Preferential oxidation, 414
Pretreatment coatings. *See also* Nonmetallic-inorganic pretreatment coatings
  alloy selected for, 64–65, 65*f*
  biofilms as, 78–79
  organic
    biofilms as, 78–79
    conductive polymer, 74–75
    controlled release coatings as, 78
    hybrid sol-gel, 72–74
    inhibitor-loaded nanocontainers and, 78
    overview of, 72–79
    polyelectrolyte multilayer films as, 77–78, 77*f*
    self-assembling, 76–77, 76*f*
  overview of, 64–66
  surface modification, 65–66
  TCP, 71–72

Propellers
axial flow, 349*f*, 350–351
inclined, 349*f*
paddle, 349*f*
radial flow, 349*f*, 352
turbine, 349*f*
Protective biofilms. *See* Protective films
Protective coatings. *See also* High performance protective coatings
culturally significant works, 641–642
for material cultural heritage conservation, 641–642
Protective films
barrier properties of, 648–649
titanium
ceramic coatings, 595–596
composites as, 594
HA as, 594
hybrid coatings, 594–595
overview of, 592–596
oxides as, 592–593
Protective organic coatings. *See also* Novel protective coatings
microcontainers-based approach to, 287–291, 326*f*
nanocontainers-based approach to, 287–291, 326*f*
self-healing and, 287–291
self-protecting and, 287–291
Pt. *See* Platinum
PU microcapsules. *See* Polyurethane microcapsules
PUF microcapsules. *See* Poly(urea-formaldehyde) microcapsules
Pulse reverse current (PRC) electrodeposition, 27
PU-PUF microcapsules. *See* Polyurethane-poly(urea formaldehyde) microcapsules
PU-UF microcapsules. *See* Polyurethane-poly(urea formaldehyde) microcapsules
PVD. *See* Physical vapor deposition
PVDF. *See* Polyvinylidene fluoride

Q

Qiu, R., 422–423
Qu, M., 426
Quasiceramic coatings, 21

R

Radhakrishnan, S., 417
Radial flow propellers, 349*f*, 352
Raman, V. C., 674
Raman optical time domain reflectometry (ROTDR), 607
Raman spectroscopy. *See also In situ* Raman spectroscopy
of coatings precursor, 369–370
of cured coatings, 369–370
normal, 677
overview of, 674–676, 677–678
surface-enhanced, 678
Rao, A., 424
Rapp, R. A., 35–36
Ratio of elements, 234*t*, 236*t*
Rawlins, J., 503–504
Raytheon, 470–471
REACH regulations. *See* Registration, Evaluation, Authorization and Restriction of Chemicals regulations
Reactors, 340–341
Rebar concrete, 435–442
Reflection, 615*f*
Registration, Evaluation, Authorization and Restriction of Chemicals (REACH) regulations, 68–69, 363–364
Reinforced concrete damage prevention, 609–612, 629–630, 630*f*
Relative humidity monitoring, 624–626, 627*t*
Relative intensities, 230*f*
Release kinetics, 320*f*
Rene 80 superalloy, 37, 38*f*
Resins
definition of, 336
overview of, 336
Rheology, 202–203, 203*t*, 211–216
Ritter, J. J., 561–562
Rodriguez, M. J., 561–562
Roller mills, 353*f*
ROTDR. *See* Raman optical time domain reflectometry
Roughness values, 265*f*, 268*f*
Rule, J., 517
Rust, 60

S

SA pretreatment coatings. *See* Self-assembling pretreatment coatings
Sacrificial anodes
advantages of, 29–30
disadvantages of, 30
overview of, 29–30
Sacrificial metallic coatings, 12–13
Sakhri, A., 415
Saliva, 597*t*
Salt coated test, 51
Salt spray exposure, 271*f*
Salt spray test, 512–517

Salt-spray chamber tests, 205, 237–239
Samadzadeh, M., 493, 494–495
Sand Mill (SM), 354–355
Sand mill route, 338–340
Sauvant-Moynot, V., 493
Savings, 18
SAXS. *See* X-ray scattering
Scanning vibrating electrode technique (SVET), 318*f*
SCC. *See* Stress corrosion cracking
Schem, M., 187
Scratched blank, 318*f*
Scully, J. R., 70–71
Seawater, 384–387
Self-assembling (SA) pretreatment coatings, 76–77, 76*f*
Self-healing, 287–291, 414–415
  microvascular-based, 500, 501, 501*f*
  properties, 152–160
  stannate coatings' functionality of, 553
Self-healing coatings. *See also* Diisocyanate-based one-part self-healing anticorrosive coating; Organic silane-based one-part self-healing anticorrosive coating; Protective organic coatings
  compact protective, 550*f*, 551*f*
  encapsulation for, 22–29
  formation of, 550*f*, 551*f*
  HDI-based
    accelerated salt immersion corrosion test of, 509–512
    anticorrosive performance of, 517–519
    capsules diameter influencing, 515*f*
    coating thickness influencing, 516*f*
    exposure time influencing, 515*f*
    formulations of, 513*t*
    healing reaction of, 512*f*
    parameters influencing, 517–519
    preparation of, 509
    salt spray test of, 512–517
    scribed regions of, 511*f*
    water's reaction with, 512*f*
    weight fraction of microcapsules influencing, 516*f*
  one-part
    design strategies of, 494–502
    examples of, 503–530
    overview of, 491–494, 530–532
    perspectives on, 530–532
    remarks on, 530–532
  polymer and, 23*f*
  polymers and, 23*f*
  POTS-based
    accelerated salt immersion corrosion test of, 525–526
    corrosion protection performance of, 526–530
    EDX analysis of, 529*f*
    HCl solution and, 526–530
    preparation of, 525
    scribed regions of, 527*f*
  vanadate, 26*f*
Self-protecting, 287–291
Self-protecting coatings
  container-based, 322–325
  organic, 322–325
  protective performance of, 322–325
Semiconductor-to-metallic phase transition (SMT), 461, 462, 464–465, 469–470, 471–472, 473–474, 475, 477, 479–480, 481
Separation, 338
SERS. *See* Surface-enhanced Raman spectroscopy
SHCs. *See* Silane hybrid coatings
Shell microcontainers, 311*f*
Shen, Q., 120–121
Ship hulls, 28–29
SHM. *See* Structural health monitoring
SHS containers. *See* Spherical hollow silica containers
SHS nanoparticles. *See* Spherical hollow silica nanoparticles
SiC precursors, 122*f*
  applications of, 117*t*
  comparison of, 123*t*
  conventional, 117*t*
  overview of, 116–121
Silane coatings
  cerium salt and, 174–191
  corrosion inhibition by, 174–191
  evaluation of, 174–191
  on HDG substrates, 174–191
  with nanoparticles, 174–191
  outlook, 192
  overview of, 135–137, 192
Silane hybrid coatings (SHCs), 136–137
  BPA influencing, 139–152
  cerium concentration influencing, 161–173
  cerium ions influencing, 139–152
  cerium nitrate, 152–160
  cerium oxide, 152–160
  corrosion protection of, 139–152, 161–173
  electrochemical assessment, 152–160
  experimental procedure
    analytical methods, 138–139
    composition of, 138*t*

Silane hybrid coatings (SHCs) *(Continued)*
overview of, 137–139
sample preparation, 137–138
on HDG substrates, 161–173
microstructural features of, 161–173
nanoparticles, 152–160
outlook, 192
overview of, 192
self-healing properties of, 152–160
on 304L stainless steel, 139–160
Silica microparticles, 293*f*, 297*f*
Silica (SiO_2) nanocomposites, 571–573
Silica precursors
CVD precursors as, 110–112
overview of, 107–112
sol-gel as, 109
Silica shell, 313*f*
Silica submicroparticles, 293*f*
Silicate nanolayer nanocomposites, 569–571
Silicon, 47–48
Simulated physiological solutions, 597*t*
Single crystal airfoils, 37
SiO_2. *See* Silica
Skin, 23–24, 501*f*
SM. *See* Sand Mill
Smart chemistry, development of, 364–367
Smart coatings
designing, 64
electrospun, 442–447
overview of, 431–434, 454, 484
rebar concrete application
overview of, 435–442
polymer selection, 438–442
vanadium dioxide
atomic oxygen irradiation influencing, 466
crystalline structure of, 462*f*
doping effects on, 466–471
infrared transmittance during, 462*f*
overview of, 461–471
phase transition of, 464–465, 466–471
properties of, 461–471
switching time of, 464–465
synthesis methods, 463–464
valence band diagrams, 463*f*
Smart green conversion coatings, sol-gel route for development of, 363–364. *See also* Green coating compositions (GCC); Smart chemistry, development of
Smart windows, 483
SMS nanoparticles. *See* Spherical mesoporous silica nanoparticles
SMT. *See* Semiconductor-to-metallic phase transition
Sodium chloride (NaCl), 552*f*
Sodium hexafluorotitanate, 297*f*
Sodium sulfate, 36*f*, 384–385, 387–389
Sol-gel, 72–74. *See also* Smart chemistry
for corrosion control
corrosion applications, 450–453
overview, 447–453
PANI and, 416*f*
scribed aluminum substrate coated with, 416*f*
as silica precursor, 109
for smart green conversion coatings, 363–364, 404–405
as titania precursor, 108–109
VO_2, 466
as zirconia precursor, 109–110
Sol-gel method, titanium
dip-coating, 588–589
overview of, 587–589
spin-coating, 589
Solid green coating composition (solid GCC), 375
Soltani, M., 469, 471–472, 473
Solution stirring, 6*f*
Solvent induced interfacial precipitation, 301–304
Solvent-based polymer pilot plant, 348*f*
Solvent-based polymeric binders, 343–347
Solvent-based resin pilot plants, 346–347
Solvents
applications of, 337
definition of, 337
overview of, 337
Song, L., 467
South Florida, 644–647, 650. *See also* Culturally significant works
Spectroscopic techniques. *See also In situ* Fourier-transform infrared spectroscopy; *In situ* Raman spectroscopy
equipment for, 677–679
ATR, 679
IR spectroscopy, 678–679
Raman spectroscopy, 677–678
GCC
FTIR analysis as, 369
NMR analysis as, 371
overview of, 368–374
Raman analysis as, 369–370
XPS analysis as, 371–374
methods as, 677–679
ATR, 679
IR spectroscopy, 678–679
Raman spectroscopy, 677–678
overview of, 673–674, 694

principles as, 674–677
IR spectroscopy, 676–677
Raman spectroscopy, 674–676
Spherical hollow silica (SHS) containers, 320*f*
Spherical hollow silica (SHS) nanoparticles, 293*f*
Spherical mesoporous silica (SMS) nanoparticles, 293*f*
Spin-coating
overview of, 589
schematics of, 589*f*
spiro[1H-isoindole-1,9-[9H]xanthen]-3(2H)-one, 3,6-bis(diethylamino)-2-[(1-methylethylidene)amino](FDI), 27–28
SPRs. *See* Surface plasmon resonances
Stabilization, 338
Standard anodization process, 66–67
Stannate conversion coatings
mitigation of corrosion using
acidic pickling surface modification in, 549*f*, 551*f*
alkaline etching surface modification in, 550*f*, 551*f*
compact protective coatings formation in, 550*f*, 551*f*
corrosion rates in, 552*t*
hydrogen evolution in, 551*t*
localized corrosion in, 549*f*
NaCl solution in, 552*f*
overview of, 547–553
performance in, 548–553
porous nonprotective coatings formation in, 549*f*
potentiodynamic in, 552*f*
self-healing coatings formation in, 550*f*, 551*f*
self-healing functionality in, 553
synthesis in, 547–548
testing in, 547–548
overview of, 553–554
remarks on, 553–554
Steckl, A. J., 116, 119
Steel corrosion sensors, 615*f*
Steel panel, 511*f*
Steel structures, 24, 28–29. *See also* Cathodic protection
Steel substrates, in ZRPs
EIS monitoring, 216–229
experiment, 216–239
GD OES, 230–231
immersion test, 216–229
investigation, 216–239
salt-spray chamber test, 237–239
XPS, 232–237
Stephenson, L. D., 24
Stern-Volmer equation, 620
Stimuli-responsive, 291, 298–300
Strain measurements, 605*f*
Stress corrosion cracking (SCC)
corrosion fatigue, 546
intergranular, 546
magnesium alloy mechanisms, 545–546
overview of, 545–546
transgranular, 546
types of, 546
Stressed aluminum-coated optical fiber corrosion sensor, 611, 612*f*
Structural health monitoring (SHM), 603–604
Styrene butylacrylate latex, 358*t*
Submicroparticles
aluminum modified, 293*f*
silica, 293*f*
Substance of very high concern (SVHC), 68–69
Substrates, 23–24. *See also* Steel substrates
characterizing, 650–652
culturally significant works, 649–650
experimental details for, 649–651
high performance protective coating, 649–650
weathered coated, 651–652
in ZRPs
EIS monitoring, 216–229
experiment, 216–239
GD OES, 230–231
immersion test, 216–229
investigation, 216–239
salt-spray chamber test, 237–239
XPS, 232–237
Sukhorukov, G. B., 307
Sulfate transport mechanism, 68–69
Super D-Gun. *See* Detonation gun spraying
Superalloys, 32–33, 32*f*
chemical composition of, 39*t*
Cr content influencing, 41
hot corrosion of, 37
nickel-based, 32–33, 32*f*, 48
under type-I corrosion conditions, 37, 38*f*, 39*f*
under type-II corrosion conditions, 38*f*
Superhydrophobic coatings
as anticorrosion coating
fabrication procedures, 421–424
overview, 419–424
theoretical background, 419–420
EAP-based, 575–580
zinc coated with, 422*f*
Superhydrophobic conducting polymers, as anticorrosion coatings, 424–427

Surface coating technologies
  diffusion coatings as, 42
  engineering techniques, 44–45
  overlay coatings as, 42–44
  overview of, 41–45
Surface engineering techniques
  EB-PVD processes as, 45
  overview of, 44–45
  preparation of, 49–50
  selection of, 49–50
  thermal spraying processes as, 44–45
Surface modification
  anodic oxidation for, 590–591
  combined methods, 592
  electrolytic deposition for, 591–592
  laser oxidation for, 590
  plasma electrolytic oxidation for, 591
  pretreatment coating, 65–66
  sol-gel method for
    dip-coating, 588–589
    overview of, 587–589
    spin-coating, 589
  titanium
    anodic oxidation, 590–591
    combined methods for, 592
    electrolytic deposition, 591–592
    laser oxidation, 590
    overview of, 587
    plasma electrolytic oxidation, 591
    sol-gel method for, 587–589
Surface morphology
  with AFM, 382
  with FESEM, 380–382
  overview of, 380–382
  with TEM, 382
Surface plasmon resonances (SPRs)
  basic structure of optical fiber sensor for, 609*f*
  metal corrosion detected by, 616, 616*f*
  overview of, 608–609
Surface-enhanced Raman spectroscopy (SERS), 678
Survey, 645*f*
Suryanarayana, C., 493, 497
SVET. *See* Scanning vibrating electrode technique
SVHC. *See* Substance of very high concern
Swain, G. M., 71–72
Sweat, 598*t*
Switches
  all-optical, 471–473
  electrical, 473
  microwave, 482*f*
Switching
  absorption, 478*f*
  time, 464–465
  transmission, 482*f*
  transmittance, 472*f*
Synthetic nanoclays, 654–658, 661–664

T

Takahashi, K., 120
TCP coatings. *See* Trivalent chromium pretreatment coatings
TEM. *See* Transmission Electron Microscopy
Tetrakis(diethyl)-aminometal, 115, 115*t*
Thermal analysis
  overview of, 374–375
  of solid GCC, 375
Thermal spraying processes
  APS as, 45
  arc spraying as, 44–45
  detonation gun spraying as, 45
  EB-PVD processes compared with, 46*t*
  flame spraying as, 44
  HVOF as, 45
  overview of, 44–45
  techniques, 44
  VPS as, 45
  warm spray process as, 45
Thermochromic, 461, 466, 483
Thermodynamics, 2–3
Thermogravimetric test, 51
Thinning, 339–340
Threads length, 324*f*
304L stainless steel, 139–160
TiCN precursors, 114–115, 114*f*
Tinting, 339–340
TiO_2. *See* Titanium dioxide
Titania precursors
  overview of, 107–112
  sol-gel as, 108–109
Titanium, 115, 115*t*
  anodic oxidation, 590–591
  electrolytic deposition, 591–592
  laser oxidation, 590
  overview of, 585–587, 599
  protective films
    ceramic coatings, 595–596
    composites, 594
    HA, 594
    hybrid coatings, 594–595
    overview, 592–596
    oxides, 592–593

sol-gel method
dip-coating, 588–589
overview of, 587–589
spin-coating, 589
surface modification
anodic oxidation, 590–591
electrolytic deposition, 591–592
laser oxidation, 590
methods, 587, 592
overview, 587
sol-gel method, 587–589
Titanium alloys, 585–587, 598*f*
Titanium dioxide (TiO_2)
crystallographic forms of, 593*f*
nanocomposites, 571–573
Tjipto, E., 305
Toohey, K., 501, 502
TRACE criteria. *See* Transparent, Reversible, Applied, Commercially available, Environment criteria
Traditional coatings, 20
Transgranular stress corrosion cracking (transgranular SCC), 546
Transition temperature, 466
Transmission Electron Microscopy (TEM), 382
Transmission spectra, 626*f*
Transmission switching, 482*f*
Transmittance switching, 472*f*
Transparent, Reversible, Applied, Commercially available, Environment (TRACE) criteria, 642
Trivalent chromium pretreatment (TCP) coatings, 71–72
TSD. *See* Twin Shaft Disperser
Tuneable metamaterial devices, 474–476
Tungsten (W)
precursors, 112–114
VO_2 co-doping with, 466–467, 468*f*, 469–471, 472*t*
Turbine propellers, 349*f*
Turn-on corrosion detector, 27–28
Twin Shaft Disperser (TSD), 352–353
Type-I hot corrosion, 34, 37, 38*f*, 39*f*
Type-II hot corrosion, 34, 38*f*

U

Ultraviolet (UV) light exposure test, 402
Ultraviolet-induced chemical vapor deposition (UVCVD), 99, 99*f*
Under deposit corrosion. *See* Crevice corrosion
Uniform corrosion. *See* General corrosion
Union Carbide, 45
United States (U.S.), 63, 283–284
University of Illinois, 24
UV light exposure test. *See* Ultraviolet light exposure test
UVCVD. *See* Ultraviolet-induced chemical vapor deposition

V

Vacuum plasma spraying (VPS), 45
Vanadate coating, 26*f*
Vanadium dioxide (VO_2)
applications
all-optical switches, 471–473
electrical switches, 473
hybrid metamaterial devices, 473–476
overview, 471–483
plasmonic devices, 476–481
RF-microwave switches, 481–483
smart windows, 483
Au and, 476–477
Au-nanoparticles and, 478
crystalline structure of, 462*f*
electrical resistivity of, 470*f*
infrared transmittance during, 462*f*
microwave switch design based on, 482*f*
nanoparticle composite, 476–477
properties of, 461–471
atomic oxygen irradiation's effects on, 466
doping effects on, 466–471
phase transition, 464–465, 466–471
switching time, 464–465
synthesis methods, 463–464
pump-probe result summary, 472*t*
RF-microwave switches based on, 481–483
SMT of, 461, 462, 464–465, 469–470, 471–472, 473–474, 475, 477, 479–480, 481
sol-gel, 466
thin films, 478
valence band diagrams, 463*f*
Vibrational spectroscopic techniques. *See* Spectroscopic techniques
VisiMix, 348
Vitreous enamel
cross-section of, 253*f*
experiment
citric acid, 264*f*, 266*f*
coating resistance, 275*f*
color changes, 264*f*, 273*f*
conclusion, 280–281
cross-section, 270*f*, 274*f*
discussion, 259–280
emission spectra, 263*f*, 276*f*, 278*f*, 279*f*, 280*f*
excitation spectra, 263*f*

Vitreous enamel *(Continued)*
gloss change, 264*f*, 267*f*, 272*f*
immersion, 264*f*, 266*f*, 267*f*
main peak, 276*f*, 278*f*, 279*f*, 280*f*
materials, 256–259
overview, 280–281
potassium pyrophosphate immersion, 267*f*, 268*f*, 269*f*, 270*f*
procedures, 256–259
results, 259–280
roughness values, 265*f*, 268*f*
salt spray exposure, 271*f*
surface, 262*f*, 269*f*, 271*f*, 273*f*
trend of intensity, 276*f*
trend of luminescent properties, 275–280
trend of protective properties, 261–275
properties of, 252–255, 261–280
protection, 261–275
VO_2. *See* Vanadium dioxide
VO_2 plasmonic devices, 476–481
VO_2-based hybrid metamaterial devices, 473–476
VO_2-based RF-microwave switches, 481–483
Volume fractions, 667–668
VPS. *See* Vacuum plasma spraying

W

W. *See* Tungsten
Wackerbarth, H., 307
Walt, D. R., 631–632
Walther, M., 503–504
Wang, P., 421–422
Warm spray process, as thermal spraying process, 45
Water, 344, 384–387, 492*f*, 512*f*, 667–668
Waterborne nanocomposites coatings, 654–657
Waterborne PVDF-clay nanocomposites, 666–667
WAXD. *See* Wide angle X-ray diffraction
Wear analysis, 379
Weathered coated substrates, 651–654
Weathering, 389–396
Weathering studies, 644–647, 650, 651
Wei, Y., 562–563
Weight fraction of microcapsules, 516*f*
Weng, C., 423–424, 426–427
Wenzel equation, 420, 421*f*
Wet corrosion, 60
Wettability conversion, 427*f*
Wetting, 338
White, S. R., 493
Wide angle X-ray diffraction (WAXD), 660–661
Wilson, L., 70
W-Ti co-doped VO_2, 469–471

X

Xanthosoma sagittifolium leaves, 575–580
X-ray photoelectron spectroscopy (XPS), 205, 232–237, 371–374
X-ray scattering (SAXS), 660–661
Xu, G., 478
Xu, Q., 424, 426

Y

Yang, H., 503–504
Yang, J., 495
Yasui, K., 117
Yeh, J. M., 563, 564, 567, 569–573, 575
Young, W., 106
Young's equation, 419–420
Yttria precursors, CVD precursors as, 110–112
Yuan, L., 496
Yuan, S., 424

Z

Zhang, F., 422–423
Zhu, Y., 426
Zinc, 422*f*
Zinc-rich paints (ZRPs)
experiment
low carbon steel substrates, 203–205
materials, 199–200
methods, 201–205
nano-size particles, 199, 201–203, 205–216
nanotubes, 201–203
overview, 199–205, 239–243
paint coatings, 200, 203–205, 216–239
preparation, 199, 200
results, 205–243
steel substrates, 216–239
synthesis, 199–200
overview of, 196–198
Zirconia precursors
CVD precursors as, 110–112
overview of, 107–112
sol-gel as, 109–110
Zirconium, 115, 115*t*
ZrCN precursors, 114–115, 114*f*
ZRPs. *See* Zinc-rich paints